Faculty of Science
Department of Physical Chemistry



Palacký University
Olomouc

Mgr. Piotr Błoński, Ph.D.

Atomic clusters and graphene: many faces of nanomagnetism

Habilitation Thesis

Olomouc 2019

Contents

Acknowledgement 1

Preface **2**

1 Introduction **3**

1.1 A concise history of magnetism 3

1.2 Magnetic information storage 8

1.3 Magnetism in graphene 20

2 Theoretical methods **42**

2.1 Density Functional Theory 42

2.1.1 Exchange-correlation functional 44

2.1.2 Spin-polarized DFT: collinear and noncollinear magnetic ordering 46

2.2 Pseudopotentials and projector-augmented-waves method 47

2.3 Plane waves 52

3 Results **54**

3.1 Structures and MAEs of small free transition-metal clusters 54

3.1.1 Dimers 55

3.1.2 Pt_{3-6} 60
3.1.3 Ni_{3-6} and Pd_{3-6} 65
3.1.4 Pt–Co and Pt–Fe trimers and tetramers 71
3.2 Structures and MAEs of small transition-metal clusters supported on graphene 76
3.2.1 Pt_{1-5} on graphene 76
3.2.2 Bimetallic dimers on graphene 82
3.2.3 Pt–Co and Pt–Fe trimers and tetramers on graphene 86
3.3 Structures and MAEs of clusters of Pt_{1-4} on graphene on Ni(111) . 89
3.4 MAEs of transition-metal dimers on graphene on Cu(111) 96
3.5 Imprinting magnetism in graphene 99
3.5.1 Magnetism induced by doping graphene with foreign atoms . 100
3.5.2 Magnetism in nanographenes 102
3.5.3 Room-temperature G(OH)F magnets 105

4 Summary and outlook **109**

Biblography **111**

Appendix 1

Reprints of papers on structures and MAEs of TM clusters 131

Appendix 2

Reprints of papers on imprinting magnetism in graphene 283

Appendix 3

Reprint of a review paper on imprinting magnetism in graphene and 2D materials 337

Acknowledgement

I would like to thank Prof. Jürgen Hafner for being a great mentor and friend during the years I spent in Vienna. I am also grateful to Prof. Michal Otyepka, Prof. Radek Zbořil, and Assoc. prof. Jiři Tuček for their constant support, friendship atmosphere, and the top-notch scientific research. Last but not least, I thank Kasia and Pola who have been always supporting me.

Preface

The work presented here concerns theoretical aspects of magnetism in reduced dimensions including free and supported transition-metal clusters, and magnetism in graphene-based systems. In this thesis I summarize investigations in the field of nanomagnetism performed by me and my co-workers at the University of Vienna and at the Department of Physical Chemistry/RCPTM Palacký University Olomouc within last ten years.

The first part of this work provides the main ideas behind the work and a summary of the most important results. Next, the theoretical methods applied in my research are described. Finally, the theoretical results of 17 selected papers are more deeply discussed. The appendices contain reprints of these 17 papers included as a set of works in this habilitation thesis. All references to the works I co-author are highlighted throughout the text in bold.

Chapter 1

Introduction

1.1 A concise history of magnetism

The history of magnetism can be divided into seven ages coeval with the history of science [1], as schematically pictured in Figure 1.1.

The history of magnetism begins with a special type of the mineral magnetite, lodestone (also spelled loadstone) possessing distinctly north-south polarity. The oldest known reference to lodestone's properties dates back to 600 BC, when the Greek philosopher Thales of Miletus (c. 624 − c. 546 BC) noticed iron's attraction to it. Thales endeavoured to rationalise the phenomenon through animism,

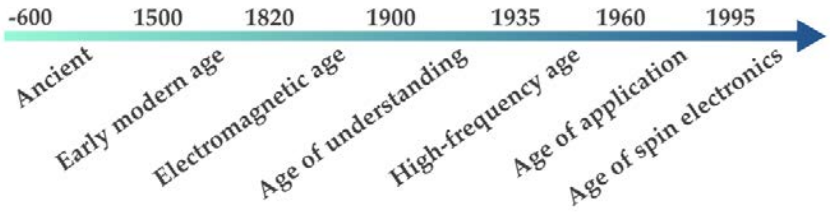


Figure 1.1: The seven ages of magnetism. Based on [1].

presuming that the lodestone possessed a soul.

Appearing in China around the 4th century BC, primitive compasses using the lodestone at first served to show the Chinese the way figuratively, helping them order and harmonize their environments and lives, as part of feng shui, an ancient Chinese practice that has evolved into a decorating trend. In time, people discovered that it can be used for navigation, too. The navigational compass was described by Shen Kua (1031 − 1095) around 1088 AC; reinvented in Europe a century later, effectively shaped the course of history.

The first truly scientific approach to the study of magnetism was taken by William Gilbert (24 May 1544 − 30 November 1603). In his monograph *De Magnete* (1600), he debunked earlier fantasy on this matter. Gilbert identified the Earth as source of the magnetic force which aligned the compass needle, rather than the stars as previously assumed. He deduced that the Earth itself was a great magnet. Around this time, René Descartes (31 March 1596 − 11 February 1650) finally laid to rest the Thales curious notion that the magnet possessed a soul. Nonetheless, magnetic research in the seventeenth and eighteenth centuries was mostly the domain of the military, particularly the British Navy, and an iconic civilian invention of that time was the horseshoe magnet.

Eighteenth century brought about the search for a relationship between electricity and magnetism. Luigi Galvani's (9 September 1737 − 4 December 1798) animal electricity, stemming from his experiments on frogs and corpses, inspired Anton Mesmer (23 May 1734 − 5 March 1815) to postulate a doctrine of animal magnetism, which was discredited in 1784 by commissioners appointed by Louis XVI. Their report was a milestone of scientific rationality. Alessandro Volta's (18 February 1745 − 5 March 1827) investigations on animal electricity led to the in-

vention of the first primitive battery, discovering that electricity can be generated through chemical processes.

Until Hans Christian Ørsted's (14 August 1777 − 9 March 1851) discovery on 21 April 1820 that an electrical current moves a compass needle, previous insights into the relationship between electricity and magnetism went largely unnoticed. The electromagnetic revolution was launched several weeks later by André-Marie Ampère (20 January 1775 − 10 June 1836) and François Arago (26 February 1786 − 2 October 1853) who wound wire into a coil and showed that the current-carrying coil was equivalent to a magnet.

In 1821 Michael Faraday (22 September 1791 − 25 August 1867) demonstrated the principle of the electric motor establishing the foundation of modern electromagnetic technology, and ten years later he discovered electromagnetic induction. In 1845 Faraday discovered that the plane of polarization of a plane-polarized light beam is rotated upon propagating through a media which is placed in a magnetic field parallel to the propagation direction. This experiment was among the firsts, which indicated the intimate relationship between the magnetic field and the light. In 1877 John Kerr (17 December 1824 − 15 August 1907) discovered of what is now called the magneto-optic Kerr effect (MOKE), i.e., the Faraday's counterpart effect in reflection. The MOKE is widely used to investigate the magnetization of materials.

In sixties of 19th century James Clerk Maxwell (13 June 1831 − 5 November 1879) unified theory of electricity, magnetism and light in the form of a set of the partial differential equations now known as Maxwell's equations. In their modern form of four partial differential equations, Maxwell's equations first appeared in his textbook *A Treatise on Electricity and Magnetism* in 1873. A remarkable con-

sequence of Maxwell's equations is the existence of a solution representing coupled oscillatory electric and magnetic fields propagating at the speed of light. It largely inspired Heinrich Rudolf Hertz's (22 February 1857 − 1 January 1894) discovery of radio transmission in 1888, which sprung techniques in television, radar and microwaves.

1824 brought about William Sturgeon's (22 May 1783 − 4 December 1850) invention of the iron-cored electromagnet. The world's first electric tram line was tested in 1880 in Sestroretsk near Saint Petersburg in Russia and soon after horses were displaced by electric trams. Beginning of 20th century brought about the households electrification.

Despite the amazing technical and intellectual triumphs of the electromagnetic revolution, ferromagnetism (FM) challenged the foundations of classical physics, and the question of how a solid could possibly be ferromagnetic remained vague. Pierre Weiss's (25 March 1865 − 24 October 1940) molecular field theory, dating from 1907 [2], successfully explained the phase transition at the Curie point above which ferromagnetic material reversibly loses its ferromagnetism. Nonetheless, magnetism, i.e., dia-, para-, as well as collective magnetism, presents a quantum mechanical effect which cannot be explained using classical mechanics and electrodynamics. This was first shown by Niels Bohr (7 October 1885 − 18 November 1962) in 1911 in his doctoral dissertation and later rediscovered by Hendrika Johanna van Leeuwen (3 July 1887 − 26 February 1974) in 1919 in her doctoral thesis; their results now refer to as a famous and often-quoted theorem of the Bohr and van Leeuwen.

Quantum mechanics and relativity, the two pillars of modern physics erected in the early years of the 20th century, made the present comprehension of mag-

netism possible. Today our understanding of magnetism is intimately related to the concept of spin, jointly proposed in 1925 by Samuel Goudsmit (11 July 1902 − 4 December 1978) and George Uhlenbeck (6 December 1900 − 31 October 1988), which arises from the relativistic description of an electron in an external electromagnetic field and becomes evince in the Dirac equation (1928) [3]. This concept results in the intrinsic spin magnetic moment and the orbital magnetic moment; the latter being due to the motion of electronic charges. Thus, atomic magnetic moments are associated with the electronic spins.

It was Werner Heisenberg (5 December 1901 − 1 February 1976) who showed [4] that the interaction between electrons, called the exchange energy, which is of electrostatic origin and is purely quantum mechanical in nature, is the basis of the Weiss molecular field. Modern theories of magnetism extensively use a Hamiltonian called the *Heisenberg exchange Hamiltonian* to investigate the magnetic properties of materials. The Hamiltonian was, however, not introduced by Heisenberg, but by Dirac in 1928. The interaction of two neighbouring atoms whose total electronic spins, in units of Planck's constant $\hbar = 1.055 \times 10^{-34}$ J s, are $\boldsymbol{S}_i$ and $\boldsymbol{S}_j$, is represented by $H = -2J\boldsymbol{S}_i \cdot \boldsymbol{S}_j$, where J is the exchange constant; J/k_B is typically in the range $1 - 100$ K. Here k_B is Boltzmann's constant, 1.3807×10^{-23} J K^{-1}. The Heisenberg Hamiltonian was not exclusively confined to the explanation of ferromagnetism. Louis Néel (22 November 1904 − 17 November 2000) in 1936 and 1948 pointed out that the exchange integral J could be negative and could thus give rise to an antiferromagnetic (AFM) or ferrimagnetic (FIM) ordering, depending on the topology of the crystal lattice. The concepts of superexchange, crystal field splitting, and domain structure and dynamics have their origin in the Heisenberg exchange mechanism.

Recent decades have witnessed an immense expansion of magnetic applications preceded by developments for the Second World War. Advances in the computer technologies, magnetic imaging, telecommunications, just to name a few, would not be possible without the forefront research areas in magnetism. Magnetic recording technology sustains the information revolution and the Internet. The discovery of the Giant Magnetoresistance (GMR) in 1988 [5] by Peter Grünberg (18 May 1939 − 7 April 2018) and Albert Fert (born 7 March 1938) awarded the 2007 Nobel Prize in Physics, allowed a tremendous enhancement of storage density. And also today technology is largely driven by the goal to develop devices which are smaller, faster, and cheaper than ever before.

The threshold to the seventh age, that of spin electronics, was in the 1980s from discoveries concerning spin-dependent electron transport phenomena in solid-state devices. Whereas electronic devices use the electrical charge of an electron to encode data, spintronic devices instead use the intrinsic angular momentum of the electron, its spin. The isolation of graphene [6] − a single layer of carbon atoms arranged in a hexagonal lattice − in 2004 by Andre Geim (born 21 October 1958) and Kostya Novoselov (born 23 August 1974) offers new vista to the design of novel devices tailored on the level of individual atomic spins, which functionality is engineered towards computing speed, storage capacity and energy saving. Andre Geim with Kostya Novoselov earned the Nobel Prize in Physics in 2010 for their isolation of graphene from graphite.

1.2 Magnetic information storage

Information storage technology has matured over last decades. An enormous progress made in the respect is pictured in Figure 1.2 showing storage of IBM



Figure 1.2: IBM record cards stored at the Federal records center in Alexandria, Virginia, (November 1959). A total of about 4.3 billion characters of data in this storage facility correspond to about the same as a 4GB flash drive. Image source: Wikimedia Commons.

record cards at the Federal records center in Alexandria, Virginia (November 1959). This storage facility held 4.3 billion characters of data, about the same as a 4GB flash drive.

Magnetic storage devices, both magnetic tapes and hard disc drives (HDDs), have been used as a crucial recording media since the birth of the information age in 1950s. The first commercial computer produced in the United States, The UNIVAC I (UNIVersal Automatic Computer I) used magnetic tape to record data (1951). Introduced by IBM in 1956 [7], HDDs became the dominant secondary storage device for general-purpose computers by the early 1960s, whereas magnetic tapes are predominantly used for backups. Over the past six decades, HDDs have come a long way, from the 1956's IBM random access method of accounting and control

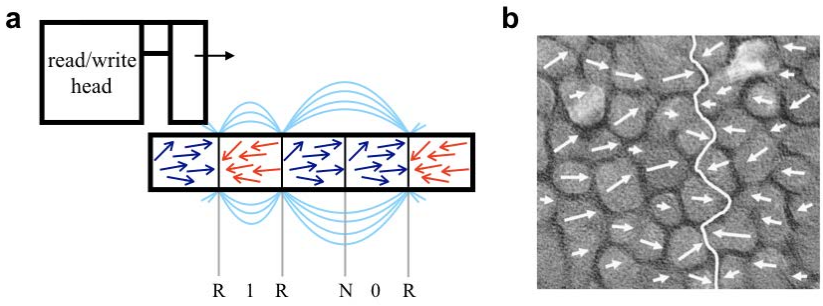


Figure 1.3: **a,** Illustration of the longitudinal magnetic recording, in which recorded magnetization lies in the plane of a layer of memory material. The domains are indicated by the regions where the magnetic moment arrows point in the same direction. A domain pointing left adjacent to one pointing right would represent a binary one, and the opposite pattern of right-left would represent a zero. Field reversal near boundary is indicated by R; N stand for no-reverse. **b,** Grains in a recording medium (Reprinted from [8]). The grains may have a random easy axis orientation as well as random grain sizes as depicted. Due to the randomness of the grains, a group of grains (creating a small magnetic domain) which have the same direction of magnetic moment stores information.

(RAMAC) 305 system being as large as two big refrigerators and using 50 24-inch platters to hold about 5MB of data at $10,000 a megabyte − about the storage that today is needed for one 5-minute MP3 encoded at 128 kilobits per second − until 2018's 12 TB HDD for around $400 enclosed in a small box of 4 in × 5.79 in (101.6 mm × 147 mm). Technologically, however, HDDs that are currently inside modern laptops are almost exactly the same as in the refrigerator-sized RAMAC system − only much smaller.

Regardless of whether it is a magnetic tape or disc, magnetic recording codes information onto a moving magnetic medium, as schematically shown in Figure 1.3. The information is coded into the current passing through a write head, acting as a tiny electromagnet. The stray field created by the write head switches the magne-

tization of the medium by overcoming the coercivity. Prior to the 1990's inductive heads were used both to write and to read the data. Since 1990's introduction of the anisotropic magnetoresistive (AMR) head by IBM, the recorded data has been read by a separate magnetoresistive (MR) sensor. Actually, it is the magnetization transitions between the recorded bits, where the stray field is greatest, that are detected. Essentially, MR material changes its resistance R in response to a magnetic field and, accordingly, modulates the current I passing through it (at fixed voltage) and thus acts as magnetic field to electrical current converter. Thus, an electrical current, either high or low representing binary one or zero, encode the information.

The recording medium is usually a thin film of metallic alloys of cobalt, platinum, and chromium composed of a dense assembly of very small, ideally single-domain grains. A single bit is recorded in the magnetization of N grains. A good signal-to-noise ratio (SNR) is achieved when the individual grains are magnetically decoupled, while SNR is approximately given by the expression $\mathrm{SNR} = 10 \log N$; if a value of 30 db is required, N has to be about 1000. SNR indicates on how reliably the bits could be read out and, therefore, on the recording performance of a recording medium. A way to increase the SNR of the recording medium is to reduce the grain size and grain size distribution, which would increase the number of grains in the bit area.

Prior to 2005, the longitudinal recording, in which the magnetizations that lie longitudinally (parallel) to the disk surface was used for storing information (Figure 1.3), dominated the magnetic recording technology. The past decade has seen a significant growth of digital information volume which, moreover, is projected to further expand to 40 Zettabytes till 2020. Besides, the gap between the amount

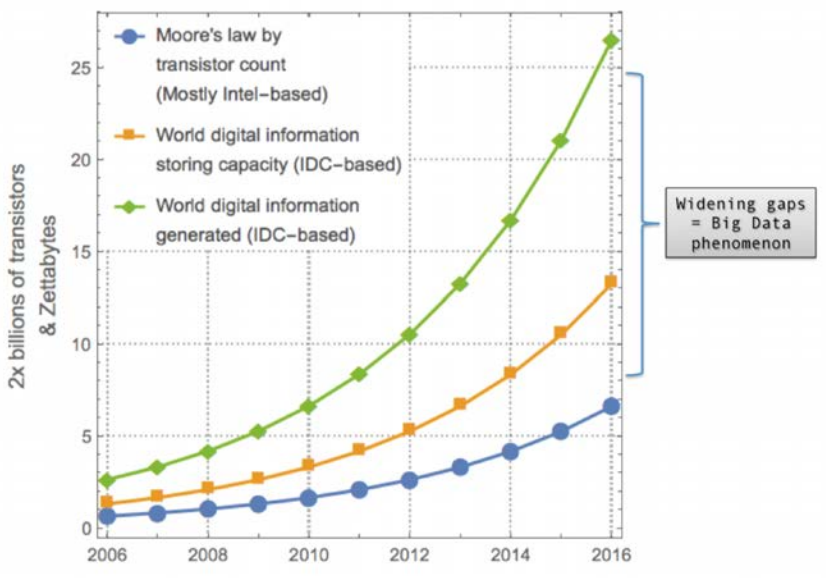


Figure 1.4: Widening the gap between digital information creation and digital data storage capacity due to the "Big Data" phenomenon. The plot shows that the gap will likely widen in the future. Reprinted from [9].

of digital information created and available digital storage will continue to widen over the next decade, as illustrated in Figure 1.4 [9] causing increasing demands for higher data storage densities. Clearly, reduction of the grain size can increase the storage capacity. Reduction of grain size below $\sim$10 nm, however, eventually leads to superparamagnetic effect, where the magnetic energy per grain becomes too small to avoid a thermally activated reversal of grain magnetization and the loss of information. Perpendicular recording getting away from the superparamagnetic limit faced by the longitudinal recording increased data storage capabilities from $\sim 100-200$ Gb in^{-2} up to $\sim$1 Tb in^{-2} [10] because it permits higher areal densities (AD = number of stored bits in^{-2}) of the magnetic records.

Unfortunately, the ongoing increase of the magnetic data storage capacity and miniaturization of the storage devices as we know it is coming to an end, unless

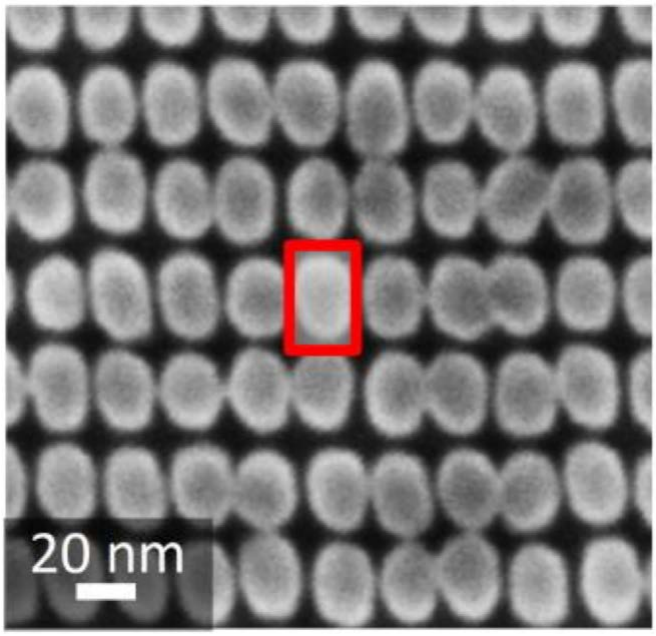


Figure 1.5: Bit patterned media. On conventional granular media, an individual bit is recorded on an ensemble of grains (Figure 1.3), while on BPM, each island stores a single bit (as indicated by the red outline). Reprinted from [11].

the superparamagnetic limit where spontaneous thermal fluctuations destroy the recorded information will be overcome by the design of novel nanocomposite materials with large intrinsic magnetic anisotropies. One solution to the problem of ultra-high-density recording is the use of a bit-patterned medium (BPM). Instead of recording a bit on an ensemble of random grains (Figure 1.3), BPM is comprised of a well-ordered array of lithographically patterned, isolated, and nanometre sized magnetic islands, each of which stores a single bit of information (Figure 1.5). BPM achieves higher SNR and thermal stability than conventional media grains. However, both mass fabrication of BPM and its integration into the recording system of HDDs is viewed as the greatest challenge for its commercialization.

A fundamental constraint for the minimal size of a bit for classical informa-

tion storage is imposed by the magnetic anisotropy energy (MAE) of the storage layer, i.e., the energy needed to orient the magnetization perpendicular to the easy-axis. The main criterion is that the energy difference between the easy and hard axes of magnetization representing a barrier for spin reorientations should exceed ambient temperatures. For practical applications, large MAEs of about $30 - 50$ meV/atom are necessary. The high bit density requires out-of-plane magnetic anisotropy to minimize dipolar interactions among adjacent magnetic moments. However, along with a reduction of magnetic bit dimensions to the atomic scale thermal stability influences the rate of magnetization switching and, moreover, quantum-mechanical excitations can start playing an important role. Thus, besides the technological challenges, the question of where downscaling of storage media ends from fundamental physics has motivated intense research efforts directed toward an improved understanding of the fundamental properties of magnetic nanostructures [12–15], **[16–20]**, [21, 22].

Magnetic anisotropy is a relativistic effect promoted by the spin-orbit coupling (SOC), which originates from the combined effect of the anisotropy in the atom's orbital angular momentum ($\boldsymbol{L}$), together with the interaction between $\boldsymbol{L}$ and the atom's spin angular momentum ($\boldsymbol{S}$). This interaction can be expressed by $H_{\mathrm{SOC}} = \xi\ \boldsymbol{L} \cdot \boldsymbol{S}$, where ξ is the atomic SOC parameter [23], **[24]**. According to Hund's rules, large spin and orbital magnetic moments are found among free transition metal (TM) atoms. However, in most magnetic compounds electron delocalization and crystal field effects compete with the intra-atomic Coulomb interactions, responsible for Hund's rules, triggering a decrease of $\boldsymbol{S}$ and quenching of $\boldsymbol{L}$ with implications for a value of MAE. Theoretical calculations, however, predict such effects to be diminished at surfaces and in low-symmetry nanostructures

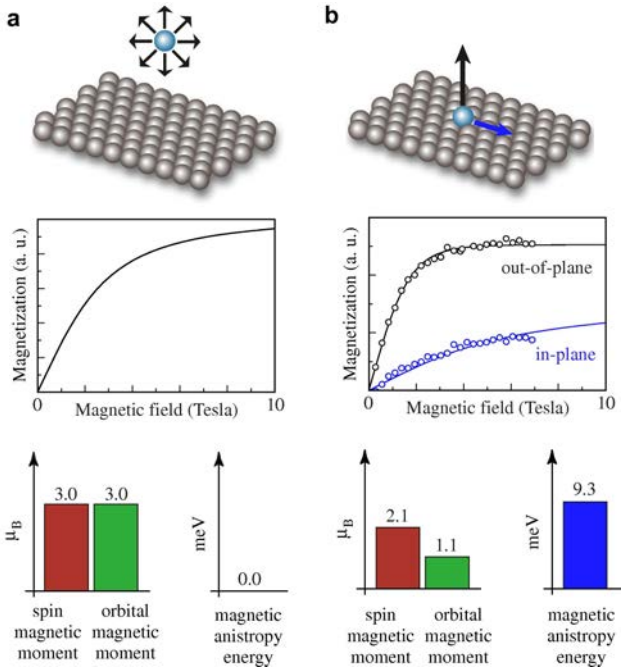


Figure 1.6: **a,** Spin and orbital magnetic moment of a gas phase Co atom (d^7 electronic configuration) according to the Hund's rules. **b,** Spin and orbital magnetic moment of an individual Co atom adsorbed on a Pt(111) surface [14]. Due to the spherical symmetry of the gas-phase atom the magnetization is isotropic, and MAE is zero. In **b,** symmetry breaking and Co-Pt coupling lead to a strong anisotropy of the magnetization measured by XMCD along the out-of-plane (black) and close to in-plane direction (blue). Reprinted from [15].

owing to the reduced coordination of TM atoms, which may also imply a substantial MAE **[16, 17, 19, 20, 24–30]**. This strategy, if specific conditions are met, could set the ultimate limit of classical data storage to a single-atom magnetic bit coordinated to a single substrate atom. Indeed, a giant MAE was found by Gambardella et al. [14] for Co atoms on a Pt(111) substrate (Figure 1.6). A high magnetic anisotropy energy requires large spin and orbital magnetic moments and a strong spin-orbit coupling. The Co atom provides the large magnetic moment,

but for Co, like for all 3d ferromagnets, the spin-orbit coupling is weak. Strong SOC is found in the heavy 5d metals such as Pt. Although, these metals are non-magnetic, significant magnetic moments can be induced in Rh, Pd, and Pt substrates in the presence of magnetic nanostructures **[16–18]**. Hence the giant MAE observed for Co/Pt(111) must have its origin in the strong coupling between the magnetic adatom and its ligands. Nanostructures of 3d metals supported on substrates of highly polarizable 5d metals may thus be a viable route to tune both the spin moments and the anisotropy energy.

Theoretical calculations for Co and Fe adatoms and ultrathin films on the (111) surfaces of Pd and Rh, and Fe adatoms on Pt(111) revealed, however, surprising results that the MAE strongly depends on the adsorption site. Moreover, due to strong quenching of the adatom orbital moments and the formation of large induced spin and orbital moments in the substrate, the latter substantially contributes to the MAE **[17, 18]**, [31].

Classical storage and spintronics devises' functionality particularly depends on long spin-relaxation times, T_1. Exchange-driven magnetic coupling of the adatom's spin to a conductive substrate may drastically limit T_1 time scale to the order of only hundreds of femtoseconds as revealed by inelastic scanning tunnelling spectroscopy (ISTS) on individual Fe atoms on a Cu(111) surface [32]. In contrast, a long spin-relaxation time in the nanosecond regime was derived from the ISTS experiment for Fe atoms adsorbed directly on a conductive Pt substrate [33], comparable to that of Fe atoms, which were decoupled from substrate conduction electron bath by thin insulating layers [34] and thus hampered electron-hole pair generation [35]. Astonishingly, magnetic remanence allowing for storing and processing information was measured by X-ray magnetic circular dichroism (XMCD)

on an ensemble of Ho atoms on ultrathin MgO(100) films grown on Ag(100), indicating a lifetime exceeding 1000 s [36]. Magnetic hysteresis up to 5.6 T and spin lifetime of 1000 s at 2.5 K was also measured for a self-assembled superlattice of noninteracting Dy atoms on graphene grown on Ir(111) [37]. More recently, Natterer et al., showed the reading and writing of the magnetic state of individual Ho atoms on MgO/Ag using a scanning tunnelling microscope (STM), and that that they retain their magnetic information over many hours (Figure 1.7) [21].

Another remarkable achievement in the field of atomic memory was by using the STM to manipulate individual chlorine atoms on the (111) crystal surface of copper to encode a series of 0s and 1s into a 8×8 array of rectangular blocks (Figure 1.8) [39]. Importantly, the chlorine lattice remained stable up to a relatively high temperature of 77 K. This re-writable atomic memory offers an areal density of 502 terabits per square inch.

Recently, the possibility of a single-atom memory originated from bistability of the orbital angular momentum (as opposite to the bistability of spin states) of an individual Co atom on semiconducting black phosphorus (BP) was demonstrated [40]. The employment of STM and ab initio calculations revealed distance-dependent-to-BP two distinct valencies of Co, each having a unique orbital population, total magnetic moment, and spatial charge density. Further, quantum chemistry calculations [41] suggested that the orbital degree of freedom may be much more robust against thermal fluctuations compared to using only the bistability of the spin ground states, and thus offering the potential for high-temperature single-atom information storage.

Last decade witnessed a tremendous progress in the field of information storage crowning with achieving the ultimate limit of writing and reading information into

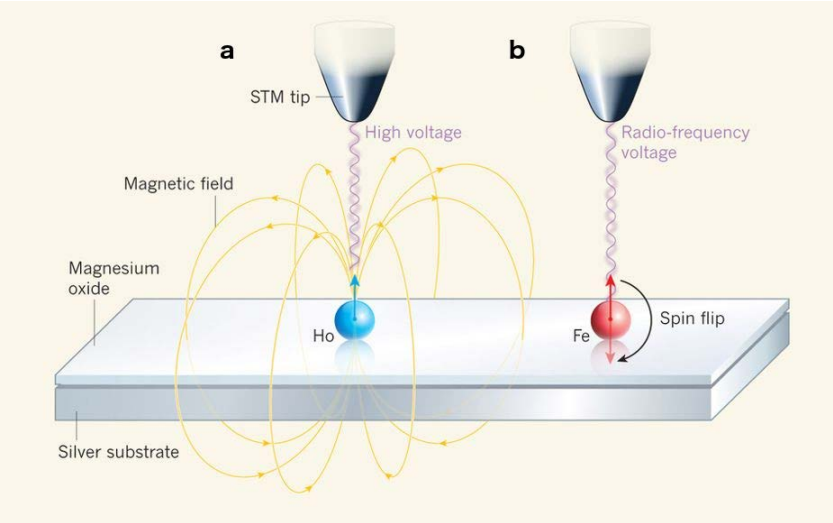


Figure 1.7: **a,** The writing and **b,** reading of the magnetic state of a single Ho atom in the vicinity of an iron (Fe) atom on a thin magnesium oxide film that decouples the two atoms from a silver substrate [21]. To write the atom's magnetic state, a high voltage (above 150 mV) was sent through the tip of a spin-polarized STM which caused the Ho atom's magnetic moment (blue arrow) to flip. The atom's magnetic state was read by measuring electrical conductance through the probed Fe atom. By applying a radio-frequency voltage from the microscope tip to the Fe atom, one can detect a change in conductance when the applied frequency matches the Larmor frequency of the Fe atom's spin. The Larmor frequency depends on the local magnetic field at the Fe site, and hence on the Ho atom's magnetic state. Reprinted from [38].

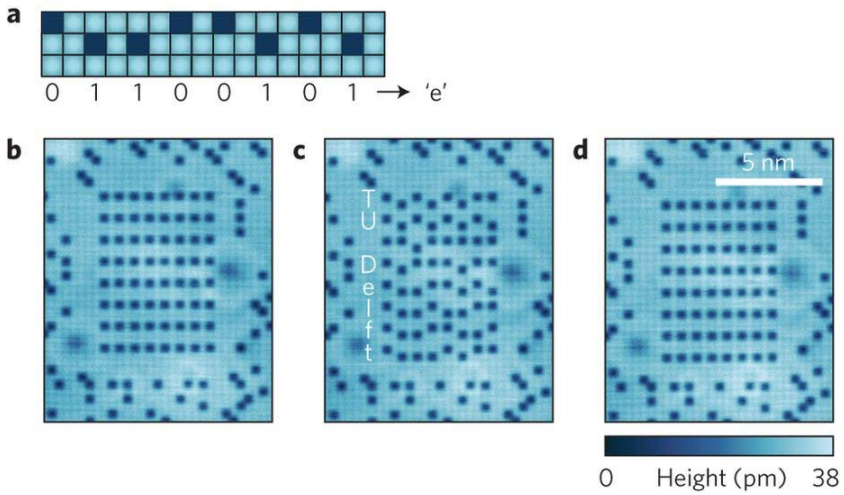


Figure 1.8: **a,** Encoding the smallest byte: The byte is set to represent the binary ASCII code for the character *e*. **b-d**, A 64-bit block, written as all 0*s* (**b**), a *TU Delft* text (**c**) and all 1*s* (**d**). Reprinted from [39].

a single-atom magnetic bit. Although, the storage and retrieval of magnetic information in a single atom is feasible, we are still far from having actual applications and, moreover several issues still need to be resolved. The methods involved are neither user-friendly nor affordable, and currently can be realized only in extreme conditions, such as in an ultrahigh vacuum and at very low temperatures.

Recent advances in ab initio simulations methods have imposed an increasingly important impact on solid-state physics and chemistry and on materials science, contributing to a deeper understanding of underlying phenomena and to materials design for future technologies [42]. Relativistic density functional calculations (RDFT) have been proved to provide an efficient tool to obtain both a thorough characterization of the potential magnetic-storage materials and a deeper understanding of the mechanisms determining the magnetic anisotropy on the electronic level in low-dimensional systems **[16–20, 24–30]**. Prominent examples include (*i*)

unveiling the important contribution to MAE from substrates hosting magnetic nanostructures **[17, 18, 27]**, (*ii*) for small TM clusters the role of the two-fold degenerate and a singly occupied state at the Fermi level (E_{F}) for achieving a large MAE **[24, 28, 29]**, and (*iii*) the prediction of an enormous MAE of 0.2 eV for heteronuclear IrCo dimers adsorbed on a graphene monolayer supported by a Cu(111) substrate **[29]**, which offers necessary barrier against loss of information even at room temperature. The MAE of bimetallic dimers stemmed from (*i*) combining a large spin moment contributed by the 3d Co atoms with a large orbital moment and strong SOC of the 5d Ir atom, (*ii*) favourable electronic structure in the vicinity of the Fermi level, i.e., SOC splitting of doubly degenerate electronic state which was occupied by only one electron at E_{F}, and (*iii*) the dimer's upright geometry with the Co atom located in a sixfold hollow of the graphene layer and the Ir atom preserving its free-atom-like characteristics. The graphene/Cu(111) supported bimetallic IrCo dimers may pave the way for high-temperature atomic-scale information storage.

Importantly, graphene intrinsically of diamagnetic nature can not only host magnetic nanostructures **[25,28,30]**, [37], but also can be equipped with magnetic properties without the presence of magnetic metallic elements, opening thus the doors towards applications in electronics, spintronics, biomedicine, and magnetic (bio)separations **[43]**.

1.3 Magnetism in graphene

Pioneering works on ferromagnetic compounds which are made up of non-metals only (i.e., C, O, H, N, and P) date back to the early 1990s. Such compounds, termed organic magnets, have unpaired p electrons and, hence, show characters

of an organic radical. The first example of an organic magnet (1991), however with FM properties only below 0.65 K, was p-nitrophenyl nitronyl nitroxide (p-NPNN) [44]. The discovery of fullerenes [45] and carbon nanotubes [46] has shifted the attention of the scientific community searching for magnetically ordered organic materials to carbon (nano)allotropes.

However, carbon, despite having two unpaired spins in the outer p-shell as an isolated atom, is diamagnetic due to the nature of bonds that are established between the carbon atoms leaving no unpaired electrons . Thus, the magnetism of carbon shows only a diamagnetic term, resulting from the motion of electrons on the orbitals, with a zero paramagnetic contribution. Pure carbon structures with mixed hybridization states (i.e., in which some of the valence electrons are not involved in a bonding process) may show unpaired spins and eventually magnetic ordering **[43]**.

Since 2004, when graphene was isolated [6], the realm of carbon has witnessed a striking attention from the scientific community to synthesize graphene and tune its unique physicochemical properties [47–50] and, moreover, equip it with features it misses, including magnetism **[43]**. Indeed, numerous theoretical works and several experimental studies confirmed successful imprinting magnetic features into graphene when defects were introduced into its lattice (see Figure 1.9) **[43]**, [51]. In short, the point defect effectively removes one p_z orbital from the graphene π cloud since once rehybridized the atom is unable to contribute its p_z orbital to the π-electron system. The point defects in the graphene bipartite lattice break the sublattice symmetry and give rise to zero-energy (mid-gap) states in the complementary sublattice, and, accordingly, to the total spin $S = |N_\alpha - N_\beta|/2$ guaranteed by a theorem by Lieb [52], where $N_\alpha - N_\beta$ is the difference between the number

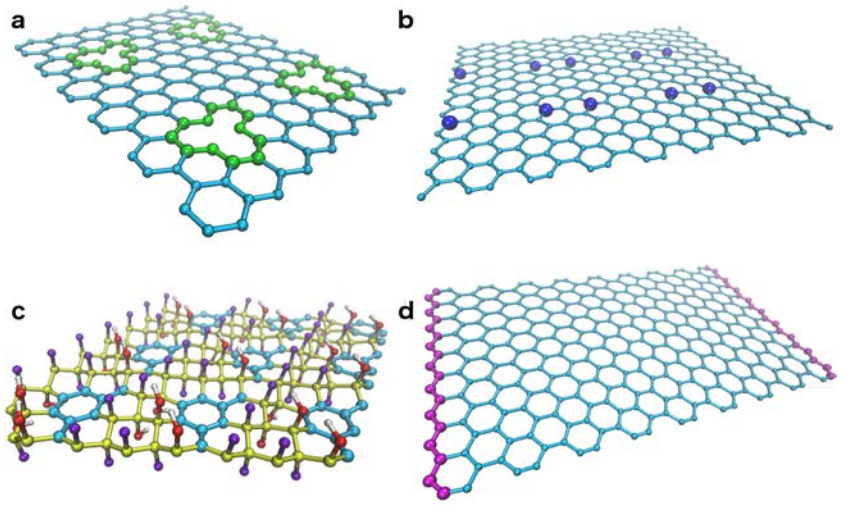


Figure 1.9: Defects in the graphene lattice: **a,** vacancies; **b,** substitution with non-carbon atoms; **c,** sp^3 functionalization; **d,** edges / spatial confinement. Reprinted from **[43]**.

of atoms in each sublattice, i.e., the sublattice imbalance. Both zero-energy states and spin densities around the defective site form characteristic $\sqrt{3} \times \sqrt{3}R30°$ superstructures with a ferromagnetic coupling between electron spins populating the quasi-localized states in the same sublattice and an antiferromagnetic coupling between different sublattices (Figure 1.10). The computed DOS plot for H-chemisorbed defect, Figure 1.10 (e), showed sharp peak close to E_{F} corresponding to the quasi-localized state induced by the defect. The peak was split by exchange giving rise to the overall magnetic moment of 1 μ_B. The removal of one carbon atom yielded a localized dangling-bond state which makes the major contribution (1 μ_B) to the intrinsic magnetic moment of the single-vacancy defect (1.1-1.5 μ_B).

Recent STM experiment matched the computed theoretical DOS with the differential conductance spectra, dI/dV, probing the energy-resolved local DOS under the STM tip position, providing thereby indirect evidence for the local magnetic moments' formation in H-defective graphene (Figure 1.11) [54]. This work further

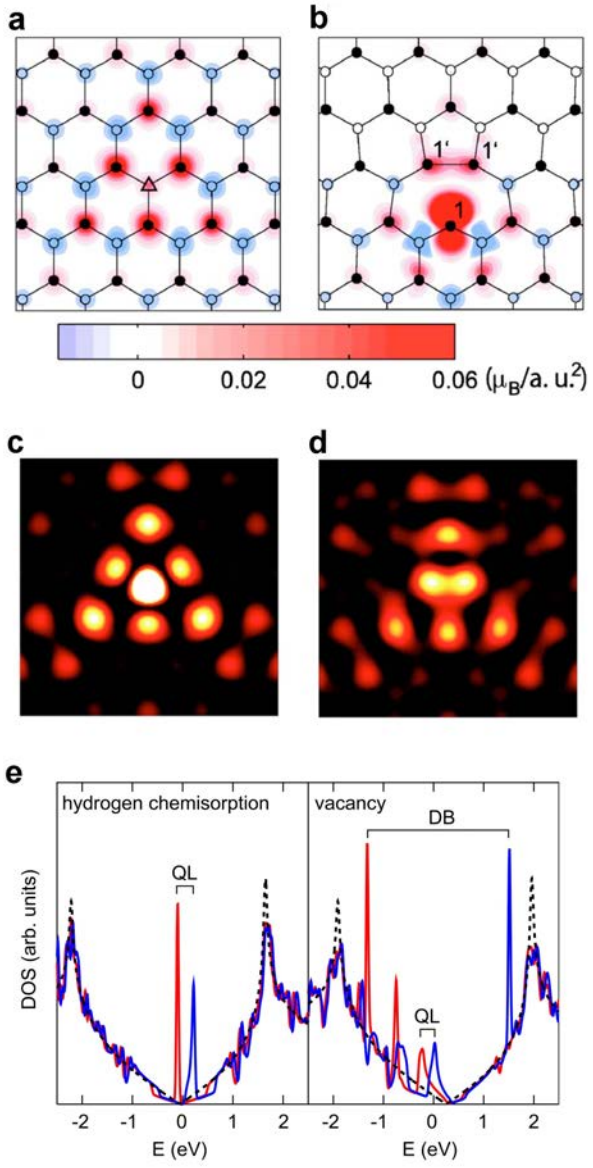


Figure 1.10: Theoretical spin-density distribution in the defective graphene sheet **a,** at the hydrogen chemisorption defect (marked by Δ) and **b,** the vacancy defect; α and β sublattices are distinguished by open and filled circles, respectively. Corresponding simulated STM images are shown in **c** and **d**, respectively. **e,** Spin-resolved density of states (DOS) for the vacancy and the hydrogen chemisorption defect showing exchange-split peaks corresponding to quasi-localized (QL) and dangling-bond (DB) states. Panels **a-d** are reprinted from [53]; panel **e** from [51].

confirmed that the zero-energy state is localized on the carbon sublattice opposite to the one where the hydrogen atom is chemisorbed, and it extends several nanometers away from the H atom driving the direct coupling between the magnetic moments at unusually long distances. One shall notice the perfect agreement between theoretical DFT predictions and experimental findings, which proved the predictive power of the theory. Further, the dI/dV spectra measured on the dimer chemisorbed on the same sublattice yielded the split state at E_{F}, as expected for a ferromagnetic coupling between the H atoms.

Importantly enough, DFT calculations showed that virtually any molecule attached to the graphene layer through a weakly polar single bond leads to the effect like that of H adsorption [55]. The spin moment of 1 μ_B was predicted for the graphene-adsorbate complexes, with the adsorption-induced spin polarization texture exhibiting remarkable similarities for various adsorbed groups (Figure 1.12). The magnetic moments align ferromagnetically on the same sublattice, while, in contrast, sp^3-functionalized opposite sublattices tend to couple antiferromagnetically. The band structure for graphene functionalized with adenine and methyl groups, indicated that the magnetization originated from a very narrow defect state pinned at E_{F}. Similarly, one spin-polarized peak appeared at E_{F} for several adsorbates chemisorbed on graphene through a single C–C bond, as indicated in Figure 1.12.

Indeed, DFT calculations predicted similar DOSs with spin-polarized mid-gap states pinned to E_{F} for carboxylated graphenes (G-COOH) [56], **[57]**. The theoretical thermodynamic stabilities of surface carboxylated graphenes indicated, however, that most of the local COOH arrangements will be thermodynamically accessible with a small energy difference between them **[57]**. This implied that the

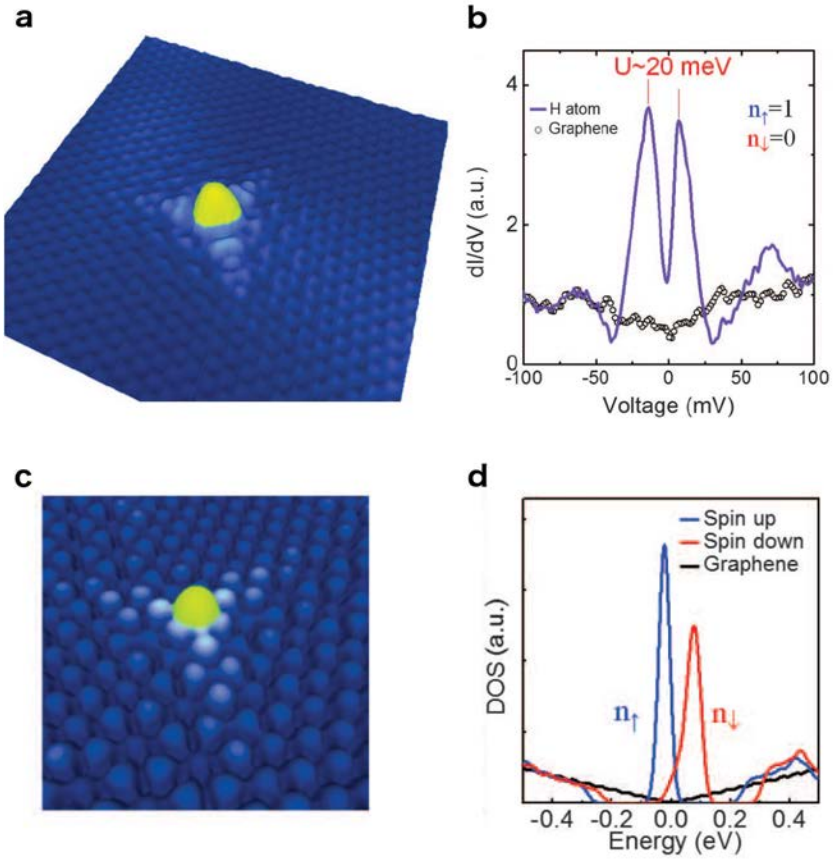


Figure 1.11: **a,** STM topography of a single H atom chemisorbed on graphene. **b,** dI/dV spectrum measured on the H atom and showing a fully polarized peak at E_{F}, and measured on bare graphene far from the H atom. **c,** DFT-simulated STM image and **d,** DOS of an H atom chemisorbed on graphene. Adapted from [54].

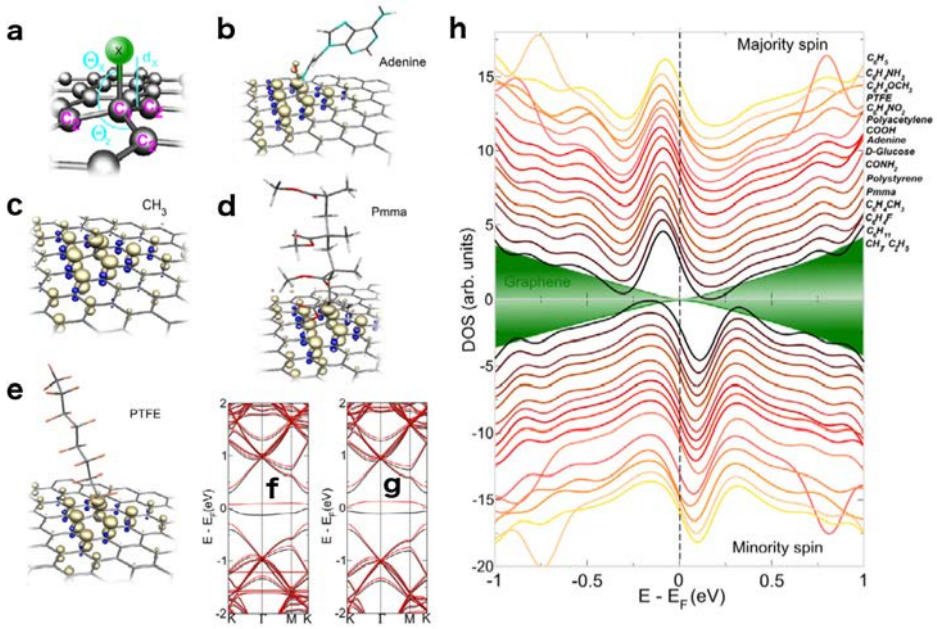


Figure 1.12: **a,** Adsorption geometry. **b-e,** Isosurfaces of the magnetization density induced on graphene by functionalization using the adenine derivatives. **f,** Spin-polarized band structures for graphene with a single adenine derivative and **g,** a CH_3 molecule chemisorbed on top of one carbon atom. **h,** Spin-polarized DOS for single molecules chemisorbed on a graphene supercell. The shaded regions indicate the DOS of pristine graphene. Adapted from [55].

topology of the carboxyl groups on the graphene surface will be given by a statistical distribution. A statistical (or random) distribution of the functional groups across the surface would prevent the formation of ferromagnetic order. Therefore, experimental verification of the emergence of magnetic order in G-COOH is highly vital.

Hydrogenation of graphene was found to be reversible [58], offering the flexibility to manipulate the coverage and to tailor its properties. It can be achieved by several techniques such as exposing graphene to hydrogen plasma, e-beam ir-

radiation, or Birch reduction of graphite oxide. The fully hydrogenated graphene derivative (termed graphane) is a non-magnetic wide-gap semiconductor. However, a H-vacancy defect in the graphane lattice led to the formation of a localized state with an unpaired spin and, accordingly, the formation of a defect level in the energy gap [59]. Further, a single-side hydrogenated graphene with H-vacancies distributed on the neighbouring carbon atoms belonging to the same graphene sublattice (termed graphone) was theoretically predicted [60] to exhibit ferromagnetic order with an estimated Curie temperature between 278 and 417 K. The induced magnetic moments localize on the unhydrogenated atoms, while the hydrogenated C atoms and H atoms carry very small magnetic moments, which is due to the strong σ bonds formed between carbon and hydrogen atoms that brakes the π-bonding network and leaves the electrons in the unhydrogenated C atoms localized and unpaired. The long-range magnetic coupling in graphone can be attributed to the large spatial extension of the valence electrons in p-states.

Fluorographene (FG), a two-dimensional (2D) stoichiometric graphene derivative is one of the thinnest insulators with a wide electronic band gap ($3.0 - 4.2$ eV) [61–63]. Theoretical calculations based on DFT anticipated that localized spin density can develop in fluorographene and can be controlled by the degree of F coverage [64]. Fluorination was experimentally confirmed to be an effective route to generate noticeable spin-half paramagnetic centres in graphene [65]. However, possibly due to the adatom clustering, the measured number of paramagnetic centres was three orders of magnitude less than the number of F adatoms in the samples and no magnetic ordering was detected at that time. Thus, the cluster edges were proposed as the only source of magnetic moments determining the nature of magnetic response. Moreover, the number of spins (N) was found to increase

monotonically with an increase in the degree of fluorination (i.e., C_1F_x, $0 \leq x \leq 1$) up to $x = 0.9$. A complete fluorination showed, in turn, a decrease in the value of N.

More recent experimental-theoretical work [66] proved that monoatomic chains of fluorine atoms on graphene led to strong magnetism in these organic graphene-based systems (see Figure 1.13). The lattice sites occupied by F atoms became inaccessible to the π-electron system. Thus, the fluorine chains acted as high-energy barriers (or a "nanoridge") for the graphene π-electron cloud. A set of localized spin states in the α-sublattice on one side of the nanoridge and the β-sublattice on the other side were created and magnetic susceptibility data yielded behaviour typical of a quantum spin-ladder system with FM legs and AFM rungs (Figure 1.13), in analogy to the exchange couplings between the zigzag edge-inherited states in graphene nanoribbons. The exchange coupling constant along the rungs was measured to be 450 K, which let consider graphene with fluorine nanoridges as a candidate for a room temperature spintronic material [66].

Fluorine atoms were also reported to form monoatomic stripes running along crystallographic directions on graphene and separated by non-fluorinated sp^2 carbon ribbons – an arrangement closely resembling that of a so-called tabby pattern [67]. As a result of tabby stripes, sp^2-sp^3 interfaces were observed to evolve with spin-polarized edge states localized on both sides of fluorine chains. Further, fluorine patterns reduced the effective dimensionality to 1D. For C_2F_x with $x < 1$, a behaviour typical for low-dimensional quantum spin ladder systems was observed, with FM ordering along the zigzag edges and AFM coupling between the opposite zigzag edges, and a thermally activated spin gap at about 450 K. Room temperature ferromagnetism found for C_2F_x with $x < 1$ was interpreted as a consequence

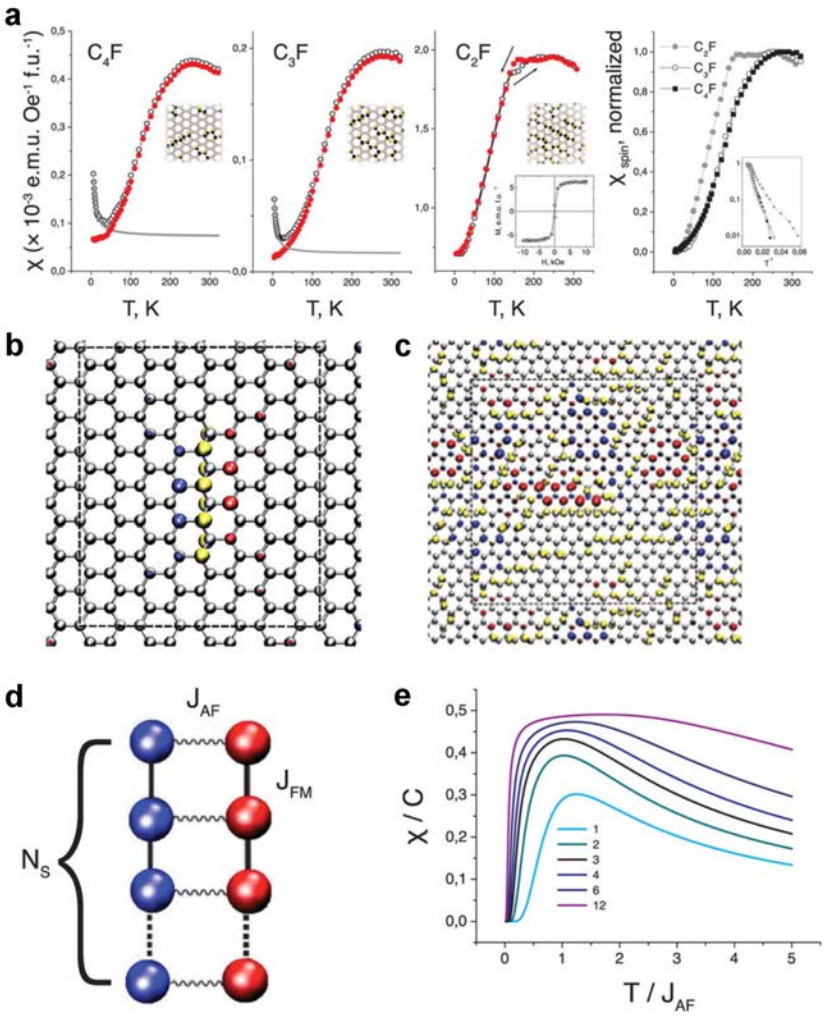


Figure 1.13: **a,** Raw data of magnetic susceptibility of the C_nF samples; C_4F and C_3F were measured at a magnetic field of 100 Oe upon being heating after zero-field cooling (open circles); the same curves with the Curie contribution (grey) subtracted are represented by red circles. C_2F was measured upon heating (filled circles) and upon cooling (open circles); inset: room-temperature hysteresis loop. Right panel: normalized spin susceptibilities; inset: spin susceptibility vs. reciprocal temperature. **b,** A zigzag chain of F atoms (yellow spheres) on graphene with opposite spins shown in red and blue. **c,** Spin densities for random fluorine chains. **d,** A spin ladder with a FM intra-leg interaction (J_{FM}) and an AFM inter-leg coupling (J_{AF}). **e,** Magnetic susceptibility (χ) for the finite size spin ladder vs. the reduced temperature. Reprinted from [66].

of a dimensional crossover due to the onset of interlayer interactions after ageing or annealing. In turn, C_2F_x with $x = 1$ exhibited a behaviour characteristic of the 2D magnetism without any signs of magnetic ordering at high temperatures; a transition to a superparamagnetic regime at 40 K was instead observed. The results demonstrated that a magnetic dimensional crossover in graphene-based systems can be induced upon changes in the fluorine content and interlayer distance.

The chemistry of FG has been recently used to develop 2D-systems, hydroxyl-substituted FG, termed hydroxofluorographene, GOHF. Depending on the F/OH ratio, hydroxofluorographenes exhibited room temperature antiferromagnetic **[68]** (Figure 1.14) or ferromagnetic **[69]** ordering (Figure 1.15). The room temperature magnetism stems from a sophisticated organization of sp^2-conjugated motifs inside an otherwise sp^3-bonded lattice and superexchange interactions via −OH functionalization **[68]** or combined contributions of itinerant π-electrons and superexchange interactions **[69]**. This new development in organic room-temperature magnetism in 2D systems pave the way to the future organic spintronic applications.

Importantly, –OH groups were also shown [70] to induce magnetic moments with high magnitudes (as high as 217 μ_B per 1000 –OH groups) on the graphene basal plane. Depending on the concentration of –OH groups (from 3 to 10 atomic percent, at%, of OH coverage) after annealing of graphene oxide at different temperatures (removing epoxy groups), the saturation magnetization was found to vary from 0.91 to 2.41 emu g^{-1}. Further, –OH groups showed high stability sustaining even at 900 °C. Thus, –OH groups were suggested as ideal sp^3-type candidates to equip graphene with robust magnetic moments [70].

It was also found that an increased level of hydroxyl groups significantly increased the local spin density up to a value of 5.17 μ_B per 1000 carbon atoms.

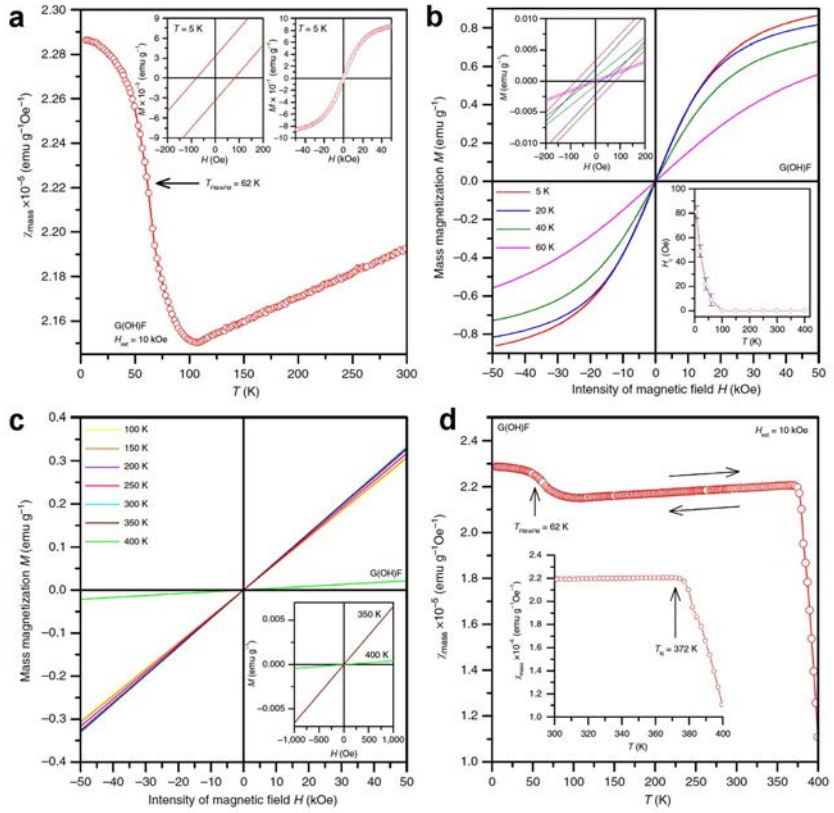


Figure 1.14: **a,** Temperature evolution of the mass magnetic susceptibility (χ_{mass}) of G(OH)F, measured under an external magnetic field of 10 kOe. The insets indicate non-zero coercivity and a saturation magnetization of ca. 1 emu g^{-1}. **b,** Isothermal magnetization curves of G(OH)F at temperatures of 5–60 K. The insets show the profile of the hysteresis loops around the origin and the temperature dependence of coercivity. **c,** Isothermal magnetization curves of G(OH)F, recorded from 100 to 400 K. The inset shows the profile of the isothermal magnetization curves at 350 and 400 K, demonstrating a transition from an AFM state to a paramagnetic state above 350 K. **d,** Temperature evolution of χ_{mass} of G(OH)F, measured under an external magnetic field of 10 kOe. The arrows show the reversibility of the measured profile on warming the sample from 5 to 400 K and then cooling from 400 to 5 K. The inset shows sudden drop of χ_{mass} above 370 K, which is indicative of a transition from an AFM state to the paramagnetic one with a Néel transition temperature of about 372 K. Reprinted from **[68]**.

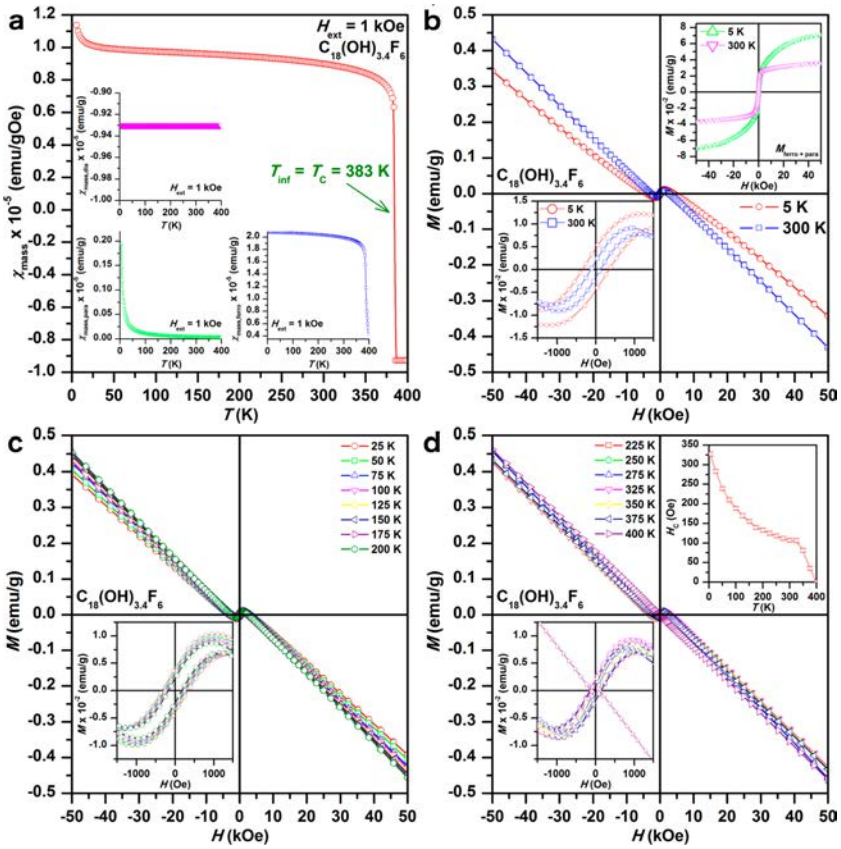


Figure 1.15: **a,** Temperature evolution of χ_{mass} of the $C_{18}(OH)_{3.4}F_6$ sample under a magnetic field of 1 kOe. Profile of the diamagnetic ($\chi_{\text{mass,dia}}$), paramagnetic ($\chi_{\text{mass,para}}$), and ferromagnetic ($\chi_{\text{mass,ferro}}$) contributions to the total χ_{mass} are shown in the insets. T_{inf} and T_{C} indicates the temperature of the inflection point and Curie temperature, respectively, and thus transition from FM to paramagnetic regime. **b,** Hysteresis loops (M vs. H curves) of $C_{18}(OH)_{3.4}F_6$ at 5 and 300 K. The lower inset provides evidence for nonzero values of the coercivity and remanent magnetization. The upper inset displays hysteresis loops after subtraction of the diamagnetic part. **c,** Hysteresis loops of $C_{18}(OH)_{3.4}F_6$ at 25 and 200 K. The inset shows the isothermal magnetization curves around the origin. **d,** Hysteresis loops of $C_{18}(OH)_{3.4}F_6$ at temperatures from 225 and 400 K. The isothermal magnetization curves around the origin is shown in the lower inset. The upper inset displays the temperature dependence of the coercivity derived from the respective hysteresis loops. Reprinted from **[69]**.

Specifically, converting epoxy groups to hydroxyl groups, combined with the Ar annealing method, increased the magnetization of graphene oxide from 0.136 to 3.11 emu g^{-1}.

Recently, room-temperature ferromagnetism was detected in reduced graphene oxide (RGO) doped with nitrogen prepared by direct reduction of graphene oxide in N_2 plasma at room temperature. The FM behaviour was attributed to pyrrolic nitrogen bonding configurations [71]. Reference [72] reports increased magnetization for RGO with increased doping with nitrogen. However, no clear scenario explaining an increase in the magnetization with increasing nitrogen content was suggested due to a complex interplay between pyridinic, pyrrolic, and graphitic nitrogen.

Doping of graphene lattice with noncarbon atoms, such as nitrogen and boron, has been theoretically shown to lead to n-type and p-type doping in the case of N- and B-doped graphene, respectively [73]. The Dirac point of graphene was downshifted in N-doped graphene and upshifted in B-doped graphene with respect to E_F, causing a semi-metal-to-metal transition in doped graphene. Moreover, if π-electrons occupy narrow bands at E_F of graphene, Stoner magnetism can emerge [74].

Indeed, it has been theoretically anticipated and experimentally confirmed that depending on the concentration and packing geometry of doping sulfur **[75]** and nitrogen **[76]** atoms, it is possible to induce FM order in graphene. Transition temperatures to the FM state were found similar in both systems, 62 and 69 K, respectively, for S- and N-doped graphene (see Figure 1.16), with graphitic dopants playing the key magnetic role, albeit significant amount of pyridinic and chemisorbed nitrogen was identified in N-doped graphene samples. Pyrrolic N was

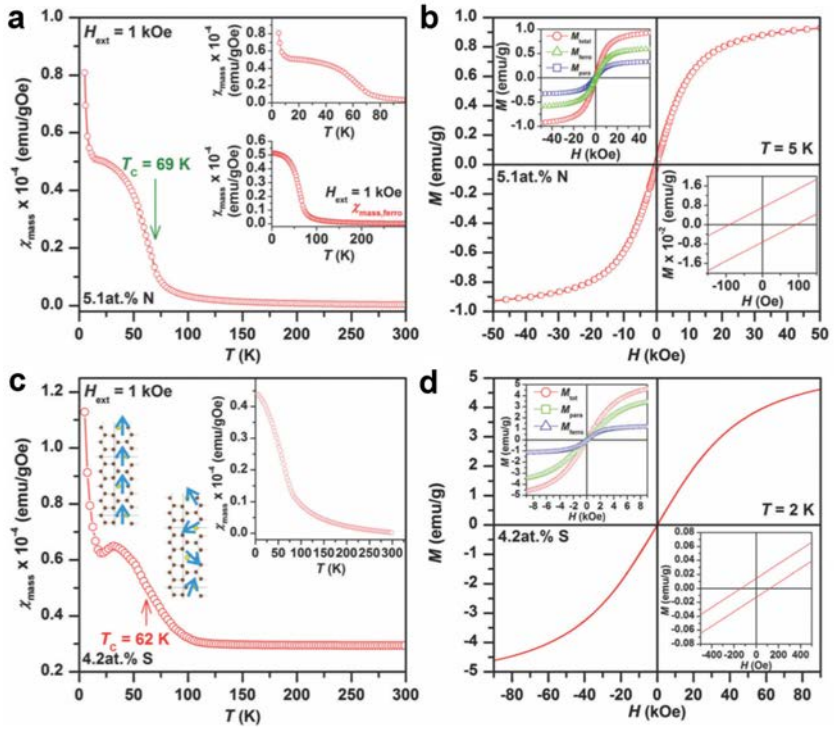


Figure 1.16: Temperature evolution of the mass magnetic susceptibility, χ_{mass}, for **a,** N and **c,** S-doped graphene at 5.1 at% (N) and 4.2 at% (S) recorded under an external magnetic field of 1 kOe with the Curie temperature, T_{C}, indicated. Insets display the ferromagnetic contributions derived from fitting of the χ_{mass} vs. T curve. For N-doped graphene, the trend of χ_{mass} at low temperatures is also shown in the inset. Hysteresis loops of **b,** N and **d,** S-doped graphene. The insets demonstrate the behaviour of the hysteresis loop around the origin with nonzero coercivity and field-dependent profiles of magnetization for the ferromagnetic, M_{ferro}, and paramagnetic, M_{para}, component. Panels **a** and **b** reprinted from **[76]**. Panels **c** and **d** reprinted from **[75]**.

not spotted in N-doped graphene, which has previously been shown to trigger a decrease in magnetization values [77]. In turn, pyrrolic nitrogen at a concentration of 6.02 at% enhanced ferromagnetism in graphene oxide [78]. A high oxygen content is, however, regarded as a dominant source of magnetism, overwhelming the effects of nitrogen doping itself, and, moreover, oxygen-containing functional groups severely reduce the electric conductivity of graphene – the main requirement for spintronics. Below 5 at% of N and 4 at% of S, graphene acted dominantly as a diamagnet; although paramagnetic centres were imprinted upon doping, they did not lead to magnetically ordered configurations. Once the doping concentration increased above these threshold values, FM states evolved when the doping-induced paramagnetic centres coupled via a π-electron system, as elucidated by theoretical calculations **[75, 76]**. Both S- and N-doping of graphene offer viable magnetic conductive materials with a huge potential in spintronic and other magnetic applications **[43]**.

Confining graphite spatially is another strategy to imprint magnetic features into carbon nanoallotropes. In fact, this approach was proposed before the first isolation of graphene (Ref. **[43]** and references therein). Graphene nanoribbons (GNRs), graphene nanoflakes and carbon quantum dots are currently regarded as prototypical examples of such carbon-based spatially confined nanostructures. Two types of edges can be formed, i.e., a zigzag or an armchair edge (Figure 1.17) [79], upon cutting a sheet of graphene into two pieces, thereby modifying its electronic band structure. The resulting edges can be terminated by hydrogen or any foreign atom to saturate σ-dangling bonds and thus enhancing the stabilization of the edges. The zigzag edge involves sites only from one graphene sublattice while both sublattices are paired along the armchair edge. Zigzag edges exhibit nonbonding

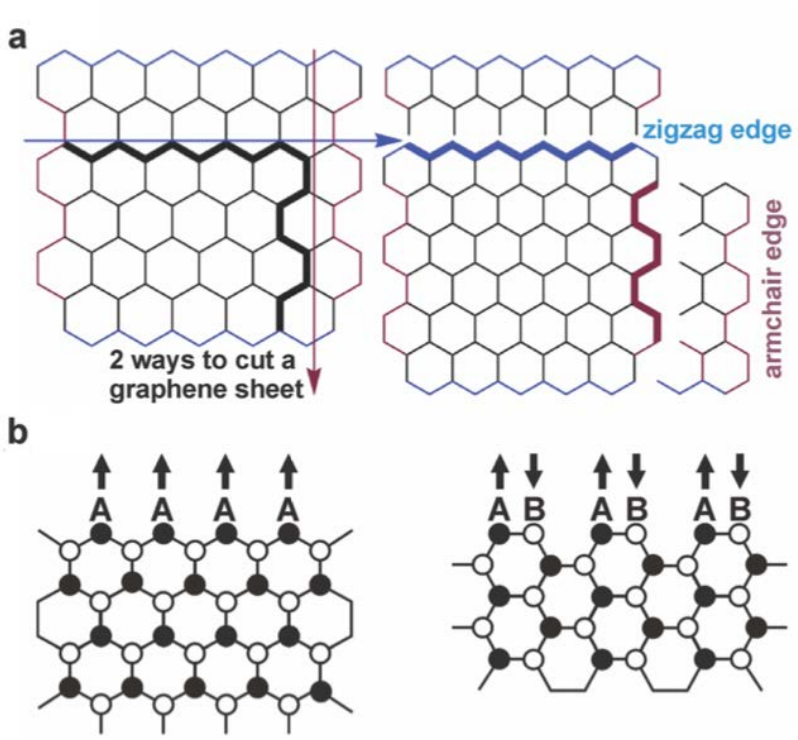


Figure 1.17: **a,** Two types of edges formed upon cutting a graphene sheet, i.e., a zigzag or an armchair edge. **b,** Zigzag and armchair edges with the A- and B-sublattice indicated. Arrows denote the pseudospins. Reprinted from **[43]** and [79].

π-electron states with an energy level appearing at the contact point of the π- and $\pi*$-bands; the occurrence of such states was documented in several experimental studies [80–82]. These states are not observed in the armchair edges. The zigzag edge states emerge due to the broken symmetry of the pseudospins. The unpaired electrons (with $S = 1/2$) in the non-bonding p-orbital of the zigzag edge are localized, thereby forming a strongly spin-polarized region. Thus, the finite-sized graphene is magnetic.

An arbitrarily-shaped sheet of nanographene having both armchair and zigzag edges is supposed to exhibit ferrimagnetic structure (Figure 1.18). Two interaction

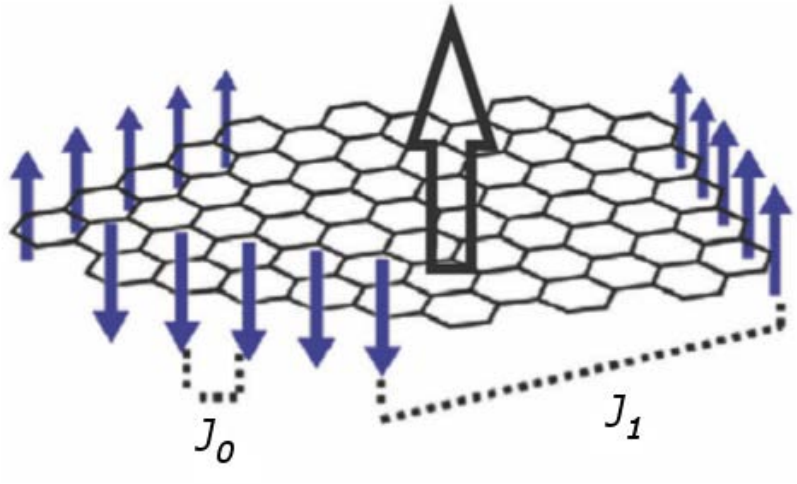


Figure 1.18: Schematic representation of an arbitrarily-shaped nanographene sheet showing the spatial distribution of edge-state spins (represented by blue filled arrows). J_0 and J_1 represent the intra-edge and inter-edge exchange interactions, respectively. The open arrow represents the net magnetic moment. Reprinted from [79].

pathways between edge-state spins in nanographene are present: (*i*) intra-edge interaction between spins on the same edge and (*ii*) inter-edge interaction between spins on opposite edges [79]. While the former exchange interaction is strong and is of FM character ($J_0 = 103$ K), the latter interaction is moderate ($J_1 = 10 - 100$ K) and can be of either FM or AFM nature depending on the geometry between the two zigzag edges. The competition between the intra-edge FM interaction and inter-edge FM/AFM interaction, the strength of which is affected by the specific geometry of the nanographene sheet, is then expected to stabilize the FIM structure with a nonzero net magnetization.

The edge-magnetism can be tuned by a chemical modification of the edges **[43]**, [79]. In particular, if the edges are fluorinated, spins located at zigzag edges are reduced. In turn, if the zigzag edge on one side of the nanographene ribbon is

dihydrogenated whereas the zigzag edge on the opposite side of the nanographene ribbon is monohydrogenated, a localized non-bonding state is supposed to appear around E_F; further, all the carbon atoms are spin-polarized even in the interior of the nanographene ribbon. If one zigzag edge is oxidized while the other zigzag edge is monohydrogenated, the side with the monohydrogenated edge is magnetic while the side with oxidized edge forms an electron conduction pathway.

Graphene nanoribbons (GNRs) are often adopted as a theoretical model system to describe and understand the role of edge and finite-size effects on the physical properties of graphene [83,84]. They also serve as a prototypical example to study the role of defects in the evolution of magnetic ordering in graphene (Ref. **[43]** and references cited therein). Armchair GNRs are non-magnetic but their zigzag counterparts show spin-polarized edge states. The electronic structure of zigzag GNRs (and, thus, bandgap and their magnetism) are believed to strongly depend on the level of quantum confinement in the width dimension and nature of intra-edge and inter-edge exchange interactions (i.e., π-conduction electron-mediated indirect interactions and direct/superexchange interactions) [85]. Following theoretical predictions, intra-edge interaction is of FM nature, whereas FM or AFM alignment is expected to evolve between opposite zigzag edges depending on the width of GNRs. Further, the change in the magnetic ordering, FM/AFM, between opposite edges is accompanied by oscillation in the conduction character of GNR between metallic- (in the FM regime) and semi-conducting fashion (in the AFM state) [86]. Many theoretical studies on the magnetic properties of GNRs have indicated that line defects [87], doping with extra carriers [88], interaction with a substrate magnetic field [89], and different saturation of opposite edges with hydrogens [90] can also influence the final magnetic properties. Therefore, interpretation

of experimental observations of edge magnetism in GNRs may be difficult, i.e., experimentally prepared GNRs may include many intrinsic defects, edge states, and also d-block-element impurities.

Graphene nanoflakes (GNFs), alternatively termed as graphene nanodisks, nanoplatelets or nanoislands, are arbitrarily shaped graphene fragments, which are finite in both dimensions (∼1 to ∼50 nm in size); they are sometimes classified as quasi 0D carbon nanostructures of sp^2 character. The regularly shaped GNFs resemble the appearance of regular convex polygons such as triangles, squares, rectangles, parallelograms, pentagons, and hexagons. The sides of GNFs consist of purely armchair or zigzag edges or their combinations. The magnetic features of GNFs are mainly predicted by theoretical studies with very rare confirmations from experimental measurements (see Ref. **[43]** for overview). Very recently, however, magnetically ordered GNFs with diverse morphologies, including nanoribbons and triangular, pentagonal, hexagonal and other polyhedral shapes, were prepared and characterized **[91]**. This material enters the ferromagnetic regime at a temperature of ∼37 K with magnetization approaching ∼0.45 emu/g under high external magnetic fields (Figure 1.19). Theoretical calculations explained that the magnetism of GNPs emerges from synergistic effects of the size, geometry of nanographenes, edge terminations, and angle between adjacent edges. In addition, they suggested a new way for preparing magnetically ordered nanoplateles with higher transition temperature. In this respect, triangular motifs with zigzag edges and reduced size to a maximum of around 3.7 × 3.7 × 3.7 nm can remain magnetically ordered up to 107 K. Based on these challenging results, further tuning of the size and morphology in spatially confined nanographenes combined with doping and sp^3 functionalization would enable preparation of magnetically ordered half-metallic

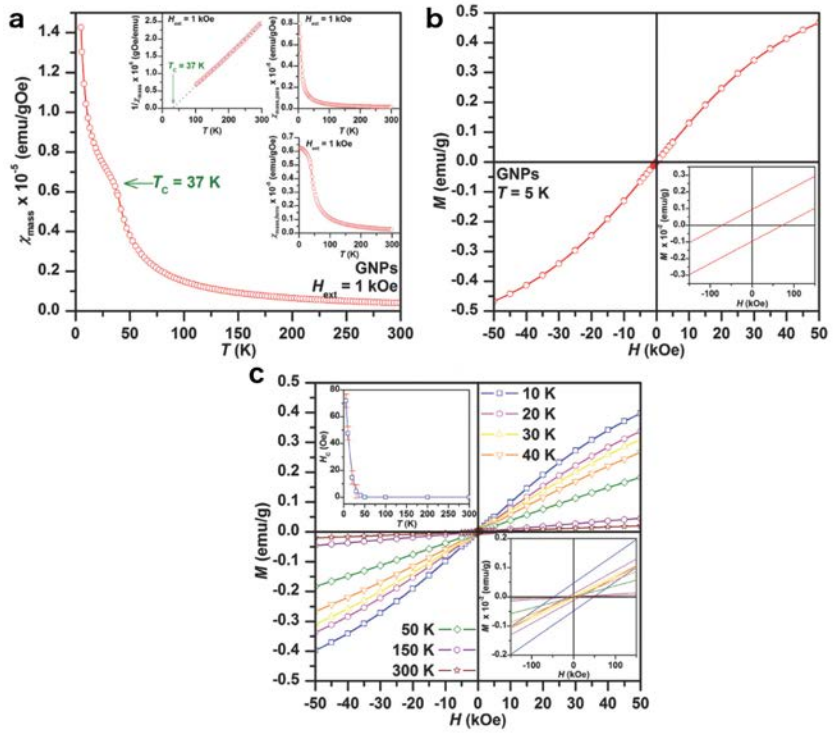


Figure 1.19: **a,** Temperature evolution of the mass magnetic susceptibility, χ_{mass}, of the GNP sample, recorded under an external magnetic field of 1 kOe, with the Curie temperature, T_{C}, indicated. In the insets the fitting of $1/\chi_{\mathrm{mass}}$ versus temperature curve with the Curie-Weiss law in the temperature range from 100 to 300 K and temperature evolution of $\chi_{\mathrm{mass,para}}$ and $\chi_{\mathrm{mass,ferro}}$ terms (as derived from the fitting model) are shown. **b,** Hysteresis loop of the GNP sample measured at a temperature of 5 K. The inset displays the behaviour of the hysteresis loop around the origin with the coercivity and remnant magnetization. **c,** Hysteresis loops of the GNP sample, recorded in the temperature range from 10 to 300 K. The insets show the behaviour of hysteresis loops around the origin and the temperature evolution of coercivity, H_{C}, derived from the respective hysteresis loops of the GNP sample. Reprinted from **[91]**.

carbon sustainable up to room temperature, thus opening new opportunities in spintronics.

Chapter 2

Theoretical methods

2.1 Density Functional Theory

The cornerstone of the development of methods for simulations of properties of materials was provided by the Hohenberg-Kohn theorem [92] density functional theory (DFT) is based upon, which casts the intractable complexity of the electron-electron interactions in many-electron systems into an effective one-electron potential, being a functional of the electron density only. This theorem states that the ground-state density $n(\boldsymbol{r})$ of a system of interacting electrons in an external potential $v(\boldsymbol{r})$ uniquely determines this potential. The density $n(\boldsymbol{r})$ is uniquely related to the external potential and the number N of electrons via $N = \int n(\boldsymbol{r}) d^3r$ and therefore it determines the full Hamiltonian. Further, it is a fundamental observable that can be directly compared to results from X-ray or neutron diffraction. The exact ground state density and energy can be determined by the minimization of the energy functional $E[n]$:

$$E_{\mathrm{tot}} = \min_{n(\boldsymbol{r})} E[n] = \min_{n(\boldsymbol{r})} \big(T[n] + V_{\mathrm{ext}}[n] + V_{\mathrm{H}}[n] + E_{\mathrm{xc}}[n] \big) \ , \tag{2.1}$$

where V_{ext} and V_{H} are, respectively, the functionals of the external potential and of the classical electrostatic interaction energy (the Hartree energy), and T is the kinetic energy functional for non-interacting electrons, i.e., the kinetic energy functional of a non-interacting reference system that is exposed to the same external potential as the true interacting system. The exchange-correlation functional E_{xc} contains all quantum mechanical many-body effects. Although, this non-local functional is not known, it has the important property that it is a universal functional of the electron density, i.e., it does not depend on any specific system or element. The kinetic energy functional T is neither well-known.

The density can be expressed as a sum over single-particle states

$$n(\boldsymbol{r}) = \sum_{i=1}^{N} \left|\psi_i(\boldsymbol{r})\right|^2 \ . \tag{2.2}$$

Making use of the variational principle for the energy functional and minimizing $E[n]$ with respect to the single particle states under the constraint of normalization, one obtains the so-called Kohn-Sham equations [93]:

$$\left\{ -\frac{\hbar^2}{2m}\nabla^2 + v_{\text{ext}}(\boldsymbol{r}) + v_{\text{H}}(\boldsymbol{r}) + v_{\text{xc}}(\boldsymbol{r}) \right\} \psi_i(\boldsymbol{r}) = \varepsilon_i \psi_i(\boldsymbol{r}) \ . \tag{2.3}$$

The sum of v_{ext}, v_{H} and v_{xc} gives the effective one-electron potential acting on the electrons, $v_{\text{eff}}(\boldsymbol{r})$. The exchange-correlation potential v_{xc} is the functional derivative of the exchange-correlation functional $E_{\text{xc}}[n]$,

$$v_{\text{xc}} = \frac{\delta E_{\text{xc}}[n]}{\delta n} \ . \tag{2.4}$$

Finally, the ground state energy can be expressed as

$$E = \sum_{i=1}^{N} \varepsilon_i + E_{\text{xc}}[n] - \int v_{\text{xc}}(\boldsymbol{r}) n(\boldsymbol{r}) d^3r - V_{\text{H}} + V_{\text{nucl-nucl}} \ . \tag{2.5}$$

The accuracy of DFT-based methods depend crucially on the particular form of exchange-correlation functional. The hierarchy of exchange-correlation functionals

after John Perdew is usually referred to as the "Jacob's ladder" of DFT (see e.g., Ref. **[94]** and references therein).

2.1.1 Exchange-correlation functional

The local density approximation (LDA) [95] for the exchange-correlation energy can be written in a simple form:

$$E_{\rm xc}[n(\boldsymbol{r})] = \int n(\boldsymbol{r})\varepsilon_{\rm xc}[n(\boldsymbol{r})]d\boldsymbol{r} \ , \tag{2.6}$$

where $\varepsilon_{\rm xc}$ is the exchange and correlation energy per electron of a uniform electron gas of density n. It is well known that the LDA tends to overestimate the bond strength in solids, thus the theoretical lattice constants are too small, cohesive energies are overestimated; also energy gaps in semiconductors and insulators are seriously underestimated. It must also be pointed out that LDA fails quite badly in predicting the ground magnetic state for transition metals, i.e., Fe is predicted to be hexagonal close-packed and non-magnetic instead of body-centered cubic and ferromagnetic [96], and body-centered cubic Cr is predicted to be non-magnetic instead of antiferromagnetic [97].

The Generalized Gradient Approximation (GGA) [98, 99] introduces a dependence of the exchange-correlation functional on the local gradient $\nabla n(\boldsymbol{r})$ of the electron density. It can be expressed as

$$E_{\rm xc}[n(\boldsymbol{r})] = \int f_{\rm xc}^{\rm GGA}[n(\boldsymbol{r}); \nabla n(\boldsymbol{r})]d\boldsymbol{r} \ . \tag{2.7}$$

Many different functional forms of $f_{\rm xc}^{\rm GGA}$ are available, for instance, the functional proposed by Perdew et al., in 1991 (PW91) [100], the Perdew-Burke-Ernzerhof (PBE) [101] functional and its revised form proposed by Hansen et al., (RPBE) [102]. The GGA corrects the overbinding tendency inherent in the LDA, albeit with a

certain tendency to overcorrect. However, the GGA produces the correct ground state for magnetic transition metals where the LSDA fails badly.

The development of more accurate exchange-correlation functionals is a very active research field. One route is the development of so-called meta-GGA that is a straightforward extension of the concept underlying the GGA, i.e., the meta GGA depends on the Laplacian of the electron density or on the local kinetic energy density [103]. Unfortunately, a systematical improvement of the properties compared to those obtained with GGA has not been obtained (see e.g., Ref. [94]).

Another step was to construct hybrid functionals mixing nonlocal Fock exchange and local or semilocal DFT exchange in a certain proportion, motivated by some hope that the deficiencies of DFT and HF will cancel out each other being in some sense complementary: band gaps predicted by DFT are too narrow, gaps calculated using HF are far too wide. The most popular hybrid in chemistry is the three-parameter B3LYP functional [104, 105], because it provides high accuracy for almost all properties of molecules, but, unfortunately, fails when applied to metals and semiconductor solids, as the correlation part of the functional is incorrect in the homogeneous electron gas limit [106, 107]. Better estimates for lattice parameters and bulk moduli of solids, and for the band gaps in semiconductors and insulators offer PBE0 [108] and HSE03 [109] hybrid functionals. Both insulating antiferromagnetic rare-earth and transition metal oxides, which are not correct with GGAs, are properly described with these hybrid functionals [110]. Hybrid functionals require much greater computational cost than standard DFT. On the other hand, atomization energies and magnetic properties of metals are more accurate through standard PBE.

2.1.2 Spin-polarized DFT: collinear and noncollinear magnetic ordering

The spin-polarized density-functional theory (SP-DFT) can be expressed in terms of a 2×2 density matrix $n^{\alpha\beta}(\boldsymbol{r})$. The spin indices α and β can take two values, either $+$ for majority spin or $-$ for minority spin. The scalar electronic density $n(\boldsymbol{r})$ and the vector of the magnetization density $\boldsymbol{m}(\boldsymbol{r})$ are given by

$$\begin{aligned} n(\boldsymbol{r}) &= \sum_{\alpha} n^{\alpha\alpha}(\boldsymbol{r}) \ , \\ \boldsymbol{m}(\boldsymbol{r}) &= \sum_{\alpha\beta} \boldsymbol{\sigma}^{\alpha\beta} n^{\alpha\beta}(\boldsymbol{r}) \end{aligned} \tag{2.8}$$

and by

$$n^{\alpha\beta}(\boldsymbol{r}) = \frac{1}{2}\big[n(\boldsymbol{r})\delta^{\alpha\beta} + m_x(\boldsymbol{r})\sigma_x^{\alpha\beta} + m_y(\boldsymbol{r})\sigma_y^{\alpha\beta} + m_z(\boldsymbol{r})\sigma_z(\boldsymbol{r})\sigma_z^{\alpha\beta}\big] \ . \tag{2.9}$$

Upper Greek indices denote 2×2 matrices and $\boldsymbol{\sigma} = (\sigma_x, \sigma_y, \sigma_z)$ is the vector of the Pauli spin matrices. The exchange-correlation energy is a functional of the electron density $n(\boldsymbol{r})$ and of the magnetization field $\boldsymbol{m}(\boldsymbol{r})$ and in the local-spin-density approximation it is defined by

$$\begin{aligned} E_{\mathrm{xc}}\big[n^{\alpha\beta}(\boldsymbol{r})\big] &= \int n_{\mathrm{Tr}}(\boldsymbol{r})\varepsilon_{\mathrm{xc}}\big[n^{\alpha\beta}(\boldsymbol{r})\big]d\boldsymbol{r} \\ &= \int n_{\mathrm{Tr}}(\boldsymbol{r})\varepsilon_{\mathrm{xc}}\big[n_{\mathrm{Tr}}(\boldsymbol{r}), |\boldsymbol{m}(\boldsymbol{r})|\big]d\boldsymbol{r} \ . \end{aligned} \tag{2.10}$$

The exchange-correlation potential consists of a scalar contributions

$$\begin{aligned} \upsilon_{\mathrm{xc}}\big[n^{\alpha\beta}\big](\boldsymbol{r}) &= \frac{\delta E_{\mathrm{xc}}\big[n^{\alpha\beta}\big]}{\delta n_{\mathrm{Tr}}(\boldsymbol{r})} \\ = \varepsilon_{\mathrm{xc}}\big[n^{\alpha\beta}\big](\boldsymbol{r}) &+ n_{\mathrm{Tr}}(\boldsymbol{r})\frac{\partial \varepsilon_{\mathrm{xc}}\big[n^{\alpha\beta}(\boldsymbol{r})\big]}{\partial n_{\mathrm{Tr}}(\boldsymbol{r})} \end{aligned} \tag{2.11}$$

and of the magnetic exchange-correlation field

$$\boldsymbol{b}\big[n^{\alpha\beta}\big](\boldsymbol{r}) = \frac{\delta E_{\mathrm{xc}}\big[n^{\alpha\beta}\big]}{\delta \boldsymbol{m}(\boldsymbol{r})}$$
$$= \boldsymbol{e}(\boldsymbol{r}) n_{\mathrm{Tr}}(\boldsymbol{r}) \frac{\partial \varepsilon_{\mathrm{xc}}\big[n^{\alpha\beta}(\boldsymbol{r})\big]}{\partial |\boldsymbol{m}(\boldsymbol{r})|} \ , \tag{2.12}$$

and

$$\boldsymbol{e}(\boldsymbol{r}) = \frac{\partial |\boldsymbol{m}(\boldsymbol{r})|}{\partial \boldsymbol{m}(\boldsymbol{r})} \tag{2.13}$$

is the local direction of the magnetization at the point $\boldsymbol{r}$.

In the LDA, one can use the exchange-correlation functional proposed by Perdew and Zunger [111] based on the quantum Monte Carlo simulations of Ceperley and Alder [112] for the interacting electron gas. The extension of the LDA to the spin-polarized case is based on the spin-interpolation proposed by Barth and Hedin [113] and by Vosko, Wilk, and Nusair [114]. The GGA incorporates the leading nonlocal corrections to the LDA. In the GGA, the exchange-correlation functional depends also on the absolute values of the gradients of charge and spin density. One can choose out of the many different GGA functionals proposed in the literature, e.g., the form proposed by Perdew et al., [115], and the approach of White and Bird [116] to calculate the spin-polarized GGA potentials. Details on the SP-DFT in the fully unconstrained noncollinear all-electron (AE) projector augmented wave (PAW) formalism are presented in Ref. [117].

2.2 Pseudopotentials and projector-augmented-waves method

The concept of pseudopotentials has been introduced to avoid the need for an explicit treatment of the strongly bound and chemically inert core electrons

hardly participating in any chemical interaction. Pseudopotentials are a necessary ingredient of all plane-wave methods, but they can also be employed in local-basis set methods to reduce the computational efforts. Although the theory of pseudopotentials is mature, in practice the construction of accurate, transferable, and efficient pseudopotentials is far from straightforward. The starting point for the generation of pseudopotentials is an all-electron calculation for the isolated atom. The one-particle wave function of a valence electron can be expressed as

$$|\psi_v\rangle = |\psi_{\rm ps}\rangle - \sum_i |\psi_{c_i}\rangle\langle\psi_{c_i}|\psi_{\rm ps}\rangle \ . \tag{2.14}$$

The ψ_{c_i} are core states with one-particle energies ε_{c_i}. In the form (2.14), the matrix element $\langle\psi_v|\psi_{c_i}\rangle$ of the valence wave-function with any core state will vanish by construction. The coefficients $\langle\psi_{c_i}|\psi_{\rm ps}\rangle$ can be chosen arbitrarily, and therefore (2.14) does not uniquely define the pseudo-wave function $|\psi_{\rm ps}\rangle$. Substituting the wave function (2.14) into an effective one-particle Schrödinger equation such as the Kohn-Sham equations (2.3) for an isolated atom leads to

$$\left\{ -\frac{\hbar^2}{2m}\nabla^2 + v_{\rm ps} \right\} |\psi_{\rm ps}\rangle = \varepsilon_v |\psi_{\rm ps}\rangle \ , \tag{2.15}$$

with the pseudopotential $v_{\rm ps}$ given by

$$v_{\rm ps} = v_{\rm eff}(\boldsymbol{r}) + \sum_i (\varepsilon_v - \varepsilon_{c_i}) |\psi_{c_i}\rangle\psi_{c_i}| \ . \tag{2.16}$$

The sum in (2.16) acts as a short-range repulsive potential. The wave function $\psi_{\rm ps}(\boldsymbol{r})$ has the same one-particle energy ε_v as the true valence wave function $\psi_v(\boldsymbol{r})$. Since pseudo-wave function does not need to be orthogonal to the core states, it does not have to have a nodal structure in the core region. Having a smooth pseudo-wave function is advantageous when the wave function is expanded in some set of basis functions. The derivation (2.14)–(2.16) captures the essentials

of the pseudopotential generation. An important feature of pseudopotentials is their transferability, which means that a pseudopotential should give reliable results independent of the particular environment in which it is used. The quality criterion of a pseudopotential is not how well it reproduces experiment, but how well it matches the results of accurate all-electron calculations. The most common pseudopotential generation methods include the *norm-conserving* pseudopotentials [118–120] and the *ultrasoft* pseudopotentials [121, 122] The nonlinearity of the exchange interaction between valence and core electrons requires elaborate non-linear core corrections [123] for systems exhibiting a non-negligible overlap between valence- and core-electron densities. This deficiency can be avoided by using the projector-augmented wave (PAW) method.

The *projector-augmented wave* method [124] aims to combine the efficiency of ultra-soft pseudopotentials with an all-electron treatment and reach the accuracy of the full-potential linearized augmented-planewave (FLAPW) method [125], which is commonly regarded as the benchmark for DFT calculations for solids. However, unlike the pseudopotential approach, the PAW method accounts for the nodal features of the valence orbitals and ensures orthogonality between valence and core wave functions. The PAW method is based on a frozen core (FC) approximation, while in the FLAPW method the core wave functions and charge densities are computed self-consistently within a spherical approximation to the one-centre effective potential.

In the PAW approach, a linear transformation [124, 126]

$$|\psi_n^{\mathrm{AE}}\rangle = |\psi_n^{\mathrm{PS}}\rangle + \sum_l \big(|\phi_i^{\mathrm{AE}}\rangle - |\phi_i^{\mathrm{PS}}\rangle\big)\langle p_i^{\mathrm{PS}}|\psi_n^{\mathrm{PS}}\rangle \ . \tag{2.17}$$

reconstructs the all-electron (AE) valence wave functions ψ_n^{AE} from the pseudo (PS) wave functions. The PS-wave functions ψ_n^{PS} (n is the band index) are the

variational quantities which are expanded in plane waves. They are identical to the AE wave functions between the PAW spheres surrounding the atoms, however inside the spheres the ψ_n^{PS} are only a bad approximation to the exact wave functions and, thus, they are used only as a computational tool. The AE partial waves ϕ_i^{AE} are solutions of the spherical scalar-relativistic Schrödinger equation for a *nonspinpolarized* atom at a reference energy ε_i in the valence regime and for an angular momentum l_i (in atomic units),

$$\left(-\frac{1}{2}\Delta + v_{\mathrm{eff}}^{\mathrm{AE}}\right)|\phi_i^{\mathrm{AE}}\rangle = \varepsilon_i|\phi_i^{\mathrm{AE}}\rangle \ , \tag{2.18}$$

with the spherical component of the AE potential, $v_{\mathrm{eff}}^{\mathrm{AE}}$. The index i is a shorthand for the reference energy ε_i, the angular momentum quantum numbers (l_i, m_i), and the atomic coordinates $\boldsymbol{R}_i$ [42]. The node-less PS partial waves ϕ_i^{PS} are identical to the AE partial wave outside a core radius r_c, approximately equal to half the nearest-neighbour distance, and match continuously to ϕ_i^{PS} inside the core. The projector functions p_i^{PS} are dual to the partial waves, $\langle p_i^{\mathrm{PS}}|\phi_j^{\mathrm{PS}}\rangle = \delta_{ij}$. They sample local properties of wave pseudofunctions inside an atomic core ensuring the reproduction of the proper charge density. The main advantage of the PAW method is an accurate description of charge density in the area of the atomic nucleus, which enables, among others, implementation of complex correlation and exchange functionals. For a comprehensive description of the PAW method the reader is referred to the paper of Kresse and Joubert [126] and references therein. The inclusion of core relaxation, including a selfconsistent optimization of the core-charge density, preserving the orthogonality between core and valence orbitals, has been made by Marsman and Kresse [127] within relaxed-core projector-augmented-wave (RC-PAW) method.

The spin-orbit coupling acts predominantly in the immediate vicinity of the

nuclei and one assumes its effects to be negligible outside of the PAW spheres. Under that assumption and provided that the PS partial waves ϕ_i^{PS} form a complete basis set within the PAW spheres, the contribution of the SOC to the PAW Hamiltonian reduces to the AE one-centre contribution

$$H_{\mathrm{SO}}^{\mathrm{PS}} = \sum_{ij} |p_i\rangle\langle\phi_i|H_{\mathrm{SO}}|\phi_j\rangle\langle p_j| \ . \tag{2.19}$$

In the zeroth-order-regular approximation, H_{SO} is given by [128]

$$H_{\mathrm{SO}}^{\alpha\beta} = \frac{\hbar^2}{(2m_e c)^2}\frac{K(r)}{r}\frac{dV(r)}{dr}\boldsymbol{\sigma}^{\alpha\beta}\cdot\boldsymbol{L} \ . \tag{2.20}$$

The angular momentum operator $\boldsymbol{L}$ is defined as $\boldsymbol{L} = \boldsymbol{r}\times\boldsymbol{p}$, and $\boldsymbol{\sigma} = (\sigma_x, \sigma_y, \sigma_z)$ are the (2×2) Pauli spin matrices, $V(r)$ is the spherical part of the effective AE potential within the PAW sphere, and

$$K(r) = \left(1 - \frac{V(r)}{2m_e c^2}\right)^{-2} \ . \tag{2.21}$$

By using $\phi_i(\boldsymbol{r}) = R_i(|\boldsymbol{r}|)Y_{l_i m_i}(\hat{\boldsymbol{r}})$, one rewrites (2.20) as

$$H_{\mathrm{SO}}^{\mathrm{PS}\alpha\beta} = \frac{\hbar^2}{(2m_e c)^2}\sum_{ij} |p_i^{\mathrm{PS}}\rangle R_{ij}\boldsymbol{\sigma}^{\alpha\beta}\cdot\boldsymbol{L}_{ij}\langle p_j^{\mathrm{PS}}| \ , \tag{2.22}$$

where

$$R_{ij} = 4\pi\int_0^{r_c} R_i(r)\frac{K(r)}{r}\frac{dV(r)}{dr}R_j(r)dr \tag{2.23}$$

and

$$\boldsymbol{L}_{ij} = \langle Y_{l_i m_i}|\boldsymbol{L}|Y_{l_j m_j}\rangle \ , \tag{2.24}$$

where Y_{lm} are real spherical harmonics. The action of the SOC operator on the PS orbitals can be expressed as

$$|\psi_n^{\mathrm{PS}\alpha}\rangle = \sum_{\alpha\beta} H_{\mathrm{SO}}^{\mathrm{PS}\alpha\beta}|\psi_n^{\mathrm{PS}\beta}\rangle \ , \tag{2.25}$$

where α and β correspond to the spin-up and spin-down components of the two-component spinor wave functions necessary to describe noncollinear magnetism **[24]**, [117, 129].

2.3 Plane waves

Modern electronic structure methods use either plane waves or localized basis functions, e.g., Gaussian-type orbitals, for the expansion of the valence orbitals, charge densities and potentials. The natural basis for a periodic structure is within plane waves

$$\psi_{\boldsymbol{k}}^{\boldsymbol{G}}(\boldsymbol{r}) = \frac{1}{\sqrt{V}} e^{i(\boldsymbol{k}+\boldsymbol{G})\cdot\boldsymbol{r}} \ , \tag{2.26}$$

being in the form of Bloch functions. In (2.26), $\boldsymbol{G}$ is a reciprocal lattice vector and $\boldsymbol{k}$ is supposed to lie within the first Brillouin zone. The symmetry properties of an infinite crystal implies that plane waves with wave vectors that do not differ by a reciprocal lattice vector do not couple, and hence the expansion of any wave function solving the Kohn-Sham equations only contains plane waves that differ by reciprocal lattice vectors. A summation over the lowest eigenvalues gives the total energy of a crystal. For infinite periodic systems, this summation has to be replaced by an integral over the first Brillouin zone

$$\sum_i \varepsilon_i \to \sum_j \frac{V}{(2\pi)^3} \int_{BZ} d^3\boldsymbol{k} \ \varepsilon_j(\boldsymbol{k}) \ , \tag{2.27}$$

where j numbers all occupied energy bands. The above integral can be approximated quite accurately by a sum over a finite set of k-points [130]. The expansion of the electronic wave functions in plane waves is computationally very efficient: A Fast Fourier Transform let an easy change from a real-space representation where

the potential energy has a diagonal representation, to momentum-space where the kinetic energy is diagonal; further, the control of basis-set convergence is rather trivial, i.e., it is sufficient to monitor the eigenvalues and total energies as a function of the cut-off energy (the highest kinetic energy of a plane-wave within the basis set). However, this expansion usually requires a periodicity of the considered system in three-dimensions. If one wants to use plane-wave codes for surface science problems or to study non-periodic molecular systems, the system has to be cast into a three-dimensional periodicity. This is doable in the so-called supercell approach, in which a system is represented by an infinite array of slabs.

Importantly, a convergence of a plane-wave expansion can be achieved only if the nodal character of the valence orbitals is eliminated. This is achieved by using e.g., the above-discussed PAW method.

Chapter 3

Results

3.1 Structures and MAEs of small free transition-metal clusters

During the last years, the magneto-structural properties of small gas-phase and supported transition-metal (TM) clusters **[16–20], [24–30]** have been in the centre of my intense research effort motivated by the quest for materials allowing an increased density of information per square inch in magnetic storage media and by potential applications in nanospintronics. A quantity of prime interest has been the magnetic anisotropy, i.e., the dependence of the total energy of the system on the orientation of the magnetic moment. The origin of the magnetic anisotropy is the coupling between the spin and orbital degrees of freedom, and thus, it is a fundamentally relativistic effect. Further, magnetic anisotropy is critically dependent on symmetry and dimensionality; typically, the magnetic anisotropy is found to be much larger in low-symmetry nanostructures than in highly symmetric bulk materials. A large magnetic anisotropy energy is necessary to inhibit the magnetization reversal due to thermal excitations.

Table 3.1: Interatomic distance d (in Å), spin multiplicity $2S+1$ from scalar-relativistic calculations, spin μ_S and orbital μ_L moments from calculations including spin-orbit coupling (in μ_B) of transition-metal dimers for axial and perpendicular orientations of the magnetization, magnetic anisotropy energy, and spin-orbit coupling constant (ξ) both in meV. The MAE is positive for any easy axis parallel to the dimer axis. Adapted from **[24]**.

Dimer	d	$2S+1$	$\mu_S^\perp$	$\mu_L^\perp$	$\mu_S^\parallel$	$\mu_L^\parallel$	MAE	ξ
Fe_2	1.98	7	5.84	0.32	5.84	0.16	0.3	24
Ru_2	2.07	5	3.98	0.00	3.94	0.24	−36.5	334
Os_2	2.10	5	3.75	−0.80	3.48	0.62	28.8	885
Co_2	1.96	5	3.90	0.78	3.90	0.32	7.1	32
Rh_2	2.21	5	3.86	1.82	3.80	0.50	47.3	136
Ir_2	2.22	5	3.88	1.96	3.42	0.94	69.8	413
Ni_2	2.09	3	1.98	0.58	1.96	0.38	6.5	101
Pd_2	2.49	3	1.96	0.02	1.98	0.36	−2.3	404
Pt_2	2.38/2.35	3	1.88	2.74	1.34	0.80	46.3	742

The results for gas-phase clusters are important for a fundamental understanding of the intrinsic properties of these clusters, and they form a reference for investigations of clusters supported on a solid surface where the orientation of the cluster is fixed by the binding to the substrate and where the magnetic anisotropy is determined by the interplay between the intrinsic anisotropy of the cluster and that imposed by the interaction with the substrate.

3.1.1 Dimers

An atomic dumbbell is the smallest cluster showing magnetic anisotropy **[24]**. Table 3.1 lists MAEs of dimers of the transition-metal atoms from groups 8 to

10 of the Periodic Table. For practical applications of magnetic nanostructures at room temperature, large MAEs of 30–50 meV are required. Thus, Pt_2, Rh_2 and Ir_2 have MAEs in the desirable range and the easy magnetic axis oriented along the dimer axis. The very large MAEs are a consequence of a transition from a high-moment state for axial to a low-moment state for magnetization perpendicular to the dimer axis induced by the change of the magnetization direction, which is most pronounced for Pt_2 whose the SOC constant is the largest. Further, SOC influenced also the bond length of Pt_2 dimer. In the scalar-relativistic mode $d = 2.33$ Å; including SOC, $d = 2.38$ Å for the easy axis and $d = 2.35$ Å for the hard magnetic axis. No similar magnetostructural effect was found for the other considered dimers.

The strong spin and orbital anisotropy calculated for the Pt dimer are in line with the results of Ref. [131] reporting strained monoatomic wires of Pt to be FM if magnetized along the wire axis, but non-magnetic if the magnetization direction was constrained to a perpendicular direction, resulting in a *giant* MAE of 36 meV/atom. Dimers and monowires demonstrated that in nanostructures with a strong SOC, a reorientation of the magnetization direction may induce a transition between high- and low-moment states or even cause the total disappearance of magnetism.

One of the main objectives of the study **[24]** was to clarify the physical mechanism determining MAEs of the dimers. This was elucidated via an analysis of the influence of SOC on the spectrum of the dimers' Kohn-Sham eigenvalues (Figure 3.1 and 3.2). In the scalar-relativistic approximation, the eigenvalue spectrum of the dimer is determined by the electronic ground state of the isolated atom, s^2d^7 for Ir, sd^8 for Rh, sd^9 for Pt, and the bonding-antibonding and exchange splittings. The highest occupied molecular orbital (HOMO) of the Rh_2 and Ir_2 dimers

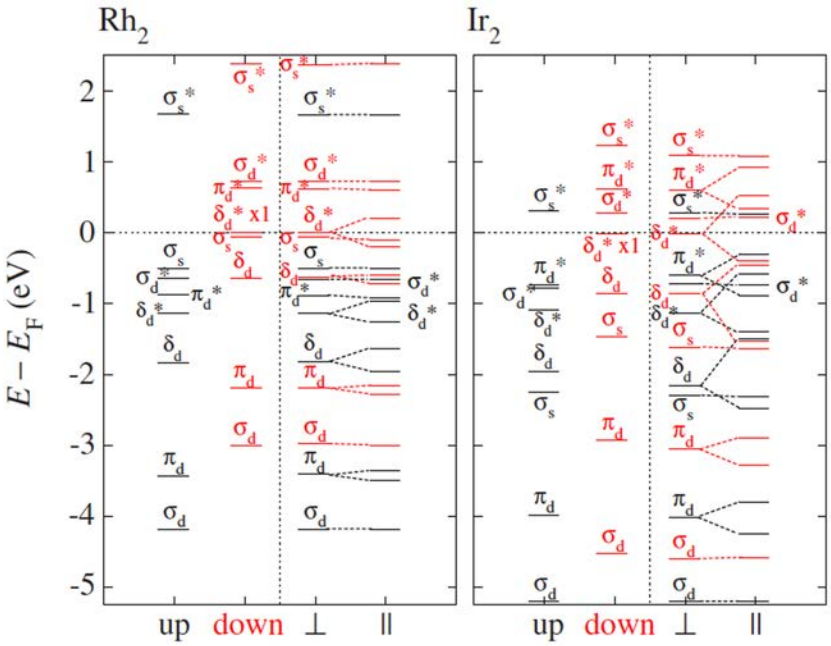


Figure 3.1: Kohn-Sham eigenvalue spectra for Rh_2 and Ir_2 dimers. The eigenvalues from the scalar-relativistic calculations are shown in the left-hand part of each graph while the right-hand part displays the eigenvalues for parallel and perpendicular orientations of the magnetic moment (with respect to the dimer axis) after adding SOC. The colouring is the same as for the scalar-relativistic eigenstates from which the fully relativistic states are derived. Reprinted from **[24]**.

is a doubly-degenerate antibonding $\delta_d^\star$ minority (spin-down) state occupied by one electron only (Figure 3.1). SOC led to a lifting of the twofold degeneracy of the δ_d and π_d states for the magnetization parallel to the dimer axis. The SOC splitting of HOMO $\delta_d^\star$ was 0.94 eV and 0.41 eV, respectively for Ir_2 and for Rh_2. The lowering of the occupied $\delta_d^\star$ states by -0.39 eV was the dominant effect determining the MAE of Ir_2 which together with an up-shift of the fully occupied $\delta_d^\star$ and δ_d states by 0.13 and 0.20 eV, respectively, yielded an energy difference of 0.06 eV–in almost perfect agreement with the calculated MAE. For Rh_2 the difference in the

sum over the eigenvalues was 0.1 eV, somewhat larger than the calculated MAE.

For the Pt_2 dimer the HOMO is the minority $\sigma_d^\star$ state; the highest majority state has the same symmetry. An antibonding $\delta_d^\star$ lies only slightly below and an empty $\pi_d^\star$ state only slightly above the HOMO. The occupied σ_s lies below the occupied bonding δ_d states (Figure 3.2). SOC led to a reordering of the eigenstates close to the Fermi level even for perpendicular orientation of the magnetization. The $\sigma_d^\star$ down-shifted below the $\delta_d^\star$ state occupied by two electrons which became the HOMO. The splitting of the doubly-degenerate $\pi_d^\star$ and $\delta_d^\star$ eigenstates at either side of the HOMO for a magnetization parallel to the dimer axis was larger than the separation of the eigenlevels. This led to a change in occupation: one electron from the $\delta_d^\star$ state was moved to the lower component of the $\pi_d^\star$ state; the $\sigma_d^\star$ state became the HOMO as in the scalar-relativistic approximation. Further, the pronounced anisotropy of the spin moment, and hence also of the exchange splitting, was reflected in the eigenvalue spectra–for some eigenstates SOC splitting was not symmetrical but accompanied by a shift in the centre of gravity of the split eigenstates. This led to contributions to the MAE of 46.3 meV which were not restricted to eigenstates close to the Fermi level.

In the DFT, the effective one-electron potential is orbital independent. In hybrid-functional calculations, mixing Hartree-Fock and hence orbital-dependent exchange with DFT exchange in a ratio of 1:3 and treating correlation at the GGA level, the bond length of Pt_2 was slightly increased by 0.05 Å. Spin moments were hardly affected but the orbital moment of the dimer increased from 2.74 μ_B to 3.02 μ_B for easy (parallel) orientation of the magnetic moment and from 0.80 μ_B to 1.06 μ_B for hard-axis orientation. The spin anisotropy was slightly reduced while the orbital anisotropy remained unchanged. The main effect of the admixture of

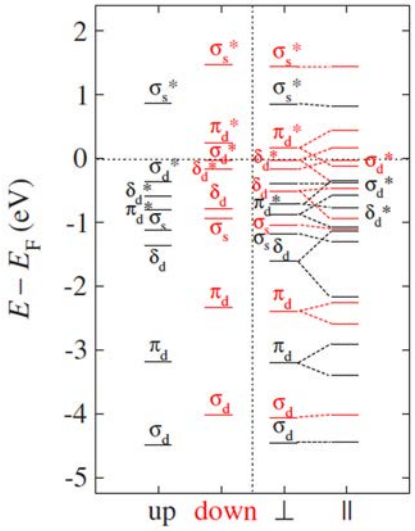


Figure 3.2: Kohn-Sham eigenvalue spectra for the Pt_2 dimer (cf. Fig. 3.1). Reprinted from **[24]**.

a fraction of Hartree-Fock exchange was to increase the exchange splitting of the partially occupied eigenstates. The exchange splitting of $\pi_d^\star$ was increased from 1.05 to 3.05 eV and for the bonding π_d states the increase was from 0.86 to 1.90 eV. The change in the occupation of the highest eigenstates was similar as with the GGA functional and led only to a reduction of the MAE from 46.5 to 30.5 meV **[24]**.

Since a high MAE requires large spin and orbital moments and a strong SOC, bimetallic nanostructures consisting of ferromagnetic 3d and heavy 5d elements are possible candidates for materials with a high MAE because of the large spin moments of the light and the strong SOC of the heavy atoms. The substitution of Ir by Co in the Ir_2 dimer left the large MAE of ∼70 meV unchanged **[28]**. For PtCo and PtFe the MAE was strongly reduced relative to the free Pt_2 dimer (18.8 and −3.2 meV, respectively); in PtFe (which is isoelectronic to IrCo) the MAE

relative to a magnetization parallel to the dimer axis even changed sign **[28]**.

For the IrCo dimer formed by homologous elements, the Fermi level coincides for perpendicular magnetization with the singly occupied $\delta_d^\star$ level whose splitting under SOC for axial magnetization represented the largest contribution to the MAE. Spin and orbital moments, as well as their anisotropies, were also of comparable magnitude to the Ir_2 dimer. For the PtCo dimer with one valence electron more, the $\delta_d^\star$ state is fully occupied, but the large SOC splitting pushed the upper component of this state above the $\sigma_d\star$ state, changing the nature of the highest occupied state. This led to a very large orbital anisotropy, but as the energy of the occupied $\sigma_d\star$ state was similar to that of the degenerate (in the absence of SOC) $\delta_d^\star$ state, only to a significantly lower MAE. For the PtFe dimer, isoelectronic to IrCo, the energy difference between the singly occupied spin-down $\delta_d^\star$ and the empty spin-up $\sigma_s\star$ states was very small, resulting in a highly mixed character of the HOMO. In this case SOC did not lead to a change in orbital occupancy, resulting in small spin and orbital anisotropies and a small MAE (Figure 3.3) **[28]**.

3.1.2 Pt_{3-6}

Theoretical calculations **[19]** revealed that for small Pt clusters SOC is of decisive importance both for the MAEs and the magnetic structures, and the equilibrium geometric structures, leading to a complex magneto-structural effects, as showed below.

For Pt_3 scalar relativistic calculations predicted the geometric structure of an equilateral triangle. SOC favoured a Jahn-Teller distortion to an isosceles triangle with the point group symmetry (PGS) $2mm$ in the Hermann-Mauguin notation. The magnetic PGS of the GS with an in-plane easy magnetic axis coinciding

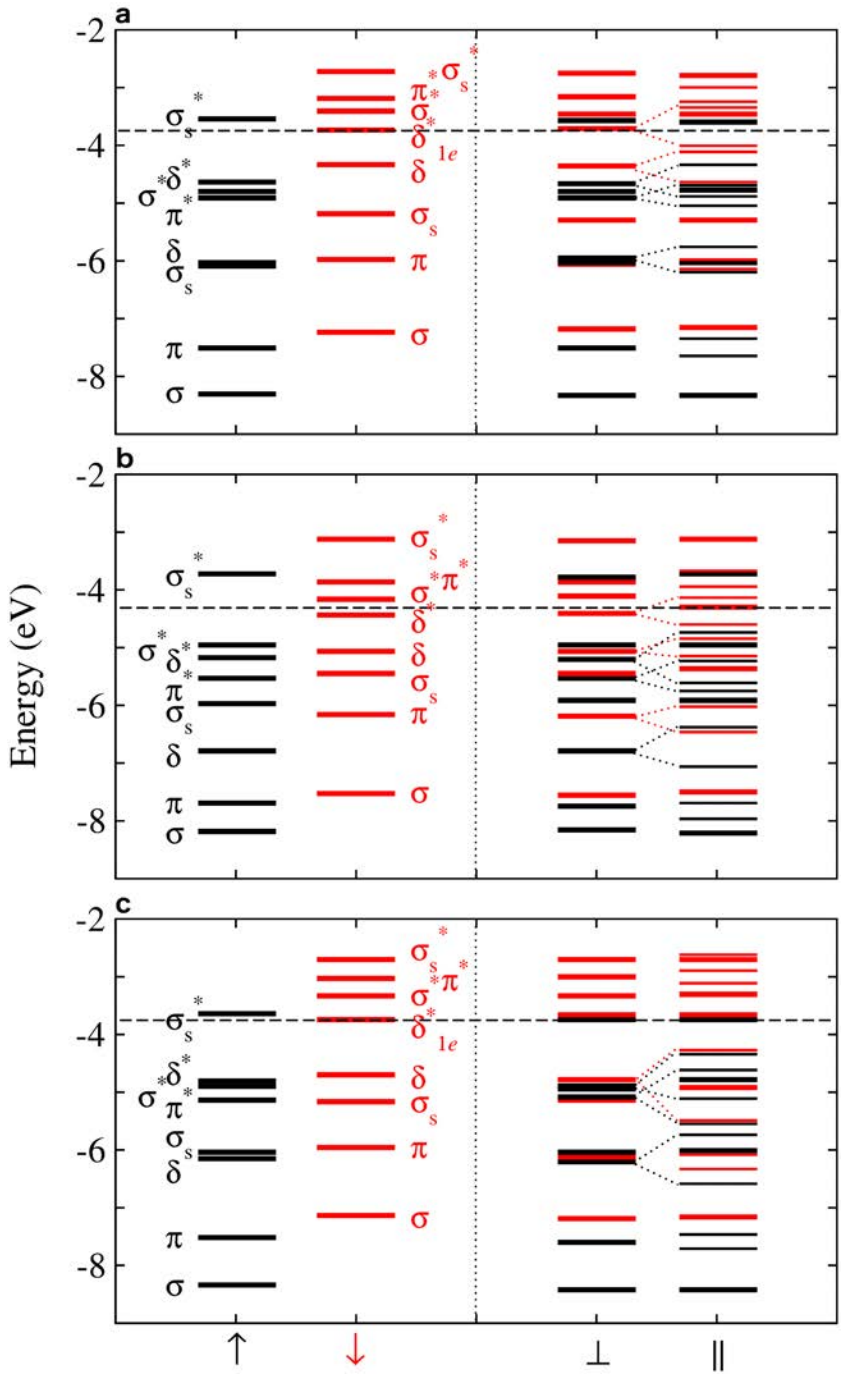


Figure 3.3: Eigenvalue spectra of free **a,** IrCo, **b,** PtCo, **c,** PtFe dimers (cf. Fig. 3.1). Reprinted from **[28]**.

with the mirror-plane of the structure was $2m'm'$ (where the prime indicates that the symmetry operation must be combined with a time-reversal operation which reverses the direction of axial vectors such as the magnetic moment). The magnetic PGS for the other stationary in-plane direction was $m'm2'$ (the in-plane MAE was only 0.2 meV/atom). For perpendicular magnetization the Pt_3 cluster changed to an equilateral triangle with a strongly reduced total magnetic moment of 1 μ_B (vs. 2.5 μ_B relative to the in-plane easy axis configuration). The perpendicular MAE was 5.1 meV/atom. The magnetic PGS of $m'm2'$ was the same as for the hard in-plane configuration. One shall note, that as for the Pt dimer, rotation of the magnetization to an orientation perpendicular of the easy plane induced a transition to a low-moment magnetic isomer.

For Pt_4 and Pt_5 clusters scalar relativistic calculations predicted, respectively, a 3D structure of tetrahedron and a trigonal bipyramid. SOC favoured a Pt_4 2D-rhombus having the geometric PGS of mmm. In the GS Pt_4 was AFM. Rotation of the AFM moments within the cluster's plane cost an energy of 4.4 meV/atom and significantly reduced local magnetic moments. The magnetic PGS of these AFM configurations was $m'm'm'$. For perpendicular magnetization an excited FM solution was found. The magnetic PGS of this FM configuration was $mm'm'$.

Relativistic calculations predicted for Pt_5 a 2D GS in a form of a slightly distorted square plus an isosceles triangle. For the stationary states of Pt_5 with crystallographic point group $2mm$, one or two of the symmetry elements have to be combined with the time-reversal operation, i.e., the time-reversal operation has to be applied to a mirror operation if the magnetization is parallel to the mirror plane and to the twofold rotation if the magnetization is perpendicular to the axis (as indicated in Figure 3.4). In the GS, the easy magnetic axis was in-

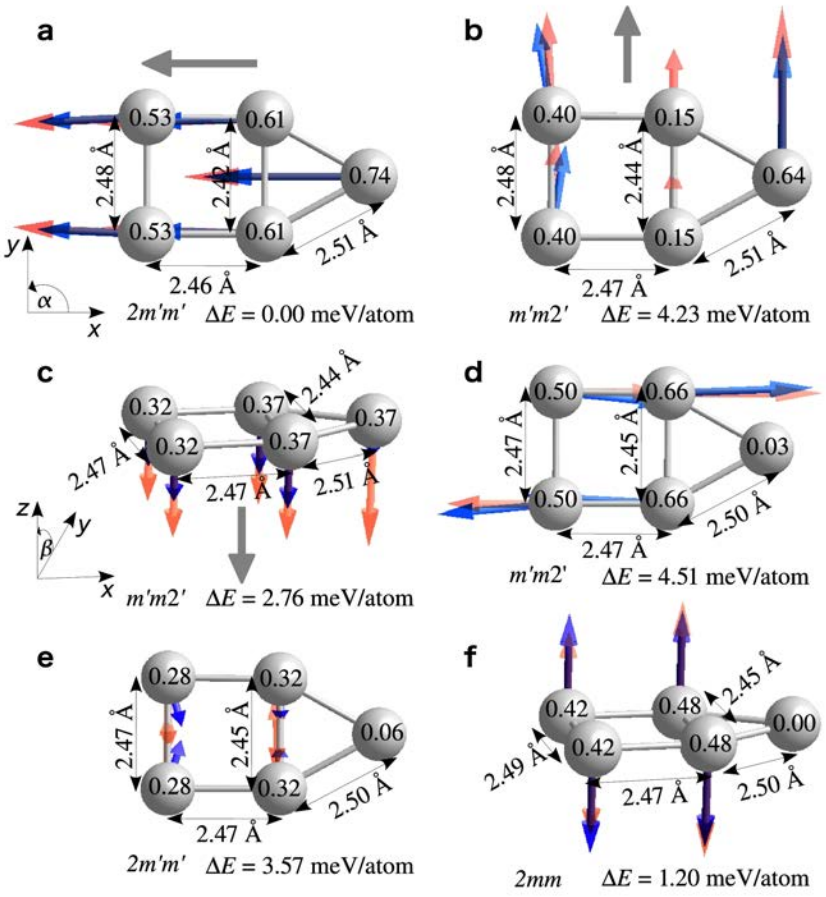


Figure 3.4: Geometric and magnetic structures of a Pt_5 cluster for perpendicular and in-plane magnetizations (as indicated by the grey arrows). Red (blue) arrows show spin (orbital) magnetic moment; the numbers on atoms give the absolute values of the local spin (upper number) and orbital (lower number) magnetic moments in μ_B. **a,** The ground state high-magnetic-moment configuration. **b–c,** Low-moment FM configurations. **d–f,** AFM configurations. The angles α and β indicates, respectively, in-plane and out-of-plane rotation of the magnetization direction. Reprinted from **[19]**.

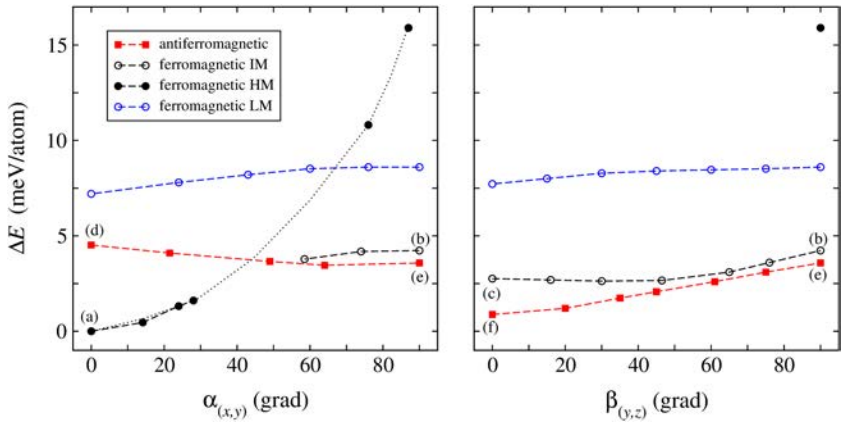


Figure 3.5: Variation of the total energies of the ferromagnetic (full and empty circles) and antiferromagnetic (squares) configurations of a Pt_5 cluster upon rotation of the magnetization direction within the (x, y) plane of the cluster and in the (y, z) plane perpendicular to the twofold symmetry axis. For the FM configurations solutions with high (HM), intermediate (IM) and low (LM) magnetic moments are indicated, cf. Fig. 3.4. Reprinted from **[19]**.

plane; the total spin and orbital moments were parallel to the twofold symmetry axis of the cluster (the magnetic point group symmetry was $2m'm'$). Rotation of the direction of magnetization by 90° within the plane of the cluster or to a perpendicular orientation led to a transition to low-moments states (Figure 3.4). Further, the FM configurations (Figure 3.4a–c) coexisted with AFM configurations (Figure 3.4d–f). The lowest barrier to a magnetization reversal was via the AFM out-of-plane configuration (Figure 3.4f). The magnetic potential-energy surface as a function of the orientation of the magnetic moment consisted of interpenetrating sheets representing different Pt_5's magnetic isomers (Figure 3.5) **[19]**.

At a scalar-relativistic level, a regular trigonal prism was found to be the ground state for the Pt_6 cluster. SOC favoured the octahedron with a noncollinear magnetic moments. In the GS, Pt_6 has a perfect octahedral geometry (PGS of $m\bar{3}m$)

but the distribution of the magnetic moments broke the octahedral symmetry to only $2'2'2$. For the first excited magnetic state, the geometric symmetry was reduced to $4/mmm$, but the magnetic symmetry was restored to $2'2'2$.

Even at a scalar relativistic level, magnetism influences the structural stability of clusters with a small energy difference between structural isomers. The stabilization of different magnetic isomers depends on the interplay between exchange splitting and spin-orbit splitting of eigenstates, the magnitude of the exchange splitting (and hence of the magnetic moment) and on the direction of magnetization. These very general considerations also suggest that similar strong spin-orbit effects can also be found in other nanostructures of the heavy 5d metals. An example has already been reported in Ref. [131] for a Pt monowire showing FM order if the moment is perpendicular to the axis of the wire, which disappears completely if the magnetization is forced to be parallel to the wire.

3.1.3 Ni_{3-6} and Pd_{3-6}

For small Pt clusters the influence of SOC is strong enough to change the energetic ordering of different structural isomers **[19]**, but even for the lighter Pd and Ni clusters RDFT calculations showed that SOC induces magneto-structural effects depending on the direction of magnetization **[20]**. Changes in the magnetic PGSs are accompanied by modest geometric distortions.

The scalar-relativistic calculations for Ni_3 and Pd_3 predicted equilateral triangles in spin triplet in the GS. Although, the highest molecular orbital was triply degenerate but occupied by only two electrons and hence it was expected that the clusters would undergo a Jahn-Teller distortion lowering the symmetry from $D_{3h} = \bar{6}m2$ to $C_{2v} = mm2$, the clusters were found stable against Jahn-Teller

distortion. SOC favoured the formation of isosceles triangles for both trimers, however, the geometric distortions were modest. SOC induced a mixing of different spin states with the largest contributions coming from low-lying spin isomers. For Ni_3, both low- and high-spin isomers had high excitation energies (larger than 77 meV) in the scalar-relativistic approximation, while for Pd_3, $S = 1$ and $S = 0$ isomers were energetically degenerate. Consequently, the relativistic calculations yielded an enhanced spin moment for Ni (2.19 μ_B), but reduced for Pd (1.66 μ_B). In the magnetic GS, the easy magnetic axis was in-plane, the magnetic point group symmetry was $m'm'2$, compatible with the parallel alignment of the local spin moments and the canting of the local orbital moments towards the twofold symmetry axis. For a magnetization axis perpendicular to the plane of the trimer the magnetic point group symmetry was $\bar{6}m'2'$, compatible with the ferromagnetic alignment of the local moments along the main symmetry axis. For in-plane and out-of-plane orientations the total energy was stationary with respect to a rotation of the magnetic axis. The difference in the total energies defines the MAE, which was 2.35 and 0.85 meV/atom for Ni and Pd trimers, respectively. A low-moment magnetic isomer was found for the Pd_3 cluster with out-of-plane magnetization, which was higher in energy by 7.9 meV/atom than the GS magnetic configuration.

On the scalar-relativistic level, the GS of Ni_4 was a distorted tetrahedron with the PGS $S_4 = \bar{4}$, a spin moment of 4 μ_B, and local moments of 1 μ_B on all four atoms. A Pd_4 cluster formed a regular tetrahedron with the PGS $T_d = \bar{4}3m$ and with a cluster magnetic moment of 2 μ_B, and with equally distributed local magnetic moments on four atoms **[20]**. While for Pt_4 SOC induced a preference for a flat structure **[19]**, for the Ni and Pd tetramers the tetrahedral structure and bond lengths remained unchanged. For Ni_4 the geometric structure was invariant

under rotations of the magnetization direction. The total energy was found to be stationary for a magnetization perpendicular to the edges of the cluster, aligned along one of the edges of the tetrahedron or parallel to one of the threefold symmetry axes. Both spin and orbital moments of the cluster were isotropic within the computational accuracy, and this was also reflected in a small MAE of 0.46 meV/atom. The symmetry of the geometric structure was reduced to $C_{2v} = mm2$; the magnetic PGS of $m'm'2$ allowed a parallel alignment of the local spin moments and a slight canting of the orbital moments relative to the spin moments in all magnetic configurations. The total magnetic moment of the cluster of 3.8 μ_B was slightly lower than the spin moment resulting from the scalar-relativistic calculation. The reduction of the spin moment was due to the existence of a $S = 1$ isomer with a low excitation energy of 27 meV, while a $S = 3$ isomer was higher in energy by 130 meV. The admixture of a low-spin state was compensated by a modest orbital moment.

SOC conserved the perfect tetrahedral symmetry of the geometric structure and the bond lengths of the Pd_4 cluster **[20]**, and thus magnetic moments initialized parallel or perpendicular to one of the edges of the tetrahedron (and hence parallel to a twofold symmetry axis) converged to energetically degenerate stationary solutions. The size of the local spin and orbital moments was the same on all four sites, the local orbital moments were slightly canted relative to the overall magnetization directions. In this easy-axis orientation the magnetic point group was $m'm'2$. For magnetic moments oriented along a threefold symmetry axis only the cluster orbital moment was slightly enhanced and the magnetic point group was $32'$. This magnetic axis was disfavoured by a small MAE of 0.26 meV/atom. Although, for Pd_4 the crystallographic symmetry was preserved, the magnetic symmetry was

reduced, because no tetrahedral point group is compatible with a ferromagnetic state. Rotational symmetry was incompatible with ferromagnetic order between moments perpendicular to the symmetry axis.

For both Ni and Pd pentamers **[20]** the scalar-relativistic calculations predicted a trigonal bipyramid (point group symmetry $D_{3h} = \bar{6}m2$) to be the GS configuration. A spin of $S = 2$ was found for Ni_5 and $S = 1$ for Pd_5. Although, SOC stabilized a planar structure of the Pt_5 cluster and the rotation of the magnetization axis led to complex transitions between different magnetic isomers **[19]**, with SOC only the interatomic distances of both Ni_5 and Pd_5 were slightly affected. The crystallographic symmetry of the latter was reduced to $C_{2v} = mm2$. In the magnetic GS the easy magnetic axis was in the equatorial plane, along a twofold symmetry axis, and the magnetic point group was $m'm'2$ for the clusters of both elements. The in-plane anisotropy was determined by a rotation of the magnetization by an angle of 60°, which preserved the magnetic PGS. The hard magnetic axis was parallel to the threefold symmetry axis and the magnetic point group was $\bar{6}m'2'$ for both Ni_5 and Pd_5. Rotation of the magnetic axis left the local spin moments hardly changed, but the orbital moments slightly decreased (by up-to 0.04 μ_B)

For the Ni_6 cluster the scalar-relativistic calculations predicted a slightly distorted octahedral geometry with the PGS of $D_{4h} = 4/mmm$ and the magnetic moment of 8 μ_B. The GS structure of Pd_6 was a non-magnetic perfect octahedron (symmetry group $O_h = m\bar{3}m$). SOC left the geometry of the Ni hexamer unchanged, the total moment per cluster was reduced to 7.12 μ_B. The easy magnetic axis was parallel to the fourfold symmetry axis, with collinear spins and local orbital moments on the equatorial atoms canted by 7° relative to the spins and

on the apices canted by 17°. The magnetic point group was $4/mm'm'$. The hard magnetic axis of Ni_6 was parallel to one of the edges of the central square of atoms (i.e., along a twofold symmetry axis). In this configuration the fourfold rotational symmetry was broken, the magnetic PGS was $mm'm'$. The local spin moments remained unchanged but the local orbital moments on the four equatorial sites were reduced and those on the apical atoms were enhanced.

Applying SOC to the calculation for the Pd_6 octahedron promoted a magnetic GS structure with a cluster moment of $\sim$2.6 μ_B. A Jahn-Teller distortion lowered the symmetry to $D_{4h} = 4/mmm$. The magnetic moments were strictly aligned. The magnetic point group was $4/mm'm'$, as for the Ni_6 cluster. Also, the hard magnetic axis of Pd_6 was parallel to one of the edges of the equatorial square and the magnetic symmetry was reduced to $mm'm'$. A rotation of the magnetization direction from the easy to the hard magnetic axis inverted both the geometry of the cluster (the bonds between equatorial atoms were shortened, while those to the apical atoms were stretched) and the relative size of the local magnetic moments.

In summary, for clusters with a symmetry axis of order $n \geq 3$, FM order was compatible with rotational symmetry if the magnetization direction was parallel to the symmetry axis, but not for perpendicular magnetization. In this case magnetism broke the crystallographic symmetry of the cluster. For clusters with higher (tetrahedral or octahedral symmetry) no magnetic subgroup was compatible with a FM state. In this case the crystallographic symmetry was broken irrespective of the direction of magnetization. The former case was realized for the dimer, trimer and pentamer, the latter for the tetramer and hexamer (but note that the symmetry can also be broken even in the absence of SOC by a Jahn-Teller mechanism) **[20]**. In any case, the MAEs were small, at most around 2 meV/atom.

Importantly enough, even for a 3d metal such as Ni, the change in the magnetic symmetry led to small geometric distortions of the cluster such that there was a contribution to the MAE from the elastic energy. However, in this case SOC was not strong enough to affect the energetic ordering between different structural isomers. For the 4d metal Pd these effects were more pronounced, but qualitatively similar as for Ni **[20]**. For a 5d metal such as Pt, SOC was strong enough to stabilize for the smallest clusters structures, which were only metastable in the scalar-relativistic limit. In this case, due to the strong SOC, the magnetic anisotropy energies can be comparable or even larger than the energy differences between different magnetic isomers **[19]**.

Using perturbation theory, a formula relating the MAE to the product of the SOC strength and the orbital anisotropy has been proposed [23]. The derivation of this relation assumes isotropic spin moments (and implicitly also a geometric structure independent of the magnetization direction) and a completely filled majority band, and postulates that the largest orbital moment is always found for easy-axis magnetization. Similarly, the description of the MAE in terms of an effective Hamiltonian with a single giant-spin degree of freedom [132] assumes that the size of the effective spin moment remains unchanged upon rotation to the magnetization directions. The theory proposed in Ref. [23] has been extended by van der Laan [133] to account for terms contributing to second order and for a possible weak anisotropy of the spin moment. Results of References **[19, 20, 24]** demonstrated that, at least for the heavier elements, the spin moments were never isotropic and that the largest orbital moment was not always found for easy-axis magnetization. For the tetrahedral Pt_4 and the planar Pt_5 clusters different initial directions of the magnetization converged to different (FM/AFM) configurations.

Further, the changes in the electronic and magnetic structures induced by a reorientation of the magnetization axis were too important to be describable by perturbation theory. Hence, a perturbation treatment postulating that the cluster geometry is frozen, the spin moments are isotropic, and that the MAE is proportional to the orbital anisotropy was not justified for these small clusters.

3.1.4 Pt–Co and Pt–Fe trimers and tetramers

For dimers the origin of a large MAE is relatively simple: the two-fold degeneracy of a singly occupied state at the Fermi level for magnetization perpendicular to the dimer axis is lifted for an axial magnetization. The geometrical properties of the dimers, however, were not affected (apart from a modest change in the bond-length reported for Pt_2). Trimers and tetramers are the smallest clusters for which magneto-structural effects could appear. For a highly symmetric cluster the possible degeneracy of the electronic eigenstates near the Fermi level can be lifted also by a Jahn-Teller distortion. For mixed clusters containing a heavy atom contributing a large SOC such as Pt the magnetic structure is much more inhomogeneous and both SOC and the direction of magnetization can affect the geometric structure.

Important differences between the Pt–Fe and the Pt–Co clusters were already shown by the scalar-relativistic DFT. Substitution of one of the Pt atoms in Pt_n clusters by Fe enhanced the weak spin moment of 2 μ_B to 4, 6, and 6 μ_B in Pt_nFe with $n = 1, 2, 3$, while substitution by Co led only to a modest enhancement of the spin moment to 3 μ_B in mixed Pt_nCo. For Pt_3Co the low-moment state with 3 μ_B was energetically degenerate with a high-moment state with 5 μ_B. In $PtFe_n$ clusters the scalar-relativistic spin-moments of 4, 8, and 12 μ_B were found respectively for

$n = 1, 2, 3$, equal to the sum of the spin moments of n free Fe atoms, while for $PtCo_n$ a corresponding relation holds only for $n = 1, 2$ with the spin moment of 3 and 6 μ_B, whereas for $PtCo_3$ the spin moment reached only 7 μ_B. This showed that the interaction between Pt and Fe stabilizes a high-moment state of the mixed cluster, while mixed Pt–Co clusters carry a weaker magnetic moment **[30]**.

Tetramers are the smallest clusters where 2D and 3D geometries are in competition. The initial geometries were created by adding a Pt or a Co(Fe) atom to the relaxed structure of the trimer such as to complete a distorted trigonal pyramid or to form a deltoid. The high-moment state of Pt_3Fe, $PtFe_3$, but also of $PtCo_3$ tetramers stabilized a flat geometry (point group symmetry $2mm$) over the 3D arrangement in form of a distorted tetrahedron which was the ground-state of all three homo-atomic tetramers. In contrast to the preference for a flat geometry in Pt_4 this was not a relativistic effect, SOC even slightly reduced the structural energy difference. For Pt_3Co the tetrahedral geometry was lower in energy **[30]**.

The magnetic energy differences between the scalar-relativistic spin-isomers are also very important for understanding the influence of SOC which leads to a mixing of low-energy spin-states. For the Pt–Fe trimers and tetramers SOC led to a reduction of the spin moment which for the Pt-rich clusters was compensated or even slightly overcompensated by the orbital moment. In the Co-rich Pt–Co clusters the loss in the spin-moment was always overcompensated by the orbital moment, while for the Pt-rich clusters SOC led to a ground state with an increased total moment. For mixed clusters SOC also had a significant influence on the geometric structure, correlated to the change in the local moments. The structural consequences of SOC were most pronounced in $PtFe_3$ where the changes in the interatomic distances reached about 0.1 Å (Figure 3.6), they were much more

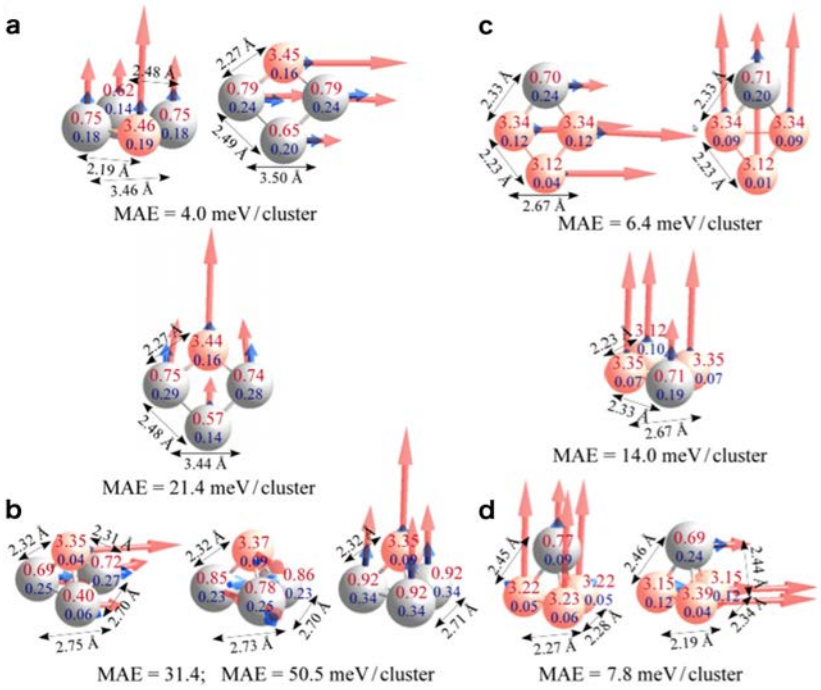


Figure 3.6: Geometric and magnetic structures of the 2D and 3D structural isomers of Pt_3Fe (**a**–**b**) and $PtFe_3$ clusters (**c**–**d**). The spin and orbital moments are represented by the red and blue arrows. Numbers on atoms denote local spin (upper value) and orbital magnetic moments (lower value) (in μ_B). The magnetic anisotropy energy is given relative to the ground state configuration. Reprinted from **[30]**.

modest in Pt–Co trimers and tetramers **[30]**.

In mixed trimers the point group symmetry was $2mm$ for all clusters. Due to the low symmetry, no degenerate electronic eigenstates exist for any orientation of the magnetization. The easy magnetic axis was in-plane, along the twofold symmetry axis and the magnetic point group symmetry was $2m'm'$ for Pt_2Co, $PtCo_2$ and Pt_2Fe. Only for $PtFe_2$ the easy axis was along the Fe–Fe edge, the magnetic point group symmetry was $m'm2'$. For all four trimers the calculations showed a strong orbital anisotropy, a weaker spin anisotropy and for some cases non-collinear local

moments and distortions of the interatomic distances as a function of the direction of magnetization. The MAE exhibited a depend on a complex interplay of (*i*) the orbital anisotropy, (*ii*) the spin anisotropy and (*iii*) the change in the geometric structure expressed by the changes in the interatomic distances. The dominant factor determining the strength of the MAE is the orbital anisotropy, but the dependence was not a simple proportionality **[30]**. Further, in some cases there were large differences in the MAE of different excited stationary configurations **[30]**. These differences are a measure for the anisotropy of the magnetic energy surface. The quantity determining the stability against a thermally induced reversal of the magnetization direction, however, is the energy of the lowest saddle point on the magnetic energy surface. For the trimers this energy varied between 6.7 meV/trimer for $PtCo_2$ and 11.3 meV/trimer for $PtFe_2$. The saddle point was associated with an in-plane rotation of the magnetic moment for $PtCo_2$ and Pt_2Fe and with a change from in-plane to perpendicular magnetization for $PtFe_2$ and vice-versa for Pt_2Co. These values were enhanced by about one order of magnitude compared to the energy barrier against in-plane rotation of the magnetization in Pt_3 of 0.6 meV/trimer **[19]** and also increased by about a factor of five compared to Co_3 and Fe_3 trimers. For the 2D tetramers the saddle-point energy varied between 3.1 meV/tetramer for $PtCo_3$ and 6.4 meV/tetramer for Pt_3Fe (in-plane rotation in both cases). The much larger MAE of the 3D Pt_3Co (Figure 3.7) was a particular case, associated with the degeneracy of different magnetic isomers without SOC. In this case a direct comparison with the Pt_4 tetramer is not possible because of antiferromagnetic ground state of the latter. The lowest barrier for the magnetization reversal of the excited FM state was 21.2 meV/tetramer **[19]**. Also, a modest enhancement compared to 3D Fe_4 and a strong one compared to Co_4 were found.

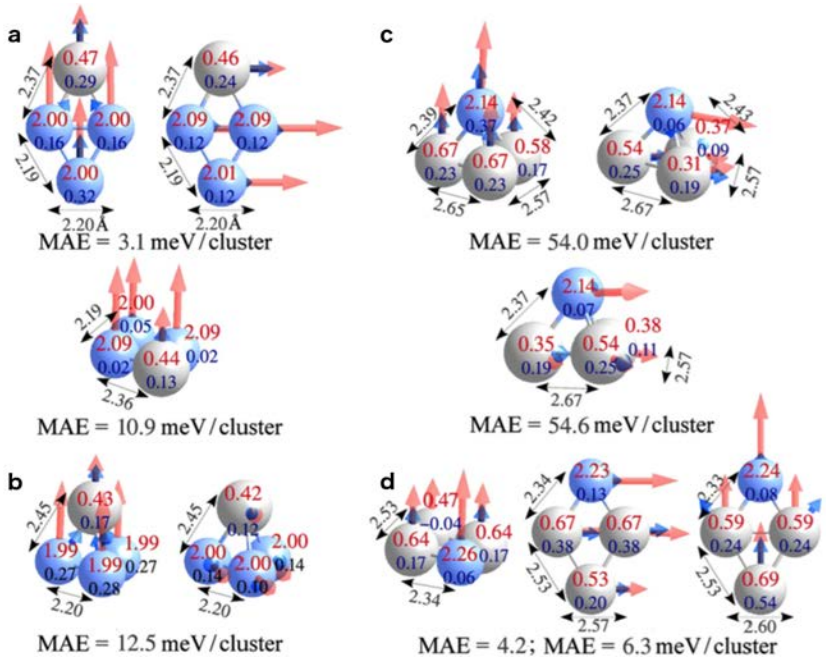


Figure 3.7: Geometric and magnetic structures of the 2D and 3D structural isomers of $PtCo_3$ (**a**–**b**) and Pt_3Co clusters (**c**–**d**). Cf. Figure 3.6. Reprinted from **[30]**.

3.2 Structures and MAEs of small transition-metal clusters supported on graphene

The results for gas-phase clusters are not of immediate practical relevance. A strong interaction between the nanostructure and support may lead to a strong quenching of the orbital moment and hence to an at least partial loss of their intriguing magnetic properties. A possible choice of a weakly reactive substrate of timely scientific interest was graphene. Apart from the unusual properties of the graphene sheet alone, the presence of metallic nanoparticles (clusters) on graphene may lead to further applications in catalysis [134–136] and in ultimately miniaturized magnetic devices [137, 138].

3.2.1 Pt_{1-5} on graphene

A single Pt atom adsorbed in the bridge (br) position between two C atoms. The adsorption energy of about -1.5 (-1.6) eV depending on the Pt coverage reflected the formation of a weak covalent bond between the p_z orbitals of the two neighbouring C atoms and the d_{xz} orbitals of the Pt atom (assuming a C–C bond parallel to the x-direction) **[25]**. The adsorption energy on top (ot) of a C atom was lower by only 0.18 eV, while the hollow site was strongly disfavoured, which showed that diffusion along the network of the C–C bonds requires an activation energy of only 0.18 eV. No magnetic moments were found on the Pt-adatom.

The Pt dimer adsorbed on graphene in an tilted configuration, i.e., its axis was tilted by 11° with respect to the surface normal, with its centre of gravity shifted by 0.115 Å from the br. The dimer carried a total magnetic moment of about 1.5 μ_B. The reduction of the magnetic moment relative to the gas phase dimer was almost

entirely due to the interaction with the support, the local magnetic moments were 0.9 μ_B on the upper and 0.55 μ_B on the lower Pt atom of the dimer. At the twice as large coverage of Pt, the adsorption energy was reduced by about 0.06 eV/Pt-atom, the distance of the lower Pt-atom from the graphene layer was increased from 2.11 to 2.26 Å, the adsorbate-induced buckling of the substrate was reduced from 0.23 to 0.14 Å. The repulsive interactions also led to an exactly upright position of the dimer. The magnetic moments remained, however, unchanged **[25]**. The binding between the Pt atoms forming the dimer was larger than in the gas-phase dimer. The adsorption energy per Pt-atom was higher for the dimer than for the isolated adatoms, and hence dimerization was predicted to be energetically favoured, in agreement with observations by STM [139] and field emission microscopy [140].

Relativistic calculations including SOC showed that the easy magnetization direction was oriented along the dimer axis at an increased total magnetic moment of 2 μ_B. The local spin and orbital moments were slightly noncollinear and both were much lower on the Pt atoms binding to graphene. Calculations initialized in a direction parallel to the graphene layer or perpendicular to the Pt dimer converge to a non-magnetic state. The energy for this magnetic to non-magnetic transition was ∼10 meV/Pt-atom **[25]**.

At the higher Pt coverage relativistic calculations predicted the easy magnetic axis again parallel to the dimer axis. The total magnetic moment was increased to ∼3 μ_B. For the magnetization perpendicular (and parallel to the graphene sheet), the total magnetic moment was only ∼1.1 μ_B. For both the easy and the hard magnetic axis, spin and orbital moments were collinear, the local orbital moments were antiparallel for the hard axis (Figure 3.8). The MAE of 11.6 meV/Pt-atom was only slightly higher than at lower Pt-coverage. A rotation of the magnetization

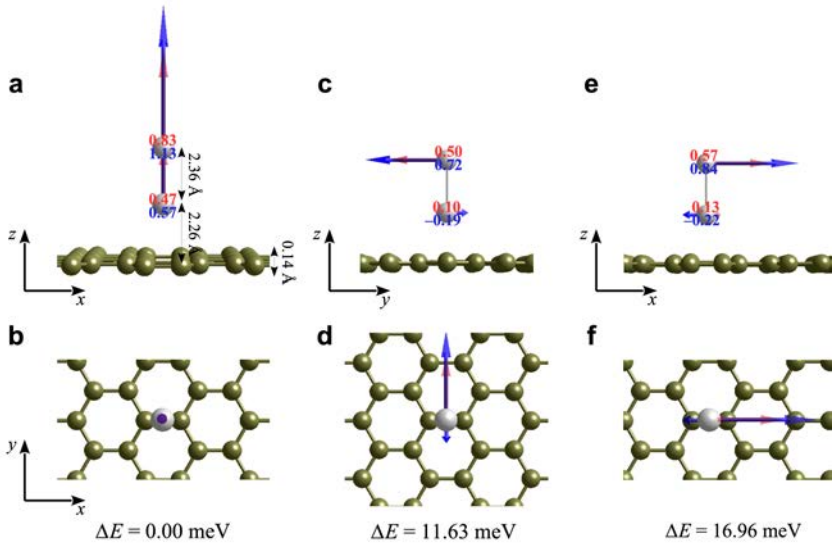


Figure 3.8: Geometric and magnetic structures of the Pt_2 cluster adsorbed on a freestanding graphene sheet. Cf. Figure 3.6. The easy magnetization direction is perpendicular to the graphene plane (**a**) and (**b**), but there is also a substantial in-plane anisotropy between configurations shown in (**c**), (**d**) and (**e**), (**f**). MAEs (ΔE in meV/Pt-atom) with respect to the easy-axis are also listed. Reprinted from **[25]**.

in a plane parallel to the graphene support cost an in-plane MAE of 5.33 meV. The formation of higher spin and orbital moments at increased coverage was due to a larger distance from and a weaker binding to the substrate. Compared to the gas-phase dimer, the MAE was reduced by more than a factor of 2, in line with a reduced anisotropy of both spin and orbital moments.

Pt_3 cluster on graphene adopted triangular geometry, similarly as in the gas-phase. Pt_3 triangle was almost perpendicular to the graphene layer and attached via either two Pt atoms (edge-down) to a position between br and ot, or via a single Pt atom (vertex-down) to a substrate atom. The former configuration was magnetic with a magnetic moment of 0.5 μ_B, the latter was non-magnetic and

higher in energy by 0.18 eV/cluster.

For the most stable edge-down configuration, the easy magnetic axis was parallel to graphene (to C–C bonds), but oblique to the triangular plane. Inversion of the magnetization direction by 180°, parallel to graphene, left total energy and total magnetic moment unchanged. The total magnetic moment of ∼1.1 μ_B was increased relative to the scalar-relativistic result, because SOC mixed different spin states. For in-plane magnetization, the calculation converged to a noncollinear solution with almost the same total magnetic moment of about 1.1 μ_B. The MAE calculated for these two magnetic solutions was only 1.72 meV/atom. This means the reduction of MAE to almost one third of the MAE of the free cluster. Spin moments were isotropic, but local orbital moments were changed by up to 0.09 μ_B relative to the easy axis.

In the optimized structures the Pt_4 cluster adapted a bent around the short diagonal rhomboidal geometry and formed only two Pt–C bounds to C atoms of the support. These two Pt atoms were two-fold coordinated by C atoms at a distance of 2.15 Å to the graphene layer. The atoms at both ends of the short diagonal bound less strongly to the graphene substrate than the remaining Pt atoms as they moved to a distance 3.87 Å above the graphene layer. The energy gain by adsorption was only modest, about 0.3 eV/Pt-atom. This structure was magnetic with a magnetic moment of 1.5 μ_B **[25]**.

Relativistic calculations including SOC were initialized with the magnetic moments perpendicular to the graphene layer, along the Pt_4 edges, and in an oblique direction **[25]**. The easy magnetic axis was perpendicular to the graphene layer, but all local moments were slightly canted away from the surface-normal. The hard axis was parallel to the graphene layer, aligned with the short diagonal of the clus-

ter. The total magnetic moment was enhanced relative to the scalar-relativistic spin-moment, because the mixing with low-spin states was overcompensated by the added orbital moment. Both spin and orbital moments were larger for the hard magnetization direction leading to a negative value of the anisotropy of the moments and only small MAE of 0.65 meV/Pt-atom.

Scalar relativistic calculations predicted for a gas-phase Pt_5 cluster a structure forming a trigonal bipyramid. However, SOC favoured a flat structure of a slightly distorted square and an isosceles triangle. With relaxed interatomic distances ranging from 2.42 to 2.51 Å this flat Pt_5 cluster fits well to the graphene layer with the Pt atoms located either on top of C atoms or at bridge sites **[25]**. The relaxation of these initial structures showed, however, that it is energetically unfavourable to former too many Pt–C bonds. In the GS configuration, Pt_5 was bound to two br sites of graphene via one edge of the triangle. The cluster remained almost flat, but rotated to an orientation almost perpendicular to graphene. Bond lengths were slightly elongated compared to the gas phase. The substrate was strongly buckled with an amplitude of 0.83 Å. The spin moment of 1.5 μ_B was lower than the spin moment of 2 μ_B of the free cluster.

Calculations including SOC converged for the noncollinear magnetic structure. This configuration was energetically degenerate with a structure in which the directions of local spin and orbital moments were reversed. The two configurations may be considered as right- and left-handed magnetic spirals turning around the point where the cluster is attached to the substrate (Figure 3.9). For the free flat Pt_5 cluster, a number of ferromagnetic high- and low-moment and also antiferromagnetic states were identified **[19]**, with energy differences comparable or even smaller than the magnetic anisotropy energies for a given magnetic state. For the

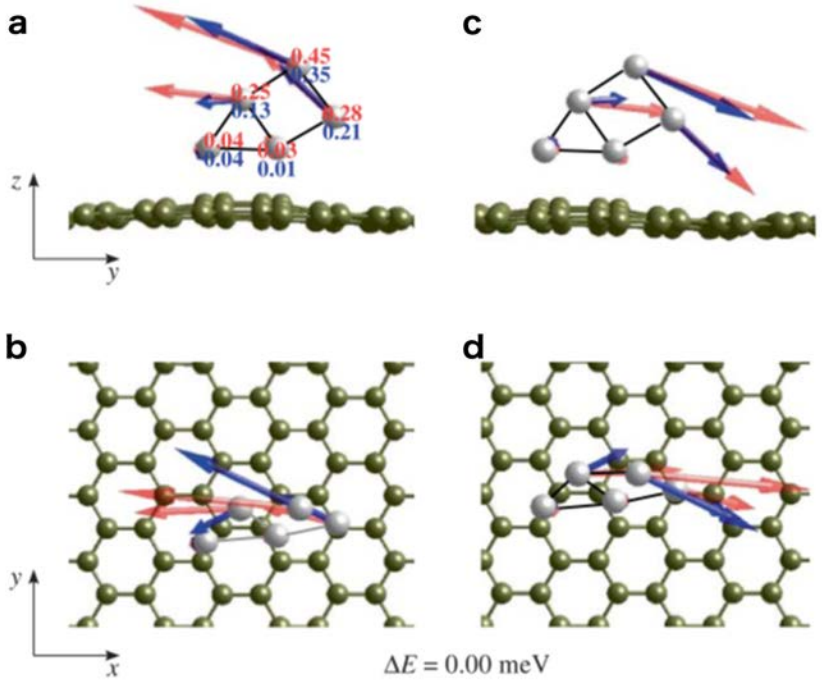


Figure 3.9: Side (**a** and **c**) and top view (**b** and **d**) of the magnetic structure of a flat Pt_5-cluster adsorbed on graphene. The two configurations are related by flipping the local spin and orbital moments to the opposite direction and they are energetically degenerate. Cf. Figure 3.6. Reprinted from **[25]**.

supported Pt_5 cluster, also a low-moment isomer with the total magnetic moment of 1.17 μ_B and a similar spiral-like noncollinear structure was found which was only 23 meV higher in energy than the GS.

Altogether, these results showed that in Pt_n clusters with two and more atoms the structure of the gas-phase cluster is preserved, although distorted, because Pt–Pt interactions were found to be much stronger than the Pt–C interactions promoting the binding to the support. The adsorption energy per atom increases with the size, favouring the growth of clusters. However, the clusters bound to

graphene only via at most two Pt–C bonds: a Pt_2 dumbbell preferred an upright position, the larger clusters bound to graphene only via one edge of the planar cluster (Pt_3 and Pt_5) or via two terminal Pt atoms of a bent Pt_4 rhombus. Evidently, the strong buckling of the graphene layer (with an amplitude increasing from 0.23 Å for the dimer to 0.83 Å for a Pt_5 cluster) induced by the Pt–C bonds prevents the formation of a larger number of cluster-support bonds. As the local spin and orbital magnetic moments were quenched on the Pt atoms forming Pt–C bonds, the magnetic structures of the supported clusters were much more inhomogeneous than the gas-phase clusters. This led to noncollinear magnetic structures and a strongly reduced MAE.

3.2.2 Bimetallic dimers on graphene

For PtCo, PtFe, and IrCo dimers supported on graphene, the strong binding within the dimer and the stronger interaction of the 3d atom with the substrate bound in a sixfold hole stabilized an upright geometry and led to free-atom like properties of the upper 5d-atom, which is very important for achieving a high MAE **[28]**.

The influence of the support on the electronic and magnetic properties of adsorbed dimers depends on the overlap of their eigenstates with the electronic DOS of graphene (Figure 3.10a–c). In the stable adsorption geometry the 3d atom of the dimer(s) was located above the centre of a sixfold hole, at a height of about 2 Å above the C atoms. The rotational invariance of the dimer eigenstates around the axis was broken and the C_∞ symmetry was replaced by C_6. The dimer–graphene interaction was realized by forming chemical bonds between the δ_d (d_{xy}, $d_{x^2-y^2}$) states of the 3d atom and the sp^2-hybrids of the C atoms, and between

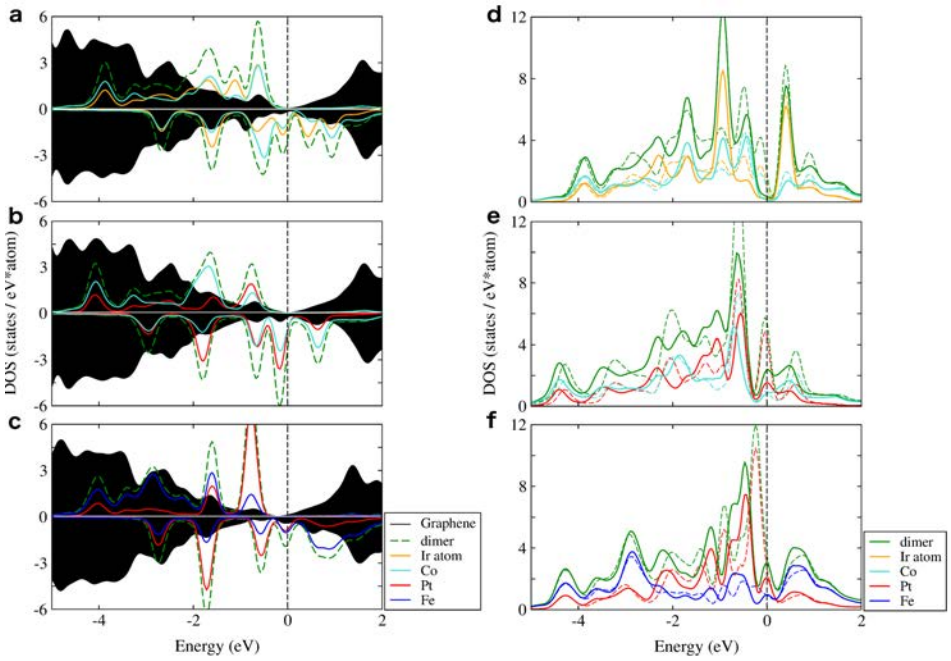


Figure 3.10: Spin-polarized scalar-relativistic DOS for **a,** IrCo; **b,** PtCo; and **c,** PtFe dimers adsorbed on a graphene layer. **d–f,** Corresponding site decomposed electronic DOS calculated including SOC for magnetization perpendicular to the support and parallel to the dimer axis (along the z-direction, full lines) and for magnetization parallel to the support and perpendicular to the dimer (along the x-direction, broken lines). Adapted from **[28]**.

the π_d (d_{xz}, d_{yz}) states and the p_z states on the C atoms. The extended σ_s and $\sigma_s^\star$ states of the dimer were up-shifted because of the Pauli repulsion. The shift of the antibonding state was particularly important for PtFe/graphene. The eigenstates of the metal atoms underwent a bonding/antibonding splitting and broadening by the hybridization with the substrate orbitals. These effects were most pronounced on the π_d states with a large weight on the 3d atom. Broadening and level shifts were less pronounced for the δ_d states where the structure of the spectrum of the free dimer was clearly recognizable in the DOS of the dimer/graphene complex.

The MAE was found to be determined by changes in the partial d-band DOS close to the Fermi level dependent on the direction of magnetization **[28]**. For IrCo/graphene the most important was the change in the δ_d partial DOS upon a rotation of the magnetic moments (Figure 3.11a). For magnetization parallel to the graphene layer and perpendicular to the dimer axis (along the x-axis), the partial DOS showed a dominant peak at the Fermi level corresponding to the singly occupied $\delta_d^\star$ state of the free dimer (Figure 3.3a). For perpendicular magnetization (along the z-axis) this peak was split into two components about ± 0.4 eV from the Fermi level, again in analogy to the splitting of the eigenvalues of the free IrCo dimer. The site-decomposed DOS revealed that for the supported dimers the change in the highest occupied eigenstates was much more pronounced on the Ir than on the Co atom and this explained the increased orbital moment on the Ir atom and the increased MAE of the graphene-supported compared to the free dimer.

The physical origin of the MAE is essentially the same for the free and the graphene-supported PtCo dimers (Figure 3.3b and Figure 3.11b), but the broadening of the eigenstates caused by the interaction with graphene reduced the influence of the SOC-induced shifts of the eigenstates on the MAE. For PtFe/graphene the large shift of the $\sigma_s^\star$ state caused by the Pauli repulsion between the extended electron density on the dimer and the charge distribution in the substrate changed the nature of the states at the Fermi level leading to an electronic structure close to the Fermi level similar to that of the isoelectronic IrCo/graphene dimer. The magnetic anisotropy was determined by the SOC-induced splitting of the partially occupied $\delta_d^\star$ state, as for the IrCo/graphene system. The easy direction was along the dimer axis, as for the other dimers, and the MAE exceeded than for PtCo

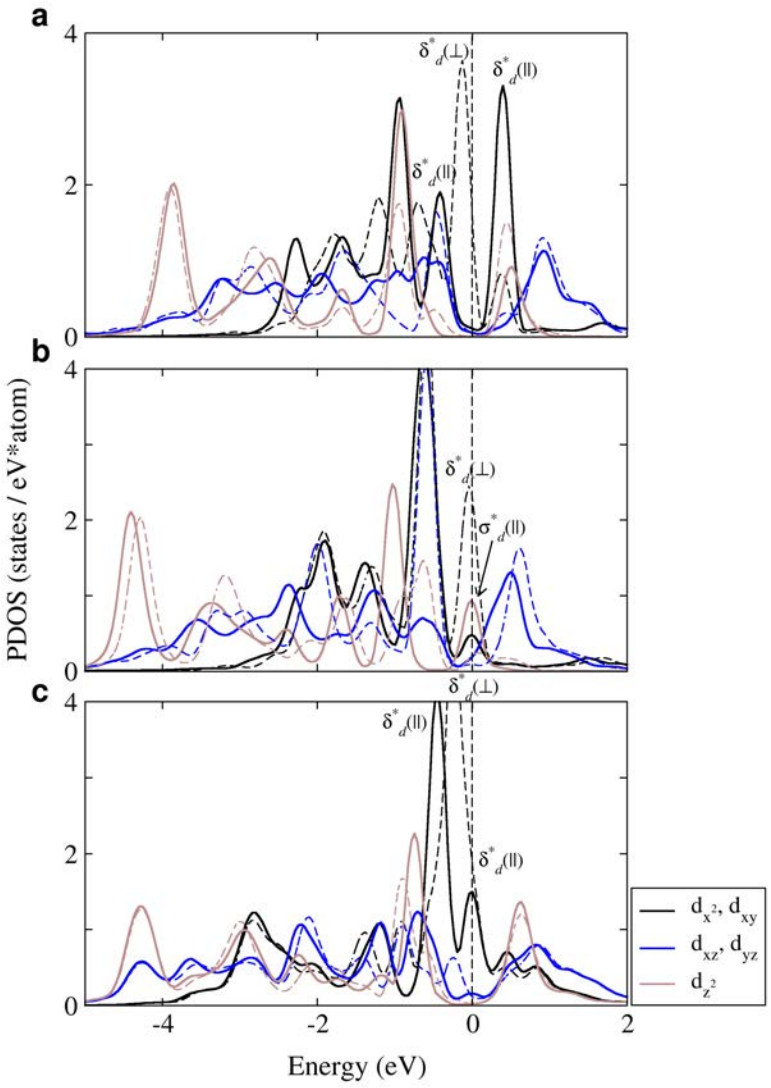


Figure 3.11: Partial d-band DOS for **a,** IrCo; **b,** PtCo and **c,** PtFe dimers adsorbed on a graphene layer, calculated including SOC for magnetization perpendicular to the support and parallel to the dimer axis (along the z-direction, full lines) and for magnetization parallel to the support and perpendicular to the dimer (along the x-direction, broken lines). Reprinted from **[28]**.

(13.4 vs. 11.7 meV/dimer) **[28]**.

3.2.3 Pt–Co and Pt–Fe trimers and tetramers on graphene

Mixed trimers adsorbed parallel to the graphene layer were found to be unstable. The trimers bound to graphene preferentially through the 3d atoms. Due to the strong cluster-substrate binding the influence of SOC on the cluster geometry was minimized. Interatomic distances changed only by less than 0.01 Å **[30]**.

In the most stable configuration both the $PtFe_2$ and $PtCo_2$ cluster bound to the graphene layer by the two Fe (Co) atoms located close to 6h sites. The PGS was $2mm$ as for the free clusters. The total magnetic moment of the $PtFe(Co)_2$/graphene complex was 6 (4) μ_B, reduced by 2 μ_B compared to the free trimers.

Calculations including SOC predicted **[30]** for both $PtFe_2$ and $PtCo_2$ an easy magnetic axis perpendicular to the graphene sheet and to the bond between 3d atoms. The total magnetic moments were enhanced in both cases relative to the scalar-relativistic spin moment largely due to the added orbital moments. The local orbital moments on the 3d atoms were non-collinear. Rotation of the magnetization to a direction parallel to the graphene layer and perpendicular to the cluster plane cost an MAE of 3.3 and 8.6 meV/cluster, respectively for $PtFe_2$ and $PtCo_2$. The total moments were slightly enhanced for $PtFe_2$, which arose from weak negative spin and orbital anisotropies on the Fe sites at the isotropic Pt moments, but reduced for $PtCo_2$ due to quenched spin and orbital moments.

In-plane rotation of the magnetic moments to the cluster plane and parallel to the bond between 3d atoms left the total spin moment of $PtFe_2$ unchanged, and led to a small negative orbital anisotropy on the Pt atom and a very modest positive orbital anisotropy on the Fe sites. This solution was 8.9 meV/cluster higher in

energy than the GS solution. The magnetic point group symmetry was $2m'm'$ for the GS and $m'm2'$ for the two magnetic excited states **[30]**. For $PtCo_2$, in turn, an in-plane solution with the total moment pointing along the Co–Co bond led to the increased spin and orbital moments, and cost an MAE of 11.3 meV/cluster. The magnetic point group symmetries were the same as for the free $PtCo_2$ trimer, but the energetic ordering of the excited states was reversed.

For mixed four-atom clusters supported on a graphene layer the 2D geometries were unstable, in all cases the structural optimization led to a transformation from the 2D-configurations parallel to the graphene layer to 3D-structures. The tetramers also bound to graphene preferentially through the 3d atoms. For the 3d-rich tetramers the stable geometry was in both cases a pyramid with the 3d-atoms close to six-fold hollows of the graphene layer. The trigonal symmetry was broken, but for $PtFe_3$ this was reflected only in a small difference in the Fe–Fe distances and not in the local spin moments, while for $PtCo_3$ the local spin moments were also different. The Fe–Fe and Co–Co distances were stretched compared to the free tetramer due to the binding to the substrate.

The total magnetic moment of the $PtFe_3$/graphene complex was 9 μ_B, reduced compared to 12 μ_B for the free tetramer. The contribution of the magnetic moments induced on the C atoms was about 0.5 μ_B, the spin on the Fe atoms was reduced by about 0.6 μ_B, the spin on the Pt atom by 0.4 μ_B compared to the free $PtFe_3$ cluster.

The easy magnetic axis of the trigonal $PtFe_3$ pyramid was perpendicular to graphene and to the basal Fe_3 triangle (magnetic point group symmetry $3m$), with a spin moment of 8.40 μ_B and an orbital moment of 0.52 μ_B. Two states with in-plane magnetization and the total moment either parallel or perpendicular to

an Fe–Fe bond were found to be energetically degenerate (these were the magnetic hard axis), with an MAE of 12.4 meV/cluster. The threefold symmetry was lost, but this was manifest only for the local orbital moments. The spin moments were strictly isotropic, the orbital moments on the Fe atoms were reduced to about half value for easy-axis magnetization.

The total magnetic moment of the $PtCo_3$/graphene complex was 5 μ_B, reduced by 2 μ_B compared to the free cluster. Small magnetic moments were induced in the slightly buckled graphene layer (-0.26 μ_B in total), oriented antiparallel to the cluster moment. In the magnetic GS of the $PtCo_3$ pyramid the local spin and orbital moments on the Co atoms were non-collinear, reflecting the asymmetry of the geometric structure. The easy magnetization direction was perpendicular to the Co–Co bond and parallel to a C–C bond of the graphene layer and tilted away from the graphene-sheet. The total magnetic moments of the cluster was 5.63 μ_B (spin/orbital moments were 5.17/0.46 μ_B). For a magnetization direction initially perpendicular to the support the relaxed local moments were canted towards the Pt–Co bonds, but their absolute values remained almost unchanged and the MAE was only 1.3 meV/cluster. For a magnetization perpendicular to another Co–Co bond, the total magnetic moment was again almost unchanged, but the energy was increased by 2.3 meV/cluster. The small MAE of supported $PtCo_3$ correlates with a very small orbital anisotropy.

Compared to the free trimers, the saddle point energy to be overcome for a magnetization reversal was lowered for $PtFe_2$ by more than a factor of 3, but remained of the same order of magnitude for $PtCo_2$. The MAE of 5.1 meV/trimer calculated for Pt_3/graphene was in-between the MAE of $PtFe_2$/graphene (3.3 meV/trimer) and $PtCo_2$/graphene (8.6 meV/trimer) **[30]**.

Compared to the free tetramers, the minimum barrier for magnetization reversal was lowered by a factor of 6 for $PtCo_3$ but almost doubled for $PtFe_3$ **[30]**. The larger MAE is related to a larger orbital anisotropy on the Fe atoms binding to graphene. Compared to the graphene-supported Pt_4 (which adopted a similar 3D structure) with a barrier energy of ∼40 meV/cluster, a reduction by about a factor of 4 for $PtFe_3$/graphene and 20 for $PtCo_3$/graphene were found. However, compared to the MAE of the GS Pt_4/graphene geometry, the graphene supported mixed $PtFe_3$ tetramers forming quite symmetric adsorption geometries exhibited an increased MAE by a factor of ∼5, but similar MAE was found for $PtCo_3$/graphene resulting from very small total spin and orbital anisotropies.

3.3 Structures and MAEs of clusters of Pt_{1-4} on graphene on Ni(111)

The study of the graphene/metal interface was motivated by several important points: (*i*) metallic substrates were demonstrated to be successfully used for the preparation of graphene layers of different thicknesses with the extraordinary quality that can be transferred onto an insulating or polymer support, (*ii*) the metallic contacts to a graphene layer determine the doping of graphene and, thus, the transport properties, (*iii*) the deeper understanding of nature of bonds at the metal-graphene interface itself is of fundamental importance, and (*iv*) from applications point-view of graphene-supported magnetic nanoclusters, the carbon sheet must be deposited on a solid substrate [141], and the the interaction between the adsorbed clusters and the metallic support across the graphene layer can heavily influence the the structural and magnetic properties of graphene-deposited metallic

clusters **[26, 27, 29]**.

Both experiment and ab initio calculations revealed that the top/fcc configuration is a stable configuration of a graphene sheet supported on Ni(111) (see **[26]** and references cited therein). Since the GGA calculations predicted no binding of the graphene sheet to the Ni substrate, the the DFT+d method of Grimme [142] was used which predicted both binding energy and distance in very good agreement with the chemisorbed state identified in the random phase approximation – adiabatic connection and fluctuation dissipation theorem (RPA-ACFDT [143]) calculations [144]. The interaction with the Ni substrate strongly influenced the electronic structure of the graphene layer (Figure 1a–b in **[26]**). The hybridization with the 3d-states of Ni led to the formation of two peaks in the C-p DOS coincident with the peaks in the substrate DOS. Due to the exchange splitting, the C-p spin-up DOS showed a local minimum, the spin-down DOS a local maximum at the Fermi level. The exchange-splitting of about 0.5 eV was in good agreement with the experimental estimate [145]. The hybridization of the π and $\pi^\star$ bands of graphene with the substrate states is essential for the stability of the C/Ni interface. At an increased distance of the graphene to the Ni(111) surface, the hybridization disappeared almost completely [144].

Although the free-standing ideal graphene sheet is non-magnetic, the binding to the Ni(111) surface induced a weak magnetic polarization of the C-atoms **[26]**. The C-atoms located on top of Ni atoms carried a magnetic moment of $-0.014\ \mu_\mathrm{B}$/atom, whereas a magnetic moment on atoms in a fcc-hollow was $+0.017\ \mu_\mathrm{B}$/atom. A weak induced magnetism of carbon atoms in the graphene/Ni(111) system has also been observed experimentally [146]. The magnetic spin moments on Ni atoms were 0.54, 0.62, and 0.65 μ_B/atom in the 1st, 2nd, and successive lay-

ers, respectively. The magnetic moment in the 1st layer of Ni(111) was quenched due to the presence of C adlayer (0.65 μ_B/atom at the clean Ni surface). The graphene/Ni(111) system exhibited a small in-plane MAE of 0.145 meV/atom. The orbital moments of the Ni atoms were 0.065, 0.054, 0.056, and 0.075 μ_B in the first and subsequent layers for in-plane magnetization, and 0.045, 0.053, 0.053, and 0.046 μ_B for perpendicular magnetization. The spin moments in adlayer and substrate were unchanged, independent of the orientation of the magnetization. Spin and orbital moments were strictly parallel. The slightly larger orbital moments for easy-axis orientation correspond to the classical picture of magnetic anisotropy.

The stable adsorption site of an isolated Pt adatom was in a bridge-position between two C atoms of the graphene layer. While the adsorption site is the same as on a free-standing graphene sheet, the adsorption energy increased almost by a factor of 2. Further, the Pt atom also induced a strong, rather complex corrugation of the graphene layer and of the top Ni layers. The bonds between the C atoms around the Pt adatom are less saturated and this led to a stronger binding between graphene and the Ni substrate such that the Pt atom is located in the centre of a deep, rather broad depression of the adlayer. Pt adatoms carried a small magnetic moment of -0.02 μ_B, which contrasts the Pt adatoms on free-standing graphene which were non-magnetic. The magnetic moments of the graphene/Ni system were hardly affected by the presence of Pt adsorbate. Only on the Ni atom almost directly below the Pt atom the magnetic moment was enhanced to 0.65 μ_B. This enhancement is remarkable because adatom and substrate were separated by the graphene layer. Calculations including spin-orbit coupling predicted a small anisotropy of the spin moment of the Pt atom, i.e., -0.022 μ_B for in-plane and -0.018 μ_B for perpendicular magnetization. The orbital moment of the Pt atom

was +0.021 μ_B for perpendicular and +0.008 μ_B for in-plane magnetizations. The easy magnetization direction of the entire complex was in-plane and the MAE was reduced to the value below 0.1 meV/atom **[26]**.

In contrast to the dimer on a free-standing graphene layer the stable configuration is a flat-lying dimer with both Pt atoms located slightly off an ot position above a C atom. The adsorption energy per Pt atom was lower than for the isolated adatom. Therefore, whereas on a free-standing graphene layer the formation of dimers and larger clusters was energetically favoured (and facilitated by a high mobility of the Pt atoms), isolated adatoms on graphene/Ni(111) were lower in energy. The formation of dimers was also hindered by an increased diffusion barrier (from 0.18 eV to 0.72 eV due to the presence of the Ni support).

The flat dimer was non-magnetic as on free-standing graphene. The upright dimer carried a magnetic moment of 1 μ_B, reduced compared to a value of 1.5 μ_B in the absence of a metallic substrate. Remarkably, the presence of the Pt dimers on the graphene/Ni(111) surface induced a re-orientation of the easy magnetization direction from in-plane to perpendicular, as for a dimer on a free-standing graphene layer. The MAE of the upright Pt dimer on graphene/Ni(111) was 49.6 meV (or 0.34 meV/atom including 96 Ni, 48 C, and 2 Pt atoms in the computational cell), to be compared with an MAE of 23.2 meV for the Pt dimer on a free graphene layer and of 46.2 meV for the gas-phase dimer **[26]**.

The Pt_3 triangle was bound to the free graphene sheet only via one of its edge. On Ni-supported graphene a flat triangle allowing a binding of all three Pt atoms with the graphene layer was, however, lower in energy by 46 meV/Pt-atom than a perpendicular configuration where the cluster binds to the substrate only via one of its edges **[27]**. The threefold symmetry of the cluster was broken

by a minimal difference of 0.02 Å in the Pt–Pt distances. The Pt atoms were located almost on top of the C atoms, slightly shifted towards the C–C bridge positions. The Pt_3 cluster induced substantial distortions of the graphene layer. It was located in the centre of an extended depression of the graphene layer, whose buckling amplitude was 0.4 Å. The local spin-moments on the Pt atoms calculated in a scalar-relativistic approach reflected the broken symmetry of the Pt_3 triangle. The spin and orbital moments per cluster calculated including SOC were smaller for the easy in-plane than for the hard perpendicular magnetization direction, leading to negative spin and orbital anisotropies. The local distribution of the magnetic moments below the cluster is similar to that for Pt adatoms and dimers on graphene/Ni(111) **[26]**. The MAE of the complex was 13.2 meV/cell or 0.089 meV/atom.

For a Pt_4 cluster on graphene/Ni(111) the equilibrium configuration was almost flat rhombus with all four Pt atoms in or close to positions on top of C atoms in the graphene layer **[27]**. This configuration was, however, only 9 meV/Pt-atom lower in energy than a trigonal pyramid with the Pt atoms forming the base located close to C atoms, slightly displaced towards the neighbouring bridge positions. In both configurations the Pt_4 cluster was located in the centre of a sink in the graphene layer, as for the smaller clusters. Also, the buckling amplitude of the graphene layer of about 0.4 Å was the same for both configurations and comparable to that induced by the smaller clusters. The binding between graphene and the Ni substrate in this region was promoted not only by dispersion forces as in the absence of adatoms, but also acquires a weak covalent component. The scalar-relativistic spin moments on the Pt atoms were 2×0.10 and 2×0.12 μ_B for the rhombus. Relativistic calculations including SOC for an easy in-plane magnetization direction

led to slightly reduced spin magnetic moments to 2×0.090 and 2×0.081 μ_{B}, and the orbital moments of 2×0.039 and 2×0.023 μ_{B}. The hard magnetic axis was out-of-plane. All local spin moments were reduced, but the orbital moments were reduced only on the sites along the long diagonal, but enhanced on the other two sites. Altogether, this led to a substantial spin anisotropy of 0.136 μ_{B} and a very low orbital anisotropy of 0.022 μ_{B}. The influence of the adsorbed cluster on the magnetic moments in the Ni layer was very similar to that caused by the smaller clusters. The MAE of the cluster/substrate complex was 15.8 meV/cell or 0.091 meV/atom.

The force theorem permits the elucidation of the electronic contributions to the MAE from the clusters, the graphene layer and from the Ni substrate. Within this formalism, the MAE may be written as **[17, 27]**

$$MAE = \sum_{i} \sum_{m_l=-2}^{2} \int_{E_B}^{E_{\mathrm{F}}} (E - E_{\mathrm{F}}) \Delta n^i_{m_l}(E) dE \ , \tag{3.1}$$

where the sum is over all atoms in the supercell and over all angular momentum quantum numbers m_l, E_B is the energy at the bottom of the valence band, and where

$$\Delta n^i_{m_l}(E) = n^i_{m_l}(E; soft) - n^i_{m_l}(E; hard) \tag{3.2}$$

is the difference in the partial local density of states for electrons with quantum number m_l at the site i for soft- and hard-axis magnetization. Integration over the $\Delta n^i_{m_l}(E)$ also yields the orbital anisotropy

$$\Delta \mu_L = 2\mu_B \sum_{i} \sum_{m_l=1,2} \int_{E_B}^{E_{\mathrm{F}}} \left[\Delta n^i_{m_l}(E) - \Delta n^i_{m_{-l}}(E) \right] dE \ . \tag{3.3}$$

A large contribution to the MAE requires a large value of $\Delta n^i_{m_l}(E)$, integrated over the valence band, irrespective of the value of m_l. A significant orbital anisotropy

arises only if $\Delta n^i_{m_l}(E)$ is different for states with $m_l = \pm 1$ and/or $m_l = \pm 2$. One shall note that since the partial DOS are based on a projection of plane wave onto spherical waves inside atom-centred spheres, the determination of the partial contributions to the MAE from integrals over the difference in partial DOS is approximate. The analysis of the MAE showed that the magnetic anisotropy of the Pt_n/graphene/Ni(111) complex was dominated by the Ni support. Although the SOC is much stronger and the orbital moment is larger for Pt than for Ni, the contribution to the MAE per Pt atom was lower than that per Ni atom at the interface with graphene. Only for the metastable upright Pt_2 dimer the spin and orbital moments on the Pt atoms were large enough to reverse the sign of the magnetic anisotropy of the graphene-covered Ni-substrate **[26, 27]**.

Similarly, significant contribution to the MAE has been found for Fe and Co adatoms **[17]** on (111) surfaces of strongly polarizable Pd and Rh substrates which are, however, non-magnetic without adsorbates. The adatom-substrate hybridization led to strong reduction of the adatom orbital moments but also to the formation of large spin and orbital moments in the substrate **[16,17]**. As a consequence, the substrate contribution can even determine the sign of the MAE. The magnitude and the sign of MAEs changed for adatoms occupying face-centered cubic (fcc) with respect to adatoms on hexagonal close-packed (hcp) hollows on the (111) surfaces **[17]**. However, in the monolayer (ML) limit, in addition the dipolar interactions between the magnetic moments significantly contributed to MAEs **[18]**. For the Co ML on Rh(111), the dipolar contribution outweighed the band contribution and determined the in-plane MAE in agreement with experiment.

3.4 MAEs of transition-metal dimers on graphene on Cu(111)

In contrast to the graphene/Ni(111) complex, on a noble-metal Cu(111) support the graphene layer was only physisorbed. The binding energy was −42 meV per C-atom at an equilibrium distance of 3.13 Å between the carbon layer and the Cu surface **[29]**.

Homoatomic Ir_2 and Pt_2 dimers preferentially bound to the graphene/Cu(111) complex in a flat configuration with both atoms binding to C–C bridge sites. The adsorption strength on graphene/Cu(111) was between that on freestanding and Ni-supported graphene. The flat dimers were only weakly magnetic with a very small MAE of ∼1 meV/dimer **[29]**.

For the mixed 5d–3d IrCo and PtCo dimers on graphene/Cu the much stronger binding of the 3d than of the 5d atoms to the support led to a preference for an upright configuration, as on freestanding graphene **[28]**. The magnetic structures of the mixed dimer is displayed in Figure 3.12. The magnetic moments on the 3d atom bound to the substrate were strongly quenched and the 5d moments were also reduced, for PtCo to values much lower than for the free dimer, whereas for IrCo they assumed intermediate values. The MAE was reduced for PtCo to 7.2 meV/dimer but enhanced for IrCo to enormous 0.2 eV/dimer. This striking difference can be understood by analysing the electronic DOS, presented in Figure 3.13. For the graphene/Cu(111) supported IrCo dimer the partially occupied spin-down $\delta_d^\star$ state is located at E_F. It is dominated by contributions from the Ir atom and almost unaffected by interaction with the substrate. A further contribution to the MAE resulted from the splitting of the bonding spin-up δ_d state at the bottom of the partial δ-DOS (formed by the $d_{x^2-y^2}$ and d_{xy} states) whose centre of gravity was

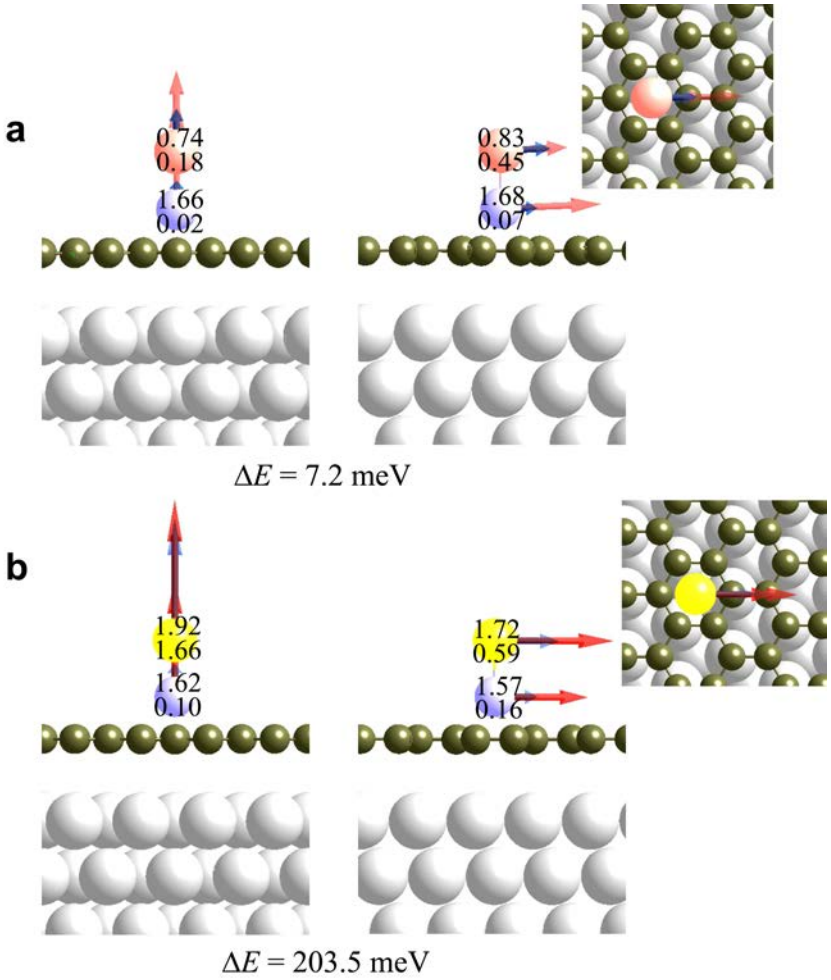


Figure 3.12: The magnetic structure of **a,** PtCo (Pt-up) and **b,** IrCo dimer (Ir-up) on graphene/Cu(1 1 1). Cf. Figure 3.6. The energy difference associated with a rotation of the magnetic moments (per dimer) are listed underneath each structure. Reprinted from **[29]**.

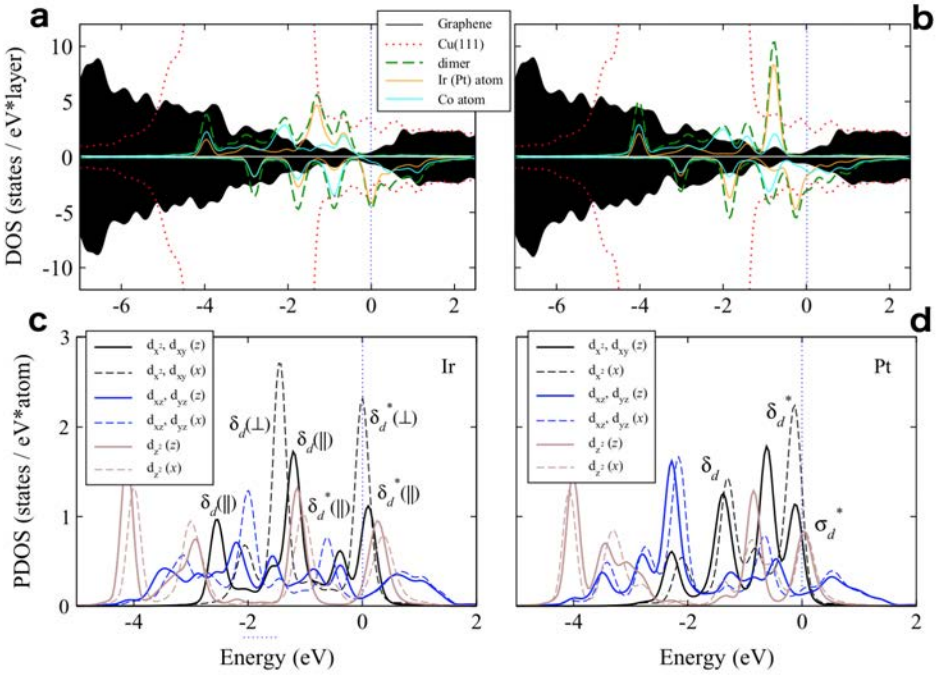


Figure 3.13: Scalar relativistic DOS (**a-b**) and atom- and orbital-resolved PDOS (**c-d**) for magnetization along the dimer axis (the z-axis, full lines) and perpendicular to it along the x-axis (broken lines) for IrCo dimer (**a** and **c**) adsorbed on graphene/Cu(111), and PtCo dimer (**b** and **d**) supported on graphene/Cu(1 1 1). Adapted from **[29]**.

shifted towards larger binding energies and contributes to the further enhancement of the MAE in the sequence: free IrCo (MAE = 69 meV/dimer) → IrCo/graphene (93 meV/dimer) → IrCo/graphene/ Cu(111) (204 meV/dimer).

For the PtCo dimer on graphene/Cu(111) the spin-down $\delta_d^\star$ state is fully occupied and located just below the Fermi level. Unlike for the free dimer, the SOC-induced splitting of the states did not reorder the energy levels and the σ_d state remained higher in energy. However, as the separation of the states is very small, the σ_d state is partially populated at the expense of the antibonding $\delta_d^\star$ state. The orbital moment on the Pt atom for PtCo/graphene/Cu(111) was lower than for

the free dimer and much lower than for PtCo/graphene, which was related to the strong mixing of the fully occupied $\delta_d^\star$ state with an energetically almost degenerate σ_d state. The mixing was even stronger for perpendicular magnetization, leading to a strong negative orbital anisotropy on the Pt atom. Together, the contribution of all eigenstates to the MAE decreases from the free to the graphene-supported and further to the dimer on graphene on Cu(111). Accordingly, the MAE decreases with increasing strength of the interaction with the support: free PtCo (MAE = 19 meV/dimer) → PtCo/graphene (12 meV/dimer) → PtCo/graphene/Cu(111) (7 meV/dimer) **[29]**.

3.5 Imprinting magnetism in graphene

Graphene – a 2D allotrope of carbon – is currently at the forefront of the scientific interest owing to its unique electronic, mechanical, optical, and transport properties. Its application potential covers a broad portfolio of disciplines, the most prominent examples include lightweight, thin, flexible, yet durable display screens, electric/photonics circuits, solar cells, and various medical, chemical and industrial processes enhanced or enabled by the use of new graphene-based materials [49, 85]. To further extend the applicability of graphene, several efforts have recently been reported to equip graphene with magnetic properties **[43]**, which are intrinsically missing in graphene due to a delocalized π-bonding network leaving no unpaired electrons. If graphene was modified to show magnetic ordering sustainable at elevated temperature, it would cause a revolution in electromagnetic, optomagnetic, and spintronic applications, opening doorways to new and effective technological concepts [147]. Without any doubt imprinting magnetic features into graphene has been considered a holy grail for physicists, chemists, and materials

scientists since the graphene isolation in 2004 [6]. The current approaches leading to equip graphene with magnetic properties include spatial confinement and edge engineering, doping of graphene lattice with foreign atoms, and sp^3 functionalization **[43, 68, 69, 75, 76, 91]**. The theoretical results presented below provided insights into the origin of magnetism in graphene-based systems.

3.5.1 Magnetism induced by doping graphene with foreign atoms

As already briefly mentioned (see Section 1.3 and Figure 1.16), doping of graphene lattice with non-carbon atoms offers a promising approach for imprinting the magnetic ordering into graphene **[75,76]**. Spin-polarized DFT calculations allowed both to gain a deeper understanding of the unique magnetic behaviour of doped graphene and decipher the effect of various bonding configurations of the dopant atoms on its the electronic and magnetic properties.

Magnetic measurements showed that doping graphene with 4.2 at% of sulfur equips it with FM properties below ∼62 K with a saturation magnetization reaching 5.5 emu/g **[75]**. Electronic-structure calculations confirmed the observed magnetic behaviour appears in a narrow concentration window (4–6 at%). Graphene doped with 2.1 at% of sulfur and above 6.25 at.% was non-magnetic. Calculations including both sulfur adsorption on a pristine graphene layer and simultaneous sulfur adatoms and substitution did not induce magnetism in graphene even when starting from an initial magnetic guess configuration. Thus, the magnetic ordering observed experimentally was solely related to the substitutional doping. The theory showed that in magnetically active configurations sulfur forms the gamma-thiothiapyrone motif in the graphene lattice (see inset in Figure 3.14a).

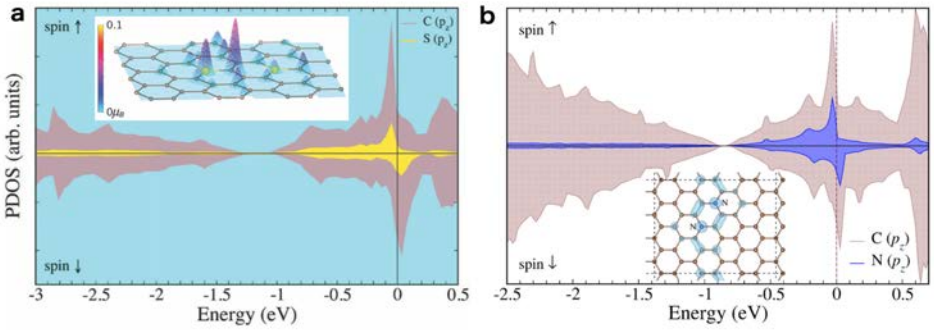


Figure 3.14: Densities of states, and spin densities and structures (shown in insets) of S (**a**) and N (**b**) doped graphene. Sulfur forms the gamma-thiothiapyrone motif and nitrogen occupies *para* positions in the graphene lattice. Panel **a** adapted from **[75]**, panel **b** from **[76]**.

Owing to its two additional electrons compared to a carbon atom, sulfur acts as an n-type (electron-donating) dopant by increasing the number of electrons in the system. Due to doping, the Dirac point was shifted below E_{F} and the doped graphene became an n-type conductor. The sustainability of the magnetism at relatively high temperatures (∼62 K) originated from the pumping of electrons from the substitutional sulfur into the graphene conduction band, strengthening the π electron system via which paramagnetic centres interact. It must be noted that Stoner magnetism can emerge if the itinerant electrons occupy narrow bands at E_{F} [74], **[75]**, as shown in Figure 3.14.

Similarly, a FM states emerged in graphene doped at 5.1 at% of nitrogen below ∼69 K **[76]**. Graphene doped below 5 at% of nitrogen was non-magnetic. High-resolution N 1s X-ray photoelectron spectroscopy (XPS) showed three distinct peaks corresponding to nitrogen in different configurations inside a graphene lattice or attached covalently to a graphene sheet, i.e., pyridinic nitrogen, graphitic nitrogen and chemisorbed N/N_2, which contrasts the S doped graphene where

sulfur was bound in the graphitic configuration inside the graphene lattice. Theoretical SP-DFT calculations were employed to address the magnetic contributions of individual N-motifs in details **[76]**. The theory revealed the particular importance of the graphitic-N motif embedded in the lattice at *para* positions (inset in Figure 3.14b) in imprinting FM order in N-doped graphene. N-doping leading to the FM state gave rise to a strong p_z electron peak at E_F in the electronic structure according to PDOS (Figure 3.14b), similar to the effect of doping of graphene with 4.2 at% of sulfur.

Although, the combined effects of all N-species was strongly FM graphene, it should be noted that coupling between pyridinic nitrogens is much less effective in maintaining the FM structure, and chemisorbed nitrogen adatoms can only generate paramagnetism. Further, chemisorbed N_2 only resulted in a non-magnetic states and pyrrolic nitrogen has no effect on magnetism in graphene. Altogether, among these structural motifs, graphitic nitrogen plays the principal magnetic role, as elucidated from SP-DFT calculations **[76]**.

3.5.2 Magnetism in nanographenes

Recently, magnetically ordered 25 nm long and 10 nm wide nanographenes (also termed graphene nanoplateles) were prepared and characterized **[91]** (Figure 1.19). SP-DFT calculations with various models of nanostructured graphene, ranging from semi-infinite nanometer-wide zigzag nanoribbons to nano-flakes of nanometer sizes and various shapes (see insets in Figure 3.15), were employed to explain the low-temperature FM with a Curie temperature of 37 K of these materials. The theory revealed that both interedge and intraedge ferromagnetism can evolve in GNPs having angles between adjacent edges smaller than 90°. This can be seen as

an excess of spin densities at the zigzag edges and in the corners between them, while deeper layers were non-magnetic. Thus, magnetism in GNPs emerged from the synergistic effects of the size, geometry of nanographenes, edge terminations, and angle between adjacent edges Moreover, SP-DFT predicted the total energy difference between FM and AFM interedge alignments in GNR with the width of ∼3.7 nm did not exceed 2 meV, and dropped below 1 meV for wider (≥8 nm) GNRs. Similar results were obtained for rectangular nanoflakes with magnetic zigzag and non-magnetic armchair adjacent edges. This further signified the important role of the intraedge ferromagnetism in nm size GNPs of rectangular shape where interedge coupling is largely suppressed **[91]**.

The theoretical Curie temperatures for GNPs of various sizes and shapes were estimated (Figure 3.15) employing the Ising model on the honeycomb lattice, which has the exact solution given as $k_{\mathrm{B}}T_{\mathrm{C}}/\mid J \mid = 0.3797$ [148], with a coupling value of $J = \Delta E/2$ [149], where ΔE is the energy difference between the magnetic ground state and non-magnetic spin-singlet. The lowest T_{C} was found for the GNRs followed by rectangular and trapezoidal flakes having both magnetic zigzag edges and non-magnetic armchair edges. Conversely, the largest T_{C} was computed for the triangular flake with an edge length of ∼3.7 nm and an excess of the spin density both in the corner between adjacent edges and on the deeper laying atoms, while the hexagonal flake and large triangular flake exhibited intermediate value of T_{C}. The median of the theoretical T_{C} was ∼47 K, which is not far from the experimentally observed T_{C} of 37 K, which is a bulk average across various morphology and size values. Upon further lowering the size of the triangular flake below 1 nm edge length, theoretical T_{C} dropped to 88 K which suggested that the Curie temperature could be theoretically enhanced by reducing the GNP size to a maximum

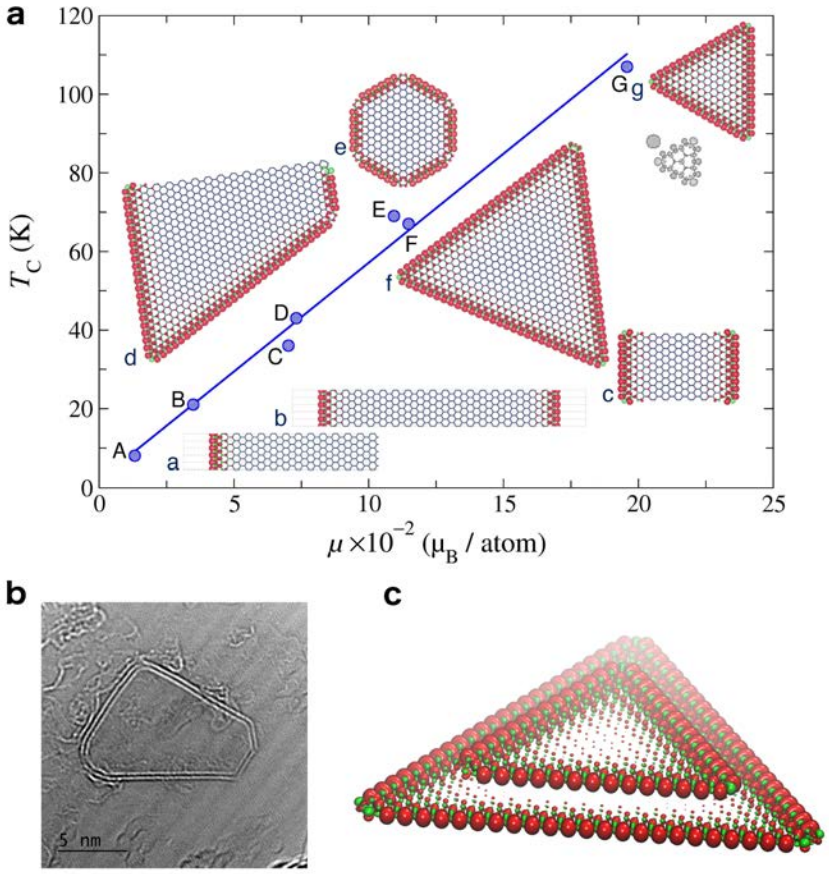


Figure 3.15: **a,** Theoretical T_C values of GNRs and GNPs vs. magnetic moments (normalized per number of atoms). The graphene flakes are labelled by small letters and the corresponding point on the plot is indicated by a capital letter. The grey point indicates T_C calculated for the smallest triangular flake (shown in grey). **b,** an example of HRTEM image of GNPs of trapezoidal shapes. **c,** Computed isosurfaces of spin densities plotted at $\pm 2 \times 10^{-3} e\text{Å}^{-3}$ for layered flakes. For clarity, C-atoms are not displayed. Both the values of magnetic moments and their distribution within the individual flakes were identical to those of single freestanding flakes. Adapted from **[91]**.

around 3.7 nm in the edge length.

3.5.3 Room-temperature G(OH)F magnets

Room-temperature magnetic ordering has recently been observed in hydroxyl-substituted fluorographene (termed hydroxofluorographene), either AFM (Figure 1.14) or FM (Figure 1.15) depending on the F/OH ratio and sophisticated organization of sp^2-conjugated motifs inside a sp^3-bonded matrix **[68, 69]**.

Specifically, the low-temperature FM and room-temperature AFM ordering in G(OH)F with an appropriate F/OH ratio stems from the presence of sp^2 diradical motifs encaged by the remaining sp^3-carbon atoms, as demonstrated by the SP-DFT calculations **[68]**. These diradical motifs are believed to emerge only above the site percolation limit of the graphene lattice, i.e., the number of sp^3 atoms must be sufficient to cage the sp^2 islands. In other words, sp^3 functionalization must reach a certain level for both the formation of diradicals and suppression of lateral diffusion of F-adatoms that would destroy the periodic magnetic pattern of sp^2 islands over the graphene surface. Importantly enough, the presence of diradical motifs in G(OH)F was confirmed experimentally by the electron paramagnetic resonance (EPR) measurements. SP-DFT showed that the $-$OH groups enable bridging among the diradical motifs and mediating interaction among them, stabilized the AFM order throughout the whole graphene lattice up to high temperatures. In particular, $-$OH groups allow communication between diradicals via superexchange interactions.

It must be noted that, from both theoretical and experimental standpoints, magnetic ordering in graphene mediated by itinerant π-electrons alone cannot be maintained at elevated temperatures. In the case of doping the magnetic order-

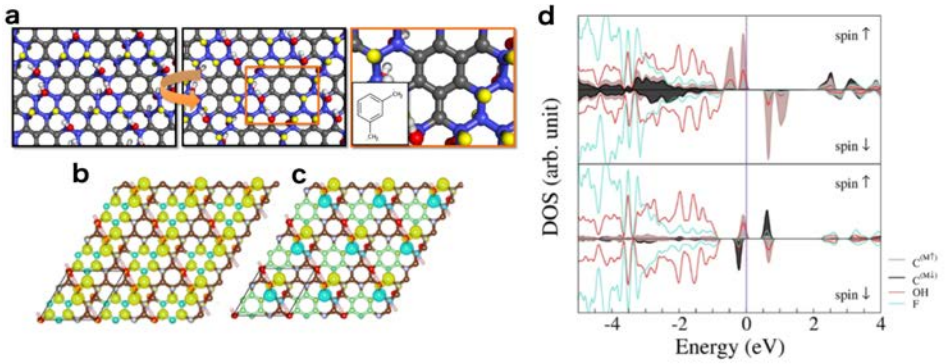


Figure 3.16: **a,** Model of m-xylylene diradical motifs in the G(OH)F system. The left and middle panels show the diradical motifs from above and below the graphene plane. The right panels shows the details of the diradical motif. Fluorine atoms are shown in yellow, hydrogen atoms in white, oxygen atoms in red, sp^3 carbon atoms in blue, and sp^2 carbon atoms in grey. **b,** Spin density distribution in FM and **c,** AFM G(OH)F. **d,** DOS of the GS FM phase (upper panel) and of the AFM phase (lower panel). Adapted from **[68]**.

ing can resist thermal disruption up to about 60–70 K **[75, 76]**. In other words, superexchange interactions seem to be much more effective than the π-electron system of graphene in maintaining the magnetic ordering to exceptionally high temperatures.

Interestingly enough, while nucleophilic substitution promotes formation of radical centres and emergence of superexchange interactions, defluorination pathways lead to the formation of the sp^2-conjugated zigzag motifs passing through sp^3 domains with radical centres either isolated in the sp^3 region or attached as a side part of the π-chain, as showed by theoretical calculations and as also evidenced by STEM and electron energy loss spectroscopy (EELS) experiments **[68, 69]** (Figure 3.17). The predicted in-plane distance between the zigzag chains was experimentally observed by high-resolution STEM. The spontaneous formation of zigzag

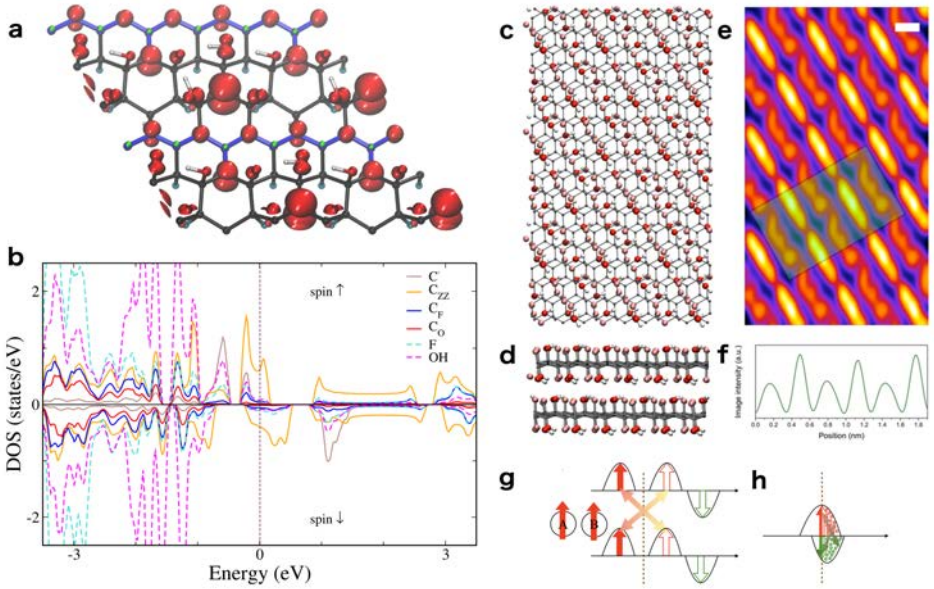


Figure 3.17: **a,** Top view of the FM G(OH)F structure with spin densities (positive shown in red and negative in green) plotted for isosurfaces at $5 \times 10^{-3} e\text{Å}^{-3}$. **b,** Corresponding DOS plot. **c,** Top view of the bilayer of FM G(OH)F. **d,** Side view. **e,** Quantitative STEM image simulation of the structure. **f,** Line profile of the area overlaid in green in panel **e**, indicating a repeating intensity variation with a period of 0.32 nm. **g,** Schematic of DOS of the two parallel-aligned magnetic moments with a ferromagnetic superexchange interaction and **h,** itinerant electron magnetism with the interaction of magnetic spins mediated by conduction π-electrons. Adapted from **[69]**.

motifs during synthesis of G(OH)F was supported by bond dissociation energies (BDEs) of fluorine atoms favouring defluorination along the motifs. This structural motif was possibly responsible for the room-temperature ferromagnetism of the G(OH)F system. A theoretical transition temperature of 440 K estimated by using the Ising model on the honeycomb lattice (see Section 3.5.2) was in good agreement with the experimentally derived T_C of 383 K. The favoured zigzag sp^2/sp^3 patterns in the basal plane strengthened interaction pathways among them via itinerant π-

electrons, as demonstrated by analyses of magnetization measurements and EPR data. This was also verified and explained by SP-DFT calculations, which revealed that the FM state was maintained by a synergistic interplay between the superexchange coupling of the radicals to the sp^2 zigzag chains and the π-electron system transferring the coupling between sp^3 strips.

These results highlight the major role of sp^2/sp^3 ratio and superorganization of radical and π-conjugated motifs in graphene for developing room-temperature nonmetallic magnets. Moreover, sp^3 functionalization offers many degrees of freedom in terms of the diversity of magnetic motifs, their architecture, combination, and organization, allowing formation of structures differing in electronic and magnetic properties tailored toward a given application.

Chapter 4

Summary and outlook

Nanomagnetism stands as one of the frontier field of magnetism. It offers new vista to high-density magnetic data storage devices on one hand, on the other hand nanomagnets exhibit a reach variety of very interesting physical phenomena, as the magneto-structural effect observed in small Pt clusters for which relativistic effects stabilized structures, which were only metastable in the scalar-relativistic limit, and that the change of directions of magnetic moments can lead to a transition between high- and low-moments states. The magnetic potential-energy surface as a function of the orientation of the magnetic moment can consist of interpenetrating sheets representing different magnetic isomers, as has been shown for Pt_5 clusters. For clusters of lighter 3d and 4d elements, the change in the magnetic symmetry leads to distortions of the clusters' geometries. These phenomena were largely unnoticed in the previous studies of TM nanostructures. The present results invalidates a perturbation analysis of magnetic anisotropy for the TM nanoclusters. The theoretical investigations of the structural and magnetic properties of TM nanostructures must be based on a simultaneous optimization of all structural and magnetic degrees of freedom and on selfconsistent calculations of the

total energies of the competing configurations.

The enormously large theoretical MAE of 0.2 eV of the IrCo dimer supported on the graphene layer deposited on Cu(111), which offers a barrier against loss of information at elevated temperatures, may pave the way for future room-temperature atomic-scale information storage. Here, the remaining challenge is the experimental realization of such supported bimetallic dimers. Also, addressing the role of structural defects in the graphnene layer both for anchoring of the clusters to the support and for the overall magnetic properties of the entire complex, remains a future task. The theory also showed that the substrate supporting TM nanostructures can be of decisive importance for the MAEs, even if it was separated from nanoclusters by the graphene layer. Magnetic and strongly polarizable metallic substrates are examples of such supports.

SP-DFT simulations provide an efficient tool to obtain a thorough characterization of both the existing and hypothetical materials and also a better understanding of the underlying phenomena in nanomagnetism. They were successfully employed to address and explain experimentally observed magnetic properties of various graphene-based systems including heteroatom doped graphene, nanoconfined graphene, and sp^3 functionalized graphene. Future directions toward preparing a wider family of graphene-based 2D high-temperature magnets with tailored properties for a given application have to combine the size and morphology aspects with other sources of magnetism, e.g., defects, doping, and functionalization.

Bibliography

[1] J. M. D. Coey, *Magnetism and Magnetic Materials* (Cambridge University Press, 2010).

[2] P. Weiss, L'hypothése du champ moléculaire et la propriété ferromagnétique. *J. Phys. Theor. Appl.* **6**, 661 (1907).

[3] P.A.M. Dirac, The quantum theory of the electron. *Proc. Roy. Soc.* **A117**, 610 (1928); *Proc. Roy. Soc.* **A118**, 351 (1928).

[4] W. Heisenberg, Zur Theorie des Ferromagnetismus. *Zeit. f. Physik* **49**, 619 (1928).

[5] M. N. Baibich, J. M. Broto, A. Fert, F. Nguyen Van Dau, F. Petroff, P. Etienne, G. Creuzet, A. Friederich, and J. Chazelas, Giant Magnetoresistance of (001)Fe/(001)Cr Magnetic Superlattices. *Phys. Rev. Lett.* **61**, 2472 (1988); G. Binasch, P. Grünberg, F. Saurenbach, and W. Zinn, Enhanced magnetoresistance in layered magnetic structures with antiferromagnetic interlayer exchange. *Phys. Rev. B* **39**, 4828(R) (1989).

[6] K. S. Novoselov, A. K. Geim, S. V. Morozov, D. Jiang, Y. Zhang, S. V. Dubonos, I. V. Grigorieva, and A. A. Firsov, Electric Field Effect in Atomically Thin Carbon Films. *Science* **306**, 666 (2004).

[7] IBM Archives: *IBM 350 disk storage unit.*

[8] S. N. Piramanayagam, Perpendicular recording media for hard disk drives. *J. Appl. Phys.* **102**, 011301 (2007).

[9] H. Zenil, *Algorithmic Data Analytics, Small Data Matters and Correlation versus Causation*, arXiv:1309.1418v9 (2017).

[10] C.-G. Stefanita, *From Bulk to Nano: The Many Sides of Magnetism* (Springer, 2008).

[11] T. R. Albrecht et al., Bit-Patterned Magnetic Recording: Theory, Media Fabrication, and Recording Performance. *IEEE Trans. Magn.* **51**, 1 (2015).

[12] P. Gambardella, A. Dallmeyer, K. Maiti, M. C. Malagoli, S. Rusponi, P. Ohresser, W. Eberhardt, C. Carbone, and K. Kern, Oscillatory Magnetic Anisotropy in One-Dimensional Atomic Wires. *Phys. Rev. Lett.* **93**, 077203 (2004).

[13] N. Weiss, T. Cren, M. Epple, S. Rusponi, G. Baudot, S. Rohart, A. Tejda, V. Repain, S. Rousset, P. Ohresser, F. Scheurer, P. Bencok, H. Brune, Uniform Magnetic Properties for an Ultrahigh-Density Lattice of Noninteracting Co Nanostructures. *Phys. Rev. Lett.* **95**, 157204 (2005).

[14] P. Gambardella, S. Rusponi, M. Veronese, S.S. Dhesi, C. Grazioli, A. Dallmeyer, I. Cabria, R. Zeller, P.H. Dederichs, K. Kern, C. Carbone, and H. Brune, Giant Magnetic Anisotropy of Single Cobalt Atoms and Nanoparticles. *Science* **300**, 1130 (2003).

[15] H. Brune and P. Gambardella, Magnetism of individual atoms adsorbed on surfaces. *Surf. Sci.* **603**, 1812 (2009).

[16] **Piotr Błoński**, J. Hafner, Density-functional theory of the magnetic anisotropy of nanostructures: an assessment of different approximations. *J. Phys.: Condens. Matter* **21**, 426001 (2009).

[17] **Piotr Błoński**, A. Lehnert, S. Dennler, S. Rusponi, M. Etzkorn, G. Moulas, P. Bencok, P. Gambardella, H. Brune, J. Hafner, Magnetocrystalline anisotropy energy of Co and Fe adatoms on the (111) surfaces of Pd and Rh. *Phys. Rev. B* **81**, 104426 (2010).

[18] A. Lehnert, S. Dennler, **Piotr Błoński**, S. Rusponi, M. Etzkorn, G. Moulas, P. Bencok, P. Gambardella, H. Brune, J. Hafner, Magnetic anisotropy of Fe and Co ultrathin films deposited on Rh(111) and Pt(111) substrates: An experimental and first-principles investigation. *Phys. Rev. B* **82**, 094409 (2010).

[19] **Piotr Błoński**, S. Dennler, J. Hafner, Strong spin-orbit effects in small Pt clusters: Geometric structure, magnetic isomers and anisotropy. *J. Chem. Phys.* **134**, 034107 (2011)

[20] **Piotr Błoński**, J. Hafner, Magneto-structural properties and magnetic anisotropy of small transition-metal clusters: a first-principles study. *J. Phys.: Condens. Matter.* **23**, 136001 (2011).

[21] F. D. Natterer, K. Yang, W. Paul, P. Willke, T. Choi, T. Greber, A. J. Heinrich, and C. P. Lutz, Reading and writing single-atom magnets. *Nature* **543**, 226 (2017).

[22] F. D. Natterer, F. Donati, F. Patthey, and H. Brune, Thermal and Magnetic-Field Stability of Holmium Single-Atom Magnets. *Phys. Rev. Lett. 121*, 027201 (2018).

[23] P. Bruno, Tight-binding approach to the orbital magnetic moment and magnetocrystalline anisotropy of transition-metal monolayers. *Phys. Rev. B* **39**, 865(R) (1989).

[24] **Piotr Błoński**, J. Hafner, Magnetic anisotropy of transition-metal dimers: Density functional calculations. *Phys. Rev. B* **79**, 224418 (2009).

[25] **Piotr Błoński**, J. Hafner, Geometric and magnetic properties of Pt clusters supported on graphene: Relativistic density-functional calculations. *J. Chem. Phys.* **134**, 154705 (2011).

[26] **Piotr Błoński**, J. Hafner, Pt on graphene monolayers supported on a Ni(111) substrate: Relativistic density-functional calculations. *J. Chem. Phys.* **136**, 074701 (2012).

[27] **Piotr Błoński**, J. Hafner, Pt_3 and Pt_4 clusters on graphene monolayers supported on a Ni(111) substrate: Relativistic density-functional calculations. *J. Chem. Phys.* **137**, 044710 (2012).

[28] **Piotr Błoński**, J. Hafner, Magnetic anisotropy of heteronuclear dimers in the gas phase and supported on graphene: relativistic density-functional calculations. *J. Phys.: Condens. Matter* **26**,146002 (2014).

[29] **Piotr Błoński**, J. Hafner, Cu(111) supported graphene as a substrate for magnetic dimers with a large magnetic anisotropy: relativistic density-functional calculations. *J. Phys.: Condens. Matter* **26**, 256001 (2014).

[30] **Piotr Błoński**, J. Hafner, On the interplay between geometrical structure and magnetic anisotropy: a relativistic density-functional study of mixed Pt–Co and Pt–Fe trimers and tetramers in the gas-phase and supported on graphene. *J. Phys.: Condens. Matter* **27**, 046002 (2015).

[31] A. A. Khajetoorians, T. Schlenk, B. Schweflinghaus, M. dos Santos Dias, M. Steinbrecher, M. Bouhassoune, S. Lounis, J. Wiebe, R. Wiesendanger, Spin Excitations of Individual Fe Atoms on Pt(111): Impact of the Site-Dependent Giant Substrate Polarization. *Phys. Rev. Lett.* **111**, 157204 (2013).

[32] A. A. Khajetoorians, S. Lounis, B. Chilian, A. T. Costa, L. Zhou, D. L. Mills, J. Wiebe, R. Wiesendanger, Itinerant Nature of Atom-Magnetization Excitation by Tunneling Electrons. *Phys. Rev. Lett.* **106**, 037205 (2011).

[33] J. Hermenau, M. Ternes, M. Steinbrecher, R. Wiesendanger, J. Wiebe, Long Spin-Relaxation Times in a Transition-Metal Atom in Direct Contact to a Metal Substrate. *Nano Lett.* **18**, 1978 (2018).

[34] W. Paul, K. Yang, S. Baumann, N. Romming, T. Choi, C. P. Lutz, A. J. Heinrich, Control of the millisecond spin lifetime of an electrically probed atom. *Nat. Phys.* **13**, 403 (2017).

[35] B. W. Heinrich, L. Braun, J. I. Pascual, K. J. Franke, Protection of excited spin states by a superconducting energy gap. *Nat. Phys.* **9**, 765 (2013).

[36] F. Donati, et al. Magnetic remanence in single atoms. *Science* **352**, 318 (2016).

[37] R. Baltic, M. Pivetta, F. Donati, C. Wackerlin, A. Singha, J. Dreiser, S. Rusponi, H. Brune, Superlattice of Single Atom Magnets on Graphene. *Nano Letters* **16**, 7610 (2016).

[38] R. Sessoli, Single-atom data storage. *Nature* **543**, 189 (2017).

[39] F. E. Kalff, M. P. Rebergen, E. Fahrenfort, J. Girovsky, R. Toskovic, J. L. Lado, J. Fernández-Rossier, A. F. Otte, A kilobyte rewritable atomic memory. *Nat. Nanotech.* **11**, 926 (2016).

[40] B. Kiraly, A. N. Rudenko, W. M. J. van Weerdenburg, D. Wegner, M. I. Katsnelson, A. A. Khajetoorians, An orbitally derived single-atom magnetic memory. *Nat. Commun.* **9**, 3904 (2018).

[41] A. N. Rudenko, F. J. Keil, M. I. Katsnelson, A. I. Lichtenstein, Adsorption of cobalt on graphene: Electron correlation effects from a quantum chemical perspective. *Phys. Rev. B* **86**, 075422 (2012).

[42] J. Hafner, Ab-initio simulations of materials using VASP: Density-functional theory and beyond. *J. Comput. Chem.* **29**, 2044 (2008).

[43] J. Tuček, **Piotr Błoński**, J. Ugolotti, A. K. Swain, T. Enoki, R. Zbořil, Emerging chemical strategies for imprinting magnetism in graphene and related 2D materials for spintronic and biomedical applications. *Chem. Soc. Rev.* **47**, 3899 (2018).

[44] M. Tamura, Y. Nakazawa, D. Shiomi, K. Nozawa, Y. Hosokoshi, M. Ishikawa, M. Takahashi, M. Kinoshita, Bulk ferromagnetism in the β-phase crystal of the p-nitrophenyl nitronyl nitroxide radical. *Chem. Phys. Lett.* **186**, 401 (1991); M. Takahashi, P. Turek, Y. Nakazawa, M. Tamura, K. Nozawa, D.

Shiomi, M. Ishikawa, M. Kinoshita, Discovery of a quasi-1D organic ferromagnet, p-NPNN. *Phys. Rev. Lett.* **67**, 746 (1991).

[45] H. W. Kroto, J. R. Heath, S. C. O'Brien, R. F. Curl, R. E. Smalley, C_{60}: Buckminsterfullerene. *Nature* **318**, 162 (1985).

[46] S. Iijima, Helical microtubules of graphitic carbon. *Nature* **354**, 56 (1991).

[47] A. H. Castro Neto, F. Guinea, N. M. R. Peres, K. S. Novoselov, A. K. Geim, The electronic properties of graphene. *Rev. Mod. Phys.* **81**, 109 (2009).

[48] M. J. Allen, V. C. Tung, R. B. Kaner, Honeycomb Carbon: A Review of Graphene. *Chem. Rev.* **110**, 132 (2010).

[49] V. Georgakilas, M. Otyepka, A. B. Bourlinos, V. Chandra, N. Kim, K. C. Kemp, P. Hobza, R. ZboĹil, K. S. Kim, Functionalization of Graphene: Covalent and Non-Covalent Approaches, Derivatives and Applications. *Chem. Rev.* **112**, 6156 (2012).

[50] V. Georgakilas, J. N. Tiwari, K. C. Kemp, J. A. Perman, A. B. Bourlinos, K. S. Kim, R. ZboĹil, Noncovalent Functionalization of Graphene and Graphene Oxide for Energy Materials, Biosensing, Catalytic, and Biomedical Applications. *Chem. Rev.* **116**, 5464 (2016).

[51] O. V. Yazyev, Emergence of magnetism in graphene materials and nanostructures. *Rep. Prog. Phys.* **73**, 056501 (2010).

[52] E. H. Lieb, Two theorems on the Hubbard model. *Phys. Rev. Lett.* **62**, 1201 (1989).

[53] O. V. Yazyev, L. Helm, Defect-induced magnetism in graphene. *Phys. Rev. B* **75**, 125408, 2007).

[54] H. González-Herrero, J. M. Gómez-RodrĂguez, P. Mallet, M. Moaied, J. J. Palacios, C. Salgado, M. M. Ugeda, J.-Y. Veuillen, F. Yndurain, I. Brihuega, Atomic-scale control of graphene magnetism by using hydrogen atoms. *Science* **352**, 437 (2016).

[55] E. J. G. Santos, A. Ayuela, D. SĂĄnchez-Portal, Universal magnetic properties of sp^3-type defects in covalently functionalized graphene. *New Journal of Physics* **14**, 043022 (2012).

[56] A. Y. S. Eng, Z. Sofer, D. Sedmidubskyý, M. Pumera, Synthesis of Carboxylated-Graphenes by the Kolbe-Schmitt Process. *ACS Nano* **11**, 1789 (2017).

[57] A. Bakandritsos, M. Pykal, **Piotr Błoński**, P. Jakubec, D. D. Chronopoulos, K. Poláková, V. Georgakilas, K. Čépe, O. Tomanec, V. Ranc, A. B. Bourlinos, R. Zbořil, M. Otyepka, Cyanographene and Graphene Acid: Emerging Derivatives Enabling High-Yield and Selective Functionalization of Graphene. *ACS Nano* **11**, 2982 (2017).

[58] D. C. Elias, R. R. Nair, T. M. G. Mohiuddin, S. V. Morozov, P. Blake, M. P. Halsall, A. C. Ferrari, D. W. Boukhvalov, M. I. Katsnelson, A. K. Geim, K. S. Novoselov, Control of Graphene's Properties by Reversible Hydrogenation: Evidence for Graphane. *Science* **323**, 610 (2009).

[59] J. Berashevich, T. Chakraborty, Sustained ferromagnetism induced by H-vacancies in graphene. *Nanotechnology* **21**, 355201 (2010).

[60] J. Zhou, Q. Wang, Q. Sun, X. S. Chen, Y. Kawazoe, P. Jena, Ferromagnetism in Semihydrogenated Graphene Sheet. *Nano Lett.* **9**, 3867 (2009).

[61] R. R. Nair, W. C. Ren, R. Jalil, I. Riaz, V. G. Kravets, L. Britnell, P. Blake, F. Schedin, A. S. Mayorov, S. J. Yuan, M. I. Katsnelson, H. M. Cheng, W. Strupinski, L. G. Bulusheva, A. V. Okotrub, I. V. Grigorieva, A. N. Grigorenko, K. S. Novoselov, A. K. Geim, Fluorographene: A TwoâDimensional Counterpart of Teflon. *Small* **6**, 2877 (2010).

[62] R. Zbořil, F. Karlický, A. B. Bourlinos, T. A. Steriotis, A. K. Stubos, V. Georgakilas, K. Šafářová, D. Jančík, C. Trapalis and M. Otyepka, Graphene Fluoride: A Stable Stoichiometric Graphene Derivative and its Chemical Conversion to Graphene. *Small* **6**, 2885 (2010).

[63] D. D. Chronopoulos, A. Bakandritsos, M. Pykal, R. Zbořil, M. Otyepka, Chemistry, properties, and applications of fluorographene. *Appl. Mater. Today* **9**, 60 (2017).

[64] H. Y. Liu, Z. F. Hou, C. H. Hu, Y. Yang, Z. Z. Zhu, Electronic and Magnetic Properties of Fluorinated Graphene with Different Coverage of Fluorine. *J. Phys. Chem. C* **116**, 18193 (2012).

[65] R. R. Nair, M. Sepioni, I. L. Tsai, O. Lehtinen, J. Keinonen, A. V. Krasheninnikov, T. Thomson, A. K. Geim, I. V. Grigorieva, Spin-half paramagnetism in graphene induced by point defects. *Nat. Phys.* **8**, 199 (2012).

[66] T. L. Makarova, A. L. Shelankov, A. A. Zyrianova, A. I. Veinger, T. V. Tisnek, E. Lähderanta, A. I. Shames, A. V. Okotrub, L. G. Bulusheva, G. N. Chekhova, D. V. Pinakov, I. P. Asanov, Ž. Šljivančanin, Edge state mag-

netism in zigzag-interfaced graphene via spin susceptibility measurements. *Sci. Rep.* **5**, 13382 (2015).

[67] T. L. Makarova, A. L. Shelankov, A. I. Shames, A. A. Zyrianova, A. A. Komlev, G. N. Chekhova, D. V. Pinakov, L. G. Bulusheva, A. V. Okotrub, E. Lähderanta, Tabby graphene: Dimensional magnetic crossover in fluorinated graphite. *Sci. Rep.* **7**, 16544 (2017).

[68] J. Tuček, K. Holá, A. B. Bourlinos, **Piotr Błoński**, A. Bakandritsos, J. Ugolotti, M. Dubecký, F. Karlický, V. Ranc, K. Čépe, M. Otyepka, R. Zbořil, Room temperature organic magnets derived from sp^3 functionalized graphene. *Nat. Commun.* **8**, 14525 (2017).

[69] J. Tuček, K. Holá, G. Zoppellaro, **Piotr Błoński**, R. Langer, M. Medved, T. Susi, M. Otyepka, R. Zbořil, Zigzag sp^2 Carbon Chains Passing through an sp^3 Framework: A Driving Force toward Room-Temperature Ferromagnetic Graphene *ACS Nano*, **12**, 12847 (2018).

[70] T. Tang, N. J. Tang, Y. P. Zheng, X. G. Wan, Y. Liu, F. C. Liu, Q. H. Xu, Y. W. Du, Robust magnetic moments on the basal plane of the graphene sheet effectively induced by OH groups. *Sci. Rep.* **5**, 8448 (2015).

[71] S. Qin, Q. Xu, Room temperature ferromagnetism in N_2 plasma treated graphene oxide. *J. Alloys Compd.* **692**, 332 (2017).

[72] Y. Liu, Q. Feng, N. J. Tang, X. G. Wan, F. C. Liu, L. Y. Lv, Y. W. Du, Increased magnetization of reduced graphene oxide by nitrogen-doping. *Carbon* **60**, 549 (2013).

[73] P. Lazar, R. Zbořil, M. Pumera, M. Otyepka, Chemical nature of boron and nitrogen dopant atoms in graphene strongly influences its electronic properties. *Phys. Chem. Chem. Phys.* **16**, 14231 (2014).

[74] D. M. Edwards, M. I. Katsnelson, High-temperature ferromagnetism of sp electrons in narrow impurity bands: application to CaB_6. *J. Phys.: Condens. Matter* **18**, 7209 (2006).

[75] J. Tuček, **Piotr Błoński**, Z. Sofer, P. Šimek, M. Petr, M. Pumera, M. Otyepka, R. Zbořil, Sulfur Doping Induces Strong Ferromagnetic Ordering in Graphene: Effect of Concentration and Substitution Mechanism. *Adv. Mater.* **28**, 5045 (2016).

[76] **Piotr Błoński**, J. Tuček, Z. Sofer, V. Mazánek, M. Petr, M. Pumera, M. Otyepka, R. Zbořil, Doping with Graphitic Nitrogen Triggers Ferromagnetism in Graphene. *J. Am. Chem. Soc.* **139**, 3171 (2017).

[77] Y. Ito, C. Christodoulou, M. V. Nardi, N. Koch, M. Kläui, H. Sachdev, K. Müllen, Tuning the Magnetic Properties of Carbon by Nitrogen Doping of Its Graphene Domains. *J. Am. Chem. Soc.* **137**, 7678 (2015).

[78] J. Li, X. Li, P. Zhao, D. Y. Lei, W. Li, J. Bai, Z. Ren, X. Xu, Searching for magnetism in pyrrolic N-doped graphene synthesized via hydrothermal reaction. *Carbon* **84**, 460 (2015).

[79] T. Enoki, *Magnetism of Nanographene*, in *Graphene: Synthesis, Properties, and Phenomena*, (Wiley-VCH Verlag GmbH & Co. KGaA, Weinheim, Germany, 2013).

[80] Y. Kobayashi, K. Fukui, T. Enoki, K. Kusakabe, Y. Kaburagi, Observation of zigzag and armchair edges of graphite using scanning tunneling microscopy and spectroscopy. *Phys. Rev. B* **71**, 193406 (2005).

[81] Y. Niimi, T. Matsui, H. Kambara, K. Tagami, M. Tsukada, H. Fukuyama, Scanning tunneling microscopy and spectroscopy studies of graphite edges. *Appl. Surf. Sci.* **241**, 43 (2005).

[82] Y. Kobayashi, K.-I. Fukui, T. Enoki, K. Kusakabe, Edge state on hydrogen-terminated graphite edges investigated by scanning tunneling microscopy. *Phys. Rev. B* **73**, 125415 (2006).

[83] K. Nakada, M. Fujita, G. Dresselhaus, M. S. Dresselhaus, Edge state in graphene ribbons: Nanometer size effect and edge shape dependence. *Phys. Rev. B* **54**, 17954 (1996).

[84] K. Wakabayashi, M. Fujita, H. Ajiki, M. Sigrist, Electronic and magnetic properties of nanographite ribbons. *Phys. Rev. B* **59**, 8271 (1999).

[85] V. Georgakilas, J. A. Perman, J. Tuček, R. Zbořil, Broad Family of Carbon Nanoallotropes: Classification, Chemistry, and Applications of Fullerenes, Carbon Dots, Nanotubes, Graphene, Nanodiamonds, and Combined Superstructures. *Chem. Rev.* **115**, 4744 (2015).

[86] G. Z. Magda, X. Jin, I. Hagymási, P. Vancsó, Z. Osváth, P. Nemes-Incze, Ch. Hwang, L. P. Biró, L. Tapasztó, Room-temperature magnetic order on zigzag edges of narrow graphene nanoribbons. *Nature* **514**, 608 (2014).

[87] M. Kan, J. Zhou, Q. Sun, Q. Wang, Y. Kawazoe, P. Jena, Tuning magnetic properties of graphene nanoribbons with topological line defects: From antiferromagnetic to ferromagnetic. *Phys. Rev. B* **85**, 155450 (2012).

[88] K. Sawada, F. Ishii, M. Saito, S. Okada, T. Kawai, Phase control of graphene nanoribbon by carrier doping: appearance of noncollinear magnetism. *Nano Lett.* **9**, 269 (2009).

[89] K. Sawada, F. Ishii, M. Saito, Magnetism in graphene nanoribbons on Ni(111): First-principles density functional study. *Phys. Rev. B* **82**, 245426 (2010).

[90] B. Xu, J. Yin, Y. D. Xia, X. G. Wan, K. Jiang, Z. G. Liu, Electronic and magnetic properties of zigzag graphene nanoribbon with one edge saturated. *Appl. Phys. Lett.* **96**, 163102 (2010).

[91] J. Tuček, **Piotr Błoński**, O. Malina, M. Pumera, C. K. Chua, M. Otyepka, R. Zbořil, Morphology-Dependent Magnetism in Nanographene: Beyond Nanoribbons. *Adv. Funct. Mater.* **28**, 1800592 (2018).

[92] P. Hohenberg, W. Kohn, Inhomogeneous electron gas, *Phys. Rev. B* **136**, B864 (1964).

[93] W. Kohn, L. Sham, Self-consistent equations including exchange and correlation effects, *Phys. Rev.* **140**, A1133 (1965).

[94] G. Carchini, N. Almora-Barrios, G. Revilla-López, L. Bellarosa, R. García-Muelas, M. García-Melchor, S. Pogodin, **Piotr Błoński**, Núria López, How Theoretical Simulations Can Address the Structure and Activity of Nanoparticles. *Top. Catal.* **56**, 1262 (2013).

[95] W. Kohn, L. J. Sham, Self-Consistent Equations Including Exchange and Correlation Effects. *Phys. Rev. A* **140**, A1133 (1965).

[96] E. G. Moroni, G. Kresse, J. Hafner, Ultrasoft pseudopotentials applied to magnetic Fe, Co, and Ni: From atoms to solids. *Phys Rev B* **56**, 15629 (1997).

[97] R. Hafner, D. Spišák, R. Lorenz, J. Hafner, Ab initio local-spin-density study of oscillatory exchange coupling in Fe/Au multilayers. *J. Phys.: Condens. Matter* **14**, 4297 (2002).

[98] D. C. Langreth, M. J. Mehl, Easily Implementable Nonlocal Exchange-Correlation Energy Functional. *Phys. Rev. Lett.* **47**, 446 (1981).

[99] D. C. Langreth, M. J. Mehl, Beyond the Local-Density Approximation in Calculations of Ground-State Electronic Properties. *Phys. Rev. B* **28**, 1809 (1983).

[100] J. P. Perdew, J. A. Chevary, S. H. Vosko, K. A. Jackson, M. R. Pederson, D. J. Singh, C. Fiolhais, Atoms, molecules, solids, and surfaces: Application of the generalized gradient approximation for exchange and correlation, *Phys. Rev. B* **46**, 6671 (1992).

[101] J. P. Perdew, K. Burke, M. Erzenhof, Generalized Gradient Approximation Made Simple, *Phys. Rev. Lett.* **77**, 3865 (1996).

[102] B. Hammer, L. B. Hansen, J. K. Nørskov, Improved adsorption energetics within density-functional theory using revised Perdew-Burke-Ernzerhof functionals. *Phys. Rev. B* **59**, 7413 (1999).

[103] J. P. Perdew, S. Kurth, A. Zupan, P. Blaha, Accurate density functional with correct formal properties: a step beyond the generalized gradient approximation. *Phys. Rev. Lett.* **82**, 2544 (1999).

[104] A. D. Becke, Density-functional thermochemistry. III. The role of exact exchange. *J. Chem. Phys.* **98**, 5648 (1993).

[105] P. J. Stevens, F. J. Devlin, C. F. Chablowski, M. J. Frisch, Ab Initio Calculation of Vibrational Absorption and Circular Dichroism Spectra Using Density Functional Force Fields. *J. Phys. Chem.* **98**, 11623 (1994).

[106] J. Paier, R. Hirschl, M. Marsman, G. Kresse, The Perdew-Burke-Ernzerhof exchange-correlation functional applied to the G2-1 test set using a plane-wave basis set. *J. Chem. Phys.* **122**, 234102 (2005).

[107] J. Paier, M. Marsman, G. Kresse, Why does the B3LYP hybrid functional fail for metals? *J. Chem. Phys.* **127**, 024103 (2007).

[108] C. Adamo, V. Barone, Toward reliable density functional methods without adjustable parameters: The PBE0 model. *J. Chem. Phys.* **110**, 6158 (1999).

[109] J. Heyd, G. E. Scuseria, M. Ernzerhof, Hybrid functionals based on a screened Coulomb potential. *J. Chem. Phys.* **118**, 8207 (2003).

[110] C. Franchini, V. Bayer, R. Podloucky, J. Paier, G. Kresse, Density functional theory study of MnO by a hybrid functional approach. *Phys. Rev. B* **72**, 045132 (2005). C. Franchini, R. Podloucky, J. Paier, M. Marsman, G. Kresse, Ground-state properties of multivalent manganese oxides: Density functional and hybrid density functional calculations. *Phys. Rev. B* **75**, 195128 (2007).

[111] J. P. Perdew, A. Zunger, Self-interaction correction to density-functional approximations for many-electron systems. *Phys. Rev. B* **23**, 5048 (1981).

[112] D. M. Ceperley, B. J. Alder, Ground State of the Electron Gas by a Stochastic Method. *Phys. Rev. Lett.* **45**, 566 (1980).

[113] U. von Barth, L. Hedin, A local exchange-correlation potential for the spin polarized case. *J. Phys. C* **5**, 1629 (1972).

[114] S. H. Vosko, L. Wilk, M. Nusair, Accurate spin-dependent electron liquid correlation energies for local spin density calculations: a critical analysis. *Can. J. Phys.* **58**, 1200 (1980).

[115] J. P. Perdew, J. A. Chevary, S. H. Vosko, K. A. Jackson, M. R. Pederson, D. J. Singh, C. Fiolhais, Atoms, molecules, solids, and surfaces: Applications of the generalized gradient approximation for exchange and correlation. *Phys. Rev. B* **46**, 6671 (1992); Erratum: *Phys. Rev. B* **48**, 4978 (1993).

[116] J. A. White, D.M. Bird, Implementation of gradient-corrected exchange-correlation potentials in Car-Parrinello total-energy calculations. *Phys. Rev. B* **50**, 4954 (1994).

[117] D. Hobbs, G. Kresse, J. Hafner, Fully unconstrained noncollinear magnetism within the projector augmented-wave method. *Phys. Rev. B* **62**, 11556 (2000).

[118] D. R. Hamann, M. Schlüter, C. Chiang, Norm-conserving pseudopotentials. *Phys. Rev. Lett.* **43**, 1494 (1979).

[119] G. B. Bachelet, D. R. Hamann, M. Schlüter, C. Chiang, Pseudopotentials that work: From H to Pu. *Phys. Rev. B* **26**, 4199 (1982).

[120] N. Troullier, J. L. Martins, Efficient pseudopotentials for plane-wave calculations. *Phys. Rev. B* **43**, 1993 (1991); N. Troullier, J.L. Martins, Efficient pseudopotentials for plane-wave calculations II. operators for fast iterative diagonalization, *Phys. Rev. B* **43**, 8861 (1991)

[121] D. Vanderbilt, Soft self-consistent pseudopotentials in a generalized eigenvalue formalism, *Phys. Rev. B* **41**, 7892 (1990).

[122] G. Kresse, J. Hafner, Norm-conserving and ultrasoft pseudopotentials for first-row and transition elements. *J. Phys.: Condens. Matter* **6**, 8245 1994.

[123] S. G. Louie, S. Froyen, M. L. Cohen, Nonlinear ionic pseudopotentials in spin-density-functional calculations. *Phys. Rev. B* **26**, 1738 (1982).

[124] P. E. Blöchl, Projector augmented-wave method. *Phys. Rev. B* **50**, 17953 (1994).

[125] D. J. Singh, *Plane Waves, Pseudopotentials and the LAPW Method* (Kluwer Academic, Norwell, MA, 1994).

[126] G. Kresse, D. Joubert, From ultrasoft pseudopotentials to the projector augmented-wave method. *Phys. Rev. B* **59**, 1758 (1999).

[127] M. Marsman, G. Kresse, Relaxed core projector-augmented-wave method. *J. Chem. Phys.* **125**, 104101 (2006).

[128] E. van Lenthe, E. J. Baerends, and J. G. Snijders, Relativistic Regular Two-Component Hamiltonians. *J. Chem. Phys.* **99**, 4597 (1993).

[129] S. Steiner, S. Khmelevskyi, M. Marsmann, G. Kresse, Calculation of the magnetic anisotropy with projected-augmented-wave methodology and the case study of disordered $Fe_{1-x}Co_x$ alloys. *Phys. Rev. B* **93**, 224425 (2016).

[130] H. J. Monkhorst, J. D. Pack, Special points for Brillouin-zone integrations. *Phys. Rev. B* **13**, 5188 (1976).

[131] A. Smogunov, A. Dal Corso, A. Delin, R. Weht, E. Tosatti, Colossal magnetic anisotropy of monatomic free and deposited platinum nanowires. *Nat. Nanotechnol.* **3**, 22-25 (2008).

[132] T. O. Strandberg, C. M. Canali, A. H. MacDonald, Transition-metal dimers and physical limits on magnetic anisotropy. *Nature Mater.* **6**, 648 (2007); Calculation of Chern number spin Hamiltonians for magnetic nano-clusters by DFT methods. *Phys. Rev. B* **77**, 174416 (2008).

[133] G. van der Laan, Microscopic origin of magnetocrystalline anisotropy in transition metal thin films. *J. Phys.: Condens. Matter* **10**, 3239 (1998).

[134] Y. Okamoto, Density-functional calculations of icosahedral M_{13} (M = Pt and Au) clusters on graphene sheets and flakes. *Chem. Phys. Lett.* **420**, 382 (2006).

[135] K. Okazaki-Maeda, S. Yamakawa, Y. Morikawa, T. Akita, S. Tanaka, S. Hyodo, M. Kohyama, Simulation of growth process of Pt-particles - first-principles calculations. *J. Phys.: Conf. Ser.* **100**, 072044 (2008).

[136] A. Bakandritsos, R. G. Kadam, P. Kumar, G. Zoppellaro, M Medved', J. Tuček, T. Montini, O. Tomanec, P. Andrýsková, B. Drahoš, R. S. Varma,

M. Otyepka, M. B. Gawande, P. Fornasiero, R. Zbořil, Mixed-Valence Single-Atom Catalyst Derived from Functionalized Graphene. *Adv.Mater.* **1900323** (2019).

[137] X.-Q. Dai, Y.-N. Tang, J.-H. Zhao, Y.-W. Dai, Absorption of Pt clusters and the induced magnetic properties of graphene. *J. Phys.: Condens. Matter* **22**, 316005 (2010).

[138] Ch. Vo-Van, Z. Kassir-Bodon, H. Yang, J. Coraux, J. Vogel, S. Pizzini, P. Bayle-Guillemaud, M. Chshiev, L. Ranno, V. Guisset, P. David, V. Salvador, O. Fruchart, Ultrathin epitaxial cobalt films on graphene for spintronic investigations and applications. *New J. Phys.* **12**, 103040 (2010).

[139] Z. Zhou, F. Gao, W. Goodman, Deposition of metal clusters on single-layer graphene/Ru(0001): Factors that govern cluster growth. *Surf. Sci.* **604**, L31 (2010).

[140] Y. Gan, L. Sun, F. Banhart, One- and Two-Dimensional Diffusion of Metal Atoms in Graphene. *Small* **4**, 587 (2008).

[141] E. Voloshina, Y. Dedkov, Graphene on metallic surfaces: problems and perspectives. *Phys. Chem. Chem. Phys.* **14**, 13502 (2012).

[142] S. Grimme, J. Antony, T. Schwabe, and C. Muück-Lichtenfeld, Density functional theory with dispersion corrections for supramolecular structures, aggregates, and complexes of (bio)organic molecules. *Org. Biomol. Chem.* **5**, 741 (2007).

[143] J. Harl, G. Kresse, Accurate Bulk Properties from Approximate Many-Body Techniques. *Phys. Rev. Lett.* **103**, 056401 (2009).

[144] F. Mittendorfer, A. Garhofer, J. Redinger, J. Klimeš, J. Harl, G. Kresse, Graphene on Ni(111): Strong interaction and weak adsorption. *Phys. Rev. B* **84**, 201401(R) (2011).

[145] Yu. S. Dedkov, M. Fonin, Electronic and magnetic properties of the graphene–ferromagnet interface. *New J. Phys.* **12**, 125004 (2010).

[146] M. Weser, Y. Rehder, K. Horn, M. Sicot, M. Fonin, A. B. Preobrajenski, E. N. Voloshina, E. Goering, Yu. S. Dedkov, Induced magnetism of carbon atoms at the graphene/Ni(111) interface. *Appl. Phys. Lett.* **96**, 012504 (2010).

[147] W Han, R. K. Kawakami, M. Gmitra, J. Fabian, Graphene spintronics. *Nat. Nanotechnol.* **9**, 794 (2014).

[148] T. Balcerzak, K. Szałowski, M. Jaščur, M. Žukovič, A. Bobák, M. Borovský, Thermodynamic description of the Ising antiferromagnet on a triangular lattice with selective dilution by a modified pair-approximation method. *Phys. Rev. E* **89**, 062140 (2014).

[149] I. P. R. Moreira, F. Illas, *Ab initio* theoretical comparative study of magnetic coupling in $KNiF_3$ and K_2NiF_4. *Phys. Rev. B* **55**, 4129 (1997).

Appendix 1

Reprints of papers on structures and MAEs of TM clusters

1. **Piotr Błoński**, J. Hafner, Magnetic anisotropy of transition-metal dimers: Density functional calculations. *Phys. Rev. B* **79**, 224418 (2009).

2. **Piotr Błoński**, S. Dennler, J. Hafner, Strong spin-orbit effects in small Pt clusters: Geometric structure, magnetic isomers and anisotropy. *J. Chem. Phys.* **134**, 034107 (2011).

3. **Piotr Błoński**, J. Hafner, Magneto-structural properties and magnetic anisotropy of small transition-metal clusters: a first-principles study. *J. Phys.: Condens. Matter.* **23**, 136001 (2011).

4. **Piotr Błoński**, J. Hafner, Geometric and magnetic properties of Pt clusters supported on graphene: Relativistic density-functional calculations. *J. Chem. Phys.* **134**, 154705 (2011).

5. **Piotr Błoński**, J. Hafner, Pt on graphene monolayers supported on a Ni(111) substrate: Relativistic density-functional calculations. *J. Chem. Phys.* **136**, 074701 (2012).

6. **Piotr Błoński**, J. Hafner, Pt_3 and Pt_4 clusters on graphene monolayers supported on a Ni(111) substrate: Relativistic density-functional calculations. *J. Chem. Phys.* **137**, 044710 (2012).

7. **Piotr Błoński**, J. Hafner, Magnetic anisotropy of heteronuclear dimers in

the gas phase and supported on graphene: relativistic density-functional calculations. *J. Phys.: Condens. Matter* **26**,146002 (2014).

8. **Piotr Błoński**, J. Hafner, Cu(111) supported graphene as a substrate for magnetic dimers with a large magnetic anisotropy: relativistic density-functional calculations. *J. Phys.: Condens. Matter* **26**, 256001 (2014).

9. **Piotr Błoński**, J. Hafner, On the interplay between geometrical structure and magnetic anisotropy: a relativistic density-functional study of mixed Pt–Co and Pt–Fe trimers and tetramers in the gas-phase and supported on graphene. *J. Phys.: Condens. Matter* **27**, 046002 (2015).

10. **Piotr Błoński**, J. Hafner, Density-functional theory of the magnetic anisotropy of nanostructures: an assessment of different approximations. *J. Phys.: Condens. Matter* **21**, 426001 (2009).

11. **Piotr Błoński**, A. Lehnert, S. Dennler, S. Rusponi, M. Etzkorn, G. Moulas, P. Bencok, P. Gambardella, H. Brune, J. Hafner, Magnetocrystalline anisotropy energy of Co and Fe adatoms on the (111) surfaces of Pd and Rh. *Phys. Rev. B* **81**, 104426 (2010).

Magnetic anisotropy of transition-metal dimers: Density functional calculations

Piotr Błoński and Jürgen Hafner*
Fakultät für Physik and Center for Computational Materials Science, Universität Wien, Sensengasse 8/12, A-1090 Wien, Austria
(Received 2 March 2009; revised manuscript received 8 May 2009; published 16 June 2009)

We present *ab initio* density functional calculations of the magnetic anisotropy of dimers of the transition-metal atoms from groups 8 to 10 of the Periodic Table. Our calculations are based on a noncollinear implementation of spin-density functional theory (DFT) where spin-orbit coupling (SOC) is included self-consistently. The physical mechanism determining the sign and magnitude of the magnetic anisotropy energy (MAE) is elucidated via an analysis of the influence of SOC on the spectrum of the Kohn-Sham eigenvalues of the dimers. The possible influence of orbital-dependent electron-electron interactions has been investigated by performing calculation with a hybrid functional (mixing Hartree-Fock and DFT exchanges) and with a DFT+U Hamiltonian introducing an orbital-dependent on-site Coulomb repulsion U. The results demonstrate that the MAE is stable with respect to the addition of such orbital-dependent interactions.

DOI: 10.1103/PhysRevB.79.224418 PACS number(s): 75.30.Gw, 75.75.+a, 36.40.Cg

I. INTRODUCTION

During the 1990s there has been an enormous interest in the magnetic properties of nanostructures, triggered by the rapid development of magnetic and magneto-optic storage technologies.[1] Much of this interest has centered on the question of the minimal size of a bit for classical information storage. The main criterion is that the energy difference between the easy and hard axes of magnetization represents a barrier for spin reorientations exceeding ambient temperatures. An important line of research has centered on molecular magnets[2] but recently there have been suggestions that very small transition-metal clusters might also satisfy this condition.

While the spin-dependent magnetic properties of transition-metal clusters have been widely investigated (see, e.g., Alonso,[3] Baletto and Ferrando,[4] Futschek *et al.*,[5,6] and further references cited therein), only very few *ab initio* investigations have addressed the problem of the magnetic anisotropy of gas-phase[7–9] or supported[10–13] transition-metal clusters. Fernandez-Seivane and Ferrer[8] performed spin-density functional calculations using pseudopotentials and a local basis set [both in the local-density (LDA) and generalized gradient (GGA) approximations] for Pd, Pt, Ir, and Au dimers. For Pd_2 the easy magnetization direction is perpendicular to the dimer axis with a magnetic anisotropy energy (MAE) of 5/2 meV (LDA/GGA) while for Pt_2 and Ir_2 the easy axis coincides with the dimer axis, in which the MAEs are much larger, 220/75 (LDA/GGA) and 100 meV (LDA) per dimer for Pt_2 and Ir_2, respectively. Strandberg *et al.*[7] used a projector-augmented-wave approach in a plane-wave basis and the GGA. They reported perpendicular anisotropy for Pd_2[MAE=2.4 meV(GGA)] and Ni_2(MAE=7 meV), and axial anisotropy for Co_2 and Rh_2 [MAE=30(Co_2) and 45 meV (Rh_2)]. Fritsch *et al.*[9] presented results for a number of 3*d* and 4*d* dimers, calculated using the LDA and a full-potential approach in a basis of numerical localized orbitals. For Pd_2 they agree with the perpendicular anisotropy predicted by the other authors [MAE=5 meV(LDA)]; for Co_2 and Rh_2 their results agree with Strandberg *et al.* on the easy axis but their MAEs are nearly twice as large (50 meV for Co_2 and 104 meV for Rh_2). For Ni_2 axial anisotropy (MAE =11 meV) is predicted in contrast to Strandberg *et al.*[7] In all calculations the MAE is determined as the difference in the total energies of the dimers with different orientations of the magnetic axis. While the calculations of Fernandez-Seivane and Ferrer[8] and of Strandberg *et al.*[7] are based on a scalar-relativistic approach and treat spin-orbit interaction in a self-consistent second-order approximation, the results of Fritsch *et al.*[9] are based on the fully relativistic Dirac equation. Strandberg *et al.* also used the results of the *ab initio* calculations to construct a giant-spin Hamiltonian quantizing the classical anisotropy energy functional. However, it is evident that the available results are too scattered to provide a clear picture of the physical mechanism determining an axial or perpendicular anisotropy or the magnitude of the anisotropy energy.

This is surprising because the calculation of the magnetic anisotropy is a problem of fundamental importance. Magnetic anisotropy, magneto-optical spectra, magnetic dichroism, and other important properties are caused by spin-orbit coupling. Within spin-density-functional theory Bruno[14] and van der Laan[15] have used perturbation theory to derive approximate expressions for the MAE. According to Bruno, for a system where the majority-spin band is completely filled, the MAE is proportional to the spin-orbit coupling (SOC) parameter ξ and to the difference in the expectation values of the orbital moment calculated for the easy and hard axes of magnetization (i.e., to the anisotropy of the orbital moment). van der Laan derived in addition a correction term which is second order in ξ and which accounts in addition for a possible anisotropy of the spin moment.

Whereas the spin magnetic moments are described quite accurately by density functional theory, the orbital moments are generally underestimated. The reason is that the variables determining the effective one-electron potential within density functional theory (the charge and spin densities) are determined as averages over occupied orbitals. For small transition-metal clusters supported on nonmagnetic substrates where the small MAE has been calculated using the force theorem or the torque force approach,[10–13] the results are generally in good qualitative and semiquantitative agreement with Bruno's and van der Laan's models. An exception

 ©2009 The American Physical Society

are, as recently pointed out by Andersson *et al.*,[16] magnetic nanostructures supported on or sandwiched by late 4*d* or 5*d* transition metals with a strong spin-orbit coupling. In these cases off-site spin-orbit coupling between the *d* states across the interface makes a dominant contribution to the MAE. The situation remains unclear for gas-phase clusters. In the studies published so far, the MAE has been calculated in terms of the difference in the total energies of two independent self-consistent calculations—the results should hence be more reliable than those based on the use of the force theorem. However, since only Fritsch *et al.*[9] report detailed results on the spin and orbital moments (but no spin-orbit coupling parameters), the validity of the perturbation formulas for the transition-metal dimers is difficult to asses—but at least for Pd_2 a larger orbital moment for parallel magnetization and an easy axis perpendicular axis are in contradiction to the perturbation treatment.

For the magnetic anisotropy of small clusters the size of the orbital moment becomes of decisive importance. Solovjev[17] has pointed out that orbital magnetism is essentially an atomic phenomenon, as it is proportional to the gradient of the effective one-electron potential which is large only in a small region around the nucleus. Many attempts have been made to devise orbital polarization corrections to the density functional Hamiltonian—an exchange-correlation field which couples to the orbital magnetic moment. The empirical orbital polarization term proposed by Brooks *et al.*[18,19] has recently been discussed by Eschrig *et al.*[20] within fully relativistic current-density functional theory, and by Solovjev[17] and Chadov *et al.*[21] in connection with the more general LDA+U (Ref. 22) and dynamical mean-field theory.[23] While the orbital polarization corrections give a fairly accurate description of orbital moment in bulk 3*d* magnets,[24] they tend to overestimate the orbital moments of dilute 3*d* impurities in noble-metal matrices[22,25] or of 3*d* adatoms on noble-metal substrates.[11,12] For the impurity cases Chadov *et al.*[21] demonstrated that an LDA+dynamic mean field theory (DMFT) approach with a modest on-site Coulomb repulsion of $U=3$ eV leads to values of the orbital moment intermediate between the LDA and orbital polarization approaches, and in better agreement with experiment. Fritsch *et al.*[9] investigated the influence of an orbital polarization contribution to the Hamiltonian on the orbital moments, and on the MAE of 3*d* and 4*d* dimers. For most of the late transition metals the orbital polarization corrections lead to a significant enhancement of the orbital magnetic moments and to a dramatic increase in the MAE. However in some cases (as for the Fe dimer) even if the anisotropy of the orbital moments is decreased, a pronounced increase in the MAE by a factor of 5 is reported. For Pd_2, orbital polarization changes the sign of the MAE which remains, however, an order of magnitude smaller than for Fe, Co, Ni, and Rh dimers where the inclusion of orbital polarization terms leads to MAEs varying between 150 and 200 meV. In contrast for dimers of the early transition metals, the correction terms have only a very modest influence on the orbital moments and leave the MAEs almost unchanged. This is surprising because the earlier work of the same group[20] had reported similar orbital polarization corrections to the total energies of the divalent cations of early and late 3*d* transition elements.

The magnetic properties of transition-metal dimers are of course closely related to those of infinite metallic chains—after all, dimers can be considered as short pieces of such chains. Although many investigations have been devoted to the magnetic order of such chains (see, e.g., Spišák and Hafner[26] and Mokrousov *et al.*,[27] and further references cited therein), only fewer studies have addressed the problem of their magnetic anisotropy.[28–33] For free-standing wires formed by the magnetic 3*d* transition metals, it has been shown[28,29,31] that the size of the orbital moment and the magnetic anisotropy energy depend very sensitively on the exact geometry of the wire (interatomic distances, straight or zigzag wire). Although the orbital moment increases with a decreasing dimensionality (from bulk to monolayer and to monowires), at equilibrium the values remain smaller than expected on the basis of x-ray circular dichroism experiments on supported monowires. Adding an orbital polarization term to the DFT Hamiltonian leads to a huge increase in the orbital moment (by a factor of 5 for Co wires) to values that are evidently too large.[28,29] Desjonquères *et al.*[33] studied the formation of orbital moments within a Hartree-Fock decoupling scheme and simpler Hamiltonians with and without orbital polarization corrections. It was concluded that the orbital polarization corrections are convenient and reliable for systems with saturated magnetic moments only. Intriguing results have been reported for the orbital moments and magnetic anisotropy energies of wires formed by 4*d* or 5*d* transition metals.[30,32] It was shown that the equilibrium interatomic distances are very close to the onset of magnetism in these wires; at equilibrium the spin moments are about μ_B, $0.2\mu_B$, and $0.5\mu_B$ in Ru, Rh, and Pd, the orbital moments are about $0.17\mu_B$, $0.37\mu_B$, and 0 for axial, and $0.05\mu_B$, 0, and $0.12\mu_B$ for perpendicular magnetization for the same series of metals. The large orbital anisotropies are reflected in large MAEs although with no proportionality between orbital anisotropy as expected from perturbation theory. Stretched nanowires display a dramatic increase in both spin and orbital moments, and reversal in the sign of the MAE without a change in the sign of the orbital anisotropy.[30] For Pt monowires is has been reported[32] that at equilibrium both spin and orbital magnetic moments exist only for parallel, but not for perpendicular, orientation of the magnetization—in such a case the MAE is determined by the energy difference between a magnetic and a nonmagnetic wire, and consequently is very large. However, at these distances the magnetic moments are still very small ($\mu_S \sim \mu_L \sim 0.2\mu_B$).

Here we present density functional calculations of the magnetic anisotropy energies for dimers of the Fe, Co, and Ni groups. Our aim is to study systematic trends in the MAE as a function of the filling of the *d* band and through a series of homologous elements from the 3*d* to the 5*d* series and to elucidate the mechanisms determining the sign and the magnitude of the MAE. In addition we briefly investigate the influence of postdensity-functional approximations (LDA+U, hybrid functionals) on orbital moments and magnetic anisotropy.

II. COMPUTATIONAL DETAILS

We have used the Vienna *ab initio* simulation package (VASP) (Refs. 34 and 35) to perform *ab initio* electronic struc-

ture calculations and structural optimizations. VASP performs an iterative solution of the Kohn-Sham equations of density functional theory within a plane-wave basis and using periodic boundary conditions. A semilocal functional in the GGA (Ref. 36) (PW91) and the spin interpolation proposed by Vosko *et al.*[37] is used to describe electronic exchange and correlation and spin polarization. The use of a semilocal functional is known to be essential for the correct prediction of the ground state of the ferromagnetic 3*d* elements in the bulk.[38] The projector-augmented wave (PAW) method[35,39] is used to describe the electron-ion interactions. The PAW approach produces the exact all-electron potentials and charge densities without elaborate nonlinear core corrections—this is particularly important for magnetic elements.

The PAW potentials have been derived from fully relativistic calculations of the atomic or ionic reference calculations. Spin-orbit coupling has been implemented in VASP by Kresse and Lebacq.[40] Following Kleinman and Bylander[41] and MacDonald *et al.*[42] the relativistic Hamiltonian given in a basis of total angular-momentum eigenstates $|j,m_j\rangle$ with $j=l\pm\frac{1}{2}$ (containing all relativistic corrections up to order α^2, where α is the fine-structure constant) is recast in the form of 2×2 matrices in spin space by reexpressing the eigenstates of the total angular momentum in terms of a tensor product of regular angular-momentum eigenstates $|l,m\rangle$ and the eigenstates of the z component of the Pauli-spin matrices. The relativistic effective potential consists of a term diagonal in spin space which contains the mass velocity and Darwin corrections, and the spin-orbit operator,

$$\mathbf{V}=\mathbf{V}^{\mathrm{sc}}+\mathbf{V}^{\mathrm{SO}}=\sum_{l,m}[V_l\cdot 1_\sigma+V_l^{\mathrm{SO}}\vec{L}\cdot\vec{\mathbf{S}}]|l,m\rangle\langle l,m|.$$

where 1_σ is the unit operator in spin space and

$$\vec{L}\cdot\vec{\mathbf{S}}=\frac{1}{2}\begin{pmatrix}L_z & L_-\\ L_+ & -L_z\end{pmatrix}.$$

The l components of the scalar V_l and spin-orbit V_l^{SO} potentials are weighted averages over the $l\pm\frac{1}{2}$ components. The Hamiltonian is therefore a 2×2 matrix in spin space. The nondiagonal elements arise from the spin-orbit coupling but also from the exchange-correlation potential when the system under consideration displays a noncollinear magnetization density. Calculations including spin-orbit coupling have, therefore, to be performed in the noncollinear mode implemented in VASP by Hobbs *et al.*[43] and Marsman and Hafner.[44]

In our calculations, the dimers have been placed into a large cubic box with an edge of 10 Å—this ensures that the separation between the periodically repeated images of the dimer is large enough to suppress any interactions. The basis set contained plane waves with a maximum kinetic energy of 500 eV. For a Co dimer test calculations have been performed with cutoff energies varying between 250 and 700 eV, leading to magnetic anisotropy energies of 7.49/7.09/7.20 meV for cutoff energies of 250/500/700 eV, indicating that a cutoff of 500 eV is a reasonable compromise between accuracy and computational effort. The calculations have been performed in two steps. First a collinear scalar-relativistic calculation has been performed, producing the correct geometry for a spin eigenstate. In those cases where there are reasons to suspect the coexistence of different spin isomers with only small differences in the total energy, fixed-moment calculations were performed for the competing spin isomers to uniquely determine the ground state. The ground state resulting from the scalar-relativistic calculations was used to initialize the noncollinear calculations including spin-orbit coupling. For each dimer at least three calculations have been performed to find the easy and hard magnetic axes and to determine the MAE. In the first two calculations, the direction of the magnetic axis was initialized along the dimer axis (chosen along [001]) or parallel to the equatorial plane of the dimer, i.e., along [100]. By symmetry, the total energy is stationary for magnetic moments in these two orientations. To cross-check the results, a third calculation was initialized with an oblique angle between the magnetic moment and the axis, and the equatorial plane of the dimer (usually the initialization was along the [111] direction). In these calculations the direction of the magnetic moment relaxed into the easy axis, and usually the difference in the total energy for easy-axis orientation was smaller than 0.01 meV. Spin-orbit coupling mixes different spin eigenstates. To control the importance of the initial value of the magnetic moment, parallel calculations have been performed. In a few cases different initializations led to different relativistic ground states—details will be discussed below. Geometric, electronic, and magnetic degrees of freedom are relaxed simultaneously until the change in total energy between successive iteration steps are smaller than 10^{-7} eV—such a stringent relaxation criterion was found to be absolutely essential.

Orbital magnetic moments are calculated directly from the wave functions as the expectation value of the components of the angular-momentum operator along the direction of magnetization. Within the group of 3*d* and 4*d* metals we observe the same trend: the orbital moment increases from Fe_2 to Co_2 and from Ru_2 to Rh_2, to decrease again in Ni and Pd dimers. This variation follows roughly the trend in the orbital moments of the isolated atoms as given by Hund's rule.

The MAE consists of two contributions: the difference in the total electronic energies for easy and hard magnetization directions induced by the spin-orbit coupling, and the magnetostatic (or shape) anisotropy to the magnetic dipolar interactions. The shape anisotropy is zero in cubic solids, usually negligible even in anisotropic solids but often relevant in ultrathin magnetic films[45] where it can trigger a magnetic reorientation transition. For monowires Tung and Guo[31] have reported a shape anisotropy which is considerably smaller than the electronic contribution. We have calculated the dipolar interaction energy for all dimers—the contributions are of the order of 0.1 meV and hence again negligible compared to the electronic term.

In addition to the DFT calculations at the GGA level, we also performed a few test calculations with hybrid functionals mixing density functional and exact (Hartree-Fock) exchange, and using the DFT+U method. The PBE0 (Ref. 46) and HSE03 (Ref. 47) functionals have been implemented in VASP by Paier *et al.*,[48] and we refer to their paper for all further details. The LDA+U approach[22] has been implemented in VASP by Rohrbach *et al.*[49] Both in the DFT+U and

TABLE I. Interatomic distance d (in Å), spin multiplicity $2S+1$ from scalar-relativistic calculations, spin μ_S and orbital μ_L moments from calculations including spin-orbit coupling (in μ_B) of transition-metal dimers for axial and perpendicular orientations of the magnetization, magnetic anisotropy energy (MAE), and spin-orbit coupling constant ξ (both in meV). The MAE is positive for any easy axis parallel to the dimer axis.

				Axial		Perp.			
Dimer		d	$2S+1$	μ_S	μ_L	μ_S	μ_L	MAE	ξ
Fe_2	PW[a]	1.98	7	5.84	0.32	5.84	0.16	0.3	24
	FKRE[b]	1.96	7	6.00	1.89	6.00	0.19	32.0	
Ru_2	PW	2.07	5	3.98	0.00	3.94	0.24	−36.5	334
Os_2	PW	2.10	5	3.75	−0.80	3.48	0.62	28.8	885
Co_2	PW	1.96	5	3.90	0.78	3.90	0.32	7.1	32
	FKRE	1.94	5	4.09	2.00	4.14	0.33	50.0	
	SCM[c]	1.98						28.0	85
Rh_2	PW	2.21	5	3.86	1.82	3.80	0.50	47.3	136
	FKRE	2.21	5	3.98	2.12	3.93	0.63	104.0	
	SCM	2.22	5					52.0	140
Ir_2	PW	2.22	5	3.88	1.96	3.42	0.94	69.8	413
	FSF[d]	2.22		4.00	1.34	4.10	1.24	100.0	
Ni_2	PW (A)	2.09	3	1.98	0.58	1.96	0.38	6.5	101
	PW (B)	2.09	3	1.98	0.12	1.98	0.38	−5.9	
	FKRE	2.05	3	1.99	0.88	1.99	0.45	11.0	
	SCM	2.10	3					−7.6	
Pd_2	PW	2.49	3	1.96	0.02	1.98	0.36	−2.3	404
	FKRE	2.93	3	1.94	0.86	1.98	0.53	−5.0	
	FSF	2.45		2.00	0.02	1.96	0.56	−2.0	
		(2.53)		(2.00)	(0.02)	(2.00)	(0.44)	(−5.0)	
	SCM	2.50	3					−1.2	
Pt_2	PW	2.38/2.35[e]	3	1.88	2.74	1.34	0.80	46.3	742
	FSF	2.38		1.90	2.40	1.65	1.20	220.0	
		(2.45)		(1.95)	(2.40)	(1.75)	(1.10)	(75.0)	

[a]Present work (GGA).
[b]Fritsch *et al.*, Ref. 9 (LDA).
[c]Strandberg *et al.*, Ref. 7 (GGA).
[d]Fernandez-Seivane and Ferrer, Ref. 8 (LDA, GGA in parentheses).
[e]Different dimer lengths for axial and perpendicular magnetizations, cf. text.

the hybrid functional approaches the exchange-correlation potential is orbital dependent and it is interesting to explore whether this changes the results derived from conventional DFT calculations.

III. RESULTS

Our results for the bond length, spin and orbital moments in axial and perpendicular orientations, magnetic anisotropy energy, and spin-orbit coupling strength are compiled in Table I. As far as available, results from the earlier studies of Fritsch *et al.* (FKRE in the following),[9] Strandberg *et al.* (SCM in the following),[7] and Fernandez-Seivane and Ferrer (FSF in the following) (Ref. 8) are also listed for comparison. But it has to be emphasized that in the paper by FSF, the values of the magnetic moments and of the bond length can be read only from small graphs, and that SCM (Ref. 7) have reported slightly different values for the MAE in their two publications. For the metals of the Co group the easy magnetic axis is always parallel to the dimer axis; the MAE increases strongly from Co_2 to Ir_2 with increasing strength of the spin-orbit coupling. In the Fe group we find a very small axial anisotropy for Fe_2, a strong perpendicular anisotropy for Ru_2, and a modest axial anisotropy for Os_2. In the Ni group the trend is also quite complex: we calculate an axial anisotropy for Ni_2 and Pt_2 (much stronger for the Pt dimer as expected from the strength of the spin-orbit coupling), but a weak perpendicular anisotropy for Pd_2. In the following sections we shall attempt to explain the variation in the MAE with band filling and increasing strength of relativistic effects in terms of a detailed analysis of their eigenvalue spectra. We begin with the Co group where the situation is relatively simple. The contributions of the magnetostatic dipolar interactions to the MAE have been calculated for all dimers. For the dimers of the 3*d* metals where the magnetic moments are

largest, the dipolar contributions to the MAE are −0.26, −0.16, and −0.04 meV/dimer for Fe_2, Co_2, and Ni_2. Except for the Fe dimer where the dipolar contribution leads to a further reduction in an already exceptionally very weak MAE, these values are entirely negligible compared to the electronic terms to which our attention is therefore restricted in the following.

A. Co group

All dimers of the metals of the Co group have the easy magnetic axis oriented along the dimer axis. The scalar-relativistic calculations lead to a ground state with $S=2$ for all three dimers. Adding SOC leaves the interatomic distance unchanged for Co_2 and Rh_2; only for the Ir dimer does the bond length increase by 0.01 Å. SOC mixes different spin eigenstates; this leads to a slight reduction in the magnetic spin moment which becomes more pronounced with increasing strength of the SOC. For Rh_2 this agrees with the results of FKRE (Ref. 9) but for Co_2 they predict an even slightly increased magnetic spin moment. A strong SOC also induces an anisotropy of the spin moment, $\Delta\mu_S=(0.0/0.06/0.46)\mu_B$ for Co/Rh/Ir, with a larger spin moment for easy-axis orientation. A much stronger anisotropy is calculated for the orbital magnetic moment, $\Delta\mu_L=(0.46/1.32/1.02)\mu_B$. For perpendicular magnetization our calculated orbital moments are in reasonable agreement with FKRE (Ref. 9) but they report larger orbital moments for parallel magnetization (in particular for Co_2). FSF (Ref. 8) report essentially a very small anisotropy of both spin and orbital magnetic moments for Ir_2—which is surprising since they also report a large MAE of 100 meV. Our calculations permit in principle a noncollinear orientation of spin and orbital moments but we always find a strictly collinear orientation.

For the Co_2 dimer our calculated MAE of 7.1 meV is substantially lower than the results reported by SCM (Ref. 7) and by FKRE.[9] The disagreement with SCM (who also reported a much stronger SOC of 85 meV) is particularly intriguing because their calculations have also been performed using the VASP code. For this reason we have checked very carefully all computational parameters. Varying the plane-wave cutoff between 250 and 700 eV left both spin and orbital moments unchanged; the calculated MAE varied only by ±0.2 meV. A different initialization of the magnetic moment also leads to the same results. Initializing the direction of the magnetic moment in an oblique direction led to convergence to the easy axis, with a difference in the total energies smaller than 0.01 meV for all values of the cutoff energy. It is difficult to asses the reasons for the discrepancy with SCM because no results for the magnetic moments and only selected details of the computational setup have been reported. Their cutoff energy was 348 eV but the decisive difference could be the criterion for terminating the self-consistent iterations. We have found that relaxing the criterion for total-energy convergence from 10^{-7} eV can lead to substantial changes in the MAE.

For a Rh_2 dimer on the other hand we note very good agreement with SCM.[7] FKRE (Ref. 9) report slightly larger spin and orbital magnetic moments and orbital anisotropy

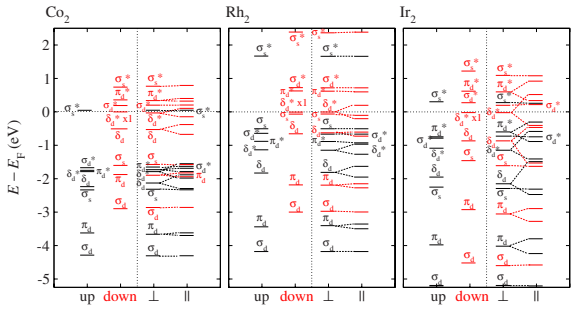


FIG. 1. (Color online) Kohn-Sham eigenvalue spectra for Co_2 (left), Rh_2 (center), and Ir_2 (right) dimers. The left-hand part of each graph shows the spin-up (black) and spin-down (red/gray) eigenvalues from the scalar-relativistic calculations while the right-hand part shows the eigenvalues for parallel and perpendicular orientations of the magnetic moment after adding spin-orbit coupling. The coloring is the same as for the scalar-relativistic eigenstates from which the fully relativistic states are derived (although they are of course not spin eigenstates). The eigenvalues refer to states with quantum numbers $m_J=m_L\pm\frac{1}{2}$.

but these differences are hardly sufficient to explain an MAE which is larger by a factor of 2. For Ir_2 the orbital anisotropy is reduced compared to Rh_2 but here we note also a rather pronounced anisotropy of the spin moment. The reduced orbital anisotropy could explain that the MAE does not increase as strongly compared to the lighter homologs as the strength of the SOC would suggest. For Ir_2 FSF (Ref. 8) report an even larger MAE but with nearly isotropic-spin and orbital magnetic moments.

It is also interesting to correlate the calculated MAEs with the perturbation theories proposed by Bruno[14] and van der Laan.[15] For Co_2 and Rh_2, where the spin anisotropy vanishes or is very small, Bruno's expression ($\mathrm{MAE}\propto\xi\mu_S\Delta\mu_L$) predicts an MAE which should be about 12 times larger for Rh_2 than for Co_2 whereas we find only an increase by a factor of 7. For Ir_2 we note a substantial anisotropy of the spin moment so that Bruno's formula cannot be expected to be valid. van der Laan's approximate expression for the MAE accounts for the spin anisotropy but only in the limit of a weak SOC—which is evidently not the case for Ir_2.

To analyze the reason for the strong axial MAE in the dimers of the Co-group metals, we follow SCM (Ref. 7) in analyzing the Kohn-Sham eigenvalue spectra of the dimers in the scalar-relativistic mode, and after adding SOC for parallel and perpendicular orientations (see Fig. 1). In the scalar-relativistic approximation, the eigenvalue spectrum of the dimer is determined by the electronic ground state of the isolated atom (s^2d^7 for Co and Ir, sd^8 for Rh), and the bonding-antibonding and exchange splittings. In all three dimers the highest occupied molecular orbital (HOMO) is a doubly-degenerate antibonding $\delta_d^\star$ minority (spin-down) state occupied by one electron only. For the Co_2 dimer where the exchange splitting is largest, the highest occupied majority state is the antibonding $\sigma_d^\star$ state but the antibonding $\delta_s^\star$ and $\pi_d^\star$ states lies just below the majority HOMO. For Rh_2 the different atomic ground state leads to an up shift of the s states relative to the d states; the highest occupied majority

state is now the bonding σ_s state. For the Ir_2 dimer the ordering of the minority levels is the same as for Co_2 but with an increased bonding-antibonding splitting and a decreased exchange splitting. For the majority states the highest occupied level is now the $\pi_d^\star$ state. SOC leads to a lifting of the twofold degeneracy of the δ_d and π_d states if the magnetization is parallel to the dimer axis. For the HOMO $\delta_d^\star$ the SOC splitting is 0.94 eV in Ir_2, 0.41 eV for Rh_2, and 0.26 eV for Co_2. The lowering of the occupied $\delta_d^\star$ states (by −0.39 eV for Ir_2) is the dominant effect determining the MAE. A similar splitting is observed also for all other doubly-degenerate eigenstates but in most cases the SOC splitting does not change the average energy—an exception are again the fully occupied $\delta_d^\star$ and δ_d states whose center of gravity is up shifted for Ir_2 by 0.13 and 0.20 eV, respectively. Taking the sum over the change in the eigenvalues yields an energy difference of 0.06 eV—in almost perfect agreement with the calculated MAE. However, this degree of agreement is a bit accidental; for Rh_2 the difference in the sum over the eigenvalues is 0.1 eV, somewhat larger than the calculated MAE. For Co_2 the eigenvalue analysis gives only a qualitative indication of the sign of the MAE; the small value requires an accurate calculation of the total-energy difference.

B. Ni group

For Ni_2 our calculations lead to two locally stable solutions with equal bond length and almost equal spin moments but widely different orbital moments for an axial orientation of the magnetization. For solution A, the orbital moment is $\mu_L = 0.58\mu_B$ for axial, and $\mu_L = 0.38\mu_B$ for perpendicular orientation. In this case we predict an easy axis parallel to the dimer axis and a modest MAE of 6.5 meV, in reasonable agreement with FKRE.[9] For solution B, the orbital moment is $\mu_L = 0.12\mu_B$ for axial, and $\mu_L = 0.38\mu_B$ for perpendicular orientation. This is also the easy axis, with an MAE of −5.9 meV, in agreement with SCM (Ref. 7) who also found a perpendicular anisotropy. The total energy for easy-axis orientation is lower by 27 meV for solution A which represents the ground state.

For Pd_2 all calculations are in agreement on a perpendicular easy axis, a weak orbital anisotropy, and a modest negative MAE of a few meV although FKRE predict a much larger orbital moment for the hard magnetic axis. For Pt_2 we predict a parallel easy axis, in good agreement with the GGA result of FSF (Ref. 8) whose LDA calculations yield, however, a much higher MAE. Both calculations also agree on a substantial spin anisotropy. We shall again attempt to analyze the origin and magnitude of the magnetic anisotropy in terms of an analysis of the eigenvalue spectra (see Fig. 2).

For the dimers of the Ni-group metals the ground state is a triplet ($S=1$) state but the Kohn-Sham eigenvalue spectra differ already at the scalar-relativistic level due to the different electronic configurations of the free atoms in their ground state. Ni has a s^2d^8 ground state. The doubly-degenerate minority $\delta_d^\star$ state occupied by two electrons is the HOMO; the highest occupied majority state has the same symmetry. The occupied bonding σ_s state lies almost in the center of the d states. Pd has a closed-shell d^{10} ground state, i.e., formation

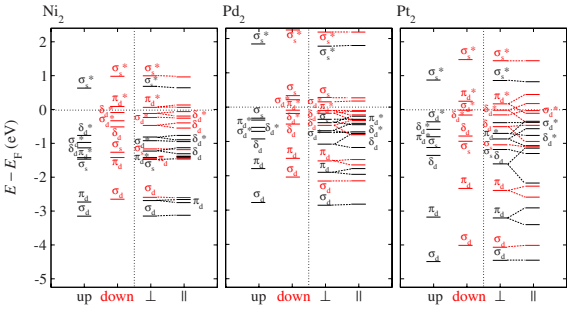


FIG. 2. (Color online) Kohn-Sham eigenvalue spectra for Ni_2 (left), Pd_2 (center), and Pt_2 (right) dimers, cf. Fig. 1.

of a stable dimer requires a promotion of at least one d electron to an s state—this is also reflected in a low binding energy of the dimer. The HOMO is the fully occupied doubly-degenerate $\pi_d^\star$ minority state while the lowest unoccupied molecular orbital is the minority $\sigma_d^\star$ state. The highest occupied majority state is σ_s. This means that the excess spin density arises from the bonding σ_s state and a hole in the d state of $\sigma_d^\star$ character. A Pt atom has a sd^9 ground state. For the dimer the HOMO is the minority $\sigma_d^\star$ state; the highest majority state has the same symmetry. For the minority electrons, an antibonding $\delta_d^\star$ lies only slightly below and an empty $\pi_d^\star$ state only slightly above the HOMO. The occupied σ_s lies below the occupied bonding d states.

The fact that all doubly-degenerate dimer eigenstates are either fully occupied by two electrons or empty suggests that the MAE will be relatively low unless SOC leads to a reordering and a change in occupation of the levels close to the Fermi energy. For the Ni_2 dimer the SOC-induced splitting of the degenerate eigenstate for parallel orientation of the magnetic moments is modest; it is largest (0.13–0.17 eV) for the highest occupied $\delta_d^\star$ and δ_d states but the center of gravity of the SOC-split states remains essentially the same (see Fig. 2). In this case the one-electron energies are not a sufficient indicator of the easy axis of magnetization which must be derived from a full total-energy calculations. For both solutions the easy axis is determined by the larger orbital moment while the magnitude of the orbital anisotropy is of the same order of magnitude. The difficulty to find a unique answer for the MAE of the Ni dimer is related to the well-known fact that the description of the electronic ground state by a single-determinant wave function (which is inherent in DFT) fails for Ni where the ground state has a multideterminant character.[50] The two solutions differing in their orbital moments might be considered as possible single-determinant solutions while a better description might by achieved with an ansatz mixing these two (and possibly other) configurations.

For Pd_2 SOC induces a splitting of the degenerate $\delta_d^\star$ and δ_d states ranging between 0.29 and 0.36 eV, and a more modest splitting of the $\pi_d^\star$ and π_d states between 0.14 and 0.24 eV. The center of gravity of the SOC-split doublets can be shifted up or down; the very small MAE is the result of a very delicate balance of up and down shifts. For the hard axis (i.e., magnetization parallel to the dimer axis) we find,

in agreement with FSF (Ref. 8) and SCM (Ref. 7) but in disagreement with FKRE,[9] an almost vanishing orbital moment. For the hard (parallel) magnetic axis of the Pd_2 dimer, FSF (Ref. 8) report for both the LDA and the GGA a discontinuous change in the orbital magnetic moment from $\mu_L \sim 0$ to $\mu_L \sim 1.0\mu_B$ if the dimer bond length is increased beyond 2.50 Å while SCM (Ref. 7) report a similar increase in the orbital moment for a bond length compressed to 2.15 Å. We find in our GGA calculations the same discontinuous variation in the orbital moment as reported by FSF. If the bond length is only very slightly increased from its equilibrium value of 2.49–2.51 Å, the orbital moment increases to $\mu_L \sim 1.0\mu_B$ while the orbital moment along the easy axis is found to be rather insensitive to the dimer length. The discontinuous change in the orbital moment reverses the sign of the orbital anisotropy but in both GGA calculations the sign of the MAE remains the same; it even increases to a large value of about 50 meV (both FSF and present work). Only for the LDA calculations a reversal of the sign of the MAE is found if the bond length is stretched beyond 2.6 Å.[8] The discrepancy with respect to the work of FKRE is related to a very large bond length of 2.93 Å reported in their work—it is difficult to understand the origin of such a large Pd-Pd distance because the LDA used in their work rather tends to underestimate the bond lengths. FSF report an LDA value of the bond length of 2.45 Å, smaller than their GGA value as expected.

For Pt_2 we calculate large strongly anisotropic spin and orbital moments—$\mu_S = 1.88(1.34)\mu_B$, $\mu_L = 2.74(0.80)\mu_B$ for the easy (hard) magnetic axis. Pt_2 is the only dimer for which SOC influences also the bond length. In the scalar-relativistic mode we find $d = 2.33$ Å (at a magnetic moment of $\mu_S = 2\mu_B$); including SOC we calculate $d = 2.38$ Å for magnetization along the easy axis and $d = 2.35$ Å for hard-axis magnetization. No similar magnetostructural effect has been found for the other $5d$ dimers Ir_2 and Os_2. SOC leads to a reordering of the eigenstates close to the Fermi level even for perpendicular orientation of the magnetization [see Fig. 2(c)]—the $\sigma_d^\star$ state is lowered below the $\delta_d^\star$ state occupied by two electrons which is now the HOMO. The splitting of the doubly-degenerate $\pi_d^\star$ and $\delta_d^\star$ eigenstates at either side of the HOMO for a magnetization parallel to the dimer axis is larger than the separation of the eigenlevels. This leads to a change in occupation: one electron from a $\delta_d^\star$ state is transferred to the lower component of the $\pi_d^\star$ state; the HOMO is now the $\sigma_d^\star$ state as in the scalar-relativistic approximation. In addition, the pronounced anisotropy of the spin moment (and hence also of the exchange splitting) is reflected in the eigenvalue spectra—for some eigenstates SOC splitting is not symmetrical but accompanied by a shift in the center of gravity of the split eigenstates. This leads to contributions to the MAE of 46.3 meV which are not restricted to eigenstates close to the Fermi level. Similar effects have also been seen for Ir_2 and (although to a much smaller extent) for Os_2; they decrease with a decreasing orbital anisotropy.

C. Fe group

For the dimers of the Fe-group metals the trend in the MAE is rather complex. Fe_2 shows axial anisotropy but with a very small MAE of only 0.32 meV, Ru_2 has perpendicular anisotropy with a large negative MAE of −36.5 meV, and Os_2 an axial anisotropy with a lower MAE of only 28.8 meV. Only for Fe_2, reference values from the work of FKRE (Ref. 9) are available; they find a much larger MAE (32 meV) related to a much higher orbital anisotropy.

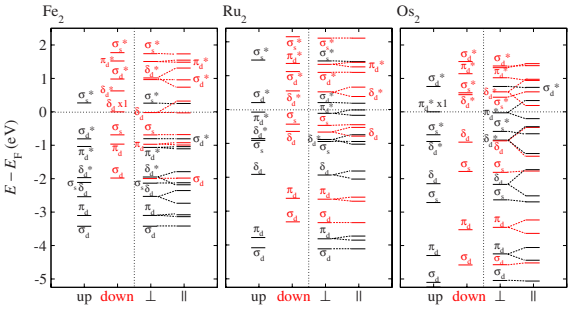


FIG. 3. (Color online) Kohn-Sham eigenvalue spectra for Fe_2 (left), Ru_2 (center), and Os_2 (right) dimers, cf. Fig. 1.

The electronic ground-state configurations are s^2d^6 for Fe and Os but sd^7 for Ru. In the scalar-relativistic approximation the ground state is $S=3$ for the Fe dimer and $S=2$ for the Ru and Os dimers. For Ru_2 we have also found solutions with $S=1$ and a lower bond length of $d=2.03$ Å, and with $S=3$ solution and $d=2.23$ Å, both are 357 and 303 meV above the ground state, respectively. Despite these relatively large energy differences, it was found that different initializations of the magnetic moment in the fully relativistic calculations can lead to different locally stable solutions. Here we report only the results for the lowest energy. Differences in the atomic ground-state configurations and in the exchange splitting lead to different eigenvalue spectra. In the scalar-relativistic approximation (and also for perpendicular magnetization if SOC is included), the HOMO of the Fe_2 dimer is the doubly-degenerate minority δ_d state occupied by one electron only while the highest occupied majority state is the antibonding $\sigma_d^\star$ state (see Fig. 3). For the Ru dimer the HOMO is the doubly-degenerate antibonding majority $\pi_d^\star$ state occupied by two electrons while the highest occupied minority state is the σ_s state. For Os_2 the HOMO is again the $\pi_d^\star$ state but, because the relativistic effects shift the antibonding $\sigma_s^\star$ state (which is unoccupied for Ru_2) below the HOMO, it is now occupied only by one electron. Hence already in a scalar-relativistic mode, all three dimers have different electronic configurations close to the Fermi edge.

For the Fe_2 the spin moment is almost unchanged by SOC and the orbital magnetic moment is very small: $0.16\mu_B$ for the hard (perpendicular) axis and $0.32\mu_B$ for the easy (parallel) axis. For the hard axis the orbital moment agrees with FKRE (Ref. 9) but for the easy axis they report a much larger orbital moment. We find that the result for the orbital magnetic moment depends critically on the initialization of the magnetic moment. If for a magnetic moment parallel to the dimer axis the relativistic calculation is started with a lower initial spin moment, it converges to a state with the same spin moment but with a much larger orbital moment of $\mu_L = 1.74\mu_B$, i.e., very close to the value reported by FKRE. If

the iterations are continued (by setting a lower convergence criterion) the calculation converges to the solution with low orbital moment (which is lower in energy by about 86 meV). We also tried to find a high-μ_L solution for the hard axis but the calculations always converged to the low-moment result. SOC splits for a parallel magnetic axis the degenerate δ_d HOMO, but as the center of gravity is up shifted, the energy gain is very modest. As the changes in the lower-lying eigenstates are balanced, this explains the very small value of the MAE.

For Ru_2 we find zero orbital magnetic moment for a magnetization along the dimer axis (as for Pd_2), and a modest orbital moment for perpendicular orientation. SOC induces for axial orientation of the magnetic moment a splitting of the degenerate and fully occupied $\pi_d^\star$ HOMO by 0.12 eV, the lower-lying $\delta_d^\star$ and δ_d states are split by 0.20–0.26 eV, and the splitting is accompanied by an up shift of the center of gravity (see Fig. 3). The change in the sum of the one-electron energies is −40 meV; this correlates rather well with the calculated perpendicular MAE of −35.5 meV.

For the Os_2 dimer we calculate a spin anisotropy of $\Delta\mu_S = 0.26\mu_B$ which is even larger than the orbital anisotropy of $\delta\mu_S = 0.18\mu_B$. The axial anisotropy with MAE=29 meV results mainly from the splitting of the doubly-degenerate $\pi_d^\star$ HOMO occupied by only one electron. The SOC-induced splitting of the lower-lying π_d and δ_d levels is quite large but symmetric; the changes in all other eigenvalues essentially balance each other.

D. Post-DFT calculations

A certain weakness of the DFT is that the effective one-electron potential is orbital independent. To test whether an orbital dependence of the electron-electron interaction has a strong influence on the calculated orbital moments and magnetic anisotropy energies, we performed some calculations using a hybrid functional mixing Hartree-Fock (and hence orbital-dependent) exchange with DFT exchange in a ratio of 1:3 and treating correlation at the GGA level, and with a DFT+U approach[22,51] adding a Hubbard-type on-site Coulomb potential U acting on the d electrons to the DFT Hamiltonian. In the version of the DFT+U proposed by Dudarev *et al.*,[51] the on-site repulsion enters only in the form $(U-J)$, where J is the on-site exchange interaction. We use a constant value of $J=1$ eV and vary U between $U=1$ eV (representing the GGA limit—but note that there might be small differences arising from incomplete cancellations between the double-counting corrections in the standard DFT and Hubbard terms) and $U=5$ eV. The on-site repulsion increases the exchange splitting for the partially occupied d states but leaves the potential acting on fully occupied or empty eigenstates essentially unchanged. We use the DFT+U approach in the form of GGA+U calculations.

The use of the GGA+U is based on the observation of Chadov *et al.*[21] that with a value of $U \sim 3$ eV for the bulk ferromagnets orbital moments in agreement with experiment are obtained while leaving the spin moment unchanged. The hybrid functional chosen is the HSE03 functional[47] (but the PBE0 functional[46] gives essentially identical results because the screening of the exchange in the HSE03 functional is long range and ineffective for isolated atoms and dimers). It must, however, be pointed out that for bulk ferromagnetic hybrid functionals lead to an overestimation of the spin moment.[52] For Fe the calculated moment is about $3\mu_B$, substantially larger than both experiment and conventional GGA calculations (which agree on a moment of $2.2\mu_B$). The results are compiled in Table II.

For Ni_2 we find that admixture of Hartree-Fock exchange increases the dimer bond length, leaves the spin moments unchanged, and leads even to a slight reduction in the orbital moment for easy-axis orientation (compared to the low-energy solution A in the GGA). Along the hard axis the orbital moment is unaffected. The MAE is reduced from 6.5 to 3.7 meV. In calculations with hybrid functionals we find only the solution with a substantial orbital moment for in-axis magnetization, in contrast to the GGA calculations.

HSE03 calculations for Pd_2 leave the bond length and the spin and orbital moments for parallel orientation of the magnetic moment unchanged; for perpendicular orientation the orbital moment is increased from $0.36\mu_B$ to $0.50\mu_B$. The MAE is very small; we find that a perpendicular orientation is still preferred but only by 0.3 meV.

In hybrid-functional calculations for Pt_2 the bond length is slightly increased by 0.05 Å. Spin moments are hardly affected but the orbital moment of the dimer increases from $2.74\mu_B$ to $3.02\mu_B$ for easy (parallel) orientation of the magnetic moment and from $0.80\mu_B$ to 1.06 μ_B for hard-axis orientation. The spin anisotropy is slightly reduced while the orbital anisotropy remains unchanged. The MAE is reduced from 46.5 to 30.5 meV.

Examination of the eigenvalue spectrum shows that the main effect of the admixture of a fraction of Hartree-Fock exchange is to increase the exchange splitting of the partially occupied eigenstates. For the Pt_2 dimer these are the $\pi_d^\star$ states where the exchange splitting is increased from 1.05 to 3.05 eV for the bonding π_d states the increase is from 0.86 to 1.90 eV. The influence is much smaller for the π- and σ-bonded d states and for the s states (all changes are smaller than 0.1 eV), whereas changes in the bonding/antibonding splitting are also modest. Although in the scalar-relativistic approximation the empty $\pi_d^\star$ state is pushed quite far above the Fermi level, due to a strongly increased SOC splitting of both the $\pi_d^\star$ and $\delta_d^\star$ states for in-axis orientation, we find a similar change in the occupation of the highest eigenstates as with the GGA functional (see Fig. 4 and compare with Fig. 2) and consequently only a reduction but no reversal of the MAE.

For Pd_2 the partially occupied d state is the antibonding $\sigma_d^\star$ state whose exchange splitting is increased to 3.32 eV but this does not introduce any change in the orbital occupancy; the perpendicular anisotropy is preserved. For Ni_2 the strongest increase in the exchange splitting is calculated for the antibonding $\delta_d^\star$ but, as the occupied majority-spin component is located at sufficiently high binding energy, this does not induce a change in the magnetic anisotropy.

We have also performed a few calculations with a GGA+U Hamiltonian and U varying between 1 and up to 5 eV.[51] The effect of the Hubbard-type on-site potential U is again to increase the exchange splitting of partially occupied eigen-

TABLE II. Interatomic distance d (in Å), spin μ_S and orbital μ_L moments (in μ_B) of transition-metal dimers for axial and perpendicular orientations of the magnetization, MAE, and spin-orbit coupling constant ξ (both in meV). The MAE is positive for any easy axis parallel to the dimer axis. The calculations have been performed with a hybrid functional.

			Axial		Perp.			
Dimer	Method	d	μ_S	μ_L	μ_S	μ_L	MAE	ξ
Ni_2	HSE03	2.27	1.98	0.50	1.96	0.30	3.7	101
	GGA+U(1 eV) (A)	2.09	1.98	0.54	1.98	0.38	9.2	101
	GGA+U(1 eV) (B)	2.08	1.98	0.02	1.98	0.38	−6.7	117
	GGA+U(2 eV) (A)	2.08	1.98	0.48	1.98	0.38	25.0	105
	GGA+U(2 eV) (B)	2.07	1.98	0.02	1.98	0.38	−6.4	117
	GGA+U(3 eV) (A)	2.08	2.00	0.42	2.00	0.36	17.0	114
	GGA+U(3 eV) (B)	2.07	1.98	0.02	2.00	0.36	−6.2	117
Pd_2	HSE03	2.50	1.96	0.02	1.98	0.50	−0.3	343
	GGA+U(1 eV)	2.49	1.96	0.02	1.98	0.62	−2.3	393
	GGA+U(3 eV)	2.50	1.94	0.02	1.98	0.40	−2.1	384
	GGA+U(5 eV)	2.50	1.94	0.04	1.98	0.40	−2.3	355
Pt_2	HSE03	2.43	1.88	3.02	1.28	1.06	30.5	743
	GGA+U(1 eV)	2.38	1.88	2.74	1.34	0.80	45.6	735
	GGA+U(2 eV)	2.38	1.90	2.82	1.40	0.84	13.3	708
	GGA+U(3 eV)	2.38	1.90	2.90	1.48	0.88	−19.5	644
	GGA+U(5 eV)	2.37	2.04	3.12	1.66	1.00	−85.0	492

states. For the Ni_2 we find for an axial orientation of the magnetization, as for the standard GGA calculations, the coexistence of solutions with high and almost vanishing orbital moment, leading to a positive and negative MAE, respectively. The solution with an easy axis parallel to the dimer axis (positive MAE) is lower in energy, independent of the value of U, with an energy difference varying between 17 and 28 meV. A modest on-site Coulomb potential leads to a slightly stronger MAE. Since this is accompanied by a decrease in the orbital anisotropy, this cannot be described by a perturbative approach. For Pd_2 only the solution with almost zero orbital moment exists for parallel magnetization, independent of U. Since there is also only a modest decrease in the perpendicular orbital moment with increasing U, the MAE is hardly affected.

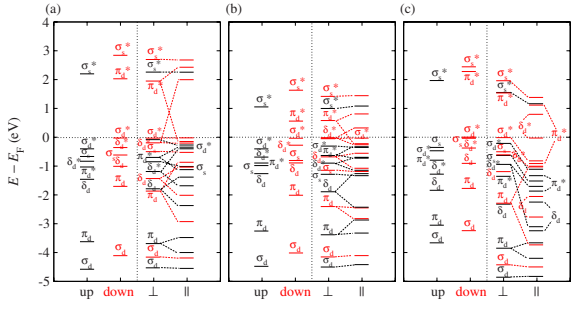


FIG. 4. (Color online) Kohn-Sham eigenvalue spectra for Pt_2 dimers for parallel and perpendicular orientations of the magnetic moments, calculated using (a) a hybrid functional and with a GGA+U approach, and (b) U=2 eV and (c) U=5 eV (cf. Fig. 2).

For the Pt dimer the GGA+U calculations predict a change in sign of the MAE with an increasing Coulomb repulsion. At a modest value of U=2 eV, the main effects are enhanced spin and orbital moments, an increased exchange splitting of the $\pi_d^\star$ states, and an increased SOC splitting—due to their combined effect, the ordering of the eigenstates near the Fermi level remains essentially the same for both axial and perpendicular orientations of the magnetization. As a result, the easy axis remains unchanged but due to shifts of lower-lying eigenstates, the MAE is reduced (see Fig. 4). For U=5 eV, the exchange splitting of the $\pi_d^\star$ states (Δ_{ex}=2.8 eV) and π_d(Δ_{ex}=1.5 eV) is increased to about the same magnitude as with the hybrid functional. For these states we also find a very large SOC splitting—even larger for the bonding component than calculated with a hybrid functional while the SOC splitting of the $\delta_d^\star$ state remain more modest. These lead to a rearrangement of the occupied eigenstates even at higher binding energies and to significant changes also in other contributions to the total energy, beyond the one-electron energies.

E. Dimers vs monowires

It is also interesting to confront our results for the magnetic properties of transition-metal dimers with the results available in the literature[30–32] for straight monowires. These results are compiled in Table III. The comparison shows that the relation between dimers and wires is entirely different for the magnetic 3d metals and for the nonmagnetic 4d and 5d metals.

For the 3d elements the interatomic distance is considerably shorter in a dimer than in an infinite monowire. The

TABLE III. Comparison of the magnetic properties of dimers and monowires: interatomic distance d (in Å), spin μ_S, and orbital μ_L moments (in μ_B) for axial and perpendicular orientations of the magnetization, and MAE (in meV/atom). The MAE is positive for any easy axis parallel to the dimer axis.

			Axial		Perp.		
Element		d	μ_S	μ_L	μ_S	μ_L	MAE
Fe_2	Dimer	1.98	2.92	0.16	2.92	0.08	0.15
Fe[a]	Wire	2.25	3.45	0.44	3.45	0.08	2.25
Co_2	Dimer	1.96	1.95	0.39	1.95	0.16	3.55
Co[a]	Wire	2.15	2.12	0.10	2.12	0.08	−0.68
Ni_2	Dimer	2.09	0.99	0.29	0.98	0.19	3.25
Ni[a]	Wire	2.18	1.20	0.50	1.20	0.06	11.43
Ru_2	Dimer	2.07	1.99	0	1.97	0.12	−18.25
Ru[b]	Wire	2.24	1.12	0.15	1.10	0.03	−10.50
Rh_2	Dimer	2.21	1.93	0.91	1.90	0.25	23.65
Rh[b]	Wire	2.31	0.30	0.36	0	0	5.00
Pd_2	Dimer	2.49	0.98	0.01	0.99	0.18	−1.15
Pd[b]	Wire	2.48	0.50	0	0.30	0.12	−5.00
Pt_2	Dimer	2.38	1.88	2.74	1.34	0.80	23.15
Pt[c]	Wire	2.39	0.19	0.17	0	0	2.00

[a]Reference 31, GGA.
[b]Reference 30, LSDA.
[c]Reference 32, GGA.

increased distance leads to an enhancement of the spin moment but not necessarily to a corresponding enhancement of the orbital moment. For the 4*d* and 5*d* elements the contraction of the bond length in the dimer is much more modest; for Pd and Pt it is the same in the dimer and in the infinite wire. Both spin and orbital moments are strongly reduced in the wire compared to the dimer.

The formation of orbital moments and the origin of a strong MAE in monowires has been discusses by Mokrousov *et al.*,[30] Smogunov *et al.*,[32] and Velev *et al.*[53] in terms very similar to the analysis we have used for dimers. The main difference is that the discrete eigenvalue spectrum of the dimer is replaced by a set of one-dimensional bands with sharp van-Hove singularities at the upper and lower edges (see, e.g., Spišák and Hafner,[26] and Mokrousov *et al.*[30] for detailed representations of the one-dimensional band structure). Under the rotational symmetry (group $C_{\infty v}$) of the wire there are two double-degenerate bands (corresponding to the π_d and δ_d states of the dimer) and a nondegenerate band (corresponding to the σ_d states). The bands are split under the influence of exchange and spin-orbit interactions. The SO splitting depends again on the direction of magnetization; for parallel magnetization the splitting of the doublets is first order in the SOC operator; for perpendicular magnetization the SOC operator has zero matrix elements within the doublets; a splitting occurs only near the band crossing points.[53] A spin moment is formed when the exchange splitting leads to a larger occupation of spin-up states while an orbital moment is formed if bands with angular momenta $\pm\mu_l$ have different occupancies. A strong effect is to be expected if the van-Hove singularity of a spin-split degenerate band occurs close to the Fermi edge.

The essential difference between the 3*d* and the heavier metals is that in the former case the exchange splitting is much larger than the SOC splitting while for the second group both are of similar magnitude. For the 3*d* elements the band narrowing resulting from the increased interatomic distance in the wire leads to an enhanced spin moment. For Fe wires the Fermi level lies just above the lower van-Hove singularity of the minority δ_d band (corresponding to the δ_d state of the dimer), while for Ni wires it lies just above the upper singularity (corresponding to the $\delta_d^\star$ state of the dimer). In these cases, the SOC-induced splitting is more efficient for the wire with large density of states (DOS) even at E_F, leading to an increased orbital moment for parallel but not for perpendicular magnetization. In a Co wire the Fermi level falls close to the DOS minimum in the δ_d band; in this case the orbital moments in the wire is even lower than in the dimer. For the heavy elements the bandwidths of the wire are strongly influenced by long-range interactions—this leads to a strong decrease in the exchange splitting and of the spin moment if the interatomic distance is lower than a critical value.[30] For all wires the equilibrium interatomic spacing is lower than this threshold; the onset of the formation of an orbital moment is coupled to the formation of a spin moment.[30,32] Hence for these elements the orbital moment in an infinite wire is decreased compared to the dimer and this is also reflected in the magnitude of the MAE. The sign of the MAE is the same for dimers and wires except for Co where the strong decrease in the orbital anisotropy leads to a small negative MAE for the infinite wire.

IV. DISCUSSION AND CONCLUSIONS

We have presented detailed DFT calculations of the influence of spin-orbit coupling (SOC) on the structural and magnetic properties, and of the magnetic anisotropy energies of dimers of metals from groups 8 to 10 of the Periodic Table. For the metals from group 10 we have also briefly examined the influence of orbital-dependent post-DFT corrections (mixing of Hartree-Fock and DFT exchange, and addition of an orbital-dependent on-site Coulomb potential to correct for the self-interaction error in DFT).

SOC has almost no influence on the dimer bond length. Only for a Pt_2 dimer a stretching of the Pt-Pt distance by 0.03 Å has been found. Due to the mixing of different spin eigenstates, the spin moment is no longer an integer multiple of μ_B when SOC is included. For all dimers considered here, SOC induces a slight reduction in the spin moment by $0.02\mu_B$–$0.25\mu_B$, increasing with the strength of the SOC. For the heavier elements the coupling between spin and orbital moments also induces an anisotropy of the spin moments which is modest for the 4*d* and rather strong for the 5*d* elements. In some cases, the determination of the relativistic ground state is hampered by the existence of multiple local minima with different orbital moments. This is the case for Ni_2 where, for a magnetic axis parallel to the dimer axis, a solution with a large orbital moment is only 27 meV lower in energy than a low-moment solution while for perpendicular

magnetization, only one solution with an intermediate value of the orbital moment is found. Hence the two solutions lead to different signs of the orbital anisotropy and of the MAE. This could also explain why DFT calculations published in the literature predict different easy-axis orientations.[7,9] For a Pd_2 dimer we find, in agreement with earlier results,[8] a discontinuous variation in the orbital moment with the length of the dimer. A further difficult case is the Fe_2 dimer. Here our result for the easy-axis orbital moment and for the MAE is much lower than the value reported by Fritsch *et al.*[9]—here again we succeeded in finding a high-moment solution but at a higher energy than the low-moment results. Altogether our analysis has demonstrated that very strict convergence criteria and a careful exploration of the potential-energy surface as a function of both spin and orbital moments is required for a reliable determination of the MAE.

One of the main objectives of our study was to elucidate the physical mechanism determining the variation in the MAE with *d*-band filling and strength of the SOC. Here we found that the analysis of the eigenvalue spectra proposed by Strandberg *et al.*[7] is very useful. For all three dimers of the Co group, the HOMO in a scalar-relativistic approximation and for perpendicular magnetization if SOC is included is a doubly-degenerate $\delta_d^\star$ state occupied by a single electron. In this case the most important factor leading to a preferred axial magnetization is the lifting of the degeneracy of the eigenstates leading to a reduction in the one-electron energies. For the dimers from the Fe and Ni groups, we find a small axial anisotropy for the 3*d* dimers, perpendicular anisotropy for the 4*d* dimers, and a rather large axial MAE for the 5*d* dimers. In these cases we could show that a decisive factor is difference in the atomic ground states (lower *d*-electron number) of the 4*d* elements. For both Ru_2 and Pd_2 the HOMO is a doubly-degenerate doubly occupied $\pi_d^\star$ state and SOC splitting stabilizes a perpendicular anisotropy as discussed in detail above. For the other four dimers an axial anisotropy is calculated.

Post-DFT calculations have been explored for the dimers of the Ni group. Mixing orbital-dependent Hartree-Fock with DFT exchange leads to an increased bond length for Ni and Pt dimers, in which spin moments remain unaffected, while orbital moments are slightly increased for Pd and Pt—but this hardly affects the MAE, adding an on-site Coulomb *U* to the *d* states. Similarly to an exact-exchange contribution, the effect of *U* is to increase the exchange splitting of the partially occupied *d* states and an increase in the SOC. Spin moments are hardly changed; orbital moments decrease with increasing *U* for Ni_2 and Pd_2 but increase for Pt_2 where a large *U* leads to a change in sign of the MAE. However, such large values of the on-site repulsion evidently lead to a rather unrealistic eigenvalue spectrum.

We also presented a comparative analysis of the formation of orbital moments and of MAEs in dimers and in infinite straight monowires. It is shown that the differences in the magnetic properties of dimers and wires can be traced back to the difference between the discrete eigenvalue spectrum of the dimer and a continuous one-dimensional DOS of the wire. This analysis also highlights the difference between the magnetic 3*d* and the nonmagnetic 4*d* and 5*d* elements.

In summary, we have presented detailed DFT calculations of the magnetic anisotropy energies of dimers of the late transition atoms from groups 8 to 10, providing an improved understanding of the physical effects determining the sign and magnitude of the MAE. Our results also illustrate some of the difficulties inherent in such calculations, associated with the difficulty of finding the relevant minima on a complex potential-energy surface and explaining certain discrepancies with regard to other calculations.[7–9] Calculations with hybrid functionals and a GGA+*U* Hamiltonian (which introduce an orbital dependence of the effective one-electron potential) introduce only modest changes with respect to conventional DFT calculations, as long as only moderate realistic values of the on-site Coulomb repulsion are admitted. The largest MAE calculated for a Pt_2 dimer corresponds to a temperature of about 500 K. However, whether this is a result that is significant for potential applications will depend on the ability to find a substrate or matrix supporting the dimer without strongly reducing the MAE.

ACKNOWLEDGMENT

This work has been supported by the Austrian Science Funds under Project. No. P19712-N16.

*Corresponding author; juergen.hafner@univie.ac.at

[1] D. Sellmyer and R. Skomski, *Advanced Magnetic Nanostructures* (Springer, New York, 2006).
[2] S. Maekawa and T. Shinjo, *Spin Dependent Transport in Magnetic Structures* (Taylor & Francis, London, 2002).
[3] J. A. Alonso, Chem. Rev. (Washington, D.C.) **100**, 637 (2000).
[4] F. Baletto and R. Ferrando, Rev. Mod. Phys. **77**, 371 (2005).
[5] T. Futschek, M. Marsman, and J. Hafner, J. Phys.: Condens. Matter **17**, 5927 (2005).
[6] T. Futschek, J. Hafner, and M. Marsman, J. Phys.: Condens. Matter **18**, 9703 (2006).
[7] T. O. Strandberg, C. M. Canali, and A. H. MacDonald, Nature Mater. **6**, 648 (2007); Phys. Rev. B **77**, 174416 (2008).
[8] L. Fernandez-Seivane and J. Ferrer, Phys. Rev. Lett. **99**, 183401 (2007); **101**, 069903(E) (2008).
[9] D. Fritsch, K. Koepernik, M. Richter, and H. Eschrig, J. Comput. Chem. **29**, 2210 (2008).
[10] B. Lazarovits, L. Szunyogh, and P. Weinberger, Phys. Rev. B **67**, 024415 (2003).
[11] B. Nonas, I. Cabria, R. Zeller, P. H. Dederichs, T. Huhne, and H. Ebert, Phys. Rev. Lett. **86**, 2146 (2001).
[12] I. Cabria, B. Nonas, R. Zeller, and P. H. Dederichs, Phys. Rev. B **65**, 054414 (2002).
[13] S. Bornemann, J. Minar, J. B. Staunton, J. Honolka, A. Enders, K. Kern, and H. Ebert, Eur. Phys. J. D **45**, 529 (2007).
[14] P. Bruno, Phys. Rev. B **39**, 865 (1989).
[15] G. van der Laan, J. Phys.: Condens. Matter **10**, 3239 (1998).
[16] C. Andersson, B. Sanyal, O. Eriksson, L. Nordström, O. Karis,

D. Arvanitis, T. Konishi, E. Holub-Krappe, and J. H. Dunn, Phys. Rev. Lett. **99**, 177207 (2007).
[17] I. V. Solovyev, Phys. Rev. Lett. **95**, 267205 (2005).
[18] M. S. S. Brooks, Physica B & C **130**, 6 (1985).
[19] O. Eriksson, M. S. S. Brooks, and B. Johansson, Phys. Rev. B **41**, 7311 (1990).
[20] H. Eschrig, M. Sargolazei, K. Koepernik, and M. Richter, Europhys. Lett. **72**, 611 (2005).
[21] S. Chadov, J. Minar, M. I. Katsnelson, H. Ebert, D. Ködderitzsch, and A. I. Lichtenstein, Europhys. Lett. **82**, 37001 (2008).
[22] V. I. Anisimov, J. Zaanen, and O. K. Andersen, Phys. Rev. B **44**, 943 (1991).
[23] G. Kotliar, S. Y. Savrasov, K. Haule, V. S. Oudovenko, O. Parcollet, and C. A. Marinetti, Rev. Mod. Phys. **78**, 865 (2006).
[24] P. Söderlind, O. Eriksson, B. Johansson, R. C. Albers, and A. M. Boring, Phys. Rev. B **45**, 12911 (1992).
[25] W. D. Brewer, A. Scherz, C. Sorg, H. Wende, K. Baberschke, P. Bencok, and S. Frota-Pessoa, Phys. Rev. Lett. **93**, 077205 (2004).
[26] D. Spišák and J. Hafner, Phys. Rev. B **66**, 052417 (2002); **67**, 214416 (2003).
[27] Y. Mokrousov, G. Bihlmayer, S. Blügel, and S. Heinze, Phys. Rev. B **75**, 104413 (2007).
[28] M. Komelj, C. Ederer, J. W. Davenport, and M. Fähnle, Phys. Rev. B **66**, 140407(R) (2002).
[29] C. Ederer, M. Komelj, and M. Fähnle, Phys. Rev. B **68**, 052402 (2003).
[30] Y. Mokrousov, G. Bihlmayer, S. Heinze, and S. Blügel, Phys. Rev. Lett. **96**, 147201 (2006).
[31] J. C. Tung and G. Y. Guo, Phys. Rev. B **76**, 094413 (2007).
[32] A. Smogunov, A. dal Corso, A. Delin, R. Weht, and E. Tosatti, Nat. Nanotechnol. **3**, 22 (2008).
[33] M. C. Desjonquères, C. Barreteau, G. Autès, and D. Spanjaard, Eur. Phys. J. B **55**, 23 (2007).
[34] G. Kresse and J. Furthmüller, Comput. Mater. Sci. **6**, 15 (1996); Phys. Rev. B **54**, 11169 (1996).
[35] G. Kresse and D. Joubert, Phys. Rev. B **59**, 1758 (1999).
[36] J. P. Perdew and Y. Wang, Phys. Rev. B **45**, 13244 (1992).
[37] S. H. Vosko, L. Wilk, and M. Nusair, Can. J. Phys. **58**, 1200 (1980).
[38] E. G. Moroni, G. Kresse, J. Hafner and J. Furthmüller, Phys. Rev. B **56**, 15629 (1997).
[39] P. E. Blöchl, Phys. Rev. B **50**, 17953 (1994).
[40] G. Kresse and O. Lebacq, *VASP Manual* http://cms.mpi.univie.ac.at/vasp/vasp/vasp.html.
[41] L. Kleinman, Phys. Rev. B **21**, 2630 (1980).
[42] A. H. MacDonald, W. E. Pickett, and D. D. Koelling, J. Phys. C **13**, 2675 (1980).
[43] D. Hobbs, G. Kresse, and J. Hafner, Phys. Rev. B **62**, 11556 (2000).
[44] M. Marsman and J. Hafner, Phys. Rev. B **66**, 224409 (2002).
[45] G. Y. Guo, W. M. Temmermann, and H. Ebert, J. Phys.: Condens. Matter **3**, 8205 (1991).
[46] J. P. Perdew, M. Ernzerhof, and K. Burke, J. Chem. Phys. **105**, 9982 (1996); K. Burke, M. Ernzerhof, and J. P. Perdew, Chem. Phys. Lett. **265**, 115 (1997).
[47] J. Heyd, G. E. Scuseria, and M. Ernzerhof, J. Chem. Phys. **118**, 8207 (2003); J. Heyd and G. E. Scuseria, *ibid.* **120**, 7274 (2004).
[48] J. Paier, M. Marsman, K. Hummer, G. Kresse, I. C. Gerber, and J. G. Angyan, J. Chem. Phys. **124**, 154709 (2006).
[49] A. Rohrbach, J. Hafner, and G. Kresse, Phys. Rev. B **69**, 075413 (2004).
[50] J. Bünemann, F. Gebhard, and W. Weber, in *Frontiers in Magnetic Materials*, edited by A. Narlikar (Springer, Berlin, 2005).
[51] S. L. Dudarev, G. A. Botton, S. Y. Savrasov, C. J. Humphreys, and A. P. Sutton, Phys. Rev. B **57**, 1505 (1998).
[52] A. Stroppa, K. Termentzidis, J. Paier, G. Kresse, and J. Hafner, Phys. Rev. B **76**, 195440 (2007).
[53] J. Velev, R. F. Sabirianov, S. S. Jaswal, and E. Y. Tsymbal, Phys. Rev. Lett. **94**, 127203 (2005).

Strong spin–orbit effects in small Pt clusters: Geometric structure, magnetic isomers and anisotropy

Piotr Błoński,[1] Samuel Dennler,[2] and Jürgen Hafner[1,a)]
[1]*Fakultät für Physik and Center for Computational Materials Science, Universität Wien, Sensengasse 8/12, A-1090 Wien, Austria*
[2]*Laboratoire des Colloïdes, Verres et Nanomatériaux, Université de Montpellier II, F-34095 Montpellier, France*

(Received 23 September 2010; accepted 3 December 2010; published online 19 January 2011)

Ab initio density functional calculations including spin–orbit coupling (SOC) have been performed for Pt_n, $n = 2$–6 clusters. The strong SOC tends to stabilize planar structures for $n = 2$–5, whereas for clusters consisting of six atoms, three-dimensional structures remain preferred. SOC leads to the formation of large orbital magnetic moments and to a mixing of different spin states. Due to the spin-mixing the total magnetic moment may be larger or smaller than the spin moment in the absence of SOC. Both spin and orbital moments are found to be anisotropic. Because of the strong SOC the energy differences between coexisting magnetic isomers can be comparable to or even smaller than their magnetic anisotropy energies. In this case the lowest barrier for magnetization reversal can be determined by a magnetic isomer which is different from the ground state configuration. © *2011 American Institute of Physics*. [doi:10.1063/1.3530799]

I. INTRODUCTION

The current interest in magnetic nanostructures is motivated by the quest for nanoscale information storage devices and by potential applications in nanospintronics.[1,2] A quantity of prime interest is the magnetic anisotropy, i.e., the dependence of the total energy of the system on the orientation of the magnetic moment. The magnetic anisotropy energy (MAE) determines the barrier to magnetization reversal due to thermal excitations; a large MAE is necessary to prevent the loss of information. The origin of the magnetic anisotropy is the coupling between the spin and orbital degrees of freedom; it is a fundamentally relativistic effect. In addition, magnetic anisotropy is critically dependent on symmetry and dimensionality; typically, the magnetic anisotropy is found to be much larger in low-symmetry nanostructures than in highly symmetric bulk materials. Prerequisites for a high magnetic anisotropy are a large spin magnetic moment and a strong spin–orbit coupling. Hence clusters or nanostructures of late 5d elements possessing an intrinsic spin moment and a strong spin–orbit coupling (SOC) are potential candidates for magnetic nanostructures with a large MAE.

However, for such clusters SOC is of decisive importance not only for the MAE but also for determining the equilibrium geometric structure. For small Pt clusters Huda *et al.*[3] have demonstrated that SOC stabilizes planar structures over the three-dimensional arrangements favored by scalar relativistic calculations, but magnetic properties have not been considered in their study. For neutral and charged Au clusters Häkkinen *et al.*[4] reported an increased preference for planar structures compared to Ag and Cu clusters, in agreement with experimental studies on mass-selected clusters by Gilb *et al.*[5] The stabilization of planar configurations has been attributed to relativistic effects shifting the 6s level closer to the 5d state and leading to a stronger s–d hybridization.

An abundant literature (including many *ab initio* studies) has been devoted to the geometric and magnetic properties of small metallic clusters (see, e.g., Refs. 6 and 7 and further references cited therein), but only a few *ab initio* calculations [8–13] have attempted to determine the MAE. For the smallest clusters, transition-metal dimers, the investigations have demonstrated that the magnetic anisotropy is determined by the nature and occupation of the electronic eigenvalues close to the Fermi level.[10–12] For magnetic moments perpendicular to the dimer axis, as in the absence of SOC, the eigenvalue spectrum consists of doubly degenerate π_d and δ_d and nondegenerate σ_d states. (Detailed representations of the eigenvalue spectra of dimers of Pt and other transition metals are given in the papers by Strandberg *et al.*[10] and Błoński and Hafner).[12] For magnetic moments aligned parallel to the dimer axis, SOC induces a splitting of the degenerate eigenstates due to the broken inversion symmetry. If the highest occupied eigenstate is doubly degenerate but occupied only by a single electron, the SOC-induced splitting of the eigenstate will stabilize an axial anisotropy.[10,12] A remarkable result of these studies is also that not only the orbital moments but also the spin moments can display a substantial anisotropy if the SOC is strong enough. The formation of orbital magnetic moments and the origin of a large MAE in monowires has been discussed by Mokrousov *et al.*,[14] Smogunov *et al.*,[15] and Velev *et al.*[16] using similar arguments. The main difference is that the discrete eigenvalue spectrum of the dimer is replaced by a set of one-dimensional bands, with sharp van Hove singularities at the upper and lower edges. Under rotational symmetry (group $C_{\infty v}$), there are doubly degenerate and nondegenerate bands corresponding to the δ_d and π_d and σ_d states of the dimer, respectively. Exchange coupling and SOC induce a

a)Author to whom correspondence should be addressed. Electronic mail: juergen.hafner@univie.ac.at.

 © 2011 American Institute of Physics

Downloaded 14 Apr 2011 to 128.130.131.2. Redistribution subject to AIP license or copyright; see http://jcp.aip.org/about/rights_and_permissions

band-splitting. For axial magnetization the SOC-induced splitting is first order; for perpendicular magnetization the SOC has zero matrix elements within the doublets and a splitting occurs only near the band crossing points. For Pt monowires Smogunov *et al.* have predicted a giant MAE—in this case the wire is ferromagnetic (FM) if the direction of magnetization is parallel to the wire, but the magnetic moments vanish if the magnetization direction is rotated to a perpendicular orientation. The spin-anisotropy predicted for the 4d and 5d dimers and the demagnetization of Pt monowires induced by a rotation of the magnetization direction indicate that the classical picture of the MAE based on perturbation theory, with a modest anisotropy of the orbital magnetic moments at isotropic spin moments,[17] cannot hold for clusters of the heavy transition metals. The same remark applies to the description of the MAE in terms of an effective "giant-spin" Hamiltonian proposed by Canali *et al.*,[18] which is also based on the assumption of isotropic spin moments.

For larger clusters, most attempts to understand the MAE have been limited to semiempirical approaches;[19,20] only a very few *ab initio* calculations have been published to date. Kortus *et al.*[8] calculated the MAE (defined as the difference in total energy for magnetic moments parallel and perpendicular to the symmetry axis) of 5- and 13-atom clusters of Co and Fe in terms of the second-order contribution from the SOC term, at a fixed geometry obtained from scalar relativistic calculations. For the five-atom clusters forming a trigonal bipyramid, MAE's of 0.1 and 0.2 meV/atom have been reported for Co and Fe clusters, respectively. For an Fe_{13} cluster forming a distorted tetrahedron, an MAE of 0.27 meV/atom was reported, while a Co_{13} cluster was described as magnetically isotropic. In mixed clusters the occupation of the sites with different atoms lowers the symmetry, leading to an enhanced MAE. The highest value of 0.37 meV/atom was reported for a $Co_{10}Fe_3$ cluster. Very recently Sahoo *et al.*[13] reported *ab initio* investigations of the MAE of 13-atom clusters of Fe, Co, and Ni, concentrating on the influence of symmetry. For clusters with the structure of an ideal icosahedron, MAEs of 1.7, 0.31, and 0.77 μeV/atom, comparable to the MAE of the bulk metals, have been reported for Fe_{13}, Co_{13}, and Ni_{13}, respectively. In this case, because of the high symmetry of the cluster, the leading contribution to the MAE is sixth-order in the SOC. A geometric distortion lowering the symmetry was found to enhance the MAE by orders of magnitude. For Fe_{13} an MAE of 0.32 meV/atom was reported for a "Jahn–Teller-distorted" cluster. However, only a restricted relaxation of the icosahedral structure describable by one-parameter models was permitted and the optimization was performed in a scalar relativistic mode, such that the possible influence of the SOC on the cluster structure was not considered. Fernandez-Seivane and Ferrer (hereafter referred to as FSF)[9] performed *ab initio* calculations of the geometric and magnetic structures of clusters of Pd, Ir, Pt, and Au with up to seven atoms, including SOC. For each cluster between two and five different "seeds" for the geometric and magnetic structures of the cluster have been used to initialize the calculations, making together five to ten different initial configurations per cluster. The MAE was defined as the energy difference between the two solutions with the lowest energies—evidently this energy difference may or may not correspond to the true magnetic anisotropy energy, as illustrated by their results for Pd_n and Pt_n. For the dimers, axial anisotropy for Pt_2 and perpendicular anisotropy for Pd_2 were reported, in semiquantitative agreement with our results.[12] For the trimers a triangular configuration with an in-plane easy axis was reported, again in partial agreement with our results to be discussed below. A Pt_4 cluster forms a rhombus with an easy axis lying in the plane—in this case we have been able to find a configuration with the same geometric but a different magnetic structure and a lower energy. For a Pt_5 cluster the ground state (GS) geometry reported by FSF (Ref. 9) is a tetragonal pyramid, whereas in their "first excited state" the cluster forms a trigonal bipyramid. Evidently in this case the energy difference between these states is not an MAE, but a structural energy difference (ignoring for the moment that there are also substantial differences in the spin and orbital moments of both configurations). It is important, however, to note that this structural energy difference is of the same order of magnitude with the MAEs reported for the smaller clusters. In addition, the work of Huda *et al.*[3] has shown that the ground state structure of a Pt_5 is not three-dimensional, but that a flat geometry is preferred.

These discussions illustrate the difficulties in achieving a correct relativistic description of clusters formed by heavy 5d metals. For these metals exchange and SOC induce a splitting of the Kohn–Sham eigenvalues which are of comparable order of magnitude. Energy differences between structural and magnetic isomers are also comparable and can be as small as magnetic anisotropy energies. In such a case an extended exploration of geometric and magnetic configurations space is required.

In the present work we investigated the structural, electronic, and magnetic properties of Pt_n clusters with $n \leq 6$ using *ab initio* density-functional theory (DFT) including SOC. Planar clusters are found to be lower in energy than three-dimensional arrangements up to $n = 5$. The energy differences between coexisting magnetic isomers with anisotropic spin and orbital moments are of the same order of magnitude with the MAE. These results lead to a picture of the physical mechanism determining the size of the MAE of the clusters, which is fundamentally different both from that suggested by low-order perturbation theory where the MAE is determined by a modest orbital anisotropy at isotropic spin moments[17] and from a description in terms of an effective giant-spin Hamiltonian such as in molecular magnets.[10,18]

II. COMPUTATIONAL SETUP

Our calculations are based on DFT as implemented in the Vienna *ab initio* simulation package VASP,[21,22] using a plane-wave basis and the projector-augmented wave approach[23] for describing the electron–ion interaction. The semilocal PW91 functional[24] in the generalized gradient approximation (GGA) and the spin-interpolation proposed by Vosko *et al.*[25] has been used for exchange and correlation. The use of a gradient-corrected functional is essential for magnetic systems. If the local-density approximation (LDA) is used, the ground state of Fe is predicted to be hexagonal-close-packed and

Downloaded 14 Apr 2011 to 128.130.131.2. Redistribution subject to AIP license or copyright; see http://jcp.aip.org/about/rights_and_permissions

nonmagnetic instead of body-centered cubic and ferromagnetic; Cr is found to be non-magnetic instead of antiferromagnetic (AFM) in the LDA ground state. In contrast, the GGA predicts the correct structural and magnetic ground states in both cases.[26] For a Pt_2 dimer an extended fully relativistic investigation of the performance of different local and semilocal exchange-correlation functionals in comparison with quantum-chemical approaches was performed by Anton *et al.*[27] It was concluded that spin-polarized GGA functionals lead to excellent agreement with the experimental bond length and binding energy. The GGA predictions are far superior to LDA results and for Pt_2 even better than quantum-chemical data.

Spin–orbit coupling has been implemented in VASP by Kresse and Lebacq.[28] Following Kleinman[29] and MacDonald *et al.*,[30] the relativistic Hamiltonian given in a basis of total angular momentum eigenstates $|j, m_j\rangle$ with $j = l \pm 1/2$ (containing all relativistic corrections up to order α^2, where α is the fine-structure constant) is recast in the form of 2×2 matrices in spin-space by reexpressing the eigenstates of the total angular momentum in terms of a tensor product of regular angular momentum eigenstates $|l, m\rangle$ and the eigenstates of the z-component of the Pauli spin matrices. The relativistic effective potential consists of a term diagonal in spin-space which contains the mass-velocity and Darwin corrections and the spin–orbit operator,

$$\mathbf{V} = \mathbf{V}^{\mathrm{sc}} + \mathbf{V}^{\mathrm{SO}} = \sum_{l,m} [V_l \cdot \mathbf{1}_\sigma + V_l^{\mathrm{SO}} \vec{\mathbf{L}} \cdot \vec{\mathbf{S}}] \, |l, m\rangle\langle l, m|,$$

where $\mathbf{1}_\sigma$ is the unit operator in spin-space and

$$\vec{\mathbf{L}} \cdot \vec{\mathbf{S}} = \frac{1}{2} \begin{pmatrix} L_z & L_- \\ L_+ & -L_z \end{pmatrix}.$$

The l-components of the scalar V_l and spin–orbit V_l^{SO} potentials are weighted averages over the $l \pm 1/2$ components, assuming that the magnetization is directed along the z-axis. The Hamiltonian is therefore a 2×2 matrix in spin-space. The nondiagonal elements arise from the spin–orbit coupling, but also from the exchange-correlation potential when the system under consideration displays a noncollinear magnetization density. Calculations including spin–orbit coupling have therefore to be performed in the noncollinear mode implemented in VASP by Hobbs *et al.*[31] and Marsman and Hafner[32] where the Hamiltonian is a functional of the 2×2 density matrix $n^{\alpha\beta}(\vec{r})$. The electron density $n(\vec{r})$ is given by the trace of the density matrix, and the density matrix may be written as a linear combination of the 2×2 unit matrix and the vector $\vec{\sigma} = (\sigma^x, \sigma^y, \sigma^z)$ of the three Pauli spin matrices,

$$n^{\alpha\beta}(\vec{r}) = \frac{[n(\vec{r})\delta_{\alpha\beta} + \vec{m}(\vec{r}) \cdot \vec{\sigma}^{\alpha\beta}]}{2},$$

with the magnetization density $\vec{m}(\vec{r}) = \sum_{\alpha\beta} n^{\alpha\beta}(\vec{r}) \cdot \vec{\sigma}^{\alpha\beta}$. For a local magnetization $\vec{m}(\vec{r})$ directed along the unit vector $\vec{n} = (\sin\theta\cos\phi, \sin\theta\sin\phi, \cos\theta)$, the exchange splitting is $b(\vec{r})\vec{n} \cdot \vec{\mathbf{S}}$ where $b(\vec{r}) = \delta E_{xc}[n^{\alpha,\beta}(\vec{r})]/\delta m(\vec{r})$ is the functional derivative with respect to the spin density $m(\vec{r}) = |\vec{m}(\vec{r})|$. The spin–orbit interaction is transformed using the Wigner spin-rotation matrices $D^{1/2}(\theta, \phi)$ to[33,34]

$$V_l^{\mathrm{SO}} D^{1/2\dagger}(\theta, \phi) \vec{\mathbf{L}} \cdot \vec{\mathbf{S}} D^{1/2}(\theta, \phi).$$

Note that both spin–orbit coupling and noncollinearity lead to a mixing of different spin-components.

Local electronic and magnetic properties can be calculated by projecting the plane-wave components of the eigenstates onto spherical waves within atomic spheres. Within each atomic sphere, spin and orbital momentums are referred to the local spin quantization axis. The local spin and orbital moments at the individual atoms have been determined by integrating the local angular-momentum- and spin-decomposed partial densities of states over occupied states. Note that the projection of the plane-wave basis states onto atomic spheres necessarily introduces a small error in the derived local quantities.

The calculations were performed for clusters placed into the center of a large cubic box with an edge length of 12 Å. For larger planar clusters the edge length was increased along the longest axis of the cluster to verify that the results are not influenced by interaction of the cluster with its periodically repeated images. The basis set contained plane waves with a kinetic energy of up to 500 eV; a convergence of the total energy within 10^{-7} eV was imposed during the self-consistency cycle. The cluster structure was relaxed without any symmetry constraints until the forces on all atoms were less than 10 meV/Å. For selected clusters and geometries we have verified that the results remain unchanged if a larger cutoff energy or a more stringent criterion for total energy and force convergence is imposed.

For the optimization of the cluster geometry, all possible geometries identified by earlier scalar relativistic calculations which are close enough in energy to the ground state geometry have been reoptimized in calculations including SOC self-consistently. For a simultaneous optimization of all geometric, electronic, and magnetic degrees of freedom, the magnetization vector relaxes to a direction where the total energy is stationary. In addition, configurations with a fixed arbitrary direction of the magnetization can be explored by constraining the direction of the magnetization vector by applying a penalty function. For each structural isomer the magnetic structure relaxes to a locally stable configuration related to the initial one by a steepest descent path. The symmetry of this configuration corresponds to one of the magnetic point groups that can be derived from the crystallographic point group of the cluster. However, as this magnetic structure is not necessarily the ground state, we have tested for each cluster a number of magnetic configurations, including structures breaking the magnetic point group symmetry (PGS).

III. RESULTS

Below we shall discuss our results for the geometries, spin and orbital magnetic moments, and the magnetic anisotropy of Pt_n clusters with $n = 2$–6. It has to be admitted that even at the level of scalar relativistic calculations, the results remain controversial. The literature published before 2006 has been summarized by Futschek *et al.*,[7] and the

Downloaded 14 Apr 2011 to 128.130.131.2. Redistribution subject to AIP license or copyright; see http://jcp.aip.org/about/rights_and_permissions

new results that have appeared meanwhile[35–38] have not always helped to achieve a converged result. The reasons for the divergent results are difficult to assess—they are related to different pseudopotentials and basis sets as well as different criteria for stopping the self-consistency iterations and the structural optimizations. Even plane-wave calculations using the same potential can produce different results because the criteria for energy and force convergence differ between 10^{-3} and 10^{-7} eV for energies and differ also widely for the residual forces. A further limitation of most calculations published so far is that static relaxation calculations always lead to a structure which is related to the initial one by a steepest–descent path. Many different initial configurations have to be used—but there is no guarantee that the global minimum has been found. To circumvent this difficulty, Futschek *et al.*[7] have used a dynamical simulated annealing at elevated temperature, followed by slow cooling and a final static optimization.

Spin–orbit effects on the cluster geometry have been reported by Huda *et al.*[3] and Sebetci;[38] geometry and magnetic anisotropy have been investigated only by FSF.[9] We will therefore compare our results for the geometry to the recent calculations but concentrate on the confrontation of our results for the MAE with those of FSF. In this context it is important to characterize briefly their computational setup. FSF used the local-orbital pseudopotential code SIESTA,[39] norm-conserving pseudopotentials,[40] and an implementation of SOC based on the so-called "on-site" approximation.[41] For dimers and trimers both LDA and GGA functionals have been used, but for clusters with four and more atoms only the LDA has been used. This must be kept in mind when the results are compared.

Our results for the Pt_2 dimer have been published before.[12] We begin our discussion with a brief recapitulation of these results, putting them into a more general context.

A. Pt_2

For a Pt_2 dimer the scalar relativistic DFT—GGA calculations predict a magnetic moment of 2 μ_B and a bond length varying between 2.33 Å (plane-wave based calculations)[3,7,35,37] and 2.45 Å (local-orbital calculations).[9,36] The calculations of Sebetci[38] based on a hybrid functional yield a bond length of 2.37 Å. The GGA result calculated in a plane-wave basis agrees with the measured bond length of 2.33 Å (Ref. 42).

If SOC is taken into account, the bond length increases slightly to 2.35 Å for axial and to 2.38 Å for perpendicular magnetization.[3,7,12] Slightly larger bond lengths of about 2.43 Å have been reported by Sebetci and FSF. A Pt_2 dimer has an easy magnetization direction parallel to the dimer axis; the very large MAE of 23.1 meV/atom is a consequence of the fact that the change of the magnetization direction induces a transition from a high-moment state with $M_J = 4.5\,\mu_B$ for axial to a low-moment state with $M_J = 2\,\mu_B$ for magnetization perpendicular to the dimer axis,[12] parallel to a contraction of the dimer bond length from 2.38 to 2.35 Å. The loss of magnetic moment arises primarily from a strong reduction of the orbital moment from $M_L \sim 2.7\,\mu_B$ to $\sim 0.8\,\mu_B$. The spin and orbital moments for the easy axis orientation are in semiquantitative agreement with FSF, who report, however, smaller spin and orbital anisotropies at a larger MAE of 37.5 meV/atom.

The strong spin and orbital anisotropy calculated for the Pt dimer corresponds to the results of Smogunov*et al.*[15] who found strained monoatomic wires of Pt to be FM if magnetized along the wire axis, but nonmagnetic if the magnetization direction is constrained to a perpendicular direction, resulting in a "giant" MAE of 36 meV/atom. Dimer and monowires are thus first examples to demonstrate that in nanostructures with a strong SOC, a reorientation of the magnetization direction may not only change the orbital moments but also induce a transition between high- and low-moment states or even cause the total disappearance of magnetism.

B. Pt_3

For the Pt_3 trimer all scalar relativistic calculations agree on a structure forming an equilateral or nearly equilateral triangle, but with bond lengths varying between 2.48–2.49 Å in the plane-wave calculations[3,7,35] and 2.53–2.57 Å in the local-orbital approaches.[9,36,43] The magnetic structure has been described as either nonmagnetic[35,36] or magnetic[7,9,43,44] with a spin moment of 2 μ_B. Futschek *et al.*[7] report an energy difference of only 14 meV/atom between the two magnetic isomers. Nonrelativistic quantum-chemical calculations[46] predict an isocele triangle with only a very small difference in the bond lengths (2.551 and 2.543 Å) and a nonmagnetic ground state.

SOC favors a Jahn–Teller distortion to an isocele triangle with two edges measuring 2.50 and one 2.51 Å, point group symmetry 2 mm in the Hermann–Mauguin notation. The easy axis is in-plane, coincident with the mirror-plane of the structure, see Fig. 1(a). The total magnetic moment is $M_J = 2.5\,\mu_B$, a reduced spin moment of 1.5 μ_B due to the mixing of different spin-states is overcompensated by a collinear total orbital moment of about 1 μ_B. A mixing of singlet and triplet states, with a dominant contribution from the triplet states, is also predicted by the quantum-chemical calculations.[46] Local spin and orbital moments are noncollinear, but the total spin and orbital moments are always aligned [see Fig. 1(a)]. In-plane rotation of the magnetization direction leaves total spin and orbital cluster moments unchanged, while the local moments undergo large variations [see Fig. 1(b)]. The in-plane MAE is very modest, only 0.2 meV/atom.

The magnetic point group is $2m'm'$ (where the prime indicates that the symmetry operation must be combined with a time-reversal operation which reverses the direction of axial vectors such as the magnetic moment)[45] for the ground state and $m'm2'$ for the hard in-plane direction. For perpendicular magnetization the Pt_3 cluster forms an equilateral triangle; both spin and orbital magnetic moments are strongly reduced; together we find $M_J = 1\,\mu_B$, with an MAE of 5.1 meV/atom relative to the in-plane easy axis configuration. The local spin and orbital moments are parallel on the site with the largest

Downloaded 14 Apr 2011 to 128.130.131.2. Redistribution subject to AIP license or copyright; see http://jcp.aip.org/about/rights_and_permissions

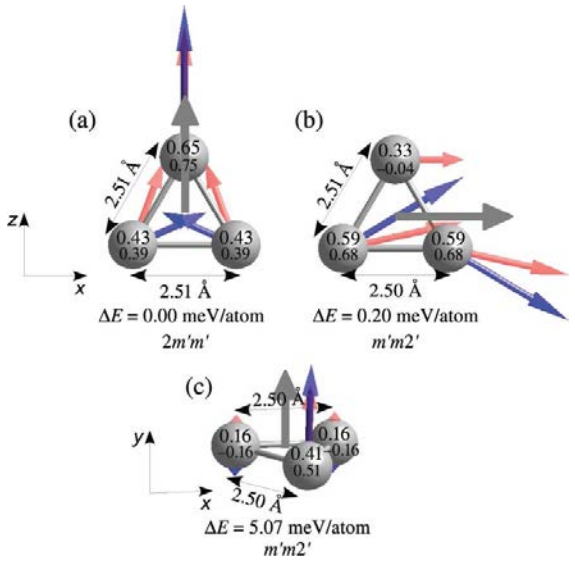


FIG. 1. Geometric and magnetic structures of a Pt_3 cluster for in-plane [(a) and (b)] and perpendicular (c) magnetization (as indicated by the grey arrows). Red (light) arrows shows spin magnetic moment and blue (dark) arrows the orbital magnetic moment; the numbers give the absolute values of the local spin (upper number) and orbital (lower number) magnetic moments $M_S(i)$ and $M_L(i)$ in μ_B. The easy axis corresponds to configuration (a), the energy for configuration (b) determines the in-plane, and (c) the axial MAE. For each configuration the magnetic point group symmetry and the energy difference relative to the ground state are listed below, cf. text.

moment, but antiparallel on the other two sites [see Fig. 1(c)]. Hence the magnetic structure breaks the threefold symmetry of the geometric arrangement; the magnetic point group symmetry is $m'm2'$ as for the hard in-plane configuration. As for the dimer, rotation of the magnetization to an orientation perpendicular of the easy plane induces a transition to a different low-moment magnetic isomer.

Our result for the GS agrees reasonably well with FSF.[9] However, FSF reported somewhat larger total moments of 2.96 μ_B and 2.19 μ_B for in-plane and perpendicular magnetization, respectively, and an MAE of 4.8 meV/atom in the GGA, comparable to our value for the perpendicular MAE. The larger magnetic moments reported by FSF are derived from a calculation of the local spin moments using a Mulliken analysis and a calculation of the local-orbital moments via the matrix elements of the orbital moment operator in their local atomic basis set. It has been shown that the Mulliken analysis based on overlapping local orbitals systematically leads to larger values of the local moments than the integration over atomic spheres.[13]

C. Pt_4

Scalar relativistic calculations predict for the Pt_4 cluster a structure forming a slightly distorted tetrahedron with an edge length of 2.60 Å and a magnetic moment of 2 μ_B, although a flat rhombus with edge length 2.50 Å and moment 4 μ_B is only 2 meV/atom higher in energy.[7] According to Sebetci,[38] Nie *et al.*,[36] and Xiao and Wang,[35] the scalar relativistic ground state is a more strongly distorted tetrahedron with a moment of 2 μ_B, whereas Bhattacharya and Majumder[37] found a high-moment rhombus with 4 μ_B to be lower in energy than the low-moment tetrahedron by 20 meV/atom. The differences in the bond length are probably due to different basis sets and more relaxed criteria for total energy and residual forces upon relaxation. A tetrahedral ground state geometry and a spin of $S = 1$ is also predicted by the quantum-chemical calculations of Dai and Balasubramanian.[47]

Calculations including SOC predict a rhombus (point group mmm) with an edge length of 2.53 Å, almost equal to the length of the short diagonal, to be lower in energy by 32 meV/atom than the tetrahedron. The higher stability of the rhombus compared to the tetrahedron agrees with Huda *et al.*[3] and FSF,[9] while Sebetci[38] finds the tetrahedron to be lower in energy. The local-orbital calculations predict slightly larger interatomic distances (2.55 Å according to FSF, 2.55–2.60 Å according to Sebetci). Surprisingly the GS is AFM with local magnetic moments $M_J(i) = \pm 0.54\ \mu_B$ on the sites connected by the short diagonal, while the other two atoms are nonmagnetic due to the frustration of the AFM interactions in triangular configurations. Rotation of the AFM moments into the plane reduces both spin and orbital moments and costs an energy of 4.4 meV/atom [see Figs. 2(a) and 2(b)]. The magnetic point group symmetries of these AFM configurations is $m'm'm'$.

For in-plane magnetization an FM state with spin and orbital moments aligned parallel to the short diagonal of the structure, $M_J = 4\,\mu_B$, $M_S = 2.6\,\mu_B$, and $M_L = 1.4\,\mu_B$ [see Fig. 2(c)] is energetically favored over the AFM state. This configuration corresponds to the scalar relativistic GS of the rhombus with $M_S = 4\,\mu_B$, with a reduced spin moment due to mixing of spin states which is just compensated by the orbital moment [Fig. 2(c)]. In-plane rotation of the FM magnetic moment to a direction parallel to the long diagonal costs an energy of 8.7 meV/atom and leads to a transition to a low-moment isomer with $M_J = 3\,\mu_B$ [see Fig. 2(d)]. For perpendicular magnetization we find an FM solution with $M_J = 3.7\,\mu_B$ with an energy intermediate between the two FM in-plane configurations [see Fig. 2(e)]. All three FM configurations have magnetic point group symmetry $mm'm'$.

Since the ground state is AFM, an MAE may be derived only for the excited FM states. The in-plane FM configuration corresponds to the ground states reported by Sebetci[38] and FSF;[9] we also note a quite good agreement of the total magnetic moments. FSF derived a large MAE of 12.5 meV/atom separating in-plane and perpendicular high-moment FM states. This energy is larger than the energy difference between our FM perpendicular and in-plane configurations of 5.3 meV/atom. The difference is due to the fact that FSF used the LDA for tetramers and larger clusters. For the smaller clusters FSF demonstrated that the LDA always leads to significantly larger values of the MAE.

For the three-dimensional structural isomer of Pt_4, the calculations including SOC predict a perfect tetrahedral geometry (point group symmetry $\bar{4}3m$, edge length 2.59 Å) and a noncollinear antiferromagnetic structure [see Fig. 3(a)]. All local moments point along one of the threefold symmetry

Downloaded 14 Apr 2011 to 128.130.131.2. Redistribution subject to AIP license or copyright; see http://jcp.aip.org/about/rights_and_permissions

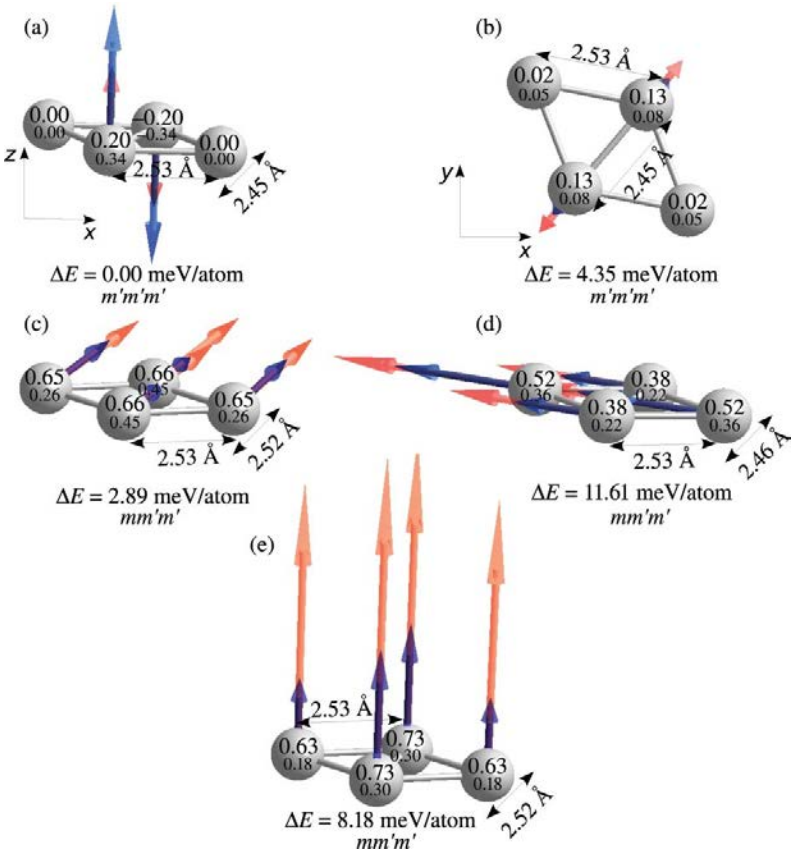


FIG. 2. Geometric and magnetic structures of a Pt_4 cluster for in-plane [(b–d)] and perpendicular [(a) and (e)] magnetization. Configurations (a) and (b) are antiferromagnetic, and (c)–(e) ferromagnetic, cf. Fig. 1.

directions; the magnetic point group is $\bar{4}'3m'$. The noncollinear orientation of the local moments relieves the frustration of the antiferromagnetic nearest-neighbor coupling in a triangular configuration. The AFM configuration of the Pt_4 tetrahedron is related not only to the AFM ground state of the planar cluster but also to the AFM ground state of the Pt_4 tetrahedron with zero spin from the scalar relativistic calculations.[7] However, as in these calculations noncollinearity was not considered, the frustration could be relieved only by lowering the tetrahedral symmetry. The total energy of this state is higher by 31 meV/atom than that for the magnetic GS of the rhombus. A noncollinear magnetic GS has also been reported by FSF (Ref. 9) for a Pd_4 tetrahedron.

A locally stable ferromagnetic state is found for a magnetization direction aligned parallel to one of the edges of the tetrahedron [see Fig. 3(b)]. In this configuration both local spin and orbital moments are enhanced relative to the ground state and slightly canted relative to the global magnetic moment. In this configuration the geometric structure is distorted in a way similar to that found in the scalar relativistic calculation; the magnetic point group symmetry is $2m'm'$. This configuration is higher in energy by 6.14 meV/atom than the noncollinear ground state.

D. Pt_5

Scalar relativistic calculations[3,7,35,36] predict that the Pt_5 cluster forms a trigonal bipyramid carrying a magnetic moment of 4 μ_B, which is found to be lower in energy by 35 meV/atom than a square pyramid with a magnetic moment of 6 μ_B. Sebetci[38] finds a capped tetrahedron to

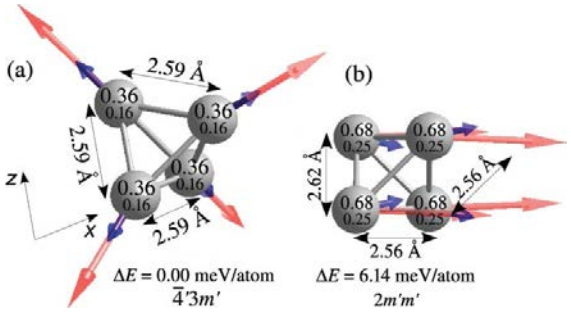


FIG. 3. (a) Noncollinear magnetic ground state structure of a Pt_4 cluster with a tetrahedral geometry. (b) Ferromagnetic state with the magnetization aligned parallel to one of the edges of the tetrahedron, forming a distorted tetrahedron, cf. Fig. 1.

Downloaded 14 Apr 2011 to 128.130.131.2. Redistribution subject to AIP license or copyright; see http://jcp.aip.org/about/rights_and_permissions

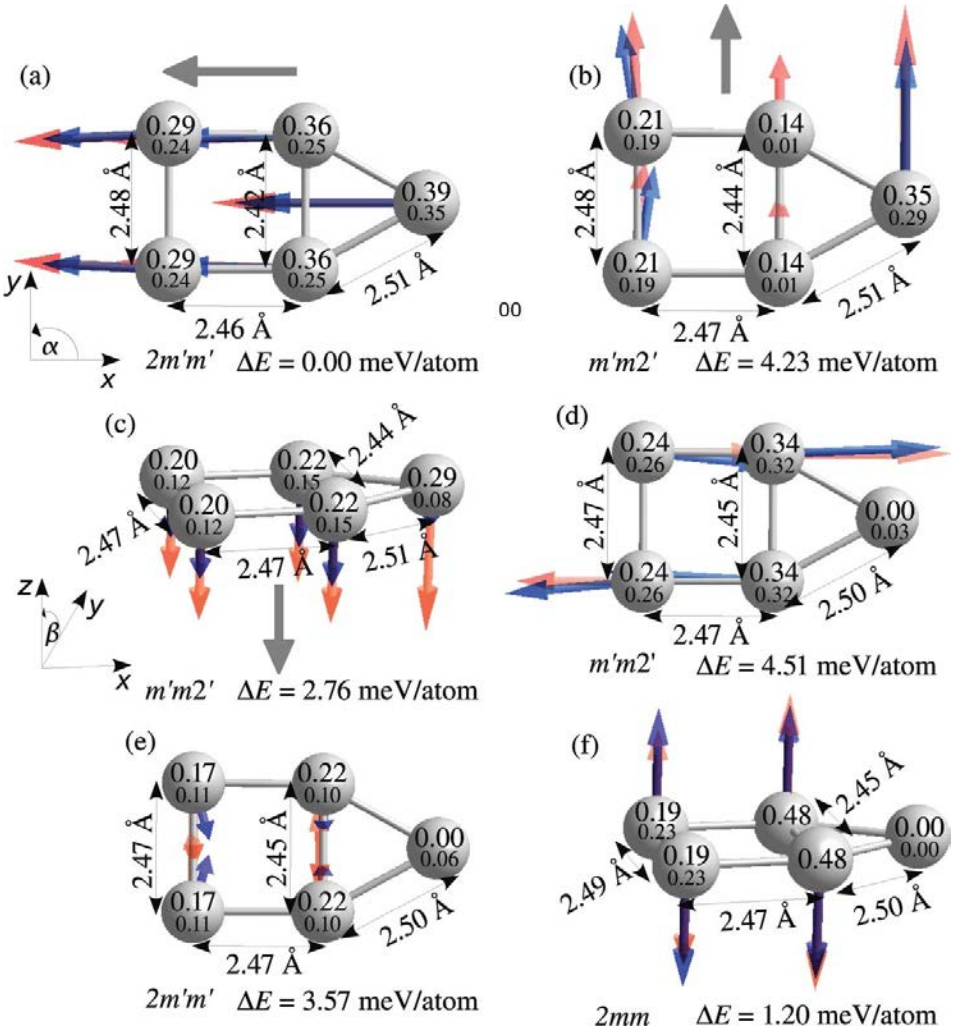


FIG. 4. Geometric and magnetic structures of a Pt_5 cluster for perpendicular and in-plane magnetizations, cf. Fig. 1. The ground state is the high-moment configuration (a), which is energetically almost degenerate with a configuration where all magnetic moments are rotated by 180°. Configurations (b) and (c) are low-moment ferromagnetic and configurations (d)–(f) antiferromagnetic. The angles α (for in-plane rotation of the magnetization direction) and β (for rotation to a perpendicular orientation) have been defined in the inset, cf. Fig. 5 and text.

be lower in energy, while Bhattacharya and Majumder[37] find a planar cluster with a moment of 2 μ_B to be favored already at the scalar relativistic level. A distorted trigonal bipyramid is predicted by the quantum-chemical calculations of Majumdar *et al.*[46]

If SOC is included, a Pt_5 cluster forms a slightly distorted square plus an isocele triangle (see Fig. 4); this planar structure is favored by 40 meV/atom over a trigonal bipyramid and by 34 meV/atom over a square pyramid. [All structural energy differences are calculated for the magnetic ground state of the respective geometrical configurations, i.e., the FM in-plane state of the planar structure (see Fig. 4), the FM in-plane state of the square pyramid [see Fig. 6(a)], and the FM in-plane state of the trigonal bipyramid [see Fig. 7(a)]. The prediction of a planar ground state geometry agrees with the results of Huda *et al.*,[3] while Sebetci[38] and FSF (Ref. 9) find the square pyramid to be the lowest in energy. Stationary magnetic states of the planar cluster for magnetization along in- and out-of-plane symmetry directions are shown in Fig. 4. In the GS [configuration (a)] with $M_J \sim 3\,\mu_B$ ($M_S = 1.7\,\mu_B$, $M_L = 1.3\,\mu_B$), the magnetization is in-plane; the total spin and orbital moments are parallel to the twofold symmetry axis of the cluster. Inversion of the direction of magnetization by 180° leaves the magnetic moments and the total energy unchanged. Rotation of the direction of magnetization by 90° within the plane of the cluster or to a perpendicular orientation leads to a transition to low-moments states [see Figs. 4(b) and 4(c)] which are 4.2 and 2.8 meV/atom above the GS. For all directions of the magnetization, the FM configurations (a)–(c) coexist with AFM configurations [see Figs. 4(d)–4(f)].

Downloaded 14 Apr 2011 to 128.130.131.2. Redistribution subject to AIP license or copyright; see http://jcp.aip.org/about/rights_and_permissions

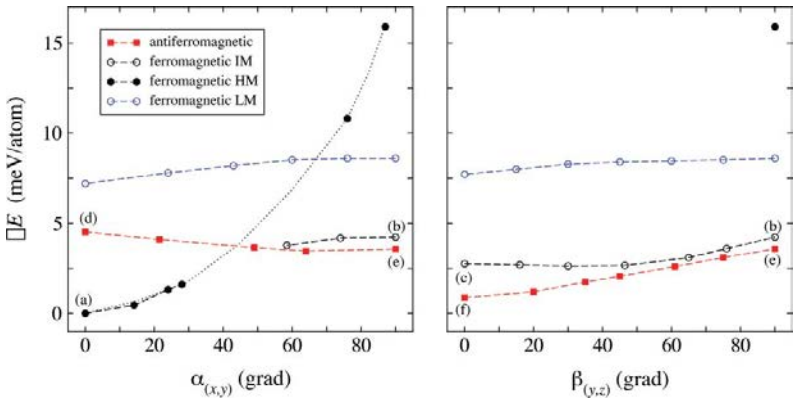


FIG. 5. Variation of the total energies of the ferromagnetic (full and empty circles) and antiferromagnetic (squares) configurations of a Pt_5 cluster upon rotation of the magnetization direction within the (*x*,*y*) plane of the cluster and in the (*y*,*z*) plane perpendicular to the twofold symmetry axis. See Fig. 4 for the definition of the angles. For the ferromagnetic configurations solutions with high (HM), intermediate (IM) and low (LM) magnetic moments are indicated, cf. Fig. 4.

Except for an orientation of the local magnetic moments parallel to the twofold symmetry axis [FM GS (a) and AFM configuration (d)], the AFM state is lower in energy. The lowest barrier to a magnetization reversal is via the AFM out-of-plane configuration (f), with an MAE of 1.2 meV/atom. The point group symmetry of the planar Pt_5 structure is 2 mm. In the magnetic point group symmetries of the stationary configurations, one or two of the symmetry elements have to be combined with the time-reversal operation, as indicated in Fig. 4.

For all clusters the magnetic potential-energy surface as a function of the orientation of the magnetic moment consists of interpenetrating sheets representing different magnetic isomers. To explore the potential-energy surfaces in more detail, we performed for Pt_5 a series of calculations with constrained orientations of the magnetic moments. If, starting from the FM high-moment ground state, we gradually rotate the magnetization direction in-plane, taking the converged charge and spin densities from the last step to initialize the self-consistency cycle, we follow a steeply ascending curve of FM high-moment states ($M_J \sim 3\,\mu_B$) ending at $\alpha = 90^\circ$ at an energy 16 meV/atom above the GS [see Fig. 5(a)]. However, for magnetization perpendicular to the twofold symmetry axis, an FM solution with a lower moment ($M_J \sim 1.75\,\mu_B$) has an energy only 4.2 meV/atom above the GS and can also be followed to smaller angles. At somewhat higher energies of about 8 meV/atom above the GS, we also found a low-moment FM solution with $M_J \sim 1\,\mu_B$ [see Fig. 5(a)]. At intermediate angles where the total energies of high- and low-moment states are comparable, it is very difficult to find a well-converged solution. Coexisting FM and AFM states are also found for magnetization directions in a plane perpendicular to the twofold symmetry axis [see Fig. 5(b)]. The AFM state (f) represents the lowest barrier to magnetization reversal relative to the magnetic GS.

FSF (Ref. 9) found for the Pt_5 cluster a ground state configuration in the form of a square pyramid and a huge magnetic moment of $M_J \sim 7\mu_B$, in contrast to the present work and that of Huda *et al.*[3] In its "first excited state" the cluster forms a trigonal bipyramid with a lower magnetic moment of $M_J \sim 4.4\,\mu_B$ ($M_S = 3.6\,\mu_B$, $M_L = 0.8\,\mu_B$). Hence energy difference between these two states of 1.1 meV/atom is not an MAE, but a structural and magnetic energy difference.

To allow a comparison with their results it is of interest to also explore the magnetic properties of the three-dimensional structural isomers of the Pt_5 cluster. For the square pyramid the three stationary magnetic states we have been able to identify are shown in Fig. 6. In the magnetic GS the fourfold symmetry of the geometric structure is broken by slightly different bond lengths of 2.56 and 2.57 Å in the basal plane; although all four atoms carry the same spin and orbital moments. The large total magnetic moment of $M_J = 5.3\,\mu_B$ ($M_S = 3.9\,\mu_B$, $M_L = 1.4\,\mu_B$) is aligned parallel to the edge of the square, but the local magnetic spin and orbital moments are slightly canted relative to the overall magnetization direction [see Fig. 6(a)], in line with the reduced symmetry. Rotation of the magnetization direction parallel to the basal

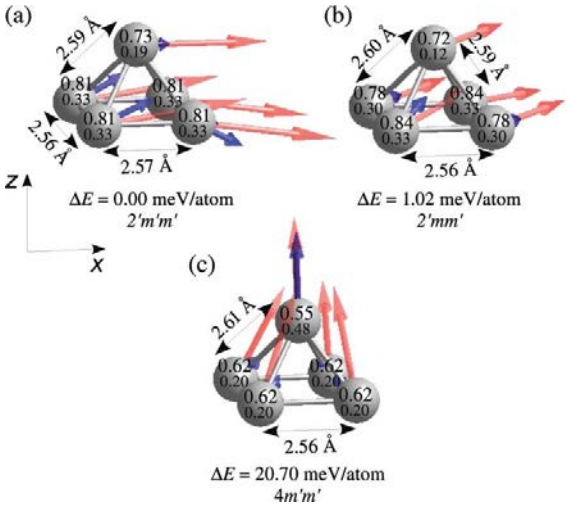


FIG. 6. Geometric and magnetic structures of a Pt_5 cluster forming a square pyramid for in-plane [(a) and (b)] and perpendicular (c) magnetizations, cf. Fig. 1 and text.

Downloaded 14 Apr 2011 to 128.130.131.2. Redistribution subject to AIP license or copyright; see http://jcp.aip.org/about/rights_and_permissions

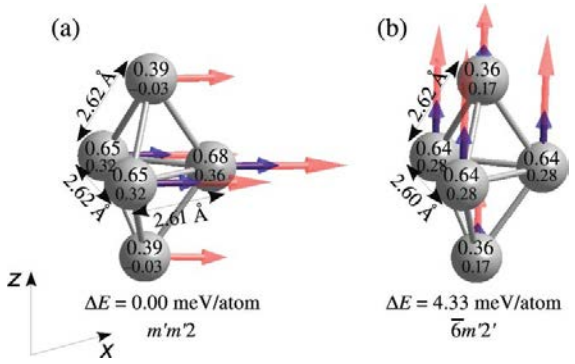


FIG. 7. Geometric and magnetic structures of a Pt_5 cluster forming a trigonal bipyramid for in-plane (a) and perpendicular (b) magnetizations, cf. Fig. 1 and text.

plane requires to overcome a modest in-plane MAE of 1.02 meV/atom. In the saddle-point configuration the magnetization is parallel to the diagonal of the base; the fourfold symmetry is broken for both the geometric and magnetic structures [see Fig. 6(b)], although the total cluster moment remains unchanged. Initialization of the magnetization along the fourfold axis leads to a stationary magnetic state with a lower total moment of $M_J = 3.9\,\mu_B$ ($M_S = 2.9\,\mu_B$, $M_L = 1.0\,\mu_B$) aligned along the axis, but again canted local moments [see Fig. 6(c)]. The bonds connecting the atoms in the basal plane to the vertex are slightly elongated by 0.02 Å. The energy of this axial low-moment state is 20.7 meV higher than that of the ground state.

Our magnetic ground state configuration for the trigonal bipyramid is shown in Fig. 7(a). The threefold rotational symmetry is broken by a slight distortion of the central triangle. The magnetic moments are ferromagnetically aligned parallel to the central triangle of the cluster and a small difference exists between the magnetic moments of the atoms occupying its vertices. The magnetic point group symmetry is $m'm'2$; the easy axis is aligned with the twofold symmetry axis. The total magnetic moment of $M_J = 3.7\,\mu_B$ is slightly lower than the moment calculated by FSF (Ref. 9) (considering the differences in the calculations of the local moments) and also lower than the spin moment of 4 μ_B derived for the scalar relativistic case. In-plane rotation of the magnetic moment to a direction parallel to one of the edges of the triangle increases the energy by only 0.06 meV/atom. Alignment of the magnetization direction parallel to the axis of the bipyramid restores the threefold symmetry axis and leads to a ferromagnetic configuration with a total moment of $M_J = 3.8\,\mu_B$ (magnetic point group $\bar{6}m'2'$) which is higher in energy by 4.3 meV/atom. In contrast to the strong anisotropy of both spin and orbital moments of the planar cluster, for the three-dimensional structure the spin moment is almost isotropic and the orbital anisotropy is modest on the three atoms occupying the central triangle and more pronounced only at the apices.

Hence for the two three-dimensional structural isomers of the Pt_5 cluster, our analysis qualitatively confirms the observation of FSF: the out-of-plane MAE of the square pyramid of 20.7 meV/atom is larger than the structural energy difference of 6 meV/atom between the square pyramid and the trigonal bipyramid in their respective magnetic ground states. However, this is a structural energy difference, and not a magnetic anisotropy energy. Also, the GS of the Pt_5 cluster is planar and the MAE of the planar cluster is lower than the structural energy difference to the three-dimensional isomers.

E. Pt_6

The predictions for the structure of a Pt_6 cluster available in the literature scatter widely. The earlier scalar relativistic calculations in our group led to the surprising result that a capped square pyramid with a magnetic moment of 6 μ_B is lower in energy by 23 meV/atom than an octahedron in the same spin-state and also lower in energy than any planar configuration.[7] Xiao and Wang[35] found the lowest energy for a planar geometry consisting of a central square capped on two sides by two triangles, lower by about 27 meV/atom than both an octahedron and a trigonal prism. Bhattacharya and Majumder[37] and Nie *et al.*[36] predicted a planar geometry consisting of four edge-sharing triangles, which was found to be favored by a large energy difference of 110 meV/atom over the most favorable three-dimensional structure (a capped trigonal bipyramid). Sebetci[38] found a distorted trigonal prism with a moment of 6 μ_B to be lower in energy by 25 meV/atom than a distorted capped square pyramid with the same magnetic moment and much lower in energy than a strongly distorted octahedron. This lack of agreement on the most basic features of the cluster prompted us to repeat the scalar relativistic calculations for all candidate structures with stringent criteria on energy and force convergence. A regular trigonal prism (interatomic distances 2.57 Å in the basal plane, height 2.51 Å) and a magnetic moment of 8 μ_B were found to be the ground state with an energy lower by 11 meV/atom than the square pyramid plus an ad-atom (magnetic moment 6 μ_B) and by 26 meV/atom than an almost perfectly symmetric octahedron with a magnetic moment of 6 μ_B. Among the planar structures the configuration reported by Xiao and Wang[35] was found to be favored (but higher in energy by more than 100 meV/atom than the three-dimensional structures).

If SOC is taken into account, the energetic order is reversed in favor of the octahedron with a noncollinear low-moment state [see Fig. 8(a)] which is found to be lower in energy by 13.8 meV/atom than the square pyramid plus ad-atom with $M_J = 5.0\,\mu_B$ [see Fig. 8(c)]. Compared to the octahedron, a trigonal prism with a magnetic moment of $M_J = 6.9\,\mu_B$ [Fig. 8(e)] is energetically disfavored by 35 meV/atom and a planar structure [similar to that of Pt_5, see Fig. 8(g)] with $M_J = 2\,\mu_B$ by 140 meV/atom. For all four structural isomers, the energy difference refers to the magnetic ground state derived from calculations with initial magnetic configurations differing in the magnitude and direction of the magnetization.

In the magnetic ground state, the Pt_6 octahedron has a perfect octahedral geometry with all interatomic distances equal to 2.62 Å but the distribution of the magnetic moments breaks the octahedral symmetry. The magnetic structure is noncollinear. The four Pt atoms occupying the equatorial plane carry spin moments of 0.26–0.27 μ_B, directed along the

Downloaded 14 Apr 2011 to 128.130.131.2. Redistribution subject to AIP license or copyright; see http://jcp.aip.org/about/rights_and_permissions

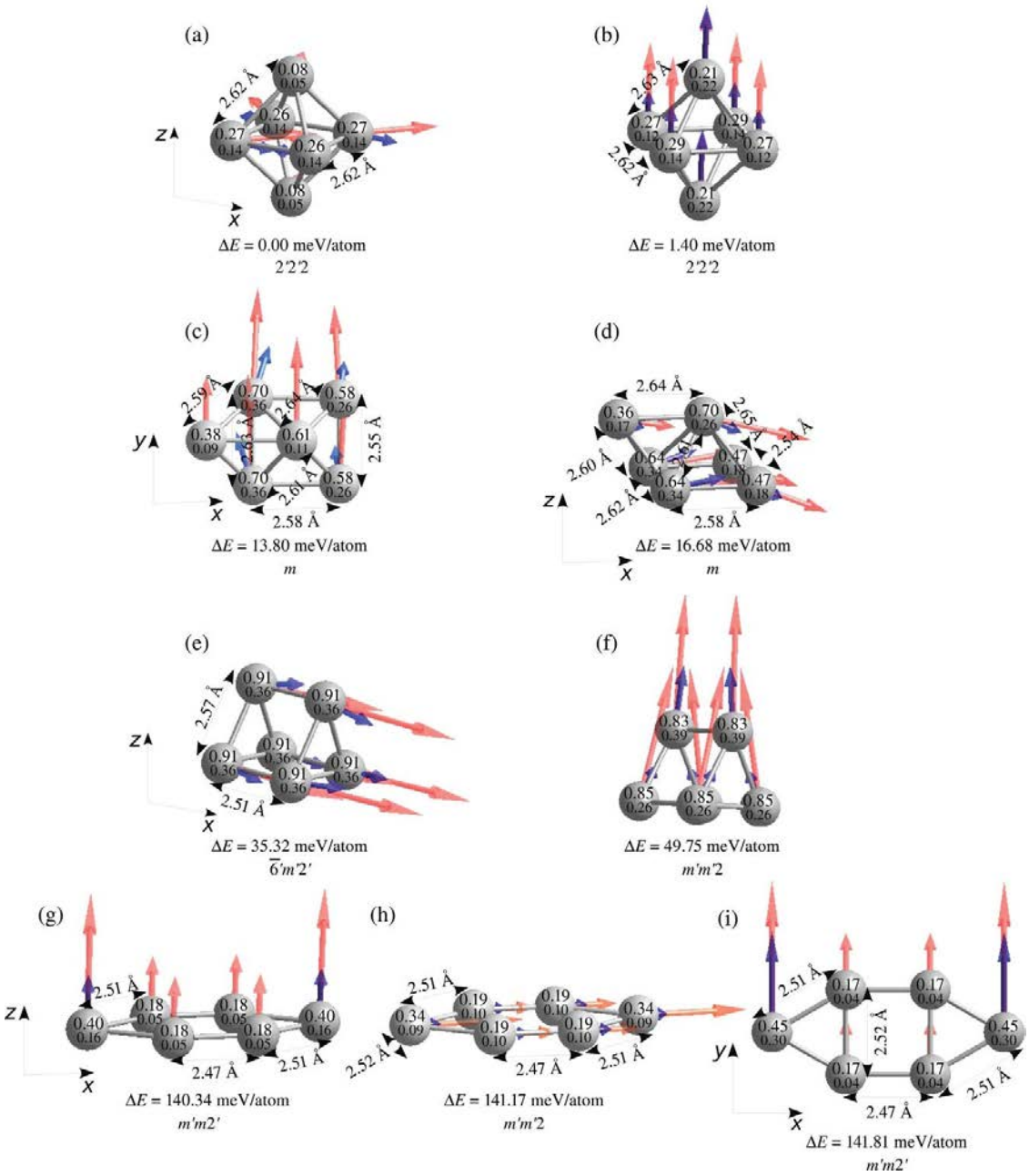


FIG. 8. Geometric and magnetic structures of a Pt_6 cluster in different configurations. (a) and (b): Octahedral ground state geometry with the magnetic structure in the easy (a) and hard (b) axis configurations. (c) and (d): Capped square pyramid magnetized along the easy (c) and hard (d) directions. (e) and (f) Trigonal prismatic configuration magnetized along the easy (e) and hard (f) directions. (g)–(i): Planar structure with perpendicular (g) and in-plane [(h) and (i)] magnetizations. Below each configuration, the energy differences relative to the GS and the magnetic point group symmetry are listed. For the definition of symbols, see Fig. 1.

face-diagonals; pairs of moments are perpendicular to each other, see Fig. 8(a). The local-orbital moments are directed along the edges of the octahedron; moments aligned parallel to the same edge point into opposite directions. The atoms on the apical sites carry small spin and orbital moments which are also parallel to the equatorial plane. The local magnetic moments add up to a cluster moment of $M_J = 0.83\,\mu_B$, directed essentially perpendicular to one of the triangular facets of the octahedron. Due to the complex magnetic structure, the magnetic symmetry group is only $2'2'2$. The hard magnetic axis points along the fourfold symmetry axis of a slightly distorted octahedron with point group symmetry $4mm$. The

Downloaded 14 Apr 2011 to 128.130.131.2. Redistribution subject to AIP license or copyright; see http://jcp.aip.org/about/rights_and_permissions

magnetic structure is collinear but breaks the fourfold symmetry; the magnetic point group symmetry is only $2'2'2$, as for the magnetic GS. Spin and orbital moments of the atoms in the equatorial plane have almost the same size as in the easy axis configuration but are rotated parallel to the overall magnetization direction. The total magnetic moment is $M_J = 2.5\,\mu_B$; the MAE is only 1.4 meV/atom. The existence of a noncollinear magnetic GS of the octahedral Pt_6 cluster might seem surprising, but the existence of competing exchange-interactions has been demonstrated already in the scalar relativistic calculations where an antiferromagnetic configuration was found to be favored over a nonmagnetic state for zero total spin and ferrimagnetic configurations were reported for low-moment isomers of the Pt_6 octahedron.

The second structural isomer is a distorted square pyramid plus an ad-atom with a low symmetry (point group m). In the magnetic ground state the spin moments are aligned parallel to one of the edges of the basal plane of the pyramid and orbital moments are slightly canted relative to the spins [see Fig. 8(c)]. The local moments add to a cluster moment of $M_J = 4.8\,\mu_B$. A rotation of the magnetization direction to a perpendicular direction in the basal plane changes the cluster moment to $M_J = 4.6\,\mu_B$ (the spin moment is reduced from 3.5 to 3.2 μ_B, while the orbital moment increases by 0.1 μ_B) and costs an "in-plane" MAE of 2.9 meV/atom [see Fig. 8(d)]. If the magnetic moment is perpendicular to the basal plane, both spin and orbital moments are reduced ($M_S = 2.7\,\mu_B$, $M_L = 1.1\,\mu_B$, $M_J = 3.8\,\mu_B$). The perpendicular MAE is 12.5 meV/atom.

The magnetic ground state for the trigonal prism in its high-moment state with $M_J = 7.6\,\mu_B$ is perpendicular to the triangular basis and the magnetic structure preserves the threefold symmetry (magnetic point group symmetry $\bar{6}'m'2'$), see Fig. 8(e). If the magnetization is perpendicular to one of the rectangular facets, the slight differences in the local spin and orbital moments break the threefold symmetry and the magnetic point group symmetry is reduced to $m'm'2$ [Fig. 8(f)]. Both spin and orbital moments are reduced, resulting in $M_J = 6.9\,\mu_B$. The MAE is 15.7 meV/atom.

For the energetically least favorable planar configuration, we calculate an easy axis perpendicular to the plane of the cluster [see Fig. 8(g)]. The cluster is in a low-moment state with $M_J = 2.0\,\mu_B$. In-plane configurations with the magnetization oriented along the long and short axes of the cluster and a total magnetic moment of about 2 μ_B [Figs. 8(h) and 8(i)] are disfavored by MAEs of 0.63 and 0.82 meV/atom, respectively. MAE and spin and orbital anisotropies are much smaller than those for the planar Pt_5 cluster.

No AFM configurations could be found for any of the structural isomers of the Pt_6 cluster. It is interesting that for both the Pt_5 and Pt_6 clusters, low-moment configurations are stabilized in the planar configurations while high-moment states are formed in the three-dimensional structures.

IV. DISCUSSION AND CONCLUSIONS

In summary we find that spin–orbit coupling has a strong influence on the geometric and magnetic structures of small Pt clusters. (i) Planar structures are stabilized up to Pt_5; for larger clusters, the energetic order of different structural isomers is changed. (ii) The clusters have large orbital magnetic moments comparable to the spin moments; both are strongly anisotropic. The anisotropy of the moments decreases with increasing size of the clusters. (iii) SOC leads to a mixing of different spin-states; the total magnetic moments can be enhanced as well as reduced compared to a scalar relativistic treatment. (iv) Local spin and orbital moments can be noncollinear, but the total spin and orbital moments of the cluster are always aligned. (v) An antiferromagnetic ground state is found for both planar and tetrahedral Pt_4 clusters. For a planar Pt_5 cluster the moments are ferromagnetically aligned, but the first excited magnetic state shows antiferromagnetic ordering. (vi) The magnetic potential-energy surface as a function of the orientation of the magnetization (or of the local magnetic moments for AFM states) consists of interpenetrating sheets representing different magnetic isomers (low- and high-moment FM as well as AFM states). (vii) The magnetic anisotropy energy (taken as the energy of the lowest saddle-point on the magnetic energy surface leading to magnetization reversal of an FM GS) can correspond to a low-moment state (Pt_2, Pt_3), an AFM isomer (Pt_5), or even to a configuration with higher total moment than that in the GS (Pt_6). No MAE can be given for Pt_4 because the GS is antiferromagnetic.

These surprising results are a consequence of the strong spin–orbit coupling inducing a splitting of the eigenstates, which is comparable to the exchange splitting and much larger than the average level spacing. In the absence of exchange splitting and SOC, the geometric structure of the nonmagnetic clusters is determined by the formation and occupation of bonding/antibonding states, depending on the hybridization of the atomic orbitals. Formation of magnetic moments leads to an exchange splitting between majority and minority spin states. For a metal with a nearly filled d-band such as Pt, the majority states will be completely occupied whereas the occupation of the antibonding minority states will be reduced (favoring the formation of a magnetic GS). Even at a scalar relativistic level, magnetism can influence the structural stability of clusters. For example, for a Pt_6 cluster with vanishing total moment, a square pyramid plus an ad-atom and an incomplete trigonal bipyramid are almost energetically degenerated and favored over the octahedron or the trigonal prism.[7] Whether SOC leads to a further splitting and a reordering of the eigenstates around the Fermi level depends on the magnetic symmetry of the cluster. Without SOC both spin-up and spin-down states can be classified according to the point group symmetry of the cluster. For example, for a Pt_2 dimer $dd\pi$ and $dd\delta$ states are twofold degenerate due to mirror and time-reversal symmetry. The degeneracy of these states is conserved for magnetization perpendicular to the dimer axis but lifted for parallel magnetization because reflection and time-reversal are no longer symmetry operations. The large SOC splitting changes the occupation of states close to the Fermi level and favors the occupation of states with a large orbital moment.[10,12] For the trimer and pentamer the geometric structure corresponds to PGS $2mm$. The magnetic PGS (Ref. 45) of the GS of Pt_3 is $m'm'2$ and that of the other two stationary configurations is $2'm'm$ (where the

Downloaded 14 Apr 2011 to 128.130.131.2. Redistribution subject to AIP license or copyright; see http://jcp.aip.org/about/rights_and_permissions

symbols m' and $2'$ indicates that the symmetry operation must by combined with a time-reversal operation which reverses the direction of axial vectors such as the magnetic moment). For the Pt_4 cluster the geometric PGS mmm is changed to $m'm'm'$ for the AFM and to $mm'm'$ for the FM states. For the FM states of Pt_5 with crystallographic point group $2mm$, the time-reversal operation has to be applied to a mirror operation if the magnetization is parallel to the mirror plane and to the twofold rotation if the magnetization is perpendicular to the axis (as indicated in Fig. 4); similar rules apply to the AFM configurations. For the GS of the Pt_6 cluster the crystallographic PGS $m\bar{3}m$ of the octahedron is reduced by different local magnetic moments on crystallographically equivalent sites to $2'2'2$. For the first excited state the geometric symmetry is reduced to $4/mmm$, but the magnetic symmetry is again $2'2'2$. Mirror and/or rotational symmetries induce degeneracies which are lifted by SOC if the symmetry is broken for a given direction of the magnetization. The stabilization of different magnetic isomers depends on the interplay between exchange splitting and spin–orbit splitting of eigenstates, depending on the magnitude of the exchange splitting (and hence of the magnetic moment) and on the direction of magnetization. These very general considerations also suggest that similar strong spin–orbit effects will also be found in other nanostructures of the heavy 5d metals. An example has already been reported by Smogunov *et al.*[15] who reported for a Pt monowire ferromagnetic order if the moment is perpendicular to the axis of the wire which disappears completely if the magnetization is forced to be parallel to the wire.

The structural and magnetic properties of the Pt clusters illustrate the complexity of the interplay of strong SOC, exchange splitting, and hybridization of the electronic eigenstates. It must be emphasized that a combined optimization of the geometric and magnetic degrees of freedom requires the absence of any symmetry constraints and extremely accurate calculations with very stringent limits on total energy and force convergence. We believe that the divergent results reported in the literature are largely due to insufficient convergence (which may indeed be very slow). It must also be emphasized that it will not be possible to test our predictions for the magnetic anisotropy experimentally because gas-phase clusters can always rotate freely such that the easy magnetic axis will be aligned with an applied magnetic field. However, these results are important for a fundamental understanding of the intrinsic properties of these clusters, and they form a reference for investigations of clusters supported on a solid surface where the orientation of the cluster is fixed by the binding to the substrate and where the magnetic anisotropy is determined by the interplay between the intrinsic anisotropy of the cluster and that imposed by the interaction with the substrate. First results for Pt clusters supported on graphene layers will be reported soon.[48]

[1] R. Wiesendanger, Rev. Mod. Phys. **81**, 1495 (2009).
[2] D. Sellmyer and R. Skomski, *Advanced Magnetic Nanostructures* (Springer, New York, 2006).
[3] M. N. Huda, M. K. Niranjan, B. R. Sahu, and L. Kleinman, Phys. Rev. A **73**, 053201 (2006).
[4] H. Häkkinen, B. Yoon, U. Landman, X. Li, H.-J. Zhai, and L.-S. Wang, J. Phys. Chem. A **107**, 6168 (2003).
[5] S. Gilb, P. Weis, F. Furche, R. Ahlrichs, and M. M. Kappes, J. Chem. Phys. **116**, 4094 (2002).
[6] F. Baletto and R. Ferrando, Rev. Mod. Phys. **77**, 371 (2005).
[7] T. Futschek, M. Marsman, and J. Hafner, J. Phys.: Condens. Matter **17**, 5927 (2005); J. Phys.: Condens. Matter **18**, 9703 (2006).
[8] J. Kortus, T. Baruah, M. R. Pederson, C. Ashamn, and S. N. Khanna, Appl. Phys. Lett. **80**, 4193 (2002).
[9] L. Fernandez-Seivane and J. Ferrer, Phys. Rev. Lett. **99**, 183401 (2007); Phys. Rev. Lett. **101**, 069903 (2008); see also supplementary material Document No. E-PRLTAO-99-018745 for detailed information on interatomic distances and local spin and orbital moments.
[10] T. O. Strandberg, C. M. Canali, and A. H. McDonald, Nature Mater. **6**, 648 (2007); Phys. Rev. B **77**, 174416 (2008).
[11] D. Fritsch, K. Koepernik, M. Richter, and H. Eschrig, J. Comput. Chem. **29**, 2210 (2008).
[12] P. Błoński and J. Hafner, Phys. Rev. B **79**, 224418 (2009).
[13] S. Sahoo, A. Hucht, M. E. Gruner, G. Rollmann, P. Entel, A. Postnikov, J. Ferrer, L. Fernández-Seivane, M. Richter, D. Fritsch, and S. Sil, Phys. Rev. B **82**, 054418 (2010).
[14] Y. Mokrousov, G. Bihlmayer, S. Heinze, and S. Blügel, Phys. Rev. Lett. **96**, 147201 (2006).
[15] A.Smogunov, A. Dal Corso, and E. Tosatti, Nat. Nanotechnol. **3**, 22 (2008).
[16] J. Velev, R. F. Sabiryanov, S. S. Jaswal, and E. Y. Tsymbal, Phys. Rev. Lett. **94**, 127203 (2005).
[17] P. Bruno, Phys. Rev. B **39**, 865 (1989).
[18] C. M. Canali, A. Cehovin, and A. H. McDonald, Phys. Rev. Lett. **91**, 046805 (2003).
[19] G. M. Pastor, J. Dorantes-Dávila, S. Pick, and H. Dreyssé, Phys. Rev. Lett. **75**, 326 (1995).
[20] A. N. Andriotis and M. Menon, Phys. Rev. Lett. **93**, 026402 (2004).
[21] G. Kresse and J. Hafner, Phys. Rev. B **47**, 558 (1993); Phys. Rev. B **49**, 14251 (1994).
[22] G. Kresse and D. Joubert, Phys. Rev. B **59**, 1758 (1999).
[23] P. E. Blöchl, Phys. Rev. B **50**, 17 953 (1994).
[24] J. P. Perdew, J. A. Chevary, S. H. Vosko, K. A. Jackson, M. R. Pederson, D. J. Singh, and C. Fiolhais, Phys. Rev. B **46**, 6671 (1992); Phys. Rev. B **48**, 4978(E) (1993).
[25] S. H. Vosko, L. Wilk and M. Nusair, Can. J. Phys. **58**, 1200 (1980).
[26] E. G. Moroni, G. Kresse, J. Hafner, and J. Furthmüller Phys. Rev. B **65** 15629 (1997).
[27] J. Anton, T. Jacob, B. Fricke, and E. Engel, Phys. Rev. Lett. **89**, 213001 (2002).
[28] G. Kresse and O. Lebacq, vasp Manual, http://cms.mpi.univie.ac.at/vasp/.
[29] L. Kleinman, Phys. Rev. B **21**, 2630 (1980).
[30] A. H. MacDonald, W. E. Pickett, and D. D. Koelling, J. Phys. C **13**, 2675 (1980).
[31] D. Hobbs, G. Kresse, and J. Hafner, Phys. Rev. B **62**, 11556 (2000).
[32] M. Marsman and J. Hafner, Phys. Rev. B **66**, 224409 (2002).
[33] G. H.O. Dalderoop, P. J. Kelly, and M. F. H. Schuurmans, Phys. Rev. B **50**, 9989 (1994).
[34] E. Abata and M. Asdente, Phys. Rev. **140**, A1303 (1965).
[35] L. Xiao and L. Wang, J. Phys. Chem A **108**, 8605 (2004).
[36] A. Nie, J. Wu, C. Zhou, S. Yao, C. Luo, R. C. Forrey, and H. Cheng, Int. J. Quantum Chem. **107**, 219 (2006).
[37] K. Bhattacharya and C. Majumder, Chem. Phys. Lett. **446**, 374 (2007).
[38] A. Sebetci, Phys. Chem. Chem. Phys. **11**, 921 (2009).
[39] J. M. Soler, E. Artacho, J. D. Gale, A. García, J. Junquera, P. Ordejón, and D. Sánchez-Portal, J. Phys.: Condens. Matter **14**, 2745 (2002).
[40] N. Troullier and J. M. Martins, Phys. Rev. B **43**, 1993 (1991).
[41] L. Fernández-Seivane, M. A. Oliveira, S. Sanvito, and J. Ferrer, J. Phys.: Condens. Matter **18**, 7999 (2006).
[42] M. M. Airola and M. D. Morse, J. Chem. Phys. **113**, 1313 (2002).
[43] A. Sebetci, Chem. Phys. **331**, 9 (2006).
[44] X. Lin, N. J. Ramer, A. M. Rappe, K. C. Hass, W. F. Schneider, and B. L. Trout, J. Phys. Chem. **105**, 7739 (2001).
[45] M. de Graef, Metall. Mater. Trans. A **41**, 1321 (2010).
[46] D. Majumdar, D. Dai, and K. Balasubramanian, J. Chem. Phys. **113**, 7919 (2000).
[47] D. Dai and K. Balasubramanian, J. Chem. Phys. **102**, 648 (1995).
[48] P. Błoński and J. Hafner, "Geometric and magnetic properties of Pt clusters supported on graphene: relativistic density-functional calculations," to be published.

Downloaded 14 Apr 2011 to 128.130.131.2. Redistribution subject to AIP license or copyright; see http://jcp.aip.org/about/rights_and_permissions

IOP Publishing Journal of Physics: Condensed Matter

J. Phys.: Condens. Matter **23** (2011) 136001 (19pp) doi:10.1088/0953-8984/23/13/136001

Magneto-structural properties and magnetic anisotropy of small transition-metal clusters: a first-principles study

Piotr Błoński and Jürgen Hafner[1]

Fakultät für Physik and Center for Computational Materials Science, Universität Wien, Sensengasse 8/12, A-1090 Wien, Austria

E-mail: juergen.hafner@univie.ac.at

Received 17 January 2011, in final form 16 February 2011
Published 14 March 2011
Online at stacks.iop.org/JPhysCM/23/136001

Abstract

Ab initio density-functional calculations including spin–orbit coupling (SOC) have been performed for Ni and Pd clusters with three to six atoms and for 13-atom clusters of Ni, Pd, and Pt, extending earlier calculations for Pt clusters with up to six atoms (2011 *J. Chem. Phys.* **134** 034107). The geometric and magnetic structures have been optimized for different orientations of the magnetization with respect to the crystallographic axes of the cluster. The magnetic anisotropy energies (MAE) and the anisotropies of spin and orbital moments have been determined. Particular attention has been paid to the correlation between the geometric and magnetic structures. The magnetic point group symmetry of the clusters varies with the direction of the magnetization. Even for a 3d metal such as Ni, the change in the magnetic symmetry leads to small geometric distortions of the cluster structure, which are even more pronounced for the 4d metal Pd. For a 5d metal the SOC is strong enough to change the energetic ordering of the structural isomers. SOC leads to a mixing of the spin states corresponding to the low-energy spin isomers identified in the scalar-relativistic calculations. Spin moments are isotropic only for Ni clusters, but anisotropic for Pd and Pt clusters, orbital moments are anisotropic for the clusters of all three elements. The magnetic anisotropy energies have been calculated. The comparison between MAE and orbital anisotropy invalidates a perturbation analysis of magnetic anisotropy for these small clusters.

(Some figures in this article are in colour only in the electronic version)

1. Introduction

In modern magnetic recording technologies, bits of information are stored in magnetically stable domains and a large magnetic anisotropy energy, determining the barrier to magnetization reversal due to thermal excitations, is therefore required to inhibit loss of information [1, 2]. A high magnetic anisotropy energy requires large spin and orbital moments and a strong spin–orbit coupling. Furthermore, a reduction of the size of the domain carrying one bit of information necessitates an increase of the magnetic anisotropy energy per atom. In nanostructures (ultrathin films, chains and clusters) the magnetic spin and orbital moments are enhanced over their bulk values because of the reduced dimensionality and reduced coordination number, and this is expected to lead to a strongly enhanced MAE. Therefore, the novel magnetic properties of nanostructures have received increasing attention during the past decade [3–6]. The ultimate limit of miniaturization is reached for small metallic clusters.

The magnetic properties of small transition-metal clusters have been studied extensively in the past, both experimentally [3–5, 7–11] and theoretically [6, 12–23]. Attention has focused in particular on 13-atom clusters, where generally

[1] Author to whom any correspondence should be addressed.

 © 2011 IOP Publishing Ltd Printed in the UK & the USA

the formation of icosahedral structures had been expected. Recent *ab initio* studies predicted different structures for the 4d and 5d metals, without, however, reaching agreement on the ground-state configurations [14–23]. Stern–Gerlach experiments found strongly enhanced magnetic moments in small Ni clusters, reaching nearly three times the value in ferromagnetic fcc Ni. It has also been demonstrated that small clusters of 4d and 5d metals, such as Rh, Pd, or Pt, which are non-magnetic in the bulk, carry a magnetic moment. Since the spin–orbit coupling in these heavy elements is much stronger than in the magnetic 3d metals, small clusters of these elements are expected to have a large MAE. From the theoretical side, spin-density-functional theory (SDFT) offers an efficient way to study magneto-structural properties of nanostructures. However, to date most theoretical studies have been performed in a non-relativistic or scalar-relativistic mode, providing detailed information on the geometrical properties and on the magnetic spin moments, but not on orbital moments and magnetic anisotropies (see [13–15, 23] and further references given therein). While the calculation of orbital magnetic moments and of the magnetic anisotropy of small metallic clusters in the gas phase has been attempted in a number of studies based on semi-empirical tight-binding schemes [24–28], only a few relativistic *ab initio* studies have addressed this problem using SDFT [23, 29–38] and quantum-chemical methods [39, 40]. In addition, relativistic studies of magnetic atoms and clusters supported on non-magnetic metallic surfaces of heavy metals using SFDT techniques have been reported [24, 28, 41–47]. In this case the magnetic anisotropy is determined by the interplay between the large magnetic moment of the adatoms and the strong spin–orbit coupling in the substrate.

Huda *et al* [30] investigated the effect of spin–orbit coupling on the geometric structures of Pt_n clusters ($n = 2, \ldots, 5$) and reported that relativistic effects lead to a preference for planar structures, but did not report any magnetic data. Piotrkowski *et al* [23] examined the effect of spin–orbit coupling on the atomic structure of 13-atom clusters formed by transition-metals and reported only modest changes in the structural energy differences for the transition metals, while for Au_{13} SOC was found to favor the formation of three-dimensional over planar structures (in contrast to the results for smaller Au clusters). Again no results on orbital moments and magnetic anisotropies were reported. The results of Huda *et al* have been contested by Sebetci [31], who reported three-dimensional structures also for Pt tetra- and pentamers. Fernández-Seivane and Ferrer [32] performed spin-density-functional calculations of the magnetic anisotropy energies for selected Pd, Pt, Ir and Au clusters with up to seven atoms, but with SOC implemented only in an on-site approximation. Strandberg *et al* [33], Fritsch *et al* [35] and Błoński and Hafner [36] investigated the magnetic anisotropy of a series of dimers of late transition metals from the Fe, Co and Ni groups and attempted to relate the MAE to the splitting of the eigenstates caused by spin–orbit coupling and the increasing filling of the d states. Strandberg *et al* [33] used the SDFT results to construct a giant-spin Hamiltonian that allows the investigation of the angular-dependence of the magnetic anisotropy energies. Later work by Strandberg *et al* [34] extended the investigations to Co_n ($n = 2, \ldots, 5$), Mn_xN_y, and Co_3Fe_2 clusters. Sahoo *et al* [38] reported *ab initio* investigations of the MAE of 13-atom clusters of Fe, Co, and Ni, concentrating on the influence of symmetry. For clusters with the structure of an ideal icosahedron, MAE's of 1.7, 0.31, and 0.77 μeV/atom, comparable to the MAE of the bulk metals, have been reported for Fe_{13}, Co_{13}, and Ni_{13}, respectively. In this case, because of the high symmetry of the cluster, the leading contribution to the MAE is sixth order in the SOC. A geometric distortion lowering the symmetry was found to enhance the MAE by orders of magnitude. For Fe_{13} an MAE of 0.32 meV/atom was reported for a 'Jahn–Teller-distorted' cluster. However, only a restricted relaxation of the icosahedral structure describable by one-parameter models was permitted and the optimization was performed in a scalar-relativistic mode, such that the possible influence of the SOC on the cluster structure was not considered. Very recently Błoński *et al* [37] performed relativistic calculations of the structural and magnetic properties of Pt_n, $n = 2$–6 clusters. In agreement with Huda *et al* it was found that for clusters consisting of up to five atoms SOC leads to a preference for planar structures and that even for a six-atom cluster the energetic ordering of different isomers is reversed. SOC leads to the formation of large orbital magnetic moments and to a mixing of different spin states. Due to the spin-mixing the total magnetic moment may be larger or smaller than the spin moment in the absence of SOC. Both spin and orbital moments are found to be anisotropic. Because of the strong SOC the energy differences between coexisting magnetic isomers can be comparable to or even smaller than their magnetic anisotropy energies. In this case the lowest barrier for magnetization reversal can be determined by a magnetic isomer that is different from the ground-state configuration. This result is closely related to the finding of Smogunov *et al* [48], who showed that for freestanding Pt–monowires ferromagnetic ordering is observed for a magnetization perpendicular to the axis of the wire, while magnetization disappears if the moments are forced to align parallel to the axis. Hence in this case the 'giant' MAE is a demagnetization energy.

These results are important for assessing the validity of simplified theories of the MAE. A well known expression for the MAE was derived by Bruno [49] within perturbation theory, assuming that the majority band is completely filled and that the spin moments are isotropic. In this case the MAE is proportional to the spin–orbit coupling parameter ξ and to the difference in the expectation values of the orbital moment calculated for the easy and hard axes of magnetization, i.e. to the anisotropy of the orbital moment. Bruno's theory has been extended by van der Laan [50] to account for terms contributing to second order and for a possible weak anisotropy of the spin moment. Similarly, the description of the MAE in terms of an effective Hamiltonian with a single giant-spin degree of freedom given by Strandberg *et al* [33, 34] assumes that the size of the effective spin moment remains unchanged upon rotation to the magnetization directions. Both descriptions cannot account for the results derived for Pt clusters and monowires.

Pt clusters with their strong SOC are a special case because only the smallest clusters are magnetic. Magnetism has been reported to disappear already for a cluster with about 13 or slightly more atoms. In the present work we have extended the investigations to Ni and Pd clusters. Clusters of the late 3d and 4d metals tend to be quite strongly magnetic [14, 15] and their larger spin moments might at least partly compensate for the weaker SOC.

2. Computational details

The electronic structure calculations and structural optimizations reported here have been performed employing the Vienna *ab initio* simulation package VASP [51, 55]. VASP performs an iterative solution of the Kohn–Sham equations of density-functional theory within a plane-wave basis and using periodic boundary conditions. A semilocal functional in the generalized gradient approximation (GGA) [52] (PW91) and the spin-interpolation proposed by Vosko *et al* [53] are used to describe electronic exchange and correlation and spin-polarization. The projector-augmented wave (PAW) method [54, 55] is employed to describe the electron–ion interactions. The PAW approach produces the exact all-electron potentials and charge densities without elaborating nonlinear core-corrections, which is particularly important for magnetic elements.

The PAW potentials have been derived from fully relativistic calculations of the atomic or ionic reference calculations. Spin–orbit coupling has been implemented in VASP by Kresse and Lebacq [56]. Following Kleinman and Bylander [57] and MacDonald *et al* [58], the relativistic Hamiltonian given in a basis of total angular momentum eigenstates $|j, m_j\rangle$ with $j = l \pm \frac{1}{2}$ (containing all relativistic corrections up to order α^2, where α is the fine-structure constant) is recast in the form of 2×2 matrices in spin-space by re-expressing the eigenstates of the total angular momentum in terms of a tensor product of regular angular momentum eigenstates $|l, m\rangle$ and the eigenstates of the z-component of the Pauli-spin matrices. The relativistic effective potential consists of a term diagonal in spin-space which contains the mass velocity and Darwin corrections, and the spin–orbit operator,

$$\mathbf{V} = \mathbf{V}^{sc} + \mathbf{V}^{\mathrm{SO}} = \sum_{l,m} [V_l \cdot \mathbf{1}_\sigma + V_l^{\mathrm{SO}} \vec{L} \cdot \vec{\mathbf{S}}] |l, m\rangle\langle l, m|,$$

where $\mathbf{1}_\sigma$ is the unit operator in spin-space and

$$\vec{L} \cdot \vec{\mathbf{S}} = \tfrac{1}{2} \begin{pmatrix} L_z & L_- \\ L_+ & -L_z \end{pmatrix}.$$

The l-components of the scalar V_l and spin–orbit V_l^{SO} potentials are weighted averages over the $l \pm \frac{1}{2}$ components, assuming that the magnetization is directed along the z-axis. The Hamiltonian is therefore a 2×2 matrix in spin-space. The nondiagonal elements arise from the spin–orbit coupling, and also from the exchange–correlation potential when the system under consideration displays a noncollinear magnetization density. Calculations including spin–orbit coupling have, therefore, to be performed in the noncollinear mode implemented in VASP by Hobbs *et al* [59] and Marsman and Hafner [60]. The Kohn–Sham equations with the relativistic effective potential have been solved self-consistently. Forces acting on the atoms have been calculated using the Hellmann–Feynman theorem.

The smallest clusters were placed into a $10 \times 10 \times 10$ Å cubic box, being large enough to suppress any interactions between the periodically repeated images of the clusters. The size of the box has been extended to $15 \times 15 \times 15$ Å for the larger 13-atom clusters. Geometric, electronic and magnetic degrees of freedom were relaxed simultaneously without any constraint until the change in total energy between successive iteration steps is smaller than 10^{-7} eV. The calculations were performed in two steps. First a collinear scalar-relativistic calculation has been performed. The geometry optimization has been performed by a static relaxation using a quasi-Newton method, starting from different initial configurations, including both three-dimensional and planar structures. For clusters with 13 atoms, in addition, molecular-dynamics simulations followed by a dynamical simulated annealing have been performed (details can by found in the paper by Futschek *et al* [14, 15]). In addition, structures proposed on the basis of other algorithms for searching global energy minima [16, 23] have been examined. In the second step the configurations resulting from the scalar-relativistic calculations were used to initialize the noncollinear calculations, including spin–orbit coupling [59, 60], allowing again for a relaxation of all geometric, electronic and magnetic degrees of freedom. For each structural isomer of a cluster a set of self-consistent calculations with different initial orientations of the magnetic moments was performed to find the easy and hard magnetic axes and to calculate the MAE in terms of the difference in the total energies. For each initial configuration all structural, electronic, and magnetic degrees of freedom have been optimized without any symmetry constraint, but for the converged solution the magnetic point group symmetry has been determined.

The basis set contained plane waves with a maximum kinetic energy of 500 eV, a convergence of the total energy within 10^{-7} eV was imposed during the self-consistency cycle. The cluster structure was relaxed without any symmetry constraints until the forces on all atoms were less than 10 meV Å^{-1}. We have checked that the results remain unchanged for higher cut-off energies and even more stringent criteria for convergence. Calculations were performed for the Γ-point of the computational cell only. The total magnetic moments of the clusters are calculated from the difference in the integrated spin-polarized densities of states. This is possible because spin and orbital cluster moments are always collinear. Local spin and orbital moments are determined by projecting the plane-wave components of the eigenstates onto spherical waves inside slightly overlapping atomic spheres. Because this projection depends on the choice of the atomic radius, the sum of the local moments is not necessarily identical to the total cluster moment.

3. Results

Some of the effects of spin–orbit coupling have already been documented in earlier studies [30, 37], and these findings have

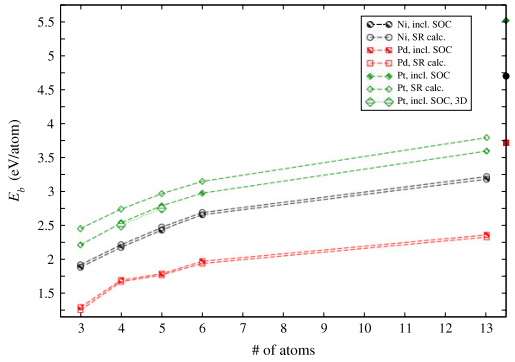


Figure 1. Binding energies of Ni, Pd, and Pt clusters calculated in the scalar-relativistic approximation and including SOC. Bulk cohesive energies are marked for comparison by full symbols at the right margin. Cf the text.

been confirmed by our calculations. (i) The SOC energies per atom (defined as the difference in the total energies with and without SOC) show only a modest variation with the size of the cluster. For Pt clusters, the values oscillate around 0.45 eV/atom [30, 37], they are much smaller for Pd (∼0.05 eV/atom) and Ni (∼0.01 eV/atom) clusters. (ii) The binding energy of the clusters, calculated with respect to the separated-atom limit, is reduced by SOC for Ni (by about 0.035 eV/atom) and Pt (by about 0.20 eV/atom) cluster, because SOC makes a larger contribution to the total energy of the isolated atoms with an open d shell (electronic configuration d^9s^1), see figure 1. For Pd clusters, SOC enhances the binding energies on average by about 0.02 eV/atom because the SOC energy of the free atoms with their closed d^{10} shell does not outweigh the corrections to the total energy of the clusters. For Ni_n, the reduction of the binding energies leads to slightly better agreement with the experimental values of Grushow and Evin [69], $E_b = 1.44/1.58/1.70/2.04$ eV/atom for $n = 3$–6, to be compared with $E_b = 1.92(1.89)/2.22(2.18)/2.47(2.43)/2.69$ (2.65) eV/atom from theory (SOC corrected values in parentheses), although it should be emphasized that experimental binding energies are subject to large uncertainties. No experimental values are available for Pd and Pt clusters. (iii) The influence of SOC on the cluster geometry is modest in most cases. Changes in bond lengths are very small, usually less than 0.01 Å. (iv) For Ni and Pd clusters the energetic order of different structural isomers remains unchanged, while for Pt_n clusters SOC favors planar structures for n up to 5 [30, 37]. In the following, the discussion will concentrate on the magneto-structural properties of transition-metal clusters, and the correlation between their geometry and magnetism.

3.1. Trimers

The scalar-relativistic calculations for Ni and Pd trimers predict a ground-state configuration forming an equilateral triangle, a magnetic spin moment of $\mu_S = 2\mu_B$ (i.e. $S = 1$, spin triplet), and bond lengths of 2.20 and 2.52 Å, respectively. For this highly symmetric configuration the highest molecular orbital is triply degenerate, but occupied by only two electrons. Hence it is expected that the cluster undergoes a Jahn–Teller distortion lowering the symmetry from $D_{3h} = \bar{6}m2$ to $C_{2v} = mm2$. According to the calculations by Futschek *et al* [14, 15], for a Ni_3 trimer a minimal distortion with a difference of 0.01 Å between one short and two long bonds occurs, while for Pd_3 and Pt_3 $\bar{6}m2$ symmetry is preserved. The stability of Pd and Pt trimers at the SDFT level against Jahn–Teller distortion is consistent with other SDFT calculations, while Balasubramanian *et al* [39, 61] and Valerio and Toulhoat [62] have shown that calculations at a multiconfiguration Hartree–Fock level or using hybrid functionals mixing Hartree–Fock and DFT exchange predict a broken symmetry. However, it must be pointed out that the deviations from perfect threefold symmetry reported there are very modest, with differences in the bond lengths around 0.01 Å and in the bond angles of the order of 0.02°–0.04°.

The calculations including spin–orbit coupling have been initialized with three different orientations of the magnetization direction: in-plane, along the z-direction (i.e. along a twofold symmetry axis of the equilateral triangle—for the definition of the coordinate system see figure 2), out-of-plane, along the y-direction, and along the [111] direction. For in-plane and out-of-plane orientations the total energy is stationary with respect to a rotation of the magnetic axis. The former represents the easy, the latter the hard magnetic axis. The difference in the total energies defines the MAE, which is 2.35 and 0.85 meV/atom for Ni and Pd trimers, respectively. For an initially oblique direction, the magnetic axis relaxes to the in-plane orientation. For the Ni_3 cluster in this relaxed state, the moments form an angle of about 30° with the easy axis, i.e. they are oriented along one of the edges of the triangle and the energy difference of 0.1 meV defines the very low in-plane anisotropy energy. For the Pd_3 trimer the angle with respect to the easy axis is about 60°, i.e. the magnetization relaxes to a symmetry-equivalent easy axis, and the total energy difference is only 0.02 meV/atom—essentially on the edge of the computational accuracy.

The orientation of the magnetic axis can break the symmetry of the cluster. For a magnetization axis perpendicular to the plane of the trimer, the threefold symmetry is conserved. The magnetic point group (MPG) symmetry $\bar{6}m'2'$ (in Hermann–Mauguin notation [63], a prime attached to a symmetry operation indicates that this operation must be combined with a time-reversal operation which reverses the direction of axial vectors such as the magnetic moment) is compatible with the ferromagnetic alignment of the local moments along the main symmetry axis. For an in-plane magnetization direction both the geometric and the magnetic symmetry are reduced to orthorhombic. We find isosceles triangles for both trimers, with two short and one long edge for the Ni_3, and two long and one short edge for the Pd_3 cluster (see figure 2). However, while the geometric distortions are modest (differences in bond lengths do not exceed 0.02 Å), large differences appear in the local magnetic moments. The MPG is $m'm'2$, compatible with the parallel alignment of the local spin moments and the canting of the local orbital moments towards the twofold symmetry axis. The local total magnetic

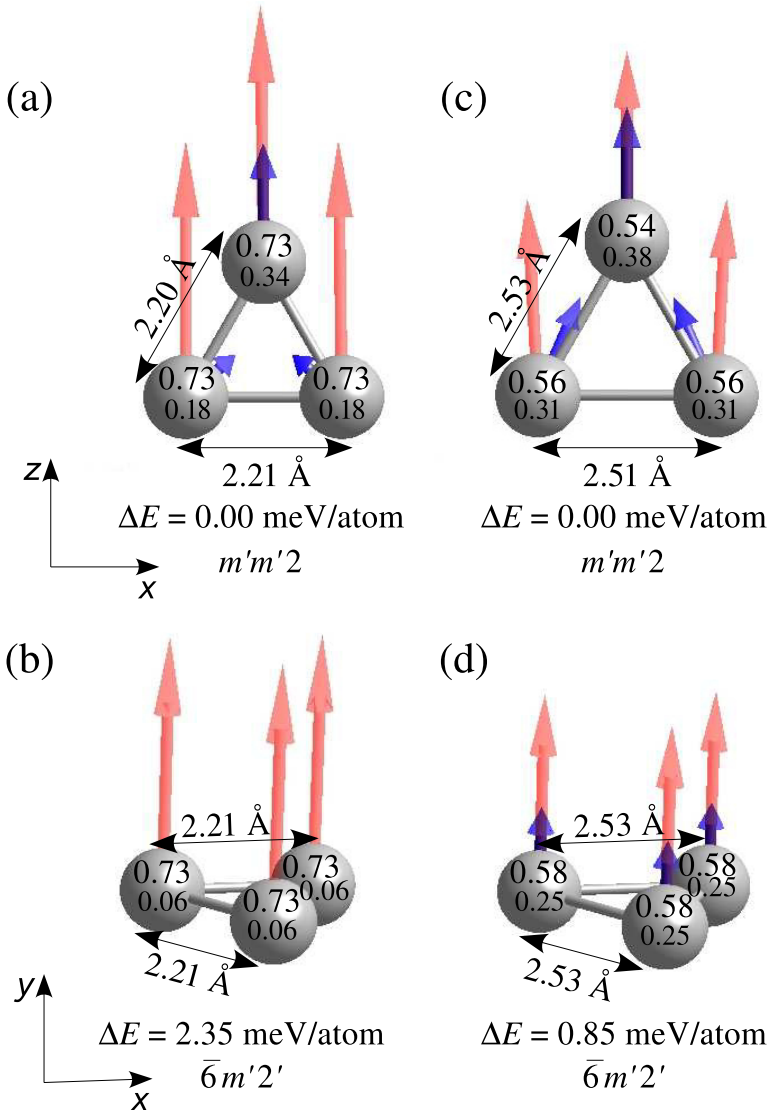


Figure 2. Structure and local spin (upper value) and orbital magnetic moments (lower value) (in μ_B) of Ni_3 ((a), (b)) and Pd_3 ((c), (d)) clusters in their easy-axis (first row) and hard-axis (second row) configurations. The spin and orbital moments are represented by the red (light gray) and blue (dark gray) arrows. For each configuration the magnetic point group symmetry and the energy difference relative to the ground state are listed below. Cf the text.

moments are larger on the atom occupying the vertex pointing along the easy axis, i.e. oriented along the mirror plane of the structure (see figure 2). Total spin and orbital moments of the cluster and the local spin and orbital moments at the site with the highest moment are always collinear, but on the other two sites spin and orbital moments are canted by angles varying between $\pm 25°$ (Pd_3), $\pm 46°$ (Pt_3) and $\pm 48°$ (Ni_3) and the local spin moments are also slightly canted relative to the global magnetization axis, see figure 2.

While in a scalar-relativistic description both trimers have a spin moment of 2 μ_B ($S = 1$), SOC induces a mixing of different spin states with the largest contributions coming from low-lying spin isomers. For the Ni trimer, both low- and high-spin isomers have high excitation energies (larger than 77 meV) in the scalar-relativistic approximation, while for Pd_3 $S = 1$ and $S = 0$ isomers are energetically degenerate [14, 15]. Consequently, the relativistic calculations yield a spin moment which is slightly enhanced for Ni ($\mu_S = 2.19\ \mu_B$), but reduced for Pd ($\mu_S = 1.66\ \mu_B$). The orbital moments increase with increasing strength of the SOC as expected, we find $\mu_L = 0.58$, 0.93 and 1.07 μ_B, and $\mu_J = 2.77$, 2.59 and 2.54 μ_B for Ni, Pd and Pt [37] in their easy-axis orientation, respectively.

Spin and orbital moments of the clusters show different degrees of anisotropy: for Ni_3 the spin moment is isotropic, but the orbital moment is strongly reduced for the out-of-plane

(hard) orientation (0.06 μ_B/atom). For Pd_3 both spin and orbital magnetic moments are only weakly anisotropic, the spin moment is lower, the orbital moment larger along the easy axis. For the Pd_3 cluster with out-of-plane magnetization we could also identify a low-moment (LM) magnetic isomer, which is higher in energy by 7.9 meV/atom than the GS magnetic configuration. For the Pt_3 trimer we had found [37] that the rotation of the magnetic moment to a direction perpendicular to the plane induces a transition to a LM isomer, with reduced spin and orbital moment. For the Pd trimer such a LM isomer exists, but it does not form the GS, for the Ni-triangle our calculations failed to find LM magnetic isomers for different orientations of the magnetization.

For triangular Pd and Pt trimers much larger MAE's of 8.3(10.0) meV/atom and 11.4(4.8) meV/atom, respectively, have been reported by Fernández-Seivane and Ferrer [32] from calculations using the local-density approximation (LDA) and gradient-corrected functionals (GGA results given in parentheses). The easy-axis orientation described in their paper is also in-plane with noncollinear local spin moments for Pt_3. The MAE is calculated as the energy difference between this ground-state configuration and the first excited magnetic isomer with out-of-plane orientation. Information on the cluster geometry and on the spin and orbital magnetic moments can be found in the supplementary information to their paper. Quite generally we find that for most clusters these authors report larger spin and lower orbital moments than we find in our work. What is more important, however, is that irrespective of the functional that has been used, Fernández-Seivane and Ferrer report much larger spin and orbital anisotropies for both trimers. It appears that the differences in the orbital moments are a consequence of the on-site approximation used for the calculation of the spin–orbit coupling matrix elements within their local orbital approach [64], while the local spin moments are derived from a Mulliken analysis. It has been demonstrated that the Mulliken analysis based on overlapping local orbitals systematically leads to larger local moments than the integration over atomic spheres [38]. The anisotropy in the total magnetic moment per trimer can be as large as 0.88 μ_B, distributed about equally between spin and orbital contributions. With such a large change in the moment, it appears to be legitimate to raise the question whether their 'excited state' really differs from the ground state only by a rotation of the magnetization direction and if it does not rather represent an excited magnetic isomer. If we add the excitation energy for the LM isomer of the Pd_3 cluster to our calculated MAE, we arrive at an energy which is very close to the value reported by Fernández-Seivane and Ferrer [32].

3.2. Tetramers

According to the scalar-relativistic calculations the ground state of the Ni_4 tetramer is a distorted tetrahedron (the point group symmetry is lowered to $S_4 = \bar{4}$, with two short edges of 2.20 Å and four long ones of 2.32 Å) and a spin moment of $\mu_S = 4\ \mu_B$ and local moments of 1 μ_B on all four atoms. A Pd_4 cluster forms a regular tetrahedron (edge length 2.61 Å, symmetry group $T_d = \bar{4}3m$) with a magnetic moment of $\mu_S = 2\ \mu_B$. For the calculations including SOC, again three different orientations of the magnetic moment have been chosen for the initial configuration: (i) along the x-axis, i.e. parallel to one of the edges of the tetrahedron (see figure 3), (ii) along the z-axis, i.e. perpendicular to one of the edges of the tetrahedron (this is parallel to a twofold symmetry axis), and (iii) along the [111] direction (for a perfect tetrahedron this would be parallel to a threefold symmetry axis).

While for a Pt_4 cluster SOC induces a preference for a flat structure (a rhombus whose short diagonal has almost the same length as one of the edges) [30, 37], for the Ni and Pd tetramers the tetrahedral structure and bond lengths remain unchanged. For Pd_4 the structural energy difference between tetrahedron and rhombus is even increased by 40 meV/atom by including SOC. For Ni_4 the total energy is found to be stationary for a magnetization perpendicular to the edges of the cluster, aligned along one of the edges of the tetrahedron or parallel to one of the threefold symmetry axes (along the [111] direction), see figures 3(a)–(c). The total magnetic moment of the cluster is $\mu_J = 3.80\ \mu_B$, i.e. slightly lower than the spin moment resulting from a scalar-relativistic calculation. The reduction of the spin moment is expected because of the existence of a $S = 1$ isomer with a low excitation energy of 27 meV, while a $S = 3$ isomer is higher in energy by 130 meV [15]. The admixture of a low-spin state is compensated by a modest orbital moment. The easy magnetization direction is perpendicular to the edge, the hard oriented parallel to an edge. Both spin and orbital moments of the cluster are isotropic within the computational accuracy, and this is also reflected in a small MAE of 0.46 meV/atom. The local orbital moments are slightly canted relative to the spin moments.

The symmetry of the geometric structure is reduced to $C_{2v} = mm2$, the magnetic point group $m'm'2$ allows a parallel alignment of the local spin moments and a slight canting of the orbital moments in all three magnetic configurations. For a magnetization oriented along the hard axis, the broken symmetry is reflected by slightly different orbital moments on pairs of atoms (see figure 3(b)), for a magnetization perpendicular to one of the triangular faces the local orbital moment is smaller on the atoms in the plane perpendicular to the magnetization and larger on the fourth atom (see figure 3(c)). For this orientation of the magnetization, the MAE is only 0.11 meV/atom. The total orbital is almost the same for all three configurations.

For the Pd_4 cluster calculations, including SOC conserves the perfect tetrahedral symmetry of the geometric structure and the bond lengths, and thus magnetic moments initialized parallel or perpendicular to one of the edges of the tetrahedron (and hence parallel to a twofold symmetry axis) converged to energetically degenerate stationary solutions with spin and orbital moments of $\mu_S = 1.84\ \mu_B$, $\mu_L = 0.48\ \mu_B$, and $\mu_J = 2.32\ \mu_B$. A slight reduction of the spin moment compared to the scalar-relativistic result is overcompensated by the orbital moment of the cluster. However, as no magnetic point group with tetrahedral symmetry is compatible with a ferromagnetic state [63], magnetization necessarily reduces the symmetry of the cluster. For the easy-axis orientation the MPG is $m'm'2$, with the total magnetic moment parallel to the twofold

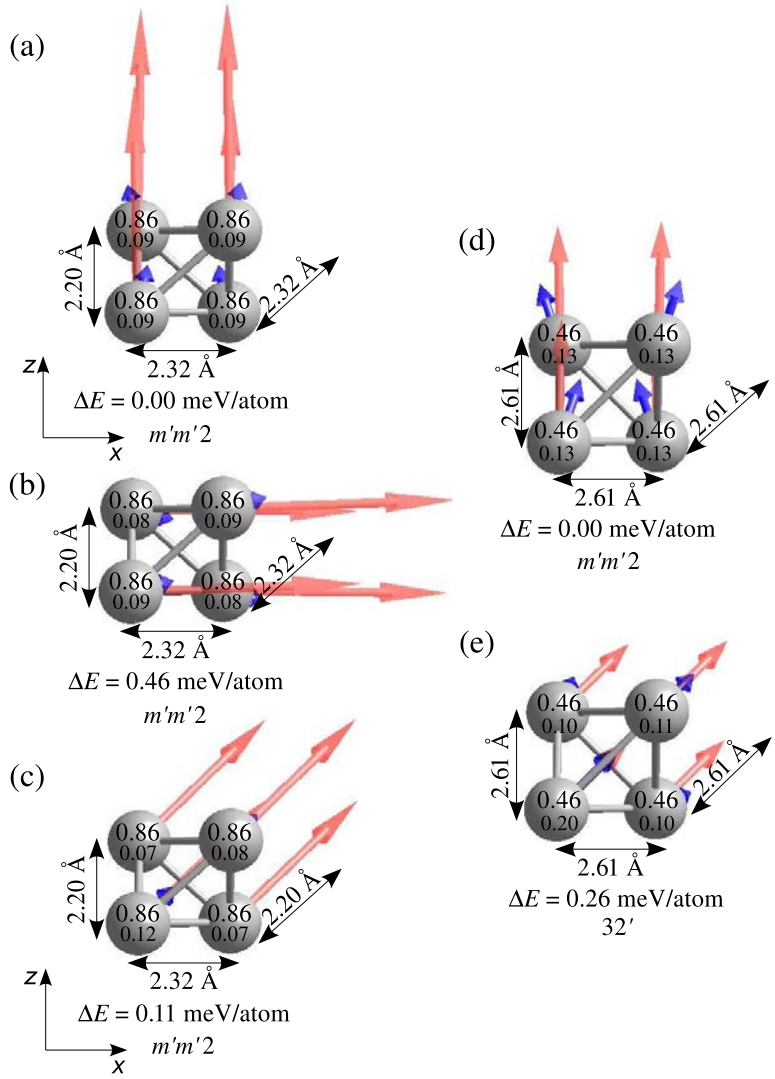


Figure 3. Structure and local magnetic moments of Ni_4 ((a), (b), and (c)) and Pd_4 ((d), (e)) clusters for different orientations of the magnetization direction. Cf figure 2 and the text.

symmetry axis. The size of the local spin and orbital moments is the same on all four sites, the local orbital moments are slightly canted relative to the overall magnetization directions (see figure 3(d)). For a magnetic moment oriented along a threefold symmetry axis the total and local spin moment are the same, but the local orbital moments are now aligned with the spin moments. The local orbital moment is significantly larger on the atom located on the threefold symmetry axis. This leads also to a small enhancement of the cluster orbital moment to $\mu_L = 0.51\ \mu_B$. The MPG is $32'$. This magnetic axis is disfavored by an MAE of 0.26 meV/atom.

For the Pt_4 cluster, inclusion of SOC not only stabilizes a planar over the tetrahedral structure (in agreement with Huda *et al* [30] and Xiao and Wang [65], but in disagreement with Sebetci [31]), it also stabilizes an antiferromagnetic ground state [37]. For a tetrahedral Pt_4 cluster a noncollinear antiferromagnetic ground state with the local moments oriented along the four threefold symmetry axes was reported. The geometric structures predicted for Pd_4 and Pt_4 structures agree with the results of Fernández-Seivane and Ferrer [32]. For the Pd_4 tetrahedron these authors report two frustrated noncollinear ferromagnetic configurations to be lower in energy than a noncollinear antiferromagnetic configuration, similar to that reported by Błoński *et al* [37] for the Pt_4 tetrahedron. In the two energetically most favorable states, a large magnetic moment exists only at one site. A total spin moment of about 1 μ_B and a modest orbital moment of about 0.2 μ_B seems to be hard to reconcile with a spin moment from the scalar-relativistic calculations, which, according to the number of valence electrons, can only be zero or an even multiple of μ_B. The energy difference between these two configurations of 3.5 meV/atom has been interpreted as the

MAE of the cluster—this would be one order of magnitude larger than our result.

3.3. Pentamers

For all pentamers the scalar-relativistic calculations predict a trigonal bipyramid (point group symmetry $D_{3h} = \bar{6}m2$) to be the ground-state configuration, with a spin of $S = 2$ for Ni_5 and Pt_5 and $S = 1$ for Pd_5. The lengths of the bonds forming the central triangle of Ni_5 (2.25 Å) are shorter than the bonds to the atoms at the apices (2.33 Å). In contrast, in the Pd pentamer the bonds forming the triangle are longer (2.91 Å) than the remaining bonds (2.56 Å). However, a structure which is closer to that of the Ni pentamer is almost energetically equivalent. The local magnetic moments of the apical atoms are always slightly lower than those on the atoms forming the central triangle: 0.74/0.84 μ_B and 0.35/0.43 μ_B for Ni_5 and Pd_5, respectively.

The calculations including SOC have been initialized with the magnetic axis parallel to the threefold symmetry axis, within the plane of the central triangle, and along the [111] direction. Adding spin–orbit coupling stretches the interatomic distances within the central Ni-triangle by 0.01 Å, the total magnetic moment of the Ni_5 cluster is $\mu_J = 4.27\ \mu_B$, $\mu_S = 3.82\ \mu_B$ and $\mu_L = 0.45\ \mu_B$ in the magnetic ground state with the easy magnetic axis in the equatorial plane, along a twofold symmetry axis (see figure 4(a)). In the ground-state configuration local spin and orbital moments are strictly collinear, both spin and orbital moments are smaller on the apical atoms. The hard magnetic axis is the threefold symmetry axis. The spin moments are isotropic, the orbital moments are the same on all atoms with $\mu_L = 0.10\ \mu_B$, leading to a slight increase of the total orbital moments to 0.50 μ_B (see figure 4(c)). A magnetization perpendicular to the threefold axis reduces the magnetic symmetry to orthorhombic (MPG $m'm'2$), without inducing a geometric distortion and with only very small differences in the local orbital moments. For the hard magnetic axis parallel to the threefold symmetry axis the MPG is $\bar{6}m'2'$. The MAE is 0.27 meV/atom relative to the in-plane orientation, although this configuration has slightly lower orbital moments. The in-plane anisotropy is determined by a rotation of the magnetization by an angle of 60° with respect to the twofold symmetry axis of the central equilateral triangle (see figure 4(b)), it amounts to only 0.09 meV/atom at almost isotropic total spin and orbital moments.

For the Pd_5 cluster SOC changes the geometry for in-plane magnetization: the equatorial plane forms an isosceles triangle with one bond shorter by 0.03 Å than the remaining two, and the distances between the apical atoms are stretched by about 0.02 Å. The crystallographic symmetry is reduced to $C_{2v} = mm2$. The easy magnetic axis lies again in the equatorial plane, in this case we also determine a larger in-plane anisotropy energy than for Ni_5: a rotation of the magnetization axis by 60° leads to an increase of the total energy by 0.91 meV/atom (see figures 4(d) and (e)). In both cases the MPG is $m'm'2$. The cluster moments for in-plane magnetization are $\mu_J = 2.38\ \mu_B$, $\mu_S = 1.81\ \mu_B$ and $\mu_L = 0.57\ \mu_B$; i.e. mixing with low-spin states is overcompensated by the orbital moment. Local orbital moments are slightly canted relative to the local spin moments only on the apical atoms. Rotation of the magnetic axis within the plane leaves the spin moments almost unchanged, but the total orbital moment slightly decreases for the hard in-plane orientation. Calculations initialized along the threefold axis always relaxed to in-plane orientation of the magnetic moments. Therefore the MAE could only be calculated for a frozen direction of the magnetization parallel to the threefold symmetry axis, resulting in an MAE of 2.1 meV/atom. For the hard axis the geometric symmetry is conserved, the magnetic symmetry is $\bar{6}m'2'$. The spin moments are slightly, and the orbital moments are strongly reduced to half of their value calculated for the easy axis (see figure 4(f) for details).

For the Pt_5 cluster SOC stabilizes a planar structure, rotation of the magnetization axis leads to complex transitions between different magnetic isomers [37]. For the Pt_5 cluster forming a trigonal bipyramid, the easy axis is again in-plane, the total magnetic moment of the cluster is $\mu_J = 3.69\ \mu_B$, with $\mu_S = 2.76\ \mu_B$ and $\mu_L = 0.93\ \mu_B$, i.e. much larger than for Pd_5. The hard axis is the threefold symmetry axis. The MAE is rather large, 4.3 meV/atom [37]. For the Pd_5 cluster Fernández-Seivane and Ferrer [32] report a stable structure in form of a trigonal bipyramid and similar spin, but lower orbital moments than our calculations. From the Supplementary Information to their paper we find out-of-plane (uniaxial) MAE of 0.4 meV/atom and a very small in-plane anisotropy of 0.1 meV/atom, in good agreement with our results. The lower orbital moments in their calculations also lead to the slightly lower value for the MAE.

3.4. Hexamers

For the Ni_6 cluster the scalar-relativistic calculations predict a slightly distorted octahedral geometry (point group symmetry reduced to $D_{4h} = 4/mmm$) with a spin moment of 8 μ_B. The local magnetic moments at the two apical atoms are reduced by 0.02 μ_B compared to those on the four equatorial atoms. The GS structure of Pd_6 is a non-magnetic perfect octahedron (symmetry group $O_h = m\bar{3}m$, bond length of 2.65 Å). Previous calculations by Futschek *et al* [14] for Pd_6 predicted the $S = 1$ state to be the GS, but note that the $S = 0$ isomer is only 10 meV/atom higher in energy. For the Pt_6 cluster a capped square pyramid with $S = 3$ was found to be preferred over a distorted octahedron with the same spin [14].

SOC leaves the geometry of the Ni hexamer unchanged, the total moment per cluster is reduced to $\mu_J = 7.12\ \mu_B$ ($\mu_S = 6.54\ \mu_B$ and $\mu_L = 0.58\ \mu_B$). The easy magnetic axis is parallel to the fourfold symmetry axis, with collinear spin and slightly canted local orbital moments (MPG $4/mm'm'$, see figure 5). The local spin moments are all 1.09 μ_B/atom, but large differences are found for the local orbital moments: 0.12 μ_B on the equatorial atoms (canted by 7° relative to the spins) and 0.05 μ_B on the apices (canted by 17°). The hard magnetic axis of Ni_6 lies parallel to one of the edges of the central square of atoms (i.e. along a twofold symmetry axis). In this configuration the fourfold rotational symmetry is broken, the MPG is $mm'm'$. The local spin moments of 1.09 μ_B/atom

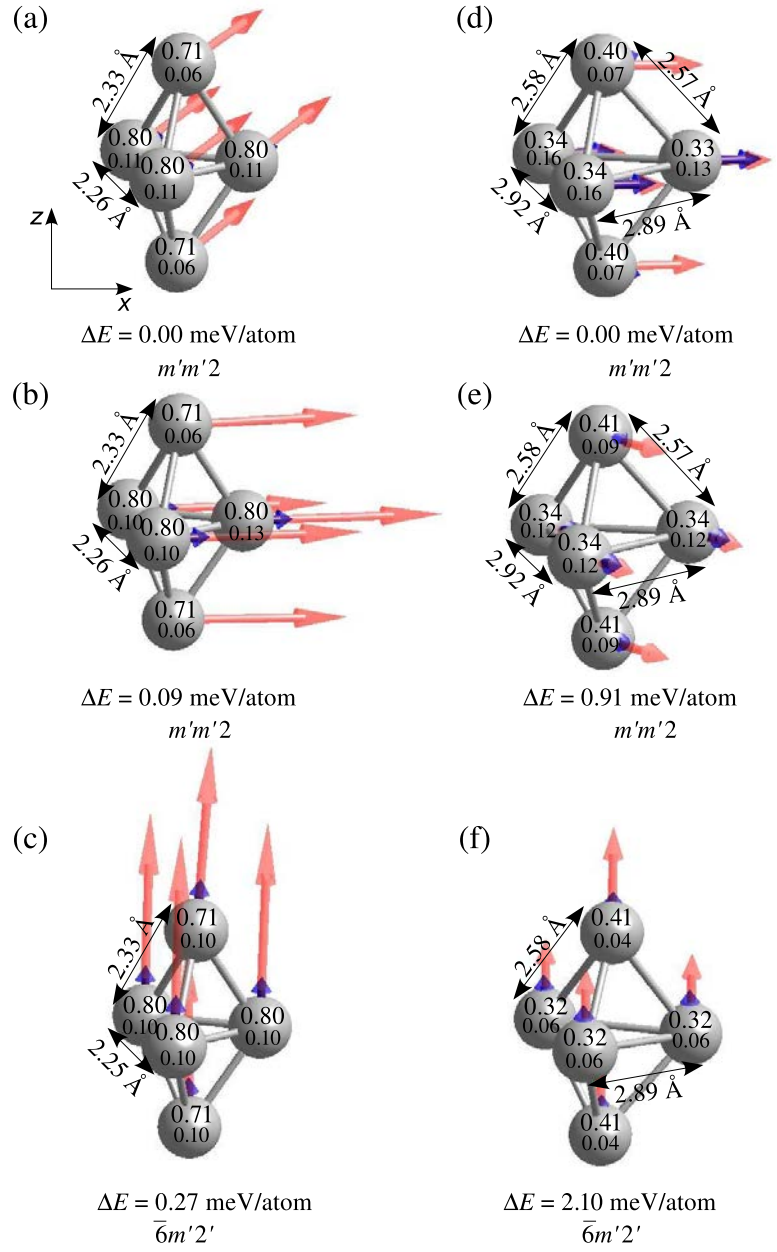


Figure 4. Structure and local magnetic moments of Ni_5 ((a)–(c)) and Pd_5 ((d)–(f)) clusters, calculated for different magnetization directions. Cf figure 2 and the text.

are completely isotropic, but the local orbital moments on the four equatorial sites are reduced to 0.09 μ_B/atom (canted by $\pm 24°$ relative to the spins), and those on the apical atoms are enhanced to 0.13 μ_B/atom and collinear to the spins. The MAE is only 0.21 meV/atom. A stationary state is also found for a magnetic axis perpendicular to one of the triangular facets (for a perfect octahedron this would be a threefold symmetry axis). The energy of this configuration is only 0.1 meV lower than for magnetization along the hard axis.

Applying SOC to the calculation for the Pd_6 octahedron promotes a magnetic GS structure with a cluster moment of ~ 2.6 μ_B ($\mu_S = 1.90$ μ_B and $\mu_L = 0.66$ μ_B). A Jahn–Teller distortion lowers the symmetry to $D_{4h} = 4/mmm$, the interatomic distances between the central square are stretched to 2.69 Å, and those to the apical atoms are unchanged. This is reflected in the local moments: the four equatorial sites carry local spin moments of 0.28 μ_B/atom and very small local orbital moments of 0.03 μ_B/atom, whereas on the apical atoms

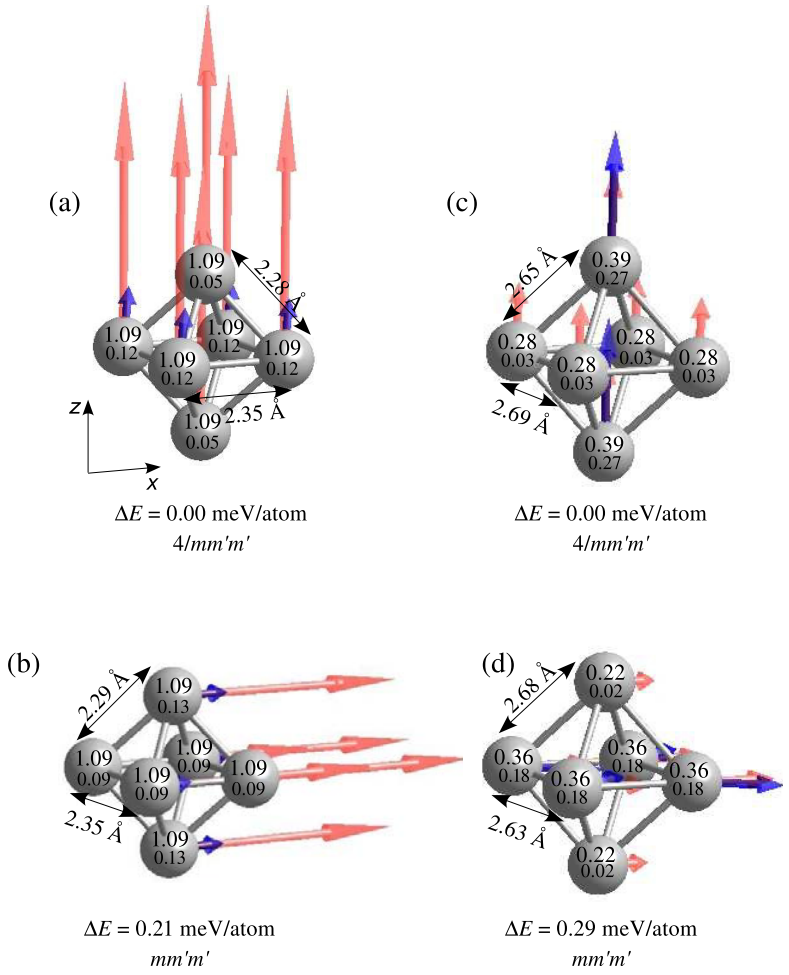


Figure 5. Structure and local magnetic moments of distorted octahedral Ni_6 ((a), (b)) and Pd_6 ((c), (d)) clusters, with magnetization along the easy ((a), (c)) and hard ((b), (d)) magnetic axes. Cf figure 2 and the text.

both the local spin and orbital moments are enhanced to 0.39 and 0.27 μ_B/atom, respectively. The magnetic moments are strictly aligned (compare figures 5(c) and (d)). The MPG is $4/mm'm'$, as for the Ni_6 cluster. Similarly as for Ni_6, the hard magnetic axis of Pd_6 lies parallel to one of the edges of the equatorial square, the magnetic symmetry is reduced to $mm'm'$. A rotation of the magnetization direction from the easy to the hard magnetic axis inverts both the geometry of the cluster (the bonds between equatorial atoms are shortened to 2.63 Å, while those to the apical atoms are stretched to 2.68 Å) and the relative size of the local magnetic moments (now, the local moments on the apical atoms are reduced, whereas those on the four equatorial sites are increased and canted by $\pm 21°$).

For Pt_6 the relativistic calculations reverse the energetic order in favor of the perfect octahedron with bond lengths of 2.62 Å [37]. In the GS, the magnetic structure of the Pt_6 cluster is rather complex, with strongly noncollinear local spin and orbital moments (local spins are oriented along the square diagonals, while the local orbital moments are aligned along the edges and they are antiparallel and slightly deviate from the equatorial plane). The cluster total moment, oriented perpendicular to one of the triangular facets, is low $\mu_J = 0.83\ \mu_B$. The hard magnetic axis is aligned along one of the edges of the equatorial square with an MAE of 1.4 meV/atom.

Fernández-Seivane and Ferrer [32] reported results only for Pd_6. Geometry and bond lengths agree reasonably with our results, but the tetragonal distortion of the octahedron is less pronounced. The GS is almost non-magnetic, with a spin moment of only 0.036 μ_B and a larger orbital moment of 0.148 μ_B. Their MAE of about 1 meV/atom is calculated for a non-magnetic excited state. We believe that the differences in magnetic moment and total energy represent rather the computational accuracy of their set-up rather than a true magnetic anisotropy.

3.5. 13-atom clusters

For a cluster formed by 13 atoms it is generally expected that the equilibrium structure is an icosahedron, because this structure allows for the formation of the maximum

number of nearest-neighbor bonds. Recent studies [12, 14–23] have demonstrated that this is not the case, without, however, converging to a generally accepted result. These calculations have been performed using different *ab initio* codes: VASP [12, 14–17, 21], SIESTA [18, 19], or GAUSSIAN03 [20, 21] and using either plane-wave (VASP) or localized (SIESTA, GAUSSIAN03) basis sets, pseudo-potentials (SIESTA) or all-electron (GAUSSIAN03, VASP) methods (note that the projector-augmented wave method implemented in VASP uses the full electron density and hence should be considered as an all-electron method). While these technical differences may account for some quantitative differences in the structural energy differences, the main origin of the discrepancies in the predicted ground-state configurations is probably in the algorithms used in searching for the global energy minimum. Futschek *et al* [14, 15] used a dynamical simulated annealing strategy starting with a high-temperature molecular-dynamics run, followed by a slow-cooling process and a final static conjugate-gradient minimization. Wang and Johnson [16] followed a procedure originally proposed by Stillinger and Weber [70, 71] for generating low-energy amorphous structures. During a high-temperature MD run, low-energy configurations are monitored, and these selected configurations are optimized by a static minimization. Kumar and Kawazoe [17] built the structure of larger clusters by sequentially adding atoms to the structures of low-energy isomers of smaller clusters. Aguilera-Granja *et al* [18, 19] use static relaxations starting from clusters with different symmetries. Fournier *et al* [20–22] used a search algorithm called 'taboo search in descriptor space' [72] attempting to interpolate in configuration space between local energy minima detected in DFT calculations using appropriately chosen descriptors, and to search for novel candidate structures.

For the Ni_{13} cluster the first calculations of Aguilera-Granja *et al* [18] predicted an icosahedral structure with a moment of 8 μ_B to be the ground state, in good agreement with Futschek *et al* [15], who found a distorted icosahedron with the same magnetic moment. More recent calculations of Aguilera-Granja *et al* [19] reported a structure in the form of a 'fragment of a double icosahedron' and a higher moment of 10 μ_B. However, no structural or magnetic energy differences with respect to the previously reported structure are given. For Pd_{13} Chang and Chou [12] and Futschek *et al* [14] reported a GS structure forming a biplanar arrangement of close-packed layers and a magnetic moment of 6 μ_B, Wang and Johnson [16] a low-symmetry structure with the same moment (but a slightly different biplanar structure was found to be only 5 meV/atom higher in energy). Aguilera-Granja *et al* [18, 19] reported the same conflicting results as for Ni_{13}. Fournier *et al* [20, 21] found distorted icosahedral structures with a magnetic moment of 8 μ_B, but the character and magnitude of the distortion were not specified. It also appears that their 'global' search algorithm did not explore layered configurations. For Pt_{13} Futschek *et al* [15] reported a similar, but non-magnetic, biplanar structure as for Pd_{13}. Wang and Johnson [16] found that the GS is a 'double triangle' structure with a magnetic moment of 2 μ_B, which is essentially a different stacking variant of the biplanar structure reported by Futschek *et al*. Kumar and Kawazoe [17] reported a triangular bilayer structure with a capping atom in a threefold site and $\mu = 2\ \mu_B$, similar to Wang and Johnson. Aguilera-Granja *et al* reported first [18] an icosahedral GS, and later [19] a structure similar to that reported by Kumar and Kawazoe. Fournier *et al* reported a structure for Pt_{13} described as an 'oblate multiply capped trigonal prism' (which we would consider rather as a kind of square pyramid) which is characterized either as non-magnetic [22] or weakly magnetic ($\mu = 2\ \mu_B$) [20]. The problem is that the results are difficult to compare—even when results for a large number of isomers are reported, the structures dealt with in the other studies cannot be found among them. The MD + static relaxation approach used by Wang and Johnson [16] seems to be able to explore the largest region of configuration space, but one has to keep in mind that the static optimization always converges to a minimum of the static potential energy connected to a selected high-temperature minimum by a steepest descent path—it is not evident that this will allow one to detect the global minimum. The simulated annealing approach used by Futschek *et al* [14, 15] depends on the quenching speed—which is always too high. The search algorithm of Fournier *et al* [72] seems to look preferentially for three-dimensional structures. A comparison of accurate total energies could decide the issue, but at the level of the structural energy differences in question, energies derived from different codes cannot be directly compared, and even if the same code has been used, the results depend on basis set completeness (cut-off energies for plane-wave codes), convergence criteria for forces and energies etc which are hardly ever reported in sufficient detail.

An alternative is to compare the structural energy differences relative to a common reference configuration, for example an ideal icosahedron. For a Ni_{13} cluster there is good agreement between the structural energy differences of a cuboctahedron of 92(88) meV/atom and of a buckled biplanar structure of 10(10) meV/atom relative to an ideal icosahedron calculated by Futschek *et al* [14] and Piotrkowski *et al* [23] (results in parentheses). Equilibrium magnetic moments of 8 μ_B for the icosahedron and 10 μ_B for the biplanar structure are also in agreement. The relaxation of the icosahedron (lowering the symmetry to C_{1h}) leads to an energy gain of 21 meV/atom, which is more than the 10 meV/atom for the lowest energy structure detected by the global search algorithm of Piotrkowski *et al*. Hence the distorted icosahedron is confirmed as the equilibrium structure of the Ni_{13} cluster.

For Pd_{13} we find that the buckled biplanar structure is lower in energy by 26 meV/atom than the ideal icosahedron. The energy difference for the asymmetric lowest energy structure of Piotrkowski *et al* [23] is 25 meV/atom, for the structure reported by Wang and Johnson [16] it is 22 meV/atom. All three calculations agree in a total magnetic moment of 8 μ_B for the icosahedron and 6 μ_B for the optimal structure. Hence for Pd_{13} we can only conclude that the energy surface in configuration space is very flat, with multiple minima differing only by a few meV/atom.

For Pt_{13} the situation is different. Relative to an ideal icosahedron with a moment of 2 μ_B the energy of

a buckled biplanar structure with zero moment is lower by 165 meV/atom (present work) and 160 meV/atom [16], respectively. Piotrkowski *et al* [23] report an energy difference of 154 meV/atom for a slightly different biplanar configuration with a moment of 4 μ_B. The good agreement shows that the comparison of the structural energy differences is meaningful. Both studies report low-energy structures which have not been detected using the dynamical simulated annealing strategy of Futschek *et al* [14]. The energetically most favorable structure of Wang and Johnson [16], with a moment of 2 μ_B, is lower in energy by 240 meV/atom, Piotrkowski *et al* [23] reported a structure with the same moment and an even larger energy difference of 271 meV/atom.

3.5.1. Ni_{13}. For the Ni_{13} cluster the scalar-relativistic calculations predict for the distorted icosahedron with 8 μ_B an excitation energy for a low-spin isomer with a ferrimagnetic structure (opposite orientation of the magnetic moment on the atom in the center) of only 24 meV/atom. This excitation energy is only slightly lower than the structural energy difference of 31 meV/atom with respect to the biplanar arrangement. The symmetry of this configuration has been described as C_{1h}, but the distortion from a threefold symmetry (point group $C_{3v} = 3m$) with respect to an axis perpendicular to the close-packed planes is only minimal. Magnetic isomers with moments of 10 and 12 μ_B are almost degenerate in energy, the local moments reflect the approximate threefold symmetry with respect to an axis perpendicular to the planes [15]. A third metastable structural variant consists of a centered distorted cube, capped on four square facets such that the point group symmetry is $D_{4h} = 4/mmm$. This configuration has spin $S = 5$, and it is higher in energy by 71 meV/atom than the distorted icosahedron.

For the Ni_{13} cluster the fully relativistic calculations confirm the icosahedral ground-state geometry with unchanged interatomic distances. The structural energy difference is slightly enhanced for the capped cube and unchanged for the biplanar structure. For the distorted Ni_{13} icosahedron we have found local equilibria for the magnetization oriented along a pseudo-threefold or a pseudo-fivefold symmetry axis—the former is the easy and the latter the hard magnetic axis (see figure 6). The distortion of the geometric structure is also reflected in small differences in the local spin and orbital moments, in the magnetic state the mirror symmetry is broken, the MPG is only 1. The MAE is 0.4 meV/atom. A calculation initialized along a twofold symmetry axis also converged to the same easy axis. For this orientation the total magnetic moment is $\mu_J = 8.97\ \mu_B$ ($\mu_S = 8.48\ \mu_B$ and $\mu_L = 0.49\ \mu_B$). The spin moment is found to be isotropic, but for the hard magnetic axis we calculate a larger orbital moment of $\mu_L = 0.82\ \mu_B$. Both the spin and orbital moments on the atom in the center of the icosahedron are reduced by about a factor of two compared to those on the outer vertices. Local spin moments vary between 0.63 and 0.73 μ_B, and local orbital moments between 0.03 and 0.05 μ_B for easy-axis, and between 0.04 and 0.08 μ_B for hard-axis magnetization, and most local orbital moments are canted relative to the local spin moments by angles up to 28°.

For the structural isomer forming a centered, capped cube slightly elongated along the tetragonal axis, the structural energy difference is slightly increased from 71 to 93 meV/atom. The easy magnetic axis is parallel to the fourfold symmetry direction of the geometric structure (see figure 6(c)). Due to small differences in the canted local orbital moments, the MPG is reduced to m', with the mirror plane parallel to the (x, y)-plane. The in-plane anisotropy is very small, only 0.06 meV/atom. In the configuration with the global magnetization direction along the x-axis a higher magnetic symmetry (MPG $m'm'2$) with the twofold axis parallel to the magnetization is conserved. The hard axis is perpendicular to the fourfold symmetry axis (y-direction). In this configuration the MPG is reduced to m', the MAE is 0.6 meV/atom. As expected, the mixing with low-spin states leads to a reduction of the magnetic moment relative to the spin moment of 10 μ_B found in the scalar-relativistic calculations, to $\mu_J = 7.03\ \mu_B$, $\mu_S = 6.14\ \mu_B$ and $\mu_L = 0.90\ \mu_B$. The spin moment is isotropic, but the orbital moments differ by $\Delta\mu_L = 0.4\ \mu_B$. On the atom in the center of the cube, the spin moment is reduced and aligned antiparallel to that on the outer sites, and the local orbital moments are completely quenched (to a value smaller than 0.01 μ_B). Local orbital moments are canted relative to the local spin moments, which are aligned relative to the chosen magnetic axis.

The structural energy difference of 31 meV/atom found for the biplanar structure relative to the icosahedron is unaffected by SOC. If the direction of magnetization is initialized parallel to the atomic planes, the direction of the moments is found to be locally stable, (see figure 6(f)), with a total cluster moment of $\mu_J = 12.48\ \mu_B$ ($\mu_S = 11.39\ \mu_B$ and $\mu_L = 1.09\ \mu_B$), i.e. comparable to the spin moment from the scalar-relativistic calculations. The magnetization reduces the symmetry to a mirror operation perpendicular to the global magnetic moment, the MPG m is compatible with the canting of the local orbital moments. If the direction of magnetization is initialized perpendicular to the atomic planes, it relaxes to an oblique orientation with unchanged spin and orbital moments. A calculation with frozen perpendicular magnetization leads to a configuration with conserved threefold symmetry (MPG 3), the MAE is 0.09 meV/atom. The spin moment is isotropic, the orbital moment is reduced from 1.23 μ_B to 1.09 μ_B.

Our result for the Ni_{13} icosahedron can be compared with the results of Sahoo *et al* for icosahedral Fe, Co, and Ni clusters [38]. If an ideal icosahedral symmetry is enforced, a Ni_{13} cluster has an MAE of only 0.77 μeV/atom. Only a restricted relaxation describable by one-parameter models has been permitted: a 'Jahn–Teller (JT) distortion' preserving the fivefold symmetry, but contracting the cluster along the fivefold axis, and a 'Mackay (M) distortion' reducing the point group symmetry from icosahedral to tetrahedral and initiating a transformation of the icosahedron into a cuboctahedron. For Ni_{13}, both JT and M relaxations lead to an energy gain of about 16 meV/cluster compared to an ideal octahedron. This is slightly smaller than the lowering of the total energy by 21 meV/atom upon unconstrained relaxation. The average values for the spin and orbital moments per atom (0.66 μ_B and 0.06 μ_B, respectively) are very close to our values, and

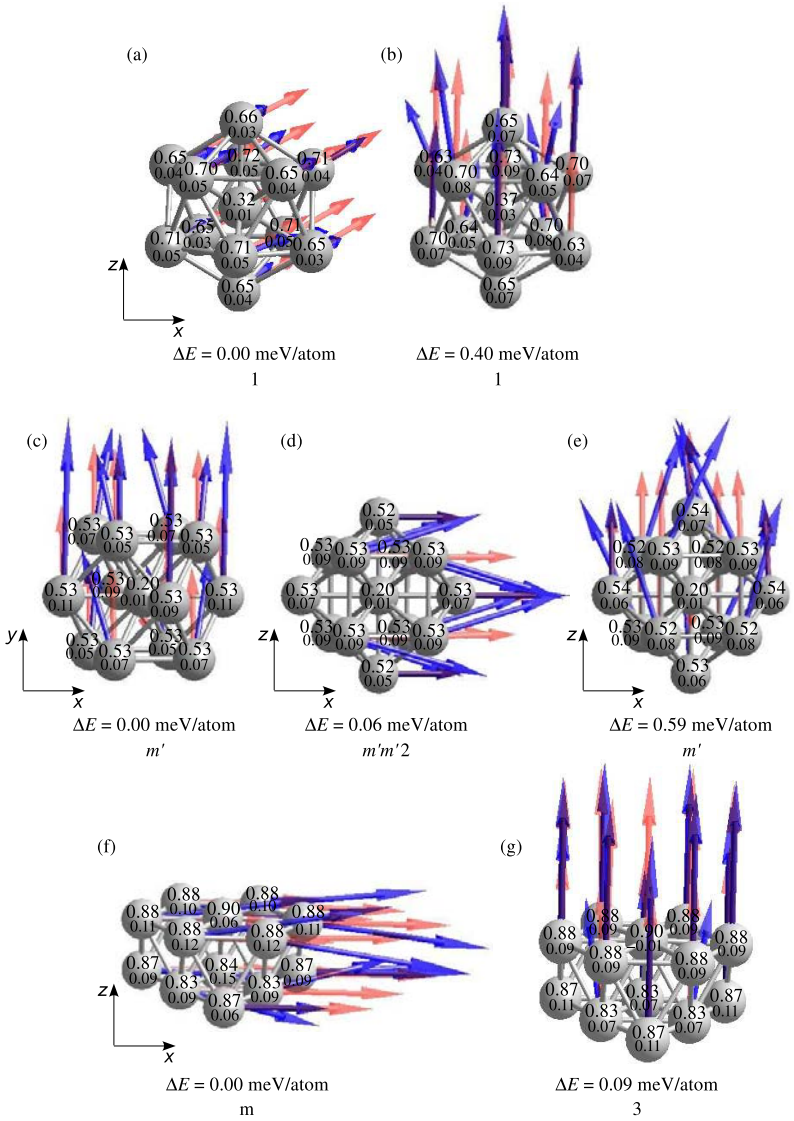


Figure 6. Geometric and magnetic structures of Ni_{13} clusters: the top row shows the icosahedral ground-state configurations, with the magnetization oriented along a threefold (a) and a fivefold (b) symmetry axis. The former is the easy magnetic axis. The second row shows the structure consisting of a centered cube capped on four square facets, with the magnetization directed along one of the Cartesian axes ((c)–(e)). The easy axis is the *y*-direction parallel to the fourfold symmetry axis (d), the hard axis in the *z*-direction (e). The bottom row shows the biplanar structure, with the magnetization initialized along the *x* and *z* directions, i.e. parallel and perpendicular to the close-packed planes ((f), (g)). Spin moments are shown by the red arrows, orbital moments by the blue arrows. For sake of clarity, the length of the arrows representing the orbital moments has been multiplied by ten. Cf figure 2 and the text.

also very close to the bulk values. No information on the anisotropy of the magnetic moments is given in their work. For a JT-distorted Ni_{13} icosahedron, an MAE of 0.688 meV/atom was reported. This MAE is about 30 times larger than that calculated for the M-distorted cluster. The MAE for the JT-distorted cluster is of the same order of magnitude as our result, although the full relaxation leads to a much lower symmetry.

3.5.2. Pd_{13}. For the Pd_{13} cluster the buckled biplanar arrangement with a magnetic moment of 6 μ_B represents the GS, and the cluster now has perfect $C_{3v} = 3m$ symmetry (although this has been overlooked in the earlier work [14]). The magnetic energy difference from the LM (4 μ_B) isomer is only 3 meV/atom, and rises to 22 meV/atom for the HM (8 μ_B) magnetic isomer, reaching a value comparable to the structural energy difference with respect to a perfect icosahedron (symmetry I_h, magnetic moment 8 μ_B) of 26 meV/atom. The structural energy difference of a capped cube with a central atom (symmetry $D_{4h} = 4/mmm$, magnetic moment 4 μ_B) is almost twice as large at 39 meV/atom [14].

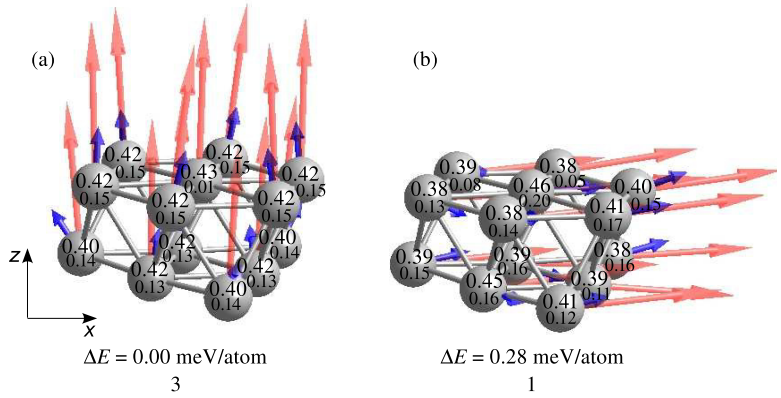


Figure 7. Magnetic structure of the Pd_{13} biplanar cluster with the easy magnetic axis oriented perpendicular to the atomic planes (a) and after rotation of the magnetization by 90° to the hard axis (b). Spin moments are shown by the red arrows, orbital moments by the blue arrows. Cf figure 2 and the text.

The calculations including SOC for Pd_{13} confirm the biplanar structure to be the ground state, but the structural energy difference with respect to the icosahedron is reduced to 13 meV/atom, whereas that of the capped cube is increased to 57 meV/atom. The modest influence of SOC on the structural energy differences is in agreement with Piotrkowski *et al* [23], who did not report any magnetic data from their relativistic calculations. The easy magnetic axis is perpendicular to the atomic planes, the total magnetic moment of the cluster is $\mu_J = 7.13\ \mu_B$ ($\mu_S = 5.41\ \mu_B$, $\mu_L = 1.72\ \mu_B$), the orbital moment leads to an increased magnetization compared to the scalar-relativistic limit. In this configuration, threefold symmetry (MPG 3) is conserved (see figure 7(a)). The hard axis lies parallel to the atomic planes, breaking the threefold symmetry (MPG 1). The MAE is 0.28 meV/atom. The small MAE is reflected in a low spin and orbital anisotropy: $\Delta\mu_S = 0.20\ \mu_B$ and $\Delta\mu_L = -0.06\ \mu_B$. For both magnetization axes, local spin and orbital magnetic moments are slightly noncollinear (see figure 7).

It is remarkable that, while for the smaller clusters, from trimer to hexamer, the easy magnetic axis is always the same for Ni and Pd clusters, for the biplanar 13-atom clusters the easy axis is in-plane for Ni and perpendicular for Pd. Different orientations of the magnetic moment in the GS have been reported for the Ni and Pd dimers [36], where they could be attributed to the different electronic configuration of the atoms.

Any initialization of a magnetization direction for the remaining Pd_{13} structures always converges to the easy magnetic axis, for the icosahedron parallel to a fivefold symmetry axis, and for the capped cube parallel to the fourfold symmetry axis.

3.5.3. Pt_{13}. For the Pt_{13} cluster we have examined the buckled biplanar structure with $C_{3v} = 3m$ symmetry found by Chang and Chou [12] and Futschek *et al* [14], as well as the lowest energy structure identified by Wang and Johnson [16]. This structure is also a biplanar arrangement, but with two triangular fragments of a close-packed plane with six atoms each stacked exactly one above the other, with the 13th atom located in a threefold hollow. Wang and Johnson reported several such triangular biplanar structures, which differ only in the location of the 13th atom and which are all lower in energy than the buckled biplanar structure. A 13-atom cluster also represents the upper size-limit for a spontaneous magnetic polarization of Pt clusters: the biplanar cluster has a non-magnetic ground state (but very low excitation energies for states with $S = 1$–4), the ground state of the lowest energy structure, as well as that of a distorted icosahedron and a distorted cubic structure has spin $S = 1$, again with low excitation energies for low- and high-spin states.

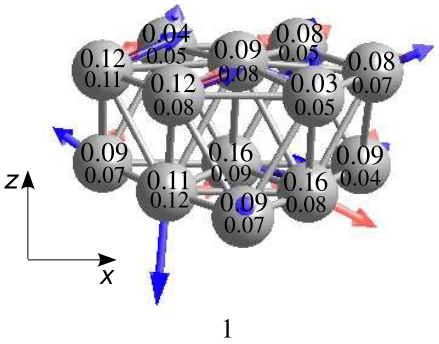


Figure 8. Magnetic structure of the biplanar Pt_{13} cluster. Cf figure 2 and the text.

Calculations including SOC and admitting a noncollinear magnetic structure converge for the biplanar structure to a magnetic state with locally fluctuating spin and orbital moments, adding to modest cluster moments of $\mu_J = 1.47\ \mu_B$ ($\mu_S = 0.88\ \mu_B$ and $\mu_L = 0.64\ \mu_B$), quite independent of the initialization. The distribution of the local moments breaks the threefold symmetry (see figure 8). No clear preference for a magnetic easy axis could be detected. This corresponds to the scalar-relativistic fixed-moment result of energetically degenerate $S = 1$ and 0 isomers.

For the lowest energy triangular structure we have initialized the magnetization along a direction perpendicular

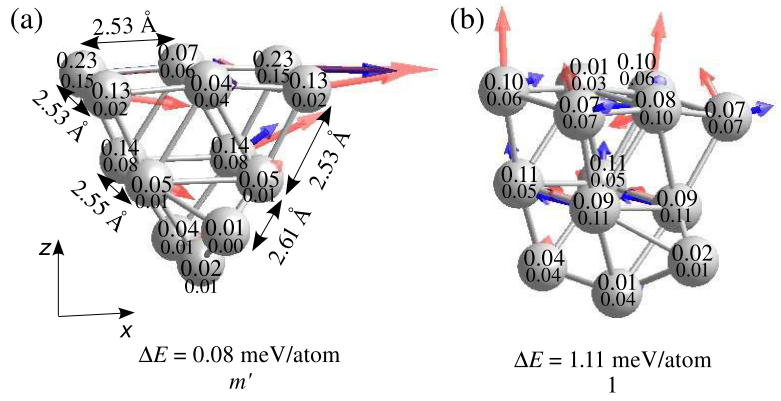


Figure 9. Magnetic structure of the triangular Pt_{13} cluster with the lowest energy. Cf figure 2 and the text.

to the two atomic layer, and along two perpendicular in-plane directions. For a perpendicular magnetization the calculations converge to a non-magnetic state—this is also the ground state. If the magnetization is initially set along the x-direction (see figure 9), along one of the edges of the triangle we find a slightly noncollinear magnetic configuration (absolute values of total, spin and orbital moment $\mu_J = 1.58\ \mu_B$, $\mu_S = 1.06\ \mu_B$, $\mu_L = 0.52\ \mu_B$) which is only 0.08 meV/atom above the ground state. The magnetic point group symmetry is m'. Initialization along a direction parallel to the mirror plane of the structure (along the y-direction) leads to a noncollinear magnetic configuration with lower moment ($\mu_J = 0.92\ \mu_B$, $\mu_S = 0.68\ \mu_B$, $\mu_L = 0.25\ \mu_B$). The in-plane MAE is 1.03 meV/atom.

For the distorted icosahedron we calculate a similar magnetic configuration, with slightly larger spin ($\mu_S = 1.67\ \mu_B$) and lower orbital ($\mu_L = 0.23\ \mu_B$) moments and a stronger canting between local spin and orbital moments. The difference between both structural isomers corresponds to a slightly larger scalar-relativistic energy difference between the icosahedral spin isomers, with a preference for the $S = 1$ state by 7 meV/atom. For the capped cubes the calculations including SOC always converged to a non-magnetic state. Altogether this confirms that a Pt cluster of this size is close to a magnetic to non-magnetic transition.

4. Discussion

We have performed a first-principles investigation of the influence of spin–orbit coupling on the structural and magnetic properties of small transition-metal clusters formed by Ni and Pd, completing our investigation of the MAE of clusters of the Pt-group elements. For Pt clusters we had found that SOC can reverse the relative stability of structural isomers (and in particular stabilize planar structures for Pt_4 and Pt_5 clusters) and lead to a large MAE comparable to the energy difference between magnetic isomers. In contrast, SOC does not affect the relative stability of different structural isomers of Ni and Pd clusters, although it can lead to modest changes in the interatomic distances and induce changes in the crystallographic and magnetic point group symmetries, depending on the orientation of the magnetization axis.

The quantities of central interest to our investigation are the orbital magnetic moment and the magnetic anisotropy of the clusters. The results are summarized in table 1, including our previous results for Pt clusters [37] and on dimers of all three elements [36]. Both the orbital moment and the MAE are found to depend on the strength of the SOC, the size and the geometry of the cluster. For the Ni_n clusters the mixing of different spin states caused by the coupling to the orbital moments leads to a reduction of the spin moment (with the exception of the trimer), the orbital moment is approximately 0.5 μ_B/cluster, varying only little with cluster size and leading to a rapidly decreasing μ_L/μ_S ratio with increasing cluster size. The total magnetic moment per cluster varies between $\mu_J = 2.77\ \mu_B$ for the trimer and $\mu_J = 8.97\ \mu_B$ for the icosahedron, the moment per atom varies around 1 μ_B for the small clusters and reaches 0.69 μ_B for the icosahedron, a value close to that in bulk Ni. The spin moment is generally isotropic, a substantial orbital anisotropy of either sign is found only for the Ni dimer and trimer ($\Delta\mu_L = 0.2\ \mu_B$ and 0.4 μ_B, respectively) and for the distorted Ni-icosahedron ($\Delta\mu_B = -0.33\ \mu_B$).

Pd atoms differ from Ni and Pt by a different electronic ground state (s^0d^{10} instead of s^1d^9). Hence, Pd clusters have a lower binding energy than both Ni or Pt clusters, because bond formation requires an opening of the closed d^{10} shell. An open d shell is also required for the formation of a magnetic moment. The Pd_2 dimer has a spin moment of $\sim$2 μ_B and an almost vanishing orbital moment, clusters with $n = 2$–6 have a small spin moment increasing from 1.66 μ_B to 1.90 μ_B and an orbital moment varying between 0.93 μ_B and 0.48 μ_B, resulting in an almost constant total magnetic moment per cluster of 2.45 $\pm$ 0.1 μ_B and a ratio μ_L/μ_S decreasing only slowly from about 0.6 for the trimer to 0.3 for the hexamer. Pd clusters show a very small spin anisotropy and a much larger orbital anisotropy of either sign—except the Pd_4 tetrahedron with isotropic spin and almost isotropic orbital moment. For the larger Pd_{13} cluster with a biplanar structure the spin moment (5.4 μ_B) is much larger and more anisotropic than the orbital moment (1.7 μ_B).

For Pt clusters the situation is very complex [37]. Dimer and trimer have a ferromagnetic ground state with $\mu_J =$

Table 1. Equilibrium geometry, magnetic point group symmetry (MPG) for easy and hard magnetization axis, magnetic anisotropy energy MAE (in meV/atom), spin- and orbital anisotropies, $\Delta\mu_S$ and $\Delta\mu_L$ (in μ_B), and ratio of orbital and spin moments μ_L/μ_S for Ni_n, Pd_n, and Pt_n clusters. If $\Delta\mu_{S,L}$ is positive, larger moments are found for the easy-axis orientation. The results for dimers are quoted after [36], for Pt clusters after [37].

			Magnetic axis					
n		Structure	Easy (MPG)	Hard (MPG)	MAE	$\Delta\mu_S$	$\Delta\mu_L$	μ_L/μ_S
2	Ni	Dimer	Axial	Perpendicular	3.2	0.02	0.20	0.29
	Pd	Dimer	Perpend.	Axial	−1.1	0.02	−0.34	0.18
	Pt	Dimer	Axial	Perpendicular	23.1	0.54	1.94	0.49
3	Ni	Triangle	In-plane $m'm'2$	Perpendicular $\bar{6}m'2'$	2.3	0.00	0.40	0.26
	Pd	Triangle	In-plane $m'm'2$	Perpendicular $\bar{6}m'2'$	0.9	−0.08	0.19	0.56
	Pt	Triangle	In-plane $m'm'2$	Perpendicular $m'm2'$	4.4	0.72	0.88	0.99
4	Ni	Tetrahedron	Perpend. edge $m'm'2$	Parall. edge $m'm'2$	0.5	0.00	0.02	0.10
	Pd	Tetrahedron	Perpend. edge $m'm'2$	Threefold axis $32'$	0.3	0.00	0.01	0.26
	Pt	Tetrahedron	Noncoll. AFM $\bar{4}'3m'$ 6					
5	Ni	Bipyramid	In-plane $m'm'2$	Threefold axis $\bar{6}m'2'$	0.3	0.00	−0.05	0.13
	Pd	Bipyramid	In-plane $m'm'2$	Threefold axis $\bar{6}m'2'$	2.1	0.03	0.33	0.31
	Pt	Bipyramid	In-plane $m'm'2$	Threefold axis $\bar{6}m'2'$	4.3	0.12	−0.24	0.34
6	Ni	Octahedron	Fourfold axis $4/mm'm'$	In-plane $mm'm'$	0.2	0.00	−0.04	0.09
	Pd	Octahedron	Fourfold axis $4/mm'm'$	In-plane $mm'm'$	0.3	0.02	−0.10	0.35
	Pt	Octahedron	Noncoll. FI $2'2'2$	Fourfold axis $2'2'2$	1.4			
13	Ni	Icosahedron	Threefold axis 1	Fivefold axis 1	0.4	0.00	−0.33	0.06
	Ni	Biplanar	In-plane m	Perpendicular 3	0.09	0.00	0.18	0.10
	Pd	Biplanar	Perpendicular 3	In-plane 1	0.3	0.20	−0.06	0.32

4.6(2.5) μ_B and $\mu_L/\mu_S = 1.5(0.7)$ for Pt_2 (Pt_3), respectively. A Pt_4 cluster has an antiferromagnetic GS for both planar and tetrahedral structural isomers. For the stable planar Pt_5 cluster, ferro- and antiferromagnetic states are very close in energy, only the less stable three-dimensional isomers have a ferromagnetic GS with substantial spin and orbital moments. Similarly, for Pt_6 a stable octahedral isomer with a low-moment GS coexists with high-moment, but less stable structures. A Pt_{13} cluster is close to the magnetic → non-magnetic transition. In the stable triangular geometry the GS is weakly magnetic in a scalar-relativistic treatment, but non-magnetic if SOC is taken into account. A weak magnetic moment can be induced by a rotation of the magnetic axis.

Trends in the magnetic anisotropy are very complex, depending on electron configuration, SOC and symmetry. Among the dimers, Ni_2 and Pt_2 have an easy magnetization direction along the dimer axis, while Pd_2 shows perpendicular anisotropy. As discussed in detail before [36], the difference arises from the different character of the states closest to the Fermi level and hence from the different electronic configurations of the free atoms. All trimers have an easy axis within the plane defined by the three atoms. For Ni_3 and Pd_3 the threefold symmetry is reduced in the GS (magnetic point group $2m'm'$), but preserved for perpendicular magnetization. The lower MAE of the Pd_3 trimer arises from the different sign in the spin and orbital anisotropies. For Pt_3 the same reduced symmetry is also found for perpendicular orientation, both spin and orbital moments are larger for the in-plane GS. For the Ni_4 cluster the tetrahedral symmetry is broken for the geometric as well as the magnetic structure (MPG $m'm'2$), irrespective of the direction of magnetization. For Pd_4 the tetrahedral crystallographic symmetry is conserved, but the magnetic symmetry is reduced to $m'm'2$ for the easy and to $32'$ for the hard magnetization axis. The Pt_4 tetrahedron has a noncollinear antiferromagnetic GS. Note that no tetrahedral magnetic point group is compatible with a ferromagnetic alignment of the local moments. For Ni_4 and Pd_4 the ratio between the modest MAEs calculated for magnetizations parallel to the twofold and (pseudo)threefold axes is the same as that between the small orbital anisotropies

(at isotropic spins), i.e. it does not reflect the stronger SOC in the Pd cluster.

For the pentamers forming a trigonal bipyramid the threefold symmetry is broken for a magnetization parallel to the equatorial plane (for Pd_5 the broken magnetic symmetry is accompanied also by a geometrical distortion), but preserved for axial magnetization. The MAE between the hard magnetization direction along the threefold axis and the easy direction in the equatorial plane is 0.3/2.1/4.3 meV/atom for Ni_5/Pd_5/Pt_5, i.e. it increases as naively expected from an increasing strength of the SOC. However, the situation is more complex: the spin moments are isotropic for Ni_5 and weakly anisotropic for Pd_5 and Pt_5, the orbital anisotropy is negative for the Ni and Pt clusters, but positive for the Pd cluster.

The octahedron is the GS geometry for all three hexamers—but note that for the Pt_6 cluster this structure is stabilized only by SOC. For Ni_6 and Pd_6 the symmetry is reduced to tetragonal (MPG $4/m'm'm'$) for the easy axis parallel to the fourfold axis. The symmetry is reduced to orthorhombic (MPG $mm'm'$) for the hard axis perpendicular to the rotational axis. The spin moments are almost isotropic, the orbital moments show a modest negative anisotropy. For Pt_6 the magnetic symmetry is further reduced to $2'2'2$, the magnetic ground state is noncollinear, with a net magnetic moment oriented perpendicular to one of the triangular facets of the cluster.

For the 13-atom clusters the GS structure is only for Ni_{13} a distorted icosahedron whose symmetry is further reduced in the magnetic state. The MAE between hard and easy magnetization directions parallel to the three- and fivefold symmetry axes of the idealized icosahedral structure is 0.4 meV/atom, the orbital anisotropy is negative. Pd_{13} clusters form a biplanar structure which is also metastable for Ni_{13}. Ni and Pd clusters with this structure have high-moment GS, a Pt cluster is only marginally magnetic. The easy magnetic axis of the biplanar clusters is in-plane for Ni (MAE 0.09 meV/atom) and perpendicular for Pd (MAE $=$ 0.28 meV/atom). The Ni_{13} cluster has isotropic spin moments and a positive orbital anisotropy of 0.14 μ_B, the Pd_{13} cluster has a positive spin, but a weak negative orbital anisotropy. For Pt_{13} our new calculations confirm that indeed the structure proposed by Wang and Johnson [16] and Kumar and Kawazoe [17] is much lower in energy than either the icosahedron or the buckled biplanar structure. The lowest energy structure is again a biplanar arrangement, but with a different stacking of the two close-packed planes. We find that a Pt cluster of this size is only marginally magnetic—the stable structure is non-magnetic in the ground state, but a solution with non-vanishing moments parallel to the atomic planes is essentially degenerate in energy.

Our results show that the factors influencing the magnetic anisotropy are much more complex than is usually assumed. Although only for small Pt_n clusters the influence of SOC is strong enough to change the energetic ordering of different structural isomers, even for the lighter Pd and Ni clusters SOC induces magneto-structural effects depending on the direction of magnetization: changes in the magnetic point group symmetries are accompanied by modest geometric distortions of the clusters. The only exceptions are the tetramers where the geometric structure is invariant under rotations of the magnetization direction. For Ni_4 clusters the tetrahedral symmetry is broken already at the scalar-relativistic level by a Jahn–Teller distortion, for Pd_4 the crystallographic symmetry is preserved, but the magnetic symmetry is reduced, because no tetrahedral point group is compatible with a ferromagnetic state. Rotational symmetry is incompatible with ferromagnetic order between moments perpendicular to the symmetry axis.

Using perturbation theory, a formula relating the MAE to the product of the SOC strength and the orbital anisotropy has been proposed [49]. The derivation of this relation assumes isotropic spin moments (and implicitly also a geometric structure independent of the magnetization direction) and a completely filled majority band, and postulates that the largest orbital moment is always found for easy-axis magnetization. Our results demonstrate that, at least for the heavier elements, the spin moments are never isotropic and that the largest orbital moment is not always found for easy-axis magnetization. For the tetrahedral Pt_4 and the planar Pt_5 clusters different initial directions of the magnetization converge to different (ferro-/antiferromagnetic) configurations [37]. In any case these results demonstrate that, for these clusters, the changes in the electronic and magnetic structures induced by a re-orientation of the magnetization axis are too important to be describable by perturbation theory.

Finally we should also point out that our approach shares a certain deficit inherent to all density-functional treatments of orbital polarization: because the calculation of the exchange-field coupling to the magnetic moment is based on averaged charge- and spin-densities, its orbital dependence is underestimated. Hence the orbital moments derived from density-functional theory are always somewhat too small. A coupling between the magnetic moments and the orbital degrees of freedom can, in principle, be achieved within the framework of current spin-density-functional theory, which has achieved some success in predicting the SOC-induced band splitting in semiconductors [66, 67]. For open-shell systems, however, the differences in the results achieved with conventional spin-polarized DFT and current spin-density functionals within an optimized effective potential (OEP) framework were found to be only minimal [67, 68]. Hence, the optimal description of orbital magnetism in complex open-shell systems, such as transition metals, remains an unsolved problem.

5. Conclusions

This work completes the *ab initio* investigations of orbital magnetic moments and magnetic anisotropy of small clusters of the metals of the Pd group. Our results provide new insights into the correlation between the symmetry and the magnetic properties of the clusters. For clusters with a symmetry axis of order $n \geqslant 3$, ferromagnetic order is compatible with rotational symmetry if the magnetization direction is parallel to the symmetry axis, but not for perpendicular magnetization. In this case magnetism breaks the crystallographic symmetry of the cluster. For clusters with higher (tetrahedral or octahedral

symmetry) no magnetic subgroup is compatible with a ferromagnetic state. In this case the crystallographic symmetry is broken irrespective of the direction of magnetization. The former case is realized for the dimer, trimer and pentamer, the latter for the tetramer and hexamer (but note that the symmetry can also be broken even in the absence of SOC by a Jahn–Teller mechanism). A novel result of our investigations is that even for a 3d metal such as Ni, the change in the magnetic symmetry leads to small geometric distortions of the cluster such that there is a contribution to the MAE from the elastic energy. However, in this case SOC is not strong enough to affect the energetic ordering between different structural isomers. For the 4d metal Pd these effects are more pronounced, but qualitatively similar as for Ni. For a 5d metal such as Pt, SOC is strong enough to stabilize for the smallest clusters structures, which are only metastable in the scalar-relativistic limit. In this case, due to the strong SOC, the magnetic anisotropy energies can be comparable or even larger than the energy differences between different magnetic isomers. Spin moments are isotropic only for Ni clusters, orbital anisotropies defined relative to the magnetic GS can have either sign. Hence, a perturbation treatment postulating that the cluster geometry is frozen, the spin moments are isotropic, and that the MAE is proportional to the orbital anisotropy is not justified for these small clusters.

Acknowledgment

This work has been supported by the VASP project.

References

[1] Plumer M L, van Ek J and Weller D 2001 *Springer Series in Surface Sciences* vol 41, ed G Ertl, R Gomer, H Lüth and D L Mills (Berlin: Springer)
[2] Sellmyer D and Skomski R 2006 *Advanced Magnetic Nanostructures* (New York: Springer)
[3] Brune H 1998 *Surf. Sci. Rep.* **31** 125
[4] Wuttig M and Liu X 2004 *Ultrathin Metal Films—Magnetic and Structural Properties* (*Springer Tracts in Modern Physics* vol 206) (Berlin: Springer)
[5] Brune H and Gambardella P 2009 *Surf. Sci.* **603** 1812
[6] Khanna S N and Castleman A W (ed) 2003 *Quantum Phenomena in Clusters and Nanostructures* (Heidelberg: Springer)
[7] Cox A J, Louderback J G, Apsel S E and Bloomfield L A 1994 *Phys. Rev.* B **49** 12295
[8] Apsel S E, Emmert J W, Deng J and Bloomfield L A 1996 *Phys. Rev. Lett.* **76** 1441
[9] Billas I, Châtelain A and de Heer W A 1997 *J. Magn. Magn. Mater.* **168** 64
[10] Knickelbein M B 1999 *Annu. Rev. Phys. Chem.* **50** 79
[11] Knickelbein M B 2002 *J. Chem. Phys.* **116** 9703
[12] Chang C M and Chou M Y 2004 *Phys. Rev. Lett.* **93** 133401
[13] Baletto F and Ferrando R 2005 *Rev. Mod. Phys.* **77** 371
[14] Futschek T, Marsman M and Hafner J 2005 *J. Phys.: Condens. Matter* **17** 5927
[15] Futschek T, Hafner J and Marsman M 2006 *J. Phys.: Condens. Matter* **18** 9703
[16] Wang L-L and Johnson D D 2007 *Phys. Rev.* B **75** 235405
[17] Kumar V and Kawazoe Y 2008 *Phys. Rev.* B **77** 205418
[18] Aguilera-Granja F, García-Fuente A and Vega A 2008 *Phys. Rev.* B **78** 134425
[19] Aguilera-Granja F, Longo R C, Gallego L J and Vega A 2010 *J. Chem. Phys.* **132** 184507
[20] Fournier R, Sun Y and Zhang M 2008 *Phys. Rev.* B **77** 075435
[21] Zhang M and Fournier R 2009 *Phys. Rev.* A **79** 043203
[22] Sun Y, Fournier R and Zhang M 2009 *Phys. Rev.* A **79** 043202
[23] Piotrkowski M, Piquini P and Da Silva J L F 2010 *Phys. Rev.* B **81** 155446
[24] Félix-Medina R, Dorantes-Dávila J and Pastor G M 2003 *Phys. Rev.* B **67** 094430
[25] Nicolas G, Dorantes-Dávila J and Pastor G M 2006 *Comput. Mater. Sci.* **35** 292
[26] Andriotis A N and Menon M 2004 *Phys. Rev. Lett.* **93** 026402
[27] Xie Y and Blackman J A 2004 *J. Phys.: Condens. Matter* **16** 3163
[28] Xie Y and Blackman J A 2006 *Phys. Rev.* B **74** 054401
[29] Kortus J, Baruah T, Pederson M R, Ashman C and Khanna S N 2002 *Appl. Phys. Lett.* **80** 4193
[30] Huda M N, Niranjan M K, Sahu B R and Kleinman L 2006 *Phys. Rev.* A **73** 053201
[31] Sebetci A 2009 *Phys. Chem. Chem. Phys.* **11** 921
[32] Fernández-Seivane L and Ferrer J 2007 *Phys. Rev. Lett.* **99** 183401
Fernández-Seivane L and Ferrer J 2008 *Phys. Rev. Lett.* **101** 069903 (erratum)
[33] Strandberg T O, Canali C M and MacDonald A H 2007 *Nat. Mater.* **6** 648
[34] Strandberg T O, Canali C M and MacDonald A H 2008 *Phys. Rev.* B **77** 174416
[35] Fritsch D, Koepernik K, Richter M and Eschrig H 2008 *J. Comput. Chem.* **29** 2210
[36] Błoński P and Hafner J 2009 *Phys. Rev.* B **79** 224418
[37] Błoński P, Dennler S and Hafner J 2011 *J. Chem. Phys.* **134** 034107
[38] Sahoo S, Hucht A, Gruner M E, Rollmann G, Entel P, Postnikov A, Ferrer J, Fernández-Seivane L, Richter M, Fritsch D and Sil S 2010 *Phys. Rev.* B **82** 054418
[39] Majumdar D, Dai D and Balasubramanian K 2000 *J. Chem. Phys.* **113** 7919
[40] Majumdar D, Dai D and Balasubramanian K 2000 *J. Chem. Phys.* **113** 7928
[41] Lazarovits B, Szunyogh L and Weinberger P 2003 *Phys. Rev.* B **67** 024415
[42] Nonas B, Cabria I, Zeller R, Dederichs P H, Huhne T and Ebert H 2001 *Phys. Rev. Lett.* **86** 2146
[43] Cabria I, Nonas B, Zeller R and Dederichs P H 2002 *Phys. Rev.* B **65** 054414
[44] Bornemann S, Minar J, Staunton J B, Honolka J, Enders A, Kern K and Ebert H 2007 *Eur. Phys. J.* D **45** 529
[45] Antal A, Udvardi L, Ujfalussy B, Lazarovits B, Szunyogh L and Weinberger P 2007 *J. Magn. Magn. Mater.* **316** 118
[46] Etz C, Lazarovits B, Zabloudil J, Hammerling R, Ujfalussy B, Szunyogh L, Stocks G M and Weinberger P 2007 *Phys. Rev.* B **75** 245432
[47] Błoński P, Lehnert A, Dennler S, Rusponi S, Etzkorn M, Moulas G, Bencok P, Gambardella P, Brune H and Hafner J 2010 *Phys. Rev.* B **81** 104426
[48] Smogunov A, dal Corso A, Delin A, Weht R and Tosatti E 2008 *Nature Nanotechnology* **3** 22
[49] Bruno P 1989 *Phys. Rev.* B **39** 865
[50] van der Laan G 1998 *J. Phys.: Condens. Matter* **10** 3239
[51] Kresse G and Furthmüller J 1996 *Comput. Mater. Sci.* **6** 15
Kresse G and Furthmüller J 1996 *Phys. Rev.* B **54** 11169
[52] Perdew J P and Wang Y 1992 *Phys. Rev.* B **45** 13244
[53] Vosko S H, Wilk L and Nusair M 1980 *Can. J. Phys.* **58** 1200
[54] Blöchl P E 1994 *Phys. Rev.* B **50** 17953
[55] Kresse G and Joubert D 1999 *Phys. Rev.* B **59** 1758
[56] Kresse G and Lebacq O 2005 VASP Manual http://cms.mpi.univie.ac.at/vasp/vasp/vasp.html
[57] Kleinman L 1980 *Phys. Rev.* B **21** 2630
[58] MacDonald A H, Pickett W E and Koelling D D 1980 *J. Phys. C: Solid State Phys.* **13** 2675

[59] Hobbs D, Kresse G and Hafner J 2000 *Phys. Rev.* B **62** 11556
[60] Marsman M and Hafner J 2002 *Phys. Rev.* B **66** 224409
[61] Balasubramanian K 1989 *J. Chem. Phys.* **91** 307
[62] Valerio G and Toulhoat H 1996 *J. Phys. Chem.* **100** 10827
[63] de Graef M 2010 *Metall. Mater. Trans.* A **41** 1321
[64] Fernández-Seivane L, Oliveira M A, Sanvito S and Ferrer J 2006 *J. Phys.: Condens. Matter* **18** 7999
[65] Xiao L and Wang L 2004 *J. Phys. Chem.* A **108** 8605
[66] Vignale G and Rasolt M 1988 *Phys. Rev.* B **37** 10685
[67] Sharma S, Pittalis S, Kurth S, Shallcross S, Dewhurst J K and Gross E K U 2007 *Phys. Rev.* B **76** 100401(R)
[68] Pittalis S, Kurth S, Helbig N and Gross E K U 2006 *Phys. Rev.* A **74** 062511
[69] Grushow A and Ervin K M 1997 *J. Chem. Phys.* **106** 9580
[70] Stillinger F H and Weber T A 1984 *J. Chem. Phys.* **80** 4434
[71] Hafner J 1988 *J. Phys. F: Metal Physics* **18** 153
[72] Fournier R 2007 *J. Chem. Theory Comput.* **3** 921

Geometric and magnetic properties of Pt clusters supported on graphene: Relativistic density-functional calculations

Piotr Błoński and Jürgen Hafner[a)]
University of Vienna, Faculty of Physics and Center for Computational Materials Science, Sensengasse 8/12, A-1090 Wien, Austria

(Received 23 February 2011; accepted 22 March 2011; published online 18 April 2011)

The geometric and magnetic structures of small Pt_n clusters ($n = 1 - 5$) supported on a graphene layer have been investigated using *ab initio* density functional calculations including spin-orbit coupling. Pt–Pt interactions were found to be much stronger than the Pt–C interactions promoting the binding to the support. As a consequence, the equilibrium structure of the gas-phase clusters is preserved if they are deposited on graphene. However, the clusters bind to graphene only via at most two Pt–C bonds: A Pt_2 dumbbell prefers an upright position, the larger clusters are bound to graphene only via one edge of the planar cluster (Pt_3 and Pt_5) or via two terminal Pt atoms of a bent Pt_4 rhombus. Evidently, the strong buckling of the graphene layer induced by the Pt–C bonds prevents the formation of a larger number of cluster-support bonds. As the local spin and orbital magnetic moments are quenched on the Pt atoms forming Pt–C bonds, the magnetic structure of the supported clusters is much more inhomogeneous as in the gas-phase. This leads to noncollinear magnetic structures and a strongly reduced magnetic anisotropy energy. © *2011 American Institute of Physics*. [doi:10.1063/1.3577517]

I. INTRODUCTION

The development of modern magnetic information storage technologies has spurred intense research efforts aimed at improving our knowledge of magnetic nanostructures. In magnetic information storage devices, bits of information are stored in magnetically stable domains and a high magnetic anisotropy energy is required to prevent loss of information by a reversal of the magnetization direction stimulated by thermal excitations.[1,2] Magnetic anisotropy arises from the coupling between the spin and orbital degrees of freedom and is hence a fundamentally relativistic effect. In nanostructures, both spin and orbital magnetic moments are enhanced over their values in the bulk, but this does not immediately lead to a high magnetic anisotropy energy which requires in addition a strong spin-orbit coupling. High magnetic moments are found in the ferromagnetic 3*d*-metals where the spin-orbit coupling is weak. Therefore, the quest for a high magnetic anisotropy has been focused on nanostructures of the 3*d*-metals supported on the surfaces of the nonmagnetic heavy 4*d*- or 5*d*-metal. The combination of the high magnetic moments of the 3*d*-atoms and the strong spin-orbit coupling in the substrate favors a high magnetic anisotropy.[3–6]

Very recently, it has been pointed out that in nanostructures 5*d*-atoms (which are nonmagnetic in the bulk) acquire an intrinsic magnetic moment and, combined with the strong spin-orbit coupling characteristic for these heavy atoms, this can lead to a very high magnetic anisotropy energy.[7–12] However, the strong relativistic effects are not restricted to the formation of large orbital moments and of a high magnetic anisotropy: (i) It has been demonstrated that spin-orbit coupling (SOC) also influences the structural stability. For Au and Pt clusters it has been shown that SOC leads to a preference of two-dimensional planar over three-dimensional structures.[12–14] (ii) In contrast to nanostructures formed by 3*d*-metals, where the anisotropy of the spin magnetic moments is often very small, and where the magnetic anisotropy energy can be calculated reasonably well within low-order perturbation theory[15–17] (being proportional to the anisotropy of the orbital moments and to the strength of the SOC); in the 5*d* nanostructures, a change in the magnetization direction can completely change the magnetic state. For freestanding Pt monowires, it has been shown that the wire has large spin and orbital moments if magnetized parallel to the axis of the wire, but is nonmagnetic if the magnetization is perpendicular to the wire.[7,9] In this case the "colossal magnetic anisotropy energy" is in fact a de-magnetization energy. Similarly, for small Pt clusters it has been demonstrated that a change of the magnetization direction can lead to a transition between high- and low-moment states.[10–12] In a Pt_5 cluster, the magnetic moments are ferromagnetically aligned in the ground state, but the first excited magnetic state (which represents also the saddle-point configuration for magnetization reversal) has antiferromagnetic character.

However, it must be admitted that the results available so far are not of immediate practical relevance, since they have been derived for freestanding monowires and clusters. Smogunov *et al.*[9] have briefly considered the effect of the substrate, but only for a wire extending along the edge of a step on a jellium surface. A strong interaction between the nanostructure and support will lead to a strong quenching of the orbital moment and hence to an at least partial loss of their intriguing magnetic properties. A possible choice of a weakly reactive substrate of timely scientific interest is graphene.

[a)]Electronic mail: juergen.hafner@univie.ac.at.

 © 2011 American Institute of Physics

Downloaded 15 Sep 2011 to 128.130.131.2. Redistribution subject to AIP license or copyright; see http://jcp.aip.org/about/rights_and_permissions

Since freestanding graphene layers have first been produced in 2004,[18] this material has been studied extensively due to its unique electronic, magnetic, and mechanical properties.[19–23] Apart from the unusual properties of the graphene-sheet alone, the presence of nanoparticles (clusters) on graphene may lead to further applications in catalysis[24,25] and in ultimately miniaturized magnetic devices.[26,27]

While the formation of small metallic clusters on metal-supported graphene has been studied quite extensively (see, e.g., Ref. 29 and further references cited therein), the properties of nanostructures on a freestanding graphene layer have received less attention. Recently, individual platinum and gold adatoms have been monitored in real time at high temperature using a high-resolution transmission electron microscope.[30] The diffusion of metal atoms and a tendency of clustering were observed. However, at the high temperature applied in the experiment, the clusters are not stable. The activation energy for the in-plane migration of both Au and Pt atoms in graphene is found to be around 2.5 eV, indicating covalent bonding between metal and carbon atoms. Theoretically, the adsorption of alkali, noble, and transition metals on graphene has been studied from first principles using spin-density functional theory.[24–28,31–36] Yazyev and Pasquarello[36] studied trends in the binding energies and adsorption sites of isolated adatoms on graphene through a series of simple and transition-metal atoms. Most of these studies have concentrated on the structural and electronic properties of the adsorbate-graphene system, and whenever magnetism come into a play, it has been considered on a scalar-relativistic level only. To the best of our knowledge, to date only Vo-Van *et al.*[27] have addressed the problem of magnetism in nanostructures on graphene using relativistic DFT calculations. They performed a combined experimental and theoretical study of the growth and the magnetic properties of a flat, epitaxial ultrathin cobalt film on graphene, demonstrating the role of the Co/graphene interface in sustaining a perpendicular magnetic anisotropy in this system.

For Pt-clusters, scalar-relativistic investigations by Dai *et al.*[26] found a preference for linear and tetrahedral structures for three- and four-atom clusters adsorbed on graphene, while Okazaki-Maeda *et al.*[25] reported for Pt_3 the formation of a triangular configuration. For the tetrahedral Pt_4 cluster, Dai *et al.*[26] reported a strong modification of the electronic structure of the graphene layer, such that the C-atoms exhibit a net magnetization. The adsorption of Pd_n cluster with $n = 1 - 5$ on graphene has been studied by Cabria *et al.*[28] For dimer and trimer planar structures, with the Pd atoms bound to C-C bridge sites, were predicted, while for tetramer and pentamer three-dimensional configurations were found to be lower in energy. The electronic structure calculations of Uchoa *et al.*[33] for Pd-coated graphene have shown that the hybridization of the graphene p_z orbital with the localized d orbitals of the ad-layer may induce itinerant magnetism in the graphene layer. On the basis of the comparison of the surface free energies of graphene and platinum, Zhou *et al.*[29] suggested that because of the substantially lower surface energy of graphene the adsorbed metal should form three-dimensional clusters at room and higher temperatures. From the experimental results, however, it appears that first a two-dimensional seed is formed, and the conversion to three-dimensional structures occurs only if the cohesive energy of the cluster exceeds the dissociative energy of the Pt–C bond.

The present work was devoted to a systematic investigation, using *ab initio* spin-density functional calculations including spin-orbit coupling, of the magneto-structural properties of Pt_n-clusters, with $n \leq 5$, supported on graphene. The comparison with the gas-phase Pt_n clusters studied in our previous work[12] should lead to an improved understanding of the role of the support in determining the geometric and magnetic structures of the clusters, including their magnetic anisotropy.

II. COMPUTATIONAL DETAILS

The electronic structure calculations and structural optimizations reported here are based on DFT as implemented in the Vienna *ab initio* simulation package VASP.[37,38] VASP performs an iterative solution of the Kohn-Sham equations within a plane-wave basis and using periodic boundary conditions. The basis set contained plane waves with a maximum kinetic energy of 500 eV. For electronic exchange and correlation effects, the semilocal PW91 functional[39] in the generalized-gradient approximation (GGA) and the spin-interpolation proposed by Vosko *et al.*[40] were used. The use of the GGA is essential for magnetic systems[41] and, in particular, for Pt-clusters.[42] The electron-ion interactions were treated in the projector-augmented-wave (PAW) formalism.[38,43] The PAW approach produces the exact all-electron potentials and charge densities and hence avoids the need to use elaborate nonlinear core-corrections, which is particularly important for magnetic elements. The PAW potentials have been derived from fully relativistic calculations of the atomic or ionic reference calculations.

Spin-orbit coupling has been implemented in VASP by Kresse and Lebacq,[44] following the approach of Kleinman and Bylander[45] and MacDonald *et al.*[46] The relativistic Hamiltonian containing all relativistic corrections up to order α^2 (where α is the fine-structure constant) is recast in the form of 2×2 matrices in spin-space by re-expressing the eigenstates of the total angular momentum in terms of a tensor product of regular angular momentum eigenstates $|\, l, m\rangle$ and the eigenstates of the z-component of the Pauli spin matrices. The relativistic effective potential consists of a term diagonal in spin-space which contains the mass-velocity and Darwin corrections. The nondiagonal contributions in spin-space arise from the spin-orbit coupling, but also from the exchange-correlation potential when the system under consideration displays a noncollinear magnetization density. Calculations including spin-orbit coupling have therefore to be performed in the noncollinear mode implemented in VASP by Hobbs *et al.*[47] and Marsman and Hafner.[48]

The graphene-sheet was represented by a periodically repeated unit cell containing 96-atoms, with a distance of 20 Å between neighboring layers, such that the interaction between the repeated images is negligible. The Brillouin zone was sampled using $3 \times 3 \times 1$ Γ-centered k-point mesh and a Gaussian smearing of 0.05 eV. To explore the influence of lateral interactions between the adsorbed nanostructures, for a single adatom and for a Pt dimer calculations have also been

Downloaded 15 Sep 2011 to 128.130.131.2. Redistribution subject to AIP license or copyright; see http://jcp.aip.org/about/rights_and_permissions

performed using a smaller model with only 48 C atoms per cell. For the smaller cell, the number of k-points has been doubled to maintain the same density of sampling points in reciprocal space. An adsorbate was placed on one side of the graphene sheet and the whole system was relaxed without any symmetry constraints until the forces on all atoms were less than 25 meV/Å. Simultaneously, the electronic and magnetic degrees of freedom were relaxed until the change in total energy between successive iteration steps was smaller than 10^{-7} eV.

The calculations were performed in two steps. First a scalar-relativistic calculation has been performed. The geometry has been optimized by a static relaxation using a quasi-Newton method, starting from different initial locations and configurations of the Pt-adatoms. In the second step, the configurations resulting from the scalar-relativistic calculations were used to initialize the calculations including spin-orbit coupling, allowing only for the relaxation of electronic and magnetic degrees of freedom. To control the effect of the SOC on the structure of supported clusters in some cases, we initialized the calculations from scratch, allowing for a simultaneous relaxation of geometric, electronic, and magnetic degrees of freedom.

To determine the magnetic anisotropy for each cluster on graphene, a set of self-consistent calculations with different initial orientations of the magnetic moments was performed. The magnetic anisotropy energy was calculated as the difference in the total energies calculated for the easy and hard magnetic axes.

III. RESULTS AND DISCUSSION

The adsorption energy per Pt-atom for a Pt_n-cluster on graphene is calculated as the total energy of the Pt_n-graphene complex, $E_{Pt_n-graph}$, minus the energy of the clean graphene layer, E_{graph}, and the total ground-state energy of the Pt_n cluster in the gas-phase, E_{Pt_n} (taken from our previous work[12]),

$$E_{ad}^{int} = \frac{1}{n}(E^{Pt_n/graph} - E^{graph} - E^{Pt_n}). \quad (1)$$

The energy defined by Eq. (1) measures the *interaction* energy of Pt-clusters of a certain size and shape with the graphene sheet. E_{ad}^{int} consists of a negative contribution from the energy gained by forming cluster-substrate bonds, and positive contributions from the elastic distortions of both cluster and graphene and (for different structural isomers realized in the adsorbate and in the gas-phase) from the structural energy difference.

The binding between the Pt atoms in the cluster is measured by the cohesive energy of the adsorption complex,

$$E_{ad}^{coh} = \frac{1}{n}(E^{Pt_n/graph} - E^{graph} - nE^{Pt}), \quad (2)$$

where E^{Pt} stands for the total energy of an isolated Pt-atom.

The relaxed C–C distance in a clean graphene layer is 1.414 Å, in very good agreement with the experimental value. For the adsorbate-graphene complex, the lattice constants of the computational supercell have been fixed at their equilibrium values for clean graphene, but the coordinates of all C and Pt atoms have been relaxed without any symmetry constraint. For the isolated Pt adatom, we have determined the equilibrium adsorption site. For the dimer and the larger clusters, the initial configuration has been chosen such as to reconcile as far as possible the structure of the gas-phase cluster with energetically favorable positions of all cluster atoms on the graphene layer. This starting structure has been relaxed without symmetry constraints.

TABLE I. Adsorption energy, E_{ad}, height of the Pt-adatom above the graphene-sheet, z, Pt–C bond length, d, and buckling amplitude of the C-layer, b, calculated for the Pt-adatom adsorbed in different sites. Values in parentheses refer to the higher surface coverage, cf. text.

Adsorption site	E_{ad} (eV)	z (Å)	d (Å)	b (Å)
br	–1.535(–1.603)	1.981(1.979)	2.110(2.109)	0.290(0.379)
ot	–1.357	2.040	2.040	0.224
6h	–0.792	1.974	2.437	0.108

A. Pt-adatoms: Adsorption energies and sites

A single Pt atom has been placed into an on-top (ot), bridge (br) or six-fold hollow (6h) position of the graphene layer, using either a 48- or 96-atom supercell. The results are summarized in Table I. In agreement with recent *ab initio* calculations[32] the bridge site is found to be energetically most favorable, followed by the on-top and hollow positions. The adsorption energy of about −1.5 eV calculated at the lower coverage reflects the formation of a weak covalent bond between the p_z orbitals of the two neighboring C atoms and the d_{xz} orbitals of the Pt atom (assuming a C–C bond parallel to the x-direction). The adsorption energy on top of a C atom is lower by only 0.18 eV, while the hollow site is strongly disfavored. The Pt atom is located 1.98 Å above the graphene layer, at a distance of 2.11 Å from both C atoms. Comparing the three adsorption sites, we find that the C-Pt distance increases with the coordination of the Pt atom, from the ot over the br to the 6h site. The adsorption of the Pt atoms causes a buckling of the graphene layer which is largest for bridge-adsorbed atoms with an amplitude of 0.29 Å—the C atoms binding the adsorbate moving outward. No magnetic moments have been found on the Pt-adatom in any of the adsorption sites.

The modest difference between the adsorption energies in ot and br sites shows that Pt atoms on graphene are rather mobile, diffusion along the network of the C–C bonds requires an activation energy of only 0.18 eV.

For the isolated Pt adatom, we have also studied adsorption using a small cell with 48 C atoms (corresponding to a coverage of about 2 pct.). The slight increase of the adsorption energy by –0.07 eV/atom reflects a modest attractive interaction, the height of the adatom remains unchanged, but the buckling induced in the graphene layer is increased.

Our adsorption geometry and energy and for the activation energy for diffusion of a Pt atom on graphene is in good agreement with the results of Yazyev and Pasquarello,[36] calculated using ultrasoft pseudpotentials at a higher

Downloaded 15 Sep 2011 to 128.130.131.2. Redistribution subject to AIP license or copyright; see http://jcp.aip.org/about/rights_and_permissions

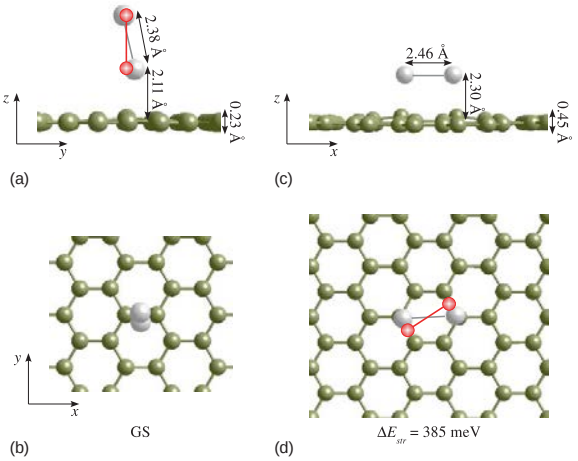


FIG. 1. Side view (a) and (c) and top view (b) and (d) of the upright tilted (a) and (b) and flat (parallel) (c) and (d) configurations of a Pt_2 dimer on graphene. The initial Pt_2 positions are shown by the red circles. The structural energy difference (ΔE_{str}) in eV/cluster with respect to the ground-state (GS) configuration is also listed.

coverage (3×3 supercell). These authors also examined trends across the transition-metal series. Adsorption in a hollow was found to be favored for most metals, with the exception of Ir, Pd, and Pt where the bridge site is favored. Dai *et al.*[26] also found bridge adsorption to be favored. For Pd atoms, Chan *et al.*[34] also found the bridge position to be favored, with an even lower activation energy for diffusion. Cabria *et al.*[28] also found bridge-adsorbed Pd atoms, with an adsorption energy of only –1.04 eV/atom. The weaker binding of Pd compared to Pt is also in good agreement with the trend reported by Yazyev and Pasquarello.[36]

B. Pt-dimer

Scalar-relativistic calculations predict for a Pt-dimer in the gas-phase a bond-length of 2.35 Å and a magnetic moment of 2 μ_B. If SOC is taken into account, the ground state is a high-moment state with a total magnetic moment of 4.5 μ_B oriented along the dimer axis. For perpendicular magnetization, the moment decreases to 2 μ_B, the magnetic anisotropy energy is 23.1 meV/atom.[12] On graphene, the distance between two bridge sites across a hollow is 2.44 Å. This suggests that a Pt-dimer could be anchored to graphene via two bridge sites. In addition, we have also examined an upright adsorption configuration, see Fig. 1. If the relaxation is started from the configuration parallel to the graphene sheet, Pt_2 rotates from the br–br configuration to a ot–ot configuration, with the Pt atoms displaced slightly from the ot positions (which are 2.83 Å apart) toward the hollows to avoid a too large stretching of the Pt–Pt bond. In the relaxed configuration, the dimer bond length is 2.46 Å, the dimer is nonmagnetic (see Table II). An upright Pt-dimer is lower in energy by about 0.39 eV. In the relaxed configuration, the dimer axis is tilted by 11° with respect to the surface normal, the center of gravity shifted by 0.115 Å from br. The bond length of 2.38 Å is only slightly longer than in the gas phase. The upright dimer is magnetic with a total spin moment of about 1.5 μ_B. The reduction of the magnetic moment relative to the gas phase is almost entirely due to the interaction with the support, the local magnetic moments are 0.9 μ_B on the upper and 0.55 μ_B on the lower Pt atom of the dimer.

TABLE II. The interaction energy, E_{ad}^{int}, adsorption energy, E_{ad}^{coh}, both in eV/Pt-atom, and the magnetic moment, μ_S (in μ_B), of Pt_n clusters adsorbed on graphene. For a Pt dimer, results in parentheses have been calculated at a higher coverage, cf. text.

	E_{ad}^{int}	E_{ad}^{coh}	μ_S
Pt_2-graphene			
upright	–0.478(–0.416)	–2.383(–2.319)	1.5(1.5)
parallel	–0.286	–2.190	0.00
Pt_3-graphene			
triangle-edge down	–0.466	–2.948	0.5
triangle-vertex down	–0.406	–2.888	0.0
chain 1	–0.273	–2.570	0.0
chain 2	–0.137	–2.434	1.0
Pt_4-graphene			
bent rhombus	–0.309	–3.034	1.5
zig-zag chain	–0.129	–2.655	1.0
straight chain	–0.012	–2.538	1.0
Pt_5-graphene			
flat, canted	–0.164	–3.197	1.5
dist. square pyramid	–0.158	–3.143	1.5
flat, parallel	–0.053	–3.086	1.5

To investigate the influence of lateral interactions between dimers, we have repeated the calculations for the upright dimer also for a cell with 48 C atoms, i.e., with twice as large coverage of Pt. At this increased coverage the adsorption energy is reduced by 62 meV/Pt-atom, the distance of the lower Pt-atom from the graphene layer is increased from 2.11 to 2.26 Å, the adsorbate-induced buckling of the substrate is also reduced from 0.23 to 0.14 Å. The repulsive interactions also lead to an exactly upright position of the dimer. The magnetic moments remain unchanged.

The analysis of the energetics shows that the binding of the Pt_2 dimer to graphene is weak, whereas the binding between the Pt atoms forming the dimer is larger than in the gas-phase dimer. The adsorption energy per Pt-atom is higher for the dimer than for the isolated ad-atoms, hence dimerization is predicted to be energetically favored, in agreement with observations by scanning tunneling microscopy[29] and field emission microscopy.[30]

Pt_2 dimers on graphene were also studied by Dai *et al.*,[26] but only flat adsorption structures have been considered. Dai *et al.* also reported much higher adsorption energies for adatoms and clusters, although they claimed to have used the same code. Their results disagree not only with ours, but also with those of other authors. For Pd dimers on graphene, binding to bridge sites was reported,[28] with a flat, nonmagnetic adsorption configuration being lower in energy by 0.3 eV/atom than an upright dimer. The adsorption energy of Pd_2 of only –1.28 eV/Pd-atom was much lower than the value we find for Pt_2. For Au dimers, an upright adsorption configuration has been predicted.[49] Mixed Pt–Au dimers have been studied by Aktürk and Tomak.[50] It was found that even when the

Downloaded 15 Sep 2011 to 128.130.131.2. Redistribution subject to AIP license or copyright; see http://jcp.aip.org/about/rights_and_permissions

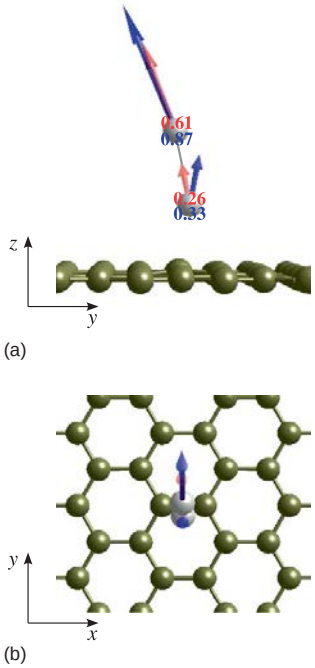


FIG. 2. Side (a) and top view (b) of the magnetic ground-state structure of a Pt_2 cluster in a tilted upright position. Red (light) arrows shows spin-, blue (dark) arrows the orbital magnetic moments, the numbers give the absolute values of the local spin (upper number), and orbital (lower number) magnetic moments in μ_B.

relaxation was started with a flat dimer and atoms located at on-top sites, the final configuration was an upright dimer with the Pt atom in a bridge position.

Calculations including SOC have been performed for the ground-state configuration and with different initial orientations of the magnetic moments, aligned with the dimer axis and hence almost perpendicular to the graphene-layer and perpendicular to the dimer and parallel to the graphene sheet. Figure 2 shows the magnetic GS at the lower coverage.

The easy magnetization direction is oriented along the dimer axis, the total magnetic moment of $\mu_J \sim 2\mu_B$ is increased compared to the spin moment of 1.5 μ_B from scalar relativistic calculations. The local spin and orbital moments are slightly noncollinear, both are much lower on the Pt atoms binding to graphene. If the magnetization direction is initialized in a direction parallel to the graphene-layer or perpendicular to the Pt-dimer the calculations converge to a nonmagnetic state. The energy for this magnetic to nonmagnetic transition amounts to 10.03 meV/Pt-atom.

The same calculation for higher coverage leads to a a slightly different scenario. The easy magnetization axis is again the dimer axis, the total magnetic moment is $M_J \sim 3\mu_B$. If the magnetization is perpendicular (and parallel to the graphene sheet), the total magnetic moment is only $\mu_J \sim 1.1\mu_B$. For both the easy and the hard magnetic axis, spin and orbital moments are collinear, both the local orbital moments are antiparallel for hard-axis magnetization

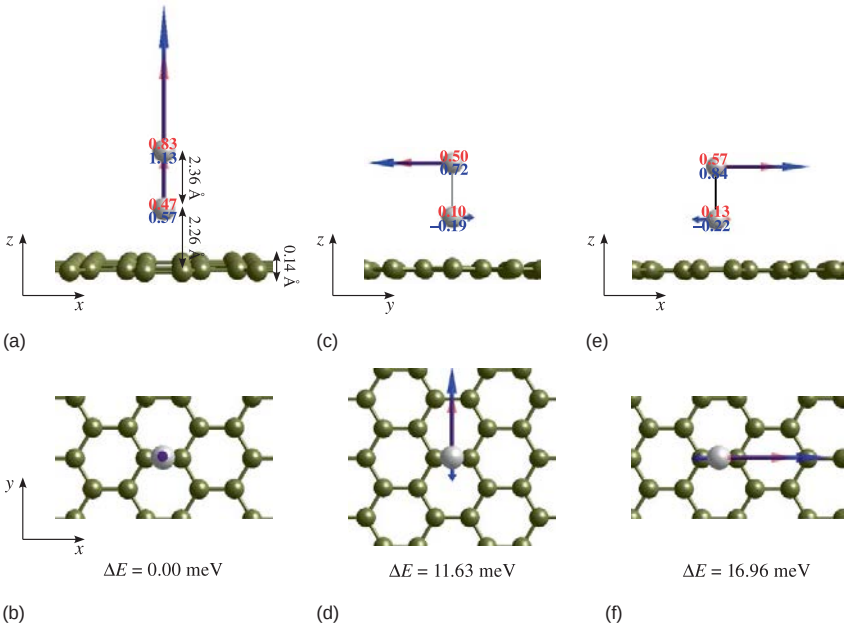


FIG. 3. Magnetic structure of a Pt_2 cluster for magnetization perpendicular (a) and (b) and parallel (c)–(f) to the graphene layer, calculated for a coverage of ∼2 pct in an upright position. The easy magnetization direction is perpendicular (a) and (b), but there is also a substantial in-plane anisotropy between magnetization perpendicular (c) and (d) and parallel (e) and (f) the C–C bridge bonding to the Pt_2 dimer. Red (light) arrows shows spin, blue (dark) arrows the orbital magnetic moments, the numbers give the absolute values of the local spin (upper number), and orbital (lower number) magnetic moments in μ_B.

Downloaded 15 Sep 2011 to 128.130.131.2. Redistribution subject to AIP license or copyright; see http://jcp.aip.org/about/rights_and_permissions

[see Figs. 3(a)–3(d)]. The MAE of 11.6 meV/Pt-atom is only slightly higher than at lower Pt-coverage. For a rotation of the magnetization in a plane parallel to the graphene support, we calculate an in-plane MAE of 5.33 meV [see also Figs. 3(e) and 3(f)]. The formation of higher spin and orbital moments at increased coverage is due to a larger distance from and a weaker binding to the substrate.

Relativistic calculations performed for a Pt-dimer parallel to the graphene sheet yield a nonmagnetic solution that is by 577 meV above the GS (tilted magnetic configuration).

Compared to the gas-phase dimer, the MAE is reduced by more than a factor of 2, corresponding to a reduced anisotropy of both spin and orbital moments. Our results for upright Pt_2 dimers are also closely related to those of Smogunov *et al.* for free Pt mono-wires and wires supported on an idealized nonreactive substrate and on a surface step, modeled by hard walls. Smogunov *et al.*[9] found the wire is ferromagnetic for parallel and nonmagnetic for perpendicular magnetization, leading to a very high MAE. Very recently, very large MAE's have also been predicted for complexes of transition-metal dimers with benzene,[51] considered as model structures for the adsorption of dimers on graphene. Upright adsorption modes with the dimer located in the center of the benzene ring were found to be preferred. The spin and orbital magnetic moments on the atom binding to benzene are strongly quenched, while the upper atom carries large moments. Huge MAE's ranging between 51 meV (Co_2) and 104 meV (Ir_2) per dimer, with the easy axis perpendicular to the benzene plane, were reported for Co_2, Ru_2, and Ir_2 dimers. The large MAE is related to a modest anisotropy of the spin and a huge anisotropy of the orbital moments on the magnetic atom. An even larger MAE of 248 meV/dimer was calculated for a mixed CoIr dimer were the Co atom provides a strong bonding to the molecule and induces a large moment on the Ir atom, while the Ir confers a strong SOC to the system.[52] For the mixed dimer also the binding to a graphene support, with the Co atom in the hollow position, was considered. This system shows an only slightly reduced MAE of 198 meV/dimer and anisotropic spin and orbital moments on both atoms.

C. Pt-trimer

For a Pt_3 trimer in the gas-phase, scalar relativistic calculations predict a structure forming a equilateral triangle with interatomic distances of 2.49 Å and a magnetic moment of 2 μ_B. SOC favors a small Jahn-Teller distortion with bond-lengths of 2.50 and 2.51 Å, the total magnetic moment is $\mu_J = 2.5\mu_B$ with an in-plane easy axis. Perpendicular magnetization is disfavored by an MAE of 5 meV/atom. A linear Pt_3 cluster has a ground-state energy higher by 0.185 eV/atom.

For Pt_3 supported on graphene, we have considered two flat triangular starting configurations with all three Pt atoms in bridge sites, with Pt–Pt distances of 2.45 and 2.12 Å, respectively (see Fig. 4), and two linear configurations with Pt atoms in bridge sites and with the same interatomic distance (see Fig. 5). Upon relaxation all four starting geometries are strongly changed. A flat-lying triangle is unstable, relaxation leads to a triangle which is almost perpendicular to the graphene layer and attached via either two Pt atoms to position between br and ot [see Figs. 4(a) and 4(b)], or via a single Pt atom to a substrate atom [see Figs. 4(c) and 4(d)]. The former configuration is magnetic with a spin moment of 0.5 μ_B, the latter is nonmagnetic and higher in energy by 0.18 eV/cluster. The energy difference arises primarily from a weak cluster-substrate bonding (see Table II).

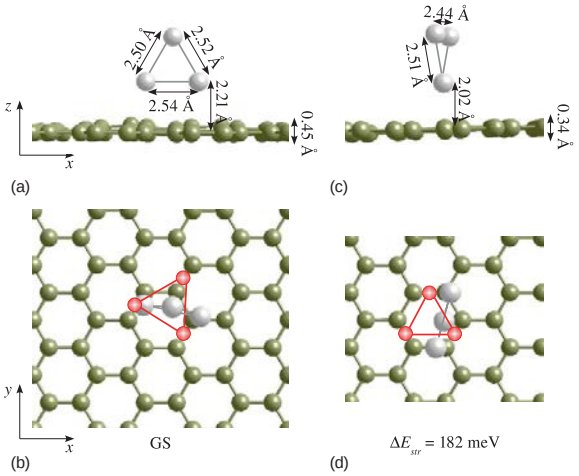


FIG. 4. Side view (a) and (c) and top view (b) and (d) of the Pt-triangle adsorption on the graphene-sheet. (a) and (b) show the magnetic ground state configuration. The flipped nonmagnetic arrangement is shown in (c) and (d). The initial Pt_3 position is shown by the red circles. The structural energy difference with respect to the ground-state configuration is also listed.

Our result that a flat configuration of a Pt_3 triangle on graphene is unstable is in contrast to the results of Cabria *et al.*[28] for Pd_3 trimers. A flat, bridge-bonded, and weakly magnetic configuration was described as the equilibrium state.

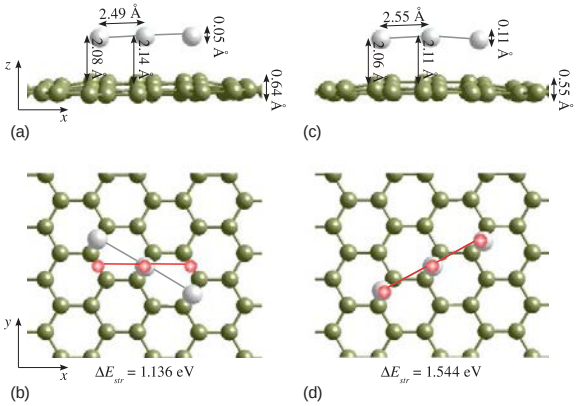


FIG. 5. Side view (a) and (c) and top view (b) and (d) of the Pt_3-chain adsorption on the graphene-sheet. (a) and (b) show the nonmagnetic configuration. The magnetic arrangement is shown in (c) and (d). The initial Pt_3 position is shown by the red circles. The structural energy difference with respect to the GS configuration shown in Fig. 4 is given below each structure.

Downloaded 15 Sep 2011 to 128.130.131.2. Redistribution subject to AIP license or copyright; see http://jcp.aip.org/about/rights_and_permissions

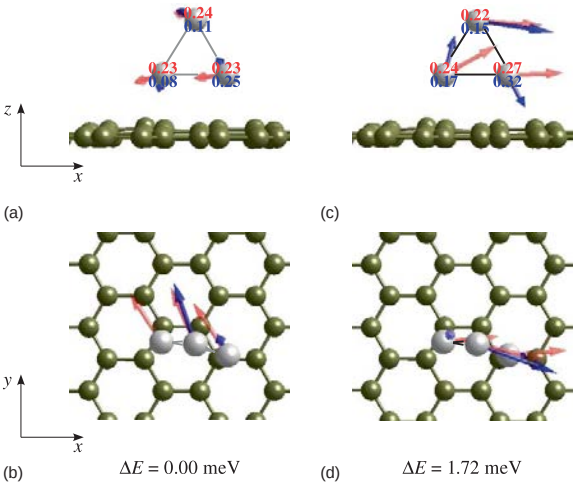


FIG. 6. Side (a) and (c) and top view (b) and (d) of the magnetic structure of a Pt_3-triangle on the graphene-sheet [cf. (a) and (b) of Fig. 4]. The easy axis corresponds to configuration (a) and (b). For each configuration, the energy difference relative to the easy magnetic axis (EA) are listed below. Red (light) arrows shows spin, blue (dark) arrows the orbital magnetic moments, the numbers give the absolute values of the local spin (upper number), and orbital (lower number) magnetic moments in μ_B.

In a linear Pt_3 cluster, in the gas-phase, the interatomic distance is 2.36 Å. Hence for the Pt_3 chain the distance of 2.12 Å between two br sites is too small, the chain rotates on the graphene sheet such as to stretch across two adjacent hexagons, with Pt–Pt distances of 2.49 Å. This allows to place all three Pt atoms almost exactly into a br site without a too large compression of the Pt–Pt bond [see Figs. 5(a) and 5(b)]. The chain is slightly bent, its adsorption induces a strong buckling in the graphene layer. In this configuration, the Pt_3 cluster is nonmagnetic, such as the flat-lying dimer.

The starting configuration with the Pt atoms in br sites at larger distances of 2.45 Å is locally stable, only the terminal atoms are slightly displaced from the br sites such as to admit a larger Pt–Pt distance of 2.55 Å. Bending and substrate buckling are similar as for the first configuration [see Figs. 5(c) and 5(d)]. Both linear Pt_3-graphene configurations are higher in energy by 1.1 to 1.5 eV than the ground state.

Relativistic calculations have been performed for all four Pt_3/graphene configurations, with the magnetization initially oriented perpendicular to the graphene layer or parallel to it, but either perpendicular or parallel to the triangle or linear chain. Our aim is to explore the influence of the dimensionality of the cluster on its magnetic anisotropy.

For the stable triangular configuration with a Pt–Pt bond parallel to the graphene layer, the easy magnetic axis is parallel to the graphene, parallel to C–C bonds, but oblique to the triangular plane, see Fig. 6(a) and 6(b). Inversion of the magnetization direction by 180°, parallel to graphene leaves total energy and total magnetic moment unchanged. The total magnetic moment of $\mu_J \sim 1.1\mu_B$ is increased relative to the scalar-relativistic result, because SOC leads to a mixing of different spin states (the spin moment is increased to about 0.70 μ_B) and an orbital moment of about 0.4 μ_B is added. For in-plane magnetization, the calculation converges to a noncollinear solution with almost the same total magnetic moment of about 1.1 μ_B, see Figs. 6(c) and 6(d). The MAE calculated for these two magnetic solutions is 1.72 meV/atom. Spin moments are almost isotropic, but local orbital moments are changed by up to 0.09 μ_B relative to the easy axis.

Surprisingly, the relativistic calculations applied to the flipped Pt-triangle [see panels (c) and (d) of Fig. 4] converge to a magnetic solution with a total magnetic moment varying between 0.74 and 1 μ_B, depending on the direction of magnetization. The easy magnetization axis is perpendicular to the graphene layer, with local orbital moments canted relative to the spin and total moments [see Figs. 7(a) and 7(b)] and total spin and orbital moments of about 0.5 μ_B each. The energy difference relative to the magnetic GS of the equilibrium geometry is increased to 222 meV.

A rotation of the magnetization within the plane of the Pt-triangle to a direction parallel to the graphene does not yield a locally stable configuration. In the converged solution, the moments are canted away from both the Pt-triangle (such as to be aligned with C–C bonds in the graphene) and also from the graphene sheet [see Figs. 7(c) and 7(d)]. The energy increases by an MAE of 3.24 meV/atom. The total spin moment increases to 0.63 μ_B and the orbital moment to 0.39 μ_B.

The rotation of the magnetization to a direction perpendicular to the Pt_3 plane but parallel to the C-layer [see Figs. 7(e) and 7(f)] costs an energy of 6.04 meV and lowers the total magnetic moment to $0.74\mu_B$. The decrease is due almost entirely to a decrease of the orbital moment, while the spin moment remains unchanged with respect to the value calculated for the easy axis.

For the linear Pt_3 chain, calculations including SOC predict a higher spin-moment of $\mu_S = 0.94\mu_B$ than for the triangle (reflecting the reduced dimension of the cluster), but a very similar orbital moment. The easy axis is parallel to the graphene layer an roughly perpendicular to the Pt_3 chain. The in-plane MAE is 3.2 meV (moments aligned with the chain), the perpendicular MAE is 5.5 meV.

D. Pt-tetramer

In the gas-phase, the equilibrium geometry of a Pt_4 tetramer is a flat rhombus which is stabilized by relativistic effects over a tetrahedral structure stable in the scalar-relativistic limit. If SOC is included, the magnetic ground state is collinear antiferromagnetic for the rhombus and noncollinear antiferromagnetic for the tetrahedron.[12] A linear Pt_4 cluster is 0.20 eV/atom higher in energy.

The bond-length in the relaxed Pt_4 rhombus is 2.53 Å; hence, a flat Pt_4 cluster with the four Pt atoms in br sites around a hexagonal hole at distances of 2.45 Å creates a structure under moderate compressive strain, see Fig. 8. Relaxation leads to a structure were the rhombus is bent around the short diagonal. The atoms at both ends of the short diagonal are three-fold coordinated, they bind less strongly to the graphene substrate than the remaining two-fold coordinated Pt atoms and move to a distance 3.87 Å above the graphene

Downloaded 15 Sep 2011 to 128.130.131.2. Redistribution subject to AIP license or copyright; see http://jcp.aip.org/about/rights_and_permissions

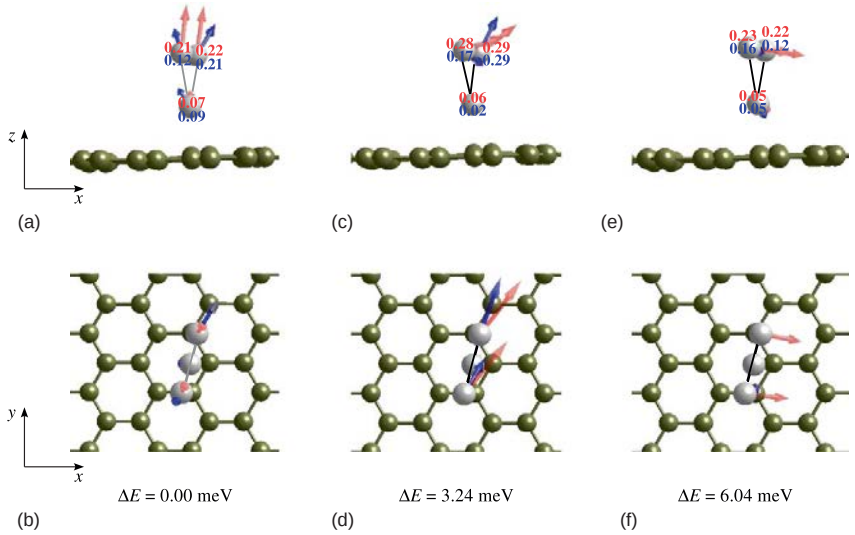


FIG. 7. Side (a), (c), and (e) and top view (b), (d), and (f) of the magnetic structure of a Pt_3-triangle in the flipped configuration on the graphene-sheet [cf. (c) and (d) of Fig. 4]. The easy axis corresponds to configuration (a) and (b). For each configuration, the energy difference relative to the EA are listed below. Red (light) arrows shows spin, blue (dark) arrows the orbital magnetic moments, the numbers give the absolute values of the local spin (upper number), and orbital (lower number) magnetic moments in μ_B.

layer. The long diagonal of the rhombus is contracted from 4.24 to 3.63 Å, such that the two Pt atoms are now much closer to on-top sites. The energy gain by adsorption is only modest, about 0.3 eV/Pt-atom. This structure is magnetic with a spin-moment of 1.5 μ_B.

For a straight Pt_4 chain, there are again two possibilities with the Pt atoms in neighboring br sites at distances of 2.12 Å or in br sites separated by 2.45 Å across a hollow. The strain on the bonds in a linear Pt_4-chain across a hollow is relaxed by moving the two central Pt atoms close to the on-top sites, resulting in the formation of a zig-zag chain which is higher in energy by about 1.5 eV/cluster. A linear chain with

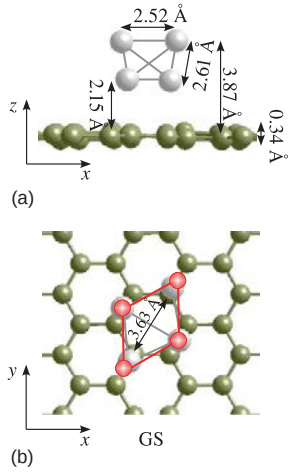


FIG. 8. Side (a) and top (b) view of the Pt_4-cluster adsorbed on the graphene-sheet forming a bent rhombus. The initial flat structure is shown by the red circles.

the Pt atoms at neighboring br sites undergoes only a modest relaxation, but this configurations is energetically even less favorable (see Table II). Both Pt-chains are slightly bent and induce a strong buckling of the graphene layer, both are magnetic with a spin moment of 1 μ_B.

For Pd_4 clusters, Cabria *et al.*[28] have compared the adsorption energies of a flat rhombus and a tetrahedron. The latter has been found to be lower in energy, but a distortion of the flat rhombus was apparently not permitted.

The calculations including SOC have been initialized with the magnetization pointing along z-axis (perpendicular both to the cluster and the graphene), along the Pt_4 edges, and in an oblique direction. Figure 9 shows the magnetic structure of the Pt-cluster obtained for the EA and hard magnetic axis (HA) of magnetization.

The EA is perpendicular to the graphene layer, but all local moments are slightly canted away from the surface-normal [see Figs. 9(a) and 9(b)]. Local spin moments are larger at the outer Pt atoms, while the local orbital moments are almost the same on all four sites. The HA is parallel to the graphene layer, aligned with the short diagonal of the cluster. In this configuration, both local spin and orbital moments are much larger on the outer Pt atoms. The total magnetic moment is enhanced relative to the scalar-relativistic spin-moment, because the mixing with low-spin states is overcompensated by the added orbital moment. The MAE is 0.65 meV/Pt-atom. Both spin and orbital moments are larger for the hard magnetization direction ($\Delta\mu_S = -0.07\mu_B$, $\Delta\mu_L = -0.08\mu_B$, a negative value of the anisotropy of the moments corresponding to larger moments for hard-axis magnetization).

We have also briefly analyzed the magnetic properties of the straight Pt_4 chains. Because all Pt-atoms in the chain are bound to C atoms of the graphene layer, the total spin moment is lower than for the rhombus. The zig-zag chain was found

Downloaded 15 Sep 2011 to 128.130.131.2. Redistribution subject to AIP license or copyright; see http://jcp.aip.org/about/rights_and_permissions

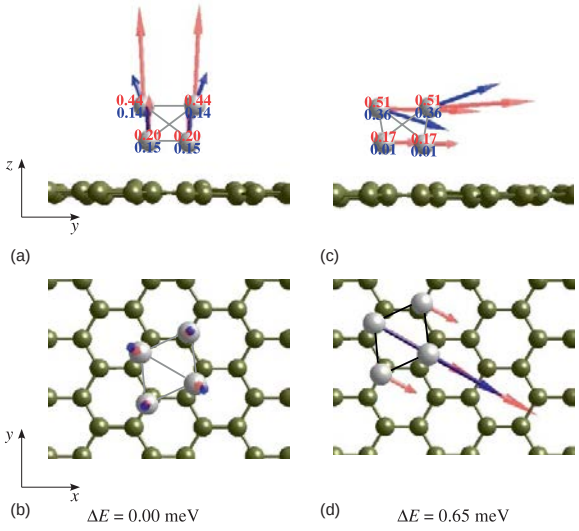


FIG. 9. Side (a) and (c) and top view (b) and (d) of the magnetic structure of a GS Pt_4-cluster adsorbed on the graphene-sheet (cf. Fig. 8). The easy axis corresponds to configuration (a) and (b). Red (light) arrows shows spin, blue (dark) arrows the orbital magnetic moments, the numbers give the absolute values of the local spin (upper number) and orbital (lower number) magnetic moments in μ_B.

to be magnetically isotropic, the straight chain has a perpendicular easy axis with an MAE of 1.4 meV for in-plane magnetization. SOC also leads to a further slight enhancement of the structural energy differences.

E. Pt-pentamer

Scalar relativistic calculations predict for a Pt_5 cluster a structure forming a trigonal bipyramid with a moment of 4 μ_B. SOC favors a flat structure consists of a slightly distorted square plus an isocele triangle, the total magnetic moment is lowered to $\mu_J = 3\mu_B$, $\mu_S = 1.7\mu_B$, and $\mu_L = 1.3\mu_B$. The saddle point on the magnetic energy surface determining the barrier for magnetization reversal (and hence the MAE) belongs to an antiferromagnetic configuration. SOC also predicts a lower energy for a square pyramid with a high magnetic moment of $\mu_J = 5.3\mu_B$ than for a trigonal bipyramid.[12]

With relaxed interatomic distances ranging from 2.42 to 2.51 Å, the flat Pt_5 cluster fits rather well to the graphene layer with the Pt atoms located either on top of C atoms [panels (a) and (b) of Fig. 10] or at bridge sites [see panels (e) and (f) of Fig. 10]. The relaxation of these initial structures shows, however, that it is energetically unfavorable to former too many Pt–C bonds—in both relaxed configurations the cluster is attached to the graphene only via two, respectively only one bond. In the GS configuration, the Pt_5 is bound to two br sites of graphene via one edge of the triangle, the cluster remains almost flat, but rotates to an orientation almost perpendicular to graphene [see Figs. 10(a) and 10(b)]. Bond lengths are slightly elongated compared to the gas phase, the substrate is strongly buckled with an amplitude of 0.83 Å. The spin moment is 1.5 μ_B, lower than the spin-moment of 2 μ_B of the free cluster.

Starting from a configuration where the Pt atoms are bound to br sites leads to a relaxed structure where only one Pt atom is strongly bound to graphene while the remaining part of the cluster drifts away from the support, but remains parallel to the graphene layer [see Figs. 10(e) and 10(f)]. Pt-Pt distances are only slightly stretched, the buckling is less pronounced than in the GS geometry. This configuration has the same spin moment, but is higher in energy by about 0.5 eV.

Panels (c) and (d) of Fig. 10 present the structure derived from a square pyramid. As four atoms forming the basal plane cannot all bind to the substrate, relaxation leads to a transformation to a distorted triangular bipyramid which is attached to

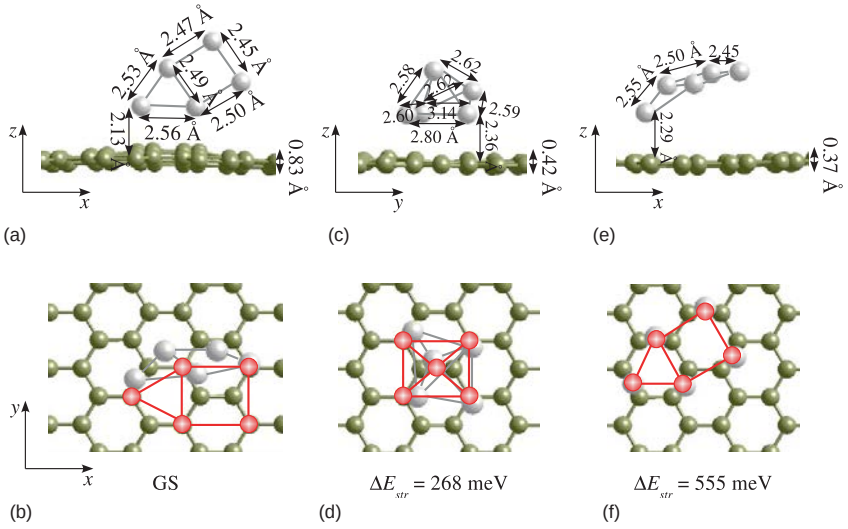


FIG. 10. Side (a), (c), and (e) and top view (b), (d), and (f) of the geometric structure of a Pt_5 cluster on graphene. For each configuration, the structural energy differences relative to the GS configuration are listed below, cf. text.

Downloaded 15 Sep 2011 to 128.130.131.2. Redistribution subject to AIP license or copyright; see http://jcp.aip.org/about/rights_and_permissions

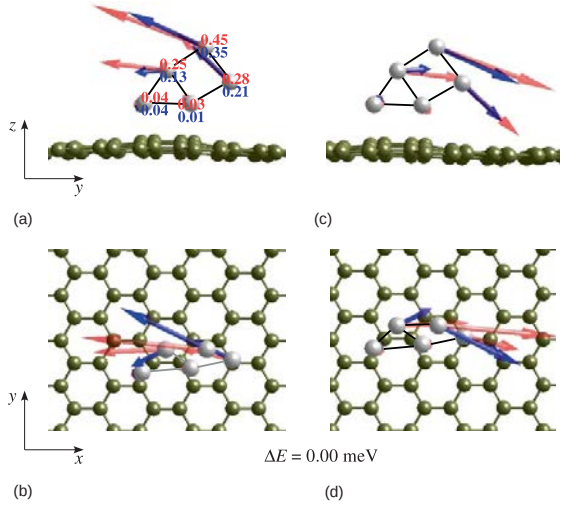


FIG. 11. Side (a) and (c) and top view (b) and (d) of the magnetic structure of a flat Pt_5-cluster adsorbed on graphene. Note that the two configurations are related by flipping the local spin and orbital moments to the opposite direction, they are energetically degenerate, cf. text.

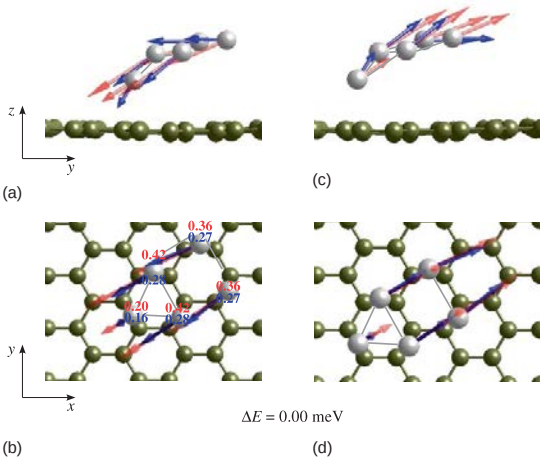


FIG. 12. Side (a) and (c) and top view (b) and (d) of the magnetic structure of a flat Pt_5-cluster parallel to the graphene sheet [cf. panels (e) and (f) in Fig. 10].

the graphene layer via weak bonding of three Pt atoms at on-top sites. Average bond lengths are slightly increased relative to the free cluster, the total magnetic moment of $\mu_J = 1.5\mu_B$ is strongly reduced relative to that of the square pyramid ($\mu_J = 5.3\mu_B$) or of the trigonal bipyramid ($\mu_J = 3.9\mu_B$) in the gas phase. The total energy is higher by 268 meV than for the GS configuration. The higher energy is due almost entirely to the less favorable binding between the Pt atoms in the cluster, while the interaction with the substrate is almost the same for both configurations (see Table II). In contrast, for Pd_5 a square pyramid, with the four Pd atoms forming the base bound to C–C bridge sites was found to be the ground state.[28]

Calculations including SOC converged for the GS geometry to the noncollinear magnetic structure shown in Fig. 11, with $\mu_S = 1.01\mu_B$ and $\mu_L = 0.65\mu_B$. This configuration is energetically degenerate with a structure in which the directions of local spin and orbital moments have been reversed. The two configurations may be considered as right- and left-handed versions of spiral structures turning around the point where the cluster is attached to the substrate.

For the flat Pt_5 cluster, we had identified a number of ferromagnetic high- and low-moment and also antiferromagnetic states, with energy differences comparable or even smaller than the magnetic anisotropy energies for a given magnetic state. For the supported Pt_5 cluster, we have also found a low-moment isomer with $\mu_J = 1.17\mu_B$ and a similar spirallike noncollinear structure which is only 23 meV higher in energy than the GS.

For the less stable configuration of a bent planar Pt_5 cluster adsorbed parallel to the support, the stable magnetic configuration is very similar to that of the flat gas-phase cluster. The local spin and orbital moments are aligned with the mirror plane of the geometric structure, a modest noncollinearity reflects the bent geometry. Again the total energy is invariant against a reversal of the direction of the local moments (see Fig. 12). Total spin and orbital moments are $\mu_S = 1.7\mu_B$ and $\mu_L = 1.2\mu_B$, almost unchanged with respect to the gas-phase. SOC reduces the energy difference relative to the geometric and magnetic ground state to 407 meV.

For both configurations of a flat Pt_5 cluster supported on graphene calculations including SOC always converged to the same magnetic state, independent of the initial magnetic structure.

For the distorted trigonal bipyramid plus adatom, two stationary magnetic configurations, one with the total moment roughly perpendicular (this is the GS) and the second with

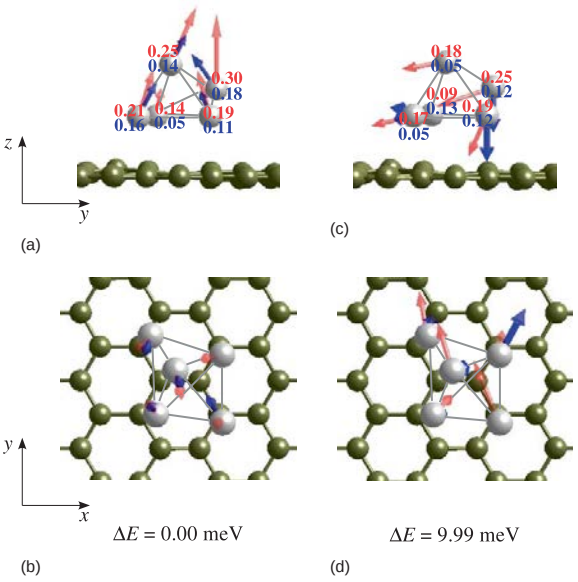


FIG. 13. Side (a) and (c) and top view (b) and (d) of the magnetic structure of a Pt_5-cluster on graphene forming a distorted trigonal bipyramid.

Downloaded 15 Sep 2011 to 128.130.131.2. Redistribution subject to AIP license or copyright; see http://jcp.aip.org/about/rights_and_permissions

the magnetization more or less parallel to the graphene layer could be determined, see Fig. 13. In this case, SOC increases the energy difference relative to the geometric and magnetic GS to 345 meV. For perpendicular magnetization, the total moment is $\mu_J = 1.57\ \mu_B$ ($\mu_S = 1.03\ \mu_B$, $\mu_L = 0.5\ \mu_B$), the local magnetic moments are canted relative to the surface normal such as to be almost parallel to the edges. Inversion of the direction of magnetization by 180° leaves the magnetic moments and the total energy unchanged. The initialization of the calculation with the magnetic moments oriented parallel to the C-layer leads to a transition to a low-moment state with $\mu_J = 1.04\ \mu_B$, which is 10 meV above the GS.

A gas-phase Pt_5 cluster with the structure of a trigonal bipyramid has an easy magnetization direction parallel to the central basal plane. As the distorted cluster is attached to the graphene layer via one of the triangular faces, this GS corresponds to out of plane magnetization. For the gas-phase cluster, the MAE is 4.3 meV/atom, with modest spin and orbital anisotropies of opposite sign. The larger MAE of the supported cluster is a consequence of the high-moment → low-moment transition coupled to the rotation of the magnetization direction.

IV. DISCUSSION

We have performed first-principles investigations of the geometric and magnetic structures of small Pt clusters supported on graphene, including spin-orbit coupling. The calculations have been started with the two-dimensional equilibrium configurations of the gas-phase clusters deposited on the graphene layer such that without constraining the Pt–Pt bonds too much the atoms are located at favorable adsorption sites. In addition linear and three-dimensional clusters have been examined. The structures of the cluster-support complex have been optimized by static relaxation. The main results can be summarized as follows (see also Table III): (i) For an isolated Pt atom, we calculate an adsorption energy of about 1.5 eV on C–C bridge sites and a low activation energy for diffusion along the network of C–C bonds. Due to the relatively strong bonding the Pt atom is nonmagnetic. (ii) In Pt_n clusters with two and more atoms, the structure of the gas-phase cluster is preserved, although distorted. The Pt–Pt bonding is much stronger than the bonding to graphene. The adsorption energy per atom increases with the size, favoring the growth of clusters. (iii) A Pt-dimer favors an upright configuration. In their optimized structures triangular Pt_3, bent rhomboidal Pt_4, and flat Pt_5 clusters form only two Pt–C bounds to C atoms of the support. As a consequence the interaction of the cluster with the support decreases with cluster size. Pt atoms on graphene form strongly bound, but rather mobile clusters. (iv) Linear chains of Pt atoms on graphene are much less stable than the two-dimensional structures. (v) The adsorption of the cluster induces a relatively strong buckling of the graphene layer, with an amplitude increasing from 0.23 Å for the upright dimer to 0.83 Å for a Pt_5 cluster. (vi) In their equilibrium geometrical configurations, the clusters are weakly magnetic, local moments are quenched on the Pt atoms binding to the support. (vii) Spin-orbit coupling enhances the total magnetic moment, but both spin and orbital moments, as well as the magnetic anisotropy energies are much lower than for the gas phase clusters. (viii) No significant magnetic moments are induced on the C atoms.

TABLE III. Comparison of gas-phase and supported Pt_n clusters: Structure, binding energy E_{coh} (in eV/atom), spin and orbital moments, μ_S and μ_L (in μ_B), and magnetic anisotropy energy MAE (in meV/atom). Results for the gas-phase clusters are taken from Ref. 12.

Cluster	Structure	E_{coh}	μ_S	μ_L	MAE
Pt_2					
gas-phase	dumbbell	1.905	1.8	2.7	37.5
supported	upright dumbbell	2.383	0.9	1.2	10.0
Pt_3					
gas-phase	triangle	2.482	1.5	1.0	5.1
supported	upright triangle	2.948	0.7	0.4	1.7
Pt_4					
gas-phase	rhombus	2.725[a]	2.6[a]	1.4[a]	8.2[a]
supported	bent rhombus	3.034	1.3	0.6	0.7
Pt_5					
gas-phase	planar	2.985	1.7	1.3	1.2[b]
supported	planar, upright	3.143	1.0	0.7	—

[a]The GS is antiferromagnetic, moments and MAE are reported for the excited ferromagnetic state.
[b]The MAE is calculated relative to the antiferromagnetic configuration with the lowest energy.

For the upright Pt_2 dumbbell, the easy magnetic axis is aligned with the dimer axis. Rotation of the magnetization parallel to the graphene support is associated with a high-moment → low-moment transition at high, respectively a magnetic → nonmagnetic transition at low coverage, in close analogy to a gas-phase dimer and to a freestanding infinite monowire. For a triangular Pt_3 cluster on graphene, the magnetic configuration corresponding to the gas-phase cluster (in the plane of the triangle and perpendicular to graphene) represents no stationary solution. The easy axis is parallel to the graphene layer, but oblique to the Pt-triangle and parallel to C–C bonds. Rotation of the magnetization direction parallel to the support costs an MAE of 1.7 meV/atom, about one third of the MAE of the free cluster. A Pt_4 rhombus is bent about the short diagonal upon adsorption, the easy axis is perpendicular to the support, with a low MAE of 0.7 meV/atom for in-plane magnetization. For both Pt_3 and Pt_4, we calculate small, but negative anisotropies of both spin and orbital moments (i.e., the moments are larger for hard-axis magnetization). The planar structure of the Pt_5 cluster is preserved upon adsorption, but bent. For the stable configuration, with the Pt-cluster perpendicular to the graphene, we find a noncollinear magnetic GS, for the less stable flat-lying configuration, we find a collinear GS very similar to that of the gas-phase cluster. The noncollinear magnetic structures are a consequence of the inhomogeneous magnetization of the clusters.

Our results for Pt_n clusters on graphene are in interesting contrast to those for Pd_n clusters reported by Cabria *et al.*[28] Free Pd_n cluster are known to have a much lower binding energy than the corresponding Ni or Pt clusters because the formation of Pd–Pd bonds requires an opening of the closed d^{10} shell of the Pd atom. Our present results demonstrate that not only the binding within the clusters is stronger for Pt, these clusters also bind more strongly to the graphene

Downloaded 15 Sep 2011 to 128.130.131.2. Redistribution subject to AIP license or copyright; see http://jcp.aip.org/about/rights_and_permissions

layer: for Pt_n the interaction energy of the cluster with the support decreases from –0.47 eV/Pt-atom for the trimer to –0.16 eV/Pt-atom, while for Pd_n it varies only between –0.19 and –0.12 eV/Pd-atom.

V. CONCLUSIONS

The structural and magnetic properties of small Pt clusters supported on graphene have been investigated using first-principles DFT methods as an example of strongly anisotropic magnetic nanostructures on a weakly interacting substrate. The calculations confirm that the binding within the clusters is much stronger than the binding to the substrate. As a consequence the structure of the gas-phase cluster is preserved also if they are deposited on graphene. In the stable configurations, the clusters bind to the support only via one or two Pt atoms whose magnetic moments are strongly quenched. Consequently, the magnetic structure of the supported clusters is rather inhomogeneous and even strongly noncollinear in triangular Pt_3 and flat Pt_5 clusters. Local spin and orbital moments and magnetic anisotropy energies are strongly reduced compared to the free clusters.

ACKNOWLEDGMENTS

This work has been supported through the VASP project.

[1] M. L. Plumer, J. van Ek, and D. Weller, in *Springer Series in Surface Sciences*, edited by G. Ertl, R. Gomer, H. Lüth, and D. L. Mills (Springer, Berlin, 2001), Vol. **41**.
[2] D. Sellmyer and R. Skomski, *Advanced Magnetic Nanostructures* (Springer, New York, 2006).
[3] H. Brune, Surf. Sci. Rep. **31**, 125 (1998).
[4] H. Brune and P. Gambardella, Surf. Sci. **603**, 1812 (2009).
[5] P. Błoński, A. Lehnert, S. Dennler, S. Rusponi, M. Etzkorn, G. Moulas, P. Bencok, P. Gambardella, H. Brune, and J. Hafner, Phys. Rev. B **81**, 104426 (2010).
[6] A. Lehnert, S. Dennler, P. Błoński, S. Rusponi, M. Etzkorn, G. Moulas, P. Bencok, P. Gambardella, H. Brune, and J. Hafner, Phys. Rev. B **82**, 094409 (2010).
[7] J. Velev, R. F. Sabiryanov, S. S. Jaswal, and E. Y. Tsymbal, Phys. Rev. Lett. **94**, 127203 (2005).
[8] Y. Mokrousov, G. Bihlmayer, S. Heinze, and S. Blügel, Phys. Rev. Lett. **96**, 147201 (2006).
[9] A. Smogunov, A. dal Corso, A. Delin, R. Weht, and E. Tosatti, Nature Nanotechnol. **3**, 22 (2008).
[10] D. Fritsch, K. Koepernik, M. Richter, and H. Eschrig, J. Comp. Chem. **29**, 2210 (2008).
[11] P. Błoński and J. Hafner, Phys. Rev. B **79**, 224418 (2009).
[12] P. Błoński, S. Dennler, and J. Hafner, J. Chem. Phys. **134**, 034107 (2011).
[13] M. N. Huda, Manish K. Niranjan, B. R. Sahu, and L. Kleinman, Phys. Rev. A **73**, 053201 (2006).
[14] H. Häkkinen, B. Yoon, U. Landman, X. Li, H.-J. Zhai, and L.-S. Wang, J. Phys. Chem. A **107**, 6168 (2003).
[15] P. Bruno, Phys. Rev. B **39**, 865 (1989).
[16] B. Lazarovits, L. Szunyogh, and P. Weinberger, Phys. Rev. B **67**, 024415 (2003).
[17] B. Nonas, I. Cabria, R. Zeller, P. H. Dederichs, T. Huhne, and H. Ebert, Phys. Rev. Lett. **86**, 2146 (2001).
[18] K. S. Novoselov, A. K. Geim, S. V. Morozov, D. Jiang, Y. Zhang, S. V. Dubonos, I. V. Grigorieva, and A. A. Firsov, Science **306**, 666 (2004).
[19] K. S. Novoselov, A. K. Geim, S. V. Morozov, D. Jiang, M. I. Katsnelson, I. V. Grigorieva, S. V. Dubonos, and A. A. Firsov, Nature (London) **438**, 197 (2005).
[20] Y. Zhang, Y.-W. Tan, H. L. Störmer, and P. Kim, Nature (London) **438**, 201 (2005).
[21] M. Y. Han, B. Özyilmaz, Y. Zhang, and P. Kim, Phys. Rev. Lett. **98**, 206805 (2007).
[22] K. I. Bolotin, K. J. Sikes, Z. Jiang, M. Klima, G. Fudenberg, J. Hone, P. Kim, and H. L. Störmer, Solid State Commun. **146**, 351 (2008).
[23] C. Lee, X. Wei, J. W. Kysar, and J. Hone, Science **321**, 385 (2008).
[24] Y. Okamoto, Chem. Phys. Lett. **420**, 382 (2006).
[25] K. Okazaki-Maeda, S. Yamakawa, Y. Morikawa, T. Akita, S. Tanaka, S. Hyodo, and M. Kohyama, J. Phys.: Conf. Ser. **100**, 072044 (2008).
[26] X.-Q. Dai, Y.-N. Tang, J.-H. Zhao, and Y.-W. Dai, J. Phys.: Condens. Matter **22**, 316005 (2010).
[27] Ch. Vo-Van, Z. Kassir-Bodon, H. Yang, J. Coraux, J. Vogel, S. Pizzini, P. Bayle-Guillemaud, M. Chshiev, L. Ranno, V. Guisset, P. David, V. Salvador, and O. Fruchart, New J. Phys. **12**, 103040 (2010).
[28] I. Cabria, M. J. Lopez, and J. A. Alonso, Phys. Rev. B **81**, 035403 (2010).
[29] Z. Zhou, F. Gao, and W. Goodman, Surf. Sci. **604**, L31 (2010).
[30] Y. Gan, L. Sun, and F. Banhart, Small **4**, 587 (2008).
[31] H. Sevinçli, M. Topsakal, E. Durgun, and S. Ciraci, Phys. Rev. B **77**, 195434 (2008).
[32] A. Ishii, M. Yamamoto, H. Asano, and K. Fujiwara, J. Phys.: Conf. Ser. **100**, 052087 (2008).
[33] B. Uchoa, C.-Y. Lin, and A. H. Castro Neto, Phys. Rev. B **77**, 035420 (2008).
[34] K. T. Chan, J. B. Neaton, and M. L. Cohen, Phys. Rev. B **77**, 235430 (2008).
[35] Ch. Cao, M. Wu, J. Jiang, and H.-P. Cheng, Phys. Rev. B **81**, 205424 (2010).
[36] O. V. Yazyev and A. Pasquarello, Phys. Rev. B **82**, 045407 (2010).
[37] G. Kresse and J. Furthmüller, Comp. Mat. Sci. **6**, 15 (1996); Phys. Rev. B **54**, 11169 (1996).
[38] G. Kresse and D. Joubert, Phys. Rev. B **59**, 1758 (1999).
[39] J. P. Perdew and Y. Wang, Phys. Rev. B **45**, 13244 (1992).
[40] S. H. Vosko, L. Wilk, and M. Nusair, Can. J. Phys. **58**, 1200 (1980).
[41] E. G. Moroni, G. Kresse, J. Hafner, and J. Furthmüller, Phys. Rev. B **65**, 15629 (1997).
[42] J. Anton, T. Jacob, B. Fricke, and E. Engel, Phys. Rev. Lett. **89**, 213001 (2002).
[43] P. E. Blöchl, Phys. Rev. B **50**, 17953 (1994).
[44] G. Kresse and O. Lebacq, vasp manual http://cms.mpi.univie.ac.at/vasp/vasp/vasp.html.
[45] L. Kleinman, Phys. Rev. B **21**, 2630 (1980).
[46] A. H. MacDonald, W. E. Pickett, and D. D. Koelling, J. Phys. C **13**, 2675 (1980).
[47] D. Hobbs, G. Kresse, and J. Hafner, Phys. Rev. B **62**, 11556 (2000).
[48] M. Marsman and J. Hafner, Phys. Rev. B **66**, 224409 (2002).
[49] R. Varns and P. Strange, J. Phys.: Condens. Matter **20**, 225005, (2008).
[50] O. Ü. Aktürk and M. Tomak, Phys. Rev. B **82**, 085417 (2009).
[51] R. Xiao, D. Fritsch, M. D. Kuzmin, K. Koepernik, and M. Richter, Phys. Rev. B **80**, 205125 (2010).
[52] R. Xiao, M. D. Kuzmin, K. Koepernik, and M. Richter, Appl. Phys. Lett. **97**, 232501 (2010).

Downloaded 15 Sep 2011 to 128.130.131.2. Redistribution subject to AIP license or copyright; see http://jcp.aip.org/about/rights_and_permissions

Pt on graphene monolayers supported on a Ni(111) substrate: Relativistic density-functional calculations

Piotr Błoński[1,2] and Jürgen Hafner[1,a)]
[1]*University of Vienna, Faculty of Physics and Center for Computational Materials Science, Sensengasse 8/12, A-1090 Wien, Austria*
[2]*Institute of Chemical Research of Catalonia (ICIQ), Avgda. Països Catalans 16, E 43007 Tarragona, Catalonia, Spain*

(Received 20 October 2011; accepted 25 January 2012; published online 15 February 2012)

The structural, energetic, and magnetic properties of Pt atoms and dimers adsorbed on a Ni-supported graphene layer have been investigated using density-functional calculations, including the influence of dispersion forces and of spin-orbit coupling. Dispersion forces are found to be essential to stabilize a chemisorbed graphene layer on the Ni(111) surface. The presence of the Ni-substrate leads not only to a stronger interaction of Pt atoms and dimers with graphene but also to a locally increased binding between graphene and the substrate and a complex reconstruction of the adlayer. The stronger binding of the dimer also stabilizes a flat adsorption geometry in contrast to the upright geometry on a free-standing graphene layer. These effects are further enhanced by dispersion corrections. Isolated Pt adatoms and flat dimers are found to be non-magnetic, while an upright Pt dimer has strongly anisotropic spin and orbital moments. For the clean C/Ni(111) system, we calculate an in-plane magnetic anisotropy, which is also conserved in the presence of isolated Pt adatoms. Surprisingly, upright Pt-dimers induce a re-orientation of the easy magnetic axis to a direction perpendicular to the surface, in analogy to Pt_2 on a free-standing graphene layer and to the axial anisotropy of a gas-phase Pt_2 dimer. © *2012 American Institute of Physics*. [http://dx.doi.org/10.1063/1.3684891]

I. INTRODUCTION

The fabrication of free-standing layers of graphene[1] in 2004 has spurred an intense interest in the outstanding structural and electronic properties of this material and its potential applications in spintronics and optoelectronics. Graphene is a two-dimensional zero-gap semiconductor, with a linear dispersion relation of the electronic eigenstates around the Fermi level. Hence, electrons with energies close to E_F can be considered as two-dimensional Dirac fermions, with the velocity of light replaced by the Fermi velocity v_F of the electrons. For this reason, graphene is of great interest for fundamental studies in quantum electrodynamics. The potential applications of graphene have also revived the interest in metal-graphene interactions. Graphene layers bound to transition-metal surfaces with a small lattice mismatch have been studied already earlier (see, e.g., Ref. 2), but very recent studies have shed new light especially on the magnetic properties of the carbon atoms in transition-metal supported graphene layers.[3–5] In recent experimental studies[6] of the interaction of transition-metal and noble-metal atoms with a suspended graphene layer it was concluded that transition-metal atoms interact only weakly with graphene, they do not form continuous films but clusters or nanocrystals. This conclusion is supported by our recent theoretical studies of the formation of Pt clusters on free graphene layers[7] where we found that the clusters bind to the graphene layer only via one or two Pt atoms. The magnetic moments on these atoms are strongly quenched, leading to a rather inhomogeneous magnetic structure of the graphene-supported clusters.

The formation of transition-metal clusters on graphene supported on non-magnetic metallic substrates such as Ir(111) (Ref. 8) or Ru(0001) (Ref. 9) has been studied experimentally and theoretically.[10] The lattice mismatch between the substrate and the graphene overlayer leads to the formation of a Moiré pattern in a corrugated graphene layer influencing the growth and morphology of clusters deposited on this substrate. From the theoretical side, recent studies[11] have shown that a correct description of the dispersion forces between the graphene layer and the metallic surface is required for a quantitatively correct description of the structural corrugation in the Moiré pattern.

This raises the question whether density-functional theory (DFT) is the proper tool for describing graphene layers on metallic substrates. Vanin *et al.*,[12] Hamada and Otani,[13] and Sławińska *et al.*[14] have presented systematic investigations of graphene layers on various close-packed transition-metal surfaces, based on the local-density approximation (LDA), the generalized gradient approximation (GGA, using the revPBE (Ref. 15) exchange-correlation functional), with and without including semi-empirical dispersion corrections as proposed by Grimme,[16,17] or using the nonlocal "van der Waals functional" (vdW-DFT) proposed by Lundqvist *et al.*[18–20] to account for dispersion forces. For the noble metals, for Pt and Al weak binding between graphene and the substrate is predicted by both LDA and vdW-DFT, whereas GGA predicts no binding at all. For Ni and Co substrates LDA predicts a too strong binding of the adlayer, with the theoretical metal-graphene distances slightly lower than estimated from experiment,[2,21]

a)Electronic mail: juergen.hafner@univie.ac.at.

 © 2012 American Institute of Physics

Downloaded 16 Apr 2012 to 128.130.131.2. Redistribution subject to AIP license or copyright; see http://jcp.aip.org/about/rights_and_permissions

while GGA finds no binding at all. According to Hamada and Otani[13] the results achieved with a nonlocal vdW-DFT correlation functional depend on the choice of a particular variant of the nonlocal vdW-correlation[18–20] and, most importantly, of the exchange functional to be combined with the nonlocal correlation functional. If the PBE exchange functional, modified such as to mimic the Hartree-Fock energy[22] is used, a large distance of ∼3.7 Å between the graphene layer and the metal surface was calculated for all substrates. If an exchange functional proposed by Cooper,[23] modified such as to yield improved agreement with high-level quantum-chemical calculations is used, significantly shorter graphene-metal distances are found, in good agreement with experiment for Ni (Refs. 2 and 21) and Pt.[24] Very recently Olsen *et al.*[25] and Mittendorfer *et al.*[26] used the random phase approximation (RPA), combined with the adiabatic connection and fluctuation dissipation theorem (ACFDT) as proposed by Harl and Kresse,[27] to investigate the adhesion of a graphene layer on metallic substrates. Lebègue *et al.*[28] had shown that this approach yields very accurate results for the interlayer distance and the cohesive energy of graphite. Both studies[25,26] demonstrated that for strong-binding substrates such as Ni or Co, the binding energy of a graphene layer has two energetically almost degenerate minima, one at larger distances of ∼3.5 Å representing a physisorbed adlayer and one at smaller distances around 2.2 Å representing the chemisorbed state. GGA calculations predict a local energy minimum at the chemisorbed state but no physisorption, the vdW-functional (in the version originally proposed[18,19]) predicts physisorption but no chemisorption.[25] A chemisorbed minimum is found with the modified vdW functionals developed recently by Klimeš *et al.*,[29] but the relative depths of the physisorbed and chemisorbed minima are found to be extremely sensitive to a judicious combination of the local and nonlocal contributions to the functional.[26]

Given the uncertainty of the proper choice of a vdW-functional and the computational complexity of the RPA-ACFDT approach (which both can currently be applied only to a fixed geometry), the simpler dispersion corrections offered by the semi-empirical force fields of Grimme[16,17] remain of interest. It has been demonstrated that the Grimme approach leads to quantitatively accurate results for graphite,[30] in good agreement with the RPA. The method has also been demonstrated to work for graphene/Au(111).[14]

For graphene/Ni(111) different structures have been proposed. From experiment Gamo *et al.*[2] found that the most stable structure is top-fcc [i.e., half of the carbon atoms are located on-top of Ni atoms and half in the face-centered cubic (fcc) hollows of the (111) surface], whereas Rosei *et al.*[31] and Klink *et al.*[32] suggested that the stable structure is hexagonal close-packed (hcp)-fcc, i.e., the carbon atoms occupy both types of three-fold hollows on the surface of the substrate. Very recently Zhao *et al.*[33] reported from combined high-resolution x-ray photoelectron spectroscopy and *ab initio* DFT calculations the co-existence of two structures for graphene/Ni(111), top-fcc and bridge-top. The DFT calculations include semi-empirical dispersion corrections[34] and find both structures to be energetically degenerate within about 0.3 kJ/mole and C–Ni distances of about 2.2 Å, in good agreement with experiment. The two competing structures have been identified by their different core-level shifts, for both configurations the DFT-calculated level shifts are in good agreement with experiment. Different structures had also been considered by Fuentes-Cabrera *et al.*[35] in calculations using both the LDA and the GGA. The GGA calculations predict that, irrespective of the structure, a graphene layer on Ni(111) does not bind to the substrate. Only for a hcp/fcc structure a weakly physisorbed layer at a distance of 3.6 Å from the Ni layer was found to be marginally stable. In LDA, the top/fcc and top/bridge structures were found to be energetically almost degenerate, with Ni-graphene distances of about 2.01 Å and 1.95 Å, respectively. This is another illustration of the well-known fact that the overbinding characteristic for the LDA predicts a binding interaction also in cases where it is promoted only by dispersion forces. For this reason, in several theoretical studies[36,37] the LDA has been preferred over the GGA. It must be emphasized, however, that physically, the binding caused by a too strong exchange contribution to the exchange-correlation functional is very different from the dynamical correlation effects promoting van der Waals interactions.

For ultrathin films of graphite sandwiched between ferromagnetic Ni(111) and Co(0001) leads, Karpan *et al.*[37] have suggested almost perfect spin filtering properties. There is almost no lattice-mismatch between graphene and these two close-packed metal surfaces, but the strong hybridization between the C-π and metal-*d* states at the interface modifies the electronic structure of the graphene layer. The recent experimental work of Dedkov and Fonin[5] based on x-ray adsorption spectroscopy and x-ray magnetic circular dichroism (XMCD) has demonstrated that a small magnetic moment is induced in the graphene layer, leading to an exchange splitting of the eigenstates at the Dirac point by about 0.3 eV and affecting the spin-filtering properties.

The present work is focused on the investigation of Pt atoms and dimers deposited on graphene support on a Ni(111) substrate. Our interest is motivated by several interesting observations: (i) Small Pt clusters in the gas phase carry a magnetic moment. (ii) Strong relativistic effects lead to the formation of a large orbital moment and a large magnetic anisotropy energy (MAE). (iii) Spin-orbit coupling (SOC) influences not only the magnetic but also the structural properties of the clusters.[38] (iv) Pt clusters bind only weakly to a graphene layer via one or two Pt atoms and preserve a large, only slightly reduced orbital moment and MAE.[7] (v) Nanostructured systems combining a ferromagnetic 3*d*-metal with a 5*d*-metal contributing a strong spin-orbit coupling are a possible way to achieve a high magnetic anisotropy energy. In the present work, our interest is concentrated on the interaction of the magnetic adatoms with the ferromagnetic substrate through the graphene layer. Our calculations are based on density-functional theory, including spin-orbit coupling effects and semi-empirical corrections for dispersion forces.

II. COMPUTATIONAL DETAILS

The electronic structure calculations and structural optimizations reported here are based on DFT as implemented in the Vienna *ab initio* simulation package VASP.[39,40] VASP

Downloaded 16 Apr 2012 to 128.130.131.2. Redistribution subject to AIP license or copyright; see http://jcp.aip.org/about/rights_and_permissions

performs an iterative solution of the Kohn-Sham equations within a plane-wave basis and using periodic boundary conditions. The basis set contained plane waves with a maximum kinetic energy of 500 eV. For electronic exchange and correlation effects the semilocal Perdew-Wang functional[41] in the GGA and the spin-interpolation proposed by Vosko *et al.*[42] were used. The electron-ion interactions were treated in the projector-augmented-wave (PAW) formalism.[40,43] The PAW approach produces the exact all-electron potentials and charge densities and hence avoids the need to use elaborate nonlinear core corrections, which is particularly important for magnetic elements. The PAW potentials have been derived from fully relativistic calculations of the atomic or ionic reference calculations.

A. Dispersion corrections

DFT calculations do not account for van der Waals (dispersion) forces. Dispersion corrections have been computed using the semi-empirical force-field proposed by Grimme *et al.*[16,17] In this method, the total energy of the system is defined as a sum of the self-consistent Kohn Sham energy ($E_{\text{KS-DFT}}$) and a semi-empirical dispersion correction (E_{disp}),

$$E_{\text{DFT}+D} = E_{\text{KS-DFT}} + E_{\text{disp}}. \tag{1}$$

The van der Waals energy is described by long-range dipole-dipole interactions,

$$E_{\text{disp}} = s_6 \sum_{i=1}^{N_{\text{at}-1}} \sum_{j=i+1}^{N_{\text{at}}} \frac{C_6^{ij}}{R_{ij}^6} f(R_{ij}), \tag{2}$$

where N_{at} denotes the total number of atoms, R_{ij} the distance between atoms i and j, and C_6^{ij} is a parameter determining the strength of the pairwise interactions. The C_6^{ij} parameters for a pair of atoms are defined as $\sqrt{C_6^i C_6^j}$ and the C_6^i parameters have been optimized to describe the bonding properties of element i in a large set of molecular systems. A cutoff function $f(R_{ij})$ is used, on one hand to prevent too strong interactions between neighboring atoms and on the other hand to restrict computational requirements for long-range interactions in solids. The scaling factor s_6 accounts for the differences between different GGA functionals. Here, we have used the parameters tabulated by Grimme *et al.*[16] for the PBE functional. The recent work of Grimme *et al.*[17] has demonstrated that the simple pair-potential approach yields van der Waals energies in good agreement with more sophisticated methods based on nonlocal exchange-correlation functionals. The pair-potential approach also permits a straightforward calculation of the dispersion forces in structural optimizations. Very recently, Grimme's DFT+d approach has been implemented in VASP code by Bučko *et al.*[30] and applied to calculate the structures and binding energies of a large number of solids where dispersion forces play an important role.

B. Spin-orbit coupling

For each system considered here, two sets of calculations were performed, one on a scalar-relativistic level, and the second-one including SOC. Spin-orbit coupling has been implemented in VASP by Kresse and Lebacq,[44] following the approach of Kleinman[45] and MacDonald *et al.*[46] The relativistic Hamiltonian containing all relativistic corrections up to order α^2 (where α is the fine-structure constant) is recast in the form of 2×2 matrices in spin-space by re-expressing the eigenstates of the total angular momentum in terms of a tensor product of regular angular momentum eigenstates $|l, m\rangle$ and the eigenstates of the z-component of the Pauli spin matrices. The relativistic effective potential consists of a term diagonal in spin-space which contains the mass-velocity and Darwin corrections. The nondiagonal contributions in spin-space arise from the spin-orbit coupling but also from the exchange-correlation potential when the system under consideration displays a noncollinear magnetization density. Calculations including spin-orbit coupling have therefore to be performed in the noncollinear mode implemented in VASP by Hobbs *et al.*[47] and Marsman and Hafner.[48] Magnetic anisotropy energies have been calculated as total energy differences from calculations with different orientations of the magnetic moments. For a more detailed description of the SOC implementation in VASP we also refer the readers to our recent paper.[7]

C. Structural model

The graphene/Ni(111) complex was represented by a periodically repeated unit cell containing the graphene layer supported on a slab with four Ni layers, containing 48 C-atoms in the graphene layer and 24 Ni atoms per layer of the substrate. Repeated slabs are separated by 20 Å of vacuum, such that the interaction between the repeated images is negligible. The Brillouin zone was sampled using $6 \times 6 \times 1$ Γ-centered k-point mesh and using a Gaussian smearing of 0.02 eV. Electronic densities of states were calculated using the tetrahedron method.

Pt atoms and dimers, with an initial geometry determined for free clusters in earlier calculations[38] were placed on top of the graphene layer. At one adatom or dimer per surface cell, the coverage is about 2 (4)% for isolated adatoms (dimers), corresponding to the higher coverage case studied in our recent work on Pt of free-standing graphene. The adsorbate/graphene/substrate complex was relaxed, keeping the two lowest Ni layers in their bulk-like positions until the forces on all atoms were less than 25 meV/Å. Simultaneously, the electronic and magnetic degrees of freedom were relaxed until the change in total energy between successive iteration steps was smaller than 10^{-7} eV.

III. RESULTS AND DISCUSSION

A. Graphene supported on Ni(111)

The C-atoms in the graphene layer have been positioned on top of the atoms and into the fcc hollows of the Ni(111) face. According to both experiment[2,33] and recent *ab initio* calculations,[26,33,50] this top/fcc configuration is a stable configuration of a graphene sheet supported on Ni(111). The possibly competing bridge/top configuration has not been considered here. The lattice constant of this lattice-matched graphene layer is 2.49 Å, which is $1/\sqrt{2}$ of the fcc-Ni lattice constant of 3.52 Å (theoretical value in agreement with

Downloaded 16 Apr 2012 to 128.130.131.2. Redistribution subject to AIP license or copyright; see http://jcp.aip.org/about/rights_and_permissions

experiment). The hexagonal lattice constant of a free-standing graphene layer is 2.44 Å (C–C distance 1.41 Å),[7] leading to a mismatch of only 2 pct.

The binding energy between the graphene layer and the Ni substrate was calculated according to

$$E_B = E^{\text{graphene}-\text{Ni}(111)} - E^{\text{Ni}(111)} - E^{\text{graph}},$$

where $E^{\text{graph/Ni}(111)}$, $E^{\text{Ni}(111)}$, and $E^{\text{graph.}}$ stand for the total energy of the graphene/Ni(111) system, the slab representing the clean Ni(111) surface, and the free-standing graphene sheet, respectively.

In accordance with the previous DFT studies (see, e.g., Refs. 12, 25, 26, and 35,) the GGA calculations predict no binding of the graphene sheet to the Ni substrate, but only a plateau or very shallow local minimum at positive (endothermic) binding energy at a graphene-Ni distance of 2.3 Å, which is accidentally only slightly larger than the experimental value of 2.1 Å.[2] The interatomic distances between the successive layers in the graphene-covered Ni-slab are 2.035, 2.038, and 2.035 Å, almost identical to the interlayer distances close to the clean, relaxed Ni(111) surface (2.034, 2.036, and 2.034 Å).

Although the free-standing ideal graphene sheet is nonmagnetic, the binding to the Ni(111) surface induces a weak magnetic polarization of the C-atoms. The C-atoms located on top of Ni atoms carry a magnetic moment of $-0.014\ \mu_B$/atom, whereas atoms in a fcc-hollow have a moment of $+0.017\ \mu_B$/atom, where $-$ (+) stands for antiparallel (parallel) orientation of the magnetic moment with respect to the magnetic moments in the Ni-slab. A weak induced magnetism of carbon atoms in the graphene/Ni(111) system has also been observed experimentally.[3,5] However, the orientation of individual magnetic moments at different atomic sites cannot be determined from the experimental XMCD data. Sawada *et al.*[51] derived from their DFT calculations magnetic moments on carbon atoms of $+0.021$ and $-0.027\ \mu_B$/atom. The Ni atoms carry magnetic spin moments of 0.54, 0.62, and 0.65 μ_B/atom in the 1st, 2nd, and successive layers, respectively. Compared to a bare Ni(111) surface only the magnetic moment in the 1st layer is quenched due to the presence of C adlayer (0.65 μ_B/atom at the clean surface).

1. Dispersion corrections

To correct the inaccurate GGA-binding energy we have repeated the calculation employing the DFT+d method of Grimme.[16] Within this method E_B is corrected to -109 meV/C-atom (negative value means that the graphene is bound to the Ni substrate), but both the graphene-Ni distance and the magnetic moments remain practically unchanged. Both binding energy and distance are in very good agreement with the chemisorbed state identified in the RPA-ACFDT calculations of Olsen *et al.*[25] and Mittendorfer *et al.*[26] [$E_B = -78(-67)$ meV/C-atom, C layer 2.3(2.17) Å above the substrate, results in parentheses are from Mittendorfer *et al.*]. The vdW correction tends, however, to shorten the Ni-interatomic distances, which within this approximation are 2.020, 2.018, and 2.020 Å, therefor the Ni-slab-geometry was taken from the standard GGA calculations and kept frozen whenever we used the vdW correction.

2. Spin-orbit coupling

Spin-orbit coupling leaves the spin moments in adlayer and substrate unchanged, independent of the orientation of the magnetization. The graphene/Ni(111) system exhibits rather small in-plane MAE of 0.145 meV/atom. The orbital moments of the Ni atoms are 0.065, 0.054, 0.056, and 0.075 μ_B in the first and subsequent layers for in-plane magnetization, and 0.045, 0.053, 0.053, and 0.046 μ_B for perpendicular magnetization. Spin and orbital moments are strictly parallel. The slightly larger orbital moments for easy-axis orientation correspond to the classical picture of magnetic anisotropy.

3. Electronic structure

The electronic structure of the graphene layer is strongly modified by the interaction with the Ni substrate. Figures 1(a) and 1(b) show the electronic density of states (DOS) of a free-standing graphene layer and a layer supported on Ni(111), with a Ni–C distance as optimized including dispersion forces. While for the free-standing layer the DOS close to the Fermi level shows the form characteristic for the linear dispersion relations, it is strongly modified by the interaction with the magnetic substrate and the spin-polarization induced in the graphene. The hybridization with the 3*d*-states of Ni leads to the formation of two peaks in the C-*p* DOS coincident with the peaks in the substrate DOS. Due to the exchange splitting, the C-*p* spin-up DOS shows a local minimum, the spin-down DOS a local maximum at the Fermi level. The exchange-splitting of about 0.5 eV is in good agreement with the experimental estimate.[5] The hybridization of the π and $\pi^\star$ bands of graphene with the substrate states is very essential for the stabilization of a chemisorbed state with a short C–Ni interlayer distances. Mittendorfer *et al.*[26] have pointed out that at the larger distance of the physisorbed state, the hybridization has disappeared almost completely.

B. Pt adatom on graphene/Ni(111)

1. Geometric properties

A single Pt atom has been placed into an on top (ot), bridge (br) or six-fold hollow (6 h) position of the graphene layer (see Fig. 2). The adsorption energy of a Pt atom or cluster is calculated as the difference in the total energies according to

$$E_{\text{ad}} = \frac{1}{n}(E^{\text{Pt}_n/\text{graphene}-\text{Ni}} - E^{\text{graphene}-\text{Ni}} - E^{\text{Pt}_n}),$$

where E^{Pt_n} stands for the total energy of an isolated Pt_n cluster (or atom for $n = 1$).

As for a Pt adatom on a free-standing graphene sheet, the br-position is found to be energetically most favorable, followed by the ot and 6 h sites. The binding of the Pt adatoms to the substrate is much stronger than in the absence of the support. The adsorption energies E_{ad} are $-3.010(-1.603)$, $-2.288(-1.357)$, and $-1.601(-0.792)$ eV/Pt-atom for br, ot,

Downloaded 16 Apr 2012 to 128.130.131.2. Redistribution subject to AIP license or copyright; see http://jcp.aip.org/about/rights_and_permissions

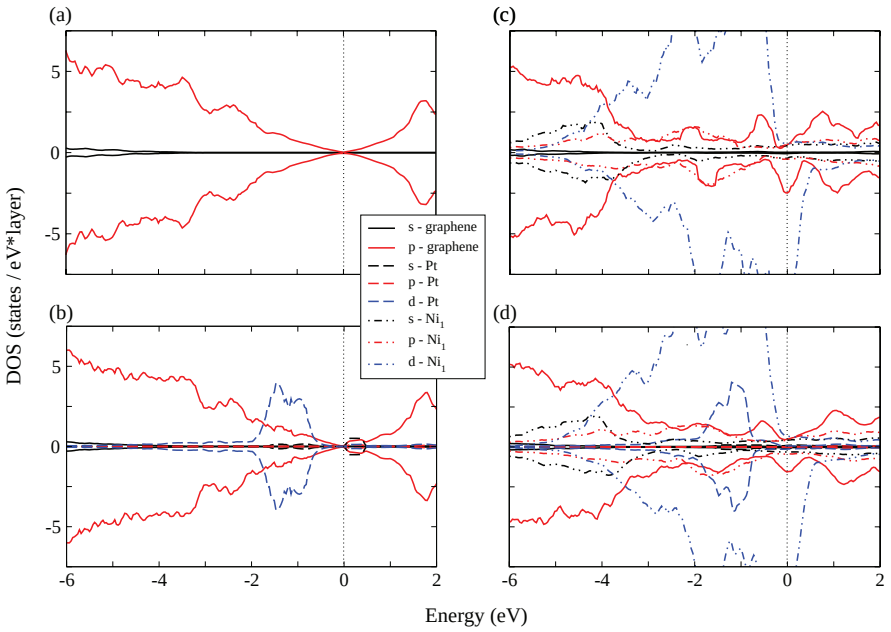


FIG. 1. Partial electronic densities of states for (a) a free-standing graphene layer, (b) a graphene layer supported on a Ni(111) substrate, (c) a graphene layer with a single Pt adatom in a bridge position, and (d) the graphene/Ni(111) complex with an isolated Pt adatom.

and 6 h, respectively. Values in parentheses refer to Pt on a free graphene layer, see also Table I. The height of the adatom above the graphene (measured relative to the average z-coordinate of the C atoms) is smallest for the 6 h site, slightly larger for the br and largest for the ot position. The presence of adatoms causes a strong, rather complex reconstruction of both the graphene sheet and the Ni layers. Due to the strong binding of the adsorbate, the bonds between the C atoms around the Pt adatom are less saturated and this leads to a stronger binding between graphene and the Ni substrate such that the Pt atom is located in the center of a deep, rather broad depression of the adlayer (see Fig. 3). The C atoms connecting directly to the Pt atoms, however, move slightly outwards (such as the C atoms of a free-standing graphene layer). A Pt atom in a br position is located 1.96 Å above the atoms forming the C–C bridge, but 2.25 Å above the average height of the C atoms. For a Pt adatom in a br site the corrugation amplitude is 0.783 Å in the C-layer, and 0.268, 0.174, 0.134 Å in the 1st, 2nd, and 3rd Ni layers. Following the trend in the adsorption energies, the corrugation of the graphene layer decreases from 0.783 Å to 0.429 Å and 0.126 Å for br-, ot-, and 6 h-positions. The Ni atoms directly below the Pt atom move outward, the buckling amplitude of the first Ni layer decreases in the same sequence: 0.268, 0.090, and 0.034 Å, for br-,ot-, and 6 h-sites. Interestingly, the mean distances between Ni layers is hardly changed, at most by about 0.005 Å.

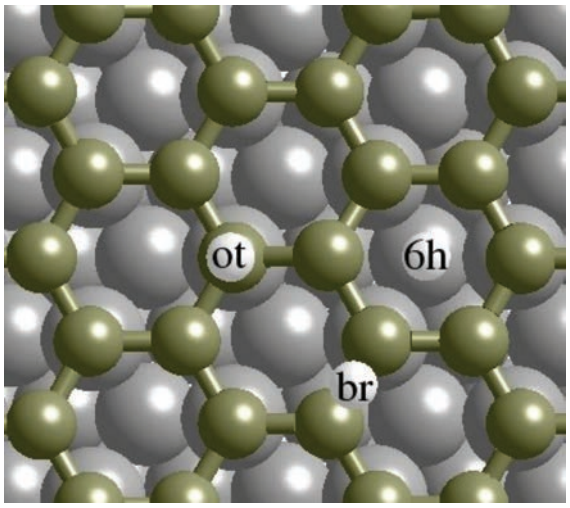


FIG. 2. Top view of the graphene/Ni(111) system (dark-gold/dark-grey circles) in a top-fcc configuration showing the Pt-adatoms (small light-grey circles) adsorption sites: bridge (br), on top a C-atom (ot), and six-fold-hollow (6 h).

TABLE I. The adsorption energy, E_{ad} and the height $z_{Pt\text{-}G}$ of a Pt adatom above the average graphene sheet, the average distance between graphene and the first Ni layer, $z_{G\text{-}Ni}$, the Pt–C bond length, $d_{Pt\text{-}C}$, and the buckling of the C layer, b_C, and Ni-first layer, b_{Ni}, calculated for the Pt adatom adsorbed in different high-symmetry sites. For the most stable br site the values in parentheses give the results including the dispersion corrections (DFT+d). The adsorption energy is given in eV/Pt atom, all distances in Å.

Adsorption	Method	E_{ad}	$z_{Pt\text{-}G}$	$z_{G\text{-}Ni}$	$d_{Pt\text{–}C}$	b_C	b_{Ni}
br	DFT	–3.010	2.251	2.346	2.055	0.78	0.27
	DFT+d	–(3.272)	(2.28)	(2.20)	(2.10)	(0.43)	(0.13)
ot	DFT	–2.288	2.332	2.320	2.002	0.43	0.09
6 h	DFT	–1.601	2.108	2.312	2.506	0.13	0.03

Downloaded 16 Apr 2012 to 128.130.131.2. Redistribution subject to AIP license or copyright; see http://jcp.aip.org/about/rights_and_permissions

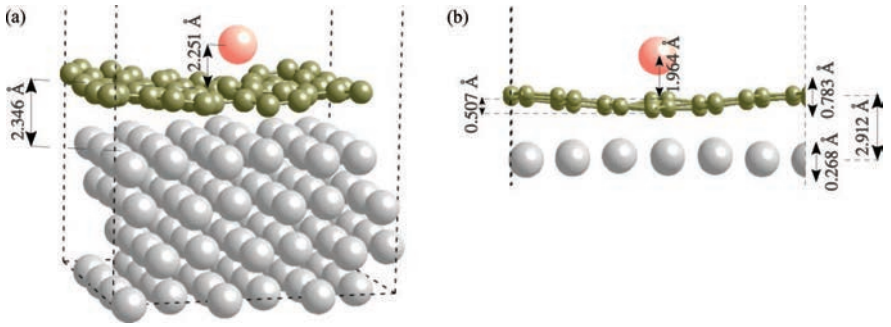


FIG. 3. (a) Graphical representation of the Pt/graphene/Ni(111) system, with the adsorbed Pt adatom in the bridge position. Part (b) shows in detail the reconstruction of the graphene layer. The distances marked in (a) are the average height of the Pt atom above the graphene layer and the average graphene-Ni interlayer distance. Part (b) reports the buckling amplitudes of the graphene and the first Ni layer, the graphene-Ni distance at the boundary of the computational cell, the height of Pt over the C–C bridge, and the height of the C–C bridge above the lowest atoms in the graphene layer. All geometrical parameters are given in Å, they refer to DFT calculations without dispersion corrections, cf. Table I and text.

2. Dispersion corrections

If dispersion corrections are taken into account (but keeping the geometry of the Ni substrate frozen as determined in the GGA calculations), the binding energy of a Pt adatom in a br position increases to −3.272 eV/Pt atom. The height of the Pt atom above the graphene layer is 2.28 Å, compared to 2.25 Å without dispersion corrections, while the graphene-Ni distance is reduced from 2.35 Å to 2.20 Å. The most important structural effect of the vdW forces is the reduction of the corrugation amplitude to 0.43 Å. If the two top layers of the Ni-substrate are also allowed to relax under the influence of the dispersion forces, the Pt–C and C–Ni distances remain unchanged, but the interlayer distances are reduced to 2.01 and 2.00 Å. The corrugation amplitude of the first Ni layer decreases to 0.13 Å.

3. Magnetic properties

Pt adatoms on graphene/Ni carry small magnetic moments, −0.02, −0.05, and −0.19 μ_B/Pt atom for br-, ot-, and 6 h-positions. This is in contrast to Pt atoms on free-standing graphene which are non-magnetic. At a frozen bulk-like geometry, the magnetic moments found for the bare graphene/Ni system are almost unaffected by the presence of adsorbate. In the top layer of the substrate the magnetic moments vary between 0.50 and 0.56 μ_B (0.54 μ_B in the absence of the Pt adatom). Only on the Ni atom almost directly below the Pt atom the magnetic moment is enhanced to 0.63 μ_B —this enhancement is remarkable because adatom and substrate are separated by the graphene layer. The induced magnetic moments on the C atoms are −0.01 and +0.02 μ_B, only on the two C atoms binding directly to Pt the magnetic moment is reduced almost to zero.

At the relaxed geometry the magnetic moments on the Ni atoms below the depression in the graphene layer are further reduced up to 0.43 μ_B, except for the atoms closest to the Pt atom which has a bulk-like moment of 0.65 μ_B. The distribution of the magnetic moments in the first Ni layer is displayed in Fig. 4. The magnetic moments in the second Ni layer vary between 0.60 and 0.66 μ_B, they are converged to the bulk value of 0.65 μ_B from the third layer onward.

4. Electronic structure

The strongly increased adsorption energy, the structural deformation of the graphene/Ni substrate and the weak induced magnetism show that there are strong interactions between the Pt adatom and the graphene, and between graphene and the Ni support. In the electronic DOS (see Fig. 1(c)) this is reflected by a broadening of the 5*d*-states of the Pt atom. In the DOS of the graphene layer the structure induced by the interaction with the Ni substrate is slightly smeared out as a consequence of the buckling of the adlayer, but the exchange-splitting remains unchanged.

5. Magnetic anisotropy

Calculations including spin-orbit coupling predict a small anisotropy of the spin moment of the Pt atom with −0.022 μ_B for in-plane and −0.018 μ_B for perpendicular

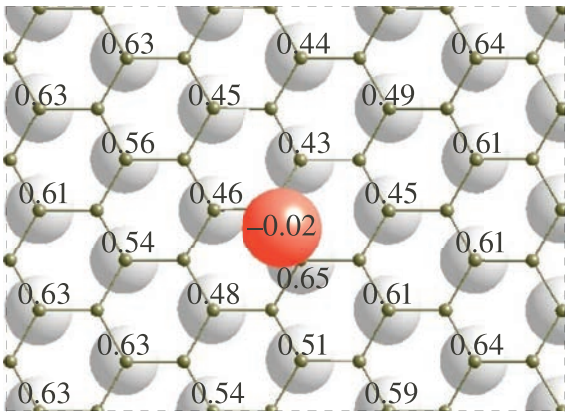


FIG. 4. Magnetic moments (in μ_B) in the top layer of a graphene-covered Ni(111) surface carrying a Pt adatom shown by the red ball. C atoms in the graphene layer are located at the vertices of the honeycomb network.

Downloaded 16 Apr 2012 to 128.130.131.2. Redistribution subject to AIP license or copyright; see http://jcp.aip.org/about/rights_and_permissions

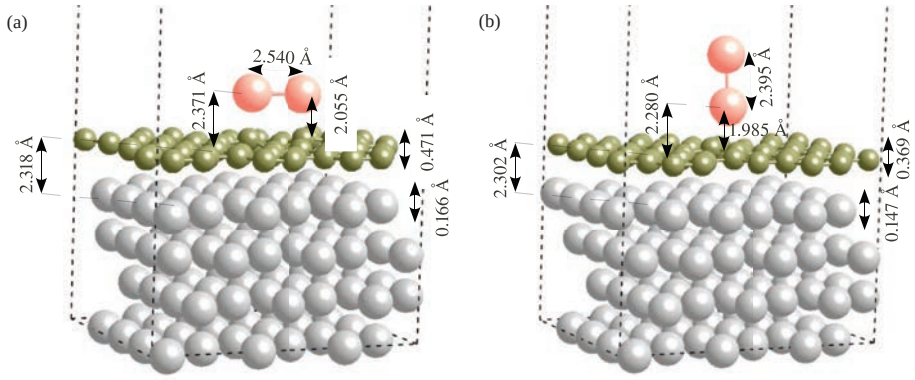


FIG. 5. Flat (a) and upright (b) configurations of a Pt_2 dimer supported on graphene/Ni(111). Geometrical parameters are from DFT calculations without dispersion corrections.

magnetization, while the spin moments on the Ni atoms remain unchanged relative to the scalar relativistic calculations. The orbital moment of the Pt atom is $+0.021\mu_B$ for perpendicular and $+0.008\mu_B$ for in-plane magnetizations. The antiparallel orientation of spin and orbital moments lead to a very small total moment on the adatom. On the Ni atoms in the first layer the orbital moments vary between 0.036 and 0.057 μ_B for perpendicular and between 0.035 and 0.075 μ_B for in-plane magnetization. The influence of the adatom on the orbital moments decreases in the deeper layers. The easy magnetization direction is in-plane, the MAE of 0.089 meV/atom is lower than without the Pt adatom.

C. Pt dimers on graphene/Ni(111)

In addition to the adsorption energy of the dimer it is also interesting to examine the strength of the binding between the Pt atoms which can be characterized by the cohesive energy of the supported dimer given by

$$E_{\text{coh}} = \tfrac{1}{2}(E^{\text{Pt}_2/\text{graph/Ni}} - E^{\text{graph/Ni}} - 2E^{\text{Pt}}),$$

where E^{Pt} stands for the total energy of an isolated Pt atom.

For a Pt dimer in the gas phase, scalar-relativistic calculations predict a bond length of 2.35 Å and a spin moment of 2 μ_B. Spin-orbit coupling favors the formation of a high-moment state with a total moment of 4.5 μ_B oriented along the dimer axis and a MAE of 23.1 meV/Pt atom.[38] On a free-standing graphene layer, a Pt dimer is adsorbed in an upright position with a bond length of 2.38 Å and a distance of 2.11 to 2.26 Å of the lower Pt atom from the buckled graphene layer, depending on coverage, and a spin moment of 1.5 μ_B. SOC favors an increased total magnetic moment of 2 μ_B at low and 3 μ_B at higher coverage, correlated to different MAE's of 5.3 and 11.6 meV/Pt atom, respectively.[7]

1. Geometric and energetic properties

The present calculation for Pt on graphene/Ni(111) corresponds to the higher coverage of about 4% studied for Pt/graphene, both upright and flat configurations have been considered, see Fig. 5. All energetic and geometric parameters are summarized in Table II. In contrast to the dimer on a free-standing graphene layer the stable configuration is a flat-lying dimer with both Pt atoms located slightly off an ot position above a C atom and $E_{\text{coh}} = -2.896$ eV/Pt atom and $E_{\text{ad}} = -0.999$ eV/Pt atom. The corresponding values for an upright dimer with the lower Pt atom in a br position are -2.733 eV and -0.836 eV/Pt atom, respectively. The adsorption energy per Pt atom is increased with respect to free-standing graphene by -0.71 eV for the flat and by -0.35 eV for the upright dimer, such that the presence of the substrate stabilizes the flat geometry. The adsorption energy per Pt atom, however, is lower than for the isolated adatom. This means that while on a free-standing graphene layer the formation of dimers and larger clusters was energetically favored (and facilitated by a high mobility of the Pt atoms),[38]

TABLE II. The adsorption energy E_{ad} and the Pt–Pt binding energy E_{coh}, and the Pt–Pt bond length $d_{\text{Pt–Pt}}$ of a Pt_2 dimer on graphene/Ni(111) for flat and upright geometries. $z_{\text{Pt-G}}$ is height of the (lower) Pt adatom above the average of the graphene sheet, $z_{\text{G-Ni}}$ the average distance between the graphene and the top Ni layers, $d_{\text{Pt–C}}$ the distance between the (lower) Pt and the nearest C atom. b_{C} and b_{Ni_1} are the buckling amplitudes of the graphene and the first Ni layers. Results of calculations without (DFT) and including dispersion corrections (DFT+d) are reported. Energies are given in eV/Pt atom, distances in Å.

Geometry	Method	E_{ad}	E_{coh}	$d_{\text{Pt-Pt}}$	$z_{\text{Pt-G}}$	$z_{\text{G-Ni}}$	$d_{\text{Pt-C}}$	b_{C} (Å)	b_{Ni} (Å)
Flat	DFT	–0.999	–2.896	2.54	2.37	2.32	2.06	0.47	0.17
	DFT+d	–1.747	–3.562	2.56	2.37	2.19	2.03	0.52	0.17
Upright	DFT	–0.836	–2.733	2.40	2.28	2.30	1.99	0.37	0.15
	DFT+d	–1.405	–3.310	2.39	2.28	2.18	1.97	0.44	0.15

Downloaded 16 Apr 2012 to 128.130.131.2. Redistribution subject to AIP license or copyright; see http://jcp.aip.org/about/rights_and_permissions

on graphene/Ni(111) isolated adatoms are lower in energy. The formation of dimers is also further hindered by a large diffusion barrier given by the difference in the adsorption energies on br and ot sites (see Table I).

The Pt–Pt distance in a flat-lying dimer is 2.54 Å—this is larger than the dimer length on a free-standing graphene layer of 2.46 Å and also slightly larger than the lattice constant of the lattice-matched graphene layer. In both cases the Pt–Pt bond stretches between two ot positions across a hexagon. The adsorbed dimer induces a corrugation of the graphene layer with an amplitude of 0.47 Å. Again the C atoms surrounding the Pt dimer move closer to the Ni substrate, but the C atoms binding directly to the Pt atoms are located slightly above their neighbors, such that the height of the Pt atoms is 2.37 Å above the average height of the C atoms but only 2.06 Å above the nearest C atoms (see Fig. 5(a)).

The Pt–Pt distance in an upright dimer is 2.395 Å, increased by 0.015 Å compared to the dimer on the free graphene layer. The lower Pt atom is located 2.28 Å above the average height of the buckled C layer but only 1.99 Å above the atoms forming the C–C bridge (see Fig. 5(b)). The buckling amplitude of the C layer is 0.369 Å, that of the first two Ni layers is 0.147 Å and 0.034 Å, respectively. Compared to Pt dimers on a free-standing graphene layer with the same coverage both Pt–Pt bond length and distance from the graphene layer are slightly increased, but the most important difference is the much larger buckling amplitude of the supported graphene layer, reflecting the substrate-induced stronger adsorption of the dimer.

2. Magnetic properties

The flat Pt_2 dimer is almost non-magnetic, only the Pt atom located almost directly above a Ni atom of the substrate has a small moment of 0.02 μ_B. C atoms directly below the Pt atoms are non-magnetic, the alternating magnetic moments on the other atoms in the graphene layer remain unchanged. The distribution of the magnetic moments in the top layer of the substrate is shown in Fig. 6, local moments vary between 0.49 and 0.63 μ_B.

The upright Pt dimer is magnetic with a total spin moment of 1 μ_B (the local moments are 0.70 μ_B on the upper and 0.3 μ_B on the lower Pt atom). The weak induced magnetism in the graphene layer is hardly affected. The magnetic moments in the top Ni layer vary between 0.52 and 0.57 μ_B, only on the Ni atom below Pt the moment is increased to 0.67 μ_B. Moments in the 2nd Ni layer range between 0.62 and 0.63 μ_B, they are converged to the bulk value of 0.65 μ_B from the third layer onward.

3. Dispersion corrections

Dispersion corrections have a strong influence on the energetics of an adsorbed Pt dimer. For the flat-lying dimer E_{ad} increases from −2.869 to −3.562 eV/Pt atom, E_{coh} from −0.999 to −1.747 eV/Pt atom. Whereas without dispersion corrections the formation of a dimer from two co-adsorbed Pt atoms is an endothermic process, it is now energetically favored by 0.290 eV/atom. The distance of the dimer from the graphene layer is unchanged, but the Pt–Pt distance increases to 2.56 Å. The buckling amplitude of the graphene layer increases to 0.52 Å. For the upright dimer E_{coh} increases from −2.733 to −3.310 eV/Pt atom, E_{ad} from −0.836 to −1.405 Å, i.e., the preference for a flat dimer becomes even more pronounced. The distance of the lower Pt atom from the graphene is unchanged, the dimer length is slightly reduced to 2.386 Å. The buckling amplitude of the graphene layer is 0.44 Å. The energies and distances calculated using the DFT+d approach are summarized in Table II. Changes in the magnetic moments as a consequence of the altered geometry are very modest.

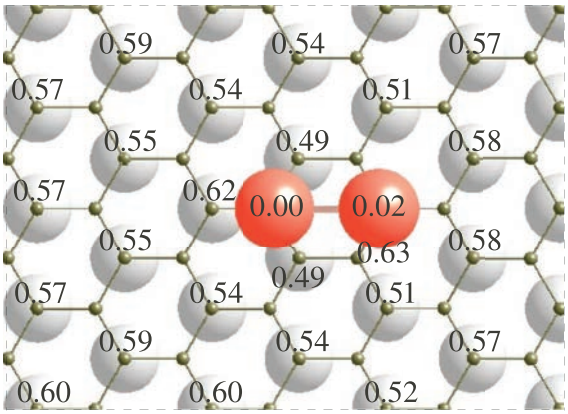


FIG. 6. Distribution of the magnetic moments in the top Ni layer below a flat-lying Pt_2 dimer supported on graphene/Ni(111). C atoms in the graphene layer are located at the vertices of the honeycomb network.

4. Influence of spin-orbit coupling—magnetic anisotropy

For a flat-lying dimer SOC does not induce the formation of a magnetic moment, the Pt dimer remains non-magnetic. The magnetism of an upright dimer, however, is strongly affected. For magnetization perpendicular to the substrate (i.e., parallel to the dimer axis), the Pt dimer has a spin moment of 0.92 μ_B and an orbital moment of 1.17 μ_B. The orbital moment on the C atoms is zero, in the first Ni layer the orbital moments vary between 0.043 and 0.047 μ_B, only the Ni atom directly below the Pt dimer has a larger orbital moment of 0.056 μ_B. In the first Ni layer the spin moments vary between 0.51 and 0.57 μ_B (only the Ni atom directly below the Pt dimer has a larger spin moment of 0.66 μ_B). Hence, they are hardly influenced by the presence of the adsorbate. In the second Ni layer the spin moment varies between 0.61 and 0.63 μ_B. For magnetization parallel to the substrate (and perpendicular to the dimer axis), the Pt dimer has lower spin and orbital moments of 0.49 μ_B and 0.36 μ_B, respectively. Again the spin moment is much larger on the upper Pt atom (0.33 μ_B) and the orbital moment is located almost entirely in this site. The spin moments in the Ni substrate are hardly changed, but in-plane magnetization permits the formation of larger orbital moments in the Ni substrate. We calculate 0.071 μ_B on the atom directly below the Pt dimer and orbital

Downloaded 16 Apr 2012 to 128.130.131.2. Redistribution subject to AIP license or copyright; see http://jcp.aip.org/about/rights_and_permissions

TABLE III. Spin and orbital moments μ_S and μ_L, spin and orbital anisotropies $\Delta\mu_S$ and $\Delta\mu_L$, and magnetic anisotropy energy MAE for a Pt_2 dimer in the gas phase, on a graphene layer, and on a graphene/Ni(111) support. All magnetic moments are given in μ_B, the MAE in meV/dimer.

	Magnetization direction[a]	μ_S	μ_L	$\Delta\mu_S$	$\Delta\mu_L$	MAE
Pt_2	Axial	1.88	2.74			0
(Ref. 49)	Perpendicular	1.34	0.80	–0.54	–1.94	46.2
Pt_2/graphene	Axial	1.30	1.70			0
(Ref. 7)	Perpendicular	0.60	0.53	–0.70	–1.17	23.2
Pt_2/graphene/Ni	Axial	0.92	1.17			
	Perpendicular	0.49	0.36	–0.43	–0.81	49.6

[a]Relative to the dimer axis.

moments between 0.050 and 0.063 μ_B on the other Ni atoms in the first layer. The easy magnetization direction is perpendicular (corresponding to the larger spin and orbital moments on the Pt dimer), with an MAE of 0.34 meV/atom.

The result of a perpendicular anisotropy of the Pt_2/C/Ni(111) system, in contrast to the in-plane anisotropy of the graphene-covered Ni(111) surface, but in agreement with the perpendicular anisotropy of an upright Pt dimer on a free-standing graphene layer[7] and the axial anisotropy of a gas-phase Pt dimer[38] is remarkable. To compare the MAE's it is important to remember that in our previous studies the MAE was given in units of meV/Pt atom, whereas the MAE calculated in the present work is calculated per atom, including all Pt, C, and Ni atoms. For the entire computational cell with 96 Ni, 48 C, and 2 Pt atoms the MAE is 49.6 meV, to be compared with an MAE of 23.2 meV for the Pt dimer on a free graphene layer and of 46.2 meV for the gas-phase dimer. The magnetic moments, spin and orbital anisotropies, and MAE's of a Pt dimer in the gas phase, on a free-standing graphene layer, and on a graphene/Ni support are collected in Table III.

The role of the support is to decrease spin and orbital moments with increasing strength of the interaction, but both remain strongly anisotropic. For a dimer in the gas phase and on graphene, the reduced MAE reflects the decrease in the orbital anisotropy. For Pt_2/graphene/Ni, however, the orbital anisotropy is further decreased, but the MAE is as large as for the isolated dimer. This means that due to the presence of the Pt dimer the contribution of the Ni support to the MAE has changed sign. This is in line with our analysis of the orbital moments of the substrate atoms which are larger for in-plane than for perpendicular magnetization for the clean graphene/Ni(111) system, whereas the orbital anisotropy is reversed in the presence of an upright Pt_2 dimer.

IV. DISCUSSION AND CONCLUSIONS

Detailed investigations of the energetic, structural, and magnetic properties of Pt atoms and dimers deposited on a graphene layer supported on a Ni(111) substrate have been presented. The influence of dispersion forces and of spin-orbit coupling has been investigated. In accordance with earlier work we find that dispersion forces are necessary to bind the graphene sheet to the Ni substrate. The magnetism of Ni induces weak magnetic moments of opposite sign on the C placed above the substrate atoms and the fcc hollows of the Ni(111) surface. The graphene–Ni distance and binding energy predicted by the simple DFT+d approach for the chemisorbed layer are in good agreement with high-level RPA-ACFDT calculations[25,26] and with experiment. Calculations including SOC predict weak orbital moments on the substrate atoms and an in-plane MAE of 0.145 meV/atom.

The stable adsorption site of an isolated Pt atom is in a bridge-position between two C atoms of the graphene layer. While the adsorption site is the same as on a free-standing graphene sheet, the adsorption energy is almost twice as large, the Pt atom also induces a strong, rather complex corrugation of the graphene layer and of the top Ni layers. Dispersion corrections increase the adsorption energy by about 9 pct and lead to a slight increase of the Pt–graphene distance by 0.03 Å. The buckling of the graphene layer induced by the adatom is stronger and qualitatively different from that found for free-standing graphene. While the C atoms of the free layer binding to Pt move outward, the adatom is located in a deep and broad depression of the supported layer. Its origin is the polarization of the graphene layer by the adatom which leads also to a locally stronger interaction between graphene and the Ni support. For the C atoms directly coordinated to Pt, however, the stronger Pt–C interaction dominates such that the atoms forming the C–C bridge are located above the surrounding part of the graphene layer.

An isolated Pt adatom is almost non-magnetic and the small magnetic moments on the C atoms remain almost unchanged. However, the Pt atom induces a slight increase of the magnetic moment of the Ni atom directly below. The weak in-plane magnetic anisotropy is further reduced by the adatom.

A Pt_2 dimer is adsorbed on graphene/Ni in a flat configuration with the Pt atoms close to on-top positions on both sides of a sixfold hollow, an upright dimer located in a C–C bridge is by 0.16 eV/Pt atom higher in energy. This is in marked contrast to a Pt_2 dimer on free-standing graphene where an upright geometry is energetically favored by 0.193 eV/Pt atom. The change in the geometry is caused by the strong interaction of the second Pt atom with the support. In both cases the graphene layer is strongly corrugated, with a geometrical pattern similar to that discussed for the adatom. Dispersion corrections increase the structural energy difference in favor of the flat dimer to 0.34 eV/Pt atom, they also stabilize the dimer relative to two isolated adatoms. The flat dimer is non-magnetic, the upright dimer carries a magnetic moment of 1 μ_B. For the flat dimer a non-magnetic state has also been found on free-standing graphene, for the upright dimer the spin moment is reduced compared to a value of 1.5 μ_B in the absence of a substrate.

Relativistic calculations have been performed only for the magnetic upright dimer. While for Pt_2 on free-standing graphene we had found at the coverage considered in the present work an enhanced total magnetic moment of $\sim$3 μ_B for the easy magnetization direction parallel to the dimer axis, on the supported graphene layer we find only a total magnetic moment of $\sim$2.1 μ_B. In both cases the orbital moment is larger than the spin moment, both spin and orbital moments

Downloaded 16 Apr 2012 to 128.130.131.2. Redistribution subject to AIP license or copyright; see http://jcp.aip.org/about/rights_and_permissions

are strongly anisotropic. The presence of Pt dimers on the C/Ni(111) surface leads to a re-orientation of the easy magnetization direction from in-plane to perpendicular, as for a dimer on a free-standing graphene layer.

The conclusions to be drawn from our results concern both the computational methodology and the physical properties of transition-metal atoms and clusters on metal-supported graphene layers. The first point to note is the reduced mobility of Pt adatoms—the diffusion barrier increases from 0.18 eV to 0.72 eV due to the presence of the Ni support. The substrate also affects the relative stability of isolated adatoms and dimers. On a free-standing graphene layer the formation of dimers and larger clusters is energetically favored. On graphene/Ni dimer formation is an endothermic process in the absence of dispersion forces but exothermic if dispersion forces are taken into account. The magnetic properties of the system are of central interest and we note that (i) a graphene-covered Ni(111) surface has a weak in-plane MAE of 0.145 meV/atom. (ii) The presence of Pt adatoms leads to a locally increased interaction between graphene and the support and a complex reconstruction of the adlayer. The easy magnetization direction remains in-plane and the MAE is further reduced. (iii) Even without dispersion corrections, a flat Pt_2 dimer is energetically more favorable on graphene/Ni(111) than an upright geometry—in contrast to the situation for unsupported graphene. (iv) A flat dimer is non-magnetic and for the upright dimer the strongly anisotropic spin and orbital magnetic moments are reduced by the presence of the substrate. (v) For the upright dimer we find an easy magnetization direction perpendicular to the substrate, as on the free-standing graphene layer and corresponding to the axial anisotropy of the gas-phase dimer. This means that the magnetic anisotropy of the dimer is strong enough to induce a re-orientation of the easy magnetic axis relative to the clean C/Ni(111) system.

Dispersion corrections of the DFT results necessary to stabilize the adhesion of a graphene layer on a Ni(111) substrate. It is important to note that the simple semi-empirical DFT+d approach predicts an adsorption energy and graphene–Ni distance in good agreement with the more elaborate and computationally much more demanding RPA-ACFDT method. This permits to extend the investigations to the much larger models required for the Pt_n/graphene/Ni system. Dispersion corrections lead to a modest increase of the adsorption energy of a Pt atom on the supported graphene layer and to a more pronounced enhancement of the adsorption energy of a dimer whose formation is energetically favored only by the dispersion forces. The preference for a flat dimer geometry is also further increased by dispersion corrections. The influence on the geometric properties is, however, very small.

The important result of this study is to demonstrate strong indirect interactions between metallic adatoms and a metallic, ferromagnetic substrate mediated by the graphene layer. These effects induce a strong reconstruction of the graphene layer and favor geometries permitting a stronger coupling between adatoms and graphene, they also reverse the relative stability of isolated adatoms and dimers. For loosely bound configurations of the dimer the stronger SOC of the heavy adsorbates dominate the magnetic anisotropy. Similar effects could also lead to a strong MAE of nanostructures on supported graphene layers which are large enough to stabilize a three-dimensional structure.

ACKNOWLEDGMENTS

This work has been supported through the VASP project.

[1] K. S. Novoselov, A. K. Geim, S. V. Morosov, D. Jiang, Y. Zhang, S. V. Dubonos, I. V. Grigorieva, and A. A. Firsov, Science **306**, 666 (2004).
[2] Y. Gamo, A. Nagashima, N. Wakabayashi, M. Terai, and C. Oshima, Surf. Sci. **374**, 61 (1997).
[3] M. Weser, Y. Rehder, K. Horn, M. Sicot, M. Fonin, A. B. Preobrajenski, E. N. Voloshina, E. Goering, and Yu. S. Dedkov, Appl. Phys. Lett. **96**, 012504 (2010).
[4] Yu. S. Dedkov, M. Sicot, and M. Fonin, J. Appl. Phys. **107**, 09E121 (2010).
[5] Yu. S. Dedkov and M. Fonin, New J. Phys. **12**, 125004 (2010).
[6] R. Zan, U. Bangert, Q. Ramasse, and K. S. Novoselov, Nano Lett. **11**, 1087 (2011).
[7] P. Błoński and J. Hafner, J. Chem. Phys. **134**, 154705 (2011).
[8] A. T. N'Diaye, S. Bleikamp, P. J. Feibelman, and T. Michely, Phys. Rev. Lett. **95**, 215501 (2006).
[9] Z. Zhou, F. Gao, and D. W. Goodman, Surf. Sci. **604**, L31 (2010).
[10] P. J. Feibelman, Phys. Rev. B **80**, 085412 (2009).
[11] D. Stradi, S. Barja, C. Diaz, M. Garnica, B. Borca, J. J. Hinarejos, D. Sánchez-Portal, M. Alcami, A. Arnau, A. L. Vázquez de Parga, R. Miranda, and F. Martin, Phys. Rev. Lett. **106**, 186102 (2011).
[12] M. Vanin, J. J. Mortensen, A. K. Kelkkanen, J. M. Garcia-Lastra, K. S. Thygesen, and K. W. Jacobsen, Phys. Rev. B **81**, 081408(R) (2010).
[13] I. Hamada and M. Otani, Phys. Rev. B **82**, 153412 (2010).
[14] J. Sławińska, P. Drabowski, and I. Zasada, Phys. Rev. B **83**, 245429 (2011).
[15] Y. K. Zhang and W. T. Yang, Phys. Rev. Lett. **80**, 890 (1998).
[16] S. Grimme, J. Antony, T. Schwabe, and C. Mück-Lichtenfeld, Org. Biomol. Chem. **5**, 741 (2007).
[17] S. Grimme, J. Antony, S. Ehrlich, and H. Krief, J. Chem. Phys. **132**, 154104 (2010).
[18] M. Dion, H. Rydberg, E. Schröder, D. C. Langreth, and B. I. Lundqvist, Phys. Rev. Lett. **92**, 246401 (2004).
[19] M. Dion, H. Rydberg, E. Schröder, D. C. Langreth, and B. I. Lundqvist, Phys. Rev. Lett. **92**, 109902 (2005).
[20] K. Lee, E. D. Murray, L. Kong, B. I. Lundqvist, and D. C. Langreth, Phys. Rev. B **82**, 081101 (2010).
[21] D. Eom, D. Prezzi, K. T. Rihm, H. Zhou, M. Lefenfeld, S. Xiao, C. Nuckolls, M. S. Hybertsen, T. F. Heinz, and G. W. Flynn, Nano Lett. **9**, 2844 (2009).
[22] E. D. Murray, K. Lee, and D. C. Langreth, J. Chem. Theory Comput. **5**, 2754 (2009).
[23] V. R. Cooper, Phys. Rev. B **81**, 161104(R) (2010).
[24] P. Sutter, J. T. Sadowski, and E. Sutter, Phys. Rev. B **80**, 245411 (2009).
[25] T. Olsen, J. Yan, J. J. Mortensen, and K. S. Thygesen, Phys. Rev. Lett. **107**, 156401 (2011).
[26] F. Mittendorfer, A. Garhofer, J. Redinger, J. Klimeš, J. Harl, and G. Kresse, Phys. Rev. B **84**, 201401(R) (2011).
[27] J. Harl and G. Kresse, Phys. Rev. Lett. **103**, 056401 (2009).
[28] S. Lebègue, J. Harl, T. Gould, J. G. Ángyán, G. Kresse, and J. F. Dobson, Phys. Rev. Lett. **105**, 196401 (2010).
[29] J. Klimeš, D. R. Bowler, and A. Michaelides, Phys. Rev. B **83**, 195131 (2011).
[30] T. Bučko, S. Lebègue, J. G. Ángyán, and J. Hafner, J. Phys. Chem. A **114**, 11814 (2010).
[31] R. Rosei, M. de Crescenzi, F. Sette, C. Quaresima, A. Savoia, and P. Perfetti, Phys. Rev. B **28**, 1161 (1983).
[32] C. Klink, I. Stensgaard, F. Besenbacher, and E. Laegsgaard, Surf. Sci. **342**, 250260 (1995).
[33] W. Zhao, S. M. Kozlov, O. Höfert, K. Gotterbarm, M. P. A. Lorenz, F. Viñes, C. Papp, A, Görling, and H. P. Steinrück, J. Phys. Chem. Lett. **2**, 759 (2011).
[34] F. Ortmann, F. Bechstedt, and W. G. Schmidt, Phys. Rev. B **77**, 205101 (2006).
[35] M. Fuentes-Cabrera, M. I. Baskes, A. V. Melechko, and M. L. Simpson, Phys. Rev. B **77**, 035405 (2008).

Downloaded 16 Apr 2012 to 128.130.131.2. Redistribution subject to AIP license or copyright; see http://jcp.aip.org/about/rights_and_permissions

[36]Z. Xu and M. J. Buehler, J. Phys.: Condens. Matter **22**, 485301 (2010).
[37]V. M. Karpan, P. A. Khomyakov, A. A. Starikov, G. Giovanette, M. Zwierzycki, M. Talanana, G. Brocks, J. Van den Brink, and P. J. Kelly, Phys. Rev. B **78**, 195419 (2008).
[38]P. Błoński, S. Dennler, and J. Hafner, J. Chem. Phys. **134**, 034107 (2011).
[39]G. Kresse and J. Furthmüller, Comput. Mater. Sci. **6**, 15 (1996), Phys. Rev. B **54**, 11169 (1996).
[40]G. Kresse and D. Joubert, Phys. Rev. B **59**, 1758 (1999).
[41]J. P. Perdew and Y. Wang, Phys. Rev. B **45**, 13244 (1992).
[42]S. H. Vosko, L. Wilk, and M. Nusair, Can. J. Phys. **58**, 1200 (1980).
[43]P. E. Blöchl, Phys. Rev. B **50**, 17953 (1994).
[44]G. Kresse and O. Lebacq, vasp Manual, see http://cms.mpi.univie.ac.at/vasp/vasp/vasp.html.
[45]L. Kleinman, Phys. Rev. B **21**, 2630 (1980).
[46]A. H. MacDonald, W. E. Pickett, and D. D. Koelling, J. Phys. C **13**, 2675 (1980).
[47]D. Hobbs, G. Kresse, and J. Hafner, Phys. Rev. B **62**, 11556 (2000).
[48]M. Marsman and J. Hafner, Phys. Rev. B **66**, 224409 (2002).
[49]P. Błoński and J. Hafner, Phys. Rev. B **79**, 224418 (2009).
[50]M. H. Kang, S. C. Jung, and J. W. Park, Phys. Rev. B **82**, 085409 (2010).
[51]K. Sawada, F. Ishii, and M. Saito, Phys. Rev. B **82**, 245426 (2010).

Downloaded 16 Apr 2012 to 128.130.131.2. Redistribution subject to AIP license or copyright; see http://jcp.aip.org/about/rights_and_permissions

Pt_3 and Pt_4 clusters on graphene monolayers supported on a Ni(111) substrate: Relativistic density-functional calculations

Piotr Błoński[1,2] and Jürgen Hafner[1,a)]
[1]*Faculty of Physics and Center for Computational Materials Science, University of Vienna, Sensengasse 8/12, A-1090 Wien, Austria*
[2]*Institute of Chemical Research of Catalonia (ICIQ), Avgda. Països Catalans 16, E 43007 Tarragona, Catalonia, Spain*

(Received 13 April 2012; accepted 25 June 2012; published online 31 July 2012)

Density-functional theory including spin-orbit coupling and corrections for dispersion forces has been used to investigate the structural and magnetic properties of Pt_3 and Pt_4 clusters deposited on a graphene layer supported on a Ni(111) substrate. It is shown that the strong interaction of the Pt atoms with the Ni-supported graphene stabilizes a flat triangular and a slightly bent rhombic structure of the clusters. Pt atoms are located nearly on top of the C atoms of the graphene layer, slightly shifted towards the bridge positions because the Pt–Pt distances are larger than the C–C distances of the graphene sheet lattice-matched to the Ni support. The strong interaction with the substrate leads to a substantial reduction of both the spin and orbital moments of the Pt atoms, not only compared to the clusters in the gas-phase, but also compared to those adsorbed on a freestanding graphene layer. The trends in the magnetic moments and in the magnetic anisotropy of the cluster/substrate complex have been analyzed and it is demonstrated that the anisotropy is dominated by the Ni support.
© *2012 American Institute of Physics*. [http://dx.doi.org/10.1063/1.4737885]

I. INTRODUCTION

In a recently published series of papers we have used density-functional theory (DFT) to explore the structural and magnetic properties of small Pt_n clusters in the gas phase[1] and supported on a freestanding graphene layer.[2] We have been able to show that free Pt clusters carry a magnetic moment and that strong relativistic effects lead to the formation of a large orbital moment and a large magnetic anisotropy energy (MAE). The spin-orbit coupling influences not only the magnetic, but also the structural properties of the clusters, leading to a preference for planar structures for clusters consisting of up to five Pt atoms, in contrast to scalar relativistic calculations predicting three-dimensional structures for trimers and tetramers.[1] Pt clusters bind only weakly to a freestanding graphene layer via one or two Pt atoms and preserve large spin and orbital moments and a substantial MAE.[2] In contrast isolated Pt atoms and Pt_2 dimers deposited on a graphene layer supported on a Ni(111) substrate are predicted to be non-magnetic. Although graphene binds to the Ni surface only very weakly by dispersion forces (included in our DFT approach by semi-empirical corrections), an adsorbed Pt atom or dimer binds much more strongly to the support and induces also a locally enhanced interaction between graphene and Ni leading to a substantial buckling of the adlayer. The dimer on the graphene/Ni support is adsorbed in a flat configuration instead of an upright one on the freestanding graphene layer. While the isolated adatom and the flat dimer are non-magnetic, an upright dimer was found to be strongly magnetic.[3]

In the present work, we extend these investigations to Pt trimers and tetramers adsorbed on a graphene/Ni(111) support, motivated by the aim to find out whether for slightly larger clusters the large magnetic moments calculated for clusters in the gas phase or adsorbed on freestanding graphene layer persist or whether the influence of the Ni substrate is strong enough to completely quench the magnetic moment as for the adatom and the dimer. Our investigations are based on spin-polarized density functional theory including spin-orbit coupling (SOC) and semi-empirical dispersion corrections.[4,5] The fully relativistic approach permits to calculate the orbital moments and the MAE, the dispersion corrections provide an accurate description of the interaction between the graphene layer and the Ni substrate. The origin of the magnetic anisotropy and the contributions from the Pt clusters, the graphene layer and from the Ni substrate are analyzed in detail.

II. COMPUTATIONAL DETAILS

The electronic structure calculations and structural optimizations reported here are based on DFT as implemented in the Vienna *ab initio* simulation package VASP.[6,7] VASP is based on the projector augmented wave method[7,10] for describing the electron ion interactions. The basis set contained plane waves with a maximum kinetic energy of 500 eV. For electronic exchange and correlation effects the semi-local Perdew-Wang functional[8] in the generalized-gradient approximation (GGA) and the spin-interpolation proposed by Vosko *et al.*[9] were used. DFT calculations do not account for van der Waals (dispersion) forces. Dispersion corrections have been computed using the semi-empirical force-field proposed by

a)Electronic mail: juergen.hafner@univie.ac.at.

 © 2012 American Institute of Physics

Downloaded 21 May 2013 to 128.130.131.2. This article is copyrighted as indicated in the abstract. Reuse of AIP content is subject to the terms at: http://jcp.aip.org/about/rights_and_permissions

Grimme *et al.*[4,5] Grimme's DFT+d approach has been implemented in VASP code by Bučko *et al.*[11] and applied to calculate the structures and binding energies of a large number of solids where dispersion forces play an important role. For graphene layers supported on metallic substrates this approach has been shown[3] to be in good agreement with calculations using the computationally much more demanding random-phase approximation.[12]

Spin-orbit coupling has been implemented in VASP by Kresse and Lebacq,[13] following the approach of Kleinman[14] and MacDonald *et al.*[15] Calculations including spin-orbit coupling have been performed in the non-collinear mode implemented in VASP by Hobbs *et al.*[16] MAE's have been calculated as (i) total energy differences from self-consistent calculations for different orientations of the magnetic moments and (ii) using the magnetic force theorem.[17,18] The force theorem allows to calculate the MAE from the differences in the sum of the band energies from non-self-consistent calculations at a frozen potential and charge density.

The force theorem permits the elucidation of the electronic origin of the MAE via the decomposition of the MAE into contributions from the adsorbed cluster, the graphene layer and from the Ni substrate. Within this formalism, the MAE may be written as

$$\mathrm{MAE} = \sum_i \sum_{m_l=-2}^{2} \int_{E_B}^{E_F} (E - E_F) \Delta n^i_{m_l}(E) dE, \qquad (1)$$

where the sum is over all atoms in the supercell and over all angular momentum quantum numbers m_l, E_B is the energy at the bottom of the valence band, and where

$$\Delta n^i_{m_l}(E) = n^i_{m_l}(E; \mathrm{soft}) - n^i_{m_l}(E; \mathrm{hard}) \qquad (2)$$

is the difference in the partial local density of states for electrons with quantum number m_l at the site i for soft- and hard-axis magnetization. The orbital anisotropy $\Delta\mu_L = \mu_L^{\mathrm{soft}} - \mu_L^{\mathrm{hard}}$ may be calculated in terms of the difference in the occupation of states with $m_l = \pm 2, \pm 1$, i.e., according to

$$\Delta\mu_L = 2\mu_B \sum_i \sum_{m_l=1,2} \int_{E_B}^{E_F} \left[\Delta n^i_{m_l}(E) - \Delta n^i_{m_{-l}}(E)\right] dE. \qquad (3)$$

Note that a large contribution to the MAE requires a large value of $\Delta n^i_{m_l}(E)$, integrated over the valence band, irrespective of the value of m_l. A significant orbital anisotropy arises only if $\Delta n^i_{m_l}(E)$ is different for states with $m_l = \pm 1$ and/or $m_l = \pm 2$. One must also remember that the expression given for the orbital anisotropy is exact, whereas the force theorem leads only an approximate value for the MAE.

The results achieved with the force theorem are necessarily less accurate than those derived from total-energy differences. The determination of the partial contributions to the MAE from integrals over the difference in partial densities of state (DOS) involves a further approximation, because the plane wave components of the eigenfunctions have to be projected onto spherical waves within atomic spheres. A detailed comparative study of the impact of these approximations on calculations of the MAE has recently been published for Fe and Co adatoms on a Pt(111) surface.[19,20] For all further computational details we refer to our previous work.[3]

A. Structural model

The graphene/Ni(111) complex was represented by a periodically repeated unit cell containing the graphene layer supported on a slab with four Ni layers, containing 48 C-atoms in the graphene layer and 24 Ni atoms per layer of the substrate. Repeated slabs are separated by 20 Å of vacuum, so that the interaction between the repeated images is negligible. The Brillouin zone was sampled using $6 \times 6 \times 1$ Γ-centered k-point mesh and using a Gaussian smearing of 0.02 eV. Electronic DOS were calculated using the tetrahedron method.

Pt trimers adopt a triangular structure in the gas phase and adsorbed on a free graphene layer. We have examined two possible configurations: one with the Pt_3 triangle parallel to the graphene sheet and a second one where the triangle is perpendicular to the surface and binds to graphene only via one of its edges (as on the free graphene layer).

For free Pt_4 clusters scalar relativistic calculations predict that the equilibrium structure is a tetrahedron, with a flat rhombus being only slightly higher in energy.[1] If SOC is included, the planar structure is preferred. Upon adsorption on graphene the initially planar structure is distorted by a contraction along the long diagonal of the rhombus so that the two Pt atoms at its ends move to positions on top of C atoms, while the two atoms occupying the short diagonal move to a larger distance from the graphene layer.[2] The resulting structure is a bent rhombus, intermediate between the planar and tetrahedral structures[3], both have been used as starting configurations in the present work. The adsorbate/graphene complex was relaxed (keeping the Ni substrate frozen as obtained from the standard GGA calculations) until the forces on all atoms were less than 25 meV/Å. Simultaneously, the electronic and magnetic degrees of freedom were relaxed until the change in total energy between successive iteration steps was smaller than 10^{-7} eV.

III. RESULTS AND DISCUSSION

A. Pt trimers

The relaxed structures of triangular Pt_3 clusters with the Pt-plane parallel (a) or perpendicular (b) to the graphene layer are shown in Figure 1, the information on the adsorption energies and the relevant geometric parameters are compiled in Table I. A flat structure that allows a binding of all three Pt atoms with the graphene layer is lower in energy by 46 meV/Pt-atom than a perpendicular configuration where the cluster binds to the substrate only via one of its edges, as on a freestanding graphene layer. Of the two energies listed in Table I, E_{ad} measures the adsorption energy of the cluster relative to the clean graphene/Ni(111) surface and the gas-phase Pt_3 cluster, whereas E_{coh} measures the energy relative to the clean substrate and three isolated Pt atoms and hence accounts for the strength of the binding between the Pt atoms in the supported cluster. With $E_{\mathrm{ad}} = -1.222$ eV/Pt-atom the binding of the cluster to the substrate is significantly weaker than

Downloaded 21 May 2013 to 128.130.131.2. This article is copyrighted as indicated in the abstract. Reuse of AIP content is subject to the terms at: http://jcp.aip.org/about/rights_and_permissions

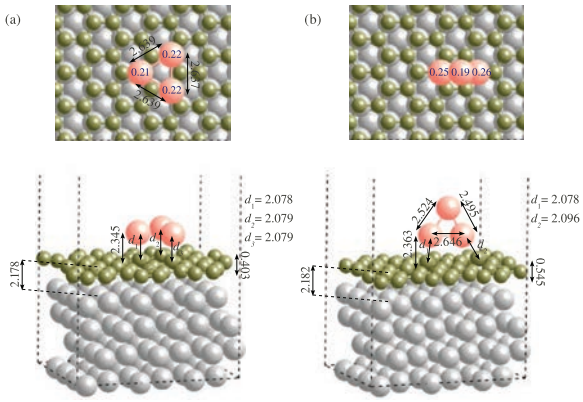


FIG. 1. Geometric structure of Pt_3 clusters. Distances are given in Å. Numbers on atoms give the values of the local spin moments as calculated in the scalar relativistic approach.

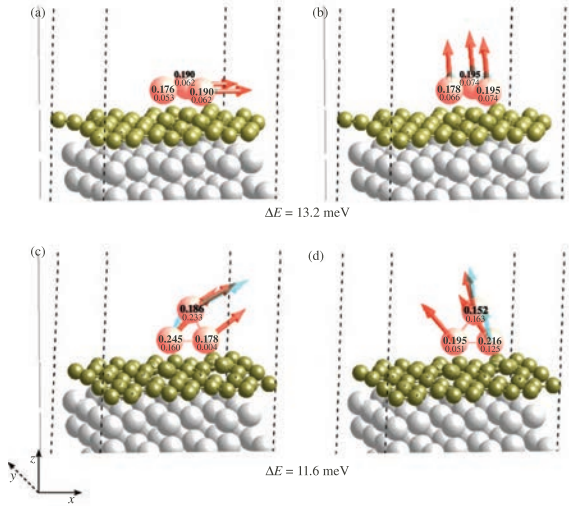


FIG. 2. Magnetic structure of Pt_3 clusters. Red (dark) arrows show spin magnetic moment and blue (light) arrows show the orbital magnetic moment; the numbers give the absolute values of the local spin (upper number) and orbital (lower number) magnetic moments μ_S^i and μ_L^i in μ_B.

for the dimer ($E_{ad} = -1.747$ eV/Pt-atom), but because E_{coh} increases by 0.045 eV/Pt-atom relative to the dimer and by 0.29 eV/Pt-atom relative to the monomer the formation of a trimer is energetically favored.

The threefold symmetry of the cluster is broken by a minimal difference of 0.02 Å in the Pt–Pt distances. The Pt atoms are located almost on top of the C atoms, slightly shifted towards the C–C bridge positions to admit for Pt–Pt distances of 2.639 Å (increased by 0.139 Å relative to the gas-phase cluster) which are larger than the C–C distances of 2.49 Å in the graphene layer lattice-matched to the Ni(111) support. The strong binding of the Pt_3 cluster to the substrate induces substantial distortions of the graphene layer. The Pt_3 triangle sits in the center of an extended depression of the graphene layer, the buckling amplitude of graphene is 0.40 Å. The C-atoms binding directly to the Pt atoms, however, are displaced outward relative to their neighbors but remain at a lower height than those at a large distance from the cluster.

In an upright triangle the Pt atoms forming the lower edge are again located close to on-top positions, slightly shifted towards the bridge (Pt–Pt distances of 2.646 Å, substantially increased compared to 2.54 Å in the upright cluster on graphene only). The Pt–C distances of the binding Pt-atoms are almost the same as for the flat triangle and only slightly increased by 0.024 Å compared to a flat dimer. The deformation of the graphene layer and of the Ni support is similar to that induced by a flat Pt-trimer, but with larger buckling amplitudes.

The spin-moments calculated in a scalar-relativistic approach reflect the broken symmetry of the Pt_3 triangles (see Figure 1). The spin-moments are only slightly changed if SOC is included, the magnetic structures for easy and hard magnetization directions are shown for both configurations in Figure 2. For the flat Pt trimer the easy magnetization direction is in-plane, the hard magnetic axis is perpendicular to the substrate. The spin and orbital moments per cluster are $\mu_S = 0.556\,\mu_B$ and $\mu_L = 0.177\,\mu_B$ for the easy and $\mu_S = 0.568\,\mu_B$ and $\mu_L = 0.214\,\mu_B$ for the hard magnetization direction, leading to negative spin and orbital anisotropies of $\Delta\mu_S = -0.012\,\mu_B$ and $\Delta\mu_L = -0.037\,\mu_B$. The spin moments in the top Ni layer vary for magnetization along the easy axis between 0.44 and 0.57 μ_B, i.e., they are reduced compared to their bulk value of 0.66 μ_B. The local distribution of the moments is similar to that reported for Pt adatoms and dimers on graphene/Ni(111), i.e., the lowest and largest values of the spin moment are found on the sites directly below the adsorbed Pt (see Figures 5 and 6 in Ref. 3). At a larger distance from the adsorbed cluster they converge to an intermediate value of 0.53 μ_B. The variation of the spin moments is already much smaller in the second Ni layer (between 0.60

TABLE I. The adsorption energy E_{ad} and the Pt–Pt binding energy E_{coh}, and the Pt–Pt bond length d_{Pt-Pt} of a Pt_3 trimer on graphene/Ni(111) for flat and upright geometries. z_{Pt-G} is the height of the (lower) Pt adatom above the average of the graphene-sheet, z_{G-Ni} is the average distance between the graphene and the top Ni layers, d_{Pt-C} is the distance between the (lower) Pt and the nearest C atom. b_C is the buckling amplitude of the graphene. Energies are given in eV/Pt-atom, distances in Å.

Geometry	Method	E_{ad}	E_{coh}	d_{Pt-Pt}	z_{Pt-G}	z_{G-Ni}	d_{Pt-C}	b_C
Flat	DFT+d	−1.222	−3.607	2 × 2.639, 2.637	2.35	2.18	2.08	0.40
Upright	DFT+d	−1.176	−3.561	2.646, 2.524, 2.495	2.36	2.18	2.08 2.10	0.55

Downloaded 21 May 2013 to 128.130.131.2. This article is copyrighted as indicated in the abstract. Reuse of AIP content is subject to the terms at: http://jcp.aip.org/about/rights_and_permissions

and 0.62 μ_B) the moments are converged to the bulk value from the third layer onwards. The orbital moments of the Ni atoms vary between 0.030 and 0.062 μ_B in the first, between 0.043 and 0.045 μ_B in the second, and 0.049 and 0.056 μ_B in the third layer. The anisotropy of the Ni spin moments is very weak, the orbital moments are slightly reduced for perpendicular magnetization, varying only between 0.034 and 0.045 μ_B in the first layer. The average orbital anisotropy is $\Delta\mu_L = 0.010\,\mu_B$ per Ni-atom. The MAE is 13.2 meV/cell or 0.089 meV/atom in the cluster/support complex (3 Pt, 48 C, and 96 Ni atoms). The contributions from cluster, graphene, and Ni support and the trends in the MAE with cluster size will be discussed below.

For the upright triangle the relativistic calculations initialized with the vector magnetic moment parallel to both the triangle and the graphene layer and parallel to the triangle, but perpendicular to the substrate converge to non-collinear stationary states are shown in Figures 2(c) and 2(d). In this case, we have calculated larger and positive spin and orbital anisotropies of $\Delta\mu_S = 0.046\,\mu_B$ and $\Delta\mu_L = 0.058\,\mu_B$. The reduction of the spin moments in the first Ni layer is smaller than below the flat Pt_3 cluster, varying between 0.47 and 0.65 μ_B, and converge more quickly towards the bulk value. Orbital moments of the Ni atoms are only marginally influenced by the configuration of the adsorbed Pt-cluster. The MAE between these two states is 11.6 meV/cell or 0.078 meV/atom.

For a Pt_3 cluster supported on a freestanding graphene layer a flat configuration is unstable, it relaxes to an upright triangle bound via one of its edges. The stationary magnetic configurations are also at least weakly non-collinear. In the magnetic ground state the magnetization direction is parallel to the graphene layer, but oblique to the triangle and parallel to the C–C bonds of the substrate [see Figure 6(a) of Ref. 2]. The total spin and orbital moments of 0.70 μ_B and 0.50 μ_B are larger by about 0.1 μ_B than in the presence of the Ni-support.

B. Pt tetramers

For a Pt_4 cluster the equilibrium configuration is an almost flat rhombus [see Figure 3(a)] with all four Pt atoms in or close to positions on top of C atoms in the graphene layer (the Pt atoms along the long diagonal are slightly shifted towards bridge positions). This configuration is only 9 meV/Pt-atom lower in energy than a trigonal Pt_4 pyramid with the Pt atoms forming the base located close to C atoms, slightly displaced towards the neighboring bridge positions [see Figure 3(b)].

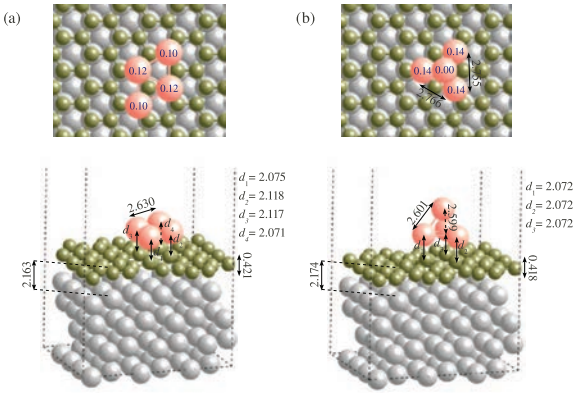


FIG. 3. Geometric structure of Pt_4 clusters. *Cf.* Fig. 1.

The adsorption energy per atom is slightly reduced compared to the smaller clusters, but the binding energy per Pt atom is larger so the Pt_4 cluster is stable against decomposition into smaller Pt ensembles (see Table II).

The Pt_4 rhombus is composed of two equilateral triangles with Pt–Pt distances of 2.630 Å, it is slightly bent because the two atoms occupying the short diagonal lie about 0.04 Å higher than those at the long diagonal which are shifted at bit more from on-top towards bridge positions. The structure of the three-dimensional Pt_4 cluster is a flattened trigonal pyramid with an edge length in the basis of 2.76 Å, longer than the edges connecting the top atom with the basis with 2.60 Å. The three Pt atoms forming the basis are 2.072 Å above their binding C-atoms. The threefold symmetry of the pyramid might be broken, but the differences in the Pt–Pt distances are at the margin of the computational accuracy and there are no differences in the heights of the Pt atoms above the substrate and in the spin moments.

In both configurations the Pt_4 cluster is located in the center of a sink in the graphene layer, as for the smaller clusters. This depression originates from the fact that due to the relatively strong binding between the adsorbed Pt and the C atoms, the graphene layer is locally electronically not saturated. Hence the binding between graphene and the Ni substrate in this region is promoted not only by dispersion forces as in the absence of adatoms, but also acquires a weak covalent component. The buckling amplitude of the graphene layer of about 0.4 Å is the same for both configurations and

TABLE II. The adsorption energy E_{ad} and the Pt–Pt binding energy E_{coh}, and the Pt–Pt bond length d_{Pt-Pt} of a Pt_4 tetramer on graphene/Ni(111) for flat and upright geometries. $z_{Pt\text{-}G}$ is the height of the (lower) Pt adatom above the average of the graphene-sheet, $z_{G\text{-}Ni}$ is the average distance between the graphene and the top Ni layers, d_{Pt-C} the distance between the (lower) Pt and the nearest C atom. b_C is the buckling amplitude of the graphene. Energies are given in eV/Pt-atom, distances in Å.

Geometry	Method	E_{ad}	E_{coh}	d_{Pt-Pt}	z_{Pt-G}	z_{G-Ni}	d_{Pt-C}	b_C
Flat rhombus	DFT+d	−1.128	−3.806	5 × 2.63	2.37	2.16	2 × 2.07, 2 × 2.12	0.42
pyramid	DFT+d	−1.119	−3.797	3 × 2.76 3 × 2.60	2.39	2.17	3 × 2.07, 2.10	0.42

Downloaded 21 May 2013 to 128.130.131.2. This article is copyrighted as indicated in the abstract. Reuse of AIP content is subject to the terms at: http://jcp.aip.org/about/rights_and_permissions

comparable to that induced by the smaller clusters. Further geometrical details are given in Table II.

The spin moments on the Pt atoms from scalar relativistic calculations are 2×0.10 and 2×0.12 μ_B for the rhombus and 3×0.14 and 0.10 μ_B for the pyramid. If SOC is taken into account, the spin moments in the flat cluster with in-plane magnetization (this is also the easy axis) are only slightly reduced to 2×0.090 and 2×0.081 μ_B, the orbital moments are 2×0.039 and 2×0.023 μ_B [see also Figure 4(a)]. The hard magnetic axis is out-of-plane. All local spin moments are reduced, but the orbital moments are reduced only on the sites along the long diagonal, but enhanced on the other two sites [see Figures 4(a) and 4(b)]. For the total cluster moments this leads to a substantial spin anisotropy of $\Delta\mu_S = 0.136\,\mu_B$ and a very low orbital anisotropy of $\Delta\mu_L = 0.022\,\mu_B$. The influence of the adsorbed cluster on the magnetic moments in the Ni layer is very similar to that reported for the smaller clusters, again we find an average modest orbital anisotropy of 0.01 μ_B on the Ni atoms. The MAE of the cluster/substrate complex is 15.5 meV/cell or 0.091 meV/atom.

For the three-dimensional Pt_4 cluster the magnetic structure becomes strongly anisotropic if SOC is included. For the in-plane easy magnetization direction the threefold symmetry is broken, the spin moments on the three Pt atoms in the basal triangle are 2×0.123 and 0.114 μ_B, whereas the Pt-atom on the top of the cluster becomes almost non-magnetic with $\mu_S = -0.009\,\mu_B$. With 2×0.046, 0.044, and 0.002 μ_B the distribution of the local orbital moments is very similar [see Figures 4(c) and 4(d)]. The hard magnetic axis is again out-of-plane, but the magnetic structure is slightly non-collinear, with the moments on the atoms in the basal plane slightly inclined towards the center of the pyramid. Both spin and orbital moments are smaller, leading to spin and orbital anisotropies of $\Delta\mu_S = 0.050\,\mu_B$ and $\Delta\mu_L = 0.011\,\mu_B$ which are much lower than for the flat cluster. This is also reflected in a lower MAE of 8.2 meV/cell or 0.057 meV/atom.

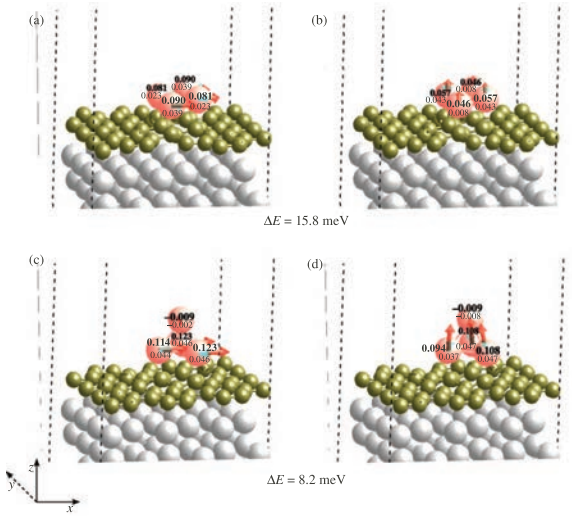


FIG. 4. Magnetic structure of Pt_4 clusters. *Cf.* Fig. 2

C. Trends in magnetic moments and anisotropy

It is interesting to confront the results for the magnetic properties of small Pt_n clusters in the gas phase with those modified by the interaction with a support. The electronic configuration of a Pt atom is $5d^9 6s^1$, which should yield spin and orbital moments of 1 μ_B each. DFT yields spin and orbital moments of 1.03 and 1.09 μ_B, respectively. For a Pt adatom on a freestanding graphene sheet, the magnetism is completely quenched while an adatom on a Ni-supported graphene layer has very small spin and orbital moments which are slightly larger for out-of plane (hard axis) magnetization (see Table III). For a gas phase dimer an easy magnetic direction has been found along the dimer axis, with spin and orbital moments which are much larger than for magnetization along the hard (perpendicular) direction. The stable configuration of a dimer on graphene is upright, perpendicular to the support and this is also the easy axis of magnetization—in agreement with the axial anisotropy of the free dimer. Spin and orbital moments are reduced and strongly anisotropic. If the graphene layer is supported on a Ni substrate, a flat Pt_2 dimer is lower in energy, and it is non-magnetic because magnetism is quenched by the much stronger binding to the substrate induced by the Ni support. An upright configuration exists as an excited state, the easy magnetic axis is again perpendicular to the substrate and parallel to the dimer axis, spin and orbital moments are further reduced compared to the same configuration on the free graphene layer (see Table III).

A Pt trimer in the gas-phase adopts a triangular configuration and has an in-plane easy axis. Spin and orbital moments are reduced compared to the dimer. The hard magnetic axis is perpendicular to the triangle, both spin and orbital moments are strongly anisotropic. On a free graphene sheet, the Pt_3 triangle is bound to the substrate only via one of its edges, resulting in an inhomogeneous distribution of the magnetic moments. Both spin and orbital components of the cluster moment are reduced by about 50% compared to the free cluster. The first excited magnetic state that determines the MAE is non-collinear with even slightly enhanced spin and orbital moments (details are given in Table III). On Ni-supported graphene a flat triangle is lower in energy, the easy magnetic axis is in plane, the hard one out of plane. The spin moment is reduced by the presence of the Ni support by about 20%, while the orbital moment is reduced by more than 50%. The spin moment is almost isotropic, the orbital moment is even slightly enhanced for magnetization along the hard direction.

The equilibrium structure of a Pt_4 tetramer is a flat rhombus, the magnetic ground state is antiferromagnetic.[1] As no antiferromagnetic configuration could be found for the supported tetramer, it is more meaningful to choose the lowest ferromagnetic state as a reference. The lowest energy ferromagnetic state of Pt_4 is found at an energy of 2.89 meV/Pt-atom above the ground state, this energy difference is lower than the MAE of the antiferromagnetic state of 4.35 meV/Pt-atom. It has a spin moment of 2.62 μ_B and an orbital moment of 1.42 μ_B. The easy magnetic axis is in plane, the hard axis perpendicular with a MAE of 8.72 meV/Pt-atom. The spin moment of the cluster has a modest negative anisotropy, in

Downloaded 21 May 2013 to 128.130.131.2. This article is copyrighted as indicated in the abstract. Reuse of AIP content is subject to the terms at: http://jcp.aip.org/about/rights_and_permissions

TABLE III. Spin and orbital moments μ_S and μ_L, and spin and orbital anisotropies $\Delta\mu_S$ and $\Delta\mu_L$, of Pt_n clusters, $n = 1$–4, in the gas phase (after Ref. 1), on a graphene layer (after Ref. 2), and on a graphene/Ni(111) support. All magnetic moments are given in μ_B.

System/structure	Magnetization direction	μ_S	μ_L	$\Delta\mu_S$	$\Delta\mu_L$
Pt atom		1.03	1.09		
Pt_1/graphene	Non-magnetic				
Pt_1/graphene/Ni	In plane[a]	− 0.018	0.008		
	Out of plane	− 0.022	0.021		
Pt_2 dimer	Axial[b]	1.88	2.74		
	Perpendicular	1.34	0.80	0.54	1.94
Pt_2/graphene	Out of plane[a]	1.30	1.70		
Upright	In plane	0.60	0.53	0.70	1.17
Pt_2/graphene/Ni	Non-magnetic				
Flat					
Pt_2/graphene/Ni	Out of plane[a]	0.92	1.17		
Upright[c]	In plane	0.49	0.36	0.43	0.81
Pt_3 trimer	In plane[d]	1.50	1.00		
Triangle	Out of plane	0.73	0.19	0.77	0.81
Pt_3/graphene	In plane[d]	0.70	0.44		
Upright triangle	Non-collinear	0.73	0.53	–0.03	–0.09
Pt_3/graphene/Ni	In plane[a]	0.56	0.18		
Flat triangle	Out of plane	0.57	0.21	− 0.01	− 0.04
Pt_4 tetramer	In plane[e]	2.62	1.42		
Rhombus (FM)	Perpendicular	2.72	0.96	− 0.10	0.46
Pt_4/graphene	In plane[a]	1.35	0.66		
Bent rhombus	Perpendicular	1.28	0.58	0.07	0.08
Pt_4/graphene/Ni	In plane[a]	0.34	0.12		
Bent rhombus	Perpendicular	0.21	0.10	0.13	0.12

[a]Relative to graphene layer.
[b]Relative to the dimer axis.
[c]Excited configuration.
[d]Relative to Pt_3 triangle.
[e]Relative to Pt_4 rhombus.

contrast to the much larger positive orbital anisotropy.[1] Upon adsorption on graphene, the Pt_4 rhombus is bent about the short diagonal, the easy magnetic axis is in plane. Both spin and orbital moments are reduced by about 50% upon adsorption, both show a modest positive anisotropy (see Table III). On a graphene layer supported on Ni, the geometry remains similar, but the bending of the rhombus is strongly reduced. For in-plane magnetization spin and orbital moments are reduced to less than 25% of the values on a free graphene layer. For the hard magnetization direction both components are further reduced.

The MAE of Pt_n clusters in the gas phase, supported on graphene and on graphene/Ni(111) are compiled in Table IV. For the clusters on the graphene/Ni support we have used both self-consistent total energy differences (TE) and the magnetic force theorem (FT) to determine the MAE and in addition we have estimated the contributions ΔE(i), i = Pt, C, Ni from the Pt_n cluster, the graphene layer and of the Ni support to the MAE from an integration over the projected partial DOS according to Eqs. (1) and (2). Note that since the partial DOS are based on a projection of plane wave onto spherical waves inside atom-centered

TABLE IV. Magnetic anisotropy energy MAE for Pt_n clusters in the gas-phase, adsorbed on a graphene sheet, and on a graphene layer deposited on a Ni(111) substrate, calculated as a total-energy difference (TE) or using the force theorem (FT) (in meV/cell). For clusters in the gas phase and adsorbed on a free graphene layer the MAE is measured relative to the ground state, for clusters supported on graphene/Ni(111) the MAE is always measured relative to in-plane magnetization. The contributions ΔE(i) of the Pt cluster, the graphene layer and of the Ni substrate to the MAE are calculated using the projected partial DOS [Eq. (4)] and given in meV/atom.

	Gas-phase	Pt_n/graphene	Pt_n/graphene/Ni(111)				
Pt_n	MAE(TE)	MAE(TE)	MAE(TE)	MAE(FT)	ΔE(Pt)	ΔE(gra)	ΔE(Ni)
Pt_0			13.9				
Pt_1			12.9	9.8	− 0.235	0.026	0.394
Pt_2 (upright dimer)	46.2	23.1	− 49.6	− 18.4	− 0.215	0.027	− 0.568
Pt_3 (triangle)	15.2	5.2	13.2	17.4	0.323	− 0.019	0.548
Pt_4 (rhombus)	8.7	2.6	15.8	23.9	0.152	− 0.019	0.932

Downloaded 21 May 2013 to 128.130.131.2. This article is copyrighted as indicated in the abstract. Reuse of AIP content is subject to the terms at: http://jcp.aip.org/about/rights_and_permissions

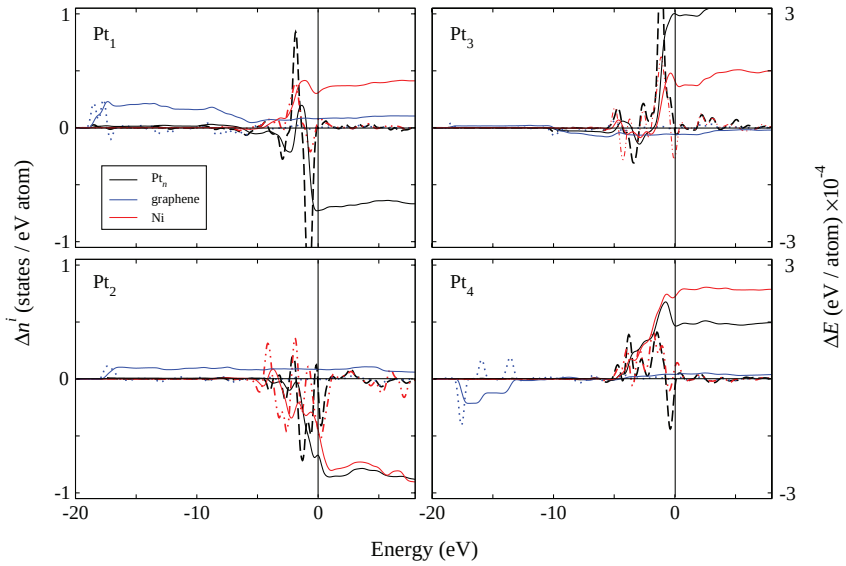


FIG. 5. Differences $\Delta n^i(E)$ in the projected electronic densities of states of Pt_n/graphene/Ni(111) clusters for soft- and hard-axis magnetization [as defined in Eq. (2)] for Pt (black dashed lines), C (blue dotted lines), and Ni (red dotted-dashed lines) atoms. The full lines show the integrated contributions to the decomposed MAE from the Pt cluster, the graphene layer, and the Ni substrate, calculated according to Eq. (1) and using the same color code. (a) Isolated Pt-adatom, (b) upright Pt_2 dimer, (c) flat Pt_3 trimer, and (d) flat Pt_4 tetramer.

spheres,

$$\mathrm{MAE}^{\star}(\mathrm{FT}) = N_{\mathrm{Pt}}\Delta E(\mathrm{Pt}) + N_{\mathrm{C}}\Delta E(\mathrm{gra}) + N_{\mathrm{Ni}}\Delta E(\mathrm{Ni}) \tag{4}$$

(where the N_{Pt}, N_{C}, and N_{Ni} are the number of atoms in the Pt-cluster, the graphene layer and in the Ni surface) can differ from MAE(FT) derived from the force theorem and the total DOS and that MAE(FT) might be less accurate than MAE(TE).

For the gas-phase clusters we note a strong decrease of the MAE from the dimer to the tetramer, parallel to a decrease in the orbital anisotropy.[1] Binding of the cluster to a graphene layer reduces the MAE by a factor of two for the dimer and by a factor of about three for the trimer and tetramer. However, one has to note that the binding of the cluster to the support via two Pt atoms only changes both the geometric and the magnetic structure.

The MAE of the clusters supported on the graphene/Ni(111) complex requires a more detailed analysis, because of the magnetism of both the adsorbed Pt cluster and the Ni support. A graphene-covered Ni(111) surface has a MAE of 13.8 meV/cell or 0.580 meV/surface-atom. An isolated Pt adatom is non-magnetic in the scalar-relativistic mode, but if SOC is included, the coupling to the magnetic substrate induces weak and slightly anisotropic spin and orbital moments leading to a slightly reduced MAE(TE) of 12.9 meV/cell. A calculation using the force theorem yields a value of MAE(FT) = 9.8 meV/cell, which illustrates the limitations of this approach. From the projected DOS we calculate contributions to the MAE of −0.235 meV/Pt-atom, 0.026 meV/C-atom, and 0.394 meV/Ni-surface-atom, together $\mathrm{MAE}^{\star}(\mathrm{FT}) = 10.46$ meV/cell. The very small contributions of the graphene layer to the MAE originate from very small induced magnetic moments on the C atoms, as discussed in more detail in Ref. 2. The $\Delta n^i_{m_l}(E)$ and the integrated contributions to the partial MAE's are shown in Figure 5. They show that the leading contributions to the MAE come from states close to the Fermi energy, changes in the electronic DOS at larger binding energies caused by the re-orientation of the magnetization direction cancel upon integration.

For the metastable upright Pt_2 dimer on graphene/Ni we have calculated a large perpendicular MAE(TE) = –49.6 meV/cell of a magnitude comparable to that of a gas-phase dimer and larger than that of a dimer on a free-standing graphene layer. In this case the force theorem yields only a qualitative agreement for the MAE, probably because the re-distribution of the electronic charge upon re-orientation of the magnetization is too large, see Table IV. Nevertheless, the decomposition of the MAE is instructive: the MAE per Pt atom is about the same as for the isolated adatom and is dramatically reduced compared to a dimer in the gas phase or on graphene only, but the contribution from the Ni substrate changes sign such that the large negative MAE is caused mainly by the Ni substrate. Figure 5(b) shows that the differences in the projected Ni-DOS as a function of the magnetization direction are rather pronounced even at higher binding energies. The analysis of the partial DOS of the flat dimer shows that the stronger interaction between dimer and support is reflected by a broadening of both the Pt and Ni states.

For a Pt_3 trimer in the gas phase and absorbed in a flat configuration on graphene/Ni the easy magnetic axis is in-plane, the MAE's are of comparable magnitude. However, the decomposition of the MAE yields contributions of 0.323 meV, −0.019 meV, and 0.548 meV per Pt, C, and Ni surface atom, adding to a value of 13.209 meV/cell which is in good

Downloaded 21 May 2013 to 128.130.131.2. This article is copyrighted as indicated in the abstract. Reuse of AIP content is subject to the terms at: http://jcp.aip.org/about/rights_and_permissions

agreement with the MAE from total-energy differences. The presence of the Pt trimer hardly affects the MAE determined by the Ni substrate. The MAE for the cluster on the free graphene layer is not directly comparable because it refers to entirely different magnetic structures. It is evident, however, that the presence of the magnetic support reduces the MAE per Pt-atom very strongly, from about 1.7 meV to 0.32 meV per Pt-atom.

For the tetramer, it is easier to compare the MAE's because its geometric structure is always a rhombus: flat for the gas-phase cluster, bent about the short diagonal for the clusters adsorbed on graphene or graphene/Ni. The decomposition of the MAE yields contributions per Pt-atom of 2.18 meV, 0.65 meV, and 0.15 meV for the free cluster and those supported on graphene and graphene/Ni, decreasing roughly parallel to the total magnetic moment of the cluster ($\mu_J = 4.04$, 2.01, 0.46 μ_B, respectively). The dominant contribution to the total MAE comes from the Ni substrate.

IV. CONCLUSIONS AND OUTLOOK

We have extended our investigations of Pt clusters on a graphene/Ni(111) support to trimers and tetramers. In both cases the clusters adopt a flat or nearly flat geometry, with the Pt atoms in positions slightly shifted from on-top of the C atoms towards bridge positions because of the mismatch between the Pt–Pt distances and the C–C distances lattice-matched to the Ni support. The flat geometry is stabilized by a much stronger binding of the Pt clusters to graphene/Ni(111) than to a freestanding graphene layer where the clusters are bound to the layer only via a Pt–Pt edge. For the Pt_4 cluster, however, the flat, slightly bent rhombus is only 9 meV/Pt-atom lower in energy than a trigonal pyramid. Due to the interaction with the adsorbate the C atoms in the graphene layer are locally electronically not saturated and this leads also to an enhanced interaction with the Ni support and a local deformation of the graphene sheet.

While for isolated adatoms and dimers the interaction with the support led to a complete quenching of the magnetism of the adsorbate, Pt trimers and tetramers are found to be magnetic, albeit with spin and orbital moments which are strongly reduced compared to the free clusters and also relative to those adsorbed on a freestanding graphene sheet. The reduction of the magnetic moments leads also to a very strongly reduced magnetic anisotropy of the Pt clusters. The analysis of the MAE shows that the magnetic anisotropy of the Pt_n/graphene/Ni(111) complex is dominated by the Ni support. Although the SOC is much stronger and the orbital moment is still larger for Pt than for Ni, the contribution to the MAE per Pt atom is lower than that per Ni atom at the interface with graphene. Only for the metastable upright Pt_2 dimer the spin and orbital moments on the Pt atoms are large enough to reverse the sign of the magnetic anisotropy of the graphene-covered Ni-substrate.

We expect that for larger Pt-clusters the strong interaction between the adatoms will stabilize three-dimensional cluster structures. However, in the case of the Pt_4 pyramid with a non-magnetic atom at the apex suggests that this will not lead to a stabilization of magnetism of the clusters. To create magnetic clusters of heavy elements with a strong SOC which can be expected to show a large magnetic anisotropy doping with strongly magnetic atoms could be an issue. At this point it is useful to recall earlier studies of the adsorption of adatoms and dimers on graphene.[21,22] Chan *et al.* have reported that while the adsorption of Fe adatoms is much stronger in a six-fold hollow, Pd adatoms are preferentially located in a bridge site (with an on-top site having an only slightly higher energy, in agreement with our studies).[21] Recently Johll *et al.*[22] studied the adsorption adatoms and dimers of Fe, Co, and Ni on graphene. Adatoms bind weakly in hollows, their spin moment is reduced by about 2 μ_B compared to the free atom, Ni adatoms are non-magnetic. Homonuclear dimers bind weakly in an upright position in the center of a hollow, with only very modest changes in the magnetic moment and bond length relative to the free dimers. The same conclusion holds also for heteroatomic dimers where the configuration with the atoms with more d electrons attached to graphene is found to be more stable. For heteroatomic dimers of a 3d atom with Pt the picture is more complex: for a Fe-Pt dimer upright configurations with the lower Pt atom bound in a top or bridge site and a magnetic moment of about 4 μ_B is most stable. Co-Pt and Ni-Pt dimers prefer to bind through the 3d atom to a hollow site, with magnetic moments of about 3 μ_B and 2 μ_B, respectively. This means that relative to the free 3d atom, the magnetic moment of the dimer is in each case enhanced by about 1 μ_B. The influence of SOC has not been investigated as yet, but mixed clusters combining one element with a large spin moments and one with a strong SOC seem to provide a way to create nanostructured clusters with a large magnetic anisotropy energy. We will follow this path in future research.

ACKNOWLEDGMENTS

Work at the Universität Wien has been supported through the VASP project.

[1] P. Błoński, S. Dennler, and J. Hafner, J. Chem. Phys. **134**, 034107 (2011).
[2] P. Błoński and J. Hafner, J. Chem. Phys. **134**, 154705 (2011).
[3] P. Błoński and J. Hafner, J. Chem. Phys. **136**, 074701 (2012).
[4] S. Grimme, J. Antony, T. Schwabe, and C. Mück-Lichtenfeld, Org. Biomol. Chem. **5**, 741 (2007).
[5] S. Grimme, J. Antony, S. Ehrlich, and H. Krief, J. Chem. Phys. **132**, 154104 (2010).
[6] G. Kresse and J. Furthmüller, Comput. Mater. Sci. **6**, 15 (1996); Phys. Rev. B **54**, 11169 (1996).
[7] G. Kresse and D. Joubert, Phys. Rev. B **59**, 1758 (1999).
[8] J. P. Perdew and Y. Wang, Phys. Rev. B **45**, 13244 (1992).
[9] S. H. Vosko, L. Wilk, and M. Nusair, Can. J. Phys. **58**, 1200 (1980).
[10] P. E. Blöchl, Phys. Rev. B **50**, 17953 (1994).
[11] T. Bučko, S. Lebègue, J. G. Ángyán, and J. Hafner, J. Phys. Chem. A **114**, 11814 (2010).
[12] F. Mittendorfer, A. Garhofer, J. Redinger, J. Klimeš, J. Harl, and G. Kresse, Phys. Rev. B **84**, 201401(R) (2011).
[13] G. Kresse and O. Lebacq, VASP Manual, see http://cms.mpi.univie.ac.at/vasp/vasp/vasp.html.
[14] L. Kleinman, Phys. Rev. B **21**, 2630 (1980).
[15] A. H. MacDonald, W. E. Pickett, and D. D. Koelling, J. Phys. C **13**, 2675 (1980).
[16] D. Hobbs, G. Kresse, and J. Hafner, Phys. Rev. B **62**, 11556 (2000).

Downloaded 21 May 2013 to 128.130.131.2. This article is copyrighted as indicated in the abstract. Reuse of AIP content is subject to the terms at: http://jcp.aip.org/about/rights_and_permissions

[17] A. R. Mackintosh and O. K. Andersen, in *Electrons at the Fermi Surface*, edited by M. Springford (Cambridge University Press, London, 1980), Sec. 3.1.
[18] V. Heine, Solid State Phys. **35**, 114 (1980).
[19] P. Błoński and J. Hafner, J. Phys.: Condens. Matter **21**, 426001 (2009).
[20] P. Błoński, A. Lehnert, S. Dennler, S. Rusponi, M. Etzkorn, G. Moulas, P. Bencok, P. Gambardella, H. Brune, and J. Hafner, Phys. Rev. B **81**, 104426 (2010).
[21] K. T. Chan, J. B. Neaton, and M. H. Cohen, Phys. Rev. B **77**, 235430 (2008).
[22] H. Johll, H. C. Kang, and E. S. Tok, Phys. Rev. B **79**, 245416 (2009).

Downloaded 21 May 2013 to 128.130.131.2. This article is copyrighted as indicated in the abstract. Reuse of AIP content is subject to the terms at: http://jcp.aip.org/about/rights_and_permissions

IOP Publishing Journal of Physics: Condensed Matter
J. Phys.: Condens. Matter **26** (2014) 146002 (12pp) doi:10.1088/0953-8984/26/14/146002

Magnetic anisotropy of heteronuclear dimers in the gas phase and supported on graphene: relativistic density-functional calculations

Piotr Błoński[1, 2] **and Jürgen Hafner**[1]

[1] University of Vienna, Faculty of Physics and Center for Computational Materials Science, Sensengasse 8/12, A-1090 Wien, Austria
[2] Institute of Nuclear Physics, Polish Academy of Sciences, ul. Radzikowskiego 152, PL-31-342 Kraków, Poland

Received 7 May 2013, revised 14 January 2014
Accepted for publication 29 January 2014
Published 20 March 2014

Abstract

The structural and magnetic properties of mixed PtCo, PtFe, and IrCo dimers in the gas phase and supported on a free-standing graphene layer have been calculated using density-functional theory, both in the scalar-relativistic limit and self-consistently including spin–orbit coupling. The influence of the strong magnetic moments of the 3d atoms on the spin and orbital moments of the 5d atoms, and the influence of the strong spin–orbit coupling contributed by the 5d atom on the orbital moments of the 3d atoms have been studied in detail. The magnetic anisotropy energy is found to depend very sensitively on the nature of the eigenstates in the vicinity of the Fermi level, as determined by band filling, exchange splitting and spin–orbit coupling. The large magnetic anisotropy energy of free PtCo and IrCo dimers relative to the easy direction parallel to the dimer axis is coupled to a strong anisotropy of the orbital magnetic moments of the Co atom for both dimers, and also on the Ir atom in IrCo. In contrast the PtFe dimer shows a weak perpendicular anisotropy and only small spin and orbital anisotropies of opposite sign on the two atoms. For dimers supported on graphene, the strong binding within the dimer and the stronger interaction of the 3d atom with the substrate stabilizes an upright geometry. Spin and orbital moments on the 3d atom are strongly quenched, but due to the weaker binding within the dimer the properties of the 5d atom are more free-atom-like with increased spin and orbital moments. The changes in the magnetic moment are reflected in the structure of the electronic eigenstates near the Fermi level, for all three dimers the easy magnetic direction is now parallel to the dimer axis and perpendicular to the graphene layer. The already very large magnetic anisotropy energy (MAE) of IrCo is further enhanced by the interaction with the support, the MAE of PtFe changes sign, and that of the PtCo dimer is reduced. These changes are discussed in relation to the relativistic electronic structure of free and supported dimers and it is demonstrated that the existence of a partially occupied quasi-degenerate state at the Fermi level favors the formation of a large magnetic anisotropy.

Keywords: clusters, magnetic moments, magnetic anisotropy, spin–orbit coupling

S Online supplementary data available from stacks.iop.org/cm/26/146002/mmedia

(Some figures may appear in colour only in the online journal)

1. Introduction

The search for materials to allow an increased density of information per square inch in magnetic storage media has stimulated intense research efforts in the field of magnetic nanostructures. The quantity of central interest is the magnetic anisotropy energy (MAE), which determines the stability of the induced direction of magnetization against

 © 2014 IOP Publishing Ltd Printed in the UK

thermally induced excitations. A high MAE requires large spin and orbital magnetic moments per atom and a strong spin–orbit coupling (SOC). 3d transition metal atoms carry large magnetic moments, but SOC is weak. SOC is strongest among the heavy 5d elements which are non-magnetic in the bulk. However, these elements may become magnetic in nanostructures like small clusters. Therefore, bimetallic nanostructures consisting of ferromagnetic 3d- and heavy 5d-elements could eventually provide a feasible route towards materials with tailored magnetic properties.

Enhanced orbital moments and magnetic anisotropy energies have been reported in experimental and theoretical studies of Fe(Co)–Pt multilayers and nanoparticles [1–8]. The investigations have concentrated on nanoparticles with diameters of a few nm and consisting of several hundreds of atoms. It is generally agreed that the magnetic properties depend on a competition between structure, chemical ordering, morphology, twinning and segregation. Theoretical studies have emphasized the importance of the hybridization between the 3d and 5d orbitals and of ligand effects for the formation of large orbital moments and a high MAE [9–11]. Chepulskii and Butler [7] have calculated the MAE for FePt nanoslabs and nanocrystals with a chemical ordering corresponding to $L1_0$-type alloys. For clusters with 20 or more atoms an MAE comparable to that of bulk $L1_0$ FePt alloys (∼1.3–1.4 meV/atom [12], extrapolated to $T = 0$ K as described in [13]) or even smaller was reported. For octahedral Fe_3Pt_3 and tetrahedral Fe_2Pt_2 clusters very large MAE's of about 10 meV/atom have been found. However, these results refer to idealized cluster geometries and fixed bulk-like interatomic distances. The effect of the interaction between 3d and 5d atoms on the magnetic properties has also been investigated by Sahoo *et al* [14] using the example of Pt–capped Fe clusters. It was shown that the capping by Pt leads to an enhancement of the orbital magnetic moment and a reduction of the spin moment of the cluster. The MAE was calculated only for a $Fe_{13}Pt_4$ cluster and found to be enhanced by a factor of ten to 7 meV/cluster compared to the value in the absence of the capping atoms. It was also emphasized that the breaking of the icosahedral symmetry due to the presence of the capping atoms is instrumental in promoting an enhanced MAE.

Very recently calculations by Xiao *et al* [15] have suggested that in free bimetallic dimers containing 3d Co and 5d Ir atoms the MAE can be as large as 0.15 eV/dimer. Moreover, the adsorption of the dimer in an upright position in the center of a hexagonal carbon-based substrate, e.g. on a benzene molecule or a graphene monolayer, with the Co atom binding to the support and the Ir atom pointing away from the carbon ring, results in a theoretical MAE of about 0.2 eV/dimer, even exceeding the value calculated for the gas phase dimer.

In our recently published articles [16–19] we have theoretically studied the magneto-structural properties of small Pt clusters in the gas phase [16], supported on a free-standing graphene sheet [17] and on a graphene layer deposited on a Ni(1 1 1) substrate [18, 19]. For free Pt_n clusters SOC stabilizes large orbital moments (which may be of the same order of magnitude as the spin moments) and a large MAE of several meV/atom, comparable to the energy difference between different magnetic isomers. For the smallest clusters up to the pentamer SOC also stabilizes planar structures over three-dimensional geometries [16].

The weak binding of the clusters to a free-standing graphene layer via only one or two Pt atoms preserves the equilibrium structure of the gas phase clusters, but their magnetic structure is much more inhomogeneous than in the gas phase, with a non-collinear orientation of the magnetic moments and a reduced anisotropy energy [17]. The magnetic moments on the Pt atoms binding to the support are strongly quenched, leading to a reduction in the cluster moments to about half their size in the gas phase and an MAE reduced to roughly one third.

An even more complex picture emerges for clusters deposited on a graphene-covered Ni substrate [18, 19]. The adsorbed cluster induces a locally enhanced interaction between the graphene layer and the Ni substrate, leading also to a stronger binding between the cluster and graphene. This results in a strong buckling of the graphene layer and of the top layers of the substrate, a stabilization of flat, two-dimensional structures of the clusters and substantial further quenching of their spin and orbital moments. Isolated Pt atoms and Pt_2 dimers on graphene/Ni(1 1 1) are nonmagnetic, supported trimers and tetramers are still weakly magnetic but the magnetic anisotropy of the cluster/support complex is dominated by that of the graphene-covered Ni(1 1 1) surface [19].

In the present work we have investigated the magnetic properties of heteronuclear Pt–Co, Pt–Fe and Ir–Co dimers (included to permit a comparison with the work of Xiao *et al* [15] and a systematic analysis of trends), both in the gas phase and adsorbed on a graphene monolayer. Recently Johll *et al* [20, 21] have reported density-functional calculations of atoms and small clusters of the magnetic 3d metals Fe, Co and Ni on graphene. It was shown that the binding to the substrate is relatively weak, such that relatively large magnetic moments are preserved. The moments on the atoms binding to the graphene layer are reduced, but large moments comparable to those in the gas phase are found on the atoms on top of an upright dimer. Thus, the total moment of the supported dimer is even larger than that calculated for the free dimer. However, the calculations were performed only in a scalar-relativistic mode so that orbital moments and magnetic anisotropy were not calculated. Nonetheless, the result that large spin moments exist in graphene-supported 3d clusters is encouraging. Here we have investigated the possibility that the combination of a large spin moment contributed by the 3d atoms with a large orbital moment and strong SOC of the 5d atom leads to an enhanced magnetic anisotropy of free and graphene-supported mixed Pt–Fe and Pt–Co dimers.

2. Computational method

2.1 Density-functional theory verses quantum-chemical methods

The properties of the smallest transition-metal clusters can be calculated either using high-level quantum-chemical methods or using density-functional theory (DFT). For quantum-chemical methods a high-level description of electronic correlation is required, and their advantage is that

the multiplet character of ground and excited states can be resolved. Within DFT the variables determining the effective potential (charge and spin densities) are calculated as averages over occupied orbitals. The lack of orbital dependence of the potential prevents a determination of the multiplet structure, but the big advantage is the much lower computational workload, which alone permits an application to clusters supported on extended substrates. Even for the problematic case of the Fe_2 dimer the results for integral properties (magnetic moment, bond length, etc) achieved using both techniques are comparable. Calculations performed using various variants of multi-reference configuration-interaction (MR-CI) methods [22–27] found spin multiplicity 7 or 9 for the ground state (GS). Coupled-cluster [CCSD(T)] calculations [28] reported the nonet state to be lower in energy. The discrepancies have been discussed in detail by Angeli and Cimiraglia [27] who argued that the difficulty in uniquely determining the GS is related to a discontinuity in the total energy of the septet state as a function of bond length and could be resolved only by using a much larger active space, which is not possible at the moment. Quantum Monte Carlo calculations by Casula *et al* [29] also reported both spin states to be very close in energy and presented arguments in favor of a septet GS. Density-functional calculations predict a GS with spin multiplicity 7 if a semilocal exchange-correlation functional is used, and spin multiplicity 9 if a hybrid–functional mixing DFT and Hartree-Fock exchange is used [24, 31, 32]. DFT calculations combined with a Hubbard U correction [28] found the nonet state to be energetically favored. DFT calculations including an orbital polarization correction [30] predict a septet state. The bond length calculated using the MR-CI variants is 2.19 Å for the nonet state, 2.06 Å for the septet state, 1.98–2.03 Å using DFT with semilocal functionals, 1.96 Å if orbital polarization is included and 2.14 Å with hybrid-DFT, to be compared with an experimental bond length [33] of 2.02 ± 0.02 Å.

For the calculation of the orbital moments and of the MAE an accurate treatment of relativistic effects, including SOC, is required. For Pt_2 first-order CI calculations using relativistic core potentials and a partial inclusion of SOC have been performed by Balasubramanian [34]. Lee *et al* [35] have presented first-order CI calculations including SOC in two-component relativistic spinor calculations and corrections for dynamical correlations using restricted coupled-cluster methods, and Varga *et al* [36] have performed four-component relativistic density-functional calculations with a generalized-gradient approximation (GGA) functional to be compared with the present work. All calculations agree on a triplet GS, with bond lengths of 2.32, 2.38 and 2.39 Å found in the three quantum-chemical calculations and 2.38 Å in the present DFT work, in reasonable agreement with the experimental value [37] of 2.33 Å. Again we find good agreement between quantum chemistry and DFT, as well as between the two- and four-component relativistic calculations and the implementation of SOC described below.

The foregoing brief comparison shows that for difficult cases such as Fe_2 the relative merits of different variants of quantum-chemical and DFT calculations is still open to debate. The combination of higher level treatments of electronic correlation with relativistic calculations accounting for SOC appears to be difficult and feasible (if at all) only for fixed geometries. Approximate treatments of correlation such as DFT+U depend on semi-empirical values of U whose transferability between different systems is questionable. Given the need to perform an accurate structural optimization of the dimer/substrate complex and our wish to analyze trends in different combinations of 3d and 5d atoms, we decided to use DFT with a semilocal GGA functional. However, one must be aware that DFT probably delivers only a lower limit of the MAE.

2.2 Details of density-functional calculations

Our investigations are based on spin-polarized DFT as implemented in the Vienna Ab-initio Simulation Package VASP [38, 39]. The electron–ion interactions were described using the projector-augmented wave (PAW) method [39, 40]. The basis set contained plane waves with a maximum kinetic energy of 500 eV. For electronic exchange and correlation effects we chose the functional of Perdew, Burke, and Ernzerhof (PBE) [41] in the GGA and the spin-interpolation proposed by Vosko *et al* [42].

SOC has been implemented in VASP by Kresse and Lebacq [43] following the approach of Kleinman and Bylander [44] and MacDonald *et al* [45]. Calculations including SOC have been performed in the non-collinear mode as implemented in VASP by Hobbs *et al* [46].

The calculations have been started in a scalar-relativistic mode, performing a full structural optimization of the free cluster or cluster/substrate complex using a quasi-Newton method until the forces on all atoms were less than 25 meV/Å. Simultaneously, the electronic and magnetic degrees of freedom were relaxed until the change in total energy between successive iteration steps was smaller than 10^{-7} eV. In the second step a self-consistent relativistic calculation including SOC was started from the relaxed configuration of the scalar-relativistic mode, allowing again for the simultaneous optimization of all geometric, electronic and magnetic degrees of freedom. Magnetic anisotropy energies have been calculated as total energy differences from self-consistent calculations for different orientations of the magnetic moments. Spin and orbital magnetic moments of the clusters have been calculated as the difference in the number of electrons in occupied majority- and minority-spin states. Local spin and orbital moments were calculated by projecting the plane-wave components of the eigenstates onto spherical waves in atom-centered atomic spheres.

The atomization energy of a free AB dimer (A = Pt,Ir, B = Co, Fe) is calculated as the total energy of the isolated atoms minus the energy of the dimer,

$$E_{\mathrm{at}} = E(\mathrm{A}) + E(\mathrm{B}) - E(AB)\,. \qquad (1)$$

The adsorption energy (equal to the negative atomization energy) for an AB dimer on graphene is calculated as the total energy of the dimer–graphene complex, $E(\mathrm{A})_{\mathrm{graph}}$, minus the energy of the clean graphene layer, E (graph), and the total GS energy of the dimer in the gas phase,

$$E_{\text{int}} = E(AB)_{\text{graph}} - E(\text{graph}) - E(AB)\,. \qquad (2)$$

The energy defined by equation (2) measures the *interaction* energy of dimers with the graphene sheet. E_{int} consists of a negative contribution from the energy gained by forming dimer–substrate bonds, and positive contributions from the elastic distortions of both dimer and graphene and (for different magnetic isomers) from the magnetic energy difference. The atomization energy of atoms from the adsorbed dimer is measured by the energy of the graphene layer and the energy of the free A and B atoms, minus the total energy of the adsorption complex,

$$E_{\text{at-ad}} = E(\text{graph}) + E(A) + E(B) - E(AB)_{\text{graph}}\,. \qquad (3)$$

The Brillouin zone was sampled using $6\times6\times1$ Γ-centered k-point mesh and a Gaussian smearing of 0.02 eV. Electronic densities of states (DOS) were calculated using the tetrahedron method. Local and partial DOS have been calculated by projecting the plane-wave components onto spherical waves inside atomic spheres. For all further computational details we refer the readers to our previous publications [16, 18, 31].

2.3 Structural model

The graphene layer was represented by a periodically repeated unit cell containing 48 C-atoms and 20 Å of vacuum, so that the interaction between the repeated images is negligible. Gas phase clusters have been placed into the center of a large periodically repeated cubic box with edges of 15 Å, which ensures that the separation between the periodically repeated images of the cluster is large enough to suppress any interactions.

The relaxed C–C distance in a clean graphene layer is 1.414 Å, in very good agreement with the experimental value. For the adsorbate–graphene complex the lattice constants of the computational supercell have been fixed at their equilibrium values for clean graphene, but the coordinates of all C and metal atoms have been relaxed without any symmetry constraint.

The calculations have been performed for PtFe, PtCo and IrCo dimers. For reference, results for the magnetic anisotropy of free homoatomic dimers are available from our earlier work [31], results for Pt_2 dimers on graphene have already been published [17], for Ir_2/graphene they are presented for completeness below. For dimers adsorbed on a graphene layer we have examined four possible starting configurations: an upright dimer in the center of an hexagonal ring with either the 3d or the 5d atom binding to the support, and a dimer placed parallel to the substrate with the atoms either in bridge (br) positions between or on top (ot) of C atoms.

3. Magnetic anisotropy of homoatomic dimers

3.1 Fe_2 and Co_2 dimers

Clusters formed by the ferromagnetic metals Fe, Co and Ni have been studied repeatedly using the density functional method (for a compilation of the literature see, e.g., the papers of Johll *et al* [20, 21]). The scalar-relativistic calculations agree on the large spin moments of the dimers ($6\mu_B$ for Fe_2, $4\mu_B$ for Co_2). Relativistic calculations for dimers of all elements of the Fe-, Co-, and Ni-groups have been published in our earlier work [31]. For Fe_2 the spin moment is slightly reduced to $m_S = 5.84\ \mu_B$, combined with a modest orbital moment of $m_L = 0.32\ \mu_B$. The easy axis is parallel to the Fe-Fe bond, a small MAE of 0.3 meV is correlated with a modest orbital anisotropy of $\Delta m_L = 0.16\,\mu_B$. For Co_2 the spin moment is also slightly reduced to $m_S = 3.90\ \mu_B$, a larger orbital moment of $m_L = 0.78\ \mu_B$ in the axial ground state is correlated to a larger MAE of 7.1 meV and a larger orbital anisotropy of $\Delta m_L = 0.46\,\mu_B$. The spin moment is isotropic for both dimers.

Scalar-relativistic calculations for graphene-supported Fe_2 and Co_2 dimers have been reported by Johll *et al* [20, 21] and Yagi *et al* [51], and for Fe_2 dimers by Longo *et al* [49] and by Srivastava *et al* [50]. For the Fe dimers where a comparison is possible, the results are widely divergent. For the Fe_2 dimer Johll *et al* and Srivastava *et al* predict an upright geometry centered at a sixfold hole at a height of 1.86 Å with a binding energy of $E_{\text{int}} \sim 0.7$ eV/dimer, a Fe-Fe distance of 2.08 and 2.07 Å and moments 3.48 (2.76) μ_B for the upper (lower) Fe atom and a total moment of $6.16\,\mu_B$. Longo *et al* found a flat-lying dimer with both Fe atoms located close to a hollow and moments of $3.44\,\mu_B$. These results merely emphasize how difficult it is to find the correct equilibrium geometry of adsorbed clusters. For Co_2 Johll *et al* [20] reported a stable upright configuration centered in a sixfold hole at a height of 1.72 Å with a binding energy of $E_{\text{int}} = 0.92$ eV/dimer. The spin moments are $2.43(1.66)\,\mu_B$ at the upper (lower) atom. Similar results for both dimers have been reported by Yagi *et al* [51].

3.2 Pt_2 and Ir_2 dimers

Results for the gas phase dimers have been published in our earlier work [31]. For Ir_2 scalar-relativistic calculations predict a quintet state. If SOC is included, the spin moment of $m_S = 3.88\mu_B$ remains almost unchanged and in addition a large orbital moment of $m_L = 1.96\mu_B$ is calculated. The easy magnetic direction parallel to the dimer axis is stabilized by a large MAE of 70 meV/dimer, and is correlated to large anisotropies of both spin and orbital moments ($\Delta m_S = 0.46\,\mu_B$, $\Delta m_L = 1.02\,\mu_B$). For Pt_2 the scalar-relativistic GS is a triplet; if SOC is included the moments are $m_S = 1.88\ \mu_B$, $m_L = 2.74$. The large axial MAE of 46 meV/dimer is correlated to even larger anisotropies of both spin and orbital moments, $\Delta m_S = 0.54\,\mu_B$, $\Delta m_L = 1.94\,\mu_B$.

Results for graphene-supported Pt clusters have been presented in [17]. At a coverage of one dimer per 48 C atoms (the same as used here) the Pt_2 dimer is weakly bound ($E_{\text{int}} = -0.96$ eV/dimer) in an upright configuration in a C-C bridge site at a height of 2.26 Å. The moments on the Pt atom binding to the substrate are quite strongly quenched, $m_S = 0.83(0.47)\ \mu_B$, $m_L = 1.13(0.57)\mu_B$ on the upper(lower) atom for the easy magnetization direction along the dimer axis and perpendicular to the substrate. The hard direction perpendicular to the Pt–Pt and C–C bonds and parallel to the graphene layer is disfavored by a reduced MAE of 12 meV/dimer and correlated to local spin and orbital anisotropies of $\Delta m_S = 0.33(0.37)\,\mu_B$ and $\Delta m_L = 0.41(0.76)\,\mu_B$ on the two

atoms. For hard-axis orientation the orbital moment is even antiparallel to the local spin moment. The properties of the supported Pt_2 dimer are coverage-dependent—at a reduced coverage of one dimer per 96 C atoms, the binding to the substrate is stronger by about 15% (as measured by the binding energy) and a reduced distance from the substrate of 2.11 Å is correlated to a total moment reduced from about $2\mu_B$ to $\sim 1.5\mu_B$. For the hard direction parallel to graphene, the magnetism of the dimer is even completely quenched.

In contrast to Pt, the magnetism of the Ir_2 dimer is found to be extremely sensitive to the interaction with a support. Xiao *et al* [15] have reported that a Ir_2 dimer bound in an upright configuration to the center of a benzene ring is nonmagnetic. Our scalar-relativistic calculations confirm that the stable adsorption configuration of the dimer on graphene is in the center of a sixfold hollow, perpendicular to the graphene layer. In accordance with the results for the benzene-supported dimer, the adsorption complex was found to be nonmagnetic. The spin moment on the Ir atom bound to graphene is zero, while for the upper Ir atom a very small moment of about $0.1\mu_B$ has been calculated. The weak moments on the dimer are compensated by very small negative induced moments on the surrounding C atoms, such that the total moment of the dimer/substrate complex is zero. As the scalar-relativistic calculations show that the magnetism of the Ir_2 dimer is destroyed by the interaction with an inert substrate, no calculations including SOC have been performed.

3.3 Trends in the MAE of free dimers

Strandberg *et al* [47] have argued that the origin of a large MAE in small clusters is closely related to the nature of the eigenstates in the immediate vicinity of the Fermi level (assuming that up to double-counting corrections, the total energy is given by the sum of the one-electron energies and that the variation of the eigenvalues dominates the MAE). For a dimer oriented along the z axis the bonding and antibonding π_d and δ_d states formed by d_{xz} and d_{yz} and d_{xy} and $d_{x^2-y^2}$ orbitals are twofold degenerate in the scalar-relativistic limit and for magnetization perpendicular to the dimer axis if SOC is taken into account, but SOC lifts the degeneracy for axial magnetization. If the degenerate state is only singly occupied, the level-splitting can lead to a large orbital anisotropy and a large MAE. This argument has been used to study the systematic trends in the MAE of dimers of the late transition metals [31]. For dimers of the Co-group the minority (spin-down) $\delta_d^\star$ state is occupied only by one electron. For this state, spin and orbital quantum numbers are $s_z = -1/2$ and $m_l = \pm 2$. For the state with spin and orbital contributions of $-1/2$ and 2, the orbital magnetization opposes the spin moment and this level will be shifted down, whereas the state with spin and orbital contributions of $-1/2$ and -2 will be shifted up. To first order in the SOC the shift of the eigenvalues is given by $\pm m_l \xi_d$ (where ξ_d is the strength of SOC for the d-electrons), and the shifts in the sub-levels will compensate each other, except if the highest eigenstate is only singly occupied. This is the case for Co_2, Rh_2 and Ir_2 and indeed large MAEs of 7, 47 and 70 meV/dimer, increasing with the strength of SOC have been calculated. For the elements of the Ni-group the degenerate eigenstates are always occupied by two electrons. A large MAE of 46 meV/dimer is found only for Pt_2 where the SOC-induced splitting is larger than the separation of the occupied $\delta_d^\star$ and empty $\pi_d^\star$ minority states—only the lower components of both are occupied if SOC is included. For the Fe-group elements only the very small MAE of the Fe_2 is of interest here. It has been demonstrated that although the $\delta^\star$ state is only singly occupied, the MAE is very low. SOC induces not only a modest level splitting, but also a small up-shift of the center of gravity of these states, leading only to a very small MAE. For all further details we refer to our prior work [31]. Below we will use a similar analysis to explain the MAE of free and graphene-supported heteroatomic dimers.

4. Heteroatomic dimers in the gas phase and supported on graphene

The central objective of our work is to study the cooperative effect of the high magnetic moments contributed by the Fe or Co atoms and the strong SOC due to Pt or Ir on the magnetic properties, in particular the MAE of mixed dimers in the gas phase and supported on a free-standing graphene layer. The results are presented in the following sections.

4.1 Ir–Co dimers

Our results for mixed IrCo dimers are compiled in table 1, where the results of Xiao *et al* [15] are also listed, calculated using the relativistic full-potential local-orbital (FPLO) code of Koepernik and Eschrig [48]. The calculations use the same GGA functional and the same k-point grid for Brillouin-zone interactions as in the present work, but use a fully relativistic Hamiltonian, a local orbital instead of a plane-wave basis, and a smaller 4×4 supercell for representing the graphene layer. A possible distortion of the graphene layer induced by the adsorbed dimer has been neglected.

In the scalar-relativistic mode both calculations predict for the free dimer a quintet state (spin moment $4\mu_B$), with a slightly shorter bond length from our plane-wave calculations. Binding with the dimer is strong, with a binding energy of $E_b = -3.87$ eV/dimer. If SOC is taken into account, the spin moment is slightly reduced, but this is overcompensated by a large orbital contribution enhancing the total moment to nearly $6\mu_B$. Both calculations predict very similar local spin and orbital moments on the Co atom, whereas Xiao *et al* find moments enhanced by $0.21\mu_B$ (orbital moment) and $0.29\mu_B$ on the Ir atom. Both calculations also agree on an easy magnetic axis parallel to the dimer bond, a weak anisotropy of the spins (with a negative spin anisotropy on the Co atom) and large orbital anisotropies of $\Delta\mu_L \sim 0.6\mu_B$ on both atoms. Given the similarities in the anisotropies of the magnetic moments, it is a bit surprising that the largest difference is found for the MAE where the value of 142 meV/dimer reported by Xiao *et al* is about twice as large as our result of 69 meV/dimer. Such a large difference was also found for homoatomic 3d and 4d dimers where Fritsch *et al* [30] consistently reported larger

Table 1. Bond length d, vertical distance z from the support (both in Å), adsorption energy $E_{\rm int}$ and atomization energy $E_{\rm at}$ (in eV/dimer), total, spin and orbital magnetic moments m_J, m_S and m_L, spin and orbital anisotropies Δm_S and Δm_L (all in $\mu_{\rm B}$), easy magnetic axis (relative to the dimer axis), MAE (in meV/dimer) for IrCo dimers in the gas phase and supported on a free-standing graphene layer. Local magnetic moments are given in parentheses. The results of Xiao *et al* [15] are given for comparison in square brackets.

Geometry	IrCo	IrCo/graphene upright
d	2.08 [2.13]	2.15[2.18]
z	—	2.22[2.25]
$E_{\rm at}$	3.87	5.10
$E_{\rm int}$	—	−1.23[−0.63]
m_J	5.45(2.60/2.85) [6.04(3.10/2.94)]	5.33(3.50/1.83) [5.83(4.00/1.83)]
m_S	3.56(1.55/2.01) [3.89(1.84/2.05)]	3.60(1.90/1.70) [3.91(2.17/1.74)]
Δm_S	0.10(0.11/−0.01) [0.13(0.04/−0.09)]	0.21(0.18/0.03) [0.05(0.13/−0.08)]
m_L	1.89(1.05/0.84) [2.15(1.26/0.89)]	1.73(1.60/0.13)] [1.92(1.83/0.09)]
Δm_L	1.20(0.59/0.61) [1.35(0.60/0.75)]	1.07(1.13/−0.06] [1.01(1.20/−0.19)]
Easy axis	Parallel	Parallel
MAE	69 [142]	93 [198]

values calculated using the FPLO code than either Blonski and Hafner [31] or Strandberg *et al* [47].

On a free-standing graphene layer a IrCo dimer adsorbs in an upright configuration through the Co atom in the center of a sixfold hole. An upright configuration with the Ir atom pointing downwards or any flat geometry with the dimer parallel to graphene is energetically disfavored by at least several tenths of an eV/dimer. Our plane-wave calculations predict a somewhat stronger adsorption, with a more pronounced elongation of the dimer bond length. Both calculations agree on a modest reduction of the total magnetic moment by about $0.2\,\mu_{\rm B}$, which is compensated by very small moments induced on the nearest C atoms such that the total moment of the dimer/substrate complex remains unchanged. Important changes, however, are found in the local magnetic moments. The magnetism of the Co atom binding to graphene is strongly quenched, the local spin moment is reduced by about $0.3\,\mu_{\rm B}$, and the local orbital moment vanishes nearly completely. In contrast, on the Ir atom the looser binding within the dimer leads to more free-atom-like properties. The spin moment is enhanced by about $0.3\,\mu_{\rm B}$, the orbital moment by about $0.55\,\mu_{\rm B}$. The easy direction of magnetization is again along the dimer axis and perpendicular to the substrate. The anisotropy of the spin moments remains very weak, and the still very strong orbital anisotropy is now entirely concentrated on the Ir atom. Together with the much stronger SOC on Ir than on Co, this leads to a further enhancement of the MAE to 93 meV/dimer—but the value reported by Xiao *et al* is again higher by a factor of two.

4.2 Pt–Co dimers

For a free PtCo dimer scalar-relativistic calculations predict a spin magnetic moment of $3\,\mu_{\rm B}$ and a bond length of 2.19 Å, at a binding energy of −1.82 eV/atom, in agreement with Johll *et al* [20]. An increase of the Pt–Co distance by only 0.01 Å has been predicted if SOC is included. The magnetic GS of a PtCo dimer is a high-moment state with a total magnetic moment of $m_J = 4\mu_{\rm B}(m_S = 2.85\mu_{\rm B},\ m_L = 1.15\,\mu_{\rm B})$ oriented along the dimer axis (see table 2 for details). For perpendicular magnetization, the total magnetic moment decreases to about $3\mu_{\rm B}(m_S = 2.56\mu_{\rm B},\ m_L = 0.50\,\mu_{\rm B})$. Compared to the IrCo dimer the spin anisotropy is increased, while the orbital anisotropy is reduced by nearly a factor of two. The important point, however, is that the largest contribution to Δm_L comes from the Co atom, while for IrCo the orbital anisotropy was evenly distributed over both atomic species. This is the main reason for the much lower MAE of 18.8 meV/dimer.

For PtCo on graphene the energetically most stable configuration ($E_{\rm int} = -1.16$ eV/dimer) is upright, with Co in the center of a carbon ring (Co-down) with a distance of 2.23 Å from the nearest C atom, and the Pt–Co bond length is reduced by only 0.01 Å, all in good agreement with [20]. The adsorbed dimer also induces a weak buckling of the graphene layer, with an amplitude of 0.08 Å. The scalar-relativistic spin moment of $3\,\mu_{\rm B}$ found for the entire adsorbate–substrate complex is the same as for the gas phase dimer. Compared to the free dumbbell, the magnetic moment on Pt is increased from $0.70\,\mu_{\rm B}$ to $0.99\,\mu_{\rm B}$ while that on the Co atom is decreased from $2.30\,\mu_{\rm B}$ to $1.88\,\mu_{\rm B}$. Quite generally the moment on the atom in contact with the substrate is reduced, whereas that on the upper atom is closer to the value for the free atom. The magnetic dimer also induces small magnetic moments on the neighboring C atoms of the order of a few $0.01\mu_{\rm B}$, completing the quantized total magnetic moment. In the second upright adsorption geometry considered here (Pt–down), the adsorption energy is only $E_{\rm int} = -0.41$ eV/dimer, and the weaker binding is also reflected in a bond length increased to 2.23 Å. The total spin moment is again $3\,\mu_{\rm B}$, with the local moment on the Pt atom binding to the graphene reduced to $0.46\mu_{\rm B}$ and an increased local moment of $2.31\mu_{\rm B}$ on the upper Co atom. For two parallel-to-graphene geometries (initially with the atoms in br–br and ot–ot positions) binding to the substrate is even weaker ($E_{\rm int} \sim -0.35$ eV).

Relativistic calculations for the Co-down dimer predict an easy magnetization direction perpendicular to the substrate, parallel to the dimer axis as for the gas phase cluster. Due to the interaction with the substrate, spin and orbital moments are strongly reduced on the Co atom and enhanced on the Pt atom, see table 2. Due to the strong SOC of the Pt atom the total magnetic moment of $4.4\,\mu_{\rm B}$ is larger than without SOC. Together the rotation of the magnetization from easy to hard direction leads to a transition from a high-moment state ($m_J^{\rm PtCo} = 4.4\mu_B$) to a lower moment magnetic isomer ($m_J^{\rm PtCo} = 3.4\mu_B$). The MAE of 11.7 meV/dimer is reduced by 32% compared to the free dimer. This is in contrast to the IrCo dimer where the interaction with the support enhances the MAE. Evidently the difference cannot be explained by the relative changes in the magnetic moments and their anisotropies alone.

For completeness we have also calculated the MAE for an upright Pt–down dimer. In this case the easy axis is in-plane, perpendicular to the dimer and parallel to the graphene layer, and magnetization perpendicular to graphene is disfavored by an MAE of 9.1 meV/dimer. Compared to the

Table 2. Bond-length d, vertical distance z from the support (both in Å), adsorption energy $E_{\rm int}$ and atomization energy $E_{\rm at}$ (in eV/dimer), total, spin and orbital magnetic moments m_J, m_S and m_L, spin and orbital anisotropies Δm_S and Δm_L (all in $\mu_{\rm B}$), easy magnetic axis (relative to the dimer axis), MAE (in meV/dimer) for a PtCo dimer in the gas phase and supported on a free-standing graphene layer. Local magnetic moments are given in parentheses.

Geometry	PtCo	PtCo/graphene upright
d	2.20	2.19
z	—	1.67
$E_{\rm int}$	—	−1.16
$E_{\rm at}$	3.64	4.80
m_J	4.00(1.29/2.71)	4.36(2.60/1.76)
m_S	2.85(0.70/2.15)	2.87(1.29/1.58)
Δm_S	0.29(0.10/0.19)	0.14(0.29/−0.15)
m_L	1.15(0.59/0.56)	1.49(1.31/0.18)
Δm_L	0.65(0.18/0.47)	0.87(0.78/0.09)
Easy axis	Parallel	Parallel
MAE	18.8	11.7

free dimer on the Pt atom in contact with graphene, both spin and orbital moments are reduced by about a factor of two; on the upper Co atom the spin moment is increased, but the orbital moment is reduced. The anisotropy of the local spin moments is weak, the larger orbital anisotropies have opposite sign. Graphical representations with details of the geometric parameters and the local moments of all configurations of free and supported Pt–Co clusters can be found in the online supplementary information[3].

4.3 Pt–Fe dimers

According to scalar-relativistic calculations, the bond length of a free PtFe dimer is 2.17 Å with a spin moment of $4\,\mu_{\rm B}$ and an atomization energy of 3.92 eV/dimer. SOC does not change the bond length, but slightly reduces the spin moment and induces a modest orbital moment which is slightly larger on the Pt atom. In the magnetic GS perpendicular to the dimer axis the total magnetic moment is $4.2\mu_{\rm B}$ ($m_S = 3.79\mu_{\rm B}$, $m_L = 0.41\,\mu_{\rm B}$, see table 3 for further details). A rotation of the magnetization by 90° parallel to the dimer axis induces a reduction of the orbital moment to $0.31\mu_{\rm B}$ and an increase of the spin moment to $3.88\,\mu_{\rm B}$, and costs a modest MAE of 3.2 meV/dimer. For a magnetization parallel to the dimer axis we also found an excited magnetic state with a total moment of $5.3\mu_{\rm B}$ ($m_S = 4.17\mu_{\rm B}$, $m_L = 1.13\,\mu_{\rm B}$) at an energy of 92.4 meV/dimer above the GS.

For a PtFe dimer adsorbed on a graphene sheet the most stable adsorption configuration is an upright (slightly canted) Fe-down dimer with the Fe atom halfway between the br and 6h position. The Pt–Fe bond length of 2.17 Å is the same as for the gas phase dimer, the adsorption energy of −0.84 eV/dimer is smaller than for the PtCo dimer. The adsorption of the dimer causes a weak buckling of the graphene layer with an amplitude of 0.12 Å. The spin moment of the cluster/graphene complex is $4\,\mu_{\rm B}$ as for the free cluster, but the local magnetic moment on the Pt atom is increased, and that on the Fe atom decreased. Adsorption with the Fe atom in the center of a hexagon and the Pt atom exactly above is only weakly exothermic ($E_{\rm int} = -0.10$ eV/cluster), in this configuration the dimer is nonmagnetic. A similar result has been reported by Johll *et al* [20], albeit with zero adsorption energy. For another upright configuration with the Pt atom located in 6h-position and the Fe atom 2.19 Å above, the adsorption energy is only −0.28 eV/cluster. The two initially parallel-to-graphene geometries were found to be unstable; upon relaxation they converged to the GS-structure. We have also tested the adsorption of the Pt–down dimer in a bridge position between two C atoms. This configuration has been reported in [20] to be the GS-geometry with an adsorption energy of $E_{\rm int} = -0.42$ eV/dimer and a spin moment of about $4\,\mu_{\rm B}$. We have found that in this configuration the dimer is non-magnetic and does not bind to graphene. It should also be noted that the adsorption energy calculated in [20] is much lower than that found here for the Fe-down GS dimer (−0.42 versus −0.84 eV).

Relativistic calculations have been performed for the upright Fe-down and Pt–down geometries. For the stable Fe-down dimer the easy magnetic axis is aligned along the dumbbell axis, in contrast to the free dimer where we had found a perpendicular easy axis. Due to the interaction with graphene, the spin and orbital moments on the Fe atom are reduced while those on the Pt atom are increased (see table 3). Together this leads to an enhanced total moment which is larger than for the free PtFe dimer. The anisotropies of the local spin moments change sign on both atoms; the orbital anisotropy on the Pt atom is positive, that on the Fe atom negative. The MAE is equal to 13.4 meV/dimer, and it is larger by almost a factor of four than that of the dimer in the gas phase.

For an upright Pt–down dimer the easy axis is again in-plane, perpendicular to the dimer axis. The MAE for the hard magnetization direction perpendicular to graphene is 5.3 meV/dimer. Local spin and orbital moments on the Fe atom are almost the same as in the free cluster, the local moments on the Pt atom are reduced to about two thirds of their value in the free cluster. Only the orbital moment on the Pt atom displays a significant anisotropy. Details of the geometric parameters of the Pt–Fe clusters are again compiled in graphical form in the supplementary information (stacks.iop.org/cm/26/146002/mmedia).

5. Electronic origin of the magnetic anisotropy in free and supported dimers

For the energetically most favorable configurations the MAE of homo- and heteroatomic dimers, defined as the difference between the total energies calculated for easy and hard axis orientations of the magnetization are summarized in table 4. For the free Ir_2 dimer the substitution of Ir by Co leaves the large MAE unchanged, while for both PtCo and PtFe the MAE is strongly reduced relative to the free Pt_2 dimer; in PtFe (which is isoelectronic to IrCo) the MAE relative to a magnetization parallel to the dimer axis even changes sign. The influence

[3] See online supplementary material (stacks.iop.org/cm/26/146002/mmedia) for graphical representations of all configurations of free and supported PtCo and Ptfe dimer, including details of the geometrical parameters and local moments.

Table 3. Bond length d, vertical distance z from the support (both in Å), adsorption energy $E_{\rm int}$ and atomization energy $E_{\rm at}$ (in eV/dimer), total, spin and orbital magnetic moments m_J, m_S and m_L, spin and orbital anisotropies Δm_S and Δm_L (all in $\mu_{\rm B}$), easy magnetic axis (relative to the dimer axis), MAE (in meV/dimer) for a PtFe dimer in the gas phase and supported on a free-standing graphene layer. Local magnetic moments are given in parentheses.

Geometry	PtFe	PtFe/graphene upright
d	2.17	2.17
z	—	2.21
$E_{\rm int}$	—	−0.84
$E_{\rm at}$	3.92	4.76
m_J	4.20(0.83/3.37)	4.72(1.53/3.19)
m_S	3.79(0.59/3.20)	4.02(0.96/3.06)
Δm_S	−0.09(−0.03/−0.06)	0.18(0.09/0.09)
m_L	0.41(0.24/0.17)	0.70(0.57/0.13)
Δm_L	0.10(0.08/0.02)	0.23(0.28/−0.05)
Easy axis	Perpendicular	Parallel
MAE	3.2	13.4

Table 4. MAE (in meV/dimer) of homo- and heteroatomic dimers of Pt, Ir, Co and Fe in the gas phase and supported on graphene (in parentheses). The MAE is given relative to a magnetization aligned with the dimer axis, which is the easy axis in all cases, except the free PtFe dimer.

Pt_2	PtCo	Co_2
46.2	18.8	7.2
(23.2)	(11.8)	
	PtFe	Fe_2
	−3.2	0.30
	(13.4)	
Ir_2	IrCo	Co_2
70	69	7.2
—	(93)	

of even a rather inert support such as graphene on the MAE is also very different. While for Pt_2 and PtCo the interaction with the support reduces the MAE by about a factor of two, it is increased and changes sign for PtFe. The magnetism of an Ir_2 dimer is extremely sensitive to the interaction with the support—on graphene as well as on benzene [15] the homoatomic dimer is nonmagnetic while the already large MAE of the mixed IrCo dimer is even further enhanced by the interaction with the support.

For free homoatomic dimers the dependence of the MAE on the d-band filling is well understood in terms of an analysis of the eigenvalue spectra proposed by Strandberg *et al* [47] (see section 3.3). For free homoatomic dimers of the late transition metal atoms we have demonstrated that the nature of the eigenstates in the vicinity of the Fermi level explains the variations of the MAE [31]; here we investigate whether the argument may be extended to heteroatomic dimers and the effect of the interaction with the substrate on the MAE.

The arguments can also be extended to heteroatomic dimers. The eigenvalue spectra of mixed IrCo, PtCo and PtFe dimers, calculated in the scalar-relativistic mode and including SOC are shown in figure 1. For the IrCo dimer formed by homologous elements, the Fermi level coincides again for perpendicular magnetization with the singly occupied $\delta_{\rm d}^{\star}$ level whose splitting under SOC for axial magnetization represents the largest contribution to the large MAE of 69 meV/dimer, equal to that calculated for Ir_2. Spin and orbital moments, as well as their anisotropies, are also of comparable magnitude.

The PtCo dimer has one electron more than IrCo, and the energetic ordering of the eigenstates near $E_{\rm F}$ for perpendicular magnetization is the same ($\delta_{\rm d}^{\star}$(occ .) < $\sigma_{\rm d}^{\star}$(empty) < $\pi_{\rm d}^{\star}$), such that the doubly degenerate $\delta_{\rm d}^{\star}$ state is now fully occupied. The SOC splitting pushes the energy of the upper component of the $\delta_{\rm d}^{\star}$ state above the $\delta_{\rm d}^{\star}$ state, changing the nature of the highest occupied state (see figure 1(*b*)). However, as the average energy of the two states is nearly the same, this only induces a large orbital anisotropy, but does not make a very large contribution to the MAE. For the Pt_2 dimer the ordering of the eigenstates is ($\sigma_{\rm d}^{\star}$(occ .) < $\delta_{\rm d}^{\star}$(occ .) < $\pi_{\rm d}^{\star}$(empty)) and due to the larger SOC splitting both the $\delta_{\rm d}^{\star}$ and $\pi_{\rm d}^{\star}$ states are singly occupied for axial magnetization, resulting in a large orbital anisotropy and a larger MAE than for PtCo.

PtFe is isoelectronic to IrCo, in the scalar-relativistic limit the total spin moment of $4\,\mu_{\rm B}$ is also the same, but the atomization energy is slightly larger for PtFe, coincident with a small increase of the bonding-antibonding splitting of the $\pi_{\rm d}$ and $\delta_{\rm d}$ states. The energy difference between the singly occupied spin-down $\delta_{\rm d}^{\star}$ and the empty spin-up $\sigma_{\rm s}^{\star}$ states is very small. If SOC is included, the energy of the $\sigma_{\rm s}^{\star}$ state is even marginally lower than that of the $\delta_{\rm d}^{\star}$ state (see figure 1(*c*)). Due to this quasi-degeneracy, the highest occupied state is of a strongly mixed character. For axial magnetization, the SOC-induced splitting of the empty $\delta_{\rm d}^{\star}$ and $\pi_{\rm d}^{\star}$ states is asymmetric, and the energy of the lower component of the $\delta_{\rm d}^{\star}$ state remains just above the $\sigma_{\rm s}^{\star}$ level, such that no change in orbital occupancy occurs. This is in line with the very low spin and orbital anisotropies. The easy axis perpendicular to the dimer with a small MAE results from the splitting of the $\delta_{\rm d}$ and $\pi_{\rm d}$ eigenstates at binding energies between 1 and 2 eV and a slight up-shift of their center of gravity.

The influence of the support on the electronic and magnetic properties of adsorbed dimers depends on the overlap of their electronic DOS with the eigenstates of the substrate. Figure 2 shows the spin-polarized DOS of the graphene layer and the adsorbed dimer, as well as the local DOS on the two metallic atoms. The DOS of graphene is zero at the Fermi level, and the electronic states in the vicinity show linear dispersion relations. In the stable adsorption geometry the 3d atom of the dimer is located above the center of a sixfold hole, at a height of about 2 Å above the C atoms. The rotational invariance of the dimer eigenstates around the axis is broken and the C_∞ symmetry is replaced by C_6. The weak interaction is realized by forming chemical bonds between the $\delta_{\rm d}(d_{xy}, d_{x^2-y^2})$ states of the 3d atom and the sp^2-hybrids of the C atoms, and between the $\pi_{\rm d}(d_{xz}, d_{yz})$ states and the p_z states on the C atoms. The extended $\sigma_{\rm s}$ and $\sigma_{\rm s}^{\star}$ states of the dimer are up-shifted because of the Pauli repulsion—the shift of the antibonding state is very important, especially for PtFe/graphene. The eigenstates of the metal atoms undergo a bonding/antibonding splitting and they are broadened by the hybridization with the substrate orbital. These effects are most pronounced on the $\pi_{\rm d}$ states with a large weight on the 3d atom, as will be discussed in detail below. The bonding between the dimer and the graphene is qualitatively similar to the bonding between an IrCo dimer and a benzene molecule, as discussed in detail by Xiao *et al* [15].

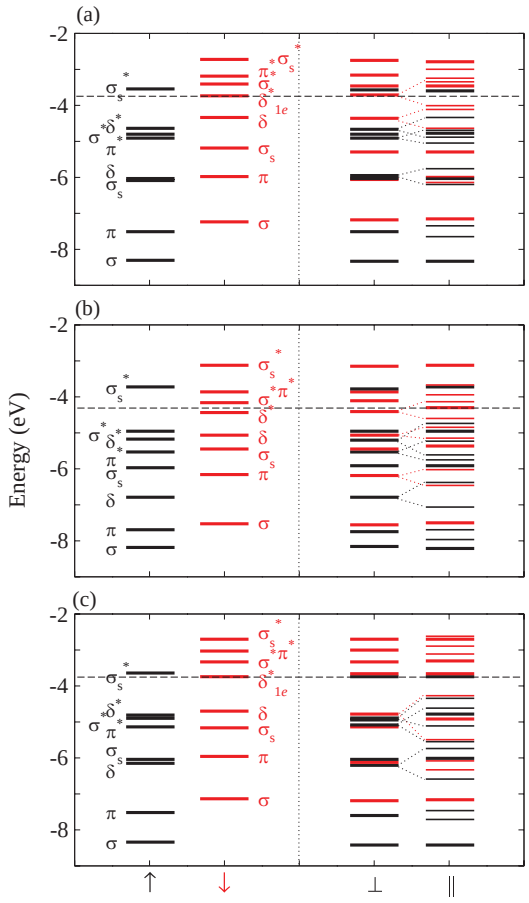


Figure 1. Eigenvalue spectra of free IrCo (*a*), PtCo (*b*), and PtFe (*c*) dimers: spin-polarized eigenvalues calculated in a scalar-relativistic approximation (spin-up in black, spin-down in red), and eigenvalues for perpendicular and parallel (axial) magnetization calculated including SOC.

Broadening and level shifts are less pronounced for the δ_d states where the structure of the spectrum of the free dimer is clearly recognizable in the DOS of the dimer/graphene complex. It is also important to note that the overlap of the 3d and 5d states is largest for IrCo (where both atoms contribute with comparable weight to all eigenstates) and smallest for PtFe (where the states close to E_F are mainly Fe-states).

The MAE is determined by changes in the partial d-band DOS close to the Fermi level and is dependent on the direction of magnetization. The relativistic total and site-decomposed DOS of the adsorbed dimers are shown in figure 3, and the partial d-states DOS on the dimer (decomposed into $\delta_d(d_{xy}, d_{x^2-y^2})$, $\pi_d(d_{xz}, d_{yz})$ and $\sigma_d(d_{z^2})$ contributions), calculated for magnetization perpendicular and parallel to the substrate, are shown for IrCo, PtCo and PtFe on graphene in figure 4. For IrCo/graphene the most important point is the change in the $\delta_d(d_{xy}, d_{x^2-y^2})$ partial DOS upon a change in the magnetization direction. For magnetization parallel to the graphene layer and perpendicular to the dimer axis (along the *x*-axis), the partial DOS shows a dominant peak at the Fermi level (see the peak labeled $\delta_d^\star(\perp)$ on the dashed line in figure 4(*a*)), corresponding to the singly occupied $\delta_d^\star$ state of the free dimer in figure 1(*a*). For perpendicular magnetization (along the *z*-axis) the $\delta_d^\star$ peak is split into two components about ±0.4 eV from the Fermi level (see the peaks labeled $\delta_d^\star(\|)$ on the full line in figure 4(*a*)), again in analogy to the splitting of the eigenvalues of the free IrCo dimer in figure 1(*a*). The site-decomposed DOS (see figure 2(*a*)) shows that for the supported dimers the change in the highest occupied eigenstates is much more pronounced on the Ir than on the Co atom and this explains the increased orbital moment on the Ir atom and the increased MAE of the graphene-supported compared to the free dimer, as listed in table 1. For in-plane magnetization the peaks associated with the π_d and $\pi_d^\star$ states are clearly recognizable in the partial DOS, with the $\pi_d^\star$ states shifted to lower binding energies due to the interaction with the substrate (see figures 1(*a*) and 4(*a*)). For perpendicular magnetization the SOC splitting strongly reduces the structure in the π_d-state DOS. The σ_d- states are almost unaffected by the change in the direction of magnetization.

For PtCo/graphene the nature of the highest occupied state depends on the direction of magnetization, as for the free dimer. For in-plane magnetization perpendicular to the dimer, the highest occupied state is a $\delta_d^\star$ state, with a quasi-degenerate state with $\delta_d^\star, \delta_d, \pi_d^\star$ and $\sigma_d^\star$ contributions at about 0.5 eV lower energy (see the broken lines in figure 4(*b*)). Due to SOC splitting the highest occupied state for axial magnetization of the dimer is predominantly a $\sigma_d^\star$ state, with only a small admixture of $\delta_d^\star$ character (see the full lines in figures 4(*b*)). The change in orbital occupancy leads to a increase in the orbital moment, as noted in table 2. In contrast to IrCo/graphene, important changes upon reorientation of the magnetization direction are also found in the DOS of the σ_d states at lower energies, induced by repulsive interactions with the down-shifted $\delta_d^\star$ states. The mechanism determining the MAE is essentially the same for the free and the graphene-supported PtCo dimers, but the broadening of the eigenstates due to the interaction with the substrate reduces the influence of the SOC-induced shifts of the eigenstates on the MAE.

For PtFe/graphene the interaction with the substrate drastically modifies the nature of the highest occupied state of the dimer. The $\sigma_s^\star$ state (which is occupied for the free dimer and quasi-degenerate with the $\delta_d^\star$ state, see figure 1(*c*)) is shifted to much higher energies due to the Pauli repulsion between the extended electron density on the dimer and the charge distribution in the substrate (see the peak at about 1 eV above the Fermi level in figure 3(*c*)). Consequently, the highest occupied state of the supported dimer for in-plane (perpendicular) magnetization is a partially occupied $\delta_d^\star$ state labeled in figure 4(*c*), as for the free and supported IrCo dimers. Due to the substrate-induced change in the orbital occupancy close to the Fermi level, the mechanism determining the magnetic anisotropy of the graphene-supported PtFe dimer is now similar to that in the isoelectronic IrCo dimer. The interaction with the substrate leads to an increase in the local spin and orbital moments of the Pt atom (see table 3), because the states located close to the Fermi level are mainly concentrated on this atom (see figure 3(*c*)). The SOC-induced splitting of the $\delta_d^\star$ state (as indicated in figure 4(*c*)) stabilizes the perpendicular (axial)

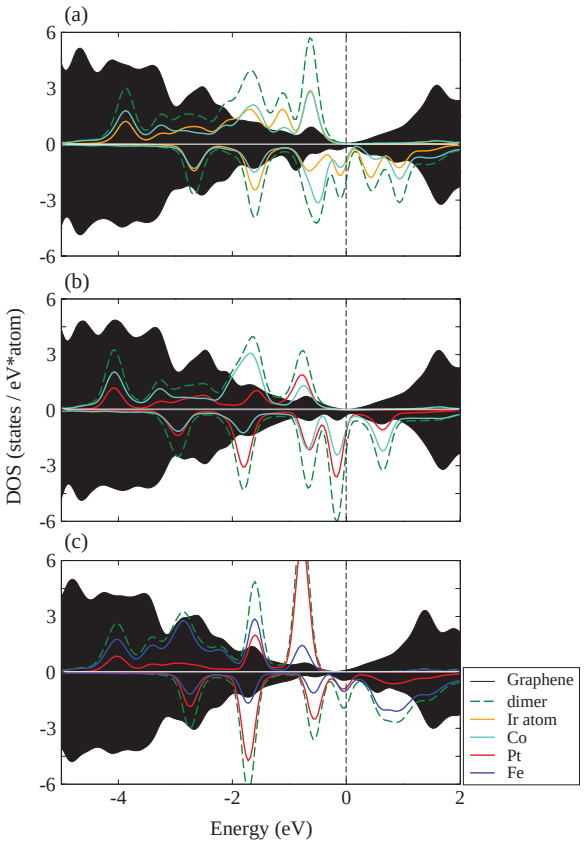


Figure 2. Spin-polarized scalar-relativistic total and local DOS for IrCo (*a*), PtCo (*b*), and PtFe (*c*) dimers adsorbed on a graphene layer.

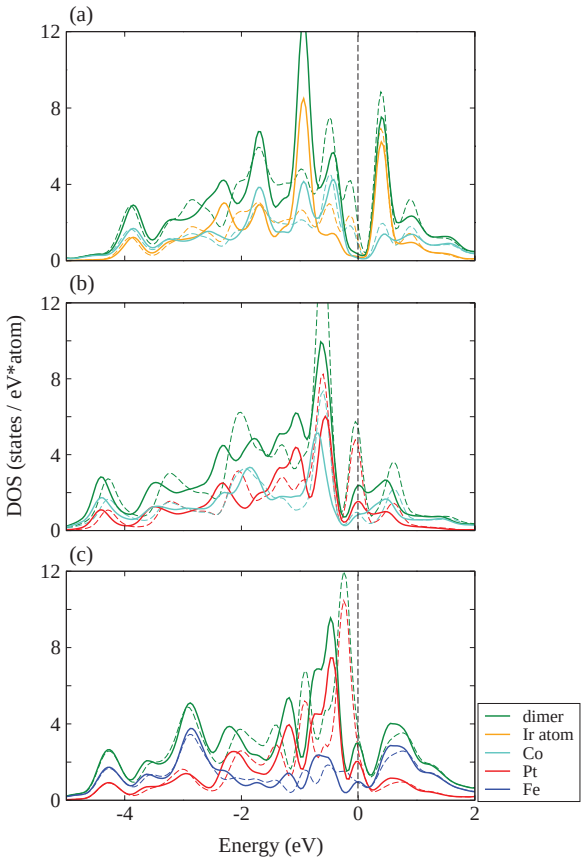


Figure 3. Total and site decomposed electronic DOS for IrCo (*a*), PtCo (*b*) and PtFe (*c*) dimers adsorbed on a graphene layer, calculated including SOC for magnetization perpendicular to the support and parallel to the dimer axis (along the *z*-direction, full lines) and for magnetization parallel to the support and perpendicular to the dimer (along the *x*-direction, broken lines).

magnetization direction and explains the change of sign in the MAE whose absolute value is also increased relative to the free dimer (see table 4).

6. Conclusions

We have presented a detailed analysis of the origin of the magnetic anisotropy of dimers consisting of heavy 5d and strongly magnetic 3d atoms (IrCo, Pt Co, and PtFe) in the gas phase and supported on a free-standing graphene layer. Density-functional calculations in the scalar-relativistic limit and self consistently including spin–orbit coupling have been performed. The magnetic anisotropy energy has been calculated as the difference of the total energies for magnetization parallel and perpendicular to the dimers axis. The magnetic anisotropy energy is found to depend very sensitively on the nature of the eigenstates in the vicinity of the Fermi level, as determined by the number of electrons, the exchange splitting, and the strength of spin–orbit coupling. The large anisotropy energy of IrCo and PtCo dimers relative to the easy direction parallel to the dimer axis is coupled to a strong anisotropy of the orbital moment on the Co atom for both dimers and also on the Ir atom in IrCo. We show that the exceptionally large MAE of IrCo arises from the SOC-induced splitting of a $\delta_d^\star$ state at the Fermi level, which is doubly degenerate in the scalar-relativistic limit and for perpendicular magnetization, but occupied by only one electron. For the PtCo dimer with one valence electron more, the $\delta_d^\star$ state is fully occupied, but the large SOC splitting pushes the upper component of the state above the $\sigma_d^\star$ state, changing the nature of the highest occupied state. This leads to a very large orbital anisotropy, but as the energy of the now occupied $\sigma_d^\star$ state is similar to that of the degenerate (in the absence of SOC) $\delta_d^\star$ state, only to a significantly lower MAE. For the PtFe dimer the energy difference between the spin-down $\delta_d^\star$ and the spin-up $\sigma_s^\star$ states is very small, resulting in a highly mixed character of the highest occupied. In this case SOC does not lead to a change in orbital occupancy, resulting in small spin and orbital anisotropies and a small MAE.

For dimers supported on graphene, the strong binding of the 3d atom to the substrate stabilizes an upright geometry, which is very important for achieving a high MAE. Spin and orbital moments on the 3d atom are strongly quenched, but because the adsorption weakens the binding within the dimer, the properties of the 5d atom are more free-atom like, with increased spin and orbital anisotropies. For IrCo/graphene the

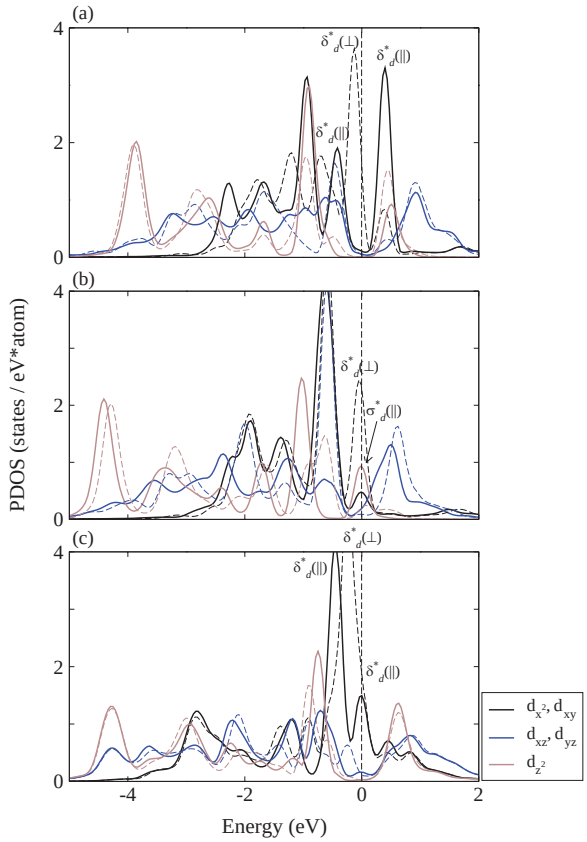


Figure 4. Partial d-band DOS ($\delta_d(d_{xy}, d_{x^2-y^2})$, $\pi_d(d_{xz}, d_{yz})$ and $\sigma_d(d_{z^2})$) for IrCo (*a*), PtCo (*b*) and PtFe (*c*) dimers adsorbed on a graphene layer, calculated including SOC for magnetization perpendicular to the support and parallel to the dimer axis (along the *z*-direction, full lines) and for magnetization parallel to the support and perpendicular to the dimer (along the *x*-direction, broken lines). The most important peaks close to the Fermi level which are strongly influenced by a reorientation of the magnetization direction are labeled according to their symmetry character and the magnetization direction.

mechanism determining the MAE is essentially the same as for the free dimer, and because the weight of the $\delta_d^\star$ state is largest on the Ir atom with enhanced spin and orbital moments, the MAE is even further increased by the interaction with the support. For PtCo/graphene the change in the nature of the occupied states close to the Fermi level is again similar to in the free dimer, but upon a rotation of the magnetization direction important changes are also found in the σ_d states at lower energy, induced by repulsive interactions with the down-shifted $\delta_d^\star$ states, resulting in a reduced MAE. For PtFe/graphene the large shift of the $\sigma_s^\star$ state caused by the Pauli repulsion changes the nature of the states at the Fermi level, leading to an electronic structure close to the Fermi level which is similar to that of the isoelectronic IrCo/graphene dimer. The magnetic anisotropy is now determined by the SOC-induced splitting of the partially occupied $\delta_d^\star$ state, as for the IrCo/graphene system. The easy direction is now along the dimer axis, as for the other dimers, and the MAE is larger than for PtCo.

In summary, we have demonstrated that the MAE of free heteroatomic dimers mixing 3d and 5d atoms does not exceed the value calculated for the free 5d-dimer. The largest MAE is found for IrCo combining elements from the same groups in the periodic table; for larger differences in the valence (such as for PtFe), the MAE can even change sign. For dimers supported on graphene, the strong binding of the 3d-atom in a sixfold hole stabilizes an upright geometry and leads to more free-atom like properties of the upper 5d-atom. For IrCo/graphene this leads to a further increase in the already large MAE. But the dominant factor is the modification of the highest occupied eigenstates through the interaction with graphene—for PtCo/graphene this leads to a reduced axial anisotropy, while for PtFe/graphene the axial anisotropy is stabilized only by the interaction with the substrate.

Acknowledgments

Work at the Universität Wien has been supported through the VASP project.

References

[1] Shick A B and Mraysov O N 2003 *Phys. Rev.* B **67** 172407
[2] Sun S, Murray C B, Weller D, Folks L and Moser A 2000 *Science* **287** 1989
[3] Miyazaki T, Kitakami O, Okamoto S, Shimada Y, Akase Z, Murakami Y, Shindo D, Takahashi Y K and Hono K 2005 *Phys. Rev.* B **72** 144419
[4] Antoniak C *et al* 2006 *Phys. Rev. Lett.* **97** 117021
[5] Gruner M E, Rollmann G, Entel P and Farle M 2008 *Phys. Rev. Lett.* **100** 087203
[6] Gruner M E 2010 *J. Phys. Conf. Ser.* **200** 072039
[7] Chepulskii R V and Butler W H 2012 *Appl. Phys. Lett.* **100** 142405
[8] Gruner M E and Entel P 2012 *Int. J. Qantum Chem.* **112** 277
[9] Anderson C, Sanyal B, Eriksson O, Norström L, Karis O, Arvanitis D, Konishi T, Holub-Krappe E and Dunn J H 2007 *Phys. Rev. Lett.* **99** 177207
[10] Błoński P, Lehnert A, Dennler S, Rusponi S, Etzkorn M, Moulas G, Bencok P, Gambardella P, Brune H and Hafner J 2010 *Phys. Rev.* B **81** 104426
[11] Lehnert A, Dennler S, Błoński P, Rusponi S, Etzkorn M, Moulas G, Bencok P, Gambardella P, Brune H and Hafner J 2010 *Phys. Rev.* B **82** 094409
[12] Ivanov O A *et al* 1973 *Phys. Met. Metallogr.* **35** 92
[13] Shick A B and Mryasov O N 2003 *Phys. Rev.* B **67** 172407
[14] Sahoo S, Hucht A, Gruner M E, Rollmann G and Entel P 2010 *Phys. Rev.* B **82** 054418
[15] Xiao R, Kuz'min M D, Koepernik K and Richter M 2010 *Appl. Phys. Lett.* **97** 232501
[16] Błoński P, Dennler S and Hafner J 2011 *J. Chem. Phys.* **134** 034107
[17] Błoński P and Hafner J 2011 *J. Chem. Phys.* **134** 154705
[18] Błoński P and Hafner J 2012 *J. Chem. Phys.* **136** 074701
[19] Błoński P and Hafner J 2012 *J. Chem. Phys.* **137** 044710
[20] Johll H, Kang H C and Tok E S 2009 *Phys. Rev.* B **79** 245416
[21] Johll H, Wu J, Ong S W and Kang Ch H 2011 *Phys. Rev.* B **83** 205408
[22] Shim I and Gingerich K A 1982 *J. Chem. Phys.* **77** 2490
[23] Noro T, Ballard C, Palmer M H and Takewaki H 1994 *J. Chem. Phys.* **100** 452

[24] Yanagisawa S, Tsuneda T and Hirao K 2000 *J. Chem. Phys.* **112** 545
[25] Hübner O and Sauer J 2002 *Chem. Phys. Lett.* **358** 442
[26] Bauschlicher C W and Ricca A 2003 *Mol. Phys.* **101** 93
[27] Angeli C and Cimiraglia R 2011 *Mol. Phys.* **109** 1503
[28] Kulik H J, Cococcioni M, Scherlis D A and Marzari N 2006 *Phys. Rev. Lett.* **97** 103001
[29] Casula M, Marchi M, Azadi S and Sorella S 2009 *Chem. Phys. Lett.* **477** 255
[30] Frisch D, Koepernik K, Richter M and Eschrig H 2008 *J. Comput. Chem.* **29** 2210
[31] Błoński P and Hafner J 2009 *Phys. Rev.* B **79** 224418
[32] Du J, Suan X and Wang H 2008 *Int. J. Quantum Chem.* **108** 1505
[33] Purdum H, Montano P A, Shenoy G K and Morrison T 1982 *Phys. Rev.* B **25** 4412
[34] Balasubramanian K 1987 *J. Chem. Phys.* **87** 6573
[35] Lee D-K Jeung G-H and Lee Y S 2009 *Int. J. Quantum Chem.* **109** 1975
[36] Varga S, Fricke B, Nakamatsu H, Mukoyama T, Anton J, Deschke G, Heitmann A, Engel E and Bastug T 2000 *J. Chem. Phys.* **112** 3499
[37] Ariola M B and Morse M D 2002 *J. Chem. Phys.* **116** 1313
[38] Kresse G and Furthmüller J 1996 *Comp. Mat. Sci.* **6** 15
Kresse G and Furthmüller J 1996 *Phys. Rev.* B **54** 169
[39] Kresse G and Joubert D 1999 *Phys. Rev.* B **59** 1758
[40] Blöchl P E 1994 *Phys. Rev.* B **50** 17953
[41] Perdew J P Burke K and Ernzerhof M 1996 *Phys. Rev. Lett.* **77** 3865
[42] Vosko S H Wilk L and Nusair M 1980 *Can. J. Phys.* **58** 1200
[43] Kresse G and Lebacq 2013 *O VASP Manual* (http://cms.mpi.univie.ac.at/vasp/vasp/vasp.html)
[44] Kleinman L 1980 *Phys. Rev.* B **21** 2630
[45] MacDonald A H, Pickett W E and Koelling D D 1980 *J. Phys. C: Solid State Phys.* **13** 2675
[46] Hobbs D, Kresse G and Hafner J 2000 *Phys. Rev.* B **62** 11556
[47] Strandberg T O, Canali C M and McDonald A H 2008 *Phys. Rev.* B **77** 174416
[48] Koepernik K and Eschrig H 1999 *Phys. Rev.* B **59** 1743
[49] Longo R C, Carrete J, Ferrer J and Gallego L J 2010 *Phys. Rev.* B **81** 115418
[50] Srivastava M, Wang Y, Kemper A F and Cheng H-P 2012 *Phys. Rev.* B **85** 165444
[51] Yagi Y, Briere T M, Sluiter M H F, Kumar V, Farajian A A and Kawazoe Y 2004 *Phys. Rev.* B **69** 075414

IOP Publishing Journal of Physics: Condensed Matter
J. Phys.: Condens. Matter **26** (2014) 256001 (11pp) doi:10.1088/0953-8984/26/25/256001

Cu(1 1 1) supported graphene as a substrate for magnetic dimers with a large magnetic anisotropy: relativistic density-functional calculations

P Błoński[1,2] and J Hafner[1]

[1] University of Vienna, Faculty of Physics and Center for Computational Materials Science, Sensengasse 8/12, A-1090 Wien, Austria
[2] Institute of Nuclear Physics, Polish Academy of Sciences, ul. Radzikowskiego 152, PL-31-342 Kraków, Poland

Received 23 March 2014, revised 15 April 2014
Accepted for publication 17 April 2014
Published 22 May 2014

Abstract

We report on our relativistic density-functional investigations of the properties of transition-metal dimers adsorbed on a graphene monolayer supported by a Cu(1 1 1) substrate, which extends our studies of dimers in the gas-phase and adsorbed on a freestanding graphene layer (Błoński and Hafner 2014 *J. Phys.: Condens. Matter* **26** 146002). The presence of the Cu(1 1 1) substrate enhances the interaction between the dimer and the support. For homoatomic dimers such as Ir_2 and Pt_2 a flat adsorption geometry is now preferred over an upright geometry, which is stable on a graphene monolayer. The magnetic moment of the dimer is strongly reduced, the magnetic anisotropy is very low—in contrast to the strong anisotropy of free and graphene-supported Ir_2 and Pt_2 dimers. For heteroatomic IrCo and PtCo dimers the upright geometry with the Co atom located in a sixfold hollow of the graphene layer is preserved, but the stronger interaction with the support leads to a further enhancement of the large magnetic anisotropy energy of IrCo to 0.2 eV/dimer, while that of PtCo is reduced. The mechanism determining the magnetic anisotropy is discussed in relation to the electronic structure of the dimers.

Keywords: magnetic anisotropy, dimers, graphene, metallic support

(Some figures may appear in colour only in the online journal)

1. Introduction

Materials with tailored magnetic properties have attracted much attention because of their potential application in high-density magnetic or magneto-optic data storage devices. A quantity of central interest is the magnetic anisotropy energy (MAE), which determines the barrier to magnetization reversal due to thermal excitations. A high MAE, which is necessary to prevent the loss of information, requires large spin and orbital moments and a strong spin-orbit coupling (SOC). Bimetallic nanostructures consisting of ferromagnetic 3d and heavy 5d elements are possible candidates for materials with a high MAE because of the large spin moments of the light and the strong SOC of the heavy atoms.

An enhanced MAE has been reported for isolated 3d atoms on the surface of heavy 4d or 5d metals [1, 2]. A striking example is the large MAE of 9.3 ± 1.6 meV per deposited atom measured for Co on a Pt(1 1 1) substrate. However, small Co clusters on this surface show only a much smaller MAE per atom, roughly inversely proportional to the number of atoms. An alternative strategy for the design of nanostructures with a large MAE is to look at mixed clusters of 3d and 5d elements.

Gas-phase transition-metal dimers are the smallest objects with a magnetic anisotropy. Very large MAEs of up to 100 meV/dimer have been predicted for dimers of 4d and 5d elements [3–5]. However, the large magnetic moments of heavy elements such as Pt are very sensitive to interactions with a supporting substrate. The large MAE of a gas-phase Pt_2 dimer

 © 2014 IOP Publishing Ltd Printed in the UK

is reduced from 46.3 to 23.2 meV/dimer if the cluster is deposited on a freestanding graphene layer [6]. If the graphene layer is supported by a Ni(1 1 1) substrate, the cluster-support interaction is strongly enhanced such that the adsorption geometry of a Pt_2 dimer changes from perpendicular to parallel and the dimer becomes essentially non-magnetic—only trimers and tetramers remain weakly magnetic [7].

A few density functional theory (DFT) results are available for mixed dimers of 3d and 5d elements. Xiao *et al* [8, 9] reported an enormous MAE of 142 meV for a IrCo dimer. We have recently presented a comparative study of the magnetic properties of IrCo, PtCo and PtFe dimers. For IrCo a large MAE of 70 meV was calculated, comparable to the MAE of an Ir_2 dimer, while for PtCo an anisotropy energy of only 17.3 meV (even smaller than for homoatomic Pt_2, but larger than for a Co_2) was reported [10]. For both the IrCo and PtCo dimers the easy magnetic direction is along the dimer axis. For a PtFe dimer with the same number of valence electrons as IrCo, a modest perpendicular anisotropy of–3.2 meV was calculated [10]. The interaction of the mixed dimers with a supporting graphene layer affects the magnetic anisotropy in a very different way. For IrCo on graphene both studies [8, 10] predict a further enhancement of the MAE by a factor of about 1.4; for PtCo/graphene the interaction with the substrate leads to a reduced MAE of 11.7 meV [10]. For a PtFe dimer on graphene the easy magnetic axis was found to be aligned with the dimer axis (in contrast to the free dimer) with an MAE of 13.4 meV, which is an increase of nearly a factor of four compared to the free dimer.

Admittedly, dimers on a freestanding graphene layer are primarily of scientific interest since, for any practical applications of graphene-supported magnetic nanoclusters, the carbon sheet must be deposited on a solid substrate (for a compilation of the literature on metal supported graphene we refer the reader to a review article by Voloshina and Dedkov [11]). Recently we have investigated the adsorption of small Pt clusters on a graphene-covered Ni(1 1 1) substrate [7, 12]. Although the interaction between graphene and the Ni surface is weak and dominated by dispersion forces, the interaction between the adsorbed clusters and the Ni support across the graphene layer was found to be sufficient to change the structural and magnetic properties of the clusters compared to those deposited on a free graphene layer. The strength of the Pt–Ni interaction is probably caused by the open 3d shell of the supporting metal. In the present work we have investigated the properties of homoatomic Pt_2 and Ir_2 and of heteroatomic PtCo and IrCo dimers on a graphene layer epitaxially grown on a Cu(1 1 1) surface, comparing them with dimers on freestanding graphene and in the gas phase.

The growth of graphene on copper foils has attracted considerable interest as a simple and low-cost method to synthesize a large area of high-quality and uniform graphene layers. [13] Recent low-energy electron microscopy investigations [14] have demonstrated that the epitaxial graphene film on a smooth Cu(1 1 1) surface is closely aligned to a single in-plane orientation, with a low number of structural defects. The graphene–Cu(1 1 1) interfacial properties have also been extensively investigated using density functional methods with different variants of the exchange-correlation functional[15–19]. The generalized gradient approximation (GGA) predicts no binding between graphene and Cu, while in the local density approximation (LDA) a weak binding at a large distance (>3 Å) from the Cu surface is obtained if one compresses Cu to match the lattice parameter of graphene. The surprisingly good performance of the LDA is fortuitous since the predicted physisorption originates largely from an overestimation of the exchange interactions, whereas dispersion forces are a purely nonlocal correlation effect. Many-body calculations [19, 20] in the random phase approximation (RPA) combined with the adiabatic connection-fluctuation dissipation theorem (ACFDT) achieved a physically realistic description of the binding between graphene and a metallic substrate. While for the surfaces of metals with an open d-shell (such as Ni(1 1 1)) a weakly chemisorbed state with a graphene–substrate distance of $d \sim 2.2 \pm 0.1$ Å coexists with a physisorbed state at $d \sim 3.25$ Å, for graphene on Cu(1 1 1) only a physisorbed state has been found. Due to the epitaxial relation between the graphene overlayer and the metallic substrate, the RPA-ACFDT calculations could be performed with a small unit cell. For the large cells required to describe an isolated cluster on the graphene/metal support, the RPA-ACFDT is computationally much too demanding. However, it has been demonstrated that for graphene on Ni(1 1 1) the binding energy and distance calculated with the semi-empirical pair-wise dispersion correction proposed by Grimme *et al* [21, 22] are in very good agreement with the chemisorbed state identified in the RPA-ACFDT calculations of Olsen *et al* [19] and Mittendorfer *et al* [20]. Therefore the same approach has been used in the present work.

Our paper is organized as follows: In section 2 we briefly discuss the computational background and the results for the graphene/Cu support interactions. The results for isolated Pt adatoms and homoatomic dimers on this support are presented in sections 3.1 and 3.2, and in section 3.3 for the mixed dimers, which are discussed in comparison with the free and graphene-supported clusters. In section 4 the results are analyzed in terms of the partial electronic density of states of the supported dimers, which we summarize in section 5.

2. Computational details

The *ab initio* studies reported are based on DFT, including dispersion corrections, as implemented in the VASP code (Vienna *Ab-initio* Simulation Package). [23, 24] VASP performs an iterative solution of the Kohn–Sham equations within a plane-wave basis set, employing periodic boundary conditions and describing the electron–ion interaction within the projector-augmented-wave formalism. [24, 25] The plane-wave basis set contained components with energies up to 500 eV. Electronic exchange and correlation are described using the functional of Perdew, Burke and Ernzerhof (PBE) [26] in the GGA approximation. The Brillouin zone was sampled using a $6 \times 6 \times 1$ Γ-centered k-point mesh and a Gaussian smearing of 0.02 eV. Electronic densities of states were calculated using the tetrahedron method. The dispersion corrections proposed

by Grimme *et al* [21, 22] with screened dispersion coefficients [27] for Cu(1 1 1) were added to the self-consistently calculated Kohn–Sham energies and forces as implemented in VASP by Bučko *et al* [28, 29]

The graphene/Cu(1 1 1) complex was represented by a periodically repeated unit cell containing the graphene layer supported on a four-layer Cu slab and a 20 Å wide vacuum layer. The C-sheet contains 48 atoms and the substrate 24 Cu atoms per layer. Previous calculations showed that there is a very weak preference for the top/fcc stacking (i.e. C atoms positioned above the Cu atoms and the fcc hollows of the Cu(1 1 1) surface), in line with a rather weak interaction and a large separation between graphene and Cu. The graphene lattice constant has been adjusted to match the in-plane lattice constant of the Cu(1 1 1) surface (a mismatch of ∼3.8%). The dispersion-corrected binding energy, E_b, of graphene to the Cu substrate is –42 meV per C-atom at an equilibrium distance of 3.13 Å between the carbon layer and the Cu surface. These values are in good agreement with the RPA-ACFDT results of Olsen *et al* [19] (E_b = –62 meV per C atom and d = 3.25 Å, respectively). Calculations with the 'vdW-functional' of Langreth *et al* [30, 31] predict a larger interfacial distance of 3.58 Å at a slightly lower binding energy of–38 meV per C-atom. [18]

Dimers with an initial geometry determined in the gas-phase were placed on top of the graphene layer, both perpendicular and parallel to the support. We have calculated both the interaction energy, E_{int}, of dimers with the graphene/Cu(1 1 1) complex, measured as the total energy difference of the entire system, the bare graphene/Cu(1 1 1) support and the dimer in the gas phase, and the cohesive energy E_b^{coh} of the supported dimer, calculated with respect to the isolated Co, Pt and Ir atoms and the bare graphene/Cu(1 1 1) complex. The adsorbate/graphene/substrate complex was relaxed until the forces on all atoms were smaller than 25 meV/Å^{-1}, keeping the two lowest Cu layers in their bulk-like positions. Simultaneously, the electronic and magnetic degrees of freedom were relaxed until the change in total energy between successive iteration steps was smaller than 10^{-7} eV.

For each system considered here, both scalar-relativistic calculations and calculations self-consistently including SOC [32, 33] were performed. Magnetic anisotropy energies have been calculated as total energy differences from self-consistent calculations for different orientations of the magnetic moments. For a more detailed description of the computational approach we refer to our earlier work [10].

3. Results

3.1. Pt-adatoms

Before discussing the results for dimers, it is interesting to study the adsorption properties of a single Pt-adatom on graphene/Cu(1 1 1), in comparison with an atom on graphene/Ni(1 1 1) [7] or on a freestanding graphene layer [6]. As for a Pt adatom on a freestanding or on Ni(1 1 1)-supported graphene, the bridge (br) position is found to be energetically most favorable (E_{int} = –2.36 eV), followed by the on-top (ot) (E_{int} = –2.21 eV) and hollow (6h) (E_{int} = –1.75 eV) sites, at vertical distances of $z_{Pt–G}$, of 2.07 (br), 2.08 (ot) and 1.87 Å (6h) to the average height of the atoms in the graphene layer, respectively (see table 1). The modest difference between the adsorption energies in br and ot sites shows that Pt atoms on graphene/Cu(1 1 1) are rather mobile, with diffusion along the network of the C–C bonds requiring an activation energy of only 0.15 eV, even lower than the diffusion barrier for Pt on freestanding graphene (0.18 eV) and much lower than that on graphene/Ni(1 1 1) (0.72 eV). This means that while the formation of dimers or larger clusters is limited by slow diffusion on Ni-supported graphene [7], it is much easier on both freestanding and Cu-supported graphene.

Table 1. Adsorption energy, E_{int}, height of the Pt-adatom above the average graphene sheet, $z_{Pt–G}$, Pt–C bond length, $d_{Pt–G}$, and buckling amplitude of the C-layer, b_G, calculated for the Pt-adatom adsorbed in br-sites on the graphene-supported on Cu(1 1 1) and Ni(1 1 1), and on the freestanding graphene.

Substrate	E_{int} (eV)	$z_{Pt–G}$ (Å)	$d_{Pt–G}$ (Å)	b_G (Å)
G/Cu(1 1 1)	–2.36	2.07	2.09	0.15
G/Ni(1 1 1)[a]	–3.27	2.20	2.10	0.43
Graphene[b]	–1.60	1.98	2.11	0.38

[a] Reference [7]
[b] Reference [6]

Due to the binding to the adatom, the interaction between the C atoms of the graphene layer is locally reduced. The slightly stretched C–C distances induce a corrugation of the graphene layer, with an amplitude increasing with the strength of the interaction: 0.03 Å (6h), 0.08 Å (ot) and 0.15 Å (br), but much smaller than the buckling calculated for freestanding and Ni-supported graphene (see table 1). The C atoms connecting directly to the adatom move outwards for Pt adsorbed on a freestanding layer and on graphene/Cu(1 1 1), in contrast to the Pt atoms on graphene/Ni(1 1 1) which are located in the center of a broad depression of the C layer. Although $z_{Pt–G}$ varies quite strongly for various supports, the Pt–C bond length of 2.10 ± 0.01 Å is almost substrate independent. In contrast to the Pt adatoms on graphene/Ni(1 1 1) which carry small magnetic moments (increasing from the br (–0.02μ_B) over the ot (–0.05μ_B) to the 6h site (–0.19μ_B)), adatoms on freestanding or Cu-supported graphene are always non-magnetic.

These results demonstrate that, while there is a strong interaction between metallic adatoms and a metallic, ferromagnetic substrate mediated by the graphene layer, these effects are much weaker for a noble-metal support on which the graphene layer is only physisorbed.

3.2. Homoatomic Pt- and Ir-dimers

Calculations for dimers in the gas phase have been published in our earlier work [5]. Scalar-relativistic calculations predict for Pt_2 (Ir_2) dimers a bond length of 2.35 (2.21) Å and a spin moment of 1.0 (2.0)μ_B/atom. SOC induces the formation of a high-moment state with the spin and orbital moments of 1.88 (3.88) and 2.74 (1.96)μ_B, respectively, oriented along the dimer axis, and an MAE of 46.3 (69.8) meV/dimer for perpendicular magnetization.

On a freestanding graphene layer [6] a Pt_2 dimer is adsorbed in an upright position at a br site, with a Pt–Pt distance of 2.36

Å and a total spin moment of 1.3μ_B and an orbital moment of 1.70μ_B. In particular, the moments on the lower Pt atom located 2.26 Å above the buckled graphene layer are reduced to less than half their value in a free dimer. The easy magnetic direction is along the dimer axis, where the MAE is reduced to 23.2 meV, in line with a reduced orbital anisotropy. The presence of a Ni substrate stabilizes a flat-lying, non-magnetic dimer with a bond length of 2.54 Å, placing both Pt atoms close to an ot site. A metastable upright dimer adsorbed in a br site is disfavored energetically by 0.34 eV, and remains magnetic with spin and orbital moments of 0.92 and 1.17μ_B. The easy magnetic axis remains perpendicular, but the MAE is dominated by the interface anisotropy of the Ni support [7].

On Cu(1 1 1)-supported graphene a flat position of the dimer with the Pt atoms in br-site is more stable than the upright one (E_{int} = −1.03 *versus* −0.88 eV/Pt-atom). The Pt–Pt distance is 2.51 Å, and the average vertical distance to the weakly buckled graphene layer (b_G = 0.16 Å) is 2.14 Å. The Pt atoms carry magnetic moments of 0.35μ_B each and the neighboring C-atoms ±0.01μ_B, completing a quantized total moment of 1μ_B. The results compiled in table 2 show that the adsorption strength on graphene/Cu(1 1 1) is between that on freestanding and Ni-supported graphene, but that the distortion of the graphene layer is much weaker than on these two substrates.

Calculations including SOC predict for the flat configuration an easy magnetic axis perpendicular to both the Pt–Pt bond of the stable dimer and to the substrate (see figure 1(*a*)), in contrast to the axial anisotropy of a Pt_2 dimer in the gas phase and on a freestanding graphene layer. The dimer has spin and orbital moments of 0.62 and 0.24μ_B in the ground state (GS). A magnetization parallel to the dimer axis and to the support leaves the spin and orbital moments almost unchanged and costs a minimal MAE of 0.7 meV. An in-plane rotation of the magnetization by 90°, perpendicular to the dimers axis, costs an MAE of 2.9 meV and leads to a slightly increased orbital moment.

For the metastable upright Pt dimer on graphene/Cu(1 1 1), calculations including SOC predict spin and orbital moments of 1.13 and 1.45μ_B, respectively, slightly reduced, compared to a dimer on freestanding graphene. The reduction of the moments occurs only on the atom in direct contact with the support, while the local moments on the upper Pt atom are essentially the same. The easy magnetic axis is parallel to the dimer axis and perpendicular to the support, the MAE for magnetization parallel to the support is 23.1 meV, correlated to large spin and orbital anisotropies on both Pt atoms. This means that the magnetic anisotropy of an upright Pt_2 dimer on graphene is almost unchanged by the Cu support. However, the interaction with the support destabilizes the upright relative to a flat configuration, which is only weakly magnetic and shows a much lower magnetic anisotropy.

As already discussed above a free Ir_2 dimer has a higher spin but lower orbital moments than Pt_2 and a larger axial magnetic anisotropy. In contrast to Pt_2, the magnetism of the Ir_2 dimer was found to be extremely sensitive to the interaction with the support. Xiao *et al* [8] have reported that a dimer bound in an upright configuration in the center of a benzene ring is non-magnetic, and the same result was found for a Ir_2 dimer on a freestanding graphene layer. The upright Ir_2 dimer is located

Table 2. The adsorption energy E_{int} and the Pt–Pt binding energy E_b^{coh}, and the Pt–Pt bond length d_{Pt-Pt} of a Pt dimer on graphene/Cu(1 1 1), graphene/Ni(1 1 1) and on the freestanding graphene for flat and upright geometries. z_{Pt-G} is the height of the (lower) Pt adatom above the average of the graphene sheet. b_G is the buckling amplitude of the graphene layer. Energies are given in eV/Pt-atom, distances in Å.

Substrate	Geometry	E_{int}	E_b^{coh}	d_{Pt-Pt}	z_{Pt-G}	b_G
G/Cu(1 1 1)	flat	−1.03	−2.88	2.51	2.14	0.16
	upright	−0.88	−2.74	2.38	2.11	0.12
G/Ni(1 1 1)[a]	flat	−1.75	−3.56	2.56	2.37	0.52
	upright	−1.41	−3.31	2.39	2.28	0.44
Graphene[b]	flat	−0.29	−2.19	2.46	2.30	0.45
	upright	−0.48	−2.38	2.38	2.11	0.23

[a] Reference [7]
[b] Reference [6]

in a 6h site, E_{int} = −0.73 eV/Ir-atom, z_{Ir-G} = 1.81 Å, the bond length is d = 2.21 Å. A weak spin moment of about 0.1μ_B was calculated for the upper atom of the dimer, while a zero moment was found for the lower atom. The weak moment of the dimer is compensated by very small moments of the opposite direction on the surrounding C atoms, such that the net moment of the dimer/substrate complex is zero. Calculations including SOC confirmed that the dimer is non-magnetic. A flat configuration with both Ir atoms close to bridge (br) sites is 0.22 eV/Ir-atom higher in energy (E_{int} = −0.51 eV/Ir-atom, z_{Ir-G} = 2.18 Å, d = 2.18 Å). In contrast to the stable upright dimer, in the metastable configuration the dimer is magnetic with spin moments of 0.66μ_B on both atoms (strongly reduced compared to local spin moments of 2μ_B in the free dimer).

On graphene/Cu(1 1 1) a flat Ir_2 dimer with both atoms located in br positions is more stable (E_{int} = −0.98 eV/Ir-atom) than an upright cluster (E_{int} = −0.91 eV/Ir-atom) positioned in a 6h site of the C-layer. The difference between these two configurations is less pronounced than for the Pt dimer. The Ir–Ir bond length is 2.33 (2.21) Å for flat (upright) configurations, the vertical distance to an average height of the graphene layer is 2.08 (1.76) Å. The buckling amplitude of the C-layer reaches 0.19 Å for the flat and 0.04 Å for the upright dimer. The scalar-relativistic spin moments on the Ir sites for the stable dimer are 0.47μ_B (reduced by 0.19μ_B compared to the flat dimer on graphene only) and, together with small moments induced on the neighboring C-atoms, the quantized moment of the entire complex is just 1μ_B. For the upright dimer the spin moment of the lower atom in direct contact with graphene is almost completely quenched to 0.02μ_B, and even that on the upper atom is only 0.25μ_B. In this case the local moment is increased compared to the dimer on graphene.

Relativistic calculations have been performed for both configurations, and the results are presented in figure 2. In the magnetic GS of the flat dimer, the magnetization is oriented perpendicular to the Ir–Ir bond and parallel to the substrate, in contrast to the axial anisotropy of the free dimer. SOC leads to a reduction of the spin moment from 0.47 to 0.36μ_B, which is not entirely compensated by the modest orbital moments. Together with the moments induced on the C atoms, the total moment is again about 1μ_B. In-plane rotation of the magnetic moments by 90°

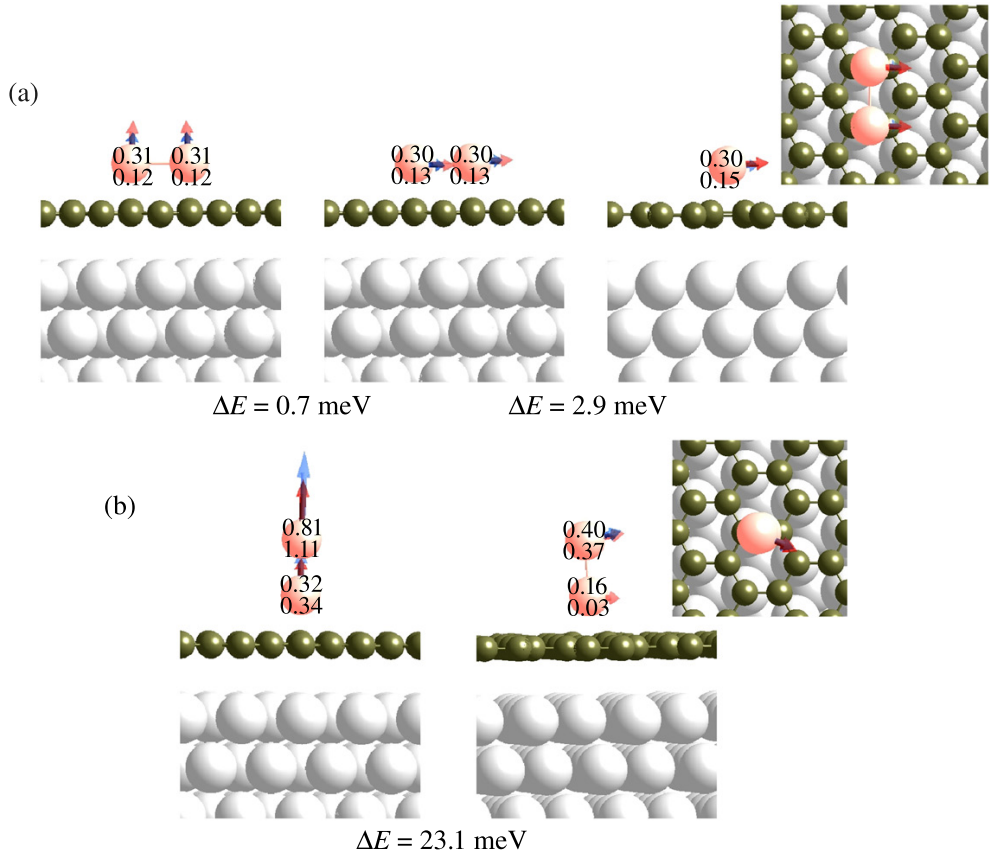


Figure 1. Magnetic structure of a Pt-dimer on Cu(1 1 1)-supported graphene in the GS (*a*) and in the metastable upright (*b*) configuration. For each configuration, the energy difference associated with a rotation of the magnetic moments are listed underneath. Red (blue) arrows show the spin (orbital) magnetic moments, the numbers give the local spin (upper number), and orbital (lower number) magnetic moments in μ_B. Top views are shown in the insets.

to a direction parallel to the support and to the dimer axis costs only a very modest MAE of 1.0 meV, although very substantial negative spin and orbital anisotropies are found ($\Delta m_S = -0.07\mu_B$, $\Delta m_L = -0.15\mu_B$). The local orbital moments are canted relative to the global magnetization direction. Magnetization perpendicular to the substrate and to the dimer axis leads to a slight increase of the local spin moments, from 0.36 to 0.39μ_B at a substantial negative orbital anisotropy (an increase from 0.08 to 0.20μ_B) and costs a small MAE of 0.7 meV.

In the metastable upright geometry the easy magnetic axis is oriented along the Ir–Ir bond. SOC strongly affects the magnetic moments on both atoms, i.e. the spin magnetic moment on the lower atom is enhanced to 0.19μ_B and on the upper one to 0.92μ_B. The local orbital moments are −0.09 and 0.79μ_B on the lower and upper Ir atoms, respectively. The rotation of the magnetic moments out of the easy axis to a direction parallel to graphene leads to a strong reduction of the spin moments to values close to the scalar-relativistic results, and the orbital moments are also strongly reduced (but the antiparallel orientation of spin and orbital moments on the lower Ir atom is not changed). The large MAE of 42.4 meV correlates with the strong spin and orbital anisotropies ($\Delta m_S = 0.83\mu_B$, $\Delta m_L = 0.51\mu_B$). The MAE is lower than that calculated for the free Ir_2 dimer, the spin anisotropy is enhanced, while the orbital anisotropy is only half as large as for the free dimer. We were also able to identify a non-magnetic state which is higher in energy than the GS by 63 meV only. This result confirms that for Ir_2 the energy difference between magnetic and non-magnetic states is very small such that stability can be changed even by very small changes in the environment.

3.3. Heteroatomic PtCo and IrCo dimers

Heteroatomic PtCo and IrCo dimers in the gas-phase and supported on a freestanding graphene layer have been investigated in our recent work. [10] Free PtCo(IrCo) in the gas-phase scalar-relativistic calculations predict a spin magnetic moment of 3 (4)μ_B and a bond length of 2.19 (2.08) Å. Calculations including SOC lead to a small increase of the Pt–Co and Ir–Co bond lengths by 0.01 Å. In the magnetic GS the total magnetic moment of 4μ_B ($\mu_S = 2.85\mu_B$, $\mu_L = 1.15\mu_B$) of the PtCo dimer is parallel to the dimer axis. For perpendicular magnetization, the total moment is only about 3μ_B($m_S = 2.56\mu_B$, $m_L = 0.50\mu_B$), the strong spin and orbital anisotropies lead to a high MAE of 18.8 meV/dimer. The local spin moments are of the same order of magnitude as in the homoatomic Pt_2

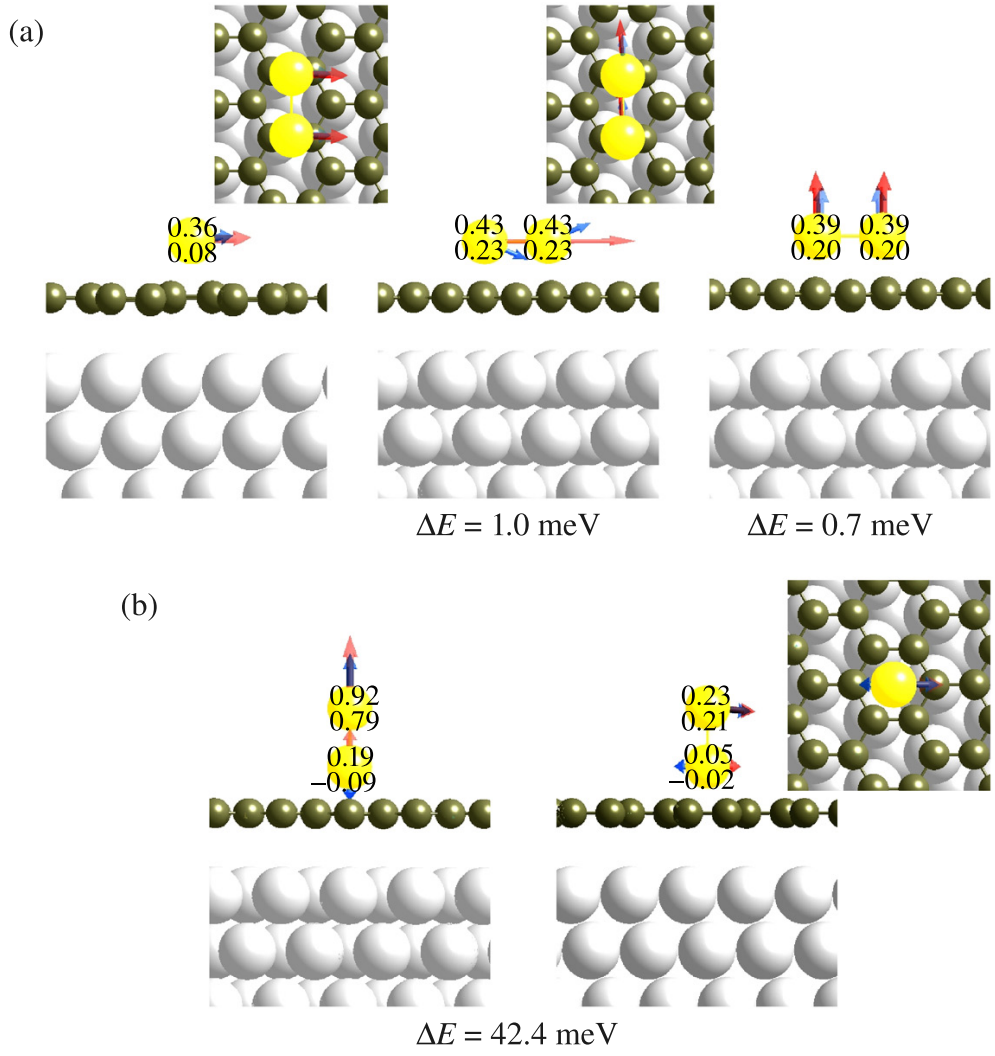


Figure 2. The magnetic structure of a Ir-dimer on a Cu(1 1 1)-supported graphene layer in the GS (*a*) and metastable (*b*) configuration. For each configuration, the energy difference associated with a rotation of the magnetic moments are listed underneath. Red (blue) arrows show the spin (orbital) magnetic moments, the numbers give the local spin (upper number), and orbital (lower number) magnetic moments in μ_B.

and Co_2 dimers, but the orbital moment is strongly reduced on Pt and increased on the Co atom. Details of the structural, energetic and magnetic properties of heteroatomic dimers in the gas phase and on a freestanding graphene layer may be found in [10].

Similarly, the magnetic GS of the IrCo dumbbell is a high-moment state with a total magnetic moment of $\sim 5.5\mu_B$($m_S = 3.56\mu_B$, $m_L = 1.89\mu_B$), oriented along the Ir–Co bond. For perpendicular magnetization the total magnetic moment decreases to $\sim 4\mu_B$($m_S = 3.46\mu_B$, $m_L = 0.69\mu_B$) at a very high anisotropy energy of 69 meV/dimer. The much higher MAE than for the PtCo dimer is correlated to a higher total orbital anisotropy ($\Delta m_L = 0.65\mu_B$ for PtCo and $1.20\mu_B$ for IrCo). One has to note that for PtCo the largest contribution to the orbital anisotropy comes from the Co atom, while for IrCo both atoms contribute evenly to the anisotropy. Together with the larger total moment this explains the larger MAE.

For IrCo these results can be compared with the fully relativistic local orbital calculations of Xiao *et al* [8]. Both calculations predict similar local spin and orbital moments on the Co atom, whereas moments enhanced by $0.2\mu_B$ (orbital moment) and $0.29\mu_B$ (spin) are predicted on the Ir atom. The largest difference is found for the MAE where the value of 142 meV/dimer reported by Xiao *et al* is about twice as large as our result. Such a large difference was also found for homoatomic 3d and 4d dimers where Fritsch *et al* [3] consistently reported larger values than either Blonski and Hafner [5] or Strandberg *et al* [4].

On freestanding graphene [8, 10] both PtCo and IrCo adsorb in an upright configuration with Co binding to the center of a carbon ring. The spin moment of the entire dimer-substrate complex is the same as for the dimer in the gas phase, however the moment on the atom in contact with the substrate is reduced, whereas that on the upper atom is closer to the value for the free atom. The Pt–Co bond length is shortened by 0.01

Table 3. Bond-length d, vertical distance z from the support (both in Å), adsorption energy $E_{\rm int}$ (in eV/dimer), total, spin, and orbital magnetic moments $m_{\rm J}$, $m_{\rm S}$ and $m_{\rm L}$, spin and orbital anisotropies $\Delta m_{\rm S}$ and $\Delta m_{\rm L}$ (all in $\mu_{\rm B}$), easy magnetic axis (relative to the dimer axis), MAE (in meV/dimer) for IrCo and PtCo dimers on graphene adsorbed on a Cu(1 1 1) surface. Local magnetic moments are given in parentheses.

Geometry	PtCo/graphene/ Cu(1 1 1) upright	IrCo/graphene/ Cu(1 1 1) upright
d	2.17	2.15
z	1.60	1.61
$E_{\rm int}$	–1.89	–1.67
$m_{\rm J}$	2.60(0.92/1.68)	5.30(3.58/1.72)
$m_{\rm S}$	2.40(0.74/1.66)	3.54(1.92/1.62)
$\Delta m_{\rm S}$	–0.11(–0.09/–0.02)	0.25(0.20/0.05)
$m_{\rm L}$	0.20(0.18/0.02)	1.76(1.66/0.10)
$\Delta m_{\rm L}$	–0.32(–0.27/–0.05)	1.01(1.07/–0.06)
Easy axis	parallel	parallel
MAE	7.0	204

Å, while that of Ir–Co is increased by 0.05 Å. Calculations including SOC predict an easy magnetization direction perpendicular to the substrate, parallel to the dimer axis as for the free cluster (for details, see [10]). Again, the rotation of the magnetization from easy to hard direction leads for both dimers on graphene to a transition from a high-moment ($m_J^{\rm PtCo} = 4.4\mu_B$, $m_J^{\rm IrCo} = 5.30\mu_B$) to a low-moment magnetic isomer, ($m_J^{\rm PtCo} = 3.4\mu_B$, $m_J^{\rm IrCo} = 4.05\mu_B$), resulting from a modest spin and a strong orbital anisotropy [8, 10]. The MAE of 11.7 meV/PtCo dimer is reduced by 32% compared to the free PtCo, while that for IrCo it is even enhanced from about 35% from 69 meV for the free dimer to 93 meV for the dimer supported on the freestanding graphene [10]. A similar enhancement has also been reported by Xiao *et al* [8].

The energetic, geometric and magnetic properties of PtCo and IrCo dimers on Cu-supported graphene are summarized in table 3. The adsorption geometry is essentially the same as on freestanding graphene, but while for PtCo both bond length and height above the substrate are slightly reduced (by 0.02 Å and 0.07 Å, respectively), for IrCo the bond length remains unchanged while the height of the Co atom above the graphene layer is reduced from 2.22 to 1.61 Å. This shows that the increased strength of the interaction with the substrate (for PtCo $E_{\rm int}$ = −1.89(−1.16) eV/dimer with and without the Cu substrate, for IrCo $E_{\rm int}$ = −1.67(−1.23) eV/dimer) influence the adsorption geometry in different ways. A Co-up configuration leads to an adsorption energy of only $E_{\rm int}$ = −0.95(−1.39) eV/dimer for PtCo(IrCo). The structural energy difference in favor of an upright configuration, as well as the increase of the adsorption energy due to the Cu substrate, are much larger for PtCo than for IrCo.

The scalar-relativistic spin moments on the Pt ($0.97\mu_{\rm B}$) and Co atoms ($1.72\mu_{\rm B}$) of the dimer are reduced compared to the dimer on freestanding graphene, reflecting the stronger interaction with the support. Relativistic calculations including SOC predict for the stable dimer a GS with perpendicular magnetization, parallel to the dimer axis. The spin moment on the Co atom is almost isotropic, while the Pt atom shows a modest negative spin anisotropy of $\Delta\,\mu_{\rm S} = 0.09\mu_{\rm B}$. The local orbital moment of Co is almost completely quenched to zero ($0.02\mu_{\rm B}$), but increases for magnetization perpendicular to the dimer and parallel to the substrate (see figure 3(*a*)). The orbital moment on the Pt atoms is largely reduced compared to the graphene-supported dimer and shows a strong negative anisotropy, increasing from $0.18\mu_{\rm B}$ in the GS to $0.45\mu_{\rm B}$ for magnetization perpendicular to the dimer axis. The negative spin and orbital anisotropies on the Pt atom contrast with the positive value found for PtCo on free graphene. The MAE is only to 7 meV/dimer, i.e. further decreased compared to the free and graphene-supported dimer.

Relativistic calculations for IrCo predict an easy magnetic axis parallel to the Ir–Co bond and perpendicular to the substrate (see figure 3(*b*)) with spin (orbital) moments of 1.92 (1.66)$\mu_{\rm B}$ on Ir and 1.62 (0.10)$\mu_{\rm B}$ on the Co atom. Compared to the free dimer both spin and orbital moment are enhanced on the Ir atom, whereas they are reduced on the Co atom. The orbital moment of Co in particular is nearly completely quenched by the interaction with the substrate. Compared to the dimer on a freestanding graphene layer, the changes are only modest. The additional effect due to the Cu support plays a minor role for the local moments, in particular the spin and orbital anisotropies on the Ir atom remain as large as without the Cu substrate. A rotation of the magnetization to a direction parallel to the support costs a large MAE of 204 meV, nearly twice as large as the MAE of 93 meV obtained for IrCo on graphene [10]. The orbital anisotropy is dominated by the contribution from Ir and is the main factor promoting the huge MAE of the IrCo dimer, quite independent of the nature of the substrate.

4. Electronic structure and magnetic anisotropy

A high MAE depends on the intrinsic properties of the dimer and on an interaction of the dimer with the substrate favoring an upright adsorption geometry. For free homoatomic dimers the dependence of the MAE on the d-band filling is well understood in terms of an analysis of the eigenvalue spectra proposed by Strandberg *et al* [4]—a high MAE will be found if a doubly degenerate orbital at the Fermi level, occupied by a single electron, exists for perpendicular magnetization and is split under the influence of SOC for axial magnetization [5]. The arguments can also be extended to heteroatomic dimers [10] and explain the exceptionally large MAE of Ir_2 and IrCo dimers.

For the supported dimers the essential point is the stable adsorption geometry–a large MAE can be achieved only for a dimer perpendicular to the substrate. On a freestanding graphene layer, an upright adsorption geometry is stable for both homo- and heteroatomic dimers, because the interaction between the metallic atoms is stronger than their binding to the support [6, 10]. However, while graphene-supported Pt_2 remains magnetic, with spin and orbital moments only reduced compared to the free dimer, an upright Ir_2 dimer on graphene is non-magnetic. Heteroatomic IrCo and PtCo dimers are bound to graphene through the Co atom whose magnetism (in particular the orbital moment) is strongly reduced, while due to the weaker binding within the dimer the moments are enhanced on the 5d atoms who become closer to the free-atom limit.

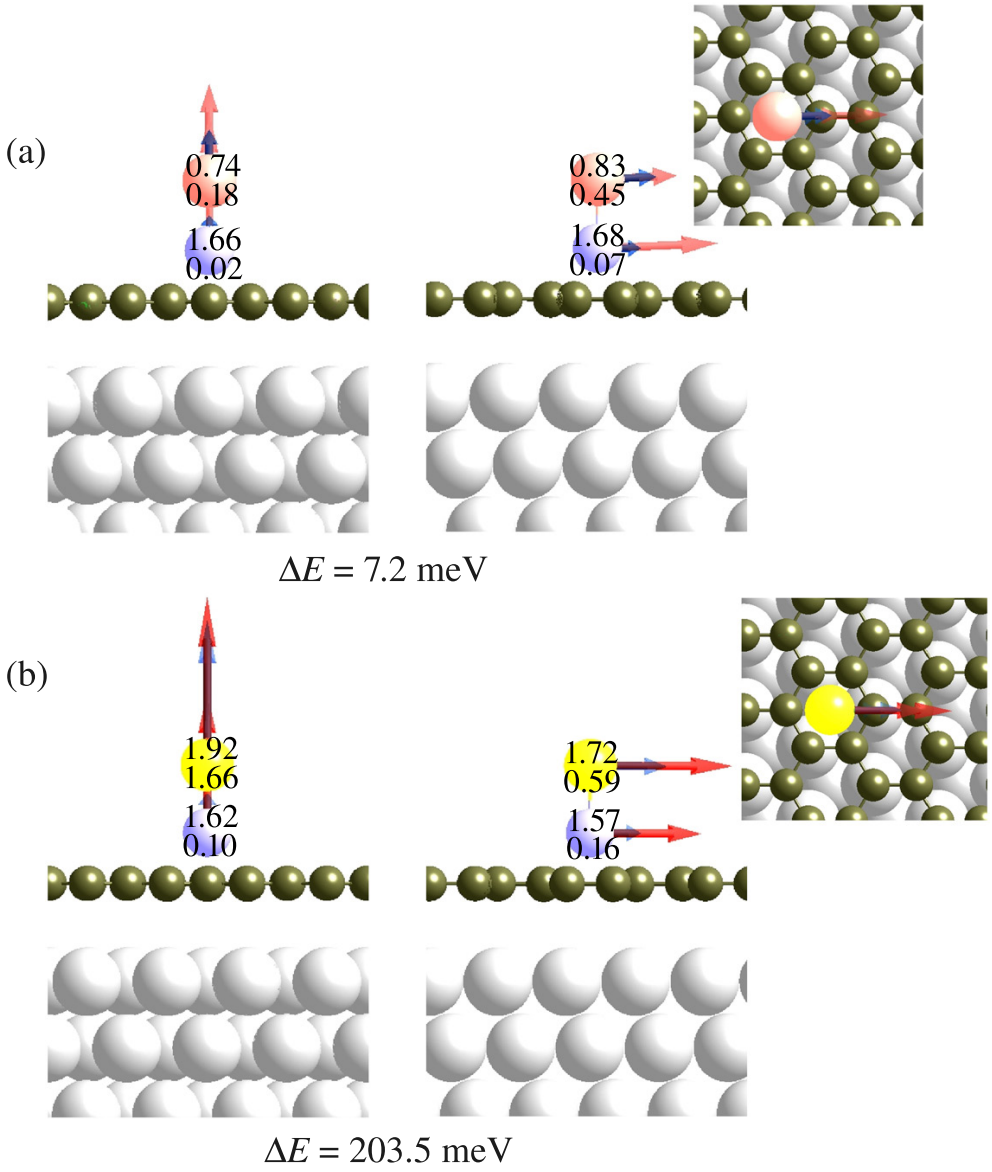


Figure 3. The magnetic structure of a PtCo (Pt-up) (*a*) and an IrCo dimer (Ir-up) (*b*) on the Cu(1 1 1) supported graphene. The energy difference associated with a rotation of the magnetic moments are listed underneath. Red (blue) arrows show the spin (orbital) magnetic moments, the numbers give the local spin (upper number), and orbital (lower number) magnetic moments in μ_B.

The interaction with graphene enhances the MAE of IrCo, but reduces that of PtCo. The mechanism determining the MAE is the same for free and graphene-supported IrCo, whereas for PtCo the broadening of the eigenstates due to the interaction with the substrate reduces the influence of the SOC-induced shift of the eigenstates on the MAE [10].

The situation is changed for graphene deposited on a matching metallic surface: for homoatomic dimers the stronger interaction of the adatoms with the substrate stabilizes a flat adsorption configuration, while an upright dimer is only metastable. Due to the stronger binding to the substrate and the increased lattice constant of the graphene layer matched to Cu(1 1 1), the interatomic distance in the dimers is stretched from 2.36 to 2.51 Å for Pt_2, and from 2.21 to 2.33 Å for Ir_2. The larger distance favors the formation of a weak magnetic moment. Both dimers are weakly magnetic with a very small MAE. In the metastable upright geometry large moments are formed on the upper atom whose large orbital anisotropy determines a large MAE reaching about 50% of that of the free dimers.

For the mixed 3d–5d dimers on graphene/Cu the much stronger binding of the 3d than of the 5d atoms to the support leads to a preference for an upright configuration. The moments on the 3d atom binding to the substrate are strongly quenched and the 5d moments are also reduced—to values much lower than for the free dimer for PtCo, whereas for IrCo

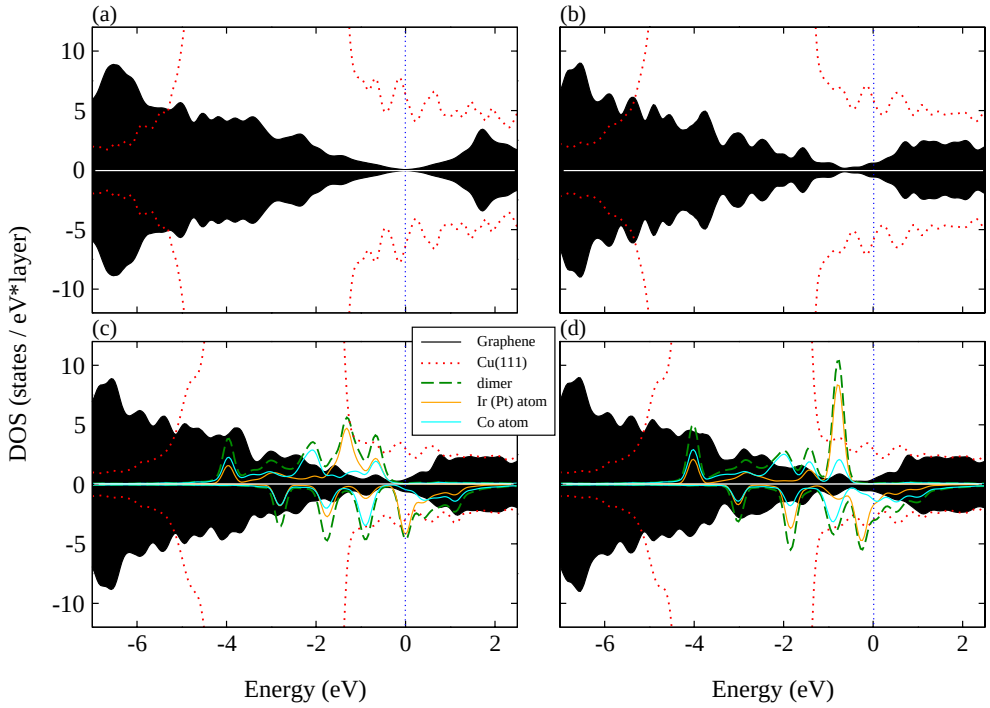


Figure 4. Spin-polarized electronic densities of states of (*a*) a freestanding graphene layer and a clean Cu(1 1 1) surface, (*b*) local densities of states for a graphene layer supported on a Cu(1 1 1) surface, (*c*) an IrCo dimer adsorbed on graphene/Cu(1 1 1), and (*d*) a PtCo dimer supported on graphene/Cu(1 1 1). The result of scalar-relativistic calculations are shown.

they assume intermediate values. This trend is also reflected in the MAE which is further increased from an already large value for IrCo, but reduced for PtCo. This striking difference can be understood by analyzing the electronic densities of states (DOS), shown in the scalar-relativistic mode in figures 4(*a*) and (*d*). The DOS of a free graphene layer is zero at the Fermi level, for graphene supported on a Cu(1 1 1) substrate the Fermi energy is determined by the support, which is located about 0.7 eV above the DOS minimum of graphene. For the supported IrCo dimer the partially occupied spin-down $\delta_d{}^\star$ state is located at E_F. It is dominated by contributions from the Ir atom and almost unchanged by interaction with the substrate. For the PtCo dimer on graphene/Cu the spin-down $\delta_d{}^\star$ state is fully occupied and located about 0.3 eV below the Fermi level.

The total, local and partial DOSs of the supported dimers are shown in figure 5. The large orbital anisotropy and the large MAE of the supported IrCo dimer is again dominated by the splitting of the antibonding $\delta_d{}^\star$ state located at the Fermi level. This state is entirely dominated by contributions from the Ir atom and uninfluenced by the interaction with the support. A further contribution to the MAE comes from the splitting of the bonding spin-up δ_d state at the bottom of the partial δ-DOS (formed by the d_{x^2} and d_{xy} states) whose center of gravity is shifted towards larger binding energies and contributes to the further enhancement of the MAE.

The situation is different for the supported PtCo/graphene/Cu dimer. The antibonding $\delta_d{}^\star$ state is now fully occupied and located just below E_F. Unlike for the free dimer, the SOC-induced splitting of the states does not reorder the energy levels and the σ_d state remains higher in energy. However, as the separation of the states is very small, the σ_d state is partially populated at the expense of the antibonding $\delta_d{}^\star$ state. The SOC-induced splitting of the $\delta_d{}^\star$ state shifts the center of gravity to slightly larger binding energies, but the mixing of the upper component with quantum numbers $s_z = -1/2$ and $m_l = -2$ with the σ_d state becomes even more pronounced and results in an increased orbital moment and negative orbital anisotropy on the Pt atom. At larger binding energies the SOC-induced splitting of the eigenstates for perpendicular magnetization is much smaller than for the supported IrCo dimer. Together, the contribution of all eigenstates to the MAE decreases from the free to the graphene-supported and further to the dimer on graphene on Cu(1 1 1).

5. Conclusions

We have used *ab-initio* DFT calculations to investigate the properties of magnetic transition-metal dimers adsorbed on a graphene monolayer supported on a Cu(1 1 1) substrate. The results show that the graphene layer does not entirely isolate the dimers from the metallic substrate. A clean graphene layer is only weakly physisorbed on the Cu(1 1 1) surface. Metallic adatoms or dimers bind quite strongly to graphene, causing a weaker binding and a local elongation of the C–C bonds and a substantial buckling of the carbon layer. For homoatomic Ir_2 and Pt_2 dimers the presence of the substrate leads to an

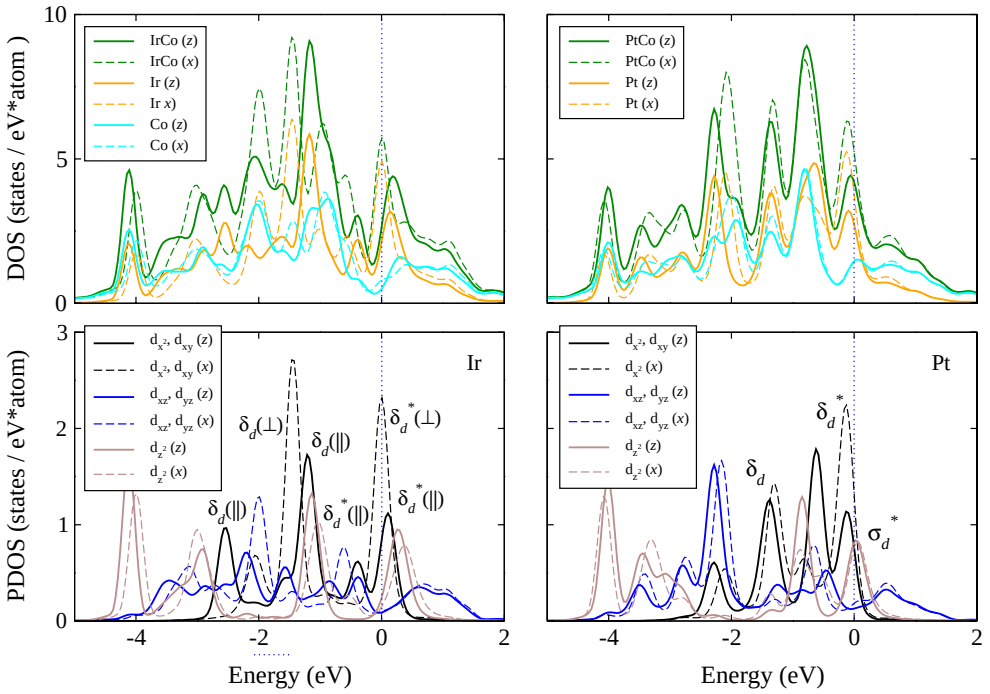


Figure 5. Total, local and partial densities of states of IrCo and PtCo dimers adsorbed on a graphene layer supported on a Cu(1 1 1) surface, calculated including SOC for magnetization along the dimer axis (the z-axis, full lines) and perpendicular to it along the x-axis (broken lines). Most important for the magnetic anisotropy is the splitting of the δ_d states (formed by the $d_{x^2-y^2}$ and d_{xy} orbitals, shown in black) upon a change in the magnetization direction. See text.

increase of the adsorption energy by about 0.2 eV/dimer, but the most important effect is that a flat adsorption geometry, with both atoms binding to C–C bridge sites, is now more stable than the upright geometry preferred on the freestanding graphene layer. The flat dimers are only weakly magnetic with a small MAE, in contrast to the strongly anisotropic magnetism of upright dimers.

For the mixed IrCo and PtCo dimers an upright configuration represents the ground state even on Cu(1 1 1)-supported graphene, but the influence of the substrate on the magnetic anisotropy is totally different. For IrCo only the local moments on the Co atom binding to graphene are quenched through the interaction of the support, while the spin and orbital moments on the Ir atom remain almost unchanged. The mechanism causing the large magnetic anisotropy of free and graphene-supported IrCo dimers (the SOC-induced splitting of a singly occupied $\delta_d{}^\star$ state at the Fermi-level) remains intact, and further contributions from states at larger binding energies leads to an MAE increasing in the sequence-free IrCo (MAE = 69 meV/dimer)–IrCo/graphene (93 meV/dimer)–IrCo/graphene/Cu(1 1 1) (204 meV/dimer). In contrast for PtCo not only the Co moments are reduced by the interaction with the support, but also the orbital moments on the Pt atom are smallest for PtCo/graphene/Cu(1 1 1), lower than for the free dimer and much lower than for PtCo/graphene. This is related to the strong mixing of the fully occupied $\delta_d{}^\star$ state with an energetically almost degenerate σ_d state. The mixing is even stronger for perpendicular magnetization, leading to a strong negative orbital anisotropy on the Pt atom. Together, the MAE decreases with increasing strength of the interaction with the support: free PtCo (MAE = 19 meV/dimer)–PtCo/graphene (12 meV/dimer)–PtCo/graphene/Cu(1 1 1) (7 meV/dimer).

Acknowledgment

Work at the Universität Wien has been supported through the VASP project.

References

[1] Gambardella P *et al* 2003 *Science* **300** 1130
[2] Blonski P, Lehnert A, Dennler S, Rusponi S, Etzkorn M, Moulas G, Bencok P, Gambardella P, Brune H and Hafner J 2010 *Phys. Rev.* B **81** 125418
[3] Fritsch D, Koepernik K, Richter M and Eschrig H 2008 *J. Comput. Chem.* **29** 2210
[4] Strandberg O, Canali C M and McDonald A H 2007 *Nature Mater* **6** 648
Strandberg O, Canali C M and McDonald A H 2008 *Phys. Rev.* B **77** 174416
[5] Błoński P and Hafner J 2009 *Phys. Rev.* B **79** 224418
[6] Błoński P and Hafner J 2011 *J. Chem. Phys.* **134** 154705
[7] Błoński P and Hafner J 2012 *J. Chem. Phys.* **136**074701
[8] Xiao R, Kuz'min M D, Koepernik K and Richter M 2010 *Appl. Phys. Lett.* **97** 232501
[9] Xiao R, Fritsch D, Kuz M D, Koepernik K, Eschrig H, Richter M, Vietze K and Seifert G 2009 *Phys. Rev. Lett.* **103** 187201
[10] Błoński P and Hafner J 2014 *J Phys.: Condens. Matter* **26** 146002

[11] Voloshina E and Dedkov Y 2012 *Phys. Chem. Chem. Phys.* **14** 13502
[12] Błoński P and Hafner J 2012 *J. Chem. Phys.* **137** 044710
[13] Li X *et al* 2009 *Science* **324** 1312
[14] Nie S, Wofford J M, Bartelt N C, Dubon O D and McCarty K F 2011 *Phys. Rev.* B **84** 155425
[15] Khomyakov P A, Giovannetti G, Rusu P C, Brocks G, van den Brink J and Kelly P J 2009 *Phys. Rev.* B **79** 195425
[16] Xu Z and Buehler M J 2010 *J. Phys.: Condens. Matter* **22** 485301
[17] Wu P, Zhang W, Li Z, Yang J and Hou J G2010 *J. Chem. Phys.* **133** 071101
[18] Vanin M, Mortensen J J, Kelkkanen A K, Garcia J M, Thygesen K S and Jacobsen K W 2010 *Phys. Rev.* B **81** 081408
[19] Olsen T, Yan J, Mortensen J J and Thygesen K S 2011 *Phys. Rev. Lett.* **107** 156401
[20] Mittendorfer F, Garhofer A, Redinger J, Klimeš J, Harl J and Kresse G 2011 *Phys. Rev.* B **84** 201401
[21] Grimme S, Antony J, Schwabe T and Mück-Lichtenfeld C 2007 *Org. Biomol.Chem.* **5** 741
[22] Grimme S, Antony J, Ehrlich S and Krief H 2010 *J Chem. Phys.* **132** 154104
[23] Kresse G, Furthmüller J 1996 *Comput. Mater. Sci.* **6** 15
Kresse G, Furthmüller J 1996 *Phys. Rev.* B **54** 11169
[24] Kresse G and Joubert D 1999 *Phys. Rev.* B **59** 1758
[25] Blöchl P E 1994 *Phys. Rev.* B **50** 17–953
[26] Perdew J P, Burke K and Ernzerhof M 1996 *Phys. Rev. Lett.* **77** 3865
[27] Ruiz V G, Liu W, Zojer E, Scheffler M and Tkatchenko A 2012 *Phys. Rev. Lett.* **108** 146103
[28] Bučko T, Lebègue S, Ángyán J G and Hafner J 2010 *J. Phys. Chem.* A **114** 11814
[29] Bučko T, Lebègue S, Hafner J and Ángyán J G 2013 *Phys. Rev.* B **87** 064110
[30] Dion M, Rydberg H, Schröder E, Langreth D C and Lundqvist B I 2004 *Phys. Rev. Lett.* **92** 246401
[31] Dion M, Rydberg H, Schröder E, Langreth D C and Lundqvist B I 2005 *Phys. Rev. Lett.* **95** 109902
[32] Kresse G and Lebacq O VASP Manual (http://cms.mpi.univie.ac.at/vasp/vasp/vasp.html)
[33] Hobbs D, Kresse G and Hafner J 2000 *Phys. Rev.* B **62** 11556

IOP Publishing Journal of Physics: Condensed Matter
J. Phys.: Condens. Matter **27** (2015) 046002 (22pp) doi:10.1088/0953-8984/27/4/046002

On the interplay between geometrical structure and magnetic anisotropy: a relativistic density-functional study of mixed Pt–Co and Pt–Fe trimers and tetramers in the gas-phase and supported on graphene

Piotr Błoński[1,2] **and Jürgen Hafner**[1]

[1] Faculty of Physics and Center for Computational Materials Science, University of Vienna, Sensengasse 8/12, A-1090 Wien, Austria
[2] Institute of Nuclear Physics, Polish Academy of Sciences, ul. Radzikowskiego 152, PL-31-342 Kraków, Poland

E-mail: juergen.hafner@univie.ac.at

Received 11 September 2014, revised 3 December 2014
Accepted for publication 8 December 2014
Published 7 January 2015



Abstract

The structural and magnetic properties of mixed Pt–Co and Pt–Fe trimers and tetramers in the gas-phase and supported on a free-standing graphene layer have been calculated using density-functional theory. The influence of the strong magnetic moments of the 3d atoms on the Pt atoms and the influence of the strong spin–orbit coupling contributed by the Pt atoms on the 3d atoms have been studied in detail. All mixed trimers form isocele triangles in the gas-phase. On a graphene layer the structure is influenced by the strong binding of the 3d atoms, leading to an asymmetric configuration for Pt-rich and more symmetric structures for 3d-rich clusters. The magnetic anisotropy energy defined as the energy difference for easy and hard magnetization directions varies between 5 and 13 meV/atom for the free trimers, but is strongly reduced to values between 0.7 and 6.6 meV/atom for the graphene-supported clusters. The saddle-point energy representing the barrier against magnetization reversal is on average 3 meV/atom for free trimers, it is reduced to 2 meV/atom for the more symmetric $PtCo(Fe)_2$ clusters, and to only about 0.3 meV/atom for the asymmetric $Pt_2Co(Fe)$ cluster on graphene. For the mixed tetramers the strong magnetism stabilizes a flat geometric structure, except for Pt_3Co which forms a distorted trigonal pyramid. The geometry of the graphene-supported tetramers is very different due to the requirement of a good match to the substrate. Large magnetic anisotropy energies are found for free Pt_3Co where the change of the magnetization direction also induces a transition from a high- to a low-moment magnetic isomer. For all other free tetramers the magnetic anisotropy energy ranges between 3 to 5 meV/atom only, it is further reduced to 0.4 to 3.8 meV/atom for the graphene-supported tetramers. The reduction is strongest for Pt_3Fe/graphene because of the asymmetric structure of the adsorption complex. The barriers against magnetization reversal range between only 0.3 meV/atom for Pt_3Fe/graphene and about 3 meV/atom for $PtFe_3$ and Pt_3Co. Altogether our results demonstrate a strong correlation between the geometric and magnetic degrees of freedom and the necessity to base investigations of the magnetic anisotropy of nanostructures on a simultaneous optimization of the total energy with respect to all geometric and magnetic parameters.

Keywords: magnetic anisotropy, geometric structure, nanoclusters, graphene, density functional theory

S Online supplementary data available from stacks.iop.org/JPCM/27/046002/mmedia

(Some figures may appear in colour only in the online journal)

 © 2015 IOP Publishing Ltd Printed in the UK

1. Introduction

The properties of magnetic nanostructures have been for a long time in the center of intense research efforts because of their potential application as information storage media. The focus is on materials with a large magnetic anisotropy where the direction of the induced magnetization is expected to be stable against thermal excitations. A high magnetic anisotropy energy (MAE) is expected in systems with large spin and orbital magnetic moments and strong spin–orbit coupling (SOC). Hence bimetallic nanostructures in which large moments are carried by ferromagnetic 3d transition-metal atoms and heavy 5d atoms contribute to a strong SOC are promising candidates.

Enhanced orbital moments and magnetic anisotropy energies have been found in experimental and theoretical investigations of Fe(Co)–Pt multilayers and nanoparticles [1–8]. While most investigations have concentrated on nanoparticles containing several hundreds of atoms an bulk-like structures, the magnetic properties of very small clusters consisting of only a few atoms deserve increased attention.

During the last years, we have investigated the magneto-structural properties of small Pt clusters in the gas-phase [9] and adsorbed on graphene, either free-standing [10] or supported on a metallic substrate [11]. For free Pt_n clusters our calculations predict large orbital moments, comparable in magnitude to the spin moments and an MAE of several meV/atom. Although the binding of the clusters to graphene layer via only one or two Pt atoms is weak, their magnetic structure is much more inhomogeneous than in the gas-phase, with a non-collinear orientation of the magnetic moments and a MAE reduced to roughly one third [10]. On metal-supported graphene layers the adsorption is stronger, leading to a further reduction of the magnetic anisotropy [11].

Recently investigations of mixed IrCo, PtCo and PtFe dimers [12–14] have reported astonishingly large MAE's for some mixed dimers. Large MAE's reaching 70 meV/dimer for Ir_2 and 46 meV/dimer for Pt_2 had been predicted before for homoatomic dimers [15]. A large magnetic anisotropy exists if the two-fold degeneracy of a singly occupied state at the Fermi level for magnetization perpendicular to the dimer axis is lifted for axial magnetization [16]. A similar argument also explains the large MAE's for IrCo (69 meV/dimer) and PtCo (19 meV/dimer) on one and the small axial anisotropy of PtFe dimers (3 meV/dimer) on the other hand [13]. For dimers adsorbed on graphene the magnetic properties are found to be very sensitive to the interaction with the support. All dimers are adsorbed in an upright configuration. While for Pt_2 bound to a C–C bridge site spin- and orbital moments and the MAE are only reduced, a Ir_2 dimer bound in the center of a sixfold hollow is almost completely demagnetized. In contrast, mixed dimers are bound through the 3d-atom to a hollow site. The binding to the substrate weakens the binding between the atoms forming the dimer so that the properties of the 5d atom become more free-atom like, with enhanced spin and orbital moments, while moments of the 3d atom are strongly quenched. Compared to the free dimers, the MAE is even enhanced for IrCo (93 meV/dimer), reduced for PtCo (12 meV/dimer) and changes sign for PtFe where the easy magnetic axis is now also parallel to the dimer axis. Again the changes in the magnetic properties can be traced back to the properties of the highest occupied electronic eigenstates. The presence of a Cu-substrate enhances the interaction between the dimer and the support. For the homoatomic dimers a flat adsorption geometry is stabilized, while for the heteroatomic IrCo and PtCo dimers the upright geometry is preserved. The stronger interaction with the support leads to an enhanced MAE for IrCo (204 meV), while that of PtCo is reduced (7 meV) [14]. Whether similar effects lead to an enhanced MAE also for larger clusters is an open question.

In the present work we have investigated the magnetic properties of heteronuclear Pt–Co and Pt–Fe trimers and tetramers, both in the gas-phase and adsorbed on a graphene monolayer. For dimers the origin of a large MAE is relatively simple: the two-fold degeneracy of a singly occupied state at the Fermi level for magnetization perpendicular to the dimer axis is lifted for an axial magnetization (see [13] and references therein). The geometrical properties of the dimers, however, are not affected (apart from a modest change in the bond-length reported for Pt_2). Trimers and tetramers are the smallest clusters for which magneto-structural effects could appear. For a highly symmetric cluster the possible degeneracy of the electronic eigenstates near the Fermi level can be lifted also by a Jahn–Teller distortion. Indeed for a Co_3 trimer an isosceles triangle has a lower energy than the more symmetric equilateral structure and also a much lower MAE [16]. For a Fe_3 trimer treated in a scalar-relativistic approach or including SOC the ground-state structure is also an isosceles triangle, although an equilateral configuration with a higher moment is only slightly higher in energy. For mixed clusters containing a heavy atom contributing a large SOC such as Pt the magnetic structure is much more inhomogeneous and both SOC and the direction of magnetization can affect the geometric structure. For clusters adsorbed on graphene the adsorption energies are only modest (a few tenths of eV/atom), because the energy gain by the formation of quite strong cluster-substrate bonds is partially compensated by the deformation of the clusters required to achieve a good match to the substrate. The binding to the substrate lowers the symmetry of the cluster and minimizes the influence of SOC on the geometry. Cluster-geometry and the interaction between 3d and 5d atoms and with the substrate have a strong influence on the magnetic anisotropies which is discussed in detail.

2. Computational method

Our investigations are based on spin-polarized density functional theory (DFT) as implemented in the Vienna *ab initio* simulation package VASP [17, 18]. The electron-ion interactions were described using the projector augmented wave (PAW) method [18, 19]. The basis set contained plane waves with a maximum kinetic energy of 500 eV. For electronic exchange and correlation effects we chose the functional of Perdew, Burke and Ernzerhof (PBE) [20] in the generalized-gradient approximation (GGA) and the spin-interpolation proposed by Vosko *et al* [21] Our motivation for the choice

Table 1. Binding energies E_b (in eV/atom), equilibrium structure, interatomic distances d_{ij} (in Å), spin and orbital moments, m_S and m_L, (in μ_B/atom) and magnetic anisotropy energy MAE (in meV/trimer) for Fe_3 and Co_3 from scalar-relativistic (SR) and fully relativistic (SOC) calculations. See text.

	Method	E_b	d_{ij}	m_S	m_L	MAE
Fe_3	SR	−1.57	3×2.29	3×4		
	SR	−1.61	2×2.14, 2.40	2×3.45, 3.05		
	SOC		2×2.14, 2.40	2×3.10, 2.75	2×0.07, 0.06	0
	SOC		2×2.14, 2.40	2×3.10, 2.75	2×0.12, 0.07	0.7
	SOC		2×2.14, 2.40	2×3.10, 2.75	2×0.08, 0.07	1.2
Co_3	SR	−1.80	2×2.17, 2.16	3×1.66		
	SOC		2×2.22, 2.08	2×1.95, 2.05	2×0.16, 0.20	0
	SOC		2×2.22, 2.08	2×1.96, 2.06	2×0.13, 0.18	1.3
	SOC		2×2.22, 2.08	2×1.95, 2.06	2×0.12, 0.15	2.1

of the PBE functional has been discussed in detail in our work on mixed dimers [13]. Spin–orbit coupling has been implemented in VASP by Kresse and Lebacq, [22] following the approach of Kleinman and Bylander [23] and MacDonald *et al* [24] Calculations including SOC have been performed in the non-collinear mode implemented in VASP by Hobbs *et al* [25] Magnetic anisotropy energies have been calculated as total energy differences from selfconsistent calculations for different orientations of the magnetic moments. For all further computational details we refer the readers to our previous publications [9, 11, 13, 15].

The calculations have been performed for Pt_2Fe, Pt_2Co, $PtFe_2$ and $PtCo_2$ trimers and Pt_3Fe, Pt_3Co, $PtFe_3$ and $PtCo_3$ tetramers. In the latter case both planar and three-dimensional structures have been explored. To create a reference, calculations including SOC for Fe and Co trimers and tetramers have been performed.

The binding energy per atom in a free Pt_mX_l cluster (X = Co, Fe) is calculated as the total energy of the cluster minus the energy of the isolated atoms ($n = m + l$),

$$E_b = \frac{1}{n}\big(E(Pt_mX_l) - m \cdot E(Pt_m) - l \cdot E(X_l)\big). \quad (1)$$

The adsorption energy for a Pt_mX_l-cluster on graphene is calculated as the total energy difference between the cluster-graphene complex, $E(Pt_mX_l)_{graph}$, the clean graphene layer, E(graph) and the cluster in the gas-phase,

$$E_{int} = \frac{1}{n}\big(E(Pt_mX_l)_{graph} - E(graph) - E(Pt_mX_l)\big). \quad (2)$$

Equation (2) provides the *interaction* energy of Pt_mX_l-clusters of a certain size and shape with the graphene sheet. The binding between atoms in the adsorbed cluster is measured by the cohesive energy of the adsorption complex minus the energy of the graphene layer and the energy of the free Pt and X atoms,

$$E_{b-ad} = \frac{1}{n}\big(E(Pt_mX_l)_{graph} - E(graph) - m \cdot E(Pt_m) - l \cdot E(X_l)\big). \quad (3)$$

For the graphene layer we have used the same model as in [13]. For trimers and tetramers on graphene both flat and upright configurations, with different locations of the binding atoms on the graphene layer have been explored. Flat clusters on graphene are unstable, the structural relaxation leads in all cases to the formation of a three-dimensional cluster, details are given below.

3. Magnetic anisotropy of homoatomic Fe and Co clusters

Clusters formed by the ferromagnetic metals Fe, Co and Ni have been studied repeatedly using density functional methods (for a compilation of the literature see, e.g. the papers of Johll *et al* [26, 27]). For Fe_3 spin moments of 8 ([28]) and 10 μ_B ([27, 29]) have been reported and Johll *et al* [27] also found a high-spin state with 12 μ_B at an only slightly increased total energy. The geometry has been described either as an equilateral [28] or an isocele [29] triangle. Johll *et al* [27] reported an equilateral triangle for the high-spin state and a distorted geometry for the ground-state. Similarly, magnetic moments of 5 or 7 μ_B and equilateral or distorted geometries were reported for Co_3 [27, 28, 30]. For the tetramers distorted tetrahedral geometries and magnetic moments of 14 μ_B for Fe_4 ([27, 31]) and 10 μ_B for Co_4 ([27, 28]) were found. The competition between structural and magnetic effects in small Fe clusters has been discussed in detail by Rollmann *et al* [32].

3.1. Trimers

Our results for trimers are summarized in table 1. For Fe_3 scalar-relativistic calculations predict a ground state with a magnetic moment of 10 μ_B forming an isocele triangle with a difference of 0.26 Å between the short and long edges. A high-spin state with a moment of 4 μ_B per atom, forming an equilateral triangle is about 40 meV higher in energy, interatomic distances are expanded by about 0.06 Å on average. These results are in good agreement with Johll *et al* [27] The geometric structure remains unchanged if SOC is included, in the ground state the magnetization is perpendicular to the plane of the isocele triangle. Spin-moments are reduced, the larger moments of 3.10 μ_B are located on the atoms separated by the longer edge, orbital moments are very small. The hard magnetic axis is in-plane, parallel to the long edge of the triangle, the MAE is 1.2 meV/cluster. Spin moments are isotropic and there is only a marginal negative orbital anisotropy of −0.01 μ_B. For in-plane magnetization parallel to the twofold symmetry axis the MAE is only 0.7 meV/trimer

Table 2. Binding energies E_b (in eV/atom), equilibrium structure, interatomic distances d_{ij} (in Å), spin and orbital moments, m_S and m_L, (in μ_B/atom) and magnetic anisotropy energy MAE (in meV/tetramer) for Fe_4 and Co_4 in three-dimensional and flat geometries from scalar-relativistic (SR) and fully relativistic (SOC) calculations. See text.

	Method	Structure	E_B	d_{ij}	m_S	m_L	MAE
Fe_4	SR	Dist. tetrahedron	−2.02	4 × 2.24, 2 × 2.54	4 × 3.5		
	SOC	Dist. tetrahedron		4 × 2.24, 2 × 2.54	2 × 3.21, 2 × 2.90	2 × 0.10, 2 × 0.06	2.8
Fe_4	SR	Rhombus	−1.96	4 × 2.23, 2.50	4 × 3.5		
	SOC	Rhombus		4 × 2.23, 2.50	2 × 3.11, 2 × 3.03	2 × 0.09, 2 × 0.08	0.69, 0.53
Co_4	SR	Dist. tetrahedron	−2.22	4 × 2.14, 2 × 2.74	4 × 2.5		
	SOC	Dist. tetrahedron		4 × 2.15, 2 × 2.75	4 × 2.19	4 × 0.14	0.5
Co_4	SR	Rhombus	−2.14	4 × 2.18, 2.29	4 × 2.5		
	SOC	Rhombus		4 × 2.18, 2.31	2 × 1.95, 2 × 1.96	2 × 0.21, 2 × 0.23	3.1, 6.8

and there is a slightly larger orbital anisotropy of $\Delta m_L = -0.05\,\mu_B$ on the atoms carrying larger local moments.

For Co_3 scalar-relativistic calculations predict a small distortion of the threefold geometry, which is not reflected in the local spin moments. Johll *et al* [27] reported energetically almost degenerate states with $7\,\mu_B$ and $5\,\mu_B$ and much more pronounced distortions of the triangular geometry, albeit at a lower binding energy of only −1.68 eV/cluster. Strandberg *et al* [16] found the $7\,\mu_B$ state with isocele geometry to be slightly lower than the $5\,\mu_B$ state forming an equilateral triangle. If SOC is taken into account, the differences in the bond lengths become much more pronounced and the broken threefold symmetry is also reflected in the increased spin moments. Orbital moments are larger than in the Fe trimer. The easy axis is in-plane, parallel to the twofold symmetry axis. In-plane rotation of the magnetization costs a small MAE of 1.3 meV/cluster and is related to a reduction of the local magnetic moments of up to $0.03\,\mu_B$. A larger MAE of 2.1 meV/cluster is required for perpendicular magnetization. This configuration is characterized by a small spin anisotropy of $0.01\,\mu_B$, the orbital moments are lowered to 2×0.12 and $0.15\,\mu_B$. The MAE of the Co_3 trimer was also calculated by Strandberg *et al* [16] using similar approach, but a fixed geometry. A perpendicular easy axis was found for both structural variants, with a MAE of 3.9 meV for the low- and of 2.4 meV for the high-symmetry variant.

For the Pt_3 trimer the easy axis is in-plane, parallel to the symmetry axis, as for Co_3. Perpendicular magnetization is disfavored by a much larger MAE of 15.2 meV/trimer, but there is only a very small in-plane MAE of 0.6 meV/trimer. Both spin and orbital moments are strongly anisotropic [9].

3.2. Tetramers

Tetramers are the smallest clusters where either three- or two-dimensional geometries can be formed. The flat configurations may be stabilized by the binding to a substrate. Our results for Fe_4 and Co_4 in both geometries are summarized in table 2. For both tetramers a distorted tetrahedral structure (point group S_4) with four short and two longer edges is more stable than a flat geometry forming a rhombus, with structural energy differences of 58.6 meV/atom for Fe_4 and 76.6 meV/atom for Co_4.

In the scalar-relativistic limit the results for 3D-Fe_4 with a total moment of $14\,\mu_B$ are in very good agreement with Johll *et al* [27] As for the Fe_3 trimer SOC leaves the structure unchanged, it is also independent of the direction of magnetization. The spin moments are reduced due to the mixing with a low-spin isomer, the orbital moments are low, as for the trimer. The easy magnetic axis is parallel to one of the long edges of the distorted tetrahedron, rotation of the magnetization direction within the plane of a triangular facet by 90° costs a small MAE of 2.8 meV/cluster, related to a reduction of two of the local orbital moments from 0.10 to $0.07\,\mu_B$. 2D-Fe_4 forms a rhombus with slightly shorter interatomic distances than in the 3D structure. Again, SOC leaves the structure unchanged, independent of the direction of magnetization. The easy axis is parallel to the short diagonal of the rhombus, in-plane rotation parallel to the long diagonal costs an MAE of 0.69 meV/tetramer, connected with an enhancement of two of the local orbital moments from 0.09 to $0.13\,\mu_B$ and a reduction of the other two from 0.08 to $0.06\,\mu_B$. Perpendicular magnetization is disfavored by 0.53 meV/tetramer and very small orbital anisotropies of 0.01 and $0.02\,\mu_B$. Spin moments remain isotropic.

For 3D-Co_4 the distortion from a perfect tetrahedral geometry is more pronounced (see table 2), in very good agreement with Johll *et al* [27] Strandberg *et al* [16] reported a structure with the same symmetry, but much shorter interatomic distances. SOC leaves the geometry almost unchanged (distances increase by 0.01 Å), the easy magnetic direction is along one of the longer edges of the tetrahedron. The local magnetic moments do not reflect the geometric distortion of the cluster. An in-plane rotation of the magnetization direction by 90° costs only 0.5 meV, both spin and orbital moments are isotropic to within $0.01\,\mu_B$. For 2D-Co_4 forming a rhombus SOC leads to an even stronger reduction of the spin moments, but to larger orbital moments than for the 3D geometry. The easy axis is parallel to the long diagonal, in-plane rotation of the magnetization costs 3.1 meV/tetramer, the perpendicular MAE is 6.8 meV/tetramer. The much larger MAE than for flat Fe_4 is related to local orbital anisotropies around $0.2\,\mu_B$.

Scalar-relativistic calculations for graphene-supported Fe_n and Co_n ($n = 1 - 4$) clusters have been reported by Johll *et al* [26, 27] and for Fe_n clusters by Longo *et al* [33] and by Srivastava *et al* [34] For Fe_3 the predicted equilibrium adsorption structure is either an upright triangle bound through an Fe–Fe edge to hole sites ([27]), an upright triangle bound only through a single Fe atom to a sixfold hole

([34]), or a triangle in an oblique orientation with respect to graphene, bound through one Fe atom to an on-top site and the upper Fe atom above a hole ([33]). The cluster moments are strongly reduced compared to the free trimer to 8.69 μ_B, 8.09 μ_B and 8.95 μ_B, respectively. For the tetramer the predicted adsorption geometries are a tetrahedron bound through one of the triangular facets to three hole sites ([27]), a top-down trigonal pyramid centered above a sixfold hole ([34]) and a zig–zag chain ([33]). The magnetic moments of 10.92 μ_B, 11.57 μ_B and 12.89 μ_B per cluster are also very different. These results merely emphasize how difficult it is to find the equilibrium geometry of adsorbed clusters. Only Johll *et al* [27] have reported results for a number of competing geometries and we think that their results are most trustworthy. In the present work homoatomic Fe and Co clusters have not been considered, because our focus is on the magnetic anisotropy which can be expected to be small in 3d clusters.

For the tetramers no direct comparison with Pt_4 is possible, because the ground state of the stable rhombic structure is antiferomagnetic and that of the metastable tetrahedral tetramer is noncollinear [9]. For the flat structure the MAE between excited ferromagnetic state with an in-plane easy axis (parallel to the short diagonal of the rhombus) and perpendicular magnetization is 21.2 meV/tetramer. The in-plane MAE for rotation to a direction parallel to the long diagonal of 34.9 meV/tetramer is even higher. These large values of the MAE are again correlated to strong spin and orbital anisotropies.

4. Heteroatomic Pt–Co and Pt–Fe trimers

The results for the stability of the free and graphene-supported mixed clusters are summarized in the supplementary information (stacks.iop.org/JPCM/27/046002/mmedia). Here it is sufficient to mention that the binding energy increases more than linearly with the cluster size such that the formation of larger clusters by coagulation of the smaller ones is energetically favored. The formation of mixed clusters is also favored by a small exothermic heat of formation around 0.1 to 0.2 eV/atom for Pt–Co clusters and 0.3 to 0.4 eV/atom for Pt–Fe clusters, both in the gas-phase and adsorbed on graphene. Here we concentrate on the magnetic properties and their correlation with the atomic structure.

4.1. Gas-phase trimers

Pt_2Fe, $PtFe_2$, Pt_2Co and $PtCo_2$ clusters form isocele triangles with scalar relativistic spin moments of 6, 8, 3 and 6 μ_B, respectively. This means that compared to the PtFe dimer the additional Pt atom in Pt_2Fe contributes a moment of 2 μ_B, the additional Fe atom in $PtFe_2$ a moment of 4 μ_B (equal to that of the free Fe atom). A contribution of 2 μ_B from the Pt atom is possible only because the binding in the trimer leads to a partial depletion of the 5d-band. The spin moment of a Pt_2Co trimer equals to that of the PtCo dimer, whereas the second Co atom in $PtCo_2$ contributes a moment of 3 μ_B, equal to that of the free Co atom. The comparison of Pt_2Co and Pt_2Fe shows that the magnetism of the Pt atom is strongly influenced by the binding to the 3d atom. Binding energies, interatomic distances, spin and orbital moments per trimer for the ground-state configurations are summarized in table 3 for SR calculations and including SOC.

4.1.1. Magnetic anisotropy of Pt–Fe trimers. For $PtFe_2$ SOC leaves the cluster geometry practically unchanged, for in-plane magnetization the Fe–Fe distance is enhanced by 0.01 Å, for perpendicular magnetization it is reduced by the same amount. The total spin moment is reduced and the reduction is not completely compensated by the orbital moment. The easy magnetization direction is parallel to the Fe–Fe edge of the triangle (see figure 1(*a*)), in agreement with the axial magnetization of the Fe_2 dimer. Parallel to the twofold symmetry axis is the hard magnetic direction with an MAE of 17.8 meV. The MAE for perpendicular magnetization is only 11.3 meV. In the states with in-plane magnetization the orbital moments on the Fe atoms are quite strongly non-collinear. In contrast the orbital moments of the Pt atom are strictly collinear to the spin moments and quite strongly anisotropic. The magnetization oriented perpendicular to the geometric symmetry axis breaks the symmetry. The magnetic point group symmetry has been discussed in detail for the Pt_n clusters [9]. For $PtFe_2$ the magnetic point group symmetry is $m'm2$ for the easy in-plane direction, $2m'm'$ for the hard in-plane magnetic axis and $m'm2'$ for perpendicular magnetization (where the prime indicates that the symmetry operation must be combined with a time-reversal operation which reverses the direction of axial vectors such as the magnetic moment) [35].

For the Pt_2Fe triangle the easy magnetic axis is parallel to the two-fold symmetry axis, perpendicular to the Pt–Pt bond, see figure 1(*b*). SOC increases Pt–Fe distances by 0.02 Å while the Pt–Pt edge is shortened by 0.05 Å. For magnetization along the Pt–Pt edge the interatomic distances are equal to those calculated in the SR limit. For magnetization perpendicular to the triangle (this is the hard magnetic axis) the Pt–Fe distances are the same as for easy-axis magnetization, while the Pt–Pt distance is reduced to 2.78 Å. Since the spin moment reduced to about 5 μ_B is compensated by an orbital moment of about 1 μ_B SOC leaves the total magnetic moment of the cluster almost unchanged. The local spin and orbital moments are collinear. An in-plane rotation of the magnetization to a direction orthogonal to the easy axis (parallel to the Pt–Pt edge of the triangle) costs an MAE of 8.5 meV. The change of the magnetization direction induces a modest reduction of the spin and orbital moments on the Pt atoms and a reduced orbital moment on the Fe atom while its spin moment is even slightly increased. The hard magnetic axis is perpendicular to the plane of the Pt_2Fe triangle, with a large MAE of about 38.9 meV. The large MAE is correlated to a strong orbital anisotropy on the Pt atoms. The magnetic point group symmetry of the three configurations is the same as for $PtFe_2$, but the energetic ordering of the two states with in-plane magnetization is reversed. Details of the local spin and orbital moments are also summarized in table III of the supplementary information (stacks.iop.org/JPCM/27/046002/mmedia).

Table 3. Binding energies E_b (in eV/atom), equilibrium structure, interatomic distances d_{ij} (in Å), spin and orbital moments, m_S and m_L, (in μ_B/atom) and magnetic anisotropy energy MAE relative to the hard-axis state (in meV/trimer) for the ground-state configurations of $PtFe_2$, Pt_2Fe, $PtCo_2$ and Pt_2Co clusters from scalar-relativistic (SR) and fully relativistic (SOC) calculations. The stable structure is always an isocele triangle. See text.

	Method	E_b	d_{X-X}	d_{Pt-X}	d_{Pt-Pt}	m_S	m_L	MAE
$PtFe_2$	SR	−2.27	2.10	2 × 2.38		8		
	SOC		2.11	2 × 2.38		7.10	0.59	17.8
Pt_2Fe	SR	−2.50		2 × 2.21	2.84	6		
	SOC			2 × 2.23	2.79	5.00	1.07	38.9
$PtCo_2$	SR	−2.24	2.06	2 × 2.37		6		
	SOC		2.06	2 × 2.37		5.14	0.85	36.0
Pt_2Co	SR	−2.41		2 × 2.31	2.53	3		
	SOC			2 × 2.32	2.52	2.80	0.70	15.3

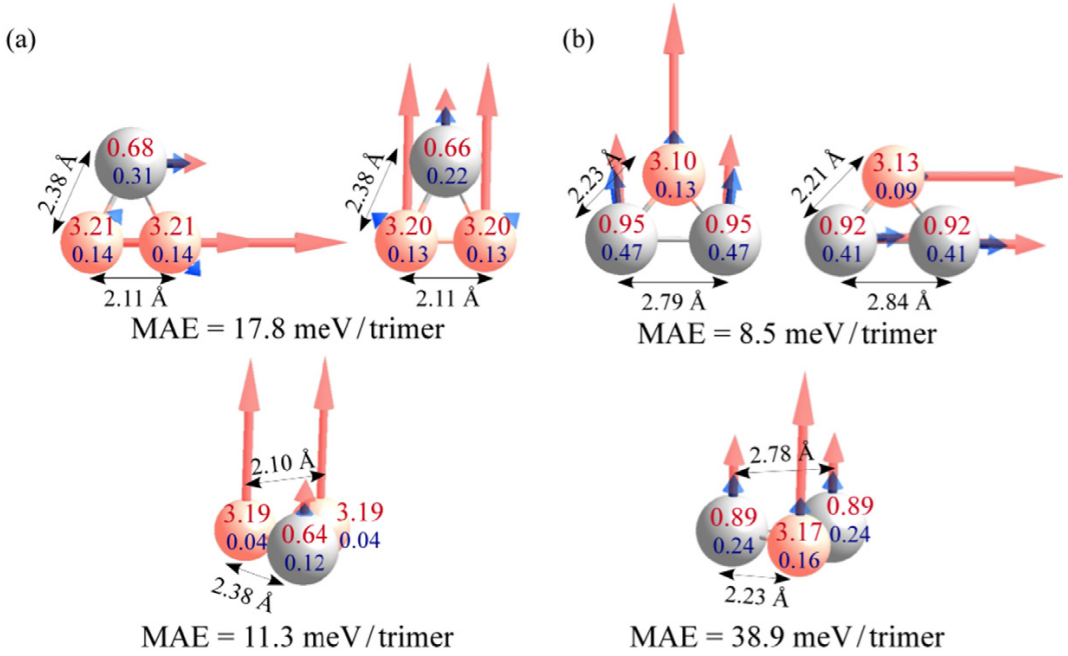


Figure 1. Geometric structure and local spin (upper value) and orbital magnetic moments (lower value) (in μ_B) of free $PtFe_2$ (*a*) and Pt_2Fe (*b*) clusters. The spin and orbital moments are represented by the red (light gray) and blue (dark gray) arrows. The magnetic anisotropy energy (the energy difference relative to the ground state) is given in meV/trimer. See text.

4.1.2. Magnetic anisotropy of Pt–Co trimers. For the $PtCo_2$ trimer SOC predicts the easy magnetic axis to be in-plane, parallel to the twofold symmetry axis of the isocele triangle (see figure 2(*a*)). The local orbital moments on the Co atoms are non-collinear, they are canted towards the twofold symmetry axis. In this configuration the interatomic distances are the same as in the scalar-relativistic limit, the reduction of the total spin moment is compensated by the orbital moment. In-plane rotation of the magnetic axis parallel to the Co–Co edge costs an energy of 6.7 meV and induces a geometric distortion of the triangle: one of the Pt–Co distances is reduced from 2.37 Å to 2.32 Å, the second is stretched to 2.50 Å. The distortion is also reflected by different magnetic moments of the two Co atoms (see figure 2(*a*)). The spin moment on the Co sites is for in-plane rotation isotropic on average and nearly isotropic on Pt. The orbital anisotropy is modest for Pt and the Co atom with the larger spin, but strong on the Co atom with the lower spin. Rotation of the magnetic axis to a direction perpendicular to the triangle costs a large MAE of 36 meV. The Co–Pt distances increase by 0.03 Å, the Co–Co distance decreases by 0.04 Å compared to the easy-axis geometry. On the Pt atom we calculate a spin anisotropy which is larger than the orbital anisotropy, while on the Co atoms a smaller spin anisotropy is accompanied by a stronger reduction of the orbital moments. The magnetic point group symmetries are $2m'm'$ for easy-axis magnetization and $m'm2'$ for vertical magnetization, while for the hard in-plane axis symmetry is completely destroyed.

For the Pt_2Co cluster SOC causes a slight change in the geometric structure (see figure 2(*b*)). Regardless of the magnetization direction we found an increase of the Pt–Co distances by 0.01 Å to 2.32 Å and a reduction of the Co–Co distance to 2.52 Å. The easy magnetic axis is in-plane, parallel to the twofold symmetry axis of the triangle as for the $PtCo_2$

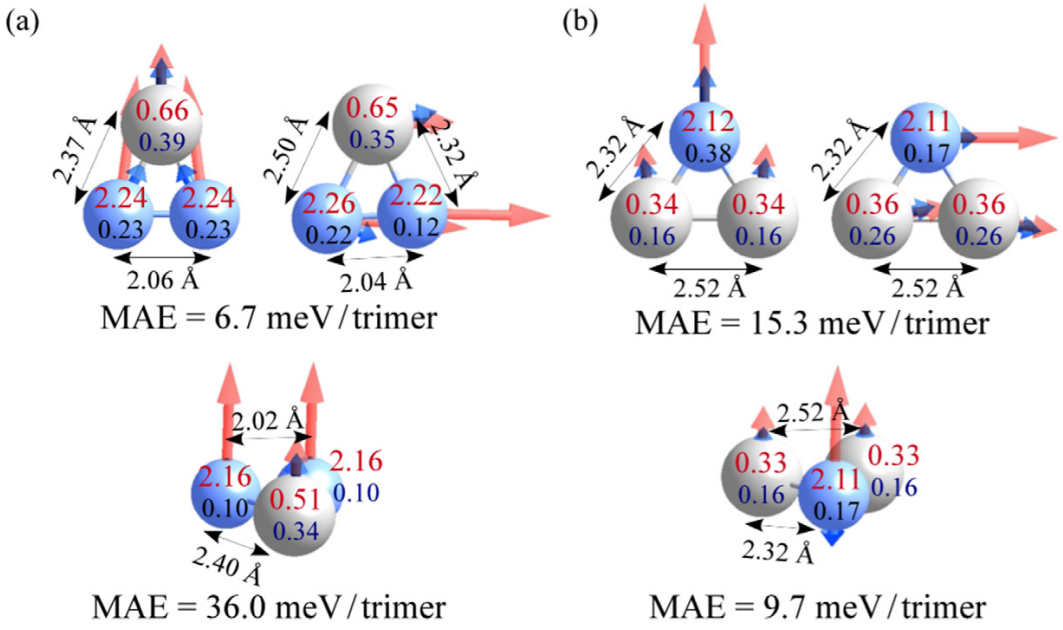


Figure 2. Geometric structure and local spin (upper value) and orbital magnetic moments (lower value) (in μ_B) of free $PtCo_2$ (*a*) and Pt_2Co (*b*) clusters. The spin and orbital moments are represented by the red (light gray) and blue (dark gray) arrows. The magnetic anisotropy energy is given in meV/cluster relative to the ground state configuration. See text.

trimer, but now all local moments are collinear. The in-plane MAE is 15.3 meV, larger that the MAE of 9.7 meV required to rotate the magnetization to a direction perpendicular to the plane of the triangle. For in-plane magnetization SOC leads to an increase of the total magnetic moment: a slight decrease of the spin moment by about $0.2\,\mu_B$ is overcompensated by a total orbital moment of $\sim 0.7\,\mu_B$. For perpendicular magnetization the total moment calculated including SOC is about equal to the scalar-relativistic spin moment. The spin anisotropy is rather modest for both species. While the orbital moment on Co is reduced by $0.21\,\mu_B$ for the in-plane hard axis and it is even anti-parallel to the spin moment for perpendicular magnetization (see figure 2(*b*)), the orbital moment on the Pt atoms is largest for magnetization along the hard axis, such that for both the easy and the hard directions (both in the plane of the triangle) the total spin and orbital moments of the cluster are almost the same, in contrast to the vanishing orbital anisotropy for magnetization perpendicular to the triangle. The magnetic point group symmetries are $2m'm'$ for easy axis magnetization and $m'm2'$ for the other two configurations. The symmetries are the same as for the Pt_3 trimer, but the magnetic ordering of the two excited states is reversed. The values of the local spin and orbital moments and the MAE for both Pt–Co trimers are given in figure 2 and summarized in table IV of the supplementary material (stacks.iop.org/JPCM/27/046002/mmedia).

4.2. Trimers supported on graphene

For the mixed trimers supported on a freestanding graphene layer we have explored a number of possible adsorption geometries to initialize the structural relaxation: parallel and perpendicular to the substrate, with the cluster atoms in contact with the support located in either bridge (br) or sixfold hollow (6h) sites. Quite generally trimers adsorbed parallel to the graphene layer were found to be unstable. In the following we report only our results for the stable or metastable configurations. The binding of the trimers to graphene is quite strong, the adsorption energies E_{int} per cluster range between -1.2 eV for Pt_2Fe and -1.70 eV for $PtCo_2$ (details are reported in the supplementary information (stacks.iop.org/JPCM/27/046002/mmedia)). Binding occurs preferentially through the 3d atom, Fe and Co atoms are located about 1.7 Å, Pt atoms between 2.2 and 2.4 Å above the graphene layer which is buckled with amplitudes between 0.12 and 0.37 Å due to the expansion of the distances between the C atoms binding to the trimer. Due to the strong cluster-substrate binding the influence of SOC on the cluster geometry is minimized. Interatomic distances change only by less than 0.01 Å.

4.2.1. Geometric and magnetic structures of Pt–Fe trimers on graphene. In the most stable configuration the $PtFe_2$ trimer is perpendicular to the graphene sheet, see figure 3(*a*). The two Fe atoms are located close to 6h sites at a distance of 2.31 Å, increased by 0.2 Å compared to the free cluster, but still slightly smaller than the distance between hollow sites in the undistorted graphene layer. The point group symmetry is 2 mm as for the free cluster. The buckling creating a depression in the layer below the adsorbate is rather modest (0.12 Å). The adsorption energy is -1.39 eV/cluster. The spin moments on the Pt and Fe atoms together with small

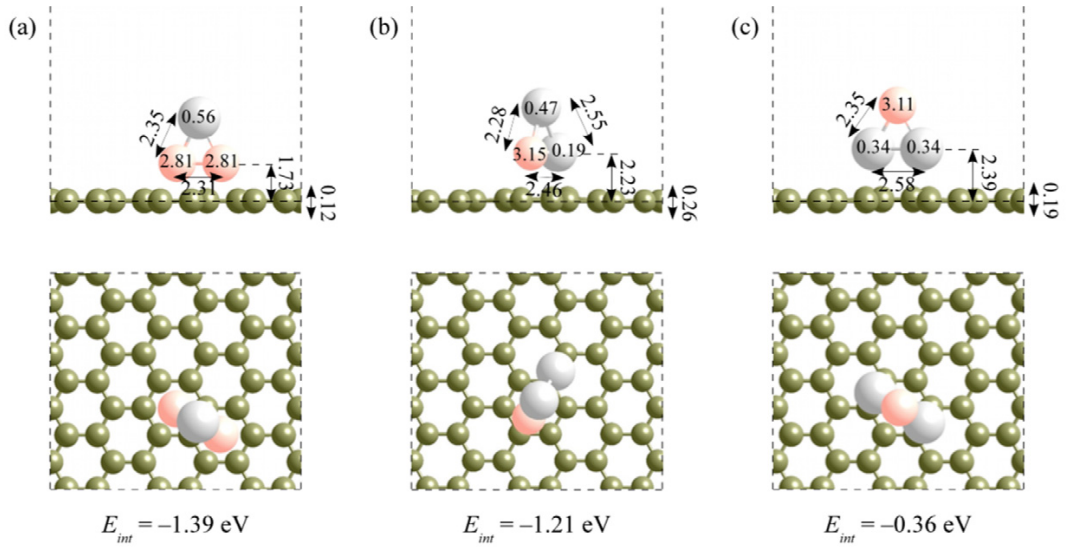


Figure 3. Side- and top-views of the adsorption geometries of a mixed Pt–Fe trimer (Pt—grey, Fe—red) on a free-standing graphene layer: (*a*) $PtFe_2$ upright, Fe–Fe edge binding to graphene, (*b*) Pt_2Fe upright, Pt–Fe edge binding to graphene (*c*) Pt_2Fe upright, Pt–Pt edge binding to graphene. All distances are in Å. Numbers on atoms denote the local magnetic moments (in μ_B) calculated in the scalar-relativistic approach.

induced antiferromagnetic moments of up to $-0.02\,\mu_B$ on the surrounding C atoms give the total moment of $6\,\mu_B$, reduced by $2\,\mu_B$ compared to the free $PtFe_2$ cluster.

Calculations including SOC (see figure 4(*a*)) predict for $PtFe_2$ an easy magnetic axis perpendicular to the graphene sheet and to the Fe–Fe bond. The total moment of $6.40\,\mu_B$ ($m_S = 6.10\,\mu_B$, $m_L = 0.30\,\mu_B$) is enhanced relative to the scalar-relativistic spin moment. The local orbital moments on the Fe atoms are non-collinear. Rotation of the magnetization to a direction parallel to the graphene-layer and perpendicular to the cluster plane costs an MAE of 3.3 meV. The total moments are all slightly enhanced: $m_J = 6.47\,\mu_B$, $m_S = 6.12\,\mu_B$, $m_L = 0.35\,\mu_B$, which arises from weak negative spin and orbital anisotropies on the Fe sites and isotropic Pt moments. In-plane rotation of the magnetization to the cluster plane leaves the total spin moment unchanged, the total orbital moment is $0.33\,\mu_B$, with a small negative orbital anisotropy on the Pt atom and a very modest positive orbital anisotropy on the Fe sites. This solution is 8.9 meV higher in energy than the GS-solution. The magnetic point group symmetry is $2m'm'$ for the ground state and $m'm2'$ for the two excited states. Detailed results for the local spin and orbital moments are collected in table V of the supplementary information (stacks.iop.org/JPCM/27/046002/mmedia).

For Pt_2Fe two different initial configurations have been examined: an asymmetric one binding to graphene through the Pt–Fe edge and a symmetric geometry (point group 2 mm) binding to the substrate through the Pt–Pt edge (see figure 3(*b*) and (*c*)). The former is stable with $E_{int} = -1.21$ eV/cluster and a total magnetic moment of $4\,\mu_B$. One of the Pt atoms is located in the br position and the Fe atom is shifted from the 6h site towards a C atom such as to accommodate a Pt–Fe distance of 2.46 Å (expanded by 0.25 Å compared to the free cluster). The buckling amplitude of the graphene layer is 0.26 Å. In this case the neighboring C atoms move outward towards the cluster. The Fe-up configuration with the Pt atoms located close to br sites is more symmetric, but only metastable with a much lower adsorption energy of $E_{int} = -0.36$ eV/cluster. The local spin moments on the Pt and Fe atoms, together with the small moments induced in the support, give a total moment of $4\,\mu_B$.

For the Pt_2Fe Pt-up triangle the easy magnetic axis with $m_J = 4.10\,\mu_B$ ($m_S = 3.75\,\mu_B$, $m_L = 0.35\,\mu_B$) is roughly in the cluster plane, tilted with respect to the graphene layer and to the Pt–Fe bond. The detailed magnetic structure for different orientations of the magnetization vector is presented in figure 4(*b*). The rotation of the magnetization to a direction orthogonal to the C-sheet and to the Pt–Fe edge costs 4.8 meV. The cluster spin and orbital magnetic moment are slightly enhanced, i.e. $m_S = 3.77\,\mu_B$, $m_L = 0.38\,\mu_B$. Rotation of the magnetization axis parallel to the support to a direction parallel to the C–C bonds, but oblique to the triangle costs only an MAE of 0.2 meV, although both the spin and orbital moments are reduced to 3.73 and $0.29\,\mu_B$, respectively. Detailed information on the local magnetic moments is compiled in table III of the supplementary information (stacks.iop.org/JPCM/27/046002/mmedia). The modest MAE of the stable graphene-supported Pt_2Fe trimer is related to the lack of symmetry. A much larger MAE of 18.9 meV/cluster between the perpendicular easy axis and in-plane magnetization is found for the metastable (but more symmetric) adsorption geometry bound through the Pt–Pt edge. Details of the magnetic structure of this metastable configuration are given in figure 1 of the supplementary information (stacks.iop.org/JPCM/27/046002/mmedia).

4.2.2. Geometric and magnetic structures of Pt–Co trimers on graphene The stable adsorption geometries of Pt–Co trimers

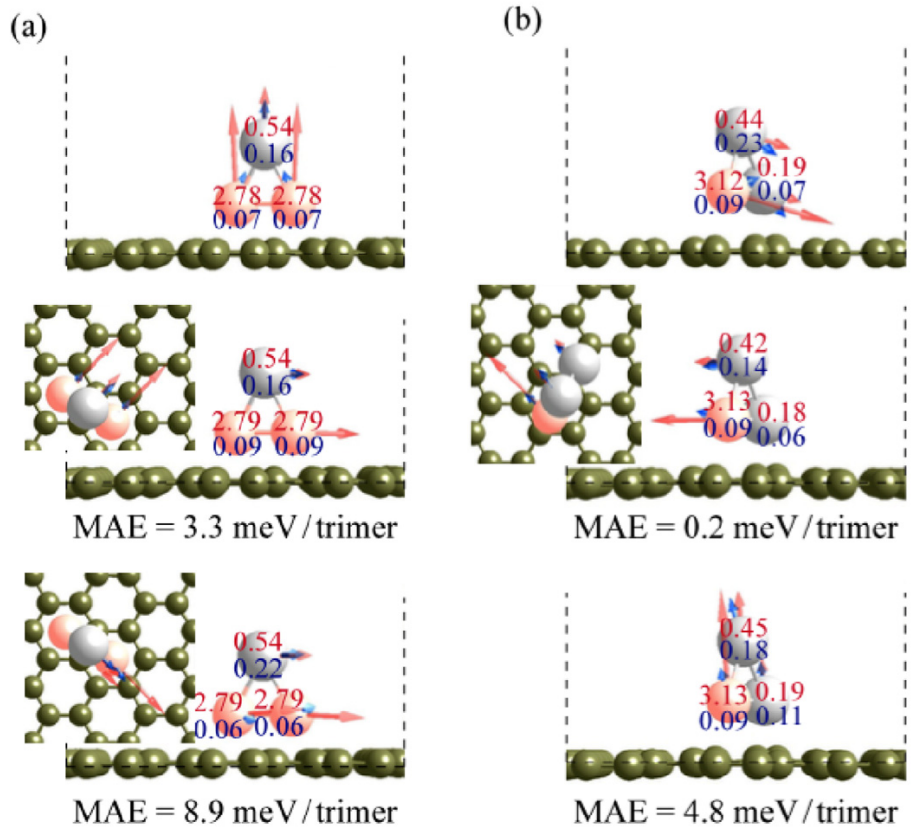


Figure 4. Side- and top-view of the magnetic structure of $PtFe_2$ (*a*) and Pt_2Fe (*b*) trimers adsorbed on graphene. Red (light) arrows show spin-, blue (dark) arrows the orbital magnetic moments, the numbers give the values of the local spin (upper number) and orbital (lower number) magnetic moments in μ_B.

resulting from the scalar-relativistic calculations are shown in figure 5. The most stable $PtCo_2$ triangle is perpendicular to the graphene layer. The cluster binds to the support through the Co–Co edge, with both Co atoms located close to 6h sites and the Pt atom above a br position. The point group symmetry is 2 mm. The Co–Co distance of 2.49 Å is strongly elongated relative to a bond length of 2.06 Å in the free cluster and it is also slightly larger (by 0.05 Å) than the distance between two 6h sites. The adsorption induces a weak buckling of the graphene with an amplitude of 0.13 Å such that the cluster is located in a shallow depression, 1.67 Å above the C atoms on average. The adsorption energy is $E_{\text{int}} = -1.70$ eV/cluster and the binding energy between the atoms in the adsorbed cluster amounts to $E_{\text{b-ads}} = -2.81$ eV/atom, while the binding energy in the free cluster is only -2.24 eV/atom. The strong interaction between cluster and substrate overcomes the distortion energy of $PtCo_2$ and graphene. The local spin moments are 1.66 μ_B on the Co atoms and 0.64 μ_B on the Pt atom. Very small magnetic moments of up to 0.02 μ_B are induced on the C atoms such that the total moment of the adsorbate-substrate complex is 4 μ_B, reduced compared to the free trimer by the quenching of the local moments on the binding Co atoms.

An initially flat configuration with all three atoms in 6h positions relaxes to the upright geometry described above, but adopts a different magnetic state. The Pt atom is non-magnetic, the Co atoms carry moments of $\pm 1.6\,\mu_B$ i.e. the cluster is antiferromagnetic. Small antiferromagnetic moments are also induced on the graphene layer. The adsorption energy of -1.51 eV/cluster corresponds to a magnetic energy difference of about 0.2 eV.

Relativistic calculations performed for the most stable $PtCo_2$/graphene structure predict an easy magnetic axis perpendicular to the graphene layer and to the Co–Co bond and in the plane of the $PtCo_2$ triangle, see figure 6(*a*). The total magnetic moment is 4.47 μ_B (a slight reduction of the spin moment is overcompensated by the orbital moment, i.e. $m_S = 3.92$, $m_L = 0.65\,\mu_B$). A rotation of the magnetization to the direction parallel to the graphene layer and perpendicular to the triangle costs an anisotropy energy of 8.6 meV. The total magnetic moment is reduced to 4.11 μ_B ($m_S = 3.77$, $m_L = 0.34\,\mu_B$). Another in-plane solution with the total moment pointing along the Co–Co bond has a total magnetic moment of 4.35 μ_B ($m_S = 3.93\,\mu_B$, $m_L = 0.42\,\mu_B$), the MAE is 19.9 meV above the GS solution. The magnetic point group symmetries are the same as for the free $PtCo_2$ trimer, but the energetic ordering of the excited states is reversed. This is related to the absence of the strong structural distortion for magnetization parallel to the Co–Co edge.

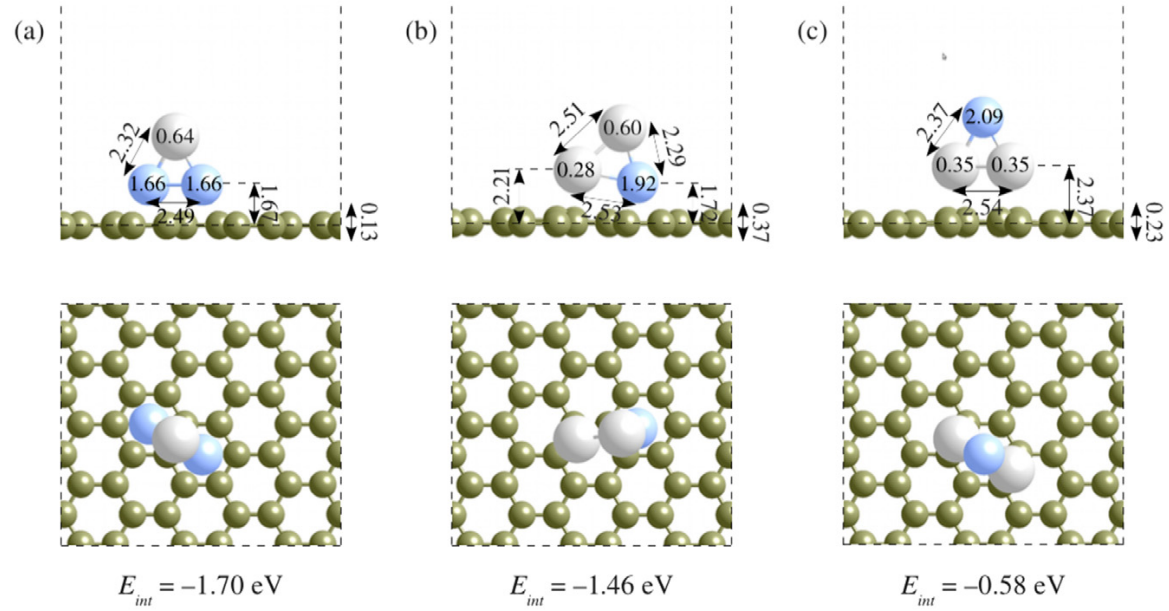


Figure 5. Side- and top-views of the adsorption geometries of a mixed Pt–Co trimer (Pt—grey, Co—blue) on a free-standing graphene layer: (*a*) $PtCo_2$ upright, Co–Co edge binding to graphene, (*b*) Pt_2Co upright, Pt–Co edge down, (*c*) Pt_2Co, upright, Pt–Pt edge binding to graphene. All distances are in Å. Numbers on atoms denote the local magnetic moments (in μ_B) calculated in the scalar-relativistic approach.

The Pt_2Co cluster was also initially placed parallel to the support with the Pt atoms in br positions and the Co atom in 6h. The relaxation led to an upright scalene triangle with Co remaining close to the 6h site and one Pt atom close to an on-top (ot) position (see panel (*b*) of figure 5). The asymmetric configuration of the adsorbate leads to a rather pronounced buckling of the graphene layer with an amplitude of 0.37 Å. The total spin moment is $3\,\mu_B$ (together with small local moments of up to $0.01\,\mu_B$ induced on the C atoms). If SOC is taken into account in the magnetic GS the total magnetic moment of $3.33\,\mu_B$ ($m_S = 2.77\,\mu_B$, $m_L = 0.56\,\mu_B$) is oriented approximately along the Pt–Pt bond (see figure 6(*b*)). This configuration results from initializations of the magnetic moments perpendicular and parallel (within the plane of Pt_2Co triangle) to graphene. The local orbital moments are strongly canted relative to the spin moments. The rotation of the magnetization to a direction almost perpendicular to the cluster plane and parallel to the graphene layer leads to a solution with $m_S = 2.70\,\mu_B$ and $m_L = 0.37\,\mu_B$, which is only 2 meV above the GS. The modest MAE is surprising in regard to the substantial orbital anisotropy, but related to the low symmetry of the adsorbed trimer (see table IV of the supplementary information (stacks.iop.org/JPCM/27/046002/mmedia)). No other stationary solution has been found.

In a more symmetric metastable configuration (point group 2 mm) the Pt_2Co cluster binds weakly through the Pt–Pt edge to br sites (see panel (*c*) of figure 5). As for the Pt_2Fe cluster we find a much higher MAE of 12.1 meV for the symmetric metastable than for the asymmetric stable configuration. Details are given in table VI and figure 1(*b*) of the supplementary information (stacks.iop.org/JPCM/27/046002/mmedia).

5. Heteroatomic Pt–Fe and Pt–Co tetramers

5.1. Gas-phase tetramers

Tetramers are the smallest clusters where two-dimensional (2D) and three-dimensional (3D) geometries are in competition. Scalar-relativistic calculations predict a tetrahedral structure for most homoatomic transition-metal tetramers, eventually distorted due to a Jahn–Teller effect. For the heavy 5d metals, however, recent studies have demonstrated [9, 36] that relativistic effects stabilize a planar rhombic over a tetrahedral configuration. For Pt_4 tetramers, however, the stabilization of the 2D geometry is not only a relativistic effect, but depends also on the magnetic moment. In the scalar-relativistic mode, a distorted tetrahedron is favored over a rhombus by 49 meV/atom for $m_S = 0$ (fixed moment calculations), the structural energy difference drops to 24 meV/atom for $m_S = 2\,\mu_B$ and for a high-spin state with $m_S = 4\,\mu_B$ the 2D geometry is favored by −22 meV/atom. Taking the magnetic energy differences into account, the distorted Pt_4 tetrahedron with $m_S = 2\,\mu_B$ is favored by only 2 meV/atom over a rhombus with $m_S = 4\,\mu_B$ [37]. SOC leads to a structural energy difference of −32 meV/atom in favor of a rhombus for an antiferromagnetic ground state with easy axis perpendicular to the plane of the rhombus. For in-plane magnetization a ferromagnetic state with $m_S = 1.6\,\mu_B$, $m_L = 2.4\,\mu_B$, $m_J = 4\,\mu_B$, however, is 1.5 meV/atom lower in energy than an antiferromagnetic state [9]. These results suggest that if a high-moment state is stabilized by substitution of Fe or Co for Pt, a flat geometry might be favored.

For mixed 3d–5d clusters the symmetry is necessarily reduced and it remains to be seen whether the strong SOC on the 5d atom is sufficient to produce effects similar to those

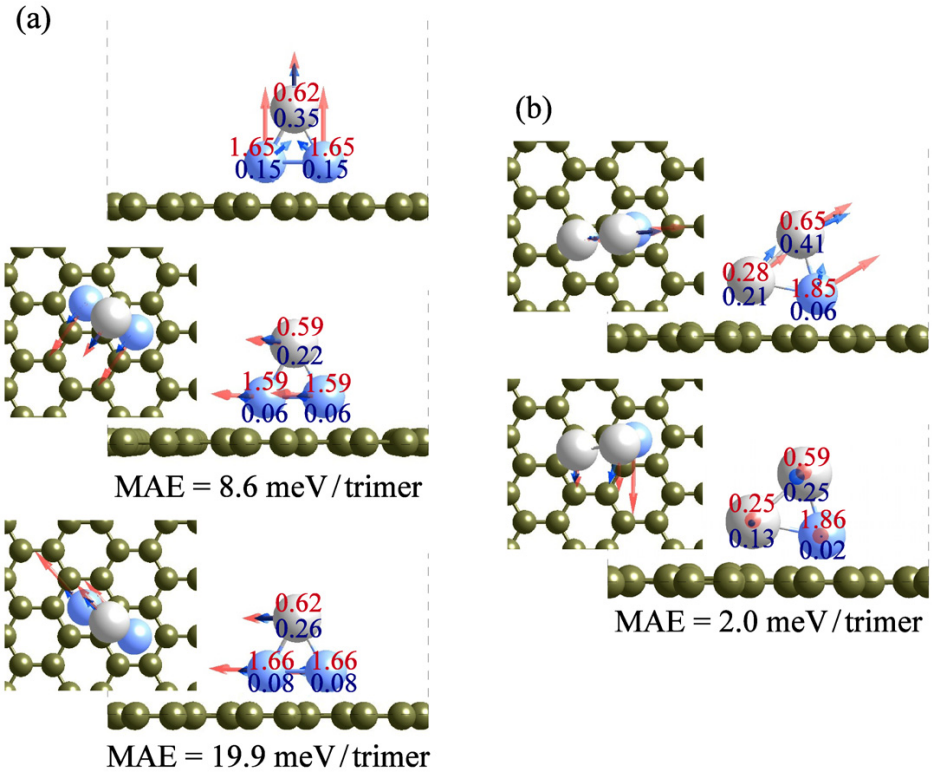


Figure 6. Side- and top-view of the magnetic structure of $PtCo_2$ (*a*) and Pt_2Co (*b*) triangles adsorbed on a graphene layer. Red (light) arrows show spin-, blue (dark) arrows the orbital magnetic moments, the numbers give the values of the local spin (upper number) and orbital (lower number) magnetic moments in μ_B. The MAE (in meV/trimer) is given relative to the ground-state configuration shown on top.

observed on homoatomic 5d clusters. In the present work we have investigated Pt_3X and PtX_3 (X = Co, Fe) clusters in 2D and 3D structures using both scalar-relativistic and relativistic methods. The initial geometries were created by adding a Pt or a Co(Fe) atom to the relaxed structure of the trimer such as to complete a distorted trigonal pyramid or to form a deltoid.

The structural, energetic and magnetic properties of all four tetramers calculated in the scalar-relativistic approximation and including SOC (for the easy axis configuration) are summarized in table 4. The most striking result is that with the exception of Pt_3Co a 2D structure in the form of a deltoid (point group symmetry 2 mm, the same as for an isocele triangle) is found to be lower in energy by about 50 to 80 meV/atom than a 3D structure forming a distorted trigonal pyramid. Only for $PtFe_3$ the 3D structure is an almost ideal tetrahedron (point group symmetry $\bar{4}3$ m).

In contrast to the preference for a flat geometry in Pt_4 this is not a relativistic effect, SOC even slightly reduces the structural energy difference. Only for Pt_3Co a 3D structure is preferred by about 96 meV/atom over the flat deltoid. In this case for the 3D tetramer a high-spin state with a total moment of 5 μ_B is found to be energetically degenerate with a geometrically distorted low-spin state with 3 μ_B. The lower moment is the same as the SR spin moment of the Pt_2Co trimer or of a free Co atom. The SR spin moment of 6 μ_B of Pt_3Fe is the same as that of the Pt_2Fe trimer and larger by 2 μ_B than the spin moment of a free Fe atom. This means that the substitution of a Pt atom by Fe leads to a much stronger magnetic polarization of the remaining three Pt atoms than a substitution by Co. The stronger magnetism of the Pt_3 group in Pt_3Fe stabilizes a flat geometry, in accordance with the observations discussed above. The differences in the structural stability and in the magnetic polarization of the Pt atoms are also correlated to significant differences in the interatomic distances: in the 2D geometries of the Pt_3X tetramers the difference between the Pt–Pt distances along the edges and through the diagonal is much larger for Pt_3Fe than for Pt_3Co, in the 3D geometry the Pt–Pt distances are larger for the cluster containing Fe.

For $PtCo_3$ the additional Co atom enhances the cluster moment by only 1 μ_B compared to $PtCo_2$, whereas for $PtFe_3$ the added Fe atom contributes a moment of 4 μ_B, equal to that of a free Fe atom. This means that while in the $PtFe_n$ dimers, trimers and tetramers the total spin moment is always equal to the sum of the moments of n free Fe atoms, for $PtCo_n$ clusters this holds only for dimers and trimers, whereas in the tetramer the interaction with Pt reduces the magnetism of the Co atoms. The different magnetic properties are also reflected in the geometries: in the flat structure of $PtCo_3$ the Co atoms form an almost equilateral triangle, while in $PtFe_3$ the Fe–Fe distance along the diagonal of the deltoid is much longer than along the edges (see table 4). In the 3D configuration $PtFe_3$ forms an almost ideal tetrahedron, while $PtCo_3$ forms a trigonal pyramid with longer Pt–Co than Co–Co distances. In $PtCo_3$ the Co–Co distances are almost equal to those in a Co_3 triangle,

Table 4. Binding energies E_b (in eV/atom), equilibrium structure, structural energy difference ΔE (in meV/atom), interatomic distances d_{ij} (in Å), spin and orbital moments, m_S and m_L, (in μ_B/atom) and magnetic anisotropy energy MAE relative to the hard-axis state (in meV/tetramer) for the 2D and 3D ground-state configurations of $PtFe_3$, Pt_3Fe, $PtCo_3$ and Pt_3Co clusters from scalar-relativistic (SR) and fully relativistic (SOC) calculations. See text.

	Method	Structure	E_b	ΔE	d_{X-X}	d_{Pt-X}	d_{Pt-Pt}	m_S	m_L	MAE
$PtFe_3$	SR	Deltoid	−2.53	0	2 × 2.23, 2.67	2 × 2.33		12		
	SOC			0	2 × 2.23, 2.67	2 × 2.33		10.50	0.52	14.0
	SR	Tetrahedron	−2.45	78	3 × 2.41	3 × 2.40		12		
	SOC			47	2 × 2.28, 2.27	3 × 2.45		10.43	0.19	7.8
Pt_3Fe	SR	Deltoid	−2.82	0		2 × 2.27	2 × 2.50, 3.55	6		
	SOC			0		2 × 2.19	2 × 2.48, 3.46	5.58	0.69	21.4
	SR	Trig. pyramid	−2.75	67		3 × 2.31	3 × 2.72	6		
	SOC			50		2 × 2.31, 2.32	2 × 2.70, 2.75	5.06	0.57	50.5
$PtCo_3$	SR	Deltoid	−2.56	0	3 × 2.19	2 × 2.36		7		
	SOC			0	2 × 2.19, 2.20	2 × 2.37		6.63	0.87	10.9
	SR	Trig. pyramid	−2.48	84	3 × 2.19	3 × 2.45		7		
	SOC			77	3 × 2.20	3 × 2.45		6.40	0.86	12.5
Pt_3Co	SR	Deltoid	−2.60	93		2 × 2.35	2 × 2.52, 2.57	5		
	SOC			96		2 × 2.34	2 × 2.53, 2.57	4.01	0.36	6.3
	SR	Pyramid	−2.69	0		2 × 2.38, 2.44	2 × 2.38, 2.74	5		
	SR	Pyramid	−2.69	0		2.36, 2.41, 2.43	2.55, 2.65, 2.68	3		
	SOC			0		2 × 2.39, 2.42	2 × 2.57, 2.65	4.06	0.99	54.6

while in $PtFe_3$ the Fe–Fe distances are enhanced on average by 0.12 Å and 0.15 Å in the 2D and 3D geometries, respectively.

SOC generally reduces the total spin moment, but in most cases the reduction is overcompensated by the orbital moment. For some of the tetramers SOC lowers the symmetry, details are discussed in the following. For the Pt_3X tetramers adsorbed on graphene the interaction with the substrate stabilizes a geometry intermediate between the 2D and 3D configurations—therefore it is important to investigate the influence of SOC on the magnetic properties of both geometric configurations. For PtX_3 tetramers the stable adsorption geometry is always a more or less distorted trigonal pyramid. In that case the flat configuration is less important as a reference.

5.1.1. Magnetic anisotropy of free Pt–Fe tetramers. For the stable 2D structure of Pt_3Fe with magnetization along the easy axis perpendicular to the deltoid (see figure 7(*a*)) SOC leads to shorter Pt–Fe and Pt–Pt distances, but does not break the symmetry (see table 4). The total moment of 6.27 μ_B ($m_S = 5.58\,\mu_B$, $m_L = 0.69\,\mu_B$) is slightly increased relative to the scalar-relativistic result. Rotation of the magnetization to an in-plane direction along the Pt–Pt diagonal leads to modest changes of the moments, but to a strong increase of the Pt–Fe interatomic distances. The geometric structure of the excited configuration is almost identical to that calculated in the absence of SOC. The magnetic moments of the cluster are slightly enhanced to $m_J = 6.52\,\mu_B$ ($m_S = 5.68\,\mu_B$, $m_L = 0.84\,\mu_B$), the MAE is 4.0 meV. In-plane rotation of the magnetization by 90° to a direction parallel to the Pt–Fe diagonal costs a larger MAE of 21.4 meV and changes the magnetic moments to $m_J = 6.36\,\mu_B$ ($m_S = 5.49\,\mu_B$, $m_L = 0.87\,\mu_B$). It also leads to very small changes in the interatomic distances. The magnetic point group symmetries are $m'm2'$ for the ground state and the first excited state and $2m'm'$ for the hard axis configuration. They are the same as for the Pt_2Fe trimer, but their energetic ordering is just the inverse.

For the metastable 3D isomer SR calculations predict a trigonal pyramid (see table 4). SOC completely destroys the symmetry for the ground state with a non-collinear magnetic structure and a global magnetization direction parallel to the basal plane, see figure 7(*b*). In-plane rotation of the magnetization direction enhances the symmetry (magnetic point group symmetry m) and leads to strongly enhanced spin and orbital moments on the Pt atoms. For perpendicular magnetization the threefold symmetry is restored (magnetic point group 3 m) and the total moment of the tetramer is increased by 1.6 μ_B compared to the GS. Hence the large MAEs of the 3D Pt_3Fe clusters are energy differences between different structural and magnetic isomers. Similarly, for Pt_n, $n = 4, 5$ it has been found that the MAE and the energy difference between magnetic isomers can be of the same order of magnitude [9].

The structure of the stable 2D $PtFe_3$ cluster is unaffected by SOC and independent of the direction of magnetization. The calculations predict an in-plane easy magnetic axis parallel to the Fe–Fe diagonal of the deltoid, see figure 7(*c*). The total cluster moment of 11.02 μ_B ($m_S = 10.50\,\mu_B$, $m_L = 0.52\,\mu_B$) is lower than without SOC. In-plane rotation of the magnetization direction by 90° (parallel to the long Fe–Pt diagonal) leaves the spin moment practically unchanged and lowers the orbital and total moments by 0.13 μ_B. The MAE for in-plane rotation is 6.4 meV. The hard magnetic axis is orthogonal to the plane of the tetramer. The MAE is 14.0 meV (with respect to the GS). The total spin and orbital moments are 10.53 and 0.43 μ_B, respectively, together $m_J = 10.96\,\mu_B$. The magnetic point group symmetries are the same as for the Pt_3Fe trimer, but the magnetic ordering of the two in-plane states is reversed.

For the geometric structure of the 3D isomer SOC leads to a reduction of the Fe–Fe distances and to an elongation of the Fe–Pt distances, transforming it from a nearly ideal tetrahedron to a distorted trigonal pyramid. The geometric distortion is modest in the ground state with magnetization

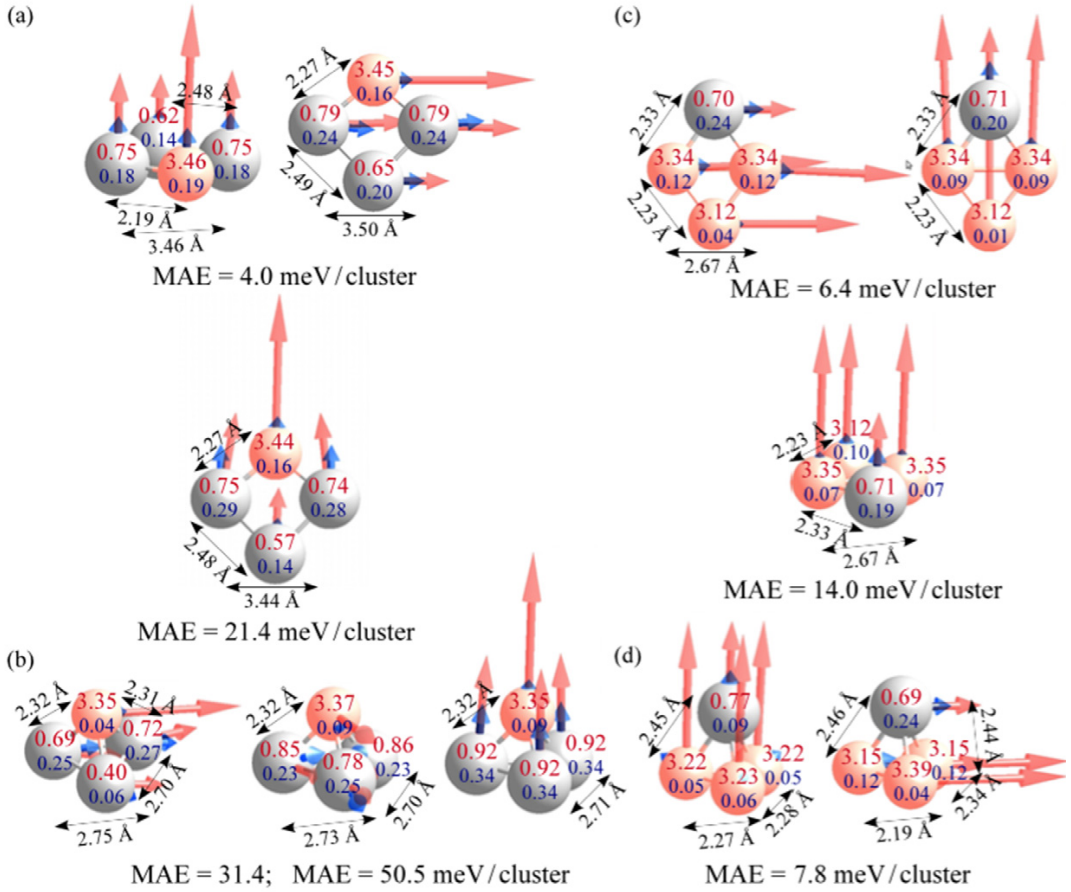


Figure 7. Geometric and magnetic structures and local spin (upper value) and orbital magnetic moments (lower value) (in μ_B) of the 2D and 3D structural isomers of Pt_3Fe (*a*) and (*b*) and $PtFe_3$ (*c*) and (*d*) clusters. The spin and orbital moments are represented by the red (light gray) and blue (dark gray) arrows. The magnetic anisotropy energy (MAE) (in meV/cluster) is given relative to the ground state configuration. See text.

perpendicular to the Fe_3 plane and much stronger for the excited state with magnetization perpendicular to the mirror plane. The magnetic structures and MAEs of 3D-$PtFe_3$ are presented in figure 7(*d*), the magnetic point group symmetry is m for the ground state and m' for the excited state. A compilation of the local and total spin and orbital moments of Pt–Fe tetramers can be found in table VII of the supplement (stacks.iop.org/JPCM/27/046002/mmedia).

5.1.2. Magnetic anisotropy of free Pt–Co tetramers. Scalar-relativistic calculations predict that the $PtCo_3$ cluster forms a deltoid (with an equilateral triangle of Co atoms), which is 84 meV/atom lower in energy than a trigonal pyramid (see table 4). For both structural variants the total spin moment is 7 μ_B. SOC leads only to a minimal change in the interatomic distances and a modest reduction of the structural energy difference. For both isomers the total spin moment is reduced, but this is overcompensated by a substantial orbital moment. For the 2D $PtCo_3$ trimer the easy magnetic axis is along the long diagonal of the deltoid (see figure 8(*a*)), in-plane rotation of the magnetization parallel to the short diagonal cost an MAE of 3.1 meV/trimer, perpendicular magnetization an MAE of 10.9 meV/trimer. The magnetic point group symmetries for easy and hard axis magnetization are $2m'm'$ and $m'm2'$, respectively, as for the $PtCo_2$ trimer. However, in contrast to the trimer the first excited state with magnetization parallel to the short diagonal has the same geometric structure than the ground state, but the magnetic point group symmetry of the hard-axis state. The MAE is correlated to a substantial orbital anisotropy ($\Delta m_L = 0.13(0.65)\,\mu_B$ for in-plane (perpendicular) MAE), which arises mostly from the local orbital anisotropy of the Co moments (see figure 8(*a*) and table VIII of the supplementary information (stacks.iop.org/JPCM/27/046002/mmedia) for details).

For the metastable 3D isomer SOC does not affect the threefold symmetry, only the Co–Co distances are increased by 0.01 Å. Calculations including SOC initialized with magnetic moments parallel to the Co_3 triangle and parallel or perpendicular to one of the Co–Co edges, converged to energetically degenerate solutions with $m_J = 6.92\,\mu_B$ ($m_S = 6.42\,\mu_B$, $m_L = 0.50\,\mu_B$) and in-plane magnetization, as presented in figure 8(*b*), which is the hard magnetic axis.

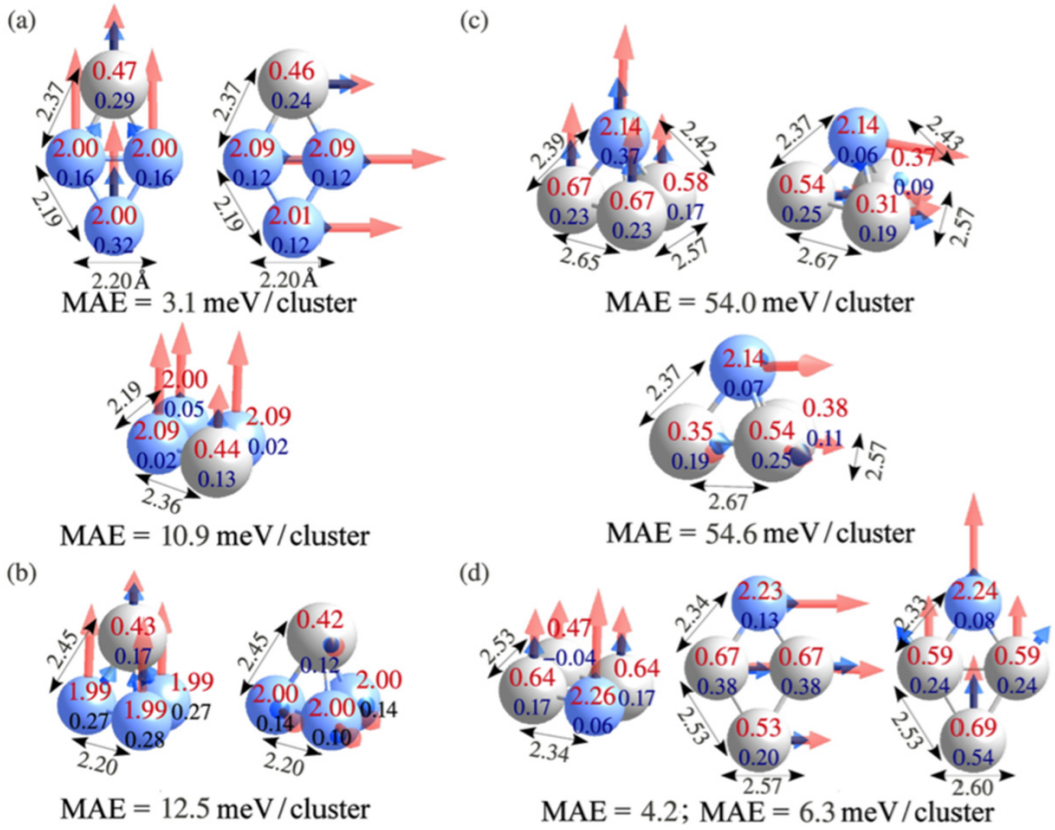


Figure 8. Geometric and magnetic structure and local spin (upper value) and orbital magnetic moments (lower value) (in μ_B) of the 2D and 3D structural isomers of $PtCo_3$ (*a*) and (*b*) and Pt_3Co (*c*) and (*d*) clusters. Interatomic distances are given in Å. Pt atoms are shown in grey, Co atoms in blue. The spin and orbital moments are represented by the red (light gray) and blue (dark gray) arrows. The magnetic anisotropy energy (MAE, in meV/cluster) is given relative to the ground state configuration. See text.

The total energy for perpendicular magnetization with $m_J = 7.26\,\mu_B$ ($m_S = 6.40\,\mu_B$, $m_L = 0.86\,\mu_B$) and non-collinear orbital moments on the Co atoms is, however, lower by an MAE of 12.5 meV (see also table VIII of the supplement (stacks.iop.org/JPCM/27/046002/mmedia) for details). The magnetic point group symmetries are $3m'$ for the ground state and m for the excited state but the loss of the threefold axis is manifest only in the orbital moments on the Co atoms.

Pt_3Co is the only tetramer for which the 3D pyramidal structure is lower in energy (by 93 meV/tetramer, 96 meV/tetramer incl. SOC) than the flat deltoid. In the SR limit two energetically degenerate magnetic isomers with total spin moments of $5\,\mu_B$ and $3\,\mu_B$ exist for the 3D tetramer. For the high-spin isomer the trigonal symmetry of the pyramid is broken, as evident from the Pt–Pt distances and Pt local moments (see table 4). The symmetry is further reduced for the low-spin isomer. SOC leads to a GS with magnetization perpendicular to the Pt_3 triangle and a total spin moment of about $4\,\mu_B$, if the orbital moments are added, the total moment is $m_J = 5.05\,\mu_B$, equal to the high-spin isomer in the SR approximation. For magnetization parallel to the Pt_3 basal plane we have identified two energetically almost degenerate states with moments parallel to a Pt-Pt edge or to the mirror plane of the structure and a very large MAE of 54.6 meV/tetramer. Both excited states have a smaller total spin moment of about $3.3\,\mu_B$ and an orbital moment of about $0.5\,\mu_B$ (see figure 8(*c*) and table VIII of the supplementary information (stacks.iop.org/JPCM/27/046002/mmedia)). Hence the exceptionally large MAE is a magnetic energy difference between high- and low-moment magnetic isomers, as for Pt_3Fe. For the ground state the magnetic structure is compatible with a mirror plane through the Co atoms and the symmetry line of the Pt_3 isocele triangle, the excited states are completely asymmetric.

For the flat 2D Pt_3Co tetramer SOC induces only small changes in the geometry (see table 4 and figure 8(*d*)). The easy magnetic axis is perpendicular, rotation of the magnetization into the plane costs an MAE of 4.2 meV/tetramer (moments parallel to the short diagonal) or 6.3 meV/tetramer (moments parallel to the long diagonal). The magnetic point group symmetries of the three configurations are the same as for the flat $PtCo_3$ cluster, but their energetic ordering is reversed. The total spin anisotropy is modest, but it is remarkable that the orbital moments are significantly larger in the excited states than in the GS. The local orbital moments

on the Pt atoms vary quite strongly with the magnetization direction (see figure 8(*d*) and table VI of the supplement (stacks.iop.org/JPCM/27/046002/mmedia)) such that the total moment of the excited states is larger by about 0.8 μ_B than in the ground state. For the ground state the total moment is $m_J = 4.37\,\mu_B$, intermediate between the low- and high-moment states of the 3D isomer, while for the excited states it is $m_J \sim 5.15\,\mu_B$. This means that the situation is just the inverse as for the 3D geometry—here the low MAE is a consequence of the partial compensation between magnetic energy difference and intrinsic MAE.

5.2. Heteroatomic tetramers supported on graphene

For mixed four-atom clusters supported on a free-standing graphene layer both initially flat and 3D geometries have been considered. The 2D geometry is unstable, in all cases the structural optimization leads to a transformation from the 2D-configuration parallel to the graphene layer to 3D-structures. A similar stabilization of a 3D structure has also be found for a graphene-supported Pt_4 cluster [10].

5.2.1. Adsorption geometries of tetramers. The geometries optimized in the SR approximation are shown in figures 9 and 10. For the 3d-rich tetramers the stable geometry is in both cases a pyramid with the 3d-atoms close to six-fold hollows (6h) of the graphene layer. The trigonal symmetry is broken, but for $PtFe_3$ this is reflected only in a small difference in the Fe–Fe distances and not in the local spin moments, while for $PtCo_3$ the local spin moments are also different. The Fe–Fe and Co–Co distances are stretched due to the binding to the substrate, while the Pt–X distance to the apical Pt atom is unchanged or even elongated compared to the free tetramer.

The binding energy E_{int} calculated for $PtFe_3$ pyramid is −1.26 eV/cluster (relative to 3D free $PtFe_3$). The total magnetic moment of the cluster/support complex is 9 μ_B, reduced compared to 12 μ_B for the free tetramer. The contribution of the moments induced on the C atoms is about 0.5 μ_B, the spin on the Fe atoms is reduced by about 0.6 μ_B, the spin on the Pt atom by 0.4 μ_B compared to the free $PtFe_3$ cluster. The buckling amplitude of the graphene-sheet is 0.26 Å, the cluster is located in a depression.

The binding energy of $PtCo_3$ is −1.12 eV/cluster (relative to the stable 2D isomer of free $PtCo_3$) or −1.46 eV/cluster relative to the 3D isomer. The trigonal symmetry is broken (as evident from the Co–Co distances and the local spin moments), the Co atoms are also slightly displaced relative to the 6h sites. The total magnetic moment of the cluster/substrate complex is 5 μ_B, reduced by 2 μ_B compared to the gas-phase cluster. In this case the small magnetic moments induced in the slightly buckled graphene layer are −0.26 μ_B in total, oriented antiparallel to the cluster moment.

The stable structure of Pt_3Fe is asymmetric, it is best described as a distorted trigonal pyramid positioned sideways on the graphene layer (see figure 9(*a*)) with $E_{int} = -1.16$ eV/cluster relative to the free 3D tetramer. The cluster induces a strong corrugation with an amplitude of 0.68 Å in the graphene-layer, the C atoms located below the cluster are pulled upwards. The magnetic moment of the Pt_3Fe/graphene complex is 4 μ_B in the scalar-relativistic limit, much lower than the magnetic moment of 7 μ_B obtained for the free 3D cluster. The reduction of the magnetic moment is due to the strong quenching of the spin on the Pt atoms while the spin on the Fe atom not in direct contact with the C atoms is only modestly reduced. A slightly lower adsorption energy ($E_{int} = -1.04$ eV/cluster) has been found for a distorted Pt_3Fe tetrahedron binding to graphene through the Pt–Fe edge, see figure 9(*b*). In this case the corrugation in the C-layer is smaller and amounts to 0.40 Å. The total magnetic moment is again 4 μ_B.

The GS geometry ($E_{int} = -1.20$ eV/cluster relative to the stable 3D isomer of the free cluster) of Pt_3Co supported on graphene is similar to that of an adsorbed Pt_4 tetramer [9]. It can be described either as a strongly distorted tetrahedron or as a deltoid bent about the short diagonal (see figure 10(*a*)). The cluster binds to the support through the Co and one of the Pt atoms, both are located between br- and ot-sites. The total moment of the cluster/graphene complex is 3 μ_B, equal to the magnetic moment of the low-spin isomer of the gas-phase 3D cluster. In a metastable variant ($E_{int} = -0.31$ eV/cluster) the supported cluster forms a distorted trigonal pyramid binding to graphene through the Pt_3 isocele triangle with the Pt atoms located near br sites, capped by the Co atom, see figure 10(*b*). In both cases, the cluster induces quite a strong corrugation in the graphene layer of 0.33 and 0.49 Å, respectively. The spin moment is again 3 μ_B.

Due to the strong binding to the substrate relativistic calculations including SOC predict only minimal changes in the adsorption geometries relative to the SR result, the SOC-induced changes in the magnetic properties and the MAE are discussed below.

5.2.2. Magnetic anisotropy of Pt–Fe tetramers on graphene. Relativistic calculations predict for the most stable Pt_3Fe cluster an easy magnetic axis parallel to the graphene layer and to the Pt–Pt edge binding to graphene (see figure 11(*a*)). The total magnetic moment is 4.15 μ_B, the slightly reduced spin moment of 3.74 μ_B is over-compensated by the orbital moment of 0.41 μ_B. Two excited magnetic configurations higher in energy by only 0.9 meV/cluster have been found, one with magnetization perpendicular to the support and one with in-plane magnetization perpendicular to the Pt_3 triangle. The spin moment is almost isotropic, the orbital anisotropy is also very small ($\Delta m_L = 0.02\,\mu_B$) under a rotation of the moment to a direction perpendicular to the graphene layer. The orbital anisotropy is larger ($\Delta m_L = 0.14\,\mu_B$) for the second excited state. The very low MAE correlates with the asymmetric geometric and magnetic structures.

A slightly larger MAE of about 1.7 meV/cluster has been calculated for the metastable adsorption geometry of Pt_3Fe. Details of the local spin and orbital moments of all Pt–Fe tetramers on graphene are summarized in table IX of the supplementary information (stacks.iop.org/JPCM/27/046002/mmedia), the magnetic structures of the the metastable Pt_3Fe tetrahedron on graphene

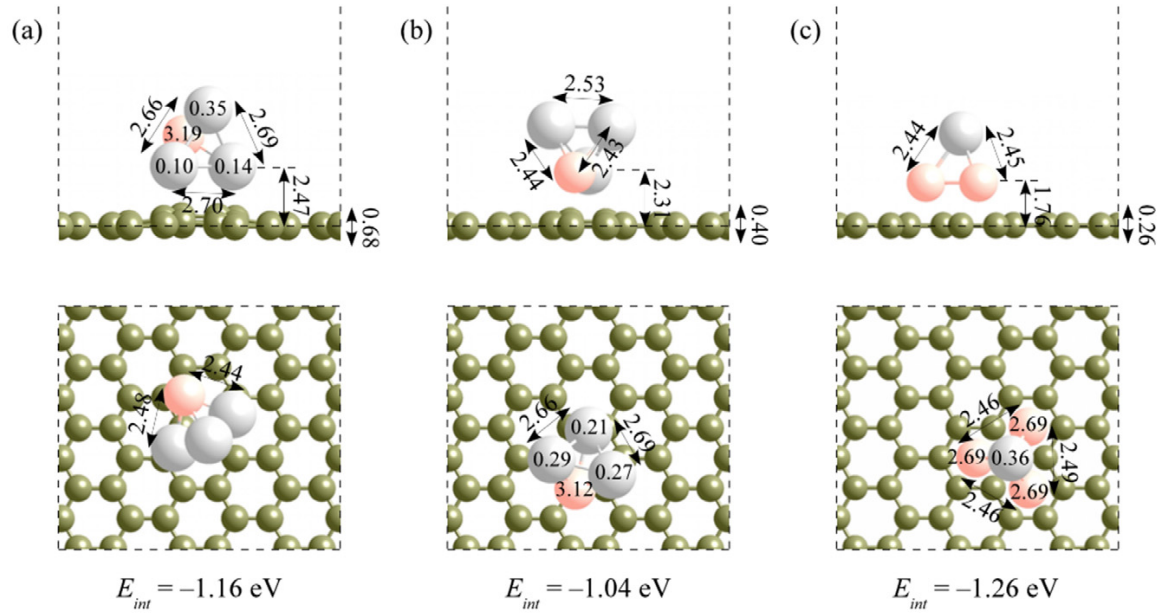


Figure 9. Side- and top-views of the adsorption geometries of a mixed Pt–Fe tetramer (Pt—grey, Fe—red) on a free-standing graphene layer: (*a*) Pt_3 pyramid, Pt–Pt edge binding to graphene, (*b*) distorted Pt_3Fe tetrahedron, Pt–Fe edge binding to graphene, (*c*) $PtFe_3$ pyramid, Pt-up. All distances are in Å. Numbers on atoms denote the local magnetic moments (in μ_B) calculated in the scalar-relativistic approach.

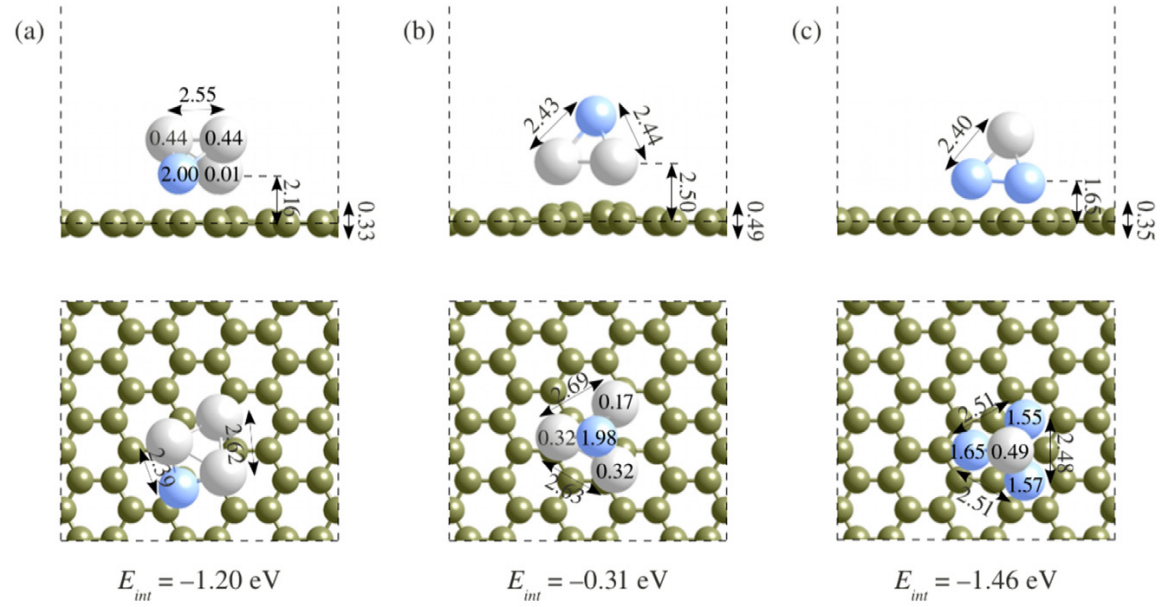


Figure 10. Side- and top-views of the adsorption geometries of a mixed Pt-Co tetramer (Pt—grey, Co—blue) on a free-standing graphene layer: (*a*) Pt_3Co ground-state, deltoid bent about the short Pt–Pt diagonal, Co and one Pt atom binding to graphene, (*b*) Pt_3Co pyramid, Co-up, (*c*) $PtCo_3$ pyramid, Pt-up. All distances are in Å. Numbers on atoms denote the local magnetic moments (in μ_B) calculated in the scalar-relativistic approach.

are displayed in figures 2(*a*) and 3 of the supplement (stacks.iop.org/JPCM/27/046002/mmedia).

The easy magnetic axis of the almost perfectly trigonal $PtFe_3$ pyramid is perpendicular to graphene and to the basal Fe_3 triangle (magnetic point group symmetry 3 m), with a spin moment of 8.40 μ_B and an orbital moment of 0.52 μ_B, see figure 11(*b*). Two states with in-plane magnetization and the total moment either parallel or perpendicular to an Fe–Fe bond are found to be energetically degenerate, with an MAE of 12.4 meV/cluster. The threefold symmetry is lost, but this is manifest only for the local orbital moments. The spin moment is strictly isotropic, the orbital moments on

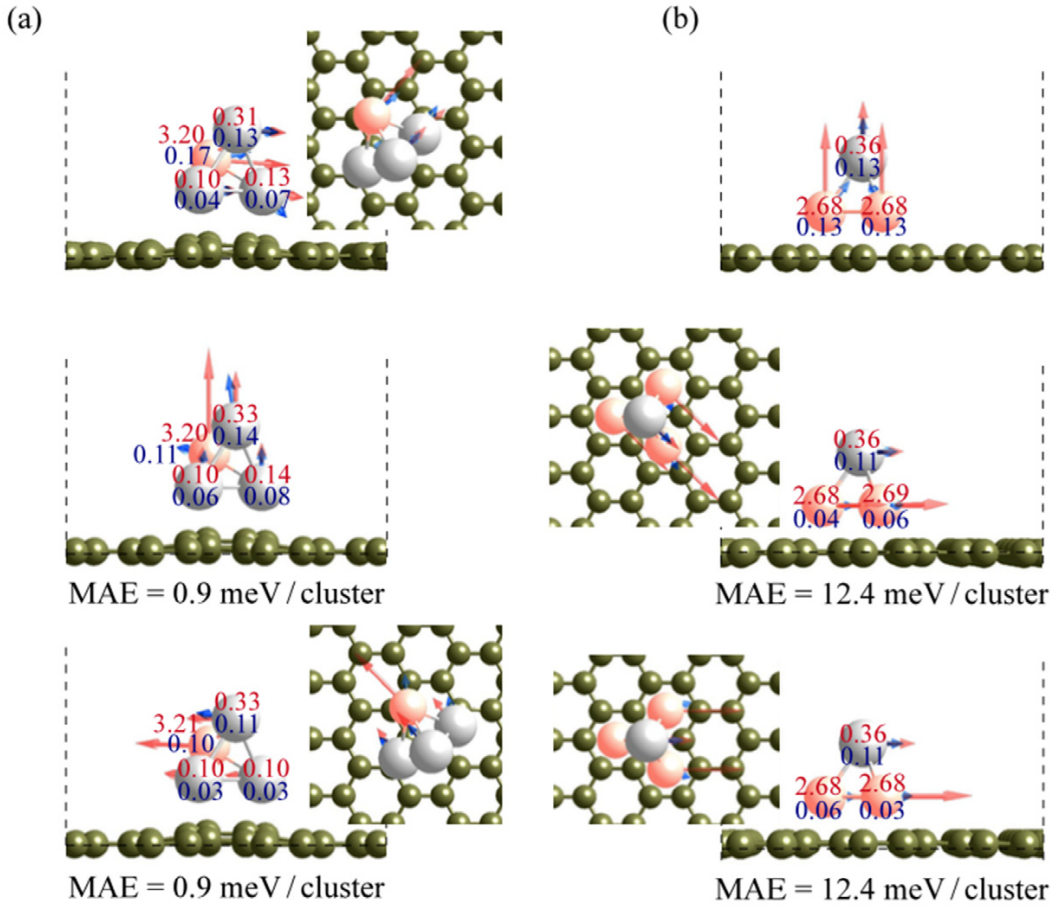


Figure 11. Side- and top-view of the magnetic structure of Pt–Fe tetramers on a free-standing graphene layer: (*a*) Pt_3Fe, equilibrium configuration, (*b*) $PtFe_3$. Red (light) arrows shows spin-, blue (dark) arrows the orbital magnetic moments, the numbers give the values of the local spin (upper number) and orbital (lower number) magnetic moments in μ_B. The MAE is given (in meV/cluster) relative to the easy axis orientation of the magnetization. See text.

the Fe atoms are reduced to about half their value for hard-axis magnetization. Table IX of the supplementary material (stacks.iop.org/JPCM/27/046002/mmedia) lists all local spin and orbital moments.

5.2.3. Magnetic anisotropy of Pt–Co tetramers on graphene. The easy magnetic axis for the stable Pt_3Co cluster on graphene is parallel to the graphene-sheet and to the upper Pt–Pt edge, but the small local spin and orbital moments on the Pt atom adjacent to graphene are antiparallel to those on the other three atoms, see figure 12(*a*). The magnetic point group symmetry is m' relative to a mirror plane passing through one Pt and Co atom and perpendicular to graphene. The spin magnetic moment of $2.73\,\mu_B$ is slightly reduced by SOC, but it is over-compensated by the orbital moment of $0.56\,\mu_B$ ($m_J = 3.29\,\mu_B$). In-plane rotation of the magnetization to a direction parallel to the Pt–Co edge costs an MAE of 13.4 meV and leads to the formation of an asymmetric configuration with strongly non-collinear local moments and a slight reduction of the total spin and orbital magnetic moments: $m_S = 2.70\,\mu_B$, $m_L = 0.49\,\mu_B$, $m_J = 3.19\,\mu_B$. The hard magnetic axis is orthogonal to the graphene layer, its energy is 15.4 meV above the GS. In this solution the magnetic moments are further reduced to $m_S = 2.65\,\mu_B$, $m_L = 0.40\,\mu_B$, $m_J = 3.05\,\mu_B$, the local moments are canted relative to the global magnetization axis. The magnetic point group symmetry is m. The MAE calculated for graphene-supported cluster is only about one third of that calculated for the free 3D Pt_3Co tetramer (which is correlated to a high- to low-moment transition), but larger than for the free 2D cluster. The value of the magnetic moment is larger than for the low-moment state of the free 3D cluster and lower than for the 2D configuration, which is primarily due to the strong quenching of the spin-moment on the Co atom binding to the support from 2.26 to $0.96\,\mu_B$. Compared to Pt_3Fe, for the Pt_3Co tetramer the reduction of the magnetic anisotropy upon adsorption on graphene is less pronounced. This is also related to the fact that the adsorption configuration of Pt_3Fe is asymmetric whereas adsorbed Pt_3 adopts a symmetric configuration intermediate between the 2D and 3D geometries of the free tetramer. The easy and hard magnetic

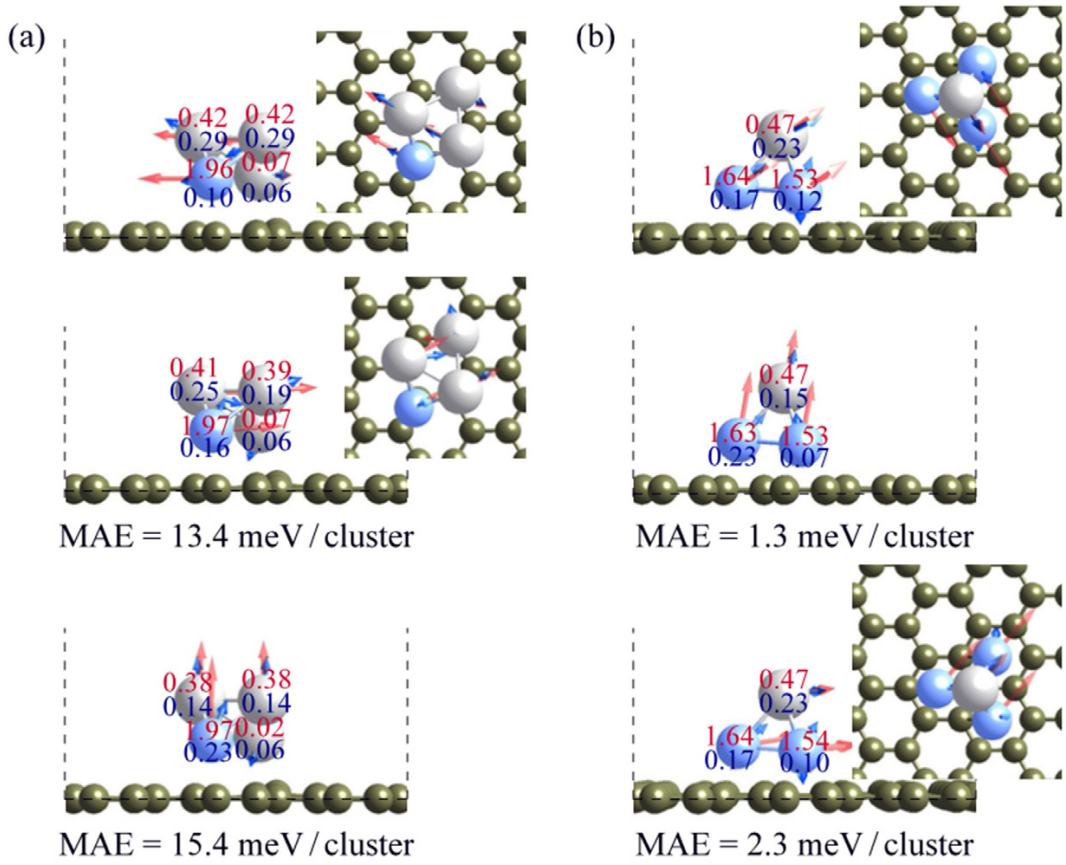


Figure 12. Side- and top-views of the magnetic structures of the stable configurations of Pt_3Co (*a*) and $PtCo_3$ (*b*) cluster supported on graphene. Blue balls represent Co atoms, light grey ball Pt atoms. Red arrows represent the spin, blue (dark) arrows the orbital magnetic moments, the numbers give the absolute values of the local spin (upper number) and orbital (lower number) magnetic moments in μ_B. The MAE is given relative to the ground state configuration. See text.

directions are oriented along the symmetry axes and parallel or perpendicular to the substrate, in contrast to the low symmetry of the stationary magnetic states of Pt_3Fe on graphene. Values of the local magnetic moments of all graphene-supported Pt_3Co tetramers are summarized in table X of the supplementary material (stacks.iop.org/JPCM/27/046002/mmedia), pictures of the magnetic configurations of the metastable adsorption state of Pt_3Co (with an MAE of 25.6 meV/cluster) are shown in figure 2(*b*) of the supplement (stacks.iop.org/JPCM/27/046002/mmedia). The MAE of the metastable configuration is even larger, because a high spin moment is preserved on the top Co atom.

In the magnetic GS of the $PtCo_3$ pyramid the local spin and orbital moments on the Co atoms are non-collinear, reflecting the asymmetry of the geometric structure. The easy magnetization direction is perpendicular to a Co–Co bond and parallel to a C–C bond of the graphene layer, tilted away from the graphene-sheet (see figure 12(*b*)). The magnetic moments of the cluster are $m_S = 5.17\,\mu_B$, $m_L = 0.46\,\mu_B$, $m_J = 5.63\,\mu_B$. For a magnetization direction initially perpendicular to the support the relaxed local moments are canted towards the Pt–Co bonds, but their absolute values remain almost unchanged and the MAE is only 1.3 meV/cluster. For a magnetization perpendicular to another Co–Co bond, equivalent to the easy-axis configuration except for the displacement of the Co atoms from the 6h sites the total magnetic moment is again almost unchanged, but the energy is increased by a small MAE of 2.3 meV/cluster. The small MAE of supported $PtCo_3$ correlates with a very small orbital anisotropy (see table X of the supplementary material (stacks.iop.org/JPCM/27/046002/mmedia) for details of the local magnetic moments).

6. Discussion

The structural and magnetic properties of mixed trimers and tetramers of transition metals in the gas-phase and supported on a graphene layer have been investigated using relativistic density-functional calculations. The focus of our investigations was on the consequences of a replacement of one or more Pt atoms in free and graphene-supported Pt_n clusters by a 3d atom such as Fe or Co on their geometric and magnetic structures and on the magnetic anisotropy in particular.

6.1. Scalar-relativistic results and spin-orbit coupling

Already at the scalar-relativistic level, important differences exist between the Pt–Fe and the Pt–Co clusters. Substitution of one of the Pt atoms in Pt_n clusters by Fe enhances the weak spin moment of $m_S = 2\,\mu_B$ to $m_S = 4$, 6, and $6\,\mu_B$ in Pt_nFe with $n = 1$, 2, 3, while substitution by Co leads only to a modest enhancement to $m_S = 3\,\mu_B$ in mixed Pt_nCo. For Pt_3Co the low-moment state with $3\,\mu_B$ is energetically degenerate with a high-moment state with $5\,\mu_B$. In $PtFe_n$ clusters containing only a single Pt atom the scalar-relativistic spin-moment is $m_S = 4$, 8 and $12\,\mu_B$ for $n = 1$, 2, 3, equal to the sum of the spin moments of n free Fe atoms, while for $PtCo_n$ a corresponding relation holds only for $n = 1, 2$ with $m_S = 3$ and $6\,\mu_B$ whereas for $PtCo_3$ the spin moment reaches only $7\,\mu_B$. This shows that the interaction between Pt and Fe stabilizes a high-moment state of the mixed cluster, while mixed Pt–Co clusters show only a weaker magnetic moment. Surprisingly, the high-moment state of Pt_3Fe, $PtFe_3$, but also of $PtCo_3$ tetramers stabilizes a flat geometry over the three-dimensional arrangement in form of a distorted tetrahedron which is the ground-state of all three homo-atomic tetramers. The stabilization of the two-dimensional geometry is closely related to the result [37] that in a high-moment state of Pt_4 with $m_S = 4\ \mu_B$ a flat geometry is preferred over the tetrahedral structure stable in the weakly magnetic ground-state with $m_S = 2\ \mu_B$. Only the magnetic energy difference leads to a very small preference for the low-spin state. For the weakly magnetic Pt_3Co the tetrahedral geometry is lower in energy.

The magnetic energy differences between the scalar-relativistic spin-isomers are also very important for understanding the influence of spin–orbit coupling which leads to a mixing of low-energy spin-states. For the Fe_n trimers and tetramers with a high-spin ground state the mixing with a low-spin isomer leads to a reduction of the spin moment if SOC is taken into account and this loss in the magnetic moment is not compensated by the small orbital moments. The situation is similar for Co_4 stable in a high-spin state while for Co_3 with a low-spin ground state SOC leads to enhancement of the spin-moments. In addition, orbital moments are always larger on the Co than on the Fe atoms (see tables 1 and 2). The situation is similar for the heteroatomic clusters: in Pt–Fe trimers and tetramers SOC leads to a reduction of the spin moment which for the Pt-rich clusters is compensated or even slightly overcompensated by the orbital moment. In the Co-rich Pt–Co clusters the loss in the spin-moment is always overcompensated by the orbital moment, while for the Pt-rich clusters SOC leads to a ground state with an increased total moment (see tables 3 and 4). For mixed clusters SOC also has a significant influence on the geometric structure, correlated to the change in the local moments. The structural consequences of SOC are most pronounced in $PtFe_3$ where the changes in the interatomic distances reach about 0.1 Å, they are much more modest in Pt–Co trimers and tetramers.

6.2. Magnetic anisotropy of free nano-clusters

The main emphasis of our investigations was on the correlation between the geometric and magnetic structures and on the magnetic anisotropy of the mixed nano-clusters in particular. The magnetic anisotropy energy is often discussed, following Bruno [38] within perturbation theory, which predicts that the easy axis is determined by the state with the largest orbital moment, the MAE being proportional to the strength ξ of the SOC, the spin moment and the anisotropy of the orbital moments, $\mathrm{MAE} \propto -\xi m_S \Delta m_L$, . However, this result is based on two essential assumptions: (1) the geometric structure is independent of SOC and of the direction of magnetization and (2) the spin moments and the exchange splitting of the electronic eigenstates are isotropic. Both are violated for magnetic nanostructures. For magnetic dimers all calculations [15, 39, 40] agree that the spin of 3d-dimers is isotropic, while 4d dimers show a small, but non-negligible spin-anisotropy and for 5d dimers Δm_S can be even comparable to the orbital anisotropy. For monowires of Pt atoms it has been shown that the magnetization direction can change the magnetic state of the systems: non-zero spin and orbital moments exist only for magnetization parallel to the axis of the wire, while a state with perpendicular magnetization is non-magnetic [41]. For monowires of other heavy elements it has been shown that at their equilibrium distances the wires are close to the onset of magnetism, but that their large MAE's are not proportional to the large spin and orbital anisotropies [42]. For Pt_2 dimers a small, but non-negligible change in the dimer length for magnetization parallel and perpendicular to the dimer axis has been reported [15].

The correlation between symmetry and MAE has been discussed by Strandberg *et al* [16]. If degenerate and only partially occupied electronic eigenstates close to the Fermi level exist for some direction of magnetization, but are lifted for other directions, this can lead to a large MAE—e.g. for the dimers of the Co-group [15]. Similarly, for a metastable Co_3 trimer forming an equilateral triangle a larger MAE has been predicted than for a trimer whose trigonal symmetry has been broken by a Jahn–Teller distortion [16]. Trimers are the smallest clusters where a degeneracy of the electronic eigenstates can be lifted either by a Jahn–Teller distortion or by the broken magnetic point-group symmetry. Another important effect influencing the MAE has already been demonstrated in our work on small Pt_n clusters: a pronounced non-collinearity and anisotropy of the local spin and orbital moments, while the total spin and orbital moments are aligned and show a smaller anisotropy [9].

In mixed trimers the point group symmetry is 2 mm for all clusters. Due to the low symmetry, no degenerate electronic eigenstates exist for any orientation of the magnetization. The easy magnetic axis is in-plane, along the twofold symmetry axis and the magnetic point group symmetry is $2m'm'$ for Pt_2Co, $PtCo_2$ and Pt_2Fe (as for all three homoatomic trimers). Only for $PtFe_2$ the easy axis is along the Fe–Fe edge, the magnetic point group symmetry is $m'm2'$. For all four trimers the calculations show a strong orbital anisotropy, a weaker spin anisotropy and for some cases non-collinear local moments and distortions of the interatomic distances as a function of the direction of magnetization (see figures 1 and 2). The MAE depends on a complex interplay of (i) the orbital anisotropy Δm_L, (ii) the spin anisotropy Δm_S and (iii) the change in

the geometric structure, measured by the change Δd_{ij} in the interatomic distances. The dominant factor determining the strength of the MAE is the orbital anisotropy, but the dependence is not a simple proportionality.

For $PtFe_2$ and Pt_2Co the geometric structure is the same for the ground state and the excited configurations, the spin anisotropy is modest—hence we expect that the MAE is dominated by the orbital anisotropy. Indeed the ground state is in both cases the state with the largest total orbital moment (see figures 1 and 2 and tables I and II of the supplementary information (stacks.iop.org/JPCM/27/046002/mmedia)), but the MAE of the excited states is not determined by the total orbital anisotropy alone. For Pt_2Co $\Delta m_L^{Co} = 0.21\,\mu_B$ for both excited states, but the in-plane MAE is larger than the perpendicular MAE because an in-plane rotation of the magnetization leads to a substantial negative orbital anisotropy on the Pt atoms, resulting in a nearly vanishing total orbital anisotropy. For $PtFe_2$ in-plane rotation of the magnetization leads to a lower orbital anisotropy, but a larger MAE than perpendicular magnetization which is also correlated to a substantial spin anisotropy.

For Pt_2Fe and $PtCo_2$ the MAE depends on Δm_L, Δm_S and substantial values of Δd_{ij}. The remarkably large perpendicular MAE of $PtCo_2$ results from the strong spin isotropy of both species, while for Pt_2Fe the increasing MAE follows the trend in Δm_L, especially the loss of the orbital moment on the Pt atoms with the much stronger SOC.

For 2D Pt_3Fe tetramers the MAE depends on substantial spin and orbital anisotropies and strong structural distortions (see figure 7(*a*)). The two excited states with in-plane magnetization have larger orbital moments on the Pt atoms than the ground state with perpendicular magnetization, but also increased Pt–Fe distances. Perpendicular magnetization is stable because the energetic cost for the change in structure overrides the magnetic energy difference. For 2D $PtFe_3$ the geometric structure is independent of SOC. In the ground state the magnetization is parallel to the Fe–Fe diagonal (see figure 8(*a*))—in accordance with the easy axis of $PtFe_2$ trimers along an Fe–Fe edge. Spin anisotropies are very small, the ground state is the state with the largest total orbital moment. The two excited states differ mainly in the sign of the orbital anisotropy on the apical Fe atom.

For 2D $PtCo_3$ the structure is again independent of SOC, spin anisotropies are modest. The easy axis is along the twofold symmetry axis, perpendicular to the Co-Co diagonal (in analogy to $PtCo_2$). For the two excited configurations the MAE increases with increasing Δm_L.

The exceptionally large MAE of 3D Pt_3Co forming a distorted trigonal pyramid results from a very large spin anisotropy (see figure 8(*b*)). For the ground state with magnetization perpendicular to the Pt_3 triangle the total spin moment is intermediate between the scalar-relativistic spin moments of the energetically degenerate low- and high-spin isomers. Together with a large orbital contribution the total moment reaches the scalar-relativistic spin moment of the high-spin isomer. For the two excited configurations the spin moment is much lower and the orbital moments are also reduced, most strongly on the Co atom.

Our calculations have shown that in some cases there are large differences in the MAE of different excited stationary configurations. These differences are a measure for the anisotropy of the magnetic energy surface. The quantity determining the stability against a thermally induced reversal of the magnetization direction, however, is the energy of the lowest saddle point on the magnetic energy surface. For the trimers this energy varies between 6.7 meV/trimer for $PtCo_2$ and 11.3 meV/trimer for $PtFe_2$. The saddle point is associated with an in-plane rotation of the magnetic moment for $PtCo_2$ and Pt_2Fe and with a change from in-plane to perpendicular magnetization for $PtFe_2$ and vice-versa for Pt_2Co. These values are enhanced by about one order of magnitude compared to the energy barrier against in-plane rotation of the magnetization in Pt_3 of 0.6 meV/trimer [9] and also increased by about a factor of five compared to Co_3 and Fe_3 trimers. For the 2D tetramers the saddle-point energy varies between 3.1 meV/tetramer for $PtCo_3$ and 6.4 meV/tetramer for Pt_3Fe (in-plane rotation in both cases). The much larger MAE of $PtCo_3$ is a particular case, associated with the degeneracy of different magnetic isomers without SOC. In this case a direct comparison with the Pt_4 tetramer is no possible because of its antiferromagnetic ground state. The lowest barrier for the magnetization reversal of the excited ferromagnetic state is much larger, 21.2 meV/tetramer. [9] Compared to the stable 3D Fe_4 and Co_4 tetramers we find a modest enhancement compared to Fe_4 and a strong one for Co_4.

6.3. Graphene-supported nano-clusters

Hetero-atomic clusters bind to graphene preferentially through the 3d atoms. This means that while for PtX_2 trimers the twofold symmetry can be preserved upon adsorption, the symmetry of free Pt_2X trimers is broken upon adsorption. Because of the need to match the distance between the preferred adsorption sites on the graphene layer, the distances between the atoms binding to the substrate are increased by 0.2 to 0.45 Å (see figures 3 and 5). Spin- and orbital moments on these atoms are reduced, 5d atoms are more affected than 3d atoms. The same observations hold also for graphene-supported tetramers. The stable adsorption geometry of Pt_3X clusters is intermediate between the 2D and 3D configurations of the free tetramers (as also observed for Pt_4, see [10]), PtX_3 tetramers form distorted trigonal pyramids with expanded X–X distances. No structural changes upon re-orientation of the magnetization have been found.

For the trimers we note a distinct difference between PtX_2 and Pt_2X clusters. The former are bound to graphene in a configuration preserving the 2 mm point group symmetry of the free clusters. The spin moments on the 3d atoms are reduced by about 0.3 μ_B for $PtFe_2$ and by 0.6 μ_B for $PtCo_2$, orbital moments are reduced by about a factor of two. On the Pt atom spin and orbital moments are reduced for $PtFe_2$, but they remain almost unchanged for $PtCo_2$. The easy axis is along the twofold symmetry axis of the trimer, perpendicular to graphene. The MAE for rotating the magnetization axis parallel to the graphene layer is significantly reduced compared to the free trimer for $PtFe_2$, but remains of the same order of

magnitude for $PtCo_2$. The dominant influence on the MAE comes from the orbital anisotropy, but for $PtCo_2$ there is also a non-negligible spin anisotropy (see parts (*a*) of figures 4 and 6 for details. The saddle point energy to be overcome for a magnetization reversal is 3.3 meV/trimer for $PtFe_2$ and 8.6 meV/trimer for $PtCo_2$. This is of the same order of magnitude than the MAE of 5.1 meV/trimer calculated for the low-symmetry configuration of Pt_3/graphene [10].

For the low-symmetry configuration of the Pt-rich trimers there is no direction for which the magnetic energy can be expected to be stationary for symmetry reason. The stationary solutions found in the simulations are asymmetric, with a certain degree of misalignment between the local spin and orbital moments (see parts (*b*) of figures 4 and 6 for details). The minimum energy for a magnetization reversal is only 0.2 meV/trimer for Pt_2Fe and 2.0 meV/trimer for Pt_2Co. These energies are much lower than that calculated for a Pt_3 trimer on graphene.

For the graphene-supported tetramers the geometric structure is again of decisive importance for the magnetic anisotropy. For the 3d-rich clusters the binding to the substrate stabilizes the slightly distorted structure of a trigonal pyramid, in contrast to the flat structure of the free tetramers. Due to the necessity to match the substrate, the distances between the 3d-atoms forming the basis are stretched by about 0.2 Å ($PtFe_3$) and 0.3 Å ($PtCo_3$) compared to the metastable 3D configuration of the free tetramers, such that the Pt atoms moves closer to the plane of the 3d-triangle. For $PtFe_3$ the spin moments of both species are reduced by adsorption and isotropic, the orbital anisotropy is largest on the Fe atoms and correlated to a large MAE of 12.4 meV/tetramer. For $PtCo_3$ the spin moments are strictly isotropic, the opposite sign of the local orbital anisotropies leads to an isotropic total orbital moment and to a small MAE (see parts (*b*) of figures 11 and 12). The easy axis is perpendicular to graphene for $PtFe_3$, but oblique for $PtCo_3$ (reflecting the broken symmetry of the adsorption structure). The minimum energy barrier for a reversal of the magnetization direction is 12.4 meV in the first, but only 1.3 meV in the second case.

Pt_3Fe tetramers are adsorbed in an asymmetric configuration, leading to a very low MAE of only 0.9 meV/tetramer. Pt_3Co is bound in a more symmetric state, adopting a structure intermediate between the 2D and 3D isomers of the free cluster. The total orbital anisotropy is low, resulting from a compensation between a large positive Δm_L on the Pt and a negative one on the Co atom. The orbital anisotropy on the Pt atoms prevails, leading to a substantial MAE for magnetization reversal of 13.4 meV/atom.

Compared to the free tetramers, the minimum barrier for magnetization reversal is lowered by a factor ranging between about 4 (Pt_3Co and Pt_3Fe) and 2 (for $PtCo_3$) Only for $PtFe_3$ the barrier height is even doubled. The larger MAE is related to a larger orbital anisotropy on the Fe atoms binding to graphene. Compared to the graphene-supported Pt_4 tetramer with a barrier-energy of 3.2 meV/tetramer we note an enhancement by about a factor of four for Pt_3Co (which adopts a similar structure) and for $PtFe_3$, but a reduction by about a similar amount for Pt_3Fe and $PtCo_3$.

7. Conclusions

The aim of our study was to investigate, at the example of Pt–Fe and Pt–Co trimers and tetramers, whether mixed magnetic nanostructures consisting of 3d and 5d atoms provide a better stability against the reversal of the magnetization direction than homoatomic clusters of either elements. An important result is that the magnetic anisotropy energy depends not only on the anisotropy Δm_L of the orbital moments (which is the dominant factor for 3d nanostructures), but also on the spin anisotropy Δm_S and on geometric distortions d_{ij} imposed by a change in magnetization direction. While the spin anisotropy is smaller than for homoatomic Pt_n clusters, the geometric distortions can be significantly more important.

For the free trimers the total energy difference calculated for easy and hard magnetization directions is of the same order of magnitude than for Pt_3 for $PtFe_2$ and Pt_2Co, but enhanced by a factor of more than two for Pt_2Fe and $PtCo_2$ due to the combination of a large total magnetic moment with a large orbital anisotropy and significant distortions of the isocele geometry. The most important result, however, is that the lowest energy of a saddle point configuration leading to a magnetization reversal ranges between about 7 and 11 meV/trimer, strongly enhanced compared to the low in-plane anisotropy energy of 0.6 meV/atom for Pt_3 (see [9]).

For free tetramers the surprising result is that, with the exception of Pt_3Co, the high magnetic moment of the free tetramers stabilizes a flat geometry. For Pt_3Co where low- and high moment states are energetically degenerate, the enhancement of the magnetic moment is not strong enough to stabilize the two-dimensional geometry. For the stable flat tetramers the energy difference between easy and hard magnetization directions varies between 12.5 and 21.4 meV/tetramer. The lowest saddle-point energy determining the stability against magnetizations reversal is lower, varying between about 3 and 6 meV/tetramer. Compared to a free Pt_4 cluster with an antiferromagnetic ground state the important effect is that in the mixed ferromagnetic ordering is stabilized. Only for 3D Pt_3Co we find a very large MAE of about 54 meV/tetramer, correlated to very large spin and significant orbital anisotropies.

However, it has to be admitted that the results for free clusters are mostly of academic interest, because for any measurement or application the cluster have to be supported on a substrate—here graphene was chosen as the example of a rather inert, weakly binding substrate. We found that because the bond strength between adatom and substrate is very different for 3d and 5d atoms, the distorted (relative to the gas-phase clusters) adsorption geometries of Pt-rich Pt_2X clusters have a very low symmetry leading to a reduced magnetic anisotropy and a lower stability against magnetization reversal. For Pt_2X trimers the saddle-point energies for magnetization reversal are strongly reduced, whereas for PtX_2 clusters conserving the symmetry they are of the same order of magnitude than for the free clusters and comparable to supported Pt_3 trimers. For tetramers the necessity to match to the substrate destabilizes the flat geometry of the free clusters. A high stability against magnetization reversal is

found for $PtFe_3$ and Pt_3Co forming more symmetric adsorption geometries, whereas the low energy barriers of Pt_3Fe and $PtCo_3$ result in the first case from the low symmetry of the cluster and in the second from very small total spin and orbital anisotropies. Only for the first two tetramers the saddle point energy of about 12 and 13 meV/tetramer is significantly larger than the value of 2.6 meV/tetramer for Pt_4 on graphene [9].

Altogether our results demonstrate that investigations of the magnetic anisotropy of mixed nanostructures must be based on a simultaneous optimization of all structural and magnetic degrees of freedom and on selfconsistent calculations of the total energies of the competing configurations.

Acknowledgments

Work at the Universität Wien has been supported through the VASP project.

References

[1] Shick A B and Mryasov O N 2003 *Phys. Rev.* B **67** 172407
[2] Sun S, Murray C B, Weller D, Folks L and Moser A 2000 *Science* **287** 1989
[3] Miyazaki T, Kitakami O, Okamoto S, Shimada Y, Akase Z, Murakami Y, Shindo D, Takahashi Y K and Hono K 2005 *Phys. Rev.* B **72** 144419
[4] Antoniak C *et al* 2006 *Phys. Rev. Lett.* **97** 117021
[5] Gruner M E, Rollmann G, Entel P and Farle M 2008 *Phys. Rev. Lett.* **100** 087203
[6] Gruner M E 2010 *J. Phys. Conf. Ser.* **200** 072039
[7] Chepulskii R V and Butler W H 2012 *Appl. Phys. Lett.* **100** 142405
[8] Gruner M E and Entel P 2012 *Int. J. Quantum Chem.* **112** 277
[9] Błoński P, Dennler S and Hafner J 2011 *J. Chem. Phys.* **134** 034107
[10] Błoński P and Hafner J 2011 *J. Chem. Phys.* **134** 154705
[11] Błoński P and Hafner J 2012 *J. Chem. Phys.* **136** 074701
[12] Xiao R, Kuz'min M D, Koepernik K and Richter M 2010 *Appl. Phys. Lett.* **97** 232501
[13] Błoński P and Hafner J 2014 *J. Phys.: Condens. Matter* **26** 146002
[14] Błoński P and Hafner J 2014 *J. Phys.: Condens. Matter* **26** 256001
[15] Błoński P and Hafner J 2009 *Phys. Rev.* B **79** 224418
[16] Strandberg T O, Canali C M and McDonald A H 2008 *Phys. Rev.* B **77** 174416
[17] Kresse G and Furthmüller J 1996 *Comput. Mater. Sci.* **6** 15
Kresse G and Furthmüller J 1996 *Phys. Rev.* B **54** 11169
[18] Kresse G and Joubert D 1999 *Phys. Rev.* B **59** 1758
[19] Blöchl P E 1994 *Phys. Rev.* B **50** 17953
[20] Perdew J P, Burke K and Ernzerhof M 1996 *Phys. Rev. Lett.* **77** 3865
[21] Vosko S H, Wilk L and Nusair M 1980 *Can. J. Phys.* **58** 1200
[22] Kresse G and Lebacq O *VASP Manual* http://cms.mpi.univie.ac.at/vasp/vasp/vasp.html
[23] Kleinman L 1980 *Phys. Rev.* B **21** 2630
[24] MacDonald A H, Pickett W E and Koelling D D 1980 *J. Phys. C: Solid State Phys.* **13** 2675
[25] Hobbs D, Kresse G and Hafner J 2000 *Phys. Rev.* B **62** 11556
[26] Johll H, Kang H C and Tok E S 2009 *Phys. Rev.* B **79** 245416
[27] Johll H, Wu J, Ong S W and Ch Kang H 2011 *Phys. Rev.* B **83** 205408
[28] Castro M, Jamorski C and Salahub D R 1997 *Chem. Phys. Lett.* **271** 133
[29] Gutsev G L, Khanna S N and Jena P 2000 *Phys. Rev.* B **62** 1604
[30] Papas B N and Schaefer H F 2005 *J. Chem. Phys.* **123** 074321
[31] Rollmann G and Entel P 2004 *Comput. Lett.* **1** 288
[32] Rollmann G, Entel P and Sahoo S 2006 *Comput. Mater. Sci.* **35** 275
[33] Longo R C, Carrete J, Ferrer J and Gallego L J 2010 *Phys. Rev.* B **81** 115418
[34] Srivastava M, Wang Y, Kemper A F and Cheng H-P 2012 *Phys. Rev.* B **85** 165444
[35] de Graef M 2010 *Metall. Mater. Trans.* A **41** 1321
[36] Huda M N, Niranjan M K, Sahu B R and Kleinman L 2006 *Phys. Rev.* A **73** 053201
[37] Futschek T, Hafner J and Marsman M 2006 *J. Phys.: Condens. Matter* **18** 9703
[38] Bruno P 1989 *Phys. Rev.* B **39** 865
[39] Frisch D, Koepernik K, Richter M and Eschrig H 2008 *J. Comput. Chem.* **29** 2210
[40] Fernandez-Seivane L and Ferrer J 2007 *Phys. Rev. Lett.* **99** 183401
Fernandez-Seivane L and Ferrer J 2008 *Phys. Rev. Lett.* **101** 069903
[41] Smogunov A, dal Corso A, Delin A, Weht R and Tosatti E 2008 *Nat. Nanotechnol.* **3** 22
[42] Mokrousov Y, Heinze S and Blügel S 2006 *Phys. Rev. Lett.* **96** 147201

IOP PUBLISHING JOURNAL OF PHYSICS: CONDENSED MATTER

J. Phys.: Condens. Matter **21** (2009) 426001 (12pp) doi:10.1088/0953-8984/21/42/426001

Density-functional theory of the magnetic anisotropy of nanostructures: an assessment of different approximations

Piotr Błoński and Jürgen Hafner[1]

Fakultät für Physik and Center for Computational Materials Science, Universität Wien, Sensengasse 8/12, A-1090 Wien, Austria

E-mail: juergen.hafner@univie.ac.at

Received 16 July 2009, in final form 27 August 2009
Published 29 September 2009
Online at stacks.iop.org/JPhysCM/21/426001

Abstract

We discuss the multiple technical choices that have to be made in *ab initio* density-functional calculations of the magnetic anisotropy of supported nanostructures: (i) choice of the exchange–correlation functional, (ii) degree of optimization of the geometry of the adsorbate/substrate complex, (iii) magnetic anisotropy energy calculated self-consistently or via the 'force theorem', (iv) calculations based on slab models of the substrate or using a Green's function describing a semi-infinite substrate, (v) full potential approach or atomic-sphere approximation. Using isolated Fe and Co atoms on Pt(111) as an example we demonstrate that by using a judicious combination of relatively crude approximations (complete neglect of structural relaxation, local exchange–correlation functional, . . .) seemingly good agreement with experimental anisotropy energies can be achieved, while the calculated orbital moments remain small. At a higher level of theory (relaxed adsorbate/substrate complex, gradient-corrected functionals, . . .) providing a realistic geometry of the adsorbate/substrate complex and hence a correct description of the interaction between the magnetic adatom and its ligands, anisotropy energies are also in semi-quantitative agreement with experiment, while the orbital moments of the adatoms are much too small. We suggest that the anisotropy energies provided by both approaches should be considered as lower limits of the real anisotropies. Without relaxation the ligand effect coupling the orbital moments of the adatom to the heavy atoms of the substrate is underestimated, while in a relaxed adsorbate/substrate complex the lack of orbital dependence of the exchange potential combined with a strong hybridization of adatom and substrate states leads to a strong underestimation of the orbital moment. We have briefly explored the influence of post-density-functional corrections. Adding a modest on-site Coulomb repulsion to the d states of the adatom (in a DFT + U approach) leads to a modest increase of spin and orbital moments of the adatom accompanied by a slow decrease of the induced moments, leaving the anisotropy energy almost unchanged.

(Some figures in this article are in colour only in the electronic version)

1. Introduction

Recently there has been great interest in the magnetic anisotropy energy (MAE) of small magnetic nanostructures supported on nonmagnetic substrates, motivated by the desire to build magnetic or magneto-optical memory storage devices with a maximal storage density [1]. A high magnetic anisotropy is required to inhibit magnetization reversal—the critical value of the MAE is about 1.2 eV/bit. Therefore a reduction of the size of the nanostructures carrying one bit of information requires an increase of the MAE per atom. In addition the dipolar magnetic interactions between neighboring bits must be sufficiently weak, and this can be achieved if the easy axis of magnetization is perpendicular to the plane of the

[1] Author to whom any correspondence should be addressed.

 © 2009 IOP Publishing Ltd Printed in the UK

substrate. The ultimate limit of a system showing magnetic anisotropy is an isolated atom on a nonmagnetic substrate. A high magnetic anisotropy energy requires large spin and orbital magnetic moments and a strong spin–orbit coupling. Large spin moments are found among the ferromagnetic 3d metals Fe and Co, but for these elements the orbital moment is small and the spin–orbit coupling is weak. Strong spin–orbit coupling is found in the heavy 5d metals, but these elements are nonmagnetic. Nanostructures of 3d metals supported on substrates of highly polarizable 5d metals are a viable route to tune both the spin moments and the anisotropy energy, and the simplest such nanostructure is of course an isolated magnetic atom on a substrate.

Using x-ray magnetic circular dichroism (XMCD) (see, e.g. Stöhr [2] and further references cited therein) it is now possible to measure the magnetic properties of adsorbed species down to surface coverages as low as 0.002 ML, extracting the spin and orbital moments as well as the magnetic anisotropy energy. However, because the focus of the x-ray beam is of the order of a few hundred μm^2, the experiment provides spatially averaged information. Consequently, information on the properties of single atoms or on well defined nanoclusters can only be achieved if surfaces with a homogeneous distribution of single atoms or monodisperse clusters can be prepared. A review of experimental investigations of the magnetism of individual atoms adsorbed on surfaces has recently been presented by Brune and Gambardella [3]. The results for isolated Co atoms on Pt(111) are characteristic for the magnetism of 3d atoms on highly polarizable substrates composed by 4d or 5d metals [3, 4]. The effective spin moment of $\mu_S^{\rm eff} = 1.8\pm0.1\ \mu_{\rm B}$ and the orbital moment of $\mu_L = 1.1\pm0.1\ \mu_{\rm B}$ measured at $T = 5.5$ K and in a magnetic field of $B = 7$ T sufficient to achieve saturation are both strongly enhanced not only compared to bulk Co (where $\mu_S = 1.52\ \mu_{\rm B}$ and $\mu_L = 0.15\ \mu_{\rm B}$), but also compared to 2D films [5–7], 1D atomic wires [8, 9], and supported nanoclusters [7, 10]. From the variation of the magnitude of the XMCD relative to the x-ray adsorption intensity measured for a magnetic field perpendicular ($\theta = 0°$) and nearly parallel ($\theta = 70°$) to the surface, a very large magnetic anisotropy of MAE $= 9.3\pm1.6$ meV was estimated. This extraordinarily large MAE has to be attributed to the reduced coordination of the Co atom and to the magnetic moments induced in the Pt substrate combined with the strong spin–orbit coupling of the Pt 5d states. The strong polarization of the substrate atoms is a consequence of the strong Stoner enhancement factor of Pt. For an isolated Co atom on the Pt(111) surface an effective moment of $\mu_S = 5.0\pm0.6\ \mu_{\rm B}$ has been estimated—this is comparable, but still lower than the effective 'giant moment' of 10 $\mu_{\rm B}$ reported for Co atoms in very dilute Co–Pt alloys [11]. This large difference in the effective moments suggests that the coordination of the magnetic impurity by the polarizable atoms is of decisive importance for the strong enhancement of the MAE of the Co atom by the coupling to the ligands.

Complementary investigations of isolated Co atoms have been performed using spin-polarized scanning tunneling microscopy (STM) and scanning tunneling spectroscopy (STS) [12]. The STM images show that the Co atoms occupy both fcc and hcp hollows of the Pt substrate. The differential conductance $\mathrm{d}I/\mathrm{d}V$ derived from the STS experiment shows no sign of hysteresis down to the lowest temperatures. This has been attributed to magnetization reversal by quantum tunneling. The curves may be fitted as a function of the magnetic field and its angle relative to the magnetic moment of the atom. Assuming an out-of-plane easy axis and MAE $=$ 9.3 meV the fit yields effective magnetic moments of μ(hcp) $= 3.9\pm0.2\ \mu_{\rm B}$ and μ(fcc) $= 3.5\pm0.2\ \mu_{\rm B}$ for the two adsorption sites, respectively. The STM studies also suggest a weak coupling between the Co-moments mediated by the conduction electrons of the substrate.

Very recently it has been claimed [13] that the STS experiments providing information on the spin-flip energy $E_{\rm sf}$ (i.e. on the energy required to change the magnetic adatom from its ground state with spin $\pm S$ to a state with $\pm(S-1)$) can also be used to obtain the MAE. If the spin is known, the MAE is approximated as $E_{\rm sf} \times S^2/(2S-1)$. Although in their analysis Balashov *et al* [13] have ignored the fact that the spin to be flipped is not the spin of the adatom alone, but the effective spin of the adatom/substrate complex, they find for Co/Pt(111) an MAE of 10.25 meV/atom in good agreement with Gambardella *et al* [4]. For an isolated Fe atom on Pt(111) again a perpendicular anisotropy and a large MAE of 6.53 meV/atom has been reported.

Experiments using XMCD and x-ray adsorption spectroscopy (XAS) on isolated Fe atoms on Pt(111) revealed a much lower ratio for orbital to effective spin moment of $L/S_{\rm eff} \sim 0.18\pm0.05$ (to be compared to $L/S_{\rm eff} \sim 0.61\pm0.05$ for Co/Pt(111)), an out-of-plane orientation of the easy axis and a very low MAE [14]. Similar values have been reported for very small Fe$_n$ clusters ($n = 2 \rightarrow 9$) adsorbed on ultrathin Ni films supported on a Cu(100) substrate [15]. For clusters of this size the ratio $L/S_{\rm eff}$ varies between 0.08 (for $n = 3$) and 0.27 (for $n = 6$).

These experiments have also motivated theoretical studies of the magnetism of supported isolated atoms based on spin-density-functional techniques [4, 16–24]. The calculation of the magnetic anisotropy is a problem of fundamental importance. Magnetic anisotropy, magneto-optical spectra, magnetic dichroism, and other important properties are caused by spin–orbit coupling, hence a relativistic calculation is required. A further complication arises from the fact that whereas spin magnetic moments are described quite accurately by density-functional theory (DFT) based on semilocal, gradient-corrected exchange–correlation functionals, the orbital moments are generally underestimated. The reason is that the variables determining the effective one-electron potential within DFT (the charge and spin densities) are determined as averages over occupied orbitals. It has been suggested that the prediction of the orbital moments should be improved by adding post-DFT calculations such as the empirical orbital polarization term proposed by Brooks *et al* [25, 26] or using the DFT $+ U$ method [27, 28] adding an on-site Coulomb repulsion U to the potential acting on the d-electrons of the magnetic atom [4, 23]. However, calculations using the full orbital polarization term tend to

produce too large orbital moments [4]. For adatoms supported on strongly polarizable substrates it is also evident that a very accurate determination of the geometry of the adatom/substrate complex is required.

Indeed a calculation of the magnetic anisotropy energy requires a number of technical choices, involving the following.

(i) The choice of an exchange–correlation functional, i.e. local spin-density approximation (LSDA) or generalized-gradient approximation (GGA). GGA calculations not only produce slightly larger (and in general more accurate) lattice constants and magnetic moments than the LSDA, but for bulk Fe the GGA is also mandatory for a correct prediction of the ground state [29].
(ii) Post-DFT corrections (orbital polarization, on-site Coulomb repulsion, . . .) which are added to the exchange–correlation functional.
(iii) Self-consistent electronic structure calculations, including spin–orbit coupling, using projector-augmented wave (PAW) [30, 31] or full potential linearized augmented wave (FLAPW) codes [32], or using multiple-scattering (screened Kohn–Korringa–Rostocker—SKKR) [34] calculations. This also implies different treatments of the effective potentials. PAW and FLAPW provide a full potential approach, while SKKR calculations rely on the atomic-sphere approximation. The spherical averaging over the atomic sphere of the adatom certainly reduces the effect of the broken symmetry of the adatom.
(iv) Modeling of the substrate: periodic slab models or semi-infinite substrate (possible only within Green's function SKKR). However, it has to be emphasized that in Green's function calculations the Dyson equation for the perturbed system is solved only for an embedded cluster surrounding the magnetic adatom which is usually smaller than the unit-cell in a slab model.
(v) Geometry of the adsorbate/substrate complex: all atoms on ideal sites continuing the crystalline lattice of the substrate (complete neglect of relaxation), relaxation of the position of the adatom only, or full relaxation of adatom plus surface.
(vi) MAE calculated as the difference in the total energies from self-consistent calculations for different orientations of the magnetic moment or, using the 'magnetic force theorem' [35] as the difference in the band energies at a fixed potential and charge density.

Using a judicious combination of different approximations (ideal bulk-like geometry—no relaxation of either adatom or surface, local spin-density approximation—no gradient corrections, atomic-sphere approximation for the effective potential within SKKR calculations, MAE calculated via the 'magnetic force theorem') quite reasonable values for the MAE can be achieved, while the calculated orbital moments are somewhat too low [4, 17, 20, 22]. However, whether these approximations are also adequate has never been questioned. Attempts have been made to cure the underestimation of the orbital moments by using an orbital polarization term—this results in moments which are now far too large [4, 23]. DFT + U calculations with a modest on-site repulsion of $U = 2 \rightarrow 3$ eV lead to a better agreement with experiment, but since the choice of U is open, this is a semiempirical approach [33]. The relaxation of the adatom–substrate complex has been calculated by Spišák and Hafner [24]. It has been shown that this leads to the formation of a large polarization cloud and a very high effective spin moment per atom, but also to a strong quenching of the orbital moment of the adatom due to an increased hybridization with the substrate.

The intention of the present work is to provide a critical analysis of the impact of all these technical choices on the calculation of the magnetic anisotropy energy. Single Fe and Co adatoms on a Pt(111) surface are used as model systems, because both experimental [4, 13] and theoretical [4, 19–23] studies are available in the literature.

2. Computational details

We have used the Vienna *ab initio* simulation package VASP [31, 37] to perform *ab initio* electronic structure calculations and structural optimizations. VASP performs an iterative solution of the Kohn–Sham equations of DFT within a plane-wave basis and using periodic boundary conditions. Either local and semilocal functionals in the GGA [38], both combined with the spin-interpolation proposed by Vosko *et al* [39] can be used to describe electronic exchange and correlation and spin polarization. The use of a semilocal functional is known to be essential for the correct prediction of the ground state of the ferromagnetic 3d elements in the bulk [29]. The PAW method [30, 31] is used to describe the electron–ion interactions. The PAW approach produces the exact all-electron potentials and charge densities without elaborate nonlinear core-corrections—this is particularly important for magnetic elements.

The PAW potentials have been derived from fully relativistic calculations of the atomic or ionic reference calculations. Spin–orbit coupling has been implemented in VASP by Kresse and Lebacq [40]. Following Kleinman and Bylander [41] and MacDonald *et al* [42] the relativistic Hamiltonian given in a basis of total angular momentum eigenstates $|j, m_j\rangle$ with $j = l \pm \frac{1}{2}$ (containing all relativistic corrections up to order α^2, where α is the fine-structure constant) is recast in the form of 2×2 matrices in spin-space by re-expressing the eigenstates of the total angular momentum in terms of a tensor product of regular angular momentum eigenstates $|l, m\rangle$ and the eigenstates of the z-component of the Pauli spin matrices. The relativistic effective potential consists of a term diagonal in spin-space which contains the mass-velocity and Darwin corrections, and the spin–orbit operator. The nondiagonal elements in spin-space arise from the spin–orbit coupling, but also from the exchange–correlation potential when the system under consideration displays a noncollinear magnetization density. Calculations including spin–orbit coupling have therefore to be performed in the noncollinear mode implemented in VASP by Hobbs *et al* [43] and Marsman and Hafner [44].

In our calculations the adatom–substrate complex has been described by a slab model. A five-layer slab with a 5×5

Table 1. The calculated adsorption energy E_{ad}, work function change $\Delta\Phi$ (with respect to the work function of the clean surface, $\Phi^{Pt} = 5.72$ eV), height z^{x} of adsorbed adatom above the Pt(111) surface, x-Pt bond length d^{x}, relaxations Δ_{ij} of the interlayer distance, and the buckling of the Pt layers, b_i^{Pt}. X denotes either the Fe or Co adatom.

Adsorption site	E_{ad} (eV)	$\Delta\Phi$ (eV)	z^{x-Pt} (Å)	d^{x} (Å)	Δ_{12} (%)	Δ_{23} (%)	b_1^{Pt} (Å)	b_2^{Pt} (Å)
			Fe/Pt					
Fcc hollow	5.566	−0.40	1.71	2.39	+0.9	−1.2	0.12	0.08
Hcp hollow	5.561	−0.41	1.69	2.40	+0.9	−1.1	0.09	0.03
			Co/Pt					
Fcc hollow	5.736	−0.35	1.69	2.40	+1.1	−0.9	0.11	0.05
Hcp hollow	5.763	−0.31	1.62	2.46	+0.8	−1.1	0.07	0.13

surface cell has been used for describing the substrate, the adatom has been placed into the center of the surface cell. This means that the nominal surface coverage is 0.04 ML, coming close to the coverage of the samples on which the XMCD experiments have been performed. Neighboring slabs are separated by a vacuum region of 16 Å—this ensures that the separation between the periodically repeated images of the slab is large enough to suppress any interactions. The basis set contained plane waves with a maximum kinetic energy of 300 eV. Test calculations with higher cut-off energies have shown that this is a reasonable compromise between accuracy and computational effort. The calculations have been performed in two steps. First a collinear scalar-relativistic calculation has been performed to determine the correct geometry of the adatom/surface complex and the correct magnetic ground state. The ground state resulting from the scalar-relativistic calculations was used to initialize the noncollinear calculations including spin–orbit coupling which allow, in principle, a further structural optimization. Two independent self-consistent calculations (including a full structural re-optimization of the adatom/substrate complex) with the magnetic axis oriented perpendicular and parallel to the surface have been performed and the magnetic anisotropy energy has been calculated as the difference in the well-converged total energies. Alternatively, the magnetic force theorem has been used to determine the MAE. Brillouin-zone integrations have been performed on $3 \times 3 \times 1$ grids, using a modest smearing to improve convergence. Test calculations with finer grids have shown that for this large supercell this leads to converged results. Final total energies are extrapolated to zero smearing. Geometric, electronic, and magnetic degrees of freedom are relaxed simultaneously until the forces acting on all atoms converge below 0.01 eV Å^{-1} and the changes in total energy between successive iteration steps are smaller than 10^{-7} eV—such a stringent relaxation criterion was found to be absolutely essential.

3. Results

3.1. Structure of clean Pt(111) surfaces

For bulk face-centered cubic Pt we calculate using the GGA a lattice constant of $a = 3.993$ Å and a bulk modulus of $B = 236$ GPa, in the LDA the corresponding values are $a = 3.910$ Å and $B = 286$ GPa, to be compared with the experimental values of $a = 3.924$ Å and $B = 230$ GPa [45]. As for all heavy elements, the lattice constant calculated using the GGA is too large by about 1.5% while the LDA value is too low. The bulk modulus, however, is definitely more accurate if calculated using the GGA. For the characterization of the (111) surface, the three top layers of the slab have been allowed to relax, while the lower two layers are kept frozen in their bulk-like positions. The relaxation leads to an expansion of the distance between the two top layers by $\Delta_{12} = 0.7\%$, while the distance between the subsurface layers is contracted by $\Delta_{23} = -1.4\%$. The predicted surface expansion is in good agreement with the LEED data of $\Delta_{12} \sim 1\%$ [47]. For the work function we find a value of $\Phi = 5.72$ eV, again in very good agreement with experiment ($\Phi = 5.6 \rightarrow 6.4$ eV) [46]. The calculations have been performed in a spin-polarized mode, initializing the magnetic moments of the surface atoms to non-zero values. However, the calculations always converged to a completely nonmagnetic solution, demonstrating that no spurious surface magnetism is induced by the reduced coordination of the surface atoms.

3.2. Fe and Co adatoms on Pt(111) surfaces

For the isolated adatom on the Pt(111) surface we have considered a location either in an fcc or in an hcp hole. The results for the adsorption geometry, the relative energy, and for the work function change from scalar-relativistic spin-polarized calculations are compiled in table 1.

For an isolated Fe atom, adsorption in an fcc hollow leads to an adsorption energy which is larger by 5.5 meV than for adsorption in an hcp hollow. The height of the Fe atom above the top Pt layer is 1.71 Å—this is reduced by 0.595 Å or 26% compared to the ideal interlayer distance in bulk Pt and corresponds to a reduction of the shortest Fe–Pt distance from 2.82 to 2.39 Å. The reduced height of the Fe adatom above the Pt surface is primarily a consequence of the large size-misfit between Fe and Pt and the desire to maintain an effective volume close to the equilibrium value in the bulk. Given the in-plane lattice constant of Pt(111) and the height of the Fe atom, we calculate an atomic volume of 11.81 Å^3 which is only slightly increased compared to bulk bcc Fe. Even this very low Fe-coverage leads to a slightly increased outward-relaxation of the distance between the top Pt layer. The adatom also induces a slight buckling of the top layers, the Pt atoms binding to the Fe atoms move outwards towards the adatom by about 0.12 Å.

Table 2. Spin μ_S, orbital μ_L, and total $\mu_{\rm tot}$ magnetic moments (all in $\mu_{\rm B}$) of Fe and Co adatoms adsorbed on a Pt(111) substrate and induced moments on the Pt-substrate atoms integrated over all atoms in the supercell. Results from scalar-relativistic calculations and including spin–orbit coupling for perpendicular and in-plane orientations of the magnetic moment are presented. The MAE is given in meV, a positive value indicates a perpendicular easy axis. The calculations are performed using the GGA and allow for a full relaxation of the adatom/substrate complex.

	Scalar-relativistic	Including SOC						
		Perpendicular			In-plane			
	μ_S	μ_S	μ_L	$\mu_{\rm tot}$	μ_S	μ_L	$\mu_{\rm tot}$	MAE
Fe (fcc hollow)	3.306	3.282	0.104	3.386	3.283	0.108	3.391	
Pt	2.377	2.153	0.402	2.555	2.172	0.518	2.690	
Effective moment	5.683	5.435	0.506	5.941	5.455	0.626	6.081	2.99
Experiment, [14] Fe								$\geqslant 0$
Experiment, [13] Fe								6.5 ± 0.1
Co (hcp hollow)	2.190	2.155	0.126	2.281	2.155	0.088	2.243	
Pt	4.826	3.319	0.684	4.003	3.325	0.829	4.154	
Effective moment	7.016	5.474	0.810	6.284	5.480	0.917	6.397	1.19
Experiment, [4] Co		2.1	1.1	3.2				9.3 ± 1.6
Experiment, [13] Co								10.3 ± 0.2

The work function is reduced by 0.4 eV—a surprisingly strong effect at such a low concentration of adatoms. This may be understood in terms of the strong adatom–substrate interaction, the large magnetic moment of the adatom and the long-range magnetic polarization induced in the substrate (see below for details).

For a Co atom, adsorption in an hcp hollow is strongly preferred over the fcc hollow, by 27.9 meV. A Co atom in an hcp hollow moves even closer to the Pt substrate (the height of the adatom is reduced by 29.7% compared to the idealized lattice position) the adsorption-induced outward-relaxation is very modest. The stronger relaxation results from an attractive interaction with a Pt atom in the subsurface layer, which is also reflected in a buckling of this layer which is more pronounced in the subsurface than in the surface layer. Shick *et al* [23] have used an LSDA$+U$ approach (with $U = 2$ eV) to determine the equilibrium height of a Co adatom at a fixed bulk-like geometry of the substrate and report a smaller relaxation by about 20%.

3.3. Magnetic moments and magnetic anisotropy

In the following we report the results of our calculations of the magnetic moments and magnetic anisotropies of Fe and Co atoms on Pt(111) substrates, calculated at different levels of theory. We begin with the results compiled in table 2, obtained for a fully relaxed adatom/substrate complex, using the spin-polarized GGA and the MAE calculated from the total-energy differences calculated self-consistently for in-plane and perpendicular orientation of the magnetic moments. For both orientations of the magnetic moments we have also allowed a complete relaxation of the geometry. However, changes in the interatomic distances with the re-orientation of the magnetization direction are very small, of the order of 0.001 Å. Within a density-functional approach, this represents the highest level of theory.

3.3.1. Relaxed geometry of adatom/substrate complex. For an isolated Co atom in an hcp hollow on Pt(111) we find a strongly enhanced spin moment of 2.15 $\mu_{\rm B}$, slightly higher than the experimental estimate of Gambardella *et al* [4], while the calculated orbital moment is much too low. The magnetic atom induces a strong polarization of the substrate. Figure 1 shows for Co/Pt(111) the induced spin and orbital moments in the three top layers of the substrate, calculated for perpendicular and in-plane orientation of the magnetization. The distribution of the induced moments is similar for Fe/Pt(111). The figure demonstrates that although the induced magnetization decays rapidly in the deeper layers, the decrease of the induced moments in the top layer with increasing distance from the adatom is slower, such that even at this low coverage the induced magnetization clouds overlap slightly. On the Pt atoms that are nearest neighbors to the Co (Fe) adatom the ratio μ_L/μ_S is 0.25(0.20) for perpendicular and 0.31(0.24) for in-plane magnetization, respectively. Hence the ratio of orbital to spin moment is much higher than for the adatom, as expected because of the stronger spin–orbit coupling.

An interesting question is also the change in the magnetization densities of adatom and substrate induced by their interaction and the small changes in the magnetization densities induced by the re-orientation of the direction of the magnetic moment. This is illustrated in figure 2 showing for Fe/Pt(111) the difference in the magnetization densities of the adatom/substrate complex and of the isolated atom plus the clean substrate. Both calculations refer exactly to the same geometry, i.e. the clean surface has been deformed such as under the influence of the adatom and the magnetization density of the free atom is centered around the relaxed adatom position. Contours of regions with increased/decreased magnetization densities are shown. The gross features of

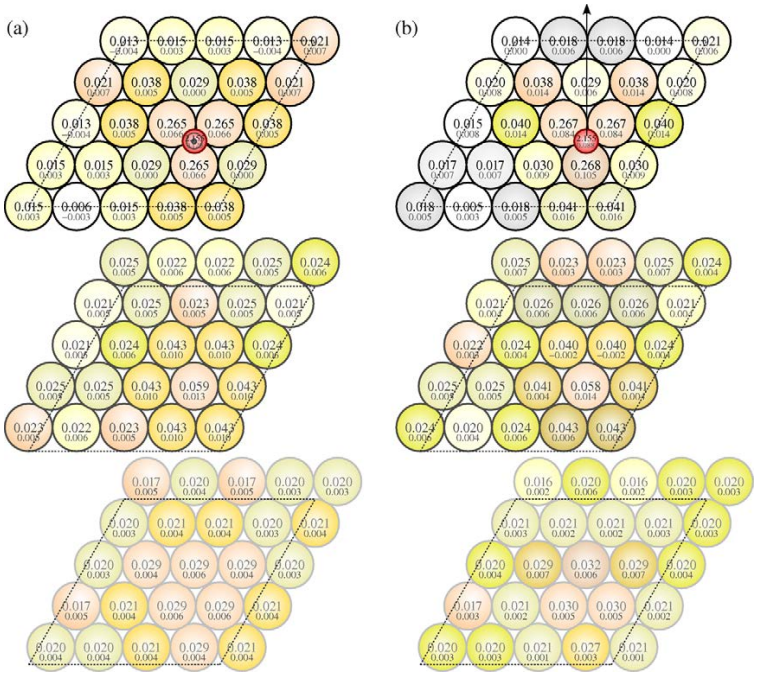


Figure 1. Spin and orbital moments induced by a Co adatom in a hcp hollow of a Pt(111) surface in the top three layers of the substrate. For each atom the top (larger) number gives the induced spin moment, the lower (smaller) number the induced orbital moment. Both are given in μ_B. Part (a) refers to perpendicular, part (b) to in-plane magnetization (as indicated by the large arrows).

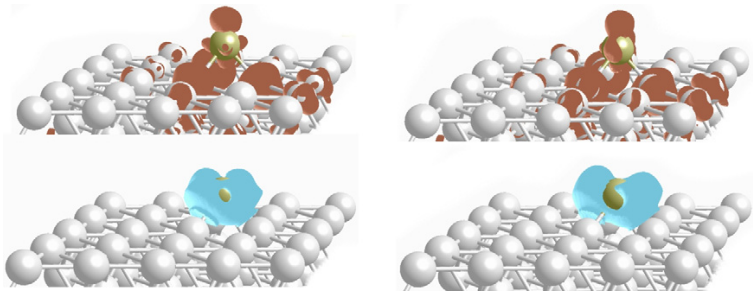


Figure 2. Constant-density surfaces showing the difference-magnetization densities for an Fe atom adsorbed in an fcc hollow on a Pt(111) surface. The upper panels (brown surfaces) show regions of increased magnetization densities visualizing the induced magnetic polarization of the substrate, but also regions of increased magnetization around the adatom. The lower panels (blue surfaces) show the regions of reduced magnetization around the adatom. The contour values are ± 0.0075 electrons Å^{-3}. The left panels refer to perpendicular, the right ones to in-plane magnetization (compare with text).

the plots demonstrate the reduced magnetic moment of the adatom relative to the large moment of the free atom and the induced polarization of the substrate. Surprisingly, there are also small regions of increased magnetization density around the adatom, extending mostly in a perpendicular direction. Most interesting in connection with the magnetic anisotropy are the small changes in these magnetization densities upon re-orientation of the magnetic axis. These changes reflect the broken symmetry for in-plane orientation.

The induced magnetization (integrated over all substrate atoms) is lower than in a scalar-relativistic calculation, because the strong spin–orbit coupling mixes different spin states. The integrated induced orbital moment is much larger than the orbital moment of the magnetic adatom and it is also much more anisotropic—in both cases the induced orbital moment is much larger for in-plane magnetization while the spin anisotropy is only modest. Interestingly, the effective spin moment per Co atom of about 5.5 μ_B is in very good agreement with the estimated effective moment of $5.0 \pm 0.6\,\mu_B$. From the difference in the total energies we deduce a magnetic anisotropy energy of 1.2 meV favoring a perpendicular easy axis of magnetization. The sign of the MAE agrees with the anisotropy of the orbital moments of the Co atoms and of the induced orbital moments and with experiment, although we find a much lower value than deduced from the XMCD experiments or estimated from the STS spectra. Our MAE of

Table 3. Spin μ_S, orbital μ_L, and total $\mu_{\rm tot}$ magnetic moments (all in $\mu_{\rm B}$) of Fe and Co adatoms adsorbed in a fcc hollow on a Pt(111) substrate and induced moments on the Pt-substrate atoms integrated over all atoms in the supercell. Results including spin–orbit coupling for perpendicular and in-plane orientations of the magnetic moment are presented. The MAE is given in meV, a positive value indicates a perpendicular easy axis. The calculations are based on an idealized bulk-like geometry (using the experimental lattice constant) and use either the GGA or the LSDA functional.

	Including SOC						
	Perpendicular			In-plane			
	μ_S	μ_L	$\mu_{\rm tot}$	μ_S	μ_L	$\mu_{\rm tot}$	MAE
Fe—LSDA, present work							
Fe	3.366	0.343	3.709	3.366	0.234	3.600	
Pt	1.363	0.227	1.590	1.457	0.325	1.782	
Effective moment	4.729	0.570	5.299	4.823	0.559	5.382	2.35
Fe—LSDA, [22]							
Fe	3.395	0.628	4.023	3.514	0.266	3.780	5.31
Fe—LSDA, [19]							
Fe	3.49	0.77	4.26				8.79
Experiment, [14]							
Fe							$\geqslant 0$
Experiment, [13]							
Fe							6.5 ± 0.1
Co—LSDA, present work							
Co	2.152	0.631	2.783	2.151	0.350	2.501	
Pt	1.135	0.194	1.329	1.258	0.279	1.537	
Effective moment	3.287	0.825	4.112	3.409	0.629	4.038	8.14
Co—GGA, present work							
Co	2.195	0.431	2.626	2.195	0.246	2.441	
Pt	1.605	0.282	1.887	1.769	0.395	2.164	
Effective moment	3.800	0.713	4.513	3.964	0.641	4.605	2.42
Co—LSDA, [22]							
Co	2.153	0.726	2.879	1.973	0.483	2.456	5.02
Co—LSDA, [19, 20]							
Co	2.27	0.60	2.87				4.76
Pt	0.40	0.07	0.47				
Co—LSDA, [23]							
Co	2.18	0.57	2.75				2.00
Co—LSDA, [4]							
Co	2.14	0.60	2.74				18.45
Experiment, [4]							
Co	2.1	1.1	3.2				9.3 ± 1.6
Experiment, [13]							
Co							10.3 ± 0.2

1.2 meV is also lower than the theoretical predictions derived for an unrelaxed surface [19, 22], a detailed discussion of the difference will be given below.

For an Fe adatom the enhancement of the spin moment compared to its value in the bulk is even more pronounced, but we find an orbital moment which is only slightly enhanced compared to the bulk. For the adatom the ratio μ_S/μ_L is only about 0.03, much smaller than the experimental estimate of $\mu_S/\mu_L \sim 0.18 \pm 0.05$ given by Lehnert [14]. For the substrate atoms, this ratio is much higher—$\mu_L/\mu_S \sim 0.20(0.29)$ for perpendicular (in-plane) magnetization. Although the anisotropy of both spin and orbital moments is very small, we calculate an MAE of 3 meV—the out-of-plane easy axis agrees with the easy axis direction found by Lehnert (no quantitative MAE could be deduced) and with the value of 6.5 meV estimated by Balashov *et al* [13] from the STS. Much larger values of the MAE have been predicted by Bornemann *et al* [19] and Etz *et al* [22], based on an ideal geometry and an LSDA functional. Tsujikawa *et al* [21] studied the MAE of a quarter of a monolayer of Fe on Pt(111) within the LSDA and allowing a restricted relaxation. An in-plane easy axis favored by about 1 meV was reported, although spin and orbital moments are not too different from our results.

3.3.2. Idealized geometry of the adatom/substrate complex. To allow a comparison of our calculations with the existing literature data, we have also performed calculations using a fixed idealized geometry based on the experimental lattice constant and either the LSDA or GGA exchange–correlation functional. In these calculations both Fe and Co have been placed into fcc hollows because this is the adsorption site assumed in the previous calculations. The results are compiled in table 3.

The LSDA calculations for Co/Pt(111) and a perpendicular orientation of the magnetic moment lead to good agreement with the published data [4, 19, 22, 23]: the spin moment of the Co atom is $\mu_S \sim 2.15 \pm 0.03\ \mu_B$, the orbital moment $\mu_L \sim 0.60 \pm 0.03\ \mu_B$ (but note that Bornemann *et al* [19] find a higher spin, and Etz *et al* [22] a higher orbital moment—these divergences are not easily understood because [4, 19] and [22] all use an SKKR Green's function code). We note that at a fixed geometry and with the same functional as in the present PAW calculations, the FLAPW calculations of Shick *et al* [23] (both using a slab model) and the SKKR calculations [4] based on a semi-infinite substrate (but solving the Dyson equation only in a finite surrounding of the adatom) lead to good agreement. Hence the two types of models are both adequate, and the difference between full potential and atomic-sphere approximations is not so important. Much larger differences are found for Fe/Pt(111)—we shall come back to this discrepancy below.

Compared to the calculations for a fully optimized adatom/substrate complex we find a strong enhancement of the orbital moment of the adatom and a pronounced decrease of both spin and orbital moments induced in the substrate. The effective spin moments per Fe or Co adatom are reduced from about 5.5 μ_B to ∼3.3–3.4 μ_B, while the effective orbital moments are almost unchanged. In the previous publications information on the magnetic moments induced on the substrate atoms is very scarce. Etz *et al* [22] report induced spin moments of $\mu_S \sim 0.1\ \mu_B$ for the nearest-neighbor Pt atoms, decreasing to about 0.01 μ_B for next-nearest neighbors, Bornemann *et al* [19] report slightly lower induced spin moments of 0.08 μ_B on nearest-neighbor sites. These values are in reasonable agreement with our findings, but hardly any information on the induced orbital moments can be found in earlier work. Only Bornemann *et al* [19] report a total induced spin moment of 0.4 μ_B and a total induced orbital moment of 0.07 μ_B for Co/Pt(111) (both per Co atom). As these values are considerably lower than our integrated values while the moments induced on nearest-neighbor sites are comparable, we can only conclude that the spatial extension of the induced polarization cloud is much smaller than derived here. This is an immediate consequence of the fact that the Dyson equation has been solved only for a small cluster surrounding the adatom. On all other substrate atoms any induced polarization has hence been suppressed

Very little information has also been given on the anisotropies of spin and orbital moments—only in the paper by Etz *et al* [22] are values of the magnetic moments given for both orientations of the magnetization. The reason for the lack of information on the direction-dependence of the magnetic moments is that the calculations of the MAE use either the magnetic force theorem [4, 22, 23] or the torque–force approach [19, 20]. In both cases, a self-consistent calculation is performed only for one direction of the magnetization and the MAE is determined as the difference in the sum of the one-electron energies, calculated at a fixed effective one-electron potential. For Fe/Pt(111) our calculations predict an isotropic spin moment and a modest anisotropy of the orbital moment of the Fe atom, $\Delta\mu_L = \mu_l(\perp) - \mu_L(\parallel) = 0.11\ \mu_B$, and an orbital anisotropy of opposite sign, $\Delta\mu_L = -0.10\ \mu_B$ induced on the Pt atoms. For the Fe atom, Etz *et al* report a substantial negative anisotropy of the spin moments, $\Delta\mu_S = -0.12\ \mu_B$, and a very large orbital anisotropy of $\Delta\mu_L = 0.36\ \mu_B$. It is intriguing that for this system, the agreement between both sets of calculations is much better for an in-plane orientation of the magnetic moment. For Co/Pt(111) both calculations lead to similar values of the orbital anisotropy ($\Delta\mu_L \sim 0.2\ \mu_B$, but Etz *et al* also report a substantial negative spin anisotropy). The additional spin anisotropy is reflected in a MAE which is lower than found in our calculations. The MAE reported by Etz *et al* [22] agrees well with Bornemann *et al* [19], while Gambardella *et al* [4] report a much larger value (even larger than experiment). Since all three calculations [4, 19, 22] are based on a SKKR Green's function approach, the same geometry and the same functional, the origin of this difference is not clear. For Fe/Pt(111) the calculated MAEs span the range between 2 meV and nearly 9 meV. The difference between our low value and the larger values reported in the SKKR calculations parallels larger orbital moments and both orbital and spin anisotropies.

3.3.3. LSDA versus GGA. To assess the influence of the choice of the exchange–correlation functional, we have also performed calculations with an idealized geometry and a GGA functional. The results for Co/Pt(111) are listed in table 3. For the adatom, the semilocal GGA functional leads to a slightly increased spin and a significantly reduced and slightly less anisotropic orbital moment. In contrast the induced spin and orbital moments are significantly enhanced with the GGA, resulting also in an enhanced effective spin and orbital moment. As with the LSDA, we note opposite signs of spin and orbital anisotropies of the adatom and of the substrate. Altogether we note that the GGA disfavors the formation of a large orbital moment on the adatom, but also leads to stronger hybridization effects. Both effects together—decreased orbital anisotropy of the adatom and increased negative orbital anisotropy of the substrate—lead to a decrease of the magnetic anisotropy energy from 8.1 to 2.4 meV, while the sign remains unchanged.

3.3.4. Self-consistent total-energy differences versus force theorem. Calculations of the MAE require a very high level of convergence of the total energies—which is rather time-consuming. Therefore many calculations are based on the 'force theorem' [35, 36] stating that to first order, the difference in the total energy calculated for magnetization along the easy and hard axes may be approximated by the difference in the sum of the one-electron energies calculated at a fixed potential. If the force theorem has been used [4, 17, 22] a self-consistent calculation has been performed for perpendicular magnetization, while for in-plane magnetization only a non-self-consistent calculation with a fixed potential has been performed. In table 4 we compare the spin and orbital moments for in-plane orientation resulting from a self-consistent calculation and from a non-self-consistent calculation using the potential and charge-distribution resulting from the self-consistent calculation for

Table 4. Spin μ_S, orbital μ_L, and total $\mu_{\rm tot}$ magnetic moments (all in $\mu_{\rm B}$) of Fe and Co adatoms adsorbed on a Pt(111) substrate and induced moments on the Pt-substrate atoms integrated over all atoms in the supercell. Results for in-plane orientation of the magnetization resulting from self-consistent calculations and from non-self-consistent calculations based on the potentials and charge-distributions calculated for perpendicular magnetization are compared. The MAE is given in meV, a positive value indicates a perpendicular easy axis.

	Self-cons. total energy				Force theorem			
	μ_S	μ_L	$\mu_{\rm tot}$	MAE	μ_S	μ_L	$\mu_{\rm tot}$	MAE
Fe—GGA, relaxed, $a_{\rm theor.}$								
Fe	3.283	0.108	3.391		3.286	0.108	3.394	
Pt	2.172	0.518	2.690		2.163	0.514	2.677	
Effective moment	5.455	0.626	6.081	2.99	5.449	0.622	6.071	2.84
Fe—LSDA, ideal geometry								
Fe	3.366	0.234	3.600		3.378	0.236	3.614	
Pt	1.457	0.325	1.782		1.330	0.295	1.652	
Effective moment	4.823	0.559	5.382	2.35	4.708	0.531	5.239	2.31
Co—GGA, relaxed, $a_{\rm theor.}$								
Co	2.155	0.088	2.243		2.137	0.088	2.255	
Pt	3.325	0.829	4.154		3.279	0.812	4.091	
Effective moment	5.480	0.917	6.397	1.19	5.416	0.900	6.316	1.20
Co—LSDA, ideal geom.								
Co	2.151	0.350	2.501		2.137	0.354	2.491	
Pt	1.258	0.279	1.537		1.095	0.240	1.335	
Effective moment	3.409	0.629	4.038	8.14	3.232	0.594	3.826	12.71

perpendicular magnetization. Indeed we find that the non-self-consistent calculation reproduces the magnetic moments with very good accuracy. For Fe/Pt(111) we also find very good agreement between the MAEs calculated from the difference in the self-consistent total energies and determined by the difference in the sum of the one-electron energies (according to the force theorem), for both the GGA at a relaxed geometry, and the LSDA and the idealized bulk-like geometry. This is remarkable, because at the idealized geometry the differences between the self-consistently calculated induced moments and the non-self-consistent calculations are not entirely negligible. For Co/Pt(111) the force theorem yields good results in GGA calculations using a fully relaxed geometry, while in LSDA calculations for an idealized geometry the force theorem leads to value of the MAE which is increased by about 4 meV compared to the self-consistent result. The largest differences are always found for the induced spin moments, they are larger in LSDA calculations and larger for Co than for Fe adatoms. The reason is that at a fixed idealized geometry (and hence a partially suppressed hybridization) even small changes in the charge- and spin densities can lead to significant changes in the magnetic moments. This shows that the compensation between the changes in the one-electron energies and double-counting corrections (Hartree- and exchange–correlation energies) predicted by the force theorem is indeed realized in most cases to a very good extent, but the case of Co/Pt(111) demonstrates that for the very small MAEs the use of the force theorem can still lead to a non-negligible quantitative error.

3.3.5. DFT + U results. To examine the influence of post-DFT corrections on the orbital moment and on the MAE, we have performed calculations using a GGA + U approach and a modest value of $U = 2 \rightarrow 3$ eV for the on-site Coulomb repulsion on the Fe 3d states. For the implementation of the GGA + U approach in VASP we refer to the work of Rohrbach *et al* [48]. $U = 2$ eV is the value also used by Shick *et al* [23] in their calculations for Co/Pt(111) and slightly smaller than the value of $U = 3$ eV recommended by Ebert *et al* to achieve agreement for the orbital moments of 3d impurities in alloys. The calculations have been performed for a fully relaxed system. Our results are compiled in table 5. With increasing U we find increasing spin and orbital moments on the adatom, accompanied by a slow decrease of the induced moments. Both effects arise immediately from the increased exchange splitting of the Fe 3d states. The effect on the calculated MAR is also very modest.

The increase of the orbital moment of the adatom is much smaller than found by Ebert *et al* for 3d impurities in a polarizable matrix. The difference is again in the different treatment of relaxation effects. In the Green's function calculations of Ebert *et al*, local relaxations are neglected—hence the impurity couples only weakly to the host and the Coulomb repulsion induces a strong exchange splitting. In our relaxed system, the effect of the added Coulomb repulsion is much smaller because of the strong coupling to the ligand states.

Our results may be compared with the work of Shick *et al* [23] on Co/Pt(111), based on an LSDA + U approach on an unrelaxed or partially relaxed system. The Co orbital moments are more sensitive to the addition of a Coulomb repulsion, again the relaxation reduces its effect. Also the effect on the MAE is found to be small—with a $U = 2$ eV the MAE increases only from 2 to 3 meV. The use of the DFT+U method requires further investigations, including realistic estimates of the strength of the Coulomb repulsion.

Table 5. Spin μ_S, orbital μ_L, and total μ_{tot} magnetic moments (all in μ_B) of Fe and Co adatoms adsorbed on a Pt(111) substrate and induced moments on the Pt substrate atoms integrated over all atoms in the supercell. Results from calculations including spin–orbit coupling for perpendicular and in-plane orientations of the magnetic moment are presented. The MAE is given in meV, a positive value indicates a perpendicular easy axis. The calculations are performed using the GGA + U and allow for a full relaxation of the adatom/substrate complex.

	Including SOC						
	Perpendicular			In-plane			
	μ_S	μ_L	μ_{tot}	μ_S	μ_L	μ_{tot}	MAE
	$U = 2$						
Fe	3.399	0.126	3.525	3.400	0.135	3.535	
Pt	2.103	0.392	2.495	2.192	0.524	2.716	
Effective moment	5.502	0.518	6.020	5.592	0.659	6.251	2.62
	$U = 3$						
Fe	3.480	0.151	3.631	3.480	0.164	3.644	
Pt	2.049	0.382	2.431	2.135	0.514	2.649	
Effective moment	5.529	0.533	6.062	5.615	0.678	6.293	2.70

4. Discussion and conclusions

We have examined the influence of different approximations (relaxed or idealized structure, local or semilocal functional, force theorem or self-consistent total-energy calculations) on density-functional calculations of the magnetic anisotropy of magnetic adatoms on Pt(111) surfaces. The surprising result of our studies is that the magnetic anisotropy energy of Fe/Pt(111) is surprisingly robust against changes in the computational setup—the results vary only between 2 and 3 meV and both easy axis orientation and the value of the MAE are in reasonable agreement with experiment [13]. For Co adatoms the variations of the MAE (between 1.2 and 12.7 meV) are much more pronounced, as a consequence of a spiky electronic density of states close to the Fermi level. But even in this case the semi-quantitative agreement with experiment is preserved, the theoretical values bracket the experimental results [4, 13]. The most important point in theoretical calculations is the description of the geometry of the adatom/substrate complex, while the remaining factors such as the choice of a functional etc are of minor importance. If relaxation is suppressed, the coupling of the magnetic adatom to the ligands with a strong SOC is strongly reduced, but this also permits the formation of a relatively large orbital moment on the adatom. If a realistic geometry is created by relaxation, the strong coupling to the ligands leads to a strong hybridization of adatom and ligand states and a larger induced moment, but the increased orbital mixing adds to the lack of orbital dependence of the exchange fields and minimizes the orbital moment of the adatom.

This important point may be illustrated by the partial local densities of states calculated for the optimized geometry of the adsorbate/substrate complex and assuming an idealized structure (see figure 3). The partial d-state densities of states (DOS) are shown for the adatom and for the atoms in the first substrate layer, for perpendicular and in-plane orientation of the magnetization. The calculations for a relaxed geometry demonstrate a strong hybridization between adatom and substrate for all states, leading to a broadening of the d states of the adatom. If an idealized geometry is assumed, the partial DOS of the d_{z^2}, d_{xy}, and $d_{x^2-y^2}$ consist of two narrow peaks located at the Fermi level and at binding energies of about -3 eV, arising from majority and minority spin states. Only the d_{xz} and d_{yz} states show a slightly stronger hybridization. The hybridization with the d band of the substrate is largely restricted to the region around the peaks in the partial Fe d-DOS. In particular, peaks just above the Fermi level are induced in the Pd d_{z^2}, d_{xz}, and d_{yz} DOS. It is also interesting to analyze the changes in the partial DOS as a function of the direction of magnetization. For perpendicular magnetization, the d_{xz} and d_{yz}, and the in-plane $d_{x^2-y^2}$ and d_{xy} states are degenerate by symmetry, for in-plane magnetization the degeneracy is lifted. As expected this splitting is more pronounced in calculations with a relaxed geometry, and—somewhat surprisingly—it is restricted to a rather narrow range of binding energies from about -4.5 to -2 eV. In this range the DOS of the d_z^2 states is more sharply peaked for out-of-plane magnetization, while for the d_{xy} and d_{yz} states whose degeneracy is also lifted, the structure in the d_{xz} DOS becomes more pronounced for in-plane magnetization while the d_{yz} DOS is more smeared out. When the partial DOSs are integrated over occupied states, the effects in the different partial DOSs largely cancel, resulting in the very small MAE of about 2 meV. The DOSs shown in figure 3 result from self-consistent calculations for both orientations of the magnetic moments—a non-self-consistent calculation with a frozen potential (as required for the use of the force theorem) gives almost identical DOS. Hence, for the elucidation of the physical mechanism determining the MAE, the partial DOSs are a too crude description of the electronic structure.

The differences in the electronic structure arising from the use of different exchange–correlation functionals on the other hand are of minor importance. The differences between the two panels of figure 3 are mostly related to the difference in the lattice constants of the substrate. The smaller lattice constant in the idealized geometry based on the smaller lattice constants calculated using the LSDA (right panel of figure 3) leads to a slightly broader Pt d band. If the Pd bands are

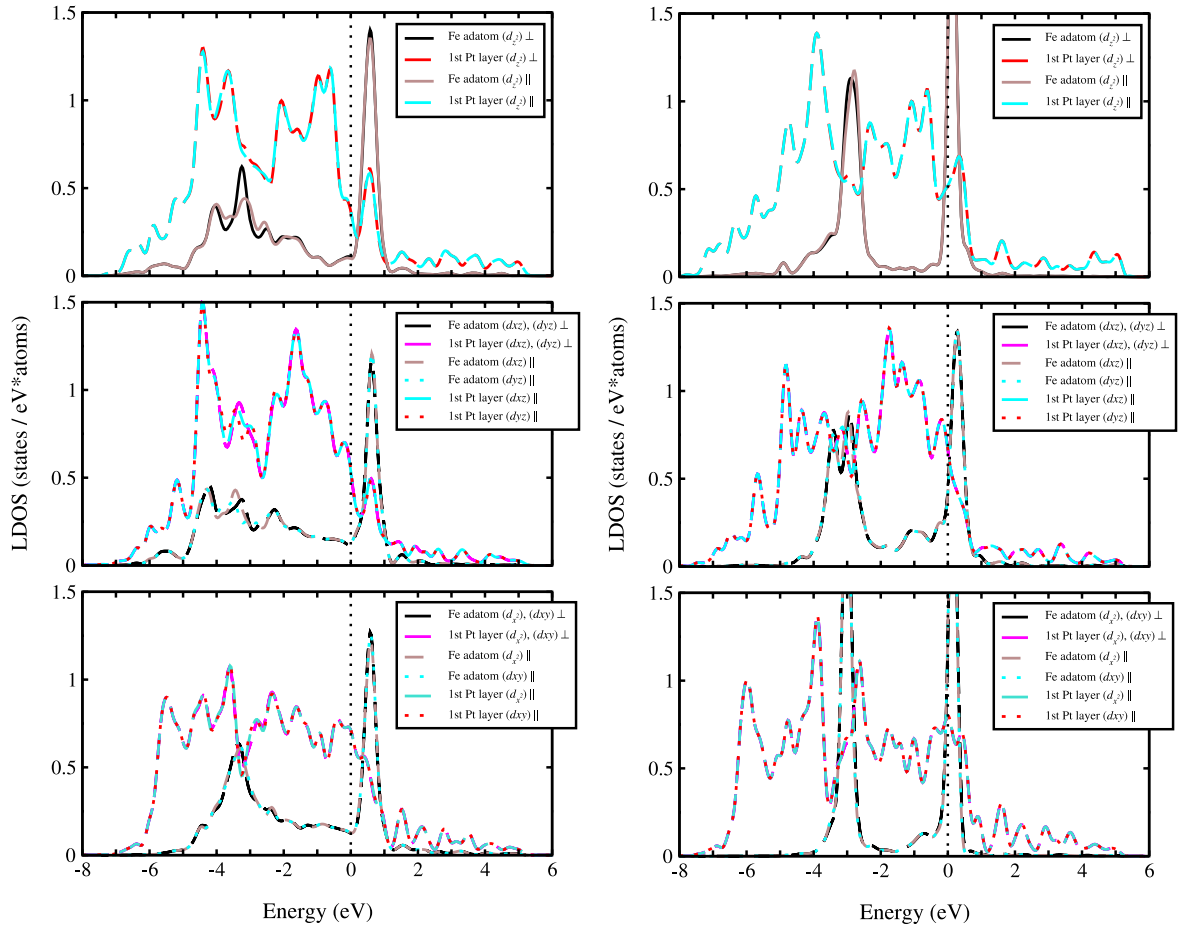


Figure 3. Partial d-electron densities of states for an Fe atom adsorbed on a Pt(111) and for the Pt atoms in the surface layer, as calculated for perpendicular and in-plane magnetization. The left panel shows the results calculated using the GGA and a fully relaxed adsorbate/substrate complex, the right one shows the results obtained using the LSDA and an idealized bulk-terminated geometry (see text).

matched at the lower band edge, the centers of gravity of the DOS for Fe majority and minority electrons are again in good agreement. An important difference—which is again mostly geometry-related—is that because of the reduced overlap of the Fe majority and minority DOSs, the Fermi level falls into a region of high Fe-DOS if an idealized geometry is used.

Altogether our analysis demonstrates that the most important approximation in DFT calculations of the magnetic anisotropy of supported nanostructures is the description of the geometry of the adsorbate/substrate complex. Calculations assuming an idealized geometry essentially attempt to cure a defect of DFT (missing orbital dependence of the exchange field) by artificially minimizing adatom/substrate hybridization. Hence while calculations based on a relaxed geometry certainly provide the more realistic scenario, both types of calculations provide a lower limit to the MAE: in one case the influence of the strong SOC on the ligands, in the other case the orbital moment of the adatom is underestimated. Future work should be based on realistic geometries and concentrate on orbital-dependent corrections to the DFT functionals, with the DFT + U being just one possible alternative. Preliminary results also demonstrate that the conclusions drawn here for isolated magnetic atoms on polarizable substrates also hold for other nanostructures (clusters, chains, ultrathin layers) composed of the same or similar elements.

Acknowledgments

This work has been supported by the Austrian Science Funds under project No. P19712-N16. We thank Anne Lehnert for communicating unpublished results and for helpful discussions.

References

[1] Sellmyer D and Skomski R 2006 *Advanced Magnetic Nanostructures* (New York: Springer)
[2] Stöhr J 1999 *J. Magn. Magn. Mater.* **200** 470
[3] Brune H and Gambardella P 2009 *Surf. Sci.* **603** 1812

[4] Gambardella P, Rusponi S, Veronese M, Dhesi S S, Grazioli C, Dallmeyer A, Cabria I, Zeller R, Dederichs P H, Kern K, Carbone C and Brune H 2003 *Science* **300** 1130
[5] Tischer M, Hjortstam O, Avranitis D, Dunn J H, May F, Baberschke K, Trygg J, Wills J M, Johansson B and Eriksson O 1995 *Phys. Rev. Lett.* **75** 1602
[6] Weller D, Stöhr J, Nakajima R, Carl A, Samat M G, Chappert C, Mégy R, Beauvillain P, Veillet P and Held G A 1995 *Phys. Rev. Lett.* **75** 3752
[7] Dürr H A, Dhesi S S, Dudzik E, Knabben D, van der Laan G, Goedekoop J B and Hillebrecht F U 1999 *Phys. Rev.* B **59** 701
[8] Gambardella P, Dallmeyer A, Maiti K, Malagoli M C, Eberhardt W, Kern K and Carbone C 2002 *Nature* **416** 301
[9] Gambardella P, Dallmeyer A, Maiti K, Malagoli M C, Rusponi S, Ohresser P, Eberhardt W, Carbone C and Kern K 2004 *Phys. Rev. Lett.* **93** 077203
[10] Koide T, Miyauchi H, Okamoto J, Shidara T, Fujimori A, Fukutani H, Amemiya K, Takeshita H, Yuasa S, Katayama T and Suzuki Y 2001 *Phys. Rev. Lett.* **87** 257201
[11] Nieuwenhuys G J 1975 *Adv. Phys.* **24** 515
[12] Meier F, Zhou L, Wiebe J and Wiesendanger R 2008 *Science* **320** 82
[13] Balashov T, Schuh T, Takacs A F, Ernst A, Ostanin S, Henk J, Mertig I, Bruno P, Miyamachi T, Suga S and Wulfhekel W 2009 *Phys. Rev. Lett.* **102** 257203
[14] Lehnert A 2009 *PhD Thesis* EPFL Lausanne
[15] Lau J T, Föhlisch A, Nietubyc R, Reif M and Wurth W 2002 *Phys. Rev. Lett.* **89** 057201
[16] Stepanyuk V S, Hergert W, Wildberger K, Zeller R and Dederichs P H 1996 *Phys. Rev.* B **53** 2121
[17] Lazarovits B, Szunyogh L and Weinberger P 2003 *Phys. Rev.* B **67** 024415
[18] Ebert H, Bornemann S, Minar J, Dederichs P H, Zeller R and Cabria I 2006 *Comput. Mater. Sci.* **35** 279
[19] Bornemann S, Minar J, Staunton J B, Honolka J, Enders A, Kern K and Ebert H 2007 *Eur. Phys. J.* D **45** 529
[20] Šipr O, Bornemann S, Minár J, Polesya S, Popescu V and Šimunek A 2007 *J. Phys.: Condens. Matter* **19** 096203
[21] Tsujikawa M, Hosokawa A and Oda T 2007 *J. Phys.: Condens. Matter* **19** 365208
[22] Etz C, Zabloudil J, Weinberger P and Vedmedenko E Y 2008 *Phys. Rev.* B **77** 184425
[23] Shick A B and Liechtenstein A I 2008 *J. Phys.: Condens. Matter* **20** 015002
[24] Hafner J and Spišák D 2007 *Phys. Rev.* B **76** 0944201
[25] Brooks M S S 1985 *Physica* B **130** 6
[26] Eriksson O, Brooks M S S and Johansson B 1990 *Phys. Rev.* B **41** 7311
[27] Anisimov V I, Zaanen J and Andersen O K 1991 *Phys. Rev.* B **44** 943
[28] Dudarev S L, Botton G A, Savrasov S Y, Humphreys C J and Sutton A P 1998 *Phys. Rev.* B **76** 195440
[29] Moroni E G, Kresse G, Hafner J and Furthmüller J 1997 *Phys. Rev.* B **56** 15629
[30] Blöchl P E 1994 *Phys. Rev.* B **50** 17953
[31] Kresse G and Joubert D 1999 *Phys. Rev.* B **59** 1758
[32] http://www.wien2k.at/
[33] Shick A B, Janis V, Drchal V and Pickett W E 2004 *Phys. Rev.* B **70** 134506
[34] Szunyogh L, Újfalussy B, Weinberger P and Kollár J 1994 *Phys. Rev.* B **449** 2721
[35] Mackintosh A R and Andersen O K 1980 *Electrons at the Fermi Surface* ed M Springfoird (London: Cambridge University Press) section 3.1
[36] Heine V 1980 *Solid State Phys.* **35** 114
[37] Kresse G and Furthmüller J 1996 *Comput. Mater. Sci.* **6** 15
Kresse G and Furthmüller J 1996 *Phys. Rev.* B **54** 11 169
[38] Perdew J P and Wang Y 1992 *Phys. Rev.* B **45** 13244
[39] Vosko S H, Wilk L and Nusair M 1980 *Can. J. Phys.* **58** 1200
[40] Kresse G and Lebacq O *VASP Manual* http://cms.mpi.univie.ac.at/vasp/
[41] Kleinman L 1980 *Phys. Rev.* B **21** 2630
[42] MacDonald A H, Pickett W E and Koelling D D 1980 *J. Phys. C: Solid State Phys.* **13** 2675
[43] Hobbs D, Kresse G and Hafner J 2000 *Phys. Rev.* B **62** 11556
[44] Marsman M and Hafner J 2002 *Phys. Rev.* B **66** 224409
[45] http://www.webelements.com
[46] Derry G N and Ji-Zhong Z 1989 *Phys. Rev.* B **39** 1940
[47] Materer N, Starke U, Barbierei A, Döll R, Heinz K, van Hove M A and Somorjai G A 1995 *Surf. Sci.* **325** 207
[48] Rohrbach A, Hafner J and Kresse G 2004 *Phys. Rev.* B **69** 075413

Magnetocrystalline anisotropy energy of Co and Fe adatoms on the (111) surfaces of Pd and Rh

Piotr Błoński,[1] Anne Lehnert,[2] Samuel Dennler,[3] Stefano Rusponi,[2] Markus Etzkorn,[2] Géraud Moulas,[2] Peter Bencok,[4] Pietro Gambardella,[5,6] Harald Brune,[2] and Jürgen Hafner[1]

[1]*Fakultät für Physik and Center for Computational Materials Science, Universität Wien, Sensengasse 8/12, A-1090 Wien, Austria*

[2]*Institute of Condensed Matter Physics, Ecole Polytechnique Fédérale de Lausanne (EPFL), CH-1015 Lausanne, Switzerland*

[3]*Laboratoire des Colloïdes, Verres et Nanomatériaux, Université de Montpellier II, F-34095 Montpellier, France*

[4]*European Synchrotron Radiation Facility, Boîte Postale 200, F-38043 Grenoble, France*

[5]*Institució Catalana de Recerca i Estudis Avançats (ICREA), E-08100 Barcelona, Spain*

[6]*Centre d'Investigació en Nanociència i Nanotecnologia (ICN-CSIC), UAB Campus, E-08193 Bellaterra, Spain*

(Received 24 November 2009; revised manuscript received 8 March 2010; published 30 March 2010)

We performed a combined theoretical and experimental investigation of the orbital magnetism and magnetocrystalline anisotropy of isolated Co and Fe adatoms on Pd(111) and Rh(111). Theoretical calculations of the spin and orbital moments are based on *ab initio* spin-polarized density-functional theory (DFT) including a self-consistent treatment of spin-orbit coupling. The calculations use a slab model to represent the adsorbate/substrate complex and allow for a complete structural relaxation leading to a strong inward displacement of the adatom and modest vertical and lateral relaxations in the substrate atoms. Compared to an idealized geometry where the atoms are kept on bulk lattice positions up to the surface, relaxation leads to a much stronger adatom/ligand hybridization. This is also reflected in the results for orbital moments and magnetocrystalline anisotropy energy (MAE). The enhanced hybridization leads to strong quenching of the adatom orbital moments but also to the formation of large induced spin and orbital moments in the substrate. As a consequence, we find that the substrate contribution to the MAE is much more important than estimated before on the basis of studies using an idealized geometry. We also find the surprising result that the MAE strongly depends on the adsorption site. The magnitude and even the sign of the MAE change for adatoms on face-centered cubic with respect to the ones on hexagonal close-packed hollow sites on the (111) surface. The dependence of the MAE on the combination of adatom and substrate has been analyzed in terms of the electronic structure, leading to a sound physical picture of the origin of the MAE. A fundamental problem, however, is the correct prediction of the size of the orbital moments of the adatoms. We suggest that this problem can be solved only via post-DFT corrections introducing an orbital dependence of the exchange potential. The theoretical results are compared to site-averaged, element-specific x-ray magnetic circular dichroism (XMCD) measurements. Low-temperature XMCD spectra and magnetization curves reveal weak out-of-plane anisotropy for Fe adatoms on both substrates. Interestingly, Co adatoms on Rh(111) present in-plane anisotropy with MAE of about −0.6 meV, contrary to the known out-of-plane anisotropy of Co on Pd(111) and Pt(111). The orbital to spin magnetic-moment ratio measured by XMCD shows that the Co adatoms present much stronger orbital magnetization components compared to Fe. The connection between orbital moments and MAE is discussed at the theoretical level including the contribution of the induced substrate magnetization.

DOI: 10.1103/PhysRevB.81.104426 PACS number(s): 75.30.Gw, 75.75.−c, 71.15.Mb, 78.70.Dm

I. INTRODUCTION

The desire to build magnetic or magneto-optical storage devices with maximal storage density[1,2] has spurred a strong interest in the properties of magnetic nanostructures supported on nonmagnetic substrates.[3] One bit of information is stored per magnetic domain, and a high magnetic anisotropy is required to inhibit magnetization reversal and hence loss of information. A reduction in the size of the nanostructure carrying one bit of information requires the increase in the magnetic anisotropy energy (MAE) per atom. In addition, the easy axis must be oriented perpendicular to the surface of the substrate to reduce the dipolar magnetic interactions between neighboring magnetic moments. The ultimate size limit of a system showing magnetic anisotropy is an isolated magnetic atom on a nonmagnetic substrate. A high MAE requires large spin and orbital moments and a strong spin-orbit coupling (SOC). Recently, a giant MAE was found by Gambardella *et al.*[4] for Co atoms on a Pt(111) substrate. In this case, the large magnetic moment is provided by the Co atom but for Co, like for all 3*d* ferromagnets, the spin-orbit coupling is weak. Strong SOC is found in the heavy 5*d* metals such as Pt but these metals are nonmagnetic. Hence the giant MAE observed for Co/Pt(111) must have its origin in the strong coupling between the magnetic adatom and its ligands. The situation is similar as for ultrathin films of 3*d* elements adsorbed on heavy-metal substrates or multilayers formed by these systems.[5]

The investigation of the MAE of supported magnetic nanostructures remains a challenge to both theory and experiment. Using x-ray magnetic circular dichroism (XMCD) (Ref. 6), it is now possible to measure the magnetic properties of submonolayers down to coverages as low as 0.002 monolayers (MLs).[7] At these coverages statistical growth, obtained by deposition at temperatures where monomer diffusion is frozen, leads almost exclusively to single adatoms.[8] Due to the spatial extent of the x-ray beam of a few hundred micrometer square, XMCD performs ensemble averages.

 ©2010 The American Physical Society

However, for ensembles containing only monomers with no mutual magnetic interactions, XMCD enables one to measure the spin and orbital moments as well as the MAE of single atoms. A review of experimental investigations of the magnetic properties of isolated atoms adsorbed on surfaces has recently been presented by Brune and Gambardella.[9] The results for Co/Pt(111) remain characteristic for the magnetism of 3*d* atoms on 4*d* or 5*d* substrates. Both spin and orbital moment of the Co atoms ($\mu_S = 1.8 \pm 0.1 \mu_B$, $\mu_L = 1.1 \pm 0.1 \mu_B$) measured at low temperature and in a magnetic field strong enough to achieve saturation are strongly enhanced compared not only to bulk Co (where $\mu_S = 1.52 \mu_B$, $\mu_L = 0.15 \mu_B$) but also in comparison to ultrathin films,[5,10] atomic wires,[11,12] and supported nanoclusters.[10,13] From the magnetization curves measured in magnetic fields perpendicular and nearly parallel to the surface, a very large MAE of 9.3 ± 1.6 meV and a total moment per Co atom (measuring the sum of the spin and orbital moments of the magnetic adatom plus the magnetization induced in the substrate) of $5.0 \pm 0.6 \mu_B$ have been estimated. A similar "giant effective moment" of about $10 \mu_B$/Co atom has been reported for very dilute Co-Pd alloys.[14] Considering the difference in the coordination between an adatom adsorbed on a surface and an atom immersed in the bulk, both estimates are in reasonable agreement.

Additional information on the structural and magnetic properties of Co atoms adsorbed on Pt(111) comes from scanning tunneling microscopy (STM) and scanning tunneling spectroscopy (STS).[15,16] The STM images confirm that the Co atoms occupy both face-centered cubic (fcc) and hexagonal close-packed (hcp) hollows of the Pt surface. The particular advantage of spin-polarized STS measurements is that they allow to probe the magnetic properties of individual adatoms.[16] Assuming a perpendicular easy axis of magnetization and a MAE of 9.3 meV taken from the XMCD experiments, a fit of the magnetization curves as a function of the applied field yields slightly different total effective moments of $\mu(\text{hcp}) = 3.9 \pm 0.2 \mu_B$ and $\mu(\text{fcc}) = 3.5 \pm 0.2 \mu_B$ for Co atoms in the two different adsorption sites. Inelastic tunneling spectroscopy observes the exchange of spin angular momentum between the tunneling electrons.[17,18] Very recently, it has been proposed that the MAE may be derived from the spin-flip energy.[19–21] However, to derive the MAE from the spin-excitation energy, the magnitude of the spin S to be flipped (consisting of the spins of the adsorbed atom plus the induced substrate moments) must be known. If $S > 1$, the excitation from the ground state with $S_z = \pm S$ to a state with $S_z = \pm (S-1)$ does not necessarily correspond to a spin reorientation by 90°. For Co/Pt(111), Balashov *et al.*[21] assumed a spin of $S = 1$ to derive an MAE compatible with the XMCD result. For Fe/Pt(111), a similar large MAE of 6.5 meV was derived from the STS data, assuming a spin of $S = 3/2$.

The determination of the spin and orbital moments and of the MAE of supported magnetic nanostructures also represents a challenge to current spin-density-functional theories (SDFTs) of magnetism. Magnetic anisotropy is caused by spin-orbit coupling, hence a relativistic calculation is required. The essential problem, however, is twofold: (i) the strong coupling between nanostructure and substrate must be correctly described. This is particularly important for isolated adatoms. The spin degeneracy of the free atom is broken only by the coupling to the ligands. (ii) All current versions of SDFT tend to underestimate the orbital moment. The reason is that the charge and spin densities determining the effective one-electron potential are determined as averages over occupied orbitals. It has been proposed that the evaluation of the orbital moments could be improved by adding semiempirical corrections such as the orbital-polarization term proposed by Brooks *et al.*[22] However, calculations based on the full orbital-polarization term produce too large moments.[4,23]

In any calculation of the MAE, a number of technical choices are required: (i) choice of the exchange-correlation functional: local or semilocal (gradient-corrected), eventually adding post SDFT corrections. (ii) Self-consistent band-structure or Green's-function calculations—this also implies the choice of the form of the one-electron potential (full-potential or atomic-sphere approximation). (iii) Spin-orbit coupling taken into account by solving the Dirac equation[24,25] or by using the second-order variational approach.[26,27] (iii) Modeling of the substrate-periodic slabs or semi-infinite (possible only within Green's-function approaches). (iv) Geometry of the adsorbate/substrate complex—all atoms in sites continuing the crystalline lattice of the bulk substrate, relaxation of the adatom only, or full relaxation of adatom plus substrate. (v) MAE determined in terms of independent total-energy calculations for different orientations of the magnetization or using the "magnetic force theorem (FT)"[28,29] as the difference in the band energies at a frozen potential and charge density. Very recently, we have published a study attempting to assess the influence of these different approximations on *ab initio* calculations of the MAE.[30]

For the archetypal systems Co/Pt(111) and Fe/Pt(111), a number of SDFT studies of orbital moments and MAE have been published.[4,21,30–35] With the exception of our recent work[30] and the work by Shick and Lichtenstein[35] and by Balashov *et al.*,[21] all these calculations are based on a Green's-function approach within the screened fully relativistic Kohn-Korringa-Rostocker (KKR) method, an idealized geometry propagating the bulk structure of the substrate, the local-density approximation, and the use of the magnetic force theorem.[4,21,31–35] In our recent assessment of the impact of the different approximations, we have demonstrated that the most important step is the description of the adsorbate/substrate complex. Calculations based on the assumption of an idealized bulklike geometry essentially attempt to cure a defect of the SDFT (missing orbital dependence of the exchange field) by artificially minimizing adatom/support hybridization. This allows to achieve a larger orbital moment and an MAE in semiquantitative agreement with experiment at the expense of an unrealistic geometry and electronic structure. Calculations based on a relaxed geometry provide a more realistic scenario but tend to underestimate the orbital moments even more strongly. Hence both types of calculations provide rather a lower limit to the MAE: in one case the influence of the strong SOC of the ligands and in the other the orbital moments of the adatom is underestimated.

In the present work, we report on a combined theoretical and experimental investigation of the spin and orbital mo-

ments as well as the MAE of isolated Co and Fe atoms on Pd(111) and Rh(111) substrates. Compared to the well-studied Co(Fe)/Pt(111) case, these systems based on 4*d* substrates differ by a reduced strength of the SOC but an increased magnetic polarizability of the substrate metals. Both Pd and Rh are known to be nearly magnetic, their density of states at the Fermi level just fails to meet the Stoner limit for ferromagnetic ordering. For both metals, there have been reports that at least their more open (100) surfaces are magnetic. This has led to a lengthy and heated discussion but the question seems now to be settled in favor of the absence of surface magnetism. Nonetheless, due to the high polarizability of the Rh atom, for Rh nanostructures (monolayers on Ag or Au substrates,[36,37] Rh nanowires,[38] and free Rh clusters[39,40]), the existence of a spontaneous magnetization has been predicted, even though not verified experimentally.[41] Experimental confirmation for the magnetism of free Rh clusters is available from Stern-Gerlach experiments.[42] For Fe/Pd, a "giant" enhancement of the magnetic moment of Fe impurities,[43,44] of embedded Fe monolayers and artificial layered FePt and FePd compounds with an $L1_0$ structure has been reported.[45] The recent SDFT studies of Rh surfaces magnetically doped with Co impurities[37] have demonstrated that the induced spin moments on Rh atoms may be as large as $0.7\mu_B$ and that the total moment per Co atom may reach $4\mu_B$. However, these studies have also demonstrated that the magnetic polarization induced by a Ruderman-Kittel-Kasuya-Yoshida mechanism is long ranged and that convergence with respect to the model size may be difficult to achieve.

II. COMPUTATIONAL SETUP

Ab initio density-functional calculations of the spin and orbital magnetic moments and of the magnetic anisotropy energy of Fe and Co adatoms on Rh and Pd (111) surfaces were performed using the Vienna *ab initio* simulation package (VASP).[46] VASP performs an iterative solution of the Kohn-Sham equations within a plane-wave basis. Electronic exchange and correlation are described within a spin-polarized generalized-gradient approximation (GGA) using the functional proposed by Perdew *et al.* (PW91 - Ref. 47) and the spin interpolation proposed by Vosko *et al.*[48] The choice of the GGA functional is motivated by the fact that for the substrate, GGA predicts slightly too large and the local-density approximation (LDA) slightly too low lattice constants, while for Co and Fe metals, the GGA predictions are definitely superior. In addition, the use of the GGA is crucial for the correct description of the structural and magnetic ground state of bulk ferromagnetic 3*d* elements.[49] The electron-ion interaction is described within the projector-augmented-wave (PAW) (Ref. 50) formalism. The PAW potentials have been derived from fully relativistic calculations for atomic reference calculations. The PAW method reconstructs the full nodal character of the exact all-electron charge distribution in the core region. Hence it is a genuine all-electron approach that avoids the necessity to include nonlinear core corrections, which is of particular importance for magnetic systems. The basis set contained plane waves with a maximum kinetic energy of 300 eV, which allows to achieve full basis-set convergence.

Magnetic anisotropy and orbital moments are relativistic effects depending on the strength of the spin-orbit coupling. Spin-orbit coupling has been implemented in VASP by Kresse and Lebacq.[51] Following Kleinman and Bylander[26] and MacDonald *et al.*,[27] the relativistic Hamiltonian given in a basis of total angular momentum eigenstates $|j,m_j\rangle$ with $j=l\pm\frac{1}{2}$ (containing all relativistic corrections up to order α^2, where α is the fine-structure constant) is recast in the form of 2×2 matrices in spin space by reexpressing the eigenstates of the total angular momentum in terms of a tensor product of regular angular momentum eigenstates $|l,m\rangle$ and the eigenstates of the z component of the Pauli-spin matrices. The relativistic effective potential consists of a term diagonal in spin space which contains the mass-velocity and Darwin corrections, and the spin-orbit operator. The nondiagonal elements in spin space arise from the spin-orbit coupling but also from the exchange-correlation potential when the system under consideration displays a noncollinear magnetization density. Calculations including spin-orbit coupling have therefore to be performed in the noncollinear mode implemented in VASP by Hobbs *et al.*[52] and Marsman and Hafner.[53]

The substrate has been modeled by periodically repeated slabs consisting of up to ten atomic layers separated by a sufficiently thick vacuum space of $\simeq 16$ Å. A 5×5 surface unit cell has been used with one adatom per surface cell. This corresponds to a coverage of 0.04 ML, only slightly larger than in experiment. Calculations on larger surface cells (and hence lower coverages) would require a much increased computational effort. In earlier experiments[12] on Co/Pt(111) for coverages varying between 0.007 and 0.03 ML, the MAE changed only from 9.2 to 8.6 meV/atom. This indicates that our surface cell represents an acceptable compromise.

The adsorbates were placed on one side of the slab only and a dipole correction[54,55] was applied to compensate for the electrical field gradient through the slab. Electronic and magnetic degrees of freedom were relaxed simultaneously until the change in total energy (TE) between successive iterations was smaller than 10^{-7} eV/cell. Such a stringent relaxation criterion is essential for an accurate MAE. The coordinates of the adatom and the positions of the atoms in the three topmost layers of the substrate were optimized using scalar-relativistic calculations until the forces on all unconstrained atoms were converged to less than 0.01 eV/Å. The geometry and electronic and magnetic ground state resulting from the scalar-relativistic calculation were used to initialize relativistic calculations including (SOC). No additional relaxation of the geometry was performed because our earlier work on Fe and Co adatom on Pt(111) has demonstrated that relaxations with and without SOC lead to almost identical results.[30] Our description of SOC allows, in principle, for a noncollinear orientation of spin and orbital moments but we always found a collinear alignment. Two sets of self-consistent calculations were performed for magnetic moments oriented perpendicular and parallel to the surface to find the easy and hard magnetic axes and to determine the MAE in terms of the difference in the total energies.

In parallel, the MAE was also calculated using the magnetic force theorem from the difference in the band energies

at a frozen potential. The results achieved from the force theorem are, in general, less accurate but using the layer and angular momentum decomposed partial local densities of states, the MAE may be decomposed into contributions from the adatom and from different layers of the substrate, as well as into contributions from different orbitals. However, the calculation of the partial local densities of states must be based on the projection of the plane-wave components of the electronic eigenstates onto spherical waves within atomic spheres. It must be kept in mind that this approximate decomposition introduces additional numerical inaccuracies. However, this decomposition is very helpful in elucidating the electronic origin of the MAE.

The calculations including SOC require a fine k-point mesh for the Brillouin-zone integrations. Test calculations were performed for a Co adatom on a Rh(111) surface for three different k-point grids: $3\times3\times1$, $3\times3\times2$, and $5\times5\times1$ generated by the Monkhorst-Pack scheme[56] and a modest Gaussian smearing of the eigenstates. A $3\times3\times1$ grid was found to provide a reasonable compromise between accuracy and computational effort. All converged total energies were extrapolated to zero smearing.

We should point out that our setup differs considerably from that used in previous calculations[4,31,32,34] of the magnetic anisotropy of supported nanostructures. Most of these calculations are based on a KKR Green's-function approach, a local exchange-correlation functional, a complete neglect of relaxation of the adsorbate/substrate complex, and the use of the magnetic force theorem for calculating the magnetic anisotropy energy. A detailed comparative study of the impact of these approximations on calculations of the magnetic anisotropy energy has recently been published for Fe and Co adatoms on a Pt(111) surface.[30]

III. COMPUTATIONAL RESULTS

A. Bulk metals and pristine surfaces

The lattice constants of fcc Pd and Rh calculated using the GGA are (experimental values are given in brackets) $a_{\mathrm{Pd}}=3.957(3.891)$ Å (Ref. 57) and $a_{\mathrm{Rh}}=3.825(3.803)$ Å,[58,59] and the bulk moduli are $B_{\mathrm{Pd}}=174(180)$ GPa (Ref. 57) and $B_{\mathrm{Rh}}=262(269)$ GPa.[58,59] These lattice parameters have been applied in all further calculations. For Pd, we performed a comparative calculation using a local LDA functional, with the results $a_{\mathrm{Pd}}=3.866$ Å and $B_{\mathrm{Pd}}=210$ GPa.

For a clean Pd(111) surface, the distances between the three top layers have been relaxed, We find interlayer relaxations of $\Delta_{12}=+0.2(0.3)\%$ and $\Delta_{23}=-0.5(-0.4)\%$ in calculations using five(ten)-layer slabs, to be compared with the available low-energy electron diffraction data finding an expansion of the first interlayer spacing by about +1%.[60–62] For the work function, we find $\Phi=5.30(5.32)$ eV while experiment yields $\Phi=5.60$ eV.[63] At this level, one is led to conclude that a five-layer slab describes the structure of a Pd(111) surface with good accuracy. A problem arises, however, from the high polarizability of the Pd atoms. A spin-polarized GGA calculation for the five-layer slab leads to a weakly magnetic slab, the largest moments of $0.4\mu_B$ are calculated for the central layer. In a calculation with a ten-layer slab, this spurious surface-induced magnetism disappears, all moments drop below $0.005\mu_B$ even if the initialization assumes a magnetic moment. The results are essentially independent of the choice of the functional, spin-polarized LDA calculations lead to almost identical results for the geometry, the maximal moment in a five-layer slab is $0.3\mu_B$. Hence it seems to be indicated to use a ten-layer slab in all calculations—however, this statement has to be revised when a magnetic atom is adsorbed at the surface.

The results for a Rh(111) surface are very similar. The surface-induced relaxations are $\Delta_{12}=-1.2/-1.1/-0.9\%$ and $\Delta_{23}=0.6/0.0/0.0\%$ for a five-layer, an eight-layer slab and in experiment.[64] The work function is $\Phi=5.25/5.22/5.30$ eV (experiments by Brault *et al.*[65]). The spurious surface-induced moments are smaller already for the five-layer slab (maximal moment $0.11\mu_B$), an eight-layer slab is nonmagnetic. However, the magnetism induced by an adatom or adlayer tends to be very long ranged and deserves attention.

B. Geometry of the adsorption complex

Table I summarizes the binding energies and the geometric data for isolated Fe and Co atoms adsorbed in threefold hollows and in twofold bridge positions on Pd and Rh (111) surfaces as calculated in a spin-polarized scalar-relativistic approach. Both fcc and hcp hollows have been considered and the binding energy at the bridge site has been calculated in order to provide an estimate for the diffusion barrier. The most important results are the following: On a Pd(111) surface, both Fe and Co adatoms prefer to occupy an hcp hollow, the difference in the binding energies is 39 meV/atom and 36 meV/atom, respectively. The diffusion barrier for Fe(Co)/Pd(111) given by the difference in the binding energies at bridge and the more stable hcp hollow sites is $E_{\mathrm{diff}}\approx144(128)$ meV. Using a typical value for the attempt frequency of $\nu_0=1\times10^{13}$ Hz, we derive onset temperatures where the jump rate is $\nu=1$ Hz of $T=41(36)$ K for the relaxation from fcc to hcp sites and of $T=56(50)$ K for surface diffusion, respectively. Thus thermal diffusion is prohibited at the substrate temperatures used for atom deposition and for recording of the XMCD spectra. It is intuitive to consider nonthermal motion over a few lattice sites along the surface possibly caused by the dissipation of the adsorption energy. However, this so-called transient mobility has been precluded for all metal/metal systems where direct atomic-scale investigations exist.[66] One example is Pt/Pt(111), for which field ion microscopy has reported an equal occupation of fcc and hcp sites at 20 K, despite the fcc site being more stable, as evidenced by diffusion from hcp to fcc hollows upon raising the temperature to 45 K.[67] Similarly for Co/Pt(111) STM has reported adsorption on both hollow sites with equal probability.[15] Based on present knowledge, metal atoms deposited at low temperature onto a metal substrate therefore come to rest at their impact site implying instantaneous dissipation of the adsorption energy of several electron volts. We conclude that Fe and Co atoms investigated in experiment are with equal probability on hcp and fcc sites on Pd(111). In both locations, they relax strongly inward by 0.63 Å (Fe) and 0.66 Å (Co), corresponding to 28% and

TABLE I. The calculated adsorption energy E_{ad}, work function change $\Delta\Phi$ (with respect to the clean surface), height z of the adatom above the surface, distance between adatom and the nearest surface atom d, relaxation Δ_{ij} of the interlayer distances, and the buckling of the substrate, b_i. The calculations are performed for five-layer thick slabs and the values quoted in brackets are obtained for a ten- and eight-layer slab for Pd and Rh substrates, respectively.

Adsorption site	E_{ad} (eV)	$\Delta\Phi$ (eV)	z (Å)	d (Å)	Δ_{12} (%)	Δ_{23} (%)	b_1 (Å)	b_2 (Å)
				Fe/Pd(111)				
hcp hollow	4.006	−0.36	1.67	2.37	+0.4	−0.3	0.06	0.07
(hcp hollow)	4.123	(−0.33)	(1.64)	(2.36)	(+0.6)	(−0.1)	(0.04)	(0.07)
fcc hollow	3.967	−0.36	1.67	2.37	+0.4	−0.3	0.07	0.04
bridge	3.862	−0.33	1.61	2.32	+0.7	−0.1	0.22	0.06
				Co/Pd(111)				
hcp hollow	3.963	−0.29	1.64	2.62	+0.3	−0.4	0.04	0.07
fcc hollow	3.927	−0.30	1.66	2.63	+0.4	+0.4	0.06	0.04
bridge	3.835	−0.28	1.62	2.66	+0.4	−0.4	0.21	0.08
				Fe/Rh(111)				
hcp hollow	5.180	−0.34	1.76	2.38	−0.7	+0.7	0.04	0.02
(hcp hollow)	5.289	(−0.37)	(1.76)	(2.38)	(−0.9)	(+0.1)	(0.05)	(0.02)
fcc hollow	5.091	−0.36	1.81	2.39	−0.6	+0.7	0.06	0.01
bridge	4.982	−0.36	1.80	2.32	−0.7	+0.7	0.07	0.03
				Co/Rh(111)				
hcp hollow	5.333	−0.28	1.73	2.36	−0.7	+0.7	0.05	0.03
(hcp hollow)	5.438	(−0.28)	(1.72)	(2.36)	(−0.9)	(+0.1)	(0.05)	(0.01)
fcc hollow	5.245	−0.29	1.76	2.37	−0.6	+0.7	0.07	0.02
bridge	5.114	−0.31	1.78	2.30	−0.7	+0.7	0.06	0.03

29% of the ideal interlayer distance. The interlayer distances in the substrate are hardly affected but the adsorption of the adatom causes also a weak buckling in the two top layers, the substrate atoms are attracted toward the adatom. The adsorption induces a decrease in the work function. Calculations based on a ten-layer slab are shown only for Fe(hcp)/Pd(111)—except for a slightly increased binding energy, the increased slab thickness has no significant effect on the adsorption geometry.

On the Rh(111) surface the preference for hcp adsorption sites is even more pronounced, the differences in the binding energies are nearly identical, 89 meV for Fe and 88 meV for Co, respectively. The diffusion barrier for Fe(Co) atoms is 198(219) meV, which is only slightly larger than twice the difference between the adsorption energies in the two hollows. The onset temperatures for relaxation from the metastable to the stable hollow are $T=42(51)$ K and the ones for surface diffusion $T=77(85)$ K. Again, from comparison of these temperatures with the temperature used in experiment, and from the absence of transient mobility, the atoms are expected to be with equal probability on fcc and hcp sites. The inward relaxation of the adatoms is slightly smaller than on the Pd surface, 21% for Fe and 22% for Co, as expected because of the smaller lattice constant of Rh. In an hcp hollow, the adatom moves closer to the surface than in a fcc site. The adsorption of an adatom also reduces the outward relaxation of the top layer of the substrate, the buckling of the surface at the adatom is weaker than on Pd(111).

C. Magnetic properties

Like magnetic impurities in highly polarizable hosts, Fe and Co adatoms on Pd and Rh surfaces induce a large polarization cloud in the substrate. Together, the moment of the adatom and the induced magnetization yield a very large total moment per magnetic atom. As shown in previous studies of the magnetic doping of transition-metal surfaces, the magnetic impurities induce a long-range oscillatory decaying polarization in the substrate.[37] In Table II, the spin moments of the adatom, the induced moments on the nearest neighbors (NNs) in the substrate, the total induced moments (integrated over all substrate atoms), and the resulting total spin moment per adatom for scalar-relativistic calculations (not including spin-orbit coupling) are compiled. The analysis of these data leads to several interesting conclusions: (i) although Fe adatoms have a higher magnetic moment than Co atoms, the magnetic moments induced by a Co adatom in a Rh(111) substrate are much larger. The reason is that due to the larger exchange splitting of the Fe d band, the overlap with the Rh d band is reduced, leading to a weaker hybridization and further to a reduced induced moment. On a Pd(111) substrate, the difference is less pronounced because as a consequence of the larger filling of the Pd d band the adatom/substrate hybridization is reduced for both adatoms. (ii) On both substrates and for both adsorption geometries, the largest induced moments are always found on the three substrate atoms directly binding to the adatom but the moments

TABLE II. Magnetic spin moments (in μ_B) of adatoms, induced spin moments on nearest (NN) and next-nearest (NNN) neighbor atoms in top layer (upper line) and subsurface layer (second line) of the substrate, total induced spin moment of the substrate, and total spin moments for isolated Fe and Co atoms on Rh(111) and Pd(111), as resulting from scalar-relativistic calculations. The results have been obtained for a five-layer slab, numbers in parentheses have been calculated for a ten- (Pd) and an eight-layer (Rh) slab, respectively.

	μ_S(Fe/Co)	$\mu_S(\mathrm{Pd})_{\mathrm{NN}}$	$\mu_S(\mathrm{Pd})_{\mathrm{NNN}}$	μ_S(Pd)	μ_S(Fe/Co+Pd)
Fe(hcp)/Pd(111)	3.39(3.39)	0.33(0.32)	0.07(0.04)	0.60(−0.53)	3.99(2.86)
		0.15(0.07)	0.10(0.03)		
Fe(fcc)/Pd(111)	3.38	0.32	0.07	0.81	4.19
		0.11	0.04		
Co(hcp)/Pd(111)	2.25	0.35	0.09	0.25	2.50
		0.17	0.13		
Co(fcc)/Pd(111)	2.23	0.33	0.08	0.62	2.85
		0.15	0.06		
	μ_S(Fe/Co)	$\mu_S(\mathrm{Rh})_{\mathrm{NN}}$	$\mu_S(\mathrm{Rh})_{\mathrm{NNN}}$	μ_S^{tot}(Rh)	μ_S(Fe/Co+Rh)
Fe(hcp)/Rh(111)	3.22(3.20)	0.27(0.26)	0.01(0.01)	1.58(0.19)	4.80(3.40)
		0.05(0.04)	−0.01(−0.01)		
Fe(fcc)/Rh(111)	3.21	0.26	0.04	2.34	5.05
		0.01	−0.01		
Co(hcp)/Rh(111)	2.10(2.07)	0.41(0.38)	0.09(0.08)	5.70(0.81)	7.80(2.89)
		0.07(0.08)	0.02(0.02)		
Co(fcc)/Rh(111)	2.06	0.38	0.10	5.39	7.45
		0.03	0.01		

induced on the more distant atoms depend on substrate and adsorption site. For an adatom in an fcc hollow on Rh(111), the second largest induced moments are found on next-nearest-neighbor (NNN) sites in the surfaces plane while the moments induced in the subsurface layer are much smaller—in contrast to adatoms in an hcp hollow which induce significant moments also in the subsurface layer. The difference is even more pronounced on Pd(111) where the second largest moment is found on the Pd atom in the second layer, directly below the adatom. This indicates that the adatom/substrate hybridization involves *d* states with different symmetry, depending on the adsorption site. (iii) While the moments induced on nearest-neighbor sites are almost independent of the slab thickness, the integrated spin moments decrease strongly for thicker slabs. This is the consequence of the slow oscillatory decay of the induced magnetization with the distance from the magnetic impurity, as discussed in detail by Dennler *et al.*[37] for magnetically doped Rh surfaces.

These results highlight one of the main difficulties of all density-functional studies of magnetic nanostructures supported on highly polarizable substrates. If the calculations are based on a slab which is sufficiently thick to produce a nonmagnetic ground state in the absence of any magnetic impurity, the integrated total induced moment depends very strongly on the thickness of the slab, in particular, we note a decrease in the induced and effective moments if the thickness of the slab is increased. This surprising result is due to the fact that at the lower surface of the slab the small induced negative moment is enhanced by the reduced coordination at the surface and the overestimation of the magnetic polarizability characteristic for the DFT. The effect is further enhanced because the very small induced moments from many atoms add up to a significant contribution. The conclusion is that a tremendous computational effort would be needed to bring the results on the magnetic properties of the adatom/substrate complex to convergence with respect to the thickness of the slab. For this reason we shall confine our calculations of the magnetic anisotropy to slabs of five layers. At this slab thickness, the induced moments at the lower surface are nearly zero (a node in the oscillatory decaying moments falls close to the surface) and thus no artificially enhanced moment exists at the lower surface. Implicitly we make the assumption that the sum over the magnetic moments induced in the deeper layers is very small, although individual induced moments might be larger.

It might appear that investigations of such systems should be based on Green's-function methods for semi-infinite substrates rather than on a slab geometry. However, this conclusion would be premature. Our setup with a restricted slab thickness corresponds in fact to the usual practice in KKR Green's-function calculations where the Dyson equation is solved only for a small cluster surrounding the adatom. On all other substrate atoms, magnetism is suppressed by construction. Usually the number of atoms in such a cluster is much smaller than the number of atoms in the computational cell used for our five-layer slab.

TABLE III. Spin μ_S, orbital μ_L, and total magnetic moments μ_{tot} (all in μ_B) of Fe and Co adatoms adsorbed in fcc or hcp hollows on a Rh(111) substrate (five-layer slab) and induced moments on the Rh-substrate atoms integrated over all atoms in the supercell. Results obtained for perpendicular and in-plane orientations of the magnetic moments are presented. MAE (in millielectron volt) denotes the energy difference between the two orientations of the magnetic moments, calculated from the difference in the total energies (TEs) and using the magnetic force theorem (FT). A positive sign corresponds to a perpendicular easy axis. The energetically more stable adsorption site is marked by boldface.

	Including SOC									
	Perpendicular				In plane					
	μ_S	μ_L	μ_L/μ_S	μ_{tot}	μ_S	μ_L	μ_L/μ_S	μ_{tot}	MAE(TE)	MAE(FT)
					Fe in hcp hollow:					
Fe	3.216	0.078	0.024	3.294	3.216	0.087	0.027	3.303	0.07	0.02
Rh	2.686	0.060	0.022	2.746	2.751	0.224	0.081	2.975		
Fe+Rh	5.902	0.138	0.023	6.040	5.967	0.311	0.052	6.278		
					Fe in fcc hollow:					
Fe	3.205	0.087	0.027	3.292	3.204	0.097	0.030	3.301	−0.58	−0.21
Rh	2.617	0.057	0.021	2.674	2.835	0.238	0.084	3.073		
Fe+Rh	5.822	0.144	0.025	5.966	6.039	0.335	0.055	6.374		
					Co in hcp hollow:					
Co	2.094	0.141	0.067	2.235	2.095	0.147	0.070	2.242	1.65	0.16
Rh	5.646	0.136	0.024	5.782	5.786	0.511	0.088	6.297		
Co+Rh	7.740	0.277	0.036	8.017	7.881	0.658	0.083	8.539		
					Co in fcc hollow:					
Co	2.061	0.158	0.076	2.219	2.060	0.166	0.081	2.226	−0.29	−0.14
Rh	3.905	0.062	0.016	3.967	4.319	0.372	0.086	4.691		
Co+Rh	5.966	0.220	0.037	6.186	6.379	0.538	0.084	6.917		

D. Orbital moments and magnetic anisotropy

Table III summarizes the results for spin and orbital moments and for the magnetic anisotropy energy of Fe and Co atoms supported on a Rh(111) surface. Both adsorption sites have been considered as they are expected to coexist in experiment.

Compared to the scalar-relativistic calculations (see Table II), the spin moment of the adatom remains almost unchanged but the total spin moment induced by an Fe adatom is strongly increased by SOC effects while for a Co adatom, the induced spin moment is decreased. The reason is that SOC leads to a mixing of different spin states, with the main contribution coming from states with a low excitation energy in the scalar-relativistic mode. Orbital moments on the adatom as well as the induced orbital moments remain small—much lower than the experimental estimates. The orbital moments are always parallel to the spin moment, as expected for late transition metals according to Hund's third rule.

While the spin moments of the adatoms are isotropic, we find a small anisotropy of the spin moments induced by Fe ($\Delta\mu_S = -0.065/-0.261\mu_B$, a negative sign indicates that the moment is larger for in-plane orientation) and a much larger one for Co ($\Delta\mu_S = -0.140/-0.414\mu_B$) adsorbed in an hcp/fcc hollow. In both cases, the induced spin moment is larger for in-plane orientation. A substantial anisotropy is found for the induced orbital moments, $\Delta\mu_L = -0.164/-0.181\mu_B$ for Fe/Rh(111) and $\Delta\mu_L = -0.375/-0.310\mu_B$ for Co/Rh(111) in the hcp/fcc hollows. The orbital moments of the adatom are nearly isotropic.

For Fe/Rh(111), we calculate from the change in the total energy a very small perpendicular magnetic anisotropy energy (MAE=0.07 meV) for an adatom in the energetically preferred hcp hollow while for the fcc hollow, we predict an in-plane easy axis (MAE=−0.58 meV). For Co(hcp)/Rh(111), we find a perpendicular anisotropy with MAE =1.65 meV, for Co(fcc) an in-plane orientation of the magnetization is preferred, with a MAE of −0.29 meV. The MAE has also been calculated using the force theorem. The results are in semiquantitative agreement with those derived from the total-energy differences, although—given the smallness of the MAE—they must certainly be considered as less reliable.

The site dependence of the magnetic anisotropy is a surprising result which has not been considered before (all earlier studies assumed that the adatom continues the bulk structure, with or without relaxation). The analysis of the anisotropies of the induced moments (which we find to be much stronger than that of the adatom) suggests that this might be a decisive factor determining the surprising change in the sign of the MAE. We find that the anisotropy of the induced spin moments is strongly site dependent—in contrast to the almost isotropic spin and orbital moments of the adatom ($\Delta\mu_{S(L)} \leq 0.01$). The induced spin and orbital moments are always larger for in-plane orientation. For both Fe and Co in fcc hollows, we find a much larger induced in-plane spin moment while for adatoms in an hcp hollow, the spin anisotropy is reduced. The orbital anisotropy on the other hand is of comparable magnitude for both adsorption

TABLE IV. Spin μ_S, orbital μ_L, and total magnetic moments μ_{tot} (all in μ_B) of Fe and Co adatoms adsorbed on a Pd(111) substrate (five-layer slab) and induced moments on the Pd-substrate atoms integrated over all atoms in the supercell. Results obtained for perpendicular and in-plane orientations of the magnetic moment are presented. The MAE has been calculated as the difference in TEs and using the magnetic FT. A positive sign of the MAE (in millielectron volt) corresponds to a perpendicular easy axis.

	Including SOC									
	Perpendicular				In plane					
	μ_S	μ_L	μ_L/μ_S	μ_{tot}	μ_S	μ_L	μ_L/μ_S	μ_{tot}	MAE(TE)	MAE(FT)
					Fe in hcp hollow:					
Fe	3.385	0.080	0.024	3.465	3.385	0.080	0.024	3.465	−1.80	−0.22
Pd	0.639	0.028	0.044	0.667	0.395	0.019	0.048	0.414		
Fe+Pd	4.024	0.108	0.027	4.132	3.780	0.099	0.026	3.879		
					Fe in fcc hollow:					
Fe	3.375	0.088	0.026	3.463	3.376	0.084	0.024	3.460	0.09	0.08
Pd	0.866	0.054	0.062	0.920	0.886	0.085	0.096	0.971		
Fe+Pd	4.241	0.142	0.033	4.383	4.262	0.169	0.040	4.431		
					Co in hcp hollow:					
Co	2.245	0.220	0.098	2.465	2.244	0.188	0.083	2.432	1.61	0.72
Pd	−0.282	−0.039	0.138	−0.321	−0.250	−0.046	0.184	−0.296		
Co+Pd	1.963	0.181	0.092	2.144	1.994	0.142	0.071	2.136		
					Co in fcc hollow:					
Co	2.236	0.247	0.110	2.483	2.244	0.218	0.097	2.462	2.27	1.88
Pd	0.117	0.022	0.188	0.139	0.941	0.107	0.114	1.048		
Co+Pd	2.353	0.269	0.114	2.622	3.185	0.325	0.102	3.510		

sites. The larger induced in-plane spin moments parallel the in-plane easy axis calculated for adatoms in the fcc hollows.

We have also investigated whether the results are affected in any way by increasing the slab thickness or the density of the *k*-point mesh. For an eight-layer slab of Co(fcc hollow)/Rh(111), the preference for in-plane MAE is reduced from −0.29 to −0.19 meV, for Fe(hcp hollow)/Rh(111), the perpendicular MAE increases from 0.07 to 0.39 meV. Induced moments on nearest-neighbor sites are unchanged, although the total induced magnetization changes appreciably. This indicates that the oscillatory varying induced moments on the more distant sites have only a limited influence on the MAE, justifying the use of thinner slabs. This also suggests that the anisotropy of the total induced moments might not be of decisive importance for the strength of the MAE. For a five-layer slab of Co/Rh(111), doubling the number of *k* points changes the MAE only from −0.29 to −0.25 meV. This demonstrates that these small energy differences are reasonably stable with respect to the computational setup.

Table IV summarizes the results for Fe and Co atoms on Pd(111). For a Co atom in an hcp/fcc hollow on Pd(111), we calculate orbital moments of $\mu_L = 0.22(0.19)/0.25(0.22)\mu_B$ for perpendicular (in-plane) magnetization, the spin moment is unchanged relative to the scalar-relativistic calculation and almost isotropic. At short distances from the adatom, induced spin and orbital moments are both parallel to the Co moment and almost independent of the direction of magnetization. The induced spin and orbital moments on the Pd atoms in the three top layers are shown in Fig. 1. At larger distances, the induced moments are aligned antiferromagnetically, leading to negative total induced spin and orbital moments and resulting in a modest total spin moment of $1.96(1.99)\mu_B$ at the hcp site. For a Co atom in an fcc hollow, the total induced spin and orbital moments remain positive, both are larger for

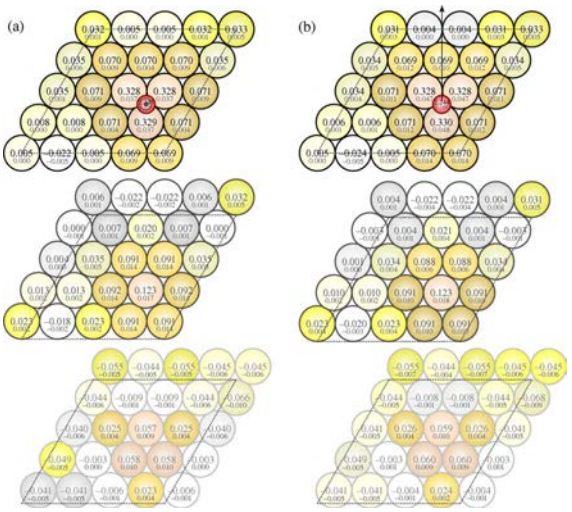


FIG. 1. (Color online) Magnetic spin (black) and orbital (gray) moments (in μ_B) induced by an isolated Co adatom (adsorbed in an hcp hollow on a five-layer Pd slab) on the Pd atoms in the first to third layer (top to bottom) with an (a) out-of-plane and (b) an in-plane orientation of the moments as shown schematically by arrows. The shape of the surface unit cell applied in the calculations is also marked.

in-plane magnetization. The anisotropy of both spin and orbital induced moments is larger for the fcc than for the hcp adsorption site but significantly lower than on the Rh substrate. We have to emphasize that the pronounced anisotropy of the induced moments is a rather long-range effect while the anisotropy of the moments induced on the nearest-neighbor sites is much more modest (see Fig. 1). This statement has general validity for all systems investigated here.

For Co in both adsorption sites, the calculation predicts a perpendicular easy axis and a MAE of 1.61 meV (hcp site) and 2.27 meV (fcc site), respectively. The MAEs derived from the force theorem are also both positive but somewhat lower.

For an Fe atom in the energetically preferred hcp hollow, we calculate isotropic spin and orbital moments for the adatom, and a modest but strongly anisotropic induced spin moment and small induced orbital moments. Both spin and orbital induced moments are larger for perpendicular magnetization. The smallness of the induced moments arises again from a compensation between parallel and antiparallel induced moments. The magnetic easy axis lies in the plane with an MAE of −1.80 meV. For an Fe atom in an fcc hollow, we find again almost isotropic spin and orbital moments (the spin moment is unchanged relative to the scalar-relativistic result) and—in contrast to an Fe atom in the hcp position—also almost isotropic induced spin and slightly anisotropic orbital moments.

The easy axis is perpendicular, the calculated MAE is 0.09 meV (total-energy differences) and 0.08 meV (force theorem). While the very low MAE for Fe in an fcc hollow corresponds to the low anisotropy of the moments of the adatom and of the ones induced in the substrate, the large negative MAE found for an adatom in an hcp hollow requires an explanation because only the induced spin moment displays a significant anisotropy, with the large value for out-of-plane magnetization.

E. Electronic origin of the MAE

Together with the previous study of Fe and Co adatoms on a Pt(111) substrate,[30] the results described above allow to discuss some interesting trends. For a Co adatom, the hcp adsorption site is always preferred and we calculate an MAE of 1.19/1.61/1.65 meV on Pt, Pd, and Rh substrates. That the anisotropy energy on the 5*d*-substrate Pt should be lower than on the 4*d*-metals Pd and Rh with a lower spin-orbit coupling might at first sight be surprising but this is readily explained in terms of a reduced adatom/substrate hybridization reflected in a smaller overlap of the *d* states of the adsorbate with the broader *d* band of the 5*d*-metal substrate. The surprising result of the present calculations, however, is the strong predicted site dependence of the MAE: for a Co atom in the less-stable fcc hollow, on Pd(111) an enhanced positive MAE of 2.27 meV is predicted while on Rh(111), we find even a change in sign of the MAE to −0.29 eV. For an Fe adatom in fcc hollows, we calculate an MAE of 2.99/0.09/−0.58 meV for Pt, Pd, and Rh substrates. The fcc site is the preferred adsorption site only on Pt, and on Pd and Rh the sign of the MAE is different for both sites: 0.09/

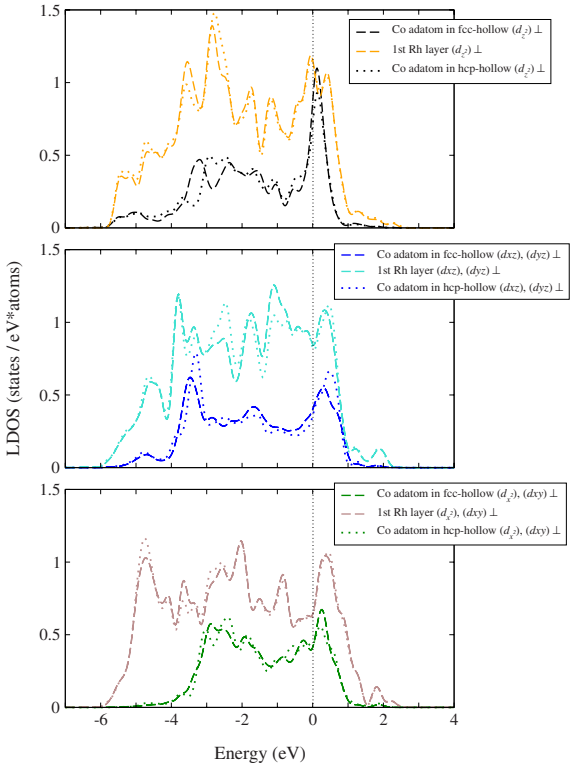


FIG. 2. (Color online) Partial electronic densities of states for a Co adatom on Rh(111) and for the Rh atoms in the surface layer, for the adatom in an fcc (dashed lines) or in an hcp (dotted lines) hollow. Cf. text.

−1.80 meV on Pd and −0.58/0.07 meV on Rh for the fcc/hcp hollows. Hence we find that on Rh the adatom shows in-plane anisotropy in the fcc and out-of-plane anisotropy in the hcp hollows while on Pd, the trend is reversed. An Fe adatom has a perpendicular easy axis in the fcc, switching to in-plane for the hcp hollow. For the Co adatom, the easy axis remains perpendicular for both hollows but the MAE is reduced for the hcp site.

The explanation of this surprising site dependence of the MAE must be sought in subtle differences in the hybridization between the *d* states of the adatom and the substrate orbitals. Figure 2 shows the partial electronic densities of states (PDOSs) for the Co adatom and for the Rh atoms in the surface layer, for both adsorption sites. To simplify the picture and because in the presence of spin-orbit coupling, the spin is not a good quantum number and because the exchange splitting is very large for the adatom but only quite modest for the substrate, we prefer to plot the spin-integrated PDOS. Note that in all cases, the majority states of the adatom are completely filled so that the peak in the Co-PDOS close to the Fermi level arises from minority states only. Due to the strong inward relaxation of the adatom, the distribution of the *d* states of the magnetic adatom is strongly broadened by the hybridization with the substrate. The bandwidth of the Co *d* states is a measure of the strength of this hybridization, it decreases in the sequence $d_{xz}, d_{yz} \rightarrow d_{z^2}$

$\rightarrow d_{xy}, d_{x^2-y^2}$. There are also subtle but significant differences between the PDOS for adatoms in the two hollows—the most important effects are found at the upper and lower band edges at the maxima associated with states that have predominantly spin-up and spin-down character. On the other hand, the changes associated with a reorientation of the magnetization direction are minimal—they hardly exceed the line thickness in these graphs. For the Co/Pd(111) system, the PDOS show a similar picture: the substrate bands are slightly narrower and due to the additional electron in the Pd *d* band the Fermi level falls close to the upper band edge. This also reduces the hybridization with the Co-minority *d* states such that the corresponding PDOS peaks fall closer to the Fermi level.

The elucidation of the electronic origin of the MAE requires an even more detailed analysis, and here the decomposition of the MAE into adatom and substrate contributions, and into contributions from different angular momentum states permitted by the force theorem and calculated in terms of the band energies by integrating the PDOS is very helpful. Within this formalism, the MAE may be written as

$$\mathrm{MAE} = \sum_i \sum_{m_l=-2}^{2} \int_{E_B}^{E_F} (E - E_F) \Delta n^i_{m_l}(E) dE, \qquad (1)$$

where the sum is over all atoms in the supercell and over all angular momentum quantum number m_l, E_B is the energy at the bottom of the valence band, and where

$$\Delta n^i_{m_l}(E) = n^i_{m_l}(E;\perp) - n^i_{m_l}(E;\parallel) \qquad (2)$$

is the difference in the partial local density of states for electrons with quantum number m_l at the site i for perpendicular ($\perp$) and in-plane ($\parallel$) magnetization. The orbital anisotropy $\Delta\mu_L = \mu_L^{\perp} - \mu_L^{\parallel}$ may be calculated in terms of the difference in the occupation of states with $m_l = \pm 2, \pm 1$, i.e., according to

$$\Delta\mu_L = 2\mu_B \sum_i \sum_{m_l=1,2} \int_{E_B}^{E_F} [\Delta n^i_{m_l}(E) - \Delta n^i_{m_{-l}}(E)] dE. \qquad (3)$$

Note that a large contribution to the MAE requires a large value of $\Delta n^i_{m_l}(E)$, integrated over the valence band, irrespective of the value of m_l. A significant orbital anisotropy arises only if $\Delta n^i_{m_l}(E)$ is different for states with $m_l = \pm 1$ and/or $m_l = \pm 2$. One must also remember that the expression given for the orbital anisotropy is exact whereas the force theorem leads only an approximate value for the MAE.

For hcp Co/Rh(111), the contributions to the MAE are 0.19/0.12/0.06 meV for the Co adatom and the first and second Rh-substrate layers. This gives altogether an MAE of 0.37 meV, to be compared with 0.16 meV calculated from the force theorem and 1.65 meV from the self-consistent total-energy difference. For fcc Co/Rh(111), the corresponding numbers are 0.06/−0.13/−0.08 meV from Co/Rh1/Rh2, together −0.15 meV to be compared with a total MAE of −0.14 meV (FT) and −0.29 meV (TE). At this point, it must be emphasized that not only the force theorem is already an approximation. In addition, the decomposition of the DOS into its local and angular momentum components resides on an atomic-sphere projection and the individual PDOS are rather noisy. Hence the decomposition of the MAE has semiquantitative validity at best but it is still very helpful for the elucidation of the physical mechanisms.

The decomposition of the MAE shows that the negative sign for Co in the less-stable fcc hollows has a double origin: a reduced positive contribution from the Co adatom and a negative contribution from the substrate. Their origin can in turn be traced back to differences in the PDOS for perpendicular and in-plane orientation of the magnetization, shown in Fig. 3. The differences in the PDOS induced by a change in the direction of magnetization are very small, at most about 1% of the PDOS. The curves look rather noisy at first sight (even after a modest filtering) but the calculations show that the oscillations at higher binding energies largely cancel out and the dominant contributions come from states very close to the Fermi edge. Inspection of the differences in the PDOS shows for the Co adatom in the hcp hollow positive contributions from the $d_z^2(m_l=0)$ and d_{xz}, $d_{yz}(m_l=\pm 1)$ states but in the fcc hollow small negative contributions from the d_{z^2} and $d_{x^2-y^2}(m_l=2)$ and small positive contributions from the d_{xz}, d_{yz} states. This analysis also explains the very small orbital anisotropy. A large $\Delta\mu_L$ would require that the degeneracy of the d_{xz}/d_{yz} and $d_{xy}/d_{x^2-y^2}$ states for perpendicular magnetization is strongly broken for in-plane magnetization while we find that, especially close to the Fermi level these states remain almost degenerate (and hence do not contribute to the orbital anisotropy, while still contributing to the MAE). For the substrate contribution, a large positive contribution for d_{z^2} and a smaller negative contribution from d_{xz}, d_{yz} states is evident for Co in the hcp hollow. The increased occupation of the $m_l=0$ states also explains the smaller orbital moment for perpendicular magnetization (although the large value listed in Table III results from an integration over all substrate atoms). For Co in an fcc hollow, the differences in the PDOS of the Rh layer are small close to E_F, hence the negative contribution results also from states at higher binding energies. The important role of d_{z^2} and d_{xz}, d_{yz} states of both adatom and substrate in determining the site dependence of the MAE shows its close relation to small but significant modifications in the *d* states extending perpendicular to the surface.

For Co/Pd(111), we find a positive (perpendicular) MAE for both adsorption sites. For the adatom in the stable hcp hollow, we calculated contributions of 0.6/0.07/0.09 meV for Co/Pd1/Pd2, i.e., together 0.76 meV, to be compared with an MAE of 0.72 meV (FT) and 1.61 meV (TE). For Co in an fcc hollow, the corresponding values are 1.11/0.22/0.34 meV from Co/Pd1/Pd2, total 1.67 meV, to be compared with an MAE of 1.88 meV (FT) and 2.27 meV (TE). In this case, the analysis of the differences in the PDOS shows almost the same picture for both adsorption sites. The dominant contributions to the MAE of both adatom and substrate come in both cases from an increased occupation of d_{z^2} states, which is more pronounced for the fcc hollow.

For Fe adatoms the situation is even more complex. On both substrates, the calculations predict that the MAE changes sign between the two different adsorption sites. The larger spin moment of the Fe adatom is coupled to a larger exchange splitting and in turn to significant differences in the electronic spectrum. The PDOS for Fe/Pd(111) is shown in

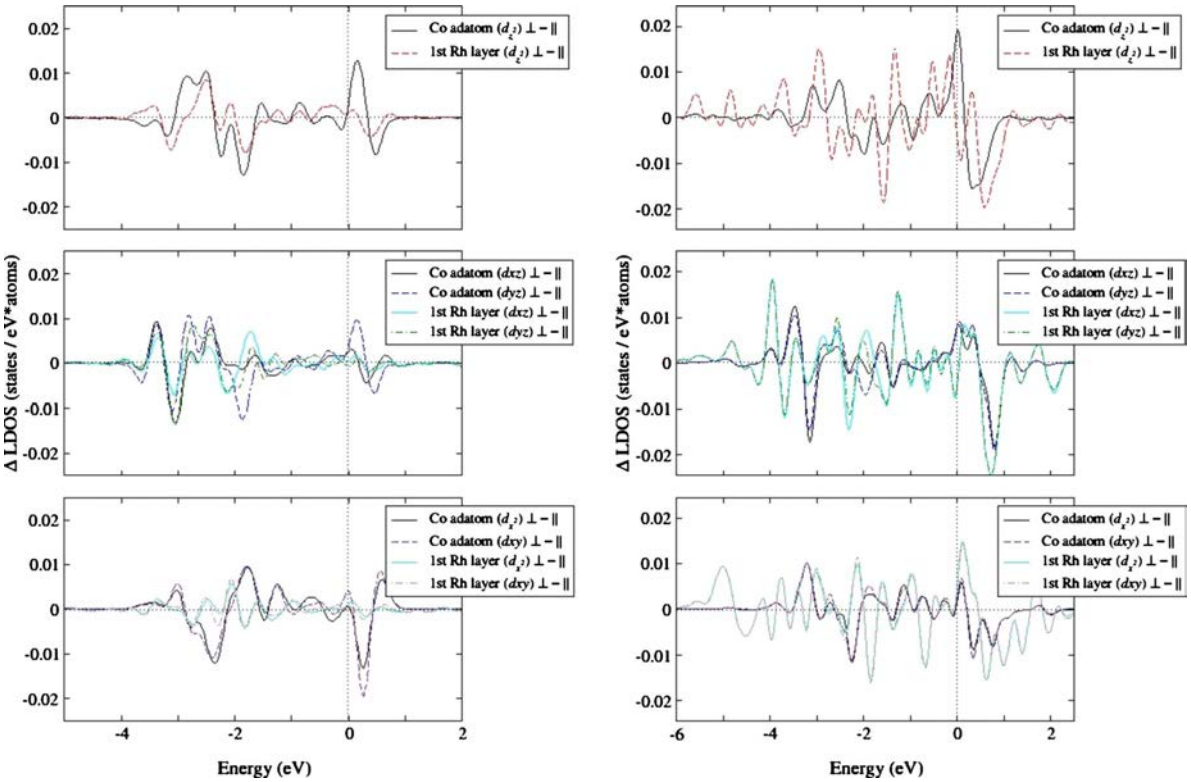


FIG. 3. (Color online) Differences in the partial electronic densities of states for a Co adatom on Rh(111) and for the Rh atoms in the surface layer as a function of the direction of magnetization, for the adatom in an fcc (left panels) and in an hcp (right panels) hollow. Cf. text.

Fig. 4. For all Fe *d* states, the minority states form a sharp peak located about 0.5 eV above the Fermi level. Hybridization of the states extending perpendicular to the surface with the substrate orbitals leads to the formation of a sharp resonance in the corresponding Pd states and the formation of a deep minimum in the Pd-PDOS at the Fermi level. Differences in the PDOS caused by a different location of the adatom are modest, the largest are found in the Fe d_{z^2} majority states and in the Pd d_{xz}, d_{yz} states. For Fe/Rh(111), the PDOS shows a similar picture but the Fermi level is downshifted due to the reduced *d*-band occupation in the substrate and the hybridization-induced PDOS minima are much less pronounced.

For hcp Fe/Pd(111), the decomposition of the MAE yields values of −0.04/−0.20/0.03 meV for Fe/Pd1/Pd2, total −0.21 meV, to be compared with an MAE of −0.22 meV (FT) and −1.80 meV (TE), for fcc Fe/Pd(111) we find 0.07/0.02/0.02 meV for Fe/Pd1/Pd2, total 0.11 meV, to be compared with an MAE of 0.08 meV (FT) and 0.09 meV (TE). The decomposition shows that the in-plane anisotropy for Fe atoms in the hcp hollows stems from a small negative contribution of the adatom and a larger one from the first substrate layer. A detailed assignment of the origin of these contributions is more difficult than for Co adatoms. The differences in the PDOS as a function of the direction of the magnetization shown in Fig. 5 are very small at E_F and for binding energies up to about −1.5 eV. Hence according to the force theorem, the leading contributions to the MAE must be assigned to a change in the occupation of states located at larger binding energies.

For hcp Fe/Rh(111), the decomposition of the MAE yields contributions of 0.04/0.05/0.03 meV for Fe/Rh1/Rh2, together 0.12 meV, in good agreement with the total MAE of 0.02 meV (FT) or 0.07 meV (TE). For fcc Fe/Rh(111), we find contributions of 0.12/−0.10/−0.02 meV from Fe/Pd1/Pd2—in this case, the contributions balance exactly to zero whereas force theorem (−0.21 meV) and total-energy differences (−0.58 meV) yield a modest negative MAE. This shows that the negative MAE for Fe in the fcc hollow stems from the substrate contribution which overcompensates a positive MAE from the adatom. The analysis of the differences in the PDOS yields again a picture very similar to that described for Fe/Pd(111). However, it must be admitted that for MAEs below 1 meV, we are certainly at the limit of the accuracy of DFT calculations and that the decomposition of the MAE according to the force theorem introduces additional approximations. The differences in the FT and TE values of the MAE should give rise to some caution against an overinterpretation of this kind of analysis. Still, the analysis of the PDOS leads to an important conclusion. Due to the large exchange splitting of the Fe *d* states, the peak in the minority DOS is located above the Fermi energy, the Fe-

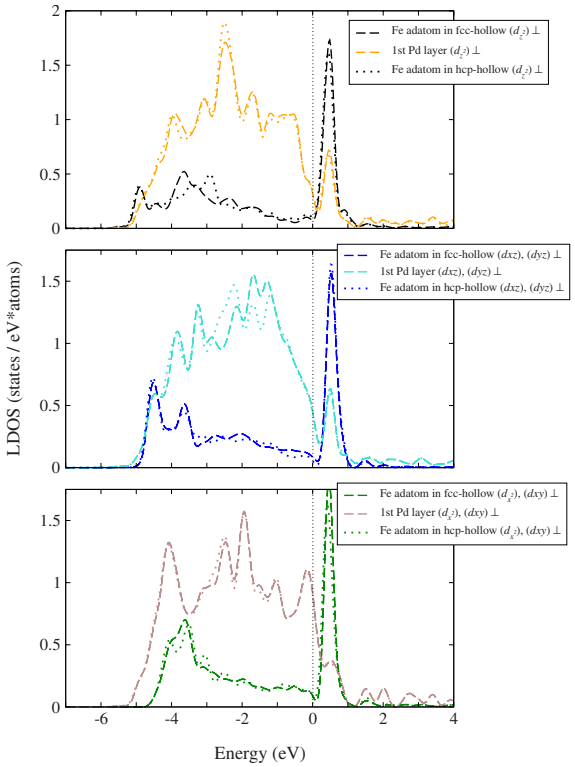


FIG. 4. (Color online) Partial electronic densities of states for an Fe adatom on Pd(111) and for the Pd atoms in the surface layer, for the adatom in an fcc (dashed lines) or an hcp (dotted lines) hollow. Cf. text.

DOS at E_F is low and undergoes only very small variations as a function of the direction of magnetization. Contributions to the MAE stem from states with higher binding energies and they are small due to cancellation effects. This leads to the conclusion that Fe adatoms and, in general, Fe nanostructures should have a much smaller MAE than those formed by Co atoms, in spite of the much larger spin moment of Fe.

Our analysis also considerably modifies the picture of the origin of the MAE derived from earlier theoretical studies based on idealized nonrelaxed geometries.[31,32,34] From LSDA calculations for Fe and Co adatoms on Pt(111) and Ir(111) substrates, Etz *et al.*[34] concluded that even the 5*d* substrates contribute only between 5.5% (for Fe/Pt) and 25% (for Fe/Ir) to the MAE and can in no case change the sign of the MAE determined by the adatom alone. Due to the weaker SOC, the contribution from a 4*d* substrate could be expected to be even weaker. However, this result is due primarily to the neglect of relaxation which largely suppresses the hybridization between adatom and substrate states. For our fully relaxed adatom/substrate complexes, we find that even for the system with the by far largest MAE [Co/Pd(111)], the substrate contributes about one third to the MAE and that as demonstrated for fcc Co/Rh(111) the substrate contribution can even determine the sign of the MAE.

Another conclusion, already suggested by the comparison of orbital anisotropies and MAE, is that the popular assumption that the MAE is directly related to the orbital moment anisotropy $\Delta\mu_L$ such that the largest orbital moment is found along the easy magnetization direction favored by the MAE, is not generally valid. This assumption is based on the perturbation treatment of the MAE proposed by Bruno[68] for materials with a single atomic species. In that case, perturbation theory predicts $\mathrm{MAE}=\frac{\xi}{4\mu_B}\Delta\mu_L$, where ξ stands for the strength of the SOC. It is evident that the relation between MAE and orbital anisotropy cannot be as simple as that if more than one atomic species is present and a strong hybridization exists between their electronic states. Andersson *et al.*[69] have shown that the MAE can be written as a sum over atomic species, i, and a double sum over occupied (s) and unoccupied (s') spin states, $\mathrm{MAE}=\Sigma_{iss'}\Delta E_i^{ss'}$, where the off-diagonal ($s\neq s'$) terms arise from the spin-orbit scattering at other sites. Even for Au/Co/Au trilayers where Co is coupled to a metal which has a strong SOC but only a very modest magnetic polarizability, Andersson *et al.* have demonstrated that the coupling to the ligands leads to strong deviations of the MAE from the linear correlation with $\Delta\mu_L$ expected on the basis of Brunos formula. For our systems, we find that only for Co/Pd(111) at least the sign of the MAE is the same as that of the orbital anisotropy but the MAE is larger for Co in an fcc site while $\Delta\mu_L$ is larger for Co in an hcp site. For the other systems, signs of MAE and orbital moment anisotropy agree as often as they disagree. The correlation is not improved if only local contributions to the MAE and local-orbital moment anisotropies are compared. This emphasizes that, not unexpectedly, the off-site spin-orbit coupling plays a very important role. A further complication arises from the fact that although the spin moments of the adatoms are almost strictly isotropic, significant anisotropies are found for the induced spin moments. van der Laan[70] has extended the perturbation approach to include spin moment anisotropy but again only for one-component systems.

IV. EXPERIMENT

The magnetic properties of Fe adatoms on the (111) surfaces of Pd and Rh, as well as the ones of Co adatoms on Rh(111), have been investigated *in situ* by means of XMCD at the ID08 beamline of the European Synchrotron Radiation Facility (ESRF) in Grenoble. Single crystal Pd(111) and Rh(111) substrates were prepared by Ar^+-ion sputtering ($E_{\mathrm{kin}}=1.3$ keV) at $T=300$ K followed by annealing at $T=800$ K at an oxygen partial pressure of $p_{O_2}=6\times10^{-8}$ mbar for 10 min to remove carbon impurities, and a final flash annealing to 1000–1100 K. Substrate cleanliness was checked by Auger electron and x-ray absorption spectroscopy (XAS). Minute amounts of Fe and Co were deposited from high-purity rods (99.995%) with an electron-beam evaporator on the substrate held at $T=8\pm1$ K. The deposition flux was 5×10^{-4} ML/s and 1×10^{-3} ML/s for Fe and Co, respectively.

As outlined in Sec. III B, thermal diffusion is inhibited at 8 K and transient mobility is absent for all investigated metal/metal systems where direct atomic-scale information is available. Therefore, the Fe and Co atoms come to rest at their site of impact. This is referred to as statistical growth.

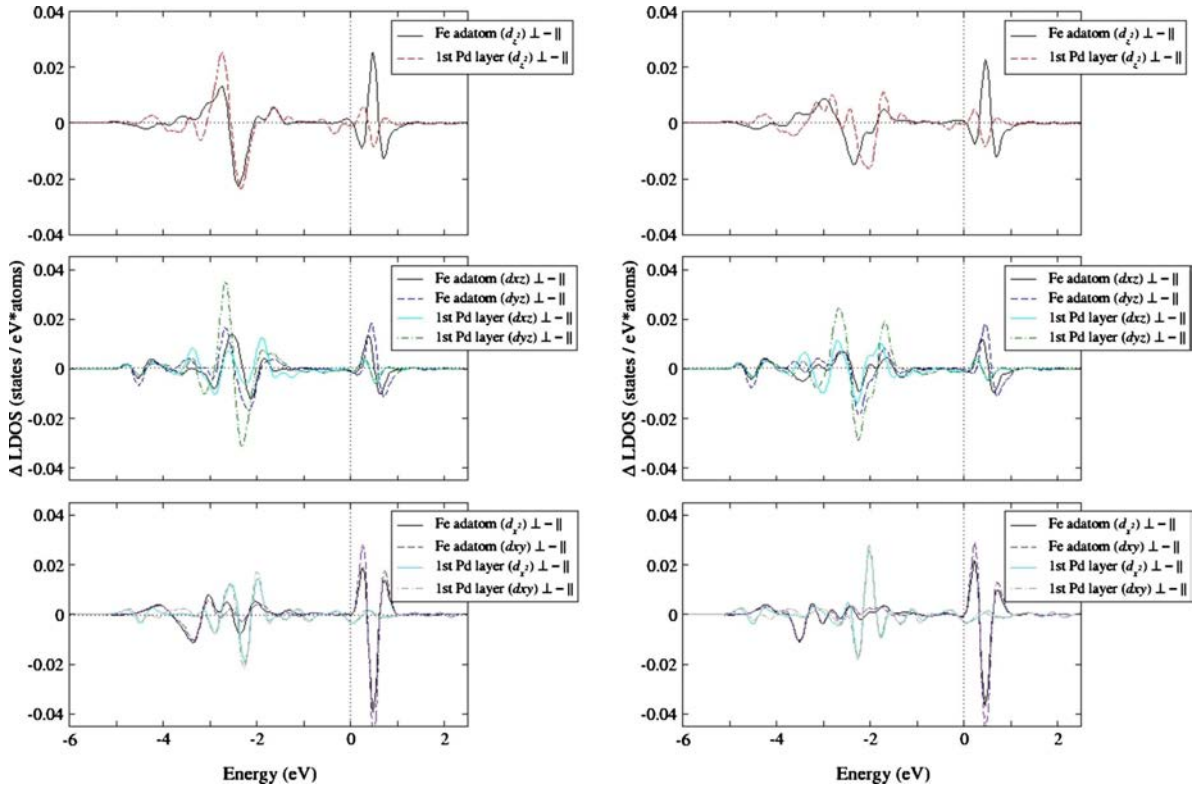


FIG. 5. (Color online) Differences in the partial electronic densities of states for an Fe adatom on Pd(111) and for the Pd atoms in the surface layer as a function of the direction of magnetization, for the adatom in an fcc (left panels) or an hcp (right panels) hollow. Cf. text.

For the coverages of $\Theta = 0.01$ ML and $\Theta = 0.02$ ML employed in this work, the probability of two adatoms landing on neighboring sites and thus forming a dimer is very low. The mean island sizes are 1.04 atoms at 0.01 ML and 1.07 atoms at 0.02 ML; 97%/3%/0% and 93%/6%/1% of the islands are monomers/dimers/trimers for 0.01 ML and 0.02 ML, respectively.[8] We therefore probe essentially single atoms residing with equal probability in the two nonequivalent hollow sites.

Since the magnitude of the XMCD signal scales as the projection of the probed atomic moments onto the x-ray incidence direction, out-of-plane vs in-plane magnetization measurements were carried out by rotating the sample position from $\theta = 0°$ to $\theta = 70°$, corresponding to normal and grazing incidence of the x-ray beam, respectively. A magnetic field up to 5 T collinear with the x-ray beam was applied. XAS experiments were performed at $T = 8 \pm 1$ K in the total electron yield (TEY) mode using $99 \pm 1\%$ circularly polarized light.

Figure 6 shows the XAS and the resulting XMCD spectra for Fe on Pd(111) and on Rh(111) taken at the Fe $L_{2,3}$ edges. The adatom XAS have relative weak absorption features compared with the Pd and Rh TEY background due to the small coverage of only 0.02 ML and 0.01 ML, respectively. The small hump of the L_2 edge is hardly visible in the XAS but a clear L_2 peak can be detected in the XMCD signal. For Fe on Pd and on Rh, the XMCD/XAS asymmetry is larger at

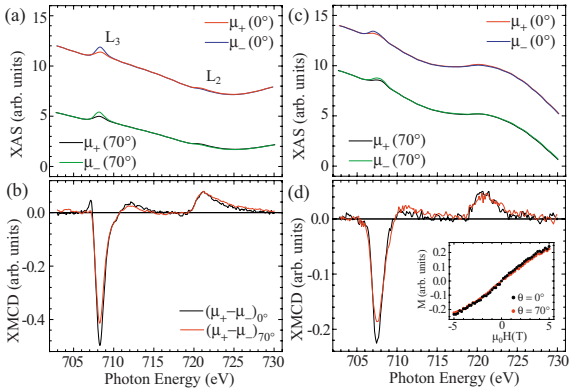


FIG. 6. (Color online) (a) and (b) 0.02 ML Fe on Pd(111), (c) and (d) 0.01 ML Fe on Rh(111): (a) and (c) XAS and (b) and (d) XMCD spectra measured at the Fe $L_{2,3}$ edges at $T = 8$ K and $B = 5$ T. In order to eliminate the dependence of the electron yield on the sample orientation, the XAS at 70° and 0° have been normalized to the background corrected area under the L_3 peak: $\int_{L_3}(\mu_+ + \mu_-)$. Inset in Fig. (d): magnetization curves at $\theta = 0°$ (black dots) and 70° [red (gray) dots] measured by taking the peak height of the L_3 XMCD intensity at 707.7 eV divided by the pre-edge intensity at 705.0 eV as a function of the applied magnetic field.

TABLE V. Orbital to spin moment ratios estimated from XMCD spectra acquired along the easy magnetization axis at $B=5$ T and MAE (millielectron volt per atom, positive values indicate out-of-plane easy axis).

	Θ (ML)	μ_L/μ_{S+7D}	MAE
Fe/Pd(111)	0.02	0.12 ± 0.05	$\gtrsim 0$
Co/Pd(111)[a]	0.02	0.70 ± 0.06	$\gtrsim 3$
Fe/Rh(111)	0.01	0.15 ± 0.05	$\gtrsim 0$
Co/Rh(111)	0.02	0.57 ± 0.04	-0.6 ± 0.1

[a]Reference 73.

0° suggesting an out-of-plane easy axis. The inset in Fig. 6(d) shows an example of field-dependent magnetization measured along the out-of-plane ($\theta=0°$) and close to in-plane ($\theta=70°$) direction for Fe/Rh(111). The $M(H)$ curves for Fe on Pd(111) are similar. At both angles, we observe two almost linear magnetization curves with similar slope, indicative of a very small MAE. Obviously, saturation is not reached and we cannot apply the XMCD sum rules[71,72] to estimate the orbital and spin magnetic moment independently. However, quantitative information can be obtained by calculating the ratio μ_L/μ_{S+7D}, where μ_D is the spin dipole moment. The obtained values along the easy axis are reported in Table V. We must caution, however, that both the magnitude[74] and the anisotropy[75] of μ_{7D} can be substantial for magnetic impurities. These effects, related to the anisotropy of the spin density within the adatom unit cell, prevent a precise determination of the orbital to spin ratio and orbital moment anisotropy based on the comparison of μ_L/μ_{S+7D} values measured along different directions.

The XAS, XMCD spectra, and magnetization curves of 0.02 ML Co/Rh(111) are shown in Fig. 7. The larger L_3 XMCD peak for 70° indicates an in-plane easy axis which is confirmed by the steeper slope of the magnetization curve at $\theta=70°$ compared to 0°. Again, saturation cannot be reached and the corresponding μ_L/μ_{S+7D} value is reported in Table V. The in-plane easy axis is quite unexpected, given that Co adatoms on both Pt(111) (Ref. 4) and Pd(111) (Refs. 73 and 74) present strong out-of-plane anisotropy. The calculations of Sec. III D, however, show that the sign of the MAE of Co/Rh(111) can indeed be negative depending on the type of adsorption site (positive for hcp and negative for fcc). Although XMCD measurements cannot distinguish between different absorption sites, these results point out the importance of the substrate and induced magnetization to determine the sign of the MAE.

The average MAE per adatom can be estimated from the magnetization curves shown in Fig. 7(c) for Co/Rh(111). The energy $E(\theta,\vartheta,\varphi)$ of a paramagnetic particle of size s being subject to uniaxial magnetic anisotropy K and exposed to an external magnetic field **B** is composed of the Zeeman term $-s\mu B\cos\vartheta$ and the MAE term $-sK(\sin\theta\sin\vartheta\cos\varphi+\cos\theta\cos\vartheta)^2$. The z axis is defined parallel to the field **B**, and ϑ and φ are the polar and azimuthal coordinates of the magnetic moment μ, θ defines the easy magnetization direction with respect to the surface normal. The mean value of the magnetization is given by Boltzmann statistics and reads

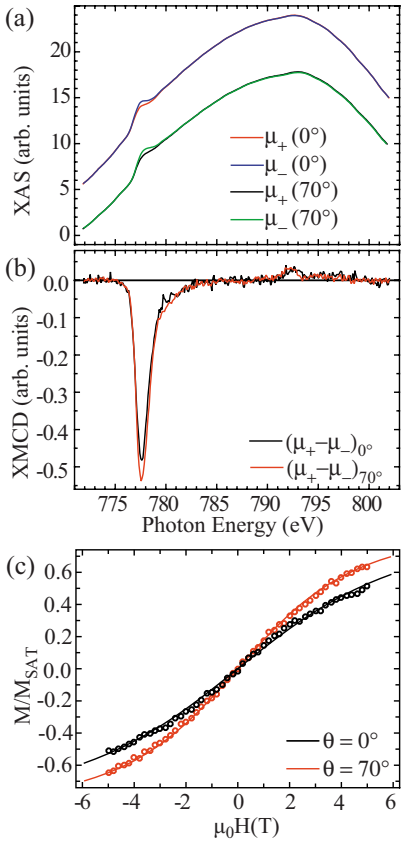


FIG. 7. (Color online) 0.02 ML Co/Rh(111) measured at $T=8$ K. (a) XAS and (b) XMCD taken at the Co $L_{2,3}$ edges at $B=5$ T. Normalization of XAS and XMCD as in Fig. 6. (c) Magnetization curves at $\theta=0°$ (black open circles) and 70° [red (gray) open circles] measured by taking the peak of the L_3 XMCD intensity at 777.0 eV divided by the pre-edge intensity at 773.5 eV as a function of the applied magnetic field. The solid lines are the best fit obtained for paramagnetic impurities of a mean size $s=1.07$ atoms with uniaxial anisotropy $K=-0.6$ meV and a total magnetic moment of $\mu=5\mu_B$.

$$M = M_{\mathrm{SAT}}\frac{\int_0^{2\pi} d\varphi \int_0^{\pi} d\vartheta \sin\vartheta\cos\varphi e^{-E(\theta,\vartheta,\varphi)/k_BT}}{\int_0^{2\pi} d\varphi \int_0^{\pi} d\vartheta \sin\vartheta e^{-E(\theta,\vartheta,\varphi)/k_BT}}. \quad (4)$$

By fitting this expression to the measured magnetization curves, one obtains the free parameters μ, K, and M_{SAT}. As pointed out before, the signal is dominated by the contribution from single adatoms. However, since the XMCD intensity corresponding to magnetic saturation cannot be determined experimentally in this case, a relatively large uncertainty remains in the fits. Moreover, to avoid increasing the number of fit parameters, no allowance is made for adatoms occupying different adsorption sites. The small amount of dimers is accounted for by using the average size of $s=1.07$ atoms at 0.02 ML coverage. In the case of Fe/Pd(111)

TABLE VI. MAE (in millielectron volt per atom), ratio μ_L/μ_S of orbital and spin magnetic moments and orbital anisotropy for Fe and Co adatoms on Rh(111), Pd(111), and Pt(111) substrates. The results for Rh and Pd substrates are from the present work, those for Pt substrate are from Refs. 4, 21, 73, and 74 (experiment) and Ref. 30 (theory). Where two entries are listed, the first refers to the hcp and the second (in parentheses) to the fcc adsorption site for the adatom.

	MAE		μ_L/μ_S		$\Delta\mu_L$
	Expt.	Theor.	Expt. $(\frac{\mu_L}{\mu_{S+7D}})$	Theor. $(\frac{\mu_L}{\mu_S})$	Theor.
Fe/Rh(111)	≥ 0	0.07(−0.58)	0.15 ± 0.05	0.03	−0.009(−0.010)
Fe/Pd(111)	≥ 0	−1.8(0.09)	0.12 ± 0.05	0.02	0.000(0.004)
Fe/Pt(111)	6.5 ± 0.1	2.99		0.03	−0.004
Co/Rh(111)	-0.6 ± 0.1	1.65(−0.29)	0.57 ± 0.04	0.07	−0.006(−0.008)
Co/Pd(111)	≥ 3	1.61(2.27)	0.70 ± 0.06	0.10	0.032(0.029)
Co/Pt(111)	9.3 ± 1.6	1.19	0.61 ± 0.09	0.06	0.038

and Fe/Rh(111), the difference between out-of-plane and in-plane magnetization curves is too small to provide a reliable fit. For Co/Rh(111), the best fit is obtained for MAE $= -0.6 \pm 0.1$ meV per atom and $\mu = 5 \pm 1 \mu_B$ per atom, where $\mu = \mu_L + \mu_S + \mu_{\text{ind}}$(Rh) includes the magnetic moment induced on the Rh sites per Co atom. A possibility to derive an experimental estimate of μ_{ind}(Rh) is by taking μ_S and μ_{S+7D} obtained for the Co monolayer film[74] and by making use of the fact that μ_S is largely independent of coordination. This way one would obtain an orbital moment of $\mu_L = 1.2\mu_B$ for the Co atom and an induced moment of μ_{ind}(Rh) $= 1.8 \pm 1.0 \mu_B$. Such an estimate, however, neglects changes in μ_{7D} from the monolayer to the adatom, which can be as large as $0.3\mu_B$.[4]

V. DISCUSSION AND CONCLUSIONS

We have presented a combined theoretical and experimental investigation of orbital magnetism and magnetic anisotropy of single Fe and Co adatoms on Rh(111) and Pd(111) substrates, complementing earlier results[4,21,30,73,74] of the same adatoms on Pt(111). Table VI confronts the collected experimental and theoretical results.

The experimental determination of the spin and orbital moments and of the MAE using XAS and XMCD spectroscopies turns out to be a very hard task because of the very weak adsorption features in the XAS spectra, the small variation in the magnetization curves with the direction of the applied magnetic field, and finally the difficulty to achieve saturation. For Fe atoms on Pd and Rh weak out-of-plane anisotropy can be inferred from the angular dependence of the L_3 XMCD peak, and the analysis of the magnetization curves suggests a very low out-of-plane MAE. As saturation cannot be achieved in fields up to 5 T, only the ratio between the effective spin and orbital moments can be determined. For Co on Rh(111), we find in-plane anisotropy with an MAE of -0.6 ± 0.1 meV/atom and significant in-plane orbital moment. Fe adatoms on both Pd(111) and Rh(111) present significantly weaker orbital-to-spin moment ratios, which, even taking into account the larger spin moment of Fe, indicate a much smaller orbital magnetization relative to Co.

Compared to the large magnetic anisotropies of both elements on Pt(111),[4,21] the MAEs of isolated atoms on the (111) surface of the two $4d$ metals investigated here are much weaker, although the spin and orbital moments of the adatoms are similar. This shows that the magnitude of the MAE is determined primarily by the interaction of the magnetic adatom with the ligands displaying a strong SOC.

The theoretical calculations of the MAE are based on spin-polarized density-functional calculations for slab models of the substrate including a self-consistent treatment of spin-orbit coupling. Self-consistent calculations have been performed for magnetization directions fixed along the surface normal and parallel to the surface of the substrate and the MAE is calculated from the difference in the total energies. In contrast to almost all previous theoretical studies of the MAE of supported nanostructures, our calculations allow for a complete relaxation of the adsorbate/substrate complex. The relaxation effects are particularly pronounced for isolated adatoms which move inward by more than 0.6 Å compared to a position continuing the bulk structure of the substrate. Evidently this leads to a much stronger hybridization between the orbitals of adatom and ligands. We have also determined the energetically most favorable adsorption site and found that a position of the magnetic adatom in an hcp hollow is preferred over the fcc site continuing the stacking sequence of the substrate lattice. We calculated the diffusion barrier limiting the mobility of the adatoms and find that the activation energy for adatom migration is on the order of 0.1 eV. Since the sample is kept at very low temperatures during deposition and measurement, this implies a random distribution of the adatoms over hcp and fcc hollows.

A characteristic property of late transition elements such as Rh and Pd is that doping with magnetic impurities induces a large magnetic polarization cloud, the total moment per magnetic atom is very large, substantially larger than the upper limit to the spin moment set by Hund's first rule. For magnetic adatoms on these highly polarizable substrates, the magnetic induction effect is even enhanced by the strong inward relaxation. We have discussed in detail the difficulties arising from these long-range polarization effects in conjunction with a slab model of the substrate. The induced magnetization is not restricted to the formation of an induced spin

moment—the induced orbital moments are comparable and sometimes even larger than the orbital moments of the adatom. While the magnetic moments of the adatom show only a modest anisotropy, both spin and orbital moments induced in the substrate display a strong anisotropy.

While our calculations yield reasonable values for the MAE (for a detailed discussion, see below), the orbital moments calculated for the adatom are much too low, by a factor of about 6. The reason for this disagreement is twofold: (i) the lack of orbital dependence of the exchange field calculated in DFT and (ii) the strong interaction between adsorbate and ligands atoms which tends to quench the orbital moment to a value comparable to that in bulk materials. In our detailed assessment of different approximations entering the calculation of orbital moments and MAE, illustrated at the example of Co and Fe atoms on Pt(111),[30] we have demonstrated that for an adatom in an idealized geometry the artificial suppression of the interaction with the ligands allows to form larger orbital moments. But to use a bulklike and, as we have shown, rather unrealistic geometry also strongly reduces the adatom-ligand coupling which is decisive for the magnitude of the MAE. Values of the MAE resulting for both approaches are comparable and tend to be lower than those derived from experiment—indicating that either way theory misses an important contribution to the MAE.

A surprising result of our study is that the MAE is found to be strongly site dependent. Except for Co/Pd(111), the MAE changes sign and magnitude if the adatom is placed in an fcc instead of an hcp hollow. Since in the experiment, the area covered by the x-ray beam contains many adatoms occupying with comparable probability hcp and fcc sites, the experimentally determined MAE must be compared with the average over the MAEs calculated for both sites. The compensation of fcc and hcp sites can explain the weak anisotropy observed for Fe on both substrates. For Co/Rh(111), however, we find a positive (out-of-plane) MAE of 1.65 meV and a very modest negative orbital anisotropy for an adatom position in hcp hollow sites and a smaller negative (in-plane) MAE of −0.29 meV and a negative orbital anisotropy for fcc sites. Thus, the arithmetic average of +0.68 meV disagrees with the experimental value of −0.6 meV, possibly due to uneven distribution of fcc vs hcp sites or numerical uncertainties. For Co/Pd(111), the calculated positive MAEs of 1.6 meV (hcp) and 2.3 meV (fcc) indicate strong out-of-plane anisotropy for the ensemble average, in good agreement with experimental estimates.[73] In these cases, a positive MAE is accompanied by a positive orbital anisotropy on the adatom. This suggest that for sufficiently large MAEs, the sign of the MAE is the same as that of the orbital anisotropy of the magnetic species (as expected on the basis of perturbation theory) while for very small MAEs, this correlation might be broken.

Good semiquantitative agreement between theory and experiment is also found for Co and Fe adatoms on Pt(111). The calculated values for spin and effective (adsorbate plus substrate) moments are in reasonable agreement with experiment. The calculated ratios of orbital to spin moment are much too low if orbital polarization is not taken into account. On the experimental side, a precise determination of the orbital moment anisotropy is made difficult by the unknown μ_{7D} contribution to the ratio of the orbital to spin moment derived from the XMCD sum rules.[71,72,75,76] Assuming small μ_{7D} anisotropy compared to μ_L, the experimental μ_L/μ_{S+7D} values would indicate positive orbital moment anisotropy for Fe on Rh(111) and Pd(111), as well as for Co on Pd(111) and Pt(111) whereas Co/Rh(111) would have negative $\Delta\mu_L$. The theoretical results agree with these estimates, except for the case of Fe/Rh(111), as for the MAE.

We have also attempted to relate the site dependence of the MAE to changes in the electronic structure, using the approximation to the MAE provided by the magnetic force theorem (MAE = difference in the band energies at fixed potential) and the projected local partial densities of states. This analysis leads to two important conclusions: (i) the contribution of the substrate to the MAE is much more important than estimated before on the basis of calculations using an idealized bulklike geometry. The substrate contribution can even invert the sign of the MAE. (ii) The site dependence is related to a rehybridization of the *d* states of both adatoms and substrate atoms extending perpendicular to the substrate. (iii) For Co adatoms, the dominant contributions to the MAE arise from a change in occupation of states very close to the Fermi edge. The contribution from the substrate is larger for Rh than for Pd because of the larger overlap of the Rh *d* band with the Co minority states. (iv) The very small MAE of Fe atoms observed on both substrates is related to the large exchange splitting of the Fe *d* states which minimizes the hybridization of the Fe minority states with the substrate.

In our view, the main problem confronted by *ab initio* calculations of the MAE is still the lack of orbital dependence of the exchange potential. To use an idealized bulklike and, as we have demonstrated, unrealistic geometry might lead to larger orbital moments. However, this does not represent an acceptable solution because it artificially reduces the adatom/ligand interactions which are the crux of the problem. A fundamental improvement of theoretical predictions of the MAE of supported magnetic nanostructures requires post-DFT corrections introducing the orbital dependence of the exchange potential.

ACKNOWLEDGMENTS

P.B. and J.H. thank Martijn Marsman for support and fruitful discussions. P.B. and J.H. acknowledge support of the Austrian Science Funds under Project. No. P19712-N16. Financial support from the Swiss National Science Foundation (Grants No. 200020-109800 and No. 200020-112322) and from the European Science Foundation (EUROCORES 05-SONS-FP-009 SANMAG) are gratefully acknowledged. P.G. acknowledges support from the Spanish Ministerio de Ciencia e Innovación (MAT2007-62341) and Agència de Gestió d'Ajuts Universitaris i de Recerca (2009 SGR 695). We thank the ESRF for provision of beam-time.

[1] M. L. Plumer, J. v. Ek, and D. Weller, in *The Physics of Ultrahigh-Density Magnetic Recording*, Springer Series in Surface Sciences, edited by G. Ertl, R. Gomer, H. Lüth, and D. L. Mills (Springer, Berlin, 2001), Vol. 41.
[2] D. Sellmyer and R. Skomski, *Advanced Magnetic Nanostructures* (Springer, New York, 2006).
[3] N. Weiss, T. Cren, M. Epple, S. Rusponi, G. Baudot, S. Rohart, A. Tejeda, V. Repain, S. Rousset, P. Ohresser, F. Scheurer, P. Bencok, and H. Brune, Phys. Rev. Lett. **95**, 157204 (2005).
[4] P. Gambardella, S. Rusponi, M. Veronese, S. S. Dhesi, C. Grazioli, A. Dallmeyer, I. Cabria, R. Zeller, P. H. Dederichs, K. Kern, C. Carbone, and H. Brune, Science **300**, 1130 (2003).
[5] M. Tischer, O. Hjortstam, D. Arvanitis, J. Hunter Dunn, F. May, K. Baberschke, J. Trygg, J. M. Wills, B. Johansson, and O. Eriksson, Phys. Rev. Lett. **75**, 1602 (1995).
[6] J. Stöhr, J. Magn. Magn. Mater. **200**, 470 (1999).
[7] P. Gambardella, S. S. Dhesi, S. Gardonio, C. Grazioli, P. Ohresser, and C. Carbone, Phys. Rev. Lett. **88**, 047202 (2002).
[8] H. Brune, Surf. Sci. Rep. **31**, 125 (1998).
[9] H. Brune and P. Gambardella, Surf. Sci. **603**, 1812 (2009).
[10] H. A. Dürr, S. S. Dhesi, E. Dudzik, D. Knabben, G. van der Laan, J. B. Goedkoop, and F. U. Hillebrecht, Phys. Rev. B **59**, R701 (1999).
[11] P. Gambardella, A. Dallmeyer, K. Maiti, M. C. Malagoli, W. Eberhardt, K. Kern, and C. Carbone, Nature (London) **416**, 301 (2002).
[12] P. Gambardella, A. Dallmeyer, K. Maiti, M. C. Malagoli, S. Rusponi, P. Ohresser, W. Eberhardt, C. Carbone, and K. Kern, Phys. Rev. Lett. **93**, 077203 (2004).
[13] T. Koide, H. Miyauchi, J. Okamoto, T. Shidara, A. Fujimori, H. Fukutani, K. Amemiya, H. Takeshita, S. Yuasa, T. Katayama, and Y. Suzuki, Phys. Rev. Lett. **87**, 257201 (2001).
[14] G. J. Nieuwenhuys, Adv. Phys. **24**, 515 (1975).
[15] Y. Yayon, X. H. Lu, and M. F. Crommie, Phys. Rev. B **73**, 155401 (2006).
[16] F. Meier, L. Zhou, J. Wiebe, and R. Wiesendanger, Science **320**, 82 (2008).
[17] A. J. Heinrich, J. A. Gupta, C. P. Lutz, and D. M. Eigler, Science **306**, 466 (2004).
[18] T. Balashov, A. F. Takács, M. Däne, A. Ernst, P. Bruno, and W. Wulfhekel, Phys. Rev. B **78**, 174404 (2008).
[19] C. F. Hirjibehedin, C. Y. Lin, A. F. Otte, M. Ternes, C. P. Lutz, B. A. Jones, and A. J. Heinrich, Science **317**, 1199 (2007).
[20] A. F. Otte, M. Ternes, K. v. Bergmann, S. Loth, H. Brune, C. P. Lutz, C. F. Hirjibehedin, and A. J. Heinrich, Nat. Phys. **4**, 847 (2008).
[21] T. Balashov, T. Schuh, A. F. Takacs, A. Ernst, S. Ostanin, J. Henk, I. Mertig, P. Bruno, T. Miyamachi, S. Suga, and W. Wulfhekel, Phys. Rev. Lett. **102**, 257203 (2009).
[22] O. Eriksson, M. S. S. Brooks, and B. Johansson, Phys. Rev. B **41**, 7311 (1990).
[23] D. Fritsch, K. Koepernik, M. Richter, and H. Eschrig, J. Comput. Chem. **29**, 2210 (2008).
[24] G. Y. Guo, H. Ebert, W. M. Temmerman, K. Schwarz, and P. Blaha, Solid State Commun. **79**, 121 (1991).
[25] L. Szunyogh, B. Ujfalussy, P. Weinberger, and J. Kollár, Phys. Rev. B **49**, 2721 (1994).
[26] L. Kleinman, Phys. Rev. B **21**, 2630 (1980).
[27] A. H. MacDonald, W. E. Pickett, and D. D. Koelling, J. Phys. C **13**, 2675 (1980).
[28] A. R. Mackintosh and O. K. Andersen, in *Electrons at the Fermi Surface*, edited by M. Springford (Cambridge University Press, London, 1980), Sec. 3.1.
[29] V. Heine, Solid State Phys. **35**, 114 (1980).
[30] P. Błoński and J. Hafner, J. Phys.: Condens. Matter **21**, 426001 (2009).
[31] S. Bornemann, J. Minar, J. B. Staunton, J. Honolka, A. Enders, K. Kern, and H. Ebert, Eur. Phys. J. D **45**, 529 (2007).
[32] O. Šipr, S. Bornemann, J. Minár, S. Polesya, V. Popescu, and A. Šimunek, J. Phys.: Condens. Matter **19**, 096203 (2007).
[33] M. Tsujikawa, A. Hosokawa, and T. Oda, J. Phys.: Condens. Matter **19**, 365208 (2007).
[34] C. Etz, J. Zabloudil, P. Weinberger, and E. Y. Vedmedenko, Phys. Rev. B **77**, 184425 (2008).
[35] A. B. Shick and A. I. Liechtenstein, J. Phys.: Condens. Matter **20**, 015002 (2008).
[36] S. Blügel, Phys. Rev. Lett. **68**, 851 (1992).
[37] S. Dennler, J. Hafner, M. Marsman, and J. Morillo, Phys. Rev. B **71**, 094433 (2005).
[38] D. Spišák and J. Hafner, Phys. Rev. B **67**, 214416 (2003).
[39] F. Aguilera-Granja, J. L. Rodriguez-Lopez, K. Michaelian, E. O. Berlanga-Ramirez, and A. Vega, Phys. Rev. B **66**, 224410 (2002).
[40] T. Futschek, M. Marsman, and J. Hafner, J. Phys.: Condens. Matter **17**, 5927 (2005); **18**, 9703 (2006).
[41] J. Honolka, K. Kuhnke, L. Vitali, A. Enders, K. Kern, S. Gardonio, C. Carbone, S. R. Krishnakumar, P. Bencok, S. Stepanow, and P. Gambardella, Phys. Rev. B **76**, 144412 (2007).
[42] A. J. Cox, J. G. Louderback, and L. A. Bloomfield, Phys. Rev. Lett. **71**, 923 (1993); A. J. Cox, J. G. Louderback, S. E. Apsel, and L. A. Bloomfield, Phys. Rev. B **49**, 12295 (1994).
[43] T. Herrmannsdörfer, S. Rehmann, W. Wendler, and F. Pobell, J. Low Temp. Phys. **104**, 49 (1996).
[44] K. Swieca, Y. Kondo, and F. Pobell, Phys. Rev. B **56**, 6066 (1997).
[45] S. Mitani, K. Takanashi, M. Sano, H. Fujimori, A. Osawa, and H. Nakajima, J. Magn. Magn. Mater. **148**, 163 (1995).
[46] G. Kresse and J. Hafner, Phys. Rev. B **47**, 558 (1993); **49**, 14251 (1994).
[47] J. P. Perdew, J. A. Chevary, S. H. Vosko, K. A. Jackson, M. R. Pederson, D. J. Singh, and C. Fiolhais, Phys. Rev. B **46**, 6671 (1992).
[48] S. H. Vosko, L. Wilk, and M. Nusair, Can. J. Phys. **58**, 1200 (1980).
[49] E. G. Moroni, G. Kresse, J. Hafner, and J. Furthmüller, Phys. Rev. B **56**, 15629 (1997).
[50] G. Kresse and D. Joubert, Phys. Rev. B **59**, 1758 (1999).
[51] G. Kresse and O. Lebacq, VASP manual, http://cms.mpi.univie.ac.at/vasp/
[52] D. Hobbs, G. Kresse, and J. Hafner, Phys. Rev. B **62**, 11556 (2000).
[53] M. Marsman and J. Hafner, Phys. Rev. B **66**, 224409 (2002).
[54] J. Neugebauer and M. Scheffler, Phys. Rev. B **46**, 16067 (1992).
[55] L. Bengtsson, Phys. Rev. B **59**, 12301 (1999).
[56] H. J. Monkhorst and J. D. Pack, Phys. Rev. B **13**, 5188 (1976).
[57] http://www.webelements.com/
[58] P. Villars and L. D. Calvert, *Pearson's Handbook of Crystallographic Data for Intermetallic Phases* (ASM, Metals Park, Ohio, 1985).
[59] C. Kittel, *Introduction to Solid State Physics*, 6th ed. (Wiley,

New York, 1986).
[60] H. Ohtani, M. A. Van Hove, and G. A. Somorjai, Surf. Sci. **187**, 372 (1987).
[61] T. E. Felter, E. C. Sowa, and M. A. Van Hove, Phys. Rev. B **40**, 891 (1989).
[62] A. Barbieri, M. A. Van Hove, and G. A. Somorjai, Surf. Sci. **306**, 261 (1994).
[63] D. R. Linde, *Handbook of Chemistry and Physics*, 78th ed. (CRC Press, London, UK, 1998).
[64] S. Schwegmann, H. Over, V. De Renzi, and G. Ertl, Surf. Sci. **375**, 91 (1997).
[65] P. Brault, H. Range, J. P. Toennies, and Ch. Wölf, Z. Phys. Chem. (Munich) **198**, 1 (1997).
[66] H. Brune, in, *Physics of Covered Solid Surfaces*, Landolt Börnstein, New Series, Group III Vol. 42, Pt. A, edited by H. P. Bonzel (Springer, Berlin, 2001).
[67] A. Gölzhäuser and G. Ehrlich, Phys. Rev. Lett. **77**, 1334 (1996).
[68] P. Bruno, Phys. Rev. B **39**, 865 (1989).
[69] C. Andersson, B. Sanyal, O. Eriksson, L. Nordström, O. Karis, D. Arvanitis, T. Konishi, E. Holub-Krappe, and J. Hunter Dunn, Phys. Rev. Lett. **99**, 177207 (2007).
[70] G. van der Laan, J. Phys.: Condens. Matter **10**, 3239 (1998).
[71] B. T. Thole, P. Carra, F. Sette, and G. van der Laan, Phys. Rev. Lett. **68**, 1943 (1992).
[72] P. Carra, B. T. Thole, M. Altarelli, and X. Wang, Phys. Rev. Lett. **70**, 694 (1993).
[73] P. Gambardella, A. Vindigni, L. Claude, S. Rusponi, K. Franke, M. Veronese, C. Grazioli, P. Bencok, C. Carbone, and H. Brune (unpublished).
[74] A. Lehnert, Ph.D. thesis, Ecole Polytechnique Fédérale de Lausanne, 2009.
[75] O. Šipr, J. Minár, and H. Ebert, EPL **87**, 67007 (2009).
[76] T. Oguchi and T. Shishidou, Phys. Rev. B **70**, 024412 (2004).

Appendix 2

Reprints of papers on imprinting magnetism in graphene

1. J. Tuček, **Piotr Błoński**, Z. Sofer, P. Šimek, M. Petr, M. Pumera, M. Otyepka, R. Zbořil, Sulfur Doping Induces Strong Ferromagnetic Ordering in Graphene: Effect of Concentration and Substitution Mechanism. *Adv. Mater.* **28**, 5045 (2016).

2. **Piotr Błoński**, J. Tuček, Z. Sofer, V. Mazánek, M. Petr, M. Pumera, M. Otyepka, R. Zbořil, Doping with Graphitic Nitrogen Triggers Ferromagnetism in Graphene. *J. Am. Chem. Soc.* **139**, 3171 (2017).

3. J. Tuček, K. Holá, A. B. Bourlinos, **Piotr Błoński**, A. Bakandritsos, J. Ugolotti, M. Dubecký, F. Karlický, V. Ranc, K. Čépe, M. Otyepka, R. Zbořil, Room temperature organic magnets derived from sp^3 functionalized graphene. *Nat. Commun.* **8**, 14525 (2017).

4. J. Tuček, K. Holá, G. Zoppellaro, **Piotr Błoński**, R. Langer, M. Medved, T. Susi, M. Otyepka, R. Zbořil, Zigzag sp^2 Carbon Chains Passing through an sp^3 Framework: A Driving Force toward Room-Temperature Ferromagnetic Graphene *ACS Nano*, **12**, 12847 (2018).

5. J. Tuček, **Piotr Błoński**, O. Malina, M. Pumera, C. K. Chua, M. Otyepka, R. Zbořil, Morphology-Dependent Magnetism in Nanographene: Beyond Nanoribbons. *Adv. Funct. Mater.* **28**, 1800592 (2018).

Sulfur Doping Induces Strong Ferromagnetic Ordering in Graphene: Effect of Concentration and Substitution Mechanism

*Jiří Tuček, Piotr Błoński, Zdeněk Sofer, Petr Šimek, Martin Petr, Martin Pumera, Michal Otyepka, and Radek Zbořil**

Since the pioneering work on the isolation of graphene in 2004,[1] there has been immense interest devoted to unveiling its properties, with discoveries of peculiar physical phenomena, such as the ambipolar effect,[1] room-temperature half-integer quantum Hall effect,[2] etc. Owing to the zero density of states at the Fermi level, graphene is described as a zero bandgap semiconductor or semi-metal.[3] Moreover, it possesses high intrinsic carrier mobility, and hence high electrical conductivity, and the charge carriers behave as massless relativistic particles with features of Dirac fermions.[3] Further, it shows a long spin lifetime and limited hyperfine interactions, favoring its potential exploitation in spintronic applications, provided it can be made magnetic.[3,4]

However, pristine graphene is diamagnetic in nature due to solely sp^2 hybridization, leaving no unpaired electrons and forming an extensive π-bonding network with delocalized π-electrons.[4–8] Localized magnetic moments are believed to evolve upon introduction of defects into the crystal lattice of graphene.[5] The defects include local topology perturbations, vacancies, noncarbon atoms in the graphene lattice, adatoms (i.e., atoms added to the surface of the graphene sheet), mixed sp^2–sp^3 hybridization, and zigzag-type edges.[5,9–19] These defects are manifested as semi-localized π "midgap" states or flat bands in the electronic band structure of graphene with the peaks in the density of states at the Fermi level showing spin polarization. In the case of vacancies and adatoms, it has been theoretically and experimentally confirmed that they carry a magnetic moment $\mu \approx \mu_B$ (where μ_B is the Bohr magneton).[20,21] The generated paramagnetic centers may then magnetically cooperate via delocalized π electrons, establishing magnetic ordering over the graphene crystal lattice. It has been theoretically proposed that if the defects are located only on one sublattice of the graphene crystal lattice, ferromagnetic alignment emerges; if defects occur on both sublattices with equal probability, graphene shows antiferromagnetic ordering.[4,5] Recently, it has been identified that both the presence of and coupling between localized magnetic moments in graphene can be effectively controlled by applying an external electric field, thus tuning the graphene magnetic features.[11] Further, localized nonbonding states are formed as a result of creation of a σ-symmetry dangling bond in the defects, exhibiting very strong exchange splitting. Thus, defects induce magnetic moments with two different contributions, i.e., from σ and π states. Moreover, owing to a finite width and peculiar edge profile, zigzag graphene nanoribbons have been shown to possess magnetic ordering when localized magnetic moments situated on one edge interact ferromagnetically with each other and in an antiferromagnetic and/or ferromagnetic manner with those sitting on the opposite edge via the π system.[12–19,22] The nature of the interedge interaction depends on the width of the zigzag graphene nanoribbon, the presence of extra carriers, edge functionalization, and line defects.[4,13–17] Surface modification of a graphene sheet with intrinsically nonmagnetic atoms (often termed as addition) and functional groups (often termed as functionalization) has been identified as an alternative way to imprint magnetism in graphene; most prominent examples include graphane,[23–25] graphone,[26] and (reduced) graphene oxide.[27–29] Such materials show ferromagnetic ordering at low temperatures. However, its sustainability at room temperature is heavily questioned as the π-electron system of graphene is too weak to maintain magnetic interactions between induced localized moments at elevated temperatures; if such a behavior is experimentally observed, it is frequently attributed to the presence of impurities of transition metal origin, stemming from either the synthesis itself or sample handling. In the ferromagnetic state, the saturation magnetization of graphane, graphone, and (reduced) graphene oxide frequently ranges between ≈0.001 and ≈2.5 emu g^{-1}, strongly depending on the degree of stoichiometry, presence of internal defects, and level of oxidation.[23–30] High saturation magnetization has been reported for vertical graphenes grown from fat-like precursors reaching up to ≈8 emu g^{-1} in the low-temperature ferromagnetic state; such a strong magnetic behavior was explained in

Dr. J. Tuček, Dr. P. Błoński, M. Petr, Prof. M. Otyepka, Prof. R. Zbořil
Regional Centre of Advanced Technologies and Materials
Department of Physical Chemistry
Faculty of Science
Palacky University
Šlechtitelů 27, 783 71 Olomouc, Czech Republic
E-mail: radek.zboril@upol.cz
Dr. Z. Sofer, Dr. P. Šimek
Department of Inorganic Chemistry
University of Chemistry and Technology Prague
Technická 5, 166 28 Prague 6, Czech Republic
Prof. M. Pumera
Division of Chemistry and Biological Chemistry
School of Physical and Mathematical Sciences
Nanyang Technological University
637371, Singapore

DOI: 10.1002/adma.201600939

© 2016 WILEY-VCH Verlag GmbH & Co. KGaA, Weinheim

terms of formation of dense atomic vacancies, hydrogenation, and edge states.[31] Recently, —OH groups were identified as an effective sp^3-type candidate for inducing robust magnetic moments on the basal plane of the graphene sheet.[32]

The doping of foreign atoms of non *d*- and *f*-block origin into the crystal lattice of graphene offers an alternative strategy to induce magnetism in graphene, as demonstrated by both theoretical and experimental approach.[4,5] It is believed that the magnetic properties of doped graphene are governed by the chemical nature of the doping element, p- and/or n-type character of the doping element, and doping concentration.[5] Moreover, chemical addition may also co-occur if the concentration of the doping element is high (i.e., exceeds the percolation limit) and/or the chemical method is mild to induce graphitic substitution. Such addition produces adatoms situated above and below the graphene sheet, which may also generate localized spins. Up to now, doping of the graphene structure has been achieved with boron,[33,34] nitrogen,[34–37] fluorine,[20] and sulfur.[38] In the case of fluorine and boron substitution, paramagnetic centers with $S = 1/2$ were shown to emerge without any apparent establishment of a magnetically ordered state at low temperatures.[20,33] In contrast, the most pronounced magnetism reported so far for graphene-based and doped systems was observed for N-doped reduced graphene oxide, which showed a transition to the ferromagnetic state at a temperature below ≈101 K and saturation magnetization of ≈1.6 emu g^{-1} at low temperatures.[28] Recently, it was experimentally shown that introduction of nitrogen in the graphene lattice decreases the magnetization values compared to those of defected graphene.[36] Identical fashion in magnetization behavior was lately observed upon doping of graphene lattice with sulfur; weakening of the magnetic response and change in the type of magnetic ordering were explained in terms of saturation of dangling bonds by sulfur atoms and, hence, quenching of local magnetic moments induced by defects existing already in undoped graphenes.[39]

In this work, we report on unique magnetic properties induced in graphene by doping with sulfur. Importantly, the S-doped graphene with the highest achieved content (4.2 at%) showed strong ferromagnetic properties below ≈62 K with a saturation magnetization reaching ≈5.5 emu g^{-1}, which is among the highest values reported so far for any graphene-based system or even carbon-based (nano)material. Density functional theory computational data proved that sulfur doping induced a ferromagnetic regime only in a narrow concentration window (sulfur content: 4–6 at%) where the doping-induced paramagnetic centers begin to actively communicate via π-electron system. Moreover, it was theoretically confirmed that the observed magnetic ordering was solely due to the substitution effect (within the graphene lattice, C—S) as addition of sulfur to a graphene sheet (C—S—C) cannot promote evolution of magnetically ordered states, and hence self-sustainable magnetism, due to nonmagnetic C—S—C configurations. In particular, the theory shows that the gamma-thiothiapyrone motif of sulfur in the graphene lattice, as magnetically active configurations, is responsible for observed magnetic ordering at low temperatures. We believe that controlled sulfur doping represents a huge step toward developing graphene derivatives exhibiting self-sustainable magnetism even at room temperature.

To study the effect of sulfur on the magnetic properties of graphene, four samples differing in the sulfur concentration in the graphene lattice were prepared. These samples were synthesized by modified literature protocol based on the thermal treatment of graphite oxide (GO) in nitrogen exploiting H_2S as the sulfur source and reaction temperature as a key variable allowing the control of the sulfur content (for details, see the Supporting Information).[38] Besides, a blank sample, i.e., sample without sulfur doping (denoted as thermally reduced graphene oxide, TRGO), was also prepared by thermal reduction of graphite oxide in nitrogen atmosphere. In order to exclude the possible role of impurities of metals of 3*d* nature, which would affect and/or degrade the magnetic features of sulfur-doped graphenes, inductively coupled plasma mass spectrometry (ICP-MS) measurements were performed. The ICP-MS analysis (see Table S1, Supporting Information) confirms the presence of Fe, Co, Ni, and Mn as main magnetic elements but with negligible contents below 20 ppm. By using the known magnetic moments of the detected elements and their measured concentrations in the samples, it is feasible to calculate their contribution to the samples' magnetic response under a 1 kOe external magnetic field. The summed mass magnetic susceptibility of the metallic elements in the samples was determined to be on the order of 10^{-8} emu gOe^{-1}, which is several orders of magnitude lower than the measured mass magnetic susceptibility of S-doped graphene samples as discussed below. The contribution of ferromagnetic elements to the samples' mass magnetic susceptibility is negligible compared to the magnetic signal originating from the sulfur doping in the graphene samples.

Prior to magnetic investigation, to quantify the amount of C, O, and S and identify the types of the bonds among elements involved, X-ray photoelectron spectroscopy (XPS) was employed. For GO and TRGO samples, the survey XPS patterns show the exclusive presence of C and O (see Figure S1, Supporting Information); no traces of nitrogen were detected for TRGO, excluding thus possible sorption of nitrogen onto the surface of graphene sheets during reduction treatment of the GO precursor. The C 1s and O 1s high-resolution XPS patterns of GO and TRGO samples are typical for graphite/graphene oxide and thermally reduced graphene oxide; C 1s and O 1s XPS profiles of GO and TRGO differ only in the amount of oxygen functionalities (see Figure S2, Supporting Information).

The survey XPS patterns for the four S-doped graphene samples are shown in Figure S1 (Supporting Information). It was confirmed that all the four samples contained only C, O, and S, with peaks located at binding energies of ≈284.5, ≈534.0, and ≈167.0 eV typical for C 1s, O 1s, and S 2p states, respectively; there are no traces of nitrogen, potassium, and chlorine from the treated compounds. Moreover, impurities of magnetic nature (such as 3*d* elements like Fe, Co, Ni, and Mn) were not detected in the XPS spectra in accordance with their negligible contents derived from the ICP-MS measurements. Deeper analysis of the XPS spectra confirmed that the amount of sulfur in the prepared samples was ≈1.1, ≈2.1, ≈3.0, and ≈4.2 at%, respectively (Figure S1, Supporting Information). Thus, based on the content of sulfur, the S-doped samples are denoted below as $GS_{0.011}$, $GS_{0.021}$, $GS_{0.030}$, and $GS_{0.042}$. Besides six carbon interactions typically observed in thermally reduced graphene

© 2016 WILEY-VCH Verlag GmbH & Co. KGaA, Weinheim

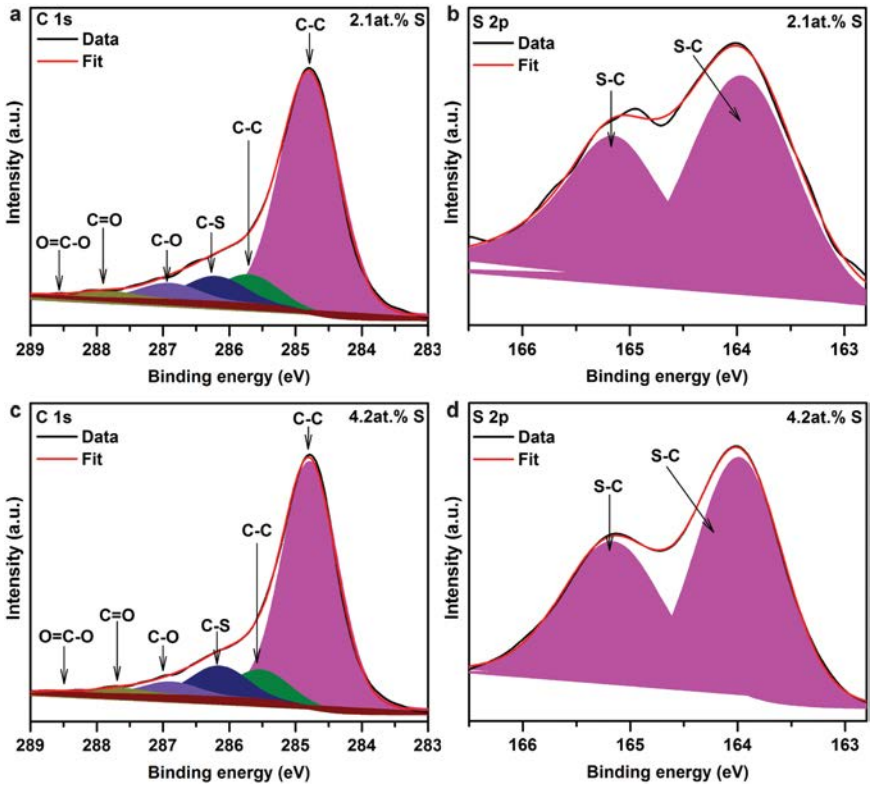


Figure 1. a,b) C 1s and S 2p high-resolution XPS spectra of the $GS_{0.021}$ sample and c,d) C 1s and S 2p high-resolution XPS spectra of the $GS_{0.042}$ sample showing identification of individual chemical bonds.

oxide, i.e., C—C (sp^2, 284.5 eV), C—C (defected, 285.7 eV), C—O (286.8 eV), C═O (288.0 eV), O—C═O (289.2 eV), and π–π (290.8 eV), all the four S-doped samples showed a C—S peak (286.5 eV) in the C 1s spectrum (see **Figure 1** and Figure S3, Supporting Information), implying structural incorporation of sulfur (i.e., graphitic substitution) into the graphene lattice. The lower binding energy of the C—S bond compared to that of the C—O bond can be explained by the higher electronegativity of oxygen. The C 1s spectra of all the four S-doped graphene samples differ only in the intensity of the C—S peak as expected reflecting different content of substituting sulfur. The S 2p spectra of the $GS_{0.011}$, $GS_{0.021}$, $GS_{0.030}$, and $GS_{0.042}$ system are identical featuring only the S—C bond (163.9 and 165.2 eV); the presence of the C—S—C bond was not witnessed in the C 1s and S 2p spectra of all the four S-doped graphene samples but cannot be definitely excluded as its peak can be masked by other more intense peaks. The O 1s high-resolution XPS patterns of all the four S-doped graphene samples were also identical to each other with only O═C (533.8 eV) and O—C (531.6 eV) bonds (see Figure S4, Supporting Information). Importantly, the total contents of oxygen in all the samples are quite comparable, the fact excluding the "magnetic effect" of oxygen on magnetic properties of sulfur doped graphenes.

The exclusive incorporation of sulfur into the graphene lattice was further supported by Raman spectra of four S-doped graphene samples (see Figure S5, Supporting Information). With an increase in the sulfur content, the D/G ratio dropped from 1.33 (TRGO) to 1.24, 1.19, 1.01, and 0.97 for $GS_{0.011}$, $GS_{0.021}$, $GS_{0.030}$, and $GS_{0.042}$, respectively, implying a decrease in the defects upon doping. If sulfur atoms would be added to the surface of graphene sheets, an increase in the D/G ratio should be observed.[38] Thus, a fall in the D/G ratio with sulfur content confirms the structural substitution of sulfur in the graphene lattice through C—S bonds, thus indirectly excluding the addition through C—S—C bonds. The presence of sulfur was also verified by chemical mapping (see Figure S6, Supporting Information); the $GS_{0.042}$ sample showed a more intense sulfur signal than that observed for the $GS_{0.021}$ sample. Moreover, the distribution of sulfur in the graphene lattice seems homogenous for both samples, thus excluding the potential clustering of sulfur atoms inside the graphene sheet.

Before experimental monitoring of the magnetic behavior of S-doped graphene samples, GO and TRGO systems were first magnetically assessed. In the case of the GO precursor, the temperature dependence of the mass magnetic susceptibility, χ_{mass}, featured three contributions, i.e., dominant diamagnetic and paramagnetic components and minor ferromagnetic response evidenced by a sign of a maximum at low temperatures (see Figure S7, Supporting Information). After subtracting the diamagnetic term, χ_{mass} can be, in the temperature interval from 50 to 300 K, well fitted (with statistical confidence at 99% level) with the Curie–Weiss law,

© 2016 WILEY-VCH Verlag GmbH & Co. KGaA, Weinheim

ADVANCED MATERIALS
www.advmat.de

Materials Views
www.MaterialsViews.com

i.e., $\chi_{mass} = C/(T - \theta)$, where θ is the Weiss temperature. The fitting gives $\theta \approx 48$ K which can be assigned to the Curie temperature, T_C. Thus, oxygen functionalities induce defects with emergence of localized magnetic moments which ferromagnetically order upon temperature decrease as already demonstrated earlier.[40] After thermal reduction of GO, ferromagnetic behavior is lost; TRGO showed only dominant diamagnetic and minor paramagnetic contribution (see Figure S7, Supporting Information). Hence, eliminating oxygen functionalities caused decrease in a number of localized magnetic moments in the graphene lattice and impossibility to establish/maintain magnetic ordering at low temperatures.

The temperature dependence of χ_{mass} for the $GS_{0.011}$, $GS_{0.021}$, and $GS_{0.030}$ sample closely followed (with statistical confidence at 99% level) the modified Curie law, i.e., $\chi_{mass} = C/T + \chi_d$, where C is the Curie constant, T is the temperature, and χ_d is the diamagnetic susceptibility. It was found that the magnetic response of all the three S-doped graphene systems was dominated by the diamagnetic contribution (see **Figure 2**). The increase in χ_{mass} at low temperatures implied the presence of paramagnetic centers with localized spins; besides sulfur substituting carbon in the graphene lattice, their emergence can be partly attributed to either residual amounts of oxygen or presence of vacancies or topological defects. However, their effects are expected to be minor compared to that connected with sulfur introduction. This is confirmed when subtracting the diamagnetic contribution as the paramagnetic term increases upon sulfur concentration in the graphene lattice (see insets in Figure 2); as Raman spectra clearly confirmed a decrease in the number of defects upon sulfur doping, presence of sulfur promoted formation of paramagnetic centers. However, the induced paramagnetic centers in the graphene lattice were distant from each other, and hence, no magnetic ordering was established down to 2 K. Thus, S-doped graphenes with a sulfur concentration of ≈1.1, ≈2.1, and ≈3.0 at% are nonmagnetic; however, the paramagnetic contribution enhances with a rise in sulfur content.

Interestingly, for the $GS_{0.042}$ sample, the temperature evolution of χ_{mass} could not be fitted with the modified Curie law; over the temperature range 70–300 K, the χ_{mass} profile closely followed the Curie–Weiss law (see **Figure 3**a). Thus, two main contributions to χ_{mass} were identified, i.e., paramagnetic and ferromagnetic behavior. Analysis of the χ_{mass} versus T dependence yielded $\theta \approx 62$ K, which can be assigned to T_C, indicating a transition from the paramagnetic state to the low-temperature ferromagnetic regime (Figure 3a). Evidently, below ≈62 K, localized spins ferromagnetically order with delocalized π electrons (of graphene itself and those supplied by S-doping, see below), acting as mediators of magnetic interactions among the paramagnetic centers. From ≈35 to ≈20 K, a slight decrease in χ_{mass} was observed, which can be explained by the presence of antiferromagnetically coupled spins, most probably favored by the distance between them. It is known that the type of interaction mediated by delocalized π electrons strongly depends on the distance between the localized magnetic moments, with oscillatory behavior between the ferromagnetic and antiferromagnetic regime. However, contrary to ferromagnetically behaving spins, the antiferromagnetic contribution is rather negligible and does not affect the overall magnetic response. On further lowering the temperature, the response from ferromagnetically coupled spins saturated and χ_{mass} increased (see Figure 3a) because some localized spins separated by a long distance behave in a paramagnetic manner independently of each other. In other words, the spins did not

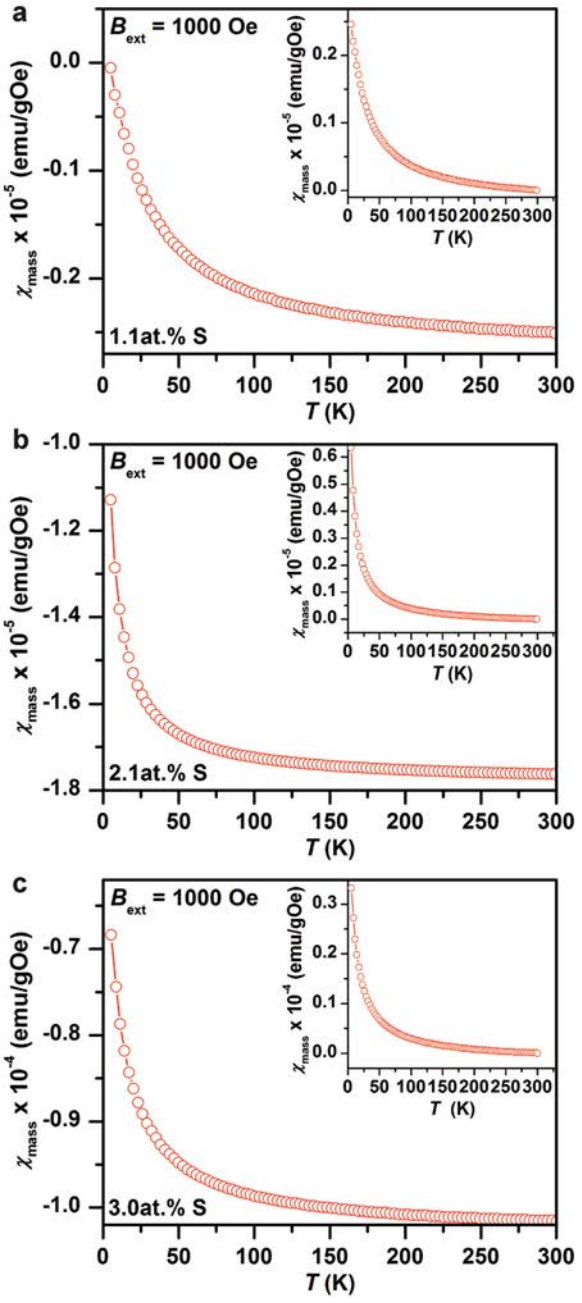


Figure 2. Temperature evolution of the mass susceptibility, χ_{mass}, of (a) $GS_{0.011}$, (b) $GS_{0.021}$, and (c) $GS_{0.030}$ sample recorded under an external magnetic field of 1 kOe. The insets show χ_{mass} versus T profiles after subtracting the diamagnetic term.

© 2016 WILEY-VCH Verlag GmbH & Co. KGaA, Weinheim

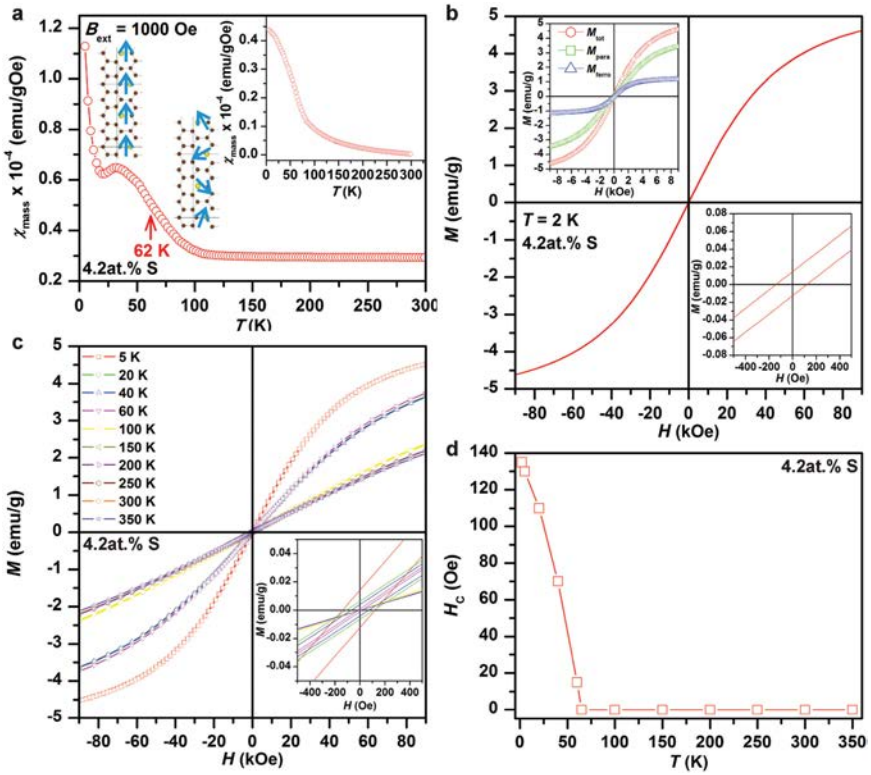


Figure 3. a) Temperature evolution of the mass susceptibility, χ_{mass}, of the $GS_{0.042}$ sample recorded under an external magnetic field of 1 kOe. The schematic inset shows ferromagnetic arrangement of localized spins inside the graphene lattice the interaction among which is mediated by π system and paramagnetic behavior at temperatures above ≈62 K. The inset in top right corner shows the ferromagnetic contribution derived from fitting of the χ_{mass} versus T curve. b) Hysteresis loop of the $GS_{0.042}$ sample, measured at a temperature of 2 K. The inset in the down right corner shows the behavior of the hysteresis loop around the origin with nonzero coercivity. The inset in the top left corner shows field-dependent profiles of magnetization for paramagnetic (M_{para}) and ferromagnetic (M_{ferro}) component. c) Hysteresis loops of the $GS_{0.042}$ sample, measured at various temperatures. d) Temperature evolution of the coercivity, H_C, of the $GS_{0.042}$ sample, derived from the recorded hysteresis loops.

form ordered magnetic clusters as the distance to other paramagnetic centers was too far, and thus magnetic interactions do not emerge. There may be several reasons for the evolution of such isolated paramagnetic centers, such as the presence of vacancies, defects of topological or edge nature, residual oxygen atoms, and separated spin sites generated by sulfur substitution. It should be stressed that the distribution of sulfur inside the graphene lattice does not need to be fully homogenous, thus allowing several possible C—S configurations/arrangements within one graphene sheet to evolve, when some of which are magnetic (giving rise to ferromagnetic and/or antiferromagnetic behavior) and others nonmagnetic (see theoretical calculations below). In order to assess the ferromagnetic response, the χ_{mass} versus T profile of the $GS_{0.042}$ sample was fitted assuming two contributions (neglecting the antiferromagnetic term), i.e., paramagnetic following the Curie law and ferromagnetic obeying Curie–Weiss law at high temperatures and Brillouin function at low temperatures within the mean field approximation (see inset in Figure 3a). The fit yields the angular momentum number $J \approx 1.4$ as an average value over all the S-doped graphene sheets in the $GS_{0.042}$ sample as the sheets can have different C—S configurations/arrangements with different net magnetic moments (see below) as already witnessed for N-doped graphene systems.[28]

The low-temperature ferromagnetic state of graphene doped with 4.2 at% of sulfur was further demonstrated by the field dependence of magnetization showing hysteresis behavior (see Figure 3b). The coercivity was found to be ≈135 Oe at 2 K, indicating emergence of magnetic anisotropy in the graphene lattice triggered by sulfur doping, and hence evolution of easy axes of magnetization inside the graphene sheet along which induced magnetic moments lie preferentially. On increasing the temperature, the coercivity falls to zero above ≈62 K (see Figure 3c,d) as expected when passing from the ferromagnetic to paramagnetic state; above ≈62 K, the isothermal magnetization curves lack hysteresis and resemble profiles typical of paramagnetic materials (see Figure 3c). More importantly, in accordance with the χ_{mass} versus T profile at low temperatures, the hysteresis loop at 2 K featured two parts, the first one originating from nonordered (isolated) paramagnetic centers and the second one stemming from ferromagnetically ordered paramagnetic centers. Following the mathematical procedure by Liu et al.[28] proposed for analyzing magnetic properties of N-doped graphene systems, it was possible to separate both

© 2016 WILEY-VCH Verlag GmbH & Co. KGaA, Weinheim

ADVANCED MATERIALS
www.advmat.de

Materials Views
www.MaterialsViews.com

contributions by employing the Brillouin function with $J \approx 1.4$ and assuming saturation character of the ferromagnetic component and mass portion of paramagnetic and ferromagnetic signal from χ_{mass} versus T curve (see inset in Figure 3b). The fitting yields a saturation magnetization of ≈1.2 emu g^{-1} and ≈4.3 emu g^{-1} for ferromagnetic and paramagnetic contribution, respectively. Such values of the saturation magnetization are among the highest reported so far among any carbon-based materials including graphene[31] and even among all reported *sp*-based systems (i.e., systems constituting of elements with only *s* and *p* orbitals). Indeed, in the ferromagnetic state, graphene with 4.2 at% of sulfur showed higher magnetization values than those observed for graphene derivatives such as graphane, graphone, doped graphenes, and graphene oxides (ranging from 0.001 to 2.5 emu g^{-1}), and other carbon nanoallotropes such as fullerenes, carbon nanotubes, and carbon dots (ranging from 0.0001 to 0.01 emu g^{-1}), securing its position among the magnetically strongest carbon-based systems known to date, with magnetism of *sp* nature (driven only by *s* and/or *p* electrons) and governed by defects. Based on the theoretical analysis presented below, it is speculated that upon further increase of sulfur concentration in the graphene lattice (up to ≈6.25 at%), the value of the saturation magnetization could further increase closely approaching ≈8 emu g^{-1}, a value reported for vertical graphenes, which are currently viewed as the magnetically strongest carbon-based systems.[31] Here, it should be stressed that indeed, sulfur atoms are embodied into the graphene lattice as a rise in the magnetization values is observed upon increase of sulfur doping; if sulfur atoms were simply added to the graphene sheets (i.e., as adatoms), they would saturate the dangling bonds and, hence, quench the magnetic moments induced by defects, resulting in a decrease in magnetization with potential alternation of the type of the magnetic state (from the ferromagnetic to paramagnetic or diamagnetic regime).[39] Such a manifestation is in line with theoretical predictions as discussed below.

To gain a deeper understanding of the unique magnetic behavior of S-doped graphenes, spin-polarized density-functional calculations were performed as theoretical methods based on density functional theory provide valuable information about the magnetic properties of graphene-based structures.[41–43] The substitutional doping was modeled by replacing carbon atoms in a graphene layer by sulfur atoms, considering doping concentrations between 1.0 and 14.6 at% at ≈1 at% (≈2 at%) intervals up to 4.2 at% (beyond 4.2 at%). Up to 8.3 at% of S, computational screening of all unique configurations was carried out, whereas beyond this threshold, only selected configurations were analyzed.

The magnetic properties varied significantly with sulfur concentration, as graphene doped up to 3.1 at% of sulfur (see Figure S8, Supporting Information) and above 6.25 at% were nonmagnetic and only structures with contents between 4.2 and 6.25 at% of sulfur provided ferromagnetic configurations. In the ferromagnetic structures, sulfur occupied positions in one sublattice, as shown for the most energetically stable ferromagnetic structure at 4.2 at% of sulfur with 0.5 μ_B magnetic moment per supercell (see **Figure 4**). Atomistic modeling identified the gamma-thiothiapyrone motif to be responsible for the observed magnetic behavior of S-doped graphene. The partial

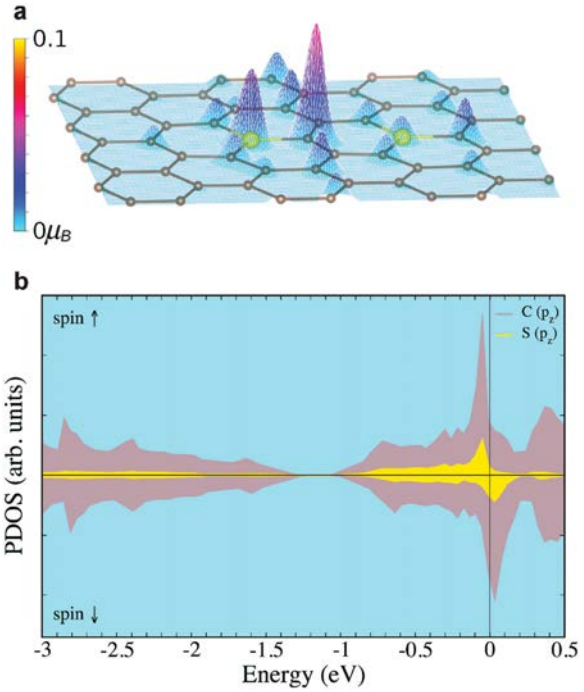


Figure 4. Computation results on graphene doped with sulfur at a concentration level of 4.2 at%: a) Structure of graphene doped by 4.2 at% of sulfur (represented by larger yellow spheres) superimposed on a 3D plot of the magnetic moment distribution within the supercell; b) The corresponding partial densities of states (PDOS).

density of states (PDOS) plot presented in Figure 4 shows that the S-doping gave rise to narrow peaks at the Fermi level for the majority and minority spin components of both the sulfur and carbon p_z orbitals. Putative electrons occupying these narrow bands cause itinerant (Stoner) magnetism with high Curie temperatures as argued by Edwards and Katsnelson.[44] The magnetic polarization was spread over an extended part of the cell and there was uneven spin-density distribution on the sulfur atoms (see Figure 4). Bader charge analysis showed larger charge transfer to graphene from S atoms carrying a larger magnetic moment (see Table S2, Supporting Information). Ground state structure of graphene doped by 4.2 at% of sulfur and possible ferromagnetically ordered graphene structure with a magnetic moment of 0.2 μ_B per supercell are shown in Figure S9, Supporting Information, together with the PDOS plots.

At 6.25 at% of sulfur, the S-doped graphene with the lowest ground state energy was magnetic with a total magnetic moment of 0.2 μ_B. Several other magnetic configurations with magnetic moment varying between 0.3 and 0.6 μ_B were found at higher energies by 0.05 to 0.36 eV with respect to the ground state structure. Substituting C by S atoms in the same sublattice led to ferromagnetic structures in which only one out of three sulfur atoms per supercell carried the magnetic moment (see **Figure 5** and Figure S10, Supporting Information). Bader charge analysis showed larger charge transfer from the spin-polarized S-atoms to graphene (see Table S2, Supporting Information).

© 2016 WILEY-VCH Verlag GmbH & Co. KGaA, Weinheim

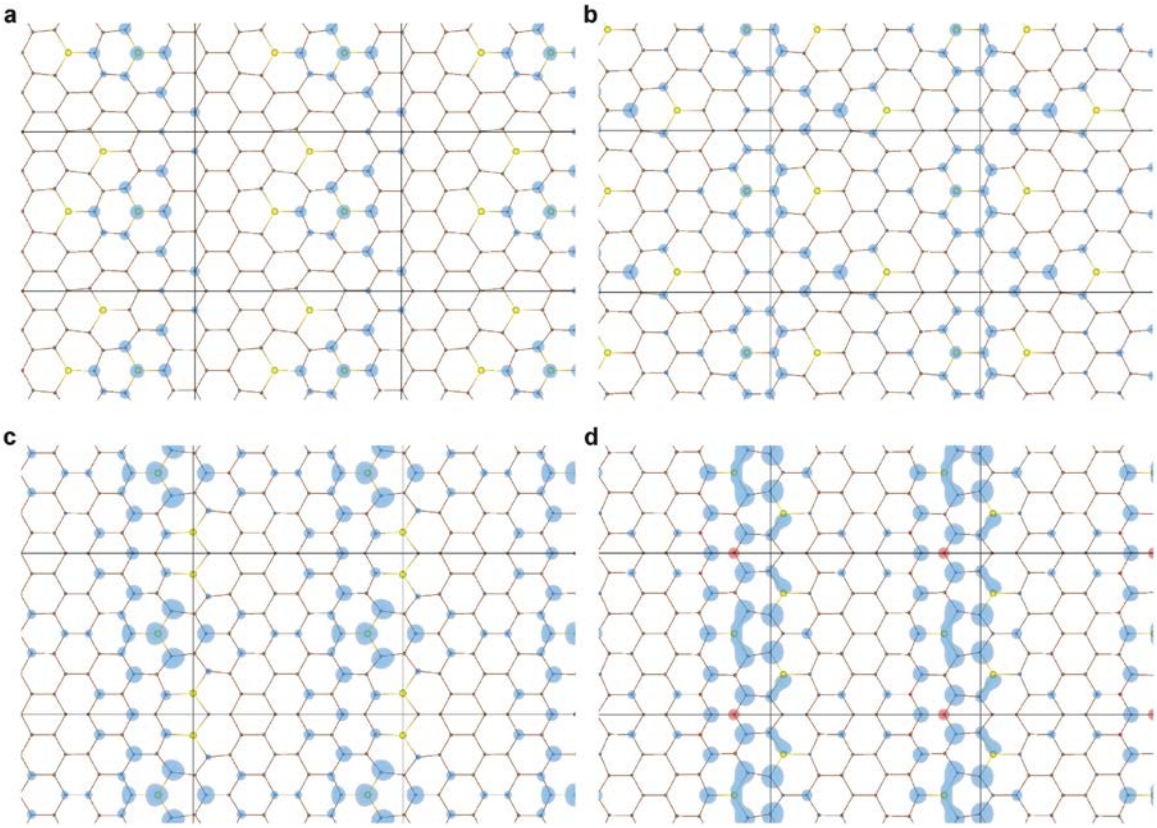


Figure 5. Top view of the magnetic structures obtained by doping graphene with 6.25 at% of sulfur (shown as yellow spheres): a) Ground state, b) 0.3 μ_B per supercell, c) 0.5 μ_B per supercell, and d) 0.6 μ_B per supercell. Positive (negative) spin densities are plotted in blue (red) for isosurfaces at 1×10^{-3} e Å^{-3}. Solid lines mark the computational cell. Partial densities of states (PDOS) for all configurations featured in panels (a)–(d) are shown in Figure S10 (Supporting Information).

To investigate whether magnetism in graphene can be induced by sulfur adatoms within the experimentally observed dopant concentrations, a large variety of structures resulting from both sulfur addition on a pristine graphene layer and simultaneous single sulfur atom addition and substitution were analyzed (see examples in Figure S11, Supporting Information). The additional doping did not induce magnetism in graphene even when starting from an initial magnetic guess configuration. Thus, we are confident that the magnetic ordering observed experimentally was solely related to the substitutional doping.

Substitution of carbon atoms by sulfur at concentrations between 1.0 and 6.25 at% did not induce any protrusion of the graphene layer, although in-plane atomic displacements were quite substantial. The distance between carbon atoms in the pristine graphene sheet was 1.424 Å, whereas the C—S bond lengths were longer by 15 to 20% at 1.0 to 6.25 at% of S, respectively. The remaining C—C distances in S-sharing hexagons deviated by up to 6% from the undoped-graphene value, but further away from the S dopant, the deviation did not exceed 3%. Needless to say that some configurations above 8 at% of S were not stable and led to unzipping of the doped graphene. The graphene honeycomb network broke down if S atoms replaced every second C atoms along the armchair direction (see Figure S12, Supporting Information). At an even higher concentration, i.e., 14.6 at%, replacing every second C by S in the hexagons along one of the cell-edges also led to graphene breakage (see Figure S12, Supporting Information). This observation may explain the experimental finding that the synthesis did not provide S-doped graphenes with higher sulfur concentrations and also agrees with recent data on N-doped graphenes.[45]

The theoretical calculations provided insights into the structure and stability of S-doped graphene and suggested that the magnetism was induced due to substitutional S atoms introducing delocalized electrons occupying narrow peaks at the Fermi level.[32] Owing to its two additional electrons compared to a carbon atom, sulfur acts as an n-type (electron-donating) dopant by increasing the number of electrons in the system. Due to doping, the Dirac point was shifted below the Fermi level and the S-doped graphenes became an n-type conductor. The enhanced magnetic properties of S-doped graphene may be attributed to the injection of two unpaired electrons by each S atom to the conducting band. These electrons are delocalized

© 2016 WILEY-VCH Verlag GmbH & Co. KGaA, Weinheim

among the S and C atoms, which contrasts with behavior of the N-doped graphenes having the injected electrons localized at the N sites, due to a high electronegativity of nitrogen.[45] This explains the higher magnetic response observed in the S-doped systems with respect to N-doped graphenes.[36] The sustainability of the magnetism at relatively high temperatures (≈62 K) can also be understood in terms of pumping the electrons from the substitutional sulfur into the graphene conduction band, strengthening the π electron system via which doping-induced paramagnetic centers interact. It should also be noted that an energy gap opens up around the Dirac point (see Table S2, Supporting Information), opening up possibilities for tuning the transport properties of graphene by adjusting the Dirac point position, e.g., by applying a gate voltage. It is also important to stress that beyond 6.25 at%, none of the dozens of examined structures exhibited spin-polarization and thus were nonmagnetic, even though the initial guess configurations were always magnetic.

In summary, we have experimentally and theoretically shown that sulfur doping in graphene induces paramagnetic centers with localized spins in the graphene lattice; these spin-carrying centers behave independently of each other if the concentration of substituting sulfur is below the threshold level (≈4.2 at%). Once the doping threshold is overcome (≈4.2 at% and above), magnetic interactions mediated by the π-electron system evolve between the substitution-generated paramagnetic centers, establishing a ferromagnetic state with a Curie temperature of ≈62 K (for ≈4.2 at%). The emergence of the ferromagnetic state at low temperatures was theoretically confirmed by computational study identifying magnetically active configurations (i.e., the gamma-thiothiapyrone motif of sulfur in the graphene lattice). At low temperatures, the observed saturation magnetization reaches ≈5.5 emu g^{-1} (ferromagnetic + paramagnetic contribution), which is among the highest values ever reported for a graphene-based system in which the magnetism is imprinted either by doping or functionalization or edge modification. The superior magnetic properties of the S-doped graphenes over the N-doped analogs can be explained in terms of injection of two unpaired electrons by each sulfur atom to the conducting band; these electrons are delocalized among the S and C atoms contrary to those injected by N-doping that are dominantly localized at the N sites. The pumping of electrons from substitutional sulfur to the graphene conduction band is also believed to promote the sustainability of the magnetism at relatively high temperatures (up to ≈62 K). Furthermore, the theory predicts that the observed magnetic behavior is solely due to a substitution mechanism; addition (or attachment) of sulfur atoms below and/or above the graphene sheet cannot promote self-sustainable magnetism. It was also shown that a rather narrow window of the doping element concentration in the graphene lattice (≈4–6 at% of sulfur) is open for viable induction of sustainable magnetism, indicating that doping studies should be carried out in a systematic manner. Finally, the magnetically ordered S-doped graphenes with a prominent saturation magnetization and coercivity offer viable highly conductive materials, which, if further functionalized, would display strengthened self-sustainable magnetism against thermal fluctuations with a huge potential in spintronics and other magnetic applications.

Supporting Information

Supporting Information is available from the Wiley Online Library or from the author.

Acknowledgements

Jiří Tuček and Piotr Błoński contributed equally to this work. The authors acknowledge the support from the Ministry of Education, Youth and Sports of the Czech Republic (LO1305) and the assistance provided by the Research Infrastructure NanoEnviCz, supported by the Ministry of Education, Youth and Sports of the Czech Republic under Project No. LM2015073. Piotr Błoński acknowledges the Palacky University institutional support. Michal Otyepka acknowledges the Neuron Fund for Support of Science and the Czech Science Foundation (P208/12/G016). Zdeněk Sofer and Petr Šimek were supported by the Czech Science Foundation (GACR No. 15-09001S) and the specific University research grant (MSMT No. 20/2016). Martin Petr acknowledges the support by the Internal Grant of the Palacky University in Olomouc, Czech Republic (IGA_PrF_2016_010). Martin Pumera acknowledges Tier 2 grant (MOE2013-T2-1-056) from Ministry of Education, Singapore. The authors thank Dr. Václav Ranc and Dr. Ondřej Tomanec (both from the Regional Centre of Advanced Technologies and Materials, Faculty of Science, Palacky University in Olomouc, Czech Republic) for performing the Raman spectroscopy measurements and microscopy (TEM/HRTEM and STEM/EDS chemical mapping) analyses, respectively.

Received: February 17, 2016
Revised: March 9, 2016
Published online: May 2, 2016

[1] K. S. Novoselov, A. K. Geim, S. V. Morozov, D. Jiang, Y. Zhang, S. V. Dubonos, I. V. Grigorieva, A. A. Firsov, *Science* **2004**, *306*, 666.
[2] C. L. Kane, E. J. Mele, *Phys. Rev. Lett.* **2005**, *95*, 226801.
[3] A. H. Castro Neto, F. Guinea, N. M. R. Peres, K. S. Novoselov, A. K. Geim, *Rev. Mod. Phys.* **2009**, *81*, 109.
[4] V. Georgakilas, J. A. Perman, J. Tucek, R. Zboril, *Chem. Rev.* **2015**, *115*, 4744.
[5] O. V. Yazyev, *Rep. Prog. Phys.* **2010**, *73*, 056501.
[6] M. Sepioni, R. R. Nair, S. Rablen, J. Narayanan, F. Tuna, R. Winpenny, A. K. Geim, I. V. Grigorieva, *Phys. Rev. Lett.* **2010**, *105*, 207205.
[7] M. Koshino, T. Ando, *Phys. Rev. B* **2007**, *75*, 235333.
[8] M. Koshino, T. Ando, *Phys. Rev. B* **2008**, *78*, 115313.
[9] B. Uchoa, V. N. Kotov, N. M. R. Peres, A. H. Castro Neto, *Phys. Rev. Lett.* **2008**, *101*, 026805.
[10] A. V. Krasheninnikov, P. O. Lehtinen, A. S. Foster, P. Pyykko, R. M. Nieminen, *Phys. Rev. Lett.* **2009**, *102*, 126807.
[11] R. R. Nair, I. L. Tsai, M. Sepioni, O. Lehtinen, J. Keinonen, A. V. Krasheninnikov, A. H. C. Neto, M. I. Katsnelson, A. K. Geim, I. V. Grigorieva, *Nat. Commun.* **2013**, *4*, 2010.
[12] J. Cervenka, M. I. Katsnelson, C. F. J. Flipse, *Nat. Phys.* **2009**, *5*, 840.
[13] M. Golor, C. Koop, T. C. Lang, S. Wessel, M. Schmidt, *Phys. Rev. Lett.* **2013**, *111*, 085504.
[14] Y. Li, W. Zhang, M. Morgenstern, R. Mazzarello, *Phys. Rev. Lett.* **2013**, *110*, 216804.
[15] O. V. Yazyev, *Phys. Rev. Lett.* **2008**, *101*, 037203.
[16] L. L. Chen, L. W. Guo, Z. L. Li, H. Zhang, J. J. Lin, J. Huang, S. F. Jin, X. L. Chen, *Sci. Rep.* **2013**, *3*, 2599.
[17] G. Z. Magda, X. Z. Jin, I. Hagymasi, P. Vancso, Z. Osvath, P. Nemes-Incze, C. Y. Hwang, L. P. Biro, L. Tapaszto, *Nature* **2014**, *514*, 608.

© 2016 WILEY-VCH Verlag GmbH & Co. KGaA, Weinheim

[18] K. Harigaya, T. Enoki, *Chem. Phys. Lett.* **2002**, *351*, 128.
[19] K. Kusakabe, M. Maruyama, *Phys. Rev. B* **2003**, *67*, 092406.
[20] R. R. Nair, M. Sepioni, I. L. Tsai, O. Lehtinen, J. Keinonen, A. V. Krasheninnikov, T. Thomson, A. K. Geim, I. V. Grigorieva, *Nat. Phys.* **2012**, *8*, 199.
[21] K. M. McCreary, A. G. Swartz, W. Han, J. Fabian, R. K. Kawakami, *Phys. Rev. Lett.* **2012**, *109*, 186604.
[22] M. Golor, S. Wessel, M. J. Schmidt, *Phys. Rev. Lett.* **2014**, *112*, 046601.
[23] A. Y. S. Eng, H. L. Poh, F. Sanek, M. Marysko, S. Matejkova, Z. Sofer, M. Pumera, *ACS Nano* **2013**, *7*, 5930.
[24] J. Berashevich, T. Chakraborty, *Nanotechnology* **2010**, *21*, 355201.
[25] C. K. Yang, *Carbon* **2010**, *48*, 3901.
[26] J. Zhou, Q. Wang, Q. Sun, X. S. Chen, Y. Kawazoe, P. Jena, *Nano Lett.* **2009**, *9*, 3867.
[27] G. Khurana, N. Kumar, R. K. Kotnala, T. Nautiyal, R. S. Katiyar, *Nanoscale* **2013**, *5*, 3346.
[28] Y. Liu, N. J. Tang, X. G. Wan, Q. Feng, M. Li, Q. H. Xu, F. C. Liu, Y. W. Du, *Sci. Rep.* **2013**, *3*, 2566.
[29] S. Qin, X. T. Guo, Y. Q. Cao, Z. H. Ni, Q. Y. Xu, *Carbon* **2014**, *78*, 559.
[30] T. Tang, F. C. Liu, Y. Liu, X. Y. Li, Q. H. Xu, Q. Feng, N. J. Tang, Y. W. Du, *Appl. Phys. Lett.* **2014**, *104*, 123104.
[31] D. H. Seo, Z. J. Yue, X. L. Wang, I. Levchenko, S. L. Kumar, S. X. Douc, K. Ostrikov, *Chem. Commun.* **2013**, *49*, 11635.
[32] T. Tang, N. J. Tang, Y. P. Zheng, X. G. Wan, Y. Liu, F. C. Liu, Q. H. Xu, Y. W. Du, *Sci. Rep.* **2015**, *5*, 8448.
[33] L. A. Ma, H. Hu, L. Y. Zhu, J. L. Wang, *J. Phys. Chem. C* **2011**, *115*, 6195.
[34] S. S. Kim, H. S. Kim, H. S. Kim, Y. H. Kim, *Carbon* **2015**, *81*, 339.
[35] Y. Liu, Q. Feng, N. J. Tang, X. G. Wan, F. C. Liu, L. Y. Lv, Y. W. Du, *Carbon* **2013**, *60*, 549.
[36] Y. Ito, C. Christodoulou, M. V. Nardi, N. Koch, M. Klaeui, H. Sachdev, K. Muellen, *J. Am. Chem. Soc.* **2015**, *137*, 7678.
[37] H. C. Wu, M. Abid, Y. C. Wu, C. O. Coileain, A. Syrlybekov, J. F. Han, C. L. Heng, H. J. Liu, M. Abid, I. Shvets, *ACS Nano* **2015**, *9*, 7207.
[38] H. L. Poh, P. Simek, Z. Sofer, M. Pumera, *ACS Nano* **2013**, *7*, 5262.
[39] J. Zhu, H. Park, R. Podila, A. Wadehra, P. Ayala, L. Oliveira, J. Hea, A. A. Zakhidov, A. Howard, J. Wilkins, A. M. Rao, *J. Magn. Magn. Mater.* **2016**, *401*, 70.
[40] N. Liaros, J. Tucek, K. Dimos, A. Bakandritsos, K. S. Andrikopoulos, D. Gournis, R. Zboril, S. Couris, *Nanoscale* **2016**, *8*, 2908.
[41] J. Zhou, Q. Wang, Q. Sun, P. Jena, *Phys. Rev. B* **2011**, *84*, 081402(R).
[42] X. W. Li, Q. Wang, *Phys. Chem. Chem. Phys.* **2012**, *14*, 2065.
[43] X. W. Li, Q. Wang, P. Jena, *J. Phys. Chem. C* **2011**, *115*, 19621.
[44] D. M. Edwards, M. I. Katsnelson, *J. Phys.: Condens. Matter* **2006**, *18*, 7209.
[45] V. V. Chaban, O. V. Prezhdo, *J. Am. Chem. Soc.* **2015**, *137*, 11688.

© 2016 WILEY-VCH Verlag GmbH & Co. KGaA, Weinheim

This is an open access article published under an ACS AuthorChoice License, which permits copying and redistribution of the article or any adaptations for non-commercial purposes.

JACS
JOURNAL OF THE AMERICAN CHEMICAL SOCIETY

Article

pubs.acs.org/JACS

Doping with Graphitic Nitrogen Triggers Ferromagnetism in Graphene

Piotr Błoński,[†,#] Jiří Tuček,[†,#] Zdeněk Sofer,[§] Vlastimil Mazánek,[§] Martin Petr,[†] Martin Pumera,[‡] Michal Otyepka,[*,†] and Radek Zbořil[*,†]

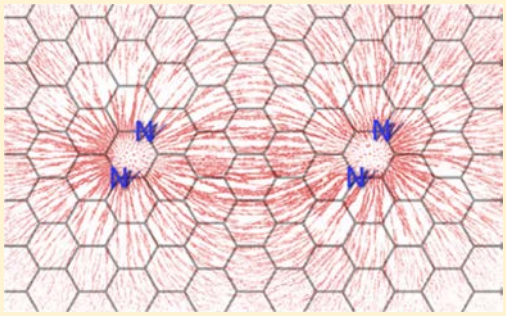
[†]Regional Centre of Advanced Technologies and Materials, Department of Physical Chemistry, Faculty of Science, Palacký University in Olomouc, 17. listopadu 1192/12, 771 46 Olomouc, Czech Republic

[§]Department of Inorganic Chemistry, University of Chemistry and Technology Prague, Technická 5, 166 28 Prague 6, Czech Republic

[‡]Division of Chemistry & Biological Chemistry, School of Physical and Mathematical Sciences, Nanyang Technological University, 637371 Singapore

Supporting Information

ABSTRACT: Nitrogen doping opens possibilities for tailoring the electronic properties and band gap of graphene toward its applications, e.g., in spintronics and optoelectronics. One major obstacle is development of magnetically active N-doped graphene with spin-polarized conductive behavior. However, the effect of nitrogen on the magnetic properties of graphene has so far only been addressed theoretically, and triggering of magnetism through N-doping has not yet been proved experimentally, except for systems containing a high amount of oxygen and thus decreased conductivity. Here, we report the first example of ferromagnetic graphene achieved by controlled doping with graphitic, pyridinic, and chemisorbed nitrogen. The magnetic properties were found to depend strongly on both the nitrogen concentration and type of structural N-motifs generated in the host lattice. Graphenes doped below 5 at. % of nitrogen were nonmagnetic; however, once doped at 5.1 at. % of nitrogen, N-doped graphene exhibited transition to a ferromagnetic state at ∼69 K and displayed a saturation magnetization reaching 1.09 emu/g. Theoretical calculations were used to elucidate the effects of individual chemical forms of nitrogen on magnetic properties. Results showed that magnetic effects were triggered by graphitic nitrogen, whereas pyridinic and chemisorbed nitrogen contributed much less to the overall ferromagnetic ground state. Calculations further proved the existence of exchange coupling among the paramagnetic centers mediated by the conduction electrons.



INTRODUCTION

The successful isolation of individual layers of graphene in 2004[1] has triggered an intense interest in its unique structural and electronic properties.[2] A very high carrier mobility along with weak spin−orbit and hyperfine interactions predestinates graphene as a promising material for spintronics, mainly if magnetic ordering can be introduced.[3] However, due to the delocalized π bonding network, ideal graphene is intrinsically nonmagnetic. Therefore, developing effective methods for synthesizing ferromagnetic (FM) graphene with high magnetization is vital for applications in novel spintronic devices combining charge and spin manipulation. A number of factors including atomic vacancies, zigzag edges, sp^3 functionalization, and chemical doping of foreign atoms can induce localized magnetic moments in graphene, which are indispensable for the existence of magnetic ordering.[4−10] Among these strategies, doping of the graphene lattice with noncarbon atoms has been identified as a promising approach for imprinting magnetic ordering into graphene while preserving/enhancing its electric/optical properties, as desirable for spintronic, optoelectronic, and magnetooptical applications.

Substitutional doping of graphene by light elements has recently attracted much attention (see, e.g., refs 11−14). In particular, nitrogen doping of the graphene lattice has been extensively studied, aimed at tuning the graphene electronic features, and hence its physical properties, in order to meet the requirements of a given application. N-doped graphenes have been tested as active materials for Li-ion batteries,[15] fuel cells,[12] field-effect transistors,[16] ultra- and supercapacitors,[17,18] and in the fields of photocatalysis[19] and electrochemical biosensing.[20] Chaban and Prezhdo have argued[21] that graphene structures containing 1/3 of nitrogen atoms or less should be stable up to 1000 K provided N−N bonds, which impair the stability, are not formed. Having similar atomic size and one additional electron compared to a carbon atom, nitrogen acts as an *n*-type

Received: December 16, 2016
Published: January 23, 2017

Downloaded via PALACKY UNIV on March 28, 2019 at 12:02:46 (UTC).
See https://pubs.acs.org/sharingguidelines for options on how to legitimately share published articles.

© 2017 American Chemical Society

DOI: 10.1021/jacs.6b12934
J. Am. Chem. Soc. 2017, 139, 3171−3180

(electron-donating) dopant by increasing the number of electrons when substituted into the graphene lattice, thus affecting the graphene electric conductivity. The substitution of carbon by nitrogen atoms in the graphene lattice necessarily leads to changes in the electronic density of states, and graphitic nitrogen can provide π electrons close to the Fermi level of graphene. If the itinerant electrons occupy narrow bands at the Fermi level, Stoner magnetism can emerge, as recently shown for graphene doped with sulfur.[22] Indeed, it has been theoretically proposed[9] that depending on the concentration and packing geometry of doping nitrogen atoms, it is possible to induce a magnetic response in graphene. However, the physical mechanism governing the emergence of magnetically ordered structures was not discussed. Until now, all the experimental attempts to imprint magnetism into graphene through N-doping have failed. Recently, a detailed theoretical and experimental magnetic study revealed that introduction of pyrrolic nitrogen into the graphene lattice decreases the magnetization values compared to those observed for defective graphene.[10] In contrast, pyrrolic nitrogen (at a concentration of 6.02 at. %) was identified to enhance ferromagnetism in highly oxidized graphene (i.e., graphene oxide) synthesized via hydrothermal reaction.[23] FM behavior has also been reported in other nitrogen-doped graphene oxide systems.[24] However, N-doped graphene oxides are unsatisfactory because a high amount of oxygen (sp^3 functionalization) is regarded as a dominant source of magnetism, overwhelming the effects of nitrogen doping itself. Moreover, oxygen-containing functional groups drastically reduce the electric conductivity of graphene—the main prerequisite for spintronic technologies. Thus, development of FM N-doped graphene with negligible oxygen content and elucidation of the effect of various nitrogen configurations (pyrrolic, pyridinic, graphitic, chemisorbed) remains a key challenge in the fields of nanotechnologies, magnetism, and spintronics.[10,25,26]

In this work, we first report the emergence of a magnetically ordered state in graphene doped solely with nitrogen. When the substitutional level exceeded ~5 at. % of nitrogen, the doping-induced paramagnetic centers commenced to interact magnetically, resulting in establishment of FM ordering at temperatures below ~69 K. In the FM state, the saturation magnetization reached ~1.09 emu/g, which is among the highest values reported so far for doped graphene-based systems. DFT calculations demonstrated that graphitic nitrogen was dominantly responsible for evolution of the magnetically active configurations. In contrast, pyridinic and chemisorbed nitrogen had a considerably lower effect on imprinting the magnetism into graphene. This finding opens possibilities for an extensive research in spintronic and magnetooptical technologies based on graphitic N-doped graphene.

EXPERIMENTAL SECTION

Materials. Graphite microparticles (2−15 μm, 99.9995%, Alfa Aesar) were used for all syntheses. Sulfuric acid (98%), nitric acid (68%), potassium chlorate (99%), hydrochloric acid (37%), silver nitrate (99.5%), and barium nitrate (99.5%) were obtained from Penta, Czech Republic. Nitrogen (99.9999% purity) and ammonia (99.9995% purity) were obtained from SIAD, Czech Republic.

Synthesis of Graphite Oxide. Graphite oxide was prepared according to the Hofmann method. Briefly, sulfuric acid (98%, 87.5 mL) and nitric acid (68%, 27 mL) were added to a reaction flask (Pyrex beaker with thermometer) containing a magnetic stir bar. The mixture was cooled by immersion in an ice bath for 30 min. Graphite (5 g) was then added to the mixture under vigorous stirring and, keeping the reaction flask in the ice bath, potassium chlorate (55 g) was slowly added. After a complete dissolution of potassium chlorate, the reaction flask was loosely capped to allow the escape of gas evolved and the mixture was continuously stirred for 96 h at room temperature. The mixture was poured into 3 L of deionized water and decanted. The obtained graphene oxide was then redispersed in HCl solution (5%, 3 L) to remove sulfate ions and repeatedly centrifuged and redispersed in deionized water until a negative reaction on chloride and sulfate ions with silver and barium nitrate was achieved. The resulting graphite oxide was dried in a vacuum oven at 50 °C for 48 h.

Synthesis of N-Doped Graphenes and Undoped Graphene. Nitrogen-doped graphenes were prepared by combined exfoliation and reduction of graphite oxide in an ammonia atmosphere. Briefly, 100 mg of graphite oxide was placed inside a quartz glass capsule connected to a magnetic manipulator and mounted in a horizontal quartz glass reactor. The reactor was repeatedly evacuated and flushed with nitrogen followed by ammonia. Subsequently, the sample was inserted in the hot zone of the reactor while the ammonia flow was kept at 1000 mL min^{-1} and the pressure was 100 kPa. The temperature of the sample was held constantly for 12 min at 400, 600 or 800 °C. After removal from the hot zone of the reactor, the sample was cooled in an ammonia atmosphere. The reactor was flushed with nitrogen before sample removal. The $GN_{0.015}$ sample was prepared at 400 °C, $GN_{0.033}$ sample was prepared at 600 °C, and $GN_{0.051}$ sample was prepared at 800 °C; the subscript reflects the level of nitrogen in the respective sample as identified from the analysis of the respective survey X-ray photoelectron spectroscopy patterns. Importantly, the oxygen content was below 4 at. % in all the samples studied. Compared to thermally reduced graphene oxide (TRGO), used as a blank undoped sample, a slight increase in the oxygen content can be explained in terms of competing processes of nitrogen incorporation and reduction of graphite oxide.

TRGO sample was prepared at 800 °C by a similar procedure using only nitrogen (1000 mL min^{-1}) as an exfoliating atmosphere.

Characterization Techniques. The residual metal content in the TRGO and N-doped graphene samples was analyzed by inductively coupled plasma mass spectrometry (ICP-MS). An exact amount of sample (10 mg) was immersed in concentrated nitric acid (≥99.999% trace metals basis) and heated for 2 h at 100 °C. Afterward, the mixture was transferred into a 10 mL volumetric flask, diluted with water and any undissolved graphene was separated using a 200 nm Millipore filter. The measured concentration of metals in the solution was recalculated to the amount in the tested sample (analogically, diluted nitric acid was used as a blank).

The atomic percent of C, O, and N, and types of bonds were assessed by X-ray photoelectron spectroscopy (XPS), employing a PHI 5000 VersaProbe II XPS system (Physical Electronics) equipped with a monochromatic Al K_α source (15 kV, 50 W) with a photon energy of 1486.7 eV. Dual beam charge compensation was used for all the measurements. All the XPS patterns were measured in a vacuum of 1.4×10^{-7} Pa and at room temperature (22 °C). For high resolution XPS patterns, a pass energy of 23.500 eV and step size of 0.200 eV were used. XPS patterns were evaluated with a MultiPak (Ulvac, PHI, Inc.) software. All binding energy values were referenced to the C 1s peak at 284.80 eV.

Raman spectra were acquired using a DXR Raman spectroscope (Thermo Scientific, U.S.A.) equipped with a laser operating at a wavelength of 633 nm. The respective sample was first deposited on a glass platform and the excitation laser was focused on its surface. Experimental parameters were tuned to maximize the respective analytic signal. The laser power on the sample was set to 5 mW and the exposition time was 20 s. Each measured Raman spectrum was an average of 16 experimental microscans.

Thermogravimetric analysis (TGA) and evolved gas analysis (EGA) curves were recorded using a Netzsch STA 449C Jupiter system with an adapted QMS 403C Aëolos quadrupole mass spectrometer. TGA/EGA measurements were performed in an open α-Al_2O_3 crucible under an argon atmosphere (80 cm^3 min^{-1}). A temperature program from 40 to 1000 °C with a heating rate of 5 K min^{-1} was used.

DOI: 10.1021/jacs.6b12934
J. Am. Chem. Soc. 2017, 139, 3171−3180

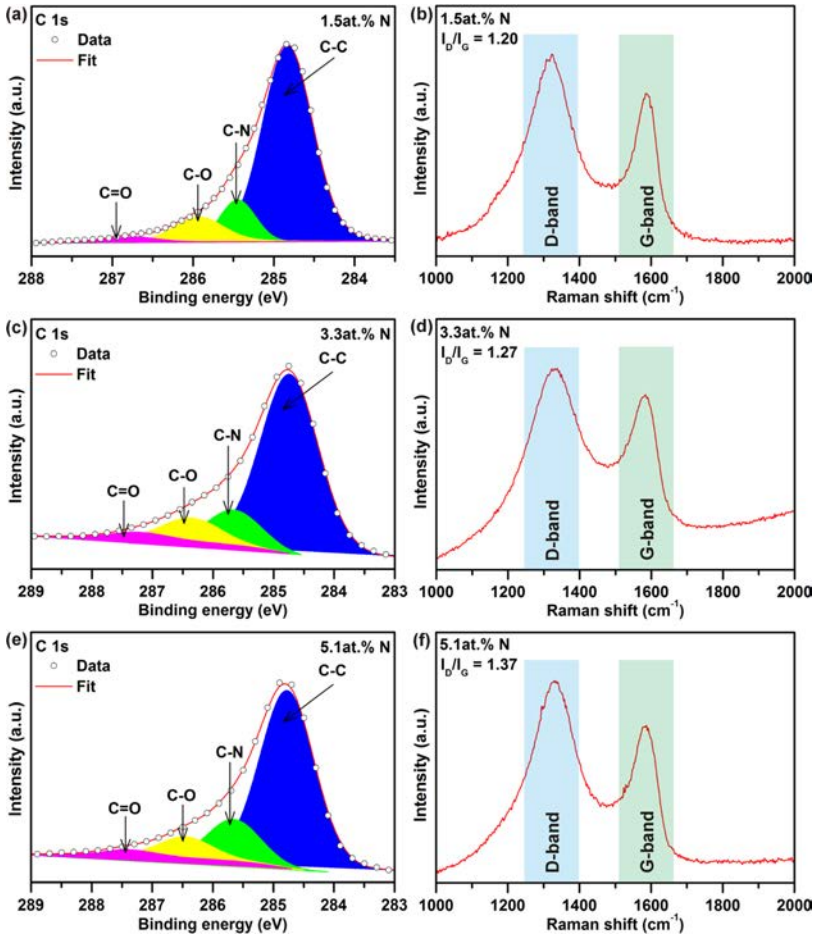


Figure 1. High-resolution C 1s XPS patterns of the (a) $GN_{0.015}$, (c) $GN_{0.033}$, (e) and $GN_{0.051}$ sample with bonds indicated. Raman spectra of the (b) $GN_{0.015}$, (d) $GN_{0.033}$, and (f) $GN_{0.051}$ sample with the I_D/I_G ratio indicated.

Magnetization measurements of the TRGO and N-doped graphene samples were performed using a physical property measurement system (PPMS) equipped with a vibrating sample magnetometer (VSM) from Quantum Design, U.S.A. Hysteresis loops were measured over the temperature range from 5 to 300 K and under static external magnetic fields ranging from −50 to +50 kOe. Temperature profiles of the mass magnetic susceptibility, χ_{mass}, were recorded in a sweep mode over a temperature range from 5 to 300 K in a field of 1 kOe after cooling in a field of 1 kOe. Magnetization values were corrected assuming the response of the sample holder, sample capsule, and respective Pascal constants.

Computational Details. Atomistic calculations were performed using a spin-polarized density functional theory (DFT) and projected augmented wave potentials (PAW) representing atomic cores as implemented in the Vienna ab initio simulation package (VASP).[27−29] Electronic exchange and correlation effects were treated by using the Perdew, Burke, and Ernzerhof (PBE)[30] generalized-gradient approximation (GGA) with a plane wave cutoff of 600 eV. Brillouin zone integrations were performed with a 6 × 6 × 1 Γ point-centered Monkhorst−Pack *k*-point mesh per conventional 4 × 3 rectangular cell (structure and cell optimization). The electronic density of states was calculated using the tetrahedron method[31] with a 21 × 21 × 1 *k*-point mesh. Partitioning of the ground state electronic density into contributions attributed to the different atoms was performed exploiting the Bader analysis.[32−34] Total magnetic moments were calculated from the difference between the number of electrons in occupied majority- and minority-spin states. Local magnetic moments were calculated by projecting the plane-wave components of all the occupied eigenstates onto spherical waves inside an atomic sphere and integrating the resulting local density of states.

A full structural optimization was performed using a quasi-Newton algorithm until the residual atomic forces were lower than 25 meV $Å^{-1}$. Simultaneously, the electronic and magnetic degrees of freedom were converged to an energy of less than 10^{-6} eV. The stability of the reported configurations was analyzed in terms of the formation energy, E_f, of the N-doped complexes using the formula given as $E_f = 1/n[E_{dpd} - E_{graph} + n(\mu_C - \mu_N)]$, where E_{dpd} and E_{graph} stand for the total energies of the doped and pristine graphene sheet, respectively, μ_C and μ_N are the chemical potentials of C and N atoms, respectively (here, approximated by the atomic energies of C and N), and n is the number of substituted atoms. A positive E_f indicates that the doping process is endothermic, although it does not hinder the formation of thermodynamically stable complexes.

The adsorption energy (E_{ad}) per N atom (n = 1 and 2) on a pristine layer was calculated as the total energy difference between the energy of an adatom-graphene complex, $E_{N/graph}$, a clean graphene layer, E_{graph}, and an isolated N atom in the gas-phase, E_N, i.e., $E_{ad} = 1/n(E_{N/graph} - E_{graph} - nE_N)$. Here, a negative E_{ad} indicates stable structures. Similarly, the adsorption energy of on-surface nitrogen on N-doped graphene was calculated as the total energy difference between the energy of a

DOI: 10.1021/jacs.6b12934
J. Am. Chem. Soc. 2017, 139, 3171−3180

doped graphene with an adatom, $E_{N/dpd}$, a doped graphene sheet, E_{dpd}, and a gas-phase N atom, i.e., $E_{ad} = E_{N/dpd} - E_{dpd} - E_N$.

RESULTS AND DISCUSSION

To study the role of N-doping on imprinting magnetic features into graphene, three samples differing in nitrogen content were prepared; the level of doping was solely controlled by the temperature, while all other synthetic parameters were kept constant. The TRGO sample was synthesized as a reference blank sample for which no source of nitrogen (i.e., ammonia atmosphere) was used during the thermal reduction of graphite oxide. The reduction process was found to be highly efficient, as evident from the very low content of oxygen (1 at. %, see the survey and high-resolution C 1s XPS pattern in Figure S1a,b in Supporting Information). The paramagnetic/FM response of graphene evolved due to defects and/or functionalization is of several orders of magnitude lower compared to that of 3*d*-block metals, such as iron, cobalt, nickel, and manganese. Hence, the results of magnetization measurements may be incorrectly interpreted if these "strong" magnetic elements are present in the system as a consequence of using reactants containing 3*d*-block metals and/or the sample handling.[35] Thus, ICP-MS was employed to quantify the presence of 3*d* metal impurities and exclude their effect on the magnetic properties of N-doped graphenes. The total concentration of Fe, Ni, Co, and Mn, regarded as the main magnetic impurities in TRGO and N-doped graphene samples, was below 10 ppm (see Table S1 in Supporting Information). Taking into account the determined concentrations and magnetic moments of the metal impurities, the total χ_{mass} of Fe, Ni, Co, and Mn was estimated to be of the order of 10^{-8} emu g^{-1} Oe^{-1} at 0 K and in a 1 kOe field. As χ_{mass} values for TRGO and N-doped graphene systems reached orders from 10^{-4} down to 10^{-6} emu g^{-1} Oe^{-1} in a 1 kOe field (see below), the contribution of Fe, Ni, Co, and Mn to the samples' χ_{mass} was assumed to be negligible in measurements of temperature evolution of χ_{mass} and hysteresis loops, thus definitely not overshadowing the magnetic properties of graphene induced solely by nitrogen doping.

Doping of graphene with nitrogen was monitored by XPS and Raman spectroscopy. In survey XPS patterns recorded for N-doped graphene samples, peaks belonging to C, N, and O were clearly observed (see Figure S2 and Table S2 in Supporting Information). The content of nitrogen was found to increase progressively with the temperature at which the thermal reduction of graphite oxide in the presence of ammonia was conducted (i.e., 400 °C, 1.5 at. % of N; 600 °C, 3.3 at. % of N; 800 °C, 5.1 at. % of N). The presence of nitrogen was further evidenced in the high-resolution C 1s XPS profile, which showed the emergence of a peak at a binding energy of around 285.5 eV corresponding to the C−N bond (see Figure 1a,c,e).[25] The C−N spectral component increased in area with the level of N-doping. A small shift in the maximum of the C−N peak witnessed for the three N-doped graphene samples can be explained in terms of impossibility to distinguish differently coordinated nitrogen atoms with carbon atoms in graphene with similar binding energy values in the C 1s domain and the significant overlap of the C−N and C−O spectral components. High-resolution N 1s XPS patterns of N-doped graphene samples (see Figure 2 and Figure S3 and Table S3 in Supporting Information) showed three distinct peaks corresponding to nitrogen in different configurations inside a graphene lattice or attached covalently to a graphene sheet (see Figure 3), i.e., pyridinic nitrogen (at ∼398.3 to ∼398.5

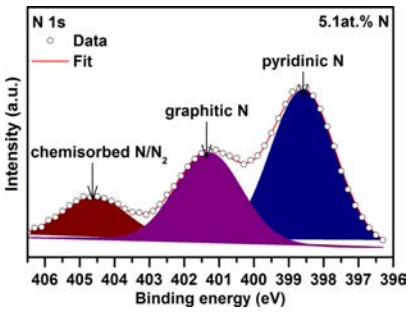


Figure 2. High-resolution N 1s XPS pattern of the $GN_{0.051}$ sample with peaks assigned to differently coordinated nitrogen.

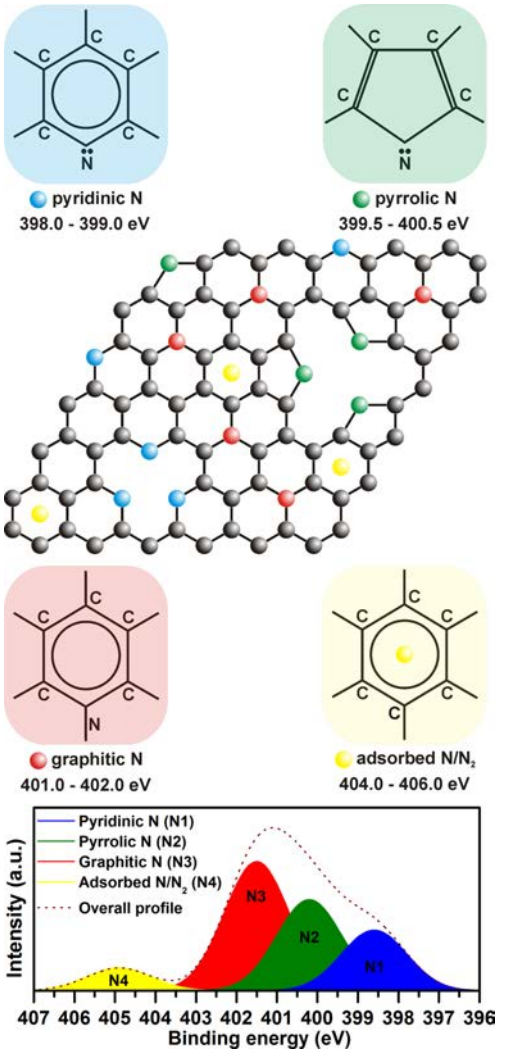


Figure 3. Scheme showing different bonding configurations of nitrogen in N-doped graphene and corresponding peaks in a simulated high-resolution N 1s XPS pattern.

DOI: 10.1021/jacs.6b12934
J. Am. Chem. Soc. 2017, 139, 3171−3180

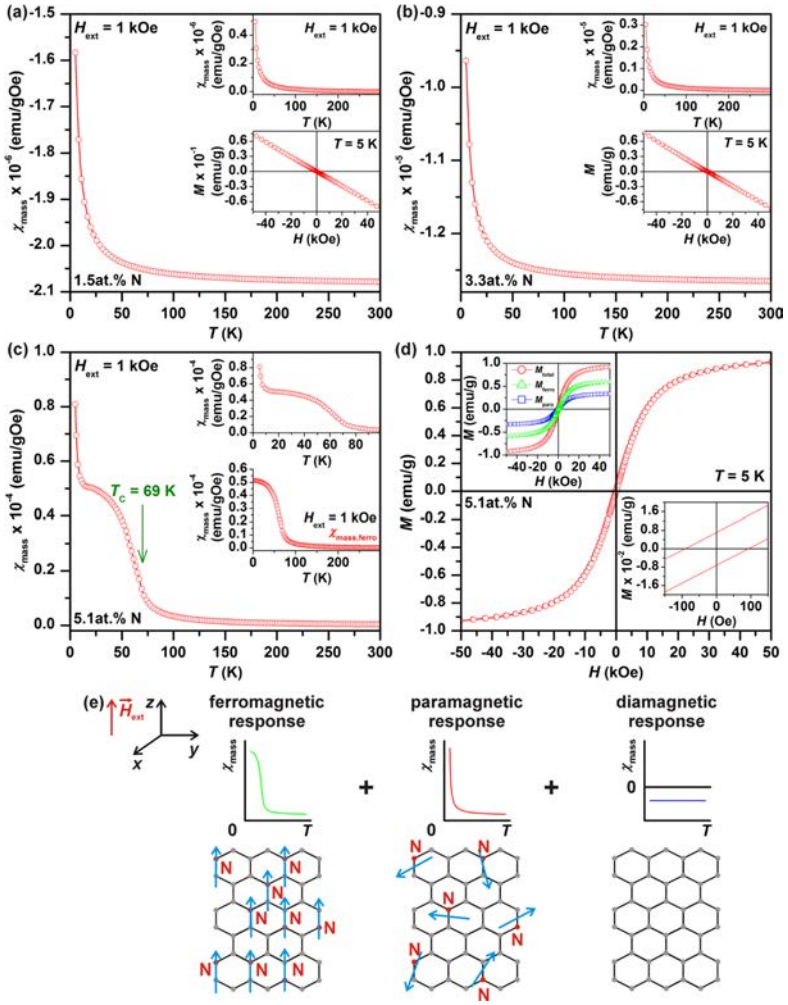


Figure 4. Temperature evolution of the mass magnetic susceptibility, χ_{mass}, of the (a) $GN_{0.015}$ and (b) $GN_{0.033}$ sample recorded under an external magnetic field of 1 kOe. The insets in panel (a) and (b) show the temperature profile of χ_{mass} after subtraction of the diamagnetic component and behavior of the 5 K hysteresis loop of the $GN_{0.015}$ and $GN_{0.033}$ sample, respectively. (c) Temperature evolution of χ_{mass} for the $GN_{0.051}$ sample recorded under an external magnetic field of 1 kOe with the Curie temperature, T_C, indicated. The insets show the trend of χ_{mass} at low temperatures and the temperature profile of the FM contribution, $\chi_{mass,ferro}$, derived from fitting the measured χ_{mass}. (d) Hysteresis loop of the $GN_{0.051}$ sample measured at a temperature of 5 K. The insets show the behavior of the hysteresis loop around the origin with the coercivity marked and field-dependent profiles of magnetization for the ferromagnetic, M_{ferro}, and paramagnetic, M_{para}, component derived from fitting the measured isothermal magnetization curve. (e) Scheme showing different magnetic fractions in the $GN_{0.051}$ sample and their respective profiles of χ_{mass}.

eV), graphitic nitrogen (at ∼401.0 to ∼401.5 eV), and chemisorbed N/N_2 (at ∼404.5 to ∼405.5 eV). In contrast, no traces of pyrrolic nitrogen, usually present at ∼400.0 eV, were observed (compare the high-resolution N 1s XPS patterns shown in Figure 2 and Figure S3 in Supporting Information with Figure 3).[36] The pyridinic and graphitic nitrogen were viewed as nitrogen incorporated inside the graphene lattice, whereas chemisorbed N/N_2 was viewed as nitrogen adsorbed as adatoms. The presence of N/N_2 was further confirmed by TGA and EGA techniques with gas electron ionization mass spectrometry, indicating emission of a fragment with m/z = 28 (for N/N_2) above 300 °C (see Figure S4 in Supporting Information). In addition, as no fragments with m/z = 30 and 48 were detected, the samples were considered free of any NO and NO_2 species, respectively. This agrees with the analysis of the Raman spectra of N-doped graphene samples as no Raman peaks around 1430 cm^{-1}, characteristic for NO and NO_2 species,[36] are observed (see Figure 1b,d,f).

Raman spectra of the $GN_{0.015}$, $GN_{0.033}$, $GN_{0.051}$, and TRGO sample are shown in Figure 1b,d,f and Figure S1c in Supporting Information. It can be seen that on increasing the level of N-doping, the D-to-G band intensity ratio, I_D/I_G, increased. It is known that if nitrogen enters the graphene lattice, the intensity of the D-band, I_D, in the Raman spectrum of graphene is enhanced due to defects that emerge upon incorporation of nitrogen into the graphene structure.[25] This provides further evidence that under the synthetic conditions used, accom-

DOI: 10.1021/jacs.6b12934
J. Am. Chem. Soc. 2017, 139, 3171−3180

modation of nitrogen into the graphene lattice was strongly favored over a simple adsorption/addition process.

If defects are introduced into graphene, paramagnetic centers emerge that may interact via suitable mediators (i.e., π-conduction electrons, overlapping orbitals favoring super-exchange mechanism, etc.) to generate long-range magnetic ordering in the 2D lattice. Under such conditions, the magnetic susceptibility of graphene, χ, involves three contributions, i.e., $\chi = \chi_{dia} + \chi_{para} + \chi_{ferro}$, where χ_{dia} is the diamagnetic term including orbital, Landau and core diamagnetic contributions, χ_{para} is the paramagnetic term including noninteracting (isolated) defect-induced paramagnetic centers, Pauli paramagnetic contribution from conduction electron and van Vleck contribution, and χ_{ferro} is the FM term describing the magnetic response of interacting defect-induced paramagnetic centers.[37] As expected, pristine TRGO behaved in a diamagnetic manner with only a tiny paramagnetic response at low temperatures (see Figure S1d in Supporting Information) due to paramagnetic centers emerging as a result of defects and/or the negligible content of oxygen functionalities, which were most likely at the edges; the profile of χ_{mass} of TRGO well matched the modified Curie law, i.e., $\chi_{mass} = \chi_{mass,dia} + C/T$, where $\chi_{mass,dia}$ is the diamagnetic contribution, C is the Curie constant, and T is the temperature.

Similarly, the temperature evolution of χ_{mass} measured for the $GN_{0.015}$ and $GN_{0.033}$ sample also obeyed the modified Curie law (see Figure 4a,b). The number of paramagnetic centers increased upon increasing the level of N-doping, as expected and evidenced by an enhanced paramagnetic Curie contribution (see insets in Figure 4a,b). However, N-doping at such levels did not imprint any magnetic configuration (as confirmed by theoretical calculations discussed below) and the induced paramagnetic centers were far from each other, precluding the establishment of a long-range magnetic ordering. Thus, the $GN_{0.015}$ and $GN_{0.033}$ sample showed dominant diamagnetic behavior, as also witnessed from the isothermal magnetization curves measured at 5 K (see insets in Figure 4a,b).

Interestingly, for the $GN_{0.051}$ sample, the temperature profile of χ_{mass} was drastically different compared to the $GN_{0.015}$ and $GN_{0.033}$ sample as it could not be described by the modified Curie law. On lowering the temperature, χ_{mass} showed a saturation tendency followed by an abrupt increase, indicating two contributions, i.e., FM and paramagnetic (see Figure 4c–e); contrary to the graphene systems with a lower N-doping, the diamagnetic term was found to be negligible here. The presence of both magnetic fractions can be explained by assuming that the N-doped graphene sheets within the sample contained nitrogen in different structural configurations, which have a different impact on the magnetism of graphene, as predicted by the theory discussed below. Moreover, it is known that even in sheets showing FM behavior, isolated paramagnetic centers may evolve owing to the presence of vacancies and defects of topological and edge nature.[4−10] In order to fit the temperature evolution of χ_{mass}, the paramagnetic term was fitted using the Curie function (i.e., $\chi_{mass} = C/T$) over the whole temperature interval, whereas a model function involving a combination of the Curie–Weiss law (i.e., $\chi_{mass} = C/(T - \theta)$, where θ is the Weiss temperature) at high temperatures and Brillouin function within the mean-field approximation at low temperatures was constructed to describe the FM contribution (see inset in Figure 4c). The fitting yielded $\theta \approx 69$ K, angular momentum number $J \approx 1.19$, and a weight-normalized ratio of ferromagnetic-to-paramagnetic contribution equal to 1.66. Note that the value of J is not an integral multiple of 0.5 as expected and must be treated as an average over all the N-doped graphene sheets in the $GN_{0.051}$ sample as the sheets can have different C–N configurations/arrangements with different net magnetic moments (see below), as already reported for N-doped and S-doped graphene systems.[22,24] Furthermore, θ can be assigned to the Curie temperature, T_C, marking the transition from the paramagnetic to FM regime on lowering the temperature. Thus, in accordance with the theory, if the concentration of nitrogen exceeds a threshold value (>5 at. % of N), magnetically active motifs inside the graphene lattice evolve, eventually leading to a magnetically ordered (i.e., FM) state at low temperatures.

Transition of graphene with ∼5.1 at. % of N to the low-temperature FM regime was further confirmed by a series of hysteresis loops measured over the temperature range from 5 to 300 K (see Figure 4d and Figure S5 in Supporting Information). At 5 K, the isothermal magnetization curve showed hysteresis with a coercivity of ∼92 Oe (see inset in Figure 4d) and saturation magnetization reaching 1.09 emu/g. The derived value of the saturation magnetization is of identical order as reported for S-doped graphenes[22] and vertical graphenes,[38] which are regarded as the magnetically strongest carbon-based systems prepared to date. The nonzero value of the coercivity implies that N-doping imprints magnetic anisotropy on the graphene lattice, establishing an easy axis of magnetization along which the magnetic moments of the generated paramagnetic centers energetically prefer to lie. Following the mathematical procedures of Liu et al.[24] and Tuček et al.[22] and assuming the J value and weighted ferromagnetic-to-paramagnetic ratio derived from the χ_{mass} vs T profile, we next attempted to separate the paramagnetic and FM contribution in the 5 K isothermal magnetization curve (see inset in Figure 4d). The fitting yielded a saturation magnetization of ∼0.65 emu/g and ∼0.37 emu/g for the FM and paramagnetic contributions, respectively. On raising the temperature, the coercivity decreased to zero (see inset in Figure S5b in Supporting Information) and the hysteresis was lost at a temperature of ∼70 K (see Figure S5a in Supporting Information), indicating a transition from the FM to paramagnetic regime.

Thus, the experimental results suggested that when the concentration of nitrogen was increased and it became firmly embedded in the crystal lattice of graphene, the number of induced paramagnetic centers increased, eventually forming magnetically active motifs with conduction electrons providing interaction pathways between them and establishing long-range magnetic ordering upon decreasing the temperature. It was hypothesized that upon further increasing the nitrogen concentration in the graphene lattice, magnetic interactions would be strengthened, as reflected by a shift of T_C to higher temperature. Moreover, the presence of more paramagnetic centers would enhance the saturation magnetization, approaching the values observed for S-doped and vertically oriented graphenes,[22,38] i.e., systems where the magnetic features are imprinted by defects. Here, it should be stated that the observed ferromagnetism above 5 at. % of N was probably a consequence of the different nitrogen motifs identified in the samples by XPS (graphitic, pyridinic, and chemisorbed N/N_2). Importantly, we did not identify pyrrolic nitrogen in the samples, which has previously been shown to cause a fall in magnetization values.[10]

DOI: 10.1021/jacs.6b12934
J. Am. Chem. Soc. 2017, 139, 3171–3180

To decipher the effect of nitrogen in various bonding configurations (as identified by XPS, Figure 2 and Figure S3 in Supporting Information) on the magnetic properties of graphene, we performed a first-principles[27−30] study of the structural, electronic, and magnetic properties of N-doped graphenes. The "magnetic contributions" of individual N-motifs were also addressed in details. We used a rectangular graphene cell containing 96 atoms, which was computationally tractable and enabled the experimentally determined total and relative (among different bonding configurations) content of nitrogen to be followed closely. Specifically, we considered chemisorbed nitrogen (both N and N_2) on the top of the graphene sheet and two graphitic and pyridinic nitrogen atoms in the graphene lattice (see Figure 5).

The computational data fully supported the experimental results. In particular, the energetically most stable structures, as presented in Figure 5a,b, exhibited FM ordering with 1.3 and 0.3 μ_B magnetic moment per supercell for N and N_2, respectively, chemisorbed on the graphene surface. The density of state (DOS) plots presented in Figure 5c,d indicated exchange coupling mediated by the conduction electrons. Moreover, the strong spin-polarized electron features at the Fermi level in the DOS structures showed a predominant contribution from the graphitic N atoms, which highlights their important role in developing Stoner-like magnetism in N-doped graphenes.[22,39] It should be noted that depending on the position of nitrogen on the graphene surface with respect to the graphitic and pyridinic nitrogen atoms, a large number of possible magnetic configurations were found with a varying effective magnetic moment per cell and exhibiting both FM and antiferromagnetic behavior or even disappearance of magnetic order. This may explain the complexity of the magnetic measurements discussed above for the $GN_{0.051}$ sample, as the experimental response represented an average over a large number of structures with different net magnetic moments.

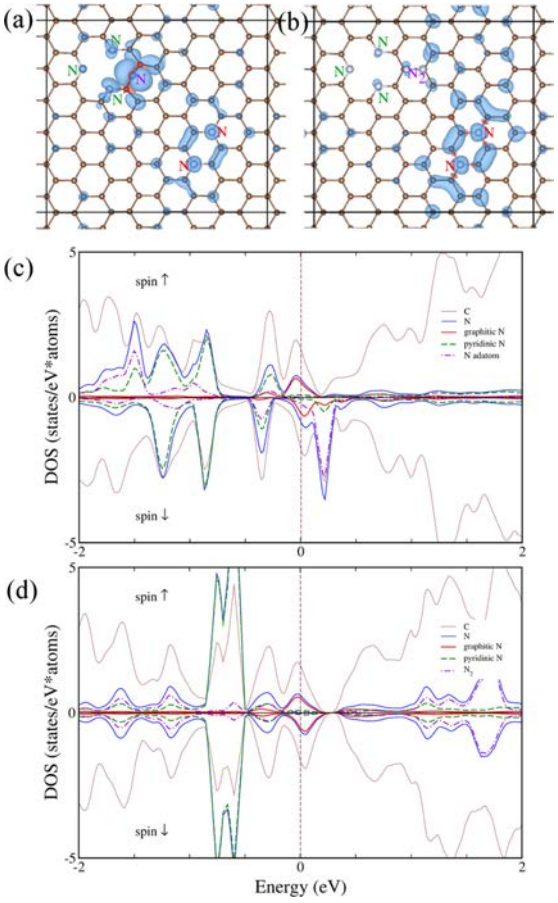


Figure 5. Top view of graphene doped with graphitic (in *para* configurations), trimerized pyridinic and chemisorbed (a) N and (b) N_2 marked respectively by red, green, and magenta, with positive (negative) spin densities plotted in blue (red) for isosurfaces at $\pm 1 \times 10^{-3}$ (panel (a)) and $\pm 2.5 \times 10^{-4}$ eÅ^{-3} (panel (b)). (c, d) The corresponding DOS plot for configuration shown in panel (a) and panel (b), respectively.

Thus, to understand the role and contribution of individual nitrogen motifs in triggering magnetism in N-doped graphenes, we carried out an extensive set of additional calculations with a smaller cell containing 48 atoms. The magnetic properties of graphene doped with graphitic nitrogen exhibited a strong dependence on both the nitrogen concentration and configurations. Nonmagnetic ground state structures doped by 2.1, 4.2, and 6.25 at. % of graphitic nitrogen (the percentages used result from the size of the cell employed in the calculations) are shown in Figure S6 in Supporting Information. The magnetism of graphene doped with graphitic nitrogen has been attributed to delocalized electrons occupying narrow peaks at the Fermi level (E_F).[22,39] Graphene doped with 2.1 at. % of nitrogen was predicted to be nonmagnetic, in accord with DFT calculations by Wang et al.,[9] and the narrow electron donor states near E_F were absent in the partial density of states (PDOS). At 4.2 at. % of nitrogen, the computational screening identified a magnetic structure with a magnetic moment of ∼0.2 μ_B per supercell in which N atoms substituted C atoms at *para* positions (see Figure 6). The same motif was responsible for triggering ferromagnetism in the larger 96-atom cell, which highlights the importance of the graphitic nitrogen motif in imprinting FM order in N-doped graphene. N-doping generating the FM state gave rise to a strong p_z electron peak at the Fermi level in the electronic structure according to PDOS, similar to recent reports for graphene doped with 4.2 at. % of sulfur.[22] The

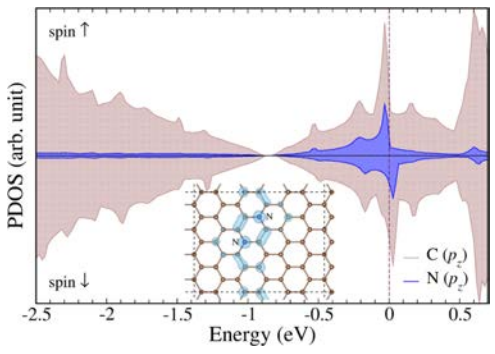


Figure 6. Partial densities of states calculated for graphene doped with nitrogen embedded in the lattice at *para* positions at a concentration of 4.2 at. %. The supercell is shown in the inset, where an isosurface of spin-density plotted at $\pm 5 \times 10^{-4}$ eÅ^{-3} is also displayed.

DOI: 10.1021/jacs.6b12934
J. Am. Chem. Soc. 2017, 139, 3171−3180

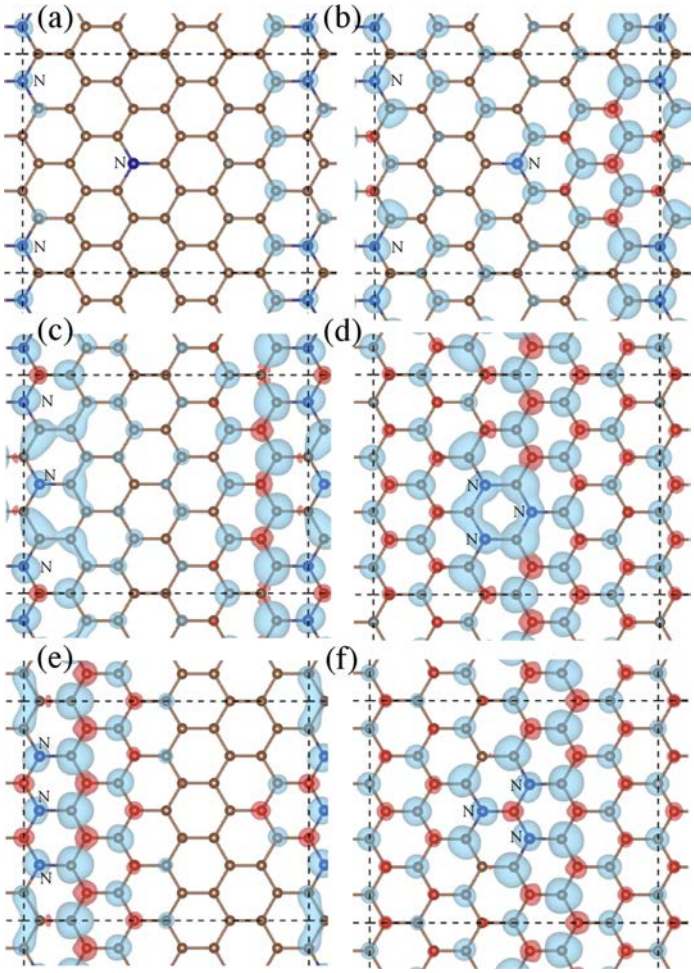


Figure 7. Top view of graphene doped with nitrogen at a concentration of 6.25 at. %. Positive (negative) spin densities are plotted in blue (red) for isosurfaces at $\pm 5 \times 10^{-4}$ e Å^{-3}: (a) 0.1, (b) 0.4, (c) 0.7, (d) 0.8, (e) 0.4, and (f) 0.6 μ_B per supercell.

magnetic polarization was confined to a narrow part of the cell, in zigzag directions between the doping atoms, as can be seen in the inset in Figure 6 presenting isosurfaces of spin densities. Importantly, formation of zigzag edges by cutting graphene along a certain crystallographic direction has been shown to give rise to peculiar edge localized states near the Fermi level responsible for the spontaneous formation of magnetic ordering in graphene nanoribbons.[40]

The DFT calculations also suggested that at 6.25 at. % of graphitic nitrogen, a greater number of magnetic configurations with the magnetic moment varying between 0.1 and 0.8 μ_B/supercell (see Figure 7 and Figure S7 in Supporting Information) were produced. These magnetic structures contained two N atoms in the *meta* configuration embedded in the graphene lattice. The magnetic behavior of this system could be tuned by changing the position of the third N atom in the host lattice as it stayed on the zigzag paths between the other two N atoms. Finally, because of the similar atomic sizes of nitrogen and carbon atoms, incorporation of nitrogen into the honeycomb network of graphene did not lead to any significant distortion of the host lattice. In-plane atomic displacements caused by nitrogen were below 2% of the C−C distance of pristine graphene and the system remained planar. Strain-induced magnetism in N-doped graphene was thus excluded.

We also considered the effect of nitrogen atoms substituting carbons in the graphene lattice (employing a 48-atom graphene cell) on pyrrolic bonding sites. A single pyrrolic nitrogen in graphene occupied a site inside the pentagonal ring in the vicinity of single vacancy (SV) or divacancy (DV) defect (see Figure S8a,b in Supporting Information). Substitution by monomeric pyrrolic nitrogen did not result in any long-range magnetic order. Importantly, replacing one of the C atoms participating in the reconstructed C−C bond with an N atom led to opening of the 5-membered ring and $S = 1/2$ paramagnetism[41] due to the carbon dangling bond. Such a bonding configuration transformed the initial pyrrolic nitrogen into pyridinic nitrogen (see Figure S8c,d in Supporting Information). We also considered the effect of adding pyrrolic nitrogen inside the octagonal ring of the DV defect (Figure S8e,f in Supporting Information), as proposed in the work of Li et al.[23] The present calculations indicated that the nitrogen

DOI: 10.1021/jacs.6b12934
J. Am. Chem. Soc. 2017, 139, 3171−3180

atom moved to the neighboring 5-membered ring, in accord with the study by Lin et al.,[42] forming a 6-membered ring upon relaxation in which nitrogen (transformed into pyridinic) was nonmagnetic.

Next, we considered the role of pyridinic nitrogen, which was also identified as an important motif in the experimental samples. Besides monomeric pyridinic nitrogen ($S = 0$ or $S = 1/2$ due to carbon dangling bonds), we also considered dimerized (with $S = 1/2$ magnetic moment due to carbon dangling bond) and trimerized pyridinic nitrogen (with a magnetic moment of 0.3 μ_B per supercell). Note that the calculated ground state arrangements of multiple pyridinic nitrogen in the graphene lattice were in agreement with annular dark-field imaging reported in the work by Lin et al.[42] However, according to DOS of the trimerized pyridinic nitrogen (see Figure S9 in Supporting Information), the electronic structure indicated that indirect exchange mediated by the conduction electrons was strongly compromised compared to the exchange coupling developed for graphene doped with graphitic nitrogen (compare Figure 6 and Figure S9 in Supporting Information). This is in line with the suppressed magnetic moment of trimerized pyridinic nitrogen in comparison to that of trimerized graphitic nitrogen (see the structure presented in Figure 7f and DOS plot in Figure S7f in Supporting Information). It is also important to mention that half-metallic properties were recently predicted for the graphene-based C_4N_3 polymer,[43] i.e., a 2D radical polymer containing many trimerized pyridinic nitrogens. In contrast, the DOS plot presented in Figure S9 in Supporting Information showed finite (nonzero) density of states above E_F in both spin-up and spin-down channel, which is most likely due to a significantly lower concentration of trimerized pyridinic nitrogen in the present study.

Finally, we investigated whether magnetism in graphene can also be induced by nitrogen adatoms/molecule, which were identified in the XPS patterns and TGA/EGA measurements. Thus, structures resulting from both nitrogen additions on a pristine graphene layer and simultaneous single nitrogen atom addition and graphitic substitution were analyzed (see Figure S10 and Figure S11 in Supporting Information).

A single N-adatom carried a magnetic moment of 0.5 μ_B, which can be understood based on an electron counting argument: two valence electrons formed covalent bonds with neighboring C atoms, two formed a lone-pair, and the fifth valence electron gave rise to the magnetic moment. However, the substrate atoms remained nonmagnetic. Adding another nitrogen atom contributed 0.5 μ_B, but no magnetic moments were induced on the C atoms. By placing another nitrogen atom in a close proximity to the preadsorbed adatom, an N_2 dimer spontaneously formed, which was adsorbed over the surface and had zero magnetic moment. Adatom addition on graphene containing 2.1 at. % of graphitic nitrogen (see Figure S11 in Supporting Information) also did not induce a magnetic response in the system.

To conclude, the computational study allowed elucidation of the synergistic effect of nitrogen atoms in various bonding configurations, as evidenced from high-resolution XPS data. To follow closely the total and relative content of nitrogen in the experimentally prepared samples, we considered graphitic nitrogen in the *para* configuration, which turned out to promote formation of the motif most important for imprinting magnetism in graphene, followed by trimerized pyridinic nitrogen and chemisorbed N adatoms. In the ground state, the structure resulting from the combined effects of all these species is strongly FM. However, it should be noted that coupling between pyridinic nitrogens is much less effective in maintaining the FM structure, and chemisorbed nitrogen adatoms can only generate paramagnetism. Further, chemisorbed N_2 only results in a nonmagnetic states. Finally, pyrrolic nitrogen has no effect on magnetism in graphene, in line with the work by Ito et al.,[10] who reported a decrease in the magnetization values with increasing concentration of pyrrolic nitrogen in the graphene lattice.

CONCLUSIONS

In summary, on the basis of electronic-structure calculations and magnetization measurements, we have provided new insights into the role of nitrogen as a highly electronegative *n*-type dopant for imprinting the magnetic properties to graphene. The magnetic features of N-doped graphene depend on both the nitrogen concentration and the configuration in the host lattice, with a complex interplay between graphitic, pyridinic, and chemisorbed nitrogen. Among these structural motifs, graphitic nitrogen plays the principal magnetic role, as corroborated by DFT calculations. Importantly, below 5 at. % of nitrogen, graphene behaves dominantly as a diamagnet; paramagnetic centers are induced upon doping; however, they do not produce magnetically active motifs. If the doping concentration is increased above the threshold doping value, magnetic interactions mediated by the conduction electron system emerge between the substitution-generated paramagnetic centers. Experimentally, graphene doped with nitrogen at a concentration level of 5.1 at. % shows a transition to an FM state at the Curie temperature of ∼69 K and saturation magnetization reaching 1.09 emu/g. Such a high value of the saturation magnetization ranks N-doped graphenes among the magnetically strongest graphene-based systems developed so far for which the magnetic properties are imprinted by defects. As N-doping is also expected to maintain or even improve the electric (i.e., conduction) features of graphene, the present work opens possibilities for further optimization of N-doped graphenes (e.g., exclusive presence of graphitic nitrogen) to produce new kinds of spintronic materials.

ASSOCIATED CONTENT

Supporting Information

The Supporting Information is available free of charge on the ACS Publications website at DOI: 10.1021/jacs.6b12934.

Figures S1−S11; Tables S1−S4 (PDF)

AUTHOR INFORMATION

Corresponding Authors

*michal.otyepka@upol.cz
*radek.zboril@upol.cz

ORCID

Martin Pumera: 0000-0001-5846-2951
Michal Otyepka: 0000-0002-1066-5677
Radek Zbořil: 0000-0002-3147-2196

Author Contributions

#P. B. and J. T. contributed equally to this work.

Notes

The authors declare no competing financial interest.

DOI: 10.1021/jacs.6b12934
J. Am. Chem. Soc. 2017, 139, 3171−3180

■ ACKNOWLEDGMENTS

The authors acknowledge the support from the Ministry of Education, Youth and Sports of the Czech Republic under Project No. LO1305 and assistance provided by the Research Infrastructure NanoEnviCz supported by the Ministry of Education, Youth and Sports of the Czech Republic under Project No. LM2015073. P. B. acknowledges Palacký University institutional support. The authors thank Mrs. Ariana Fargašová and Dr. Juri Ugolotti (both from the Regional Centre of Advanced Technologies and Materials, Faculty of Science, Palacky University in Olomouc, Czech Republic) for Raman spectroscopy and TGA/EGA measurements, respectively. Z. S. and V. M. were supported by the Czech Science Foundation (GACR No. 15-09001S) and by specific university research (MSMT No. 20-SVV/2016). M. O. acknowledges funding from an ERC Consolidator grant (H2020) No. 683024. M.P. acknowledges a Tier 2 grant (MOE2013-T2-1-056; ARC 35/13) from the Ministry of Education, Singapore.

■ REFERENCES

(1) Novoselov, K. S.; Geim, A. K.; Morosov, S. V.; Jiang, D.; Zhang, Y.; Dubonos, S. V.; Grigorieva, I. V.; Firsov, A. A. *Science* **2004**, *306* (5696), 666−669.
(2) Geim, A. K.; Novoselov, K. S. *Nat. Mater.* **2007**, *6* (3), 183−191.
(3) Tombros, N.; Jozsa, C.; Popinciuc, M.; Jonkman, H. T.; van Wees, B. J. *Nature* **2007**, *448* (7153), 571−574.
(4) Yazyev, O. V.; Helm, L. *Phys. Rev. B: Condens. Matter Mater. Phys.* **2007**, *75* (12), 125408.
(5) Yazyev, O. V.; Katsnelson, M. I. *Phys. Rev. Lett.* **2008**, *100* (4), 047209.
(6) Palacios, J. J.; Fernández-Rossier, J. *Phys. Rev. B: Condens. Matter Mater. Phys.* **2008**, *77* (19), 195428.
(7) Červenka, J.; Katsnelson, M. I.; Flipse, C. F. J. *Nat. Phys.* **2009**, *5* (11), 840−844.
(8) Soriano, D.; Leconte, N.; Ordejón, P.; Charlier, J.-C.; Palcios, J.-J.; Roche, S. *Phys. Rev. Lett.* **2011**, *107* (1), 016602.
(9) Wang, Z.; Qin, S.; Wang, C. *Eur. Phys. J. B* **2014**, *87* (4), 88.
(10) Ito, Y.; Christodoulou, C.; Nardi, M. V.; Koch, N.; Kläui, M.; Sachdev, H.; Müllen, K. *J. Am. Chem. Soc.* **2015**, *137* (24), 7678−7685.
(11) Poh, H. L.; Pumera, M. *ChemElectroChem* **2015**, *2* (2), 190−199.
(12) Qu, L.; Liu, Y.; Baek, J.-B.; Dai, L. *ACS Nano* **2010**, *4* (3), 1321−1326.
(13) Wang, X.; Li, X.; Zhang, L.; Yoon, Y.; Weber, P. K.; Wang, H.; Guo, J.; Dai, H. *Science* **2009**, *324* (5928), 768−771.
(14) Wang, Z. G.; Li, P. J.; Chen, Y. F.; Liu, J. B.; Zhang, W. L.; Guo, Z.; Dong, M. D.; Li, Y. R. *J. Mater. Chem. C* **2015**, *3* (24), 6301−6306.
(15) Reddy, A. L. M.; Srivastava, A.; Gowda, S. R.; Gullapalli, H.; Dubey, M.; Ajayan, P. M. *ACS Nano* **2010**, *4* (11), 6337−6342.
(16) Kwon, O. S.; Park, S. J.; Hong, J. Y.; Han, A. R.; Lee, J. S.; Lee, J. S.; Oh, J. H.; Jang, J. *ACS Nano* **2012**, *6* (6), 1486−1493.
(17) Jeong, H. M.; Lee, J. W.; Shin, W. H.; Choi, Y. J.; Shin, H. J.; Kang, J. K.; Choi, J. W. *Nano Lett.* **2011**, *11* (6), 2472−2477.
(18) Chen, L. F.; Zhang, X. D.; Liang, H. W.; Kong, M. G.; Guan, Q. F.; Chen, P.; Wu, Z. Y.; Yu, S. H. *ACS Nano* **2012**, *6* (8), 7092−7102.
(19) Huang, X.; Qi, X. Y.; Boey, F.; Zhang, H. *Chem. Soc. Rev.* **2012**, *41* (2), 666−686.
(20) Wang, Y.; Shao, Y. Y.; Matson, D. W.; Li, J. H.; Lin, Y. H. *ACS Nano* **2010**, *4* (4), 1790−1798.
(21) Chaban, V. V.; Prezhdo, O. V. *J. Am. Chem. Soc.* **2015**, *137* (36), 11688−11694.
(22) Tuček, J.; Błoński, P.; Sofer, Z.; Šimek, P.; Petr, M.; Pumera, M.; Otyepka, M.; Zbořil, R. *Adv. Mater.* **2016**, *28* (25), 5045−5053.
(23) Li, J. Y.; Li, X. H.; Zhao, P. H.; Lei, D. Y.; Li, W. L.; Bai, J. T.; Ren, Z. Y.; Xu, X. L. *Carbon* **2015**, *84*, 460−468.
(24) Liu, Y.; Tang, N. J.; Wan, X. G.; Feng, Q.; Li, M.; Xu, Q. H.; Liu, F. C.; Du, Y. W. *Sci. Rep.* **2013**, *3*, 2566.
(25) Wang, H.; Maiyalagan, T.; Wang, X. *ACS Catal.* **2012**, *2* (5), 781−794.
(26) Lazar, P.; Zbořil, R.; Pumera, M.; Otyepka, M. *Phys. Chem. Chem. Phys.* **2014**, *16* (27), 14231−14235.
(27) Kresse, G.; Furthmüller, J. *Phys. Rev. B: Condens. Matter Mater. Phys.* **1996**, *54* (16), 11169−11186.
(28) Kresse, G.; Joubert, D. *Phys. Rev. B: Condens. Matter Mater. Phys.* **1999**, *59* (3), 1758−1775.
(29) Blöchl, P. E. *Phys. Rev. B: Condens. Matter Mater. Phys.* **1994**, *50* (24), 17953−17979.
(30) Perdew, J. P.; Burke, K.; Ernzerhof, M. *Phys. Rev. Lett.* **1996**, *77* (18), 3865−3868.
(31) Blöchl, P. E.; Jepsen, O.; Andersen, O. K. *Phys. Rev. B: Condens. Matter Mater. Phys.* **1994**, *49* (23), 16223−16233.
(32) Bader, R. *Atoms in Molecules: A Quantum Theory*; Oxford University Press: New York, 1990.
(33) Henkelman, G.; Arnaldsson, A.; Jonsson, H. *Comput. Mater. Sci.* **2006**, *36* (3), 354−360.
(34) Sanville, E.; Kenny, S. D.; Smith, R.; Henkelman, G. *J. Comput. Chem.* **2007**, *28* (5), 899−908.
(35) Nair, R. R.; Tsai, I.-L.; Sepioni, M.; Lehtinen, O.; Keinonen, J.; Krasheninnikov, A. V.; Castro Neto, A. H.; Katsnelson, M. I.; Geim, A. K.; Grigorieva, I. V. *Nat. Commun.* **2013**, *4*, 2010.
(36) Zhao, L. B.; Huang, Y. F.; Liu, X. M.; Anema, J. R.; Wu, D. Y.; Ren, B.; Tian, Z. Q. *Phys. Chem. Chem. Phys.* **2012**, *14*, 12919.
(37) Makarova, T. L.; Shelankov, A. L.; Zyrianova, A. A.; Veinger, A. I.; Tisnek, T. V.; Lahderanta, E.; Shames, A. I.; Okotrub, A. V.; Bulusheva, L. G.; Chekhova, G. N.; Pinakov, D. V.; Asanov, I. P.; Sljivancanin, Z. *Sci. Rep.* **2015**, *5*, 13382.
(38) Seo, D. H.; Yue, Z. J.; Wang, X. L.; Levchenko, I.; Kumar, S. L.; Douc, S. X.; Ostrikov, K. *Chem. Commun.* **2013**, *49* (99), 11633−11637.
(39) Edwards, D. M.; Katsnelson, M. I. *J. Phys.: Condens. Matter* **2006**, *18* (31), 7209−7225.
(40) Fujita, M.; Wakabayashi, K.; Nakada, K.; Kusakabe, K. *J. Phys. Soc. Jpn.* **1996**, *65* (7), 1920−1923.
(41) Nair, R. R.; Sepioni, M.; Tsai, I.-L.; Lehtinen, O.; Keinonen, J.; Krasheninnikov, A. V.; Thomson, T.; Geim, A. K.; Grigorieva, I. V. *Nat. Phys.* **2012**, *8* (3), 199−202.
(42) Lin, Y. C.; Teng, P. Y.; Yeh, C. H.; Koshino, M.; Po-Chiu, P. W.; Suenaga, K. *Nano Lett.* **2015**, *15* (11), 7408−7413.
(43) Lee, E. C.; Choi, Y. C.; Kim, W. Y.; Singh, N. J.; Lee, S.; Shim, J. H.; Kim, K. S. *Chem. - Eur. J.* **2010**, *16* (40), 12141−12146.

DOI: 10.1021/jacs.6b12934
J. Am. Chem. Soc. 2017, 139, 3171−3180

nature COMMUNICATIONS

ARTICLE

Received 4 Oct 2016 | Accepted 9 Jan 2017 | Published 20 Feb 2017

DOI: 10.1038/ncomms14525 OPEN

Room temperature organic magnets derived from sp^3 functionalized graphene

Jiří Tuček[1], Kateřina Holá[1], Athanasios B. Bourlinos[1,2], Piotr Błoński[1], Aristides Bakandritsos[1], Juri Ugolotti[1], Matúš Dubecký[1], František Karlický[1], Václav Ranc[1], Klára Čépe[1], Michal Otyepka[1] & Radek Zbořil[1]

Materials based on metallic elements that have *d* orbitals and exhibit room temperature magnetism have been known for centuries and applied in a huge range of technologies. Development of room temperature carbon magnets containing exclusively *sp* orbitals is viewed as great challenge in chemistry, physics, spintronics and materials science. Here we describe a series of room temperature organic magnets prepared by a simple and controllable route based on the substitution of fluorine atoms in fluorographene with hydroxyl groups. Depending on the chemical composition (an F/OH ratio) and sp^3 coverage, these new graphene derivatives show room temperature antiferromagnetic ordering, which has never been observed for any *sp*-based materials. Such 2D magnets undergo a transition to a ferromagnetic state at low temperatures, showing an extraordinarily high magnetic moment. The developed theoretical model addresses the origin of the room temperature magnetism in terms of sp^2-conjugated diradical motifs embedded in an sp^3 matrix and superexchange interactions via –OH functionalization.

[1] Regional Centre of Advanced Technologies and Materials, Department of Physical Chemistry, Faculty of Science, Palacky University in Olomouc, Slechtitelu 27, Olomouc 783 71, Czech Republic. [2] Physics Department, University of Ioannina, Ioannina 45110, Greece. Correspondence and requests for materials should be addressed to R.Z. (email: radek.zboril@upol.cz).

Since the first isolation of graphene—2D carbon allotrope—in 2004 (ref. 1), vast efforts have been made to understand its unique mechanical, electronic, optical and transport properties[2–8]. Among other properties, it exhibits superior mechanical strength,[4] a very large specific surface area[9], high carrier mobility[2], transparency[10] and thermal conductivity[6]. Moreover, several peculiar physical phenomena have been observed in graphene such as the ambipolar effect[1], room temperature half-integer quantum Hall effect[7], nonlinear Kerr effect[11] and Casimir effect[12]. Because of its remarkable properties, graphene has great potential in a broad portfolio of technical applications[13] including robust lightweight, thin and flexible display screens[14], field-effect and ballistic transistors[15], spin transistors and spin logic devices[16], photosensitive transistors[17], organic photovoltaic cells[18], organic light-emitting diodes[19] and conductive plates in supercapacitors and lithium-ion, lithium-sulfur and lithium-air batteries[9,20,21].

However, the practical applications of graphene are limited by its zero band gap, hydrophobicity and absence of long-range magnetic ordering. One potentially effective way of eliminating these drawbacks is to instead use covalently functionalized graphene derivatives in which specific atoms or functional groups are covalently bound to the graphene sheet to tune its physicochemical and biochemical properties[22]. Important examples of covalently modified graphene derivatives include graphene oxide[23], graphane[24] and fluorographene[25]. In particular, graphene oxide and fluorographene can be further readily functionalized with various other functional groups (for example, –Cl, –I and –SH), offering further scope for band gap tuning and the introduction of new electronic, optical and sensing properties[23,26,27].

Covalent functionalization has thus made it possible to produce graphene derivatives with modified band gap properties and altered hydrophilicity/hydrophobicity[22,28]. However, development of graphene derivative with room temperature magnetic behaviour is a major unaddressed challenge despite the investment of considerable effort into imprinting stable magnetic centres into graphitic structures and inducing long-range magnetic ordering across 2D carbon networks[29,30]. Several key strategies have been suggested to induce spin-carrying sp^3 (paramagnetic) states in graphene-related structures[29,30] such as formation of defects and vacancies,[30] insertion of non-carbon atoms (for example, boron, nitrogen and sulfur) into the graphene lattice[31–33], cutting of graphene sheets creating edges with a specific geometry (for example, zigzag graphene nanoribbons)[34], covalent functionalization with functional groups[29,30,35–37], light-atom adsorption (that is, adatoms)[38–40], transition-metal-atom adsorption[41] and electric field engineering[42]. Particularly, the pioneering work of Nair *et al.*[43] suggested that it may be possible to imprint paramagnetic centres into graphene by combining defects arising from partial fluorination with appropriate (C–F) functionalization. All these approaches demonstrate the possibility to combine various sources for creation and π-electron system-based coupling of spin-carrying sp^3 states to induce magnetism into graphene. However, π-electron system-mediated interactions are weak and, hence, magnetic ordering collapses at relatively low temperatures (< 100 K). Thus, room temperature magnetism in graphene and graphene derivatives, maintained by the π-electron system, is heavily questioned in literature[13]; if such a behaviour was experimentally observed, the presence of impurities of transition metal origin (Fe, Ni, Co), originating from either the synthesis itself or sample handling, was not properly excluded, leading to misinterpretation of results and inaccurate conclusions[13].

Here we report a discovery of organic graphene-based magnets with a magnetic ordering sustainable up to room temperature due to the suitable sp^3 functionalization. A series of magnetic carbons designated as hydroxofluorographenes are prepared from fluorographene by exchanging some of its fluorine atoms for hydroxyl groups. The chemical composition of hydroxofluorographenes can be controlled through reaction conditions and choice of –OH-containing precursors. Strikingly, hydroxofluorographenes with an appropriate composition (an F/OH ratio) exhibit antiferromagnetic ordering at room temperature, a magnetic behaviour not previously observed for any graphene derivative or *sp*-based material. At low temperatures, these hydroxofluorographenes undergo a transition to a ferromagnetic state with one of the highest magnetization values reported among graphene-based material. Based on the set of experimental data and high throughput first principles calculations on a large number of atomic configurations with varying F/OH ratio, we establish that the unique magnetism is attributed to a network of functionalization-induced sp^2-conjugated carbon diradical motifs embedded in an sp^3 matrix, and the ability of –OH groups to stabilize magnetically ordered state up to room temperature due to emergence of superexchange interactions. Moreover, the suggested theoretical model for hydroxofluorographene system has a universal nature and covers both 'diradical motifs-induced magnetism' appearing at high sp^3 coverages and sustaining up to room temperature and 'defect-induced magnetism', which emerges at lower degrees of sp^3 functionalization with limited sustainability at higher temperatures.

Results

Physicochemical properties of hydroxofluorographenes. The synthesis of hydroxofluorographenes is based on the chemistry of fluorographene (GF), which has been investigated experimentally and computationally by our group, leading to the development of practical procedures for the direct nucleophilic substitution of fluorine[26,27]. The series of five hydroxofluorographenes differing in degree of sp^3 functionalization, an F/OH ratio, and magnetic features were prepared by ultrasonic exfoliation of fluorographite (C_1F_1) in *N,N*-dimethylformamide (DMF), after which the exfoliated material was treated with –OH-containing precursors for various reaction temperatures and time. For detailed chemical, structural, morphological and magnetic characterization, we have selected the representative sample, denoted as G(OH)F, prepared by reaction of fluorographene with tetramethylammonium hydroxide in DMF for 3 days (Fig. 1; for more details, see 'Methods' section below).

The overall chemical composition of G(OH)F sample was determined by X-ray photoelectron spectroscopy (XPS) analysis (Supplementary Fig. 1), revealing the average contents of oxygen, fluorine, carbon and nitrogen to be 6.1, 27.2, 65.4 and 1.3 at.%, respectively. To exclude the presence of metals, which would affect magnetic features of the system, we performed inductively coupled plasma mass spectrometry (ICP-MS) analysis confirming their negligible contents generally below 24 ppm (Supplementary Table 1). The C/F ratio of G(OH)F (2.4/1) found from XPS analysis is greater than that of its precursor, fluorographene (1/1), reflecting the sample's partial defluorination and formation of some aromatic sp^2 regions during G(OH)F synthesis. The presence of oxygen, fluorine, carbon and nitrogen was inferred from energy-dispersive X-ray (EDX) spectrum measured for the G(OH)F sample (Supplementary Fig. 2). The small content of nitrogen comes from DMF solvent residues as clearly seen in the thermogravimetric curve (Supplementary Fig. 3a) exhibiting a negligible loss (0.41 wt.%) up to 100 °C due to release of adsorbed water, while the secondary weight decrease (1.11 wt.%) between 108 and 140 °C is evidently related to DMF evolution. To confirm the presence of fluorine and hydroxyl groups in the G(OH)F structure, the G(OH)F sample was

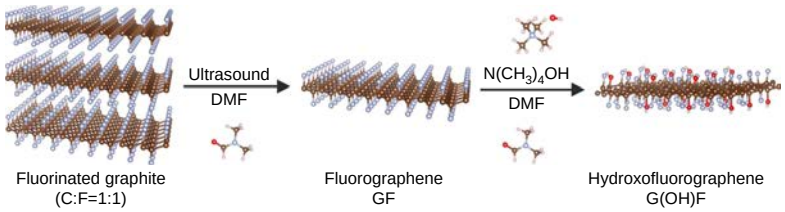


Figure 1 | Representative preparation of G(OH)F. The scheme depicting the chemical procedure towards G(OH)F.

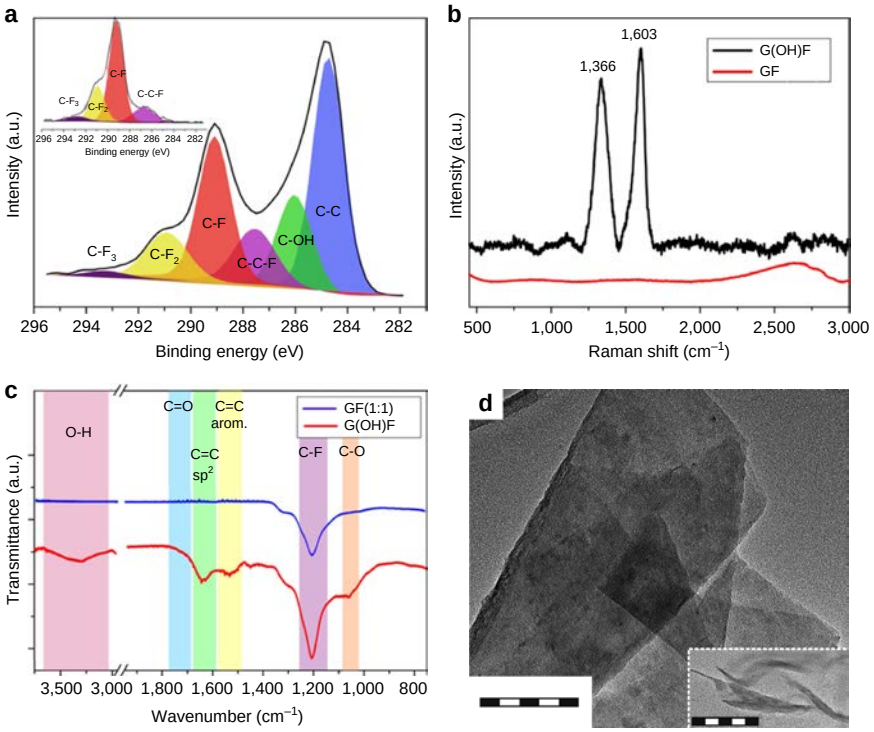


Figure 2 | Physicochemical characterization of GF and G(OH)F. (**a**) High-resolution C 1s spectrum of G(OH)F and GF precursor (inset). (**b**) Raman spectra of G(OH)F (black line) and GF (red line). (**c**) FT-IR spectra of G(OH)F (red line) and GF (blue line). (**d**) HRTEM image (scale bar, 100 nm) of a G(OH)F sheet with an inset (scale bar, 100 nm) demonstrating a single-sheet character of G(OH)F.

subjected to thermal decomposition under nitrogen atmosphere, heating from room temperature to 900 °C, and the release of gases and ions was monitored by mass spectrometry (Supplementary Fig. 3b). The release of hydroxyl ions started once the temperature rose above 200 °C; this was attributed to the removal of covalently attached –OH groups because the adsorbed water molecules were released at temperatures of up to 100 °C. The two peaks appearing in the evolved gas profile for the –OH groups can be well explained in terms of the stability of –OH groups in G(OH)F strongly dependent on their local environment (Supplementary Fig. 3c). Hence, the first peak, with maximum at 220 °C, corresponds to the evolution of less stable –OH groups, which are released before any evolution of fluorine, while the second peak, centred at 260 °C, corresponds to –OH groups released after the onset of fluorine evolution, which would radically change their local environment and stability (Supplementary Fig. 3c). The fluorine ions were detected in a broad range of temperatures with the maximum of fluorine released at 500 °C. Importantly, carbon dioxide and carbon monoxide, whose release typically indicates the presence of carboxylic and epoxy groups, were not detected at any temperature.

The successful attachment of hydroxyl groups was also confirmed by high-resolution C 1s XPS data (Fig. 2a) showing that the product contained C–O and C–C bonds, which were not present in the XPS pattern of the GF precursor (inset in Fig. 2a). Formation of aromatic sp^2 regions was also indicated by Raman spectroscopy (Fig. 2b): Raman spectrum of the G(OH)F sample exhibited a characteristic G-band at 1,603 cm^{-1} and a disorder-induced D-band at 1,366 cm^{-1}, whereas pristine fluorographene is Raman-inactive[44]. The Fourier transform infrared (FT-IR) spectrum of G(OH)F featured vibrations in the range of 1,510–1,670 cm^{-1} corresponding to aromatic regions, and C–F vibrations at 1,200 cm^{-1} (Fig. 2c). Importantly, its FT-IR spectrum also showed peaks associated with covalent C–OH bonds that were not observed in the FT-IR spectrum of fluorographene, namely a C–O vibration peak at 1,058 cm^{-1} and a broad O–H vibration peak at

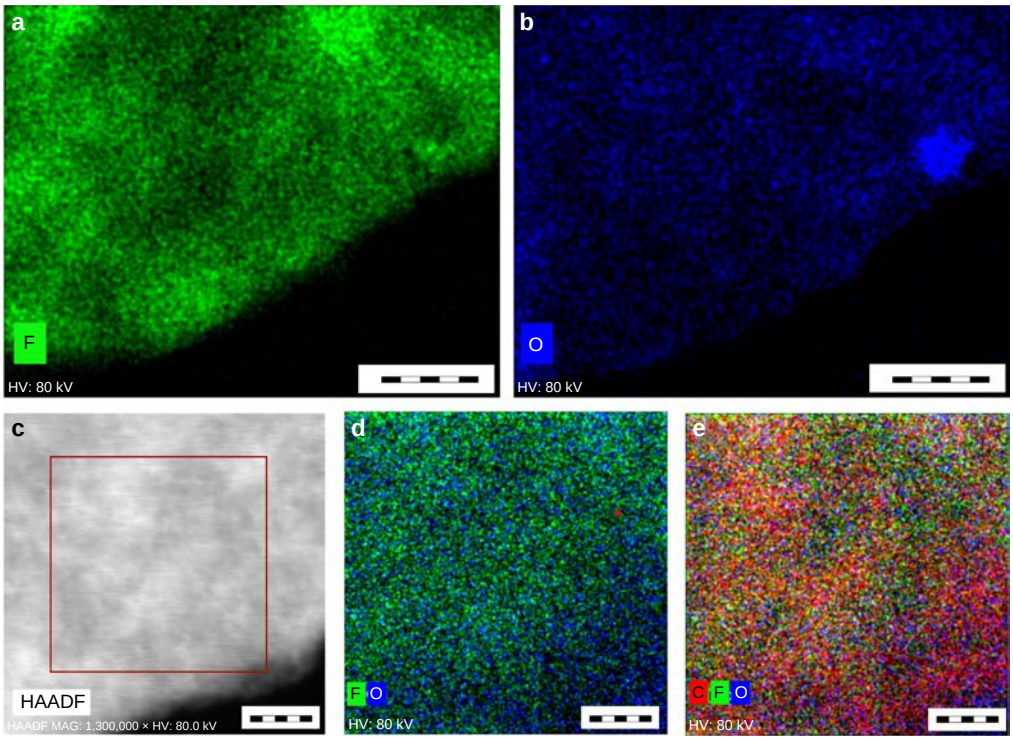


Figure 3 | Chemical mapping of a G(OH)F sheet by STEM–HAADF. (**a**) Distribution of fluorine atoms on the G(OH)F sheet (scale bar, 50 nm). (**b**) Distribution of oxygen atoms on the G(OH)F sheet (scale bar, 50 nm). (**c**) STEM/HAADF image of the G(OH)F sheet (scale bar, 10 nm). (**d**) Combined F/O chemical mapping of the G(OH)F sheet (scale bar, 6 nm). (**e**) Combined C/F/O chemical mapping of the G(OH)F sheet (scale bar, 6 nm).

3,250 cm^{-1}. These results indicate that a well-defined covalently modified graphene derivative containing aromatic rings and two characteristic functional groups, C–OH and C–F, can be prepared from fluorographene via a simple synthetic procedure involving chemical exfoliation followed by nucleophilic substitution. The stoichiometric formula for this representative material is approximately $C_{18}(OH)_{1.8}F_{7.2}$ with C_{18} as a supercell used in the theoretical model (see below).

Atomic force microscopy experiments indicated that after the exfoliation process, the sample consisted of single-layered sheets less than 1 nm thick (Supplementary Fig. 4), however, a few-layered sheets with thickness of several nanometres were observed as well. Similarly, very thin highly transparent single sheets were observed by high-resolution transmission electron microscopy (HRTEM) (Fig. 2d). The distribution of fluorine and oxygen within the sheet was investigated by scanning transmission electron microscope–high-angle annular dark-field imaging (STEM–HAADF) chemical mapping (Fig. 3), which showed that fluorine and oxygen (–OH) groups were distributed rather homogeneously within the G(OH)F structure, without any large fluorine (or oxygen) islands (Fig. 3e).

Magnetic properties of hydroxofluorographenes. To exclude the effect of tetramethylammonium hydroxide and possible trace impurities contained in this precursor on magnetic behaviour of the system, we measured the temperature evolution of mass magnetic susceptibility (χ_{mass}), confirming its solely diamagnetic character within the whole temperature range (Supplementary Fig. 5). In the case of other precursor, GF, the temperature profile of χ_{mass} can be fitted employing the Curie law ($\chi_{mass} = C/T$, where C is the Curie constant and T is the temperature) and temperature-independent diamagnetic contribution (Supplementary Fig. 6). However, the paramagnetic response of GF is very weak due to minor defects in the GF structure; its magnetic behaviour is dominated by the diamagnetic term in accordance with the previous study[43]. Thus, both precursors used for synthesis of G(OH)F exhibit non-magnetic behaviour.

Importantly, the substitution of some of F atoms of GF by –OH groups produces a material with radically different magnetic properties. Observed magnetic features are not definitely driven by tiny impurities identified by ICP-MS as the sum of their χ_{mass}, considering the magnetic moments of detected elements and recalculating their magnetic response to their weight in the sample and under an external magnetic field of 10 kOe, is four orders lower than the measured χ_{mass} of G(OH)F. Contrary to GF, the temperature dependence of χ_{mass} for G(OH)F is not described by the Curie or Curie–Weiss laws from 5 to 300 K, implying a magnetically ordered state up to room temperature. More strikingly, at room temperature, G(OH)F exhibits antiferromagnetic (AFM) behaviour as χ_{mass} (or $1/\chi_{mass}$) decreases (or increases) with lowering the temperature (Fig. 4a and Supplementary Fig. 7). Thus, at room temperature, G(OH)F shows AFM ordering, a behaviour never observed for any 2D organic material having only *s* and/or *p* electrons. At low temperatures, an abrupt increase in χ_{mass} is observed followed by a saturation trend, which is characteristic of ferromagnetic (FM) materials. The passage from the AFM to FM regime is also clearly evident from the $1/\chi_{mass}$ versus temperature curve with an inflection point at ~62 K (Supplementary Fig. 7). Thus, below ~62 K (the FM/AFM transition temperature,

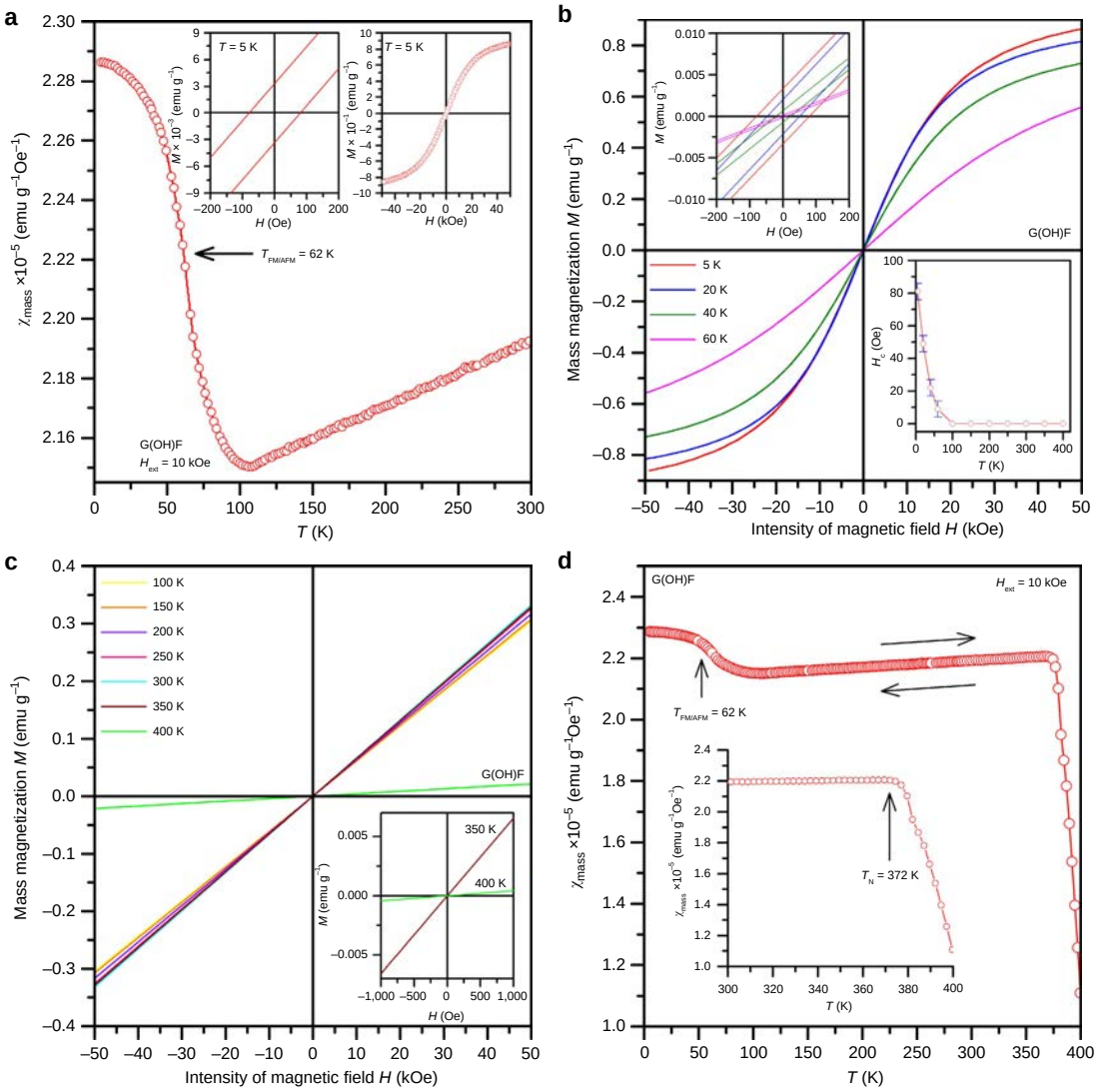


Figure 4 | Magnetization measurements. (**a**) Temperature evolution of the mass magnetic susceptibility (χ_{mass}) of G(OH)F, measured under an external magnetic field (H_{ext}) of 10 kOe. The insets show the hysteresis loops of G(OH)F at 5 K, which indicate non-zero coercivity and a saturation magnetization of almost 1 emu g^{-1}. (**b**) Isothermal magnetization curves of G(OH)F at temperatures of 5–60 K. The insets show the profile of the hysteresis loops around the origin and the temperature dependence of coercivity (H_C). (**c**) Isothermal magnetization curves of G(OH)F, recorded from 100 to 400 K. The inset shows the profile of the isothermal magnetization curves at 350 and 400 K, demonstrating a dramatic decrease in the curve's gradient upon increasing temperature above 350 K; this implies a transition from an AFM state to a paramagnetic regime. (**d**) Temperature evolution of χ_{mass} of G(OH)F, measured under an external magnetic field of 10 kOe. The arrows show the reversibility of the χ_{mass} profile on warming the sample from 5 to 400 K and then cooling from 400 to 5 K. The inset depicts the behaviour of χ_{mass} between 300 and 400 K including its sudden drop above 370 K, which is indicative of a transition from an AFM state to the paramagnetic regime with a Néel transition temperature of about 372 K. Note: the paramagnetic signal from the non-interacting paramagnetic centres was subtracted from the χ_{mass} data.

$T_{FM/AFM}$), G(OH)F behaves in an FM manner. In other words, the FM state is a ground magnetic state for G(OH)F and the AFM regime can be regarded as thermally excited state. It is worth noting that similar FM-AFM transitions have been observed in various molecular radical-based systems[45]. The low-temperature FM state was further supported by G(OH)F isothermal magnetization curve, measured at 5 K: the curve exhibits hysteresis with a coercivity of ~80 Oe (inset in Fig. 4a). Moreover, the magnetization of G(OH)F saturates above a value of 1 emu g^{-1}, placing G(OH)F among the strong magnetic graphene-based systems including doped and functionalized graphenes and graphene derivatives. However, unlike other graphene-based materials, which also show FM features at low temperatures[13,28], G(OH)F synthesized as described above does not lose its magnetic ordering at room temperature; instead, it passes from an FM to AFM state as the temperature raises.

To address the evolution/sustainability of the magnetic properties of G(OH)F, we performed measurements of the material's hysteresis loops and χ_{mass} under heating from

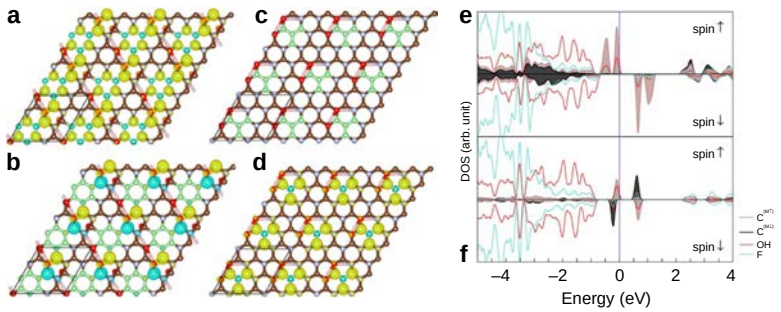


Figure 5 | Spin densities and densities of states. (**a**,**b**) The *m*-xylylene-like motif (green) of G(OH)F embedded in an sp^3 lattice with the corresponding FM (**a**) and AFM (**b**) phases, with up/down spin densities shown in yellow/blue. (**c**,**d**) sp^3-embedded trimethylenemethane-like motif with the corresponding FM spin density. Brown/green, blue, red and pink balls represent carbon, fluorine, oxygen and hydrogen atoms, respectively. (**e**) DOS of the GS FM phase. (**f**) DOS of the AFM phase. For (**e**) and (**f**), orbital contributions of individual atoms (labelled in the inset legend) are presented in both spectra. Electronic states of carbon atoms with up/down magnetic moments are plotted by brown/black line. Electronic states with the same spin direction can hybridize with each other. The hybridization involves the occupied and unoccupied spin-up states (**e**) and the occupied and unoccupied spin-up or spin-down states (**f**). Such kind of coupling not involving a finite density of states at E_F is termed as the superexchange interaction. Both DOS spectra show a significant contribution of oxygen orbitals to the midgap states, which implies an important role of -OH group in the superexchange interactions.

5 to 400 K and cooling from 400 to 5 K (Fig. 4b–d and Supplementary Fig. 7). Between 5 and 60 K, the isothermal magnetization curves of G(OH)F reveal hysteresis with non-zero coercivity and remanent magnetization that both decrease with increasing temperature as would be expected for an FM ground state (Fig. 4b and its insets). Above 60 K, the hysteretic behaviour disappears and profiles of the isothermal magnetization curves are consistent with those expected for an AFM system (Fig. 4c). Importantly, above 350 K, the gradient of the magnetization versus field curve decreases sharply, implying a transition from an AFM to paramagnetic regime (inset in Fig. 4c,d), with the Néel temperature of $\sim$372 K (see the sudden increase and/or drop in $1/\chi_{mass}$ and/or χ_{mass}, respectively, above 370 K in Fig. 4d and Supplementary Fig. 7). Importantly, the profile of the χ_{mass} versus T curve is reversible at temperatures of 5–400 K, meaning that mild thermal treatment does not cause any irreversible structural or magnetic changes in the material (arrows in Fig. 4d). In the paramagnetic region, the χ_{mass} profile fits well with the Curie–Weiss law ($\chi_{mass} = C/(T+\theta)$, where θ is the Weiss temperature) for AFM materials with $\theta \approx 186$ K. The difference between the values of T_N and θ can be explained by different (not defects-like) origin of magnetic moments in the G(OH)F system and AFM state not being the ground magnetic state. More strikingly, the temperature evolution of coercivity and remanent magnetization in the FM state does not follow any formulas valid for *d*-electron driven magnetism (that is, Brillouin function, Bloch function and so on), further indicating a completely new source of magnetic moments—motifs—induced in the G(OH)F lattice (insets in Fig. 4b).

Discussion

To explain the origin and sustainability of magnetism in G(OH)F systems and effect of chemical composition on magnetic features, we applied a high throughput theoretical screening of random structures of $C_{18}(OH)_yF_x$ (that is, with a large number (more than 1,400) of configurations, see Supplementary Table 2 listing abundances of FM and AFM ground states in % of $C_{18}(OH)_yF_x$), simulating thus reliably a random nature of the derivatization. We focused on identification of the nature of magnetic motifs driving room temperature magnetism, origin of FM-AFM transition, role of –OH groups in magnetic communication of these motifs and effect of $C_{18}(OH)_yF_x$ (an F/OH ratio) on magnetic properties of the system.

Regarding the magnetism origin, we identified energetically stable diradical motifs, typically consisting of sp^2-conjugated islands embedded in an sp^3 matrix, which were responsible for the observed magnetic behaviour. A prototypical example is the *m*-xylylene motif, which comprises eight sp^2 carbon atoms and has an FM ground state (GS) with a spin moment $S=1$ and an FM-AFM spin-flip gap of 0.012 eV (Fig. 5a,b). Another important motif consists of four conjugated sp^2 carbon atoms in a triangular configuration that resembles trimethylenemethane (Fig. 5c,d). Structures containing the trimethylenemethane motif have a spin moment $S=1$ (FM GS) and an FM-AFM spin-flip gap of 0.012 eV. It is worth noting that both *m*-xylylene and trimethylenemethane are typical organic diradicals that are known sources of molecular magnetism[46]. Structural details of both prototypical diradical motifs are depicted in Supplementary Fig. 8. The presence of diradical motifs with FM GS and small FM-AFM spin-flip gap is consistent with the experimental FM-AFM transition observed for G(OH)F at $\sim$62 K.

The electronic structure displayed as density of states (DOS) of G(OH)F with the *m*-xylylene-like motif both in the FM and AFM phase (Fig. 5e,f) provides insight into the nature of G(OH)F magnetism. The DOS in the vicinity of the Fermi level (E_F) is dominated by spin-polarized midgap states. Two midgap states per spin channel are visible in the FM phase (Fig. 5e), and only one channel is occupied. The midgap states reflect an imbalance of graphene bipartite lattice, $N = N_A - N_B$, where N_A and N_B are the number of atoms belonging to each sublattice. As the GS spin of imbalanced bipartite lattice is given by $2S = |N_A - N_B|$ (ref. 47), both diradical motifs have $N=2$ and, hence, $S=1$. The spin-polarized midgap states and bulk of positive (up) spin density reside within the diradical motif on the majority sublattice, while the electronic states of the minority sublattice form a band extending from 2.1 eV above E_F. Note that the electronic states with the same spin direction hybridize with each other.

The DOS plot indicates on the superexchange interactions[48] in maintaining the GS FM ordering within the diradical motifs. A substantial contribution of the oxygen *p* states of the bridging hydroxyl group (located between diradical motifs) to the midgap states (Fig. 5e) shows the important role of –OH groups in

stabilizing the FM GS through the coupling between magnetic diradical motifs. The importance of –OH functionalization in self-sustainability of magnetic ordering is further demonstrated by the fact that fully fluorinated analogue of the *m*-xylylene motif, that is, the system comprising *m*-xylylene-like sp^2 island surrounded by a fully fluorinated sp^3 network, is predicted to have a paramagnetic GS with an AFM-FM spin-flip energy of 0.001 eV (ref. 43). Introduction of a single –OH group to the supercell only slightly enhances the stability of the *m*-xylylene motif's FM state, by about -0.03 eV with respect to its fully fluorinated counterpart. A more significant stabilization of the FM GS was observed when two hydrogen-bonded –OH groups were introduced in close proximity to the sp^2 island; this increased the stability of the FM state relative to the AFM state by 0.08 eV. In addition, a strong overlap of the –OH and –F orbitals in a broad binding energy range starting from –18.5 eV highlights the importance of –OH groups preventing migration of fluorine atoms over the graphene surface and suppressing formation of non-magnetic islands, which are formed in partially fluorinated graphenes[43,49,50].

The DOS spectra of the AFM phase (Fig. 5f) are virtually identical as those for FM one up to the valence band maximum. The important differences appear in the occupation of the midgap states. The occupied (unoccupied) spin-up (spin-down) states are localized on the C atoms carrying positive spin density, while the opposite occupation resides on the C atoms with negative spin density. As hydroxyl group substantially contributes to the midgap states, we conclude that the AFM superexchange is driven by the magnetic coupling[48,51] in which –OH group plays the significant role. Needless to say that the orientation of the hydroxyl group does not affect the FM-AFM transition observed at $\sim$62 K as both *ab initio* molecular dynamic simulations and arbitrary rotation of the –OH groups did not induce the phase change. Thus, the experimentally observed FM-AFM transition, inherent to organic-based materials with radical motifs[42], is in good agreement with a low-energy gain of superexchange interaction of the FM state, which is inversely proportional[52] to the energy difference between hybridized states ($\sim$2.6 eV).

It is worth to mentioning that magnetism of graphene-based materials is intimately related to the appearance of midgap states in their electronic structure[28,29]. The origin of these midgap states is usually ascribed to defects or edges in the structure of graphene-based materials. Here we first identify the new principal source of magnetism in graphene derivatives based on creation of diradical domains through an appropriate sp^3 functionalization. Such diradical motifs embedded in an sp^3 lattice are thus clearly necessary but not sufficient for maintenance of the magnetic regime, which is further stabilized by the presence of neighbouring –OH groups. They show multiple roles in the system contributing to formation and stabilization of diradical motifs, superexchange interaction among them and suppression of adatoms lateral diffusion.

To support the principle role of –OH groups on magnetism, we further performed a high-temperature treatment of the G(OH)F sample. If it is exposed to a temperature above 200 °C, the room temperature magnetism is lost (after thermal treatment, G(OH)F behaves in a diamagnetic manner; Supplementary Fig. 9) as –OH groups start to leave the structure of G(OH)F (see, for comparison, Supplementary Fig. 3b). It confirms that –OH groups have an essential role on establishing and maintaining magnetically ordered state up to room temperature. In addition, defects such as vacancies, voids and edges cannot be considered as key factors capable to imprint the observed FM and AFM behaviour at low and room temperature, respectively.

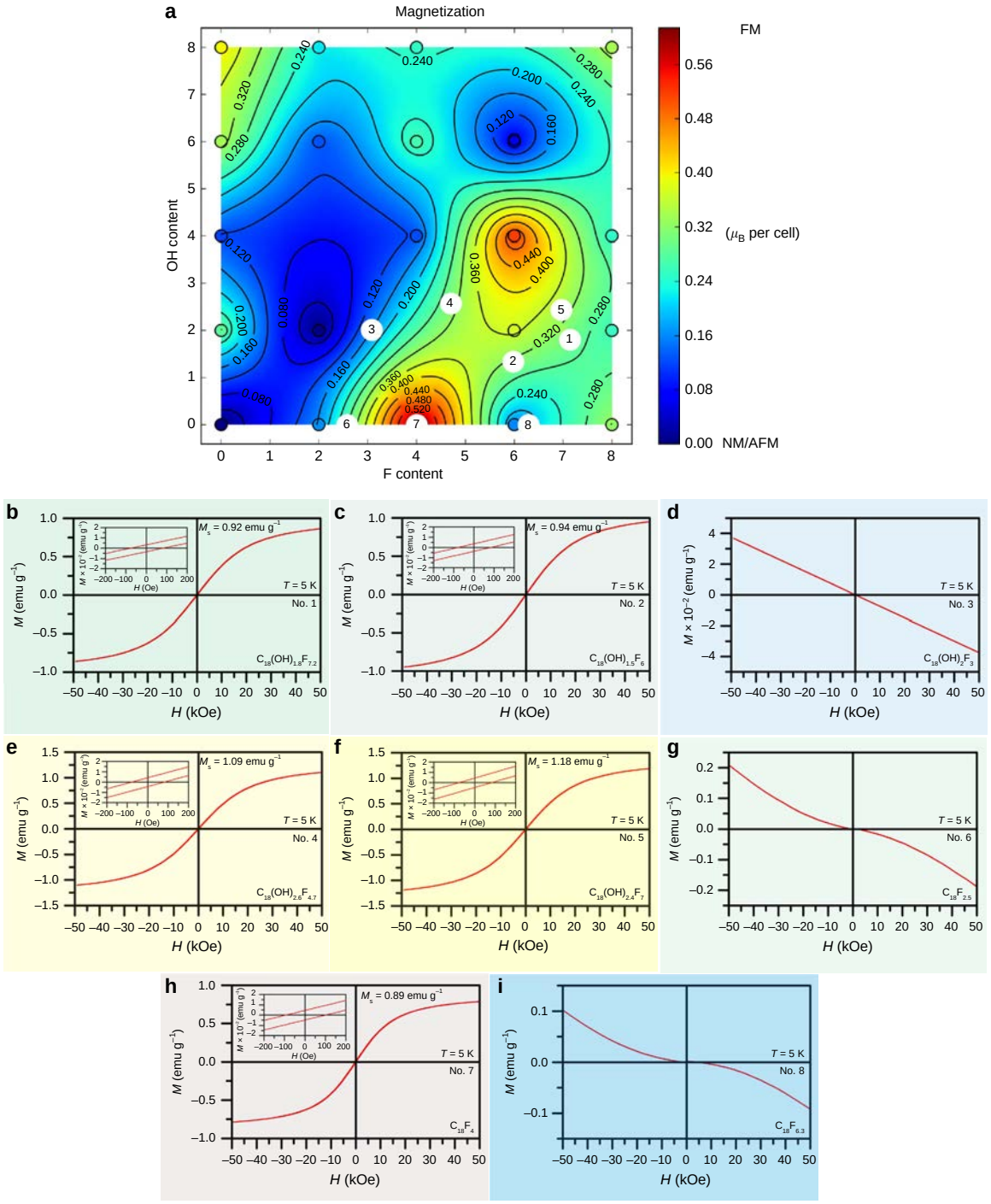
Furthermore, we modelled the effect of the partial 3D layering of G(OH)F sheets on the magnetic features of the G(OH)F system. Here the individual layers in bulk G(OH)F samples were supposed to be bound by both dispersive forces and hydrogen-bonding between –OH groups. The theoretical calculations show that the magnetic properties of bulk G(OH)F are identical to those of the monolayered material (Supplementary Fig. 10). This indicates that magnetism of G(OH)F originates from the individual sheets and is not a consequence of their stacking. In other words, the potential contribution of 3D layering to the observed magnetism can be clearly ruled out.

To address the effect of chemical composition (OH and F contents) on magnetic properties of hydroxofluorographenes, we then constructed the magnetization map based on density functional theory (DFT) calculations for the $C_{18}(OH)_yF_x$ basic studied cell (Fig. 6). The magnetization map shows the propensity for the formation of FM ground states as a function of the F and OH content of the material (as also listed in Supplementary Table 2). Importantly, there are regions corresponding to the magnetically ordered FM ground states ranging from green to magnetically strongest red parts depending on the particular composition. Nevertheless, the blue regions corresponding to non-magnetic states are also present in a significant portion—the fact evidencing for a principal effect of chemical composition on magnetic features of G(OH)F system. In particular, two magnetically interesting islands appear, that is, upper island corresponding to G(OH)F systems with relatively high sp^3 functionalization (above $\sim$50%) and higher OH and F contents and lower island with considerably lower degree of sp^3 functionalization, centred at the $C_{18}F_4$ stoichiometry, surprisingly with very low OH content. Importantly, the stoichiometry of the G(OH)F sample, thoroughly discussed above, lies within the region of the upper island (sample denoted as No. 1 in the magnetization map in Fig. 6), where the magnetism originates from the presence of sp^2-conjugated diradical motifs embedded in an sp^3 matrix. Computational predictions are thus consistent with available experimental data. In this region, the $sp^3/(sp^2+sp^3)$ ratio is above the site percolation limit of honeycomb lattice (0.697)[52], which indicates that the number of sp^3 atoms is sufficient (above 5.5 for the supercell containing 18 carbon atoms) to cage the sp^2 islands.

To confirm the presence of diradical motifs experimentally, we prepared and measured the electron paramagnetic resonance (EPR) spectra (Supplementary Fig. 11) for the $C_{18}F_{11.5}$ sample whose $sp^3/(sp^2+sp^3)$ ratio was above the percolation limit (0.735), favouring the emergence of diradical motifs according to our theory. This sample exhibited a similar level of sp^3 functionalization like G(OH)F sample, which is, however, antiferromagnetic ($S=0$) and thus EPR silent. The EPR resonances recorded at two different temperatures clearly indicate the presence of radical species. In particular, overlapping signals originating from uncoupled $S=1/2$ centres (strong resonance signals around $g\approx2$) together with spin-coupled $S=1/2$ systems were observed, leading to the formation of triplet species ($S=1$). The EPR signatures of $S=1$ systems exhibited small E/D ratios (about 0.1) and became clearly visible upon lowering the temperature. The axial zero-field-splitting parameter (D) for the $S=1$ system was found to be equal to $\sim$790 MHz, which corresponds to an average distance of $\sim$4.6 Å between the interacting $S=1/2$ spins (point-dipole approach). Note that the distance between the two interacting $S=1/2$ spins corresponds well with the distance between the methylene groups in the *m*-xylylene motif ($\sim$4.887 Å). The EPR data thus unambiguously confirmed the presence

of diradical motifs in fluorographene systems of sufficiently high sp^3 content.

To validate the theoretical magnetization map, we further prepared four additional samples (samples denoted as No. 2–No. 5 in Fig. 6) exploiting various reaction conditions and –OH sources (for details, see 'Methods' section below) and determined their chemical composition by XPS (Supplementary Figs 12 and 13). Here it is worth noting that the experimental scope for preparing the strongest magnetic systems will be limited by thermodynamics (Supplementary Fig. 14) and ability to prepare hydroxofluorographene systems with suitable and stable distributions of –OH and –F moieties (in this context, the facile migration of fluorines in lightly fluorinated graphenes may be problematic[43]). Nevertheless, the magnetic properties of all four additional derivatives with chemical compositions of $C_{18}(OH)_{1.5}F_6$, $C_{18}(OH)_2F_3$, $C_{18}(OH)_{2.6}F_{4.7}$ and $C_{18}(OH)_{2.4}F_7$



fit to the magnetization map with an excellent correlation and confirm the profound influence of the $C_{18}(OH)_yF_x$ stoichiometry (Fig. 6 and Supplementary Figs 12 and 13). In particular, $C_{18}(OH)_2F_3$ is a diamagnet, in full accordance with the map (it lies in one of the blue regions in Fig. 6). Conversely, $C_{18}(OH)_{1.5}F_6$, $C_{18}(OH)_{2.6}F_{4.7}$ and $C_{18}(OH)_{2.4}F_7$ are magnetically sustainable 2D materials with an FM GS (all lying in green-yellow region) and very similar transition temperature to the AFM state at $\sim$62 K. The identical transition temperature, thus independent on chemical composition, is viewed as another proof of the same source of magnetism based on diradical motifs. The slight changes in saturation magnetization (from $\sim$0.9 to $\sim$1.2 emu g^{-1}; Fig. 6) stem from different strength of superexchange interactions associated to the content of –OH groups.

To further validate our theory, provide additional support for the essential role of –OH groups in the magnetism of hydroxofluorographenes, and explore the potentially different origins of magnetism in fluorographene and hydroxofluorographene systems, we also synthesized three partially fluorinated fluorographenes without –OH groups by simple thermal defluorination of the exfoliated C_1F_1 sample (for details on synthesis, see the 'Methods' section). The stoichiometries of these new systems are $C_{18}F_{2.5}$, $C_{18}F_4$ and $C_{18}F_{6.3}$ and the samples are denoted as No. 6, 7 and 8, respectively, in the magnetization map in Fig. 6 (for detailed XPS and magnetic characterization, see Supplementary Figs 15, 16 and 17). In full agreement with the magnetization map derived from our computational studies (Fig. 6), $C_{18}F_{2.5}$ is diamagnetic but contains some paramagnetic centres in perfect correspondence with the work by Nair *et al.*[43] reporting such behaviour for fluorographenes with lower fluorine coverages. Importantly, beyond the study by Nair *et al.*[43], the $C_{18}F_4$ exhibits even an FM GS as predicted by our magnetic model and experimentally confirmed (Fig. 6). However, it undergoes a transition to a paramagnetic state with the Curie temperature of 22 K. The different nature of transition temperature and inability to maintain magnetic ordering up to room temperature imply the different origin of magnetism in fluorographenes compared with hydroxofluorographenes. In particular, the structure of $C_{18}F_4$ can be considered as sp^3 structural defect in the sp^2 graphene lattice (Supplementary Fig. 18). This is further confirmed experimentally by detailed magnetic analysis of $C_{18}F_4$ (Supplementary Fig. 17). In particular, the temperature evolution of coercivity and saturation magnetization of $C_{18}F_4$ agrees very closely with predictions based on theoretical expressions for magnetism due to *d*-electrons (that is, models based on Brillouin and Bloch functions), implying that its magnetism is due to localized defect-induced magnetic moments[53,54]. These results starkly contrast with our observations for G(OH)F systems that exhibit room temperature magnetic ordering, whose experimental saturation magnetization and coercivity data cannot be fitted using models based on expressions for *d*-electron magnetism. Finally, the $C_{18}F_{6.3}$ sample is again diamagnetic with some paramagnetic centres in agreement with the theoretical magnetization map (Fig. 6). Here the magnetic ordering is lost due to a lack of conduction electrons related to the increased degree of functionalization.

The comparison of magnetic behaviour of GF and G(OH)F systems demonstrates the differences between the 'defect-induced magnetism' observed for GF systems with lower levels of sp^3 functionalization and the 'diradical motif-based magnetism' observed in the highly functionalized G(OH)F system. At the same time, these data show that our theoretical model (that is, the magnetization map presented in Fig. 6) is robust, universal and capable of explaining the behaviour of both system types with different origins of magnetism.

In summary, we report a new class of graphene derivatives, which behave as antiferromagnetic materials at room temperature, representing examples of *sp*-based systems with room temperature magnetism. They become ferromagnets as the temperature is lowered showing remarkable magnetization. These organic magnets are prepared via simple, scalable and controllable reactions of fluorographene with suitable –OH-containing organic precursors. An interplay between thermodynamically preferred defluorination and nucleophilic substitution affects the products' final stoichiometry and thus their magnetic features. The magnetism in hydroxofluorographenes with an appropriate stoichiometry stems from the presence of diradical motifs coupled via superexchange interactions and stabilized by –OH groups, which also mediate the coupling. The newly constructed theoretical model addresses the effect of system stoichiometry on magnetic features in an excellent agreement with experimental data. More importantly, this robust model has a universal character covering the aspects of the 'defect-induced magnetism' and 'diradical motif-triggered magnetism' appearing in the field of graphene magnetism depending on degree of sp^3 functionalization.

We believe that this work would open the doors for preparing a wider family of graphene-based 2D room temperature magnets whose magnetic properties can be tuned by controlling the sp^3 functionalization. Definitely, the theoretical model based on diradical motifs communicating through superexchange interactions should be further extended also for other graphene-based systems. The developed room temperature carbon magnets also offer a huge space for testing in potential applications in various fields including, for example, spintronics and magnetically separable nanocarriers.

Methods

Chemicals. Fluorinated graphite (C_1F_1) and tetramethylammonium hydroxide (25% w/w aqueous solution) were purchased from Sigma-Aldrich. Partly fluorinated graphites ($C_1F_{0.55}$ and $C_1F_{0.8}$) were purchased from Alfa Aesar.

Figure 6 | Magnetic properties as a function of $C_{18}(OH)_yF_x$ stoichiometry. (**a**) The mean magnetization map indicates which $C_{18}(OH)_yF_x$ ($x = 0$–8, $y = 0$–8) stoichiometries are likely to exist in ferromagnetic and non-magnetic ground states. Both –F and –OH groups are assumed to be randomly distributed across the sample (as suggested by STEM–HAADF elemental mapping, cf. Fig. 3) at zero temperature and the possibility of kinetically controlled –F/–OH migration is not considered. The white circles indicate experimentally studied samples: 1—$C_{18}(OH)_{1.8}F_{7.2}$ (ferromagnetic in the ground state), 2—$C_{18}(OH)_{1.5}F_6$ (ferromagnetic in the ground state), 3—$C_{18}(OH)_2F_3$ (diamagnetic in the ground state), 4—$C_{18}(OH)_{2.6}F_{4.7}$ (ferromagnetic in the ground state), 5—$C_{18}(OH)_{2.4}F_7$ (ferromagnetic in the ground state), 6—$C_{18}F_{2.5}$ (diamagnetic in the ground state), 7—$C_{18}F_4$ (ferromagnetic in the ground state) and 8—$C_{18}F_{6.3}$ (diamagnetic in the ground state). (**b**) The isothermal magnetization (*M*) curve of $C_{18}(OH)_{1.8}F_{7.2}$ (Sample No. 1) as a function of an external magnetic field (*H*), recorded at a temperature of 5 K. (**c**) *M* versus *H* curve of $C_{18}(OH)_{1.5}F_6$ (Sample No. 2), recorded at a temperature of 5 K. (**d**) *M* versus *H* curve of $C_{18}(OH)_2F_3$ (Sample No. 3), recorded at a temperature of 5 K. (**e**) *M* versus *H* curve of $C_{18}(OH)_{2.6}F_{4.7}$ (Sample No. 4), recorded at a temperature of 5 K. (**f**) *M* versus *H* curve of $C_{18}(OH)_{2.4}F_7$ (Sample No. 5), recorded at a temperature of 5 K. (**g**) *M* versus *H* curve of $C_{18}F_{2.5}$ (Sample No. 6), recorded at a temperature of 5 K. (**h**) *M* versus *H* curve of $C_{18}F_4$ (Sample No. 7), recorded at a temperature of 5 K. (**i**) *M* versus *H* curve of $C_{18}F_{6.3}$ (Sample No. 8), recorded at a temperature of 5 K. The insets in panel (**b**,**c**,**e**,**f** and **h**) show the behaviour of the respective hysteresis loops around the origin with the saturation magnetization (M_S) indicated.

DMF (p.a. grade) was obtained from PENTA, Czech Republic, and used without further purification.

Detailed synthesis of samples. To synthesize a few-layered fluorographene (GF) dispersion in DMF, fluorinated graphite (C:F, 1:1) (250 mg, Aldrich, grey powder) was suspended in 50 ml DMF. The mixture was sonicated for 2 h in an ultrasound bath and the temperature of the bath was kept below 30 °C. The suspension was then left to stand for 1 day to allow any undispersed material to settle. The clear, pale grey supernatant colloid was then collected and used in the preparation of hydroxofluorographene.

To synthesize hydroxofluorographene (G(OH)F, $C_{18}(OH)_{1.8}F_{7.2}$), 2 g of an aqueous tetramethylammonium hydroxide solution (25% w/w, Aldrich) was added to 50 ml of a fluorographene (C_1F_1) dispersion in DMF (prepared as described above) with a concentration of 0.8 mg ml^{-1}. The base initially precipitates in DMF but the precipitate gradually dissolves upon stirring. After 3 days' stirring at room temperature in a sealed vessel, the suspension was centrifuged at 5,000 r.p.m. for 10 min. The centrifuged solid was washed several times with water until its pH became neutral and then re-suspended in 6–8 ml water by sonication in an ultrasound bath (45 min). This dispersion was left to stand for 1 day to allow undispersed particles to settle and then centrifuged at 1,000 r.p.m. for 20 min to yield a clear black colloid containing aqueous dispersed hydroxofluorographene layers. Completely the same synthetic procedure was also applied to prepare hydroxofluorographenes ($C_{18}(OH)_2F_3$ and $C_{18}(OH)_{1.5}F_6$, respectively) from partly fluorinated graphites ($C_1F_{0.55}$ and $C_1F_{0.8}$, respectively).

Among several pathways tested for obtaining different hydroxylated graphene fluoride derivatives, two such reactions are described, as more appropriate for the scope of the present work. To synthesize $C_{18}(OH)_{2.6}F_{4.7}$, 50 mg of graphite fluoride was dispersed in 2 ml DMF and 0.7 ml H_2O_2 (30%, Aldrich) was added. The $C_{18}(OH)_{2.4}F_7$ sample was prepared by adding 0.7 ml tert-butyl hydroperoxide solution in decane (5.0–6.0 M, Aldrich) and 50 mg potassium tert-butoxide (Aldrich) in a 50 mg graphite fluoride dispersion in 2 ml DMF. Both mixtures were heated under stirring at 90 °C for 3 days. Work up of products was performed similarly with the previous ones.

Partially fluorinated fluorographenes, that is, with a composition of $C_{18}F_{2.5}$, $C_{18}F_4$ and $C_{18}F_{6.3}$, and the sample with the composition of $C_{18}F_{11.5}$ used for the EPR measurements, were obtained by thermal treatment of commercial fluorinated graphite under inert atmosphere at 800 °C for 4 h, at 625 °C for 4 h, at 550 °C for 5 h and at 550 °C for 1 h 52 min, respectively. The thermal treatments were performed in an open α-Al_2O_3 crucible using a Netzsch STA 449C Jupiter instrument. A temperature programme with a heating rate of 5 °C min^{-1} (10 °C min^{-1} for $C_{18}F_{11.5}$) from 40 °C to the final temperature was used. According to XPS analysis, the samples presented also small amounts of nitrogen and oxygen (atomic content, $C_{18}F_{2.5}$: N 2.0%, O 2.1%; $C_{18}F_4$: N 1.0%, O 1.4%; $C_{18}F_{6.3}$: O 0.6%; $C_{18}F_{11.5}$: O 3.1%).

Thermal annealing of G(OH)F. G(OH)F was thermally annealed by heating under inert atmosphere from room temperature to 220 °C at a rate of 5 °C min^{-1}, with a subsequent 3 h isotherm at 220 °C.

Characterization techniques. The exact composition of the precursors ($C_1F_{0.55}$, $C_1F_{0.8}$ and C_1F_1) and derived G(OH)F and partially fluorinated graphene (that is, $C_{18}F_x$, $x = 2.5$, 4, 6.3 and 11.5) samples was determined by XPS carried out with a PHI VersaProbe II (Physical Electronics) spectrometer using an Al K_α source (15 kV, 50 W). The obtained data were evaluated with the MultiPak (Ulvac-PHI, Inc.) software package. The detection of residual metal content in the G(OH)F sample was performed by ICP-MS. The exact amount of the G(OH)F sample (10 mg) was immersed in a concentrated nitric acid (≥99.999% trace metals basis) and heated for 2 h at 100 °C. Afterwards, the mixture was transferred into 10 ml volumetric flask, diluted with water and the undissolved graphene was caught by a 200 nm Millipore filter. The obtained concentration of metals in the solution was recalculated to the amount of the tested sample (analogically, diluted nitric acid was used as a blank). FT-IR spectra were obtained using an iS5 FT-IR spectrometer (Thermo Nicolet) with a Smart Orbit ZnSe ATR technique (650–4,000 cm^{-1}). Raman spectra were recorded on a DXR Raman microscope using the 532 nm excitation line of a diode laser. HRTEM images were obtained using an FEI TITAN 60–300 HRTEM microscope with an X-FEG type emission gun, operating at 300 kV. STEM–HAADF analyses for EDX mapping of elemental distributions on the G(OH)F sheets were performed with an FEI TITAN 60–300 HRTEM microscope operating at 80 kV. For HRTEM, STEM–HAADF and EDX experiments, an aqueous solution of G(OH)F with a concentration of 0.1 mg ml^{-1} was redispersed by ultrasonication for 5 min. A drop of the sonicated sample was then deposited on a carbon-coated copper grid and slowly dried at laboratory temperature for 24 h to reduce its content of adsorbed water. Atomic force microscopy images and appropriate height profiles were recorded in semi-contact mode (HA-NC tips, mica substrate) on an NTEGRA Aura instrument. Thermogravimetric analysis and evolved gas analysis were performed on a STA449 C Jupiter-Netzsch instrument with a heating rate of 1 °C min^{-1}. The masses of released gases in the range of 12–60 *m/z* were determined with a QMS 403 Aolos mass spectrometer (Netzsch), starting at 100 °C to avoid overloading the spectrometer with adsorbed water. A superconducting quantum interference device magnetometer (MPMS XL-7 type, Quantum Design, USA) was employed for the magnetization measurements. The temperature dependence of the magnetization of tetramethylammonium hydroxide, C_1F_1 precursor and seven final products (that is, $C_{18}(OH)_2F_3$, $C_{18}(OH)_{1.5}F_6$, $C_{18}(OH)_{2.6}F_{4.7}$, $C_{18}(OH)_{2.4}F_7$, $C_{18}F_{2.5}$, $C_{18}F_4$ and $C_{18}F_{6.3}$) was recorded in the sweep mode over the temperature interval from 5 to 300 K under an external magnetic field of 10 kOe; the temperature evolution of magnetization of the $C_{18}(OH)_{1.8}F_{7.2}$ sample was monitored in the sweep mode over the temperature interval from 5 to 400 K and back under an external magnetic field of 10 kOe. The hysteresis loops of the $C_{18}(OH)_{1.8}F_{7.2}$ and $C_{18}F_4$ samples were measured at a series of temperatures in the interval from 5 to 400 K and from 5 to 300 K, respectively, in external magnetic fields ranging from −50 to +50 kOe. The hysteresis loops of the $C_{18}(OH)_2F_3$, $C_{18}(OH)_{1.5}F_6$, $C_{18}(OH)_{2.6}$ $F_{4.7}$, $C_{18}(OH)_{2.4}F_7$, $C_{18}F_{2.5}$ and $C_{18}F_{6.3}$ samples were measured at a temperature of 5 K and in external magnetic fields from −50 to +50 kOe. The magnetization values were corrected assuming the response of the sample holder, sample capsule and respective Pascal constants. EPR spectra were recorded on a JEOL JES-X-320 operating at X-band frequency (~9.15 GHz), equipped with a variable temperature control ES 13060DVT5 apparatus, and were performed on the powder $C_{18}F_{11.5}$ sample (~2 mg loaded onto the EPR tube). The cavity Q quality factor was kept above 6,000, highly pure quartz tube was employed (Suprasil, Wilmad, <0.5 OD) to load the sample powders. The *g* value accuracy was obtained by comparing the resonance signals of the $C_{18}F_{11.5}$ sample with that of MnO standard (JEOL-internal standard). The experimental conditions for measuring EPR spectra were adjusted as follows: frequency = 9.15584 GHz, modulation frequency = 100 kHz, modulation amplitude = 0.8 mT, time constant = 30 ms, applied microwave power = 0.8 mW, sweep time = 480 s and phase = 0°s.

Computational methods. Atomistic calculations were performed using the spin-polarized DFT and projected augmented wave potentials representing atomic cores as implemented in the VASP package[55–57]. The PBE xc functional[58] was used with a plane wave cutoff of 500 eV. The Brillouin zone integrations were performed with $2 \times 2 \times 1$ (structure and cell optimization) and $10 \times 10 \times 1$ (final runs; magnetism) Γ point-centred *k*-point Monkhorst-Pack meshes[59] per 3×3 supercell. The electronic density of states was calculated using the tetrahedron method[60] employed denser *k*-point sampling $16 \times 16 \times 1$. Open circles in Fig. 6 label the explored 21 unique stoichiometries $C_{18}(OH)_yF_x$. For each stoichiometry at least 64 random structures were generated. The optimized structures were converged to energy of less than 10^{-4} eV, and a convergence criterion of 10^{-6} eV for each SCF cycle. The thermodynamic stability of all reported configurations was analysed in terms of the stabilization energy $E_{stab} = [E(\text{model}) - N_F{*}E(\text{F}) - N_{OH}{*}E(\text{OH}) - N_C{*}E(\text{C})]/(N_F + N_{OH} + N_C)$, where E(model), E(F) and E(OH) denote the total energy of the supercell model, F atom, –OH group and C atom, respectively and N_F, N_{OH} and N_C denote the number of F atoms, –OH groups and C atoms, respectively. The spin coupling constant or spin-flip gap per supercell was calculated as $E_{SF} = E_{LS} - E_{HS}$, where E_{LS} and E_{HS} are the total low-spin and total high-spin energy for a given configuration, respectively. The mean magnetization was obtained as average over 32 low-energy samples from 64 per cell as a function of x and y in the formula of $C_{18}(OH)_yF_x$. The colour-coded maps were generated by linear fitting among valid data points represented by circles.

To address the role of 3D stacking on the magnetic properties of the G(OH)F system, calculations including vdW-correction DFT-D3 of Grimme[61] were carried out for a hypothetical bulk. We considered typical stacking patterns, namely AA and AB; the relaxed interlayer distance for the most energetically stable structure was 5.9 Å. The energetically most stable structure together with the corresponding density of states plot is presented in Supplementary Fig. 10.

Data availability. The data that support the findings of this study are available from the corresponding author upon request.

References

1. Novoselov, K. S. *et al.* Electric field effect in atomically thin carbon films. *Science* **306,** 666–669 (2004).
2. Novoselov, K. S. *et al.* Two-dimensional gas of massless Dirac fermions in graphene. *Nature* **438,** 197–200 (2005).
3. Zhang, Y. B., Tan, Y. W. & Stormer, H. L. Experimental observation of the quantum Hall effect and Berry's phase in graphene. *Nature* **438,** 201–204 (2005).
4. Lee, C., Wei, X. D., Kysar, J. W. & Hone, J. Measurement of the elastic properties and intrinsic strength of monolayer graphene. *Science* **321,** 385–388 (2008).
5. Castro Neto, A. H., Guinea, F., Peres, N. M. R., Novoselov, K. S. & Geim, A. K. The electronic properties of graphene. *Rev. Modern Phys.* **81,** 109–162 (2009).
6. Balandin, A. A. *et al.* Superior thermal conductivity of single-layer graphene. *Nano Lett.* **8,** 902–907 (2008).
7. Kane, C. L. & Mele, E. J. Quantum spin Hall effect in graphene. *Phys. Rev. Lett.* **95,** 226801 (2005).

8. Geim, A. K. & Novoselov, K. S. The rise of graphene. *Nat. Mater.* **6,** 183–191 (2007).
9. Stoller, M. D., Park, S. J., Zhu, Y. W., An, J. H. & Ruoff, R. S. Graphene-based ultracapacitors. *Nano Lett.* **8,** 3498–3502 (2008).
10. Nair, R. R. *et al.* Fine structure constant defines visual transparency of graphene. *Science* **320,** 1308 (2008).
11. Tse, W. K. & MacDonald, A. H. Giant magneto-optical Kerr effect and universal Faraday effect in thin-film topological insulators. *Phys. Rev. Lett.* **105,** 057401 (2010).
12. Fialkovsky, I. V., Marachevsky, V. N. & Vassilevich, D. V. Finite-temperature Casimir effect for graphene. *Phys. Rev. B* **84,** 035446 (2011).
13. Georgakilas, V., Perman, J. A., Tucek, J. & Zboril, R. Broad family of carbon nanoallotropes: classification, chemistry, and applications of fullerenes, carbon dots, nanotubes, graphene, nanodiamonds, and combined superstructures. *Chem. Rev.* **115,** 4744–4822 (2015).
14. Bae, S. *et al.* Roll-to-roll production of 30-inch graphene films for transparent electrodes. *Nat. Nanotechnol.* **5,** 574–578 (2010).
15. Tapaszto, L., Dobrik, G., Lambin, P. & Biro, L. P. Tailoring the atomic structure of graphene nanoribbons by scanning tunnelling microscope lithography. *Nat. Nanotechnol.* **3,** 397–401 (2008).
16. Han, W., Kawakami, R. K., Gmitra, M. & Fabian, J. Graphene spintronics. *Nat. Nanotechnol.* **9,** 794–807 (2014).
17. Sun, Z. H. & Chang, H. X. Graphene and graphene-like two-dimensional materials in photodetection: Mechanisms and methodology. *ACS Nano* **8,** 4133–4156 (2014).
18. Liu, Z. F. *et al.* Organic photovoltaic devices based on a novel acceptor material: Graphene. *Adv. Mater.* **20,** 3924–3930 (2008).
19. Wu, J. B. *et al.* Organic light-emitting diodes on solution-processed graphene transparent electrodes. *ACS Nano* **4,** 43–48 (2010).
20. Xu, Y. X. *et al.* Holey graphene frameworks for highly efficient capacitive energy storage. *Nat. Commun.* **5,** 4554 (2014).
21. Zhao, M. Q. *et al.* Unstacked double-layer templated graphene for high-rate lithium-sulphur batteries. *Nat. Commun.* **5,** 3410 (2014).
22. Georgakilas, V. *et al.* Functionalization of graphene: covalent and non-covalent approaches, derivatives and applications. *Chem. Rev.* **112,** 6156–6214 (2012).
23. Joshi, R. K., Alwarappan, S., Yoshimura, M., Sahajwalla, V. & Nishina, Y. Graphene oxide: the new membrane material. *Appl. Mater. Today* **1,** 1–12 (2015).
24. Elias, D. C. *et al.* Control of graphene's properties by reversible hydrogenation: evidence for graphane. *Science* **323,** 610–613 (2009).
25. Zboril, R. *et al.* Graphene fluoride: a stable stoichiometric graphene derivative and its chemical conversion to graphene. *Small.* **24,** 2885–2891 (2010).
26. Urbanova, V. *et al.* Thiofluorographene-hydrophilic graphene derivative with semiconducting and genosensing properties. *Adv. Mater.* **27,** 2305–2310 (2015).
27. Dubecky, M. *et al.* Reactivity of fluorographene: a facile way toward graphene derivatives. *J. Phys. Chem. Lett.* **6,** 1430–1434 (2015).
28. Kuila, T. *et al.* Chemical functionalization of graphene and its applications. *Prog. Mater. Sci.* **57,** 1061–1105 (2012).
29. Yazyev, O. V. Emergence of magnetism in graphene materials and nanostructures. *Rep. Prog. Phys.* **73,** 056501 (2010).
30. Palacios, J. J., Fernandez-Rossier, J. & Brey, L. Vacancy-induced magnetism in graphene and graphene ribbons. *Phys. Rev. B* **77,** 195428 (2008).
31. Yazyev, O. V. & Helm, L. Defect-induced magnetism in graphene. *Phys. Rev. B* **75,** 125408 (2007).
32. Ito, Y. *et al.* Tuning the magnetic properties of carbon by nitrogen doping of its graphene domains. *J. Am. Chem. Soc.* **137,** 7678–7685 (2015).
33. Tuček, J. *et al.* Sulfur doping induces strong ferromagnetic ordering in graphene: effect of concentration and substitution mechanism. *Adv. Mater.* **28,** 5045–5053 (2016).
34. Magda, G. Z. *et al.* Room-temperature magnetic order on zigzag edges of narrow graphene nanoribbons. *Nature* **514,** 608–611 (2014).
35. Khurana, G., Kumar, N., Kotnala, R. K., Nautiyal, T. & Katiyar, R. S. Temperature tuned defect induced magnetism in reduced graphene oxide. *Nanoscale* **5,** 3346–3351 (2013).
36. Eng, A. Y. S. *et al.* Searching for magnetism in hydrogenated graphene: using highly hydrogenated graphene prepared *via* birch reduction of graphite oxides. *ACS Nano* **7,** 5930–5939 (2013).
37. Zhou, J. *et al.* Ferromagnetism in semihydrogenated graphene sheet. *Nano Lett.* **9,** 3867–3870 (2009).
38. Gonzalez-Herrero, H. *et al.* Atomic-scale control of graphene magnetism by using hydrogen atoms. *Science* **352,** 437–441 (2016).
39. Li, Y., Ren, J. C., Zhang, R. Q., Lin, Z. J. & van Hove, M. A. Atomic nitrogen chemisorption on graphene with extended line defects. *J. Mater. Chem.* **22,** 21167–21172 (2012).
40. Wang, Z. G., Qin, S. J., Wang, C. L. & Hui, Q. Fluorine adsorption on the graphene films: from metal to insulator. *Comput. Mater. Sci.* **97,** 14–19 (2015).
41. Cao, C., Wu, M., Jiang, J. Z. & Cheng, H. P. Transition metal adatom and dimer adsorbed on graphene: Induced magnetization and electronic structures. *Phys. Rev. B* **81,** 205424 (2010).
42. Nair, R. R. *et al.* Dual origin of defect magnetism in graphene and its reversible switching by molecular doping. *Nat. Commun.* **4,** 2010 (2013).
43. Nair, R. R. *et al.* Spin-half paramagnetism in graphene induced by point defects. *Nat. Phys.* **8,** 199–202 (2012).
44. Nair, R. R. *et al.* Fluorographene: a two-dimensional counterpart of teflon. *Small.* **6,** 2877–2884 (2010).
45. Cho, D., Ko, K. C. & Lee, J. Y. Organic magnetic diradicals (radical-coupler-radical): standardization of couplers for strong ferromagnetism. *J. Phys. Chem. A* **118,** 5112–5121 (2014).
46. Rajca, A. Organic diradicals and polyradicals: from spin coupling to magnetism? *Chem. Rev.* **94,** 871–893 (1994).
47. Lieb, E. H. 2 theorems on the Hubbard model. *Phys. Rev. Lett.* **62,** 1201–1204 (1989).
48. Belhadji, B. *et al.* Trends of exchange interactions in dilute magnetic semiconductors. *J. Phys. Condens. Matter* **19,** 436227 (2007).
49. Ao, Z. *et al.* Enhancement of the stability of fluorine adatoms on defective graphene and at graphene/fluorographene interface. *ACS Appl. Mater. Interfaces* **7,** 19659–19665 (2015).
50. Sadeghi, A., Neek-Amal, M. & Peeters, F. M. Diffusion of fluorine on and between graphene layers. *Phys. Rev. B* **91,** 014304 (2015).
51. Kim, S. W., Kim, H. J., Choi, J. H., Scheicher, R. H. & Cho, J. H. Contrasting interedge superexchange interactions of graphene nanoribbons embedded in h-BN and graphane. *Phys. Rev. B* **92,** 035443 (2015).
52. Feng, X. M., Deng, Y. J. & Blote, H. W. J. Percolation transitions in two dimensions. *Phys. Rev. E* **78,** 031136 (2008).
53. Makarova, T. L. *et al.* Edge state magnetism in zigzag-interfaced graphene *via* spin susceptibility measurements. *Sci. Rep.* **5,** 13382 (2015).
54. Enoki, T. & Takai, K. The edge state of nanographene and the magnetism of the edge-state spins. *Solid State Commun.* **149,** 1144 (2009).
55. Kresse, G. & Furthmüller, J. Efficient iterative schemes for ab initio total-energy calculations using a plane-wave basis set. *Phys. Rev. B* **54,** 11169–11186 (1996).
56. Kresse, G. & Joubert, D. From ultrasoft pseudopotentials to the projector augmented-wave method. *Phys. Rev. B* **59,** 1758–1775 (1999).
57. Blöchl, P. E. Projector augmented-wave method. *Phys. Rev. B* **50,** 17953–17979 (1994).
58. Perdew, J. P., Burke, K. & Ernzerhof, M. Generalized gradient approximation made simple. *Phys. Rev. Lett.* **77,** 3865–3868 (1996).
59. Monkhorst, H. J. & Pack, J. D. Special points for Brillouin-zone integrations. *Phys. Rev. B* **13,** 5188–5192 (1976).
60. Blöchl, P. E., Jepsen, O. & Andersen, O. K. Improved tetrahedron method for Brillouin-zone integrations. *Phys. Rev. B* **49,** 16223–16233 (1994).
61. Grimme, S., Antony, J., Ehrlich, S. & Krieg, S. A consistent and accurate ab initio parametrization of density functional dispersion correction (dft-d) for the 94 elements H-Pu. *J. Chem. Phys.* **132,** 154104 (2010).

Acknowledgements

The authors acknowledge the support from the Ministry of Education, Youth and Sports of the Czech Republic (LO1305) and the assistance provided by the Research Infrastructure NanoEnviCz, supported by the Ministry of Education, Youth and Sports of the Czech Republic under Project No. LM2015073. M.O. acknowledges the Neuron fund for supporting science and the Czech Science Foundation (P208/12/G016) and ERC grant (ERC-2015-CoG). The authors deeply thank Dr. Giorgio Zoppellaro (from the Regional Centre of Advanced Technologies and Materials, Faculty of Science, Palacky University in Olomouc, Czech Republic) for measuring and interpreting the EPR spectra. The authors also thank Dr. Joelle Hoggan and her team at Sees-editing Ltd., UK, for professional language corrections of the manuscript.

Author contributions

J.T. performed magnetization data analysis and participated in writing the manuscript, K.H. prepared the samples and performed data analysis, A.B.B. and J.U. prepared the samples, A.B. prepared the samples and performed data analysis, P.B., M.D. and F.K. carried out theoretical computations and participated in writing the manuscript, V.R. performed Raman and FT-IR measurements, K.C. performed microscopic experiments, M.O. carried out theoretical computations and participated in writing the manuscript and R.Z. came with the idea of imprinting magnetism to a graphene-based system through functionalization, designed the experiments and participated in writing the manuscript.

Additional information

Supplementary Information accompanies this paper at http://www.nature.com/naturecommunications

Competing financial interests: The authors declare no competing financial interests.

Reprints and permission information is available online at http://npg.nature.com/reprintsandpermissions/

How to cite this article: Tuček, J. *et al.* Room temperature organic magnets derived from sp^3 functionalized graphene. *Nat. Commun.* **8,** 14525 doi: 10.1038/ncomms14525 (2017).

Publisher's note: Springer Nature remains neutral with regard to jurisdictional claims in published maps and institutional affiliations.

This work is licensed under a Creative Commons Attribution 4.0 International License. The images or other third party material in this article are included in the article's Creative Commons license, unless indicated otherwise in the credit line; if the material is not included under the Creative Commons license, users will need to obtain permission from the license holder to reproduce the material. To view a copy of this license, visit http://creativecommons.org/licenses/by/4.0/

© The Author(s) 2017

ACS NANO
Cite This: ACS Nano 2018, 12, 12847−12859
www.acsnano.org

ARTICLE

Zigzag sp^2 Carbon Chains Passing through an sp^3 Framework: A Driving Force toward Room-Temperature Ferromagnetic Graphene

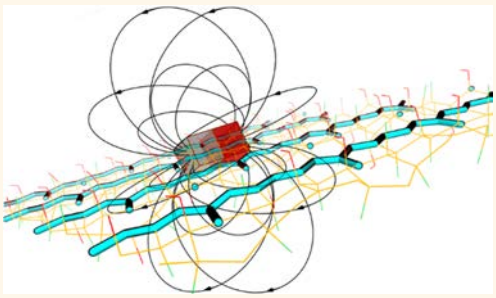
Jiří Tuček,[†] Kateřina Holá,[†] Giorgio Zoppellaro,[†] Piotr Błoński,[†] Rostislav Langer,[†] Miroslav Medveď,[†] Toma Susi,[‡] Michal Otyepka,*[,†] and Radek Zbořil*[,†]

[†]Regional Centre of Advanced Technologies and Materials, Department of Physical Chemistry, Faculty of Science, Palacký University in Olomouc, Šlechtitelů 27, 783 71 Olomouc, Czech Republic

[‡]Faculty of Physics, University of Vienna, Boltzmanngasse 5, 1090 Vienna, Austria

Supporting Information

ABSTRACT: **Stabilization of ferromagnetic ordering in graphene-based systems up to room temperature remains an important challenge owing to the huge scope for applications in electronics, spintronics, biomedicine, and separation technologies. To date, several strategies have been proposed, including edge engineering, introduction of defects and dopants, and covalent functionalization. However, these techniques are usually hampered by limited temperature sustainability of ferromagnetic ordering. Here, we describe a method for the well-controlled sp^3 functionalization of graphene to synthesize zigzag conjugated sp^2 carbon chains that can act as communication pathways among radical motifs. Zigzag sp^2/sp^3 patterns in the basal plane were clearly observed by high-resolution scanning transmission electron microscopy and provided a suitable matrix for stabilization of ferromagnetic ordering up to room temperature due to combined contributions of itinerant π-electrons and superexchange interactions. The results highlight the principal role of sp^2/sp^3 ratio and superorganization of radical motifs in graphene for generating room-temperature nonmetallic magnets.**



KEYWORDS: *hydroxofluorographene, fluorographene, magnetic carbon, hydroxyl, DFT calculations, density of states, 2D magnets, spintronics*

Graphene, a two-dimensional (2D) layer of sp^2-bonded carbon atoms arranged in hexagons, has attracted continuous attention of the scientific community over the past decade owing to its exceptional mechanical, electric, transport, and optical properties, which stem from its peculiar atomic organization and electronic structure.[1,2] It has been successfully tested in or proposed for a broad spectrum of applications[3] in various fields, such as electronics,[4] generation and storage of energy,[5,6] optics,[7] medicine,[8] printing technologies,[9] treatment of the environment,[10] and mechanical reinforcements.[11] However, despite its unique physical features, several drawbacks have been identified that hamper its use for specific processes and utilization. They include its high hydrophobicity, zero bandgap, and lack of magnetic response. In many cases, functionalization has been shown to be an effective strategy for overcoming these drawbacks.[12] For instance, it has been used to synthesize a number of graphene derivatives, such as graphene oxide,[13] graphane,[14] fluorographene[15,16] and other halogenated graphenes,[17] thiographene,[18] cyanographene,[19] graphene acid,[19,20] and hydroxographene,[21] significantly extending the application potential of graphene-based materials and providing attractive/competitive alternatives in fields where pristine graphene fails.

More than two decades ago, it was theoretically suggested that in a single layer of graphite, intrinsically diamagnetic, localized magnetic moments may emerge if an sp^3-type defect is formed in the hexagonal carbon lattice. Since the first isolation of graphene in 2004,[1] the introduction of defects has become accepted as a promising way to endow graphene with the magnetic properties it lacks.[22,23] In general, defects formed or introduced in the graphene lattice are of diverse nature; for example, they can emerge due to (i) structural/topological disorders, such as point and line defects (*i.e.*, vacancies, interstitial atoms, periodically repeating pentagonal-heptagonal

Received: October 22, 2018
Accepted: December 5, 2018
Published: December 5, 2018

Downloaded via PALACKY UNIV on March 28, 2019 at 12:05:47 (UTC).
See https://pubs.acs.org/sharingguidelines for options on how to legitimately share published articles.

© 2018 American Chemical Society

DOI: 10.1021/acsnano.8b08052
ACS Nano 2018, 12, 12847−12859

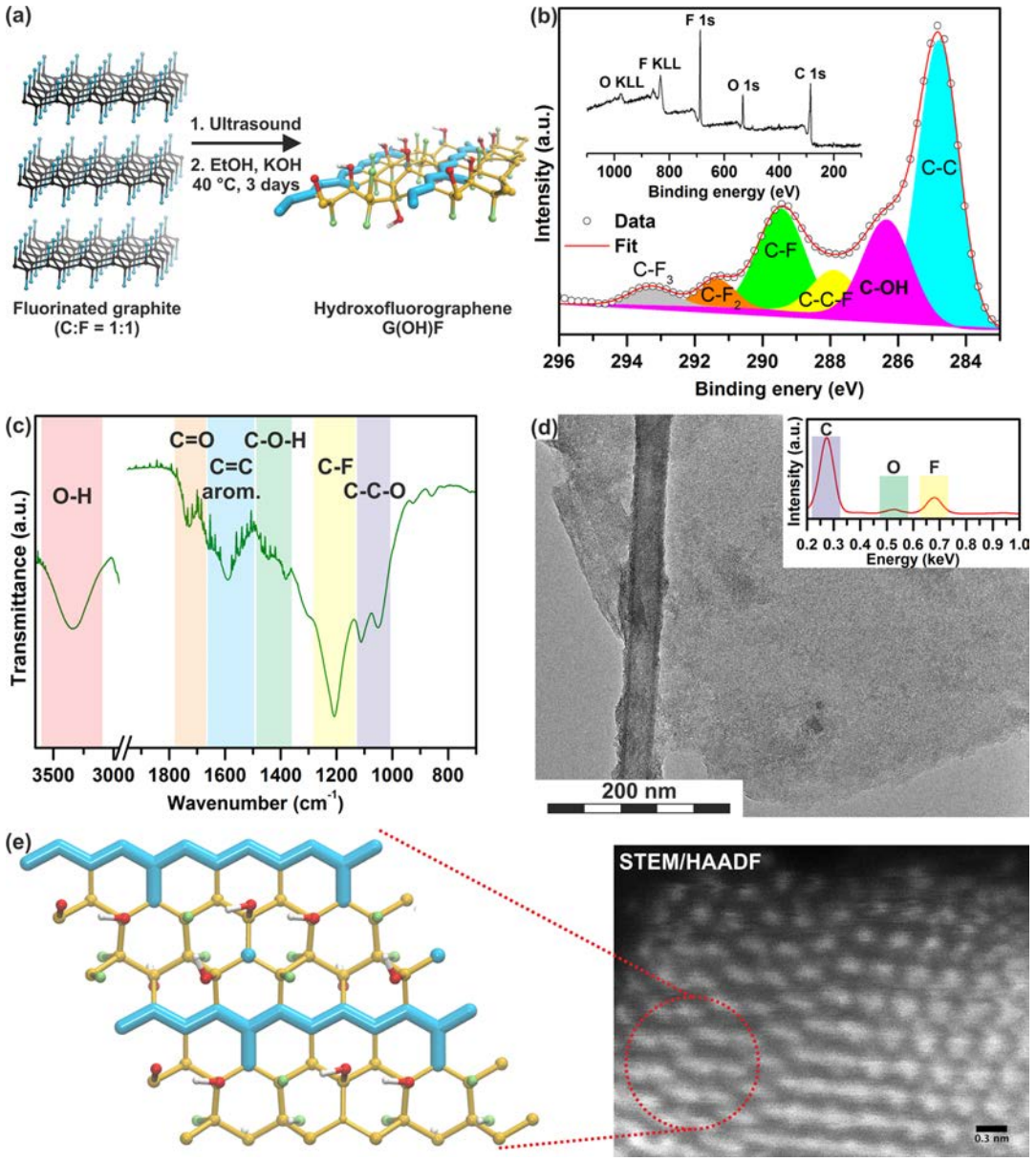


Figure 1. Physicochemical characterization of the G(OH)F system. (a) Schematic of the synthetic protocol for preparing G(OH)F. (b) High-resolution C 1s XPS pattern of G(OH)F with bonds indicated. The inset shows the survey XPS pattern of G(OH)F with element peaks indicated. (c) FT-IR spectrum of G(OH)F with bands corresponding to the significant bonds marked. (d) Representative HRTEM image of a G(OH) sheet. The inset shows the EDS pattern, which confirms that only carbon, fluorine, and oxygen were present in the system. (e) Scanning transmission electron microscopy/high-angle annular dark-field imaging (STEM/HAADF) image (right) of a thin region near the edge of a G(OH)F aggregate, with evident zigzag patterning in agreement with the model representation of zigzag routes in the structure of G(OH)F (left).

or pentagonal-octagonal motifs) and Thrower−Stone−Wales defects,[24,25] (ii) substitutional non-carbon atoms (*i.e.*, nitrogen, boron, sulfur),[26,27] (iii) adatoms (*i.e.*, light atoms such as hydrogen, fluorine, *etc.*),[28−32] (iv) functionalizing groups,[33,34] and (v) special edge architectures and related confinement effects.[35,36] The presence of defects substantially modifies the electronic structure of graphene, resulting in evolution of midgap states or flat bands appearing at or in close proximity to the Fermi level (E_F). Most importantly, these new band features are spin polarized, implying they are associated with increased magnetic moments due to defect-promoted formation of unpaired electrons that no longer participate in bonding.

DOI: 10.1021/acsnano.8b08052
ACS Nano 2018, 12, 12847−12859

As graphene can be regarded as a bipartite system with two interpenetrating triangular lattices, the relative positions of the magnetic moments determine the type of the magnetic ground state according to the Lieb's theorem.[37] The generated magnetic moments, alternatively termed paramagnetic centers, may interact with each other once a communication medium is available. As a result, ferromagnetic and/or antiferromagnetic ordering can develop with sustainability against thermal fluctuations up to a finite temperature determined by the strength of the magnetic interactions among the defect-induced magnetic moments. Originally, the conductive π-electron system of graphene was proposed as a mediator of magnetic coupling with attributes resembling those of the Ruderman−Kittel−Kasuya−Yosida (RKKY) interaction.[22,23] Thus, the concept of the Stoner magnetism is sometimes adopted to account for magnetic ordering in graphene mediated by itinerant π-electrons occupying narrow bands at E_F. However, it has often been argued, from both theoretical and experimental standpoints, that the π-electron system of graphene is generally too weak for maintaining the magnetic coupling over the whole structure at elevated temperatures.[23,38] It has also been shown that in the case of doping the magnetic ordering can resist thermal disruption to some extent depending on the chemical nature of the dopant, its electronic features (*i.e.*, n-/p-type), and its concentration and configurations of foreign atoms in the graphene lattice.[26,27] In such cases, the magnetic transition temperatures can be up to 100 K. In cases where room-temperature magnetic ordering has been observed, it has been heavily questioned due to the highly probable or lately confirmed presence of impurities of d-block elements stemming from the synthesis itself or sample handling.[39,40]

Recently, sp^3 functionalization of a graphene sheet has been identified as an effective approach to induce huge magnetic moments at low temperatures.[41] In addition, suitable sp^3 functionalization promotes the formation of a new type of magnetic centers in graphene, known as diradical motifs, as demonstrated very recently by Tuček *et al.*,[33] whereas previous concepts have heavily relied on monoradical-(defect-)induced magnetism. These diradical motifs are believed to emerge only above the site percolation limit of the graphene lattice, *i.e.*, when the number of sp^3-carbon atoms is sufficient to encage the remaining sp^2-conjugated islands. In other words, sp^3 functionalization must reach a defined level for both the generation of diradical motifs and suppression of lateral diffusion of adatoms that ruin the periodic pattern of sp^2 magnetic islands over the graphene sheet. Most importantly, apart from acting as sources of magnetic moments, the functionalizing groups enable bridging among the diradical motifs, eventually mediating interaction among them and stabilizing the magnetic order throughout the whole graphene lattice up to high temperatures.

In particular, hydroxofluorographenes with an appropriate F/OH ratio are examples of such sp^3-functionalized graphene platforms where −OH groups act as a driving force for establishing diradical motifs by supporting their stabilization and allowing communication *via* superexchange interactions.[33] Although these systems show a ferromagnetic ground state, they undergo transition to an antiferromagnetic regime upon heating, which is stable up to room temperature. In other words, superexchange interactions seem to be much stronger than the π-electron system of graphene at maintaining the magnetic ordering to exceptionally high temperatures. Thus, development of the functionalization approach to generate ferromagnetic ordering sustainable up to room temperature *via* strengthening the role of itinerant π-electrons and, at the same time, the synergistic effect of other magnetic exchange mechanisms remains a challenging task.

In this work, we report a simple synthetic strategy based on the chemistry of fluorographene to prepare hydroxyl- and fluoro-functionalized 2D graphenes with superorganization of zigzag sp^2 carbon chains/paths inside an otherwise sp^3-bonded lattice. The prepared graphene derivative exhibited room-temperature ferromagnetic ordering stemming from the synergistic interplay between itinerant π-electrons and superexchange interactions mediated by −OH groups. The synthesis of a ferromagnetic nonmetallic carbon-based material could stimulate an interest in exploiting such 2D systems for advanced applications in various fields of electronics, biomedicine, spintronics, targeted delivery, and separation processes.

RESULTS AND DISCUSSION

To prepare a magnetically ordered graphene derivative, we synthesized graphene containing zigzag sp^2 motifs embedded in an otherwise sp^3 lattice with a suitable functional group that enabled magnetic interaction among the individual zigzag motifs.[42] We employed a fluorographene chemistry, which allowed tailored functionalization of graphene and preparation of a wide portfolio of graphene derivatives.[43−45] We chose −OH groups as a functionality for establishing efficient magnetic interaction among magnetic centers embedded in the graphene lattice.[33] We reacted fluorographene with KOH in ethanol at an elevated temperature (see Figure 1a and Figure S1 in the Supporting Information) to prepare hydroxofluorographene (denoted hereafter as G(OH)F) and found that it exhibited ferromagnetic ordering sustainable up to room temperature (see below).

X-ray photoelectron spectroscopy (XPS) analyses performed on as-formed G(OH)F revealed the presence of only carbon, fluorine, and oxygen, as can be seen in the XPS survey spectrum in the inset of Figure 1b. The content of these elements was 65.8%, 21.9%, and 12.3%, respectively, giving a total chemical composition of $C_{18}(OH)_{3.4}F_6$. The high proportion of oxygen in the material was also reflected in the ratio between the C−OH and various C−F bonds in the high-resolution C 1s XPS (see Figure 1b) pattern. The high-resolution O 1s XPS pattern also showed that oxygen in the sample was mostly present as hydroxyl groups (see Figure S2a in the Supporting Information). The low amount of oxygen as carbonyl/carboxyl groups was probably due to the harsh reaction conditions. Quantification of various metals as potential magnetic contaminants was carried out by inductively coupled plasma mass spectrometry (ICP-MS) technique (see Table S1 in the Supporting Information). The ICP-MS analysis confirmed that the mass amounts of Fe, Ni, and Co were below 15 ppm. If the determined mass amounts of Fe, Ni, and Co and the magnitudes of their magnetic moments were considered, the total mass magnetic susceptibility (χ_{mass}) of these d-block elements was estimated to be on the order of 10^{-8} emu g^{-1} Oe^{-1} at 0 K under a 1 kOe field. Since the measured χ_{mass} values for the G(OH)F sample were on the order of 10^{-5} to 10^{-6} emu g^{-1} Oe^{-1} under a 1 kOe field (see below), the contribution of Fe, Ni, and Co to the sample's χ_{mass} was assumed negligible and not responsible for the observed magnetic phenomena.

DOI: 10.1021/acsnano.8b08052
ACS Nano 2018, 12, 12847−12859

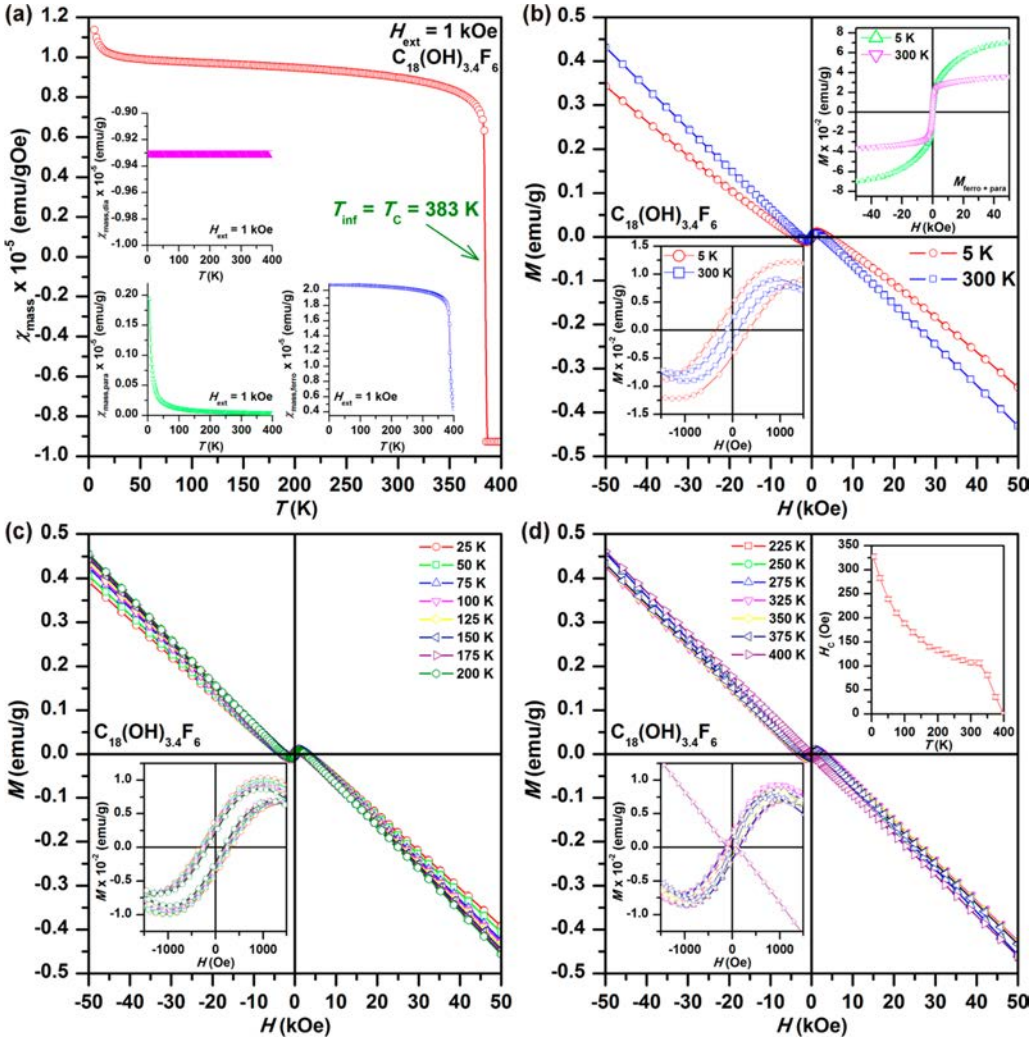


Figure 2. Magnetization measurements of the G(OH)F system. (a) Temperature evolution of the mass magnetic susceptibility (χ_{mass}) recorded for the $C_{18}(OH)_{3.4}F_6$ sample under an external magnetic field (H_{ext}) of 1 kOe. The insets show the profile of the diamagnetic ($\chi_{mass,dia}$), paramagnetic ($\chi_{mass,para}$), and ferromagnetic ($\chi_{mass,ferro}$) contribution to the total χ_{mass} obtained from analysis of the χ_{mass} plot. T_{inf} and T_C correspond to the temperature of the inflection point and Curie temperature, respectively, and indicate transition from a ferromagnetic state to paramagnetic regime upon warming the sample in the chamber of the magnetometer. (b) Hysteresis loops (M *vs* H curves) of the $C_{18}(OH)_{3.4}F_6$ sample measured at temperatures of 5 and 300 K. The lower inset shows the behavior of the isothermal magnetization curves around the origin, providing evidence for nonzero values of the coercivity and remanent magnetization. The upper inset displays hysteresis loops after subtraction of the diamagnetic part ($M_{ferro+para}$ denotes the magnetization of the ferromagnetic and paramagnetic fraction together). (c) Hysteresis loops (M *vs* H curves) of the $C_{18}(OH)_{3.4}F_6$ sample at temperatures of 25 and 200 K. The lower inset shows the behavior of the isothermal magnetization curves around the origin, providing evidence for nonzero values of the coercivity and remanent magnetization. (d) Hysteresis loops (M *vs* H curves) of the $C_{18}(OH)_{3.4}F_6$ sample measured at temperatures from 225 and 400 K. The lower inset shows the behavior of the isothermal magnetization curves around the origin, providing evidence for nonzero values of the coercivity and remanent magnetization. The upper inset displays the temperature dependence of the coercivity (H_C), derived from the respective hysteresis loops.

The Raman spectrum of G(OH)F (see Figure S2b in the Supporting Information) exhibited typical features of functionalized graphenes, *i.e.*, a D-band at 1323 cm^{-1}, a G-band at 1608 cm^{-1}, and an I_D/I_G intensity ratio of 1.22. The Fourier-transform infrared (FT-IR) spectrum of G(OH)F (see Figure 1c) showed dominant peaks at 1105 and 1044 cm^{-1} typical of a C−C−O asymmetric stretching mode and also a peak at 1385 cm^{-1} assigned to O−H bending. Finally, characteristic peaks of a C−F bond at 1200 cm^{-1} and an aromatic C═C bond at 1596 cm^{-1} were observed along with minor signs of a C═O bond at 1725 cm^{-1} in accordance with the XPS results.

High-resolution transmission electron microscopy (HRTEM) images demonstrated the existence of relatively large sheets of G(OH)F with lengths and widths exceeding 1

DOI: 10.1021/acsnano.8b08052
ACS Nano 2018, 12, 12847−12859

μm (see Figure 1d). Moreover, the sheets were observed to have a few-layered character, as also confirmed by atomic force microscopy (AFM) topology and AFM height profile evidencing a sheets' thickness of ~1.1 nm (see Figure S3 in the Supporting Information). In the energy-dispersive X-ray spectroscopy (EDS) pattern, only peaks belonging to carbon, oxygen, and fluorine were detected (see inset in Figure 1d). No traces of other elements were observed, in agreement with the XPS analysis. More importantly, from aberration-corrected scanning transmission electron microscopy (STEM) imaging, a periodic pattern could be seen with an appearance closely resembling the expected zigzag motifs (see Figure 1e). Thus, it seems that at such a F/OH ratio, a peculiar organization of −OH groups and −F adatoms favors formation of sp^2 zigzag chains separated by sp^3 strips (see scheme in Figure 1e). This was found to be crucial not only for the emergence of magnetic ordering in G(OH)F but also for its sustainability at exceptionally high temperatures, as we shall discuss below.

To assess the magnetic features of the G(OH)F system, its χ_{mass} as a function of temperature was first measured (see Figure 2a). It is well known that when defects, of whatever nature, are introduced into graphene, unpaired spins emerge with evolution of localized magnetic moments that can communicate with each other *via* charge carriers (π-electrons, holes) and/or exchange interactions. χ_{mass} of the defected graphene can then be expressed by eq 1:

$$\chi_{mass} = \chi_{mass,dia} + \chi_{mass,para} + \chi_{mass,ferro/antiferro} \quad (1)$$

where $\chi_{mass,dia}$ is a diamagnetic term involving orbital, Landau, and core diamagnetic contributions, $\chi_{mass,para}$ is a paramagnetic term including a Curie-like response of noninteracting (isolated) defect-induced paramagnetic centers, a paramagnetic Pauli contribution from the conduction electrons, and a paramagnetic van Vleck contribution, and $\chi_{mass,ferro/antiferro}$ represents the ferromagnetic/antiferromagnetic term appearing only when the interaction among the defect-induced paramagnetic centers becomes feasible. As shown in Figure 2a, χ_{mass} exhibited complex temperature-dependent behavior with a dramatic drop in values above ~375 K, indicating the onset of a magnetic transition. From the second derivative of χ_{mass}, an inflection point (T_{inf}) was identified at a temperature of ~383 K, which is a characteristic signature of ferromagnetic materials when passing from a ferromagnetic state to a paramagnetic regime upon warming.

To mathematically analyze the χ_{mass} profile recorded for the G(OH)F system, several assumptions were adopted to relate the temperature evolution of the individual contributions to the sample's χ_{mass}. On a phenomenological level, $\chi_{mass,para}$ was well described by the Curie law (*i.e.*, C/T, where C is the Curie constant and T is the temperature), whereas $\chi_{mass,dia}$ was temperature-independent with a constant negative value over the entire temperature range of the measurement. Moreover, above the inflection point, χ_{mass} was expected to obey well the Curie−Weiss law (*i.e.*, $C/(T-\theta)$, where C is the Curie−Weiss constant, T is the temperature, and θ is the Weiss temperature). Assuming that $\chi_{mass,para}$ tended to zero at high temperatures, only the Curie−Weiss law with the $\chi_{mass,dia}$ term was used for fitting χ_{mass} above 385 K. The analysis yielded $\theta \approx$ 380 K and $\chi_{mass,dia} \approx -9.3 \times 10^{-6}$ emu/gOe (see inset in Figure 2a). The profile of $\chi_{mass,para}$ was derived (see inset in Figure 2a) after subtracting $\chi_{mass,dia}$ and assuming that the ferromagnetic contribution showed a saturation tendency at low temperatures. The temperature behavior of $\chi_{mass,ferro}$ was obtained by subtraction of $\chi_{mass,para}$ and $\chi_{mass,dia}$ from the χ_{mass} data (see inset in Figure 2a).

The measured χ_{mass} profile confirmed the existence of a magnetically ordered fraction within the G(OH)F sheets. The positive value of θ implies that magnetic moments, induced by partial −OH substitution of −F in fluorographene, interacted ferromagnetically among each other. Since the values of T_{inf} and θ were, within the experimental error, nearly identical, T_{inf} was ascribed to the Curie temperature (T_C), at which transition from a ferromagnetic to paramagnetic state occurs. Thus, $C_{18}(OH)_{3.4}F_6$ behaved in a ferromagnetic manner at room temperature. Note that the existence of a ferromagnetic ground state in hydroxofluorographene systems is due to the presence and peculiar organization of diradical-based motifs. Importantly, no transition from a ferromagnetic to antiferromagnetic state was observed for the studied $C_{18}(OH)_{3.4}F_6$ system with zigzag architecture, playing a crucial role in preservation of the ferromagnetic ground state up to high temperatures, as shown by theoretical calculations below.

The temperature sustainability of the ferromagnetic behavior was further evidenced from measuring and analyzing hysteresis loops for the G(OH)F system recorded over the temperature range from 5 to 400 K (see Figure 2b−d and Figure S4 in the Supporting Information). At 5 K, the magnetization *vs* field curve showed a complex profile with a diamagnetic profile dominating at high applied magnetic fields and hysteresis trend at low external magnetic fields. After subtracting the diamagnetic component, the isothermal magnetization curve featured contributions from both the paramagnetic and ferromagnetic fraction in the G(OH)F sheets (see inset in Figure 2b). Note the relatively high value of coercivity amounting to ~320 Oe (see inset in Figure 2b), which implies that the magnetic anisotropy within the G(OH)F structure holding the magnetic moments in preferential orientations is favored by the 2D character of the G(OH)F sheet, the organization of magnetic motifs, and interactions between them.

Upon increasing the temperature, the hysteresis profile of the isothermal magnetization curves persisted (see Figure 2c,d and Figure S4 in the Supporting Information). However, although the coercivity of the ferromagnetic fraction gradually decreased (see inset in Figure 2d), it did not strictly follow the function valid for the expected magnetic response from defect-induced localized magnetic moments. This signifies a different nature of the magnetic moments, *i.e.*, similar to diradical-based motifs, as previously proposed for hydroxofluorographene systems with an $sp^3/(sp^2 + sp^3)$ ratio over the percolation limit,[33] and complex temperature behavior of magnetic anisotropy associated with the magnetically active patterns. Most importantly, the hysteresis was observed even at 300 K (see Figure 2b) with a coercivity value of ~105 Oe, further confirming the stability of the ferromagnetic fraction up to room temperature. The hysteresis was lost between 375 and 400 K, implying transition to a paramagnetic regime, in accordance with the χ_{mass} data; at 400 K, the isothermal magnetization curve exhibited only the diamagnetic and paramagnetic profiles (see Figure 2d and Figure S4 in the Supporting Information). The hysteresis loops collected for $C_{18}(OH)_{3.4}F_6$ in the temperature range from 5 to 400 K displayed a notable diamagnetic contribution. Such a feature can be explained by the presence of a significant number of itinerant π-electrons in $C_{18}(OH)_{3.4}F_6$, which orbit around (or pass along) the benzene rings in the lattice similarly to those in

DOI: 10.1021/acsnano.8b08052
ACS Nano 2018, 12, 12847−12859

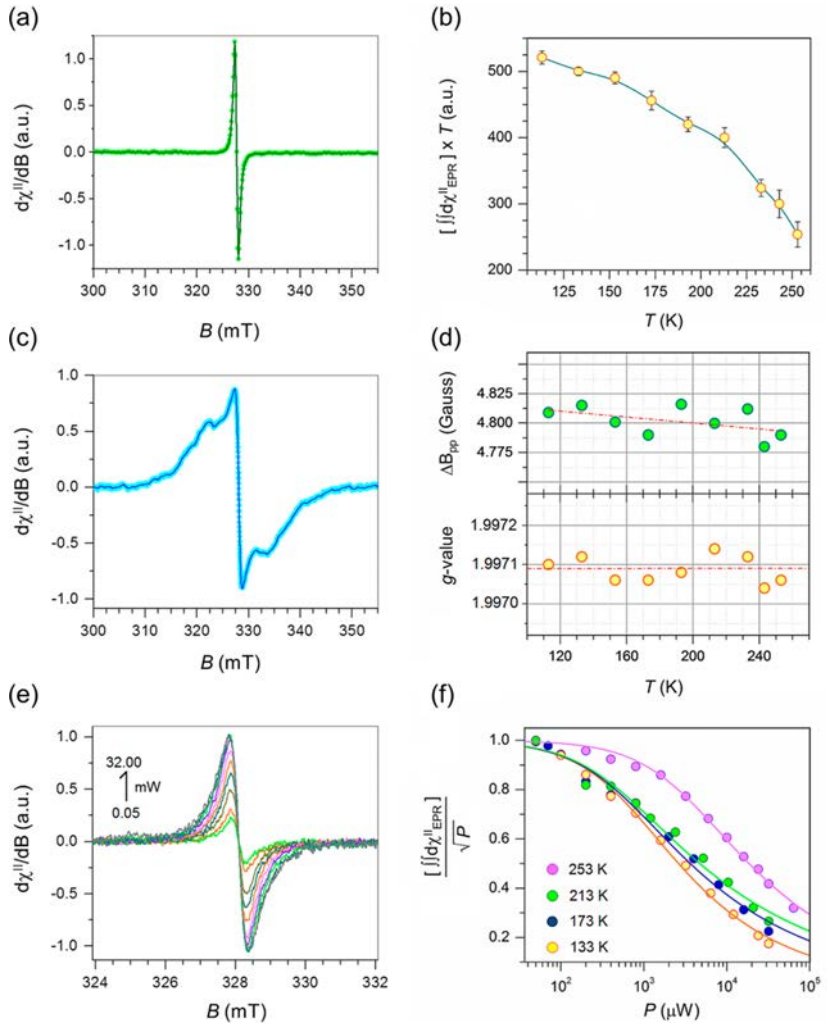


Figure 3. EPR measurements and analyses of the G(OH)F system. (a) X-band (9.17 GHz) EPR spectrum of $C_{18}(OH)_{3.4}F_6$, recorded at 113 K with 100 kHz modulation frequency, 0.2 mT modulation width, 100 μW microwave power, 4 min sweep time, and 0.03 s time constant, 4 scan accumulated and averaged. (b) Temperature dependence of the spin population obtained for $C_{18}(OH)_{3.4}F_6$ (circles) plotted in the form of $\int\int\chi_{EPR} \times T$ *vs* T. (c) X-band (9.17 GHz) EPR spectrum of commercial fluorographene ($C_1F_{1.1}$), recorded at 113 K with 100 kHz modulation frequency, 0.2 mT modulation width, 100 μW microwave power, 4 min sweep time, and 0.03 s time constant, 4 scan accumulated and averaged. (d) Variation of g_{eff} and peak-to-peak line width (ΔB_{pp}) for $C_{18}(OH)_{3.4}F_6$ recorded as a function of the sample temperature. (e) EPR power-saturation resonance signals (from 0.05 to 32 mW) recorded at 133 K for $C_{18}(OH)_{3.4}F_6$. (f) Power saturation plots with values normalized to the nonsaturating condition. The fitting analysis (solid lines) results were obtained from Portis and Castner's saturation equation.

ideal, defect-free graphene. This suggests that the itinerant π-electrons might assist in the interaction mechanism with superexchange interactions, encouraging the persistence of a ferromagnetic ground state against the temperature.

Electron paramagnetic resonance (EPR) spectroscopy was used as a complement to the bulk χ_{mass} analysis and allowed further probing of the nature and dynamics of the spin species in the high-temperature region (100−300 K) where the anomalous χ_{mass} behavior was evident (see Figure 3 and related Figures S5−S23 in the Supporting Information). The X-band EPR spectrum of powder $C_{18}(OH)_{3.4}F_6$ recorded at 113 K is shown in Figure 3a. This material exhibited a resonance signature consistent with an organic-based radical very different from the EPR spectrum of the commercial fluorographene ($C_1F_{1.1}$) precursor (see Figure 3c). The observed signal for $C_{18}(OH)_{3.4}F_6$ did not show g-anisotropy nor ^{19}F and ^{1}H-hyperfine splitting associated with soluble OH residues from the starting potassium hydroxide. Instead, it exhibited only a narrow EPR signal (ΔB_{pp} = 0.482 mT) centered at g_{eff} = 1.9971(1) (validated against $Mn^{II}MgO$ standard) (see Figure S6 and Figures S9−S17 in the Supporting Information). Resonance signals ascribable to other soluble paramagnetic species/contaminants were not detected in the broad range (see Figure S5 in the Supporting

DOI: 10.1021/acsnano.8b08052
ACS Nano 2018, 12, 12847−12859

Information). The absence of Dysonian-shaped signals,[46,47] which are known to be associated with itinerant spins, in conduction electron spin resonance (CESR) spectroscopy indicated that the spins were localized in $C_{18}(OH)_{3.4}F_6$. The integrated $C_{18}(OH)_{3.4}F_6$ resonance signal was well described by the Voigt shape function (see Figure S7 in the Supporting Information), similar to the findings of Rao *et al.*[48] in ultrasmall double-walled carbon nanotubes embedded in zeolite, but with dominant Lorentzian character (W_G, Gaussian weight of 2.33 × 10^{-5}, and W_L, Lorentzian weight equal to 0.90).

The narrow peak-to-peak line width indicated that the unpaired electrons collectively experienced the fast exchange regime, known as the exchange narrowing effect. Such a phenomenon stems from the occurrence of exchange interactions among unpaired electrons (H_{ex}) with strength large enough to yield a random frequency modulation. When $H_{ex} \gg H_{dip}$, where H_{dip} corresponds to dipolar interactions arising from radical centers in close space proximities, the effect on the spin system due to frequency modulation is to average out the dipolar interactions. Hence, the resonance line associated with the entire spin packets approached that of the isolated, noninteracting electron spin moment. The observation of an electronic transition at half-field (around $g \approx 4$; see Figure S8 in the Supporting Information) further indicated that the radical system description was under a strong exchange regime.

Theoretically, the effect of exchange narrowing has been elucidated by van Vleck, Kubo, and Tomita and by Andersson.[49−52] From the EPR spectrum shown in Figure 3a, the spin−spin relaxation time (T_2) was estimated using the relation (eq 2)

$$T_2 = 1/\gamma\Delta\upsilon_L \tag{2}$$

where $\Delta\upsilon_L = (2/\sqrt{3})\Delta B_L$ and ΔB_L corresponds to the peak-to-peak field width (in magnetic units) of the unsaturated Lorentzian line. The calculated T_2 value was 1.36 × 10^{-8} s for $C_{18}(OH)_{3.4}F_6$. This value is much smaller than that estimated for neat fluorographene (T_2 of 2.6 ± 10^{-5} s) by Panich *et al.*[53] The temperature dependence of the EPR signals of $C_{18}(OH)_{3.4}F_6$ recorded in the range of 113−253 K did not show changes from the Voight-shape resonance profile, appreciable changes in the peak-to-peak width (ΔB_{pp}), or any spread in g_{eff} (see Figures S8−S17 in the Supporting Information). Figure 3d presents experimental values determined for g_{eff} *vs* T (lower panel) and ΔB_{pp} *vs* T (upper panel) from linear fitting analysis (red line; ΔB_{pp} = 4.82 ± 0.01 G, slope equals 8.3 × 10^{-5}; g_{eff} = 1.9970 ± 0.0001, slope equals 1.69 × 10^{-9}).

The variation of the spin-population of $C_{18}(OH)_{3.4}F_6$ recorded as a function of the temperature is shown in Figure 3b ($\chi_{EPR} \times T$ *vs* T, with T from 113 to 253 K), where the term $\int\int d\chi_{EPR}$ represents the double integrated EPR signal intensity recorded at a fixed microwave power (0.1 mW). The observed increase of the spin-population shows a clear departure from Curie-like behavior. Hence, the trend is not consistent with that expected for paramagnetic species. This is consistent with the above-mentioned χ_{mass} data. The clear increase of the $\chi_{EPR} \times T$ product shows that the unpaired electrons must be correlated together *via* exchange interactions and the correlation is ferromagnetic in nature. To gain further understanding of the system spin dynamics, power saturation experiments were performed at four selected temperatures. The saturation results are shown in Figure 3f. Figure 3e shows, as an example, the evolution of the $C_{18}(OH)_{3.4}F_6$ EPR signals recorded at 133 K as a function of increasing microwave power (from 0.05 mW to 32 mW, drawn as a simple superimposition) to investigate the possible effect of itinerant electrons on the magnetic regime. Results from other experiments at various temperatures and microwave powers are shown in Figures S18−S23 in the Supporting Information.

To analyze the saturation trends, first-derivative EPR spectra recorded at different microwave powers (P) were fitted using Portis and Castner's theory (eq 3):[54,55]

$$\iint S = \frac{k \times \sqrt{P}}{[1 + (P/P_{1/2})]^{b/2}} \tag{3}$$

where the term $\int\int S$ indicates the double integrated signal intensity, P is the applied microwave power, b is the relaxation factor (b = 1 for inhomogeneous line broadening (Gaussian line) and b = 3 for homogeneous line broadening (Lorentzian line)), $P_{1/2}$ is the power at which the signal is half-saturated, and k is an experimental constant associated with the instrument. From global fitting analysis, a (spin-correlated) b value of 0.62 ± 0.01 was obtained for all the microwave powers and temperatures examined. The $P_{1/2}$ value, which was $\propto 1/T_1T_2$, showed a strong dependence on the sample temperature. In the high-temperature regime (T = 253 K), $P_{1/2}$ was rather large, with a half-saturation value of 2.283 ± 0.102 mW. At lower temperatures, there was a sudden drop in the half-saturation value, which became nearly temperature independent ($P_{1/2}$ of 0.544 ± 0.061 mW at 213 K; $P_{1/2}$ of 0.427 ± 0.124 mW at 173 K; $P_{1/2}$ of 0.317 ± 0.030 mW at 133 K). Since the relaxation factor b converges to less than 1, lying outside the region of uncorrelated spins, a fast exchange regime of the collective spin system in $C_{18}(OH)_{3.4}F_6$ is therefore validated.

Taking together the results from the bulk χ_{mass} and EPR analyses, the present findings can be interpreted as follows. The mechanism for the appearance of magnetism in carbon-based materials is widely accepted to involve C-based defects (nonbonding localized states, dangling bonds, states localized on edge carbon atoms), giving rise to spin-polarized π-electrons of carbon. However, taken together, the results from the bulk χ_{mass} and EPR analyses indicate that in the case of $C_{18}(OH)_{3.4}F_6$ the observed ferromagnetic interaction and power saturation trends of the fast exchange regime cannot simply be explained by strong correlation between localized spins. Spin−spin interactions in organic-based materials containing strongly correlated localized spins usually show saturation values that are much larger than those observed here.[56] Furthermore, from Portis and Castner's theory, the $P_{1/2}$ value cannot remain nearly constant, as observed here in the 133−213 K regime. Systems that express a CESR signal are expected the show an emergence of (T-independent) Pauli-type spin susceptibility, which translates into a strong dependence of the signal width in response to cooling, and a substantial g_{eff}-shift from that of the free electron value (g_{eff} > 2.00232) due to spin−orbit coupling.[57] Since these effects were not observed, the recorded EPR envelope for $C_{18}(OH)_{3.4}F_6$, together with its saturation and magnetic behavior, cannot be exclusively ascribed to conduction electrons. On the other hand, it has been reported that the occurrence of Heisenberg (S = 1/2) chain-type interaction between localized spins mediated by itinerant spins can produce ferromagnetism in proton-irradiated graphite (*i.e.*, activated carbon fibers).[58,59] Therefore, we suggest that a

DOI: 10.1021/acsnano.8b08052
ACS Nano 2018, 12, 12847−12859

similar scenario may occur in $C_{18}(OH)_{3.4}F_6$; that is, the observed magnetic behavior results from exchange interaction among localized spins mediated by itinerant π-electrons. In other words, the presence of itinerant π-electrons, witnessed from the magnetization and EPR measurements, implied the existence of sp^2-conductive pathways organized within the $C_{18}(OH)_{3.4}F_6$ structure. Formation of a similar π-electron-based conductive network was previously reported for less-fluorinated regions of fluorographene prepared by fluorination of graphene grown by a chemical vapor deposition technique.[60] A highly inhomogeneous fluorine coverage was found to produce multilayer islands, folds, wrinkles, and ripples, all containing a lower content of fluorine, consequently forming a conductive superstructure through which the charge transport, mediated by itinerant π-electrons, occurred preferentially.[60]

Density functional theory (DFT) calculations using $C_{18}(OH)_4F_6$ as a model (see Supporting Information for further details and respectively Figure S24 and Figure S25 in the Supporting Information) with stoichiometry very close to the experimental one identified a structural motif (see Figure 4a) possibly responsible for the room-temperature ferromagnetism of the $C_{18}(OH)_{3.4}F_6$ system. The motif consisted of sp^2-conjugated zigzag chains passing through sp^3 domains with radical centers that were isolated in the sp^3 region and attached as a side part of the π-chain, as also evidenced by further STEM and electron energy loss spectroscopy (EELS) experiments (see below). The spontaneous formation of zigzag motifs during synthesis of G(OH)F is supported by bond dissociation energies (BDEs) of fluorine atoms favoring defluorination along the motif (see Figure S26 in the Supporting Information). A transition temperature of 440 K estimated for $C_{18}(OH)_4F_6$ by using the Ising model on the honeycomb lattice[61,62] (see Methods section below for details) indicated that the ferromagnetically ordered state was stable up to temperatures exceeding 300 K, in good agreement with the experimentally derived T_C. The electronic structure displayed as density of states (DOS) of the $C_{18}(OH)_4F_6$ model provided insights into the magnetic exchange mechanism in the G(OH)F system (see Figure 4b). The DOS of $C_{18}(OH)_4F_6$ in the ferromagnetic state exhibited a continuum of states at E_F predominantly composed of π-chain states. Importantly, the electronic states of the radicals, −OH groups, and −F adatoms contributed significantly to the DOS at E_F. A complex exchange mechanism can therefore be anticipated for the ferromagnetic G(OH)F system, with both superexchange coupling of the radicals to the sp^2 zigzag chains and the π-electron system transferring the coupling between sp^3 strips, in line with both the magnetization and EPR measurements. Theoretical calculations for close stoichiometries, *i.e.*, $C_{18}(OH)_4F_5$ and $C_{18}(OH)_3F_5$, showed the same features. Thus, similar types of magnetism arise from similar structural and electronic characteristics, demonstrating the robustness of the model in explaining the observed magnetism (see Supporting Information for further details and respectively Figure S27 and Figure S28 in the Supporting Information). In summary, the theoretical calculations indicated that the magnetic ordering sustainable up to very high temperatures exceeding room temperature originated from a complex organization of radical motifs and zigzag-conjugated sp^2 carbon chains embedded in an sp^3-functionalized graphene lattice, allowing for combined contributions of superexchange interactions

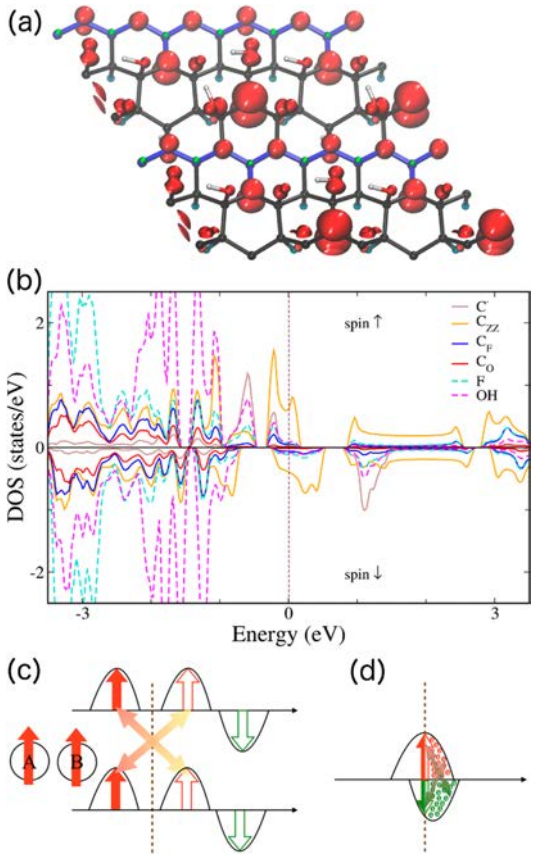


Figure 4. Theoretical calculations performed for the G(OH)F system. (a) Top view of the prototypical ferromagnetic $C_{18}(OH)_4F_6$ structure (the same structure as shown in Figure 1e) with spin densities (positive shown in red and negative in green) plotted for isosurfaces at 5×10^{-3} e Å^{-3}. (b) Corresponding atom-resolved spin-polarized DOS plot. The plot is zeroed at E_F. (c, d) Schematic of DOS of the two parallel-aligned magnetic moments with a ferromagnetic superexchange interaction (panel (c)) and itinerant electron magnetism with the interaction of magnetic spins mediated by conduction π-electrons (panel (d)).

mediated through the F/OH functionalization and indirect exchange *via* itinerant π-electrons.

The validity of the computational structural models was further demonstrated by STEM imaging (see Figure 5 and Supporting Information for further details), which revealed a repeating linear contrast with a periodicity close to 0.29 nm (see Figure 5c,f). Although the repeating linear contrast of the theoretical monolayer structures of G(OH)F does not directly match the experimental images (see Figure S29 in the Supporting Information), considering that the imaged area contains several layers, we simulated STEM images of bilayer G(OH)F material, which yields an apparent feature separation in very good agreement with the experimental data (see Figure S30 in the Supporting Information). Furthermore, EELS mapping of the O K-edge revealed the presence of oxygen, with a line shape characteristic of −OH groups (see Figure 5e,g). Importantly, theoretical calculations showed that

DOI: 10.1021/acsnano.8b08052
ACS Nano 2018, 12, 12847−12859

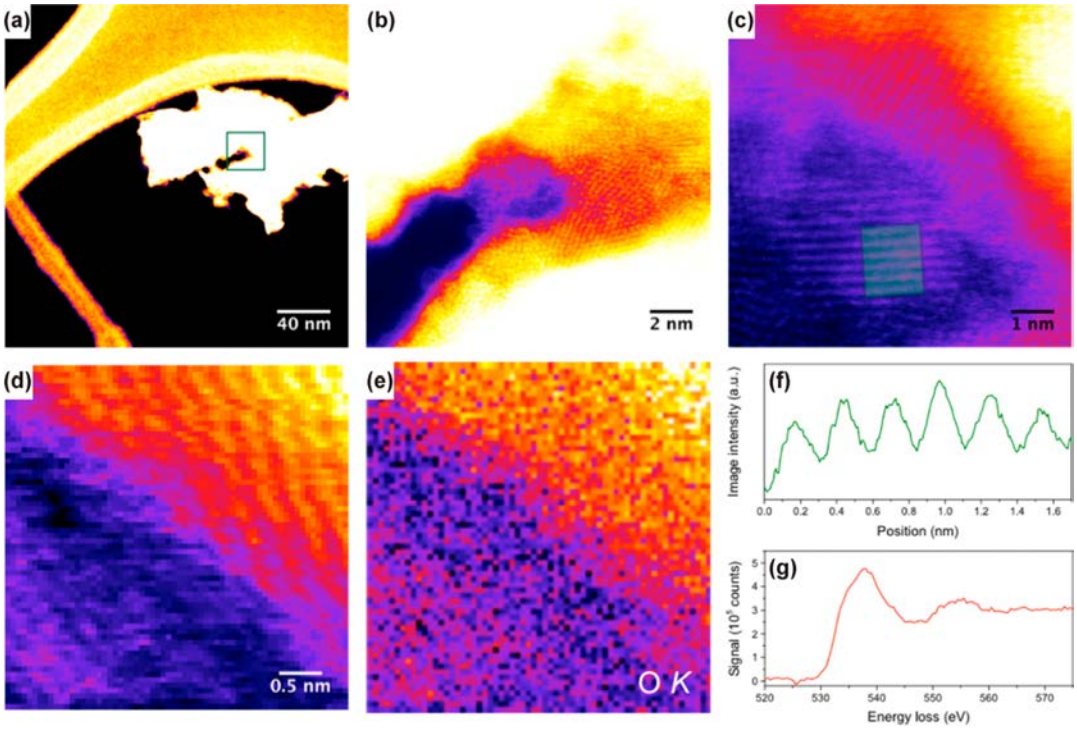


Figure 5. STEM/EELS characterization of the G(OH)F system. (a) STEM/MAADF image of an aggregate dispersed on a holey carbon support film. MAADF stands for medium-angle annular dark-field imaging. (b) Close-up of the region indicated by the green open square in panel (a). (c) STEM/HAADF image of a region near the left edge of that shown in panel (b). The green rectangle is overlaid on the repeating linear features and indicates the location of the line profile plotted in panel (f). (d) STEM/HAADF image recorded during a spectrum map of a region near the center of panel (c). (e) Mapped intensity of the background-subtracted EELS signal integrated over the O K-edge. All panels are colored with the ImageJ lookup table "Fire". (f) Line profile perpendicular to the linear features in panel (c), with a period of 0.29 nm. (g) Background-subtracted EELS O K-edge spectrum integrated over panel (e), which is highly consistent with −OH chemical groups.

layering of G(OH)F does not significantly affect its electronic and magnetic features compared to single free-standing sheets (see Figure S30e in the Supporting Information), regardless of the stacking sequence of the sheets.

CONCLUSION

In summary, we exploited the concept of functionalization for preparation of a graphene derivative showing a ferromagnetic behavior sustainable at room temperature. In particular, we focused on hydroxofluorographenes and experimentally found a member with a robust ferromagnetic ground state. It was demonstrated that for a suitable F/OH coverage of a graphene sheet, functionalization-promoted magnetic motifs—sources of magnetic moments—strongly interacted with each other to retain ferromagnetic properties up to an exceptionally high temperature of ~383 K when the paramagnetic state became established. Theoretical calculations showed that at such a F/OH ratio, sophisticated organization of magnetic motifs emerged, consisting of sp^2-conjugated zigzag chains passing through sp^3 domains with radical centers either isolated in the sp^3 region or attached as a side part of the π-chain. The predicted in-plane distance between the zigzag chains was experimentally observed by high-resolution STEM. The structural configuration in hydroxofluorographene was found to be influenced not only by the thermodynamic stability of the individual structures but also by the kinetics and random organization of defects over the surface of the starting fluorographene. The favored arrangement of magnetically active motifs strengthened interaction pathways among them *via* itinerant π-electrons, as demonstrated by analyses of magnetization measurements and EPR data. Such a scenario was further verified and explained by theoretical calculations, which suggested that the ferromagnetic state is maintained by a synergistic interplay between the superexchange coupling of the radicals to the sp^2 zigzag chains and the π-electron system transferring the coupling between sp^3 strips. In addition, while nucleophilic substitution promotes formation of radical centers and emergence of superexchange interactions, defluorination pathways lead to the formation of the sp^2 zigzag motif with strengthening the role of itinerant π-electrons, as confirmed by theoretical computations.

The presented results highlight the importance of considering sp^3 functionalization when designing and preparing graphene-based materials possessing sp-driven magnetism that is stable even at room temperature. Moreover, it provides many degrees of freedom in terms of the diversity of magnetic motifs, their architecture, combination, and organization, allowing formation of structures with various sp^2/sp^3 ratios differing in electric and magnetic properties targeted toward a given application. We believe that the presented concept will

DOI: 10.1021/acsnano.8b08052
ACS Nano 2018, 12, 12847−12859

stimulate further interest and research in graphene-based organic magnets with features tunable by varying the level of sp^3 functionalization. This will enable optimal structures to be identified that guarantee the emergence and temperature preservation of magnetic ordering, thus extending the application portfolio of graphene and graphene derivatives for use in spintronics, biomedicine, and other related fields.

METHODS

Materials. Fluorinated graphite $(C_1F_{1.1})_n$ and potassium hydroxide (KOH) were purchased from Sigma-Aldrich. The solvents for synthesis and purification were obtained from PENTA, Czech Republic. Dialysis tubing (12.4 kDa cutoff) was purchased from P-lab (Czech Republic). All the chemical were used without further purification.

Synthesis. Potassium hydroxide (250 mg) was solubilized in 8 mL of ethanol overnight. Afterward, 250 mg of fully fluorinated graphite was added and the solution was sonicated for 2 h. The formed suspension was heated to 40 °C and then stirred at this temperature for 72 h. The resulting material was purified (see Figure S1 in the Supporting Information) by washing sequentially with aliquots of acetone (2×), ethanol (2×), and water (2×) separated by centrifugation at 20000*g*. The final pellet after centrifugation of the water suspension was redispersed in ethanol and centrifuged at 3000*g* to obtain the most hydrophilic fraction of the prepared material in the supernatant. The supernatant fraction was afterward dialyzed against water in the dialysis tube with a 12.4 kDa cutoff for 3 days to remove residual potassium ions. The material was either lyophilized or stored as a water suspension. The yield of this very fine fraction was 2−3%.

Characterization Methods. XPS measurements were performed on a PHI VersaProbe II (Physical Electronics) spectrometer fitted with an Al Kα source (15 kV, 50 W) and controlled by MultiPak software (Ulvac-PHI, Inc.). The data were referenced relative to the C 1s peak at 284.80 eV.

FT-IR characterization was conducted on an iS5 Thermo Nicolet spectrometer utilizing the Smart Orbit ZnSe ATR technique. A DXR Raman microscope with a 780 nm excitation line of a diode laser was used for Raman measurements.

An ICP-MS Agilent 7700x device was used for detection of residual metals in the prepared G(OH)F sample. Prior to the detection, 3 mg of the G(OH)F sample was kept at 100 °C in 10 mL trace metal basis nitric acid for 2 h. The insoluble residues were afterward removed by passing through a 200 nm filter, and the solution was diluted with nitric acid to 25 mL in a volumetric flask. The final solution was used as a blank sample of trace metal basis nitric acid.

A physical property measurement system (PPMS, Quantum Design, U.S.A.) equipped with a vibrating sample magnetometer (VSM) was employed for collecting magnetization data of the G(OH)F sample. The temperature dependence of the G(OH)F sample's magnetization was measured upon warming in the temperature interval from 5 to 400 K under an external magnetic field of 1 kOe after cooling in a field of 1 kOe. Hysteresis loops of the G(OH)F sample were recorded in an external magnetic field ranging from −50 to +50 kOe and at various temperatures from 5 to 400 K. Prior to analysis, the magnetization values were corrected by considering the response of the sample holder, sample capsule, and respective Pascal constants.

EPR spectra of the powder G(OH)F sample were recorded on a JEOL JES-X-320 spectrometer operating at the X-band frequency (~9.14−9.17 GHz) equipped with a variable-temperature control ES 13060DVT5 apparatus. The cavity quality factor (Q) was kept above 6000 in all the measurements. Highly pure quartz tubes were employed (Suprasil, Wilmad, ≤0.5 OD), and accuracy on g-values was obtained against a Mn^{II}/MgO standard (JEOL standard).

HRTEM images were obtained and STEM/HAADF analyses for EDS mapping of elemental distributions on the G(OH)F sample were performed with a FEI TITAN 60-300 HRTEM device equipped with an extreme field emission gun (X-FEG) electron source operating at 80 kV. For the HRTEM, STEM-HAADF, and EDS experiments, an aqueous solution of the G(OH)F sample at a concentration of 0.1 mg mL^{-1} was redispersed by ultrasonication for 5 min. A drop of the sonicated sample was then deposited on a carbon-coated copper grid and slowly dried at laboratory temperature for 24 h to reduce its content of adsorbed water. The G(OH)F sample for AFM measurements was prepared following the protocol identical for HRTEM, STEM-HAADF, and EDS experiments; the solution was just deposited on a mica substrate, and the AFM measurements were performed on an NTEGRA Aura instrument.

The G(OH)F sample was further imaged in an aberration-corrected Nikon UltraSTEM100 scanning transmission electron microscope operated at an acceleration voltage of 60 kV. The beam current was around 50 pA, the beam convergence semiangle was 30 mrad, and the detector angular ranges were 60−200 mrad for the MAADF option and 80−300 mrad for the HAADF option. Images were colored with the ImageJ lookup table "Fire" to highlight relevant details. Core-loss EELS was performed on the same instrument using a Gatan PEELS 666 spectrometer retrofitted with an Andor iXon 897 electron-multiplying charge-coupled device (EMCCD) camera.[63] The energy dispersion was 0.1 eV/pixel (with an instrumental broadening of 0.4 eV), and the EELS collection semiangle was 35 mrad.

To simulate STEM images, we used the PyQSTEM interface[64] to the Quantitative TEM/STEM Simulations (QSTEM) code.[65] The model structures were first relaxed with DFT, and then MAADF or HAADF images were simulated using our experimental STEM parameters, with scattering potentials described using the independent atom approximation.[66]

Computational Methods. *Plane-Wave (PW) DFT Calculations with Periodic Boundary Condition (PBC).* DFT-PBC computations were performed using the Vienna *ab initio* simulation package (VASP)[67] employing the Perdew, Burke, and Ernzerhof (PBE)[68] exchange and correlation functional and projected augmented wave potentials (PAW)[69,70] to represent atomic cores. The wave functions were expanded in the PW basis set with a cutoff of 500 eV. Brillouin zone integrations were performed with an 11 × 11 × 1 Γ point-centered Monkhorst−Pack k-point mesh[71] per 3 × 3 graphene supercell (structure and cell optimization). The electronic DOS were calculated using the tetrahedron method with a 21 × 21 × 1 k-point mesh. For each $C_{18}(OH)_xF_y$ (x = 3, 4; y = 5, 6) stoichiometry, at least 100 random structures were generated, and an extensive study of their structural, electronic, and magnetic properties was accomplished. Full structural optimization was performed using a quasi-Newton algorithm until the residual atomic forces were lower than 25 meV $Å^{-1}$. Simultaneously, the electronic and magnetic degrees of freedom were converged to an energy of less than 10^{-6} eV.

By relating the energy difference (ΔE) between the ferromagnetic state and spin singlet with all electrons paired (typically higher in energy by up to several hundreds of meV depending on both the stoichiometry and structural features of the G(OH)F system) to the Ising model of the honeycomb lattice, the transition temperature (T_C) was estimated.[61,62] The exact solution for the honeycomb lattice resulted in $k_BT_C/|J| = 0.3797$, with $J = \Delta E/2z$ for z pairs of spins on radical sites (with k_B being the Boltzmann constant). In the Ising model, one usually relates the magnetic coupling constant (J) to the energy difference between the ferromagnetic and antiferromagnetic spin arrangements.[72] We shall note, however, that the G(OH)F system is known to exhibit complex temperature-dependent magnetic behavior.[33] Moreover, our calculations converged to the ferromagnetic state, and the spin-flip led to solutions with nonzero total magnetic moments, *i.e.*, ferrimagnetic states with spin-flip energy below 60 meV (see the Supporting Information for details). Therefore, we modeled the paramagnetic state by a spin singlet with all electrons paired, although the paramagnetic state can be maintained by thermal effects with local moments pointing in random directions. Thus, our approach may provide an upper estimate of T_C. However, besides inherent difficulties of DFT in describing the dynamic magnetic disorder in the paramagnetic state, such local disorder goes beyond the Ising model and has been shown to provide excellent agreement with the measured magnetic transition temperature.[62]

DOI: 10.1021/acsnano.8b08052
ACS Nano 2018, 12, 12847−12859

Quantum Mechanical Finite Model Calculations. The initial model structures of partially fluorinated graphene, *i.e.*, $C_{18}F_{10}$, and $C_{18}(OH)_4F_6$ for the kinetic stability study were extracted from the PW-DFT-PBC, and linked hydrogen atoms were added to saturate any dangling bonds. The structures were reoptimized at the ωB97X-D/6-31+G(d) level of theory[73−75] (keeping the boundary carbon atoms frozen) using the Gaussian09 program (revision D.01).[76] The size of the model structures was chosen based on the local chemical environment criterion; that is, all carbon atoms in the vicinity of a reaction site were considered. Reaction energies and activation barriers were obtained by geometry optimizations of the local region containing the two carbon atoms at the reaction site as well as the closest neighboring atoms with their substituents but keeping the rest of the structure frozen.

ASSOCIATED CONTENT

Supporting Information

The Supporting Information is available free of charge on the ACS Publications website at DOI: 10.1021/acsnano.8b08052.

Scheme showing purification conditions for the preparation of the G(OH)F system, high-resolution O 1s XPS pattern of the G(OH)F sample, Raman spectrum of the G(OH)F system, AFM topology and height profile of the G(OH)F sample, profiles of the hysteresis loops of the G(OH)F system at low applied magnetic fields, additional EPR spectra of the G(OH)F sample, theoretical calculations of the G(OH)F structures, additional STEM measurements and simulations, and content of various selected metals in the synthesized G(OH)F sample determined from the ICP-MS technique (PDF)

AUTHOR INFORMATION

Corresponding Authors

*E-mail: michal.otyepka@upol.cz.
*E-mail: radek.zboril@upol.cz.

ORCID

Jiří Tuček: 0000-0003-2037-4950
Giorgio Zoppellaro: 0000-0003-2304-2564
Toma Susi: 0000-0003-2513-573X
Michal Otyepka: 0000-0002-1066-5677
Radek Zbořil: 0000-0002-3147-2196

Author Contributions

J.T. was responsible for the concept development and performed analysis of magnetization measurements. K.H. performed synthesis and physicochemical characterization of the prepared systems. G.Z. performed EPR measurements and analysis. P.B. performed modeling of magnetic features. R.L. performed theoretical calculations on defluorination process and formation of zigzag patterns. M.M. performed stability calculations. T.S. performed STEM and EELS measurements and their analyses. M.O. was responsible for the theoretical concept and interpreted the theoretical data. R.Z. was responsible for the concept development, performed the design of experiment, set the strategy of the work, and came up with the idea presented in the work. All the authors have given approval to the final version of the manuscript.

Notes

The authors declare no competing financial interest.

ACKNOWLEDGMENTS

The authors acknowledge the support from the Ministry of Education, Youth and Sports of the Czech Republic under Project No. LO1305, the support by the Operational Programme Research, Development and Education−European Regional Development Fund, Project No. CZ.02.1.01/0.0/0.0/16_019/0000754 of the Ministry of Education, Youth and Sports of the Czech Republic, the assistance provided by the Research Infrastructure NanoEnviCz supported by the Ministry of Education, Youth and Sports of the Czech Republic under Project No. LM2015073, and the support from the Internal Student Grant Agency (IGA) of the Palacký University in Olomouc, Czech Republic (Project No. IGA_PrF_2018_021). P.B. acknowledges Palacký University institutional support. T.S. acknowledges the Austrian Science Fund (FWF) Project P 28322-N36 and the European Research Council (ERC) Grant (H2020) No. 756277-ATMEN. M.O. acknowledges funding from the ERC Consolidator Grant (H2020) No. 683024.

REFERENCES

(1) Novoselov, K. S.; Geim, A. K.; Morozov, S. V.; Jiang, D.; Zhang, Y.; Dubonos, S. V.; Grigorieva, I. V.; Firsov, A. A. Electric Field Effect in Atomically Thin Carbon Films. *Science* **2004**, *306*, 666−669.

(2) Castro Neto, A. H.; Guinea, F.; Peres, N. M. R.; Novoselov, K. S.; Geim, A. K. The Electronic Properties of Graphene. *Rev. Mod. Phys.* **2009**, *81*, 109−162.

(3) Novoselov, K. S.; Fal'ko, V. I.; Colombo, L.; Gellert, P. R.; Schwab, M. G.; Kim, K. A Roadmap for Graphene. *Nature* **2012**, *490*, 192−200.

(4) Tapaszto, L.; Dobrik, G.; Lambin, P.; Biro, L. P. Tailoring the Atomic Structure of Graphene Nanoribbons by Scanning Tunnelling Microscope Lithography. *Nat. Nanotechnol.* **2008**, *3*, 397−401.

(5) Zhu, Y. W.; Murali, S.; Stoller, M. D.; Ganesh, K. J.; Cai, W. W.; Ferreira, P. J.; Pirkle, A.; Wallace, R. M.; Cychosz, K. A.; Thommes, M.; Su, D.; Stach, E. A.; Ruoff, R. S. Carbon-Based Supercapacitors Produced by Activation of Graphene. *Science* **2011**, *332*, 1537−1541.

(6) Qu, L. T.; Liu, Y.; Baek, J. B.; Dai, L. M. Nitrogen-Doped Graphene as Efficient Metal-Free Electrocatalyst for Oxygen Reduction in Fuel Cells. *ACS Nano* **2010**, *4*, 1321−1326.

(7) Liu, Z. F.; Liu, Q.; Huang, Y.; Ma, Y. F.; Yin, S. G.; Zhang, X. Y.; Sun, W.; Chen, Y. S. Organic Photovoltaic Devices Based on a Novel Acceptor Material: Graphene. *Adv. Mater.* **2008**, *20*, 3924−3930.

(8) Min, S. K.; Kim, W. Y.; Cho, Y.; Kim, K. S. Fast DNA Sequencing with a Graphene-Based Nanochannel Device. *Nat. Nanotechnol.* **2011**, *6*, 162−165.

(9) Zhu, C.; Han, T. Y. J.; Duoss, E. B.; Golobic, A. M.; Kuntz, J. D.; Spadaccini, C. M.; Worsley, M. A. Highly Compressible 3D Periodic Graphene Aerogel Microlattices. *Nat. Commun.* **2015**, *6*, 6962.

(10) Han, Y.; Xu, Z.; Gao, C. Ultrathin Graphene Nanofiltration Membrane for Water Purification. *Adv. Funct. Mater.* **2013**, *23*, 3693−3700.

(11) Shin, M. K.; Lee, B.; Kim, S. H.; Lee, J. A.; Spinks, G. M.; Gambhir, S.; Wallace, G. G.; Kozlov, M. E.; Baughman, R. H.; Kim, S. J. Synergistic Toughening of Composite Fibres by Self-Alignment of Reduced Graphene Oxide and Carbon Nanotubes. *Nat. Commun.* **2012**, *3*, 650.

(12) Georgakilas, V.; Otyepka, M.; Bourlinos, A. B.; Chandra, V.; Kim, N.; Kemp, K. C.; Hobza, P.; Zboril, R.; Kim, K. S. Functionalization of Graphene: Covalent and Non-Covalent Approaches, Derivatives and Applications. *Chem. Rev.* **2012**, *112*, 6156−6214.

(13) Dreyer, D. R.; Park, S.; Bielawski, C. W.; Ruoff, R. S. The Chemistry of Graphene Oxide. *Chem. Soc. Rev.* **2010**, *39*, 228−240.

(14) Elias, D. C.; Nair, R. R.; Mohiuddin, T. M. G.; Morozov, S. V.; Blake, P.; Halsall, M. P.; Ferrari, A. C.; Boukhvalov, D. W.;

DOI: 10.1021/acsnano.8b08052
ACS Nano 2018, 12, 12847−12859

Katsnelson, M. I.; Geim, A. K.; Novoselov, K. S. Control of Graphene's Properties by Reversible Hydrogenation: Evidence for Graphane. *Science* **2009**, *323*, 610−613.
(15) Zboril, R.; Karlicky, F.; Bourlinos, A. B.; Steriotis, T. A.; Stubos, A. K.; Georgakilas, V.; Safarova, K.; Jancik, D.; Trapalis, C.; Otyepka, M. Graphene Fluoride: A Stable Stoichiometric Graphene Derivative and Its Chemical Conversion to Graphene. *Small* **2010**, *6*, 2885−2891.
(16) Nair, R. R.; Ren, W. C.; Jalil, R.; Riaz, I.; Kravets, V. G.; Britnell, L.; Blake, P.; Schedin, F.; Mayorov, A. S.; Yuan, S. J.; Katsnelson, M. I.; Cheng, H. M.; Strupinski, W.; Bulusheva, L. G.; Okotrub, A. V.; Grigorieva, I. V.; Grigorenko, A. N.; Novoselov, K. S.; Geim, A. K. Fluorographene: A Two-Dimensional Counterpart of Teflon. *Small* **2010**, *6*, 2877−2884.
(17) Karlicky, F.; Datta, K. K. R.; Otyepka, M.; Zboril, R. Halogenated Graphenes: Rapidly Growing Family of Graphene Derivatives. *ACS Nano* **2013**, *7*, 6434−6464.
(18) Urbanova, V.; Hola, K.; Bourlinos, A. B.; Cepe, K.; Ambrosi, A.; Loo, A. H.; Pumera, M.; Karlicky, F.; Otyepka, M.; Zboril, R. Thiofluorographene-Hydrophilic Graphene Derivative with Semiconducting and Genosensing properties. *Adv. Mater.* **2015**, *27*, 2305−2310.
(19) Bakandritsos, A.; Pykal, M.; Blonski, P.; Jakubec, P.; Chronopoulos, D. D.; Polakova, K.; Georgakilas, V.; Cepe, K.; Tomanec, O.; Ranc, V.; Bourlinos, A. B.; Zboril, R.; Otyepka, M. Cyanographene and Graphene Acid: Emerging Derivatives Enabling High-Yield and Selective Functionalization of Graphene. *ACS Nano* **2017**, *11*, 2982−2991.
(20) Jankovsky, O.; Novacek, M.; Luxa, J.; Sedmidubsky, D.; Fila, V.; Pumera, M.; Sofer, Z. A New Member of the Graphene Family: Graphene Acid. *Chem. - Eur. J.* **2016**, *22*, 17416−17424.
(21) Ghaderi, N.; Peressi, M. First-Principle Study of Hydroxyl Functional Groups on Pristine, Defected Graphene, and Graphene Epoxide. *J. Phys. Chem. C* **2010**, *114*, 21625−21630.
(22) Georgakilas, V.; Perman, J. A.; Tucek, J.; Zboril, R. Broad Family of Carbon Nanoallotropes: Classification, Chemistry, and Applications of Fullerenes, Carbon Dots, Nanotubes, Graphene, Nanodiamonds, and Combined Superstructures. *Chem. Rev.* **2015**, *115*, 4744−4822.
(23) Yazyev, O. V. Emergence of Magnetism in Graphene Materials and Nanostructures. *Rep. Prog. Phys.* **2010**, *73*, 056501.
(24) Červenka, J.; Katsnelson, M. I.; Flipse, C. F. J. Room-Temperature Ferromagnetism in Graphite Driven by Two-Dimensional Networks of Point Defects. *Nat. Phys.* **2009**, *5*, 840−844.
(25) Yazyev, O. V.; Helm, L. Defect-Induced Magnetism in Graphene. *Phys. Rev. B: Condens. Matter Mater. Phys.* **2007**, *75*, 125408.
(26) Tucek, J.; Blonski, P.; Sofer, Z.; Simek, P.; Petr, M.; Pumera, M.; Otyepka, M.; Zboril, R. Sulfur Doping Induces Strong Ferromagnetic Ordering in Graphene: Effect of Concentration and Substitution Mechanism. *Adv. Mater.* **2016**, *28*, 5045−5053.
(27) Blonski, P.; Tucek, J.; Sofer, Z.; Mazanek, V.; Petr, M.; Pumera, M.; Otyepka, M.; Zboril, R. Doping with Graphitic Nitrogen Triggers Ferromagnetism in Graphene. *J. Am. Chem. Soc.* **2017**, *139*, 3171−3180.
(28) Zhou, J.; Wang, Q.; Sun, Q.; Chen, X. S.; Kawazoe, Y.; Jena, P. Ferromagnetism in Semihydrogenated Graphene Sheet. *Nano Lett.* **2009**, *9*, 3867−3870.
(29) Nair, R. R.; Sepioni, M.; Tsai, I. L.; Lehtinen, O.; Keinonen, J.; Krasheninnikov, A. V.; Thomson, T.; Geim, A. K.; Grigorieva, I. V. Spin-Half Paramagnetism in Graphene Induced by Point Defects. *Nat. Phys.* **2012**, *8*, 199−202.
(30) Eng, A. Y. S.; Poh, H. L.; Sanek, F.; Marysko, M.; Matejkova, S.; Sofer, Z.; Pumera, M. Searching for Magnetism in Hydrogenated Graphene: Using Highly Hydrogenated Graphene Prepared *via* Birch Reduction of Graphite Oxides. *ACS Nano* **2013**, *7*, 5930−5939.
(31) Eng, A. Y. S.; Sofer, Z.; Huber, S.; Bousa, D.; Marysko, M.; Pumera, M. Hydrogenated Graphenes by Birch Reduction: Influence of Electron and Proton Sources on Hydrogenation Efficiency, Magnetism, and Electrochemistry. *Chem. - Eur. J.* **2015**, *21*, 16828−16838.
(32) Gonzalez-Herrero, H.; Gomez-Rodriguez, J. M.; Mallet, P.; Moaied, M.; Palacios, J. J.; Salgado, C.; Ugeda, M. M.; Veuillen, J. Y.; Yndurain, F.; Brihuega, I. Atomic-Scale Control of Graphene Magnetism by Using Hydrogen Atoms. *Science* **2016**, *352*, 437−441.
(33) Tucek, J.; Hola, K.; Bourlinos, A. B.; Blonski, P.; Bakandritsos, A.; Ugolotti, J.; Dubecky, M.; Karlicky, F.; Ranc, V.; Cepe, K.; Otyepka, M.; Zboril, R. Room Temperature Organic Magnets Derived from sp^3 Functionalized Graphene. *Nat. Commun.* **2017**, *8*, 14525.
(34) Boukhvalov, D. W.; Katsnelson, M. I. sp Electron Magnetic Clusters with a Large Spin in Graphene. *ACS Nano* **2011**, *5*, 2440−2446.
(35) Kobayashi, Y.; Fukui, K.; Enoki, T.; Kusakabe, K.; Kaburagi, Y. Observation of Zigzag and Armchair Edges of Graphite Using Scanning Tunneling Microscopy and Spectroscopy. *Phys. Rev. B: Condens. Matter Mater. Phys.* **2005**, *71*, 193406.
(36) Magda, G. Z.; Jin, X. Z.; Hagymasi, I.; Vancso, P.; Osvath, Z.; Nemes-Incze, P.; Hwang, C. Y.; Biro, L. P.; Tapaszto, L. Room-Temperature Magnetic Order on Zigzag Edges of Narrow Graphene Nanoribbons. *Nature* **2014**, *514*, 608−611.
(37) Lieb, E. H. 2 Theorems on the Hubbard Model. *Phys. Rev. Lett.* **1989**, *62*, 1201−1204.
(38) Hong, J.; Bekyarova, E.; de Heer, W. A.; Haddon, R. C.; Khizroev, S. Chemically Engineered Graphene-Based 2D Organic Molecular Magnet. *ACS Nano* **2013**, *7*, 10011−10022.
(39) Makarova, T. L.; Sundqvist, B.; Hohne, R.; Esquinazi, P.; Kopelevich, Y.; Scharff, P.; Davydov, V. A.; Kashevarova, L. S.; Rakhmanina, A. V. Magnetic Carbon. *Nature* **2001**, *413*, 716−718.
(40) Makarova, T. L.; Sundqvist, B.; Hohne, R.; Esquinazi, P.; Kopelevich, Y.; Scharff, P.; Davydov, V. A.; Kashevarova, L. S.; Rakhmanina, A. V. Retraction: Magnetic Carbon. *Nature* **2006**, *440*, 707.
(41) Tang, T.; Tang, N. J.; Zheng, Y. P.; Wan, X. G.; Liu, Y.; Liu, F. C.; Xu, Q. H.; Du, Y. W. Robust Magnetic Moments on the Basal Plane of the Graphene Sheet Effectively Induced by OH Groups. *Sci. Rep.* **2015**, *5*, 8448.
(42) Tucek, J.; Blonski, P.; Ugolotti, J.; Swain, A. K.; Enoki, T.; Zboril, R. Emerging Chemical Strategies for Imprinting Magnetism in Graphene and Related 2D Materials for Spintronic and Biomedical Applications. *Chem. Soc. Rev.* **2018**, *47*, 3899−3990.
(43) Pumera, M.; Sofer, Z. Towards Stoichiometric Analogues of Graphene: Graphane, Fluorographene, Graphol, Graphene Acid and Others. *Chem. Soc. Rev.* **2017**, *46*, 4450−4463.
(44) Sturala, J.; Luxa, J.; Pumera, M.; Sofer, Z. Chemistry of Graphene Derivatives: Synthesis, Applications, and Perspectives. *Chem. - Eur. J.* **2018**, *24*, 5992−6006.
(45) Chronopoulos, D. D.; Bakandritsos, A.; Pykal, M.; Zboril, R.; Otyepka, M. Chemistry, Properties, and Applications of Fluorographene. *Appl. Mater. Today* **2017**, *9*, 60−70.
(46) Petit, P.; Joguelet, E.; Fischer, J. E.; Rinzler, A. G.; Smalley, R. E. Electron Spin Resonance and Microwave Resistivity of Single-Wall Carbon Nanotubes. *Phys. Rev. B: Condens. Matter Mater. Phys.* **1997**, *56*, 9275−9278.
(47) Likodimos, V.; Glenis, S.; Guskos, N.; Lin, C. L. Antiferromagnetic Behavior in Single-Wall Carbon Nanotubes. *Phys. Rev. B: Condens. Matter Mater. Phys.* **2007**, *76*, 075420.
(48) Rao, S. S.; Stesmans, A.; Noyen, J. V.; Jacobs, P.; Sels, B. Electron Spin Resonance Investigation of Ultra-Small Double Walled Carbon Nanotubes Embedded in Zeolite Nanochannels. *J. Phys.: Condens. Matter* **2011**, *23*, 455801.
(49) van Vleck, J. H. The Dipolar Broadening of Magnetic Resonance Lines in Crystals. *Phys. Rev.* **1948**, *74*, 1168−1183.
(50) Anderson, P. W.; Weiss, P. R. Exchange Narrowing in Paramagnetic Resonance. *Rev. Mod. Phys.* **1953**, *25*, 269−276.
(51) Kubo, R.; Tomita, K. A General Theory of Magnetic Resonance Absorption. *J. Phys. Soc. Jpn.* **1954**, *9*, 888−919.

DOI: 10.1021/acsnano.8b08052
ACS Nano 2018, 12, 12847−12859

(52) Anderson, P. W. A Mathematical Model for the Narrowing of Spectral Lines by Exchange or Motion. *J. Phys. Soc. Jpn.* **1954**, *9*, 316−319.
(53) Panich, M.; Shames, A. I.; Nakajima, T. On Paramagnetism in Fluorinated Graphite: EPR and Solid State NMR Study. *J. Phys. Chem. Solids* **2001**, *62*, 959−964.
(54) Castner, T. G. Saturation of the Paramagnetic Resonance of a V Center. *Phys. Rev.* **1959**, *115*, 1506−1515.
(55) Portis, A. M. Electronic Structure of F-Centers − Saturation of the Electron Spin Resonance. *Phys. Rev.* **1953**, *91*, 1071−1078.
(56) Zoppellaro, G.; Geies, A.; Andersson, K. K.; Enkelmann, V.; Baumgarten, M. Synthesis, Optical Properties and Magnetic Studies of 2,6-bis(pyrazolylmethyl)pyridine Functionalized with Two Nitronyl Nitroxide Radicals. *Eur. J. Org. Chem.* **2008**, *2008*, 1431−1440.
(57) Kosaka, M.; Ebbesen, T. W.; Hiura, H.; Tanigaki, K. Electron Spin Resonance of Carbon Nanotubes. *Chem. Phys. Lett.* **1994**, *225*, 161−164.
(58) Shibayama, Y.; Sato, H.; Enoki, T.; Endo, M. Disordered Magnetism at the Metal-Insulator Threshold in Nano-Graphite-Based Carbon Materials. *Phys. Rev. Lett.* **2000**, *84*, 1744−1747.
(59) Lee, K. W.; Lee, C. E. Electron Spin Resonance of Proton-Irradiated Graphite. *Phys. Rev. Lett.* **2006**, *97*, 137206.
(60) Wang, B.; Wang, J. J.; Zhu, J. Fluorination of Graphene: A Spectroscopic and Microscopic Study. *ACS Nano* **2014**, *8*, 1862−1870.
(61) Balcerzak, T.; Szalowski, K.; Jascur, M.; Zukovic, M.; Bobak, A.; Borovsky, M. Thermodynamic Description of the Ising Antiferromagnet on a Triangular Lattice with Selective Dilution by a Modified Pair-Approximation Method. *Phys. Rev. E* **2014**, *89*, 062140.
(62) Tuček, J.; Błoński, P.; Malina, O.; Pumera, M.; Chua, C. K.; Otyepka, M.; Zbořil, R. Morphology-Dependent Magnetism in Nanographene: Beyond Nanoribbons. *Adv. Funct. Mater.* **2018**, *28*, 1800592.
(63) Susi, T.; Hardcastle, T. P.; Hofsass, H.; Mittelberger, A.; Pennycook, T. J.; Mangler, C.; Drummond-Brydson, R.; Scott, A. J.; Meyer, J. C.; Kotakoski, J. Single-Atom Spectroscopy of Phosphorus Dopants Implanted into Graphene. *2D Mater.* **2017**, *4*, 021013.
(64) Susi, T.; Madsen, J.; Ludacka, U.; Mortensen, J. J.; Pennycook, T. J.; Lee, Z.; Kotakoski, J.; Kaiser, U.; Meyer, J. C. Efficient First Principles Simulation of Electron Scattering Factors for Transmission Electron Microscopy. *Ultramicroscopy* **2019**, *197*, 16−22.
(65) Koch, C. *Determination of Core Structure Periodicity and Point Defect Density along Dislocations*. Ph.D. Thesis, Arizona State University, 2002.
(66) Rez, D.; Rez, P.; Grant, I. Dirac-Fock Calculations of X-ray Scattering Factors and Contributions to the Mean Inner Potential for Electron Scattering. *Acta Crystallogr., Sect. A: Found. Crystallogr.* **1994**, *50*, 481−497.
(67) Kresse, G.; Furthmuller, J. Efficient Iterative Schemes For *Ab Initio* Total-Energy Calculations Using a Plane-Wave Basis Set. *Phys. Rev. B: Condens. Matter Mater. Phys.* **1996**, *54*, 11169−11186.
(68) Perdew, J. P.; Burke, K.; Ernzerhof, M. Generalized Gradient Approximation Made Simple. *Phys. Rev. Lett.* **1996**, *77*, 3865−3868.
(69) Blöchl, P. E. Projector Augmented-Wave Method. *Phys. Rev. B: Condens. Matter Mater. Phys.* **1994**, *50*, 17953−17979.
(70) Kresse, G.; Joubert, D. From Ultrasoft Pseudopotentials to the Projector Augmented-Wave Method. *Phys. Rev. B: Condens. Matter Mater. Phys.* **1999**, *59*, 1758−1775.
(71) Monkhorst, H. J.; Pack, J. D. Special Points for Brillouin-Zone Integrations. *Phys. Rev. B* **1976**, *13*, 5188−5192.
(72) Moreira, I. P. R.; Illas, F. *Ab Initio* Theoretical Comparative Study of Magnetic Coupling in $KNiF_3$ and K_2NiF_4. *Phys. Rev. B: Condens. Matter Mater. Phys.* **1997**, *55*, 4129−4137.
(73) Chai, J.-D.; Head-Gordon, M. Long-Range Corrected Hybrid Density Functionals with Damped Atom-Atom Dispersion Corrections. *Phys. Chem. Chem. Phys.* **2008**, *10*, 6615−6620.
(74) Hehre, W. J.; Ditchfield, R.; Pople, J. A. Self-Consistent Molecular Orbital Methods. XII. Further Extensions of Gaussian-Type Basis Sets for Use in Molecular-Orbital Studies of Organic-Molecules. *J. Chem. Phys.* **1972**, *56*, 2257−2261.
(75) Clark, T.; Chandrasekhar, J.; Spitznagel, G. W.; Schleyer, P. V. R. Efficient Diffuse Function-Augmented Basis-Sets for Anion Calculations. 3. The 3-21+G Basis Set for 1st Row Elements, Li-F. *J. Comput. Chem.* **1983**, *4*, 294−301.
(76) Frisch, M. J.; Trucks, G. W.; Schlegel, H. B.; Scuseria, G. E.; Robb, M. A.; Cheeseman, J. R.; Scalmani, G.; Barone, V.; Petersson, G. A.; Nakatsuji, H.; Li, X.; Caricato, M.; Marenich, A.; Bloino, J.; Janesko, B. G.; Gomperts, R.; Mennucci, B.; Hratchian, H. P.; Ortiz, J. V.; Izmaylov, A. F.; Sonnenberg, J. L.; Williams-Young, D.; Ding, F.; Lipparini, F.; Egidi, F.; Goings, J.; Peng, B.; Petrone, A.; Henderson, T.; Ranasinghe, D.; Zakrzewski, V. G.; Gao, J.; Rega, N.; Zheng, G.; Liang, W.; Hada, M.; Ehara, M.; Toyota, K.; Fukuda, R.; Hasegawa, J.; Ishida, M.; Nakajima, T.; Honda, Y.; Kitao, O.; Nakai, H.; Vreven, T.; Throssell, K.; Montgomery, J. A., Jr.; Peralta, J. E.; Ogliaro, F.; Bearpark, M.; Heyd, J. J.; Brothers, E.; Kudin, K. N.; Staroverov, V. N.; Keith, T.; Kobayashi, R.; Normand, J.; Raghavachari, K.; Rendell, A.; Burant, J. C.; Iyengar, S. S.; Tomasi, J.; Cossi, M.; Millam, J. M.; Klene, M.; Adamo, C.; Cammi, R.; Ochterski, J. W.; Martin, R. L.; Morokuma, K.; Farkas, O.; Foresman, J. B.; Fox, D. J. *Gaussian 09*, Revision D.01; Gaussian, Inc.: Wallingford, CT, 2016.

DOI: 10.1021/acsnano.8b08052
ACS Nano 2018, 12, 12847−12859

Morphology-Dependent Magnetism in Nanographene: Beyond Nanoribbons

Jiří Tuček, Piotr Błoński, Ondřej Malina, Martin Pumera, Chun Kiang Chua, Michal Otyepka, and Radek Zbořil**

Imprinting self-sustainable magnetic features into graphene has recently generated much interest owing to its potential application in spintronics. Several strategies for imprinting magnetic features into graphene are proposed theoretically. However, only a few of them are realized experimentally. Here, the first scalable synthesis of magnetic graphene nanoplatelets with diverse morphologies, including nanoribbons and triangular, pentagonal, hexagonal, and other polyhedral shapes, is reported. This material enters the ferromagnetic regime at a temperature of ≈37 K with magnetization approaching ≈0.45 emu g^{-1} under high external magnetic fields. Theoretical calculations are used to explain this sort of morphology-driven magnetism of graphene nanoplatelets, which emerges from the synergistic effects of the size, geometry of nanographenes, edge terminations, and angle between adjacent edges. In addition, they suggest a new way for preparing magnetically ordered graphene nanoplatelets with a higher transition temperature. In this respect, triangular motifs with zigzag edges represent the most promising morphology of graphene nanoplatelets, which can remain magnetically ordered up to ≈107 K. Based on these challenging results, further tuning of the size and morphology in spatially confined nanographenes combined with doping and sp^3 functionalization will enable the preparation of magnetically ordered half-metallic carbon sustainable up to room temperature, thus opening new opportunities in spintronics.

1. Introduction

Graphene, a single 2D sheet of carbon atoms with an arrangement mimicking the honeycomb hexagonal architecture, has captured immense interest from the scientific community since its isolation in 2004.[1] It is widely recognized as an intriguing material with remarkable physicochemical properties emerging from its 2D atomic organization and peculiar electronic structure.[2] Several unusual physical phenomena have been observed in graphene, such as an ambipolar electric field effect,[1] half-integer quantum Hall effect,[3,4] bipolar supercurrent,[5] positive piezoconductive effect,[6] photo-thermoelectric effect,[7] nonlinear Kerr effect,[8] and Casimir effect.[9] Owing to its appealing mechanical, electric, optical, transport, and thermal features that can be readily tuned upon its doping by foreign elements or functionalization/surface modification,[10] a broad portfolio of potential applications is possible covering various fields, such as electronics (ultralight flexible displays and touch panels,[11] field effect, high-speed, and ballistic transistors,[12] spin transistors and spin logic devices,[13] light-emitting diodes,[14] components of radio-frequency-integrated circuits,[15] and nano-electromechanical systems[16]), energy storing, and generating devices (electrodes in ultra/supercapacitors,[17] Li-ion batteries,[18] and fuel cells[19]), optics (photoactive medium in solar cells,[20] photodetectors,[21] and broadband polarizers[22]), printing technologies (conductive inks[23] and inks for electromagnetic shielding[24]), medicine (DNA sequencing,[25] agents for cellular imaging, and carriers of drugs/biomolecules[26]), environment- and water-treating technologies (sensors and sorbents of pollutants[27] and water desalination[28]), and additives for improving the mechanical properties of composites (car bumpers[29]).

Among other properties, graphene shows strong ballistic transport, a long spin lifetime and spin relaxation length, weak spin–orbit coupling, and limited hyperfine interactions, i.e., prerequisites highly required in spintronics.[13] Unfortunately, pristine graphene is intrinsically diamagnetic due to solely sp^2 bonding, leaving no unpaired electrons, and hence preventing emergence of localized magnetic moments. Thus, in order to create magnetic moments in graphene, sp^2 hybridization must be altered by introducing defects in the graphene lattice,[30,31] e.g., topology perturbations,[32] vacancies,[33] substitutional atoms,[34,35] adatoms (not of d-block nature),[36,37] sp^3 functionalizing groups,[38,39] special edge geometries,[40,41] and confined

Dr. J. Tuček, Dr. P. Błoński, Dr. O. Malina, Prof. M. Otyepka, Prof. R. Zbořil
Regional Centre of Advanced Technologies and Materials
Department of Physical Chemistry
Faculty of Science
Palacký University in Olomouc
17. listopadu 1192/12, 771 46 Olomouc, Czech Republic
E-mail: michal.otyepka@upol.cz; radek.zboril@upol.cz
Prof. M. Pumera, Dr. C. K. Chua
Division of Chemistry and Biological Chemistry
School of Physical and Mathematical Sciences
Nanyang Technological University
Singapore, 637371 Singapore
The ORCID identification number(s) for the author(s) of this article can be found under https://doi.org/10.1002/adfm.201800592.

DOI: 10.1002/adfm.201800592

 © 2018 WILEY-VCH Verlag GmbH & Co. KGaA, Weinheim

states.[42] Such perturbations equip the electronic structure of graphene with spin-polarized peaks and/or flat bands at the proximity of the Fermi level, E_F. Once evolved, the magnetic moments are believed to interact with each other via conduction electrons and/or direct exchange or superexchange interactions, establishing the magnetically ordered (ferromagnetic (FM) and/or anti-ferromagnetic (AFM)) state over the entire graphene lattice that can preserve eventually up to room temperature depending on the nature and strength of the interaction.

Spatially confined carbon nanoallotropes have received significant attention as promising candidates showing magnetic features which can be imprinted and fine-tuned by edge engineering, proving experimentally the concepts of edge magnetism. Graphene nanoribbons (GNRs) and graphene nanoflakes/quantum dots are frequently regarded as prototypical examples of such carbon-based nanostructures.[31,41,42] In particular, GNRs are strips of graphene with a width of less than 50 nm; they were theoretically introduced as a model system to study edge and nanoscale-size effects in graphene.[43] They are sometimes referred to as a "pseudo" 1D sp^2 carbon nanoallotrope and are commonly classified into two groups with respect to the edge geometry, i.e., armchair and zigzag GNRs.[31] While armchair GNRs are nonmagnetic, their zigzag counterparts show spin-polarized edge states. The electronic structure and, hence, bandgap and magnetic features of zigzag GNRs are believed to strongly depend on the level of quantum confinement in the width dimension and nature of intraedge and interedge magnetic interactions (i.e., π-conduction electron-mediated indirect interactions and direct/superexchange interactions).[31] It has been theoretically predicted that magnetic moments localized on the same edge of GNR always interact among each other in an FM manner, whereas FM or AFM alignment is expected to evolve between opposite zigzag edges depending on the GNR width.[31] Importantly, the change in the magnetic ordering between opposite edges is accompanied by oscillation in the conduction features of GNR between metallic behavior (in the FM regime) and semiconducting fashion (in the AFM state). Many theoretical works devoted to the magnetic properties of GNRs have shown that line defects,[44] injected extra carriers (electron/holes),[45,46] interaction with a substrate magnetic field,[47] and different saturation of opposite edges with hydrogens[48] can also affect the final magnetic behavior. These facts complicate interpretation of experimental observations of edge magnetism in GNRs because experimentally prepared GNRs may naturally include many intrinsic irregularities, defects, edge states, and d-block element impurities. Moreover, it has been theoretically argued that long-range magnetic ordering over the zigzag GNR cannot evolve if quantum fluctuations are strong enough to form rung singlets.[49] Other phenomena restricting/eliminating the existence of edge states include edge reconstruction, edge passivation, and edge closure.[50] Graphene nanoplatelets (GNPs, also termed as graphene nanoflakes or graphene quantum dots) are considered as 0D sp^2 carbon allotropes which can bear magnetic ordering. The magnetism is triggered by termination of the carbon lattice in the two dimensions and depends on the GNP size, shape, and symmetry.[51–54] Theoretically, various magnetically ordered regimes for GNPs have been suggested, including FM, AFM, and mixed states, all resulting from application of Lieb's theorem with on-site Coulombic interaction. In addition, strain,[55] electric[56] and magnetic[57] fields, layered character,[53] and doping with charge carriers (i.e., electrons and holes)[58] and other elements (e.g., N and B)[59] can affect the electronic structure of GNPs, thus altering the magnetic response. Despite their promising magnetism, material of this nature has not been prepared yet.

In this work, we prepared and characterized magnetically ordered GNPs ≈25 nm long and ≈10 nm wide. They exhibited low-temperature ferromagnetism with a Curie temperature of ≈37 K. The hysteresis loop recorded at 5 K displayed a coercivity of ≈72 Oe and remnant magnetization of $\approx 10^{-3}$ emu g^{-1}, confirming the low-temperature FM regime. The magnetization at high applied magnetic fields reached a value of ≈0.45 emu g^{-1} (at 5 K), comparable with another magnetic graphene-based systems, e.g., doped graphenes and graphene derivatives. The negligible concentration of d-block elements impurities could not be considered as a source of the observed magnetism. Therefore, the observed magnetism is an inherent property of GNPs. Theoretical calculations have been used to explain the nature of magnetic ordering, which stems particularly from their finite size, zigzag geometry of edges, and sharp angles between the edges. In addition, they suggested that the Curie temperature could theoretically be enhanced by reducing the GNP size to a maximum of around $3.7 \times 3.7 \times 3.7$ nm.

2. Results and Discussion

The size, morphological, and geometrical characteristics of the GNP system were analyzed by employing high-resolution transmission electron microscopy (HRTEM). As clearly seen from the HRTEM images (see **Figure 1**a–h; Figure S1a–d, Supporting Information), GNPs show various shapes described in terms of *n*-sided polygons. Most frequently, triangles, rectangles, pentagons, and hexagons were observed. To determine the lateral size of GNPs, their shape was approximated as a rectangle. Within this approximation, the length was found to lie in the interval from ≈5 to ≈60 nm and the width varied from ≈2 to ≈20 nm; the aspect ratio changed from ≈1.5 to ≈4. The distribution of the length, width, and aspect ratio values of GNPs followed a Gaussian curve with an average value of 25 nm, 10 nm, and 2.5, respectively (see Figure 1i–k). HRTEM images showed both a single- and a few-layered character. Nevertheless, the stacking was not responsible for the observed magnetic features of GNPs, as demonstrated by theoretical calculations (see the following sections). Regarding the chemical nature of the GNP system, only signals originating from carbon and oxygen were detected in the energy-dispersive X-ray spectroscopy (EDX) pattern (see Figure S1e in the Supporting Information); the intensity of the C peak was much higher compared to that of the O peak, demonstrating that the content of oxygen was very low in the sample.

Figure 2a shows the Raman spectrum of GNPs with two peaks at 1335 and 1597 cm^{-1}, ascribed to the D- and G-bands, respectively. The G-band is characteristic of an ideal graphene; it reflects the presence of optical E_{2g} phonons at the Brillouin zone center, which are generated from bond stretching (i.e., in-plane vibrations) of sp^2 carbon–carbon pairs in rings and chains. The appearance of the D-band in the Raman spectrum

© 2018 WILEY-VCH Verlag GmbH & Co. KGaA, Weinheim

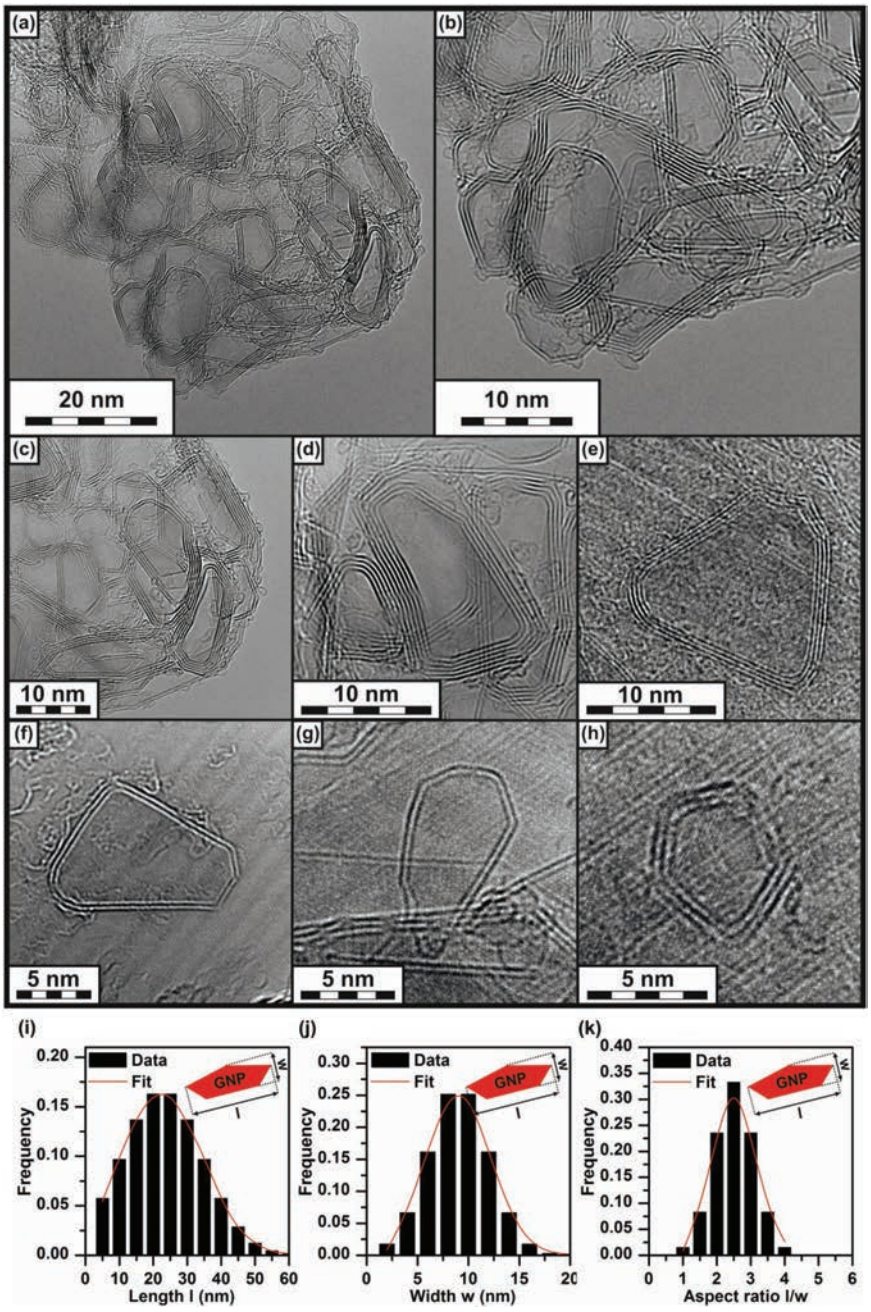


Figure 1. HRTEM measurements: a–h) representative HRTEM images of GNPs of different shapes; i–k) HRTEM-derived histograms with theoretical fits showing the distribution of length, width, and aspect ratio values of GNPs within the sample.

indicates disorder, defects (e.g., sp^3 carbons), and edge states in graphene,[60] causing emergence of breathing modes (i.e., out-of-plane vibrations) of aromatic rings. The I_D/I_G ratio was equal to 1.54, implying defective graphene and agrees with Raman spectroscopy studies for GNRs,[61,62] where the emergence of the D-band was ascribed to the edge states. The broadening and upshift (by 16 cm^{-1} with respect to ideal graphene) of the G-band further confirm the nanosized character of GNPs, as previously observed for GNRs with decreasing width.[61]

To identify the chemical nature, composition, and types of chemical bonds, X-ray photoelectron spectroscopy (XPS) technique was employed for the synthesized GNPs. The survey

 © 2018 WILEY-VCH Verlag GmbH & Co. KGaA, Weinheim

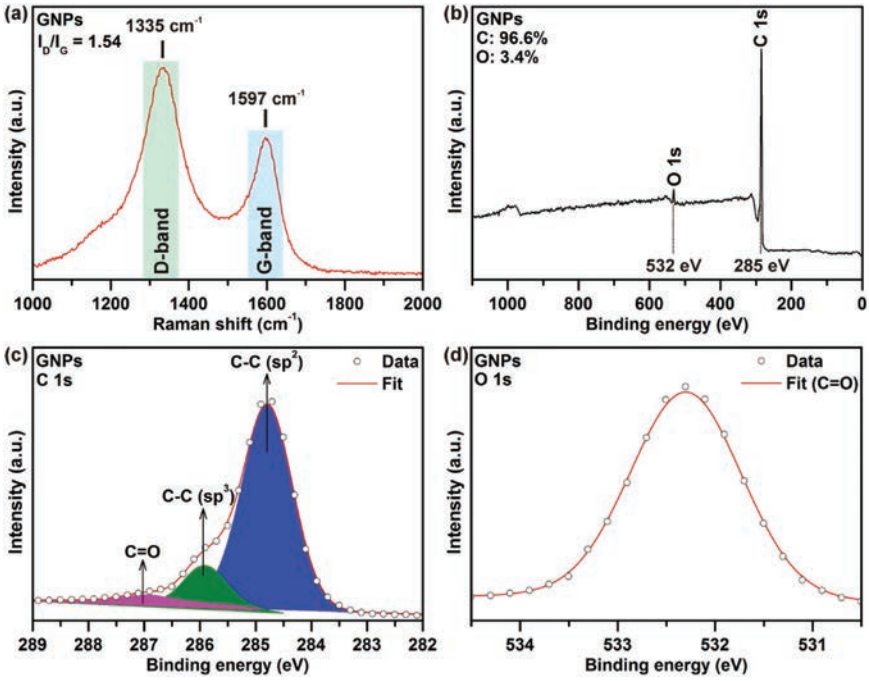


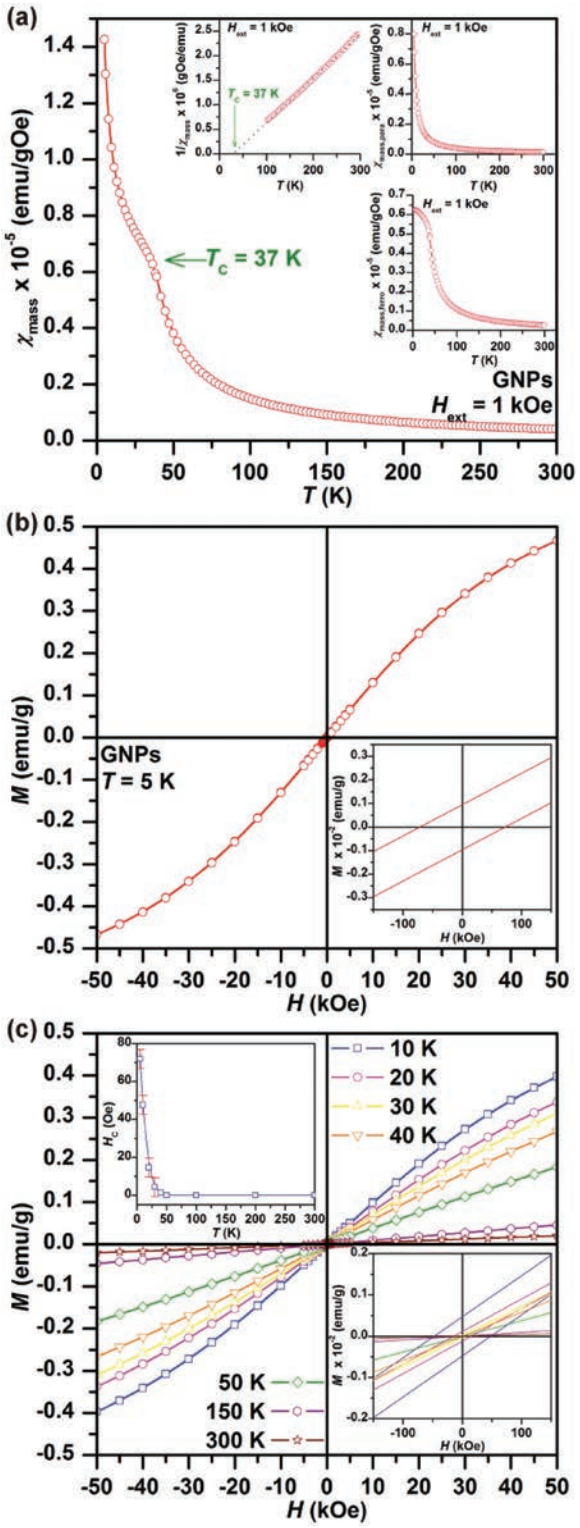
Figure 2. Raman and XPS measurements: a) Raman spectrum of the GNP sample with the D- and G-bands indicated. b) Survey XPS pattern of the GNP sample with peaks corresponding to carbon and oxygen indicated. c) High-resolution C 1s XPS pattern of the GNP sample with types of bonds indicated. d) High-resolution O 1s XPS pattern of the GNP sample.

XPS pattern (see Figure 2b) of the GNP system showed two sharp peaks, i.e., one intense maximum at a binding energy of ≈285 eV corresponding to the C 1s peak and the other one with weak intensity at ≈532 eV corresponding to the O 1s peak. Spectral integration of the survey XPS profile showed 96.6 and 3.4 at% of carbon and oxygen, respectively. However, the level of oxygen was very low, in accordance with the EDX analysis and was not believed to induce/alter the magnetic features of GNPs, as previously demonstrated for N- and S-doped graphene systems.[34,35] The types of bonds in GNPs can be clearly seen from the high-resolution C 1s XPS pattern, where three peaks were identified, i.e., at 284.78, 285.92, and 286.96 eV assigned to C—C (sp^2), C—C (sp^3), and C=O, respectively (see Figure 2c). Besides the C—C (sp^2) peak inherent in the pristine graphene, the C—C (sp^3) component corresponds to defects of sp^3 origin and agrees with the Raman spectrum analysis. Since C=O bonds as only oxygen-containing bonds were found in the high-resolution C 1s and high-resolution O 1s XPS patterns (see Figure 2c,d), it can be deduced that oxygen atoms are attached dominantly to the edges of GNPs as often reported for thermally reduced graphene oxide systems.[63–65]

Besides carbon and oxygen, no other elements were detected by XPS technique. As the XPS detection limit in the survey mode was about 0.1 at% (i.e., 1000 ppm), trace amounts of d-block elements (in particular, Fe, Ni, Co, and Mn), considered as main magnetic impurities in the carbon-based systems, would not have to been seen. Thus, an inductively coupled plasma mass spectrometry (ICP-MS) technique (with a detection limit in units of ppt) was employed to determine the concentration of d-block metals in the GNP sample (see Table S1 in the Supporting Information). ICP-MS analysis confirmed that the mass amounts of Fe, Ni, Co, and Mn were below 5 ppm. If the determined mass amounts of Fe, Ni, Co, and Mn, and magnitudes of their magnetic moments were considered, the total mass magnetic susceptibility, χ_{mass}, of magnetically significant elements was estimated to be of the order of 10^{-8} emu g^{-1} Oe^{-1} at 0 K and under a 1 kOe field. Since the measured χ_{mass} values for the GNP sample lie in the interval with orders from 10^{-4} to 10^{-6} emu g^{-1} Oe^{-1} under a 1 kOe field (see the following sections), the contribution of Fe, Ni, Co, and Mn with the given mass amount to the sample's χ_{mass} was assumed negligible. In other words, the measured magnetic signal stemmed solely from the GNP system and was not affected at all by the trace amounts of impurities of d-block element origin, precluding any incorrect interpretations.

To experimentally probe the magnetic features of the system composed of GNP, its mass magnetization, M_{mass}, as a function of temperature, T, and external magnetic field, H_{ext}, was measured and thoroughly analyzed (see **Figure 3**). In particular, as clearly seen from the temperature evolution of the sample's mass magnetic susceptibility, χ_{mass} ($=M_{mass}/H_{ext}$), recorded under H_{ext} of 1 kOe (see Figure 3a), it does not strictly resemble a simple hyperbolic trend (i.e., the Curie law) characteristic for ideal paramagnetic systems without any long-range magnetic ordering down to 0 K. The χ_{mass} profile shows a sign of a saturation behavior at around

 © 2018 WILEY-VCH Verlag GmbH & Co. KGaA, Weinheim



40 K followed by a steep increase upon lowering the temperature, implying the onset of an FM regime coexisting with the paramagnetic state.

Generally, it is well known that defects introduced into the graphene lattice locally break the sp^2 bonding with emergence of unpaired electrons, and hence paramagnetic centers. Then, χ_{mass} of a defective graphene can be expressed as the sum of three components, i.e., $\chi_{mass} = \chi_{mass,dia} + \chi_{mass,para} + \chi_{mass,ferro}$. More specifically, $\chi_{mass,dia}$ is a diamagnetic term involving orbital, Landau, and core diamagnetic contributions, and $\chi_{mass,para}$ represents a paramagnetic term including Curie-like response of noninteracting (isolated) defect-induced paramagnetic centers, paramagnetic Pauli contribution from conduction electrons and paramagnetic van Vleck contribution. If an interaction pathway is established among defect-induced paramagnetic centers (mediated by the graphene π-electron network, direct exchange, or superexchange), a magnetically ordered regime (frequently of FM nature) evolves, as manifested by the appearance of the $\chi_{mass,ferro}$ term in the total χ_{mass}.

In the case of GNPs, χ_{mass} was analyzed assuming a weighted linear combination of $\chi_{mass,para}$ and $\chi_{mass,ferro}$. $\chi_{mass,para}$ is expressed by the Curie law (i.e., C/T, where C is the Curie constant) in the whole temperature interval, whereas the Curie–Weiss law (i.e., $C/(T - \Theta)$, where C is the Curie–Weiss constant and Θ is the Weiss temperature) was considered for mathematical description of $\chi_{mass,ferro}$ at temperatures above 50 K. Since χ_{mass} was still positive at 300 K and extrapolation of χ_{mass} above 300 K gave $\chi_{mass,dia}$ of the order of 10^{-8}, $\chi_{mass,dia}$ was further neglected, implying that the diamagnetic signal, typical for ideal graphene, was significantly suppressed and hugely exceeded in intensity by the paramagnetic response from the defect-induced centers. Mathematical analysis of χ_{mass} then yielded $\Theta \approx 37$ K. Considering the profile of the $\chi_{mass,para}$ contribution (see the inset in Figure 3a), the temperature dependence of the $\chi_{mass,ferro}$ term was then obtained by subtracting $\chi_{mass,para}$ from the total χ_{mass} (see the inset in Figure 3a). In other words, $\chi_{mass,para}$ reflects the presence of defect-induced magnetic moments localized too far from each other, preventing any interaction among them, while $\chi_{mass,ferro}$ features those magnetic moments preferentially evolved at the edges of GNPs, sitting at a distance providing an effective interaction among each other. Regarding $\chi_{mass,para}$, it also includes response from the regions at the edges with attached oxygen atoms (as C=O bonds, as evidenced from high-resolution XPS patterns, see Figure 2c,d).

Figure 3. Magnetization measurements: a) Temperature evolution of the mass magnetic susceptibility, χ_{mass}, of the GNP sample, recorded under an external magnetic field of 1 kOe, with indication of the Curie temperature, T_C. The insets show the fitting of $1/\chi_{mass}$ versus temperature curve with the Curie–Weiss law in the temperature range from 100 to 300 K and temperature evolution of $\chi_{mass,para}$ and $\chi_{mass,ferro}$ terms, as derived from the fitting model. b) Hysteresis loop of the GNP sample measured at a temperature of 5 K. The inset shows the behavior of the hysteresis loop around the origin with the coercivity and remanent magnetization indicated. c) Hysteresis loops of the GNP sample, recorded at various temperatures in the temperature range from 10 to 300 K. The insets show the behavior of the hysteresis loops around the origin and the temperature evolution of the coercivity, H_C, derived from the respective hysteresis loops of the GNP sample.

© 2018 WILEY-VCH Verlag GmbH & Co. KGaA, Weinheim

In the case of FM contribution, from the analysis of χ_{mass} data, it was not possible to state whether it stemmed dominantly from either interaction between adjacent edges or from intraedge interaction or both types of interactions that are equivalently relevant.

As Θ is positive, the interaction among induced magnetic moments is of FM nature. For ideal GNRs, it is well known that intraedge interactions are FM while interedge interactions can be either FM or AFM depending on the nanoribbon's width. For GNPs, it turns out that FM interactions of both intraedge and interedge characters govern their magnetic behavior. It seems that AFM interactions are most probably absent, as also demonstrated by rough fitting (i.e., ignoring $\chi_{mass,para}$) of $1/\chi_{mass}$ with the Curie–Weiss law over the temperature range of 100–300 K, dissecting the temperature axis at the positive value (≈37 K; see the straight line in the inset of Figure 3a). Thus, Θ can be ascribed to the Curie temperature, T_C, at which the system enters the FM state on lowering the temperature.

The magnetic properties of GNPs were further monitored by measuring the isothermal magnetization curves at various temperatures from 5 to 300 K (see Figure 3b,c). At 5 K, a hysteretic behavior was observed with nonzero values of coercivity (≈72 Oe) and remanent magnetization (≈10^{-3} emu g^{-1}; see Figure 3b and its inset), confirming the low-temperature FM regime of the system. Under high applied magnetic fields, i.e., 50 kOe, magnetization was observed to reach a value of ≈0.45 emu g^{-1}, one order of magnitude lower than those reported for doped, surface-functionalized and/or vertically oriented graphene-based systems.[34–36,66,67] The nonsaturation behavior of the hysteresis loop indicated a significant presence of noninteracting paramagnetic centers, as already witnessed from the analysis of χ_{mass}, with a reluctance to align in the direction of the external magnetic field. As the temperature was raised, the hysteresis of the isothermal magnetization curves was gradually reduced until it vanished at a temperature of 40 K (see Figure 3c), implying passage from the FM state to the paramagnetic regime. More importantly, the fall in the values of coercivity (see the inset in Figure 3c) was found to strictly obey the mathematical expression valid for FM systems consisting of d-block elements. This implies that magnetic moments are of localized nature, and hence emerge at the edges as spin-polarized states. Unfortunately, the macroscopic character of magnetization measurements did not allow identification of the exact interaction pathways, role of interedge and intraedge interactions and interaction mediators responsible for establishment of the low-temperature FM behavior of the prepared GNP system.

To gain a deeper insight into the interplay between the structural, electronic, and magnetic features of GNPs, we performed plane wave–density functional theory (PW-DFT) calculations with various models of nanostructured graphene, ranging from semi-infinite nanometer-wide zigzag nanoribbons to nanoflakes of nanometer sizes and various shapes (see Figure S2 in the Supporting Information). Both zigzag and armchair terminations were considered with both bare and H-passivated edge atoms. Regardless of the shape of nanostructured graphene-based systems, zigzag edges host spin-polarized electronic states, whereas armchair edges are nonmagnetic (see Figures S3 and S4 in the Supporting Information). The nearest-neighbor carbon atoms interact in an AFM manner, and, thus different sublattices have opposite magnetic moment. The spin density at the edge atoms is higher than on atoms located deeper into the bulk. Furthermore, all atoms at the zigzag edge belong to the same sublattice. Therefore, they have the same magnetic moment. This leads to a local imbalance of the total magnetic moment and to edge ferromagnetism. The magnetic moments localized on edge carbon atoms were ≈0.2 μ_B (≈0.7 μ_B without H-passivation of dangling bonds), but deeper layers were nonmagnetic. It should be noted that recent scanning tunneling spectroscopy experiments on on-surface synthesized GNRs with zigzag edge topology confirmed the existence of localized states at the zigzag edge.[68]

Although GNRs exhibit intraedge ferromagnetism, depending on the width of GNRs, either FM or AFM alignment is expected to evolve between opposite zigzag edges.[31] Present calculations indicated that the total energy difference between FM and AFM interedge alignments in GNR with the width of ≈3.7 nm did not exceed 2 meV, and dropped below 1 meV for wider (≳8 nm) GNRs. Similar results hold for rectangular nanoflakes with zigzag (magnetic) and armchair (nonmagnetic) adjacent edges. This signifies the important role played by the intraedge ferromagnetism in nm size GNPs of rectangular shape, whereas interedge coupling was largely suppressed as indicated by the declined contribution from the deeper layers to the peaks near E_F in the density of states (DOS) plots shown in Figure S5 (Supporting Information).

HRTEM images revealed that the angle between the adjacent sides of GNPs varied from ≈30° to ≈150°; there are also many instances when the angle between the GNP adjacent sides did not exceed 45°. Theoretical calculations for triangular and trapezoidal graphene nanoflakes indicated that both interedge and intraedge ferromagnetism can evolve in GNPs having angles between adjacent edges smaller than 90°. This can be respectively seen as an excess of spin densities at the zigzag edges and in the corners between them (see Figures S3 and S4 in the Supporting Information). Note the higher spin densities at the edges than in between them, and for the large flakes, complete suppression of magnetism in the bulk (in line with suppressed exchange interaction in deeper layers of GNRs, as indicated by their declined contribution to the peaks near E_F in the DOS plots shown in Figure S5 (Supporting Information), which highlights the dominant intraedge ferromagnetism in GNPs.

The energy difference, ΔE, between the magnetic ground state and nonmagnetic spin-singlet computed for graphene flakes of various sizes and shapes indicate the trend of Curie temperatures, adopting the Ising model. **Figure 4** shows that the lowest T_C was found for the rectangular and trapezoidal flakes having both magnetic zigzag edges and nonmagnetic armchair edges. Conversely, the largest T_C (≈107 K) was computed for the triangular flake with an edge length of ≈3.7 nm and an excess of the spin density both in the corner between adjacent edges and on the deeper laying atoms, while the hexagonal flake and large triangular flake exhibited intermediate value of T_C. Moreover, a similar T_C predicted among the latter flakes could be related to the leading intraedge interactions. Further, among the flakes with zigzag edges and sharp angles between the adjacent edges and when only the zigzag edge atoms were considered (including the second row of atoms), ΔE differed by only several meV among various flakes. This further highlights the additional role (to the dominant intraedge coupling) of the interedge interaction in maintaining a high T_C.

© 2018 WILEY-VCH Verlag GmbH & Co. KGaA, Weinheim

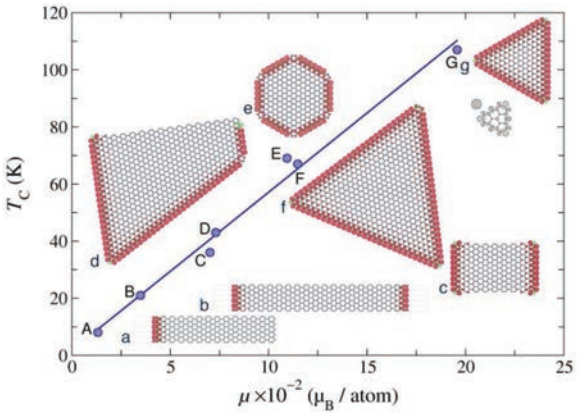


Figure 4. Predicted T_C values of various GNR and GNP structures: The calculated T_C for graphene flakes of various shapes and sizes (as shown in the insets) versus magnetic moments (normalized per number of atoms) indicating stability of the ground FM state. The graphene flakes are labeled by small letters; the corresponding point on the plot is indicated by a capital letter. The gray point indicates T_C calculated for the smallest triangular flake (shown in gray). The median of the theoretical T_C amounts to ≈47 K, which is not far from the experimentally observed T_C, which is a bulk average across various morphology and size values.

Importantly, upon further lowering the size of the triangular flake below 1 nm edge length, T_C dropped to ≈88 K which suggested that the Curie temperature could be theoretically enhanced by reducing the GNP size to a maximum around $3.7 \times 3.7 \times 3.7$ nm.

Furthermore, we theoretically considered a possible role of 3D layering of graphene flakes (evidenced from HRTEM images, see Figure 1a–h) on their magnetic features. It should be noted that the individual flakes of stacked GNPs are bound by London dispersive forces. The theoretical calculations showed that both the values of magnetic moments and their distribution within the individual flakes were identical to those of single freestanding flakes (see Figure S6 in the Supporting Information). This indicates that magnetism of GNPs was neither a consequence of nor influenced by their stacking. In other words, the potential contribution of 3D layering to the observed magnetism can be ruled out.

3. Conclusion

In the present study, a scalable synthetic method involving an oxidative scissoring of graphene nanofibers was reported leading to GNPs bearing intrinsic magnetic properties. The as-prepared GNPs were ≈25 nm long and ≈10 nm wide, and contained various polyhedral shapes. GNPs were dominantly composed of sp^2 carbon atoms and contained less than 3.5 at% of the oxygen atoms as evidenced by EDX and XPS techniques. Upon lowering the temperature, some GNPs in the system were found to enter an FM regime with the Curie temperature of ≈37 K; the magnetization was observed to reach a value of ≈0.45 emu g^{-1} at 5 K and in high applied magnetic fields comparable with those reported for other magnetic graphene-based systems, e.g., doped graphenes and graphene derivatives. Theoretical calculations showed that the magnetism emerges from zigzag edges and is enhanced by the sharp angles between edges observed experimentally. In addition, theoretical calculations suggested the triangular GNPs as suitable magnetic motifs the Curie temperature of which could be further enhanced up to ≈107 K by reducing their size down to 3.7 nm in the edge length. This work points to the upper limit in sustainable magnetism based on GNRs and GNPs and indicates that magnetic ordering sustainable up to room temperature has to be achieved by combining the size and morphology aspects with other sources of magnetism, e.g., defects, doping, and functionalization.

4. Experimental Section

Synthesis: GNPs were prepared according to the modified Hummers method from stacked graphene nanofibers (Strem). Stacked graphene nanofibers (0.5 g) were stirred with 23.0 mL of H_2SO_4 (95–98%) for 20 min at 0 °C prior to addition of $NaNO_3$ (0.5 g) in portions. The mixture was left to stir for 1 h. $KMnO_4$ (3 g) was then added in portions at 0 °C. The mixture was subsequently heated to 35 °C for 1 h. Water (40 mL) was then added into the mixture and resulted in the temperature of the mixture rising to 90 °C. The temperature was maintained at 90 °C for 30 min. Additional water (100 mL) was added into the mixture. This was followed by slow addition of 30% H_2O_2 (≈10 mL). The warm solution was filtered (with regenerated cellulose (RC) membrane filter, 0.22 µm) and washed with warm water (100 mL). The solid was subsequently washed with a copious amount of water until a neutral pH was obtained. The materials were kept in the oven at 60 °C for 5 d prior to further thermal treatment and analyses. Consequently, dried samples were thermally reduced/exfoliated at 1000 °C. Oxidized nanofibers were placed in a porous quartz glass capsule connected to a magnetic manipulator inside a vacuum-tight tube furnace with a controlled atmosphere. Use of the magnetic manipulator enabled application of a temperature gradient of over 1000 °C min^{-1}. The sample was flushed with nitrogen by repeated evacuation of the tube furnace to remove any traces of oxygen and then quickly inserted using a magnetic manipulator to a preheated furnace and held in the furnace for 12 min. The flow of nitrogen (99.9999% purity) during the exfoliation procedure was 1000 mL min^{-1} to remove any by-products of the exfoliation procedure.

Characterization Techniques: HRTEM images were obtained using an HRTEM Titan 60–300 microscope equipped with an extreme field-emission gun (X-FEG) operating at 300 kV. Scanning transmission electron microscopy/high-angle annular dark-field imaging (STEM/HAADF) analyses for EDX mapping of elemental distributions on GNPs were performed with an FEI Titan HRTEM microscope operating at 80 kV. For HRTEM, STEM-HAADF, and EDX experiments, an aqueous solution of GNPs with a concentration of 0.1 mg mL^{-1} was redispersed by ultrasonication for 5 min. A drop of the sonicated sample was then deposited on a carbon-coated copper grid and slowly dried at laboratory temperature for 24 h to reduce the content of adsorbed water.

The detection of residual metal content in the GNP sample was performed by ICP-MS. The exact amount of the GNP sample (10 mg) was immersed in concentrated nitric acid (≥99.999% trace metals basis) and heated for 2 h at 100 °C. Afterward, the mixture was transferred into a 10 mL volumetric flask, diluted with water, and undissolved GNPs were trapped by a 200 nm Millipore filter. The obtained concentration of metals in the solution was recalculated to the amount of the tested sample (analogously, diluted nitric acid was used as a blank).

The atomic percent of C and O and types of bonds were assessed by XPS technique, employing a PHI 5000 VersaProbe II XPS system (Physical Electronics) equipped with a monochromatic Al Kα source (15 kV, 50 W) with a photon energy of 1486.7 eV. Dual beam charge compensation was used for all the measurements. All the XPS patterns were measured in a vacuum of 1.4×10^{-7} Pa and at room temperature

© 2018 WILEY-VCH Verlag GmbH & Co. KGaA, Weinheim

(22 °C). For high-resolution XPS patterns, a pass energy of 23.500 eV and a step size of 0.200 eV were used. Spectra were evaluated with MultiPak (Ulvac—PHI, Inc.) software. All binding energy values were referenced to the C 1s peak at 284.80 eV.

Raman spectra were acquired using a DXR Raman spectroscope (Thermo Scientific, USA) equipped with a laser operating at a wavelength of 633 nm. The GNP sample was first deposited on a glass platform and the excitation laser was focused on its surface. Experimental parameters were tuned to maximize the respective analytic signal. The laser power on the sample was set to 5 mW and the exposition time was 20 s. Each measured Raman spectrum was an average of 16 experimental microscans.

Magnetization measurements were performed using a physical property measurement system equipped with a vibrating sample magnetometer from Quantum Design, USA. Hysteresis loops were measured at various temperatures in the range from 5 to 300 K and under static external magnetic fields ranging from −50 to +50 kOe. Temperature profiles of χ_{mass} were recorded in a sweep mode over a temperature range of 5 to 300 K in a field of 1 kOe after cooling in a field of 1 kOe. Magnetization values were corrected assuming the response of the sample holder, sample capsule, and respective Pascal constants.

Computational Details: All calculations were performed by using DFT-based VASP[69] code with a generalized gradient approximation and the Perdew–Becke–Erzenhof[70] exchange-correlation functional. Atomic cores represented by projected augmented wave potentials were used.[71,72] The PW basis set contained components with energies up to 400 eV. All the structures were relaxed until the forces on all the atoms were smaller than 25 meV Å^{-1}. Simultaneously, the electronic and magnetic degrees of freedom were relaxed until the change in total energy between successive iteration steps was smaller than 10^{-6} eV.

Structural models employed in this study (see Figure S2 in the Supporting Information for more details) included (i) semi-infinite zigzag nanoribbons with widths of ≈3.7, ≈8, and ≈20.8 nm and vacuum layers of ≈2 nm in aperiodic directions; (ii) rectangular flakes ((≈3.7) × (≈2.2) nm) with zigzag and armchair terminations on adjacent edges; (iii) equilateral triangular flakes with zigzag termination of edges of ≈3.7 and ≈7.1 nm in length; (iv) trapezoidal flakes ((≈6.7) × (≈2) × (≈7.6) × (≈5.7) nm) with zigzag and armchair terminations on the adjacent edges; and (v) hexagonal flakes ((≈1.9) × (≈1.9) nm). Both, bare and H-passivated edges were considered. All the flakes were surrounded by an in-plane ≈2 nm vacuum layer, which was large enough to avoid interactions from the neighboring images. The nanometer sizes of the computational models were chosen to be as close as possible to the sizes of experimental GNPs and still computationally feasible. Brillouin zone integrations for the narrower nanoribbons were performed with a 1 × 50 × 1 Γ-centered *k*-point mesh and a Gaussian smearing of 0.02 eV, and appropriately adjusted for wider nanoribbons. Properties of graphene flakes were computed at the Γ point.

Exchange interactions between the localized moments were evaluated by calculating the total energy difference normalized per number of atoms between the magnetic ground state and spin singlet with all the electrons paired. By relating the energy difference to the Ising model on the honeycomb lattice,[73] which has the exact solution given as $k_B T_C/|J| = 0.3797$, with a coupling value of $J = \Delta E/2$,[74] T_C can be estimated. In the Ising model, the magnetic coupling constant, *J*, is usually related either to the energy difference between the FM and AFM spin arrangements or the energy difference corresponding to the FM state and the broken-symmetry solution.[74] However, it should be noted that graphene-based systems may exhibit a complex temperature-dependent behavior, including AFM ground state and FM excited state that can pass to a paramagnetic regime on further increasing the temperature.[38] Thus, the paramagnetic state was modeled by using a spin singlet, albeit that the paramagnetic state can be maintained by thermal effects pointing the local moments in random directions. Nonetheless, this approach might provide an upper estimate of T_C. However, besides inherent difficulties of DFT in describing the dynamic magnetic disorder in the paramagnetic state, such a disorder local model goes beyond the Ising model, which, despite its simplicity, provides a perfect agreement with the measured magnetic transition temperature.

Supporting Information

Supporting Information is available from the Wiley Online Library or from the author.

Acknowledgements

The authors gratefully acknowledge the support from the Ministry of Education, Youth and Sports of the Czech Republic under Project No. LO1305, the support by the Operational Programme Research, Development and Education—European Regional Development Fund, Project No. CZ.02.1.01/0.0/0.0/16_019/0000754 of the Ministry of Education, Youth and Sports of the Czech Republic, and the assistance provided by the Research Infrastructure NanoEnviCz supported by the Ministry of Education, Youth and Sports of the Czech Republic under Project No. LM2015073. P.B. acknowledges Palacký University institutional support. M.O. acknowledges funding from an ERC Consolidator grant (H2020) No. 683024. J.T. thanks Dr. Michaela Tučková for assistance with design and optimization of measuring protocols for magnetization measurements (supported by the Martina Roeselová Memorial Fellowship). The authors thank Dr. Ariana Opletalová, Dr. Martin Petr, and Dr. Ondřej Tomanec (all from the Regional Centre of Advanced Technologies and Materials, Faculty of Science, Palacký University in Olomouc, Czech Republic) for Raman spectroscopy, XPS, and HRTEM measurements, respectively.

Conflict of Interest

The authors declare no conflict of interest.

Keywords

confinement, edge engineering, graphene, magnetism, spintronics

Received: January 23, 2018
Published online: March 25, 2018

[1] K. S. Novoselov, A. K. Geim, S. V. Morozov, D. Jiang, Y. Zhang, S. V. Dubonos, I. V. Grigorieva, A. A. Firsov, *Science* **2004**, *306*, 666.
[2] A. H. Castro Neto, F. Guinea, N. M. R. Peres, K. S. Novoselov, A. K. Geim, *Rev. Mod. Phys.* **2009**, *81*, 109.
[3] K. S. Novoselov, A. K. Geim, S. V. Morozov, D. Jiang, M. I. Katsnelson, I. V. Grigorieva, S. V. Dubonos, A. A. Firsov, *Nature* **2005**, *438*, 197.
[4] Y. B. Zhang, Y. W. Tan, H. L. Stormer, P. Kim, *Nature* **2005**, *438*, 201.
[5] H. B. Heersche, P. Jarillo-Herrero, J. B. Oostinga, L. M. K. Vandersypen, A. F. Morpurgo, *Nature* **2007**, *446*, 56.
[6] K. Xu, K. Wang, W. Zhao, W. Z. Bao, E. F. Liu, Y. F. Ren, M. Wang, Y. J. Fu, J. W. Zeng, Z. G. Li, W. Zhou, F. Q. Song, X. R. Wang, Y. Shi, X. G. Wan, M. S. Fuhrer, B. G. Wang, Z. H. Qiao, F. Miao, D. Y. Xing, *Nat. Commun.* **2015**, *6*, 8119.
[7] D. Basko, *Science* **2011**, *334*, 610.
[8] R. Shimano, G. Yumoto, J. Y. Yoo, R. Matsunaga, S. Tanabe, H. Hibino, T. Morimoto, H. Aoki, *Nat. Commun.* **2013**, *4*, 1841.
[9] I. V. Fialkovsky, V. N. Marachevsky, D. V. Vassilevich, *Phys. Rev. B* **2011**, *84*, 035446.
[10] V. Georgakilas, M. Otyepka, A. B. Bourlinos, V. Chandra, N. Kim, K. C. Kemp, P. Hobza, R. Zboril, K. S. Kim, *Chem. Rev.* **2012**, *112*, 6156.
[11] S. Park, G. Wang, B. Cho, Y. Kim, S. Song, Y. Ji, M. H. Yoon, T. Lee, *Nat. Nanotechnol.* **2012**, *7*, 438.

 © 2018 WILEY-VCH Verlag GmbH & Co. KGaA, Weinheim

[12] L. Tapaszto, G. Dobrik, P. Lambin, L. P. Biro, *Nat. Nanotechnol.* **2008**, *3*, 397.
[13] W. Han, R. K. Kawakami, M. Gmitra, J. Fabian, *J. Nat. Nanotechnol.* **2014**, *9*, 794.
[14] S. J. Han, A. V. Garcia, S. Oida, K. A. Jenkins, W. Haensch, *Nat. Photonics* **2012**, *6*, 105.
[15] S. J. Han, A. V. Garcia, S. Oida, K. A. Jenkins, W. Haensch, *Nat. Commun.* **2014**, *5*, 3086.
[16] O. Y. Loh, H. D. Espinosa, *Nat. Nanotechnol.* **2012**, *7*, 283.
[17] Y. W. Zhu, S. Murali, M. D. Stoller, K. J. Ganesh, W. W. Cai, P. J. Ferreira, A. Pirkle, R. M. Wallace, K. A. Cychosz, M. Thommes, D. Su, E. A. Stach, R. S. Ruoff, *Science* **2011**, *332*, 1537.
[18] M. Q. Zhao, Q. Zhang, J. Q. Huang, G. L. Tian, J. Q. Nie, H. J. Peng, F. Wei, *Nat. Commun.* **2014**, *5*, 3410.
[19] L. T. Qu, Y. Liu, J. B. Baek, L. M. Dai, *ACS Nano* **2010**, *4*, 1321.
[20] Z. F. Liu, Q. Liu, Y. Huang, Y. F. Ma, S. G. Yin, X. Y. Zhang, W. Sun, Y. S. Chen, *Adv. Mater.* **2008**, *20*, 3924.
[21] F. N. Xia, T. Mueller, Y. M. Lin, A. Valdes-Garcia, P. Avouris, *Nat. Nanotechnol.* **2008**, *4*, 839.
[22] Q. L. Bao, H. Zhang, B. Wang, Z. H. Ni, C. H. Y. X. Lim, Y. Wang, D. Y. Tang, K. P. Loh, *Nat. Photonics* **2011**, *5*, 411.
[23] C. Zhu, T. Y. J. Han, E. B. Duoss, A. M. Golobic, J. D. Kuntz, C. M. Spadaccini, M. A. Worsley, *Nat. Commun.* **2015**, *6*, 6962.
[24] J. J. Liang, Y. Wang, Y. Huang, Y. F. Ma, Z. F. Liu, J. M. Cai, C. D. Zhang, H. J. Gao, Y. S. Chen, *Carbon* **2009**, *47*, 922.
[25] S. K. Min, W. Y. Kim, Y. Cho, K. S. Kim, *Nat. Nanotechnol.* **2011**, *6*, 162.
[26] X. M. Sun, Z. Liu, K. Welsher, J. T. Robinson, A. Goodwin, S. Zaric, H. J. Dai, *Nano Res.* **2008**, *1*, 203.
[27] Y. Han, Z. Xu, C. Gao, *Adv. Funct. Mater.* **2013**, *23*, 3693.
[28] J. Abraham, K. S. Vasu, C. D. Williams, K. Gopinadhan, Y. Su, C. T. Cherian, J. Dix, E. Prestat, S. J. Haigh, I. V. Grigorieva, P. Carbone, A. K. Geim, R. R. Nair, *Nat. Nanotechnol.* **2017**, *12*, 546.
[29] M. K. Shin, B. Lee, S. H. Kim, J. A. Lee, G. M. Spinks, S. Gambhir, G. G. Wallace, M. E. Kozlov, R. H. Baughman, S. J. Kim, *Nat. Commun.* **2012**, *3*, 650.
[30] O. V. Yazyev, *Rep. Prog. Phys.* **2010**, *73*, 056501.
[31] V. Georgakilas, J. A. Perman, J. Tucek, R. Zboril, *Chem. Rev.* **2015**, *115*, 4744.
[32] J. Cervenka, M. I. Katsnelson, C. F. J. Flipse, *Nat. Phys.* **2009**, *5*, 840.
[33] O. V. Yazyev, L. Helm, *Phys. Rev. B* **2007**, *75*, 125408.
[34] J. Tucek, P. Blonski, Z. Sofer, P. Simek, M. Petr, M. Pumera, M. Otyepka, R. Zboril, *Adv. Mater.* **2016**, *28*, 5045.
[35] P. Blonski, J. Tucek, Z. Sofer, V. Mazanek, M. Petr, M. Pumera, M. Otyepka, R. Zboril, *J. Am. Chem. Soc.* **2017**, *139*, 3171.
[36] J. Zhou, Q. Wang, Q. Sun, X. S. Chen, Y. Kawazoe, P. Jena, *Nano Lett.* **2009**, *9*, 3867.
[37] R. R. Nair, M. Sepioni, I. L. Tsai, O. Lehtinen, J. Keinonen, A. V. Krasheninnikov, T. Thomson, A. K. Geim, I. V. Grigorieva, *Nat. Phys.* **2012**, *8*, 199.
[38] J. Tucek, K. Hola, A. B. Bourlinos, P. Blonski, A. Bakandritsos, J. Ugolotti, M. Dubecky, F. Karlicky, V. Ranc, K. Cepe, M. Otyepka, R. Zboril, *Nat. Commun.* **2017**, *8*, 14525.
[39] D. W. Boukhvalov, M. I. Katsnelson, *ACS Nano* **2011**, *5*, 2440.
[40] Y. Kobayashi, K. Fukui, T. Enoki, K. Kusakabe, Y. Kaburagi, *Phys. Rev. B* **2005**, *71*, 193406.
[41] G. Z. Magda, X. Z. Jin, I. Hagymasi, P. Vancso, Z. Osvath, P. Nemes-Incze, C. Y. Hwang, L. P. Biro, L. Tapaszto, *Nature* **2014**, *514*, 608.
[42] A. D. Guclu, P. Potasz, O. Voznyy, M. Korkusinski, P. Hawrylak, *Phys. Rev. Lett.* **2009**, *103*, 246805.
[43] K. Nakada, M. Fujita, G. Dresselhaus, M. S. Dresselhaus, *Phys. Rev. B.* **1996**, *54*, 17954.
[44] M. Kan, J. Zhou, Q. Sun, Q. Wang, Y. Kawazoe, P. Jena, *Phys. Rev. B* **2012**, *85*, 155450.
[45] M. Kabir, T. Saha-Dasgupta, *Phys. Rev. B* **2014**, *90*, 035403.
[46] K. Sawada, F. Ishii, M. Saito, S. Okada, T. Kawai, *Nano Lett.* **2009**, *9*, 269.
[47] K. Sawada, F. Ishii, M. Saito, *Phys. Rev. B* **2010**, *82*, 245426.
[48] B. Xu, J. Yin, Y. D. Xia, X. G. Wan, K. Jiang, Z. G. Liu, *Appl. Phys. Lett.* **2010**, *96*, 163102.
[49] M. Golor, S. Wessel, M. J. Schmidt, *Phys. Rev. Lett.* **2014**, *112*, 046601.
[50] J. Kunstmann, C. Ozdogan, A. Quandt, H. Fehske, *Phys. Rev. B* **2011**, *83*, 045414.
[51] S. Ganguly, M. Kabir, T. Saha-Dasgupta, *Phys. Rev. B* **2017**, *95*, 174419.
[52] H. X. Yang, M. Chshiev, D. W. Boukhvalov, X. Waintal, S. Roche, *Phys. Rev. B* **2011**, *84*, 214404.
[53] B. Sahu, H. K. Min, S. K. Banerjee, *Phys. Rev. B* **2010**, *81*, 045414.
[54] S. Dutta, K. Wakabayashi, *Sci. Rep.* **2015**, *5*, 11744.
[55] S. Cheng, J. M. Yu, T. X. Ma, N. M. R. Peres, *Phys. Rev. B* **2015**, *91*, 075410.
[56] K. Szalowski, *Carbon* **2017**, *118*, 78.
[57] K. Szalowski, *J. Appl. Phys.* **2013**, *114*, 243908.
[58] A. Valli, A. Amaricci, A. Toschi, T. Saha-Dasgupta, K. Held, M. Capone, *Phys. Rev. B* **2016**, *94*, 245146.
[59] W. Sheng, Z. Y. Ning, Z. Q. Yang, H. Guo, *Nanotechnology* **2010**, *21*, 385201.
[60] A. C. Ferrari, D. M. Basko, *Nat. Nanotechnol.* **2013**, *8*, 235.
[61] S. Ryu, J. Maultzsch, M. Y. Han, P. Kim, L. E. Brus, *ACS Nano* **2011**, *5*, 4123.
[62] T. Kato, R. Hatakeyama, *Nat. Nanotechnol.* **2012**, *7*, 651.
[63] C. Mattevi, G. Eda, S. Agnoli, S. Miller, K. A. Mkhoyan, O. Celik, D. Mastrogiovanni, G. Granozzi, E. Garfunkel, M. Chhowalla, *Adv. Funct. Mater.* **2009**, *19*, 2577.
[64] H. J. Shin, K. K. Kim, A. Benayad, S. M. Yoon, H. K. Park, I. S. Jung, M. H. Jin, H. K. Jeong, J. M. Kim, J. Y. Choi, Y. H. Lee, *Adv. Funct. Mater.* **2009**, *19*, 1987.
[65] Y. L. Huang, H. W. Tien, C. C. M. Ma, S. Y. Yang, S. Y. Wu, H. Y. Liu, Y. W. Mai, *J. Mater. Chem.* **2011**, *21*, 18236.
[66] D. H. Seo, Z. J. Yue, X. L. Wang, I. Levchenko, S. L. Kumar, S. X. Douc, K. Ostrikov, *Chem. Commun.* **2013**, *49*, 11635.
[67] T. Tang, N. J. Tang, Y. P. Zheng, X. G. Wan, Y. Liu, F. C. Liu, Q. H. Xu, Y. W. Du, *Sci. Rep.* **2015**, *5*, 8448.
[68] P. Ruffieux, S. Y. Wang, B. Yang, C. Sanchez-Sanchez, J. Liu, T. Dienel, L. Talirz, P. Shinde, C. A. Pignedoli, D. Passerone, T. Dumslaff, X. L. Feng, K. Mullen, R. Fasel, *Nature* **2016**, *531*, 489.
[69] G. Kresse, J. Furthmuller, *Phys. Rev. B* **1996**, *54*, 11169.
[70] J. P. Perdew, K. Burke, M. Ernzerhof, *Rev. Lett.* **1996**, *77*, 3865.
[71] P. E. Blöchl, *Phys. Rev. B* **1994**, *50*, 17953.
[72] G. Kresse, D. Joubert, *Phys. Rev. B* **1999**, *59*, 1758.
[73] T. Balcerzak, K. Szałowski, *Phys. Rev. E* **2014**, *89*, 062140.
[74] I. P. R. Moreira, F. Illas, *Phys. Rev. B* **1997**, *55*, 4129.

© 2018 WILEY-VCH Verlag GmbH & Co. KGaA, Weinheim

Appendix 3

Reprint of a review paper on imprinting magnetism in graphene and 2D materials

1. J. Tuček, **Piotr Błoński**, J. Ugolotti, A. K. Swain, T. Enoki, R. Zbořil, Emerging chemical strategies for imprinting magnetism in graphene and related 2D materials for spintronic and biomedical applications. *Chem. Soc. Rev.* **47**, 3899 (2018).

Published on 26 March 2018. Downloaded by Univerzita Palackého v Olomouci on 2/28/2019 2:05:03 PM.

Chem Soc Rev

REVIEW ARTICLE

View Article Online
View Journal | View Issue

Check for updates

Cite this: *Chem. Soc. Rev.*, 2018, **47**, 3899

Emerging chemical strategies for imprinting magnetism in graphene and related 2D materials for spintronic and biomedical applications

Jiří Tuček,[a] Piotr Błoński,[a] Juri Ugolotti,[a] Akshaya Kumar Swain,[a] Toshiaki Enoki[b] and Radek Zbořil*[a]

Graphene, a single two-dimensional sheet of carbon atoms with an arrangement mimicking the honeycomb hexagonal architecture, has captured immense interest of the scientific community since its isolation in 2004. Besides its extraordinarily high electrical conductivity and surface area, graphene shows a long spin lifetime and limited hyperfine interactions, which favors its potential exploitation in spintronic and biomedical applications, provided it can be made magnetic. However, pristine graphene is diamagnetic in nature due to solely sp^2 hybridization. Thus, various attempts have been proposed to imprint magnetic features into graphene. The present review focuses on a systematic classification and physicochemical description of approaches leading to equip graphene with magnetic properties. These include introduction of point and line defects into graphene lattices, spatial confinement and edge engineering, doping of graphene lattice with foreign atoms, and sp^3 functionalization. Each magnetism-imprinting strategy is discussed in detail including identification of roles of various internal and external parameters in the induced magnetic regimes, with assessment of their robustness. Moreover, emergence of magnetism in graphene analogues and related 2D materials such as transition metal dichalcogenides, metal halides, metal dinitrides, MXenes, hexagonal boron nitride, and other organic compounds is also reviewed. Since the magnetic features of graphene can be readily masked by the presence of magnetic residues from synthesis itself or sample handling, the issue of magnetic impurities and correct data interpretations is also addressed. Finally, current problems and challenges in magnetism of graphene and related 2D materials and future potential applications are also highlighted.

Received 20th October 2017

DOI: 10.1039/c7cs00288b

rsc.li/chem-soc-rev

1. Introduction

Over the past one hundred years, most of the solid-state magnetic phenomena and features, occurring at both macroscopic and nanoworld levels, have been thoroughly described experimentally and theoretically for compounds with 3d- and 4f-block elements addressing the origin of magnetism, its quantum nature, essence of magnetic ordering, and various types of magnetically self-sustainable regimes (*i.e.*, ferromagnetism, antiferromagnetism, ferrimagnetism, *etc.*). To widely recognize the significance of magnetic phenomena and their numerous applications, the 1970 Nobel prize in Physics was awarded to Louis Néel for his pioneering studies on the magnetic properties of solids. However, in the late 1980s, it was speculated that compounds which are made up of non-metals only (*i.e.*, C, O, H, N, and P) could have shown magnetic ordering and, hence, self-sustainable magnetism. Such compounds must have an unpaired p electron and, hence, must show features of an organic radical; they represent a new class of magnetic substances termed organic magnets. In 1991, *p*-nitrophenyl nitronyl nitroxide (*p*-NPNN) was the first example of an organic magnet with ferromagnetic (FM) properties below 0.65 K.[1,2] Despite the diversity of organic chemistry, there exist only a few purely organic compounds with unpaired p electrons and magnetic moments that can magnetically order, but only at low temperature. Thus, with the discovery of fullerenes[3] and, especially, carbon nanotubes,[4] the attention of the scientific community searching for magnetically active organic materials was shifted to carbon (nano)allotropes.

Carbon is the building block of all the forms of life on Earth and is the fourth most abundant element in the solar system. The ground-state electronic configuration of carbon is given by $1s^2 2s^2 2p^2$; carbon can form single, double or triple bonds with

[a] *Regional Centre of Advanced Technologies and Materials, Department of Physical Chemistry, Faculty of Science, Palacký University in Olomouc, Šlechtitelů 27, 783 71 Olomouc, Czech Republic. E-mail: radek.zboril@upol.cz; Fax: +420 585634761; Tel: +420 585634337*

[b] *Tokyo Institute of Technology, 2 Chome-12-1 Ookayama, Meguro, Tokyo 152-8550, Japan*

Published on 26 March 2018. Downloaded by Univerzita Palackého v Olomouci on 2/28/2019 2:05:03 PM.

another carbon atom. However, it is known that carbon, despite having two unpaired spins in the outer p-shell as an isolated atom, is diamagnetic due to the nature of bonds that are established between the carbon atoms. In particular, adopting the concept of molecular orbital theory (see Fig. 1), four electrons are paired in the carbon π-bonding orbital. In other words, carbon always forms four bonds, leaving no unpaired electrons. Thus, the magnetic moment of carbon shows only a diamagnetic term, resulting from the motion of electrons on the orbitals, with a zero paramagnetic contribution. As a result, all the carbon (nano)allotropes/nanostructures, known so far or predicted to exist, with an identical character of bonds between the carbon atoms are supposed to lack any magnetic features.

Carbon (nano)allotropes/nanostructures can be classified depending on various criteria.[5] Most frequently, dimensionality is selected as a standard for placing them into four groups, *i.e.*, (i) 0D (*e.g.*, fullerenes, quantum dots, nanodiamonds), (ii) 1D (*e.g.*, carbon nanotubes, nanohorns, and nanoribbons), (iii) 2D (*e.g.*, graphene), and (iv) 3D (*e.g.*, graphite, diamond) structures. With regard to morphology, carbon (nano)allotropes/nanostructures fall into two categories, *i.e.*, (i) open/flat (*e.g.*, graphene) and closed/hollow (*e.g.*, fullerenes, carbon nanotubes) structures. Another classification involves the type of bonds between carbon atoms. In general, carbon tends to readily hybridize its 2s and 2p orbitals upon bonding with other carbon atoms. Three different hybridized states in carbon are recognized, *i.e.*, (i) sp,



Jiří Tuček

Dr Jiří Tuček received his PhD in Applied Physics from the Palacký University in Olomouc, Czech Republic, in 2008. In 2013, he became an associate professor at the Faculty of Science of the Palacký University in Olomouc, Czech Republic. He is currently a Senior Researcher and the head of the "Magnetic Nanostructures" group at the Regional Centre of Advanced Technologies and Materials (RCPTM), Palacký University in Olomouc, Czech Republic. In 2015, he received The Zasshi-kai Lectureship Award from The Tokyo University, Japan, for young scientists for the contribution in the field of magnetism of nanostructured objects. His research interests include magnetism in the nanoworld, particularly the magnetic behavior and properties of carbon nanostructures (in particular, graphene) and iron-containing compounds such as iron and iron oxide nanosystems.



Piotr Błoński

Dr Piotr Błoński obtained his PhD degree in physics from the University of Wrocław, Poland (2006). After his PhD, he undertook several postdoctoral stays, at the University of Vienna, Austria, at the Institute of Chemical Research of Catalonia, Spain, and at the Institute of Nuclear Physics, Polish Academy of Sciences in Kraków. Currently, he is an assistant professor at the Department of Physical Chemistry and a junior researcher at the Regional Centre of Advanced Technologies and Materials (RCPTM), Palacký University in Olomouc, Czech Republic. His research focuses on modelling magnetic nanomaterials with an emphasis on carbon nanostructures.



Juri Ugolotti

Dr Juri Ugolotti is a researcher at the Regional Centre of Advanced Technologies and Materials (RCPTM) of the Palacký University in Olomouc, Czech Republic. He completed his undergraduate studies in Applied Chemistry in the UK and Italy, and he received his PhD in Chemistry from Imperial College London, UK. After post-doctoral spells at the University of Münster, Germany, and at the Academy of Science of the Czech Republic in Prague, he started working at RCPTM in 2014. His research interests span the synthesis, characterization and application of magnetic inorganic and organometallic materials and of carbon-based nanostructures.



Akshaya Kumar Swain

Dr Akshaya Kumar Swain obtained his PhD degree in materials science, which was jointly awarded by IIT Bombay-India and Monash University-Australia in 2015. He also obtained his MTech degree in solid state materials from IIT Delhi-India. He is currently working as an assistant professor of physics at the GITAM University-India and pursuing research on functional nanomaterials for application in spintronics and cancer therapy. His research interests include synthesis and magnetism of low-dimensional materials, particularly belonging to the carbon family.

This journal is © The Royal Society of Chemistry 2018

Published on 26 March 2018. Downloaded by Univerzita Palackého v Olomouci on 2/28/2019 2:05:03 PM.

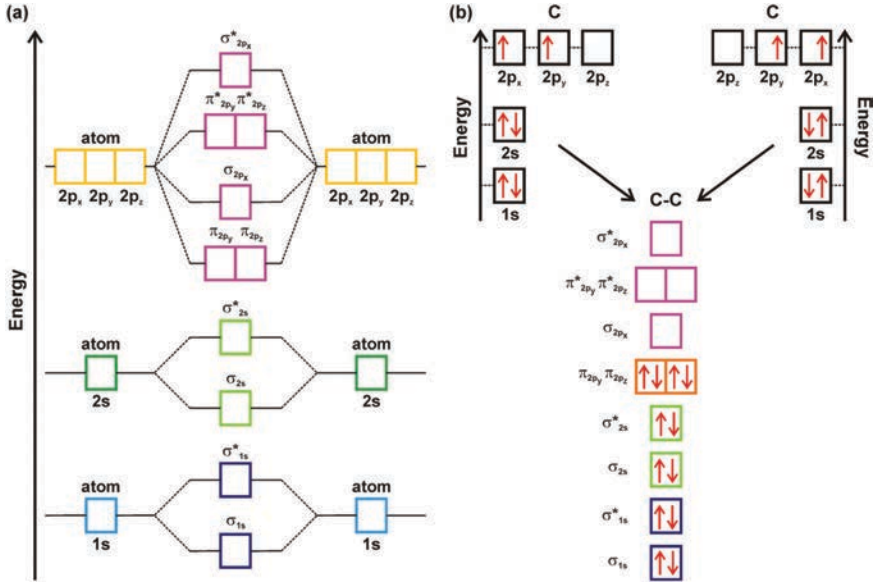


Fig. 1 (a) General molecular orbital energy-level diagram for the first two energy levels showing the formation of molecular bonding (σ, π) and antibonding (σ*, π*) orbitals. (b) Bonding scheme for two carbon atoms providing evidence for pairing of all the spins, confirming thus the diamagnetic nature of the C–C pair.

(ii) sp^2, and (iii) sp^3 (see Fig. 2a), depending on the number of σ-bonds established between the carbon atoms. In the case of sp^3 hybridization, carbon atoms present four single bonds with a tetrahedral arrangement while one double bond and two single bonds are characteristic of sp^2 hybridization with trigonal planar geometry (see Fig. 2a). The configuration showing one single and one triple bond conforms to sp hybridization with carbon atoms lying on a line (see Fig. 2a). Various hybridization states and their combinations generate a broad spectrum of already existing carbon (nano)allotropes/nanostructures as demonstrated in Fig. 2b.[5,6] Other structures with C atoms in various sp/sp^2/sp^3 ratios were predicted such as high-pressure phases or hypothetical forms found thermodynamically stable from theoretical calculations, all waiting to emerge from properly designed/optimized synthetic protocols.[5]



Toshiaki Enoki

Professor Toshiaki Enoki received his PhD in 1974 from Kyoto University. He was a research associate at the Institute for Molecular Science (1977–1987) and a visiting scientist at the Massachusetts Institute of Technology in 1984. In 1987, he moved to the Department of Chemistry at the Tokyo Institute of Technology as an associate professor, and then became a professor. Currently, he is a professor emeritus at the institute. He was a visiting professor at the University of Rennes I (2000, 2004, 2005), the Institute for Molecular Science (2003–2004), an honorary professor at Durham University (2010) and an honorary member of Ioffe Institute, Russian Academy of Sciences in 2013. His current research interests are focused on the electronic and magnetic structures of π-electron-based materials, such as nanographene, nanodiamond, and organic charge transfer complexes.



Radek Zbořil

Professor Radek Zbořil received his PhD degree from the Palacký University in Olomouc, Czech Republic. After his doctoral studies, he did several foreign stays at universities around the world in locations such as Tokyo, Delaware, and Johannesburg. Currently, he is a professor in the Department of Physical Chemistry and a General Director of the Regional Centre of Advanced Technologies and Materials at the Palacký University in Olomouc, Czech Republic. His research interests focus on nanomaterial research including iron- and iron oxide-based nanoparticles, silver nanoparticles, carbon nanostructures, and magnetic nanoparticles, their synthesis, physicochemical characterization, and applications in catalysis, water treatment, antimicrobial treatment, medicine, and biotechnology. He is an author and co-author of more than 450 scientific papers with more than 15 000 citations.

Published on 26 March 2018. Downloaded by Univerzita Palackého v Olomouci on 2/28/2019 2:05:03 PM.

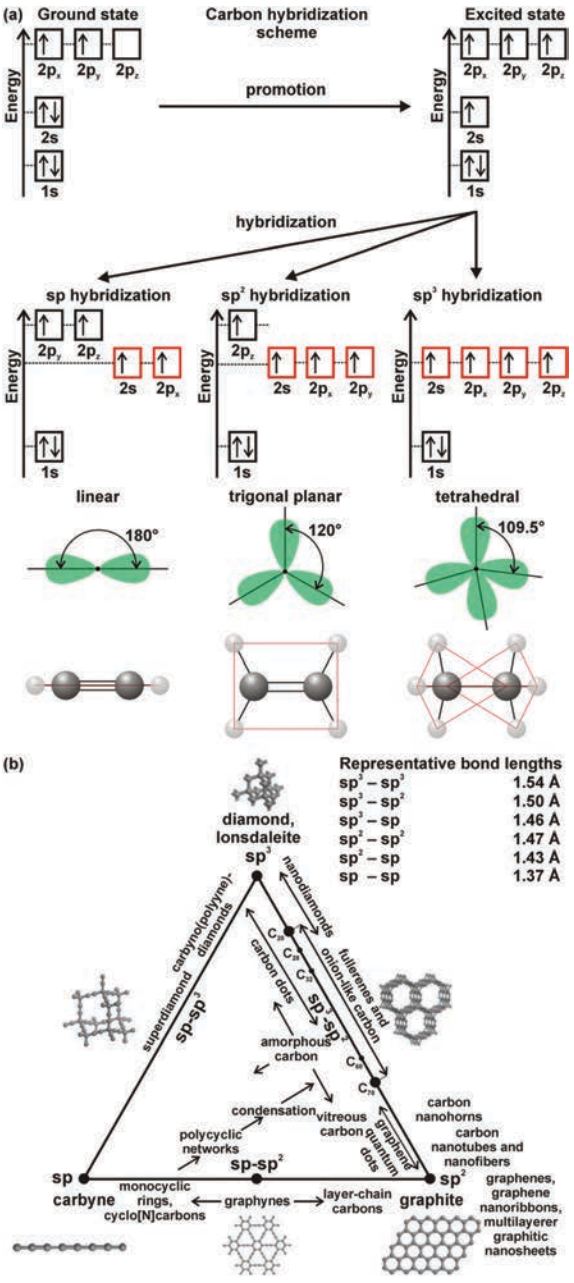


Fig. 2 (a) Schematic description of sp, sp^2, and sp^3 hybridization in carbon with an illustration of the bonding structure. (b) Ternary phase diagram of carbon (nano)allotropes/nanostructures depending on the hybridization state they show. The positions/intervals of the most common carbon (nano)allotropes/nanostructures are indicated. Carbon forms with a single hybridization state are found at the vertices of the triangle, carbon species with mixed hybridization states lie along the sides of the triangle, and carbon compounds with all the three hybridization states are placed inside the triangle. The representative bond lengths between carbon atoms with specific hybridizations are also listed. Panel (b) reprinted with permission from ref. 5. Copyright 2015 American Chemical Society.

Due to the participation of all the valence electrons in establishing strong sp^3, sp^2, and sp bonds, carbon is regarded as an element with the least probability to retain unpaired electrons, thus behaving largely in a diamagnetic manner. Indeed, besides superconductors, graphite is ranked as a material with the most negative magnetic susceptibility reported so far ($\sim -50 \times 10^{-6}$ emu g^{-1}).[7] The diamagnetic behavior of graphite is solely caused by delocalization of electrons which move along the graphitic rings in the plane; due to small contribution of motion of electrons in the direction perpendicular to the graphitic rings, the diamagnetic susceptibility of graphite is highly anisotropic. In diamond, three contributions to its magnetic susceptibility were identified, *i.e.*, two diamagnetic terms originating from s (core) and p (valence) electrons and a van Vleck (paramagnetic) term emerging from magnetic dipole transitions occurring between the valence and conduction bands with a strong dependence on the symmetry of the chemical bond.[7] As the van Vleck term is relatively small, diamond shows a dominant diamagnetic response (with a magnetic susceptibility of $\sim -0.5 \times 10^{-6}$ emu g^{-1}). Carbyne, an example of purely sp carbon (nano)allotrope, is also diamagnetic due to electron currents flowing along its structure.

Other carbon nanostructures such as carbon nanotubes and carbon nanohorns were found to be magnetically unattractive. In particular, single-walled and multi-walled carbon nanotubes, composed entirely of sp^2 bonds, are diamagnetic. If magnetic features for carbon nanotubes were reported, they were ascribed to the presence of catalyst particles (*e.g.*, Fe, Co). However, a few exceptions exist in the literature. The possibility of imprinting stable magnetization in carbon nanotubes was addressed by theoretical computations and experiments; it was found that a magnetic ground state may emerge for finite-sized zigzag-cut carbon nanotubes in the case of hydrogenation, truncation with edge termination, and capping by fullerene hemispheres.[8,9] FM behavior was then explained in terms of larger exchange splitting compared to energy loss due to breaking the bonding states in some carbon nanotubes; the FM response was found to strongly depend on the chirality and diameter of the nanotubes. Another hypothesis introduces the concept of emergence of free radicals communicating *via* the itinerant electrons of the carbon nanotube network.[10] The magnetic ground state can be alternatively stabilized by topological line defects involving pentagon and octagon rings with emergence of peculiar edge-localized states similar to those of graphite flakes.[11] The theory predicts that metallic carbon nanotubes may behave in an FM (antiferromagnetic (AFM)) manner if localized spins occupy the same (different) sublattice while semiconducting carbon nanotubes may show a dominant FM response with weak dependence on the distribution of the localized spins over respective sublattices; the communication pathways are believed to be maintained by an isotropic Heisenberg interaction and anisotropic Ruderman–Kittel–Kasuya–Yosida (RKKY) interaction of Ising and Dzyaloshinskii–Moriya nature, the latter emerging due to spin–orbit interactions breaking the SU(2) spin symmetry of the system.[12] In the case of carbon nanohorns (*i.e.*, short single-walled carbon nanotubes

 This journal is © The Royal Society of Chemistry 2018

Published on 26 March 2018. Downloaded by Univerzita Palackého v Olomouci on 2/28/2019 2:05:03 PM.

closed on one side), diamagnetic features were reported; it is speculated that a large diamagnetic contribution originating from the sp^2 network is partly cancelled by a constant van Vleck paramagnetic term.[13] Similar to carbon nanotubes, carbon nanohorns are diamagnetic in nature; emergence of magnetic features in nanohorns was observed upon adsorption of oxygen.[14]

The hope that pure carbon structures may show unpaired spins and eventually magnetic ordering is redirected to such carbon (nano)allotropes with mixed hybridization states (*i.e.*, sp^2/sp^3 ratio) in which some of the valence electrons are not involved in a bonding process. In particular, fullerenes with "pseudo" sp^3 and sp^2 bonds, the ratio of which depends on the number of carbon atoms (see Fig. 2b), show both diamagnetic and paramagnetic behavior. The diamagnetic contribution originates from electrons moving around the hexagonal rings,[15] while motion of electrons around double bonds which are adjacent to the vertices of pentagons is identified to be responsible for the paramagnetic term.[16] It is then assumed that the diamagnetic contribution should gradually increase with the size of fullerenes (*i.e.*, with increasing number of hexagons), eventually reaching the value of the diamagnetic susceptibility of graphite.[17] However, it was observed that the diamagnetic susceptibility of fullerenes with a number of carbon atoms less than 100 varies in a random manner, most probably resulting from a dependence of the characteristics of bonds in pentagons and hexagons on the structure.[18] For larger fullerenes, diamagnetic susceptibility increases as expected. For C_{60}, the most studied fullerene, the paramagnetic and diamagnetic contributions are almost equal; hence, C_{60} is non-magnetic. In order to increase the paramagnetic term in C_{60}, several strategies have been proposed such as intercalation with oxygen or intrinsic defects (*e.g.*, C_{60}^- ions). FM/AFM features were observed for some fullerene derivatives such as C_{60} charge transfer complexes (*e.g.*, C_{60}–TDAE (tetrakis-dimethylamino-ethylene)–$C_2N_4(CH_3)_8$),[19] $C_{60}R_n$ compounds (where R is H, F, CF_3 or polymer fragments, and n is odd),[20–22] and fullerenes polymerized by irradiation or introduction of under pressure (orthorhombic, tetragonal, and rhombohedral fullerene polymers).[23–25] Among them, C_{60}–TDAE, a donor–acceptor type system, has been studied heavily; it undergoes a transition to the FM state at $\sim$16 K.[19] The emergence of the FM regime was explained in terms of formation of an ion-radical ($TDAE^{+\bullet}$–$C_{60}^{-\bullet}$) pair due to charge transfer from the π-orbitals of a donor molecule (TDAE) coupled by strong spin-exchange. If TDAE is replaced with other donating compounds, FM behavior is preserved;[26] however, with C_{70}, no long-range magnetic ordering was ever observed. $(ND_3)K_3C_{60}$ is another example of a fullerene-based compound behaving in AFM manner stabilized up to $\sim$37 K by spatial disorder and inhomogeneity effects.[27] Nanodiamonds – close dimensional relatives to fullerenes – with a core–shell structure composed of a diamond core (sp^3 carbon atoms), a middle layer (sp^{2+x} carbon atoms), and a graphitic outer shell (sp^2 carbon atoms) with dangling bonds terminated by functional groups[5] – were found to be largely diamagnetic with minor paramagnetic centers whose existence is further promoted by the introduction of nitrogen vacancies.[28] However, no magnetic ordering has been observed so far for nanodiamonds. Similar to non-functionalized fullerenes, onion-like carbon shows a large diamagnetic contribution and a small paramagnetic term.

In the beginning of the nineties of the 20th century, it was theoretically predicted that carbon may become magnetic once the structure adopts an arrangement with a mixture of planar 3-fold coordinated sp^2- and tetrahedral sp^3-hybridized carbon atoms.[29,30] In particular, for a hypothetical layered intermediate graphite-diamond structure with 50% of sp^2-bonded and 50% of sp^3-bonded carbon atoms, resulting in a high level of unpaired electrons (0.59 per carbon atom), the saturation magnetization was estimated to reach 230 emu g^{-1}, similar to that of α-Fe (220 emu g^{-1}). Carbon nanofoam, firstly synthesized in 1999, is an example of a carbon (nano)allotrope with a $sp^3/(sp^2 + sp^3)$ bonding ratio of 35% on average and a structure resembling hyperbolic schwarzite.[31] Carbon nanofoam is modelled as a tetrapod with 12 heptagons surrounded by hexagons with tetravalent carbon atoms (with heptagons showing trivalent carbon radicals with a lone electron). Magnetic carbon nanofoam shows a Curie temperature of $\sim$92 K and a saturation magnetization of $\sim$0.42 emu g^{-1} (at 1.8 K). The origin of magnetic moments in carbon nanofoam was explained considering several factors: (i) the presence of carbon rings other than 6-membered rings causing localization of the π-electron cloud encouraging localization of unpaired spins; (ii) sp^3-bond carbon atoms providing cross-linking between different schwarzite layers and preventing π-electron delocalization; (iii) potential presence of carbon vacancies; and (iv) presence of hydrogen and oxygen promoting spin formation and localization by disrupting the conjugated C–C bond system.[32] However, it seems that establishment of an interaction pathway is strongly dependent on the $sp^3/(sp^2 + sp^3)$ ratio with a non-trivial trend. Moreover, magnetic carbon nanofoam is highly unstable losing its magnetic features within several months after synthesis if not protected against a chemical attack by formation of strongly convoluted sheets and/or impermeable frameworks.

Similarly, if the structure contains both sp- and sp^2-bonded carbon atoms, magnetic moments are observed to evolve;[33,34] the examples of carbon nanoallotropes with mixed sp and sp^2 hybridization states include graphyne and graphdiyne.[5] In graphdiyne, the magnetic moments are believed to arise due to the unique construction of the carbon matrix and specific sp-hybridization. They can be enhanced if the structure of graphdiyne is doped with nitrogen with a pyridine configuration.[35] Graphdiyne then behaves in a paramagnetic manner (*i.e.*, spin-half paramagnet) without any magnetic ordering; an AFM ground state was observed for annealed graphdiyne when hydroxyl groups, adsorbed on the graphdiyne sheet and forming a chain-like motif, were identified as the major sources of magnetic moments.[34]

In 2004, when graphene was firstly isolated,[36] the realm of carbon witnessed a striking attention from the scientific community to synthesize graphene, study, understand, and tune its unique physicochemical properties[37–40] and, eventually, equip it with features it misses, including a magnetic response. Since then, dozens of theoretical and experimental papers have

Published on 26 March 2018. Downloaded by Univerzita Palackého v Olomouci on 2/28/2019 2:05:03 PM.

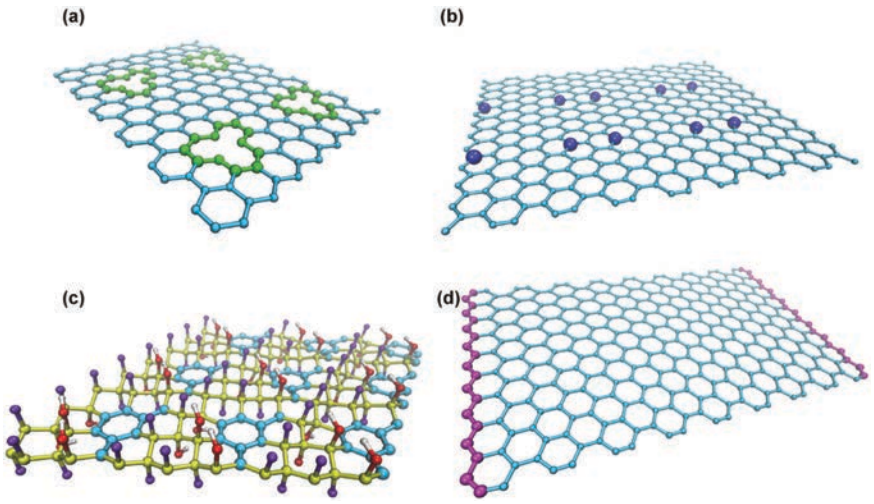


Fig. 3 Defects imprinting a magnetic behavior into graphene: (a) vacancies; (b) substitution with non-carbon atoms; (c) sp^3 functionalization; (d) edges.

appeared reporting attempts to synthesize "magnetically-active" graphene-based systems which would be competitive with traditional inorganic magnets thus opening the doors towards applications in electronics,[41] spintronics,[42] biomedicine,[43] and magnetic (bio)separations.[44]

Graphene, intrinsically of diamagnetic nature due to a delocalized π-bonding network, was found to show magnetic features only in cases when defects were introduced into its lattice as indicated by numerous theoretical works and confirmed by several experimental studies.[45] The defects include local topology perturbations,[46] vacancies,[47] Stone–Wales (SW) defects,[48] pentagonal–octagon pairs,[49] substitution with non-carbon atoms in the graphene lattice,[50,51] adatoms (*i.e.*, atoms attached to the surface of the graphene sheet),[52,53] mixed sp^2/sp^3 hybridization (*i.e.*, covalent sp^3 functionalization),[54,55] and zigzag-type edges (*i.e.*, confinement-related phenomena) (see Fig. 3).[56,57] In short, these defects are manifested as semi-localized π "midgap" states or flat bands in the electronic band structure of graphene with the peaks in the density of states at the Fermi level (E_F) showing spin polarization, giving rise to localized magnetic moments. Defect-induced FM behavior in graphene and its derivatives (*e.g.*, graphone, graphane) has been experimentally observed to evolve at low temperatures; however, its sustainability at room temperature is heavily questioned as the π-electron system of graphene is too weak to maintain magnetic interactions (*i.e.*, RKKY-like interactions) between induced localized moments at elevated temperatures. Recently, several reports have appeared demonstrating the possibility of preparing graphene-based systems with magnetic ordering stable up to room temperature. Currently, the imprinting of self-sustainable magnetism at room temperature to graphene and/or its derivatives is widely recognized as a key challenge for further development of 2D carbon-based materials with a tremendous potential, especially, in spintronics and biomedical fields.

Several review works have been published so far aimed at giving an overview about the recent advancements in magnetism of graphene and related 2D materials;[42,58–60] however, they have focused only on the theoretical aspects of imprinting self-sustainable magnetic features in graphene or have chosen only particular defects without any systematization and critical assessment or have concentrated solely on the application potential of magnetically active graphene systems and their 2D analogs. Moreover, in this respect, substitution and functionalization of graphene sheets as new emerging approaches toward magnetism in graphene have been ignored so far. The present review thus aspires to comprehensively and critically cover the issue of magnetism in graphene, its derivatives and 2D analogs with regard to a recent huge progress in the field from the theoretical, experimental, and application perspective. The aims include to systematically classify the methods used to equip graphene with magnetic properties, evaluate the effectiveness of various approaches in imprinting of magnetism in graphene and discuss their possible exploitation for challenging future applications. Particularly, in Section 2, graphene is introduced with an emphasis on its structure and electronic features, highlighting areas of its potential applications. Moreover, the models providing description and understanding of defect-induced magnetic behavior in graphene are briefly discussed. Section 3 is devoted to point and line defects in graphene, their nature, experimental creation and their role in the evolution of magnetic features in graphene. Section 4 reviews confined graphene-based systems including graphene nanoribbons, graphene nanoflakes, and graphene quantum dots. The attention is devoted to identifying the role and effect of the intrinsic parameters of the system (*e.g.*, edge geometry, size, lattice doping, and edge modification) and external stimuli (*e.g.*, electric field and strain) on the evolution and tuning of the magnetic response of confined graphene-based representatives. In Section 5, the issue of doping of the graphene lattice with non-carbon elements (*i.e.*, nitrogen, sulfur) is addressed; here, the type (n-type/p-type), chemical nature, and concentration of the dopant are discussed as crucial parameters affecting directly the

 This journal is © The Royal Society of Chemistry 2018

Published on 26 March 2018. Downloaded by Univerzita Palackého v Olomouci on 2/28/2019 2:05:03 PM.

electronic structure of graphene and, hence, evolved magnetic properties. Section 6 introduces the concept of chemical covalent functionalization of the graphene surface with various adatoms (*e.g.* hydrogen, nitrogen, fluorine) and functional groups (*e.g.*, –OH, –COOH) as a promising strategy to develop graphene-based systems with a magnetic ordering sustainable up to room temperature. Section 7 briefly summarizes recent advancements in magnetically active graphene intercalated compounds. In Section 8, the emergence of magnetism in graphene analogues and other selected 2D materials is discussed; in particular, the attention is devoted to transition metal dichalcogenides, metal dihalides, metal dinitrides, MXenes, hexagonal boron nitride, and other relevant 2D compounds/molecules. Since the magnetic behavior of graphene imprinted with defects of whatever nature can be incorrectly interpreted as due to magnetic impurities (*i.e.*, d-block elements), Section 9 sheds light on the proper determination of magnetic admixtures in the sample (*i.e.*, magnetic residues from synthesis itself or sample handling) and discusses experimental approaches to quantify/exclude them, thus preventing misleading interpretations. Moreover, mathematical procedures used to correctly analyze the measured magnetization data and separate individual magnetic contributions are also briefly outlined. Finally, the review summarizes the current status in the field of graphene magnetism, highlights the potential future challenges, and envisages application fields where "magnetic" graphene could become a prominent material.

2. Graphene, its structure, properties and applications and theoretical models providing an understanding of defect-induced magnetic behavior in graphene

Carbon atoms in graphene are sp^2-hybridized leaving a free p_z orbital perpendicular to the plane (see Fig. 4). The in-plane sp^2-orbitals form the σ-bonds. The honeycomb lattice of graphene is formed by three sp^2-bonded carbon atoms.[37] However, the Bravais lattice of graphene is different from the honeycomb lattice and is superposition of two triangular Bravais lattices (termed as A- and B-sublattice, or alternatively denoted as α- and β-sublattice, respectively). Hence, the honeycomb lattice of graphene provides two free electrons per unit cell.[61]

Graphene follows a linear dispersion relation, reflecting the relativistic nature of the electrons and holes in graphene, which behave as massless Dirac fermions in a biparticle lattice.[37,61] The corresponding Hamiltonian can then be represented adopting the relativistic Weyl equation,[37] *i.e.*,

$$H = \sigma V_F p, \quad (1)$$

where p is the momentum, V_F is the Fermi velocity and σ is the pseudospin operator. Cone-shaped electronic bands (also called Dirac cones) for the π-valence and π*-conduction states can be obtained by solving the relativistic Weyl equation. These Dirac cones touch each other at a point called the Dirac point resulting in a zero-gap semiconducting behavior. In other words, the π- and π*-bands equip graphene with most of its remarkable electronic properties *via* the half-filled band that permits free-moving electrons.

The peculiar electronic structure of graphene is responsible for emergence of unusual physical phenomena including, for example, the half-integer quantum Hall effect,[62,63] ambipolar electric field effect,[36] non-linear Kerr effect,[64] Casimir effect,[65] photothermoelectric effect,[66] bipolar supercurrent,[67] and positive piezoconductive effect.[68] Due to its structural and electronic features, graphene is equipped with superior properties such as, for example, a high charge carrier mobility (up to 200 000 $cm^2 V^{-1} s^{-1}$ at room temperature at a carrier density of 10^{12} cm^{-2}), very low resistivity (10^{-6} Ω cm), large thermal conductivity (1500–2500 W $m^{-1} K^{-1}$), high optical transmittance (97.7% for red light), large surface area (2630 $m^2 g^{-1}$), and high tensile strength (130.5 GPa) and Young's modulus (~1 TPa). The physicochemical characteristics of graphene can be further easily/appropriately tuned by doping its lattice with non-carbon atoms, functionalizing its surface with various atoms, molecules, functional groups or deposition on various substrates,[39] significantly extending its portfolio of applications. So far, graphene has been suggested as a promising material in various fields such as, for example, electronics (ultralight flexible displays and touch panels,[69] field-effect, high speed and ballistic transistors,[70] spin transistors and spin logic devices,[42] light-emitting diodes,[71] components

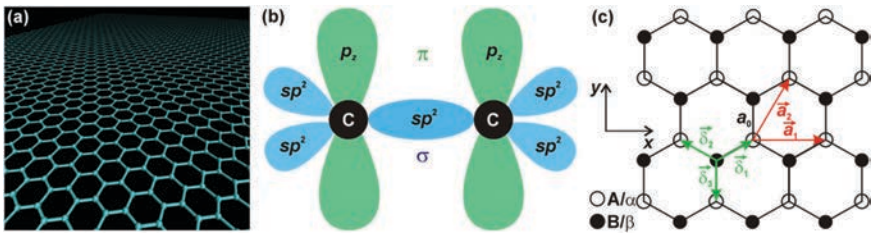


Fig. 4 (a) Pictorial representation of graphene sheet and (b) sp^2 hybridization in graphene. (c) The honeycomb lattice structure of graphene. The atoms in the sublattice are separated by a_0 = 0.142 nm. The basis vectors of the Bravais lattice are represented by a_1 and a_2 and are given as $a_1 = a_0\sqrt{3}(1; 0)$ and $a_2 = a_0\sqrt{3}(1/2; \sqrt{3}/2)$. The nearest vectors that connect the atoms from the A-(α-) to the B-(β-)sublattice are represented by δ_1, δ_2, and δ_3 and given as $\delta_1 = a_0/2(\sqrt{3}; 1)$, $\delta_2 = a_0/2(-\sqrt{3}; 1)$, and $\delta_3 = a_0/2(0; -1)$.

Published on 26 March 2018. Downloaded by Univerzita Palackého v Olomouci on 2/28/2019 2:05:03 PM.

of radio frequency integrated circuits[72] and nanoelectromechanical systems[73]), energy storing and generating devices (electrodes in ultra-/super-capacitors,[74] Li-ion batteries,[75] and fuel cells[76]), optics (photoactive medium in solar cells,[77] photodetectors,[78] and broadband polarizers[79]), printing technologies (conductive inks,[80] inks for electromagnetic shielding[81]), medicine (DNA sequencing,[82] agents for cellular imaging and carriers of drugs/biomolecules[83]), environment- and water-treating technologies (sensors and sorbents of pollutants,[84] water desalination[85]), and additives improving mechanical properties of composites (car bumpers[86]). However, most of the proposed applications of graphene are still in the laboratory stage as problems are frequently faced with scaling-up the production of graphene-based systems, preserving, at the same time, their purity, chemical identity, and, hence, application-desired physicochemical properties.

Besides, graphene shows strong ballistic transport, long spin lifetime and spin relaxation length, limited hyperfine interactions, and weak spin–orbit coupling (a result of low nuclear charge and orthogonality of π- and σ-bands), *i.e.*, prerequisites, which are highly required in spintronics. Importantly, due to the spin–orbit coupling, the quantum spin Hall effect emerges in graphene, when the spin-up and spin-down carriers move in the opposite directions along the same edge.[87] However, as already mentioned above, it misses localized magnetic moments in its pristine state. Thus, defects of whatever nature are needed to free electrons from bonding resulting in evolution of unpaired spins. Magnetic susceptibility (χ_{mass}) of the defected graphene is then given by $\chi_{mass} = \chi_{mass,dia} + \chi_{mass,para} + \chi_{mass,ferro}$, where $\chi_{mass,dia}$ is the diamagnetic term involving orbital, Landau, and core diamagnetic contributions, $\chi_{mass,para}$ stands for a paramagnetic term including Curie-like response of non-interacting (isolated) defect-induced paramagnetic centers, paramagnetic Pauli contribution from conduction electrons, and paramagnetic van Vleck contribution, and $\chi_{mass,ferro}$ represents the ferromagnetic term reflecting the establishment of interaction pathways between the defect-induced paramagnetic centers.

A theoretical understanding of graphene magnetism can be well described by the tight-binding model, Hamiltonian model, Hubbard model, mean field approximation (Hartree–Fock, Monte Carlo, renormalization, *etc.*), density functional theory (DFT) approach, *etc.* From the theoretical viewpoint, the electron–electron interaction as the diagonal elements of the Hamiltonian matrix plays an important role. The problem can be solved with an appropriate guess that could tackle the matrix self-consistently breaking the spin–lattice symmetry.

The one-orbital mean-field Hubbard model is probably the simplest model to analyze the magnetic properties of sp^2 carbon nanostructures. The unhybridized p_z atomic orbitals of sp^2 carbon atoms in graphene give rise to low energy π-symmetry electronic states. The mean-field Hubbard model considers these π-symmetry electronic states. The Hamiltonian is given as

$$H = H_0 + H_I, \tag{2}$$

where H_0 and H_I are the kinetic and interaction parts of the Hamiltonian, respectively. H_0 represents the nearest-neighbor tight-binding Hamiltonian given as

$$H_0 = -t\sum_{\langle i,j\rangle\sigma}\left[c_{i\sigma}^{\dagger}c_{j\sigma} + \text{h.c.}\right], \tag{3}$$

where $c_{i\sigma}^{\dagger}$ and $c_{j\sigma}$ are the creation and annihilation operators, respectively, that create and annihilate an electron at site i with spin σ. The term "h.c." is the Hermitian conjugate part of the Hamiltonian. The consideration of nearest-neighbor atoms is denoted by the angular bracket ($\langle\rangle$). The hopping integral $t \approx 2.7$ eV. The elements of the Hamiltonian matrix are determined by the atomic structure. If the atoms i and j are covalently bonded, the off-diagonal matrix elements are set to $-t$. The eigenvalues of the Hamiltonian matrix have electron–hole symmetry. Thus, the bonding (occupied) and anti-bonding (unoccupied) states are always in pairs with an energy relation given as $\varepsilon = -\varepsilon^*$. The mid-gap states with energy $\varepsilon = 0$ are called the zero-energy states. Although the tight-binding model can predict the electronic structure of sp^2 carbon atoms, addition of the on-site Coulomb interaction helps in explaining the emergence of magnetism. Thus, the interaction part of the mean-field Hubbard model is given as

$$H_I = U\sum_i n_{i\uparrow}n_{i\downarrow}, \tag{4}$$

where U is the magnitude of the on-site Coulomb interaction. The spin-resolved electron density at the i-site is given by $n_{i\sigma} = c_{i\sigma}^{\dagger}c_{j\sigma}$. It should be noted that this model involves only the nearest neighbor interactions. Thus, only two electrons are considered that occupy the same p_z atomic orbital. This limitation can be overcome by using a mean-field approximation where an electron with spin-up/-down at the i-site interacts with the average electron density with spin-down/-up. Hence, the Hamiltonian in the mean-field approximation is given by

$$H_{mf} = U\sum_i\left\{n_{i\uparrow}\langle n_{i\downarrow}\rangle + \langle n_{i\uparrow}\rangle n_{i\downarrow} - \langle n_{i\uparrow}\rangle\langle n_{i\downarrow}\rangle\right\}. \tag{5}$$

The diagonal terms in the Hamiltonian are only effected by such formulation. This can be solved self-consistently by arbitrarily choosing a value for $\langle n_{i\sigma}\rangle$. In the case when the chosen value breaks the spin spatial symmetry, AFM solutions can be obtained.[88,89] With a right guess for the starting value of $\langle n_{i\sigma}\rangle$, one can easily converge the solution with repeated iterations. Eventually, the spin density at each i-atom is obtained self-consistently and is given by

$$M_i = \frac{1}{2}\left(\langle n_{i\uparrow}\rangle - \langle n_{i\downarrow}\rangle\right) \tag{6}$$

The total spin (S) of the system is given by $S = \sum_i M_i$. The induced magnetic moment in the carbon nanostructure mainly depends on U/t. With a right guess for U/t, one can easily obtain similar solutions compared to those from the first-principles calculations.

Doubts can be raised on the suitability of the above-discussed model by demanding further clarifications. Does the graphene

 This journal is © The Royal Society of Chemistry 2018

Published on 26 March 2018. Downloaded by Univerzita Palackého v Olomouci on 2/28/2019 2:05:03 PM.

system follow the mean-field approximation? How does it compare to the results obtained by a method that considers all the electrons? What could be the best guesses for U/t to get a converged solution? The validity of the mean-field approximation can be checked by comparing its results with that obtained using the exact diagonalization and quantum Monte Carlo simulations.[90] If the empirical value of the parameter U/t is chosen wisely, a close match between the mean-field Hubbard model and first-principles computations can be achieved.[91–93] It should be noted that the equivalence of all electrons or ignoring the localized atomic core states, which are performed in the first-principles methods, actually does not play any important role. However, it does if one computes the hyperfine interactions because the spin polarization of the 1s carbon atoms can effectively contribute.[88,94] Else, choosing a suitable value of $U/t \approx 1.3$, the results achieved by the DFT model, considering an exchange–correlation function belonging to a generalized-gradient-approximation (GGA) family, can be reproduced. Similarly, choosing $U/t \approx 0.9$, the local-spin-density approximation results can also be predicted.[93] A suitable range for $U \approx 3.0$–3.5 eV was reported from magnetic resonance studies of *trans*-polyacetylene which is very similar to a zigzag-edged graphene nanoribbon with a minimum width.[95,96] The DFT model using GAA employs the identical interval of U/t, *i.e.*, 1.1–1.3. A Mott–Hubbard transition of AFM ordering in graphene can be obtained in the case in which one chooses the value of U/t to be greater than 2.23.[97]

Alternatively, the benzenoid graph theory can be used to compute and analyze the tight-binding Hamiltonian spectrum of graphene. For a thorough description of the benzenoid graph theory, one is advised to read the work by Fajtowicz *et al.*[98] In short, the theory is based on counting principles. The number of zero-energy states in the tight-binding model can be predicted (counted) from the graph's nullity in the benzenoid theory and is given by

$$\eta = 2\alpha - N, \tag{7}$$

where N is the total number of sites and α is the possible maximum number of sites that are not nearest to each other. Further, the Stoner criterion decides the onset of magnetism. The Stoner criterion is based on the competition between the loss of kinetic energy and the gain in exchange energy due to spin polarization of a system. The exchange splitting of the electronic states in the spin polarization system can cause a gain in the exchange energy,[99] *i.e.*,

$$\Delta S = \varepsilon_{\uparrow} - \varepsilon_{\downarrow} = \frac{U}{2}\sum_i n_i^2, \tag{8}$$

where $\sum_i n_i^2$ measures the degree of localization of the corresponding state. The loss of kinetic energy is proportional to this state. Thus, irrespective of the degree of localization, for any $U > 0$, the spin polarization occurs by the zero-energy states. In other words, spin polarization is a medium to prevent the instability of low-energy states in the system. The benzenoid theory is limited as it does not give the alignment of the spins in these states. Lieb's theorem[100] can be used to extract such information and, hence, to compute the total spin of the system. This theorem does not require any periodicity of the lattice structure and is valid in all the dimensions. Interestingly, both of the counting principles described above are linked as $\eta \geq N_A - N_B$, where N_A and N_B are number of sites on the A- and B-sublattice of graphene, respectively.

As mentioned above, the Stoner criteria decide on the evolution of ferromagnetism considering a competition between the exchange and kinetic energy. Usually, the s- and p-block elements have higher kinetic energy than the exchange energy. Thus, they tend to be non-magnetic as the loss of kinetic energy dominates over the gain in exchange energy. The energy effects become considerably important when the dimension of the system is reduced. The energies are also modified by the presence of defects and other atoms in the interface or surface. As a result, intrinsically non-magnetic s- and p-block elements may become magnetic.

3. Defected graphene: morphology and magnetic properties

The presence of defects in the graphene structure modifies its chemical, mechanical and electronic properties and can lead to the formation of magnetic moments. While pristine, defect-free graphene is diamagnetic, a sizeable amount of theoretical and experimental research has shown how defects can impart magnetic ordering to graphene and how this magnetism can be predicted, generated and tuned. The seminal work at the start of the current century by Esquinazi *et al.*[101–103] on irradiated graphite has generated a vast array of publications, and comprehensive reviews on the topic have been published.[45,104–108] In order to fully understand the impact of defects on the magnetism of graphene, it is necessary to review at the same time the types of defects that can be present on a graphene sheet, with particular focus on the magnetism-generating defects.[37,109–111] These involve point defects (0D), line defects (1D) and grain boundaries (2D), whereas 3D defects, like voids, are present in graphite. The defects, moreover, can be due to single or multiple vacancies when one or more atoms are removed, can be of topological type only, thus not involving any loss or gain of atoms (for example, Thrower-Stone–Wales (TSW) defects[112,113]), or can be due to internal or external adatoms and impurities, and to adatom/vacancy interactions. By extending the study to multilayer graphene, interstitial atoms can also be included among the defects. Moreover, a unique property of extended sp^2 carbon-based materials is the ability to reconstruct defects by forming non-hexagonal units with limited or no dangling bonds, and defects can also migrate or interact with each other, as in the case of the adatom/vacancy interactions. Here, the effect on magnetism of vacancies and TSW/line defects is covered, while among the external impurities only hydrogen will be considered. The theoretical works reviewed in this section are in particular devoted to the understanding of the exact source of this magnetism and to the estimation of the formation energy and mechanism of the various defects. Experimentally, mainly electron and ion

Published on 26 March 2018. Downloaded by Univerzita Palackého v Olomouci on 2/28/2019 2:05:03 PM.

(proton) irradiation, epitaxial growth and chemical treatment have been employed to create defects, with crucial support from surface techniques like scanning tunneling microscopy (STM) and transmission electron microscopy (TEM) to detect and also to generate them.

3.1. Defects of graphene: formation and morphology

Removal of one or more carbon atoms from a graphene sheet creates a vacancy that can be a single vacancy, divacancy or, in general, multivacancy depending on the number of atoms involved (see Fig. 5). The simple expulsion of a carbon atom generates a defect with D_{3h} symmetry in which three dangling σ bonds form around the missing atom. However, a reconstruction can take place, driven by an energy-lowering Jahn–Teller distortion in which two of the carbon atoms with dangling bonds create a "soft" σ C–C bond, resulting in a defect, called V_1(5-9), with one dangling bond left and C_{2v} symmetry.[114–117] The new bond formed has a calculated length of ∼2 Å. A further distortion can take place in which the C atom with the dangling bond is displaced out-of-plane (see Fig. 6).[115,118,119] The formation energy of the graphene monovacancy has been consistently calculated at values of 7.4–7.8 eV.[114,115,118,120,121] This relatively high value accounts for the presence of a carbon atom with an unsaturated bond. Moreover, the reconstructed defect imparts strain to the graphene lattice surrounding the defect.[122] The electronic environment of the V_1(5-9) vacancy also reflects the newly formed bond and the dangling one. In particular, a localized spin density is present at the unsaturated C center (see Fig. 7).[116]

Monovacancies have been experimentally detected. Aberration corrected high resolution transmission electron microscopy (AC-HRTEM) and high angle annular dark field scanning transmission electron microscopy (HAADF-STEM) techniques in particular have been used for creation of defects by irradiation at energies above 80 keV and for their visualization (see Fig. 8).[122–127] Interestingly, both symmetric and reconstructed defects, corresponding to Fig. 8a and d, have been detected.

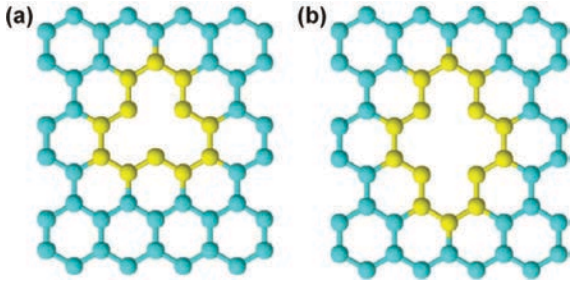


Fig. 5 Examples of (a) single vacancy and (b) double vacancy before reconstruction. Reprinted with permission from ref. 117. Copyright 2017 Elsevier B.V.

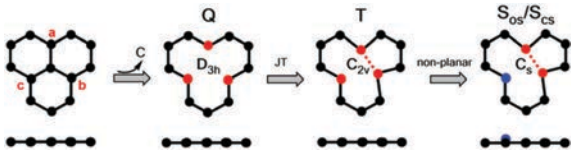


Fig. 6 Top and side views of a graphene single vacancy, with the respective point groups, type of distortion (JT: Jahn–Teller) and spin multiplicity (Q: quintet, T: triplet, S: singlet, OS: open shell, CS: closed shell). Reprinted with permission from ref. 119. Copyright 2017 American Chemical Society.

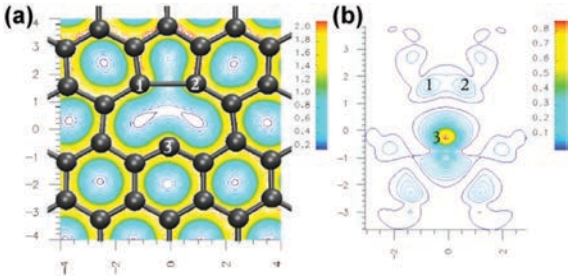


Fig. 7 C monovacancy: structure with (a) charge density (in e $Å^{-3}$) and (b) spin density (in e $Å^{-3}$). Reprinted with permission from ref. 116. Copyright 2004 American Physical Society.

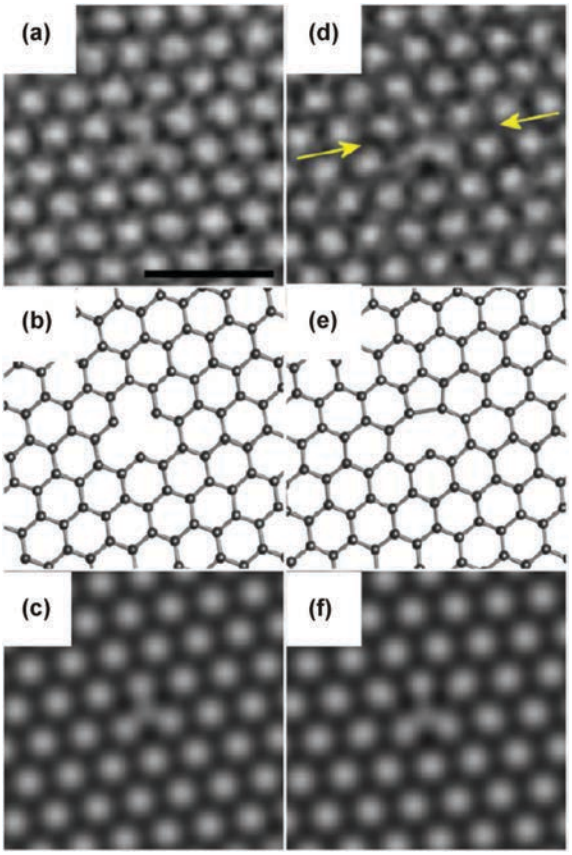


Fig. 8 AC-HRTEM images of (a) a symmetric C monovacancy and (d) after reconstruction. Panels (b and e) are the DFT calculated models and panels (c and f) the multislice TEM simulations of images in panels (a and d), respectively. Reprinted with permission from ref. 122. Copyright 2013 American Chemical Society.

This journal is © The Royal Society of Chemistry 2018

Published on 26 March 2018. Downloaded by Univerzita Palackého v Olomouci on 2/28/2019 2:05:03 PM.

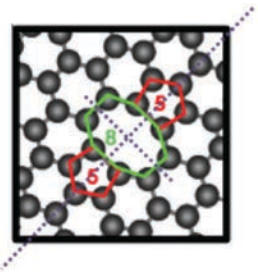


Fig. 9 Depiction of a V_2(5-8-5) divacancy defect. Reprinted with permission from ref. 132. Copyright 2012 American Physical Society.

Single vacancies can diffuse in the graphene lattice. The calculated barrier for this diffusion depends on the model used to simulate the migration, and is between 0.9 and 1.7 eV.[114,128] Experimentally, the diffusion of single vacancies does not take place at room temperature within the timescale of the measurements.[123] The migration and coalescence of vacancies can however be influenced by the presence of multiple vacancies, which induce bond strain extending into the lattice portion where the vacancies are present.[129]

When two connected carbon atoms are simultaneously displaced, or when two single vacancy defects coalesce, a divacancy forms. Also in this case, a reconstruction can take place. By formation of the long σ bonds analogous to that of the single vacancy, a corresponding V_2(5-8-5) structure appears (see Fig. 9).[130–132] However, this structure can convert into one with a lower energy, V_2(555-777). Other possible reconstructions are V_2(5555-6-7777), which lies at an intermediate energy between the other two, V_2(585) with dangling bonds and V_2(555-777) with a tilted carbon dimer. All these structures have been characterized by electron microscopy and confirmed by simulations (see Fig. 10).[133,134] The formation energy of divacancies is of the same order of magnitude as that of single vacancies (~8 eV), accounting for ~4 eV per atom.[114,121,135] The much lower energy per atom needed with respect to monovacancies is due to the absence of dangling bonds left after the structure reconstruction. On the other hand, the migration barrier is much higher than that of single vacancies, being estimated to be ~7 eV,[114] thus allowing the accessible visualization of the defect by electron microscopy.

Studies of the influence of strain on graphene with vacancies have provided an insight into the mechanical and electronic properties of the material. For vacancy content up to 0.2%, the elastic modulus of graphene sheets increases by nearly 100%, and then decreases with higher defect density, while the fracture strength instead decreases in the presence of defects (see Fig. 11 for a STM image of defected graphite used for investigation of the influence of strain).[136,137] Also, the energy required for vacancy formation in graphene can be reduced by ~37% by the application of biaxial tensile strain.[138] A tensile strain lower than ~50% is needed to open a band gap in defected graphene when compared to pristine graphene.[139]

The reactivity of graphene single vacancies is determined by the presence of the dangling bond, which can be saturated by

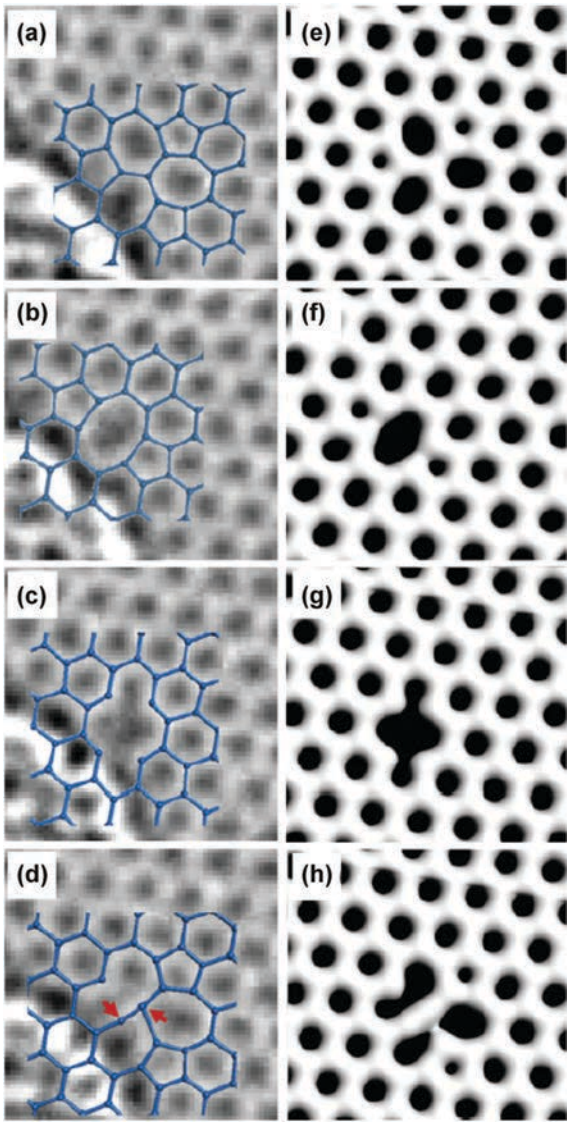


Fig. 10 (a–d) Structures of different double vacancy defect reconstructions ((a): V_2(555-777); (b): V_2(585); (c): V_2(585) with dangling bonds; (d): V_2(555-777) with a tilted carbon dimer, shown by the red arrows). (e–h) Corresponding charge density plots obtained from *ab initio* calculations. Reprinted with permission from ref. 134. Copyright 2011 American Physical Society.

adatoms, thus further changing the properties and structure of the defect.[140,141] In this section, only the influence of H as a chemisorbed adatom, isolated or connected to a vacancy, will be discussed, for cases in which single or limited H atoms are present on graphene structures thus constituting a defect rather than a functionalization. Chemisorption and physisorption of H atoms on graphene have both been studied, mainly from the theoretical point of view, but experimental works have also been published.[142–149] Various models have been proposed, including pyrene, coronene and a 4 × 4 supercell, and coronene has been

Published on 26 March 2018. Downloaded by Univerzita Palackého v Olomouci on 2/28/2019 2:05:03 PM.

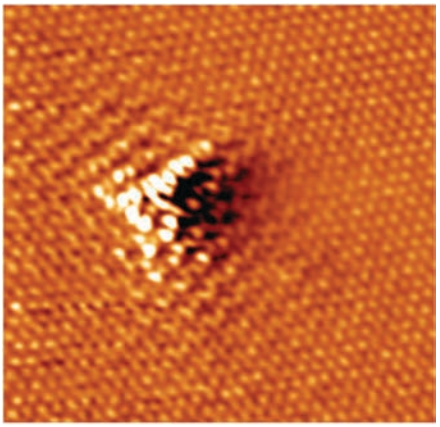


Fig. 11 STM image of a defect on graphite created by Ar^+ irradiation at 140 eV (image taken in air at room temperature). Reprinted with permission from ref. 136. Copyright 2014 Macmillan Publishers Limited.

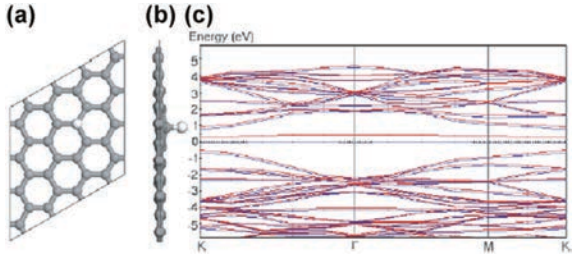


Fig. 13 (a) Top view, (b) side view, and (c) band structure for an H atom adsorbed on a graphene sheet (32-atom model). Reprinted with permission from ref. 142. Copyright 2004 American Physical Society.

suggested as the one with the minimum size suitable for calculations of H chemisorption on graphene (see Fig. 12).[146]

The C–H bond formed, in which the C atom hybridizes to sp^3 and its p_z orbital is removed from the general graphene π-system,[45] has been calculated as being of length 1.11–1.13 Å.[142,146] Studies performed at the PB3-D3/cc-pVZD level of theory indicate that the energy barrier for H chemisorption is mainly attributed to the structural work connected to the defect reconstruction. The presence of the bond creates a band gap of 1.25 eV, containing two non-dispersing states (see Fig. 13). This effect has been attributed to the influence of the H^+ ionic core.[142]

When a pair of hydrogen atoms is chemisorbed on graphene, four different outcomes are possible, depending on whether the two H atoms are on the same or opposite side of the graphene sheet and whether they are on C atoms which are part of the same or different sublattices. Calculations have suggested that the formation energy of the pairs in all four cases is dependent on the distance between the C atoms carrying the H atoms, resulting in lower energies for distances up to 5 Å and then increasing at larger distances.[144] The presence of chemisorbed H atoms can affect the mechanical properties of graphene, leading to deterioration of the material. Atomistic simulations have shown that the fracture strain and fracture stress of hydrogenated graphene decrease substantially in both armchair and zigzag directions when compared to pristine graphene.[148]

TSW defects in graphene are generated by the 90° rotation of a C–C bond. Upon this rotation, two C–C bonds are formally broken and two new bonds are formed, with the result that four hexagons turn into two pentagons and two heptagons, a so called SW(55-77) structure (see Fig. 14).[150] The opposite curvature of pentagons and heptagons results in the formal conservation of

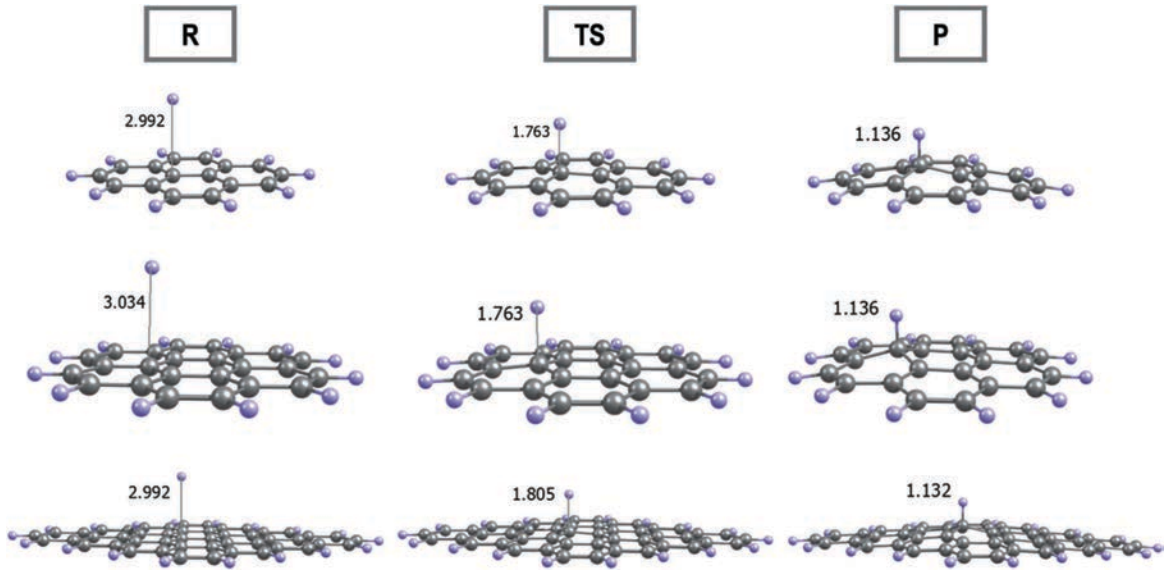


Fig. 12 C–H distances (in Å) in the physisorbed state (R), transition state (TS) and chemisorbed state (P) for the three different models, *i.e.*, pyrene (top), coronene (center) and 4 × 4 supercell (bottom). Reprinted with permission from ref. 146. Copyright 2014 AIP Publishing LLC.

 This journal is © The Royal Society of Chemistry 2018

Published on 26 March 2018. Downloaded by Univerzita Palackého v Olomouci on 2/28/2019 2:05:03 PM.

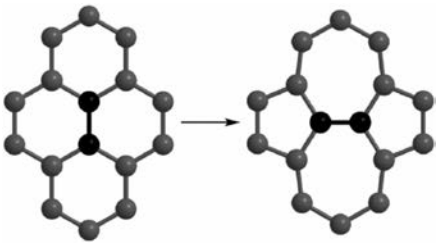


Fig. 14 TSW transformation by C–C bond rotation (in black) with the formation of a SW(55-77) defect. Reprinted with permission from ref. 150. Copyright 2015 Pleiades Publishing, Ltd.

the planar structure; it is worth reminding that the presence instead of 12 pentagons along with hexagons but without heptagons generates a spherical allotrope as in the case of fullerene.[151,152] Calculations have pointed out that the most stable geometry of a graphene single layer with a SW(55-77) defect has an out-of-plane sinusoidal shape, with the sine-like structure having the lowest energy (see Fig. 15).[153–155] As already mentioned, the TSW defect leaves the total number of atoms unchanged and also the hybridization of the components of the system is not mutated, each carbon atom being bonded to three neighboring atoms. However, the bond lengths in the SW(55-77) system diverge substantially from the periodic C–C bond of 1.46 Å of pristine graphene. Calculated values obtained from DFT methods indicate bond lengths down to 1.28 Å for the common heptagon–heptagon bond[140] within the defect area.[110]

The calculated formation energy associated with flat TSW defects reported in several works is of ~5 eV, with small variations depending on the type of codes used for the calculations,[140,153,155,156] whereas structures presenting sine-like distortions have in average slightly lower calculated formation energies.[135,150,156] The kinetic barrier to overcome for the simultaneous 90° rotation of the two C atoms producing the TSW defect is of 10 eV, whereas the opposite rearrangement with recreation of the hexagonal structure is 5 eV, making the TSW defect, once formed, rather stable.[140] AC-HRTEM at <100 keV with different electron fluxes has been employed to successfully visualize TSW defects and their rapid healing.[157,158]

TSW defects are reported to affect the mechanical,[159–161] chemical[142] and electronic[107,162–165] properties of graphene. TSW defects from defect reconstruction are deemed responsible for enhanced chemical reactivity due to the locally changed π-electron density,[167] whereas the bond rotation responsible for the TSW defect has the effect of creating a band with energy ~0.5 eV higher than E_F, due to the displaced p_z orbitals of the atoms of the defect site.[162]

The reconstruction of multiple defects in a graphene lattice can lead to the formation of line defects,[166–170] which can be seen as the 1D analogue of the 2D grain boundary defects in graphite.[171,172] However, it must be noted that "grain boundary" is often used as a synonym of "line defect" in graphene (see Fig. 16). Line defects can consist of the periodic repetition of pentagonal–heptagonal or pentagonal–optagonal motifs as well as disordered distributions of different polygons. The planar nature of the graphene sheet allows for rearrangements not present in their 3D counterparts, resulting in the formation of peaks in "3D landscapes" upon structural relaxation and consequent reduction of the defect energy. The height of the peaks has been calculated as being close to the distance between the defects (see Fig. 17).[173,174] Moreover, the relative stability of defects created by pairs of 5-7 defects against extended Haeckelite-like structures has also been assessed,[166] whereas simulations performed using GGA for DFT with spin polarization have shown the formation of pentagonal–octagonal-based line defects on graphene sheets upon inclusion of C and N adatoms.[175]

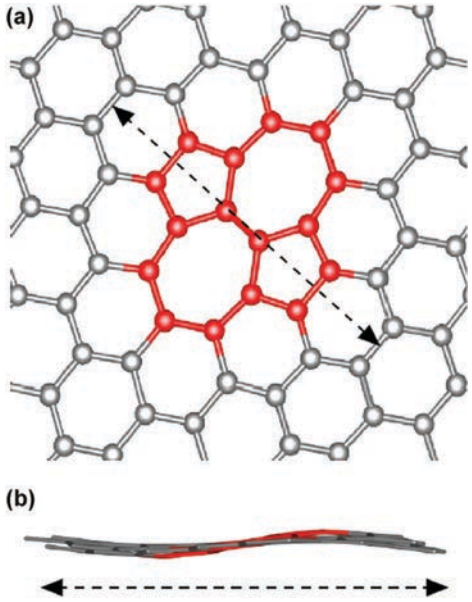


Fig. 15 (a) Top and (b) side views of a SW(55-77) defect, in which the sinusoidal distortion is shown. Reprinted with permission from ref. 154. Copyright 2014 American Physical Society.

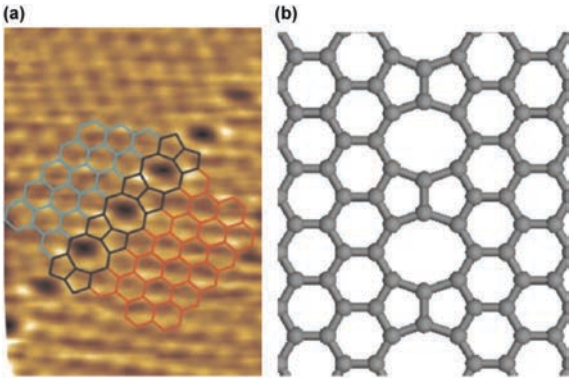


Fig. 16 (a) STM image of a line defect in graphene and (b) schematic representation of the defect. Reprinted with permission from ref. 170. Copyright 2014 Elsevier B.V.

Published on 26 March 2018. Downloaded by Univerzita Palackého v Olomouci on 2/28/2019 2:05:03 PM.

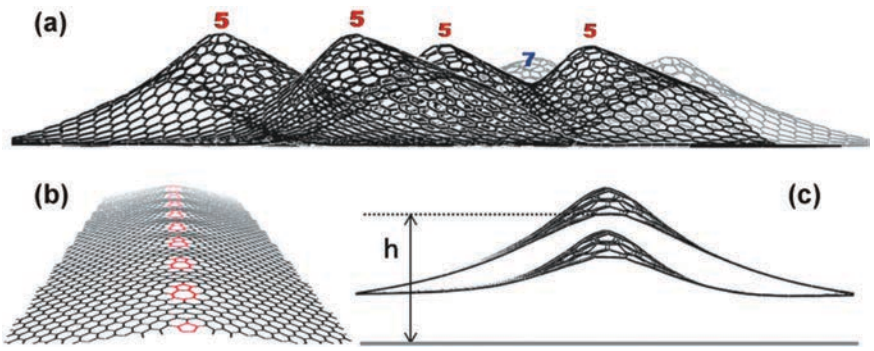


Fig. 17 (a) Calculated peak formation in the presence of scattered pentagonal (5) and heptagonal (7) defects (full relaxation mode). (b) Ridge-like deformation from regular pentagonal–heptagonal defect distribution. (c) Computed flattening effect generated by the van der Waals attraction to the substrate. Reprinted with permission from ref. 173. Copyright 2010 American Chemical Society.

STM has been successfully employed to characterize line defects and the design of graphene sheets with specific line defects has been reported.[167,176–178] In particular, deposition of graphene on a Ni(111) surface results in the formation of various line defects corresponding to the different orientations of graphene on the metallic surface, and the material produced in this way can be transferred to other substrates upon dissolution of the Ni layer.[167] Migration of grain boundary defects in graphene has also been observed atom-by-atom using AC-HRTEM.[179] The migration takes place when a significant curvature of the boundary is present.

The presence of line defects and grain boundaries influences the mechanical properties of the material. Graphene sheets can be strengthened or weakened by the presence of line defects, depending on their density and arrangement (see Fig. 18). According to molecular dynamics (MD) and DFT calculations, for both zigzag- and armchair-oriented graphene layers the strength of the sheet increases with the angle of the grain boundary, because the strain induced in the structure containing the line defect decreases with the increase of such an angle. However, if the distribution of the defects is not regular, the opposite behavior can be observed, in which the grain boundary induces weakening of the structure.[180,181]

Grain boundaries on graphene also affects the electronic properties of the material. Computational studies combined with STM and scanning tunneling spectroscopy (STS) on graphite have pointed out the main superlattice periodicities of the line defects and have identified grain-boundary structures of low formation energy.[165,182] Moreover, STS measurements of structures with specific superlattice periodicity have shown the presence of two localized states at positions of −0.3 and +0.4 V, respectively. These strong states, which were not detected on pristine graphite, extend to a distance up to 4 nm.[182]

3.2. Magnetism of defected graphene

Defect-induced magnetism in graphene is well documented, with the experimental roots around the turn of the millennium

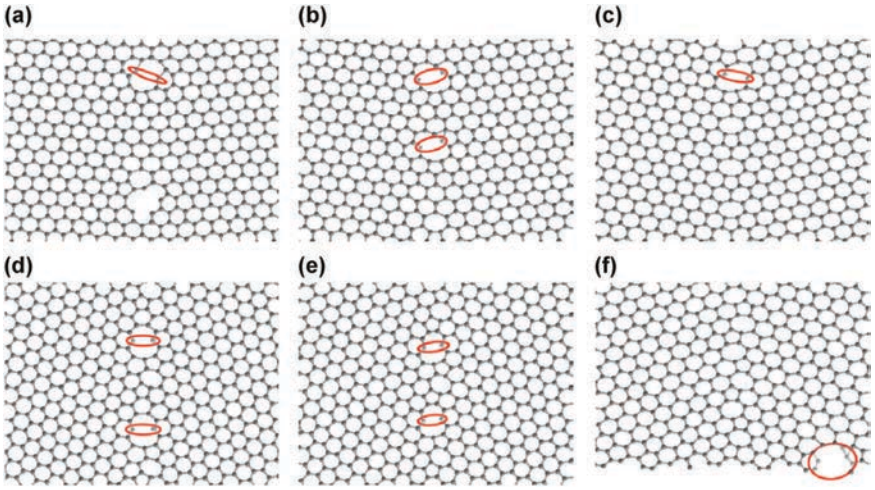


Fig. 18 Starting phase of structural failure in (a–c) zigzag-oriented and (d–f) armchair-oriented graphene upon strain applied perpendicularly to the grain boundary defect. Reprinted with permission from ref. 181. Copyright 2010 American Association for the Advancement of Science.

 This journal is © The Royal Society of Chemistry 2018

Published on 26 March 2018. Downloaded by Univerzita Palackého v Olomouci on 2/28/2019 2:05:03 PM.

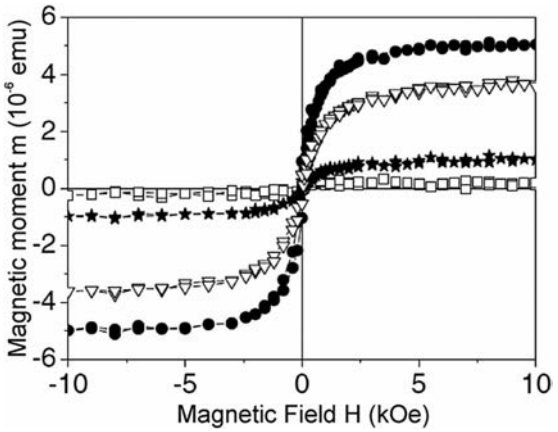


Fig. 19 Magnetic moment of graphite samples (sample holder subtracted) after different irradiation conditions (□ = first irradiation stage, ★ = second irradiation stage, ● = third irradiation stage, and ▽ = fourth irradiation stage). Reprinted with permission from ref. 103. Copyright 2003 American Physical Society.

when the studies on irradiated graphite by Esquinazi *et al.*[101–103] appeared alongside analogous works focused on other carbon allotropes.[25,183,184] The proton irradiation of pyrolytic graphite at high energy and different doses in these early studies showed triggering of magnetic ordering (*i.e.*, of FM and AFM nature). Moreover, this magnetic ordering appeared to be stable at room temperature.[103] Measurements of the magnetic moment with the applied field parallel to the graphene sheets produced different magnetic responses depending on the intensity and dose of the irradiation (see Fig. 19). A similar result was obtained with the magnetic field oriented perpendicularly to the graphene plane. Soft X-ray dichroism technique on irradiated graphitic material suggested that the observed ferromagnetism originated only from the π-electrons.[185] A substantial part of these early works was dedicated to the assessment of the influence on magnetism by possible metallic (Fe-based in particular) impurities. While this factor dictated in some case the retraction of the study,[186,187] it became soon clear that the observed magnetic ordering was in most instances an intrinsic property of the material and not due to external impurities, and consequently several works focusing on the explanation of this behavior were published.

Vacancies and H chemisorption have been in particular investigated as the source of magnetism in defected graphene. As pointed out in several theoretical studies, magnetic moments in the presence of vacancies are due to the formation of localized states at E_F because of the lattice distortions generated by the defect and consequent electron–electron interactions.[45,47,89,116,125,188,189] In the case of single vacancies, the single dangling bond formed upon reconstruction of the defect contributes to the creation of an intrinsic magnetic moment (see Fig. 20).[45,47] The quantification of this magnetic moment covers values between 1 and 2 μ_B depending on the type of calculations performed and the evaluation of the effect of surrounding defects.[47,119,138,190–194] In particular, different results between the calculations based

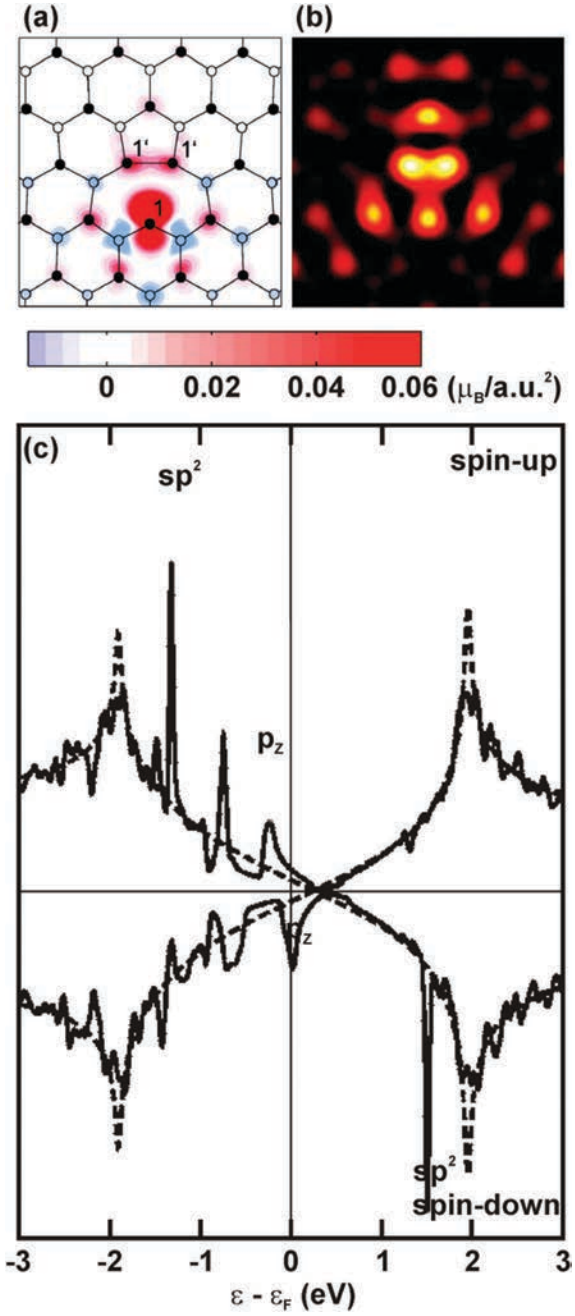


Fig. 20 Graphene single vacancy: (a) theoretical spin-density distribution (C atoms of the two different sublattices are represented by empty and filled circles, respectively); (b) corresponding simulated STM image; (c) density of states for n = 4. Reprinted with permission from ref. 47. Copyright 2007 American Physical Society.

on periodic LDA or GGA functionals and those in which hybrid functional methods like B3LYP-D* were used have been reported.[119] The average magnetic moment of 1.5 μ_B for a single vacancy is the result of the sum of the σ component related to

Published on 26 March 2018. Downloaded by Univerzita Palackého v Olomouci on 2/28/2019 2:05:03 PM.

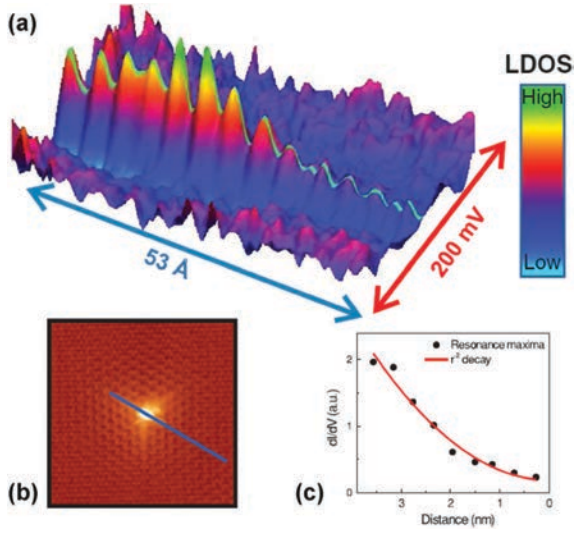


Fig. 21 (a) LDOS as a function of voltage and position (blue line in image (b)) of a graphite vacancy, (b) STM image of the defect, and (c) r^{-2} decay of the intensity of the resonance. Reprinted with permission from ref. 125. Copyright 2010 American Physical Society.

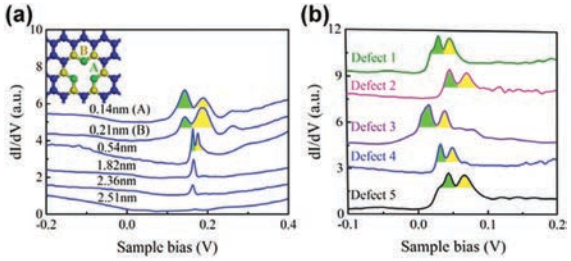


Fig. 22 STS spectra of graphene with monovacancy: (a) appearance of a spin-split resonance peak at decreasing distances from the vacancy. The two top spectra are measured in correspondence to the A and B atoms shown in the inset, respectively; (b) spin-split resonance peaks of five different vacancies. Reprinted with permission from ref. 196. Copyright 2016 American Physical Society.

the newly formed C–C bond upon reconstruction, of value 1 μ_B, and the π component ascribed to the dangling unsaturated bond. The formula $(1 + x)\ \mu_B$ for the total magnetic moment of the defect has been proposed, where the x value is subjected to the variations ascribed to the chosen model. The evaluation of the competition between the symmetric planar configuration of the single vacancy and the nonplanar reconstruction is also responsible for the spread values reported, with metastable states corresponding to local energy minima also taken into consideration.[194,195]

STM measurements supported by calculations have proved to be a powerful instrument for the detection of magnetism in graphene with vacancies. Through this technique, it has been shown in correspondence to the Fermi energy at the vacancy sites a sharp electronic resonance, thus confirming the theoretical studies (see Fig. 21). Moreover, differential conductance measurements have indicated that the magnetic moment generated by defects in a surface graphitic layer is influenced by the presence of the layers underneath.[125]

Studies on graphene with monovacancies synthesized on metal foils, for instance on Rh or Pt, have supplied important information about the magnetism of the defected 2D material. In particular, the contribution of the π electrons to the local magnetic moment generated by a single carbon vacancy in graphene, connected to the presence of two spin-split density-of-states peaks located in the proximity of the Dirac point, has been assessed by STM and STS.[196] Spectra collected at decreasing distance from a monovacancy on graphene on Rh foil reveal the appearance of a resonance peak, that splits into two states for distances from the vacancy <0.6 nm, in agreement with theoretical studies (see Fig. 22).[47] Remarkably, the detected spin-split states are still present even at energies distant from E_F. According to first-principles calculations, n- and p-doped graphene should also present the spin-split states.

In order to find ways to tune the magnetism of defected graphene, the application of various types of strain to graphene with monovacancies has been investigated. In the case of shear distortion, a DFT study has shown that reversible electronic transition between two magnetic states is achieved when a deformation of a shear angle of 1 degree is applied. The magnetic moment undergoes a variation of 0.8–1.2 μ_B depending on the size of the calculated supercell and remains nearly constant at deformations >1 degree. This behavior is attributed to the breakage of the local symmetry of the monovacancy induced by the shear distortion, influencing both the σ and π bands of the states of the vacancy (see Fig. 23).[197] On the other hand, strain applied in the form of compression up to 2% to graphene with a single vacancy can result in the weakening and eventually disappearance of magnetism together with the formation of ripples, thus showing a correspondence between local curvature and magnetism. With the application of compressive strain of 3% and above, the rippling leads to a reconstruction of the defect, with formation of two pairs of deformed pentagons and hexagons and no magnetic behavior (see Fig. 24).[198]

The number and location of the vacancies also play a major role in the establishment of a magnetic moment. Due to the bipartite structure of the graphene lattice, the presence of vacancies solely on one sublattice leads to FM coupling, whereas a defect distribution on both sublattices results in AFM coupling (see Fig. 25).[47] Models have therefore been proposed in order to predict and tune the magnetic moment in systems with multi-vacancies through manipulation of the position of the defects and n- and p-doping.[199–201]

For experimental evidence such as the magnetism of irradiated graphite, the simple vacancies alone are not the main source for this property due to their likely annihilation taking place *via* the interaction with adatoms and interstitials.[47,116] A source of defect-related magnetism is the presence of H atoms chemisorbed on the graphene lattice. As mentioned before, the bonding with H by a graphene C atom without vacancy removes the p_z orbital of that atom from the π-system of the graphene lattice, thus creating the same effect of a C vacancy but without

 This journal is © The Royal Society of Chemistry 2018

Published on 26 March 2018. Downloaded by Univerzita Palackého v Olomouci on 2/28/2019 2:05:03 PM.

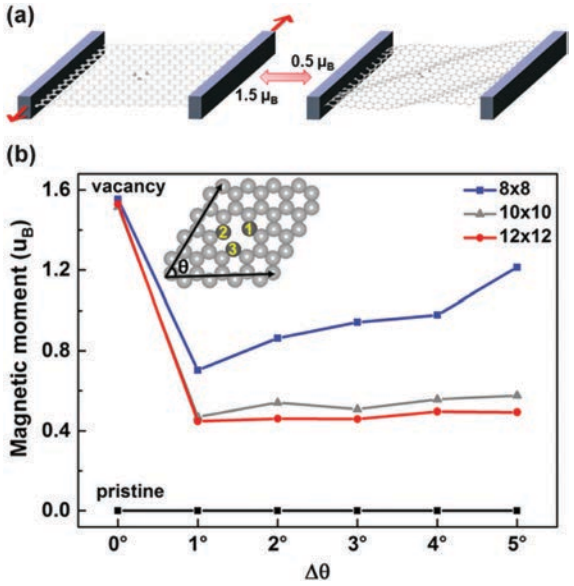


Fig. 23 (a) Representation of the reversible change of magnetism of a graphene sheet with single vacancy upon shear deformation. (b) Variation in magnetic moment of graphene supercells of different sizes under shear deformation of 0–5° compared to pristine graphene (initial angle = 60°, see inset). Reprinted with permission from ref. 197. Copyright 2017 Macmillan Publishers Limited.

the presence of unsaturated bonds. The H chemisorption brings the C atom bonded to H slightly out of plane and generates a small displacement of the surrounding portion of lattice.[47,143] STM experiments (see Fig. 26) have shown that the adsorption of a single H atom contributes to the formation of a magnetic moment, and that interaction due to direct exchange is possible. In agreement with the theory and with works dealing with monovacancies,[47,196] two spin-split states have been detected, but in the case of H chemisorption they are visible only in the vicinity of E_F and they do not survive n- or p-doping.[143]

Theoretical and experimental studies have pointed out that if two H atoms adsorb in the same sublattice then FM coupling takes place, whereas the absorption in two different sublattices leads to a non-magnetic interaction, with the non-magnetic configuration being the one of lower energy.[144] By manipulating

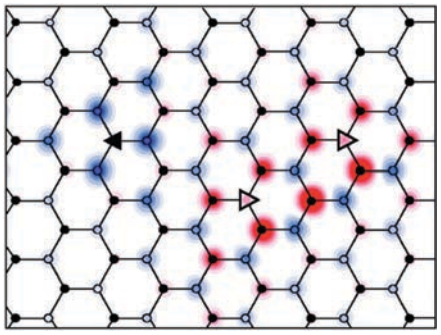


Fig. 25 Theoretical spin-density distribution in graphene with two defects on the A-sublattice (empty triangles) and one on the B-sublattice (filled triangle). Reprinted with permission from ref. 47. Copyright 2007 American Physical Society.

the number of H atoms chemisorbed in the two different sublattices, the corresponding variations in the net magnetic moment have been detected.[143] In the case of graphite, H adsorbed *via* irradiation at low fluence has been evaluated together with the H already present in the sample. It has been reported that the magnetic moments formed undergo FM coupling with Curie temperatures above 300 K.[202] The triggering of ferromagnetism in multilayer materials has been attributed to the stacking order of the layers upon irradiation. This can generate a mechanism by which the graphene sublattices become inequivalent depending on the position of chemisorbed H in the underlying layer.[45,89]

Chemisorbed hydrogen can be present as a single type of defect or associated with vacancies, in which case it is bonded to the carbon atom that carries the dangling bond upon reconstruction. The influence of adsorbed hydrogens in association with vacancy defects can impart half-metallic properties to graphene. This half-metallicity depends on the number of C atoms intercalated between two H atoms, appearing only when this number is odd. The magnetism in these systems is mainly regulated by the p_z orbitals of the C atoms surrounding the vacancy.[203]

Among other experimental techniques, muon spectroscopy has also been employed to study the origin of magnetism in graphene.[204] Muon spectroscopy is a very powerful spectroscopic technique as muons are very sensitive probes of local magnetic

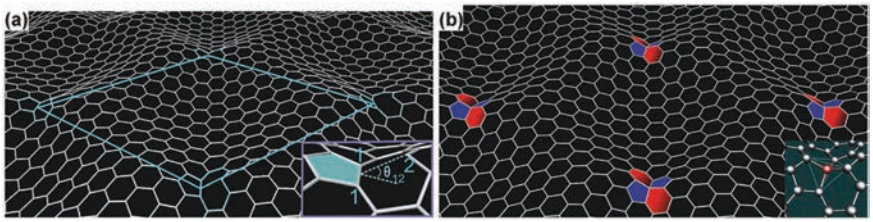


Fig. 24 (a) Rippling of a graphene sheet with vacancies (with highlighted 10 × 10 supercell) upon compression of 1.2%. The inset shows the resulting geometry of the vacancies. (b) Vacancy reconstruction upon an isotropic compression just below 3%. Reprinted with permission from ref. 198. Copyright 2012 American Chemical Society.

Published on 26 March 2018. Downloaded by Univerzita Palackého v Olomouci on 2/28/2019 2:05:03 PM.

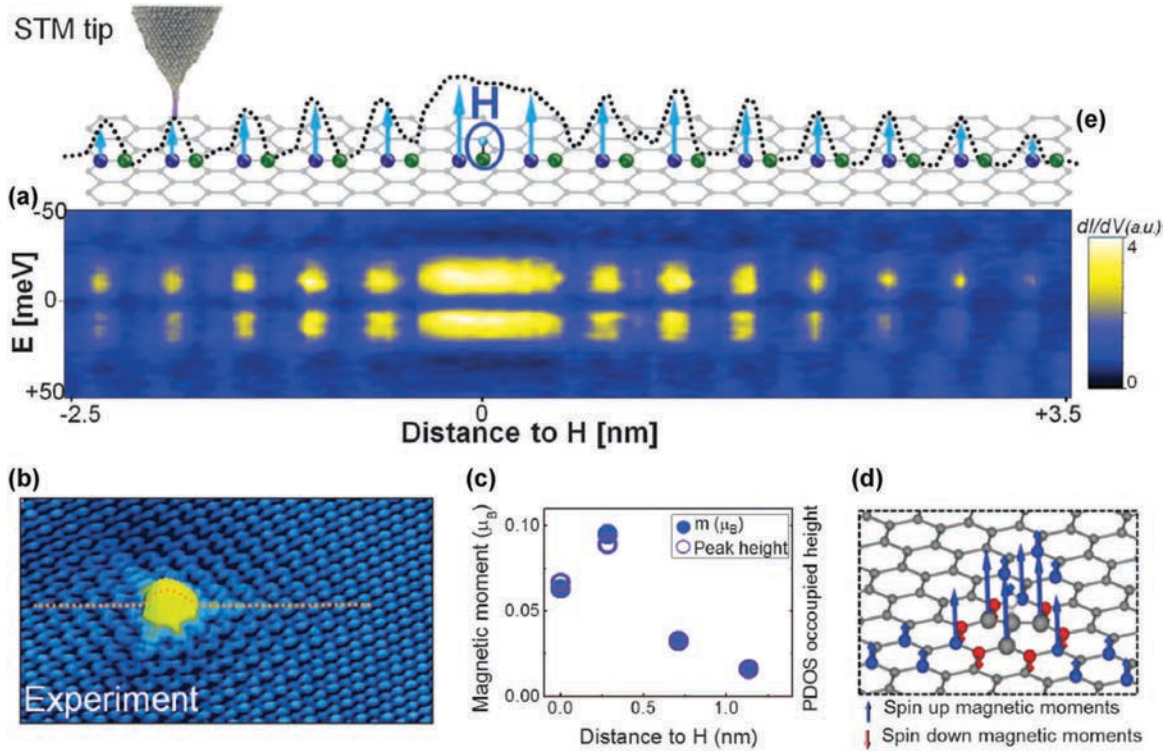


Fig. 26 Chemisorbed H on graphene: (a) conductance map obtained by the STM technique; (b) STM topography; (c) comparison between the values of the local magnetic moment computed by DFT calculations and the heights of the occupied projected density-of-states peak; (d) magnetic moments (calculated) generated by the chemisorbed hydrogen; (e) schematic representation of the structure of graphene along the dashed line shown in panel (b). The green (purple) balls denote the positions of carbon atoms that are part of the same (opposite) sublattice with regard to the site of H chemisorption. The dotted line then shows the profile of the height corresponding to the measured occupied peak; the arrows denote the relative contribution to the magnetic moment of each carbon atoms. The STM measurements were performed at a temperature of 5 K. Reprinted with permission from ref. 143. Copyright 2016 American Association for the Advancement of Science.

fields and can interact with hydrogen. In particular, the muons which are, after being thermalized, implanted into graphene can capture an electron to form the atom ''muonium'' (Mu). In defective graphene, the muon precession was found to originate from the nuclear dipolar interaction with a single proton, located at a distance of 1.7 Å from the muon. As the amplitude correlates with the density of defects in graphene, increasing drastically after hydrogenation of graphene samples, formation of a CH-Mu group is suggested to occur, which is stable up to 1200 K. However, these results exclude the presence of magnetic ordering evolving in the chemically derived defective graphene systems. Nevertheless, as strongly highlighted in a muon spectroscopic study, these conclusions do not automatically rule out the appearance of magnetism in other experimentally proven cases such as proton-irradiated graphite, synthesized small graphene fragments or graphene nanoribbons.[204]

From the point of view of the magnetic properties, the TSW defects do not create sublattice imbalance in the graphene structure since they do not involve loss of atoms, thus according to Lieb's theorem,[100] $S = 1/2(N_A - N_B) = 0$, and no magnetization is expected.[89] However, the TSW defects can perturb the magnetic state of the lattice *via* interaction with other defects such as adsorbed hydrogen atoms,[205] and they can be a source of magnetism in size-confined systems.[206]

The presence of grain boundaries has been proposed as a reason for the magnetism of defective highly oriented pyrolytic graphite (HOPG).[46] At the 2D array of point defects due to the grain boundary, localized electron states take place together with self-doping, with establishment of ferromagnetism. The magnetic moment associated with the defect has been evaluated to be 0.2–1.5 μ_B, for distances between defects ranging from 0.5 to 4 nm. Similar considerations have been drawn for single graphene sheets. In the presence of line defects generated by repeating V_2(5-8-5) defects, the presence of magnetic ordering and self-doping has been detected using first-principles calculations.[207] The evolution of the electronic structure as a function of the distance between the defects was studied, and the establishment of magnetic ordering and n-doping on the graphene sheets with reduction of the distance was found. The formation energies and spin distribution of systems with different number of zig-zag chains (N) between the two central carbon atoms of the pentagonal–octagonal periodic defects (C_2) have been evaluated, with detection of three stable magnetic configurations (see Fig. 27).

 This journal is © The Royal Society of Chemistry 2018

Published on 26 March 2018. Downloaded by Univerzita Palackého v Olomouci on 2/28/2019 2:05:03 PM.

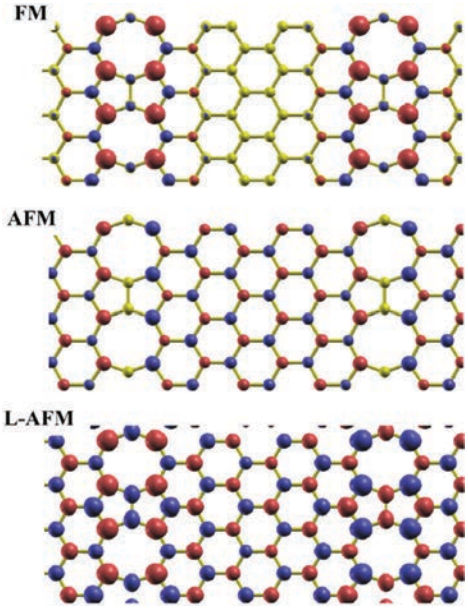


Fig. 27 Spin-density distribution for N = 6 showing FM, AFM and FM ordering at the line defect but AFM ordering in the surrounding line defect (L-AFM) arrangements (red color: isosurfaces of spin-up density; blue color: isosurfaces of spin-down density). Reprinted with permission from ref. 207. Copyright 2015 American Physical Society.

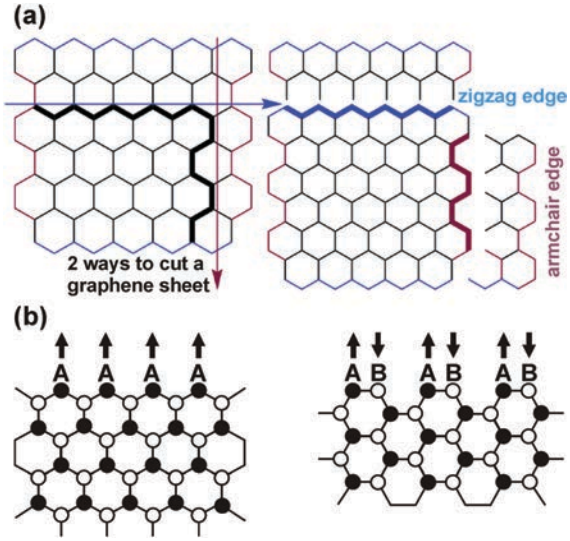


Fig. 28 (a) Two ways of cutting a graphene sheet with a formation of zigzag or armchair edged graphene. (b) Zigzag and armchair edges with the A- and B-sublattice indicated and an arrow denoting the pseudospins. Panel (b) reprinted with permission from ref. 212. Copyright 2013 Wiley-VCH Verlag GmbH & Co. KGaA.

Ab initio calculations based on CVD-grown graphene have shown how small C-rings, made of three or four units, can initially form at the boundary region of two graphene fragments.[208] The fusion of these small rings with larger ones leads to the formation of periodic defects in which high localization of electrons takes place, with establishment of net magnetization. The bipartite structure of the graphene lattice collapses at the line defect, thus the magnetization observed at the boundary cannot be attributed to lattice inequality as seen, in agreement with Lieb's theorem, in the case of other types of defects. Moreover, selected application of strain along extended line defects can tune the magnetism induced by the defects. In particular, calculations have shown that tensile strain applied along the zigzag direction of the defect can enhance the magnetism and its stability, up to a certain critical value that however does not correspond to structural breakage. On the other hand, tensile strain applied along the armchair direction induces an immediate reduction of magnetism, up to breakage of the structure.[209]

4. The role of confinement and edges on emergence of magnetism in graphene

Confining graphite spatially is widely considered as a pioneering strategy to imprint magnetic features into all-carbon materials. It is an approach proposed before the first isolation of graphene; the confined species of carbon were termed nanographenes or nanographites (*i.e.*, stacked nanographene sheets) and their magnetic properties were covered in the review papers by Enoki and Takai,[210] Enoki *et al.*,[211] and Enoki.[212] Currently, three spatially confined carbon forms derived from graphene are recognized: (i) graphene nanoribbons, (ii) graphene nanoflakes, and (iii) graphene quantum dots.

The theoretical calculations predict that the magnetism of finite size graphite/graphene strongly depends on its shape. If a sheet of graphene is cut into two pieces, two types of edges can be formed, *i.e.*, a zigzag or an armchair edge (see Fig. 28), thereby modifying its electronic band structure. Graphene with zigzag and armchair edges mimics the structure of *trans*- and *cis*-polyacetylenes, respectively. The resulting edges can be terminated by hydrogen or any foreign atom to create edges without σ-dangling bonds, *i.e.*, saturating the edge structure and promoting its stabilization. As graphene can be represented by the two sublattices in its unit cell, the zigzag edge involves sites only from one sublattice while both sublattices are paired along the armchair edge. Following the theoretical predictions, zigzag edges are manifested as non-bonding π-electron edge states with an energy level appearing at the contact point of the π- and π*-bands; the presence of such states was documented by several experimental studies.[56,211,213–217] These states are absent in the case of the armchair edges. The edge states along the zigzag edges emerge due to the broken symmetry of the pseudospins. The unpaired electrons (with S = 1/2) in the non-bonding π-orbital of the zigzag edge are localized, thereby forming a strongly spin-polarized region. As a result, the finite-sized graphene becomes magnetic.

Published on 26 March 2018. Downloaded by Univerzita Palackého v Olomouci on 2/28/2019 2:05:03 PM.

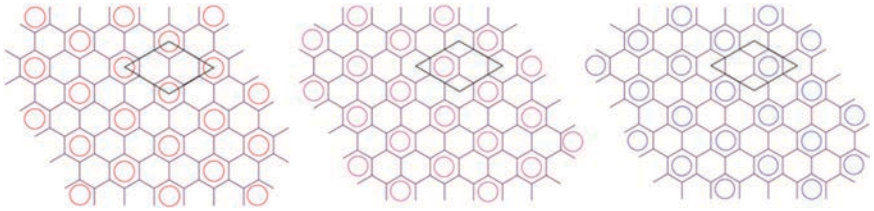


Fig. 29 Triply degenerate Clar's representations of graphene. The unit cell of the honeycomb lattice is manifested by a parallelogram that has two independent sublattice sites.

In this context, Clar's aromatic sextet rule[218] can be considered in order to describe the electronic stability of aromatic molecules. Its concept can be extended to graphene in the limit when the size of the graphene systems becomes infinite. The sextet rule states that a molecule that has the maximum number of sextets is more stable. Thus, every three hexagons in the honeycomb lattice of graphene would give rise to one sextet forming a triply degenerate superlattice as shown in Fig. 29. As the sextets are placed only on 1/3 of the hexagon rings, it implies that graphene is less stable, which leads to an electronic activity of the graphene sheet. The electronic properties of graphene sheets then get modified based on the type of edges they carry after being cut into pieces.[212] Graphene with the zigzag edges (represented as, *e.g.*, triangular and linear molecules with zigzag edges, see Fig. 30) is described by a fewer number of sextets while for graphene with armchair edges (represented as armchair molecules, see Fig. 30), the sextet rule gives a larger number of sextets. Hence, graphene with armchair edges is energetically favored in comparison to that having zigzag edges featuring unpaired electrons of π-origin. In the case of zigzag-edged graphene (see Fig. 30), the unpaired electrons exist in the non-bonding π-orbitals. Following Hund's rule, it can be readily shown that the triangular molecules that have 3, 6, and 10 hexagon rings behave in an FM manner due to the presence of 1, 2, and 3 unpaired electrons, respectively. In contrast, linear molecules (see Fig. 30) show an AFM state, as the interaction between the spins is of an AFM character. The final ground magnetic state of the system is then determined by the dominance of the nature of the interaction among these edge states (*i.e.*, non-bonding states).[212] The theoretical and experimental results on various nanographenes' sizes and shapes confirm that magnetism in graphene emerges largely due to the π-electrons forming strongly spin-polarized edge states. In addition to the edge states, the defects of the σ-electron nature in graphene can give rise to localized spins. For instance, non-bonding carbon atoms can be created by virtue of any chemical attack or ion bombardment on the π-electron conjugated network of the graphene sheet. This can also result in magnetic graphene due to the σ-dangling bond with a localized spin ($S = 1/2$). Thus, a variety of magnetic states can be expected due to the simultaneous presence of defects and edge states. In the past few years, there have been more efforts devoted to understanding the basic difference between the edge states and the σ-dangling bonds that have helped in comprehending the origin of magnetism in carbon nanostructures.[89,219–223]

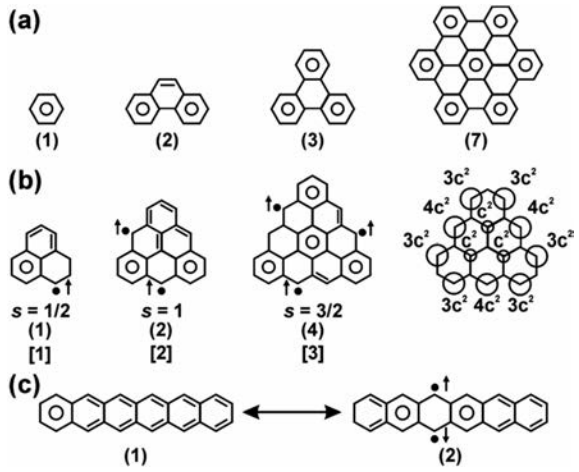


Fig. 30 Clar's representation for (a) armchair-edged molecules, (b) zigzag-edged triangular molecules, and (c) zigzag-edged linear molecules. The right structure of panel (b) displays the spatial distribution of the local density of states in a zigzag-edged triangular molecule with six hexagons. The numbers in () and [] represent the number of sextets and unpaired electrons, respectively. The spin state of the particular structure is given by *s*. Reprinted with permission from ref. 212. Copyright 2013 Wiley-VCH Verlag GmbH & Co. KGaA.

As already mentioned in Sections 2 and 3, Lieb's theorem[100] can be helpful in computing the spin state of graphene, *i.e.*, $S = 1/2(N_A - N_B)$, where N_A and N_B are the number of spins in the A- and B-sublattice. It can then be readily confirmed that the armchair-edged nanographene is non-magnetic while its zigzag-edged counterpart displays a magnetic ordering of either FM or AFM nature depending particularly on its geometry. The edge-state-driven magnetism is then described by the mean-field Hubbard Hamiltonian given as (see Section 2)[212]

$$H = -t\sum_{\langle i,j\rangle,\sigma}\left(c_{i\sigma}^{+}c_{j\sigma} + \text{h.c.}\right) + U\sum_{i}\left(n_{i\uparrow}\langle n_{i\downarrow}\rangle + n_{i\downarrow}\langle n_{i\uparrow}\rangle\right), \quad (9)$$

where the first term is the single-orbital Hamiltonian (with t indicating the transfer integral between neighboring i-th and j-th sites belonging to the A- and B-sublattice, respectively) and the second term stands for the on-site Coulomb interaction. As clearly seen, the appearance of the second term implies formation of magnetic moments. When solved, for example, for triangular-shaped nanographene with all the three edges of

 This journal is © The Royal Society of Chemistry 2018

Published on 26 March 2018. Downloaded by Univerzita Palackého v Olomouci on 2/28/2019 2:05:03 PM.

zigzag character, a spin gap emerges around E_F, showing a spin polarization in the edge-state spins (*i.e.*, imbalance in spin channels ↑ and ↓). Spins sitting on the A-sublattice are oriented in an antiparallel manner to that on the B-sublattice; they are well localized near the zigzag edges and their strength rapidly decays from the edge to the interior of the triangular-shaped nanographene. At edges, atoms belonging to only the A-sublattice (or B-sublattice) are present, implying that the spins at the edges show parallel arrangement. Hence, the FM structure evolves with a non-zero spontaneous magnetization. For hexagonal-shaped nanographene with all the six edges of zigzag nature, spins with orientation ↑ sit along three edges while spins with orientation ↓ occupy the other three edges. As spins on the adjacent edges are oriented opposite to each other, the AFM structure is established over the hexagonal-shaped nanographene with no spontaneous magnetization. The expected magnetic behavior of both triangularly- and hexagonally-shaped nanographene sheets coincides exactly with the prediction from Lieb's theorem. Here, it should be highlighted that due to a weak spin–orbit interaction in carbon (~ 5 cm^{-1}), edge-state spins are weakly anisotropic. Then, the edge-state-driven magnetic structure is predicted by treating nanographene in the approximation of a weakly anisotropic Heisenberg spin system in a low-dimensional lattice.[212]

For an arbitrarily-shaped sheet of nanographene with a combination of armchair and zigzag edges (see Fig. 31), a ferrimagnetic (FIM) structure is supposed to be established. In particular, two interaction pathways between edge-state spins are recognized: (i) intra-edge interaction between spins lying along the same edge and (ii) inter-edge interaction between spins on opposite edges.[212] The intra-edge exchange interaction (expressed by the exchange integral J_0) is strong and is of FM character ($J_0 \approx 10^3$ K). The opposite FM edges can magnetically communicate by an inter-edge interaction (expressed by the exchange integral J_1) mediated by the conduction π-electrons. The inter-edge interaction is moderate ($J_1 \approx$ 10–100 K) and can be of either FM or AFM nature depending on the mutual geometrical relationship between the two zigzag edges. The competition between the strong intra-edge FM interaction and moderate inter-edge FM/AFM interaction, the strength of which is affected by the particular shape of the nanographene sheet, is then expected to stabilize the FIM structure with a nonzero spontaneous magnetization as antiferromagnetically coupled FM spin clusters are compensated.[211,212]

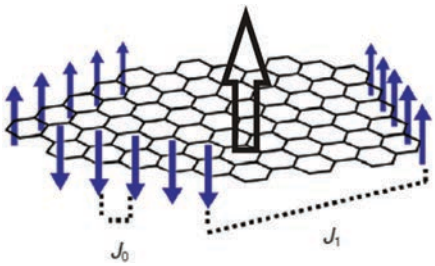


Fig. 31 Schematic representation of an arbitrarily-shaped sheet of nanographene showing the spatial distribution of edge-state spins (with blue filled arrows). J_0 and J_1 denote the intra-edge and inter-edge interactions, respectively. The white open arrow represents the net magnetic moment given as a vector sum of FM moments sitting on the zigzag edges. Reprinted with permission from ref. 212. Copyright 2013 Wiley-VCH Verlag GmbH & Co. KGaA.

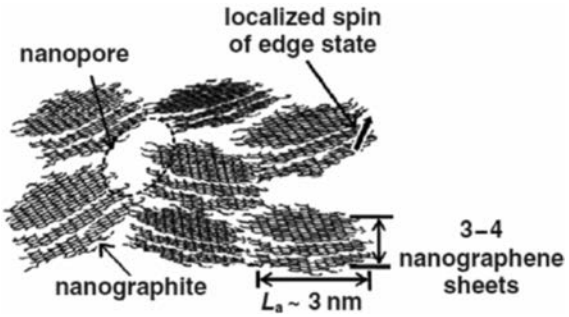


Fig. 32 Schematic representation of nanoporous activated carbon fiber with the localized edge-state spins sitting on the zigzag edges. The organization of nanographite domains in the activated carbon fiber favors the formation of a nanopore. Reprinted with permission from ref. 212. Copyright 2013 Wiley-VCH Verlag GmbH & Co. KGaA.

If the edges are fluorinated, spins located at zigzag edges are reduced. In contrast, if the zigzag edge on one side of the nanographene ribbon is dihydrogenated while the zigzag edge on the opposite side of the nanographene ribbon is monohydrogenated, a fully localized non-bonding state is supposed to appear around E_F; all the carbon atoms are spin-polarized even in the interior of the nanographene ribbon.[212] Another example involves oxidation of one side with the zigzag edge; in such a case, the side with the monohydrogenated zigzag edge is magnetic while the side with oxidized edge forms an electron conduction pathway. Thus, roles of edges can be tuned by their chemical modification (see below).[212]

If nanographites with the localized spins at the edges form a network (known as activated carbon fibers, see Fig. 32), a spin-glass behavior is observed maintained by the π-conduction electron-mediated interaction between the edge-state spins, similar to the s–d interaction in traditional metallic magnets.[211,212,224] It was found that the adsorption/desorption of water into the micropore space in the networked nanographite domains reduces/enhances the effective magnetic moments of the edge-state spins, which was explained in terms of encouraging the exchange interaction among the edge-state spins on the adjacent nanographene sheets by reduction of the inter-sheet distance caused by the internal pressure of water, eventually squeezing the nanographite domains. Such a phenomenon seems very promising in detection of guest molecules which, upon physisorption, switch on/off the magnetic response of the networked nanographite domains.[211,212]

4.1. Graphene nanoribbons

Graphene nanoribbons (GNRs) are strips of graphene sheets with a finite width not exceeding 50 nm (usually with a high aspect ratio).[5] They are classified as quasi-one-dimensional

Published on 26 March 2018. Downloaded by Univerzita Palackého v Olomouci on 2/28/2019 2:05:03 PM.

carbon nanoallotropes and are often adopted as a theoretical model system to describe and understand the role of edge and finite-size effects on the physical properties of graphene.[215,225,226] Currently, they are viewed as a prototypical example to study both theoretically and experimentally the role of various defects in the evolution of self-sustainable magnetic ordering in graphene.

Currently, three main approaches are used to synthesize GNRs, *i.e.*, (i) cutting from graphene employing lithographical procedures or catalytic particles, (ii) bottom-up synthesis from polycyclic molecules, and (iii) unzipping the carbon nanotubes.[5,227–229] With lithographic techniques, GNRs can be prepared by etching the exfoliated graphene flakes, graphene grown on metallic surfaces by chemical vapor deposition or epitaxial graphene on SiC. However, smooth edges are difficult to achieve even if other techniques are used such as TEM, STM or atomic force microscopy. Moreover, the yield of lithographic techniques is low. Alternatively, graphene can be cut by catalytic particles such as Fe or Ni in the presence of a hydrogen atmosphere. The problem is faced with unpredictability of cutting directions, resulting thus in a wide variety of shapes of graphene nanostructures. Recently, plasma etching was suggested as a tool providing engineering of the edge termination. The chirality of the edge segments was found to strongly depend on the initial chirality of the GNR itself, local environments, and out-of-equilibrium nature of the hydrogen plasma etching. By plasma etching, the edges are flat without structural reconstructions and terminated with hydrogen atoms preventing any hybridization of the outermost carbon edge atoms.[230]

Bottom-up syntheses of GNRs are based on growing them from molecular precursors.[231] They involve several steps, starting from monomeric precursors which react at the surface of an appropriate catalytic metal. Upon sublimation at a modestly hot metallic surface (with a temperature of $\sim$200 °C), polymer chains are formed. Dehydrogenation/cyclization of polymer chains at higher temperatures ($\sim$400 °C) results in the formation of GNRs. They are very narrow with a narrow size distribution and show an atomically precise edge configuration. However, in bottom-up synthetic procedures, metallic substrates are always required, limiting thus a bulk production of GNRs. This approach has not been fully explored yet and is widely viewed as a synthetic technique with future advancements.

The third approach to prepare GNRs involves unrolling or unzipping multi-walled carbon nanotubes. Several strategies to unzip multi-walled carbon nanotubes have been reported so far (see Fig. 33);[5,227] most of them exploit solution-based processes. The edge structure and crystallinity of GNRs were found to depend on various parameters such as the degree of nanotube crystallinity and uniformity in the length, diameter, and number of layers of carbon nanotubes. GNRs from unzipped carbon nanotubes can be produced in high yields with significantly lower costs compared to the other two approaches. However, as GNRs are prone to stack due to van der Waals interactions, setting of suitable conditions for their large-scale production should be carefully considered in order to avoid agglomeration, entanglement, and wrinkling of graphene strips.

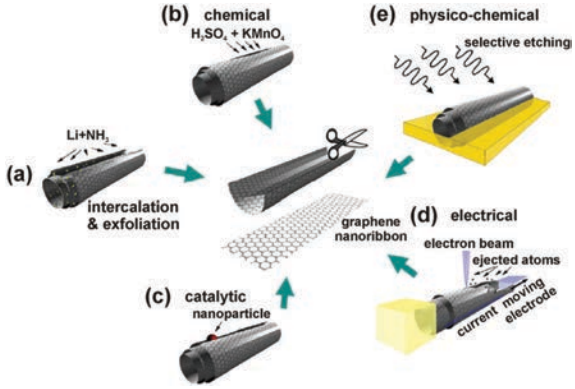


Fig. 33 Various strategies exploited for the preparation of GNRs involving unrolling or unzipping the carbon nanotubes: (a) intercalation/exfoliation of multi-walled carbon nanotubes by unzipping them by treatment in liquid NH_3 and Li, followed by exfoliating the graphene strips by HCl and heat treatment; (b) chemical procedures involving oxidizing agents (*e.g.*, $KMnO_4$, H_2SO_4) which break the C–C bonds; (c) catalytic cutting of multi-walled carbon nanotubes by exposing to metal nanoparticles (*e.g.*, Fe, Co, Ni) facilitating cutting of the carbon nanotubes along their length; (d) electrical cutting with an electrical current applied through the carbon nanotube; (e) physicochemical approach involving embedding of multi-walled carbon nanotubes in the polymer matrix, followed by etching the walls by an Ar plasma. Reprinted with permission from ref. 227. Copyright 2010 Elsevier Ltd.

Two canonical types of GNRs are recognized depending on the geometrical termination of their edges, *i.e.*, armchair and zigzag GNRs.[5] The edge pattern is defined considering the GNR's orientation with respect to the graphene lattice. From the geometrical aspect, armchair and zigzag edges are configurations with a high symmetry. In the case of zigzag GNRs, the edge consists of two sides of each hexagon resembling the periodic triangular appearance (see Fig. 34).[5] For armchair GNRs, the edge is formed by the hexagonal sides with adjacent hexagons contributing alternatively with one and three sides in a periodic manner (see Fig. 34).[5] The width of armchair GNR is defined by

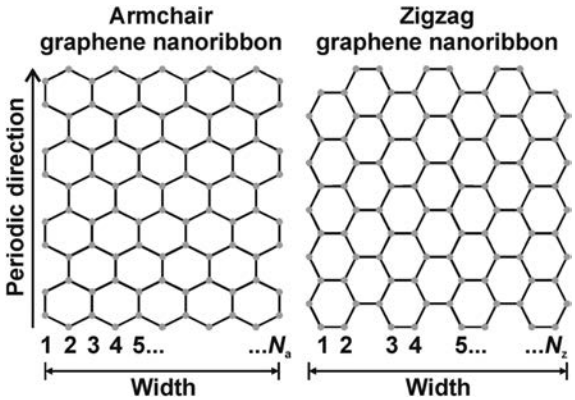


Fig. 34 Structures of the armchair and zigzag GNRs with their width given by the number of dimer lines (N_a) and zigzag chains (N_z), respectively.

This journal is © The Royal Society of Chemistry 2018

Published on 26 March 2018. Downloaded by Univerzita Palackého v Olomouci on 2/28/2019 2:05:03 PM.

the number of dimer lines (N_a) while for zigzag GNR, the width is given by the number of zigzag chains (N_z; see Fig. 34).[5] All other ordered orientations are of chiral nature. Here, it should be stressed that the carbon atoms sitting at the edge are not saturated. In the case of armchair GNRs, no edge reconstructions occur as the armchair edges are stable, hence preserving the planar patterns. However, zigzag edges are metastable undergoing spontaneous reconstructions even at room temperature. A pattern consisting of a pentagon and heptagon formed upon transformation of two hexagons was suggested as a potential reconstruction of the zigzag edge, resembling the appearance of an edge cut through a Haeckelite structure of a line of the SW defects. Thus, hydrogen atoms are often introduced to saturate the carbon atoms at the zigzag edge to preserve the planar structures of zigzag GNRs.[5] Moreover, a partial hydrogenation was theoretically identified to produce narrower GNRs from their wider counterparts.[232] The hydrogenation proceeds from the edges to the interior of GNRs, maximizing the number of carbon–carbon π–π bonds; the adsorption of hydrogen is of alternating nature skipping from one edge to another edge, terminated once all the hydrogen atoms available are adsorbed. The theoretical calculations imply that partially hydrogenated GNRs show similar electronic and magnetic features compared to those of narrow GNRs, which represent their graphene parts.[232]

It has been shown by tight-binding calculations that the band structure of GNRs depends heavily on the edge termination.[233] Armchair GNRs are predicted to behave as semiconductors with an extremely low carrier effective mass and a finite band gap which increases with a decrease in the width of the nanoribbon. Based on the size of the energy gap and its dependence on the nanoribbon's width, armchair GNRs can be classified into three families with $N_a = 3p$, $N_a = 3p + 1$, and $N_a = 3p + 2$, where p is an integer (see Fig. 35).[233] It is believed that the semiconducting behavior of armchair GNRs is driven by the quantum confinement effect together with a significant role of edge effects. As the carbon atoms sitting at the edge of armchair GNRs are passivated with hydrogen atoms, distinct bonding of carbon atoms at the edge is expected compared to that of carbon atoms in the interior. The carbon atoms at the edge show bond lengths shorter than those of carbon atoms in the interior of the armchair GNR, eventually opening its band gap. More importantly, the theory predicts that the electronic structure of all three classes of armchair GNRs is more or less similar, with the presence of four important subbands.[234] Their origin stems from π-bonds of carbon atoms; as they have different shapes, it is possible to alter them by external stimuli, further tuning the electronic structure and, hence, physical properties of armchair GNRs. However, unmodified armchair GNRs are not magnetic.[233] If the number of layers is increased, multilayered armchair GNRs fall into three classes, *i.e.*, two semiconducting and one metallic. For a given width, the band gap in multilayer armchair GNRs is expected to be smaller than that in their bilayered counterparts.[235]

Similar to armchair GNRs, zigzag counterparts show a direct energy gap, behaving in a metallic or semiconducting manner depending on the edge spin orientation. More importantly, their electronic structure is described by a set of doubly degenerate flat edge-state bands appearing at E_F, resulting in a large density of states at E_F.[233,236] At E_F, the peak of density of states is half-filled, implying emergence of the Stoner instability, a prerequisite for evolution of magnetic states. If spin degrees of freedom are introduced into the theoretical calculations, a magnetic insulating ground state was predicted for zigzag GNRs with FM ordering at the edge and antiparallel spin orientation between the two edges;[233,236] moreover, the intra-edge FM correlations were proposed to be significantly strengthened by the on-site Coulomb interaction.[237] The band gap is inversely proportional to the width of zigzag GNRs identically as in the case of their armchair analogues. The generated spin states are located mainly at the edges on carbon atoms (see Fig. 36);[233] the moments sitting on the edge atoms were predicted to be weakly dependent on the width of the nanoribbon, implying that the dependence of the band gap on the width of the nanoribbon results purely from the quantum confinement of orbitals.[238] The evolution of spin-polarized edge states is more energetically favored compared to non-spin-polarized solutions; upon an increase in the width of

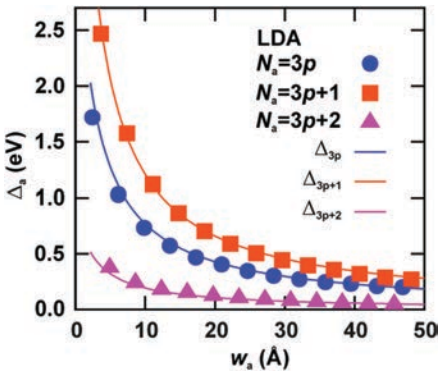


Fig. 35 Variations in band gaps for armchair GNRs as a function of their widths (w_a). Reprinted with permission from ref. 233. Copyright 2006 American Physical Society.

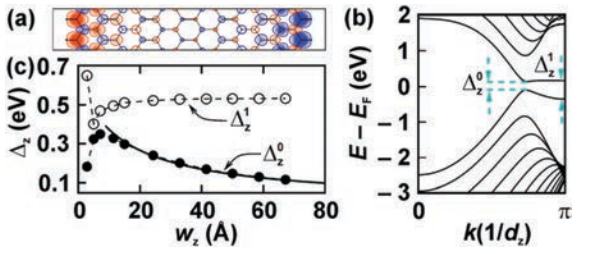


Fig. 36 (a) Spatial modulation of spin density for zigzag GNR with N_z = 12. (b) Band structure of zigzag GNR (with N_z = 12). The spin states in the A- and B-sublattice are degenerate in all the energy bands. Δ_z^0 and Δ_z^1 represent the direct band gap and the energy splitting at $kd_z = \pi$, respectively. (c) Profile of Δ_z^0 and Δ_z^1 with the width (w_z) of zigzag GNRs. Reprinted with permission from ref. 233. Copyright 2006 American Physical Society.

Published on 26 March 2018. Downloaded by Univerzita Palackého v Olomouci on 2/28/2019 2:05:03 PM.

zigzag GNRs, the energy difference between the spin-polarized and non-spin-polarized edge states increases. The existence of spin-polarized edge state is further encouraged by FM coupling along the edge.[233] The temperature dependence of the electron paramagnetic resonance linewidth implies that the edge-state spins are strongly coupled with the conduction π carriers.[239] It is believed that the edge states can withstand potential fluctuations due to electron–electron interactions. However, if the potential disorder is strong enough, electron–hole puddles (*i.e.*, inhomogeneous charge distributions) evolve inducing a magnetic transition when the coupling between the opposite zigzag edges is switched from AFM to FM character. The electron–hole puddles are formed as a consequence of a local breaking of charge neutrality.[240] In general, the difference between FM and AFM inter-edge coupling decreases with an increase in the width of zigzag GNRs, becoming negligible once the width significantly exceeds the decay length of spin-polarized edge states. The energy gaps in zigzag GNRs are believed to emerge as a result of staggered sublattice potentials from magnetic ordering. In other words, it can be inferred that the band gap stems from the exchange difference on the two sublattices of the graphene lattice. Moreover, it turns out that the spins occupying the A- and B-sublattice are degenerate in all the bands and show identical band gap.[233] For bilayered GNRs (*i.e.*, two identical graphene strips in a layered structure), the magnetic ordering at the edge atoms is predicted to disappear due to coupling of edge states between the top and bottom layers for particular stacking configurations. For various stacking arrangements, different band gaps and edge magnetizations are expected to evolve due to energy competition between inlayer and interlayer interactions, encouraging stabilization of ground magnetic state of either non-magnetic or FM or AFM origin. Moreover, metal–semiconductor transitions and splitting of spin-up and spin-down states can also be observed depending on the stacking configurations, spin arrangements, and widths of GNRs.[241,242] For example, if the layers are shifted by 0.61 Å (perpendicular to the ribbon's axis), such stacking of the two layers is favored in terms of thermodynamics showing, however, a non-magnetic ground state. If the shifts are larger than 1.42 Å, AFM inlayer and interlayer states develop, which are found to be the most stable among others.[243] In order to prevent losing magnetic ordering in bilayered zigzag GNRs, the two layers must alternatively have different widths. While edges at one side are pinched due to interlayer coupling, resulting in no magnetic ordering, the edges at the other side are coupled antiferromagnetically between the layers analogously as in the case of opposite edges in the monolayered zigzag GNRs.[244] If placed in an external electric field, asymmetric energy-gap opening for spin-up and spin-down occurs, leading to a half-metallic behavior in bilayered zigzag GNRs with different widths of layers.[244] For multilayered zigzag GNRs, the value of the gap then depends on the type of edge alignment.[235]

However, the existence and stability of edge states were heavily questioned by several theoretical studies. It was proposed that edge states can be suppressed, weakened or even eliminated by three mechanisms, which include edge reconstruction, edge passivation, and edge closure.[245] Moreover, quantum fluctuations were identified to play an eminent role, eventually ruining the long-range spin correlations by forming rung singlets.[246] In particular, this happens in cases when decoherence, which is affected by the environment interactions, is slower than the quantum dynamics. Similarly, edge magnetic moments are supposed to get reduced upon increasing the strength of nonlocal Coulomb interactions when spin- and charge-density fluctuations compete with each other.[247] As a result, dispersion of the edge states is renormalized, eventually generating a single-particle gap. However, no phase transition is observed, indicating that FM coupling along the edges, encouraged by the on-site interaction, is not affected by the competing short-range charge correlations, which are favored due to the long-range Coulomb interactions.[247] Suppression of spin polarization and, hence, stability of spin states in GNRs were predicted to occur for edge defects (*e.g.*, vacancies) and impurities; upon increasing their concentration, edge states at E_F are reduced or removed.[248] In particular, GNRs become non-magnetic if the concentration of defects exceeds a critical value of $\sim$0.10 Å^{-1}. Moreover, the local edge spins can completely disappear once two defects are positioned within a distance smaller than 3 unit edge segments (see Fig. 37). In other words, a tiny randomness

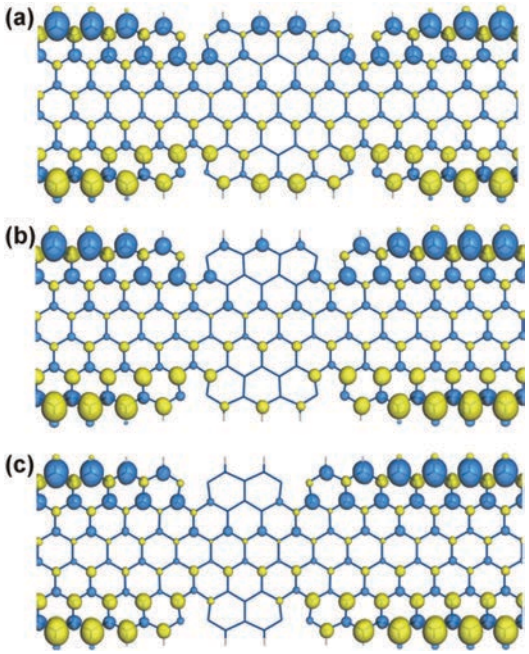


Fig. 37 Isosurfaces of the charge difference between the spin-up and spin-down states when vacancies are introduced at the edges of GNRs: (a) edge vacancies separated by 5 unit edge segments; (b) edge vacancies separated by 4 unit edge segments; (c) edge vacancies separated by 3 unit edge segments. The range of isovalues is set at (−0.004, 0.004) μ_B Å^{-1}. Reprinted with permission from ref. 248. Copyright 2008 American Physical Society.

 This journal is © The Royal Society of Chemistry 2018

Published on 26 March 2018. Downloaded by Univerzita Palackého v Olomouci on 2/28/2019 2:05:03 PM.

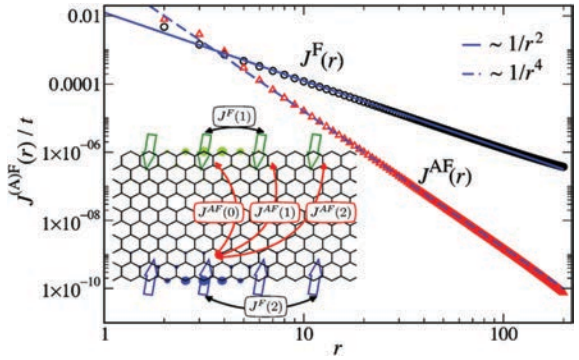


Fig. 38 Evolution of effective FM intra-edge [$J^{F}(r)$] and AFM inter-edge [$J^{AF}(r)$] interactions as a function of lateral distance (r) for a zigzag GNR with a width of 10. The inset schematically shows the structure of the zigzag GNR with some effective exchange interactions of the effective spin-ladder model indicated. The circles correspond to the amplitudes of the Wannier functions calculated for the two of these edge states on the nanoribbon's sites (one shown on the upper edge and one shown on the lower edge). Reprinted with permission from ref. 249. Copyright 2017 American Physical Society.

in the edge structure can even ruin edge magnetism and spin transport in GNRs.[248]

Very recently, the issue of edge magnetism in zigzag GNRs was theoretically addressed adopting the effective spin-ladder models constructed within the large-scale quantum Monte Carlo simulations; more specifically, zigzag GNRs are mathematically described as two antiferromagnetically coupled FM Haldane–Shastry spin-half-chains.[249] The results showed that FM intra-edge interactions decay relatively weakly with a lateral distance, r (proportional to $1/r^2$), while AFM inter-edge interactions fade away much faster with r following the $1/r^4$ power-law (see Fig. 38). In addition, the quantum disordered region appears if the strength of AFM inter-edge coupling exceeds a finite critical value, determining a quantum critical point; such a region was identified as a spin-gapped ground state of the effective quantum spin model for chiral GNRs.[246] In other words, upon increasing the strength of AFM inter-edge interactions, the system undergoes a quantum phase transition from the gapless state to the phase of quantum-disordered-region nature for which dominant singlets are observed to form along the inter-chain bonds.[249]

Experimentally, FM properties were observed for potassium-split GNRs and oxidatively unzipped and chemically converted GNRs;[250] in both cases, multi-walled carbon nanotubes were used as a starting material for GNRs. FM ordering was found to be self-sustainable up to room temperature for potassium-split GNRs; for oxidatively unzipped and chemically converted GNRs, vanishing of the FM response upon increasing the temperature was explained in terms of potential reconstruction, passivation, or closing by an oxidative unzipping process of majority of edges. The analysis of magnetization data confirmed clustering of spins with $S = 1/2$ in both types of GNRs. Moreover, a co-existence of AFM regions with the FM structure was observed, manifested by a non-zero exchange bias. The negative exchange bias was detected for potassium-split GNRs suggesting the existence of smooth edges. From electron spin resonance (ESR) spectra, carbon-related localized states were identified to be responsible for the emerged magnetism.[250]

Besides extensively studied armchair and zigzag edge terminations, the existence of other types of edge structures was reported. These include extended Klein's edges, cove edges, and reconstructed edges. The extended Klein's edge, predicted theoretically and observed experimentally, is defined as an array of single atom carbon atoms extending from a zigzag edge, *i.e.*, with an atomic site showing a π-orbital on the edge.[251–253] The Klein edges are favored to form among other edge terminations in the tearing process of graphene; hydrogenated Klein's and reconstructed Klein's edges were proposed to be energetically favored over hydrogen-terminated zigzag edges, with stabilities approaching those reported for the armchair edges.[254] It was shown that if the Klein's bearded bonds are partially attached to the GNR with both armchair and zigzag edges, partial flat bands appear at zero energy even for $|N_A - N_B| = 0$, which gives rise to a spin polarization near the edge.[255] The cove-shaped GNRs contain protruding phenyl rings along both edges and can thus be described as alternating armchair and zigzag segments;[256,257] however, the spin-polarized flat bands were found to emerge only once modified with the Klein's bearded bonds.[255] Reczag edges, already mentioned above and defined as the zigzag-57 edge with alternating 5- and 7-membered rings (*i.e.*, a structure with two under-saturated carbon atoms moved adjacent to each other), are energetically more stable than zigzag edges; in the electronic structure, they are manifested as flat bands extended around E_F, *i.e.*, a prerequisite for evolution of edge magnetic moments.[258] Other reported edge geometries involve ac(677) and ac(56) edges; the ac(677) edge structure is formed when the two separate ''armrest'' hexagons are merged into the adjacent heptagons by the Stone–Wales mechanism while the ac(56) edge motif is established upon diffusion of carbon atoms from the distant armrests to the seat positions.[258] These reconstructed armchair edges need more energy for stabilization than pure armchair edges and are not magnetic.[258]

The stability, edge states, and aromaticity of various types of edges can drastically vary depending on the level of hydrogenation (see Fig. 39 and Table 1).[259] The theoretical results imply that GNRs are magnetic only at an extremely low hydrogen concentration (see Table 1); however, they show metastability as they are very reactive. On the other hand, non-magnetic GNRs are considered as the most stable systems with a low reactivity at a standard/high level of hydrogenation (see Table 1).[259] Moreover, the Clar's rule can be applied to decide about the aromaticity of the structure; for pure graphene with an ideal aromaticity, a value of 1/3 is expected. It turns out (see Table 1) that some zigzag edges and mono- and di-hydrogenated armchair edges show 1/3 aromaticity of graphene and, hence, are not magnetic and non-metallic. If the edges have an aromaticity lower than graphene, a competition between the bulk and edge is expected to occur. As a result, some carbon atoms are forced to have less or more than four saturated bonds, eventually leading to the evolution of the edge states.[259]

Published on 26 March 2018. Downloaded by Univerzita Palackého v Olomouci on 2/28/2019 2:05:03 PM.

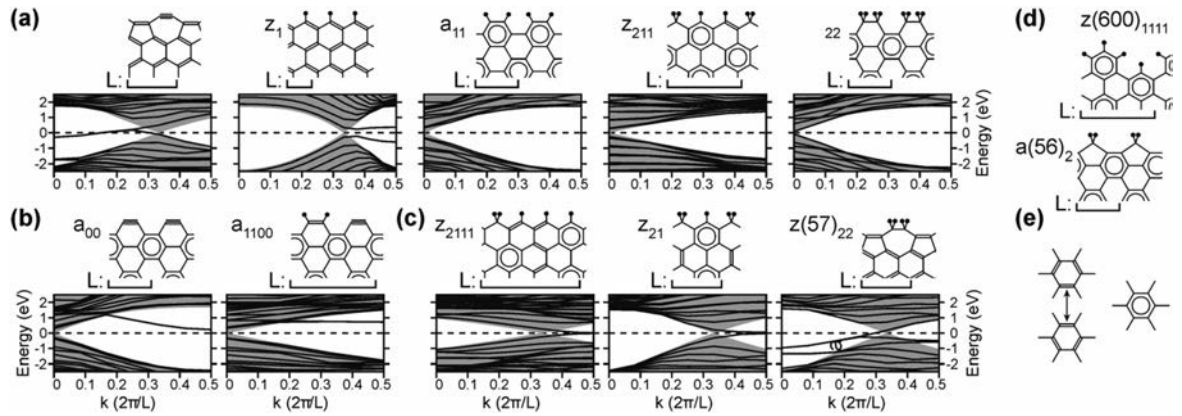


Fig. 39 (a) Schemes and electronic band structures of the five most stable hydrogen-passivated edges of GNRs. Hydrogen atoms are marked with filled circles. The systems considered show a periodicity along the ribbon's edge indicated by *L*. The grey area in the electronic structures corresponds to the electronic bands allowed in bulk graphene and the dashed line marks E_F. (b) Other stable armchair edge structures. (c) Other stable zigzag and reconstructed zigzag edge structures. (d) Structures of other reconstructed armchair and zigzag edges. (e) Standard representation of the benzenoid aromatic carbon ring used for computation of the aromaticity of various edge motifs considered. Reprinted with permission from ref. 259. Copyright 2008 American Physical Society.

Table 1 Formation energy (E_{H2}) and hydrogen density (ρ_H) for various edge structures. $z_{n_1n_2\ldots n_x}$ represents GNRs with zigzag edges, where n_i denotes the number of hydrogen atoms on a given site and *x* is the number of adjacent edge sites within the periodicity, *L* (see Fig. 39), $a_{m_1m_2m_3m_4}$ represents GNRs with armchair edges for the supercells with one (m_1m_2) and two ($m_1m_2m_3m_4$) hexagon columns, where m_i denotes the number of hydrogen atoms attached to the *i*-th carbon site, and $z(57)_{ij}$, $z(600)_{ijkl}$, and $a(56)_i$ represent GNRs with reconstructed zigzag and armchair edges, where the subscripts *i*, *j*, *k*, and *l* indicate the number of hydrogen atoms on a given site. Adopted with permission from ref. 259. Copyright 2008 American Physical Society

Edge type	ρ_H (Å^{-1})	E_{H_2} (eV Å^{-1})	Edge features
$z(57)_{00}$	0.000	0.9650	Non-magnetic and metallic edge, non-aromatic
z_0	0.000	1.1452	Magnetic and metallic edge, non-aromatic
z_{100}	0.136	0.7854	Magnetic and metallic edge, non-aromatic
z_{200}	0.271	0.7260	Magnetic and metallic edge, non-aromatic
z_{110}	0.271	0.4306	Magnetic and metallic edge, non-aromatic
$z(57)_{11}$	0.407	0.3337	Non-magnetic and metallic edge, non-aromatic
z_1	0.407	0.0809	Magnetic and metallic edge, non-aromatic
z_{211111}	0.474	0.0463	Magnetic and metallic edge, non-aromatic
z_{21111}	0.488	0.0397	Magnetic and metallic edge, non-aromatic
z_{2111}	0.508	0.0257	Magnetic and metallic edge, non-aromatic
z_{211}	0.542	0.0119	Non-magnetic and non-metallic edge, aromatic
$z(600)_{111}$	0.542	0.0459	Non-magnetic and non-metallic edge, aromatic
z_{21}	0.610	0.0382	Non-magnetic and metallic edge, non-aromatic
z_{221}	0.678	0.1007	Magnetic and metallic edge, non-aromatic
z_2	0.813	0.2224	Magnetic and metallic edge, non-aromatic
$z(57)_{22}$	0.813	0.2171	Non-magnetic and metallic edge, non-aromatic
$a(56)_0$	0.000	1.4723	Magnetic and metallic edge, non-aromatic
a_{00}	0.000	1.0078	Non-magnetic and non-metallic edge, aromatic
$a(56)_1$	0.235	0.7030	Non-magnetic and metallic edge, non-aromatic
a_{1100}	0.235	0.4946	Non-magnetic and non-metallic edge, aromatic
a_{10}	0.235	0.6273	Magnetic and metallic edge, non-aromatic
a_{11}	0.469	0.0321	Non-magnetic and non-metallic edge, aromatic
$a(56)_2$	0.469	0.4114	Non-magnetic and non-metallic edge, aromatic
a_{21}	0.704	0.2092	Magnetic and metallic edge, non-aromatic
a_{2211}	0.704	−0.0163	Non-magnetic and non-metallic edge, aromatic
a_{22}	0.939	−0.0710	Non-magnetic and non-metallic edge, aromatic

The presence of edges offers a potentiality to modify their chemical and electronic features with defects, doping with foreign atoms, hydrogenation, oxidation, functionalization with various functional groups and with adsorption of some gas molecules or when exposed to external stimuli such as strain and external electric and magnetic fields. In general, the type of edge modification determines whether the GNR is a conductor or a semiconductor; a conducting behavior is associated with the decorating atom and its covalent bond while a semiconducting feature is closely related to the edge-induced magnetic moments.

If GNRs are doped with nitrogen and boron creating holes and carriers, respectively, in their structure, the triplet state is

 This journal is © The Royal Society of Chemistry 2018

Published on 26 March 2018. Downloaded by Univerzita Palackého v Olomouci on 2/28/2019 2:05:03 PM.

expected to be more stable compared to the singlet state, thus favoring an FM ground state.[260] For armchair GNRs, both the band gap and ionization potential gradually decrease as their widths increase. In zigzag GNRs, the dependence of band gap and ionization potential on their widths shows a distinct trend whether unpaired electrons are present or not.[260] Lately, from theoretical calculations seeking the most energetically favorable atomic configurations in doped GNRs, it was suggested that nitrogen atoms preferentially substitute carbon atoms at both armchair and zigzag edges. In the case of boron (as a p-type dopant), the preference for site substitution is different for armchair and zigzag GNRs. While carbon atoms are substituted by boron at zigzag edges, in armchair GNRs, boron replaces carbon atoms at positions (*i.e.*, three-coordinated sites) next to the edge. In zigzag GNRs, boron induces a spin-dependent donor-like state if it is located at the edge while acceptor states are formed as boron atoms move to the center of the nanoribbon. For nitrogen n-type doping, the opposite effect is expected, *i.e.*, acceptor-like states with nitrogen at the edge and donor-like states with nitrogen located in the GNR inner regions.[261,262] More specifically, if pyridine- and pyrrole-like N-doping defects are introduced into zigzag GNRs, they turn them into half-metals or spin-gapless semiconductors;[263] they tend to be localized near the edge of GNRs. A similar effect is expected for nitrogen atoms attached to only one zigzag edge.[264] As a result, the two edge states separate near E_F; the system adopts the FM ground state due to reduction of the magnetic moments at the doped side. Appropriate charge doping is thus expected to give rise to half-metallic and single-edge conducting zigzag GNRs.[264] In the case of co-doping zigzag GNRs simultaneously with nitrogen and boron, it was theoretically predicted that for an AFM ground state, the BN defect states destroy the doped-side spin-polarized edge currents promoting their flowing at the undoped side near the conduction band-edge region with almost a perfect one-spin-channel transmission.[265] On the other hand, fully spin-polarized currents flowing along the undoped side of zigzag GNR were identified to evolve near E_F. Such BN-induced spin-polarized states are robust with regard to the width of GNRs, doping concentration, and geometries of heterojuctions.[265] Half-metallic behavior can also be observed for hybrid C/BN zigzag GNRs (*i.e.*, with a BN row introduced into the nanoribbon's structure) for a specific nanoribbon's width and ratio between C and BN; the unexpected half-metallicity was proposed to originate from the competition between the charge and spin polarizations and π orbital hybridization between C with B and N, breaking the electronic symmetry of the two edge states.[266]

Despite showing a non-magnetic response, magnetic states can be induced in armchair GNRs if periodically repeating defects such as vacancies or divacancies are introduced into their lattice. They are found to promote metallic character and net magnetization due to the spin polarization of the local defect states. Besides the geometry of the defect, the band gap is significantly affected by the repeating periodicity of the defect and its position within the GNR structure relative to the edge.[267] Moreover, a magnetic state induced by vacancies in armchair GNRs can be tuned by applying a strain as evidenced for a two-vacancy system when singlet–triplet splitting was found to strongly depend on the product of strain and inter-vacancy distance.[268] Alternatively, a magnetic ground state may develop if armchair GNRs are doped with extra electrons. The spin polarization then stems from the localized edge state appearing around the Brillouin zone boundary. Moreover, if some electrons are injected, indirect-gap armchair GNRs show half-metallic properties while heavily doped direct-gap armchair GNRs become antiferromagnets.[269] More specifically, a dominant AFM behavior appears around half-filling with electrons while an FM ground state is favored with electron filling lower than 0.8 and can be manipulated by the gate voltage. Thus, FM interactions are believed to be strengthened substantially by the next-nearest-neighbor hopping energy.[270]

As shown theoretically, the magnetism in armchair GNRs can be induced and tuned if a line defect composed of two pentagons and one octagon (*i.e.*, 558-type line defect), is introduced as a grain boundary in the nanoribbon's lattice.[271] If the end configuration of the 558 grain boundary is varied, the structures were found to fall into three groups. For some particular configurations, a transition from the non-magnetic to FM state occurs in defective armchair GNRs. In FM systems, the evolved magnetic features stem from the zigzag chains of the 558 grain boundary which are closely correlated with the spin splitting of the energy bands.[271]

If passivated with oxygen, planar armchair GNRs may adopt a degenerate magnetic ground state due to emptying the O lone-pair electrons.[272] The degenerate magnetic ground state established over planar armchair GNRs involves metallic FM ordering and AFM ordering with three families distinguished upon the band gap, *i.e.*, one metallic and two semiconducting classes. Due to steric interactions between oxygen atoms and more beneficent hybridization of atomic orbitals, non-planar geometries are energetically favored over planar appearance of oxygen-functionalized GNRs, becoming eventually non-magnetic and classified into three semiconducting families depending on the behavior of the band gap.[272] On the other hand, for GNRs with armchair edges saturated with H_2, the theoretical calculations lead to shifted labeling of the three nanoribbon's classes with $N = 3p$, $3p - 1$ and $3p + 1$ ($p = 1, 2, 3, \ldots$).[273] The shift in classes, and, hence, in width values, was explained by modification of sp^2-hybridization to sp^3-like hybridization by interaction of π orbitals of graphene on the outermost edge and hydrogen orbitals.[273]

Besides boron and nitrogen, armchair GNRs were doped or edge-modified by other elements such as Mg, Mn, Fe, and Au.[274–277] In particular, Fe atoms are preferentially doped at the center of GNRs and their magnetic moments vary from 1.95 to 2.93 μ_B depending on the doping site. Fe atoms are supposed to break the degeneracy of the opposite spin states. Spin polarization can reach 60% and can be tuned upon varying the position of Fe atoms in the nanoribbon's lattice. Due to a number of conduction channels that cross E_F, the system shows a high metallicity, which does not depend on the nanoribbon's width or position of the Fe atom.[275] In contrast, Au atoms were identified to preferentially substitute carbon atoms near the edge of armchair GNRs. The Au-doped armchair GNRs behave as semiconductors with an FM configuration showing a lower

Published on 26 March 2018. Downloaded by Univerzita Palackého v Olomouci on 2/28/2019 2:05:03 PM.

energy compared to an AFM case. The spin-up and spin-down states are completely degenerate as no spin dependence in the band structure is observed. Moreover, the edge substitution modifies the band gap, encouraging the occurrence of the semiconductor–metal transitions in Au-substituted armchair GNRs.[276]

Recently, it was shown that if armchair GNRs are exposed to a strain along the armchair direction, edge states can evolve even for a very small intrinsic spin–orbit coupling.[278] Moreover, the edge-state conductivity was found to be quantized. A deeper theoretical analysis identified the helical nature of edge states, confirming the presence of the spin Hall effect. A transition from the quantum spin Hall state to a trivial insulator regime was then observed upon reaching a critical value of strain. Compared to zigzag GNRs, the emerged spin texture in armchair GNRs was found to be invariant to the Fermi energy with spin directions of the edge states opposite to each other on the same boundary.[278]

As a weak spin–orbit interaction exists in carbon resulting in small magnetic anisotropy energy, it is heavily questioned, whether magnetic ordering in GNRs can sustain thermal fluctuations and magnetic impetus. It was theoretically proposed that if suitably ligated GNRs are further functionalized with 3d transition metals, the system becomes equipped with large magnetic moments and large magnetic anisotropy energy.[279] The suggested concept was verified for GNRs edge-functionalized with –F and –CN groups and then decorated with Co and Mn atoms. If GNRs are terminated with –CN groups and Co atoms, high magnetic anisotropy energy is expected; the direction of their magnetization can be then changed by applying an external electric field. For –CN-terminated GNRs with Mn atoms attached, a half-metallic behavior with giant magnetic moments was observed, which seems to be more stable than that reported for half-metallic zigzag GNRs.[279]

In the case of zigzag GNRs, it has been shown that the nature of coupling between opposite edges can be altered by their width.[57] Upon increasing the nanoribbon's width, a transition from the AFM state to the FM regime is witnessed; in the AFM state, zigzag GNRs behave as direct-band gap semiconductors while metallic features are observed for FM zigzag GNRs.[57] In addition, opposite edges of zigzag GNRs can interact in an FM manner if (i) extra carriers (*i.e.*, electron/holes) are injected into the lattice of GNRs by doping (*e.g.*, N or B),[280] (ii) GNRs interact with an internal magnetic field on a suitable substrate during graphene deposition,[281] and (iii) one edge is saturated by two hydrogen atoms and the other edge by only one hydrogen atom.[282] More specifically, upon increasing the level of doping with electrons/holes, the angle (θ) between the directions of spins at the opposite edges continuously decreases from 180° (AFM state) to 0° (FM state). The canted, non-collinear spin structures appear for $0^\circ < \theta < 180^\circ$ (see Fig. 40).[283] Furthermore, if boron atoms are attached to both edges, the FM ground state is promoted showing a half-metallic behavior irrespective of the width of zigzag GNRs. However, if nitrogen atoms are introduced at both zigzag edges, the system preserves an AFM ground state with the metallic behavior.[284] Recent theoretical works confirmed that half-metallicity can be imprinted in zigzag GNRs once functionalized on either edge with species of donor and acceptor nature. As a result, an effective potential gradient emerges. Other strategy involves hybrid modification at one edge manifested by evolution of spin-polarized impurity state at E_F. For example, if zigzag edges are decorated with CH_3–NO_2 pair, the spin-down channel is metallic while semiconducting behavior is expected for the spin-up channel; the spin density is distributed largely over the carbon atoms at the edges.[285] Half-metallic state can be alternatively induced by introducing a BN defect in the structure of zigzag GNRs.[286] As the zigzag C–C chains located in the middle part of the ribbon are gradually replaced with BN segments, the system eventually transforms to the zigzag BN nanoribbons with electronic features dependent on the level of substitution. If the doping concentration exceeds a threshold value, when carbon atoms, resembling the arrangement of terminated polyacene C chains, are located only at the edges and all the interior carbon atoms are replaced with BN chains, the hybrid system becomes a half-metallic antiferromagnet for all the widths. The evolution of half-metallicity was explained in terms of charge transfer from the adjacent carbon atoms to boron atoms promoted by the Lewis acid nature of boron, leading eventually to the generation of the interface potential gradient similar to the case of applying an external electric field.[286] On the other hand, if holes are pumped in zigzag GNRs, they become conductive, accompanied by the reduction of their spin gaps. Above the threshold value of hole doping, the spin gap is closed and the system shows a magnetic ground state with a net magnetic moment over the structure.[287] If the structure of zigzag GNRs shows periodically repeating protruded edge step segments (with a length of less than 9.776 Å), the system undergoes a transition from the non-magnetic semiconducting state through the metallic regime and eventually to a magnetic semiconducting state as the step-to-step distance gradually increases.[288]

Recently, it was shown that square-shaped carbon tetragons, connecting asymmetrically the two segments of zigzag GNRs, can serve as spin switches changing the orientation of magnetic moments at the two edges (see Fig. 41);[289] the switching process was predicted to occur for a large variety of acene dimer configurations, representing the narrowest zigzag GNRs. Moreover, such spin switches can lift the spin degeneracy, eventually providing to tune the magnetic ground state of the system by charge doping, stabilizing a half-metallic and FM behavior.[289]

Vacancies and divacancies are considered as point defects modifying the ground magnetic state of zigzag GNRs. It is believed that if a vacancy is introduced into zigzag GNRs, it reconstructs and then interacts with the edge states. The structural local reconstruction of the lattice and, hence, emerging spin polarization of the orbitals at the close proximity of the defect are responsible for evolution of net magnetic moments. As a result, the AFM ground state is altered with establishment of the FIM state.[267] The effect of the vacancy defect on the electronic and magnetic properties of zigzag GNRs can be fine-tuned by its symmetry, size, and position within the lattice with respect to the edges.[290]

 This journal is © The Royal Society of Chemistry 2018

Published on 26 March 2018. Downloaded by Univerzita Palackého v Olomouci on 2/28/2019 2:05:03 PM.

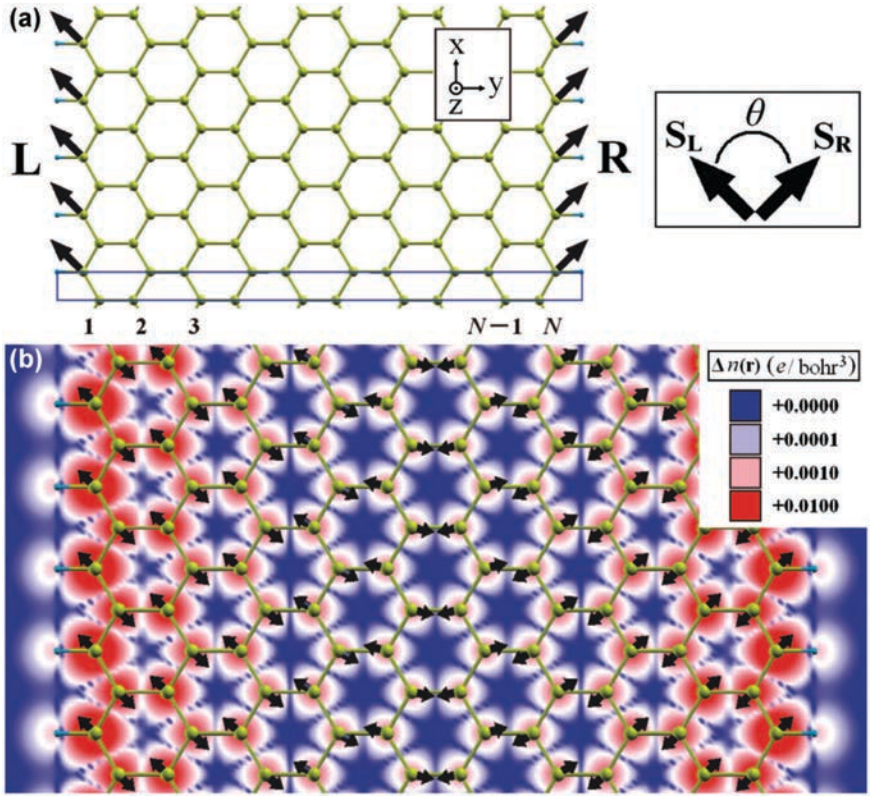


Fig. 40 (a) Schematic representation of a GNR with yellow and light blue balls corresponding to C and H atoms, respectively. The blue rectangle stands for the unit cell and N is the ribbon's width. The black arrows represent the orientation of the magnetic moments at the left (S_L) and right (S_R) edge and θ denotes the relative angle between S_L and S_R. (b) Spatial distribution of the spin density in the canted magnetic state for θ = 90° and doping concentration x = 0.16 e nm^{-1}. The black arrows denote the calculated directions of the magnetic moments of the respective carbon atoms. Reprinted with permission from ref. 283. Copyright 2009 American Chemical Society.

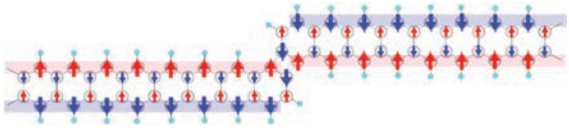


Fig. 41 Scheme of the spin configuration for different zigzag GNRs connected with a carbon tetragon as a spin switch. Reprinted with permission from ref. 289. Copyright 2016 American Physical Society.

A transition from the AFM to the FM ground state was observed if the line defects of 558-type (*i.e.*, two pentagons and one octagon) were introduced into zigzag GNRs (see Fig. 42) and exposed to strain or doped with nitrogen and boron.[291] In the case when no strain is applied or zigzag GNRs with the array of 558-type defects are not doped, opposite sides are coupled antiferromagnetically (see Fig. 42) as there is no moment at the C_I and C_{II} positions and the spins linked with them are in an antiparallel arrangement. FM coupling appears in the case of application of uniaxial tension or doping of nitrogen, boron, aluminum, or phosphorous (with a number of valence electrons different from carbon by one); the C_I and C_{II} positions become magnetically active and mediate FM interactions across the GNR.[291] Lately, it was proposed that without strain, 558-type line defects form near the zigzag edges.[292] If the defects move from the interior of the GNR to its edge, the system gradually undergoes a transition from the AFM conducting through AFM half-metallic to FM metallic state. Upon an increase in strain, the band gaps of AFM semiconducting GNRs are reduced gradually becoming AFM half-metals. A further increase in strain forces GNRs to adopt FM metallic behavior. The threshold values of strain for these transitions decrease upon movement of the 558-type line defect to the edge. Moreover, the occurrence of magnetic transitions is found to heavily depend on the nanoribbon's width.[292] More importantly, if the 558-type line defect sits at one edge, the defective zigzag GNRs are supposed to show a long-range magnetic ordering at edges with a high Curie temperature of up to 276 K.[293] Doping with nitrogen and boron at the particular sites of the 558-type defect can tune the magnetic response of defective zigzag GNRs.[294] If A and B sites are doped (see Fig. 43),[294] AFM spin alignment is preferred while non-magnetic states emerge for other doped sites. The exception involves doping the D site with boron favoring the FM state across the GNR. More importantly, if carbon atoms are replaced by nitrogen and boron at the A site,

Published on 26 March 2018. Downloaded by Univerzita Palackého v Olomouci on 2/28/2019 2:05:03 PM.

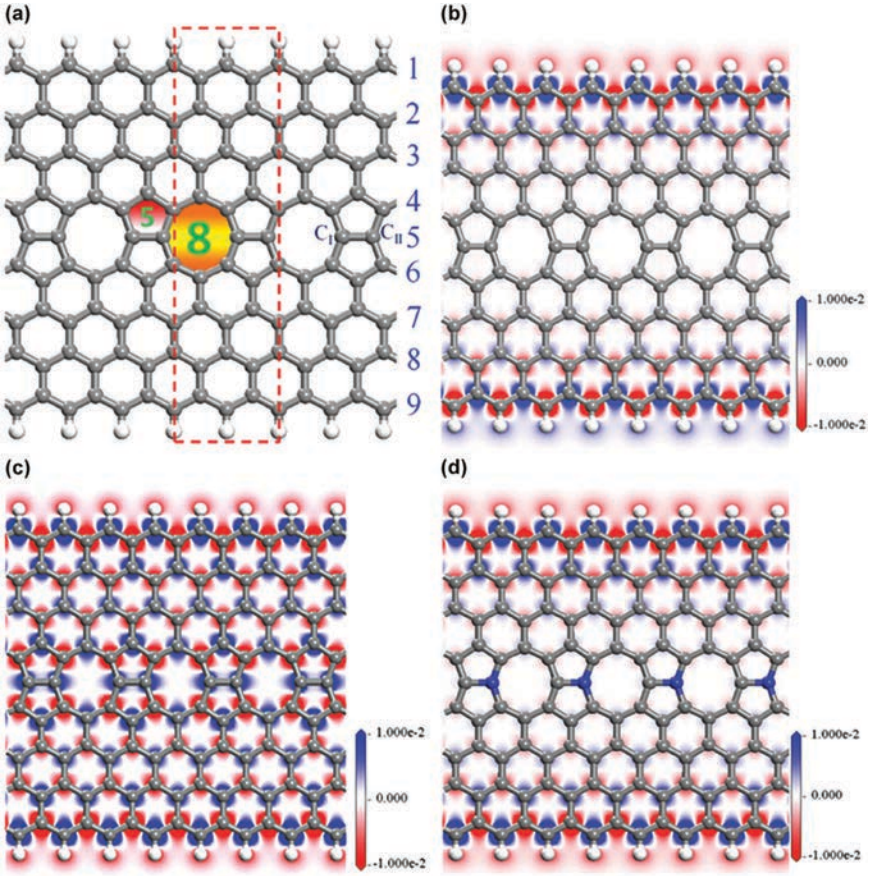


Fig. 42 (a) Scheme of the structure of a zigzag GNR with the 558-defect in its lattice with the C_I and C_{II} positions indicated. (b) Spin-density plot of the zigzag GNR with the 558-defect. (c) Spin-density plot of the zigzag GNR with the 558-defect when exposed to a uniaxial tension. (d) Spin-density plot of the zigzag GNR with the 558-defect doped with nitrogen at the C_{II} position. Reprinted with permission from ref. 291. Copyright 2012 American Physical Society.

half-metallicity appears. For boron doping the B and D sites of defective GNRs, the system becomes a spin-gapless semiconductor upon applying a transverse electric field. The eminent spin filtering capacity of suitably doped defective zigzag GNRs was then explained in terms of breaking the symmetry of the transmission channel.[294]

A pair made of a pentagon and a heptagon ring, periodically repeating along the nanoribbon's length, was recently considered as another line defect in zigzag GNRs.[295] The 5-7 line defect separates the GNR into two non-defective regions (*i.e.*, upper and lower parts) terminated with the zigzag edges. If the 5-7 line defect is positioned close to one edge of the GNR, the system behaves as a ferromagnet with a metallic character and non-degenerate spin state. The electronic features can be changed by varying the nanoribbon's width or the position of the 5-7 line defect within the lattice of the zigzag GNR. Once the symmetry about the 5-7 line defect is removed, the degeneracy in the spin-up and spin-down states vanishes. A transition from an AFM semi-metal to an AFM semi-metal semiconducting state occurs upon changing the position of the 5-7 line defect within the nanoribbon's structure towards its edge. The degeneracy of spin-up and spin-down states of zigzag GNRs with the 5-7 line defect can be lifted by doping with boron and nitrogen atoms, tuning thus the magnetic polarization.[295]

Interesting electric and magnetic features useful for applications were predicted for zigzag GNRs with SW defects.[296] Due to the asymmetry of the SW defects, they are believed to induce finite magnetic moments in the lattice of defective zigzag GNRs. If the defect moved from the position near the edge of the GNR to its interior, the net magnetic moment of defective zigzag GNRs was found to decrease to zero; reduction in the net magnetic moment was accompanied by a transition from the metallic to semi-half-metallic and even to semiconducting state. If an extra defect was placed close to the opposite side of the defective zigzag GNR symmetrically with the firstly introduced defect, the net magnetic moment vanished and the electronic features were found to depend on the distance between the defect and the closer side of the GNR.[296] If the zigzag edges are reconstructed with the SW defects, a new type of edge state is theoretically expected to appear; they show a dispersive character with non-zero amplitudes in both graphene sublattices.[297]

 This journal is © The Royal Society of Chemistry 2018

Published on 26 March 2018. Downloaded by Univerzita Palackého v Olomouci on 2/28/2019 2:05:03 PM.

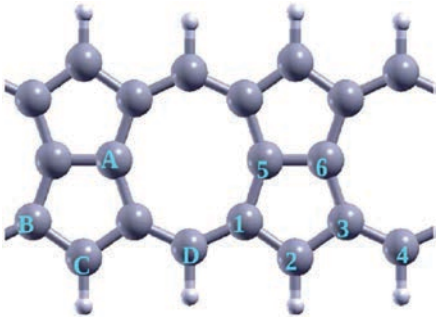


Fig. 43 Structure of defective zigzag GNR with various doping sites denoted as A–D and 1–6. The grey and white balls represent the carbon and hydrogen atoms, respectively. Reprinted with permission from ref. 294. Copyright 2014 The Royal Society of Chemistry.

Moreover, two components were identified in the wave functions amplitudes; they have different decay lengths with the distance from the edge. The decay length for one amplitude component is finite even at the Dirac point while for the other amplitude component, it diverges.[297] In the case of the SW line defect, it was theoretically shown that it sits most favorably near the edge; such defective zigzag GNRs behave as AFM semiconductors with an indirect band gap.[298] If they are exposed to an axis tensile strain, the band gap of AFM semiconducting systems progressively enlarges. Transitions from semiconducting, half-metallic, and metallic states accompanied by an AFM-to-FM passage are expected to occur with shifting of the SW line defect from the center of the nanoribbon to its edge by increasing the tensile strain.[298]

If zigzag GNRs are curved by an angle θ (see Fig. 44), alteration in the ground magnetic state was suggested to happen. For curvatures of $89^\circ \leq \theta < 180^\circ$, the AFM ground state persists.[299] However, if $\theta \leq 88^\circ$, the system is expected to undergo a magnetic transition from the AFM to a non-magnetic state upon increasing the curvature. Upon further bending, the AFM state is finally restored (see Fig. 44). Such a behavior was explained in terms of the overlap of the wave functions localized on the carbon atoms at the curving sites and inter-layered coupling evoked by a large bending of the structure.[299] However, if a divacancy is introduced into the lattice of zigzag GNRs, a distinct transition sequence occurs upon increasing the curvature. In particular, the system is predicted to show AFM, FM, and non-magnetic states if $164^\circ \leq \theta \leq 180^\circ$, $142^\circ \leq \theta \leq 163^\circ$, and $65^\circ \leq \theta \leq 141^\circ$, respectively.[300] In contrast, no change in the magnetic ground state was observed upon twisting zigzag GNRs despite a decrease in the atomic bonding energies and, hence, variation of gaps between the lowest unoccupied and the highest occupied molecular orbitals; AFM coupling between the opposite edges still persists with an appearance of spin flip at some sites at zigzag edges.[301]

Adsorption of hydrogen atoms on the surface of zigzag GNRs was identified to equip them with additional magnetic features.[302] As hydrogen atom is adsorbed, the spin density evolves on the surrounding orbitals; its symmetry and extent of localization were predicted to depend on the distance between the site with the adsorbed hydrogen atom and the edge. The interaction among such induced magnetic moments can be of either FM or AFM nature, dictated by the number of adsorbed hydrogen atoms at each graphene sublattice. Moreover, the magnitude of these interactions was found to strongly vary if the position of the adsorbed hydrogen atoms, relative to the edge, was changed.[302]

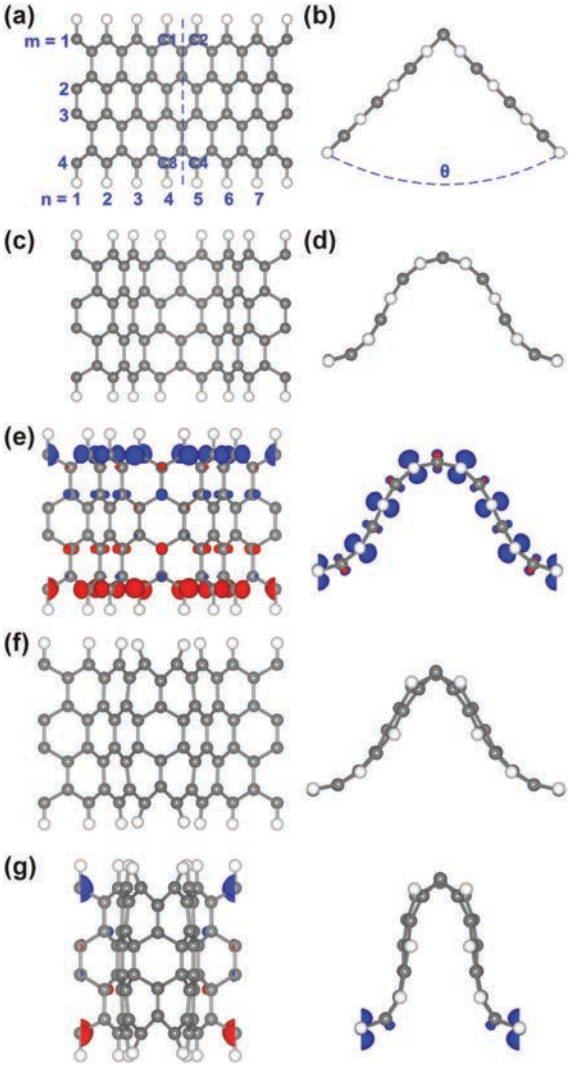


Fig. 44 (a) Top and (b) side views of a bent zigzag GNR. C_1, C_2, C_3, and C_4 denote edge carbon atoms close to the curving site and θ represents the bending angle. (c) Top and (d) side views of the zigzag GNR relaxed after bending by $\theta = 89^\circ$. The top (left) and side (right) views of the spatial spin distribution for the zigzag GNR relaxed after bending by an angle of (e) 89°, (f) 88°, and (g) 52°. Reprinted with permission from ref. 299. Copyright 2012 American Institute of Physics.

Hydrogenation, *i.e.*, edge modification with hydrogen atoms, was suggested as another approach to alter the ground magnetic state of zigzag GNRs.[303] If one zigzag edge is saturated with one

Published on 26 March 2018. Downloaded by Univerzita Palackého v Olomouci on 2/28/2019 2:05:03 PM.

hydrogen atom and the opposite edge with two hydrogen atoms, zigzag GNRs become FM semiconductors. In such cases, the difference between the energy of the AFM and FM states varies inversely with the nanoribbon's width.[303] With introduction of a line defect (of 558-type) into the asymmetrically hydrogen-edge terminated zigzag GNRs, they can become spin-polarized metals, metals with a Dirac point, or half-metals depending on the position of the line defect in the nanoribbon's lattice. In particular, half-metallicity is observed when the line defect is positioned far away from the edge. If the line defect then moves to the edge, a behavior resembling that of spin-polarized metals or metals with a Dirac point is observed, regardless of the nanoribbon's width.[304] Alternatively, if doped with p-type or n-type entities, a perfect spin filtering effect may further emerge.[305] Interestingly, with the zigzag edges passivated with H_2, a magnetic-to-non-magnetic transition is observed for a critical value of the nanoribbon's width, which changes with the number of nanoribbon's layers.[273]

Similarly to the case of hydrogenation, equipping the zigzag edges with hydroxyl groups may facilitate transition from AFM to FM coupling between the opposite nanoribbon's sides.[306] If the edges are passivated asymmetrically with hydroxyl groups, different potentials emerge at the two edges, eventually resulting in spin splitting in the bands. If the concentration of –OH groups is higher than 70%, the energy difference between the ground AFM and excited FM states becomes small, providing tuning between AFM semiconducting and FM half-metallic phases upon applying a small external magnetic field. The small energy difference between FM and AFM states for –OH concentrations higher than 70% allows for tuning between AFM semiconducting and FM half-metallic regimes by applying a small magnetic field.[306] Similarly, for asymmetrical adsorption of CO_2 molecules at the two zigzag edges, the FIM state is developed with a lower stabilization energy compared to that of the AFM state and new edge states appearing in the gap of CO_2-edge passivated zigzag GNRs.[307]

The zigzag edges of GNRs can be oxidized by terminating them with various oxygen-containing groups such as hydroxyl, lactone, ketone, and ether.[308] It was theoretically predicted that the oxidized GNRs are more stable compared to hydrogen-terminated GNRs except for ether groups. The stable oxidized GNRs show a spin-polarized ground state with an AFM ordering of opposite edges, similar to fully hydrogenated analogues (see Fig. 45).[308] More strikingly, apart from the edge modification by ketone groups, edge oxidation causes lowering of the critical electric field needed for entering the half-metallicity state. If the external magnetic field is further increased, a drastic decrease in the magnetization is witnessed, eventually vanishing at a certain intensity of the electric field when all the oxidized GNRs become non-magnetic.[308]

Interestingly, the electronic features and nature of the magnetic ground state can be observed in systems composed of joint structures with decorated polydiacetylene (PDA) derivatives deposited on zigzag GNRs with perfect, 57-reconstructed, and partially hydrogen-terminated edge patterns.[309] Zigzag GNRs with hydrogen-terminated edges adopt a half-metallic or

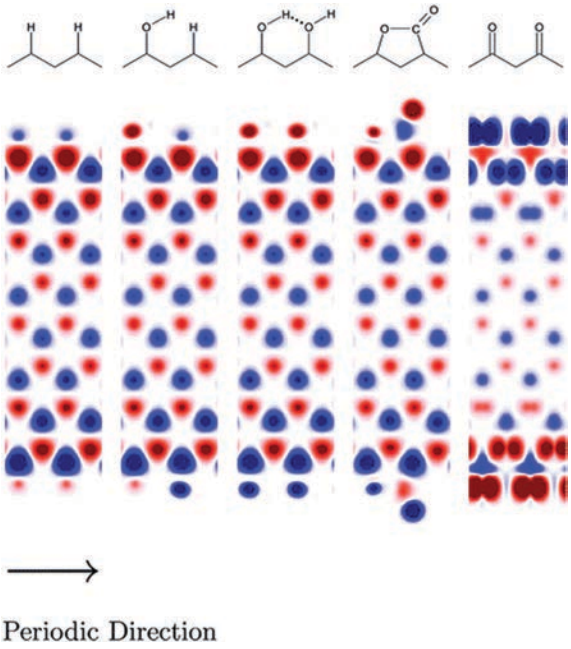


Fig. 45 Ground-state spin densities of the zigzag GNR oxidized by hydroxyl, lactone, ketone, and ether groups including the fully hydrogenated system for comparison. The red color denotes the spin density at the A-sublattice and the blue color stands for the spin density at the B-sublattice of the zigzag GNR. Reprinted with permission from ref. 308. Copyright 2007 American Chemical Society.

metallic behavior once decorated with PDA derivatives with several pairs of acceptor/donor groups (*i.e.*, NO_2/NH_2, F/H, Cl/H, or CN/CH_3) attached. Such systems may undergo transitions between spin-gapless semiconducting, half-metallic, and metallic regimes accompanied by an AFM-to-FM passage upon changing the nanoribbon's width or increasing the number of –C≡C– bonds present in the linking bridge of the NO_2/NH_2 groups bound to the PDA derivatives (see Fig. 46).[309] Similar transitions (*i.e.*, between AFM spin-gapless semiconducting, FM half-metallic, AFM metallic, and non-magnetic metallic states), triggered by the width and number of –C≡C– bonds, were reported for joint systems of the PDA derivatives decorating zigzag GNRs with 57-reconstructed edge patterns. Partial hydrogenation was found to eliminate the effect of edge reconstruction and electronic and magnetic features of the relevant joint structures with zigzag GNRs with perfect edges. The diverse spectra of electronic and magnetic properties of these joint structures are believed to evolve due to a floating dipole–dipole field, induced by the donor/acceptor groups bridging the ladder-structure PDA derivatives with a remarkably delocalized π-conjugated backbone and transferred by π–π interactions.[309]

It is worth mentioning that the type of the intra-edge interaction can be modified if the nanoribbon's zigzag edges are decorated with fluoranthene groups.[310] If a single fluoranthene group (FAG) was attached to a zigzag edge, the two FAG-separated segments were predicted to be correlated in an

 This journal is © The Royal Society of Chemistry 2018

Published on 26 March 2018. Downloaded by Univerzita Palackého v Olomouci on 2/28/2019 2:05:03 PM.

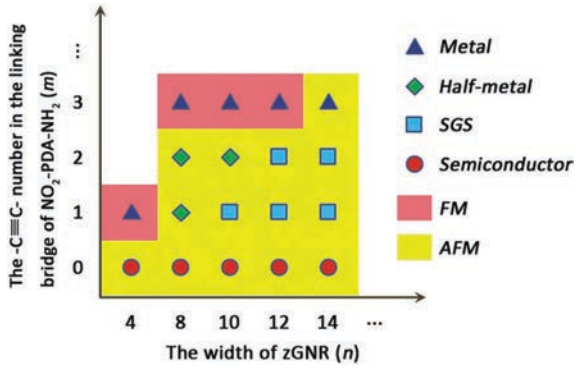


Fig. 46 Influence of the width of zigzag GNRs and the number of $-C\equiv C-$ bonds in the linking bridge on the electronic and magnetic behavior of the n-NO_2–(m)PDA–NH_2 joint systems where n = 4, 8, 10, 12, and 14 and m = 1, 2, and 3. Reprinted with permission from ref. 309. Copyright 2013 WILEY-VCH Verlag GmbH & Co. KGaA.

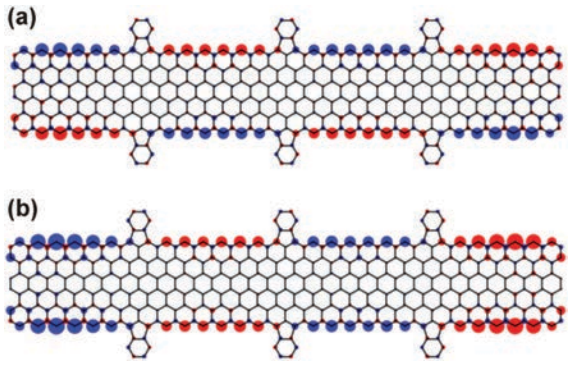


Fig. 47 Calculated profile of magnetization for GNRs with zigzag edges functionalized with several FAGs for (a) ground-state configuration and (b) excited state. Red and blue colors denote the sign of the magnetic moment and the size of the colored ball represents its magnitude. Reprinted with permission from ref. 310. Copyright 2016 American Physical Society.

AFM fashion (see Fig. 47) contrary to the edge-unmodified GNRs in which spins are always ferromagnetically coupled along the zigzag edge. As the introduction of a pentagonal defect breaks down the bipartite nature of the graphene lattice, the relation between the sign of the interaction between the edge spins and the sublattice degree of freedom is no longer valid. In addition, the presence of FAGs can revert AFM inter-edge interactions for sufficiently narrow GNRs. In other words, pentagon defects attached to the zigzag edges of GNRs can be viewed as an agent providing engineering of the spin exchange interactions.[310] Moreover, if only one edge is perturbed with topological defects such as discontinuous patches of pentagons and heptagons, emerging competing magnetic orderings result in spin frustration accompanied by a maximum suppression of magnetic order in the vicinity of these defects at the edge.[311] Thus, the FIM ground state is stabilized due to nonequivalence of the edges. Moreover, depending on the type of localization and spin polarization of the defect-induced edge states, non-uniform energy shifts are predicted to be observed promoted by exchange interactions due to the occupied states of the zigzag GNR localized close to the defect sites. Thus, spatial separation occurs between the states that are localized on the unmodified edge and those sitting at the defect-altered edge.[311] As a result, a complex pattern of occupied and unoccupied frontier bands evolves dictating the magnetic properties of the system. More importantly, the topological defects at the edges can open an energy window for transport of electrons with the minority spin at the edge of the conduction band above a narrow band gap, eventually leading to a half-metallicity feature without the need for involving any non-carbon element.[311]

As radicals and various coupling agents possess unpaired electron(s) and, hence, inherent magnetic moments, functionalizing the zigzag edges with them was suggested as a promising idea to modify the magnetic features of GNRs. The relevance of the proposed concept was theoretically tested for zigzag GNRs with edges terminated with trimethylenemethane (TMM) and 6-oxoverdazyl (OVER) radicals in *syn–syn*, *anti–anti*, and *syn–anti* configurations (see Fig. 48);[312] TMM is an example of a *syn* radical while OVER is classified as an *anti* radical (see Fig. 49). For *syn–syn* and *anti–anti* configurations, the AFM (low-spin) ground state is expected to evolve while for zigzag GNRs terminated with the *syn* radical at one side and the *anti* radical at the opposite side, the FM (high-spin) state is favored with a strong magnetic coupling across the nanoribbon. Furthermore, the spin alternation rule and classification scheme for radicals and couplers were thoroughly described providing identification of such terminating configurations stabilizing the FM ground state.[312]

As edges of GNRs are highly reactive, they can be easily chemically modified under experimental conditions and sample handling. However, such a functionalization of edges may cause suppression or disappearance of their magnetic features. Among several organic compounds considered, C_2H_4 was identified as an ideal terminating group for zigzag GNRs to preserve the edge magnetism.[313] Zigzag GNRs with C_2H_4-terminated edges can be produced under mild experimental conditions with electronic and magnetic properties reproducing those of zigzag GNRs with edges terminated by hydrogen. The enhanced stability of the sp^2 coordinated edges in the C_2H_4-terminated zigzag GNRs was explained in terms of multiple hyper-conjugation interactions. In this context, it was stressed that even a pure sp^2 termination does not need to be a sufficient guarantee for the edge magnetism as, for example, in the case of zigzag edges terminated with C_2H_2, the magnetism is destroyed due to coupling of C_2H_2 terminating groups with the π-electron system of zigzag GNRs.[313] Besides C_2H_4, the pure sp^2 coordinated edge states can be preserved and stabilized by iodine termination.[314] The sp^3 coordination is usually suppressed due to the strong steric effect of iodine atoms.

Similarly to their armchair counterparts, zigzag GNRs can be doped with elements other than boron and nitrogen. The examples include Ni, Ti, and Au atoms.[315–317] In particular, it was proposed that Ni atoms are preferentially located along the zigzag edges; however, their presence quenches the local

Published on 26 March 2018. Downloaded by Univerzita Palackého v Olomouci on 2/28/2019 2:05:03 PM.

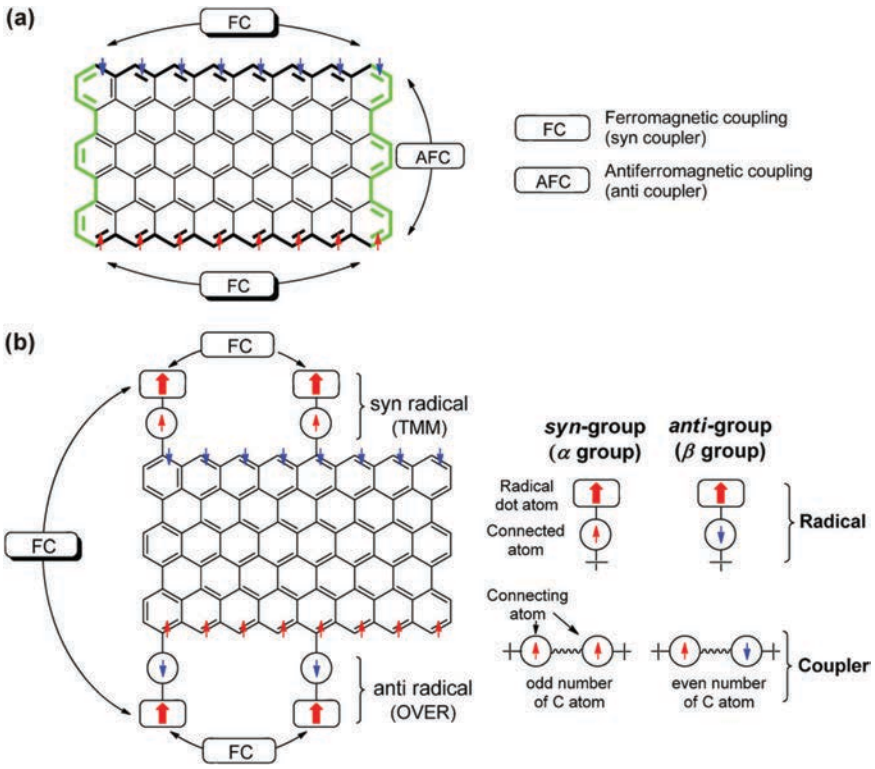


Fig. 48 (a) Scheme showing distribution of spins on each edge of a zigzag GNR (N_z = 8). (b) Scheme showing a ferromagnetically coupled zigzag GNR terminated by a radical and classification of radical couplers into *syn* and *anti* groups. Reprinted with permission from ref. 312. Copyright 2015 American Chemical Society.

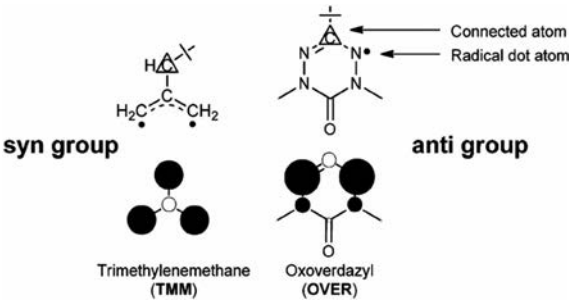


Fig. 49 Structure and spin-density plot of TMM and carbon-connected OVER belonging to the *syn* and *anti* groups, respectively. The hollow and filled circles represent spin-up and spin-down density, respectively. Reprinted with permission from ref. 312. Copyright 2015 American Chemical Society.

magnetic moments of C atoms bound to Ni atoms by a factor of nearly five. The quenching decays fast with distance and is negligible at sites farther than 9 Å from the position of the Ni atom. If Ni atoms are present only at one zigzag edge, AFM coupling between the opposite sides of zigzag GNRs is still preserved. Nevertheless, the adsorbed Ni atoms give rise to d-related states appearing above and below E_F, responsible for spin-dependent transport.[315] A similar effect is observed for Ti atoms which suppress the edge magnetic moments if positioned near the zigzag edge. They are supposed to introduce extra sub-bands showing spin polarization, which neutralizes the magnetic moments of edge carbon atoms.[316] In the case of Au atoms, an FM or AFM ground state was observed depending on the positions of Au atoms in the lattice of zigzag GNRs. The system was found to behave as a spin-gapless semiconductor once Au atoms were placed in the center and edge sites of zigzag GNRs. More importantly, for such a configuration, spin-gapless semiconducting feature is still present irrespective of the nanoribbon's width. Moreover, besides site dependence, the spin-gapless semiconducting behavior was identified to be fine-tuned by impurity atom concentration.[317] Interestingly, the FM ground state can be stabilized by doping zigzag GNRs with planar tetrahedrally coordinated carbon; such defective zigzag GNRs are not only magnetic but are also equipped with metallic features.[318]

Another strategy to alter the magnetic features of zigzag GNRs is to place them on various substrates. Different hybridization between the 2p orbitals of graphene and those of substrates and eventual charge transfer between the surface and zigzag GNR are theoretically predicted to suppress or destroy the edge magnetism. Alternatively, it was suggested that the net magnetization of zigzag GNRs deposited on a substrate is reduced due to inversion of occupied/unoccupied bands (*i.e.*, reordering of edge bands).[319] In this context, it was

 This journal is © The Royal Society of Chemistry 2018

Published on 26 March 2018. Downloaded by Univerzita Palackého v Olomouci on 2/28/2019 2:05:03 PM.

found that the edge magnetic states are not affected only in the case of zigzag GNRs with hydrogen-terminated edges deposited on an Au(111) substrate.[320] Another example involves depositing zigzag GNRs on a zigzag hybrid fluorographene–graphane substrate. The spin-up and spin-down band gaps can then be tuned in the opposite direction by varying the fluorographene-to-graphane ratio in the hybrid substrate. If the interlayer spacing is lowered, a transition from half-semiconducting to half-metallic behavior occurs in zigzag GNRs.[321] For electrically polarized substrates like PTO, the AFM ground state is preserved; the ferroelectric substrate polarization causes only a decrease in the local magnetic moments of all the carbon atoms due to substrate-induced charge transfer.[322]

An electric field is often employed as an external stimulus to alter the magnetic features of zigzag GNRs. For zigzag GNRs with antiferromagnetically coupled opposite sides, it was predicted that in-plane homogeneous electric fields applied across the zigzag edges induce half-metallic behavior.[323] Its origin was explained in terms of the effect of the external electric field on energy levels of the edge states shifting them either up or down depending on the orientation of spins at the particular edge. Due to the antiparallel arrangement of spins at the opposite zigzag edges, the external electric field is supposed to move the occupied and unoccupied β-spin states closer together in energy while further separating the occupied and unoccupied α-spin states (see Fig. 48).[323] As the magnitude of the external magnetic field increases, the electrostatic potential is increased on the right side while it is reduced on the left side of the nanoribbon. As a result, right-sided localized edge states show an upward shift in energy while energies for edge states localized at the left side of the nanoribbon are shifted downwards, leaving eventually states with only one spin direction at E_F (see Fig. 50).[323] In other words, the system becomes conductive for one spin direction while remains insulating for another spin orientation.[323] Such a behavior occurs only if a critical electric field is reached; its value is found to decrease as the nanoribbon's width increases since the electrostatic potential difference between the opposite sides is proportional to the size of the system. Moreover, the critical electric field needed to establish a half-metallic or a non-magnetic state can be reduced if edges are functionalized with suitable functional groups in a configuration with an electron donating group at one edge and an electron withdrawing group at the opposite edge (*e.g.*, O−H/C−N, N−O_2/N−H_2, and O−H/N−O_2).[324] As a result, such functionalized zigzag GNRs are equipped with a perfect spin filtering feature if placed in an external electric field.

Moreover, it was suggested that if the electric field is increased, AFM coupling between the opposite edges is reduced as a result of decreased magnetic moments at the edges. This is reflected in the profile of the spin wave dispersion, indicating potentiality to manipulate the spin wave lifetime by the electric field, without inducing magnetic instability in the system.[325]

Despite their similar electronic band structure and magnetic properties, symmetric and asymmetric zigzag GNRs were found to show different transport behavior under an applied bias voltage; the symmetry/asymmetry of zigzag GNRs is inferred

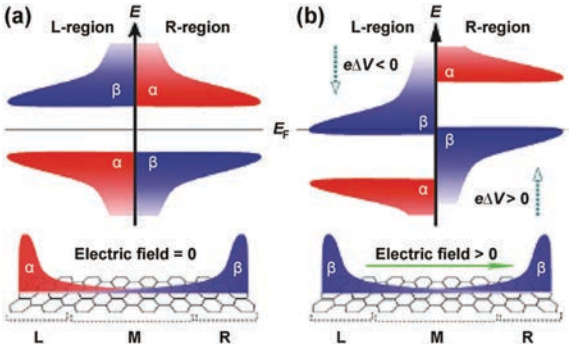


Fig. 50 (a) Diagram of electronic states for zigzag GNRs without application of an external electric field. On the left (L) side, α- and β-spin states represent the occupied and unoccupied localized edge states, respectively, while on the right (R) side, α- and β-spin states represent the unoccupied and occupied localized edge states, respectively. Note that the energy gap is identical at both sides. The bottom plot shows the spatial distribution of spin corresponding to the highest occupied valence band states without application of an external electric field. (b) Diagram of electronic states for GNRs with application of a transverse electric field. With the electric field, the electrostatic potential on the left side of the zigzag GNR is lowered (by $e\Delta V < 0$) while it is increased on the right side of the zigzag GNR (*i.e.*, by $e\Delta V > 0$). The bottom plot shows that only the β-spin states lie at E_F. Reprinted with permission from ref. 323. Copyright 2006 Nature Publishing Group.

from the existence/absence of the mirror plane.[326] While asymmetric zigzag GNRs strictly follow the characteristics of conventional conductors with one conductance quantum under bias voltages, symmetric counterparts show unexpectedly small currents and conductance gap around E_F. The difference in transport properties of asymmetric and symmetric zigzag GNRs was explained in terms of distinct coupling between π and π* sub-bands due to the different nanoribbon's symmetry. Furthermore, the current can be increased for symmetric zigzag GNRs once the symmetry of their electronic structure is broken, *e.g.*, by introducing the asymmetric edge terminations.[326]

Strain is another external parameter providing control over the magnetic response of zigzag GNRs. Recently, it was theoretically shown that if the strain is applied along the zigzag edge, FM behavior can be stabilized and preserved at very high temperatures (~400 K).[327] Enhancement in edge magnetism was explained in terms of reduction of critical Coulomb interaction with increasing strain.[327]

In chiral GNRs, a potential evolution of magnetic behavior was predicted to be dictated by the percentage of carbon atoms at the zigzag edges.[328] If the percentage of carbon atoms with zigzag arrangement equals 50%, chiral GNRs show an AFM semiconducting ground state. In other cases, they behave as spin degenerate semiconductors. The critical chiral angle that guarantees the appearance of spin polarization was theoretically estimated to be 13.9°. The FM state was identified as metastable, the occurrence of which strongly depends on the width of chiral GNRs. Its metastability results from a weaker character of inter-edge FM coupling compared to that of inter-edge AFM interactions.[328] Furthermore, other theoretical data

Published on 26 March 2018. Downloaded by Univerzita Palackého v Olomouci on 2/28/2019 2:05:03 PM.

confirmed that FM interactions among the zigzag segments along nanoribbon's edges become dominant beyond the armchair limit.[329] If the nanoribbon's width increases, AFM inter-edge interactions strongly weaken, leading to correlation lengths comparable with a long-range FM edge response. This is consistent with the appearance of a typical low-energy peak along the nanoribbon's edge, implying formation of enhanced electronic correlations. More specifically, its position in the energy spectrum linearly depends on the interaction strength and chirality angle.[329] In addition, it seems that local magnetization in sufficiently wide chiral GNRs is dominantly governed by chirality with negligible dependence on the nanoribbon's width.[330]

Besides armchair, zigzag, and chiral types, structurally complex GNRs with various heterojunctions were experimentally observed or theoretically predicted. They are commonly classified as hybrid GNRs and are composed of armchair and zigzag segments *via* rotating the cutting direction. They show irregular edge morphologies with a mixture of armchair and zigzag heterojunctions; the most prominent examples include wedge-like zigzag/zigzag (zigzag/armchair),[331] chevron-like armchair/armchair,[332] L-shaped,[333] Y-shaped,[334] Z-shaped,[335] sawtooth-shaped,[336] and cross-shaped[337] junctions. These heterojunctions are believed to affect the carrier scattering and, hence, imprint the electronic and magnetic features onto hybrid GNRs distinct to those of GNRs with ideal armchair or zigzag edges. Their presence in real samples is expected to be unavoidable due to current limitations of traditional production methods including lithographic etching and chemical synthesis.

In general, hybrid GNRs undergo a transition from the non-magnetic to the magnetic semiconducting state by increasing the length of zigzag segments (see Fig. 51).[338] It was theoretically confirmed that introducing the armchair segments as ''impurities'' will not alter the electronic and magnetic features shown by zigzag GNRs. Although the opposite zigzag edges are coupled in an AFM manner, the magnetization on two edges is not equal. The electronic and magnetic properties of hybrid GNRs were found to be tuned not only by the length of the zigzag segments but also by the nanoribbon's width. More importantly, if placed in an external transverse electric field, a half-metallic behavior was expected to appear for magnetic hybrid GNRs.[338]

For sawtooth zigzag-edged GNRs with edges passivated with hydrogen, an FM ground state was proposed irrespective of their size.[339] They behave as magnetic semiconductors whose spin splitting energy is modulated periodically with the nanoribbon's width. Moreover, such structures may show a dual spin-filtering effect with a 100% spin polarization and high-performance dual spin diode effect. More importantly, if sawtooth zigzag-edged GNRs are placed inside the transverse electric field (see Fig. 52), they become spin conductors with spin carriers that are both spin-polarized in energy space and spatially separated at the two opposite edges of GNRs.[340] In other words, electrons of one spin direction conduct the current at one edge while the holes of the other spin orientation conduct the current at the opposite edge with a different energy. In addition,

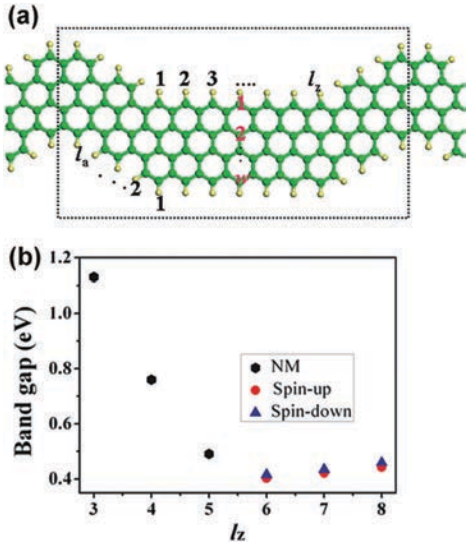


Fig. 51 (a) Structure of hybrid GNRs with a different width (w) and length of armchair (l_a) and zigzag (l_z) segments. Carbon and hydrogen atoms are represented by green and light yellow balls, respectively. One unit supercell in the direction of the nanoribbon's axis is marked with a rectangle. (b) Variation of the band gap on the length of the zigzag segment (l_z). The black dots stand for the band gaps of non-magnetic hybrid GNRs while red dots and blue triangles represent the band gaps of magnetic hybrid GNRs with spin-up and spin-down configurations, respectively. Reprinted with permission from ref. 338. Copyright 2012 American Chemical Society.

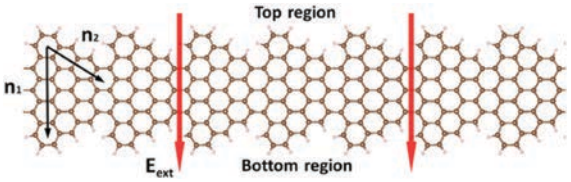


Fig. 52 Structure of a sawtooth zigzag-edged GNR with (n_1, n_2) denoting its size and E_{xt} representing the electric field applied across the sawtooth zigzag-edged GNR. Reprinted with permission from ref. 340. Copyright 2013 American Physical Society.

these states were found to be robust against the edge disorder. Thus, the suggested concept offers another degree of freedom for the manipulation and control of spins in spintronic devices.[340]

Triwing zigzag GNRs consist of three ribbon wings which can be joined together with either sp^2 or sp^3 junctions. The structures with sp^2 hybridized junctions behave as FM metals whose magnetic moments increase with the width of the wing (see Fig. 53a and b).[341] On the other hand, the systems with sp^3 hybridized junctions show features of FIM conductors with a universal magnetic moment equal to 1 μ_B (see Fig. 53c and d). The electric field does not seem to change the metallic behavior of triwing zigzag GNRs with sp^2 hybridized junctions while its application in parallel and perpendicular directions tunes the bands from the *l*-wing or *m*-/*n*-wings, respectively, for the counterparts with sp^3 hybridized junctions. Thus, half-metallicity may

 This journal is © The Royal Society of Chemistry 2018

Published on 26 March 2018. Downloaded by Univerzita Palackého v Olomouci on 2/28/2019 2:05:03 PM.

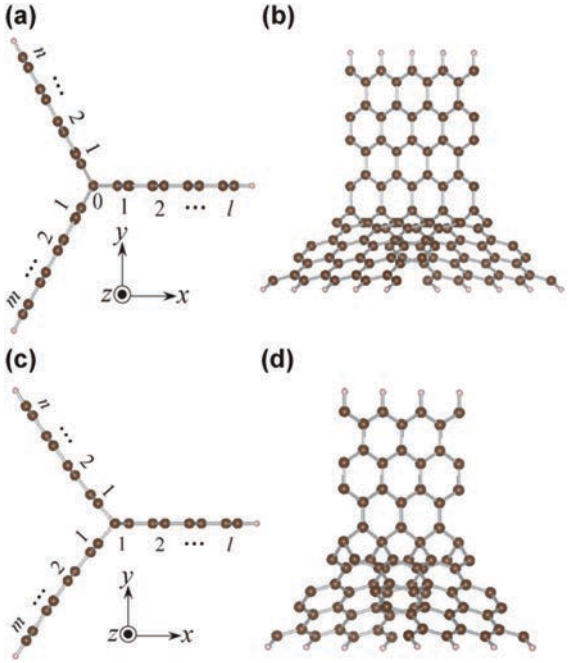


Fig. 53 (a) Top and (b) side views of the geometric structure of a triwing zigzag GNR consisting of three wings joined together *via* a linear carbon array with sp^2 hybridization. (c) Top and (b) side views of the geometric structure of the triwing zigzag GNR composed of three wings joined together *via* their inner edge carbon atoms. Reprinted with permission from ref. 341. Copyright 2012 The Royal Society of Chemistry.

appear for the sp^3-hybridized-junctioned structures.[341] Alternatively, asymmetrical BN doping can induce the half-metallic behavior and suppress the spin polarization of the doped wings.[342]

4.2. Graphene nanoflakes

Graphene nanoflakes (GNFs) are arbitrarily shaped graphene fragments, which are finite in both dimensions; they are sometimes classified as quasi zero-dimensional carbon nanostructures of sp^2 character. They are alternatively termed as graphene nanodisks, graphene nanoplatelets or graphene nanoislands. They are from $\sim$1 to $\sim$50 nm in size and show various regular or irregular shapes. The regularly shaped GNFs resemble the appearance of regular convex polygons such as triangles, squares, rectangles, parallelograms, pentagons, and hexagons. The sides of GNFs consist of purely armchair or zigzag edges or their combinations. Various types of GNFs are schematically shown in Fig. 54.[343] To synthesize them, methods used for the preparation of GNRs are very frequently adopted; most of the synthetic protocols rely on bottom-up approaches starting from molecular carbon-based precursors. However, cutting them to a specific shape is very problematic and needs sophisticated optimization in future procedures. Thus, the magnetic features of GNFs are largely predicted by theoretical studies with very rare confirmations from experimental observations. Theoretically, GNFs are frequently represented by all-benzenoid polycyclic aromatic hydrocarbon molecules.

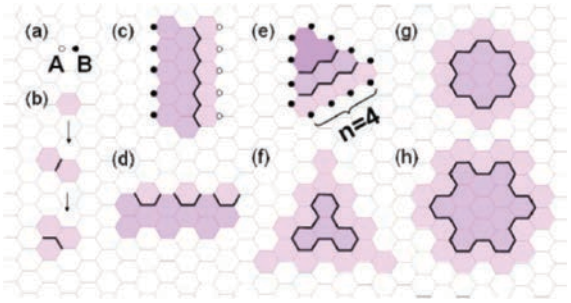


Fig. 54 Various types of GNFs that can be constructed by stitching up (with black lines) from smaller sub-flakes (darker shade): (a) A- and B-sublattice of graphene; (b) GNF formed by stitching up the A–B balanced hexagons; (c) GNF corresponding to zigzag GNR; (d) GNF corresponding to armchair GNR; (e) zigzag-edged triangularly-shaped GNF; (f) armchair-edged triangularly-shaped GNF; (g) zigzag-edged hexagonally-shaped GNF; (h) armchair-edged hexagonally-shaped GNF. Reprinted with permission from ref. 343. Copyright 2008 American Chemical Society.

In this context, a hexagonal fragment can be well described with the model of a coronene molecule whereas a triangular fragment closely resembles the shape of a hypothetical triangulane molecule.

Graphene nanodisks are spatially confined structures with closed edges; they are formed by connecting the benzene rings the number of which defines their size and edge patterns. Typical examples of graphene nanodisks are shown in Fig. 55.[344]

Alike to GNRs, GNFs with zigzag edges show a magnetic ground state as demonstrated by experiments employing the ESR technique.[49] The theory predicts that non-zero net spin exists for triangular GNFs with all the three edges of zigzag nature; the net spin is believed to emerge due to a topological frustration of π-bonds.[243] From a computational viewpoint, GNFs can be constructed by stitching up the sub-flakes as shown in Fig. 54. The stitch is then defined as a single path of bonds merging the two sub-flakes together; an even stitch contains an even number of atoms and *vice versa*. This implies that for an even stitch, the number of A- and B-sites is equal while one extra A- or B-site is present in an odd stitch. Thus, the odd stitch is supposed to create or annihilate one non-bonding state while the number of non-bonding states is not changed for the even stitch. Adopting the proposed counting rule then

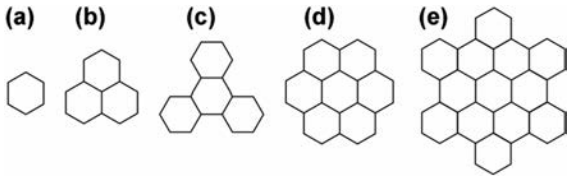


Fig. 55 Various types of graphene nanodisks: (a) benzene; (b) trigonally-shaped zigzag-edged nanodisk (phenalene); (c) trigonally-shaped armchair-edged nanodisk (triphenylene); (d) hexagonally-shaped zigzag-edged nanodisk (coronene); (e) hexagonally-shaped armchair-edged nanodisk (hexabenzocoronene). Reprinted with permission from ref. 344. Copyright 2007 American Physical Society.

Published on 26 March 2018. Downloaded by Univerzita Palackého v Olomouci on 2/28/2019 2:05:03 PM.

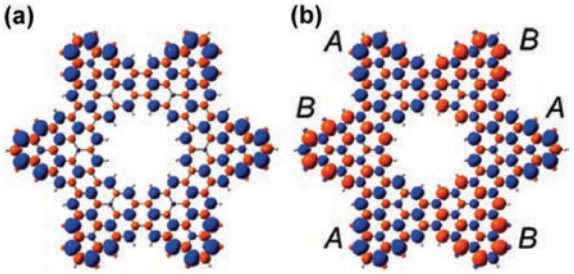


Fig. 56 Two spin configurations of the structure known as the "Star of David" with (a) $S = 3$ and (b) $S = 0$ for an antisymmetric broken-symmetry ground state. Positive and negative spin densities are shown with blue and red, respectively. Regions with dominating A- and B-sublattice are marked with letters A and B. Reprinted with permission from ref. 345. Copyright 2008 American Chemical Society.

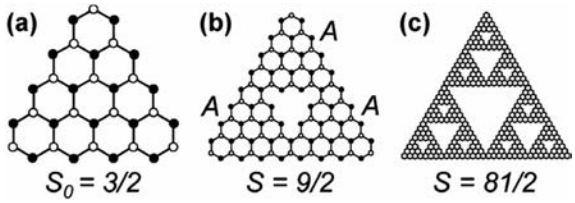


Fig. 57 Suggested Sierpinski sieve fractal structures of GNFs: (a) elementary triangularly-shaped building block; (b) fractal structure with a fractal level of 2; (c) fractal structure with a fractal level of 4. The A- and B-sublattices are denoted with filled and open circles, respectively; the A-sublattice globally dominates. S_0 and S represent the total spin of the fractal structures ($S_q = S_0 3^q$, where q is the fractal level). Reprinted with permission from ref. 345. Copyright 2008 American Chemical Society.

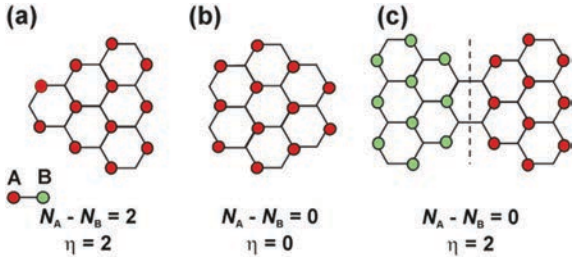


Fig. 58 (a and b) Structures of GNFs belonging to Class I with $\eta = |N_A - N_B|$. (c) Structure of the bowtie-shaped GNF falling into Class II with a zero sublattice imbalance but $\eta = 2$ (*i.e.*, $N_A = N_B = 19$ and $\alpha = 20$). The colored sites conform to a maximum set of non-adjacent sites. Reprinted with permission from ref. 346. Copyright 2009 American Physical Society.

provides constructing GNFs with geometries showing non-zero spin by stitching together hexagonal units with intrinsic zero spin. Moreover, non-bonding states in GNFs and flat edge states in GNRs differ in evolution; non-bonding states originate from singularities of the hopping matrix while flat edge states approach E_F asymptotically due to size effects. As a result, GNRs must have zero spin while GNFs can host a large spin. Non-bonding states are expected to emerge due to topology constraints; they have a half-filled character with a behavior resembling that of the outer shell of an FM atom. In zigzag-edged triangular GNFs, FIM ordering is established between the spins occupying A- and B-sites due to asymmetry in spatial distribution. A "Star of David" structure (see Fig. 56) is another example to accommodate a large spin.[343] It is a fractal that is constructed by repeatedly overlapping two triangles in the opposite direction with the overlap portion removed. The total spin of the "Star of David" structure is found to increase exponentially with the fractal level. The increase in the total spin is related to an increase in the boundary length, which enhances the probability of topological frustrations of π-bonds.[343] However, later calculations for the "Star of David" structure confirmed the existence of broken-symmetry configurations, eventually leading to AFM correlations of locally spin-polarized regions and zero net spin. Thus, other fractal structures – with a spin-polarized triangular fragment as a building unit – were proposed to host the large spin (see Fig. 57); they can be drafted adopting the Sierpinski sieve construction.[345]

Based on their magnetic behavior, GNFs are classified into two main categories, *i.e.*, finite structures with a large net spin and systems with AFM coupling between groups with an electron spin (see Fig. 58).[346] To classify them, a criterion of topological frustration is followed. The topological frustration emerges once all the p_z orbitals cannot be simultaneously paired in a given structure. GNFs with one sublattice showing topological frustration are grouped into Class I. For such structures, $\beta = \min\{N_A, N_B\}$, where β is the maximum number of non-adjacent edges and N_A and N_B are the number of carbon atoms on the A- and B-sublattice, respectively.[346] The number of zero-energy eigenstates, termed as nullity (*i.e.*, $\eta = \alpha - \beta$, where α is the maximum number of non-adjacent vertices), is given as $\eta = |N_A - N_B|$. In other words, if the sublattices are balanced, *i.e.*, $N_A = N_B$, η is zero. All highly symmetric forms of GNFs fall into Class I. Class II includes GNFs with both sublattices topologically frustrated. For such structures, $\beta \leq \min\{N_A, N_B\}$, implying that $\eta > |N_A - N_B|$.[346] The nullity is finite even for GNFs showing balanced sublattices. Further considering the Lieb's theorem, the total spin of the magnetic ground state of GNFs in Class I and II is given as $S = \eta/2$ and $S < \eta/2$, respectively. In other words, all spins in singly occupied orbitals are aligned in a parallel manner for structures belonging to Class I while AFM ordering is expected for structures of Class II.[346] Here, it should be stressed that except for the topological frustration, AFM coupling can arise from polarization of the low-energy states which approach E_F upon increasing the size of the system. Such an effect cannot cause evolution of the net spin; the energy of the non-interacting eigenstates is not E_F (with an exception for infinite systems) and the magnetic ordering develops only in the case where the interaction energy exceeds a positive threshold value, *i.e.*, when a critical size of a system is reached as valid for GNRs or hexagonal GNFs.[346]

For triangularly-shaped GNFs with zigzag edges (see Fig. 59a),[91] the total spin is always non-zero for all sizes; such systems are described as metallic ferromagnets. The states with zero energy are localized on one sublattice (*i.e.*, A-sublattice) and the magnetic ground state has a finite spin given as

 This journal is © The Royal Society of Chemistry 2018

Published on 26 March 2018. Downloaded by Univerzita Palackého v Olomouci on 2/28/2019 2:05:03 PM.

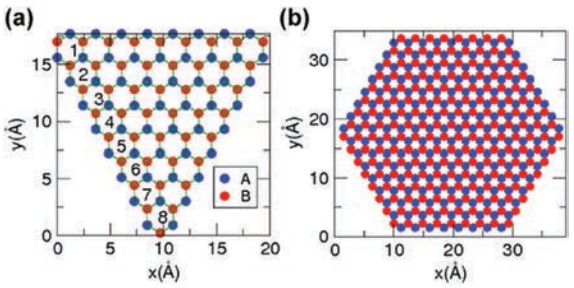


Fig. 59 Structure of (a) triangularly-shaped and (b) hexagonally-shaped GNFs. Reprinted with permission from ref. 91. Copyright 2007 American Physical Society.

$S = (N_A - N_B)/2$ for interactions included. In other words, zigzag triangular GNFs have an excess of unpaired electrons on one sublattice the number of which increases as the nanoflake's size increases. Thus, an FM ground state is expected as all the three zigzag edges are coupled in an FM manner.[347] Note that all the carbon atoms are spin-polarized. On the other hand, GNFs with a hexagonal shape and zigzag edges (see Fig. 59b) show $S = 0$, implying a potential AFM ground state.[91] For smaller hexagonally-shaped GNFs, hybridization is strong, thus avoiding evolution of magnetic ordering. However, if a critical size of hexagonal GNF is exceeded, exchange interactions become strong enough to magnetize the edges. Thus, local magnetic moments emerge above the critical size which was predicted to be equal to 1.5 nm. In other words, below a size of 1.5 nm, hexagonal GNFs behave as paramagnets while they become ferrimagnets if their size is larger than 1.5 nm.[91]

GNFs with zigzag edges can be classified whether they show lattice imbalance (*i.e.*, $N_A \neq N_B$) or not (*i.e.*, $N_A = N_B$).[348] In particular, triangularly- and pentagonally-shaped GNFs belong to the $N_A \neq N_B$ group, while rhombohedrally- and hexagonally-shaped GNFs fall into the $N_A = N_B$ class (see Fig. 60).[348] GNFs with sublattice imbalance can be non-magnetic or exhibit a fully compensated magnetic ordering satisfying $S = 0$. Such GNFs may undergo a quantum transition upon a change in their size. Actually, if the size of the sublattice-balanced GNFs exceeds a threshold value, a transition to a magnetic state occurs; the new structure shows attributes of FIM nature. The critical size, at which the sublattice-balanced GNFs adopt a new magnetic ordering, is dictated by the armchair defect concentration. In order words, uncompensated spins suddenly develop beyond the critical size of GNF.[348] In contrast, sublattice-imbalanced GNFs are always magnetic regardless of their size. In particular, for triangular GNFs, the inter-edge coupling is of FM nature. In pentagonal GNFs, viewed as an integration of triangularly- and hexagonally-shaped finite systems, the commensurate magnetic structure is predicted when identical and different sublattices are coupled in an FM and AFM manner, respectively.[348] Upon doping with charge carriers, a transition from the AFM to FM regime is expected for sublattice-balanced GNFs while for sublattice-imbalanced GNFs, the magnetic response is suppressed, eventually vanishing for high charge carrier concentration.[348]

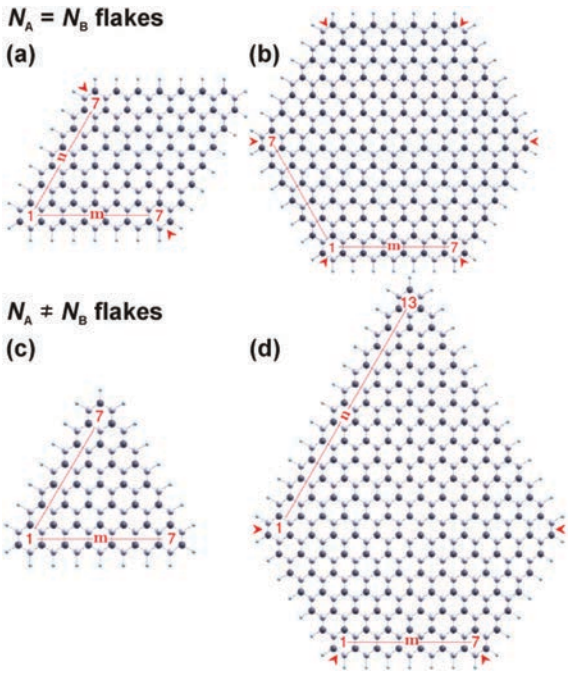


Fig. 60 Structure of (a) rhombohedrally-shaped, (b) hexagonally-shaped, (c) triangularly-shaped, and (d) pentagonally-shaped GNFs. Carbon atoms which belong to the two sublattices are marked with black and white. The nanoflake's size is determined by the number of hexagonal rings along the edge. Armchair defects are highlighted by red arrows and their number is equal to 2, 6, 4, and 0 for rhombohedrally-shaped, hexagonally-shaped, pentagonally-shaped, and triangularly-shaped GNFs, respectively. Reprinted with permission from ref. 348. Copyright 2017 American Physical Society.

Besides changes in magnetic features of both sublattice-balanced and sublattice-imbalanced GNFs, their electronic structure is altered if charge carriers are introduced into their lattice. In particular, initially semiconducting sublattice-balanced GNFs become metallic while in sublattice-imbalanced GNFs, a transition from semiconducting to half-metallic behavior and from semiconducting through half-metallic to metallic regime is predicted to occur for triangular and pentagonal members, respectively. More interestingly, a fully polarized spin transport is expected in the half-metallic state.[348] Similarly, spin-polarized currents were predicted for pure-hydrogenated rectangular GNFs if the electrodes are connected to the nanoflake partially along the zigzag-edge directions or if transition metal adatoms (*e.g.*, vanadium) are introduced over the nanoflake's surface, altering the symmetry in the spin-dependent scattering rates of the transmitted electrons.[349]

Other theoretical works have proposed that due to a different spin polarization at the A- and B-sublattice, zigzag triangular GNFs show a FIM structure as a ground magnetic state.[350] If foreign atoms (such as B, N, O, and F) are introduced into the lattice of zigzag triangular GNFs, they preferentially occupy the sublattice forming the edge. If GNFs are doped with boron and nitrogen, the net magnetic moment is reduced irrespective of

Published on 26 March 2018. Downloaded by Univerzita Palackého v Olomouci on 2/28/2019 2:05:03 PM.

the doping site.[350] In the case of oxygen and fluorine, both an increase and a decrease in the net magnetic moment were observed depending on the doping position.[350] The enhancement/reduction in the magnetic response was explained in terms of different behaviors of the dopants and the interactions between the dopants and the neighboring carbon atoms (especially those sitting on the edge-forming sublattice). A perfect spin filtering effect was proposed for the undoped and boron-doped zigzag triangular GNFs, for which majority states are conducting.[350] In contrast, minority states are conducting for nitrogen-, oxygen-, and fluorine-doped systems, implying that the type of the spin conduction channel can be selected by appropriate doping.[350]

For hexagonal GNFs with zigzag edges, the theoretical calculations identified an AFM structure as a ground magnetic state (see Fig. 61a).[351] If doped with charge carriers (*i.e.*, holes and electrons), the FM state (see Fig. 61b) or mixed phase states are expected to evolve due to the competition between carrier doping (favoring FM coupling) and on-site Coulomb interactions (favoring AFM coupling).[351] In other words, at half-filling, a fully compensated AFM state is expected considering the potential energy gain characteristic of the weak-coupling mechanism. Upon injection of the charge carriers into the hexagonal GNFs, a magnetic state with an uncompensated net magnetic moment is stabilized as a result of effective FM exchange coupling among the ordered spins which is mediated by the introduced charge carriers localized in the proximity of the edges.[352] Alternatively, the encouragement of FM coupling over the AFM ground state can be understood in terms of contribution from indirect charge carrier mediated RKKY interactions once an odd number of charge carriers is doped/removed into/from the nanoflake. Such an alteration in the magnetic coupling involving impurities and their neighbors is, however, predicted to happen only for some geometries of hexagonal GNFs.[353] The magnetic phase diagram then becomes richer once the edges of zigzag hexagonal GNFs are functionalized with hydrogen; AFM, FM, mixed, and non-magnetic phases can appear depending on the level of doping and strength of the on-site Coulomb interaction (see Fig. 62). More importantly, if the temperature is increased, FM solution is more favored for both pure and carrier-doped zigzag hexagonal GNFs,[351] confirming its temperature stability as observed experimentally up to room temperature.[354]

As clearly seen above, hydrogen is viewed as a powerful agent to tune electronic and magnetic features of GNFs.[355] For both hexagonal and triangular GNFs with zigzag edges, increasing content of hydrogen activates a sequential transition from a behavior of a small-gap semiconductor through half-metal to a wide-gap semiconductor. Besides, raising the level of hydrogenation causes the occurrence of a magnetic transition from the FM to the non-magnetic state for triangular GNFs and from the AFM through FM to the non-magnetic state for hexagonal GNFs (see Fig. 63). The non-magnetic behavior for fully hydrogenated GNFs is expected as all the carbon π-bonds become saturated, leaving no unpaired electron.[355] If GNFs of both shapes are half hydrogenated, strong spin polarization arises

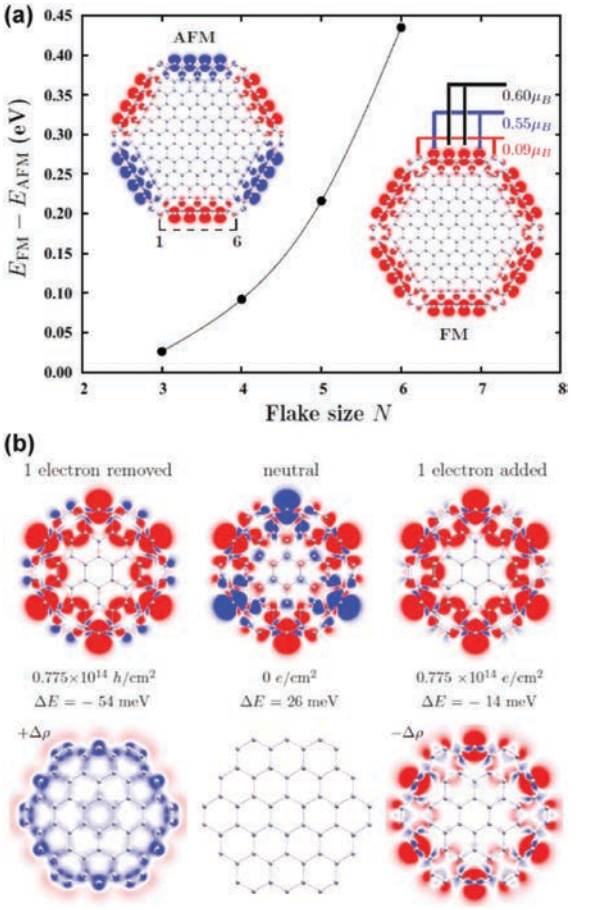


Fig. 61 (a) Evolution of the energy difference between the AFM ground state and the excited FM state upon increasing the size of the hexagonally-shaped zigzag-edged GNF without any charge doping. Red and blue color correspond to the spin-up and spin-down density, respectively. (b) Spin-density plots for the hexagonally-shaped zigzag-edged GNF for cases when one electron is removed (*i.e.*, a hole is introduced; upper left), system is neutral (upper middle), and one electron is doped (upper right). Again, red and blue color indicate spin-up and spin-down density, respectively. The bottom panel displays the difference in charge density between the neutral and charge-doped GNFs. It is worth mentioning that the doped carrier (hole or electron) is distributed only along the edges of the hexagonally-shaped zigzag-edged GNF. Reprinted with permission from ref. 351. Copyright 2014 American Physical Society.

around E_F, manifested by a large net magnetic moment which scales with a power of two with the nanoflake's size. The induced spin magnetizations are found to align parallel, showing a collective character promoted by a long-range magnetic coupling; such GNFs can act as spin filters.[356]

Within the family of nanodisks, trigonal zigzag members were found to show half-filled degenerate zero-energy states, behaving as metallic ferromagnets.[344] The degeneracy can be tuned arbitrarily by changing the nanodisk's size. Moreover, the relaxation time of these systems is quite long at low temperatures, depending on their size.[344]

 This journal is © The Royal Society of Chemistry 2018

Published on 26 March 2018. Downloaded by Univerzita Palackého v Olomouci on 2/28/2019 2:05:03 PM.

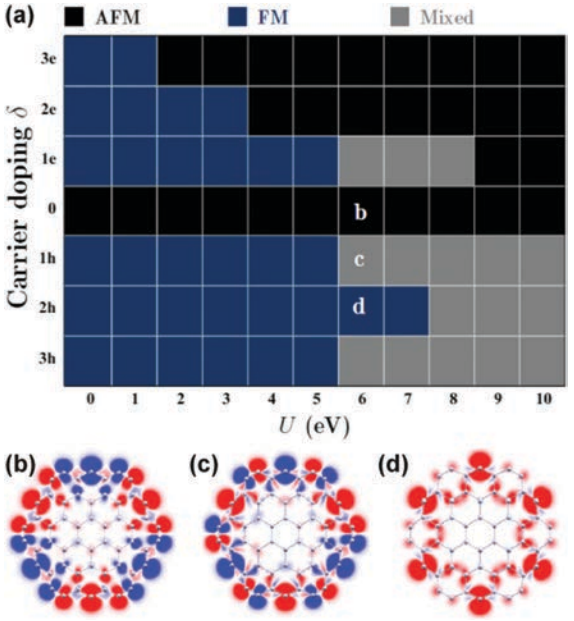


Fig. 62 Magnetic phase diagram as a function of varied on-site Coulomb interaction (U) and charge doping (δ) for a hexagonally-shaped zigzag-edged GNF (with N = 3). Representative spin-density plots for (b) AFM, (c) mixed, and (d) FM configurations (for U = 6 eV). Reprinted with permission from ref. 351. Copyright 2014 American Physical Society.

Bowtie-shaped GNFs (see Fig. 64) are peculiar systems with an immense potential as a molecular switch.[357] Their structure consists of two triangular GNFs with zigzag edges oppositely oriented and connected with a hexagon. Zero-energy states are supposed to evolve; they are spin-polarized due to the Coulomb repulsion between electrons. Bowtie-shaped GNFs show an AFM ground state with S = 0 (*i.e.*, zero net spin) when the direction of the spin of a carbon atom is opposite to that of its nearest neighbors. In the AFM ground state, spin-up and spin-down components are symmetric; the occupied spin-up energy levels are localized in the left triangle while the occupied spin-down energy levels lie in the right triangle of the bowtie-shaped GNF (see Fig. 65).[357] Identically, unoccupied spin-up and spin-down energy levels are found in the left and right triangles of the bowtie-shaped GNF, respectively. In contrast, in the FM state, the spin-up and spin-down energy levels are delocalized and distributed over the whole bowtie-shaped GNF (see Fig. 65). As a result, FM bowtie-shaped GNFs show a perfect spin filtering effect with a much higher conductance contrary to their AFM counterparts.[357] Moreover, if exposed to an external magnetic field, bowtie-shaped GNFs undergo an AFM-to-FM transition, acting as a switch from an OFF to ON state.[357,358] If bowtie-shaped GNF is doped with a single charge carrier, the FIM ground state is favored; in such a case, a sequential transition from the FIM to metamagnetic and, eventually, to the FM state is expected to occur upon an increase in the external magnetic field. The value of the critical transition-inducing field depends on the nanoflake's size; it decreases upon an increase in the size of the system. Moreover, the critical fields are believed to be affected more significantly by an off-diagonal disorder in contrast to a diagonal disorder, resulting in a substantial widening of the critical-field-distribution.[358] Conversely, if the bowtie-shaped GNFs are placed in an external electric field, the AFM ground state is destroyed; the non-magnetic behavior is

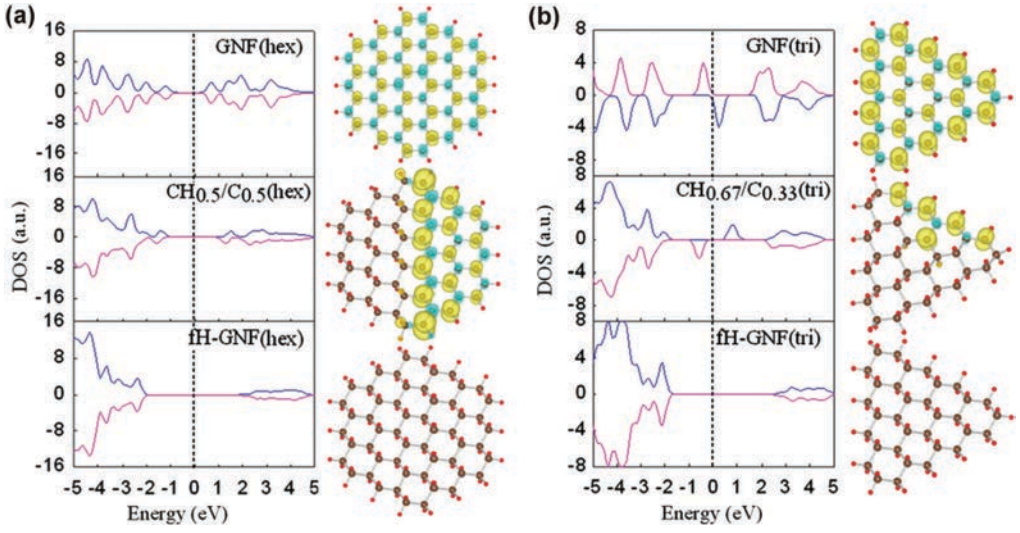


Fig. 63 Spin-polarized density of states and the isosurface of spin-polarized charge density for (a) differently hydrogenated hexagonally-shaped GNFs (*i.e.*, non-hydrogenated, half-hydrogenated ($CH_{0.5}/C_{0.5}$), and fully hydrogenated GNFs) and (b) differently hydrogenated triangularly-shaped zigzag-edged GNFs (*i.e.*, non-hydrogenated, extendedly ($CH_{0.67}/C_{0.33}$), and fully hydrogenated GNFs). H and C atoms are represented by red and brown balls, respectively. Yellow and blue isosurfaces correspond to the values of +0.006 e Å^{-3} and −0.006 e Å^{-3}, respectively. Reprinted with permission from ref. 355. Copyright 2013 Elsevier B.V.

Published on 26 March 2018. Downloaded by Univerzita Palackého v Olomouci on 2/28/2019 2:05:03 PM.

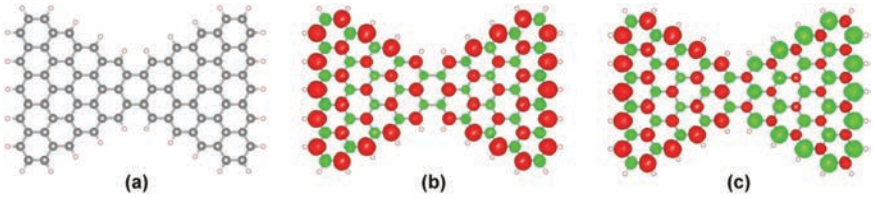


Fig. 64 (a) Structure of a bowtie-shaped GNF. Spin density for (b) FM and (c) AFM bowtie-shaped GNF. Red and green color indicate spin-up and spin-down orientation, respectively. Reprinted with permission from ref. 357. Copyright 2012 American Institute of Physics.

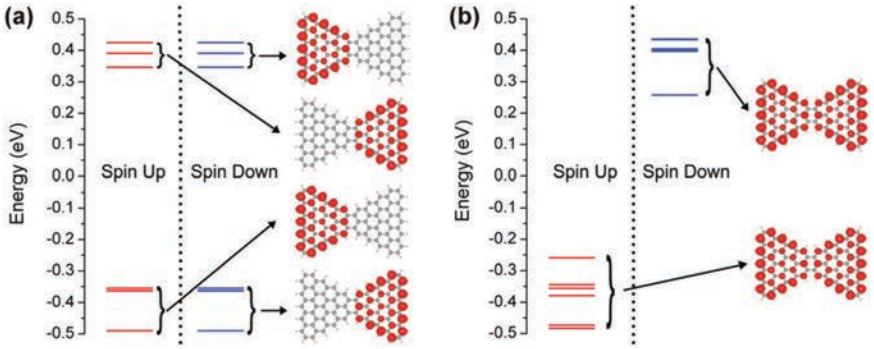


Fig. 65 Energy level spectra for (a) AFM and (b) FM bowtie-shaped GNFs. Reprinted with permission from ref. 357. Copyright 2012 American Institute of Physics.

favored after reaching a critical value of the applied electric field. Surprisingly, upon an increase in the electric field, the FM ground state was not observed at all as for GNRs. The occurrence of the AFM-to-non-magnetic transition was explained in terms of breaking the sublattice symmetry, eventually bringing enough energy to split the originally degenerate zero-energy states.[359] Moreover, the number of zero-energy states can be well controlled by asymmetric connection of the two zigzag-edged triangular GNFs in the bowtie-shaped arrangement; the level of topological frustration, varying the nullity, was found to modulate the strength of AFM coupling between the two zigzag-edged triangular GNFs.[360]

Alternatively, the two zigzag triangular GNFs can be connected together with chains of carbon atoms (see Fig. 66).[361] The two GNFs then interact in an FM manner if the chains are composed of an odd number of carbon atoms. In the case of an even number of carbon atoms, no coupling is established between the two GNFs. Such a behavior can be understood considering the singlet–triplet rule for a chain of carbon atoms, the anti-pattern rule for a magnetic bipartite graphene structure, and the Lieb-Mattis criterion determining the total magnetic moment.[361] Note that the singlet–triplet rule elucidates the ground state of a single hydrogen-terminated chain of carbon atoms; for odd or even number of carbon atoms, the chain shows a triplet or singlet ground state, respectively. Zigzag triangular GNFs can be assembled to form two-dimensional structures when individual GNFs in the network are linked by 1,3,5-benzenetriyl units.[362] Such a two-dimensional system behaves as a ferromagnet; the magnetic moments of the zigzag

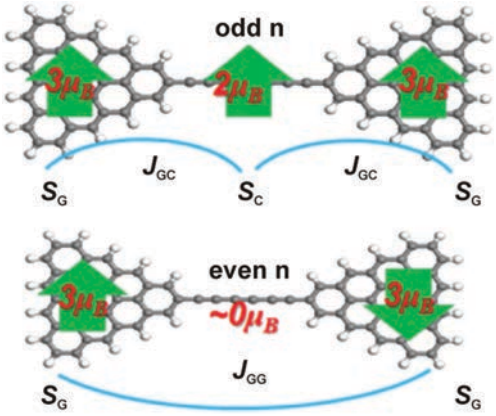


Fig. 66 Schematic representation of the two triangularly-shaped zigzag-edged GNFs connected with an odd and even number (n) of carbon atoms in a linear chain. J_{GC} denotes the exchange integrals characterizing the magnetic interaction between the carbon atom chain and GNFs on opposite sides, J_{GG} is the exchange integral characterizing the magnetic interaction only between the two GNFs on the opposite side of the carbon atom chain, and S_G and S_C are the total magnetic moments of GNFs and the carbon atom chain, respectively. The green arrows indicate the orientation and total magnetic moment carried by each triangularly-shaped zigzag-edged GNF. Reprinted with permission from ref. 361. Copyright 2011 American Physical Society.

triangular GNFs increase with their size. More importantly, if the carbon atoms at the zigzag edges of triangular GNFs are doubly hydrogenated, the strength of the magnetic interaction

 This journal is © The Royal Society of Chemistry 2018

Published on 26 March 2018. Downloaded by Univerzita Palackého v Olomouci on 2/28/2019 2:05:03 PM.

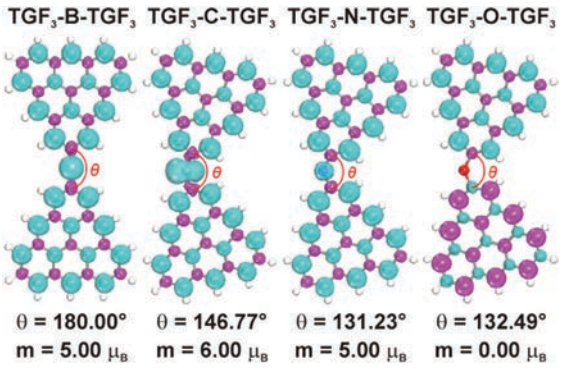


Fig. 67 Spin-density isosurfaces of two zigzag-edged triangular GNFs (with a length N = 3; TGF_3) connected together with B, C, N, and O atoms. θ denotes the angle between the linking atom and its nearest two carbon atoms and m represents the magnetic moment of the structure. The different colors indicate the opposite spin orientations; the magnetic moment was identified to originate mainly from 2p orbitals of the C atoms. Reprinted with permission from ref. 363. Copyright 2012 IOP Publishing Ltd and Deutsche Physikalische Gesellschaft.

among GNFs is enhanced stabilizing the FM state over the whole structure.[362]

Triangular GNFs with zigzag edges were theoretically used as building units to construct two-dimensional superstructures known as magnetic kagome lattices.[363] In particular, C, O, B, and N atoms served as bridging atoms (see Fig. 67). The ground magnetic state of designed kagome lattice was found to strongly depend on the chemical nature of the linking atom and lattice's size. If linked with C, B, and N atoms, zigzag-edged triangular GNFs interacted in an FM manner while an AFM coupling was favored for O as a linking atom. In other words, C, B, and N atoms were identified as mediators of FM coupling, the strength of which can be varied by changing the size of the zigzag-edged triangular GNFs and the bridging atom. Such two-dimensional kagome lattices, semiconducting in nature, were predicted to show a Curie transition temperature above 300 K and could be thus well suited for spintronic applications.[363]

Besides a perfect spin filtering effect and giant magnetoresistance,[364] a magnetoelectric effect is another application-promising phenomenon that was predicted to emerge in GNFs if deposited on a suitable substrate. In particular, it involves induction of magnetization by an electric field and induction of polarization by a magnetic field. To study the magnetoelectric effect, $C_{13}H_9$ as the smallest magnetic GNF was suggested as a model system.[365] The magnetoelectric effect was found to strongly depend on the chemical activity of the substrate affecting the distribution of the electronic states around E_F of GNF by interlayer interactions. In particular, a non-linear magnetoelectric effect observed in GNFs evolved from the interaction with the graphene substrate (see Fig. 68).[365] If an h-BH sheet was inserted between the GNF and graphene support, the magnetoelectric effect showed a linear nature accompanied by an enhancement of its coefficients (see Fig. 69).[365]

Experimentally, the issue of origin of magnetism in GNFs was addressed by the ESR technique; the surface areas of

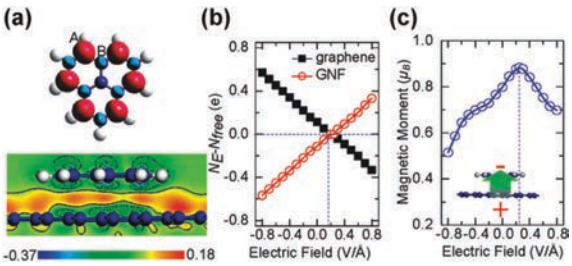


Fig. 68 (a) Spin density of GNF (*i.e.*, $C_{13}H_9$; magenta color for spin-up and light blue color for spin-down orientation) and charge redistribution induced by adsorbing GNF onto graphene (with red and blue colors indicating charge accumulation and depletion regions, respectively). (b) Amount of transferred electrons in the GNF and graphene in dependence on the strength of the electric field. (c) Dependence of the net magnetic moment of the GNF on the strength of the electric field. The inset in panel (c) shows the structure of the GNF lying on the graphene substrate with the bias electric field (green and gray balls marking carbon and hydrogen atoms, respectively). Reprinted with permission from ref. 365. Copyright 2012 American Chemical Society.

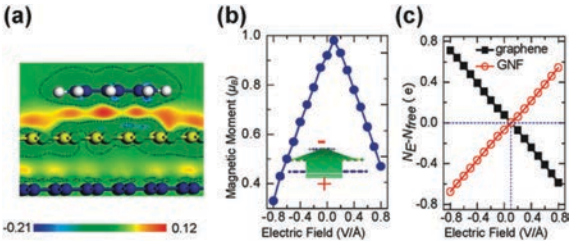


Fig. 69 (a) Charge redistribution induced by adsorbing the GNF (*i.e.*, $C_{13}H_9$) on h-BN-sheet/graphene with red and blue colors indicating charge accumulation and depletion regions, respectively (blue, green, yellow, and gray balls used for representation of carbon, nitrogen, boron, and hydrogen atoms, respectively). (b) Dependence of the net magnetic moment of the GNF on the strength of the electric field with the inset showing the structure of the GNF on the h-BN-sheet/graphene substrate with the bias electric field. (c) Variation in amounts of transferred electrons in the GNF and graphene as a function of the strength of the electric field. Reprinted with permission from ref. 365. Copyright 2012 American Chemical Society.

synthesized GNFs were ≤ 1 μm^2. The analysis of ESR spectra identified a broad component showing a transition to the FM state at 25 K as demonstrated by changes in the intensity and linewidth of the signal and g-factor. Assisted with DFT calculations considering various extended defects (*e.g.*, sheet edges, zigzag chains of chemisorbed H atoms, pentagon–octagon rows), the magnetic moments were proposed to evolve at C atoms in their vicinities. At low temperatures, FM coupling then develops among the magnetic moments emerging due to the H-saturated C atoms.[49]

4.3. Graphene quantum dots

Graphene quantum dots (GQDs) are finite carbon nanostructures with sizes ranging from 2 to 20 nm; they are classified as 0D carbon nanoallotropes.[5] They are composed largely of sp^2 hybridized carbon atoms, are crystalline and monolayered.

Published on 26 March 2018. Downloaded by Univerzita Palackého v Olomouci on 2/28/2019 2:05:03 PM.

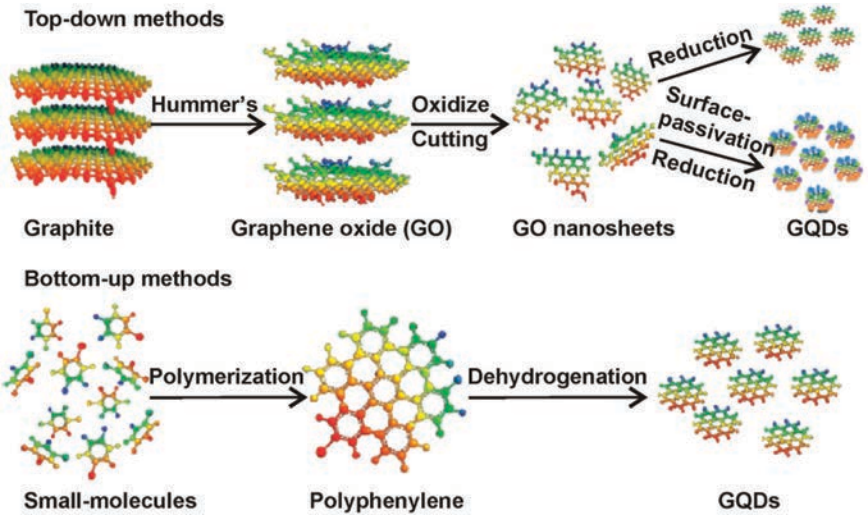


Fig. 70 Top-down and bottom-up procedures for the synthesis of GQDs. Reprinted with permission from ref. 366. Copyright 2012 The Royal Society of Chemistry.

However, in practice, they often consist of a few stacked graphene monolayers due to graphitic nanosheet nature of the precursors. Their physical properties are driven by quantum confinement and edge effects; the most prominent feature includes size- and functionalization-tunable photoluminescence.[5]

Several synthetic methods were developed for preparing GQDs. In general, they fall into two groups, *i.e.*, top-down and bottom-up approaches (see Fig. 70).[366] A general feature of all the top-down methods is to cut graphene sheets into GQDs; they include chemical ablation, electrochemical oxidation, and oxygen plasma treatment. As a starting material to cut, carbon black, coal, graphite, graphite fibers, single-walled and multi-walled carbon nanotubes, graphene or graphene oxide are used. In bottom-up methods, GQDs are assembled from small aromatic molecules.[5]

In many aspects, the magnetic properties of GQDs are identical to those of GNFs. In particular, the ground magnetic state depends strongly on the size, geometry, and symmetry of GQDs.[367] It was theoretically predicted that the magnetic response in GQDs emerges due to electron edge states with energy location within the finite-size quantization pseudo-gap.[368] Two types of edge states, *i.e.*, the zero-energy states and dispersed edge states, then determine the magnetic ground state of GQDs. While zero-energy states are related to the existence of a spin, the presence of dispersed edge states with almost zero energy establishes a diamagnetic behavior. Thus, GQDs (hexagonal, circular, and arbitrarily shaped) which contain mainly dispersed edge states are found to be diamagnetic. The susceptibility of variously shaped GQDs (with sizes from 2 to 7 nm) is shown in Fig. 71.[368] The shaded regions in the plots correspond to the pseudo-gap. The results presented in Fig. 71 match the analytical calculations of previously reported studies for a graphene sheet with a band gap of 2Δ.[226,369] The zero-energy states located at the zero-energy Dirac point are responsible for the Curie paramagnetism and are found in the triangular GQDs. The small triangular GQDs show spin paramagnetism at low temperatures, while orbital magnetism dominates at high temperatures for bigger triangular systems.

Among GQDs with various shapes, those with triangular appearance and zigzag edges have caught significant attention with regard to their magnetic behavior. Zigzag triangular GQDs show an FM ground state; however, its robustness against thermal fluctuations is heavily questioned as it can be destroyed even at low temperatures. Moreover, the FM ground state in triangular GQDs is predicted to be destabilized upon introduction of sufficiently strong disorder. The loss in magnetization is ascribed both to the bulk and edge disorder; while the bulk disorder alters the density of states around the van Hove singularities, the edge disorder affects the energy states in the vicinity of E_F where the edge states appear.[370] Similarly, the FM ground state in zigzag triangular GQDs can be ruined by edge reconstruction.[371] The theory predicts that triangular GQDs with pentagon–heptagon edges (see Fig. 72) are more stable than those with perfect zigzag edges in the absence of hydrogen passivation. If the zigzag edges are passivated with hydrogen, the stability of triangular GQDs significantly increases; they become more energetically favorable than those with reconstructed edges. If the edge reconstruction occurs, the band with zero-energy states still exists; however, the distinction between the two sublattices is smeared out. Moreover, due to a reduction in the symmetry of GQD upon edge reconstruction, the band with zero-energy states shows an increased dispersion. The mixing of the two sublattices then lowers the splitting between the spin-up and spin-down bands. These two effects appearing simultaneously are believed to be responsible for the loss of the net magnetization.[371] In contrast, for triangular GQDs with ideal zigzag edges, the splitting between the spin-up and spin-down energy states is always larger even though the dispersion of the zero-energy band increases with an increase in GQD size.

 This journal is © The Royal Society of Chemistry 2018

Published on 26 March 2018. Downloaded by Univerzita Palackého v Olomouci on 2/28/2019 2:05:03 PM.

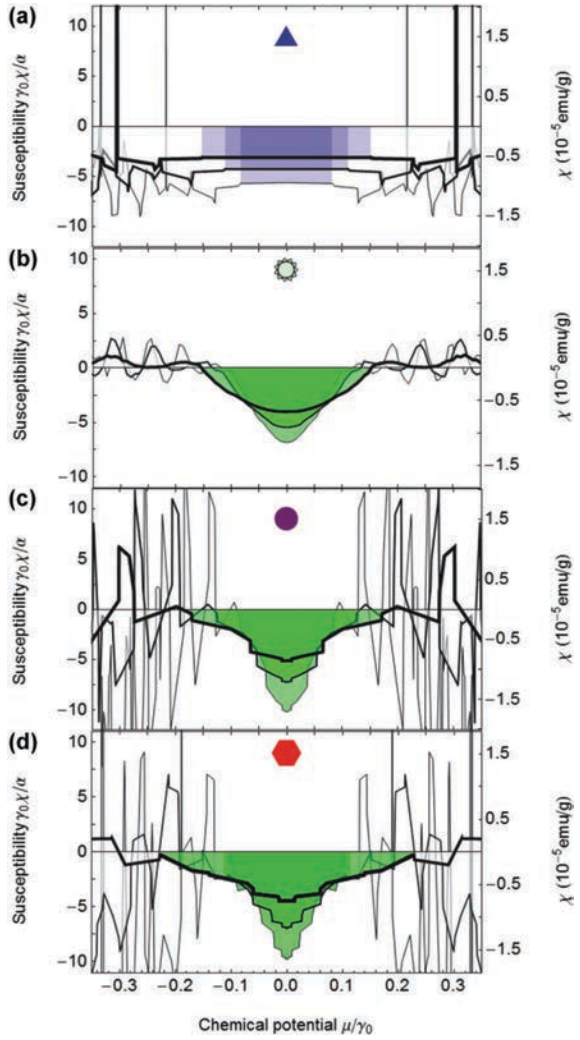


Fig. 71 Susceptibility of 2–7 nm sized GQDs with (a) triangular, (b) random, (c) circular, and (d) hexagonal shape. The pseudo-gap is indicated by the shaded regions. Reprinted with permission from ref. 368. Copyright 2013 American Physical Society.

This implies that magnetism in triangular GQDs with perfect zigzag edges should survive even for infinitely large dot-based systems.[371] Indeed, the magnetism originating from the zigzag edges in GQDs was found to be robust against imperfections such as the presence of other types of edges (regular or irregular) and random terminations. In particular, it was shown that the shape irregularities do not destroy the edge-state magnetism if the zigzag edges in GQDs are longer than three to four repeating units.[372]

On the other hand, if exposed to strain, FM correlations in GQDs with zigzag edges are significantly enhanced.[367,373] The strengthening of FM interactions is predicted to result from altering the nearest-neighbor hopping integrals upon increase in the strain. At the same time, the local magnetic moments in

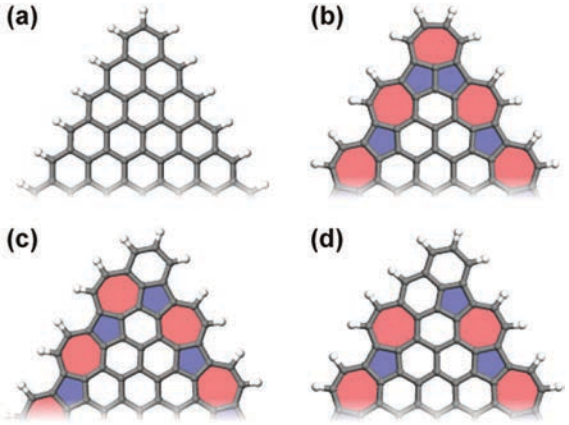


Fig. 72 Triangular GQDs with (a) ideal zigzag edges, (b) reconstructed edges with a pentagon–heptagon–pentagon corner, (c) reconstructed edges with a heptagon–hexagon–pentagon corner, and (d) reconstructed edges with a hexagon–hexagon–pentagon corner. Reprinted with permission from ref. 371. Copyright 2011 American Physical Society.

the ground state are modified and can drift from the zigzag to the armchair edges in the rectangularly-shaped GQDs.[368]

It was theoretically demonstrated that magnetic moments emerging at the zigzag edges of GQDs can be significantly affected by the intrinsic spin–orbit interaction.[374,375] Magnetic anisotropy, driven by spin–orbit coupling, was then found to determine the arrangement of magnetic moments at the edges energetically favoring their in-plane configuration with edge states gapped over the out-of-plane alignment.[374,375]

Similar to GNRs and GNFs, an external electric field can significantly modify the electronic and magnetic structure of GQDs. In particular, zigzag triangular GQDs in a bilayered arrangement are coupled in an FM state in the absence of the external electric field (see Fig. 73).[376] However, if the electric field is applied vertically (see Fig. 73), the FM behavior can be turned off or the total spin of the system can be reduced to a single electron/hole spin. The single electron/hole spin is found to be isolated in a charge neutral structure in an applied electric field, regardless of GQD size and without decoherence due to contacts.[376]

Following the theoretical predictions, the bisanthrene isomer of $C_{28}H_{14}$ molecule was identified as the smallest graphene derivative to show a spin-polarized state.[221] The shape of such a molecule resembles that of rectangular GQDs with spins aligned in an AFM manner at the two zigzag edges. The zigzag edges were found to be spin-polarized for a length of three consecutive units in minimum if the width of the system was 1 nm or wider. If the zigzag edges are 1 nm and longer, AFM ordering persists up to room temperature; for longer systems, spin wave structures were proposed to appear in some high-spin multiplicity states.[221] Upon increasing the length of the zigzag edges, oscillations were observed in the energy gap, however, with a smaller amplitude compared to that found in GNRs with infinitely long edges. More importantly, in an external in-plane electric field, the predicted half-metallic behavior seemed to survive even for finite systems with extremely short edges.[221]

Published on 26 March 2018. Downloaded by Univerzita Palackého v Olomouci on 2/28/2019 2:05:03 PM.

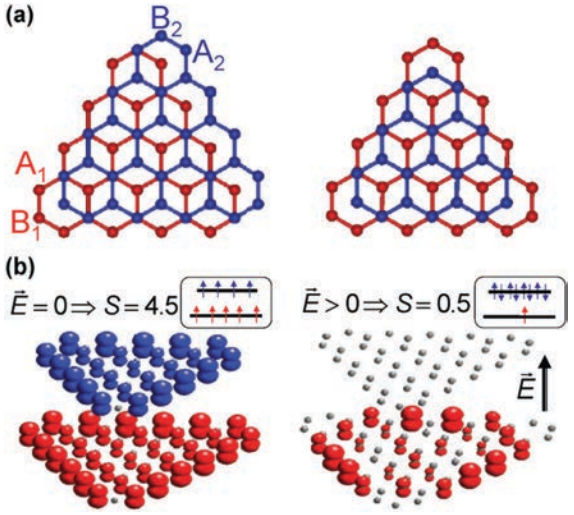


Fig. 73 (a) Structure of bilayered GQDs with zigzag edges and with equal (left) and different (right) sizes. (b) Isosurface plot of the difference in the spin-up and spin-down densities for cases with and without an external magnetic field (E). S denotes the total spin of the system. Reprinted with permission from ref. 376. Copyright 2011 American Physical Society.

Distinct magnetic features were experimentally reported for GQDs or graphene oxide quantum dots depending on their size and surface modification. In particular, GQDs with an average size and height of 4.2 and 6.6 nm, prepared by oxidative cutting of size reduced graphene oxide sheets by UV radiation, were found to show FM behavior even at room temperature (see Fig. 74a).[377] The reduced graphene oxide used for the synthesis of GQDs was diamagnetic at all temperatures down to 10 K, as reported by several other studies.[378,379] The FM response of GQDs was further verified by plotting hysteresis loops as displayed in Fig. 74b. The FM behavior evolving in these GQDs was explained in terms of the presence of defects similar to the case of GNRs, nanographites, and other systems exhibiting defect based magnetism.[250,380,381]

In contrast, graphene oxide quantum dots, synthesized by oxidative cutting, were mostly diamagnetic.[382] Particularly, in three systems with an average dot size of 1.6, 3.3, and 4.1 nm, the ratio of paramagnetic quantum dots increased from 1/70 to 1/15 and to 1/14, respectively, upon an increase in size. Hydroxyl groups were identified as a main source of magnetism in these graphene oxide quantum dots.[382] The suppression of edge state magnetism was explained in terms of a high-degree irregularity of the edge structure or spin cancellation between various magnetic fragments of the boundary. Besides, if the magnetic correlation length is smaller compared to the CQD size, CQD then behaves like a system with a single spin. Alternatively, the edge of such a GQD breaks into smaller fundamental magnetic order units which act more or less independently.[382] Here, it should be stressed that the magnetic correlation length was estimated to be 1 nm at room temperature and more than 100 nm at 2 K.

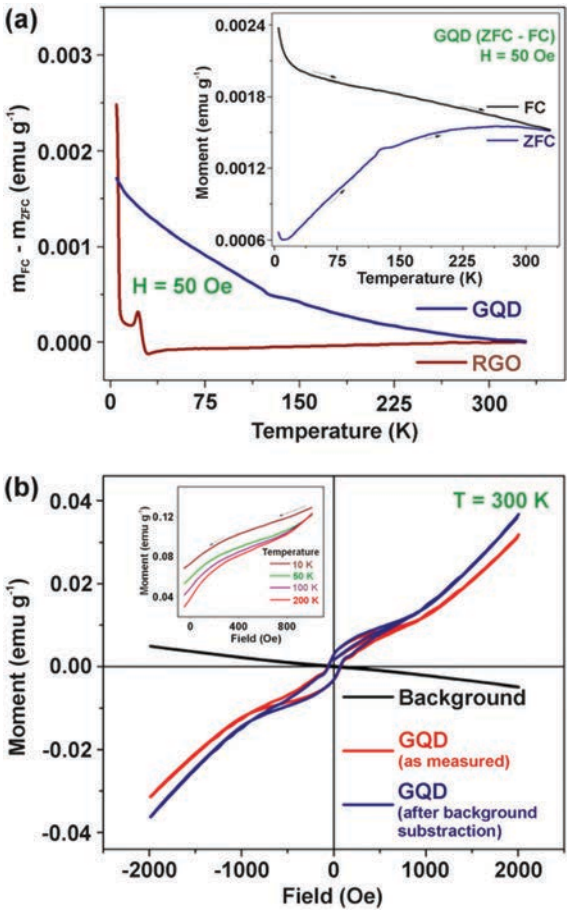


Fig. 74 (a) Comparison of zero-field-cooled (ZFC)/field-cooled (FC) measurements (*i.e.*, $m_{FC} - m_{ZFC}$) of GQDs and reduced graphene (RGO) quantum dots at H = 50 Oe. The inset in panel (a) shows the magnetic moment at various temperatures. (b) Moment *vs.* field measurement of the background and GQDs (with and without background subtraction). The inset shows the profile of the moment *vs.* temperature curve (only the first quadrant) at various temperatures. Reprinted with permission from ref. 377. Copyright 2013 Elsevier Ltd.

FM ordering self-sustainable up to room temperature was observed for very small GQDs (with an average diameter of 2.21 nm) and a composite containing mat-like polyaniline nanofibers and 0.315 wt% of GQDs (see Fig. 75).[383] The increase in the saturation magnetization of the composite (see Fig. 76) was ascribed to the electron transfer from the nitrogen atoms of mat-like polyaniline nanofibers to the encapsulated GQDs.[383]

5. Magnetism in graphene induced by doping with foreign atoms

Creating defects in a lattice is equivalent to disturbing its chemical surrounding. This can be achieved either by changing the nature of bonding or by disturbing the bonds. The most popular approach to generating defects in graphene involves

 This journal is © The Royal Society of Chemistry 2018

Published on 26 March 2018. Downloaded by Univerzita Palackého v Olomouci on 2/28/2019 2:05:03 PM.

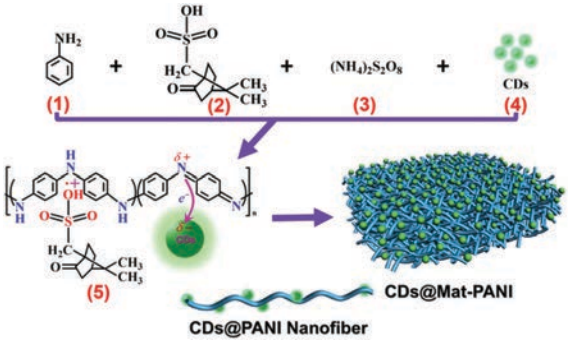


Fig. 75 Synthetic route towards a composite containing graphene quantum dots (CDs) and mat-like polyaniline nanofibers (Mat-PANI). Reprinted with permission from ref. 383. Copyright 2017 Macmillan Publishers Limited.

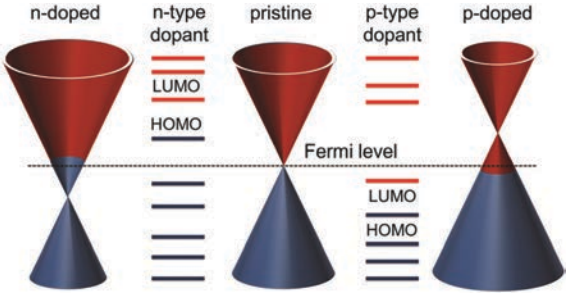


Fig. 77 Schematic showing n- and p-type dopants' Fermi level with respect to that of pristine graphene. Reprinted with permission from ref. 388. Copyright 2015 The Royal Society of Chemistry.

adopting a sequential oxidation and reduction path to produce graphene from graphite. The adsorption of oxygen in the basal plane of graphite during the oxidation of graphite can alter the chemical properties of the graphitic surface. Thus, defects can be easily formed due to the interaction of the carbon atoms with any foreign molecule. This can also be achieved by sintering the material in a suitable atmosphere. Another widely used technique to reduce the van der Waals forces between the layers of graphite involves intercalating a foreign species that could result in the formation of defects.

The carriers in graphene can be selected to be either electrons or holes by controlling the metals or molecules on the surface of graphene. n-Type doping in graphene can be achieved by using n-type dopants such as K, Ti, Fe, Cr atoms or NH_3 molecules.[384–386] Similarly, p-type doping can be realized by dopants such as NO_2 molecules.[387] In either of the cases, the electronic configuration of the system modifies by changing the position of E_F. The position of the highest occupied molecular orbital (HOMO) and the lowest unoccupied molecular orbital (LUMO) of the dopant with respect to the Dirac point in graphene is important in determining the direction of the charge transfer (see Fig. 77).[388] In the process of doping, exchange of electrons occurs between the dopant and graphene. Besides, the electrons may get confined in the orbital if it has a higher energy than E_F of graphene. In addition, redox reactions at the surface of graphene can also cause doping effects in graphene.[389] Doping with suitable dopants can be achieved by irradiating graphene.

Doping of graphene lattice with heteroatoms, such as nitrogen and boron, has been theoretically shown to stimulate n-type and p-type behavior in the case of N- and B-doped graphene, respectively.[390] The Dirac point of graphene was downshifted in N-doped graphene and upshifted in B-doped graphene with respect to E_F (see Fig. 78),[390] inducing a semi-metal-to-metal transition in doped graphene. Importantly, if π-electrons occupy narrow bands at E_F of graphene, Stoner magnetism can emerge.[391]

Indeed, it has been theoretically proposed and experimentally confirmed that depending on the concentration and packing geometry of doping sulfur[50] and nitrogen[51] atoms, it is possible to induce FM order in graphene. Both systems yielded similar transition temperatures to the FM state, 62 and 69 K, respectively, for S- and N-doped graphene (see Fig. 79), with graphitic dopants playing the principal magnetic role, albeit significant amount of pyridinic and chemisorbed nitrogen was identified in N-doped graphene samples. Pyrrolic nitrogen was not detected in N-doped graphene, which has previously been shown to cause

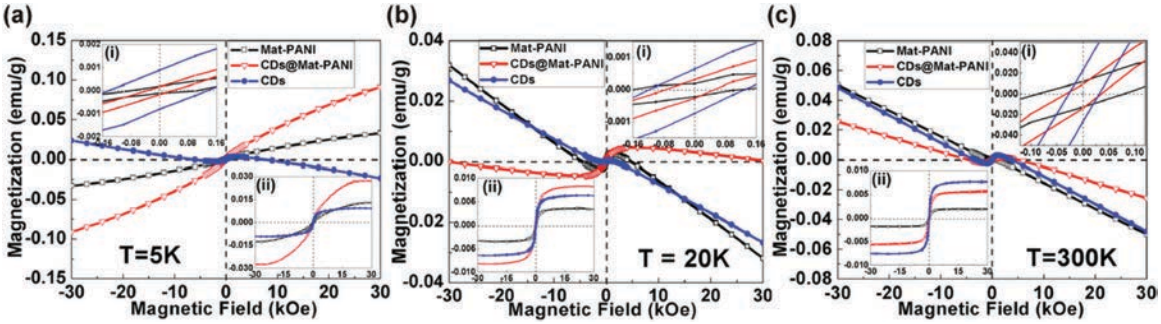


Fig. 76 Hysteresis loops of mat-like polyaniline nanofibers (Mat-PANI), graphene quantum dots (CDs), and a composite consisting of mat-like polyaniline nanofibers and graphene quantum dots recorded at a temperature of (a) 5 K, (b) 20 K, and (c) 300 K. The upper inset in panel (a–c) shows the behavior of the hysteresis loops at low applied magnetic fields. The lower inset in panel (a–c) shows the hysteresis loops after a subtraction of the diamagnetic component. Reprinted with permission from ref. 383. Copyright 2017 Macmillan Publishers Limited.

Published on 26 March 2018. Downloaded by Univerzita Palackého v Olomouci on 2/28/2019 2:05:03 PM.

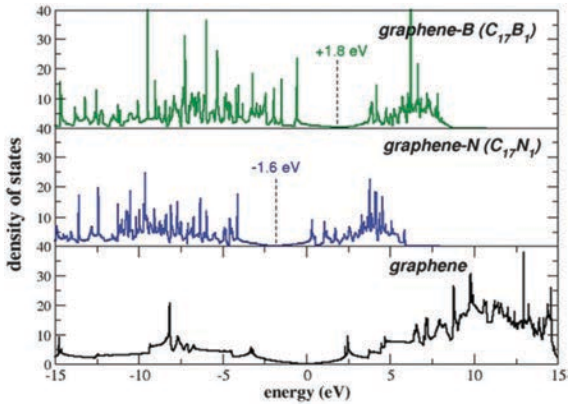


Fig. 78 Theoretical density of states of B- and N-doped graphene. B atoms serve as p-type dopants and N atoms as n-type dopants. Reprinted with permission from ref. 390. Copyright 2014 The Royal Society of Chemistry.

a decrease in magnetization values.[392] However, N-doped graphene with a solely pyrrolic nitrogen configuration at a very high concentration (~11.17 at% of N) was found to stabilize FM ordering up to ~678 K; the Curie temperature of pyrrolic N-doped graphenes was observed to decrease with increasing defect concentration.[393] Similarly, pyrrolic nitrogen at a concentration of 6.02 at% enhanced ferromagnetism in graphene oxide.[394] One shall note that a high oxygen content is regarded as a dominant source of magnetism, overwhelming the effects of nitrogen doping itself, and, moreover, oxygen-containing functional groups drastically reduce the electric conductivity of graphene – the main prerequisite for spintronics. Below 5 at% of nitrogen and ~4 at% of sulfur, graphene behaved dominantly as a diamagnet; although paramagnetic centers were imprinted upon doping, they did not lead to magnetically active configurations. Upon an increase in the doping concentration above these threshold doping values, FM states evolved when the

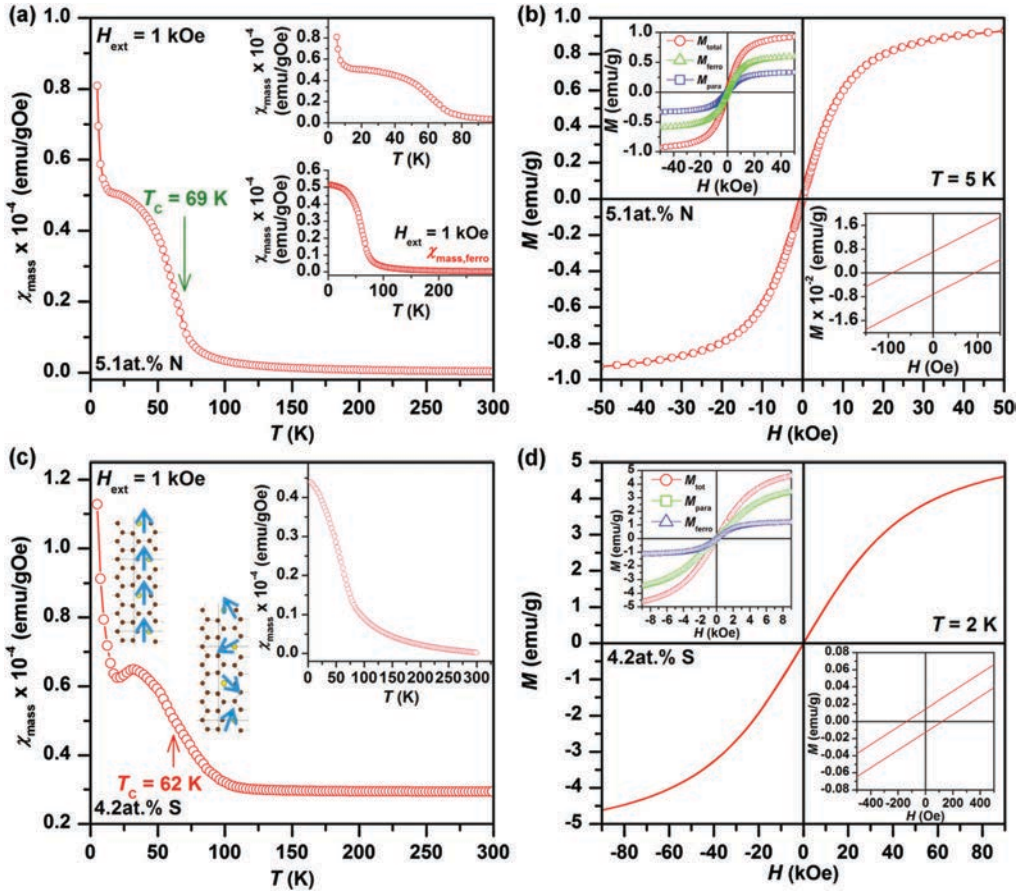


Fig. 79 Temperature evolution of the mass magnetic susceptibility (χ_{mass}) for (a) N- and (c) S-doped graphene at 5.1 at% (N) and 4.2 at% (S) recorded under an external magnetic field of 1 kOe with the Curie temperature (T_C), indicated. The ferromagnetic contributions derived from fitting of the χ_{mass} *vs.* *T* curve are shown in the insets. For N-doped graphene, the trend of χ_{mass} at low temperatures is also shown in the inset. Hysteresis loops of (b) N- and (d) S-doped graphene. The insets show the behavior of the hysteresis loop around the origin with nonzero coercivity and field-dependent profiles of magnetization for the ferromagnetic (M_{ferro}) and paramagnetic (M_{para}) components. Panel (a and b) reprinted with permission from ref. 51. Copyright 2017 American Chemical Society. Panel (c and d) reprinted with permission from ref. 50. Copyright 2016 WILEY-VCH Verlag GmbH & Co. KGaA.

 This journal is © The Royal Society of Chemistry 2018

Published on 26 March 2018. Downloaded by Univerzita Palackého v Olomouci on 2/28/2019 2:05:03 PM.

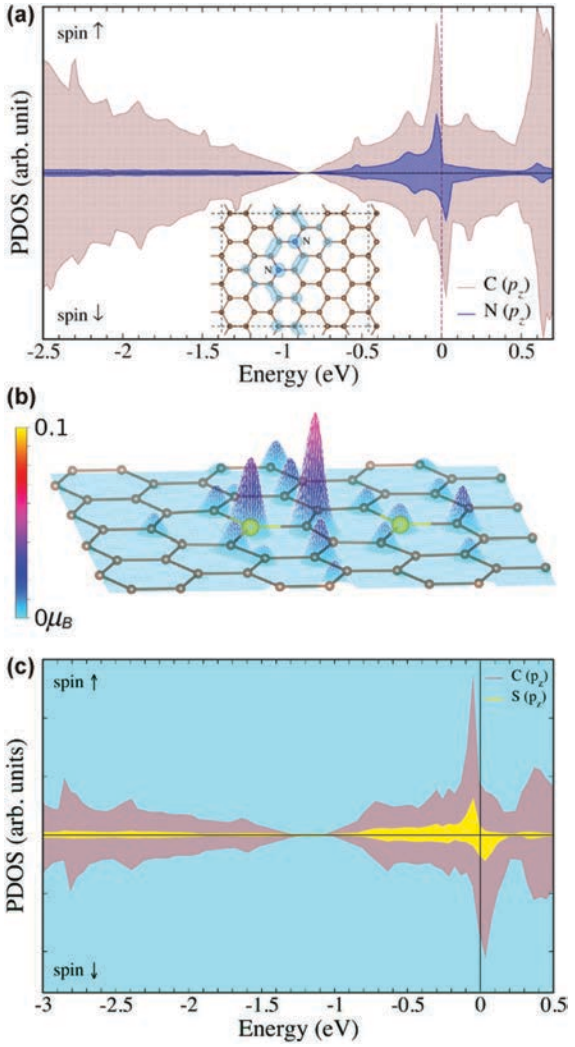


Fig. 80 (a) Theoretical partial densities of states (PDOS) calculated for N-doped graphene at 5.1 at% of N, where nitrogen occupies para positions in graphene. The supercell and an isosurface of spin density are shown in the inset. (b) Magnetic configuration of S-doped graphene at 4.2 at% of S superimposed on a 3D plot of the magnetic moment distribution within the supercell. (c) The corresponding calculated PDOS plot. Panel (a) reprinted with permission from ref. 51. Copyright 2017 American Chemical Society. Panel (b and c) reprinted with permission from ref. 50. Copyright 2016 WILEY-VCH Verlag GmbH & Co. KGaA.

doping-induced paramagnetic centers coupled *via* a π-electron system (see Fig. 80).[50,51] At low temperatures, the observed saturation magnetization reached ~1 emu g^{-1} (N-doped graphene) and ~5.5 emu g^{-1} (S-doped graphene), which is among the highest values ever reported for a graphene-based system in which the magnetism is imprinted either by doping or functionalization or edge modification. It must be noted that both S- and N-doping offer viable magnetic conductive materials with a huge potential in spintronic and other magnetic applications. In contrast, upon doping sulfur into the graphene lattice, a decrease in the saturation magnetization was witnessed accompanied by a change in the nature of magnetic ordering. These observations were explained in terms of saturation of dangling bonds at vacant and edge sites by sulfur atoms and, hence, quenching of local magnetic moments induced by vacancies and edges existing already in undoped graphenes.[395]

Recently, an ultralow energy ion implantation was exploited to incorporate different ion species (B, C, and N) into the graphene lattice. E_F gets reduced or increased due to doping by B or N, respectively,[396] and defects are formed when graphene is bombarded with carbon ions. STM images of graphene with different dopant atom species are shown in Fig. 81.[396] The electronic and magnetic properties can be tuned by selecting the type of dopant and its location in the structure. For example, N or B edge substitutions in armchair GNRs do not show any change in band gap[397] while a semiconductor–metal transition can occur due to N, B, and pyridine-like substitutions.

Besides boron, nitrogen, and sulfur, graphene can be doped with transitions metals. However, as their atomic radii are larger than that of a carbon atom, most of the transition metals are displaced outwards from the plane of graphene. They tend to form transition metal-vacancy complexes (*i.e.*, Au, Cu, V, Cr, Co, and Mn), which are predicted to show an interesting magnetic behavior.[398] For example, if an iron atom is substituted in the place of a single vacancy, it becomes non-magnetic; however, if doped in the site of a double vacancy, it shows a high magnetic moment. Similarly, a non-magnetic behavior is observed for a nickel atom substituting at a single vacancy. In such a case, a magnetic moment can emerge when exposed to a uniaxial strain.[399,400] On the other hand, cobalt atoms behave in a different manner as they give spin polarization, when doped at a single vacancy in graphene (see Fig. 82a). The cobalt atom was found to stabilize a symmetric structure of the carbon vacancy; in the electronic structure of the Co-substituted defect, a single level appears at E_F with a strong contribution stemming from the p_z orbitals of the neighboring carbon atoms, resembling a single vacancy (see Fig. 82b–d). Then, each Co-substituted defect possesses a magnetic moment of 1 μ_B. The total spin value of the system obeys Lieb's theorem. If the Co-substituted defects occupy only one sublattice of graphene, FM coupling is predicted while an AFM interaction is favored once the Co-substituted defects are on the opposite sublattices.[398]

6. Effect of functionalization on magnetic properties of graphene

In general, functionalization of graphene has been countlessly approved as an effective strategy to alter its physicochemical features tuning them appropriately for a given application. It involves modification of the graphene surface in both non-covalent and covalent manner by various adatoms, molecules, functional groups, and adsorbates. Particularly, functionalization leads to tuning of the band gap and hydrophobicity/hydrophilicity of graphene, eliminating its drawbacks in the pristine state. Moreover, it prevents stacking and aggregation of

Published on 26 March 2018. Downloaded by Univerzita Palackého v Olomouci on 2/28/2019 2:05:03 PM.

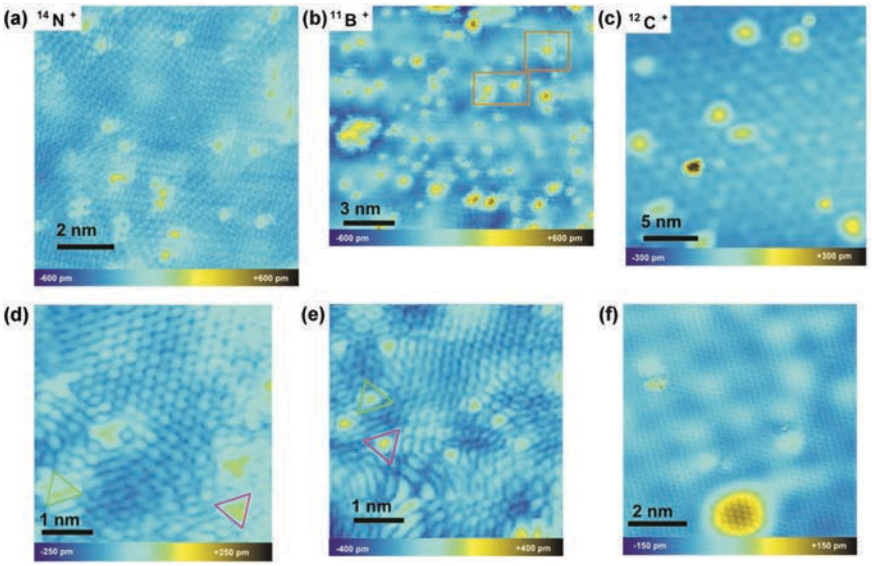


Fig. 81 STM images of graphene with different dopant atom species incorporated by ultralow energy ion implantation: (a) nitrogen-implanted; (b) boron-implanted; (c) carbon-implanted. Defects are seen on a larger scale; zoom of single atoms of (d) nitrogen and (e) boron. Both sublattice orientations were found (red and green triangles); (f) carbon-implanted sample. Reprinted with permission from ref. 396. Copyright 2015 American Chemical Society.

graphene sheets, facilitating its further processing with solvent-assisted techniques. Here, it should be stressed that functionalization with intrinsically magnetic species (*i.e.*, oxides of transition metals) is not discussed as the magnetic properties of such surface-modified graphene systems are solely driven by covalently or non-covalently attached magnetic compounds significantly overshadowing potential magnetic moments induced in graphene by functionalization; the topic of graphene functionalization with iron oxide nanoparticles was, for example, thoroughly covered in the review by Tuček *et al.*[401]

Graphene defects can be due to the presence of carbon adatoms, a consequence, for example, of a knock-on process that removed the atom from its position in the graphene lattice but with the atom still connected in some form to the sheet itself. Carbon adatoms can occupy various positions on the graphene sheets, for example, bridge (above a C–C bond), top (directly above a C atom), hollow (above the center of a hexagonal ring) and others (see Fig. 83). GGA calculations have shown that the ''bridge'' position has the lowest formation energy (position A in Fig. 83).[140] The calculated perpendicular distance of the adatom from the underlying graphene sheet is 1.87 Å. The two C atoms bonded to the adatom present a sp^2–sp^3 hybridization, while the adatom itself is sp^2 hybridized (see Fig. 84). The energy required to adsorb a C atom is 1.40 eV, nearly 1 eV lower than that necessary to adsorb directly above a lattice C. The diffusion of C adatoms through two bridge positions has a barrier of 0.47 eV, whereas migration across the graphene sheets requires energy 4 times higher.[141]

An atomistic simulation using the three-center tight-binding potential for carbon was performed to obtain low-energy defect structures.[402] Fig. 85 shows the low-energy structures for adsorption of 1–4 carbon atoms on graphene including their formation energies. A linear chain of the carbon adatoms is preferred. The lowest formation energy was found for adsorption of two atoms. Moreover, the formation energy of carbon adatom insertion into graphene is much higher than that of carbon adatom adsorption on graphene.

Carbon adatoms formed upon displacement are responsible for magnetism. As discussed above, adatoms can diffuse on the graphene sheet surface. Calculations have shown that the diffusing atoms migrate as non-magnetic units, but they become magnetic when they reach the equilibrium (bridge) position. Carbon adatoms contribute to magnetism with a magnetic moment of 0.5 μ_B. The paramagnetic/FM oscillations at various calculated cell size indicate that among the adatoms, RKKY interactions take place. Annihilation of magnetism can take place at high temperatures, unless clusters are formed, thus ''pinning'' the magnetism.[141]

Interestingly, it was found that the magnetism evoked by adatoms (and vacancies) can be effectively controlled by doping resulting in switching 'ON' and 'OFF' of the magnetic moments; nitric acid (HNO_3) or NO_2 gas were chosen as hole dopants whereas aniline as an electron dopant.[403] Such an observation unambiguously proved the itinerant nature of magnetic moments in graphene, *i.e.*, the existence of π magnetism. More specifically, if a graphene sheet with vacancies is sufficiently doped with charge carriers (*i.e.*, when $|E_F| \geq U_C$, where U_C is the Coulomb repulsion), the contribution to the magnetic moment originating from a singly occupied π state completely vanishes while the other contribution from an unsaturated σ bond remains unaffected. In other words, only half of the magnetism generated by a vacancy can be switched off by charge doping,

 This journal is © The Royal Society of Chemistry 2018

Published on 26 March 2018. Downloaded by Univerzita Palackého v Olomouci on 2/28/2019 2:05:03 PM.

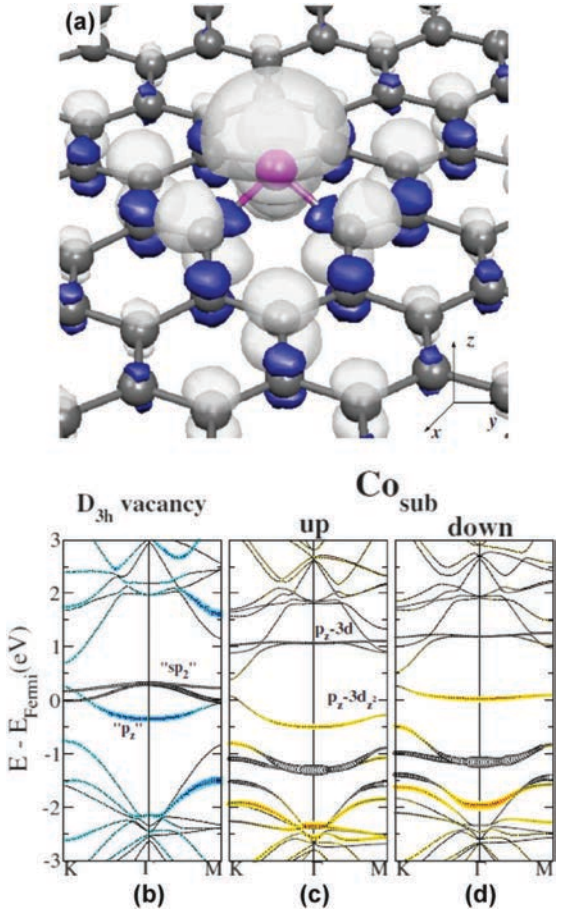


Fig. 82 (a) Isosurface of the spin density induced by the Co-substituted defect. Spin-up and spin-down densities are represented by light and dark colors, respectively, with isovalues of ± 0.008 e$^-$ Bohr^{-3}. (b) Spin-unpolarized band structure of a vacancy. (c) Majority spin-band structure of the Co-substituted defect; (d) minority spin-band structure of the Co-substituted defect. Reprinted with permission from ref. 398. Copyright 2010 American Physical Society.

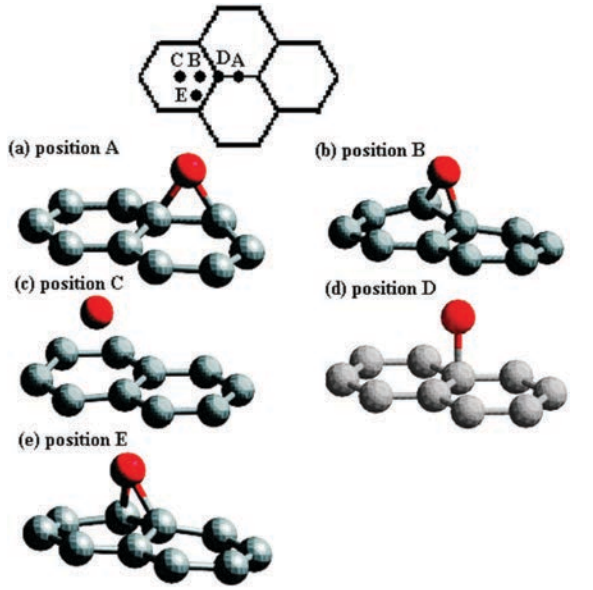


Fig. 83 Various adatom configurations on a graphene lattice. Reprinted with permission from ref. 140. Copyright 2005 American Physical Society.

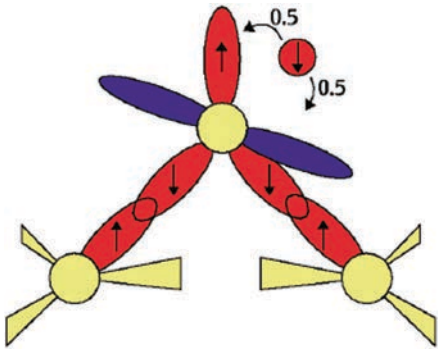


Fig. 84 Schematic of the bond orbital configuration in the case of an adatom at the bridge (equilibrium) position. Reprinted with permission from ref. 141. Copyright 2003 American Physical Society.

providing the potential to control the spin transport and, hence, spin diffusion in graphene.[403]

Importantly enough, density-functional calculations indicated that virtually any molecule attached to a carbon layer through a weakly polar single bond leads to an effect like that of hydrogen adsorption.[404] The graphene–adsorbate complexes exhibited a spin moment of 1 μ_B. The adsorption-induced spin polarization texture was shown to be remarkably similar for various adsorbed groups (see Fig. 86). The magnetic moments align ferromagnetically on the same sublattice, with an exchange coupling that falls off very slowly with the distance (r) between adsorbates ($\sim r^{-(1+\varepsilon)}$, $\varepsilon \approx 0.20$). In contrast, sp^3-functionalized opposite sublattices tend to couple antiferromagnetically. The band structure for graphene functionalized with adenine and methyl groups (see Fig. 86) showed that the magnetization comes from a very narrow defect state pinned at E_F. Similarly, one spin-polarized peak appeared close to E_F for various adsorbates chemisorbed on graphene through a single C–C bond (see Fig. 86).[404]

Various chemical routes such as hydrogen passivation, molecular grafting, or functionalization with various functional groups can be adopted to produce defects in graphene.[405–409] It was proved that atomic hydrogen can change the hybridization type in the parent graphene lattice from sp^2 to sp^3 bonding.[408] Fig. 87 shows the density of states for one-sided functionalization of bilayer graphene with several functional groups such as CN, NH_2, CH_3, COOH, and a combination of dopants and hydrogen.[406] The chemical nature of the dopant is independent of the band gap (0.6–0.7 eV) generated due to one-sided doping. However, functionalization by halogens or their combination

Published on 26 March 2018. Downloaded by Univerzita Palackého v Olomouci on 2/28/2019 2:05:03 PM.

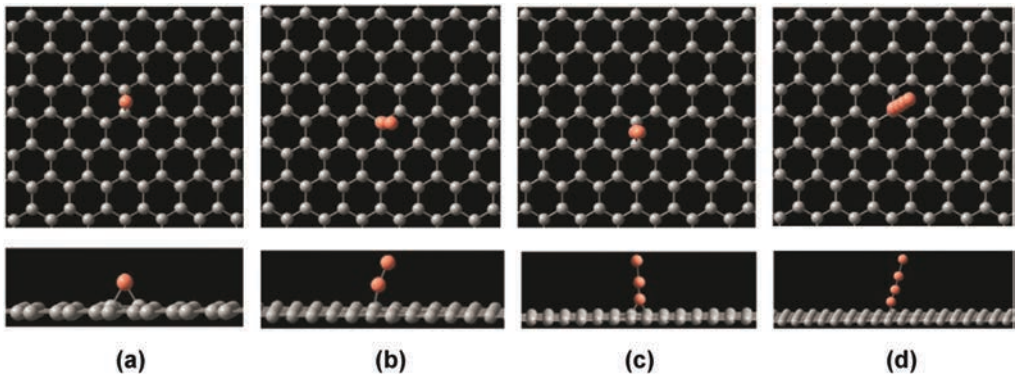


Fig. 85 Top and perspective views of the low-energy structures and formation energies (in eV) of adsorption of one, two, three, and four carbon atoms on graphene calculated by tight-binding approximation: (a) 5.52 eV; (b) 4.42 eV; (c) 7.58 eV; (d) 6.7 eV. Reprinted with permission from ref. 402. Copyright 2016 IOP Publishing Ltd.

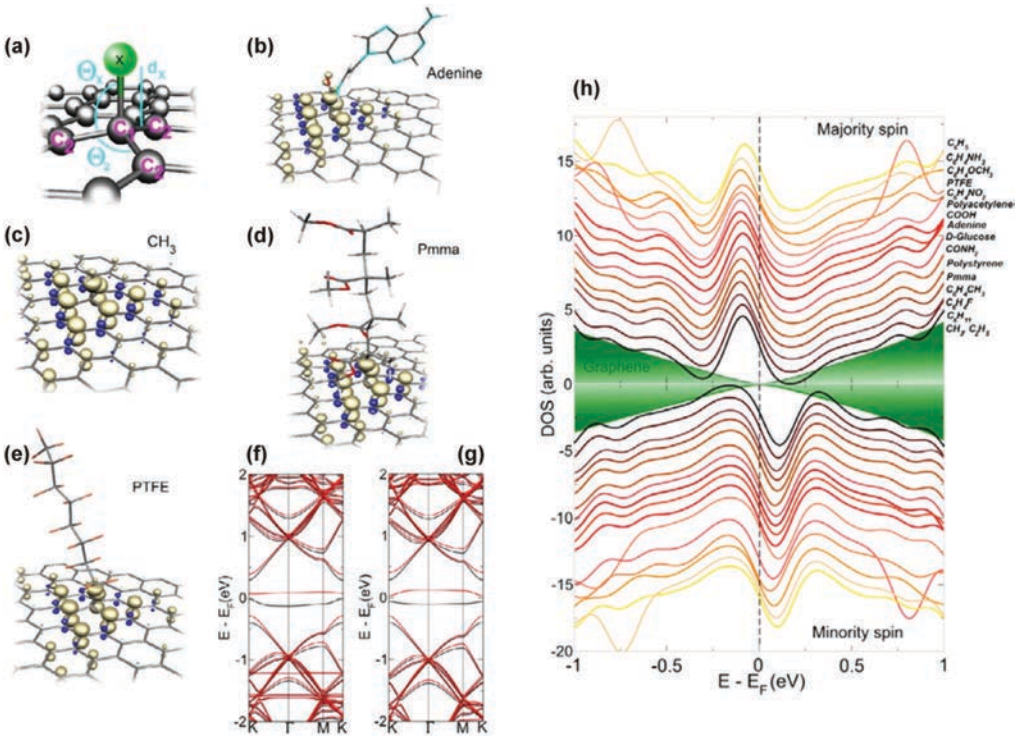


Fig. 86 (a) Adsorption geometry. (b–e) Isosurfaces of the magnetization density induced on graphene by functionalization using the adenine derivatives. Spin-polarized band structures for graphene with (f) a single adenine derivative and (g) a CH_3 molecule chemisorbed on top of one carbon atom. (h) Spin-polarized density of states (DOS) for a single molecule chemisorbed on a graphene supercell. The shaded regions indicate the density of states of pristine graphene. Reprinted with permission from ref. 404. Copyright 2012 IOP Publishing Ltd and Deutsche Physikalische Gesellschaft.

with hydrogen atoms was found to equip graphene with a wider band gap (1–3 eV).

Graphane, the fully hydrogenated graphene derivative, is a non-magnetic wide-gap semiconductor ($\sim$3.5 eV). Hydrogen can form a strong covalent bond with the carbon atom in graphene, thereby, consuming the π-electron to form sp^3 hybridization. This results in a strong resonance near E_F and increases the spin–orbit coupling. More specifically, the change from sp^2 to sp^3 states confines the p_z electrons into the chemical bonds, which is manifested by the disappearance of π-bands; the σ-bands are observed to move to the top of the valence band, which is accompanied by a large opening of the band gap. Although the hexagonal lattice of graphene is preserved in graphane, the periodicity decreases. Multilayered graphane, also

 This journal is © The Royal Society of Chemistry 2018

Published on 26 March 2018. Downloaded by Univerzita Palackého v Olomouci on 2/28/2019 2:05:03 PM.

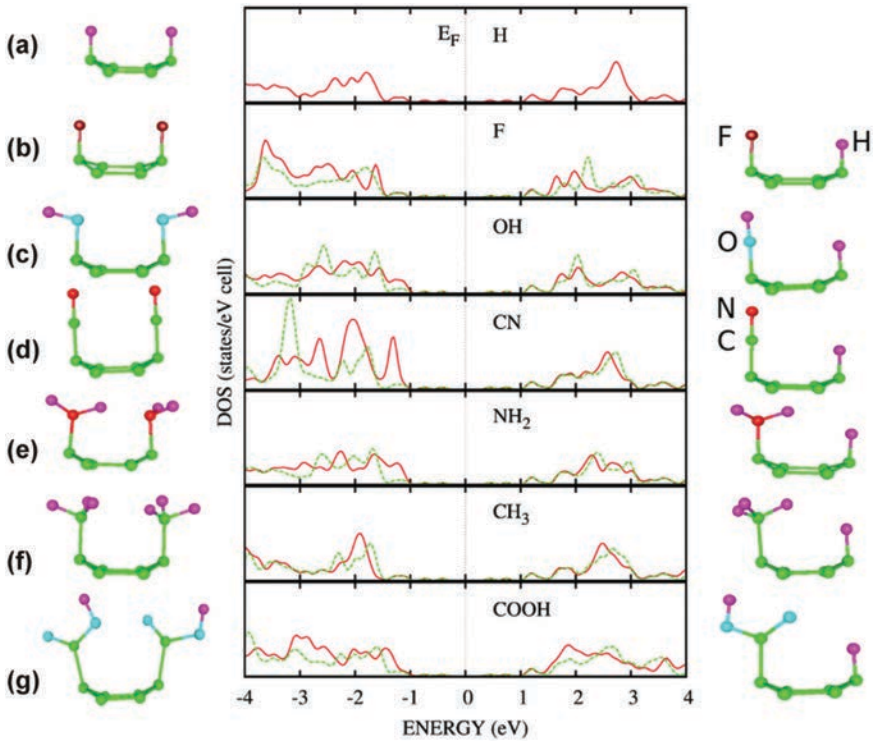


Fig. 87 Optimized configurations and total densities of states for one-sided functionalization of bilayer graphene. Left panel and red solid lines correspond to the case of two identical dopants, *e.g.*, F···F, per hexagon; right panel and dashed green lines correspond to the case when one dopant group per hexagon is replaced by hydrogen atoms, *e.g.*, F···H. Reprinted with permission from ref. 406. Copyright 2008 American Physical Society.

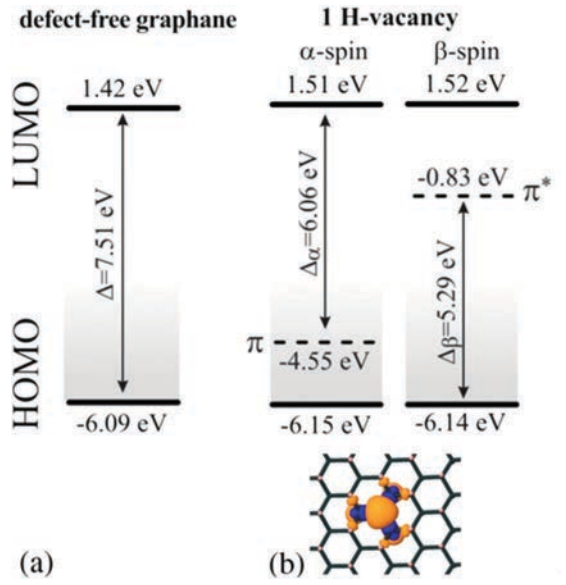


Fig. 88 Energetics of the bands in graphane with the defect levels (π and π*) induced by H-vacancy (dashed lines): (a) defect-free graphane; (b) graphane containing a single H-vacancy. The α- and β-spin states correspond to spin-up and spin-down states. Inset displays isosurfaces of spin-densities. Reprinted with permission from ref. 412. Copyright 2010 IOP Publishing Ltd.

called hydrographite, is a stable compound with a hexagonal crystal structure.[410] Hydrogenation of graphene was found to be reversible,[408] providing the flexibility to manipulate the coverage and to tailor its properties. Hydrogenation of graphene can be achieved by several techniques such as exposing graphene to hydrogen plasma, e-beam irradiation, or Birch reduction of graphite oxide. Graphane was found to show FM behavior that can resist against thermal fluctuations up to room temperature; the stability of the FM state was explained in terms of large extent of hydrogenation as proved theoretically. Besides, it was reported that AFM contribution can be detected arising as a result of multiple defects in agreement with computational predictions.[411]

Furthermore, a H-vacancy defect in the graphane lattice leads to the formation of a localized state with an unpaired spin and, accordingly, the formation of a defect level in the energy gap (see Fig. 88).[412] The armchair graphane is non-magnetic but AFM ordering can be seen on the same edge of zigzag edged graphane nanoribbons. Like GNRs, where spin states can be confined in zigzag GNRs by periodically repeating edge profiles, graphane nanoribbons can also produce similar effects.[413,414] Fig. 89 shows the energy-band diagram and band-projected charge density isosurfaces of various states of such a superlattice that mimics the edge roughness. The superlattice in Fig. 89 is a periodically repeating heterostructure of narrow (N_z = 6) and

Published on 26 March 2018. Downloaded by Univerzita Palackého v Olomouci on 2/28/2019 2:05:03 PM.

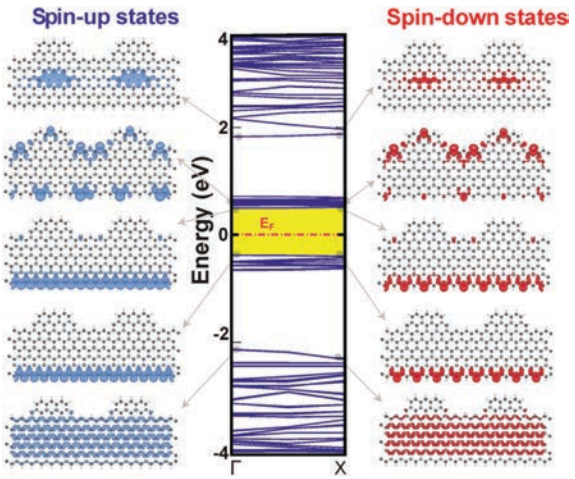


Fig. 89 The atomic and electronic band structure of a graphane nanoribbon including edge roughness. The yellow/gray shaded region is the band gap between the edge states. E_F is considered as the zero band energy. Reprinted with permission from ref. 414. Copyright 2010 American Physical Society.

wide (N_z = 8) segments of graphane nanoribbons, where N_z is the number of zigzag carbon chains along the nanoribbon's axis. It can be seen that at specific regions of periodic edge roughness, electronic states can be confined. On the other hand, it was proposed that edge states should theoretically disappear as a result of the absence of delocalized π-electrons due to completely sp^3 hybridized carbon atoms. Thus, only inner carbon atoms and hydrogen atoms determine predominantly the electronic structure of graphane nanoribbons, implying that they can be additionally modified in order to observe an emergence of magnetism.[415] Thus, spin polarization can be formed by creating domains of H-vacancies and CH-divacancies.[413] First-principles calculations using the Vienna ab initio simulation package (VASP) show that transition-metal-atom-embedded graphanes have larger magnetic moments in comparison to that of their corresponding graphene structure embedded with transition metal atoms or pristine graphane. The magnetic moment in graphane can be tailored by selecting a suitable dopant.[416] In particular, a maximum magnetic moment of 3.5 μ_B was found when Mn atoms were embedded in graphane.[417] More importantly, if a heterojunction structure with different transition metals (*i.e.*, nickel and vanadium), substituted in graphane, is theoretically considered, the spin-down current is observed to be totally suppressed and the spin-up current increases upon the application of the negative bias voltage.

Semi-hydrogenated graphene, known as graphone, shows a band gap of ~2.45 eV.[418,419] DFT calculations reveal that rectangular graphone is the most stable structure. Triangular graphone can undergo transitions to attain its stable structure by moving its two hydrogen atoms to the nearest carbon atoms at the starting point of the trigonal geometry. Fig. 90 shows the electron densities of triangular and rectangular graphone. The electrons in triangular graphone are localized around the hydrogen atom, while the electrons in rectangular graphone are not localized around the hydrogen atom. Thus, there exists a strong (weak) interaction between the two nearest hydrogen atoms in rectangular (triangular) graphone. This enhances the stability of rectangular graphone. Such kind of mutual interaction that exists between the two nearest neighbor hydrogen atoms in the rectangular graphone encourages AFM behavior. The unstable triangular graphone exhibits FM behavior with an indirect band gap of ~0.67 eV. Further, for single-side hydrogenated graphene with H-vacancies distributed on the neighboring carbon atoms belonging to the same graphane sublattice (graphone), the theory predicted[52] FM ordering with the estimated Curie temperature between 278 and 417 K. Fig. 91 shows that the induced magnetic moments are localized on the unhydrogenated atoms, while the hydrogenated C atoms and H atoms carry very small magnetic moments, which is due to the formation of strong σ-bonds between carbon and hydrogen atoms that break the π-bonding network and leave the electrons in the unhydrogenated C atoms localized and unpaired. The long-range magnetic coupling in graphone can be attributed to the large spatial extension of the valence electrons in the p-states.

The stability of graphone can be increased by fluorination. In fact, graphane (hydrogenated graphone) is less stable than a 100% fluorinated graphene.[420] DFT calculations show a dramatic change of electronic and magnetic properties upon fluorinating graphone. The insulating AFM graphone can be changed to an FM half-metallic fluorinated graphone. As the magnetism in graphone arises due to the localized and unpaired electrons originating from the unhydrogenated carbon atoms, any subsequent bond formation at these carbon atoms can quench the magnetic ordering. Further DFT study showed a two- and four-fold decrease in total magnetization upon adhesion of graphone on quartz and copper substrates, respectively.[421] However, in reality, no quenching of magnetization can be observed if polycrystalline copper or

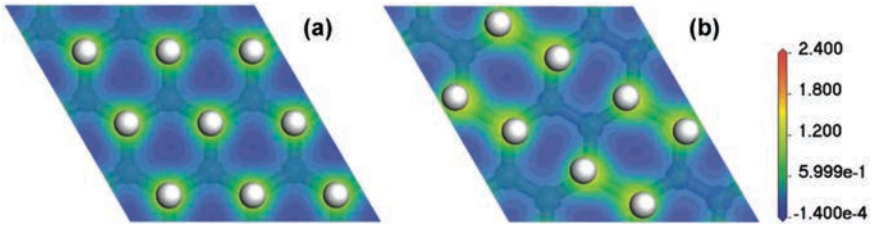


Fig. 90 Electron densities of (a) triangular (b) rectangular graphone. Reprinted with permission from ref. 419. Copyright 2012 AIP Publishing LLC.

 This journal is © The Royal Society of Chemistry 2018

Published on 26 March 2018. Downloaded by Univerzita Palackého v Olomouci on 2/28/2019 2:05:03 PM.

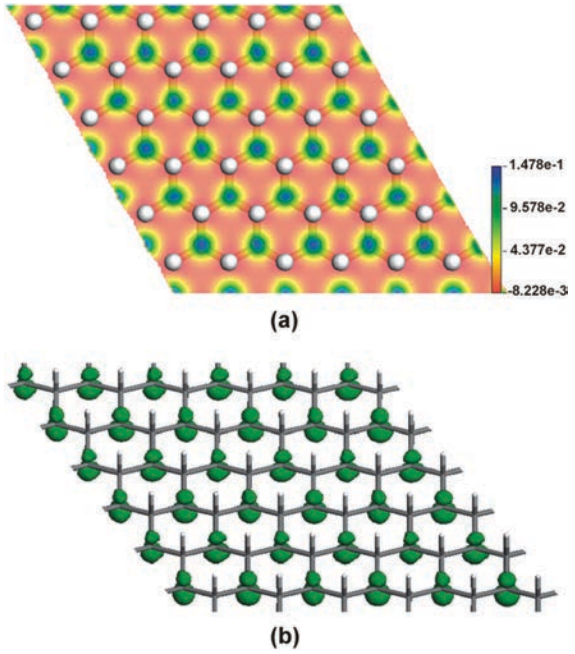


Fig. 91 (a) 2D plot of calculated spin-density difference (between spin-up and spin-down density) of graphone and (b) isosurface computed at a value of 0.26 e $Å^{-3}$. Reprinted with permission from ref. 52. Copyright 2009 American Chemical Society.

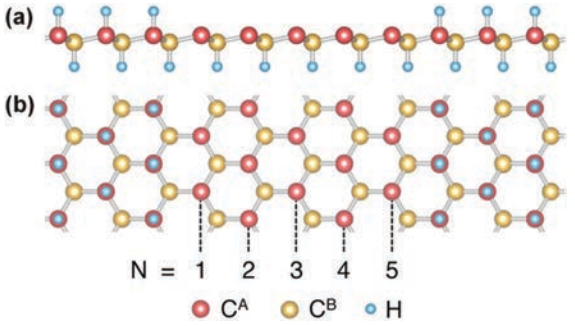


Fig. 92 (a) Side and (b) top views of the zigzag-edged semi-hydrogenated graphene nanorod in the fully-hydrogenated graphene layer where *N* denotes the width of the nanorod. Reprinted with permission from ref. 422. Copyright 2017 American Chemical Society.

amorphous silica substrates are used. This is due to the lack of effective bonding between the substrate and the corresponding C atoms.

Recently, an architecture comprising a semi-hydrogenated graphene nanorod incorporated into a fully-hydrogenated graphene sheet was theoretically proposed to show a robust ferromagnetism and bipolar semiconducting behavior (see Fig. 92).[422] Due to the areal magnetization promoted by half-hydrogenation, the FM response is not affected by the variation in the width and orientation of the nanorod in contrast to the magnetic behavior of related systems, relying solely on the edge states, and hence potentially ruined by chemical contamination and structural defects.[422]

Halogenation of the graphene system generates several interesting features by constructing a change in electron/hole density due to chemical adsorption. Fluorine doping can result in extra charge formation. For example, recent DFT calculations addressed the effect of doping on the magnetic properties of hydrogenated and fluorinated graphene.[423] A carbon atom can gain one unpaired electron when its neighboring carbon atom is attached to a functional group. Eventually, this process can occur in a series to gain unpaired electrons which would facilitate magnetism. The magnetic nature of the doped system is decided based on the presence of the unpaired electrons in the sublattices. Fluorinated and hydrogenated graphene possesses about 0.72 and 2.0 μ_B, respectively, without doping. The spin-up and spin-down density was found to vary depending upon the doping of extra charges (electrons/holes). The C–F bond length can be extended by adding more electrons by fluorination. Fig. 93 shows the band structures of the fluorinated graphene with various charge contents.[423] It is well known that E_F shifts due to doping of extra charges (see Section 5). E_F can shift down or up due to doping of holes or electrons, respectively. Hence, the spin polarization states of both spin-up and spin-down vary upon charge doping. However, fluorine doping has different effect on the graphene systems. In addition to the shift in E_F, spin-up and spin-down band distances also move disparately. In this respect, it was shown that the relative distance between E_F and the spin-up band lines hardly changes if the system is doped with positive charges that are smaller than 0.6 *e*. Fig. 94a and b display the geometrical structures of the hydrogenated and fluorinated carbon, respectively.[423] Hydrogen, carbon, and fluorine atoms are represented as white, cyan, and grey solid spheres, respectively. The unseen connections between the carbon atoms are shown by green triangles. The torsions of the two geometrical structures are also displayed. As is clear from Fig. 94c–f, the hydrogenated graphene has a maximum spin moment when it is not doped, while the spin moment decreases linearly upon doping (electrons/holes).[423] The fluorinated graphene has its maximum spin moment when doped with a positive charge of 0.6 *e*. It could undergo a change in the magnetic phase to become non-magnetic if it is doped with negative charges (−0.6 *e*). This can happen due to a change in the bond length as a result of the presence of extra charges.

Evolution of potential magnetic response in fluorinated graphite was studied with regard to various F/C ratios.[424] By employing the ESR technique, it was found that fluorinated graphites showed paramagnetic behavior with a *g*-value of ~2, typical for paramagnetic defects and free radicals. A generation of local magnetic moments was proposed originating from dangling bonds that are formed due to the conversion of sp^2-bonds to sp^3-bonds as a result of carbon–fluorine reactions. Interestingly, strong exchange interactions were observed between the localized moments of F atoms in a partially fluorinated sample while the localized spins in highly fluorinated samples behaved like isolated spins.

Published on 26 March 2018. Downloaded by Univerzita Palackého v Olomouci on 2/28/2019 2:05:03 PM.

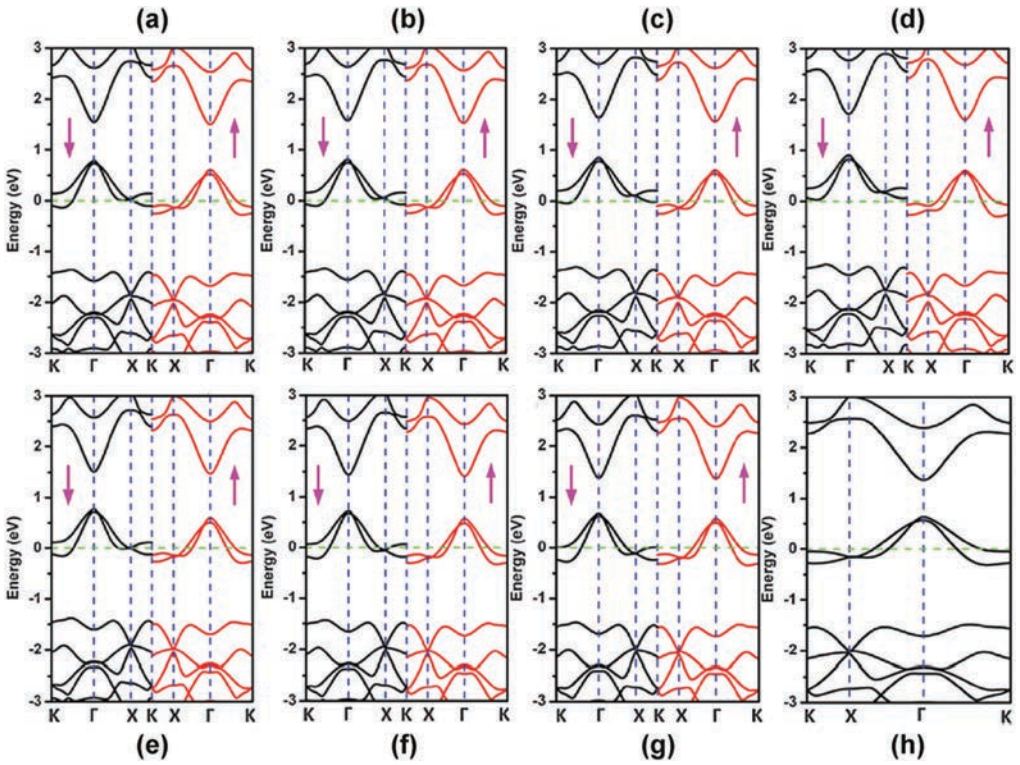


Fig. 93 Fluorinated graphene's band structures with charge (a) 0 *e*, (b) 0.1 *e*, (c) 0.3 *e*, (d) 0.6 *e*, (e) −0.1 *e*, (f) −0.3 *e*, (g) −0.5 *e*, and (h) −0.6 *e*. *e* is the unit of charge. The spin-up and spin-down bands are shown with red and black lines, respectively. E_F is marked with a green dashed line and set to zero. Reprinted with permission from ref. 423. Copyright 2013 The Royal Society of Chemistry.

Fluorographene, a two-dimensional stoichiometric graphene derivative, is one of the thinnest insulators with a wide electronic band gap (from 3.0–4.2 eV).[425–427] In fluorographene, the sp^3-hybridized C–C and C–F bond lengths are 1.58 and 1.37 Å, respectively. Density-functional calculations predicted that localized spin density can emerge in fluorographene and can be modulated by the degree of F coverage.[428] Fluorination was experimentally confirmed to be an effective route to generate noticeable spin-half paramagnetic centers in graphene (see Fig. 95).[53] However, possibly due to the adatom clustering, the measured number of paramagnetic centers was three orders of magnitude less than the measured number of F adatoms in the samples (see Fig. 95) and no long-range magnetic ordering was detected at that time. Thus, the cluster edges were proposed as the only source of magnetic moments that would determine the nature of magnetic response. Moreover, the number of spins (N) was found to increase monotonically with an increase in the degree of fluorination (*i.e.*, C_1F_x, $0 \leq x \leq 1$) up to $x \approx 0.9$. However, a complete fluorination showed a decrease in the value of N.[53]

More recently, in a combined experimental–theoretical work, Makarova *et al.*[429] proved that monoatomic chains of fluorine atoms on graphene led to strong magnetism in these purely organic graphene-based systems (see Fig. 96). The lattice sites that were occupied by F atoms became unavailable to the π-electron system, *i.e.*, the fluorine chains acted as high-energy barriers (a "nanoridge") for the graphene π-electron cloud. Thus, two edges separated by a nearly impenetrable CF-nanoridge were created, where one may expect a set of localized spin states in the A-sublattice on one side of the nanoridge and the B-sublattice on the other side. Magnetic susceptibility data yielded behavior typical of a quantum spin-ladder system with FM legs and AFM rungs (see Fig. 97), in analogy to the exchange couplings between the zigzag edge-inherited states in GNRs. The exchange coupling constant along the rungs was measured to be 450 K, which is strong enough to consider graphene with fluorine nanoridges as a candidate for a room temperature spintronic material.[429]

Like graphone, single-side semifluorinated graphene (C_2F) – a graphene derivative that was recently prepared experimentally[430] – should be FM according to Lieb's theorem since the fluorine atoms adsorb on the same sublattice of graphene. Very recently, the theoretical description of the magnetic moments by using the Wannier functions highlighted the direct exchange interaction in maintaining FM order in functionalized graphene, C_2F and C_2H.[431] Unlike graphone, C_2F was predicted to be at the edge of the AFM–FM instability, which in combination with the Dzyaloshinskii–Moriya interaction can lead to a skyrmion state at finite temperatures and magnetic fields (see Fig. 98).[431]

 This journal is © The Royal Society of Chemistry 2018

Published on 26 March 2018. Downloaded by Univerzita Palackého v Olomouci on 2/28/2019 2:05:03 PM.

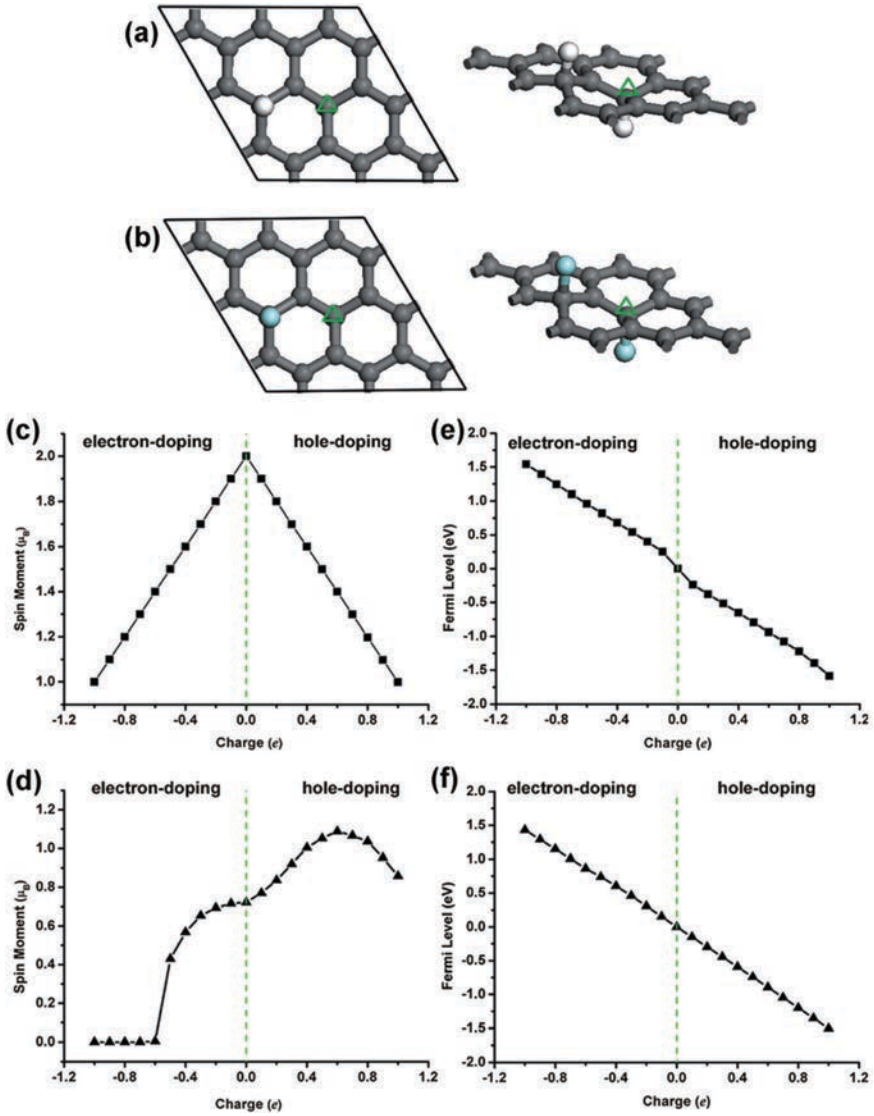


Fig. 94 Geometrical structures and relations between spin moment and charge of (a and c) hydrogenated and (b and d) fluorinated graphene. The relation between E_F and charge for (e) hydrogenated and (f) fluorinated graphene. E_F corresponding to the zero charge is set to zero. Reprinted with permission from ref. 423. Copyright 2013 The Royal Society of Chemistry.

Intriguing magnetic behavior was observed for graphene sheets functionalized with fluorine atoms with an arrangement closely resembling that of a so-called tabby pattern.[432] In particular, the attached fluorine atoms form monoatomic stripes which run along crystallographic directions, and are separated by non-fluorinated sp^2 carbon ribbons. As a result of bonds developed between the sp^3-hybridized carbon atoms and zigzag fluorine chains, sp^2–sp^3 interfaces were observed to evolve with spin-polarized edge states localized on both sides of chains. More importantly, fluorine patterns induced reduction of the effective dimensionality to 1D. For C_2F_x with $x < 1$, a behavior typical for low-dimensional quantum spin ladder systems was observed, with FM ordering along the zigzag edges and AFM coupling between the opposite zigzag edges. In addition, a thermally activated spin gap was detected at about 450 K. Ferromagnetism stable at room temperature was also found for C_2F_x with $x < 1$ and interpreted as a consequence of a dimensional crossover due to the onset of interlayer interactions after ageing or annealing. In contrast, the C_2F_x system with $x \approx 1$ exhibited a behavior characteristic of the two-dimensional magnetism without any signs of magnetic ordering at high temperatures; instead, a transition to a superparamagnetic regime at 40 K was observed. Thus, the results demonstrated that a magnetic dimensional crossover in

Published on 26 March 2018. Downloaded by Univerzita Palackého v Olomouci on 2/28/2019 2:05:03 PM.

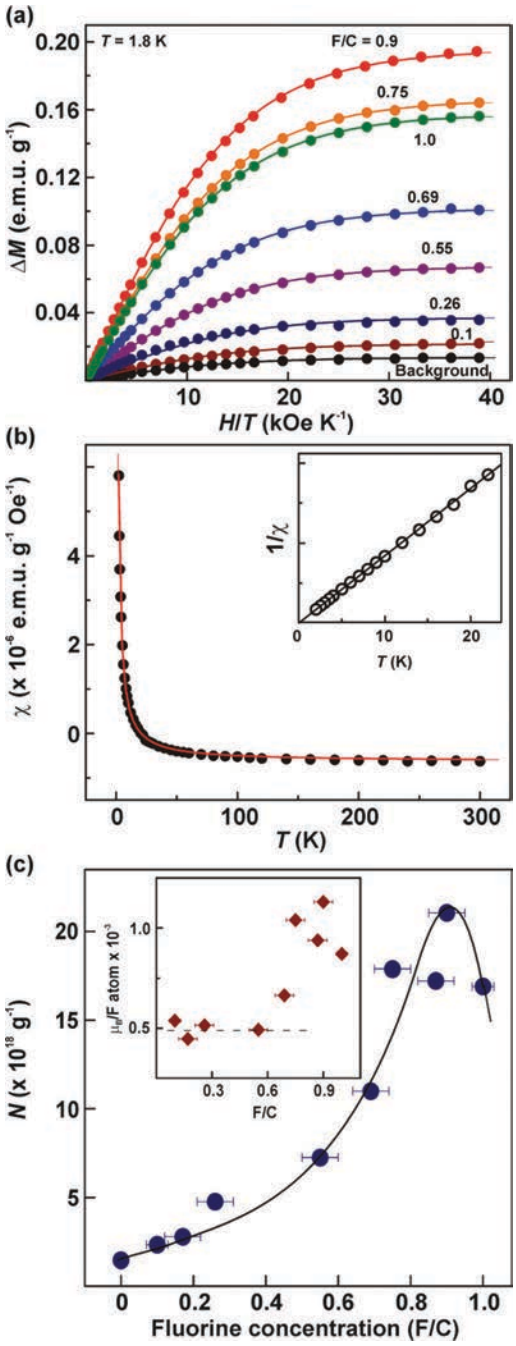


Fig. 95 (a) Magnetic moment as a function of parallel field for different F/C ratios. Symbols represent the measurements and solid curves are fits to the Brillouin function with $S = 1/2$ and assuming $g = 2$. (b) Example of the temperature dependence of magnetic susceptibility ($\chi = M/H$) in a parallel external magnetic field (H) of 3 kOe for F/C = 0.9. The inset shows the inverse magnetic susceptibility *vs.* temperature plot demonstrating the linear, purely paramagnetic behavior with no sign of magnetic ordering. (c) Number of spins (N) extracted from the Brillouin fits as a function of the F/C ratio. The inset shows the same N normalized to the concentration of adatoms in each sample. Reprinted with permission from ref. 53. Copyright 2012 Macmillan Publishers Limited.

graphene-based systems can be induced upon changes in the fluorine content and interlayer distance.[432]

The chemistry of fluorographene has been recently used to develop room-temperature magnetically ordered 2D systems.[54] While partially fluorinated graphene samples (*i.e.*, C_1F_x), prepared by thermal defluorination of exfoliated C_1F_1, were either diamagnetic but contained some paramagnetic centers or exhibited even an FM ground state with the Curie temperature of 22 K, hydroxyl-substituted fluorographene (termed hydroxofluorographene) prepared *via* simultaneous reductive defluorination and nucleophilic substitution with –OH groups showed room-temperature AFM ordering with a high saturation magnetization of $\sim$1 emu g^{-1}, and underwent a transition to an FM state at 62 K (see Fig. 99), as predicted by theoretical models and confirmed experimentally (see Fig. 100).[54] The different transition temperatures and failure/ability to establish magnetic order up to room temperature highlighted the different origin of magnetism in fluorographene and hydroxofluorographene. Magnetism of fluorographene with low levels of sp^3 functionalization stems from localized defect-induced magnetic moments. The magnetism in hydroxofluorographenes with an appropriate stoichiometry stemmed from the presence of aromatic islands forming diradicals that coupled through OH-enabled superexchange interactions (see Fig. 101). These new developments in sp^2-based room-temperature magnetism in 2D systems pave the way to the future organic spintronic applications.[51]

Adding atoms or molecules in a material through covalent bonding can influence several properties including the magnetic behavior.[433] The effects of addition of monovalent and divalent adsorbates with different electronegativity onto graphene were studied using first-principles calculations based on spin-polarized DFT. The energy difference between the magnetic and non-magnetic states (ΔE) was used to understand the stability of magnetic orderings in graphene systems. The atom/functional group X representing F, H, OH, CN, CH_3, and NH_2 was considered for monovalent adsorption while C, N, O, CH_2, and NH were selected as a divalent adsorbate. The monovalent adsorbate X would make a single covalent bond between carbon and the X atom. As a result, the bond length and bond angle, corresponding to sp^3 hybridization, change. The magnetic moment of the supercell then decreases with an increase in the size of the supercell.[433] A very high adsorption concentration of fluorine is required to establish a magnetic ground state due to its high electronegativity. Thus, the magnetism in the graphene system with monovalent addition becomes a charge-transfer-dependent process. However, H adsorption was found to induce the highest moment with a narrow energy gap. This is because the charge transfer is dependent on the electronegativity. The exchange interaction between sp^3 carbon and localized states is weakened by the electron transfer process. The spin split of density of states of graphene with various supercells for H and N adsorption is shown in Fig. 102.[433] The red and black arrows in the density-of-state plot for N addition can be attributed to the spin-polarized p_z orbital (see Fig. 102e–h).[433] Similar results were obtained by adopting LSDA+U calculations except that the positions of

 This journal is © The Royal Society of Chemistry 2018

Published on 26 March 2018. Downloaded by Univerzita Palackého v Olomouci on 2/28/2019 2:05:03 PM.

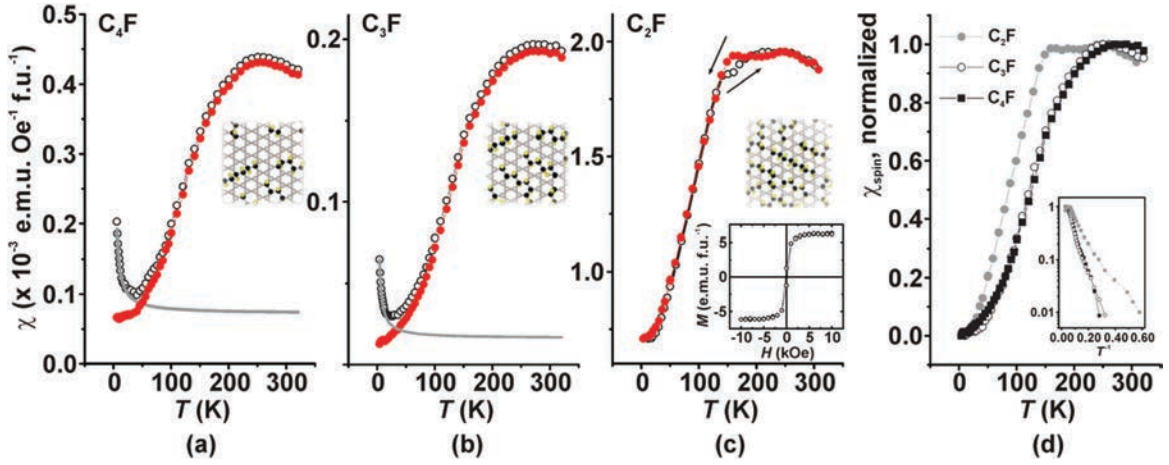


Fig. 96 (a–c) Raw data of magnetic susceptibility (χ) of the C_nF samples (n = 2, 3, and 4). C_4F and C_3F samples were measured at an applied magnetic field of 100 Oe upon heating after zero-field cooling (open circles); the same curves with the Curie contribution (grey) subtracted are represented by filled red circles. A C_2F sample was measured upon heating (filled circles) and upon cooling (open circles). The inset in panel (c) shows the room-temperature hysteresis loop of the C_2F sample. (d) Normalized spin susceptibilities for C_4F, C_3F and C_2F samples with the inset showing dependence of the spin susceptibility on reciprocal temperature for these samples. Reprinted with permission from ref. 429. Copyright 2015 Macmillan Publishers Limited.

localized states (on N atoms) for the spin-up branch were deeper in the valence band for U_{eff} = 4.6 eV.

In contrast, the induced magnetic moment in the case of divalent adsorption was found to be more stable and less dependent on the concentration of the adsorbates.[433] The π-bond breaks after the divalent adsorption and sp^3-like hybridization is seen at the carbon sites. However, the magnetic contribution from this π-bond breakage is very small because the hybridized carbon atoms belong to different sublattices of graphene. The adsorption of O, CH_2, and NH did not yield any magnetic ordering in the ground states due to the absence of any unpaired p_z electron. N adsorption induces a larger moment compared to C atom adsorption. ΔE for the divalent adsorption does not follow any regular fashion. Like the monovalent adsorption, the exchange interactions for the divalent adsorption on graphene were found to be distance-dependent.[433]

Covalent adsorption of an aromatic radical onto a graphene sheet can also imprint magnetic behavior and band gap opening. For example, attaching a phenyl group onto graphene was theoretically found to generate a band gap by modifying the band structure, thereby creating two spin-dependent states around E_F.[434] A nonzero magnetic moment can be induced due to an imbalance between the two sublattices in graphene caused by an aromatic adsorption on one of the carbon atoms in the sublattice. As a result, the corresponding p_z orbital is removed leaving the other sublattice unpaired. However, graphene is found to be less sensitive to adsorption of an aromatic molecule.

The magnetic ground state can vary depending on whether the adsorbate is physically or chemically adsorbed. Employing DFT calculations, it was predicted that the magnetic response for such adsorption emerges at a femtosecond time-scale due to core level excitations.[435] The dominant interaction between the physisorbed molecule and graphene is primarily governed by the van der Waals forces. In such cases, the ground state of the system is non-magnetic. The magnetic ground state is altered by the degree of electron transfer that happens at the femtosecond time-scale. This non-magnetic ground state can be magnetic only after a core electron gets excited and retains its magnetic state until the core electron is de-excited. In contrast, for covalently bonded molecules, the ground state is of magnetic nature and the magnetic state is suppressed by the excitation of a core electron.

Alternatively, ferromagnetism was observed in hydrogenated epitaxial graphene grown on SiC substrates.[436] The effect of substrate on the evolution of magnetic behavior in graphene was studied by growing a quasi-freestanding monolayer graphene which was prepared by intercalating hydrogen between the SiC substrate and the buffer layer. Due to the exchange coupling interaction between the localized states in the hydrogenated graphene layer and the localized states of the buffer layer, the hydrogenated epitaxial graphene was found to show FM ordering.[436] Moreover, a paramagnetic response for the buffer layer was observed, signifying the presence of localized magnetic moments at the defect sites. Upon hydrogenation, sp^3 defect states were created by virtue of C–H bonds. These newly generated states were believed to undergo a spin split in the vicinity of E_F due to the Coulombic interaction of the Si dangling bonds. Thus, the FM state was stabilized with the Curie temperature of 300 K or higher.[436] Even in the absence of the substrate, hydrogenated graphene was reported to exhibit an intrinsic ferromagnetism with the lower Curie temperature. The emergence of FM behavior was further confirmed by measuring the remanent magnetization by magnetic force microscopy (MFM, see Fig. 103).[436] A difference in the MFM signal is seen in between the single (1L) and bilayer (2L) areas implying a change in the degree of magnetization correspondingly; it was explained by the difference in hydrogen coverage by both layers. Fig. 103c then clearly shows a switching

Published on 26 March 2018. Downloaded by Univerzita Palackého v Olomouci on 2/28/2019 2:05:03 PM.

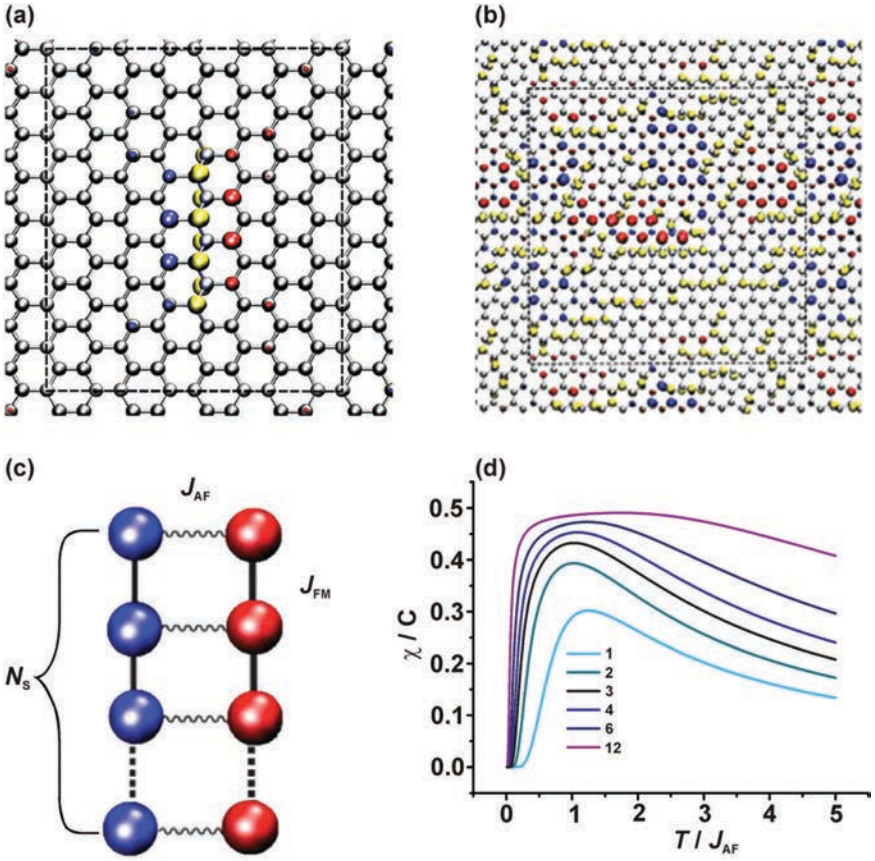


Fig. 97 (a) A zigzag chain of fluorine on graphene. Opposite spin orientations are shown in red and blue. F atoms are represented by yellow spheres. (b) The calculated spin density for a random distribution of fluorine chains. (c) A model of a spin ladder with an infinitely strong FM intra-leg interaction (J_{FM}) and an AFM inter-leg coupling (J_{AF}). (d) A plot of the magnetic susceptibility (χ) for the finite size spin ladder as a function of the reduced temperature. The numbers near the curves correspond to length of the spin ladder (N_S). Reprinted with permission from ref. 429. Copyright 2015 Macmillan Publishers Limited.

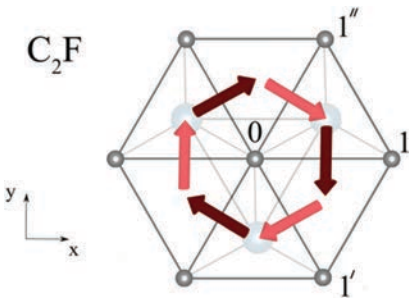


Fig. 98 Schematic representation of the Dzyaloshinskii–Moriya vectors in C_2F. Light and dark red arrows denote the Dzyaloshinskii–Moriya vectors with positive and negative z components, respectively. Reprinted with permission from ref. 431. Copyright 2016 American Physical Society.

mechanism in the presence of different layers.[436] The MFM signal changes its direction upon reversing the external magnetic field (visible through color inversion of the MFM images in Fig. 103a and b).[436] These MFM measurements clearly support the present FM behavior of hydrogenated graphene, thereby ruling out any previous doubts on the evolution of magnetism in graphene by magnetic contaminations.[436]

If a graphene sheet is functionalized with –OH groups, magnetic moments with high magnitudes can be induced on its basal plane; depending on the concentration of –OH groups (from 3 to 10 at% of OH coverage) after annealing of graphene oxide at different temperatures (removing epoxy groups), the saturation magnetization was found to vary from 0.91 to 2.41 emu g^{-1}.[437] More importantly, an inducing efficiency as a high as 217 μ_B per 1000 OH groups was observed. In addition, –OH groups showed high stability sustaining even at 900 °C. Thus, –OH groups were suggested as ideal sp^3-type candidates to equip graphene with robust magnetic moments.[437]

Unlike graphene which is hydrophobic in nature, graphene oxide forms stable dispersions in many solvents due to its oxygen-rich functional groups (*e.g.*, –OH, –O–, –COOH, C=O). In particular, epoxy and hydroxyl groups sit on the basal plane of the graphene oxide sheet (*i.e.*, in the interior region) while carbonyl and carboxyl groups are attached at its edge sites.[438]

 This journal is © The Royal Society of Chemistry 2018

Published on 26 March 2018. Downloaded by Univerzita Palackého v Olomouci on 2/28/2019 2:05:03 PM.

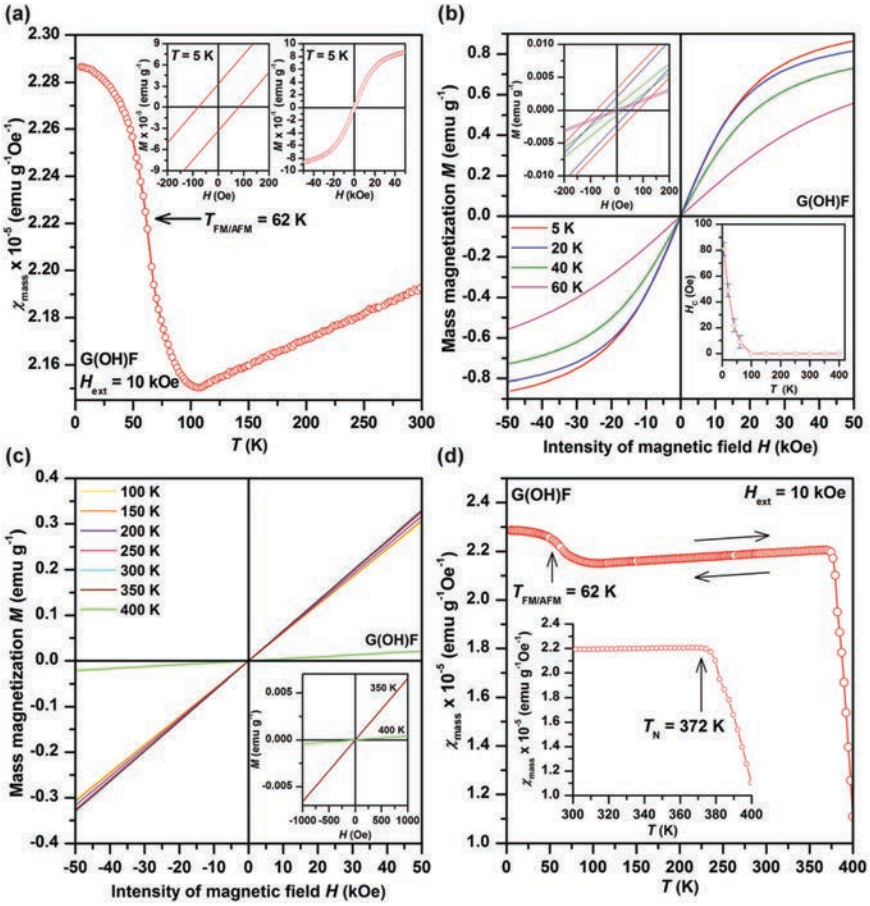


Fig. 99 (a) Temperature evolution of the mass magnetic susceptibility (χ_{mass}) of hydroxofluorographene (G(OH)F), measured under an external magnetic field of 10 kOe, with TFM/AFM indicating a transition from the FM to AFM state upon warming. The insets show the hysteresis loops of G(OH)F at 5 K, which indicate a non-zero coercivity and a saturation magnetization of $\sim$1 emu g^{-1}. (b) Isothermal magnetization curves of G(OH)F at temperatures of 5–60 K. The insets show the profile of the hysteresis loops around the origin and the temperature dependence of coercivity (H_C). (c) Isothermal magnetization curves of G(OH)F, recorded from 100 to 400 K. The inset shows the profile of the isothermal magnetization curves at 350 and 400 K, demonstrating a transition from an AFM state to a paramagnetic regime above 350 K. (d) Temperature evolution of χ_{mass} of G(OH)F, measured under an external magnetic field of 10 kOe. The arrows show the reversibility of the χ_{mass} profile on warming the sample from 5 to 400 K and then cooling from 400 to 5 K. The inset shows a sudden drop of χ_{mass} above 370 K, which is indicative of a transition from an AFM state to a paramagnetic regime with a Néel transition temperature (T_N) of about 372 K. Note: the paramagnetic signal from the non-interacting paramagnetic centers was subtracted from the χ_{mass} data. Reprinted with permission from ref. 54. Copyright 2017 Macmillan Publishers Limited.

Thus, graphene oxide contains a mixture of both sp^2 and sp^3 bonds and is regarded as an insulator with a band gap depending on the relative fraction of individual oxygen-containing groups (between $\sim$0.2 and $\sim$4.2 eV). Upon reduction, graphene oxide may undergo a transition from the insulating through semiconducting to the semi-metal state. A single epoxy group is found to be non-magnetic as it induces equal defects in the A- and B-sublattice of the graphene lattice. On the other hand, a single hydroxyl group can effectively generate a localized spin ($\sim$1 μ_B) sitting on the basal plane of the graphene sheet.

It was found that high-content hydroxyl groups can be formed on the basal plane of graphene oxide upon ring opening of the epoxy group. An increase in the level of hydroxyl groups caused a significant increase in the local spin density reaching a value of 5.17 μ_B per 1000 carbon atoms. In other words, converting epoxy groups to hydroxyl groups, combined with the Ar annealing method, increased the magnetization of graphene oxide from 0.136 to 3.11 emu g^{-1}.[439] Similarly, higher magnetization values were experimentally observed for graphene oxide after thermal annealing in Ar for 2 h. It was suggested that the elevated temperatures promote migration of epoxy groups over the surface of the graphene oxide sheets, eventually self-assembling into several long chains with a zigzag motif. The increase in the number of zigzag edges was then responsible for a higher value of the magnetic moment. Moreover, the density of epoxy groups was identified as crucial for cutting the graphene oxide sheets to small structures with a higher number of zigzag edges.[440]

Published on 26 March 2018. Downloaded by Univerzita Palackého v Olomouci on 2/28/2019 2:05:03 PM.

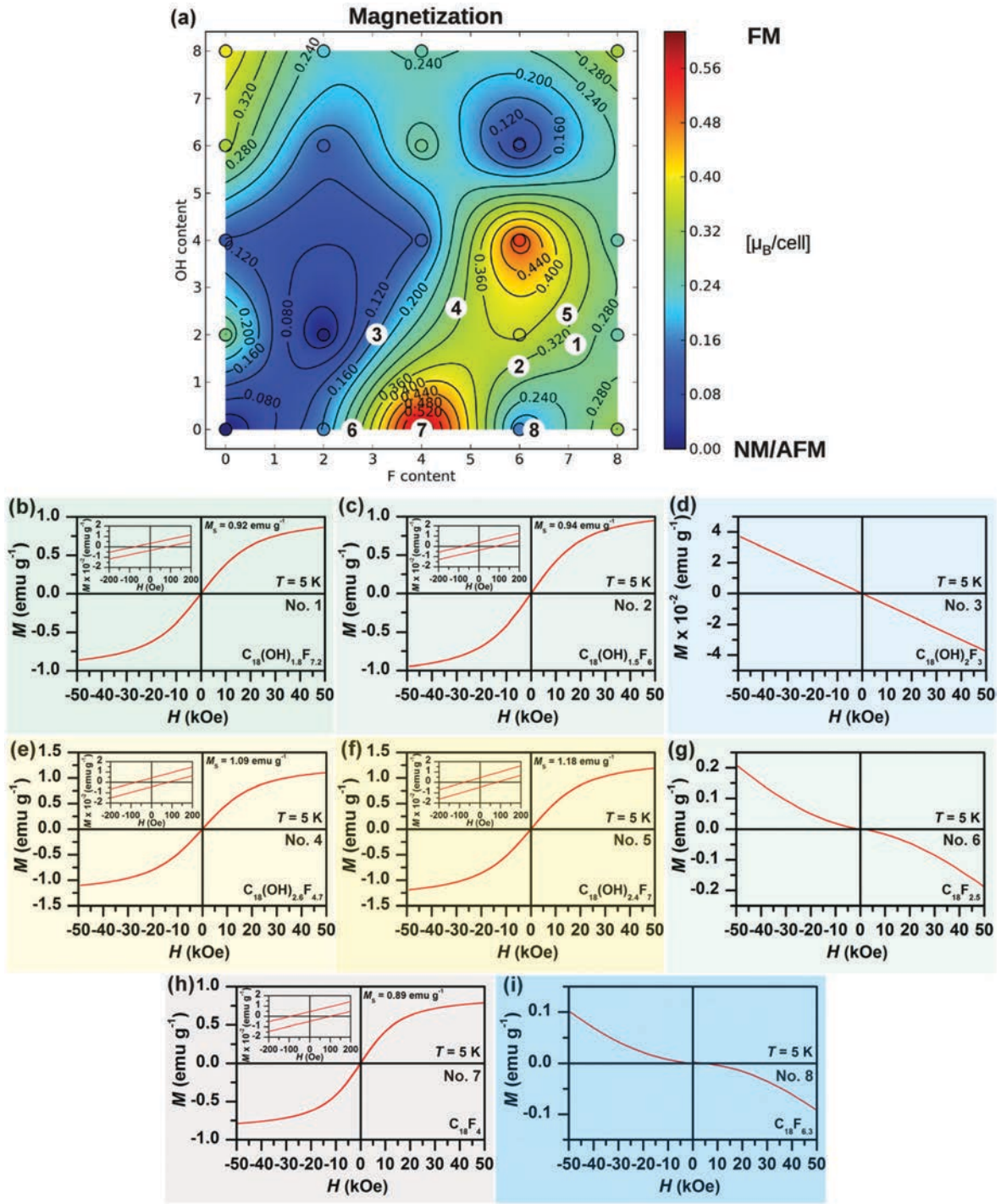


Fig. 100 (a) The theoretical mean magnetization map indicates which $C_{18}(OH)_yF_x$ stoichiometries are likely to exist in ferromagnetic (FM) and non-magnetic (NM) ground states. The white circles indicate experimentally studied samples (b–i) for which the isothermal magnetization (M) curves as a function of an external magnetic field (H), recorded at a temperature of 5 K are shown. The insets in panels (b, c, e, f and h) show the behavior of the respective hysteresis loops around the origin with the saturation magnetization (M_S) indicated. Reprinted with permission from ref. 54. Copyright 2017 Macmillan Publishers Limited.

 This journal is © The Royal Society of Chemistry 2018

Published on 26 March 2018. Downloaded by Univerzita Palackého v Olomouci on 2/28/2019 2:05:03 PM.

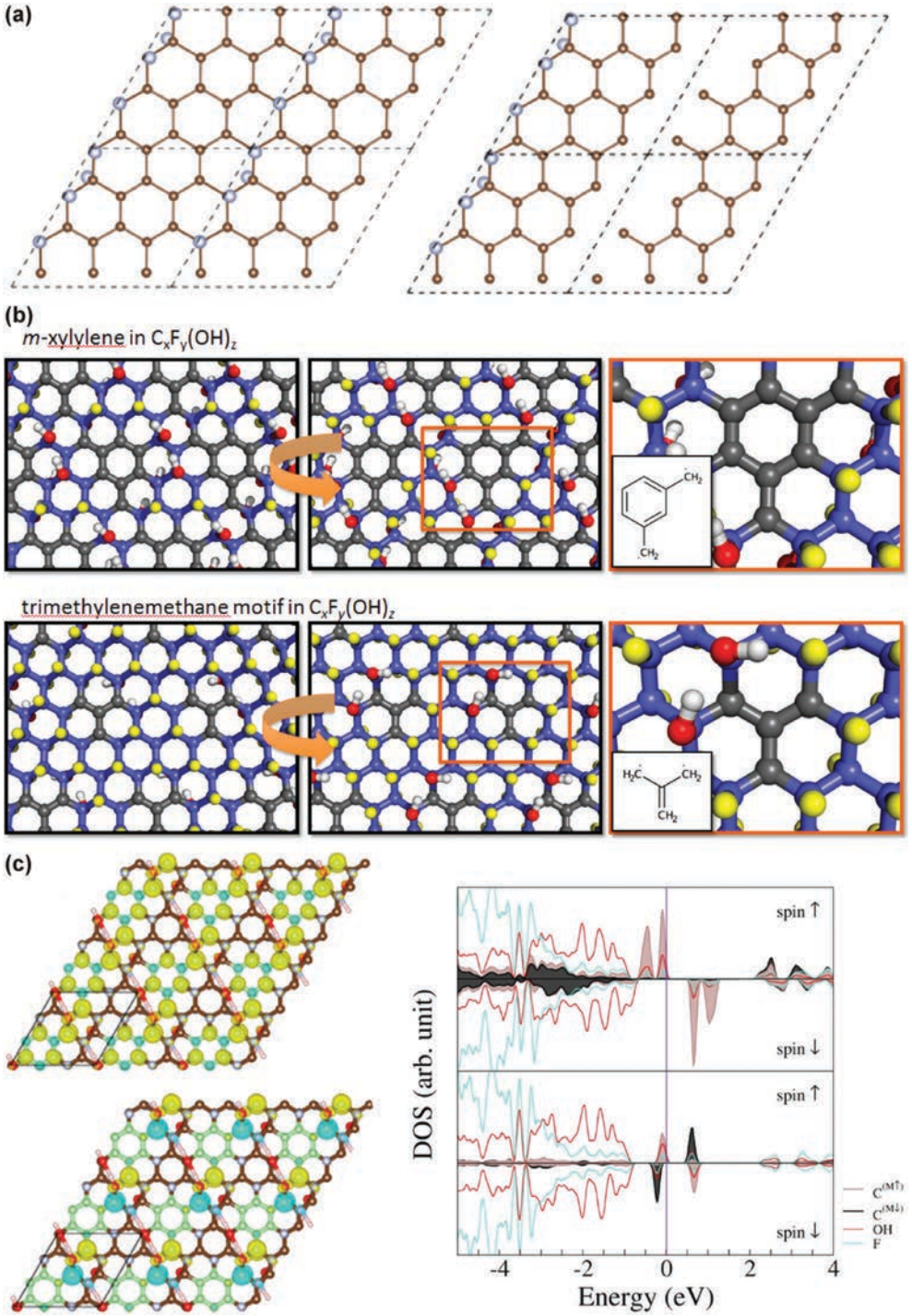


Fig. 101 (a) Structure of $C_{18}F_4$ which can be considered as an sp^3 structural defect in the sp^2 graphene lattice; the sp^3 carbon atoms due to F adsorption (shown in cyan) cut the graphene plane along the zig-zag line and virtually generate a graphene ribbon with a zig-zag edge. (b) Models of diradical motifs in the hydroxofluorographene system (shown in grey) leading to its room-temperature AFM properties. (c) Spin densities in the *m*-xylylene motif embedded in an sp^3 lattice of hydroxofluorographene with the corresponding FM and AFM phases, with spin-up and spin-down densities shown in yellow/blue. Right panels display corresponding densities of states which indicate the important role of –OH group in the superexchange interactions. Reprinted with permission from ref. 54. Copyright 2017 Macmillan Publishers Limited.

Published on 26 March 2018. Downloaded by Univerzita Palackého v Olomouci on 2/28/2019 2:05:03 PM.

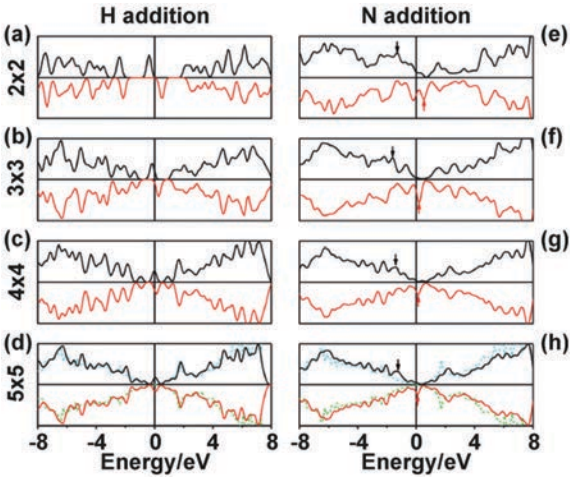


Fig. 102 Spin-split density of states of graphene with various supercell sizes for (a–d) H and (e–h) N additions. The black line represents spin-up and the red line represents spin-down. For comparison in the 5 × 5 supercell, the density of states of graphene is also shown in cyan (spin-up) and green (spin-down) dashed lines. Reprinted with permission from ref. 433. Copyright 2009 The Royal Society of Chemistry.

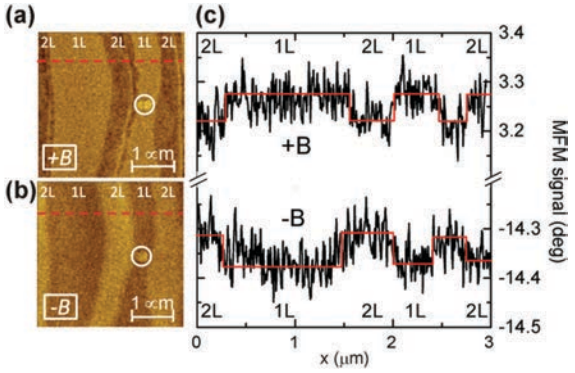


Fig. 103 MFM measurements of hydrogenated epitaxial graphene (1L and 2L) post applying a magnetic field (positive and negative) and the cross section of its magnetization. Reprinted with permission from ref. 436. Copyright 2013 American Physical Society.

Furthermore, theoretical studies have shown that the magnetic behavior in graphene oxide originating from hydroxyl groups is more stable than that observed in graphene surface-functionalized with hydrogen.[441] In particular, the energy barrier for migration was found to be three times higher for hydroxyl groups than for hydrogen, encouraging the magnetic stability in graphenes modified with hydroxyls. Moreover, the migration energy can be further increased upon increasing the number of water molecules linked to hydroxyl groups.[441] Magnetic configurations were predicted to form upon migration of hydroxyl groups from the solvent, facilitated by the ripples on graphene, during the production of graphene laminate. A magnetic configuration containing seven –OH groups was proposed as stable reflecting the symmetry of the graphene lattice. The as-formed clusters carry a large magnetic moment between 4 and 5 μ_B; the clusters were found to be structurally stabilized if the distance between them was larger than 3 nm, behaving thus as paramagnetic centers with negligible exchange interactions.[55]

Following several experimental and theoretical studies published so far, it is not currently clear which oxygen-containing group dominantly governs the magnetic properties in graphene oxide. It was recently reported that if the epoxy groups are destroyed by heat and/or chemical (by NaOH) treatment, the magnetic response of graphene oxide is significantly reduced.[442] This suggests that epoxy groups are responsible for the evolution of unpaired spins on carbon radicals, acting thus as sources of magnetism in graphene oxide.[442] Moreover, if organized as an epoxy-chain pair at various positions on zigzag GNRs, the FM ground state was theoretically predicted.[443] On the other hand, hydroxyl groups were identified to significantly enhance the magnetic response in graphene oxide as they are believed to induce paramagnetic centers with a spin of 5/2.[444] However, the emergence of magnetic moments from hydroxyl groups was found to strongly depend on the their configuration on the graphene oxide sheets; the generation of unpaired spins was predicted only for a case when two non-neighboring hydroxyl-bonded carbon atoms were connected with one carbon atom sitting in between them in the ring.[445]

The concentration of paramagnetic centers in graphene oxide can be increased by increasing the sp^3 content. The effect of degree of oxidation on the magnetic behavior of graphene oxide was recently studied in the work by Liaros *et al.*[446] Fig. 104 shows the temperature evolution of the mass susceptibility for graphene oxide with increasing oxidation ($GO_3 > GO_2 > GO_1$). The Curie temperature was found to increase by increasing the degree of oxidation in graphene oxide. The paramagnetic centers can magnetically communicate to exhibit FM behavior provided they are separated by a small distance. Else, the paramagnetic behavior will be preserved. The magnetic interaction between the localized magnetic moments at sp^3 states is realized by delocalized π-electrons.[446] Although the amount of paramagnetic centers can be increased by increasing the degree of oxidation, the number of delocalized π-electrons is believed to be reduced. Thus, it seems to be necessary to optimize the degree of oxidation to achieve a desired magnetic ordering sustainable at sufficiently high temperatures. Alternatively, the Curie temperature of FM graphene oxide can be increased by doping with nitrogen; if the content of nitrogen reached 8.80 at% (calculated as 100 N/C at%), N-doped graphene oxide showed FM behavior with a saturation magnetization of 1.66 emu g^{-1} (at 2 K) self-sustainable up to 100 K.[447]

Upon chemical, electrochemical, thermal, photocatalytic, or electric-current reduction, the amount of oxygen-containing groups is decreased and graphene oxide is transformed into a reduced form.[438] In general, the reduction of graphene oxide increases the sp^2/sp^3 ratio, resulting in a decrease in the band gap and an increase in the conductivity. However, the conversion of graphene oxide to reduced graphene oxide does

 This journal is © The Royal Society of Chemistry 2018

Published on 26 March 2018. Downloaded by Univerzita Palackého v Olomouci on 2/28/2019 2:05:03 PM.

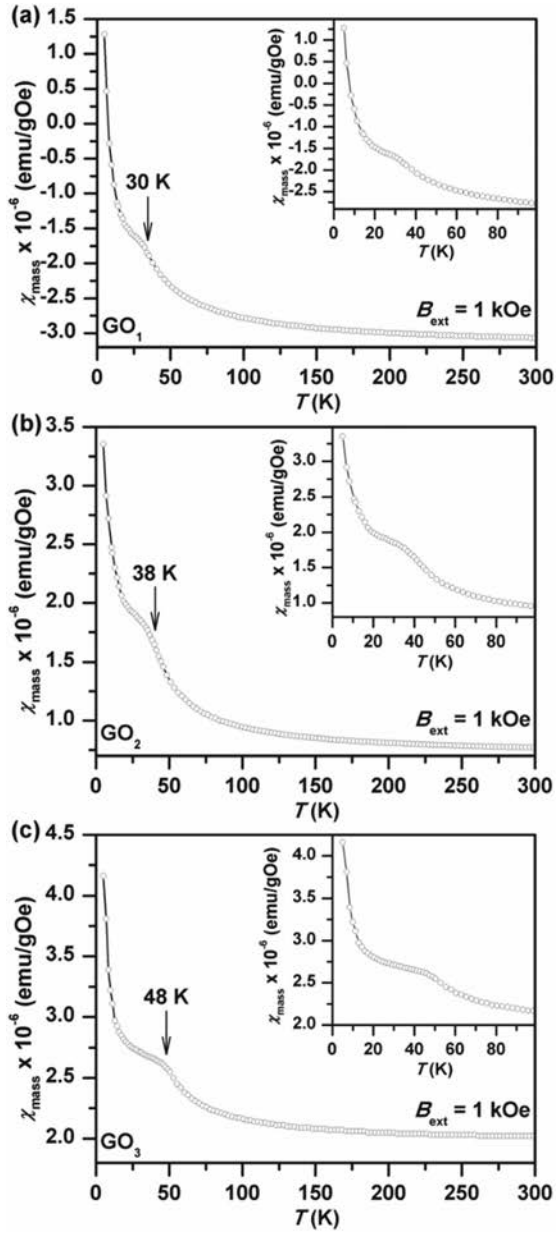


Fig. 104 (a–c) The temperature dependence of mass susceptibility (χ_{mass}) for graphene oxide with different degrees of oxidation ($GO_3 > GO_2 > GO_1$). The insets show the behavior of χ_{mass} at low temperatures. Reprinted with permission from ref. 446. Copyright 2016 The Royal Society of Chemistry.

not restore the features of pristine graphene since the conductivity of the reduced form is 10–100 times lower than that observed for ideal graphene. Moreover, besides residual oxygen-containing groups, reduced graphene oxide possesses structural defects including topological vacancies and pentagon–heptagon defects. A complete reduction to graphene was theoretically suggested to be hardly achieved due to a difficult removal of highly stable carbonyl and ether groups. Several studies reported FM behavior in reduced graphene oxide sustainable even at room temperature.[440,448,449] Fig. 105a shows an example of a sample composed of reduced graphene oxide sheets with saturation magnetization of ~2.73 and ~0.79 emu g^{-1} at 2 K and room temperature, respectively.[450] The origin of the FM response was explained in terms of defect states in the sheets of reduced graphene oxide. The defect states were found to be healed through several processes. Fig. 105b then displays the magnetization *vs.* field curves of reduced graphene oxide sheets annealed at various temperatures (in the interval from 200–800 °C). A sharp decrease in the value of the saturation magnetization (~0.08 emu g^{-1}) was noticed when reduced graphene oxide was annealed at 600 °C. At 600 °C, it was proposed that the defect states mend themselves by a self-repair mechanism that removes various vacancies and the C–C bond is reconstructed. The saturation magnetization then showed an increase with a further increase in the annealing temperature (700 and 800 °C). The increase in the saturation magnetization was understood as a result of the cleavage of the C–C bonds, which produces defects contributing towards an evolution of magnetism in reduced graphene oxide.[450] The paramagnetic centers in graphene oxide and reduced graphene oxide can be easily studied employing the ESR technique. A recent ESR study confirmed the formation of defect states in graphene oxide and its reduced form during the synthesis.[451] The shape of the ESR spectrum and the *g*-value then provide valuable information on the paramagnetic electrons and their interactions with the surrounding states.

A strong room-temperature FM ordering was observed for reduced graphene oxide prepared by high-temperature annealing of weakly oxidized graphene oxide in an Ar atmosphere.[452] The intrinsic nature of the witnessed ferromagnetism was confirmed by hysteresis in magnetoresistance. Graphene can exhibit both positive[453] and negative[454,455] magnetoresistance. The chiral nature of electrons in graphene is then believed to be responsible for a weak antilocalization manifested by a positive magnetoresistance.[456] The random resistor network caused by the inhomogeneous distribution of charged impurities was also suggested to produce a positive magnetoresistance.[364] In contrast, the formation of cyclotron orbits and delocalization effect under the influence of a magnetic field are then responsible for a negative magnetoresistance in graphene.[457–462] Fig. 106 and its inset display the temperature dependence of magnetoresistance and resistance, respectively, in weakly oxidized graphene oxide. Non-magnetic graphene does not show any hysteresis loop in either positive or negative magnetoresistance. The spin-dependent scattering of FM defects then causes the hysteresis of negative magnetoresistance.

Diamantopoulou *et al.*[463] studied the emergence of magnetism in graphene oxide and its alteration upon chemical reduction by sodium borohydride. Contrary to other experimental works, paramagnetic behavior with a saturation magnetization of ~1.2 emu g^{-1} and weak AFM interactions were observed for pristine graphene oxide sheets. By employing the ESR technique, the presence of spatially isolated magnetic clusters carrying high spin moments (up to $S = 2$) was detected besides expected spin-half paramagnetic defect centers. If reduced, the saturation

Published on 26 March 2018. Downloaded by Univerzita Palackého v Olomouci on 2/28/2019 2:05:03 PM.

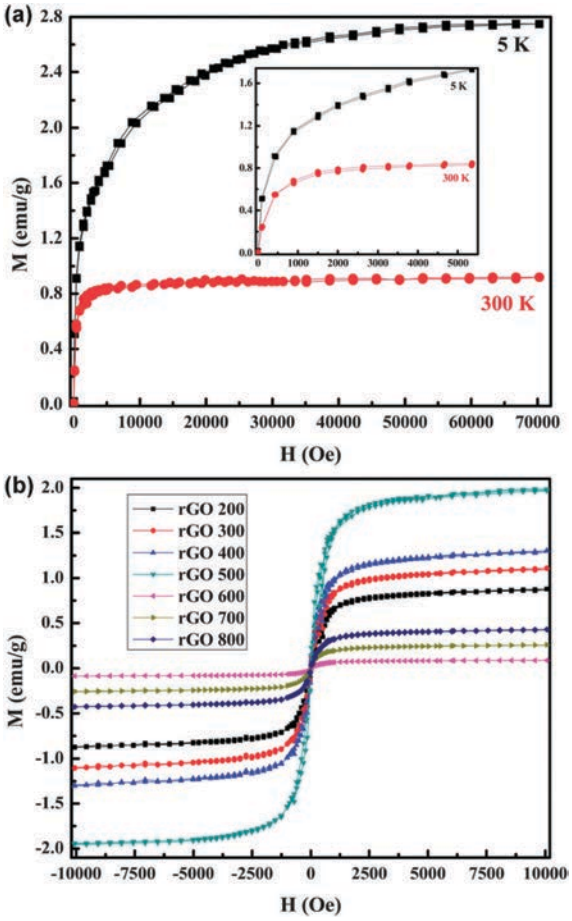


Fig. 105 Magnetization *vs.* field measurements for (a) reduced graphene oxide at 5 and 300 K and (b) reduced graphene oxide annealed at various temperatures (200–800 °C). Reprinted with permission from ref. 450. Copyright 2013 The Royal Society of Chemistry.

magnetization of the system dropped to ~0.17 emu g^{-1} with enhancement of a diamagnetic contribution, implying a dramatic elimination of paramagnetic centers and growth of sp^2 domains. From analysis of the ESR spectrum, two distinct spin systems were identified in chemically reduced graphene oxide, *i.e.*, localized π-defect states coupled strongly with the itinerant spins occurring within the formed sp^2 cluster and edge/vacancy defect spins, attributed to the persistent structural inhomogeneity in reduced graphene oxide after chemical reduction.[463]

Recently, room-temperature ferromagnetism was detected in reduced graphene oxide doped with nitrogen; such a system was prepared by direct reduction of graphene oxide in N_2 plasma at room temperature. The induced FM behavior was attributed to pyrrolic nitrogen bonding configurations; at low temperatures, pyrrolic nitrogen is predicted to be more stable than pyridinic and graphitic nitrogen.[464] Increased magnetization was found for reduced graphene oxide with increased doping with nitrogen; here, the N-doped reduced graphene samples were synthesized by annealing reduced graphene oxide,

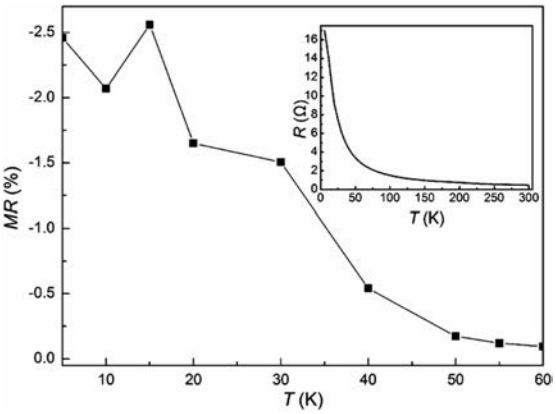


Fig. 106 Temperature dependence of magnetoresistance (MR) for weakly oxidized graphene oxide. The inset shows the temperature dependence of resistance (*R*) of weakly oxidized graphene oxide. Reprinted with permission from ref. 452. Copyright 2014 Elsevier Ltd.

pre-prepared by annealing graphene oxide in an Ar atmosphere at 700 °C for 1 h, in NH_3 at various temperatures (in the interval from 400 to 900 °C) for 1 h.[465] However, no clear scenario explaining an increase in the magnetization with increasing nitrogen content was suggested due to a complex interplay between pyridinic, pyrrolic, and graphitic nitrogen.[465]

The possibility of imprinting magnetism into graphene by covalent derivatization leading to graphene acid was recently suggested by DFT calculations (see Fig. 107).[466,467] The theoretical study of the thermodynamic stabilities of surface carboxylated graphenes, $C_x(COOH)_y$, with *x*/*y* ratios of up to the experimental value of 6.6 indicated, however, that most of the local COOH arrangements will be thermodynamically accessible with a small energy difference between them.[466] This implied that the topology of the carboxyl groups on the graphene surface will be given by a statistical distribution. One shall, however, notice that a statistical (random) distribution of the functional groups across the surface would prevent the formation of FM order. Therefore, experimental verification of the emergence of magnetic order in graphene acid is highly vital.

7. Magnetic ordering in graphene-based materials due to intercalation

Graphite intercalation compounds (GICs) have been extensively studied for more than a century; the earliest publication dates to 1840.[468–470] The advent of 2D materials has renewed interest in this field; reports on the intercalation of various species such as $FeCl_3$,[471–474] Ca,[475] Ce,[476] and Li[477] in few-layer graphene (FLG) have offered a new route to synthesizing graphene-based materials both for novel flexible displays and photovoltaics, as the associated electronics require materials that are flexible, optically transparent and electrically conductive, and for energy storage, magnetic/spintronic and superconductive applications. For the timely and comprehensive review of the recent progress

 This journal is © The Royal Society of Chemistry 2018

Published on 26 March 2018. Downloaded by Univerzita Palackého v Olomouci on 2/28/2019 2:05:03 PM.

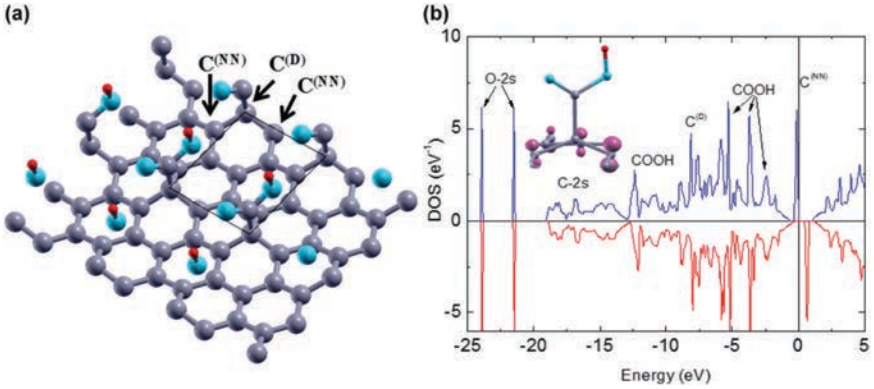


Fig. 107 (a) Model of carboxylated graphene sheet. (b) Theoretical density of states (DOS) of C_8COOH showing spin-polarized midgap states. The electron density associated with the spin-up channel of midgap states is shown in the inset. Reprinted with permission from ref. 467. Copyright 2017 American Chemical Society.

on intercalation methods, as well as tailored properties and potential applications offered by intercalation, the reader is referred to the work by Wan *et al.*[478]

The magnetic properties of $FeCl_3$ GICs have received significant attention in the last five decades mainly because they provide a model system for studying the magnetic phase transition of a 2D spin system.[479] *Ab initio* numerical simulations employing the Hubbard parameter (U), which reflects the strength of the on-site Coulomb interaction, and the J-parameter, which adjusts the strength of the exchange interaction, led to a theoretical understanding of the structural, electronic, and magnetic properties in $FeCl_3$-FLG.[480] It was reported that stage-1 $FeCl_3$-FLG has an AFM ground state and stage-2 $FeCl_3$-FLG exhibits FM ordering at the ground state (see Fig. 108). At the same time, the magnetic moments of $FeCl_3$ are expected to align ferromagnetically in the same intercalant layer.

More recently, Bointon *et al.*[481] *via* successful uniform intercalation of large area (1 cm^2) epitaxial FLG grown on 4H-SiC with $FeCl_3$ (see Fig. 109a and b) provided the evidence for magnetic ordering in the 2D limit of graphene. Fig. 109c shows the measured weak localization contribution to the magneto-conductance at various temperatures, which allowed extraction of the corresponding phase coherence length (L_φ; see Fig. 109d). Large values of L_φ for $T < 30$ K, a temperature matching the 2D magnetic correlations in the plane of $FeCl_3$, and a saturation of L_φ for T lower than $\sim$4 K, a temperature corresponding to three-dimensional (3D) AFM coupling between planes of $FeCl_3$, showed

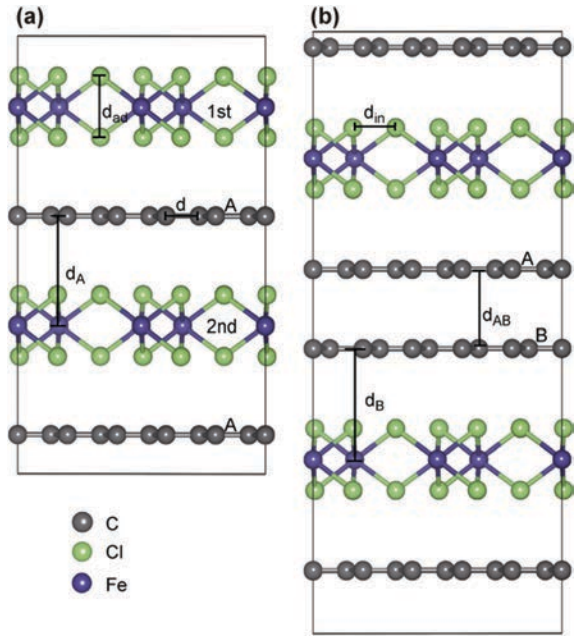


Fig. 108 GICs classified by the number of graphene layers between adjacent intercalant layers: (a) stage-1 $FeCl_3$-based GICs; (b) stage-2 $FeCl_3$-based GICs. Reprinted with permission from ref. 480. Copyright 2013 Elsevier B.V.

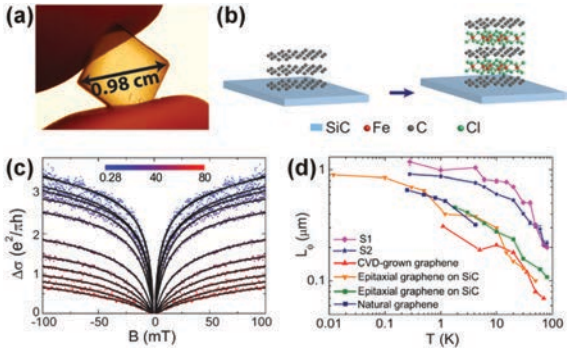


Fig. 109 (a) Intercalated FLG on 4H−SiC and (b) schematic crystal structure of trilayered stage-1 $FeCl_3$-FLG. (c) The measured weak localization contribution to the magneto-conductance (scatter points) and theoretical fits (solid line). (d) Temperature dependence of L_φ for pristine graphene prepared by different methods. The values are compared to the estimated values of $FeCl_3$/FLG. Reprinted with permission from ref. 481. Copyright 2014 American Chemical Society.

Published on 26 March 2018. Downloaded by Univerzita Palackého v Olomouci on 2/28/2019 2:05:03 PM.

indeed that $FeCl_3$-FLG is a good platform for studying magnetic ordering in the extreme 2D limit of graphene.[481]

Graphene-based FM heterostructures have been considered as ideal candidates for a new class of tunnel magnetoresistance (TMR) or giant magnetoresistance (GMR) devices. Cutting-edge spin-polarized scanning tunneling microscopy (SP-STM) experiments combined with state-of-the-art first-principles calculations revealed an extremely high magnetic anisotropy energy for a cobalt-intercalated graphene/Ir(111) heterostructure (see Fig. 110a) with an out-of-plane easy axis (see Fig. 110b).[482] A series of spin-polarized dI/dV measurements of large surface areas, containing 33 intercalation regions of different sizes and various shapes acquired with a different out-of-plane magnetic field in the order of 0 T → −6.5 T → +6.5 T → −6.5 T and plotted as the percentage of area among all intercalation regions which were aligned in the +z direction *vs.* the applied field, showed a hysteresis loop (see Fig. 110c).[482] This indicated that even an upper field limit was not able to align 100% of the intercalation regions and, thus, the actual coercive field was higher than the value of ~4.5 T inferred from the loop. Further, the graphene layer presented a magnetic Moiré pattern with a high corrugation on the underlying cobalt monolayer. First-principles calculations showed that its origin lies in the variation of a site-dependent magnetization of the graphene: at top sites, the graphene was coupled ferromagnetically to the cobalt underneath, while it was antiferromagnetically coupled at fcc and hcp sites (see Fig. 111).[482]

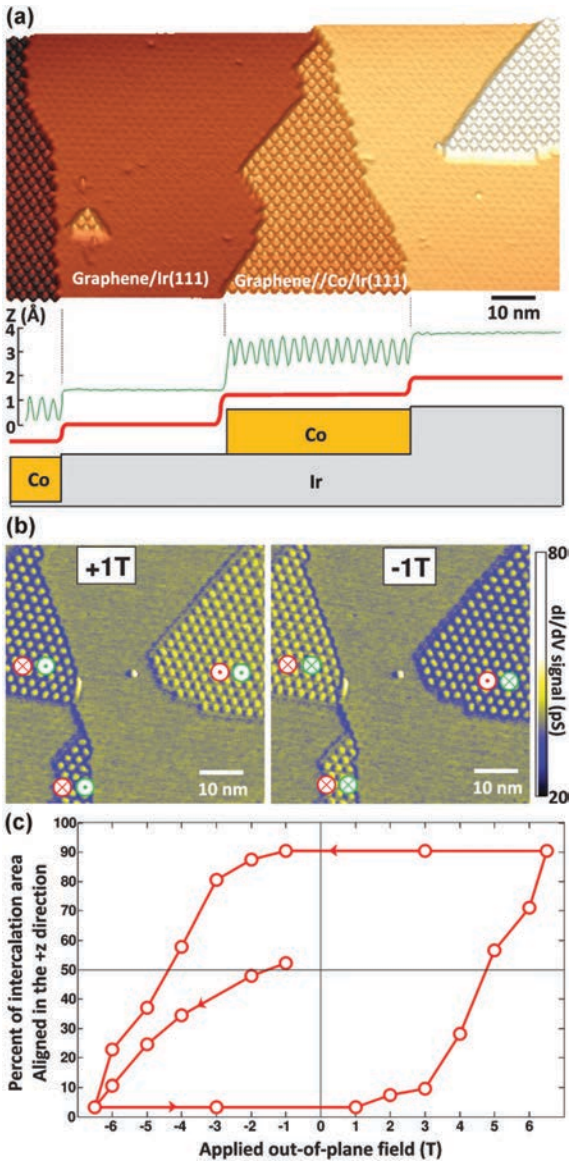


Fig. 110 (a) Topography of the graphene/Ir(111) surface. The line profile illustrates the difference between graphene/Ir(111) and graphene/Co/Ir(111) Moiré corrugations. (b) Maps of the spin-resolved differential tunneling conductance (dI/dV map) of the same area with an out-of-plane applied magnetic field of +1 T and −1 T, respectively. Green symbols represent magnetic orientation of the SP-STM tip and red symbols correspond to magnetic orientation of the intercalation regions. (c) Hysteresis loop obtained from large-scale spin-resolved dI/dV maps presenting 33 intercalation regions. Reprinted with permission from ref. 482. Copyright 2013 American Physical Society.

More recent spin-polarized low-energy electron microscopy (SPLEEM) experiments confirmed out-of-plane magnetization in thin-enough films of cobalt intercalated at the graphene/Ir(111) interface, while it is in-plane for thicker films.[483] Magnetization was purely out-of-plane for Co films thinner than 13 monolayers, while it was purely in-plane for Co films thicker than 24 monolayers. In the intermediate thickness range, magnetization exhibited a canted state. Vectorial imaging of magnetic domains revealed an unusually gradual thickness-dependent spin reorientation transition, in which magnetization rotated from out-of-the-film plane to the in-plane direction by less than 10° per cobalt monolayer. During this transition, cobalt films exhibit a meandering spin texture, characterized by a complex 3D, wavy magnetization pattern with a short wavelength, in which magnetic domains with a uniform magnetization separated by domain walls cannot be defined as the pattern resembles a flux closure configuration in three dimensions (see Fig. 112).[483]

Clearly, graphene-based magnetic heterostructures thus have the potential to open new prospects in nanomagnetism and surface magnetism.

8. Magnetism in selected graphene analogues and 2D materials

The recent progress in imprinting magnetism in otherwise non-magnetic graphene has aroused significant attention in the scientific community and prompted research on other 2D layered materials, of which layered transition metal dichalcogenides (TMDCs) are vital members.[484] While graphene is single atom thick, TMDC consists of transition metals in between two layers of chalcogen atoms. TMDCs are described by the formula MX_2, where M is the transition metal (*e.g.*, Mo, W, Ti, Nb, Re, V, Zr, Ta, Hf, *etc.*) and X denotes the chalcogen atom (*e.g.*, S, Se, or Te). The layers in any TMDC

 This journal is © The Royal Society of Chemistry 2018

Published on 26 March 2018. Downloaded by Univerzita Palackého v Olomouci on 2/28/2019 2:05:03 PM.

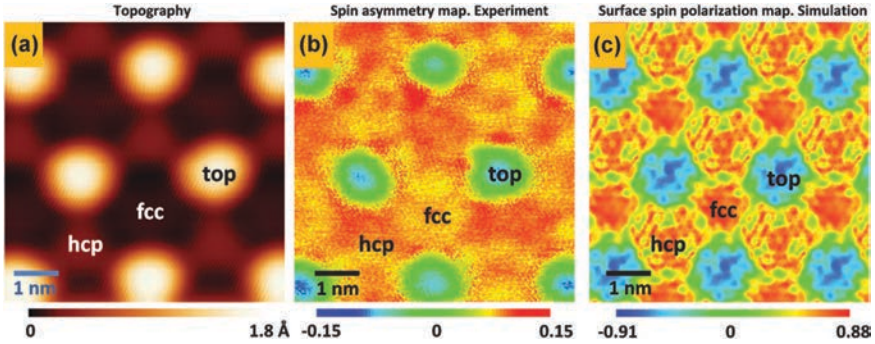


Fig. 111 (a) Topography of the Co-intercalated graphene/Ir(111) region. (b) Spin-asymmetry map of the region shown in panel (a). (c) Simulated surface spin polarization map. Panels (b and c) define a magnetic Moiré pattern of the graphene–Co/Ir(111) intercalation region. Reprinted with permission from ref. 482. Copyright 2013 American Physical Society.

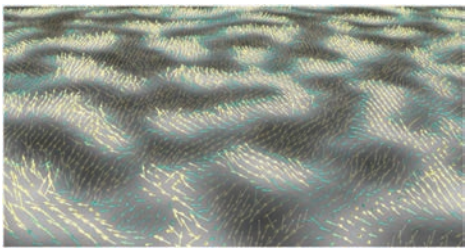


Fig. 112 Three-dimensional representation of the magnetization vector (arrows) in the case of 16 monolayers of graphene/Ir(111) intercalated Co. Dark and light domains represent the out-of-plane component of the magnetization vector. The magnetization vector is represented by colored arrows (yellow when magnetization is out-of-plane, green when it is in-plane) and smoothly rotates in all space directions in the form of waves across the field of view, like a wheat field in the wind. Reprinted with permission from ref. 483. Copyright 2016 Macmillan Publishers Limited.

are held tight by van der Waals interactions. Three crystallographic arrangements are recognized for such layered materials: (i) semiconducting 2H (trigonal prism) form, (ii) metallic 1T (octahedral) form, and (iii) semiconducting 3R (trigonal prism) form.[484–486]

Various single- and few-layered TMDCs have been synthesized and characterized so far.[487] They are frequently prepared by exfoliation, chemical vapor deposition, or molecular beam epitaxy techniques. There have been several reports on the magnetism of TMDCs published so far in the literature.[488–493] The pristine bulk form of molybdenum disulfide (MoS_2) shows only diamagnetism. Moreover, ESR studies on inorganic fullerene-like MoS_2 nanoparticles[494] confirmed the presence of a large density of dangling bonds carrying unpaired electrons that signifies a more defective nature than that of its bulk form. Like highly oriented pyrolitic graphite, MoS_2 exhibited room-temperature FIM order upon exposure to a 2 MeV proton beam with a Curie temperature of 895 K (see Fig. 113).[495] Proton irradiation can induce defects such as atomic vacancies, displacements, and saturation of a vacancy by the implanted protons which are all regarded as a possible source of the high-temperature magnetism. Recently, intriguing physical properties were theoretically proposed for the 1T′ phase of MoS_2.[496] In particular, it was found that the 1T′ phase of MoS_2, semi-metallic in nature, can host lattice imperfections more readily than its 2H phase; they preferentially form at the S atom closer to the Mo atomic plane. Local magnetic moments are then induced by the Mo adatoms and Mo antisites. In contrast, S vacancies, S adatoms, and Mo vacancies do not cause emergence of any spin polarization.[496]

The room-temperature ferromagnetism in MoS_2 has been mainly attributed to edge states, vacancies, vacancy clusters, and reconstruction of the lattices. Edge-oriented MoS_2 nanosheet-like films were shown to exhibit room-temperature ferromagnetism due to the presence of a high density of prismatic edges containing unsaturated Mo and S atoms.[497] Similarly, magnetization measurements on MoS_2 nanosheets of different sizes prepared by exfoliation of bulk MoS_2 in dimethylformamide solution revealed room-temperature ferromagnetism (see Fig. 114).[498] The X-ray photoelectron spectroscopy, TEM, and ESR results suggested that the origin of such FM order is related to the presence of edge spins on the edges of the nanosheets. Field-cooled (FC) and zero-field-cooled (ZFC) magnetization (see Fig. 114d) diverged from about 300 K. Such divergence of ZFC and FC magnetization curves is expected in magnetically frustrated systems (*e.g.*, spin glasses) where FM and AFM domains are randomly distributed. The nanosheets are non-magnetic beyond a certain thickness.[499] First-principles calculations on MoS_2 clusters showed a magnetic ordering arising due to the unsaturated metal center with partially filled d orbitals.[500] Besides, the FM response was detected in MoS_2 partly due to the presence of zigzag edges in the magnetic ground state.[501] Similar to GNRs, magnetic edge states were theoretically identified in MoS_2.[502] It was claimed that the magnetic ordering can evolve only due to the presence of sulfur-terminated edges resulting from splitting of metallic edge states at E_F. Moreover, first-principles calculations[503] predicted spin-polarized states in zigzag MoS_2 nanoribbons and spin-unpolarized ground states in armchair MoS_2. FM and metallic nature of zigzag-edged MoS_2 nanoribbons is independent of their width and

Published on 26 March 2018. Downloaded by Univerzita Palackého v Olomouci on 2/28/2019 2:05:03 PM.

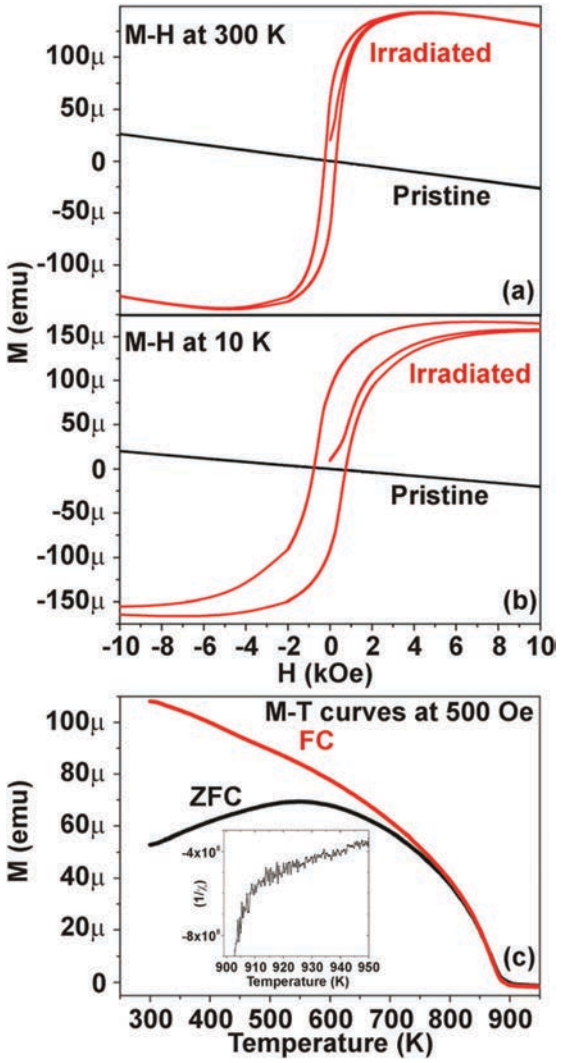


Fig. 113 Magnetization *vs.* magnetic field (*M vs. H*) curves (a) at 300 K and (b) at 10 K for an untreated and irradiated MoS_2. (c) Zero-field-cooled (ZFC) and field-cooled (FC) magnetization *vs.* temperature measurements in an applied field of 500 Oe for an irradiated MoS_2 at 5×10^{18} ions cm^{-2}. The inset shows the inverse of the estimated magnetic susceptibility *vs.* temperature plot near the Curie temperature (900–950 K). The estimated value of the Curie temperature is 895 K. Reprinted with permission from ref. 495. Copyright 2012 American Institute of Physics.

thickness, while the armchair nanoribbons are non-magnetic with a semiconducting behavior.

The possibility of imprinting FM behavior, sustainable at room temperature, by adsorption of light elements (*i.e.*, H, F, and Li) and exposed to strain was theoretically explored for MoS_2 monolayers.[504] Besides shifting E_F of MoS_2 in the conduction or valence band (depending on the charge polarity of the adsorbed atom), no induction of magnetic moments was found for adsorption at the S site. However, when the strain was applied increasing the density of states at E_F, magnetic moments emerged in MoS_2 with H, F, and Li adsorbed. Moreover, it was suggested that the FM state is more energetically stable than the AFM regime. Importantly, half-metallic ferromagnetism was found to emerge for the MoS_2 monolayers with H and F atoms adsorbed on their surfaces.[504]

Analogous to MoS_2, tungsten disulfide (WS_2) is non-magnetic in the bulk form. More recently, structural and magnetic properties of MoS_2 and WS_2 exfoliated using various alkali metal intercalating compounds such as butyllithium and sodium naphthalenide were thoroughly analyzed.[505] It has been shown that effective exfoliation, leading to the formation of a single layer of TMDCs by using sodium naphthalenide, and a corresponding phase transition from semiconducting 2H to metallic 1T polymorph along with the formation of defects on the edges of TMDC sheets resulted in the development of a room-temperature FM phase (see Fig. 115).[505] This effect was observed neither in bulk TMDCs nor in the butyllithium exfoliated samples. The latter exhibited a considerably lower degree of exfoliation and, accordingly, a lower concentration of defects on the edges of individual sheets as compared with sodium naphthalenide exfoliated materials, which further highlighted the role of structural disorder on the sheet edges in the conductive metallic phase of TMDCs for the room-temperature ferromagnetism.

Mao *et al.*[506] measured the saturation magnetization of WS_2 reaching a value of about 0.004 emu g^{-1} at 10 K. The corresponding magnetization *vs.* magnetic field plots of bulk and nanosheets at various temperatures are shown in Fig. 116.[506] The Curie temperature of WS_2 nanosheets estimated from the ZFC/FC plots, shown in Fig. 116c, is found to be $\sim$330 K.[506] Like graphene, the zigzag edges contribute to the ferromagnetism of WS_2 layers. In addition, the impurities can also trigger FM behavior in WS_2. DFT calculations show that doping of V, Nb, and Ta in WS_2 is preferred when WS_2 is rich in S instead of W. The doping causes a coupling between the dopant's unpaired d orbital and the nearest neighbors of W 5d and S 3p states, thereby inducing ferromagnetism. This signifies that the magnetic properties of such materials could be tuned using metal dopants.[507] First-principles theoretical computations for monolayered WS_2 nanoribbons suggest that zigzag edges are responsible for FM metallic behavior.[507] The magnetic moments reside at the W and S edge atoms. The magnetic ordering can be varied by changing the width of zigzag WS_2 nanoribbons.[507] In contrast, armchair WS_2 nanoribbons show a semiconducting behavior similar to their MoS_2 counterparts.

Recently, vanadium disulfide (VS_2) attracted significant attention due to the $3d^1$ electronic configuration of quadrivalent vanadium and strong electron coupling manifested, among others, by collective electronic behaviors including charge density wave order. More importantly, existence of intrinsic magnetic ordering was theoretically proposed to occur in VS_2 when the magnetic coupling can be readily tuned by a strain. The room-temperature FM ordering in VS_2 can be stabilized by a few-layered architecture;[508] if properly engineered, the van der Waals interactions were identified to play a crucial role providing regulation of spin properties and band gap in VS_2. Specifically, enlarging the van der Waals interactions was found to encourage a metal-

 This journal is © The Royal Society of Chemistry 2018

Published on 26 March 2018. Downloaded by Univerzita Palackého v Olomouci on 2/28/2019 2:05:03 PM.

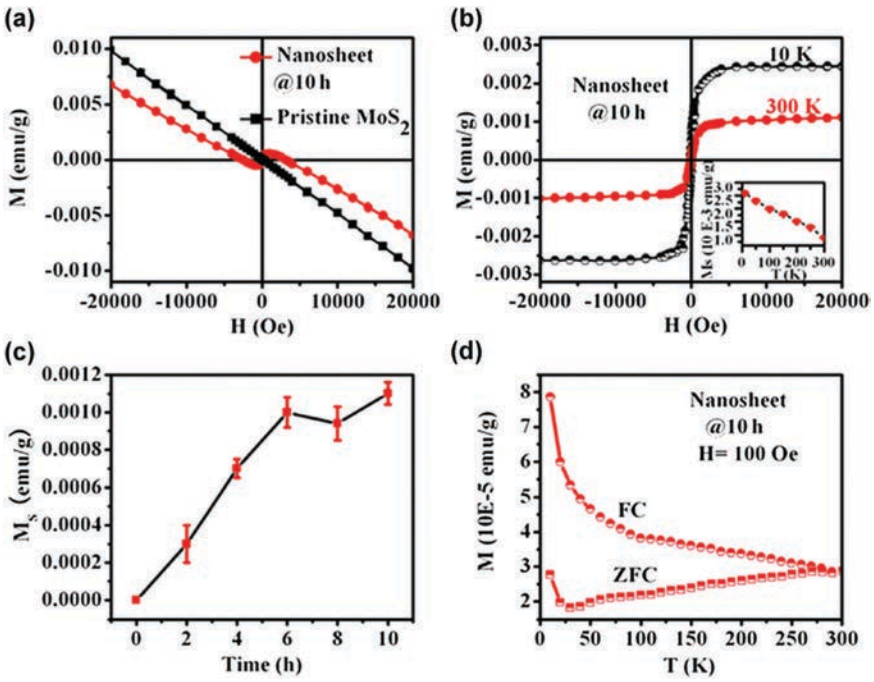


Fig. 114 (a) Room-temperature magnetization *vs.* magnetic field (*M vs. H*) curves for MoS_2 pristine powders and the exfoliated nanosheets (sonicated in dimethylformamide for 10 h). The exfoliated MoS_2 nanosheets show the FM signal in the lower field region, in contrast to MoS_2 powders which show only the diamagnetic signal. (b) *M vs. H* curves for MoS_2 nanosheets measured at 10 and 300 K. After deducting the diamagnetic signal, the saturation magnetizations (M_S) are 0.0025 and 0.0011 emu g^{-1} at 10 and 300 K, respectively, which are comparable to other dopant-free diluted magnetic semiconductors. (c) M_S of MoS_2 nanosheets increases as the ultrasonic time increases, and then becomes invariable when the ultrasonic time exceeds 6 h. (d) ZFC and field-cooled FC magnetization curves for the exfoliated MoS_2 nanosheets sonicated in DMF for 10 h. FC and ZFC magnetization curves diverge from about 300 K. Reprinted with permission from ref. 498. Copyright 2013 Springer.

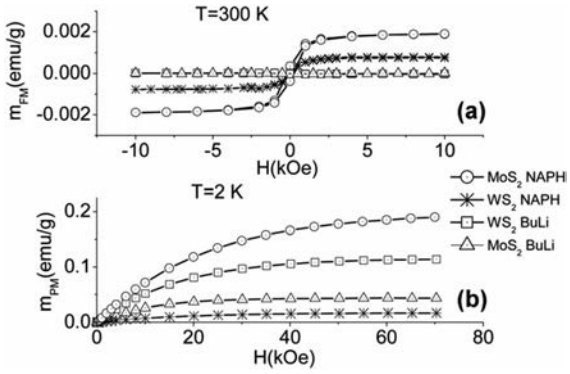


Fig. 115 Magnetization curves for MoS_2 and WS_2 at (a) T = 300 K and (b) at T = 2 K (measured data are depicted by symbols, lines correspond to theoretical calculations with S = 1) exfoliated by using butyllithium (BuLi) and sodium naphthalenide (NAPH). Reprinted with permission from ref. 505. Copyright 2016 The Royal Society of Chemistry.

to-semiconductor transition while compression of van der Waals interactions was responsible for strengthening the metallic behavior of VS_2 resulting from an increased overlap of chalcogens between the neighboring layers. Thus, both charge and spin degrees of freedom can be precisely tuned within the VS_2 lattice, which is viewed as highly promising for future generation of spintronic devices.[508]

Although ReS_2 is an inorganic analogue of graphene belonging to the TMDC family, it exhibits a unique distorted orthogonal structure with an in-plane structural anisotropy.[509] Re atoms in ReS_2 are dimerized due to the Peierls distortion to form the zigzag chains. Thus, the layers in ReS_2 are decoupled electronically and vibrationally, thereby reducing the layer-dependent physical and chemical properties. ReS_2 behaves as a diamagnetic semiconductor with a direct gap. If sulfur vacancies are present, they stabilize non-magnetic semiconducting ground states. In contrast, rhenium vacancies promote generation of spin-polarized ground states with localized magnetic moments ranging from 1 to 3 μ_B; however, the formation of a Re vacancy needs much larger energy and is, thus, less likely to occur.[509] Moreover, the theoretical calculations suggest the formation of mid-gap states due to fluorination of the Re chains.[510] AFM coupling between Re chains and FM coupling within Re chains are observed for the metallic mid-gap states, while the semiconducting mid-gap states show no magnetic couplings. Recently, ReS_2 was also found to possess FM behavior at its wrinkled regions.[511] In addition, adsorption of nitrogen and phosphorus atoms on the ReS_2 sheets was found to generate spin-polarized defect states, leading to a half-semiconducting behavior.[512]

Published on 26 March 2018. Downloaded by Univerzita Palackého v Olomouci on 2/28/2019 2:05:03 PM.

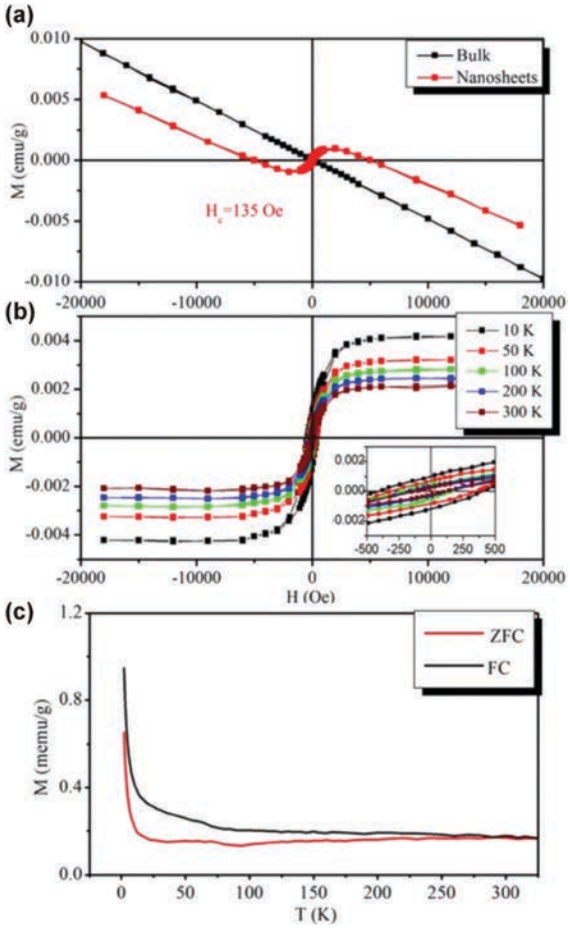


Fig. 116 (a) Magnetization *vs.* magnetic field (*M vs. H*) curves for bulk and nanosheets of WS_2, (b) *M vs. H* plot of WS_2 nanosheets at different temperatures with background correction, and (c) ZFC/FC magnetization curves of WS_2 nanosheets. Reprinted with permission from ref. 506. Copyright 2013 Springer.

Significant attention was also devoted to $MoSe_2$-, WSe_2-, and $ReSe_2$-type TMDCs with potential evolution of magnetically-ordered regimes. In particular, room-temperature FM behavior was observed for WSe_2 nanosheets; employing the MFM technique, the magnetic regions were identified to be located at the edges.[513] The existence of edge magnetic moments was also confirmed by the theoretical calculations, originating from unsaturated Se and W atoms at the edges. More specifically, FM ground states were found to exist only in cases when the edges are terminated fully or by 50% terminated by Se atoms. Upon increasing the thickness of the WSe_2 nanosheets, FM response was observed to decrease rapidly, disappearing at a critical number of layers (*i.e.*, 6 atomic layers).[513] Alternatively, application-promising magnetic features can be tuned by doping as proved for the $MoSe_2$ nanosheets.[514] The recent theoretical study on doped $MoSe_2$ systems showed that if N and F atoms are substituted (at a concentration of 3.12 at%) at the Se-sites (*i.e.*, under Mo-rich conditions) to the $MoSe_2$ crystal structure, an FM ground state is expected. More interestingly, a half-metallic ferromagnetism appeared for the Cl-, Br-, and I-doped $MoSe_2$ nanosheets. The origin of magnetism in such atom-substituted systems was then explained in terms of the p–d hybridization between the p orbitals of doped atoms and the d orbitals of the neighboring three Mo atoms.[514] Similarly, a room-temperature ferromagnetism was recently reported for the Re-doped $MoSe_2$ systems stemming from ordering of the next nearest-neighboring Re pairs.[515] In the $ReSe_2$-based systems, the magnetic ground state can evolve due to a cationic defect (*i.e.*, Re vacancy), resulting in the reconstruction and orbital hybridization between neighboring Se atoms; the magnetic response can be significantly regulated by the external strain, modifying the distribution of the spin polarization among neighboring Se atoms.[516]

Monolayered metal dihalides, *i.e.*, MX_2 where X = Cl, Br, I, are regarded as a new class of 2D materials with crystal structures closely resembling those of TMDCs; in metal dihalides, a layer of transition metal atoms is sandwiched between two layers of halogen atoms. In the family of metal halides, $GaBiCl_2$, ZrBr, and HfCl monolayered nanosheets were found to behave as room-temperature quantum spin Hall insulators with large and nontrivial band gaps.[517,518] FM ordering was, for example, observed for monolayered $FeCl_2$[519] and CrI_3,[520] the former with a half-metallic feature and the latter with a remarkable out-of-plane spin orientation. Very recently, an FM ground state was reported for 2D $FeCl_2$, $FeBr_2$, FeI_2, $NiCl_2$, $NiBr_2$, NiI_2, $CoCl_2$, and $BoBr_2$ whereas an AFM ground state was identified for VCl_2, VBr_2, VI_2, $CrCl_2$, $CrBr_2$, CrI_2, $MnCl_2$, $MnBr_2$, and MnI_2 nanosheets; the existence of different magnetic states in metal halides was explained in terms of the competition between AFM direct nearest-neighbor d–d exchange interactions and FM exchange interactions mediated by the halogen p-states.[521] In addition, it was proposed that the values of the Curie temperature calculated for transition metal halides are comparable to those of TMDCs due to a tight ionic bonding in halides, significantly encouraging the superexchange interactions between the magnetic metal ions *via* the halogen atoms.[521] Furthermore, a half-metallic feature was predicted for a family of iron dihalides, *i.e.*, $FeCl_2$, $FeBr_2$, and FeI_2 (see Fig. 117a).[522] They show a large magnetic moment of 4 μ_B, originating from high-spin d^6 Fe^{2+} octahedral coordination, and an easy magnetization plane characterized by no energy requirement for rotation of the magnetic moment within the plane of the 2D layer. In addition, large half-metallic spin gaps were identified for iron dihalides, *i.e.*, 6.4, 5.5, and 4.0 for $FeCl_2$, $FeBr_2$, and FeI_2, respectively, resulting from a quantum confinement effect. Such 2D materials can then be used in a potential spintronic device illustrated schematically in Fig. 117b;[522] the hypothetical magnetic tunnel junction is composed of a BN tunneling layer sandwiched between two half-metallic contacts, one from $FeCl_2$ and the other from $FeBr_2$. Here, the magnetoresistance is maximized by the 100% spin polarization of 2D $FeCl_2$, $FeBr_2$, and FeI_2. Moreover, such 2D half-metals can be used in Datta–Das spintronic transistors or spin transistors with a high

 This journal is © The Royal Society of Chemistry 2018

Published on 26 March 2018. Downloaded by Univerzita Palackého v Olomouci on 2/28/2019 2:05:03 PM.

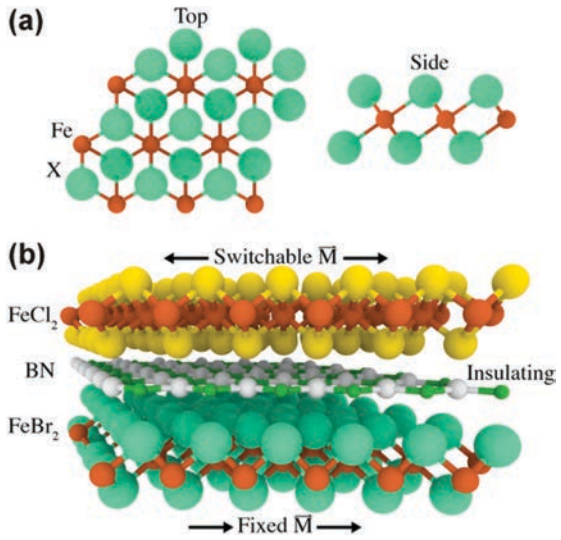


Fig. 117 (a) Top and side views of the crystal structure of 2D iron dihalides ($FeCl_2$, $FeBr_2$, and FeI_2). (b) Scheme of a hypothetical magnetic junction based on 2D iron dihalides. The magnetization of the top layer can be reoriented by an external magnetic field while the magnetization of the bottom layer is pinned by a suitable substrate. The junction operates in "ON" and "OFF" states corresponding to parallel and antiparallel orientation of the layers, respectively. Reprinted with permission from ref. 522. Copyright 2017 American Chemical Society.

transmissivity (promoted by spin–orbit coupling from an appropriate insulating layer).[522]

Transition metal dinitrides are regarded as another class of atomic-scale materials. MoN_2 is a typical example of 2D transition metal dinitrides; due to inability of Mo to saturate all three 2p orbitals of N, a spontaneous magnetic moment is believed to emerge at N sites.[523] 2D MoN_2 was proposed to behave as a ferromagnet with a theoretically calculated Curie temperature of 420 K. The advantage of MoN_2 over other 2D materials relies on the nature of magnetism originating from electron-deficient N orbitals when no doping or structure modification is needed to imprint magnetic features. Moreover, MoN_2 can be turned to a half-metal once exposed to a tensile stress. In contrast, YN_2 and 1T-TaN_2 are intrinsically half-metallic with an FM ground state;[523,524] in 1T-TaN_2, the magnetic moments and half-metallic behavior are mainly ascribed to the p orbitals of N instead of d orbitals of Ta atoms, which is believed to be beneficial to overcome a problem with a short spin relaxation time caused by a large spin coupling of transition metal atoms.[524] Other recently studied 2D half-metallic materials with a robust FM ground state and high Curie temperature include, for example, Fe_2Si,[525] Co_9Se_8,[526] and g-C_4N_3;[527] moreover, Fe_2Si shows a large magnetic anisotropic energy.[525]

The half-metallic behavior was also theoretically suggested to occur in free-standing 2D purely organic dimethylmethylene-bridged triphenylamine (DTPA) porous sheets.[528] The structure of a DTPA molecule closely resembles that of triangular zigzag-edged GNF, when the central carbon atom is substituted with a nitrogen atom; isolated DTPA molecule is magnetic and

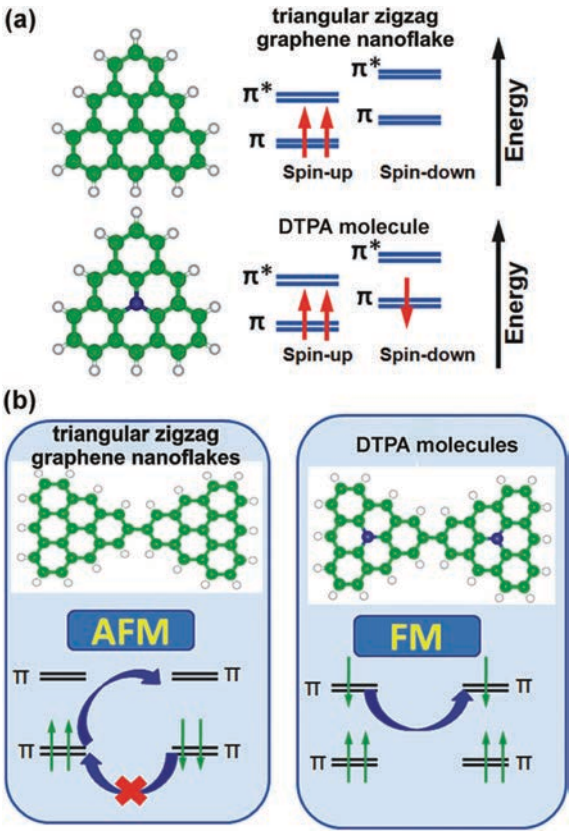


Fig. 118 (a) Structures and schematic diagrams of spin-resolved orbital energy levels for a triangular zigzag-edged GNF and a DTPA molecule. (b) Schematic diagrams showing exchange mechanisms for 2D sheets composed of triangular GNFs and DTPA molecules. AFM/FM ground state is favored by virtual hopping. In panels (a and b), the blue, green, and white balls represent nitrogen, carbon, and hydrogen atoms. Reprinted with permission from ref. 528. Copyright 2012 American Chemical Society.

carries a magnetic moment of 1 μ_B (see Fig. 118a). If 2D DTPA molecules form a network, an FM ground state is favored contrary to an AFM ground state for a 2D sheet composed of GNF molecules (see Fig. 118b). Moreover, the band gap in the semiconducting channel was estimated to be $\sim$1 eV and half-metallicity was found to be robust if the 2D DTPA porous sheet was exposed to a strain with values well beyond those evoked by a substrate.[528]

MXenes belong to another emerging family of 2D materials; they include 2D-transition metal carbides, nitrides, and carbonitrides and are described by the general formula $M_{n+1}X_nT_x$, where M denotes a transition metal, X represents C and/or N, T stands for O, OH and/or F, and n = 1, 2, or 3. Currently, the class features more than 100 members, both theoretically predicted and experimentally synthesized. Thus, it is highly expected to achieve desired magnetic properties for MXenes upon suitable combinations of the transition metal involved and surface termination groups used. Among MXenes, Cr_2N and Cr_2C monolayers were found to be very appealing as they

Published on 26 March 2018. Downloaded by Univerzita Palackého v Olomouci on 2/28/2019 2:05:03 PM.

intrinsically show the FM ground state and half-metallic behavior.[529] However, their magnetic features can be dramatically altered by surface terminating groups (*i.e.*, F, OH, H, and Cl), eventually losing their ferromagnetism and half-metallicity and, instead, becoming AFM semiconductors.[530] Nearly half-metallic ferromagnetism was proposed for Ti_2C and Ti_2N monolayers;[531] while Ti_2C is supposed to undergo a phase transition from a nearly half-metallic state to a half-metallic, spin-gapless semiconducting, and metallic regime upon a gradual increase in the biaxial strain, Ti_2N retains its nearly half-metallic properties irrespective of the biaxial strain applied. On the other hand, V_2C and V_2N, showing AFM and non-magnetic ground states, respectively, can be equipped with large magnetic moments once exposed to the biaxial tensile and compressive strains.[531] Recently, theoretical calculations were used to comprehensively address the issue of magnetism in nitride MXenes, particularly focusing on identification of those representatives with intrinsic FM ground states that are stable and robust enough with regard to the surface terminations and thermal fluctuations at room temperature.[532] Due to an additional electron from nitrogen, the FM phase is energetically favored in nitride MXenes in line with the Stoner criterion. In addition, the two oxidation states of the transition metal atom can coexist in nitride MXenes promoting evolution of the double exchange mechanism. More specifically, Mn_2NF_2, Mn_2NO_2, $MnN(OH)_2$, Ti_2NO_2, and Cr_2NO_2 were found to show a robust FM ground state with a magnetic moment per formula unit reaching up to 9 μ_B.[532] For these systems, the interlayer and intralayer couplings are of FM nature and the Curie temperatures lie in the interval from 566 to 1877 K. Moreover, a half-metallic behavior was predicted for Mn_2N MXenes with a wide band gap for the minority spins for all three surface terminations (*i.e.*, F, O, and OH). In contrast, an AFM ground state was calculated for Ti_2NF_2, $Ti_2N(OH)_2$, V_2NF_2, V_2NO_2, $V_2N(OH)_2$, Cr_2NF_2, and $Cr_2N(OH)_2$ monolayers; for these systems, the interlayer interaction is of FM character while AFM interactions are expected within one layer.[532] The stabilization of either FM or AFM ground state in nitride MXenes can be understood in terms of relative strengths of the superexchange and double exchange interactions. From the theoretical analysis, it can then be inferred that oxygen termination should be considered in syntheses of nitride MXenes as it encourages a robust FM ground state.[532] High magnetic moments (from 3 to 4 μ_B per unit cell) and high Curie temperatures (from 495 to 1133 K) were also predicted for $Hf_2MnC_2O_2$, $Hf_2VC_2O_2$, and $Ti_2MnC_2T_x$ (with T = O, OH, and F) monolayers.[533] Moreover, if exposed to the tensile in-plane strains, these double-transition metal MXene structures are expected to show semi-metal-to-semiconductor and FM-to-AFM phase transitions.[533]

Among graphene-related materials, hexagonal boron nitride (h-BN) has also received significant attention, as the h-BN polymorph, which is remarkably similar to graphene with the alternating B and N atoms forming two-dimensional layers of strong sp^2 bonds within a honeycomb arrangement, can be well suited for integration with graphene as their lattice constant mismatch is less than 2%.[534,535] Furthermore, h-BN shows enhanced chemical and thermal stability resulting from a bond ionicity that can localize the electron states. There is, however, an important difference, *i.e.*, due to the chemically inequivalent sublattices, h-BN is an insulator with a band gap of 6.0 eV.[536] Similar to graphene, h-BN can also form nanotubes, nanoribbons and other similar structures.

Theoretical calculations predicted that several factors may give rise to the magnetic state in h-BN systems, including defects in the atomic network,[537–539] substrate-induced magnetism,[540,541] and bare-edge localized states.[542] Many growth techniques yielded few-layered h-BN.[543] Recently, magnetization measurements performed on few-layered h-BN nanosheets, exfoliated from bulk by using a mechanical cleavage approach, revealed room-temperature FM order with a Curie temperature above 400 K (see Fig. 119),[543] in contrast to the pristine diamagnetic h-BN system. Further, DFT calculations and spherical-aberration

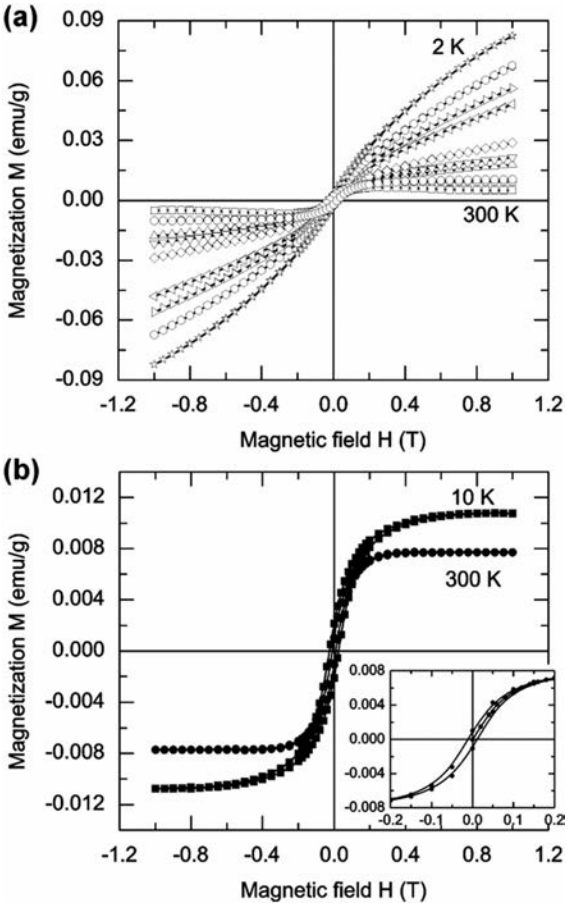


Fig. 119 (a) Magnetization *vs.* magnetic field (*M vs. H*) curves of few-layered h-BN nanosheets for various temperatures in the range of 2–300 K from top to bottom. (b) Magnetization (*M*) after subtracting the paramagnetic and diamagnetic signals as a function of magnetic field (*H*) at a temperature of 10 and 300 K. The inset shows a smaller field region of the hysteresis loop at T = 300 K, which exhibits a typical FM character. Reprinted with permission from ref. 543. Copyright 2014 AIP Publishing LLC.

 This journal is © The Royal Society of Chemistry 2018

Published on 26 March 2018. Downloaded by Univerzita Palackého v Olomouci on 2/28/2019 2:05:03 PM.

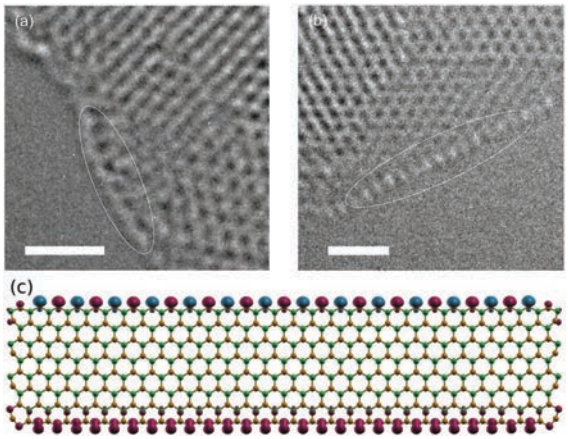


Fig. 120 SACS-TEM images of h-BN showing (a) distorted pentagonal rings and (b) zigzag edges. The scale bars are set to 1 nm. (c) Theoretical h-BN nanoribbon and the corresponding spin-density distributions (red and blue isosurfaces denote spin-up and spin-down, respectively), where distorted pentagonal rings at the armchair edges and magnetic moment localized mainly at the zigzag edges are visible. Boron and nitrogen atoms are represented by yellow and green spheres, respectively. Reprinted with permission from ref. 543. Copyright 2014 AIP Publishing LLC.

corrected transmission electron microscopy (SACS-TEM) revealed a hexagonal–pentagonal ring transition at the armchair edges. The distorted armchair edges carried relatively small magnetic moments. The main FM contribution stemmed, however, from the FM ordering at the N-zigzag edges, whereas B-zigzag edges exhibited AFM coupling (see Fig. 120).[543]

It was theoretically proposed that the magnetic properties of h-BN are independent of the N-vacancy defects.[538] The nearest nitrogen atoms get the spin polarization by the B-vacancy defects, thereby creating a magnetic moment of 0.87 μ_B within the muffin-tin radius. Only a weak spin polarization of about 0.1 μ_B evolves due to the B-adatom defects, while in the case of the N-adatom defects, a larger magnetic moment of about 0.38 μ_B is predicted to emerge. Furthermore, another set of first-principles calculations were employed to understand the effect of non-magnetic impurities on the magnetism of BN sheets.[538] To do so, a rectangular supercell with cell dimensions of 20.05 and 17.37 Å was constructed (see Fig. 121a).[538] Be, B, C, N, O, Al, and Si atoms were selected to replace B or N atoms to change the density of states and spatial distribution of defect states. Fig. 121b then shows the calculated magnetic moments as a function of the nearest-neighbor distance (d_D).[538] The partially filled defect bands produced finite magnetic moments. Moreover, C and Ge atoms were found to preferentially dope the B-sites than the N-sites; for the 3-fold doping configurations, the spins were localized dominantly on the Ge-p/d orbitals and C-p orbitals.[544] In contrast, the 4-fold C_{BN} and Ge_{BN} doping configurations did not cause evolution of any magnetism due to sp^2d and sp^3 type of hybridization. Nevertheless, a spin filtering phenomenon was observed under various bias voltages for h-BN systems doped with carbon at the B- and N-sites and germanium at the B-sites.[544] Spontaneous magnetization can also be induced by adsorption of single H atoms on the external surface of BN nanotubes. However, adsorption of two H atoms on two neighboring N atoms or on two neighboring B and N atoms results in no magnetic ordering. The magnetic moment can be induced if the two adsorbed H atoms are attached to the two B atoms, which are separated. The hydrogenated BN nanotubes exhibited zero magnetic moment if an odd number (1 or 3) of H atoms were adsorbed on a vacancy defect, while an even number of H-atom adsorptions induced a finite magnetic moment.[538] This clearly illustrates the general criteria for the existence of magnetism due to unpaired electrons. Such a magnetic behavior is very promising

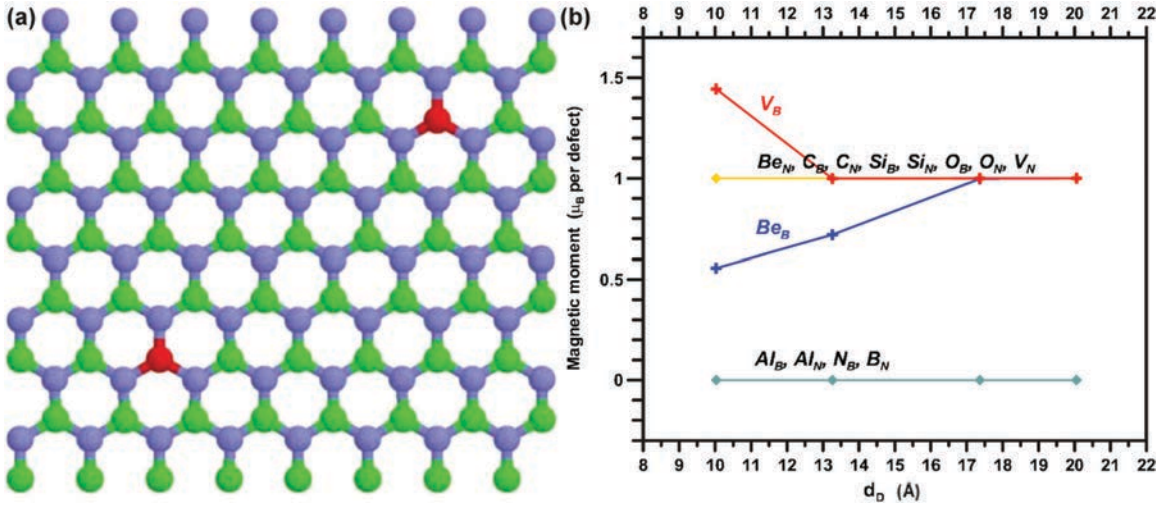


Fig. 121 (a) Rectangular supercell structure containing 64 primitive cells of BN sheets (dimensions: 20.05 and 17.37 Å). (b) Magnetic moment of the supercell as a function of the nearest-neighbor distance (d_D). Reprinted with permission from ref. 538. Copyright 2007 American Physical Society.

Published on 26 March 2018. Downloaded by Univerzita Palackého v Olomouci on 2/28/2019 2:05:03 PM.

for realizing devices only when it could be tuned by application of an external force.[538] The ground state magnetic moment of the defects can be tailored by modifying the geometry by a stress.[545] In this respect, it was shown that a triangular shape of defects may create strong spin localization in the magnetic state. The magnetic moment of these defect states and the N–N distance are strongly related to each other.

Similar to the case of graphene, the magnetic properties of h-BN predominantly vary upon functionalization. A suitable surface functionalization may result in h-BN becoming FM, AFM or magnetically degenerate.[546] As h-BN is heteroatomic in nature, doping can generate anisotropic structures with interesting electronic and magnetic features. Hydrogenation and fluorination in h-BN are endothermic and exothermic processes, respectively. The band gap of h-BN sheet can vary from 4.7 to 0.6 eV depending upon the degree of hydrogenation while graphene undergoes a metal-to-insulator transition when it is fully hydrogenated. Theoretical calculations[547] showed that a spontaneous magnetization is induced upon chemisorption of F atoms on the B atoms in an h-BN nanotube. The evolved magnetic ordering can disappear if both B and N atoms are equally fluorinated. Similarly, fluorination was predicted to promote room-temperature ferromagnetism with a half-metallic feature for h-BN single layers; the partially filled bands were proposed to develop due to the large number of holes.[548] Experimentally, after exfoliation, h-BN nanosheets can be readily fluorinated with ammonium fluoride (NH_4F); such fluorinated h-BN single layers were observed to show FM behavior up to the deduced Curie temperature of $\sim$580 K.[549] From the theoretical calculations, it also turned out that the magnetic moments evolved from the spin polarization of F and three N atoms sitting nearest to the sp^3-hybridized B atom underlying the F atom.[549]

Finally, very recent computational discovery of new 2D materials with a high Néel temperature[550] and Curie temperature[551,552] must be mentioned. The former includes Cr_2CFCl, Cr_2CClBr, Cr_2CHCl, Cr_2CHF, and Cr_2CFOH for which a Néel temperature reaching 400 K has been predicted (see Fig. 122).[550] The latter includes Mn_2CF_2 with a Curie temperature of 520 K (see Fig. 123a–c)[551] and $NiCl_3$ with a Curie temperature of $\sim$400 K (see Fig. 123d).[552]

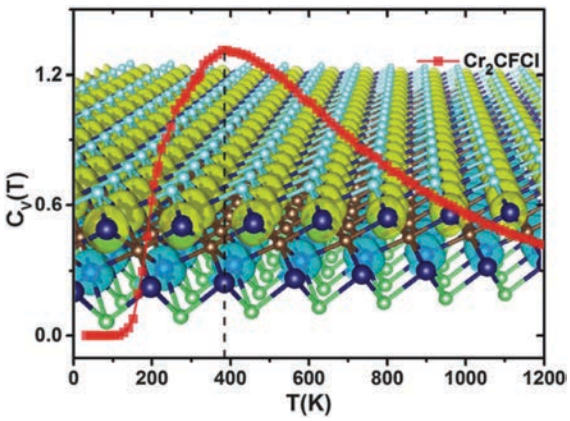


Fig. 122 Specific heat (C_V) *vs.* temperature plot simulated for Cr_2CFCl. The background figure displays spin-polarized charge densities, where spin-up (-down) densities are shown in yellow (cyan). Reprinted with permission from ref. 550. Copyright 2016 The Royal Society of Chemistry.

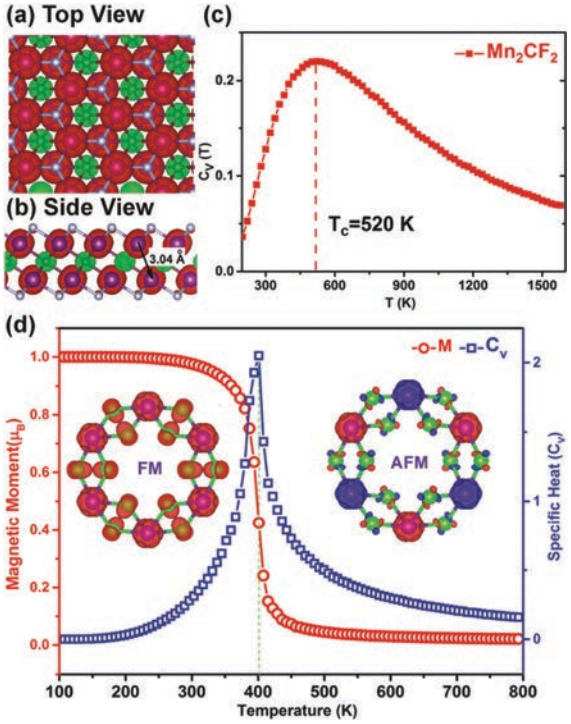


Fig. 123 (a and b) Theoretical spin-polarized charge densities of Mn_2CF_2, where spin-up (-down) densities are shown in red (green). (c) Specific heat (C_V) *vs.* temperature plot simulated for Mn_2CF_2 with the Curie temperature (T_C) indicated. Reprinted with permission from ref. 551. Copyright 2016 The Royal Society of Chemistry. (d) Average magnetic moment (red) and C_V (blue) *vs.* temperature plot calculated for a monolayer of $NiCl_3$. Isosurfaces of spin-polarized charge densities are depicted in the insets. Reprinted with permission from ref. 552. Copyright 2017 The Royal Society of Chemistry.

9. Magnetic impurities in graphene-based systems and methods of deconvolution of individual contributions to the magnetic response

The magnetism of carbon-based materials containing only s- and p-electrons is very intriguing and a much debated topic in the literature. Here, it should be stressed that the observed magnitude of magnetization is comparable to that of the background. Thus, it is very important that the measurement process is accurate and free of errors. Several errors can often happen during data collection in the measurement. Briefly, we present a few important issues that are constantly faced by experimentalists

 This journal is © The Royal Society of Chemistry 2018

Published on 26 March 2018. Downloaded by Univerzita Palackého v Olomouci on 2/28/2019 2:05:03 PM.

during the data collection process and should be taken into consideration for accurate measurements/interpretations.

Magnetic impurities like Fe, Co, Ni, and Mn (*i.e.*, 3d-block elements) are the main hindrances that ignite doubts when dealing with magnetism of low-magnetic-moment materials. Even traces of materials with such high magnetization can contribute equally and can lead to wrong conclusions. For example, 1 ng of Fe impurity in the matrix can produce a magnetic moment of ~0.22 μemu.[553] Thus, one should very accurately measure the impurity concentration to avoid misleading results. The measured magnetization of a material is the sum of all the contributions that arise from the sample itself, sample holder, and any other cavity that are used to mount the samples. Usually, the sample holders (Teflon wraps, straws, cavities, *etc.*) exhibit a diamagnetic response, which should be subtracted from the final measured value.[554] Because the magnetization of such low-magnetic-moment materials is comparable to that of the background, a careful treatment of such data is essential to understand the origin of magnetism. Sometimes, it can be surprising to see that a negative moment becomes positive after the background subtraction. For a better representation of magnetic susceptibility *vs.* temperature data, one can simply plot the difference of ZFC and FC magnetization curves against temperature. This will clearly remove the background and any common errors of the measurement.[553,555] Another typical source of error comes from the Teflon tapes used to wrap powder samples for recording the magnetic data. Although Teflon tapes are diamagnetic in nature, they can induce an FM signal when tempered. Any tempering in the form of mechanical stretching, cutting or heating can change the true magnetic nature by creating dangling bonds.[554] In turn, these dangling bonds can interact with the neighboring carbon atoms to produce a defect-mediated magnetic order that is comparable to that of the primary material under consideration. Although the sensitivity of the superconducting quantum interference device (SQUID)-type magnetometer is very high, the errors due to instrumental artifacts can never be ignored. The common instrumental artifacts come from sensors and the sequence used for measuring the data. Synchronization between the data collection process and temperature or field ramp is necessary to avoid any unusual spikes/transitions. Fig. 124a shows the effect of different heating rates on the ZFC magnetization plots. A noticeable hump can be seen when the heating rate is changed. Fig. 124b shows the change in the profile of the plot when magnetization data are collected with transitions in heating rates. Subsequently, this effect is then clearly manifested in the magnetization *vs.* temperature plots, which could lead to misguided results. However, if the transition and data collection rates are in sync, one can easily avoid such instrumental errors.

Inductively coupled plasma mass spectrometry (ICP-MS) is very efficient in detecting metals and several non-metals at very low concentrations (parts per quadrillion, ppq). The ICP-MS technique is very popular due to its high precision, fast speed, and sensitivity. X-ray magnetic circular dichroism (XMCD) and X-ray absorption spectroscopy (XAS) are useful in determining

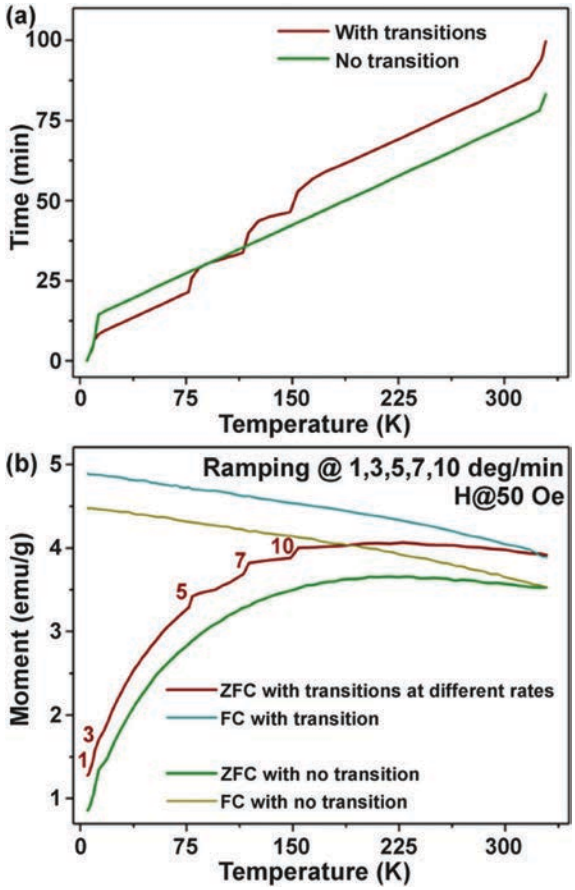


Fig. 124 (a) Effect of heating rate on ZFC magnetization data. (b) Effect of transitions in heating rate on the magnetic moment of the material.

the presence of d-shell elements and their contribution as impurities in graphene-based systems. However, the requirement of synchrotron radiation and a cryomagnetic environment to operate XMCD makes the technique disadvantageous for routine studies of d-shell impurities. The ESR technique is widely used to measure the presence of unpaired electrons and their interactions with the surroundings. The presence of FM centers would have a different nature of ESR patterns and *g*-value in comparison to those characteristic of conduction/paramagnetic centers. X-ray powder diffraction (XRD) is very useful and sensitive in sensing a small wt% of magnetic impurities.

There have been many reports on simultaneous occurrence of ferromagnetism, antiferromagnetism, paramagnetism, and diamagnetism in graphene and its derivatives. In the absence of any magnetic impurities, the important factors that would decide the magnetic state of a material include the density of states, defect states, temperature, external fields, and possible interactions within the system. The delocalized π-electrons due to sp^2 hybridization in graphene can trigger many interactions between the guest and the host lattice. Moreover, magnetic ordered states can be maintained by exchange interactions.

Published on 26 March 2018. Downloaded by Univerzita Palackého v Olomouci on 2/28/2019 2:05:03 PM.

In general, the magnetic susceptibility (χ) of a system is basically a mixture of all the forms of magnetic contributions, *i.e.*,

$$\chi = \chi_{BG} + \chi_{dia} + \chi_{para} + \chi_{FM/AFM}, \quad (10)$$

where χ_{BG} corresponds to the contribution of the background, χ_{dia} is the diamagnetic response, χ_{para} stands for the paramagnetic term, and $\chi_{FM/AFM}$ denotes the FM/AFM contribution (for details, see Section 2). To understand the true nature of such a mixed state, it is essential to separate various contributions to χ of the system. Swain *et al.*[553,556] proposed a low field-high field technique to deconvolute the mixed magnetic state. The basic principle of the suggested procedure lies in the physics of interaction between the states and the external field. The paramagnetic (diamagnetic) susceptibility is directly (inversely) proportional to the external field. The FM/AFM states do not show a linear dependence to the field and rather exhibit hysteresis. The diamagnetic background can be easily separated by measuring the susceptibility in the absence of the material. After getting rid of the background contribution, any further paramagnetic (plus diamagnetic) contribution can be calculated from the slope of the linear portion of the magnetization *vs.* field curve at high fields. As FM materials saturate at high magnetic fields, the presence of any saturation in magnetization can be seen once both background and paramagnetic contributions are deducted as shown in Fig. 125.[556] In addition, the FM/AFM states can be noticed from low-field ZFC/FC magnetization measurements by virtue of their transition temperatures.

The low-magnetic-moment materials usually show a very high magnetization value at very low temperatures. The abrupt increase in magnetization is mainly due to a strong internal molecular field that boosts the collective magnetic order at low temperatures (below 10 K). The internal molecular field at such temperatures is at least 1000 times stronger than the applied magnetic field.[557] Thus, the magnetic centers experience a very strong effective field, thereby giving rise to a very high magnetic moment.

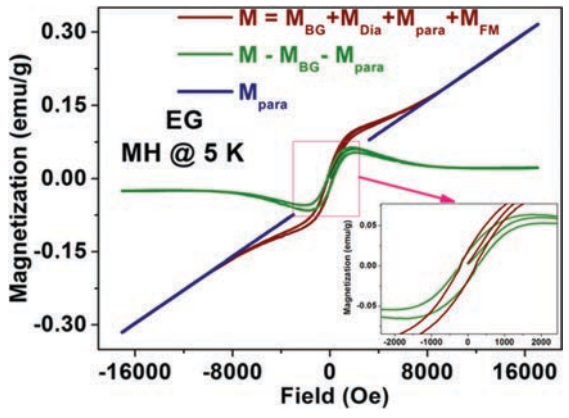


Fig. 125 FM response deduced after subtraction of both diamagnetic and paramagnetic contributions. Reprinted with permission from ref. 556. Copyright 2014 AIP Publishing LLC.

10. Conclusions, applications of "magnetic" graphene in spintronics and biomedicine and future challenges

The goal of the review was to systematically classify and thoroughly describe the approaches used to imprint magnetic behavior into intrinsically non-magnetic graphene. To do so, several strategies must be adopted, all relying on the introduction of defects into graphene. In general, the defects, to some extent, disturb the ideal structure of graphene, modifying its electronic features, leading, among others, to an evolution of magnetic moments that can interact with each other if a suitable communication medium is provided and interaction pathways are secured. The diverse theoretical studies identified various ground magnetic states evolved depending on the nature of the defects and how they can be altered upon doping, functionalization, edge engineering, spatial confinement, and external stimuli. A significant number of experimental works confirmed the predictions from calculations synthesizing graphene-based systems with magnetic ordering effectively resisting the thermal fluctuations and preserving even up to room temperature. The examples of room-temperature ferromagnets/antiferromagnets include, in particular, functionalized graphenes where the communication among the defect-induced localized magnetic moments is suggested to result from a complex interplay between interaction mechanisms of various natures. Sustainable magnetism can also emerge in graphene analogues and other classes of 2D materials such as transition metal dichalcogenides, metal dihalides, metal dinitrides, MXenes, h-BN or 2D organic porous sheets, implying that the concept of equipping magnetic features to 2D materials by defects seems to be of universal character for originally non-magnetic systems. However, false interpretations on observed magnetic behavior may happen in cases, when magnetic impurities (especially, 3d-block elements) are present either from the synthesis itself or from sample handling as they often overshadow the magnetic signal from the carbon-based materials.

Several challenges still remain untouched. Most of them are connected with experimental difficulties to synthesize graphene-based systems with introduction of defects in a controllable manner. Moreover, the issue of homogeneity of distribution of defects within each sheet is still experimentally unsolved and very hard to tackle as it needs a sophisticated optimization of the synthetic protocols. Frequently, only a certain portion of defect-modified graphene sheets in the sample show a desired magnetic behavior in agreement with the theoretical predictions. The defects may induce a large number of configurations when some of them are magnetically-active whereas others are non-magnetic. The energy differences between magnetic and non-magnetic configurations can be, in some cases, very tiny favoring stabilization of non-magnetic states during the synthetic conditions used. Moreover, the defects have different tendencies for localization in particular sites in graphene (*i.e.*, in the interior, close to the edges, at the edges), resulting in potential commutation at preferred regions.

 This journal is © The Royal Society of Chemistry 2018

Published on 26 March 2018. Downloaded by Univerzita Palackého v Olomouci on 2/28/2019 2:05:03 PM.

For adatoms, migration energy barriers should be carefully considered, preventing their movement on the graphene surface and grouping at positions hindering evolution of whatever magnetic ordering. Another challenge involves experimental engineering of size and edges in spatially confined graphene representatives. Currently, there are only a few ways to cut graphene into pieces with a proper edge structure and geometry, most of them exploiting conditions of ultra-high vacuum and microscopy-based techniques. Due to the high reactivity of edges, post-process treatments are necessary to preserve the edge structure, which can be chemically highly demanding. Thus, for example, for GNRs, it is very hard to experimentally reproduce the theoretical results in terms of altering the magnetic states by width, edge termination or doping. Another option to imprint magnetic ordering into graphene, which has not been synthetically explored, involves combination of defects of various natures. For example, confined carrier-doped graphene sheets with an appropriate edge structure and surface functionalization would show magnetic features that can be sustainable up to room temperature. Here, it should be stressed that for every strategy exploited, a threshold value exists when the number of defects breaks the graphene structure or completely modifies its electronic features, precluding emergence of magnetic states. Moreover, the sustainability of the magnetic ordering against thermal fluctuations is closely related to the strength of the interactions among the defect-induced magnetic moments. Thus, competition/interplay among various types of interactions (*i.e.*, π-electron-mediated interactions, exchange interactions, *etc.*) should be thoroughly engineered all positively contributing to the stabilization of magnetic ordering up to high temperatures. Alternatively, the magnetism in graphene (or graphene derivatives) can be induced by the generation of radical-like magnetic moments; here, a vast space for theoretical modeling and experimenting is, in particular, viewed in evaluating the thermodynamic stability of radicals and their motifs, identification of magnetically-active motifs, potential arrangement (*i.e.*, hierarchical organization) of radical motifs in "magnetic superstructures" encouraging a long-range magnetic ordering, and development of sophisticated synthetic protocols providing engineering of the suitable structure(s) of motifs and their homogeneous distribution within each single sheet of graphene in the specimen. Tuning the magnetically-active motifs and interaction pathways may then further lead to a stabilization of the magnetic ordering with Curie and/or Néel temperature above the room temperature, opening doors to new applications of graphene. Equally important, strengthening the magnetic anisotropy in graphene is an experimentally challenging task requiring control over intrinsic and extrinsic sources of spin–orbit coupling or introducing other types of coupling such an exchange bias. In this respect, graphene analogues and other 2D materials can be regarded as equal competitors offering much higher Curie/Néel temperatures and stronger magnetic anisotropies, showing intrinsically without a need to introduce defects; however, overwhelming majority of these rivals have been only predicted theoretically and, nowadays, it is very hard to anticipate the difficulties and problems associated with their synthesis in order to reproduce completely the theoretical behaviors. Last but not least, from the practical viewpoint, a fundamental challenge is viewed in connecting "magnetic" graphenes and other 2D materials to other functional components in devices in a way not degrading or destroying the spin transport and magnetic response.

Once graphene or its 2D analogues become magnetic, it can be applied in branches requiring a sustainable magnetic response of a material. Recently, "magnetic" graphene has been suggested as a promising candidate in spintronic applications. In general, spintronics exploits the spin degree of freedom of electrons, thus developing the new technological concepts for information storage and logic devices; in other words, its main goals are to understand mechanisms behind the control of spin configurations and spin currents and to design/discover materials with suitable spin generation and transport features. Spin-based information technology offers several advantages over classical electronics such as high speed of data processing, high circuit integration density, low-power operation, and reconfigurable option. In order to both meet the criteria for ideal spintronic materials on one hand and to find an optimal design and fabrication procedure of a spintronic device on the other hand, several challenges have been identified so far such as generation of fully-polarized carriers and injection into spin devices, long-distance spin propagation (and, hence, long spin lifetime), and manipulation and detection of spin orientation of the carriers. Regarding the materials appealing for spintronics, a behavior intrinsic to half metals, spin-gapless semiconductors and/or bipolar magnetic semiconductors is highly desirable. As proved by a number of theoretical and experimental studies, graphene and/or its 2D analogues can behave as a half metal, spin-gapless semiconductor or bipolar magnetic semiconductor depending on the structure modification/functionalization or exposure to external stimuli or combination of both approaches. In particular, in half metals, one spin channel is metallic while the other spin channel is insulating or semiconducting (see Fig. 126a).[60] However, for preservation of half-metallicity at room temperature, a high Curie temperature is not a sufficient prerequisite; in addition, a wide half-metallic gap is required to avoid occurrence of thermally-agitated spin–flip transitions. In graphene, a half-metallic property is often observed upon an appropriate chemical modification; however, its stabilization needs exclusion of non-local exchange interactions stemming from impurities and improper (irregular) incorporation of foreign elements or sheet and edge functionalization. Equally important, the occurrence of half-metallicity in graphene without applying an external electric field or strain is highly unlikely. For a spin-gapless semiconductor, the valence band maximum and conduction band minimum touch each other exactly at E_F and at least one of the valence band maximum and conduction band minimum is fully spin-polarized (see Fig. 126b).[60] In spin-gapless semiconductors, excitation of an electron from the valence band to the conduction band does not require any threshold energy; more importantly, the excited carriers may then show a full spin polarization. In graphene, for example, the emergence of spin-gapless semiconducting behavior strongly

Published on 26 March 2018. Downloaded by Univerzita Palackého v Olomouci on 2/28/2019 2:05:03 PM.

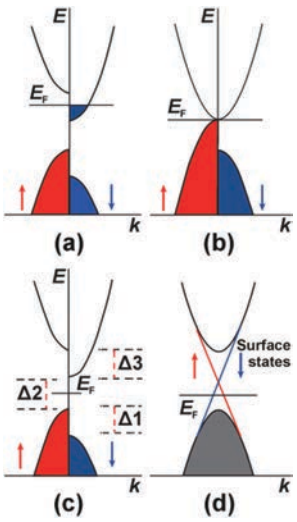


Fig. 126 Schematic band structure of (a) half metal, (b) spin-gapless semiconductor, (c) bipolar magnetic semiconductor, and (d) topological insulator, where k is the wave vector, E represents the energy, and E_F denotes the Fermi level. In panel (c), Δ1, Δ2, and Δ3 correspond to the spin–flip gap in the valence band, band gap, and spin–flip gap in the conduction band, respectively. Reprinted with permission from ref. 60. Copyright 2016 Oxford University Press on behalf of China Science Publishing & Media Ltd.

depends on the dopant and vacancy sites and distances between them, which could be hardly controlled during the synthesis. Bipolar magnetic semiconductors, for which the valence band maximum and conduction band minimum are completely spin-polarized in the opposite spin direction (see Fig. 126c),[60] offer fully spin-polarized currents with reversible spin polarization which can be readily controlled by applying a gate voltage. However, such a feature was theoretically predicted for GNRs with a special morphology and edge geometries that can be hardly achieved by currently mastered experimental top-down or bottom-up procedures. Currently, equipping graphene with properties resembling those of topological insulators is regarded as a challenging task. To imprint such a behavior when the metallic surface states are symmetry-protected and the electrons with spin-up and spin-down move in the opposite direction on the 2D surface (see Fig. 126d),[60] an appropriate functionalization strategy of graphene should be identified theoretically and verified experimentally.

Due to a long spin lifetime and spin diffusion length defined by a weak spin–orbit coupling, graphene has been suggested to effectively work as a spin conserver which can provide transmission of the spin-encoded information across a device with high fidelity. The theory predicts that the spin relaxation time in graphene can reach $\sim$1 μs; however, the values observed for synthesized graphenes lie in the interval from tens of picoseconds to units of nanoseconds. Such a difference between the experimental and theoretical values of the spin relaxation times is often explained in terms of the presence of impurities, defects, and static ripples. Thus, introduction of defects to raise magnetism in graphene should not significantly alter the spin relaxation time towards lower values as it could then ruin an effective spin transport through the device.

Besides, materials involving only sp elements have been predicted to show high magnitudes of spin-wave stiffness and, hence, higher magnetic transition (Curie/Néel) temperatures. However, to realize a robust magnetic ordering in graphene-based systems, the existence and significant strength of magnetic anisotropy are highly needed besides high values of Curie/Néel temperature. For such systems, the spin–orbit coupling is responsible for magnetic anisotropy. Adopting a simple model, it can be inferred that for temperatures sufficiently higher than the so-called crossover temperature, T_X ($\approx$ 10 K), the spin correlation length, ξ, is inversely proportional to the temperature, *i.e.*, $\xi \propto T^{-1}$, as a weak magnetic anisotropy is not expected to play any role above T_X.[45] Below T_X, ξ is supposed to increase exponentially upon lowering the temperature. Thus, $\xi \approx 1$ nm at 300 K.[45] In order to increase T_X and, hence, ξ at room temperature, it is necessary to modify appropriately the magnetic anisotropy. To do so, several approaches have been suggested so far, most of them relying on the introduction of foreign atoms with an intrinsically large anisotropy into the graphene lattice, surface functionalization with suitable adatoms and/or functional groups or deposition on a substrate. Besides, the magnetic anisotropy of graphene can be alternatively controlled by the Rashba effect and associated Rashba coupling originating from the π–σ hybridization. Increasing the magnetic anisotropy in graphene is believed to encourage its new role as a spin generator when combined with transport currents. Moreover, the ''magnetic'' graphene could effectively work as a component in magnetoresistive junctions used in the sensors of magnetic fields; a very high magnetoresistive ratio has already been reported for an architecture composed of GNRs placed between the two FM contacts.

Apart from electronics and spintronics, a vast number of experimental studies have proved graphene's prominent application potential in biomedicine. However, as graphene is hydrophobic, its surface must be functionalized with appropriate functional groups in order to make it hydrophilic. Moreover, surface functionalization significantly improves its colloidal stability, another feature highly required for biomedical applications. Regarding the toxicity issues, GQDs have been identified as low toxic graphene-based systems.[5] They currently work as photoluminescence agents for biomedical imaging; if equipped with the paramagnetic centers, they could offer an option of dual imaging, *i.e.*, in fluorescence and magnetic domain. Moreover, it is speculated that due to a slightly different nature of spins in sp-based systems (*i.e.*, existence of pseudospin) compared to that of the traditional d-block-element- or f-block-element-containing magnetic materials, the spin–lattice and spin–spin relaxation may provide interesting contrast properties in T_1- or T_2-weighted magnetic resonance images. Moreover, once spatially confined, the magnetic moment of graphene is believed to show magnetic phenomena activated by external stimuli including temperature, light, and external magnetic field; such magnetic features would be promising in designing graphene-based imaging agents.

 This journal is © The Royal Society of Chemistry 2018

Published on 26 March 2018. Downloaded by Univerzita Palackého v Olomouci on 2/28/2019 2:05:03 PM.

Besides, as graphene possesses a large surface area, if magnetic, graphene or its derivatives can be further functionalized with biomolecules and other compounds, thus serving as a platform for active drug targeting. Experimentally, size, morphology, functionalization, long-term toxicity, repeatability, and yield aspects are currently considered as highly challenging with a potentially long journey to achieve biomedically-appealing ''magnetic'' graphenes in the near future.

Abbreviations

AC-HRTEM	Aberration corrected high resolution transmission electron microscopy
AFM	Antiferromagnetic
CVD	Chemical vapor deposition
DFT	Density functional theory
DTPA	Dimethylmethylene-bridged triphenylamine
E_F	Fermi level
ESR	Electron spin resonance
FAG	Fluoranthene group
FC	Field-cooled
FIM	Ferrimagnetic
FLG	Few-layered graphite
FM	Ferromagnetic
GGA	Generalized gradient approximation
GIC	Graphite intercalation compound
GMR	Giant magnetoresistance
GNRs	Graphene nanoribbons
GNFs	Graphene nanoflakes
GQDs	Graphene quantum dots
HAADF-STEM	High angle annular dark field scanning transmission electron microscopy
HOMO	Highest occupied molecular orbital
HOPG	Highly oriented pyrolytic graphite
ICP-MS	Inductively coupled plasma mass spectrometry
LUMO	Lowest unoccupied molecular orbital
MD	Molecular dynamics
MFM	Magnetic force microscopy
OVER	6-Oxoverdazyl
PDA	Polydiacetylene
RKKY	Ruderman–Kittel–Kasuya–Yosida
SACS-TEM	Spherical-aberration corrected transmission electron microscopy
SPLEEM	Spin-polarized low-energy electron microscopy
SP-STM	Spin-polarized scanning tunneling microscopy
SQUID	Superconducting quantum interference device
STM	Scanning tunneling microscopy
STS	Scanning tunneling spectroscopy
SW	Stone–Wales
TDAE	Tetrakis-dimethylaminoethylene
TEM	Transmission electron microscopy
TMDC	Transition metal dichalcogenide
TMM	Trimethylenemethane
TMR	Tunnel magnetoresistance
TSW	Thrower–Stone–Wales
VASP	Vienna ab initio simulation package
XAS	X-ray absorption spectroscopy
XMCD	X-ray magnetic circular dichroism
XRD	X-ray powder diffraction
ZFC	Zero-field-cooled

Conflicts of interest

There are no conflicts to declare.

Acknowledgements

The authors gratefully acknowledge the support from the Ministry of Education, Youth and Sports of the Czech Republic under Project No. LO1305 and the support by the Operational Programme Research, Development and Education – European Regional Development Fund, Project No. CZ.02.1.01/0.0/0.0/16_019/0000754 of the Ministry of Education, Youth and Sports of the Czech Republic.

References

1 M. Tamura, Y. Nakazawa, D. Shiomi, K. Nozawa, Y. Hosokoshi, M. Ishikawa, M. Takahashi and M. Kinoshita, *Chem. Phys. Lett.*, 1991, **186**, 401–404.
2 M. Takahashi, P. Turek, Y. Nakazawa, M. Tamura, K. Nozawa, D. Shiomi, M. Ishikawa and M. Kinoshita, *Phys. Rev. Lett.*, 1991, **67**, 746–748.
3 H. W. Kroto, J. R. Heath, S. C. O'Brien, R. F. Curl and R. E. Smalley, *Nature*, 1985, **318**, 162–163.
4 S. Iijima, *Nature*, 1991, **354**, 56–58.
5 V. Georgakilas, J. A. Perman, J. Tucek and R. Zboril, *Chem. Rev.*, 2015, **115**, 4744–4822.
6 R. B. Heimann, S. E. Evsvukov and Y. Koga, *Carbon*, 1997, **35**, 1654–1658.
7 T. L. Makarova, *Superconductors*, 2004, **38**, 615–638.
8 A. Oshiyama, S. Okada and S. Saito, *Physica B*, 2002, **323**, 21–29.
9 S. Okada and A. Oshiyama, *J. Phys. Soc. Jpn.*, 2003, **72**, 1510–1515.
10 L. W. Chang and J. T. Lue, *J. Nanosci. Nanotechnol.*, 2009, **9**, 1956–1963.
11 S. Okada, K. Nakada, K. Kuwabara, K. Daigoku and T. Kawai, *Phys. Rev. B: Condens. Matter Mater. Phys.*, 2006, **74**, 121412.
12 J. Klinovaja and D. Loss, *Phys. Rev. B: Condens. Matter Mater. Phys.*, 2013, **87**, 045422.
13 S. Bandow, F. Kokai, K. Takahashi, M. Yudasaka and S. Iijima, *Appl. Phys. A: Mater. Sci. Process.*, 2001, **73**, 281–285.
14 S. Bandow, T. Yamaguchi and S. Iijima, *Chem. Phys. Lett.*, 2005, **401**, 380–384.
15 R. C. Haddon, *Science*, 1993, **261**, 1545–1550.
16 R. Zanasi and P. Fowler, *Chem. Phys. Lett.*, 1995, **238**, 270–280.

Published on 26 March 2018. Downloaded by Univerzita Palackého v Olomouci on 2/28/2019 2:05:03 PM.

17 R. C. Haddon and A. Pasquarello, *Phys. Rev. B: Condens. Matter Mater. Phys.*, 1994, **50**, 16459–16463.
18 M. Saunders, A. Jimenez-Vazquez, R. J. Cross, W. E. Billups, C. Gesenberg, A. Gonzalez, W. Luo, R. C. Haddon, F. Diederich and A. Herrmann, *J. Am. Chem. Soc.*, 1995, **117**, 9305–9308.
19 P.-M. Allemand, K. C. Khemani, A. Koch, F. Wudl, K. Holczer, S. Donovan, G. Gruner and J. D. Thompson, *Science*, 1991, **253**, 301–303.
20 M. Ata, M. Machida, H. Watanabe and J. Seto, *Jpn. J. Appl. Phys.*, 1994, **33**, 1865–1871.
21 Y. M. Shul'ga, A. S. Lobach, I. N. Ivleva, Y. G. Morozov, V. N. Spector and A. A. Ovchinnikov, *Mol. Cryst. Liq. Cryst. Sci. Technol., Sect. C*, 1998, **10**, 201–206.
22 A. S. Lobach, Y. M. Shul'ga, O. S. Roshchupkina, A. I. Rebrov, A. A. Perov, Y. G. Morozov, V. N. Spector and A. A. Ovchinnikov, *Fullerene Sci. Technol.*, 1998, **6**, 375–391.
23 Y. Iwasa, T. Arima, R. M. Fleming, T. Siegrist, O. Zhou, R. C. Haddon, L. J. Rothberg, K. B. Lyons, H. L. Carter, Jr., A. F. Hebard, R. Tycko, G. Dabbagh, J. J. Krajevski, G. A. Thomas and T. Yagi, *Science*, 1994, **264**, 1570–1572.
24 M. Nuñez-Regueiro, L. Marques, J.-L. Hodeau, O. Berthoux and M. Perroux, *Phys. Rev. Lett.*, 1995, **74**, 278–281.
25 R. A. Wood, M. H. Lewis, M. R. Lees, S. M. Bennington, M. G. Cain and N. Kitamura, *J. Phys.: Condens. Matter*, 2002, **14**, L385–L391.
26 A. Mrzel, A. Omerzu, P. Umek, D. Mihailovic, Z. Jaglicic and Z. Trontelj, *Chem. Phys. Lett.*, 1998, **298**, 329–334.
27 K. Prassides, S. Margadonna, D. Arcon, A. Lappas, H. Shimoda and Y. Iwasa, *J. Am. Chem. Soc.*, 1999, **121**, 11227–11228.
28 L. Rondin, J. P. Tetienne, T. Hingant, J. F. Roch, P. Maletinsky and V. Jacques, *Rep. Prog. Phys.*, 2014, **77**, 056503.
29 A. A. Ovchinnikov and I. L. Shamovsky, *THEOCHEM*, 1991, **251**, 133–140.
30 A. A. Ovchinnikov, I. L. Shamovsky and K. V. Bozhenko, *THEOCHEM*, 1991, **251**, 141–151.
31 A. V. Rode, E. G. Gamaly, A. G. Christy, J. G. Fitz Gerald, S. T. Hyde, R. G. Elliman, B. Luther-Davies, A. I. Veinger, J. Androulakis and J. Giapintzakis, *Phys. Rev. B: Condens. Matter Mater. Phys.*, 2004, **70**, 054407.
32 D. Arčon, Z. Jagličič, A. Zorko, A. V. Rode, A. G. Christy, N. R. Madsen, E. G. Gamaly and B. Luther-Davies, *Phys. Rev. B: Condens. Matter Mater. Phys.*, 2006, **74**, 014438.
33 G. D. Yu, Z. Liu, W. Z. Gao and Y. S. Zheng, *J. Phys.: Condens. Matter*, 2013, **25**, 285502.
34 Y. P. Zheng, Y. H. Chen, L. H. Lin, Y. Y. Sun, H. B. Liu, Y. L. Li, Y. W. Du and N. J. Tang, *Appl. Phys. Lett.*, 2017, **111**, 033101.
35 M. J. Zhang, X. X. Wang, H. J. Sun, N. Wang, Q. Lv, W. W. Cui, Y. Z. Long and C. S. Huang, *Sci. Rep.*, 2017, **7**, 11535.
36 K. S. Novoselov, A. K. Geim, S. V. Morozov, D. Jiang, Y. Zhang, S. V. Dubonos, I. V. Grigorieva and A. A. Firsov, *Science*, 2004, **306**, 666–669.
37 A. H. Castro Neto, F. Guinea, N. M. R. Peres, K. S. Novoselov and A. K. Geim, *Rev. Mod. Phys.*, 2009, **81**, 109–162.
38 M. J. Allen, V. C. Tung and R. B. Kaner, *Chem. Rev.*, 2010, **110**, 132–145.
39 V. Georgakilas, M. Otyepka, A. B. Bourlinos, V. Chandra, N. Kim, K. C. Kemp, P. Hobza, R. Zboril and K. S. Kim, *Chem. Rev.*, 2012, **112**, 6156–6214.
40 V. Georgakilas, J. N. Tiwari, K. C. Kemp, J. A. Perman, A. B. Bourlinos, K. S. Kim and R. Zboril, *Chem. Rev.*, 2016, **116**, 5464–5519.
41 P. Avouris, Z. H. Chen and V. Perebeinos, *Nat. Nanotechnol.*, 2007, **2**, 606–615.
42 W. Han, R. K. Kawakami, M. Gmitra and J. Fabian, *Nat. Nanotechnol.*, 2014, **9**, 794–807.
43 J. M. Yoo, J. H. Kang and B. H. Hong, *Chem. Soc. Rev.*, 2015, **44**, 4835–4852.
44 G. Z. Kyzas, E. A. Deliyanni and K. A. Matis, *J. Chem. Technol. Biotechnol.*, 2014, **89**, 196–205.
45 O. V. Yazyev, *Rep. Prog. Phys.*, 2010, **73**, 056501.
46 J. Červenka, M. I. Katsnelson and C. F. J. Flipse, *Nat. Phys.*, 2009, **5**, 840–844.
47 O. V. Yazyev and L. Helm, *Phys. Rev. B: Condens. Matter Mater. Phys.*, 2007, **75**, 125408.
48 A. Carpio, L. L. Bonilla, F. de Juan and M. A. H. Vozmediano, *New J. Phys.*, 2008, **10**, 053021.
49 L. Ciric, D. M. Djokic, J. Jacimovic, A. Sienkiewicz, A. Magrez, L. Forro, Z. Sljivancanin, M. Lotya and J. N. Coleman, *Phys. Rev. B: Condens. Matter Mater. Phys.*, 2012, **85**, 205437.
50 J. Tucek, P. Blonski, Z. Sofer, P. Simek, M. Petr, M. Pumera, M. Otyepka and R. Zboril, *Adv. Mater.*, 2016, **28**, 5045–5053.
51 P. Blonski, J. Tucek, Z. Sofer, V. Mazanek, M. Petr, M. Pumera, M. Otyepka and R. Zboril, *J. Am. Chem. Soc.*, 2017, **139**, 3171–3180.
52 J. Zhou, Q. Wang, Q. Sun, X. S. Chen, Y. Kawazoe and P. Jena, *Nano Lett.*, 2009, **9**, 3867–3870.
53 R. R. Nair, M. Sepioni, I. L. Tsai, O. Lehtinen, J. Keinonen, A. V. Krasheninnikov, T. Thomson, A. K. Geim and I. V. Grigorieva, *Nat. Phys.*, 2012, **8**, 199–202.
54 J. Tucek, K. Hola, A. B. Bourlinos, P. Blonski, A. Bakandritsos, J. Ugolotti, M. Dubecky, F. Karlicky, V. Ranc, K. Cepe, M. Otyepka and R. Zboril, *Nat. Commun.*, 2017, **8**, 14525.
55 D. W. Boukhvalov and M. I. Katsnelson, *ACS Nano*, 2011, **5**, 2440–2446.
56 Y. Kobayashi, K. Fukui, T. Enoki, K. Kusakabe and Y. Kaburagi, *Phys. Rev. B: Condens. Matter Mater. Phys.*, 2005, **71**, 193406.
57 G. Z. Magda, X. Z. Jin, I. Hagymasi, P. Vancso, Z. Osvath, P. Nemes-Incze, C. Y. Hwang, L. P. Biro and L. Tapaszto, *Nature*, 2014, **514**, 608–611.
58 E. J. Kan, Z. Y. Li and J. L. Yang, *NANO*, 2008, **3**, 433–442.
59 W. Q. Liu and Y. B. Xu, *Curr. Opin. Solid State Mater. Sci.*, 2016, **20**, 388–395.
60 X. X. Li and J. L. Yang, *Natl. Sci. Rev.*, 2016, **3**, 365–381.
61 S. Das Sarma, S. Adam, E. H. Hwang and E. Rossi, *Rev. Mod. Phys.*, 2011, **83**, 407–470.
62 K. S. Novoselov, A. K. Geim, S. V. Morozov, D. Jiang, M. I. Katsnelson, I. V. Grigorieva, S. V. Dubonos and A. A. Firsov, *Nature*, 2005, **438**, 197–200.
63 Y. B. Zhang, T. W. Tan, H. L. Stormer and P. Kim, *Nature*, 2005, **438**, 201–204.

 This journal is © The Royal Society of Chemistry 2018

Published on 26 March 2018. Downloaded by Univerzita Palackého v Olomouci on 2/28/2019 2:05:03 PM.

64 R. Shimano, G. Yumoto, J. Y. Yoo, R. Matsunaga, S. Tanabe, H. Hibino, T. Morimoto and H. Aoki, *Nat. Commun.*, 2013, **4**, 1841.
65 I. V. Fialkovsky, V. N. Marachevsky and D. V. Vassilevich, *Phys. Rev. B: Condens. Matter Mater. Phys.*, 2011, **84**, 035446.
66 D. Basko, *Science*, 2011, **334**, 610–611.
67 H. B. Heersche, P. Jarillo-Herrero, J. B. Oostinga, L. M. K. Vandersypen and A. F. Morpurgo, *Nature*, 2007, **446**, 56–59.
68 K. Xu, K. Wang, W. Zhao, W. Z. Bao, E. F. Liu, Y. F. Ren, M. Wang, Y. J. Fu, J. W. Zeng, Z. G. Li, W. Zhou, F. Q. Song, X. R. Wang, Y. Shi, X. G. Wan, M. S. Fuhrer, B. G. Wang, Z. H. Qiao, F. Miao and D. Y. Xing, *Nat. Commun.*, 2015, **6**, 8119.
69 S. Park, G. Wang, B. Cho, Y. Kim, S. Song, Y. Ji, M. H. Yoon and T. Lee, *Nat. Nanotechnol.*, 2012, **7**, 438–442.
70 L. Tapaszto, G. Dobrik, P. Lambin and L. P. Biro, *Nat. Nanotechnol.*, 2008, **3**, 397–401.
71 T. H. Han, Y. Lee, M. R. Choi, S. H. Woo, S. H. Bae, B. H. Hong, J. H. Ahn and T. W. Lee, *Nat. Photonics*, 2012, **6**, 105–110.
72 S. J. Han, A. V. Garcia, S. Oida, K. A. Jenkins and W. Haensch, *Nat. Commun.*, 2014, **5**, 3086.
73 O. Y. Loh and H. D. Espinosa, *Nat. Nanotechnol.*, 2012, **7**, 283–295.
74 Y. W. Zhu, S. Murali, M. D. Stoller, K. J. Ganesh, W. W. Cai, P. J. Ferreira, A. Pirkle, R. M. Wallace, K. A. Cychosz, M. Thommes, D. Su, E. A. Stach and R. S. Ruoff, *Science*, 2011, **332**, 1537–1541.
75 M. Q. Zhao, Q. Zhang, J. Q. Huang, G. L. Tian, J. Q. Nie, H. J. Peng and F. Wei, *Nat. Commun.*, 2014, **5**, 3410.
76 L. T. Qu, Y. Liu, J. B. Baek and L. M. Dai, *ACS Nano*, 2010, **4**, 1321–1326.
77 Z. F. Liu, Q. Liu, Y. Huang, Y. F. Ma, S. G. Yin, X. Y. Zhang, W. Sun and Y. S. Chen, *Adv. Mater.*, 2008, **20**, 3924–3930.
78 F. N. Xia, T. Mueller, Y. M. Lin, A. Valdes-Garcia and P. Avouris, *Nat. Nanotechnol.*, 2008, **4**, 839–843.
79 Q. L. Bao, H. Zhang, B. Wang, Z. H. Ni, C. H. Y. X. Lim, Y. Wang, D. Y. Tang and K. P. Loh, *Nat. Photonics*, 2011, **5**, 411–415.
80 C. Zhu, T. Y. J. Han, E. B. Duoss, A. M. Golobic, J. D. Kuntz, C. M. Spadaccini and M. A. Worsley, *Nat. Commun.*, 2015, **6**, 6962.
81 J. J. Liang, Y. Wang, Y. Huang, Y. F. Ma, Z. F. Liu, J. M. Cai, C. D. Zhang, H. J. Gao and Y. S. Chen, *Carbon*, 2009, **47**, 922–925.
82 S. K. Min, W. Y. Kim, Y. Cho and K. S. Kim, *Nat. Nanotechnol.*, 2011, **6**, 162–165.
83 X. M. Sun, Z. Liu, K. Welsher, J. T. Robinson, A. Goodwin, S. Zaric and H. J. Dai, *Nano Res.*, 2008, **1**, 203–212.
84 Y. Han, Z. Xu and C. Gao, *Adv. Funct. Mater.*, 2013, **23**, 3693–3700.
85 J. Abraham, K. S. Vasu, C. D. Williams, K. Gopinadhan, Y. Su, C. T. Cherian, J. Dix, E. Prestat, S. J. Haigh, I. P. Grigorieva, P. Carbone, A. K. Geim and R. R. Nair, *Nat. Nanotechnol.*, 2017, **12**, 546–550.
86 M. K. Shin, B. Lee, S. H. Kim, J. A. Lee, G. M. Spinks, S. Gambhir, G. G. Wallace, M. E. Kozlov, R. H. Baughman and S. J. Kim, *Nat. Commun.*, 2012, **3**, 650.
87 C. L. Kane and E. J. Mele, *Phys. Rev. Lett.*, 2005, **95**, 226801.
88 O. V. Yazyev, *Nano Lett.*, 2008, **8**, 1011–1015.
89 O. V. Yazyev, *Phys. Rev. Lett.*, 2008, **101**, 037203.
90 H. Feldner, Z. Y. Meng, A. Honecker, D. Cabra, S. Wessel and F. F. Assaad, *Phys. Rev. B: Condens. Matter Mater. Phys.*, 2010, **81**, 115416.
91 J. Fernandez-Rossier and J. J. Palacios, *Phys. Rev. Lett.*, 2007, **99**, 177204.
92 D. D. Gunlycke, D. A. Areshkin, J. Li, J. W. Mintmire and C. T. White, *Nano Lett.*, 2007, **7**, 3608–3611.
93 L. Pisani, J. A. Chan, B. Montanari and N. M. Harrison, *Phys. Rev. B: Condens. Matter Mater. Phys.*, 2007, **75**, 064418.
94 O. V. Yazyev, I. Tavernelli, L. Helm and U. Röthlisberger, *Phys. Rev. B: Condens. Matter Mater. Phys.*, 2005, **71**, 115110.
95 H. Thomann, L. K. Dalton, M. Grabowski and T. C. Clarke, *Phys. Rev. B: Condens. Matter Mater. Phys.*, 1985, **31**, 3141–3143.
96 S. Kuroda and H. Shirakawa, *Phys. Rev. B: Condens. Matter Mater. Phys.*, 1987, **35**, 9380–9382.
97 S. Sorella and E. Tosatti, *Europhys. Lett.*, 1992, **19**, 699.
98 S. Fajtlowicz, P. E. John and H. Sachs, *Croat. Chem. Acta*, 2005, **78**, 195–201.
99 J. J. Palacios, J. Fernandez-Rossier and L. Brey, *Phys. Rev. B: Condens. Matter Mater. Phys.*, 2008, **77**, 195428.
100 E. H. Lieb, *Phys. Rev. Lett.*, 1989, **62**, 1201–1204.
101 Y. Kopelevich, P. Esquinazi, J. H. S. Torres and S. Moehlecke, *J. Low Temp. Phys.*, 2000, **119**, 691–702.
102 P. Esquinazi, A. Setzer, R. Höhne, C. Semmelhack, Y. Kopelevich, D. Spemann, T. Butz, B. Kohlstrunk and M. Lösche, *Phys. Rev. B: Condens. Matter Mater. Phys.*, 2002, **66**, 024429.
103 P. Esquinazi, D. Spemann, R. Höhne, A. Setzer, K.-H. Han and T. Butz, *Phys. Rev. Lett.*, 2003, **91**, 227201.
104 Z. Li and F. Chen, *Appl. Phys. Rev.*, 2017, **4**, 011103.
105 R. Singh, *J. Magn. Magn. Mater.*, 2013, **346**, 58–73.
106 F. Banhart, J. Kotakoski and A. V. Krasheninnikov, *ACS Nano*, 2011, **5**, 26–41.
107 O. V. Yazyev and Y. P. Chen, *Nat. Nanotechnol.*, 2014, **9**, 755–767.
108 S. Nigar, Z. Zhou, H. Wang and M. Imtiaz, *RSC Adv.*, 2017, **7**, 51546–51580.
109 S. T. Skowron, I. V. Lebedeva, A. M. Popov and E. Bichoutskaia, *Chem. Soc. Rev.*, 2015, **44**, 3143–3176.
110 H. Terrones, R. Lv, M. Terrones and M. S. Dresselhaus, *Rep. Prog. Phys.*, 2012, **75**, 062501.
111 R. H. Telling and M. I. Heggie, *Philos. Mag.*, 2007, **87**, 4797–4846.
112 P. A. Thrower and R. M. Mayer, *Phys. Status Solidi A*, 1978, **47**, 11–37.
113 A. J. Stone and D. J. Wales, *Chem. Phys. Lett.*, 1986, **128**, 501–503.
114 A. A. El-Barbary, R. H. Telling, C. P. Ewels, M. I. Heggie and P. R. Briddon, *Phys. Rev. B: Condens. Matter Mater. Phys.*, 2003, **68**, 144107.
115 Y. Ma, P. O. Lehtinen, A. S. Foster and R. M. Nieminen, *New J. Phys.*, 2004, **6**, 68.
116 P. O. Lehtinen, A. S. Foster, Y. Ma, A. V. Krasheninnikov and R. M. Nieminen, *Phys. Rev. Lett.*, 2004, **93**, 187202.

Published on 26 March 2018. Downloaded by Univerzita Palackého v Olomouci on 2/28/2019 2:05:03 PM.

117 S. F. Asbaghian Namin and R. Pilafkan, *Phys. E*, 2017, **93**, 257–264.
118 A. V. Krasheninnikov, P. O. Lehtinen, A. S. Foster and R. M. Nieminen, *Chem. Phys. Lett.*, 2006, **418**, 132–136.
119 C. Ronchi, M. Datteo, D. Perilli, L. Ferrighi, G. Fazio, D. Selli and C. Di Valentin, *J. Phys. Chem. C*, 2017, **121**, 8653–8661.
120 R. Singh and P. Kroll, *J. Phys.: Condens. Matter*, 2009, **21**, 196002.
121 X. Q. Dai, J. H. Zhao, M. H. Xie, Y. N. Tang, Y. H. Li and B. Zhao, *Eur. Phys. J. B*, 2011, **80**, 343–349.
122 A. W. Robertson, B. Montanari, K. He, C. S. Allen, Y. A. Wu, N. M. Harrison, A. I. Kirkland and J. H. Warner, *ACS Nano*, 2013, **7**, 4495–4502.
123 A. Hashimoto, K. Suenaga, A. Gloter, K. Urita and S. Iijima, *Nature*, 2004, **430**, 870–873.
124 M. H. Gass, U. Bangert, A. L. Bleloch, P. Wang, R. R. Nair and A. K. Geim, *Nat. Nanotechnol.*, 2008, **3**, 676–681.
125 M. M. Ugeda, I. Brihuega, F. Guinea and J. M. Gómez-Rodríguez, *Phys. Rev. Lett.*, 2010, **104**, 096804.
126 J. C. Meyer, F. Eder, S. Kurasch, V. Skakalova, J. Kotakoski, H. J. Park, S. Roth, A. Chuvilin, S. Eyhusen, G. Benner, A. V. Krasheninnikov and U. Kaiser, *Phys. Rev. Lett.*, 2012, **108**, 196102.
127 H. I. Rasool, C. Ophus and A. Zettl, *Adv. Mater.*, 2015, **27**, 5771–5777.
128 G.-D. Lee, C. Z. Wang, E. Yoon, N.-M. Hwang, D.-Y. Kim and K. M. Ho, *Phys. Rev. Lett.*, 2005, **95**, 205501.
129 T. Trevethan, C. D. Latham, M. I. Heggie, P. R. Briddon and M. J. Rayson, *Nanoscale*, 2014, **6**, 2978–2986.
130 P. A. Denis and F. Iribarne, *J. Phys. Chem. C*, 2013, **117**, 19048–19055.
131 A. R. Botello-Méndez, X. Declerck, M. Terrones, H. Terrones and J.-C. Charlier, *Nanoscale*, 2011, **3**, 2868–2872.
132 M. M. Ugeda, I. Brihuega, F. Hiebel, P. Mallet, J.-Y. Veuillen, J. M. Gómez-Rodríguez and F. Ynduráin, *Phys. Rev. B: Condens. Matter Mater. Phys.*, 2012, **85**, 121402.
133 Ç. Ö. Girit, J. C. Meyer, R. Erni, M. D. Rossell, C. Kisielowski, L. Yang, C.-H. Park, M. F. Crommie, M. L. Cohen, S. G. Louie and A. Zettl, *Science*, 2009, **323**, 1705–1708.
134 Y. Kim, J. Ihm, E. Yoon and G.-D. Lee, *Phys. Rev. B: Condens. Matter Mater. Phys.*, 2011, **84**, 075445.
135 A. Zobelli, V. Ivanovskaya, P. Wagner, I. Suarez-Martinez, A. Yaya and C. P. Ewels, *Phys. Status Solidi B*, 2012, **249**, 276–282.
136 G. López-Polín, C. Gómez-Navarro, V. Parente, F. Guinea, M. I. Katsnelson, F. Pérez-Murano and J. Gómez-Herrero, *Nat. Phys.*, 2015, **11**, 26–31.
137 G. López-Polín, M. Jaafar, F. Guinea, R. Roldán, C. Gómez-Navarro and J. Gómez-Herrero, *Carbon*, 2017, **124**, 42–48.
138 Y. Zhang, M. P. K. Sahoo and J. Wang, *Nanotechnology*, 2016, **27**, 435206.
139 I. Y. Sagalianov, T. M. Radchenko, Y. I. Prylutskyy, V. A. Tatarenko and P. Szroeder, *Eur. Phys. J. B*, 2017, **90**, 112.
140 L. Li, S. Reich and J. Robertson, *Phys. Rev. B: Condens. Matter Mater. Phys.*, 2005, **72**, 184109.
141 P. O. Lehtinen, A. S. Foster, A. Ayuela, A. Krasheninnikov, K. Nordlund and R. M. Nieminen, *Phys. Rev. Lett.*, 2003, **91**, 017202.
142 E. J. Duplock, M. Scheffler and P. J. D. Lindan, *Phys. Rev. Lett.*, 2004, **92**, 225502.
143 H. González-Herrero, J. M. Gómez-Rodríguez, P. Mallet, M. Moaied, J. J. Palacios, C. Salgado, M. M. Ugeda, J.-Y. Veuillen, F. Yndurain and I. Brihuega, *Science*, 2016, **352**, 437–441.
144 D. W. Boukhvalov, M. I. Katsnelson and A. I. Lichtenstein, *Phys. Rev. B: Condens. Matter Mater. Phys.*, 2008, **77**, 035427.
145 F. Karlický, B. Lepetit and D. Lemoine, *J. Chem. Phys.*, 2014, **140**, 124702.
146 D. Cortés-Arriagada, S. Gutiérrez-Oliva, B. Herrera, K. Soto and A. Toro-Labbé, *J. Chem. Phys.*, 2014, **141**, 134701.
147 B. Lepetit and B. Jackson, *Phys. Rev. Lett.*, 2011, **107**, 236102.
148 J. Zhang, Y. Yan, W. Zong, A. Li, Z. Qiao and T. Sun, *J. Phys.: Condens. Matter*, 2017, **29**, 195001.
149 K. M. McCreary, A. G. Swartz, W. Han, J. Fabian and R. K. Kawakami, *Phys. Rev. Lett.*, 2012, **109**, 186604.
150 A. I. Podlivaev and L. A. Openov, *Phys. Solid State*, 2015, **57**, 820–824.
151 J. González, F. Guinea and M. A. H. Vozmediano, *Phys. Rev. B: Condens. Matter Mater. Phys.*, 2001, **63**, 134421.
152 M. Marcaccio and F. Paolucci, Making and Exploiting Fullerenes, Graphene, and Carbon Nanotubes, in *Topics in Current Chemistry*, Springer-Verlag, Berlin Heidelberg, 2014, pp. 1–270.
153 J. Ma, D. Alfè, A. Michaelides and E. Wang, *Phys. Rev. B: Condens. Matter Mater. Phys.*, 2009, **80**, 033407.
154 K. Ulman and S. Narasimhan, *Phys. Rev. B: Condens. Matter Mater. Phys.*, 2014, **89**, 245429.
155 A. I. Podlivaev and L. A. Openov, *Phys. Lett. A*, 2015, **379**, 1757–1761.
156 N. S. Shirodkar and U. V. Waghmare, *Phys. Rev. B: Condens. Matter Mater. Phys.*, 2012, **86**, 165401.
157 J. Kotakoski, J. C. Meyer, S. Kurasch, D. Santos-Cottin, U. Kaiser and A. V. Krasheninnikov, *Phys. Rev. B: Condens. Matter Mater. Phys.*, 2011, **83**, 245420.
158 S. T. Skowron, V. O. Koroteev, M. Baldoni, S. Lopatin, A. Zurutuza, A. Chuvilin and E. Besley, *Carbon*, 2016, **105**, 176–182.
159 N. Jing, Q. Xue, C. Ling, M. Shan, T. Zhang, X. Zhou and Z. Jiao, *RSC Adv.*, 2012, **2**, 9124–9129.
160 B. Mortazavi and S. Ahzi, *Carbon*, 2013, **63**, 460–470.
161 A. Verma and A. Parashar, *Phys. Chem. Chem. Phys.*, 2017, **19**, 16023–16037.
162 A. Lherbier, S. M.-M. Dubois, X. Declerck, Y.-M. Niquet, S. Roche and J.-C. Charlier, *Phys. Rev. B: Condens. Matter Mater. Phys.*, 2012, **86**, 075402.
163 X. Peng and R. Ahuja, *Nano Lett.*, 2008, **8**, 4464–4468.
164 L. Vicarelli, S. J. Heerema, C. Dekker and H. W. Zandbergen, *ACS Nano*, 2015, **9**, 3428–3435.
165 O. V. Yazyev and S. G. Louie, *Phys. Rev. B: Condens. Matter Mater. Phys.*, 2010, **81**, 195420.

 This journal is © The Royal Society of Chemistry 2018

Published on 26 March 2018. Downloaded by Univerzita Palackého v Olomouci on 2/28/2019 2:05:03 PM.

166 B. W. Jeong, J. Ihm and G.-D. Lee, *Phys. Rev. B: Condens. Matter Mater. Phys.*, 2008, **78**, 165403.
167 J. Lahiri, Y. Lin, P. Bozkurt, I. I. Oleynik and M. Batzill, *Nat. Nanotechnol.*, 2010, **5**, 326–329.
168 S. Malola, H. Häkkinen and P. Koskinen, *Phys. Rev. B: Condens. Matter Mater. Phys.*, 2010, **81**, 165447.
169 P. Y. Huang, C. S. Ruiz-Vargas, A. M. van der Zande, W. S. Whitney, M. P. Levendorf, J. W. Kevek, S. Garg, J. S. Alden, C. J. Hustedt, Y. Zhu, J. Park, P. L. McEuen and D. A. Muller, *Nature*, 2011, **469**, 389–393.
170 J.-R. Yin, W.-H. Wu, W. Xie, Y.-H. Ding and P. Zhang, *Phys. E*, 2015, **68**, 102–106.
171 T. R. Albrecht, H. A. Mizes, J. Nogami, S.-I. Park and C. F. Quate, *Appl. Phys. Lett.*, 1988, **52**, 362–364.
172 P. Simonis, C. Goffaux, P. A. Thiry, L. P. Biro, P. Lambin and V. Meunier, *Surf. Sci.*, 2002, **511**, 319–322.
173 Y. Liu and B. I. Yakobson, *Nano Lett.*, 2010, **10**, 2178–2183.
174 D. Berger and C. Ratsch, *Phys. Rev. B: Condens. Matter Mater. Phys.*, 2016, **93**, 235441.
175 Y. Li, R.-Q. Zhang, Z. Lin and M. A. Van Hove, *Appl. Phys. Lett.*, 2012, **101**, 253105.
176 W. T. Pong, J. Bendall and C. Durkan, *Surf. Sci.*, 2007, **601**, 498–509.
177 Q. Yu, L. A. Jauregui, W. Wu, R. Colby, J. Tian, Z. Su, H. Cao, Z. Liu, D. Pandey, D. Wei, T. F. Chung, P. Peng, N. P. Guisinger, E. A. Stach, J. Bao, S.-S. Pei and Y. P. Chen, *Nat. Mater.*, 2011, **10**, 443–449.
178 B. Yang, H. Xu, J. Lu and K. P. Loh, *J. Am. Chem. Soc.*, 2014, **136**, 12041–12046.
179 S. Kurasch, J. Kotakoski, O. Lehtinen, V. Skákalová, J. Smet, C. E. Krill III, A. V. Krasheninnikov and U. Kaiser, *Nano Lett.*, 2012, **12**, 3168–3173.
180 Y. Wei, J. Wu, H. Yin, X. Shi, R. Yang and M. Dresselhaus, *Nat. Mater.*, 2012, **11**, 759–763.
181 R. Grantab, V. B. Shenoy and R. S. Ruoff, *Science*, 2010, **330**, 946–948.
182 J. Červenka and C. F. J. Flipse, *Phys. Rev. B: Condens. Matter Mater. Phys.*, 2009, **79**, 195429.
183 V. N. Narozhnyi, K.-H. Müller, D. Eckert, A. Teresiak, L. Dunsch, V. A. Davydov, L. S. Kashevarova and A. V. Rakhmanina, *Phys. B*, 2003, **329–333**, 1217–1218.
184 T. L. Makarova and F. Palacio, in *Carbon Based Magnetism: An Overview of the Magnetism of Metal Free Carbon-based Compounds and Materials*, Elsevier, Amsterdam, 2006.
185 H. Ohldag, T. Tyliszczak, R. Höhne, D. Spemann, P. Esquinazi, M. Ungureanu and T. Butz, *Phys. Rev. Lett.*, 2007, **98**, 187204.
186 T. L. Makarova, B. Sundqvist, R. Höhne, P. Esquinazi, Y. Kopelevich, P. Scharff, V. A. Davydov, L. S. Kashevarova and A. V. Rakhmanina, *Nature*, 2001, **413**, 716–718.
187 T. L. Makarova, B. Sundqvist, R. Höhne, P. Esquinazi, Y. Kopelevich, P. Scharff, V. A. Davydov, L. S. Kashevarova and A. V. Rakhmanina, *Nature*, 2006, **440**, 707.
188 M. A. H. Vozmediano, M. P. López-Sancho, T. Stauber and F. Guinea, *Phys. Rev. B: Condens. Matter Mater. Phys.*, 2005, **72**, 155121.
189 V. M. Pereira, F. Guinea, J. M. B. Lopes dos Santos, N. M. R. Peres and A. H. Castro Neto, *Phys. Rev. Lett.*, 2006, **96**, 036801.
190 J. J. Palacios and F. Ynduráin, *Phys. Rev. B: Condens. Matter Mater. Phys.*, 2012, **85**, 245443.
191 B. Wang and S. T. Pantelides, *Phys. Rev. B: Condens. Matter Mater. Phys.*, 2012, **86**, 165438.
192 V. Antonov, D. Borisova and A. Proykova, *Int. J. Quantum Chem.*, 2013, **113**, 792–796.
193 L. Rodrigo, P. Pou and R. Pérez, *Carbon*, 2016, **103**, 200–208.
194 H. Padmanabhan and B. R. K. Nanda, *Phys. Rev. B: Condens. Matter Mater. Phys.*, 2016, **93**, 165403.
195 W. S. Paz, W. L. Scopel and J. C. C. Freitas, *Solid State Commun.*, 2013, **175-176**, 71–75.
196 Y. Zhang, S.-Y. Li, H. Huang, W.-T. Li, J.-B. Qiao, W.-X. Wang, L.-J. Yin, K.-K. Bai, W. Duan and L. He, *Phys. Rev. Lett.*, 2016, **117**, 166801.
197 F. Gao and S. Gao, *Sci. Rep.*, 2017, **7**, 1792.
198 E. J. G. Santos, S. Riikonen, D. Sánchez-Portal and A. Ayuela, *J. Phys. Chem. C*, 2012, **116**, 7602–7606.
199 R. Faccio and A. W. Mombrú, *J. Phys.: Condens. Matter*, 2012, **24**, 375304.
200 S. Lei, B. Li, E. Kan, J. Huang, Q. Li and J. Yang, *J. Appl. Phys.*, 2013, **113**, 213709.
201 W. L. Scopel, W. S. Paz and J. C. C. Freitas, *Solid State Commun.*, 2016, **240**, 5–9.
202 J. Barzola-Quiquia, P. Esquinazi, M. Rothermel, D. Spemann, T. Butz and N. García, *Phys. Rev. B: Condens. Matter Mater. Phys.*, 2007, **76**, 161403.
203 Q. Zhou, Y. Yong, W. Ju, X. Su and X. Li, *Phys. E*, 2017, **91**, 65–71.
204 M. Riccò, D. Pontiroli, M. Mazzani, M. Choucair, J. A. Stride and O. V. Yazyev, *Nano Lett.*, 2011, **11**, 4919–4922.
205 M. P. López-Sancho, F. de Juan and M. A. H. Vozmediano, *Phys. Rev. B: Condens. Matter Mater. Phys.*, 2009, **79**, 075413.
206 P. Lu, Z. Zhang and W. Guo, *Phys. Lett. A*, 2009, **373**, 3354–3358.
207 J.-C. Ren, Z. Ding, R.-Q. Zhang and M. A. Van Hove, *Phys. Rev. B: Condens. Matter Mater. Phys.*, 2015, **91**, 045425.
208 S. Dutta and K. Wakabayashi, *Sci. Rep.*, 2015, **5**, 11744.
209 L. Kou, C. Tang, W. Guo and C. Chen, *ACS Nano*, 2011, **5**, 1012–1017.
210 T. Enoki and K. Takai, Unconventional Magnetic Properties of Nanographite, in *Carbon-Based Magnetism*, ed. T. L. Makarova and F. Palacio, Elsevier B.V., 2006, pp. 397–416.
211 T. Enoki, Y. Kobayashi and K.-I. Fukui, *Int. Rev. Phys. Chem.*, 2007, **26**, 609–645.
212 T. Enoki, Magnetism of Nanographene, in *Graphene: Synthesis, Properties, and Phenomena*, ed. C. N. R. Rao and A. K. Sood, Wiley-VCH Verlag GmbH & Co. KGaA, Weinheim, Germany, 2013, pp. 131–157.
213 S. E. Stein and R. L. Brown, *J. Am. Chem. Soc.*, 1987, **109**, 3721–3729.
214 K. Tanaka, S. Yamashita, H. Yamabe and T. Yamabe, *Synth. Met.*, 1987, **17**, 143–148.

Published on 26 March 2018. Downloaded by Univerzita Palackého v Olomouci on 2/28/2019 2:05:03 PM.

215 M. Fujita, K. Wakabayashi, K. Nakada and K. Kusakabe, *J. Phys. Soc. Jpn.*, 1996, **65**, 1920–1923.
216 Y. Niimi, T. Matsui, H. Kambara, K. Tagami, M. Tsukada and H. Fukuyama, *Appl. Surf. Sci.*, 2005, **241**, 43–48.
217 Y. Kobayashi, K.-I. Fukui, T. Enoki and K. Kusakabe, *Phys. Rev. B: Condens. Matter Mater. Phys.*, 2006, **73**, 125415.
218 E. Clar, *The Aromatic Sextet*, Wiley, London, 1972.
219 K. Wakabayashi, M. Sigrist and M. Fujita, *J. Phys. Soc. Jpn.*, 1998, **67**, 2089–2093.
220 M. Bendikov, H. M. Duong, K. Starkey, K. N. Houk, E. A. Carter and F. Wudl, *J. Am. Chem. Soc.*, 2004, **126**, 7416–7417.
221 O. Hod, V. Barone and G. E. Scuseria, *Phys. Rev. B: Condens. Matter Mater. Phys.*, 2008, **77**, 035411.
222 D. E. Jiang and S. Dai, *J. Phys. Chem. A*, 2008, **112**, 332–335.
223 J. C. Freitas, W. L. Scopel, W. S. Paz, L. V. Bernardes, F. E. Cunha-Filho, C. Speglich, F. M. Araujo-Moreira, D. Pelc, T. Cvitanic and M. Pozek, *Sci. Rep.*, 2015, **5**, 14761.
224 Y. Shibayama, H. Sato, T. Enoki and M. Endo, *Phys. Rev. Lett.*, 2000, **84**, 1744–1747.
225 K. Nakada, M. Fujita, G. Dresselhaus and M. S. Dresselhaus, *Phys. Rev. B: Condens. Matter Mater. Phys.*, 1996, **54**, 17954–17961.
226 K. Wakabayashi, M. Fujita, H. Ajiki and M. Sigrist, *Phys. Rev. B: Condens. Matter Mater. Phys.*, 1999, **59**, 8271–8282.
227 M. Terrones, A. R. Botello-Mendez, J. Campos-Delgado, F. Lopez-Urias, Y. I. Vega-Cantu, F. J. Rodriguez-Macias, A. L. Elias, E. Munoz-Sandoval, A. G. Cano-Marquez, J. C. Charlier and H. Terrones, *Nano Today*, 2010, **5**, 351–372.
228 Y. Segawa, H. Ito and K. Itami, *Nat. Rev. Mater.*, 2016, **1**, 1.
229 M. Yagmurcukardes, F. M. Peeters, R. T. Senger and H. Sahin, *Appl. Phys. Rev.*, 2016, **3**, 041302.
230 X. W. Zhang, O. V. Yazyev, J. J. Feng, L. M. Xie, C. G. Tao, Y. C. Chen, L. Y. Jiao, Z. Pedramrazi, A. Zettl, S. G. Louie, H. J. Dai and M. F. Crommie, *ACS Nano*, 2013, **7**, 198–202.
231 P. Ruffieux, S. Y. Wang, B. Yang, C. Sanchez-Sanchez, J. Liu, T. Dienel, L. Talirz, P. Shinde, C. A. Pignedoli, D. Passerone, T. Dumslaff, X. L. Feng, K. Mullen and R. Fasel, *Nature*, 2016, **531**, 489–492.
232 H. J. Xiang, E. J. Kan, S. H. Wei, M. H. Whangbo and J. L. Yang, *Nano Lett.*, 2009, **9**, 4025–4030.
233 Y. Son, M. Cohen and S. Louie, *Phys. Rev. Lett.*, 2006, **97**, 216803.
234 L. Sun, Q. Li, H. Ren, H. Su, Q. Shi and J. Yang, *J. Chem. Phys.*, 2008, **129**, 074704.
235 B. Sahu, H. K. Min and S. K. Banerjee, *Phys. Rev. B: Condens. Matter Mater. Phys.*, 2010, **82**, 115426.
236 F. Wu, E. Kan, H. Xiang, S. Wei, M. Whangbo and J. Yang, *Appl. Phys. Lett.*, 2009, **94**, 223105.
237 S. Y. Li, L. L. Shi, L. Wen and T. X. Ma, *J. Phys.: Condens. Matter*, 2016, **28**, 086001.
238 B. Sahu, H. Min, A. H. MacDonald and S. K. Banerjee, *Phys. Rev. B: Condens. Matter Mater. Phys.*, 2008, **78**, 045404.
239 V. L. J. Joly, M. Kiguchi, S. J. Hao, K. Takai, T. Enoki, R. Sumii, K. Amemiya, H. Muramatsu, T. Hayashi, Y. A. Kim, M. Endo, J. Campos-Delgado, F. Lopez-Urias, A. Botello-Mendez, H. Terrones, M. Terrones and M. S. Dresselhaus, *Phys. Rev. B: Condens. Matter Mater. Phys.*, 2010, **81**, 245428.
240 H. U. Ozdemir, A. Altintas and A. D. Guclu, *Phys. Rev. B: Condens. Matter Mater. Phys.*, 2016, **93**, 014415.
241 S. L. Chang, B. R. Wu, J. H. Wong and M. F. Lin, *Carbon*, 2014, **77**, 1031–1039.
242 S. L. Chang, B. R. Wu, P. H. Yang and M. F. Lin, *RSC Adv.*, 2016, **6**, 64852–64860.
243 K. K. Paulla and A. A. Farajian, *J. Phys.: Condens. Matter*, 2013, **25**, 115303.
244 G. Kim and S. H. Jhi, *Appl. Phys. Lett.*, 2010, **97**, 263114.
245 J. Kunstmann, C. Ozdogan, A. Quandt and H. Fehske, *Phys. Rev. B: Condens. Matter Mater. Phys.*, 2011, **83**, 045414.
246 M. Golor, S. Wessel and M. J. Schmidt, *Phys. Rev. Lett.*, 2014, **112**, 046601.
247 M. Raczkowski and F. F. Assaad, *Phys. Rev. B: Condens. Matter Mater. Phys.*, 2017, **96**, 115155.
248 B. Huang, F. Liu, J. Wu, B. L. Gu and W. H. Duan, *Phys. Rev. B: Condens. Matter Mater. Phys.*, 2008, **77**, 153411.
249 C. Koop and S. Wessel, *Phys. Rev. B: Condens. Matter Mater. Phys.*, 2017, **96**, 165114.
250 S. S. Rao, S. N. Jammalamadaka, A. Stesmans, V. V. Moshchalkov, J. van Tol, D. V. Kosynkin, A. Higginbotharn-Duque and J. M. Tour, *Nano Lett.*, 2012, **12**, 1210–1217.
251 D. J. Klein, *Chem. Phys. Lett.*, 1994, **217**, 261–265.
252 D. J. Klein and L. Bytautas, *J. Phys. Chem. A*, 1999, **103**, 5196–5210.
253 K. He, A. W. Robertson, S. Lee, E. Yoon, G. D. Lee and J. H. Warner, *ACS Nano*, 2014, **8**, 12272–12279.
254 P. Wagner, V. V. Ivanovskaya, M. Melle-Franco, B. Humbert, J. J. Adjizian, P. R. Briddon and C. P. Ewels, *Phys. Rev. B: Condens. Matter Mater. Phys.*, 2013, **88**, 094106.
255 K. Wakabayashi, S. Okada, R. Tomita, S. Fujimoto and Y. Natsume, *J. Phys. Soc. Jpn.*, 2010, **79**, 034706.
256 L. P. Chen, L. J. Wang and D. Beljonne, *Carbon*, 2014, **77**, 868–879.
257 J. Z. Liu, B. W. Li, Y. Z. Tan, A. Giannakopoulos, C. Sanchez-Sanchez, D. Beljonne, P. Ruffieux, R. Fasel, X. L. Feng and K. Mullen, *J. Am. Chem. Soc.*, 2015, **137**, 6097–6103.
258 P. Koskinen, S. Malola and H. Hakkinen, *Phys. Rev. Lett.*, 2008, **101**, 115502.
259 T. Wassmann, A. P. Seitsonen, A. M. Saitta, M. Lazzeri and F. Mauri, *Phys. Rev. Lett.*, 2008, **101**, 096402.
260 F. J. Owens, *J. Chem. Phys.*, 2008, **128**, 194701.
261 E. Cruz-Silva, Z. M. Barnett, B. G. Sumpter and V. Meunier, *Phys. Rev. B: Condens. Matter Mater. Phys.*, 2011, **83**, 155445.
262 J. Lan, X. H. Zheng, L. L. Song, R. N. Wang and Z. Zeng, *Solid State Commun.*, 2012, **152**, 1635–1640.
263 Y. F. Li, Z. Zhou, P. W. Shen and Z. F. Chen, *ACS Nano*, 2009, **3**, 1952–1958.
264 S. Q. Zhao, Y. Lu, W. G. Lu, W. J. Liang and E. G. Wang, *Chin. Phys. B*, 2014, **23**, 067305.
265 S. S. Kim, H. S. Kim, H. S. Kim and Y. H. Kim, *Carbon*, 2015, **81**, 339–346.

 This journal is © The Royal Society of Chemistry 2018

Published on 26 March 2018. Downloaded by Univerzita Palackého v Olomouci on 2/28/2019 2:05:03 PM.

266 E. J. Kan, X. J. Wu, Z. Y. Li, X. C. Zeng, J. L. Yang and J. G. Hou, *J. Chem. Phys.*, 2008, **129**, 084712.
267 M. Topsakal, E. Aktürk, H. Sevinçli and S. Ciraci, *Phys. Rev. B: Condens. Matter Mater. Phys.*, 2008, **78**, 235435.
268 D. Midtvedt and A. Croy, *J. Phys.: Condens. Matter*, 2016, **28**, 045302.
269 K. Sawada, F. Ishii and M. Saito, *J. Phys. Soc. Jpn.*, 2011, **80**, 044712.
270 T. X. Ma, S. H. Liu, P. Gao, Z. B. Huang and H. Q. Lin, *J. Appl. Phys.*, 2012, **112**, 073922.
271 Q. Q. Dai, Y. F. Zhu and Q. Jiang, *Phys. Chem. Chem. Phys.*, 2014, **16**, 10607–10613.
272 A. J. Simbeck, D. Y. Gu, N. Kharche, P. V. Satyam, P. Avouris and S. K. Nayak, *Phys. Rev. B: Condens. Matter Mater. Phys.*, 2013, **88**, 035413.
273 B. Sahu, H. Min and S. K. Banerjee, *Phys. Rev. B: Condens. Matter Mater. Phys.*, 2011, **84**, 075481.
274 N. Gorjizadeh, A. A. Farajian, K. Esfarjani and Y. Kawazoe, *Phys. Rev. B: Condens. Matter Mater. Phys.*, 2008, **78**, 155427.
275 N. K. Jaiswal and P. Srivastava, *IEEE Trans. Nanotechnol.*, 2013, **12**, 685–691.
276 P. Srivastava, S. Dhar and N. K. Jaiswal, *Phys. Lett. A*, 2015, **379**, 835–842.
277 Z. Zhu, D. Wang, Z. H. Zhang and M. Qiu, *Carbon*, 2016, **106**, 252–259.
278 Z. F. Liu, Q. P. Wu, A. X. Chen, X. B. Xiao, N. H. Liu and G. X. Miao, *Sci. Rep.*, 2017, **7**, 8854.
279 M. H. Wu, X. C. Zeng and P. Jena, *J. Phys. Chem. Lett.*, 2013, **4**, 2482–2488.
280 K. Sawada, F. Ishii, M. Saito, S. Okada and T. Kawai, *Nano Lett.*, 2009, **9**, 269–272.
281 K. Sawada, F. Ishii and M. Saito, *Phys. Rev. B: Condens. Matter Mater. Phys.*, 2010, **82**, 245426.
282 B. Xu, J. Yin, Y. D. Xia, X. G. Wan, K. Jiang and Z. G. Liu, *Appl. Phys. Lett.*, 2010, **96**, 163102.
283 K. Sawada, F. Ishii, M. Saito, S. Okada and T. Kawai, *Nano Lett.*, 2009, **9**, 269–272.
284 S. Dutta and S. K. Pati, *J. Phys. Chem. B*, 2008, **112**, 1333–1335.
285 E. J. Kan, Z. Y. Li, J. L. Yang and J. G. Hou, *J. Am. Chem. Soc.*, 2008, **130**, 4224–4225.
286 S. Dutta, A. K. Manna and S. K. Pati, *Phys. Rev. Lett.*, 2009, **102**, 096601.
287 S. Dutta and K. Wakabayashi, *Sci. Rep.*, 2012, **2**, 519.
288 W. Z. Wu, Z. H. Zhang, P. Lu and W. L. Guo, *Phys. Rev. B: Condens. Matter Mater. Phys.*, 2010, **82**, 085425.
289 P. Cui, Q. Zhang, H. B. Zhu, X. X. Li, W. Y. Wang, Q. X. Li, C. G. Zeng and Z. Y. Zhang, *Phys. Rev. Lett.*, 2016, **116**, 026802.
290 K. Tarawneh and N. Al-Aqtash, *J. Nano Res.*, 2014, **27**, 65–73.
291 M. Kan, J. Zhou, Q. Sun, Q. Wang, Y. Kawazoe and P. Jena, *Phys. Rev. B: Condens. Matter Mater. Phys.*, 2012, **85**, 155450.
292 Q. Q. Dai, Y. F. Zhu and Q. Jiang, *J. Phys. Chem. C*, 2013, **117**, 4791–4799.
293 G. P. Tang, Z. H. Zhang, X. Q. Deng, Z. Q. Fan and H. L. Zhu, *Phys. Chem. Chem. Phys.*, 2015, **17**, 638–643.
294 B. Mandal, S. Sarkar, A. Pramanik and P. Sarkar, *RSC Adv.*, 2014, **4**, 49946–49952.
295 C. Chakravarty, B. Mandal and P. Sarkar, *Phys. Lett. A*, 2017, **381**, 307–313.
296 P. Lu, Z. H. Zhang and W. L. Guo, *Phys. Lett. A*, 2009, **373**, 3354–3358.
297 J. N. B. Rodrigues, P. A. D. Goncalves, N. F. G. Rodrigues, R. M. Ribeiro, J. M. B. Lopes dos Santos and N. M. R. Peres, *Phys. Rev. B: Condens. Matter Mater. Phys.*, 2011, **84**, 155435.
298 W. X. Zhang, C. He, T. Li and S. B. Gong, *RSC Adv.*, 2015, **5**, 33407–33413.
299 X. H. Hu, L. T. Sun and A. V. Krasheninnikov, *Appl. Phys. Lett.*, 2012, **100**, 263115.
300 X. D. Tan, X. P. Liao and L. T. Sun, *Physica E*, 2017, **85**, 302–307.
301 S. Y. Yue, Q. B. Yan, Z. G. Zhu, H. J. Cui, Q. R. Zheng and G. Su, *Carbon*, 2014, **71**, 150–158.
302 D. Soriano, F. Muñoz-Rojas, J. Fernández-Rossier and J. J. Palacios, *Phys. Rev. B: Condens. Matter Mater. Phys.*, 2010, **81**, 165409.
303 B. Xu, J. Yin, Y. D. Xia, X. G. Wan, K. Jiang and Z. G. Liu, *Appl. Phys. Lett.*, 2010, **96**, 163102.
304 Z. Y. Guan, C. Si, S. L. Hu and W. H. Duan, *Phys. Chem. Chem. Phys.*, 2016, **18**, 12350–12356.
305 J. Kang, F. M. Wu and J. B. Li, *Appl. Phys. Lett.*, 2011, **98**, 083109.
306 H. Z. Zhang, S. Meng, H. F. Yang, L. Li, H. X. Fu, W. Ma, C. Y. Niu, J. T. Sun and C. Z. Gu, *J. Appl. Phys.*, 2015, **117**, 113902.
307 W. C. Yi, W. Liu, L. Zhao, R. Islam, M. S. Miao and J. Y. Liu, *RSC Adv.*, 2017, **7**, 27932–27937.
308 O. Hod, V. Barone, J. E. Peralta and G. E. Scuseria, *Nano Lett.*, 2007, **7**, 2292–2299.
309 J. Guan, W. Chen, Y. F. Li, G. T. Yu, Z. M. Shi, X. R. Huang, C. C. Sun and Z. F. Chen, *Adv. Funct. Mater.*, 2013, **23**, 1507–1518.
310 R. Ortiz, J. L. Lado, M. Melle-Franco and J. Fernández-Rossier, *Phys. Rev. B: Condens. Matter Mater. Phys.*, 2016, **94**, 094414.
311 J. Bhattacharjee, *J. Chem. Phys.*, 2012, **137**, 094705.
312 D. Cho, K. C. Ko, H. Park and J. Y. Lee, *J. Phys. Chem. C*, 2015, **119**, 10109–10115.
313 Y. F. Li, Z. Zhou, C. R. Cabrera and Z. F. Chen, *Sci. Rep.*, 2013, **3**, 2030.
314 Y. Wang and Y. F. Li, *Theor. Chem. Acc.*, 2014, **133**, 1548.
315 V. A. Rigo, T. B. Martins, A. J. R. da Silva, A. Fazzio and R. H. Miwa, *Phys. Rev. B: Condens. Matter Mater. Phys.*, 2009, **79**, 075435.
316 G. D. Yu, X. L. Lu, Y. S. Zheng and W. J. Tian, *J. Appl. Phys.*, 2012, **111**, 033707.
317 X. H. Hu, W. Zhang, L. T. Sun and A. V. Krasheninnikov, *Phys. Rev. B: Condens. Matter Mater. Phys.*, 2012, **86**, 195418.

Published on 26 March 2018. Downloaded by Univerzita Palackého v Olomouci on 2/28/2019 2:05:03 PM.

318 M. M. Zhong, C. Huang and G. Z. Wang, *J. Mater. Sci.*, 2017, **52**, 12307–12313.
319 P. P. Shinde, O. Groning, S. Y. Wang, P. Ruffieux, C. A. Pignedoli, R. Fasel and D. Passerone, *Carbon*, 2017, **124**, 123–132.
320 Y. Li, W. Zhang, M. Morgenstern and R. Mazzarello, *Phys. Rev. Lett.*, 2013, **110**, 216804.
321 S. B. Tang and X. R. Cao, *Phys. Chem. Chem. Phys.*, 2014, **16**, 23214–23223.
322 G. D. Belletti, S. D. Dalosto and S. Tinte, *J. Phys.: Condens. Matter*, 2016, **28**, 435002.
323 Y. W. Son, M. L. Cohen and S. G. Louie, *Nature*, 2006, **444**, 347–349.
324 M. R. Rezapour, J. Yun, G. Lee and K. S. Kim, *J. Phys. Chem. Lett.*, 2016, **7**, 5049–5055.
325 F. J. Culchac, R. B. Capaz, A. T. Costa and A. Latgé, *J. Phys.: Condens. Matter*, 2014, **26**, 216002.
326 Z. Y. Li, H. Y. Qian, J. Wu, B. L. Gu and W. H. Duan, *Phys. Rev. Lett.*, 2008, **100**, 206802.
327 G. Yang, B. Y. Li, W. Zhang, M. Ye and T. X. Ma, *J. Phys.: Condens. Matter*, 2017, **29**, 365601.
328 L. L. Sun, P. Wei, J. H. Wei, S. Sanvito and S. M. Hou, *J. Phys.: Condens. Matter*, 2011, **23**, 425301.
329 M. Golor, T. C. Lang and S. Wessel, *Phys. Rev. B: Condens. Matter Mater. Phys.*, 2013, **87**, 155441.
330 A. R. Carvalho, J. H. Warnes and C. H. Lewenkopf, *Phys. Rev. B: Condens. Matter Mater. Phys.*, 2014, **89**, 245444.
331 X. Li, X. Wang, L. Zhang, S. Lee and H. Dai, *Science*, 2008, **319**, 1229–1232.
332 J. Cai, P. Ruffieux, R. Jaafar, M. Bieri, T. Braun, S. Blankenburg, M. Muoth, A. P. Seitsonen, M. Saleh, X. Feng, K. Mullen and R. Fasel, *Nature*, 2010, **466**, 470–473.
333 Y. P. Chen, Y. E. Xie and X. H. Yan, *J. Appl. Phys.*, 2008, **103**, 063711.
334 L. Zhu, J. Wang, T. Zhang, L. Ma, C. W. Lim, F. Ding and X. C. Zeng, *Nano Lett.*, 2010, **10**, 494–498.
335 Z. F. Wang, Q. Li, Q. W. Shi, X. Wang, J. G. Hou, H. Zheng and J. Chen, *Appl. Phys. Lett.*, 2008, **92**, 133119.
336 X. Wu and X. C. Zeng, *Nano Res.*, 2008, **1**, 40–45.
337 T. Jayasekera and J. W. Mintmire, *Nanotechnology*, 2007, **18**, 424033.
338 Y. F. Li, Z. Zhou, P. W. Shen and Z. F. Chen, *J. Phys. Chem. C*, 2012, **116**, 208–213.
339 D. Wang, Z. Zhang, Z. Zhu and B. Liang, *Sci. Rep.*, 2014, **4**, 7587.
340 Z. F. Wang, S. Jin and F. Liu, *Phys. Rev. Lett.*, 2013, **111**, 096803.
341 Y. Ding and Y. L. Wang, *Phys. Chem. Chem. Phys.*, 2012, **14**, 2040–2049.
342 L. A. Ma, H. Hu, L. Y. Zhu and J. L. Wang, *J. Phys. Chem. C*, 2011, **115**, 6195–6199.
343 W. L. Wang, S. Meng and E. Kaxiras, *Nano Lett.*, 2008, **8**, 241–245.
344 M. Ezawa, *Phys. Rev. B: Condens. Matter Mater. Phys.*, 2007, **76**, 245115.
345 O. V. Yazyev, W. L. Wang, S. Meng and E. Kaxiras, *Nano Lett.*, 2008, **8**, 766.
346 W. L. Wang, O. V. Yazyev, S. Meng and E. Kaxiras, *Phys. Rev. Lett.*, 2009, **102**, 157201.
347 A. M. Silva, M. S. Pires and V. N. Freire, *J. Phys. Chem. C*, 2010, **114**, 17472–17485.
348 S. Ganguly, M. Kabir and T. Saha-Dasgupta, *Phys. Rev. B: Condens. Matter Mater. Phys.*, 2017, **95**, 174419.
349 H. Sahin and R. T. Senger, *Phys. Rev. B: Condens. Matter Mater. Phys.*, 2008, **78**, 205423.
350 W. Sheng, Z. Y. Ning, Z. Q. Yang and H. Guo, *Nanotechnology*, 2010, **21**, 385201.
351 M. Kabir and T. Saha-Dasgupta, *Phys. Rev. B: Condens. Matter Mater. Phys.*, 2014, **90**, 035403.
352 A. Valli, A. Amaricci, A. Toschi, T. Saha-Dasgupta, K. Held and M. Capone, *Phys. Rev. B: Condens. Matter Mater. Phys.*, 2016, **94**, 245146.
353 K. Szałowski, *Phys. Rev. B: Condens. Matter Mater. Phys.*, 2011, **84**, 205409.
354 S. K. Saha, M. Baskey and D. Majumdar, *Adv. Mater.*, 2010, **22**, 5531–5536.
355 X. Guo, C. D. Wang and Y. G. Zhou, *Phys. Lett. A*, 2013, **377**, 993–996.
356 Y. G. Zhou, Z. G. Wang, P. Yang, X. Sun, X. T. Zu and F. Gao, *J. Phys. Chem. C*, 2012, **116**, 5531–5537.
357 J. Kang, F. M. Wu and J. B. Li, *J. Appl. Phys.*, 2012, **112**, 104328.
358 K. Szałowski, *J. Appl. Phys.*, 2013, **114**, 243908.
359 A. P. Zhou, W. D. Sheng and S. J. Xu, *Appl. Phys. Lett.*, 2013, **103**, 133103.
360 Y. Ge, J. L. Ji, Z. Z. Shen, Q. Zhang, A. Q. Jian, Q. Q. Duan, C. Wang, J. Jiang, W. D. Zhang and S. B. Sang, *Carbon*, 2018, **127**, 432–436.
361 J. Zhou, Q. Wang, Q. Sun and P. Jena, *Phys. Rev. B: Condens. Matter Mater. Phys.*, 2011, **84**, 081402.
362 X. W. Li and Q. Wang, *Phys. Chem. Chem. Phys.*, 2012, **14**, 2065–2069.
363 X. W. Li, Q. Wang, X. S. Chen, Y. Kawazoe and P. Jena, *New J. Phys.*, 2012, **14**, 033043.
364 K. Gopinadhan, Y. J. Shin, I. Yudhistira, J. Niu and H. Yang, *Phys. Rev. B: Condens. Matter Mater. Phys.*, 2013, **88**, 195429.
365 P. Lu, Z. H. Zhang, C. H. Woo and W. L. Guo, *J. Phys. Chem. C*, 2012, **116**, 626–631.
366 J. Shen, Y. Zhu, X. Yang and C. Li, *Chem. Commun.*, 2012, **48**, 3686–3699.
367 J. Viana-Gomes, V. M. Pereira and N. M. R. Peres, *Phys. Rev. B: Condens. Matter Mater. Phys.*, 2009, **80**, 245436.
368 T. Espinosa-Ortega, I. A. Lukyanchuk and Y. G. Rubo, *Phys. Rev. B: Condens. Matter Mater. Phys.*, 2013, **87**, 205434.
369 M. Koshino and T. Ando, *Phys. Rev. B: Condens. Matter Mater. Phys.*, 2010, **81**, 195431.
370 B. Jaworowski, P. Potasz and A. Wójs, *Superlattices Microstruct.*, 2013, **64**, 44–51.
371 O. Voznyy, A. D. Guclu, P. Potasz and P. Hawrylak, *Phys. Rev. B: Condens. Matter Mater. Phys.*, 2011, **83**, 165417.

 This journal is © The Royal Society of Chemistry 2018

Published on 26 March 2018. Downloaded by Univerzita Palackého v Olomouci on 2/28/2019 2:05:03 PM.

372 S. Bhowmick and V. B. Shenoy, *J. Chem. Phys.*, 2008, **128**, 244717.
373 S. Cheng, J. M. Yu, T. X. Ma and N. M. R. Peres, *Phys. Rev. B: Condens. Matter Mater. Phys.*, 2015, **91**, 075410.
374 J. L. Lado and J. Fernández-Rossier, *Phys. Rev. Lett.*, 2014, **113**, 027203.
375 I. Weymann, J. Barnas and S. Krompiewski, *Phys. Rev. B: Condens. Matter Mater. Phys.*, 2015, **92**, 045427.
376 A. D. Guclu, P. Potasz and P. Hawrylak, *Phys. Rev. B: Condens. Matter Mater. Phys.*, 2011, **84**, 035425.
377 A. K. Swain, D. Li and D. Bahadur, *Carbon*, 2013, **57**, 346–356.
378 H. S. S. R. Matte, K. S. Subrahmanyam and C. N. R. Rao, *J. Phys. Chem. C*, 2009, **113**, 9982–9985.
379 R. McIntosh, M. A. Mamo, B. Jamieson, S. Roy and S. Bhattacharyya, *Europhys. Lett.*, 2012, **97**, 38001.
380 O. E. Andersson, B. L. V. Prasad, H. Sato, T. Enoki, Y. Hishiyama, Y. Kaburagi, M. Yoshikawa and S. Bandow, *Phys. Rev. B: Condens. Matter Mater. Phys.*, 1998, **58**, 16387–16395.
381 R. Hohne and P. Esquinazi, *Adv. Mater.*, 2003, **14**, 753–756.
382 Y. Y. Sun, Y. P. Zheng, J. Chen, W. L. Zhang, N. J. Tang and Y. W. Du, *Appl. Phys. Lett.*, 2016, **108**, 033105.
383 J. Liu, H. Bi, P. C. Morais, X. Zhang, F. P. Zhang and L. Hu, *Sci. Rep.*, 2017, **7**, 2165.
384 A. S. Arico, P. Bruce, B. Scrosati, J. M. Tarascon and W. van Schalkwijk, *Nat. Mater.*, 2005, **4**, 366–377.
385 X. Wang, X. Li, L. Zhang, Y. Yoon, P. K. Weber, H. Wang, J. Guo and H. Dai, *Science*, 2009, **324**, 768–771.
386 H. Pinto, R. Jones, J. P. Goss and P. R. Briddon, *Phys. Status Solidi A*, 2010, **207**, 2131–2136.
387 S. Y. Zhou, D. A. Siegel, A. V. Fedorov and A. Lanzara, *Phys. Rev. Lett.*, 2008, **101**, 086402.
388 K. S. Mali, J. Greenwood, J. Adisoejoso, R. Phillipson and S. De Feyter, *Nanoscale*, 2015, **7**, 1566–1585.
389 J. Jin, X. Fu, Q. Liu, Y. Liu, Z. Wei, K. Niu and J. Zhang, *ACS Nano*, 2013, **7**, 4764–4773.
390 P. Lazar, R. Zboril, M. Pumera and M. Otyepka, *Phys. Chem. Chem. Phys.*, 2014, **16**, 14231–14235.
391 D. M. Edwards and M. I. Katsnelson, *J. Phys.: Condens. Matter*, 2006, **18**, 7209–7225.
392 Y. Ito, C. Christodoulou, M. V. Nardi, N. Koch, M. Klaui, H. Sachdev and K. Mullen, *J. Am. Chem. Soc.*, 2015, **137**, 7678–7685.
393 Q. H. Miao, L. D. Wang, Z. Y. Liu, B. Wei, F. B. Xu and W. D. Fei, *Sci. Rep.*, 2016, **6**, 21832.
394 J. Y. Li, X. H. Li, P. H. Zhao, D. Y. Lei, W. L. Li, J. T. Bai, Z. Y. Ren and X. L. Xu, *Carbon*, 2015, **84**, 460–468.
395 J. Zhu, H. Park, R. Podila, A. Wadehra, P. Ayala, L. Oliveira, J. He, A. A. Zakhidov, A. Howard, J. Wilkins and A. M. Rao, *J. Magn. Magn. Mater.*, 2016, **401**, 70–76.
396 P. Willke, J. A. Amani, A. Sinterhauf, S. Thakur, T. Kotzott, T. Druga, S. Weikert, K. Maiti, H. Hofsass and M. Wenderoth, *Nano Lett.*, 2015, **15**, 5110–5115.
397 F. Cervantes-Sodi, G. Csanyi, S. Piscanec and A. C. Ferrari, *Phys. Rev. B: Condens. Matter Mater. Phys.*, 2008, **77**, 165427.
398 E. J. G. Santos, D. Sanchez-Portal and A. Ayuela, *Phys. Rev. B: Condens. Matter Mater. Phys.*, 2010, **81**, 125433.
399 E. J. G. Santos, A. Ayuela, S. B. Fagan, J. Mendes Filho, D. L. Azevedo, A. G. Souza Filho and D. Sanchez-Portal, *Phys. Rev. B: Condens. Matter Mater. Phys.*, 2008, **78**, 195420.
400 E. J. G. Santos, A. Ayuela and D. Sanchez-Portal, *J. Phys. Chem. C*, 2012, **116**, 1174–1178.
401 J. Tucek, K. C. Kemp, K. S. Kim and R. Zboril, *ACS Nano*, 2014, **8**, 7571–7612.
402 W. Zhang, W. C. Lu, H. X. Zhang, K. M. Ho and C. Z. Wang, *J. Phys.: Condens. Matter*, 2016, **28**, 115001.
403 R. R. Nair, I. L. Tsai, M. Sepioni, O. Lehtinen, J. Keinonen, A. V. Krasheninnikov, A. H. C. Neto, M. I. Katsnelson, A. K. Geim and I. V. Grigorieva, *Nat. Commun.*, 2013, **4**, 2010.
404 E. J. G. Santos, A. Ayuela and D. Sánchez-Portal, *New J. Phys.*, 2012, **14**, 043022.
405 D. W. Boukhvalov and M. I. Katsnelson, *Nano Lett.*, 2008, **8**, 4373–4379.
406 D. W. Boukhvalov and M. I. Katsnelson, *Phys. Rev. B: Condens. Matter Mater. Phys.*, 2008, **78**, 085413.
407 F. P. OuYang, B. Huang, Z. Y. Li, J. Xiao, H. Y. Wang and H. Xu, *J. Phys. Chem. C*, 2008, **112**, 12003–12007.
408 D. C. Elias, R. R. Nair, T. M. Mohiuddin, S. V. Morozov, P. Blake, M. P. Halsall, A. C. Ferrari, D. W. Boukhvalov, M. I. Katsnelson, A. K. Geim and K. S. Novoselov, *Science*, 2009, **323**, 610–613.
409 P. Laaksonen, M. Kainlauri, T. Laaksonen, A. Shchepetov, H. Jiang, J. Ahopelto and M. B. Linder, *Angew. Chem., Int. Ed.*, 2010, **49**, 4946–4949.
410 V. E. Antonov, I. O. Bashkin, A. V. Bazhenov, B. M. Bulychev, V. K. Fedotov, T. N. Fursova, A. I. Kolesnikov, V. I. Kulakov, R. V. Lukashev, D. V. Matveev, M. K. Sakharov and Y. M. Shulga, *Carbon*, 2016, **100**, 465–473.
411 A. Y. S. Eng, H. L. Poh, F. Sanek, M. Marysko, S. Matejkova, Z. Sofer and M. Pumera, *ACS Nano*, 2013, **7**, 5930–5939.
412 J. Berashevich and T. Chakraborty, *Nanotechnology*, 2010, **21**, 355201.
413 H. Sahin, C. Ataca and S. Ciraci, *Appl. Phys. Lett.*, 2009, **95**, 222510.
414 H. Sahin, C. Ataca and S. Ciraci, *Phys. Rev. B: Condens. Matter Mater. Phys.*, 2010, **81**, 205417.
415 Y. Li, Z. Zhou, P. Shen and Z. Chen, *J. Phys. Chem. C*, 2009, **113**, 15043–15045.
416 C.-K. Yang, *Carbon*, 2010, **48**, 3901–3905.
417 H. Da, Y. P. Feng and G. Liang, *J. Phys. Chem. C*, 2011, **115**, 22701–22706.
418 N. Kharche and S. K. Nayak, *Nano Lett.*, 2011, **11**, 5274–5278.
419 L. Feng and W. X. Zhang, *AIP Adv.*, 2012, **2**, 042138.
420 D. W. Boukhvalov, *Physica E*, 2010, **43**, 199–201.
421 F. Buonocore, A. M. Conte and N. Lisi, *Physica E*, 2016, **78**, 65–72.
422 L. X. Liu, S. D. Liu, Z. Y. Zhang and W. G. Zhu, *J. Phys. Chem. C*, 2017, **121**, 24824–24830.
423 M. Wang and C. M. Li, *Phys. Chem. Chem. Phys.*, 2013, **15**, 3786–3792.

Published on 26 March 2018. Downloaded by Univerzita Palackého v Olomouci on 2/28/2019 2:05:03 PM.

424 A. M. Panich, A. I. Shames and T. Nakajima, *J. Phys. Chem. Solids*, 2001, **62**, 959–964.
425 R. Zboril, F. Karlicky, A. B. Bourlinos, T. A. Steriotis, A. K. Stubos, V. Georgakilas, K. Safarova, D. Jancik, C. Trapalis and M. Otyepka, *Small*, 2010, **6**, 2885–2891.
426 R. R. Nair, W. C. Ren, R. Jalil, I. Riaz, V. G. Kravets, L. Britnell, P. Blake, F. Schedin, A. S. Mayorov, S. J. Yuan, M. I. Katsnelson, H. M. Cheng, W. Strupinski, L. G. Bulusheva, A. V. Okotrub, I. V. Grigorieva, A. N. Grigorenko, K. S. Novoselov and A. K. Geim, *Small*, 2010, **6**, 2877–2884.
427 D. D. Chronopoulos, A. Bakandritsos, M. Pykal, R. Zboril and M. Otyepka, *Appl. Mater. Today*, 2017, **9**, 60–70.
428 H. Y. Liu, Z. F. Hou, C. H. Hu, Y. Yang and Z. Z. Zhu, *J. Phys. Chem. C*, 2012, **116**, 18193–18201.
429 T. L. Makarova, A. L. Shelankov, A. A. Zyrianova, A. I. Veinger, T. V. Tisnek, E. Lahderanta, A. I. Shames, A. V. Okotrub, L. G. Bulusheva, G. N. Chekhova, D. V. Pinakov, I. P. Asanov and Z. Sljivancanin, *Sci. Rep.*, 2015, **5**, 13382.
430 R. J. Kashtiban, M. A. Dyson, R. R. Nair, R. Zan, S. L. Wong, Q. Ramasse, A. K. Geim, U. Bangert and J. Sloan, *Nat. Commun.*, 2014, **5**, 4902.
431 V. V. Mazurenko, A. N. Rudenko, S. A. Nikolaev, D. S. Medvedeva, A. I. Lichtenstein and M. I. Katsnelson, *Phys. Rev. B: Condens. Matter Mater. Phys.*, 2016, **94**, 214411.
432 T. L. Makarova, A. L. Shelankov, A. I. Shames, A. A. Zyrianova, A. A. Komlev, G. N. Chekhova, D. V. Pinakov, L. G. Bulusheva, A. V. Okotrub and E. Lahderanta, *Sci. Rep.*, 2017, **7**, 16544.
433 W. F. Li, M. W. Zhao, Y. Y. Xia, R. Q. Zhang and Y. G. Mu, *J. Mater. Chem.*, 2009, **19**, 9274–9282.
434 H. Lin, G. Fratesi and G. P. Brivio, *Phys. Chem. Chem. Phys.*, 2015, **17**, 2210–2215.
435 A. Ravikumar, A. Baby, H. Lin, G. P. Brivio and G. Fratesi, *Sci. Rep.*, 2016, **6**, 24603.
436 A. J. M. Giesbers, K. Uhlirova, M. Konecny, E. C. Peters, M. Burghard, J. Aarts and C. F. Flipse, *Phys. Rev. Lett.*, 2013, **111**, 166101.
437 T. Tang, N. J. Tang, Y. P. Zheng, X. G. Wan, Y. Liu, F. C. Liu, Q. H. Xu and Y. W. Du, *Sci. Rep.*, 2015, **5**, 8448.
438 X. Huang, X. Y. Qi, F. Boey and H. Zhang, *Chem. Soc. Rev.*, 2012, **41**, 666–686.
439 J. Chen, W. L. Zhang, Y. Y. Sun, Y. P. Zheng, N. J. Tang and Y. W. Du, *Sci. Rep.*, 2016, **6**, 26862.
440 K. Bagani, M. K. Ray, B. Satpati, N. R. Ray, M. Sardar and S. Banerjee, *J. Phys. Chem. C*, 2014, **118**, 13254–13259.
441 D. W. Boukhvalov, *Phys. Chem. Chem. Phys.*, 2010, **12**, 15367–15371.
442 D. Lee, J. Seo, X. Zhu, J. M. Cole and H. B. Su, *Appl. Phys. Lett.*, 2015, **106**, 172402.
443 M. Wang and C. M. Li, *New J. Phys.*, 2010, **12**, 129801.
444 T. Tang, F. Liu, Y. Liu, X. Li, Q. H. Xu, Q. Feng and N. J. Tang, *Appl. Phys. Lett.*, 2014, **104**, 123104.
445 M. Wang, W. Huang, M. B. Chan-Park and C. M. Li, *Nanotechnology*, 2011, **22**, 105702.
446 N. Liaros, J. Tucek, K. Dimos, A. Bakandritsos, K. S. Andrikopoulos, D. Gournis, R. Zboril and S. Couris, *Nanoscale*, 2016, **8**, 2908–2917.
447 Y. Liu, N. J. Tang, X. G. Wan, Q. Feng, M. Li, Q. H. Xu, F. Liu and Y. W. Du, *Sci. Rep.*, 2013, **3**, 2566.
448 S. K. Sarkar, K. K. Raul, S. S. Pradhan, S. Basu and A. Nayak, *Physica E*, 2014, **64**, 78–82.
449 P. Z. Sun, K. L. Wang, J. Q. Wei, M. L. Zhong, D. H. Wu and H. W. Zhu, *Nano Res.*, 2014, **7**, 1507–1518.
450 G. Khurana, N. Kumar, R. K. Kotnala, T. Nautiyal and R. S. Katiyar, *Nanoscale*, 2013, **5**, 3346–3351.
451 L. Majchrzycki, M. A. Augustyniak-Jablokow, R. Strzelczyk and M. Mackowiak, *Acta Phys. Pol., A*, 2015, **127**, 540–542.
452 S. Qin, X. T. Guo, Y. Q. Cao, Z. H. Ni and Q. Y. Xu, *Carbon*, 2014, **78**, 559–565.
453 S. B. Kumar and J. Guo, *Nanoscale*, 2012, **4**, 982–985.
454 J. Bai, R. Cheng, F. Xiu, L. Liao, M. Wang, A. Shailos, K. L. Wang, Y. Huang and X. Duan, *Nat. Nanotechnol.*, 2010, **5**, 655–659.
455 W. Shu-Wei, H. E. Lin, L. Huang-De, K. Y. Chen, T. Kun-Hua, C. W. Chen, C. Ju-Ying, L. Cheng-Hua, C. T. Liang and Y. F. Chen, *Nanotechnology*, 2011, **22**, 335701.
456 E. McCann, K. Kechedzhi, V. I. Fal'ko, H. Suzuura, T. Ando and B. L. Altshuler, *Phys. Rev. Lett.*, 2006, **97**, 146805.
457 N. M. R. Peres, A. H. Castro Neto and F. Guinea, *Phys. Rev. B: Condens. Matter Mater. Phys.*, 2006, **73**, 195411.
458 N. M. R. Peres, A. H. Castro Neto and F. Guinea, *Phys. Rev. B: Condens. Matter Mater. Phys.*, 2006, **73**, 241403.
459 Y. C. Huang, C. P. Chang and M. F. Lin, *Nanotechnology*, 2007, **18**, 495401.
460 J. Liu, A. R. Wright, C. Zhang and Z. Ma, *Appl. Phys. Lett.*, 2008, **93**, 041106.
461 C. Ritter, S. S. Makler and A. Latgé, *Phys. Rev. B: Condens. Matter Mater. Phys.*, 2008, **77**, 195443.
462 T. S. Li, Y. C. Huang, S. C. Chang, C. P. Chang and M. F. Lin, *Philos. Mag.*, 2009, **89**, 697–709.
463 A. Diamantopoulou, S. Glenis, G. Zolnierkiwicz, N. Guskos and V. Likodimos, *J. Appl. Phys.*, 2017, **121**, 043906.
464 S. Qin and Q. G. Xu, *J. Alloys Compd.*, 2017, **692**, 332–338.
465 Y. Liu, Q. Feng, N. J. Tang, X. G. Wan, F. C. Liu, L. Y. Lv and Y. W. Du, *Carbon*, 2013, **60**, 549–551.
466 A. Bakandritsos, M. Pykal, P. Blonski, P. Jakubec, D. D. Chronopoulos, K. Polakova, V. Georgakilas, K. Cepe, O. Tomanec, V. Ranc, A. B. Bourlinos, R. Zboril and M. Otyepka, *ACS Nano*, 2017, **11**, 2982–2991.
467 A. Y. S. Eng, Z. Sofer, D. Sedmidubský and M. Pumera, *ACS Nano*, 2017, **11**, 1789–1797.
468 C. Schafhaeutl, *J. Prakt. Chem.*, 1840, **21**, 129–157.
469 M. S. Dresselhaus and G. Dresselhaus, *Adv. Phys.*, 1981, **30**, 139–326.
470 M. S. Dresselhaus, *Phys. Scr.*, 2012, **T146**, 014002.
471 N. Kim, K. S. Kim, N. Jung, L. Brus and P. Kim, *Nano Lett.*, 2011, **11**, 860–865.
472 I. Khrapach, F. Withers, T. H. Bointon, D. K. Polyushkin, W. L. Barnes, S. Russo and M. F. Craciun, *Adv. Mater.*, 2012, **24**, 2844–2849.
473 Y. Lia and Q. Yue, *Physica B*, 2013, **425**, 72–77.

 This journal is © The Royal Society of Chemistry 2018

Published on 26 March 2018. Downloaded by Univerzita Palackého v Olomouci on 2/28/2019 2:05:03 PM.

474 T. H. Bointon, I. Khrapach, R. Yakimova, A. V. Shytov, M. F. Craciun and S. Russo, *Nano Lett.*, 2014, **14**, 1751–1755.
475 S. Ichinokura, K. Sugawara, A. Takayama, T. Takahashi and S. Hasegawa, *ACS Nano*, 2016, **10**, 2761–2765.
476 J. Kim, P. Lee, M. Ryu, H. Park and J. Chung, *RSC Adv.*, 2016, **6**, 114219–114223.
477 N. A. Kaskhedikar and J. Maier, *Adv. Mater.*, 2009, **21**, 2664–2680.
478 J. Wan, S. D. Lacey, J. Dai, W. Bao, M. S. Fuhrer and L. Hu, *Chem. Soc. Rev.*, 2016, **45**, 6742–6765.
479 M. Suzuki and I. S. Suzuki, *Phys. Rev. B: Condens. Matter Mater. Phys.*, 1998, **58**, 371–384.
480 Y. Li and Q. Yue, *Physica B*, 2013, **425**, 72–77.
481 T. H. Bointon, I. Khrapach, R. Yakimova, A. V. Shytov, M. F. Craciun and S. Russo, *Nano Lett.*, 2014, **14**, 1751–1755.
482 R. Decker, J. Brede, N. Atodiresei, V. Caciuc, S. Blügel and R. Wiesendanger, *Phys. Rev. B: Condens. Matter Mater. Phys.*, 2013, **87**, 041403(R).
483 A. D. Vu, J. Coraux, G. Chen, A. T. N'Diaye, A. K. Schmid and N. Rougemaille, *Sci. Rep.*, 2016, **6**, 24783.
484 S. Manzeli, D. Ovchinnikov, D. Pasquier, O. V. Yazyev and A. Kis, *Nat. Rev. Mater.*, 2017, **2**, 17033.
485 B. Schonfeld, J. J. Huang and S. C. Moss, *Acta Crystallogr., Sect. B: Struct. Sci.*, 1983, **39**, 404–407.
486 F. Wypych and R. Schollhorn, *J. Chem. Soc., Chem. Commun.*, 1992, 1386–1388.
487 M. K. Jana and C. N. R. Rao, *Philos. Trans. R. Soc., A*, 2016, **374**, 20150318.
488 H. Pan and Y.-W. Zhang, *J. Phys. Chem. C*, 2012, **116**, 11752–11757.
489 C. N. Rao, H. S. Matte and U. Maitra, *Angew. Chem., Int. Ed.*, 2013, **52**, 13162–13185.
490 Y. Zhou, Q. Su, Z. Wang, H. Deng and X. Zu, *Phys. Chem. Chem. Phys.*, 2013, **15**, 18464–18470.
491 M. Sagynbaeva, P. Panigrahi, L. Yunguo, M. Ramzan and R. Ahuja, *Nanotechnology*, 2014, **25**, 165703.
492 Z. Yang, D. Gao, J. Zhang, Q. Xu, S. Shi, K. Tao and D. Xue, *Nanoscale*, 2015, **7**, 650–658.
493 Z. H. Zhang, X. F. Liu, J. Yu, Y. Hang, Y. Li, Y. F. Guo, Y. Xu, X. Sun, J. X. Zhou and W. L. Guo, *WIREs Comput. Mol. Sci.*, 2016, **6**, 324–350.
494 A. M. Panich, A. I. Shames, R. Rosentsveig and R. Tenne, *J. Phys.: Condens. Matter*, 2009, **21**, 395301.
495 S. Mathew, K. Gopinadhan, T. K. Chan, X. J. Yu, D. Zhan, L. Cao, A. Rusydi, M. B. H. Breese, S. Dhar, Z. X. Shen, T. Venkatesan and J. T. L. Thong, *Appl. Phys. Lett.*, 2012, **101**, 102103.
496 M. Pizzochero and O. V. Yazyev, *Phys. Rev. B: Condens. Matter Mater. Phys.*, 2017, **96**, 245402.
497 J. Zhang, J. M. Soon, K. P. Loh, J. H. Yin, J. Ding, M. B. Sullivian and P. Wu, *Nano Lett.*, 2007, **7**, 2370–2376.
498 D. Q. Gao, M. S. Si, J. Y. Li, J. Zhang, Z. P. Zhang, Z. L. Yang and D. S. Xue, *Nanoscale Res. Lett.*, 2013, **8**, 129.
499 H. Li, X. Y. Qi, J. Wu, Z. Y. Zeng, J. Wei and H. Zhang, *ACS Nano*, 2013, **7**, 2842–2849.
500 P. Murugan, V. Kumar, Y. Kawazoe and N. Ota, *Phys. Rev. A: At., Mol., Opt. Phys.*, 2005, **71**, 063203.
501 S. Tongay, S. S. Varnoosfaderani, B. R. Appleton, J. Wu and A. F. Hebard, *Appl. Phys. Lett.*, 2012, **101**, 123105.
502 A. Vojvodic, B. Hinnemann and J. K. Nørskov, *Phys. Rev. B: Condens. Matter Mater. Phys.*, 2009, **80**, 125416.
503 Y. Li, Z. Zhou, S. Zhang and Z. Chen, *J. Am. Chem. Soc.*, 2008, **130**, 16739–16744.
504 A. U. Rahman, G. Rahman and V. M. Garcia-Suarez, *J. Magn. Magn. Mater.*, 2017, **443**, 343–351.
505 J. Luxa, O. Jankovsky, D. Sedmidubsky, R. Medlin, M. Marysko, M. Pumera and Z. Sofer, *Nanoscale*, 2016, **8**, 1960–1967.
506 X. Mao, Y. Xu, Q. Xue, W. Wang and D. Gao, *Nanoscale Res. Lett.*, 2013, **8**, 430.
507 H. P. Li, S. Liu, S. L. Huang, D. Q. Yin, C. S. Li and Z. C. Wang, *Ceram. Int.*, 2016, **42**, 2364–2369.
508 Y. Q. Guo, H. T. Deng, X. Sun, X. L. Li, J. Y. Zhao, J. C. Wu, W. S. Chu, S. J. Zhang, H. B. Pan, X. S. Zheng, X. J. Wu, C. Q. Jin, C. Z. Wu and Y. Xie, *Adv. Mater.*, 2017, **29**, 1700715.
509 R. Rahman, K. Davey and S. Z. Qiao, *Adv. Funct. Mater.*, 2017, **27**, 1606129.
510 G. C. Loh and R. Pandey, *Phys. Chem. Chem. Phys.*, 2015, **17**, 18843–18853.
511 S. X. Yang, C. Wang, H. Sahin, H. Chen, Y. Li, S. S. Li, A. Suslu, F. M. Peeters, Q. Liu, J. B. Li and S. Tongay, *Nano Lett.*, 2015, **15**, 1660–1666.
512 X. O. Zhang and Q. F. Li, *J. Appl. Phys.*, 2015, **118**, 064306.
513 L. Tao, F. C. Meng, S. D. Zhao, Y. L. Song, J. X. Yu, X. J. Wang, Z. G. Liu, Y. Wang, B. S. Li, Y. Wang and Y. Sui, *Nanoscale*, 2017, **9**, 4898–4906.
514 X. Zhao, X. N. Zhang, T. X. Wang, S. Y. Wei and L. Yang, *RSC Adv.*, 2017, **7**, 26673–26679.
515 V. Kochat, A. Apte, J. A. Hachtel, H. Kumazoe, A. Krishnamoorthy, S. Susarla, J. C. Idrobo, F. Shimojo, P. Vashishta, R. Kalia, A. Nakano, C. S. Tiwary and P. M. Ajayan, *Adv. Mater.*, 2017, **29**, 1703754.
516 M. Meng, C. G. Shi, T. Li, S. E. Shi, T. H. Li and L. Z. Liu, *Appl. Surf. Sci.*, 2017, **425**, 696–701.
517 L. Li, O. Leenaerts, X. Kong, X. Chen, M. W. Zhao and F. M. Peeters, *Nano Res.*, 2017, **10**, 2168–2180.
518 L. Zhou, L. Kou, Y. Sun, C. Felser, F. M. Hu, G. C. Shan, S. C. Smith, B. H. Yan and T. Frauenheim, *Nano Lett.*, 2015, **15**, 7867–7872.
519 E. Torun, H. Sahin, C. Bacaksiz, R. T. Senger and F. M. Peeters, *Phys. Rev. B: Condens. Matter Mater. Phys.*, 2015, **92**, 104407.
520 B. Huang, G. Clark, E. Navarro-Moratalla, D. R. Klein, R. Cheng, K. L. Seyler, D. Zhong, E. Schmidgall, M. A. McGuire, W. Yao, D. Xiao, P. Jarillo-Herrero and X. D. Xu, *Nature*, 2017, **546**, 270–273.
521 V. V. Kulish and W. Huang, *J. Phys. Chem. C*, 2017, **5**, 8734–8741.
522 M. Ashton, D. Gluhovic, S. B. Sinnott, J. Guo, D. A. Stewart and R. G. Hennig, *Nano Lett.*, 2017, **17**, 5251–5257.
523 F. Wu, C. X. Huang, H. P. Wu, C. Lee, K. M. Deng, E. J. Kan and P. Jena, *Nano Lett.*, 2015, **15**, 8277–8281.

Published on 26 March 2018. Downloaded by Univerzita Palackého v Olomouci on 2/28/2019 2:05:03 PM.

524 J. Y. Liu, Z. F. Liu, T. L. Song and X. Cui, *J. Phys. Chem. C*, 2017, **5**, 727–732.
525 Y. J. Sun, Z. W. Zhuo, X. J. Wu and J. L. Yang, *Nano Lett.*, 2017, **17**, 2771–2777.
526 X. D. Zhang, J. J. Zhang, J. Y. Zhao, B. C. Pan, M. G. Kong, J. Chen and Y. Xie, *J. Am. Chem. Soc.*, 2012, **134**, 11908–11911.
527 A. J. Du, S. Sanvito and S. C. Smith, *Phys. Rev. Lett.*, 2012, **108**, 197207.
528 E. J. Kan, W. Hu, C. Y. Xiao, R. F. Lu, K. M. Deng, J. L. Yang and H. B. Su, *J. Am. Chem. Soc.*, 2012, **134**, 5718–5721.
529 M. Khazaei, M. Arai, T. Sasaki, C. Y. Chung, N. S. Venkataramanan, M. Estili, Y. Sakka and Y. Kawazoe, *Adv. Funct. Mater.*, 2013, **23**, 2185–2192.
530 C. Si, J. Zhou and Z. Sun, *ACS Appl. Mater. Interfaces*, 2015, **7**, 17510–17515.
531 G. Y. Gao, G. Q. Ding, J. Li, K. L. Yao, M. H. Wu and M. C. Qian, *Nanoscale*, 2017, **8**, 8986–8994.
532 H. Kumar, N. C. Frey, L. Dong, B. Anasori, Y. Gogotsi and V. B. Shenoy, *ACS Nano*, 2017, **11**, 7648–7655.
533 L. Dong, H. Kumar, B. Anasori, Y. Gogotsi and V. B. Shenoy, *J. Phys. Chem. Lett.*, 2017, **8**, 422–428.
534 B. Sachs, T. O. Wehling, M. I. Katsnelson and A. I. Lichtenstein, *Phys. Rev. B: Condens. Matter Mater. Phys.*, 2011, **84**, 195414.
535 L. Ci, L. Song, C. H. Jin, D. Jariwala, D. X. Wu, Y. J. Li, A. Srivastava, Z. F. Wang, K. Storr, L. Balicas, F. Liu and P. M. Ajayan, *Nat. Mater.*, 2010, **9**, 430–435.
536 K. Watanabe, T. Taniguchi and H. Kanda, *Nat. Mater.*, 2004, **3**, 404–409.
537 M. S. Si and D. S. Xue, *Phys. Rev. B: Condens. Matter Mater. Phys.*, 2007, **75**, 193409.
538 R.-F. Liu and C. Cheng, *Phys. Rev. B: Condens. Matter Mater. Phys.*, 2007, **76**, 014405.
539 P. Dev, Y. Xue and P. Zhang, *Phys. Rev. Lett.*, 2008, **100**, 117204.
540 M. N. Huda and L. Kleinman, *Phys. Rev. B: Condens. Matter Mater. Phys.*, 2006, **74**, 075418.
541 N. Joshi and P. Ghosh, *Phys. Rev. B: Condens. Matter Mater. Phys.*, 2013, **87**, 235440.
542 V. Barone and J. E. Peralta, *Nano Lett.*, 2008, **8**, 2210–2214.
543 M. S. Si, D. Q. Gao, D. Z. Yang, Y. Peng, Z. Y. S. Zhang, D. S. Xue, Y. S. Liu, X. H. Deng and G. P. Zhang, *J. Chem. Phys.*, 2014, **140**, 204701.
544 S. K. Gupta, H. Y. He, I. Lukacevic and R. Pandey, *Phys. Chem. Chem. Phys.*, 2017, **19**, 30370–30380.
545 E. Machado-Charry, P. Boulanger, L. Genovese, N. Mousseau and P. Pochet, *Appl. Phys. Lett.*, 2012, **101**, 132405.
546 J. Zhou, Q. Wang, Q. Sun and P. Jena, *Phys. Rev. B: Condens. Matter Mater. Phys.*, 2010, **81**, 085442.
547 F. Li, Z. G. Zhu, X. D. Yao, G. Q. Lu, M. W. Zhao, Y. Y. Xia and Y. Chen, *Appl. Phys. Lett.*, 2008, **92**, 102515.
548 E. J. Kan, H. J. Xiang, F. Wu, C. Tian, C. Lee, J. L. Yang and M. H. Whangbo, *Appl. Phys. Lett.*, 2010, **97**, 122503.
549 M. Du, X. L. Li, A. Z. Wang, Y. Z. Wu, X. P. Hao and M. W. Zhao, *Angew. Chem., Int. Ed.*, 2014, **53**, 3645–3649.
550 J. J. He, P. B. Lyu, L. Z. Sun, A. M. Garcia and P. Nachtigall, *J. Mater. Chem. C*, 2016, **4**, 6500.
551 J. He, P. Lyu and P. Nachtigall, *J. Mater. Chem. C*, 2016, **4**, 11143–11149.
552 J. J. He, X. Li, P. B. Lyu and P. Nachtigall, *Nanoscale*, 2017, **9**, 2246–2252.
553 A. K. Swain and D. Bahadur, *RSC Adv.*, 2013, **3**, 19243–19246.
554 Y. W. Ma, Y. H. Lu, J. B. Yi, Y. P. Feng, T. S. Herng, X. Liu, D. Q. Gao, D. S. Xue, J. M. Xue, J. Y. Ouyang and J. Ding, *Nat. Commun.*, 2012, **3**, 727.
555 T. Scheike, W. Bohlmann, P. Esquinazi, J. Barzola-Quiquia, A. Ballestar and A. Setzer, *Adv. Mater.*, 2012, **24**, 5826–5831.
556 A. K. Swain and D. Bahadur, *Appl. Phys. Lett.*, 2014, **104**, 242413.
557 L. Chen, L. Guo, Z. Li, H. Zhang, J. Lin, J. Huang, S. Jin and X. Chen, *Sci. Rep.*, 2013, **3**, 2599.

 This journal is © The Royal Society of Chemistry 2018